NASA TECHNICAL TRANSLATION

NASA TT F-601

NASA TT F-601

ROCKET AERODYNAMICS

by N. F. Krasnov (Editor), V. N. Koshevoy, A. N. Danilov, and V. F. Zakharchenko

"Vysshaya Shkola" Press, Moscow, 1968

NATIONAL AERONAUTICS AND SPACE ADMINISTRATION • WASHINGTON, D. C. • JUNE 1971

NASA TECHNICAL TRANSLATION

NASA TT F-601

NASA TT F-601

ROCKET AERODYNAMICS

by N. F. Krasnov (Editor), V. N. Koshevoy, A. N. Danilov, and V. F. Zakharchenko

"Vysshaya Shkola" Press, Moscow, 1968

NATIONAL AERONAUTICS AND SPACE ADMINISTRATION • WASHINGTON, D. C. • JUNE 1971

ROCKET AERODYNAMICS

By N. F. Krasnov (Editor), V. N. Koshevoy,
A. N. Danilov, and V. F. Zakharchenko

Translation of "Aerodinamika Raket"
"Vysshaya Shkola" Press
Moscow, 1968

NATIONAL AERONAUTICS AND SPACE ADMINISTRATION

For sale by the National Technical Information Service, Springfield, Virginia 22151
$9.00

PREFACE

/3*

Modern aerodynamics is developing in two basic directions, one of which is concerned with further development and improvement of methods for determining the forces exerted by a medium on a body moving in it, and the other with the investigation and calculation of thermal processes on the walls of the vehicle, which are accompanied by various physicochemical transformations. The second trend has become an independent division of the aerodynamic sciences — aerothermodynamics. Aerothermodynamic research is advancing for the most part independently, using data from conventional ("force") aerodynamics. In recent years, as the mathematical apparatus has been perfected, more and more of the aerodynamic problems associated with determination of the force effects and heat transfer are being solved jointly. In many cases, however, it is practically justifiable to assume that the force and thermal processes are independent of one another and to compute them separately. Accordingly, the distribution of gas variables in flow over a surface (pressure, friction stress, temperature, etc.) is found without consideration of heat transfer at the wall. Heat flows, on the other hand, can be calculated separately using these variables.

The distributions of pressure, temperature, and density (the so-called "inviscid" variables) are studied by solving the corresponding gasdynamic equations for an inviscid (ideal) gas. The resulting "inviscid" variables are used to solve the boundary-layer equations and compute the distribution of tangential [shearing] stresses over the surface of the vehicle.

When the vehicles move at very high speeds, the air near the surface of the body is heated to very high temperatures, at which chemical reactions take place. Consideration of the effect of these reactions on the magnitude and distribution of pressure, temperature, and other variables is a salient feature of modern aerodynamics that has been treated in the present volume.

The book devotes considerable space to study of nonsteady flow past bodies of various shapes, which is currently of major importance.

An examination of the general propositions of aerodynamics prefaces our discussion of applied problems in the aerodynamic synthesis of various types of wings and fuselages and combinations thereof. The general material forms Part 1, which deals with the notions of forces, moments, and aerodynamic coefficients (Chapter I), describes the forms of the vehicles and their elements (Chapter II), the basic relationships of [illegible]-flow theory

*Numbers in the margin indicate pagination in the [illegible]ign text.

(Chapter III), and general methods of solution of aerodynamic problems (Chapter IV).

In considering the aerodynamic characteristics, it is very important from a practical standpoint to decompose the resultant values of these characteristics into individual components that have the property of additivity.

The principle of decomposition of the aerodynamic characteristics into individual components is applied for isolated bodies and wings and for bodies and wings in combination. In the latter case, the aerodynamic forces and moments are determined in the form of sums of the corresponding characteristics (for isolated bodies, wings, and fins) and interference corrections. This principle also forms the basis for discussion of the problems of nonstationary aerodynamics, in which case the aerodynamic characteristics are calculated separately with consideration of appropriate nonstationary secondary flows that are superimposed on the stationary flow over the body. /4

Modern aerodynamics has accumulated considerable experience in the determination of aerodynamic characteristics for isolated bodies and wings and for various vehicle configurations. Chapter II is devoted to the most commonly encountered shapes of individual vehicle elements, classifies rockets built for various purposes on the basis of aerodynamic layouts and flight properties, analyzes the general aerodynamic properties of present-day vehicles, the various types of steering devices, and their aerodynamic characteristics.

The differential equation system of aerogasdynamics, on which solution of the flow problems is based, is examined separately for two basic forms of motion: free flow and flows in the boundary layer. The free-flow equation system generally permits calculation of strongly disturbed turbulent flow with consideration of the effects of high temperatures, which may cause dissociation and ionization. Solution of the equations for the boundary layer enables us to find the friction and heat-transfer variables in the presence of chemical reactions and diffusion due to the presence of molecular, ionic, and electronic components in the layer.

Solution of the supersonic-flow problems involves study of flow behind compression shocks. For this purpose, the general relationships determining the flow variables behind shocks are examined for the most general case, with consideration of the chemical processes taking place in the gas behind the shock waves at hypersonic speeds. Consideration is given here to the relaxation effects, since the excitation processes may be characterized by substantial lag times.

The method of finite differences (method of sinks) is

effectively used to solve aerodynamic problems. Finite differences are used, for example, in calculations of the method of characteristics, whose basic relationships are set forth in the book for the general cases of two-dimensional dissociated vortex flows (plane and three-dimensional axisymmetric). A group of scientific staff members of the Mathematics Institute, Academy of Sciences USSR (K.I. Babenko, G.P. Voskresenskiy, and others [4]) has made a major contribution to the development of the net-point method in application to calculation of three-dimensional flow past sharp-nosed bodies in the general case in which chemical reactions are considered.

In the discussion of aerodynamic design of isolated wings and bodies, much attention is given to methods of determining the variables of flow over thin bodies at moderate supersonic speeds (the source and small-disturbance methods).

Application of the method of characteristics makes it possible in flow calculations to pass to bodies of arbitrary shape and to arbitrary free-stream Mach numbers.

Methods of calculating force effects and heat transfer at hypersonic flow speeds are dwelt upon in some detail in the discussion of wing and body aerodynamics.

The aerodynamic characteristics of isolated wings and bodies are also examined for subsonic and transonic speeds.

Together with the aerodynamics of tapered wings and bodies, research on flow past blunt surfaces has been developing. The results of this research that are considered in the present book pertain in particular to determination of shock-wave detachment and shape and to calculation of pressure and velocity on the blunt leading edge of the surface and flow over peripheral zones of the blunted body. Practical interest attaches to solution of problems of flow at large angles of attack (up to 90°) past a wing in the form of a flat plate and circular flow over a body.

Study of the disturbed flow that results from bluntness has established the existence of an "inviscid," high-entropy, low-velocity layer, whose properties have also been determined. Proper use of these properties makes it possible to reduce the heat flows by choosing optimum shape and dimensions for the blunt nose. Thus, blunting must be regarded in a certain sense as a means for heat protection of the vehicle. /5

This book reflects theoretical and experimental results obtained in investigation of heat transfer on surfaces that have, in the general case, an arbitrary leading edge. Calculation of heat flows on blunt bodies is examined, with consideration of the prior history of the boundary layer and chemical reac-

taking place in it.

With increasing flight speeds, diffusive heat transfer, the notion of which is set forth for the cases of finite chemical reaction rate and infinitely fast recombination, becomes substantial along with heat transfer by conduction in the boundary layer. Ways to control diffusive heat transfer are indicated in the discussion of these problems; they consist in the use of contacting materials with unlike catalytic activities.

Aerodynamic calculation of isolated wings is of the auxiliary nature and forms a component part of the determination of the over-all aerodynamic characteristics of the vehicles, which represent combinations of a body with various lifting, stabilizing, and control surfaces. Wing aerodynamics will acquire independent importance as "flying-wing" vehicles make their appearance. Aerodynamic study of bodies of arbitrary shape and especially solids of revolution may have independent importance, since many rocket-type vehicles have solid-of-revolution aerodynamic layouts or are made in the form of a body whose shape is nearly that of a solid of revolution. For this reason, the aerodynamics of the body (solid of revolution) is set forth in greatest detail in the present volume. Along with the problems noted above, which are shared by wings and bodies, a number of specific questions of body aerodynamics are illuminated.

In its aerodynamic layout, the modern high-speed aircraft represents a combination of a body (usually a solid of revolution), wings, fins, and control devices. Owing to aerodynamic interference between these elements, the total forces and moments for the combination are not equal to the sums of the corresponding characteristics for the body, wings, fins and control surfaces taken separately. In calculating the over-all aerodynamic characteristics, therefore, the effects of interaction must be taken into account. The last part of the book sets forth interference problems on the basis of aerodynamic slender-body theory for both stationary and nonstationary flow over the slender (thin) component configurations. The methods of calculating interference that are developed in this theory are extended to the case of linearized flow in which the effect of Mach number is taken into account. High-speed interference of composite bodies of arbitrary thickness is the least developed problem of contemporary aerodynamics. It has been established experimentally that the interactions become less important with increasing supersonic speed. This is explained by narrowing of the reciprocal-effect zones. For this reason, the high-speed aerodynamic characteristics of a combination of bodies with lifting, stabilizing, and control devices can be determined in approximation by adding the corresponding aerodynamic characteristics for the isolated elements of this combination.

Present-day guided vehicles are provided with aerodynamic, gasdynamic, or combined controls. Selection of the type of control device is governed by the design features, purpose, and flight conditions of the vehicle. Determination of the controlling effort is an important part of the aerodynamic calculation, since it determines in many respects the flight properties of the vehicle as a whole. For this reason, the book devotes much attention to calculation of the effectiveness of controls of these three types. The force and moment characteristics of aerodynamic controls are set forth within the framework of aerodynamic slender-body theory, using corrections obtained from the linearized theory. For other types of controls, the calculation of the effectiveness is set forth on the basis of available experimental data, with application of the elementary relationships of gasdynamics. Aerodynamic problems related to controls have not been developed adequately. Further theoretical and experimental study is necessary. /6

On the whole, the book will familiarize the reader with the basic theoretical premises of modern high-speed aerodynamics, methods of calculating force and heat effects of the environment on the vehicle and its individual elements, and the most important characteristics of gas flows in various gas states.

To facilitate conversion of the units used for the physical quantities to the new ones conforming to the accepted International System (SI), a special conversion table is given at the end of the book. Quantities derived using the International System are given for comparison in numerical examples.

Prof. N.S. Arzhanikov, Honored Worker of Science and Engineering, and Prof. I.P. Ginzburg accomplished a major task in reviewing the manuscript and submitted highly valuable recommendations and comments, which were taken into consideration in final editing of the book.

The authors acknowledge that their work may not be without shortcomings, and will welcome all readers' comments.

TABLE OF CONTENTS /767

Preface iii
Abstract 1

PART ONE. GENERAL DEFINITIONS OF AERODYNAMICS

Chapter I. The Concepts of Forces, Moments, and Aerodynamic Coefficients 3
§ I-1. Coordinate Systems 3
§ I-2. Forces, Moments, and Their Aerodynamic Coefficients. 6
§ I-3. Frontal Drag 11
Winged Vehicles 11
The Body. 15
Wings (Lifting Surface) 18
§ I-4. Lift 23
Winged Vehicle. 23
Body. 25
Wings (Lifting Surface) 27
§ I-5. Moment 29
Winged Vehicle. 29
Body 30
Wing and Profile. 32
§ I-6. Application of Aerodynamic Characteristics to the Study of Flight Stability of Bodies. 33
Static Stability. 33
Dynamic Stability 36
§ I-7. Aerodynamic Characteristics of Vehicles in Nonsteady Motion 43

Chapter II. Shapes of the Vehicles and Their Elements
§ II-1. Shapes of Vehicle Bodies. 54
§ II-2. Shapes of Lifting, Controlling, Stabilizing, and Auxiliary Surfaces. 63
§ II-3. Controls. 74
§ II-4. Aerodynamic Configurations of Aircraft. 84
§ II-5. Influence of Mission and Tactical-Technical Requirements on Selection of Vehicle Aerodynamic Layouts. 92
Vehicle Type and Aerodynamic-Layout Features 93
Powerplant Type and Aerodynamic-Layout Features. . . . 99

Chapter III. Fundamental Relationships in the Theory of Gas Flows
§ III-1. Peculiarities of Gas Flow at Very High Speeds. . . 102
Change in Physicochemical Properties and Thermodynamic Characteristics of Air with Temperature. 102
Dissociation and Ionization. 104
Basic Relationships for a Diatomic Dissociating Gas. . 111
Relaxation Effects 118

Diffusion Effects in the Boundary Layer. 125
§ III-2. The System of Fundamental Equations. 129
Equation of Motion 130
Continuity Equation. . . . . 137 /768
The Diffusion Equation 144
Equation of Momentum 145
The Energy Equation. 146
The Equation of State. 151
Condition of Entropy Conservation. 152
Initial and Boundary Conditions. 153
§ III-3. Isentropic Flow. 155
§ III-4. Fundamental Relationships for Determination of Parameters Behind Compression Shock. 159
Equations of the Oblique Compression Shock 159
Calculation of Oblique Compression Shock with Tables or Curves of the Thermodynamic Functions for Air at Very High Temperatures 162
Compression Shock in Gas Flow with Constant Heat Capacities 169
Relaxation Effects in Shock Waves. 177

Chapter IV. General Methods of Solution of Aerodynamic Problems
§ IV-1. The Method of Characteristics 181
General Equations for the Characteristics. 181
Characteristics of Plane Potential Flow. 188
Scheme for Problem Solution by the Method of Characteristics 191
Characteristics in a Dissociating Gas. 197
§ IV-2. Conical Flows 199
§ IV-3. The Method of Sources 201
§ IV-4. Theory of Supersonic Flow Past Slender Bodies with Arbitrary Cross Section 203
Solution of the Potential Equation 203
Aerodynamic Forces and Moments 210
The Method of Conformal Transformation 214
§ IV-5. Flow-Reversibility Method 218
§ IV-6. General Expressions for the Stability Derivatives of a Finned Solid of Revolution. The Method of Attached Masses 219
§ IV-7. Approximate Methods of Calculation of Flow Over Surfaces. 229
§ IV-8. Aerodynamic Heating 241
The Parameters of Heat Transfer. 242
Heat Transfer in the Laminar Boundary Layer on a Curved Surface 258
§ IV-9. Influence of Viscous Interaction on Flow Parameters 271
§ IV-10. Peculiarities of Flow Past Bodies with Blunted Nose Section 273

PART TWO. AERODYNAMICS OF LIFTING, STABILIZING, AND CONTROL SURFACES

Chapter V. Calculation of the Aerodynamic Coefficients. . . 280
§ V-1. Subsonic and Transonic Speeds. 280
Influence of Compressibility on Pressure 280
Lift [6] 286
Frontal Drag 298
Moment and Aerodynamic Center (Center of Pressure) . . 306
§ V-2. Supersonic Speeds. 309
Flow Around a Thin Plate 309
Profile in Supersonic Flow 313
§ V-3. Lift and Moment of Thin Finite-Span Wings. Drag Dependent on Lift. 323
§ V-4. Drag of Wings of Finite Thickness. 343
§ V-5. The Nonlinear Problem of Supersonic Flow Around Wings. 355
Application of the Method of Characteristics 355
Aerodynamic Characteristics at Very High (Hypersonic) Speeds 360
§ V-6. Wake Drag. Viscous Interaction . . . . . 379 /769
§ V-7. Aerodynamics of Blunt Wedges at High Supersonic Speeds 385
Flow Around Profile with Blunt Leading Edge. 385
Bluntness in the Form of a Flat Plate 389
Profile with Small Bluntness 395
§ V-8. Annular Wings. 400
§ V-9. Cruciform Wings. 403
§ V-10. Nonstationary Wing Aerodynamics 405
Plate in Supersonic Flow 405
Wings in Subsonic Flow 408
Wings in Supersonic Flow (Slender-Body Theory) 412
Influence of Wing Aspect Ratio and M_∞ on Stability Derivatives. 418

Chapter VI. Friction and Heat Transfer on Wings
§ VI.1. Parameters of Friction in Flow Around a Flat Plate. 429
Homogeneous Boundary Layer 429
Mixed Boundary Layer 445
Friction on a Plate Set at an Angle of Attack. 450
§ VI-2. Heat Transfer on a Flat Plate 453
Incompressible Flow. 453
Influence of High Velocities 454
Heat Transfer on a Plate Set Perpendicular to the Oncoming Flow (Laminar Boundary Layer) 457
§ VI-3. Friction and Heat Transfer on Wings of Finite Thickness 461
Wing with Sharp Leading Edge 461
Heat Transfer on Blunt Wing Surface. 470
§ VI-4. Wall Temperature. 473
Steady-State Heating 473
Nonsteady Heating. 475

Wall Temperature in the Presence of Solar Heating. . . 477
§ VI-5. Wing Leading Edge Bluntness for Maximum Reduction of Heat Flows 478

PART THREE. BODY AERODYNAMICS

Chapter VII. Aerodynamic Coefficients at Subsonic and Transonic Speeds 484
§ VII-1. Subsonic Speeds. 484
§ VII-2. Transonic Speeds 487
Similarity of Transonic Flows. 487
Total Drag of Various Solids of Revolution at Transonic Speeds 495
Chapter VIII. The Cone in Supersonic Flow 502
§ VIII-1. Axisymmetric Supersonic Flow Past a Cone. 502
Equation System. 502
Constant Heat Capacities 503
Influence of Dissociation and Ionization 514
Influence of Nonequilibrium. 522
§ VIII-2. Cone at Angle of Attack 523
Certain Results from Calculation of Supersonic Conical Flows. 523
Analysis of Calculated Results for Flow Around Cones . 525
Kopal's Tables 528
Approximate Calculation of Flow at High Velocities . . 530

Chapter IX. Application of Difference Methods to Calculation of Flow Around Bodies with Curved Generatrices . . 531
§ IX-1. Calculation of Axisymmetric Supersonic Flow Around a Sharp Solid of Revolution by the Method of Characteristics [17]. 531
§ IX-2. The Net-Point Method. . . . . 543 /770
§ IX-3. Influence of Attack Angle on Frontal Drag 546

Chapter X. Hypersonic Velocities. 548
§ X-1. Flow Around Slender Bodies at Very High Speeds . . . 548
The Equation System. 548
Flow Calculation 554
§ X-2. Use of Approximate Methods to Calculate Flow Around Solids of Revolution at Very High Speeds 563
"Local Cone" Method. 563
Method Combining Conical and Expansion Flows 565
§ X-3. The Newton Method. 571
Pressure 571
Coefficient of Axial Force 572
Shape of Nose Section with Minimum Drag. 578
Normal-Force Coefficient 583
Coefficients of Moment and Center of Pressure. 593
Similarity Law for Nonaxisymmetric Flow. 600
Estimation of Error in Approximate Methods 602

Chapter XI. Aerodynamics of Slender Bodies in Linearized Flow. 604
§ XI-1. Application of the Method of Sources. 604
§ XI-2. Axisymmetric Flow 612
Calculation of Velocity and Pressure 612
The Wave Drag Coefficient. 621
Very Slender Body. 630
Shape of Solid of Revolution with Minimum Wave Drag. . 632
§ XI-3. Flow Around Solids of Revolution at an Angle of Attack. 633
Pressure Distribution in Nonaxisymmetric Flow. 633
Normal-Force Coefficient 640
Coefficient of Moment of Forces. 648
Center of Pressure Coefficient 651
Drag Due to Lift 660

Chapter XII. Aerodynamics of Blunt Solids of Revolution
§ XII-1. Inviscid Flow Around a Blunted Nose. 662
General Solution for a Nose of Arbitrary Shape 662
§ XII-2. Approximate Methods of Calculating Flow Around Noses with Various Shapes. 665
Spherical Nose 665
Flat Face. 680
Other Blunted Nose Shapes. 685
Spherical Surface with "Blunted" Forward End 689
§ XII-3. Flow at High Velocities Around Cylindrical and Conical Bodies with Small Bluntness. 690
Analogy with Nonsteady Motion of Piston. 690
Flow Around a Blunted Cylinder 694
Flow Around a Slender Cone with a Small Bluntness. . . 699
§ XII-4. Application of the Method of Characteristics to Calculation of Flow Past Blunt Solids of Revolution. . 705
§ XII-5. Influence of Attack Angle. 711
§ XII-6. The Newton Method. 712
§ XII-7. Flow Around Blunt Bodies of Curvilinear Shape. . . 718
§ XII-8. Influence of Nonequilibrium on Parameters of Inviscid Flow Around Blunt Bodies. 729
Nonequilibrium Flow in Regions with Strong Overexpansion and Small Pressure Gradients. 729
Effect of Nonequilibrium on Position and Shape of Shock Wave 734

Chapter XIII. Nonstationary Aerodynamics of Bodies. . . . . 739 /771
§ XIII-1. Linearized Flow Around Solids of Revolution . . . 739
Basic Relationships. 739
Aerodynamic Coefficients under the Conditions of Low-Frequency Oscillations 745
§ XIII-2. Application of the Newton Method. 750
Tapered Solid of Revolution. 750
Blunted Cone 754
§ XIII-3. Action of Additional Forces Due to Rotation of Body About Longitudinal Axis. 758

Chapter XIV. Friction and Heat Transfer at High Velocities
§ XIV-1. Friction and Heat Transfer of the Body 762
§ XIV-2. Influence of Viscosity on Drag. Wake Drag. 769
Influence of Viscous Interaction on Flow Variables . . 769
Friction 772
Wake Drag. 775
§ XIV-3. Determination of the Degree of Bluntness for Maximum Reduction of Heat Flows. 782
§ XIV-4. Heat Transfer on the Body. 792
Curvilinear Surface. 792
Sharp Body 792
§ XIV-5. Total Stagnation Point on Blunt Nose 794
§ XIV-6. Curvilinear Blunted Surface. 799
Laminar Heat Transfer. 799
Heat Transfer Across Turbulent Boundary Layer. 810
§ XIV-7. Comparison of Friction and Heat Flows on Sharp and Blunt Cones. 817
§ XIV-8. Viscosity Effect on External Flow Around a Blunt Body. 820

PART FOUR. AERODYNAMIC CHARACTERISTICS OF THE VEHICLE

Chapter XV. Steady-State Flow
§ XV-1. Calculation of Aerodynamic Coefficients with Consideration of Interference for a Slender-Body-Wing Combination 827
General Definitions. 827
Relationships for Aerodynamic Calculation with Consideration of Interference. 829
Calculation of Interference for "Nonslender" Combinations. 842
§ XV-2. Change in Tail Aerodynamic Properties under the Influence of the Wing 851
General Expression for Normal Force. 851
Downwash Angle Behind Wing 852
Lifting Capacity of a Vehicle with Fixed Wings and Tail at Supersonic Speeds 854
§ XV-3. Effect of Interference on Aerodynamic Characteristics of Controls. 869
All-Moving Plane Controls. 869
All-Moving Cruciform Controls. 880
Interaction Between Controls 881
Controls Along Trailing Edges of Lifting Surfaces. . . 883
Nonlinear Effects. 887
Hinge Moment of All-Moving Wings 890
Example of Aerodynamic-Characteristic Calculation for a Body-Wing-Tail Combination. Experimental Data . . . 893
§ XV-4. Damping Moment of Vehicle Due to Motion of Fuel and Combustion Products 916
§ XV-5. Design of Rollerons 917

§ XV-6. Frontal Drag. . . . . 921 /772
Drag at Zero Lift. 921
Drag at $c_y \neq 0$ 927
Lift/Drag Ratio. 930

Chapter XVI. Aerodynamics of Controls
§ XVI-1. Forces Created by Aerodynamic Controls 933
Spoilers 933
Increasing Lift of Aerodynamic Controls by Blowing Gas into Boundary Layer. 936
§ XVI-2. Calculation of Forces Developed by Gasdynamic Controls. 938
Calculation of Thrust of Gasdynamic Controls with Consideration of Losses in Air Intakes. 938
Fixed and Movable Control Engines. 945
Pivoting Nozzles 946
Rotary Mouthpieces 948
Deflectors 950
Gas Vanes. 952
Control of Gas Injection into Supersonic Section of Nozzle 957
Throttling Individual Nozzles. 961
Determination of Controlling Efforts Created by Gasdynamic Controls in Nozzle Assemblies with a Central Body 962
§ XVI-3. Calculation of Forces Set Up by Combined Controls. 964
Controls with Fixed Slot Nozzle on Trailing Edge of a Plate. 964
Controls with Rotating Slot Nozzle on Wing Trailing Edge at Subsonic Speeds. 969
Controls in the Form of a Fixed Slot Nozzle on a Cylindrical Body Surface at Supersonic Speeds 973
§ XVI-4. Determination of Hinge Moments of Gasdynamic and Combined Controls. 974

Chapter XVII. Nonstationary Characteristics of the Vehicle
§ XVII-1. Determination of Stability Derivatives from Slender-Body Aerodynamic Theory 977
§ XVII-2. Damping Coefficients. 980
§ XVII-3. Analysis of Stability Derivatives for Finned Body 984
§ XVII-4. The Magnus Effect 991
Appendix No. 1. 995
Appendix No. 2. 1023
Appendix No. 3. 1024
References 1026

NASA TT F-601

ROCKET AERODYNAMICS

N.F. Krasnov (Editor), V.N. Koshevoy,
A.N. Danilov and V.F. Zakharchenko

ABSTRACT: The book is designed to familiarize the reader with the basics of modern high-speed aerodynamic theory, calculation of force and heat effects of the environment on the vehicle, and the most important characteristics of flows for various states of the gas. Two trends are discerned: study of the forces that the medium exerts on the body moving in it and thermal and chemical processes on the skin of the vehicle. Pending refinement of joint-solution methods, the effects of thermochemical reactions on the gasdynamic variables and their distributions are determined separately. Much attention is given to nonsteady flows past bodies of various shapes. Part One is a general discussion of forces, moments, and aerodynamic characteristics, vehicle and vehicle-element shapes, gas-flow theory, and the general methods of solution of aerodynamic problems (characteristics, sources, slender-body-theory, conformal-mapping, reversibility, attached-mass, etc.). Parts Two, Three, and Four, respectively, deal with applications to lifting, stabilizing, and control surfaces; bodies; and combinations of these elements that constitute vehicles, with consideration of interference between the parts and operation of aerodynamic and gasdynamic controls. Aspects of the treatment include nonsteady flows over bodies of various shapes with emphasis on blunt forms, additive components of aerodynamic characteristics, consideration of diffusive heat transfer and relaxation behind the shock in supersonic problems, use of the net-point method as developed at the Mathematics Institute, USSR Academy of Sciences(Babenko and Voskresenskiy), shock-wave shape and detachment for blunt bodies with determination of $\underline{p}$ and V on tapering nose sections, and determination of the properties of the "inviscid" high-entropy, low-velocity layer on blunt bodies and their use to control heat transfer.

Part One

GENERAL DEFINITIONS OF AERODYNAMICS

THE CONCEPTS OF FORCES, MOMENTS, AND AERODYNAMIC COEFFICIENTS

§I-1. COORDINATE SYSTEMS

Forces exerted by the medium. The action of the medium on a body in motion in it reduces to the appearance of continuously distributed normal-pressure forces on its surface, along with tangential [shearing] stresses governed by the medium's viscosity. All of these forces (Fig. I-1-1) are reduced to a single principal aerodynamic-force vector $\bar{F}$ and a principal vector $\bar{M}$ of the moment of these forces about some reference point. This may be any point of the body, e.g., its center of gravity, the point of its nose, etc. In engineering practice, we deal not with the vectors $\bar{F}$ and $\bar{M}$, but with their projections onto the axes of some coordinate system. Most common among these systems are the wind (drag) and body axes.

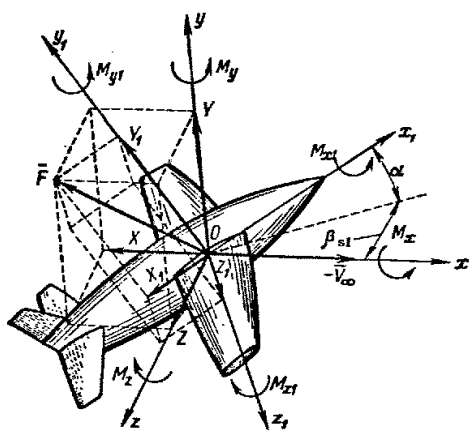

Figure I-1-1. Diagram of Aerodynamic Forces and Moments Acting on Aircraft in Wind (x, y, z) and Body (x_1, y_1, z_1) Coordinate Systems.

The wind (drag) coordinate system. In this coordinate system (Fig. I-1-1), the longitudinal axis x coincides with the direction of flight velocity, the y-axis lies in the vertical plane of symmetry of the body in the flow, and the z-axis is perpendicular to the x, y-plane and directed in such a way that the axes x, y, and z form a right-hand coordinate system.

The wind system is sometimes applied in another form. Its longitudinal axis x coincides with the direction of flow velocity and its y-axis lies in the plane in which the velocity vector $\bar{V}_\infty$ and the body axis x_1 are located.

Body axes. In this system, which is rigidly bound to the vehicle (see Fig. I-1-1), the x_1-axis points toward the nose parallel to the wing chord, and, for a vehicle with an axisymmetric body, coincides with the body's longitudinal axis of symmetry. The y_1 axis of the body system lies in the vertical plane

of symmetry and the z_1-axis points along the span of the right wing (right-hand coordinate system).

The body system whose axes are shown in Fig. I-1-2 is used occasionally. The x_1 axis is directed downstream from the nose to the tail of the body. With horizontal and vertical symmetry, the z_1- and y_1-axes lie respectively in the horizontal and vertical planes of symmetry, forming a right-hand coordinate system.

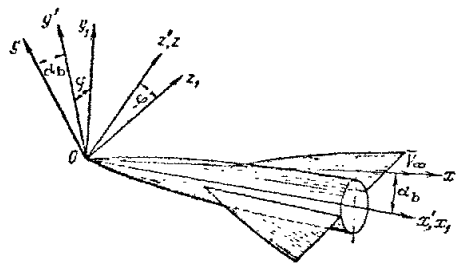

Figure I-1-2. Body (x_1, y_1, z_1) and Wind (x, y, z) Coordinates.

Together with the wind and body axes, aerodynamics research sometimes makes use of the so-called semibound axes. In this system, the longitudinal axis x_2 coincides with the projection of the velocity vector $\overline{V}_\infty$ onto the vehicle's vertical plane of symmetry. The vertical axis y_2 is also in this plane, which is known as the angle of attack plane. The z_2 axis coincides with the z_1 of the body system. /10

Relative positions of the axes of the various systems. At a given speed, the magnitude and direction of forces and moments depend on the orientation of the body relative to the velocity vector, or, for the converse motion, relative to the direction of the oncoming-flow velocity $\overline{V}_\infty$. Consequently, the magnitude and direction of forces and moments depend on the relative positions of the coordinate systems bound to the flow and the body.

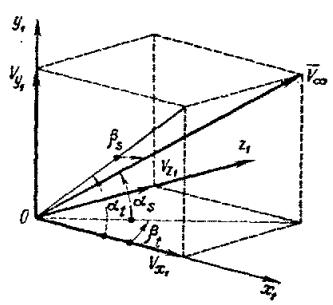

Figure I-1-3. Attack and Slip Angles (components of velocity $\overline{V}_\infty$ are given in the body system).

The relative positioning of the wind and body systems is determined (see Fig. I-1-1) by the attack angle α, the angle between the Ox_1-axis and the projection of vector $\overline{V}_\infty$ onto the x_1Oy_1 plane and by the slip angle β_{sl}, the angle between the vector $\overline{V}_\infty$ and the x_1Oy_1 plane.

Knowing the angles α and β_{sl}, we can proceed from given coordinates of a point, say in the wind axes, to find its coordinates in the body system and vice-versa. This is done by the appropriate formulas of analytical geometry, which give the coordinates to be converted as functions of the cosines of the angles

practice therefore the visible figure of Venus may be considered to be a globe. The altitude of the cloud layer over the surface of the planet, and therefore the diameter and shape of the planet itself, are unknown.

The mass of Venus is 408,500±160 times less than the mass of the sun [138], which corresponds to 0.815 of the earth. The density of Venus is 4.86 g/cm^3. For the earth the corresponding quantity is equal to 5.52 g/cm^3. Acceleration of gravity on the surface of Venus g_{φ} = 835 cm · sec^{-2}. The second cosmic speed near the surface of Venus is equal to 10.2 km/sec.

3. The Atmosphere and the Cloud Layer

The atmosphere of Venus was discovered in 1761 by M. V. Lomonosov [66] after having observed the passage of the planet across the solar disk. However, up to the present time the composition of the atmosphere, temperature and the pressure are practically unknown. Such a situation results mainly from the fact that due to the nontransparence of the atmosphere of Venus in the optical range only the upper layers of the gaseous-aerosol clouds of the planet are accessible to our immediate investigation. At the present time the lower cloud layers remain the subject of diverse hypotheses.

An evaluation of the pressure in that part of the atmosphere above the clouds of Venus was carried out by Dolfus [27], Moroz [71, 72] and Vaucouler and Menzel [323]. Dolfus investigated the difference in polarity in the red and green parts of the spectrum. Interpreting this as a result of molecular scattering, he determined that the equivalent altitude of the atmosphere of Venus at the level of the cloud layer was equal to 800 meters. Under a force of gravity somewhat less than that of earth, this corresponds to a pressure at the top of the cloud layer of 90 mb*. V. I. Moroz in widening the band of absorption CO_2 λ 1.575 and 1.606 μ defined the pressure at the level of the cloud layer as equal to 300 mb. /12

Vaucouler and Menzel [323] in accordance with observations of the screening of Regulus by Venus, evaluated the pressure at a level of 70 km above the cloud layer as equal to 2.6 x 10^{-3} mb. In accordance with these observations the altitude of the similar atmosphere in the layer above the clouds of Venus equals H = 6.8 km according to the calculation of the authors, and H = 6 km according to the calculation of Martynov and Pospergelis [67].

According to a calculation of Sagan [282] based upon measurements of the bands of absorption CO_2 λ 0.8 μ [302] and 1.6 μ [191], and the screening of Regulus by Venus [323], the pressure at the level of the cloud layer for the illuminated side of Venus was determined to be equal to 600 mb.

---

* We are reminded that 1 atm = 1013 mb.

An attempt to estimate the pressure in that part of the atmosphere under the clouds was undertaken by Spinrad [302]. He processed old spectrograms of the spectrum band 7820 Å, obtained by Adams and Dunham [102]. They calculated the pressure at the level of the reflecting layer from 1.1 to 4.6 atm according to the spread of the spectral lines. In connection with the fact that high pressures correspond as a rule with high temperatures, they interpreted the result as an indication of change in the altitude of the reflecting layer. At the lowest measured level the pressure approached 5 atm.

The chemical composition of the atmosphere of Venus has been the subject of numerous spectroscopic investigations. Nevertheless, thus far carbon dioxide is the single satisfactorily explained component of the atmosphere of the planet.

Estimates of the content of CO_2 in the atmosphere of Venus have been extremely diverse. Until recently the most accepted estimates have been those of Adams, Dunham [102] and Kuiper [41]. According to these estimates there exists above the cloud layer 10^5 atm-centimeters* of CO_2, which appears to be the basic component of the atmosphere of Venus. Completely different results were obtained recently by Spinrad [302]. Having processed the old spectrograms of Adams and Dunham he determined the CO_2 content to be equal to 2×10^5 atm-centimeters. However, in accordance with measurements of the width of the lines of absorption, he came to the conclusion that the indicated quantity of CO_2 is maintained above the level at which the pressure comprises 7 atm. In this case there is above the cloud layer (under a pressure at the level of this layer of 90 mb) only 4×10^3 atm-centimeters of CO_2, and the relative content of carbon dioxide in the atmosphere of Venus consists in all of 4% (according to the mass). /13

According to an estimate of Kaplan [193] the relative content of CO_2 in the atmosphere of Venus comprises 15%.

Under earth conditions, atmospheric carbon dioxide reacts with silicates, which are components of soil. This process, decreasing the content of CO_2 in the atmosphere, demands the presence of water in the liquid state as a catalytic agent. The liberation of CO_2 into the atmosphere proceeds simultaneously with this. The speed of these processes is determined by the

---

* 1 Atm-centimeter is the thickness in cm of the layer of specified gas which would be obtained if the gas were isolated and compressed to a pressure of 1 atmosphere under the influence of a standard temperature.

equilibrium of Urey. The abundance of CO_2 in the atmosphere of Venus in comparison with that of earth indicates apparently a disturbance in the equilibrium of Urey. A possible reason for this may be the lack of water on Venus.

A series of attempts to detect water in the atmosphere of Venus have been undertaken.

In 1921 John and Nicholson [188] investigated at Mt. Wilson the line of water vapor near λ 5,900 Å. This line was not detected. They calculated the upper limit of the water vapor content above the reflecting layer of Venus as equal to 1 mm of precipitated water, i.e. about 14% of the content of water vapor in the atmosphere of the earth over Mt. Wilson in winter.

Adams and Dunham [102] carried out analogous investigations of the line near 8,200 Å and estimated the upper limit of the water vapor content on Venus as equal to 5% of the earth's level.

In 1960, with the aid of an apparatus raised on a stratospheric balloon in order to decrease terrestrial lines, Strong and others undertook measurements of the band of absorption of water vapor near λ 1.13 μ. It was found that the water vapor content above the reflecting clouds in the atmosphere of Venus comprises $(1.9 \pm 1.6) \cdot 10^{-3}$ cm, i. e. (19 ± 16) μ of precipitated water. However, in connection with the fact that the water vapor content measured by Strong and others is commensurate with that found in the atmosphere of earth [243], the cited data were subject to doubt.

In 1962 Spinrad [301] reprocessed some old Mt. Wilson spectrograms near λ 8,180 Å. He detected no line of absorption of water vapor. He calculated the upper limit of water vapor content in the atmosphere of Venus as $7 \cdot 10^{-3}$ $g \cdot cm^{-2}$ (70 μ). From a comparison with former work defining the pressure in accordance with the spreading of lines of absorption of CO_2 [302] he considered that the experiment referred to the level at which the pressure consisted of 8 atm and therefore the relative content of water vapor in the atmosphere of Venus would be less than $9 \cdot 10^{-7}$ (according to the mass). This calculation was reduced to $<10^{-5}$ because of a series of indefinite quantities.

The next attempt to detect water vapor was undertaken by Dollfus [150] in 1963 by measurements of the band of H_2O near λ 1.4 μ. In comparing the spectrum of Venus and the moon under conditions of equal zenithal distances he detected that in all cases the intensity of the band of H_2O in the spectrum of Venus was higher than in the spectrum of the moon. He determined that the average water content of the Venus disk was equal to $2.8 \cdot 10^{-2}$ $g \cdot cm^{-2}$. These measurements were carried out with a phase angle of 91° which corresponds to 4 as the average optical path of the reflected ray. From this the water vapor content in a vertical column was calculated as equal to $0.7 \cdot 10^{-2}$ $g \cdot cm^{-2}$, i.e. 70 μ. Providing that the calibration of the apparatus was carried out under pressure of 1 atm and that the pressure

/14

of the layer observed on Venus was significantly lower, the true content of H_2O must be lower than indicated.

In 1964 Strong, together with Bottema and Plummer, [116 and 117] repeated the stratospheric balloon measurements of water vapor in the atmosphere of Venus. Under atmospheric pressure the absorption of water vapor in the line of H_2O λ 1.1 μ was detected corresponding to $9.8 \cdot 10^{-3}$ g $\cdot$ cm^{-2} (98 μ). The interpretation of the data obtained depends upon the pressure at the level of the cloud layer and the distribution of water vapor by altitude. For a gravitational atmosphere the experimental data corresponds to $22.2 \cdot 10^{-3}$ g $\cdot$ cm^{-2} of water vapor at a pressure at the level of the cloud layer of 90 mb and $5.3 \cdot 10^{-3}$ g $\cdot$ cm^{-2} at a pressure of 600 mb. The relative water vapor content in the atmosphere of Venus is calculated as equal to $2.5 \cdot 10^{-4}$ and $0.87 \cdot 10^{-5}$ respectively.

Recent measurements of water vapor were carried out by Spinrad [304] at the line 8,200 Å in July and August of 1964. Water vapor content above the cloud layer was estimated by him at less than 20 μ [306].

Prokof'ev and Petrova [76, 77] undertook an extremely successful attempt to reveal molecular oxygen in the atmosphere of Venus. In 1961 and 1962 they obtained a spectrum in the region of the telluric α band of oxygen displaying nonsymmetry of line caused apparently by a weak band of absorption of oxygen in the atmosphere of Venus. In 1964 the deduction concerning the possible presence of oxygen in the atmosphere of Venus was conclusively confirmed by Prokof'ev's [78] new investigations into the region of the B band of telluric oxygen. A preliminary evaluation of the oxygen content in the cloud layer over Venus made by Prokof'ev revealed 0.1% of the earth's level, i.e. approximately 170 atm-cm.

Spectroscopic measurements by Spinrad [305] gave a negative result. He estimates the O_2 content in the layer above the clouds of Venus at less than 50 atm-cm. /15

Concerning other gases which have been examined spectroscopically, Sinton [296] points to weak lines of absorption which may be ascribed to CO. These lines were also obtained by Moroz [70] who evaluated the CO content as equal to 5 atm-cm. However, analogous measurements by Kuiper [210] did not reveal the indicated bands of absorption. In agreement with Kuiper's estimates, the content of CO in the atmosphere of Venus is less that 3 atm-cm.

Table I.1, which we have borrowed from [70], presents estimates of the upper limit of the content of several other gases which have yielded negative results to spectroscopic investigations in the atmosphere of Venus.

$$m_z^{\prime} = m_z^{\prime} + \frac{x_1^{\prime} - x_1^{\prime}}{l} c_{y1} - \frac{y_1^{\prime} - y_1^{\prime}}{l} c_{x1}, \qquad \text{(I-2-6)}$$

where ℓ is a characteristic length, for example, the length of a solid of revolution or the chord b of a wing (Fig. I-2-2).

The polar curve. Vehicle lift/drag ratio. The polar curve and lift/drag ratio are extremely important aerodynamic characteristics of a vehicle. The polar establishes the relation between lift and frontal drag or between normal and axial forces. The $c_{x_1} = f_1(c_y)$ curve is known as a polar of the first kind, and the relation $c_{x_1} = f_2(c_{y_1})$ [or $c_R = f_2(c_N)$] as a polar of the second kind.

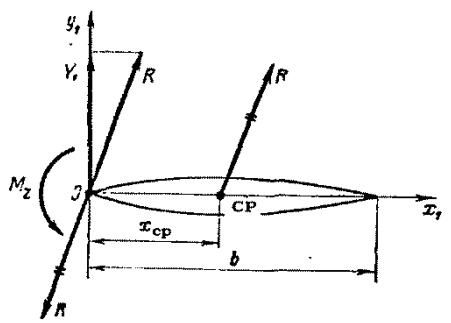

Figure I-2-3. Diagram Illustrating Definition of Center of Pressure.

The lift/drag ratio of a vehicle /14

$$K = \frac{c_y}{c_x}. \qquad \text{(I-2-7)}$$

Center of pressure and aerodynamic center. The center of pressure of a vehicle is the point of application of the aerodynamic-force resultant. The center of pressure coefficient (Fig. I-2-3) is a dimensionless quantity and is defined as the ratio of the distance of the center of pressure from some fixed characteristic point to the characteristic length (ℓ or b):

$$c_{c.p.} = \frac{x_{c.p.}}{b}. \qquad \text{(I-2-8)}$$

The coefficient $c_{c.p}$ can be computed from known values of the pitching moment and normal force and can be expressed in terms of the aerodynamic coefficients:

$$c_{c.p.} = \frac{M_z}{Nb} = \frac{m_z}{c_N}. \qquad \text{(I-2-8')}$$

For vehicles that do not have horizontal symmetry, flight properties are more conveniently evaluated not with respect to the center of pressure, but with respect to the center distance.

To establish the sense of the "vehicle aerodynamic center" concept, we shall use the familiar relationship for the coefficient of moment calculated about an arbitrary point with coordinate x_n on the chord of the unsymmetrical profile,

$$m_z = m_{z0} + \frac{\partial m_z}{\partial c_y} c_y + \frac{x_n}{b} c_y, \qquad \text{(I-2-9)}$$

where m_{z_0} is the coefficient of the moment about the leading edge at zero lift.

The second term in the right member determines the moment increment associated with a change in attack angle. The profile chord $\underline{b}$ is taken as the characteristic linear dimension. Here we are concerned with small attack angles, for which $c_y \approx c_N$.

It follows from (I-2-9) that a point $x_n = x_F$ (an aerodynamic center) such that the moment about it does not depend on c_y can be found on the chord.

The aerodynamic-center coordinate

$$\left.\begin{aligned} x_F &= -b\frac{\partial m_z}{\partial c_y}, \\ \bar{x}_F &= \frac{x_F}{b} = -\frac{\partial m_z}{\partial c_y} \end{aligned}\right\} \qquad \text{(I-2-10)}$$

Obviously, the aerodynamic center is a point about which the aerodynamic moment remains constant and independent of attack angle, i.e., the point of application of the resultant of all additional forces produced by the attack angle. The relation between the center of pressure and the aerodynamic center is given by

$$c_{c.p.} = \frac{m_z}{c_y} = \frac{m_{z0} + (\partial m_z/\partial c_y) c_y}{c_y} = c_{c.p.0} + \bar{x}_F, \qquad \text{(I-2-11)}$$

where $c_{c.p_0} = m_{z_0}/c_y$, and $\bar{x}_F$ is the absolute value.

For bodies with symmetrical configuration, m_{z_0}, and, consequently, $c_{c.p._0}$ are zero, and the center of pressure coincides with the aerodynamic center. If $c_y \to 0$ for a symmetrical body /15

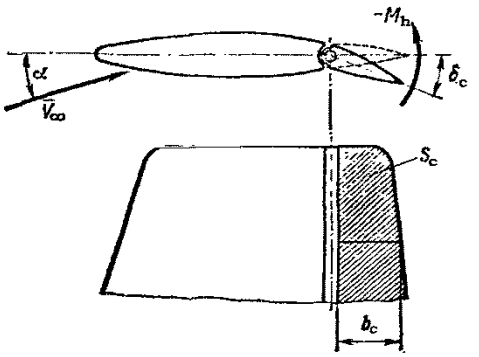

Figure I-2-4. Hinge Moment of Control Surface.

then $m_z \to 0$ also; the center of pressure coefficient tends to a finite value of

$$c_{c.p.} = \left(\frac{\partial m_z}{\partial c_y}\right)_{c_y=0}.$$

For an unsymmetrical body, e.g., a profile, the moment coefficient tends to a finite value m_{z_0} as $c_y \to 0$, and hence $c_{c.p} \to \infty$.

Hinge moment. This moment acting on a control surface

$$M_h = m_h q b_c S_c, \qquad \text{(I-2-12)}$$

where m_h is the hinge moment coefficient, and b_c and S_c are the mean geometric chord and planform of the control device (surface).

For given flight conditions (speed, altitude), the moment coefficient m_h is a function of the vehicle's attack angle α and the control-surface deflection angle δ_c (Fig. I-2-4).

§I-3. FRONTAL DRAG

Winged Vehicles

The frontal drag coefficient c_x of a vehicle can be expressed as the sum of a coefficient c_{x_0}, that owes its origin to viscosity and compressibility and is unrelated to lift, and an additional coefficient c_{xi} which is governed by lift (induced-drag coefficient). Accordingly, the over-all drag coefficient

$$c_x = c_{x0} + c_{xi}. \qquad \text{(I-3-1)}$$

The drag coefficient c_{x_0} can be represented as the sum of the corresponding drag coefficients for the body, wings, fins, controls, and other elements of the vehicle taken separately, plus an additional quantity that arises from interference between the vehicle's various elements.

Let us consider, for example, a combination consisting of a body, pivoting wings, and fixed tail stabilizers (Fig. I-3-1). The value of c_{xi} depends on the lift coefficient of the particular combination, which is calculated by (I-4-1').

At small body angles of attack α and small wing incidence angles δ (small deflections of the wing chord from the rocket's longitudinal axis), the induced drag coefficient

$$c_{xi} = [c_{N\,b(wg,tl)} + c_{N\,tl(b,wg)}]\alpha + c_{N\,wg(b)}(\alpha+\delta), \qquad (I\text{-}3\text{-}2)$$

where $c_{N\,b(wg,\,tl)}$, $c_{N\,tl(b,\,wg)}$, and $c_{N\,wg(b)}$ are the normal-force coefficients of, respectively, the body in the presence of the wing and tail; the tail in the presence of the body and wing; the wing in the presence of the body. /16

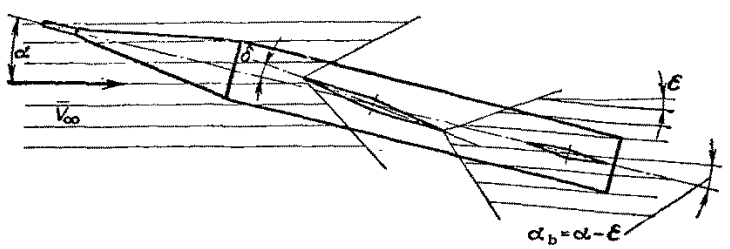

Figure I-3-1. Downwash Behind Wing.

Here it has been remembered that an additional drag-coefficient component $\delta c_{N\,wg(b,\,tl)}$ appears when the wing is deflected through an angle δ with respect to the axis of the body. Substituting the aerodynamic coefficients in (I-3-2) in accordance with their values from (I-4-3) and dropping the term containing the product of small quantities $\alpha\varepsilon$ (ε is the downwash angle, see Fig. I-3-1), we obtain

$$c_{xi} = K_1\alpha^2 + K_2\delta^2 + K_3\alpha\delta, \qquad (I\text{-}3\text{-}3)$$

where K_1, K_2, K_3 are the corresponding combinations of angle derivatives.

We then transform the resulting expression, dividing it by c_N^2, where c_N is the normal force coefficient of the combination and is determined by (I-4-5). As a result, Expression (I-3-3)

assumes the form

$$\frac{c_{xi}}{c_N^2} = \left[K_1\left(\frac{\alpha}{\delta}\right)^2 + K_2 + K_3\frac{\alpha}{\delta}\right]\left(c_N^{\alpha}\frac{\alpha}{\delta} + c_N^0\right)^{-2}. \qquad \text{(I-3-4)}$$

Since the attack and incidence angles are small, we can substitute c_y for c_N in (I-3-4). Further denoting the right member of (I-3-4) by K, we obtain the drag formula (I-3-1) in the form

$$c_x = c_{x0} + Kc_y^2. \qquad \text{(I-3-5)}$$

The curve defined by this equation is known as the parabolic drag polar.

We see from the equation that for K ≈ const, the drag varies as a square-law function of lift. Here c_{x_0}, the minimum of c_x, is reached at zero lift.

Research has indicated that a similar parabolic relationship

$$c_x - c_x^0 = K(c_y - c_y^0)^2 \quad \text{or} \quad \Delta c_x = K(\Delta c_n)^2 \qquad \text{(I-3-6)}$$

may also obtain in the more general case of flow in which the attack angles do not necessarily remain small. This more general case is characterized by minimum drag c_x^0 being reached not at zero lift, but at a certain finite lift c_y^0.

The curve representing this relation is shown in Fig. I-3-2. Parameter K characterizes the increase in drag on an increase in lift and is constant. The tangent drawn to the parabola from the origin determines the maximum lift/drag ratio

$$\left(\frac{c_y}{c_x}\right)_{max} = \frac{1}{2}\left[(c_{y\,optm} - c_y^0)K\right]^{-1}, \qquad \text{(I-3-7)}$$

where the optimum lift coefficient /17

$$c_{y\,optm} = \sqrt{(c_y^0)^2 + \frac{c_x^0}{K}}. \qquad \text{(I-3-8)}$$

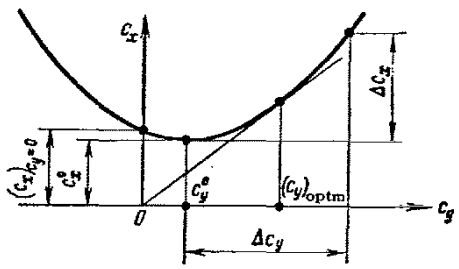

Figure I-3-2. Drag Polar.

The coefficient c_y^0 is zero for a vehicle with horizontal symmetry.

Aerodynamic properties can be analyzed with the aid of the drag curve either for combinations of bodies with lifting, controlling, and stabilizing surfaces or for the component parts in isolation. In all cases, these properties will be defined fully by the appropriate values of c_x^0, c_y^0, and K [see (I-3-6)].

The generalized polar. In a more general case, the frontal drag coefficient c_x varies in accordance with the law

$$c_x = c_{x0} + Kc_y^n. \qquad \text{(I-3-5')}$$

The curve of this equation is known as the generalized polar. The coefficient K and the exponent n are functions of M_∞ and Re.

According to (I-3-5'), the maximum lift-drag ratio

$$\left(\frac{c_y}{c_x}\right)_{max} = \frac{1}{n}\left(\frac{n-1}{c_{x0}}\right)^{\frac{n-1}{n}} K^{-\frac{1}{n}}. \qquad \text{(I-3-7')}$$

The value of $(c_y/c_x)_{max}$ corresponds to the optimum lift coefficient

$$c_{y\,optm} = \left[\frac{c_{x0}}{K(n-1)}\right]^{\frac{1}{n}} \qquad \text{(I-3-8')}$$

and to

$$\frac{Kc_y^n}{c_{x0}} = \frac{1}{n-1}.$$

For vehicles with thin-profile wings, we may set $n \approx 2$ for subsonic, transonic, and moderate supersonic speeds. At hypersonic speeds, a better approximation for such vehicles is $n \approx 3/2$.

The Body

There are various approaches to resolution of the resistance offered by the air to motion of the body into component parts. In the most general case, drag can be resolved into a component governed by pressure forces acting normal to the surface and a component associated with tangential friction that arises at the surface owing to the viscosity of the air.

The former component of drag is known as pressure drag and the latter as friction drag.

Usually, pressure drag is resolved, in turn, into two components, namely the drag due to pressure on the lateral surface (nose drag) and the drag due to pressure at the base section (wake drag).

Thus, the total drag /18

$$X = X_p + X_{wke} + X_f, \qquad \text{(I-3-9)}$$

where the terms on the right represent the nose, wake and friction drags, respectively.

Converting to the aerodynamic coefficients, we write an expression for the total drag coefficient referred to the area S_{mid} of the maximum (midships) section of the solid of revolution:

$$c_x = \frac{X}{qS_{mid}} = c_{xp} + c_{x\,wke} + c_{xf}, \qquad \text{(I-3-9')}$$

where the coefficients of nose, wake and friction drag, respectively, are represented on the right.

If the distribution of normal pressure over the surface is known,

$$c_{xp} = \frac{1}{S_{mid}} \int_{(S_{nde})} \bar{p} \cos(n, \bar{V}_\infty)\, dS_{nde}; \qquad \text{(I-3-10)}$$

$$c_{x\,wke} = \frac{1}{S_{mid}} \int_{(S_{wke})} \bar{p} \cos(n, \bar{V}_\infty)\, dS_{wke} \qquad \text{(I-3-11)}$$

where $\bar{p} = (p - p_\infty)/q$ is the pressure coefficient, cos $(n, \bar{V}_\infty)$ is the cosine of the angle between vector $\bar{V}_\infty$ and the normal $\underline{n}$ to the

surface of the body at the point under examination, and S_{sid} and S_{wke} are the side and base areas of the body, respectively.

For a flat base section, where cos $(n, \bar{V}_\infty)$ = const, the pressure is usually assumed constant at all points. If we assume that the normal $\underline{n}$ to the plane of the section coincides with the direction of the longitudinal axis, cos $(n, \bar{V}_\infty)$ = cos α. Then

$$c_{x\ wke} = \bar{p}_{wke} \cos\alpha \bar{S}_{wke} \qquad \text{(I-3-11')}$$

where $\bar{S}_{wke} = S_{wke}/S_{mid}$.

For small angles of attack

$$c_{x\ wke} = \bar{p}_{wke} \bar{S}_{wke}. \qquad \text{(I-3-11")}$$

The friction drag coefficient is determined from the tangential-stress distribution:

$$c_{xf} = \frac{1}{S_{mid}} \int\limits_{(S_{sde})} c_{fx} \cos(t, \bar{V}_\infty)\, dS_{sde}, \qquad \text{(I-3-12)}$$

where $c_{fx} = \tau/q$ is the local coefficient of friction and $\cos(t, \bar{V}_\infty)$ is the cosine of the angle between vector $\bar{V}_\infty$ and the tangent $\underline{t}$ to the body surface.

In aerodynamic research, it is more convenient to deal with the axial force, which coincides in direction with the body axis. The total axial force

$$R = R_p + R_{wke} + R_f, \qquad \text{(I-3-13)}$$

i.e., it is equal to the sum of three components, namely the axial force R_p from the pressure on the nose (or simply the axial pressure force), the axial force R_{wke} from the wake pressure (base axial force) and the friction axial force R_f. Converting to force coefficients, /19

$$c_R = \frac{R}{qS_{mid}} = c_{Rp} + c_{R\,wke} + c_{Rf}, \qquad \text{(I-3-13')}$$

where c_R is the coefficient of total axial force; c_{Rp}, $c_{R\ wke}$, and c_{Rf} are the respective coefficients of the pressure, wake, and friction axial forces.

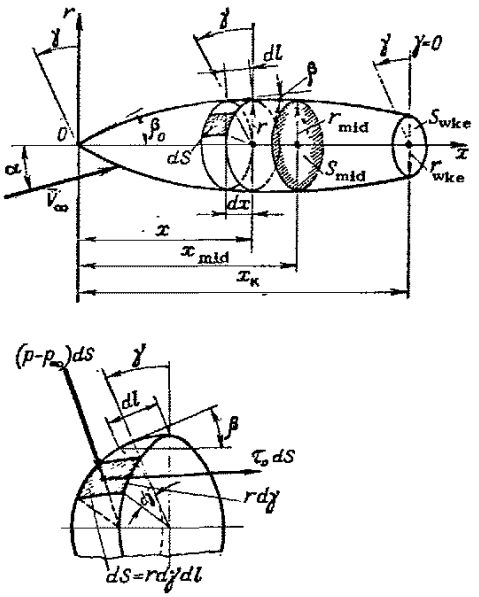

Figure I-3-3. Illustrating Derivation of Relationships Determining Aerodynamic Characteristics of Solid of Revolution from Known Distribution of Normal and Tangential Stresses.

The axial-force components and their coefficients can be determined if we know the distributions of normal pressure and tangential stress over the surface of the body.

Considering a body in the form of a solid of revolution and using the diagram in Fig. I-3-3, we can derive the following expressions for the coefficients of the total axial force components:

$$c_{Rp} = \frac{R_p}{qS_{mid}} = \frac{1}{\pi}\int_0^1 \frac{d\bar{r}^2}{d\tilde{x}}\,d\tilde{x}\int_0^\pi \bar{p}\,d\gamma; \quad \text{(I-3-14)}$$

$$c_{R\,wke} = \frac{R_{wke}}{qS_{mid}} = \bar{p}_{wke}\bar{S}_{wke}; \quad \text{(I-3-15)}$$

$$c_{Rf} = \frac{R_f}{qS_{mid}} = \frac{4\lambda_к}{\pi}\int_0^1 \bar{r}\,d\tilde{x}\int_0^\pi c_{fx}\,d\gamma. \quad \text{(I-3-16)}$$

Here $\bar{r} = r/r_{mid}$ is the ratio of the body's radius in a certain section to the radius of the midships section, $\tilde{x} = x/x_b$ is the axial distance to this section referred to the length of the body, and $\lambda_b = x_b/2r_{mid}$ is the fineness ratio of the solid of revolution.

Expressions (I-3-14) and (I-3-16) have been written for the general case of unsymmetrical flow over a body of revolution when the attack angle is not zero. At zero angle of attack (axisymmetric flow),

$$c_{Rp} = \int_0^1 \bar{p}\,\frac{d\bar{r}^2}{d\tilde{x}}\,d\tilde{x}; \quad \text{(I-3-14')}$$

$$c_{Rf} = 4\lambda_b\int_0^1 c_{fx}\bar{r}\,d\tilde{x}. \quad \text{(I-3-16')}$$

Wings (Lifting Surface)

Drag components. The drag of a lifting surface

$$X = X_p + X_f, \qquad \text{(I-3-17)}$$

where X_p is the pressure drag and X_f is the friction drag.

We can convert from forces to aerodynamic coefficients: /20

$$c_x = c_{xp} + c_{xf}, \qquad \text{(I-3-17')}$$

where c_x is the over-all drag coefficient, c_{xp} is the pressure drag coefficient, and c_{xf} is the friction drag coefficient.

The drag coefficients are usually referred to the wing plan area S_{wg}. If the pressure distribution over the wing surface is known,

$$c_{xp} = \frac{X_p}{qS_{wg}} = \frac{1}{S_{wg}} \int\limits_{(S_{wg})} \bar{p} \cos(n, \bar{V}_\infty)\, dS_{wg}. \qquad \text{(I-3-18)}$$

The friction drag coefficient is calculated from the tangential-stress distribution:

$$c_{xf} = \frac{X_f}{qS_{wg}} = \frac{1}{S_{wg}} \int\limits_{(S_{wg})} c_{fx} \cos(t, \bar{V}_\infty)\, dS_{wg}. \qquad \text{(I-3-19)}$$

Formula (I-3-18) applies for wings of any shape and, in particular, for wings with sharp or blunt trailing edges. For a wing with a blunted trailing edge, pressure drag also includes drag from the vacuum formed behind the edge. This component, which is analogous to the wake drag of a solid of revolution, is known as trailing-edge drag.

The trailing-edge drag coefficient can be found from a known distribution of the pressure $p_{b.e}$ on the blunt wing surface $S_{b.e}$:

$$c_{x\,b.e.} = \frac{1}{S_{wg}} \int\limits_{(S_{b.e.})} \bar{p}_{b.e.} \cos(n, \bar{V}_\infty)\, dS_{b.e.}, \qquad \text{(I-3-19')}$$

where $\bar{p}_{b.e}$ is the coefficient of pressure on the trailing edge at the point under consideration and $\cos(n, \bar{V}_\infty)$ is the cosine of the angle between vector $\bar{V}_\infty$ and the normal $\underline{n}$ to the blunt surface of the wing at the same point.

Retaining the symbol c_{xp} for the coefficient of pressure drag of the nose of the wing, we write the expression for the total drag coefficient

$$c_x = c_{xp} + c_{x\,b.e.} + c_{xf}. \qquad \text{(I-3-17")}$$

The profile. Let us now apply our relationships to calculation of the aerodynamic characteristics of a wing profile, assuming that the distribution of pressure and frictional stress over the profile is known.

The drag coefficient from the normal pressure, referred to chord $\underline{b}$ of the profile (Fig. I-3-4), is

$$c_{xp} = \frac{1}{b}\oint \bar{p}\cos(n, \bar{V}_\infty)\,ds. \qquad \text{(I-3-20)}$$

where $\oint$ is the line integral over the profile contour, and ds is an arc element of the contour.

The friction drag coefficient can also be found by evaluating the line integral

$$c_{xf} = \frac{1}{b}\oint c_{fx}\cos(t, \bar{V}_\infty)\,ds. \qquad \text{(I-3-21)}$$

The total profile drag coefficient will be equal to the sum of the coefficients c_{xp} and c_{xf}. Here the total coefficient, like its components, is calculated from the area of a wing of unit width $b \cdot 1$. /21

Let us consider how the corresponding aerodynamic coefficients are computed in the body coordinate system whose horizontal x_1-axis coincides with the chord (Fig. I-3-4).

The coefficient of the axial pressure force

$$c_{Rp} = \frac{1}{b}\oint \bar{p}\cos(n, x_1)\,ds, \qquad \text{(I-3-22)}$$

and the coefficient of the axial friction force

$$c_{Rf} = \frac{1}{b}\oint c_{fx}\cos(t, x_1)\,ds, \qquad \text{(I-3-23)}$$

where cos (n, x_1) and cos(t, x_1) are the respective cosines of the angles between the outer normal $\underline{n}$ and the tangent $\underline{t}$ to the contour at the particular point and the x_1- axis.

If $\cos(t, x_1) = \cos\beta$, then $\cos(n, x_1) = \sin\beta$. For ds, we have the relation $ds = dx_1/\cos\beta$. On converting from line to ordinary integrals, therefore, we obtain the following expressions for the aerodynamic-coefficient components:

$$c_{Rp} = \int_0^1 \bar{p}_u \left(\frac{dy_1}{dx_1}\right)_u d\bar{x}_1 + \int_1^0 \bar{p}_l \left(\frac{dy_1}{dx_1}\right)_l d\bar{x}_1; \qquad \text{(I-3-24)}$$

$$c_{Rf} = \int_0^1 (c_{fx})_u\, d\bar{x}_1 + \int_0^1 (c_{fx})_u\, d\bar{x}_1, \qquad \text{(I-3-25)}$$

where $\bar{x}_1 = x_1/b$; dy_1/dx_1 is the derivative of the function $y_1 = f(x_1)$, and is defined by the contour equation.

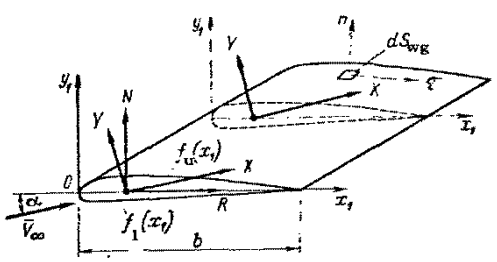

Figure I-3-4. Forces Acting on Wing.

The subscripts "l" and "u" indicate that the respective parameters are taken on the lower and upper segments of the profile contour.

The total axial force coefficient

$$c_R = c_{Rp} + c_{Rf}. \qquad \text{(I-3-26)}$$

The value of c_{Rp} may also include the drag of a blunt trailing edge if there is one. However, it is more convenient to separate this drag component and, assuming that the edge lies along the normal to the x_1-axis, to represent it as follows:

$$c_{R\,b.e.} = \bar{p}_{b.e}\bar{c}_{b.e}, \qquad \text{(I-3-27)}$$

where $c_{b.e} = c_{b.e}/b$ is the dimensionless height of the trailing edge.

Accordingly, the axial-force coefficient

$$c_R = c_{Rp} + c_{Rb.e.} + c_{Rf}. \qquad \text{(I-3-26')}$$

For a rectangular wing of infinite span, the drag coefficient is equal to the value found for the profile. On a section of such a wing with area S_{wg}, the drag force $X = c_x q S_{wg}$.

To determine the drag coefficient of an arbitrary planform wing of finite span and area S_{wg}, it is necessary to know the values of the coefficients c_x for a series of sections (profiles) taken along the span ℓ (Fig. I-3-5). The corresponding wing drag coefficient is determined by integration over the span: /22

$$c_x = \frac{X}{qS_{wg}} = \frac{2}{S_{wg}} \int_0^{l/2} c_x b(z)\, dz. \qquad \text{(I-3-28)}$$

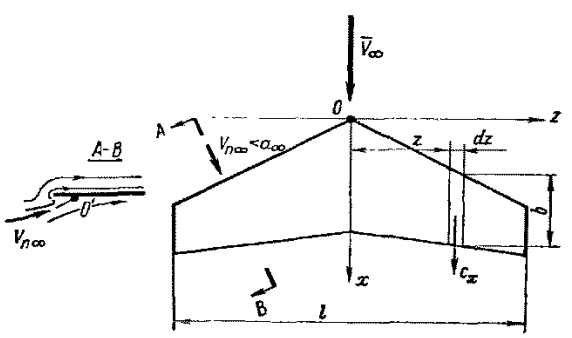

Figure I-3-5. Illustrating Determination of Wing Aerodynamic Characteristics.

Other forms of drag representation. In resolving wing drag into components, it is possible to isolate the component associated with lift. This component X_i is known as the <u>induced drag</u>. When it is added to that part of drag that is not associated with formation of lift and is known as the <u>wing profile drag</u> X_{pr}, the result is the total drag $X = X_{pr} + X_i$.

If $c_{x\,pr}$ and c_{xi} are the coefficients of profile and induced drag, respectively, the expression for the total drag coefficient is represented as the sum

$$c_x = c_{x\,pr} + c_{xi}. \qquad \text{(I-3-29)}$$

Profile drag consists of the pressure and friction drags and determines the total drag when c_{xi} is zero.

The profile drag coefficient can be written by analogy with (I-3-6) in the form (see Fig. I-3-2):

$$c_x = c_{x\,pr} + Kc_y(c_y - 2c_y^0). \qquad \text{(I-3-30)}$$

The component $c_{x\,pr}$, which does not depend on attack angle, and the component c_{xi}, which is governed by lift, have been separated in this formula. The former component

$$c_{x\,pr} = c_x^0 + K(c_y^0)^2; \qquad \text{(I-3-31)}$$

and the latter

$$c_{xi} = Kc_y(c_y - 2c_y^0). \qquad \text{(I-3-32)}$$

For horizontal symmetry, $c_y^0 = 0$ and $c_{x\,pr} = c_x^0$, while $c_{xi} = Kc_y^2$.

Properties of wing drag peculiar to supersonic speeds. In calculating the drag of wings moving at supersonic speeds, certain peculiarities of the flow over them must be taken into consideration. These pertain to wings with subsonic leading edges. Subsonic and supersonic wing edges will be discussed in greater detail on page 67. A wing leading edge will be subsonic if the velocity component $V_{n\infty}$ of the free stream perpendicular to it is smaller than the speed of sound a_∞. The wing profile is then in subsonic flow (see Fig. I-3-5). At the critical point 0' (point of total stagnation), which is situated not far from the leading edge on the bottom side of the wing at an angle of attack, the flow branches, and part of it moves forward, flowing over the leading edge. If the flow does not separate, a vacuum zone forms at the leading edge, creating a suction force that lowers drag. Research has shown that this force is proportional to a coefficient equal in magnitude to αc_y. If the proportionality coefficient is denoted by μ, the suction force will be $\mu\alpha c_y$. /23

Let us further denote by c_{Rp} the coefficient of the axial pressure force, which does not depend on suction force, for a wing with a symmetrical profile. Then the over-all axial-force coefficient at a certain angle of attack will be

$$c_R = c_{Rp} + \mu\alpha c_y + c_{Rf}.$$

Assuming that the attack angles are small, so that $c_N \approx c_y$, we obtain according to (I-2-3)

$$c_x = -\alpha c_y (1-\mu) + c_{Rp} + c_{Rf}. \qquad \text{(I-3-33)}$$

For $\alpha = 0$

$$c_x = c_{x0} = (c_{Rp})_0 + (c_{Rf})_0. \qquad \text{(I-3-33')}$$

The wing's aerodynamic properties can be characterized by the coefficient of drag increase

$$K = \frac{\Delta c_x}{c_y^2} = \frac{c_x - c_{x0}}{c_y^2} = -\frac{(1-\mu)}{c_y^\alpha} + \frac{c_{Rp} - (c_{Rp})_0}{c_y^2} + \frac{c_{Rf} - (c_{Rf})_0}{c_y^2}, \qquad \text{(I-3-34)}$$

where $c_y^\alpha = \partial c_y / \partial \alpha = c_y / \alpha$.

Research has shown that the principal term determining K is the first, $-(1 - \mu)/c_y^\alpha$, which is basically determined by the pressure drag, whose distribution is governed by wave phenomena and interaction between the external flow and the vortex trail behind the wing. The coefficient μ is nonzero for subsonic leading edges and zero for supersonic leading edges.

The second term in Formula (I-3-34) is governed by the difference between the axial forces, which depend on pressure, for $\alpha \neq 0$ and $\alpha = 0$. Study has shown that this difference is proportional to the product of the profile thickness ratio Δ/b by the attack angle. The quantity $c_{Rp} - (c_{Rp})_0$ may increase as a result of boundary-layer separation.

Finally, the third term is associated with the variation of friction as a function of attack angle. This variation is so slight that it may be disregarded in practice.

§I-4. LIFT

Winged Vehicle

Let us examine the general expression for the lift of the vehicle formed by combining a body, wing, and tail, for which we derived the drag relationship above. The lift

$$Y = Y_{b(wg,t)} + Y_{wg(b)} + Y_{t(b,wg)}. \qquad \text{(I-4-1)}$$

where $Y_{b(wg,tl)}$ is the body's lift in the presence of the wing and tail; $Y_{wg(b)}$ is the wing lift in the presence of the body; $Y_{tl(b,wg)}$ is the tail lift in the presence of the body and wing. /24

The corresponding lift coefficient

$$c_y = c_{y\,b(wg,tl)} + c_{y\,wg(b)} + c_{y\,tl\,(b,wg)}. \qquad (I\text{-}4\text{-}1')$$

These expressions take account of the effect of interference between the individual elements of the vehicle on total lift. If we succeed in separating the individual interference-dependent components from the total lift, the lift coefficient

$$c_y = c_{y\,b} + c_{y\,wg} + c_{y\,tl} + \Delta c_{y\,b(wg,tl)} + \Delta c_{y\,wg(b)} + \Delta c_{y\,tl(b,wg)}$$

where the first three components pertain to the body, wings, and tail in isolation, and the others determine the secondary, interference components of lift.

Instead of lift and its components, we might consider the normal force and its corresponding components, which characterize the lifting capability of the vehicle.

The total coefficient of normal force

$$c_N = c_{N\,b(wg,tl)} + c_{N\,wg(b)} + c_{N\,tl(b,wg)}. \qquad (I\text{-}4\text{-}2)$$

From the normal-force coefficient we can find the lift coefficient by using the formula for conversion from body to wind axes. Let us assume that together with small attack angles α, we also have small wing setting angles δ relative to the body axis. Then the normal-force components

$$\left.\begin{aligned} c_{N\,b(wg,tl)} &= c^{\alpha}_{N\,b(wg,tl)}\,\alpha; \\ c_{N\,wg(b)} &= c^{\alpha}_{N\,wg(b)}\alpha + c^{\delta}_{N\,wg(b)}\delta; \\ c_{N\,tl(b,wg)} &= c^{\alpha}_{N\,tl(b,wg)}\,(\alpha - \varepsilon), \end{aligned}\right\} \qquad (I\text{-}4\text{-}3)$$

where the superscripts "α" and "δ" are the partial derivatives of the normal-force coefficient with respect to α and δ, respectively; ε is the angle of downwash behind the wing.

Thus, the total coefficient of normal force

$$c_N = c_N^{\alpha}\alpha + c_N^{\delta}\delta - c_{N\ tl(b,wg)}^{\alpha}\varepsilon, \qquad (I\text{-}4\text{-}4)$$

where

$$c_N^{\alpha} = c_{N\ wg(b)}^{\alpha} + c_{N\ b(wg,tl)}^{\alpha} + c_{N\ tl(b,wg)}^{\alpha};\ c_N^{\delta} = c_{N\ wg(b)}^{\delta}$$

The last term in the right member of (I-4-4) characterizes the effect of interference of the wing with the tail on the normal force. This effect is small if we remember that the tail area is relatively small. However, the effect of interference on moment may be substantial in view of the long arm at which the tail acts.

Disregarding the interference term on the right side of (I-4-4), we find the relation

$$\frac{c_N}{\delta} = c_N^{\alpha}\frac{\alpha}{\delta} + c_N^{\delta}, \qquad (I\text{-}4\text{-}5)$$

which characterizes the sensitivity of the vehicle to controlling efforts set up by the wing. The controllability parameter c_N/δ depends only on the ratio α/δ for a given vehicle design and a given flight speed.

Body /25

The lift Y of the body can be represented as the sum of two components Y_p and Y_f, the first of which depends on the normal-pressure distribution, while the second is a function of tangential-stress distribution. The total lift coefficient

$$c_y = c_{yp} + c_{yf}, \qquad (I\text{-}4\text{-}6)$$

where c_{yp} is the lift coefficient due to normal pressure and c_{yf} is the lift coefficient due to friction.

The components of the lift coefficient can be computed if we know the distribution of pressure and tangential stress over the body:

$$c_{yp} = \frac{1}{S_{\text{mid}}} \int_{(S)} \bar{p} \sin(n, \bar{V}_\infty)\, dS; \qquad \text{(I-4-7)}$$

$$c_{yf} = \frac{1}{S_{\text{mid}}} \int_{(S)} c_{fx} \sin(t, \bar{V}_\infty)\, dS. \qquad \text{(I-4-8)}$$

Here S is the total area of the body, including its sides and the base-section area. Usually, the effect of the lift component due to friction behind the base is not taken into account because of its smallness; hence we set $S = S_{\text{sid}}$ in (I-4-8).

Although it remains small, the lift component that arises from the wake pressure may still influence body lift more strongly than the frictional component. The coefficient of the lift component due to wake pressure

$$c_{y\,\text{wke}} = \frac{1}{S_{\text{mid}}} \int_{(S_{\text{wke}})} \bar{p}_{\text{wke}} \sin(n, \bar{V}_\infty)\, dS_{\text{wke}}. \qquad \text{(I-4-9)}$$

If $c_{y\ \text{wke}}$ is computed separately, $S = S_{\text{sid}}$ should be used in (I-4-7), thus determining the lift component that depends on the distribution of normal pressure over the lateral surface.

If the base section is flat, $\sin(n, \bar{V}_\infty) = \sin\alpha$. Assuming further that $\bar{p}_{\text{wke}} = \text{const}$ behind the base, we find

$$c_{y\,\text{wke}} = \bar{p}_{\text{wke}} \sin\alpha \bar{S}_{\text{wke}}. \qquad \text{(I-4-9')}$$

For small α, the coefficient $c_{y\ \text{wke}} = \bar{p}_{\text{wke}} \alpha \bar{S}_{\text{wke}}$.

The normal-force coefficient

$$c_N = c_{Np} + c_{Nf}, \qquad \text{(I-4-10)}$$

where c_{Np} is the component governed by the normal pressure on the lateral surface and c_{Nf} is the component generated by friction.

For a solid-of-revolution body (see Fig. I-3-3), the component c_{Np} of the normal-force coefficient can be found from the known pressure distribution by the formula

$$c_{Np} = \frac{N_p}{qS_{\text{mid}}} = -\frac{4\lambda_{\text{H}}}{\pi} \int_0^1 \bar{r}\, d\bar{x} \int_0^\pi \bar{p} \cos\gamma\, d\gamma. \qquad \text{(I-4-11)}$$

The second component c_{Nf} is calculated from the known tangential-stress distribution:

$$c_{Nf} = \frac{N_f}{qS_{mid}} = -\frac{4\lambda_b}{\pi}\int_0^1 \bar{r}\,\mathrm{tg}\,\beta\, d\bar{x}\int_0^{\pi} c_{fx}\cos\gamma\, d\gamma, \qquad \text{(I-4-12)}$$

where tan β = dr/dx.

Wings (Lifting Surface) /26

The lift of a wing or of lifting surfaces in general can be expressed, like the body lift, as the sum of two components, one of which is governed by the action of normal pressure forces and the other by friction. Accordingly, the total lift coefficient is expressed by Formula (I-4-6).

The components are calculated by the formulas

$$c_{yp} = \frac{1}{S_{wg}}\int_{(S_{wg})} \bar{p}\sin(n, \bar{V}_\infty)\, dS_{wg}, \qquad \text{(I-4-13)}$$

$$c_{yf} = \frac{1}{S_{wg}}\int_{(S_{wg})} c_{fx}\sin(t, \bar{V}_\infty)\, dS_{wg}. \qquad \text{(I-4-14)}$$

If the wing has a blunt trailing edge, it is advisable to separate the part of the lift that originates from suction at the trailing edge from the component c_{yp}. The coefficient of this lifting force is

$$c_{y\,b.e} = \frac{1}{S_{wg}}\int_{(S_{b.e.})} \bar{p}\sin(n, \bar{V}_\infty)\, dS_{b.e.}, \qquad \text{(I-4-15)}$$

The frictional lift coefficient is usually calculated without consideration of the influence of friction at the trailing edge.

Formulas (I-4-13) and (I-4-14) are used to determine profile lift components. Setting the profile chord equal to b and referring the aerodynamic coefficients to the area b·1, we write

$$c_{yp} = \frac{1}{b}\oint \bar{p}\sin(n, \bar{V}_\infty)\, ds; \qquad \text{(I-4-16)}$$

$$c_{yf} = \frac{1}{b}\oint c_{fx} \sin(t, \bar{V}_\infty)\, ds. \qquad \text{(I-4-17)}$$

Here, instead of integrating over the area S_{wg}, a line integral over an arc of the profile contour s is evaluated.

Let us examine general expressions for the profile's normal-force coefficient and its components. For the over-all normal-force coefficient, we have Formula (I-4-10), in which c_{Np} is the wing normal force coefficient, computed from the normal pressure distribution and c_{Nf} is the normal force coefficient computed from the tangential stress distribution. The working formulas for these coefficients are:

$$c_{Np} = \frac{1}{b}\oint \bar{p} \sin(n, x_1)\, ds; \qquad \text{(I-4-18)}$$

$$c_{Nf} = \frac{1}{b}\oint c_{fx} \sin(t, x_1)\, ds. \qquad \text{(I-4-19)}$$

We can convert from line to ordinary integrals:

$$c_{Np} = \int_0^1 \bar{p}_u d\bar{x}_1 + \int_1^0 \bar{p}_l d\bar{x}_1; \qquad \text{(I-4-20)}$$

$$c_{Nf} = \int_0^1 (c_{fx})_u \left(\frac{dy_1}{dx_1}\right)_u d\bar{x}_1 + \int_1^0 (c_{fx})_l \left(\frac{dy_1}{dx_1}\right)_l d\bar{x}_1. \qquad \text{(I-4-21)}$$

Knowing the coefficient of normal force and its components, and using the appropriate formulas for conversion from body to wind axes, we can determine the profile's lift coefficient. /27

The lift $Y = c_y q S_{wg}$ is computed from the coefficient $c_y = c_{yp} + c_{yf}$ for a section of an infinite-span rectangular wing with area S_{wg}.

For a wing of finite span and arbitrary planform, the total lift coefficient is found by integrating the elementary lift values over the span:

$$c_{y\,wg} = \frac{Y}{qS_{wg}} = \frac{2}{S_{wg}} \int_0^{l/2} c_y b(z)\, dz, \qquad \text{(I-4-22)}$$

where c_y is the profile lift coefficient.

§I-5. MOMENT

Winged Vehicle

An aerodynamic moment acting on a vehicle of arbitrary shape can be computed with respect to any point. In aerodynamic research, it is more convenient to choose a fixed point as this point of reduction, one that is bound to the body and does not change position during flight. We shall henceforth refer this calculation to the body nose of the vehicle or its center of gravity, regarding the position of the latter as fixed.

In general form, for a vehicle consisting of individual elements (body, wing, tail, etc.), moment is determined as the sum of body, wing, tail, and other components with consideration of interference effects.

Let us consider the general expression for pitching moment. The coefficients of the rolling and yawing moments can be presented similarly. For a body-pivoting wing-stabilizer combination, we have

$$m_z = m_{z\,b(wg,tl)} + m_{z\,wg(b)} + m_{ztl(b,wg)}. \qquad (I\text{-}5\text{-}1)$$

Here the subscripts have the same significance as above.

In turn, each moment-coefficient component can be determined if we know the normal and axial force components and the corresponding arms, i.e., the distances along the $\underline{x}$- and $\underline{y}$-axes to the center of pressure.

For the body, for example, the component $m_{z\,b(wg,\underline{tl})} = (c_N\bar{x}_{c.p} + c_R\bar{y}_{c.p})_{b(wg,tl)}$, where $\bar{x}_{c.p} = x_{c.p}/x_b$ and $\bar{y}_{c.p} = y_{c.p}/x_b$ ($x_{c.p}$ and $y_{c.p}$ are the coordinates of the center of pressure and x_b is a characteristic linear dimension). For the vehicle as a whole, the moment coefficient

$$m_z = \sum_{i=1}^{3} (c_N\bar{x}_{c.p.} + c_R\bar{y}_{c.p.})_i, \qquad (I\text{-}5\text{-}2)$$

where the summation is extended over all elements (body, wing, tail).

In calculating the moment, the positive direction corresponds to rotation along the shortest arc from the x-axis to the y-axis.

For a body-pivoting wing-stabilizer combination, the moment coefficient at a given speed can be represented as a function $m_z = f(\alpha,\delta)$. For small angles α and δ, the moment is a linear function of attack angle and wing deflection, /28

$$m_z = m_z^{\alpha}\alpha + m_z^{\delta}\delta + m_{z0}, \qquad \text{(I-5-3)}$$

where m_{z_0} is the moment coefficient for $\alpha = \delta = 0$. For a design with horizontal symmetry, $m_{z_0} = 0$.

Body

Like a force, an aerodynamic moment acting on the body can be represented as a sum of two components — moments of pressure and friction forces. Accordingly, the total coefficient of pitching moment

$$m_z = m_{zp} + m_{zf}, \qquad \text{(I-5-4)}$$

where m_{zp} is the moment coefficient of the normal pressure forces and m_{zf} is the friction moment coefficient.

The two components can be determined by integrating elementary moments created by normal-pressure and tangential-stress forces, respectively, over the area of the body. The component

$$m_{zp} = \frac{1}{x_b}\int_{(S)}\left(x\frac{dc_{Np}}{dS} - y\frac{dc_{Rp}}{dS}\right)dS, \qquad \text{(I-5-5)}$$

or

$$m_{zp} = \frac{1}{S_{mid}x_b}\int_{(S)}\bar{p}\left[x\sin(n, x_1) - y\cos(n, x_1)\right]dS. \qquad \text{(I-5-6)}$$

Figure I-3-3 can be used to determine the signs of the components. The surface element dS is so selected that $dr/dx > 0$ for it and, consequently, the moments from the elementary normal and axial forces will be negative. Since, according to Fig. I-3-3, dc_{Np} is negative, the plus sign is taken before the first terms in the expressions for m_{zp}.

The frictional component of the moment coefficient

$$m_{zf} = \frac{1}{x_b} \int_{(S)} \left(x \frac{dc_{Nf}}{dS} - y \frac{dc_{Rf}}{dS} \right) dS, \qquad \text{(I-5-7)}$$

or

$$m_{zf} = \frac{1}{S_{mid} x_b} \int_{(S)} c_{fx} [x \sin(t, x_1) - y \cos(t, x_1)] \, dS. \qquad \text{(I-5-7')}$$

In investigating the moment characteristics of the body, the influence of the base section can be excluded, since it is very small in practice. Then integration will be performed over the side surface in all of the formulas given above.

Let us consider the moment characteristics for a solid-of-revolution body (see Fig. I-3-3) for the condition that the moment and its components are calculated with respect to the nose. The moment coefficient of the normal-pressure forces

$$m_{zp} = \frac{M_{zp}}{qS_{mid} x_b} = -\frac{4\lambda_b}{\pi} \int_0^1 \bar{r}\bar{x} \, d\bar{x} \int_0^\pi \bar{p} \cos\gamma \, d\gamma - \\ -\frac{2}{\pi} \int_0^1 \bar{r}^2 \operatorname{tg}\beta \, d\bar{x} \int_0^\pi \bar{p} \cos\gamma \, d\gamma. \qquad \text{(I-5-8)}$$

If the body is slender, the second term in this formula will be small. /29

The frictional component of the moment is also found by surface integration:

$$m_{zf} = \frac{M_{zf}}{qS_{mid} x_b} = -\frac{4\lambda_b}{\pi} \int_0^1 \bar{x}\bar{r} \operatorname{tg}\beta \, d\bar{x} \int_0^\pi c_{fx} \cos\gamma \, d\gamma - \\ -\frac{2}{\pi} \int_0^1 \bar{r}^2 \, d\bar{x} \int_0^\pi c_{fx} \cos\gamma \, d\gamma. \qquad \text{(I-5-9)}$$

The moment component, like the friction-dependent aerodynamic-force components, is not always the same in order of magnitude as the normal-pressure components. Studies have shown that friction has a stronger influence for long slender bodies in flow at large angles of attack.

Wing and Profile

The moment and the corresponding coefficient for a wing are usually computed with respect to a z-axis passing through the wing apex (see Fig. I-3-5). The total moment coefficient is decomposed into a component m_{zp} that depends on the normal pressure distribution and a component m_{zf} that depends on tangential-stress distribution.

By analogy with the corresponding expressions for the body

$$m_{zp} = \frac{1}{S_{wg} b_{MAC}} \int_{(S_{wg})} [x\bar{p} \sin(n, x_1) - y\bar{p} \cos(n, x_1)]\, dS_{wg}; \qquad \text{(I-5-10)}$$

$$m_{zf} = \frac{1}{S_{wg} b_{MAC}} \int_{(S_{wg})} [xc_{fx} \sin(t, x_1) - yc_{fx} \cos(t, x_1)]\, dS_{wg}. \qquad \text{(I-5-11)}$$

It follows from the formulas that the moment coefficients are referred to the wing plan area S_{wg} and the mean aerodynamic chord b_{MAC}.

The corresponding working relationships for the profile have the form of line integrals:

$$m_{zp} = \frac{1}{b^2} \oint \bar{p} [x \sin(n, x_1) - y \cos(n, x_1)]\, ds; \qquad \text{(I-5-12)}$$

$$m_{zf} = \frac{1}{b^2} \oint c_{fx} [x \sin(t, x_1) - y \cos(t, x_1)]\, ds, \qquad \text{(I-5-13)}$$

which are evaluated over an arc of contour s.

Determining the moment, which is calculated in this case about the leading edge, as the sum of the moments for the upper and lower parts of the contour, we obtain

$$m_{zp} = \int_0^1 \left[\bar{x}_1 \bar{p}_u - \bar{y}_{1u} \left(\frac{dy_1}{dx_1}\right)_B \bar{p}_u\right] dx_1 + \int_1^0 \left[\bar{x}_1 \bar{p}_1 - \bar{y}_{11} \left(\frac{dy_1}{dx_1}\right)_H \bar{p}_1\right] d\bar{x}_1; \qquad \text{(I-5-14)}$$

$$m_{zf} = \int_0^1 \left[\bar{x}_1 (c_{fx})_u \left(\frac{dy_1}{dx_1}\right)_u - \bar{y}_{1u} (c_{fx})_u\right] d\bar{x}_1 +$$

$$+ \int_1^0 \left[\bar{x}_1 (c_{fx})_1 \left(\frac{dy_1}{dx_1}\right)_1 - \bar{y}_{11} (c_{fx})_1\right] d\bar{x}_1, \qquad \text{(I-5-15)}$$

where $\bar{x}_1 = x_1/b$; $\bar{y}_1 = y_1/b$.

The profile moment coefficient is equal to the sum of the components, i.e., $m_z = m_{zp} + m_{zf}$. If the spanwise distribution of the m_z is known for a wing of given planform (see Fig. I-3-5), the total coefficient of the wing moment about the z_1-axis can be found: /30

$$m_{z\,wg} = \frac{M_{z\,wg}}{qS_{wg}b_{MAC}} = \frac{2}{S_{wg}b_{MAC}}\left[\int_0^{l/2} x_1(z)\,b(z)\,c_N\,dz + \int_0^{l/2} b^2(z)\,m_z\,dz\right], \quad \text{(I-5-16)}$$

where x_1 is the distance from the z_1-axis to the wing leading edge.

If the wing has a dihedral, the moment coefficient

$$m_{z\,wg} = \frac{2}{S_{wg}b_{MAC}}\left[\int_0^{l/2} x_1(z)\,b(z)\,c_N\,dz + \int_0^{l/2} b^2(z)\,m_z\,dz \mp \int_0^{l/2} c_R b(z)\,y\,dz\right]. \quad \text{(I-5-16')}$$

For a positive dihedral (vee wings), the minus sign should appear in front of the third term in the right member; the plus sign appears for negative dihedral (drooped wings).

§I-6. APPLICATION OF AERODYNAMIC CHARACTERISTICS IN STUDY OF FLIGHT STABILITY OF BODIES

Static Stability

Longitudinal and lateral stability. Random disturbances (the initial jolt on leaving the launcher, wing gusts, deviations from nominal engine output, etc.) may result in changes of the attack and slip angles of a body in motion. The moment that appears as a result causes a further change in these angles after the disturbance has ceased to act.

If the angles α and β_{s1} tend to return to their original values, flight is said to be statically stable. If the deviation continues to increase, we have static instability.

Static stability is resolved into longitudinal static stability, directional static or weathercock stability, and lateral static stability.

In the presence of longitudinal static stability, the pitching moment that arises will be stabilizing, i.e., it will tend to restore the original attack angle. In this case, the direction of change of the moment M_z (and, accordingly, of the coefficient m_z) will be opposed to the direction in which the angle α has changed. Consequently, the longitudinal static stability condition can be expressed by the inequalities $\partial M_z/\partial\alpha < 0$ or $\partial m_z/\partial\alpha = m_z^{\alpha} < 0$.

In the case of longitudinal static instability, a destabilizing tumbling moment appears and tends to change the attack angle even more. Consequently, the condition for longitudinal static instability will be the inequality $\partial m_z/\partial\alpha = m_z^{\alpha} > 0$.

Obviously, directional static stability is characterized by the inequality $\partial M_y/\partial\beta_{sl} < 0$ or $\partial m_y/\partial\beta_{sl} = m_y^{\beta} < 0$; directional static stability will be characterized by $\partial M_y/\partial\beta_{sl} > 0$ or $\partial m_y/\partial\beta_{sl} = m_y^{\beta} > 0$. The directions of the changes in yawing moment and slip angle are different in the former case and the same in the latter. Accordingly, the moments will be stabilizing and destabilizing directional moments. /31

The derivative $\partial M_x/\partial\beta_{sl}$ or $\partial m_x/\partial\beta_{sl} = m_x^{\beta}$ is a measure of lateral static stability (or static stability in roll). If the derivative $m_x^{\beta} < 0$, the vehicle has lateral static stability. If $m_x^{\beta} > 0$, we have lateral static instability.

A vehicle is neutral as regards longitudinal static stability, weathercock stability, or lateral static stability if $m_z^{\alpha} = 0$, $m_y^{\beta} = 0$, $m_x^{\beta} = 0$.

Center of pressure coefficient. Aerodynamic center. The center of pressure coefficient is one of the parameters of static stability. For example, the center of pressure coefficient is a parameter of longitudinal static stability and is defined from the condition $\bar{x}_{c.p} = x_{c.p}/\ell = m_z/c_N$, where $x_{c.p}$ is the distance from the center of pressure to the point about which the longitudinal moment is determined.

Suppose that this point is the nose of the body. Then we can take the distance between the center of gravity $x_{c.g}$ and the center of pressure $x_{c.p}$ as a characteristic (criterion) of static stability. If the difference $\bar{x}_{c.p} - \bar{x}_{c.g}$ is positive ($\bar{x}_{c.g} = x_{c.g}/\ell$), i.e., the center of pressure lies aft of the center of gravity, flight will be statically stable. If the center of

pressure is forward (the difference $\bar{x}_{c.p} - \bar{x}_{c.g}$ is negative), we have static instability.

The criterion $\bar{x}_{c.p} - \bar{x}_{c.g}$ is sometimes known as the static stability margin. It may be positive (static stability), negative (static instability), or zero (neutral longitudinal stability).

If the pitching moment is determined about the center of gravity, the parameter $\bar{x}_{c.p}$ itself can be treated as a stability criterion. In the linear range of attack angles, $\bar{x}_{c.p}$ can be presented in the form $\bar{x}_{c.p} = \partial m_z/\partial c_N$. If $\partial m_z/\partial c_N < 0$, flight will be statically stable; when $\partial m_z/\partial c_N > 0$, it is unstable. The parameter $\bar{x}_{c.p} = \partial m_z/\partial c_N$ is known as the longitudinal stability coefficient.

For unsymmetrical designs or symmetrical ones with deflected controls, it is more convenient to use the dimensionless center distance instead of the center of pressure coefficient as a static criterion. Applying (I-2-9) we write the equality

$$m_{z1} = -(c_{c.p.} - \bar{x}_b) c_N = m_z + \bar{x}_T c_N = m_{z0} + \left(\frac{\partial m_z}{\partial c_N} + \bar{x}_b\right) c_N, \qquad \text{(I-6-1)}$$

which determines the coefficient m_{z_1} of the moment about a lateral axis passing through a certain point with coordinate $\bar{x}_b$ in terms of the coefficient m_z of the moment about the nose of the vehicle and the normal lift coefficient c_N. The signs in (I-6-1) have been so selected that the moment is positive when it acts to increase attack angle and negative when it acts in the opposite direction.

The point with the coordinate $\bar{x}_b = \bar{x}_F$, at which $\partial m_z/\partial c_N + \bar{x}_F = 0$, is the aerodynamic center. The dimensionless center coordinate x_F is determined by the formula

$$\bar{x}_F = -\frac{\partial m_z}{\partial c_N}. \qquad \text{(I-6-2)}$$

Thus, /32

$$m_{z1} = m_{z0} - (\bar{x}_F - \bar{x}_b) c_N, \qquad \text{(I-6-3)}$$

where $\bar{x}_b$ may be the dimensionless coordinate of the center of gravity. Then it follows from (I-6-3) that flight will be statically stable if the aerodynamic center is aft of the center of gravity and unstable if it is forward of it, i.e., the vehicle's degree of static stability depends on the relative positions of its aerodynamic and gravity centers.

The trim condition. This condition, which is necessary for statically stable straight-line flight in the longitudinal plane, takes the form $m_z = 0$. This condition is satisfied by deflecting the elevator through the appropriate angle. Setting $m_z = 0$ in (I-5-3), we obtain the equation of trimmed flight:

$$m_z^\alpha \alpha + m_z^\delta \delta + m_{z0} = 0. \qquad \text{(I-6-4)}$$

The trim characteristic, the ratio of attack angle to control deflection angle, is found from this equation. For a given design and speed, this characteristic is a function of the angle δ. For a symmetrical design, the trim ratio α/δ is independent of control-surface deflection and given by the formula

$$\frac{\alpha}{\delta} = -\frac{m_z^\delta}{m_z^\alpha}. \qquad \text{(I-6-5)}$$

Dynamic Stability

The concept of dynamic stability. Analysis of the derivatives of the aerodynamic moments with respect to α or β_{s1} makes is possible to establish whether the body has one or another form of static stability. However, this analysis is not sufficient to evaluate the flight properties of the body in motion, since it does not answer the question as to the nature of the body's motion after cessation of a disturbance, or of the magnitude of the parameters determining this motion. Indeed, if we know, for example, that the derivative $\partial m_z/\partial\alpha$ is negative and that, consequently, the pressure center is aft of the center of gravity, we may infer only longitudinal static stability. But we cannot tell, for example, the amplitude of the attack-angle fluctuations at a given value of the initial disturbance parameter or how it varies in time. Dynamic stability theory gives the answers to all of these and other questions.

Dynamic stability theory is based on aerodynamic research results obtained under conditions of nonstationary flow. Thus, in contrast to static conditions, a body whose orientation varies with time will be acted upon by additional aerodynamic loads whose influence depends on time.

Damping moment. One of these loads is the damping moment that arises when the body performs rotational motion about its center of mass on its flight trajectory. This moment is restoring in nature and hence directed opposite to the rotation.

Let us examine the expression for the damping moment set up by the tail in the particular case when the vehicle is moving without slip at constant speed and simultaneously rotating at a certain angular velocity $\Omega_z(t)$ about a z-axis passing through its center of mass (Fig. I-6-1). As a result of this motion, the tail gives rise to an aerodynamic pitching moment M_z that depends on the components V_x and V_y of the translational velocity and on the angular velocity Ω_z, i.e., $M_z = f(V_x, V_y, \Omega_z)$. /33

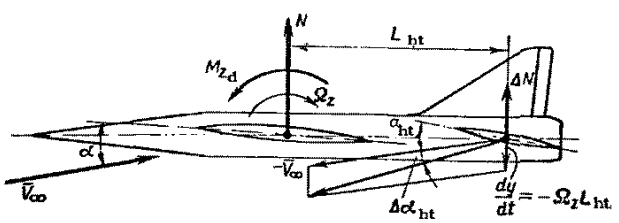

Figure I-6-1. Diagram Illustrating Origin of Tail Damping Moment.

Introducing the nomenclature $V_y/V_\infty = \alpha$; $\Omega_z L_{h.t}/V_\infty = \Delta\alpha_{h.t}$, where $L_{h.t}$ is the distance from the vehicle's center of mass to the tail aerodynamic center and $\Delta\alpha_{h.t}$ is the tail attack angle increment due to the rotation, and setting $V_x/V_\infty \approx 1$, we can write an expression for the moment coefficient in the form $m_z = M_z/qS\ell = \phi(\alpha, \Delta\alpha_{h.t})$. Here ϕ is a function of attack angle and the increment $\Delta\alpha_{h.t}$. Assuming α and $\Delta\alpha_{h.t}$ to be small, we can represent the function ϕ for symmetrical designs in the form of a sum $\phi = \phi^{\alpha}\alpha + \phi^{\Delta\alpha_{h.t}}\Delta\alpha_{h.t}$, where the derivatives ϕ^{α} and $\phi^{\Delta\alpha_{h.t}}$ are constant.

If $\varphi^{\alpha} = m_z^{\alpha}$ and $\varphi^{\Delta\alpha_{h.t.}} = m_z^{\omega_z}\left(\omega_z = \Delta\alpha_{h.t.} = \frac{\Omega_z L_{h.t.}}{V_\infty}\right)$,

$$M_z = m_z^{\alpha} qSl\alpha + m_z^{\omega_z} qSl\omega_z. \qquad \text{(I-6-6)}$$

The second moment component, which depends on angular velocity, is known as the damping moment and denoted by $M_{zd} = m_{zd}^{\omega_z} qSl\omega_z$

or

$$M_{zd} = m_{zd}^{\omega_z} \rho_\infty V_\infty \Omega_z l^2 S, \qquad \text{(I-6-7)}$$

which defines the damping moment as a function of the damping moment coefficient m_{zd} and the angular velocity of the rotation.

Studies have shown that (I-6-7) can be applied to the vehicle as a whole. The damping coefficient will depend in its linear range of angular-velocity variation only on the design features of the vehicle.

Dynamic stability criteria. As for static stability, there are criteria of dynamic stability. To consider these criteria, we shall use the equation of oscillatory rotary motion of a body about its center of gravity:

$$A \frac{d^2\alpha}{dt^2} = M_z, \qquad \text{(I-6-8)}$$

where A is the equatorial moment of inertia and M_z is the pitching moment about the center of gravity, as defined by (I-6-6).

We shall consider a motion in which the trajectory inclination varies insignificantly. The derivative $m_z^{\omega_z}$ can be represented in the form $m_z^{\omega_z} = m_z^{\alpha} V_\infty / l$, since $\Omega_z = \alpha' = d\alpha/dt$. Consequently, (I-6-8) reduces to the form /34

$$\ddot{\alpha} + a_1 \dot{\alpha} + a_2 \alpha = 0, \qquad \text{(I-6-9)}$$

where

$$a_1 = -m_z^{\dot{\alpha}} q S l A^{-1}, \quad a_2 = -m_z^{\alpha} q S l A^{-1}.$$

Let us assume for further analysis that velocity does not vary along the trajectory and, consequently, that the aerodynamic coefficients remain constant. If we also assume that A = const, the coefficients a_1, a_2 in (I-6-9) will be constant. The general solution of such an equation is as follows:

$$\alpha = C_1 e^{k_1 t} + C_2 e^{k_2 t}, \qquad \text{(I-6-10)}$$

where k_1, k_2 are the roots of the characteristic equation $k^2 + a_1 k + a_2 = 0$, and are given by the expression

$$k_{1,2} = -\frac{a_1}{4} \pm \sqrt{\frac{a_1^2}{4} - a_2}.$$

The constants C_1 and C_2 are found from the initial conditions. Research has shown that flight stability is most strongly influenced by an initial jolt characterized at time $t = 0$ by the initial angular velocity $\dot{\alpha} = \dot{\alpha}_0$ and by the angle $\alpha = 0$. For these conditions, the constants

$$C_1 = -C_2 = \frac{1}{2}\dot{\alpha}_0 \left(\frac{a_1^2}{4} - a_2\right)^{-\frac{1}{2}},$$

and the solution (I-6-10) becomes

$$\alpha = \frac{1}{2}\dot{\alpha}_0 b^{-1} e^{-\lambda_1 t}(e^{bt} - e^{-bt}), \qquad \text{(I-6-10')}$$

where

$$b = \sqrt{\lambda_1^2 - a_2}, \quad \lambda_1 = a_1/2.$$

Let us examine the case of static stability, in which the derivative $m_z^{\alpha} < 0$ and, consequently, $a_2 > 0$. If we remember that the damping moment is substantially smaller than the stabilizing moment under real conditions and that, as a result, $|a_2| > \lambda_1^2$, we can derive for α

$$\alpha = \dot{\alpha}_0 \bar{b}^{-1} e^{-\lambda_1 t} \sin(\bar{b}t), \qquad \text{(I-6-10")}$$

in which $\bar{b} = \sqrt{|a_2| - \lambda_1^2}$.

It is evident from (I-6-10") that the variation of attack angle takes the form of periodic oscillations. Since λ_1 is always positive, these oscillations will damp and, consequently, the moving body will have longitudinal oscillatory stability.

Analyzing (I-6-10") for the attack angle, we can establish certain criteria of oscillatory stability (for dynamic stability). These include the period of the oscillations

$$T = 2\pi \left(|m_z^{\alpha}| qSlA^{-1} - \lambda_1^2\right)^{-\frac{1}{2}} \qquad \text{(I-6-11)}$$

and their frequency

$$\omega = \frac{2\pi}{T} = \left(|m_z^{\alpha}| qSlA^{-1} - \lambda_1^2\right)^{\frac{1}{2}}. \qquad \text{(I-6-12)}$$

An important oscillatory-stability criterion is the logarithmic damping decrement, which is equal to the natural logarithm of the ratio of the amplitudes at the respective times t_1 and $t_1 + T$, i.e., /35

$$\varepsilon = \lambda_1 T. \qquad \text{(I-6-13)}$$

The value of this criterion depends on the period of the oscillations and on the parameter

$$\lambda_1 = \frac{1}{2} |m_z^{\dot{\alpha}}| qSlA^{-1}. \qquad \text{(I-6-14)}$$

The larger the aerodynamic damping coefficient $|m_z^{\dot{\alpha}}|$, the larger will be the logarithmic decrement and the more rapidly will the oscillations damp out.

Together with the logarithmic decrement, the time for the amplitude to diminish by half is another dynamic stability criterion:

$$t_2 = \lambda_1^{-1} \ln 2. \qquad \text{(I-6-15)}$$

The parameter λ_1, which determines both of the above criteria, is also regarded as an independent dynamic stability characteristic and is known as the damping factor.

Finally, we present yet another criterion of stability – the wavelength of the oscillations as determined from the expression

$$\lambda = TV_{\infty} = \frac{2\pi V_{\infty}}{\sqrt{|a_2| - \lambda_1^2}}. \qquad \text{(I-6-16)}$$

In practice, it is advisable to endow the moving body with aerodynamic properties such that the damping coefficient is sufficiently large, since the time t_2 will then be small, although at the expense of some increase in the wavelength, which is undesirable. Usually, an effort is made to reduce wavelength. For this purpose, it is necessary to increase the stabilizing moment, which, in turn, has the desirable effect of lowering the oscillation amplitudes.

Above, we examined the case in which the body has static stability, which also endows it with longitudinal oscillatory stability. A similar analysis might be carried out for a body that does not have static stability, i.e., for which the derivative $m_x^{\alpha} > 0$.

Solving (I-6-9), we obtain a relation for α that indicates nondamping aperiodic motion, which will now no longer be oscillatory. With time, the attack angle will increase without limit. In this case, the body has longitudinal dynamic instability.

Generalized method for stability analysis of vehicle motion. An expression more general than (I-6-10) for the attack angle of a ballistic missile is cited in [55] and takes the form

$$\alpha = e^{l_1 v - \beta y}\left[C_1 J_0(v) + C_2 Y_0(v)\right], \qquad \text{(I-6-17)}$$

where $J_0(v)$ and $Y_0(v)$ are zero-order Bessel functions of the first and second kinds, respectively, of the argument

$$v = \sqrt{l_2}\, e^{-\frac{1}{2}\beta y}. \qquad \text{(I-6-18)}$$

The parameter l_1 is the "dynamic stability" factor:

$$l_1 = \frac{\varepsilon \rho_3 S_{mid}}{4\beta G \sin\theta_0}\left[c_x - c_y^{\alpha} + (m_z^{\omega_z} + m_z^{\dot{\alpha}})\left(\frac{r_b}{R_{ro}}\right)^2\right], \qquad \text{(I-6-19)}$$

while the parameter l_2 is the "static stability" factor: /36

$$l_2 = -\frac{\varepsilon \rho_3 S_{mid}}{2\beta^2 G r_b \sin^2\theta_0} m_z^{\alpha}\left(\frac{r_b}{R_{ro}}\right)^2. \qquad \text{(I-6-20)}$$

In these relationships, G is the weight of the vehicle, θ_0 is the

initial inclination of the trajectory to the horizon, x_b is the length of the vehicle, R_{ro} is its radius of inertia, and c_y^α and m_z^α are the derivatives with respect to α: $c_y^\alpha = \partial c_y/\partial\alpha$, $m_z^\alpha = \partial m_z/\partial\alpha$.

The other two derivatives of the moment coefficient are given by the expressions

$$m_z^{\omega_z} = \frac{\partial m_z}{\partial \omega_z}; \quad m_z^{\dot{\alpha}} = \frac{\partial m_z}{\partial \dot{\alpha}}, \tag{I-6-21}$$

with

$$\omega_z = \frac{\Omega_z x_b}{2V_\infty}; \quad \dot{\alpha} = \frac{\dot{\alpha} x_b}{2V_\infty} \quad \left(\dot{\alpha} = \frac{\partial \alpha}{\partial t}\right). \tag{I-6-22}$$

Solution (I-6-17) was derived for nonuniform flight conditions of the ballistic missile in the atmosphere, in which the density variation is defined by an exponential law:

$$\rho = \rho_g e^{-\beta y},$$

where ρ_g is the density at sea level, β is the altitude gradient of density, which is assumed constant, and y is the altitude above sea level.

The constants of integration C_1 and C_2 in (I-6-17) are determined by the initial conditions at entry into the dense atmospheric layers. If the initial angular velocity of rotation $\Omega_{z_0} = 0$, and the attack angle $\alpha = \alpha_0 \neq 0$, the constant $C_2 = 0$, and the solution assumes the form

$$\alpha = \alpha_0 e^{-l_1 v^2 - \beta y} J_0(v). \tag{I-6-23}$$

In the most common cases, the static stability factor l_2 is of the order of $\sim 10^5$.

The dynamic stability factor l_1 may differ markedly from the value indicated. For example, when damping has a strong effect on oscillatory motion, l_1 may become negative (e.g., $l_1 = -10$). As

altitude decreases in this case, the attack angle will oscillate around zero with sharply reduced, near-zero amplitude. If the dynamic stability factor $\ell_1 = 0$, the oscillations will damp more slowly and the amplitude may be nonzero at the ground.

For $\ell_1 > 0$ (e.g., $\ell_1 \approx 10$), we have a case of practically undamped motion in which damping ceases at a certain altitude and a marked amplitude increase is observed with the approach to the ground.

The effect of vehicle oscillations can be taken into account in computing heat transfer, the rate of which varies somewhat from the rate in the absence of oscillations. This change in heat transfer can, of course, be taken into consideration by the design of an appropriate cooling system.

§I-7. AERODYNAMIC CHARACTERISTICS OF VEHICLES IN NONSTEADY MOTION /37

General relation for force or moment. Above, we examined relationships determining forces, moments, and their coefficients. These relationships answered only the question as to how an aerodynamic characteristic can be found if the distributions of normal pressure and tangential stress are known, and did not tell us the conditions under which these distributions originated. At the same time, importance attaches to the prior history of the motion, i.e., the manner in which the body arrived at a particular position on its trajectory as given by attack and slip angle values, for investigation of the real vehicle's aerodynamic characteristics and, in particular, for investigation of the pressure and tangential stress distribution. For example, was the attitude arrived at under conditions under which there was no rotation and the body moved progressively with its center of mass at constant speed on its trajectory, or was it reached under conditions in which the body's motion was characterized not only by the velocity of its center of mass, but also by an angular velocity of rotation of the body about its center of mass.

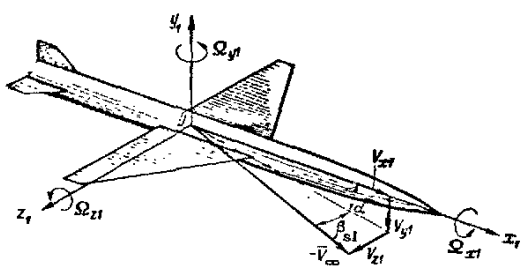

Figure I-7-1. Diagram Showing Action of Rotational Moments.

Strictly speaking, the former case is not realized in flight, but it can be reproduced in aerodynamic test installations and obviously corresponds to steady-state flow at fixed attack and slip angles. The aerodynamic coefficients obtained as a result of the experiment are known as the static coefficients.

Nonsteady flow corresponds to the second case of motion of the body, that characterized by rotation. Flow of this type causes a change in the distribution of local forces from the steady-state distribution. Additional dynamic components of the aerodynamic forces and moments appear as a result. One such component is the damping moment, an expression for which was derived for the particular case of plane (zero-slip) motion characterized by constant translational velocity $-\overline{V}_\infty$ and angular velocity $\overline{\Omega}_z$.

In the most general case, nonsteady motion of a vehicle will be determined by the three components $V_{x1}(t)$, $V_{y1}(t)$, $V_{z1}(t)$ of the velocity $-\overline{V}_\infty(t)$ of the center of gravity in the body system (Fig. I-7-1) and by the components $\Omega_{x1}(t)$, $\Omega_{y1}(t)$, $\Omega_{z1}(t)$ of the angular velocity $\overline{\Omega}(t)$ in the same system, with all of these components dependent on time.

Any force or moment can be represented in the form of a functional relationship

$$F = f(V_{x1}, V_{y1}, V_{z1}, \Omega_{x1}, \Omega_{y1}, \Omega_{z1}, \dot{V}_{x1}, \dot{V}_{y1}, \dot{V}_{z1}, \dot{\Omega}_{x1}, \dot{\Omega}_{y1}, \dot{\Omega}_{z1}), \quad \text{(I-7-1)}$$

which indicates that the nonsteady aerodynamic characteristics are determined not only by the instantaneous dynamic state of the body, i.e., the parameters V_{x1}, V_{y1}, V_{z1}, Ω_{x1}, Ω_{y1}, Ω_{z1} at the particular time on the trajectory, but also by the first time derivatives of these parameters $\dot{V}_{x1}$, $\dot{V}_{y1}$, $\dot{V}_{z1}$, $\dot{\Omega}_{x1}$, $\dot{\Omega}_{y1}$, $\dot{\Omega}_{z1}$. /38

In the particular case with smooth variation of the parameters, we can limit ourselves to the functional relation

$$F = f(V_{x1}, V_{y1}, V_{z1}, \Omega_{x1}, \Omega_{y1}, \Omega_{z1}). \quad \text{(I-7-2)}$$

In practice, nonsteady-flow problems are associated with changes in the geometric shapes of vehicles in flight due, in particular, to elastic strains. The influence of this shape change on the aerodynamic characteristics can be taken into account by introducing a parameter $\delta(x_1, y_1, z_1, t)$ equal in magnitude to the increment in local attack angle and the time derivative $d\delta/dt$ of this parameter.

Dimensionless kinematic parameters. In investigation of the aerodynamic force and moment coefficients, these coefficients are regarded as functions of dimensionless kinematic parameters in the form

$$\left.\begin{aligned} u = \frac{V_{x1}}{V_\infty};\ \dot{\bar{u}} = \frac{dV_{x1}}{dt}\frac{l}{2V_\infty^2};\ \alpha = \frac{V_{y1}}{V_\infty};\ \dot{\bar{\alpha}} = \frac{d\alpha}{dt}\frac{l}{2V_\infty};\\ \beta_{s1} = \frac{V_{z1}}{V_\infty};\ \dot{\bar{\beta}}_{s1} = \frac{d\beta_{s1}}{dt}\frac{l}{2V_\infty};\ \omega_x = \Omega_{x1}\frac{l}{2V_\infty};\ \dot{\omega}_x = \frac{d\Omega_{x1}}{dt}\frac{l^2}{2V_\infty^2};\\ \omega_y = \Omega_{y1}\frac{l}{2V_\infty};\ \dot{\omega}_y = \frac{d\Omega_{y1}}{dt}\frac{l^2}{2V_\infty^2};\ \omega_z = \Omega_{z1}\frac{l}{2V_\infty};\ \dot{\omega}_z = \frac{d\Omega_{z1}}{dt}\frac{l^2}{2V_\infty^2};\\ \dot{\bar{\delta}} = \frac{d\delta}{dt}\frac{l}{2V_\infty}. \end{aligned}\right\} \qquad \text{(I-7-3)}$$

Here α, and β_{s1} are the attack and slip angles, respectively, and l is the characteristic length.

For example, we have for the coefficient of normal force and pitching moment

$$C_N = f_1(u, \dot{\bar{u}}, \alpha, \dot{\bar{\alpha}}, \beta_{s1}, \dot{\bar{\beta}}_{s1}, \omega_x, \dot{\omega}_x, \omega_y, \dot{\omega}_y, \omega_z, \dot{\omega}_z, \delta, \dot{\bar{\delta}}); \qquad \text{(I-7-4)}$$

$$m_z = f_2(u, \dot{\bar{u}}, \alpha, \dot{\bar{\alpha}}, \beta_{s1}, \dot{\bar{\beta}}_{s1}, \omega_x, \dot{\omega}_x, \omega_y, \dot{\omega}_y, \omega_z, \dot{\omega}_z, \delta, \dot{\bar{\delta}}). \qquad \text{(I-7-5)}$$

Stability derivatives. Let us assume that the functional relationships (I-7-4) and (I-7-5) can be expanded in Taylor series with respect to a point defined by certain initial-velocity values $V_{\infty 0}$, $V_{x_{10}}$, $V_{y_{10}}$, $V_{z_{10}}$ and zero angular velocity $\Omega_0 = 0$.

A linear law of variation of the aerodynamic coefficients with kinematic parameters is valid at small nonsteady disturbances. Then, excluding the parameters δ and $\dot{\delta}$ from consideration, i.e., disregarding the effect of strains, we obtain the following expressions for the aerodynamic coefficients:

$$c_N = c_{N0} + c_N^u u + c_N^{\dot{u}}\dot{\bar{u}} + c_N^\alpha \alpha + c_N^{\dot{\alpha}}\dot{\bar{\alpha}} + c_N^{\omega_x}\omega_x + c_N^{\dot{\omega}_x}\dot{\omega}_x + \ldots; \qquad \text{(I-7-6)}$$

$$m_z = m_{z0} + m_z^u u + m_z^{\dot{u}}\dot{\bar{u}} + m_z^\alpha \alpha + m_z^{\dot{\alpha}}\dot{\bar{\alpha}} + m_z^{\omega_x}\omega_x + m_z^{\dot{\omega}_x}\dot{\omega}_x + \ldots. \qquad \text{(I-7-7)}$$

The derivatives $c_N^u = \partial c_N/\partial u$, $c_N^{\dot{u}} = \partial c_N/\partial \dot{\bar{u}}$, etc, are known as the stability derivatives.

Let us examine the accepted stability-derivative classification. Stability derivatives of the form c_N^u, c_N^α, c_N^{β}, etc., which are determined by differentiation of the coefficients with respect to u, α, and β_{s1}, respectively, are known as static /39

stability derivatives and are assigned to the first group of derivatives.

The partial derivatives of the coefficients with respect to one of the variables ω_x, ω_y, ω_z, etc., form the second group and are known as rotary derivatives ($c_N^{\omega_x}$, $c_N^{\omega_y}$, $c_N^{\omega_z}$ etc.).

The third group of stability derivatives is made up of the acceleration derivatives, which are defined as the partial derivatives of the coefficients with respect to one of the derivatives $\dot{\bar{u}}$, $\dot{\omega}_x$, $\dot{\omega}_y$ or $\dot{\omega}_z$.

Remembering that the derivatives $c_N^{\dot{\bar{\alpha}}}$, $c_N^{\dot{\bar{\beta}}}$, etc., are computed by differentiating the aerodynamic coefficients also with respect to derivatives (in this case with respect to $\dot{\bar{\alpha}}$, $\dot{\bar{\beta}}_{st}$, etc.), we shall arbitrarily classify these stability derivatives among the acceleration derivatives. Thus, this group includes the derivatives $c_N^{\dot{\bar{u}}}$, $c_N^{\dot{\omega}_x}$, $c_N^{\dot{\omega}_y}$, $c_N^{\dot{\bar{\alpha}}}$, etc.

Since the number of aerodynamic force and moment coefficients is six, the first group embraces 18 static stability derivatives and the second 18 rotary derivatives. The third group will number 36 acceleration derivatives.

If the nonstationary disturbances cease to be small, the nonlinearity of the relationships characterizing flow over the body becomes an essential feature. In this case, it is necessary to leave terms of order higher than the first in the expansions (I-7-6) and (I-7-7). For example, on retaining quadratic terms, we obtain second-order derivatives such as $m_y^{\alpha\omega_x} = \partial^2 m_y / \partial\alpha\,\partial\omega_x$ and others.

Studies have shown that only some of the first-order derivatives and a few of the second-order derivatives are of practical importance. These derivatives are listed in Table I-7-1.

Some of the stability derivatives given in Table I-7-1 are of special interest for investigation of vehicle dynamic properties and have specific names. Among these derivatives, we might mention the static stability derivatives previously dealt with, m_z^{α}, m_y^{β}, m_x^{β}, which characterize important properties like the "stiffnesses" of the vehicle's longitudinal, lateral, and transverse oscillatory motions, respectively, and determine the frequencies of these oscillations.

The derivative m_z^{α} is often called the static longitudinal stability derivative, m_y^{β} the static directional stability

derivative or the weathercock stability coefficient, and m_x^{β} the static transverse stability derivative.

TABLE I-7-1. STATIC DERIVATIVES

Static derivatives

c_R^u	c_R^α	c_R^β	m_x^u	m_x^α	m_x^β
c_N^u	c_N^α	c_N^β	m_y^u	m_y^α	m_y^β
c_z^u	c_z^α	c_z^β	m_z^u	m_z^α	m_z^β

Rotary derivatives

$c_R^{\omega_x}$	$c_R^{\omega_y}$	$c_R^{\omega_z}$	$m_x^{\omega_x}$	$m_x^{\omega_y}$	$m_x^{\omega_z}$
$c_N^{\omega_x}$	$c_N^{\omega_y}$	$c_N^{\omega_z}$	$m_y^{\omega_x}$	$m_y^{\omega_y}$	$m_y^{\omega_z}$
$c_z^{\omega_x}$	$c_z^{\omega_y}$	$c_z^{\omega_z}$	$m_z^{\omega_x}$	$m_z^{\omega_y}$	$m_z^{\omega_z}$

Acceleration derivatives

$c_R^{\dot{\alpha}}$	$c_R^{\dot{\beta}}$	$c_R^{\dot{\omega}_x}$	$m_x^{\dot{\beta}}$	$m_x^{\dot{\alpha}}$	$m_x^{\dot{\omega}_x}$
$c_N^{\dot{\alpha}}$	$c_N^{\dot{\beta}}$	$c_N^{\dot{\omega}_x}$	$m_y^{\dot{\beta}}$	$m_y^{\dot{\alpha}}$	$m_y^{\dot{\omega}_x}$
$c_z^{\dot{\alpha}}$	$c_z^{\dot{\beta}}$	$c_z^{\dot{\omega}_x}$	$m_z^{\dot{\beta}}$	$m_z^{\dot{\alpha}}$	$m_z^{\dot{\omega}_x}$

Second acceleration derivatives

$m_x^{\alpha\beta}$	$m_x^{\alpha\omega_x}$	$m_x^{\beta\omega_x}$	$m_y^{\alpha\omega_x}$

The rotary derivatives and acceleration derivatives act on the motion as damping parameters. Accordingly, the derivatives $m_z^{\omega_z}$, $m_z^{\dot{\alpha}}$ are known as the longitudinal damping coefficients $m_y^{\omega_y}$, $m_y^{\dot{\beta}}$ as the yaw damping coefficients, and $m_x^{\omega_x}$ is called the roll damping coefficient.

The Magnus effect is important for the rotational motion. It consists in the appearance of a force and moment proportional

to the product $\alpha\Omega_x$ or $\beta_{sl}\Omega_x$ on a body in longitudinal rotation at angular velocity Ω_x and in the presence of an attack or slip angle, with these forces directed perpendicular to the planes in which the angles α and β_{sl} lie. The aerodynamic coefficients /40 of these forces (moments) are proportional to $\alpha\omega_x$ and $\beta_{sl}\omega_x$, respectively. Hence the derivatives of the coefficients with respect to $\alpha\omega_x$ and $\beta_{sl}\omega_x$, e.g., $c_N^{\alpha\omega_x}$, $c_N^{\beta_{ск}\omega_x}$, $m_z^{\alpha\omega_x}$, $m_z^{\beta_{ск}\omega_x}$, are known as the Magnus stability derivatives.

The forces and moments of the other group are associated with simultaneous rotation of the vehicle about two axes and are therefore gyroscopic in nature. The gyroscopic forces and moments are proportional to the product of the two angular velocities. For example, in simultaneous rotation about the x- and y-axes, these additional forces and moments are proportional to the product $\Omega_x\Omega_y$ and the corresponding aerodynamic coefficients to the product $\omega_x\omega_y$. Hence the derivatives of the coefficients with respect to $\omega_x\omega_y$ ($c_N^{\omega_x\omega_y}$, $m_z^{\omega_x\omega_y}$, etc.) are known as the gyroscopic stability derivatives.

Particular cases of motion. To simplify investigation of /41 the stability characteristics, we can use a method in which the composite motion of the vehicle is broken down into its individual components. In each such particular case of motion, stability is studied independently of other forms of motion. This method presupposes isolation of individual characteristic motion forms or combinations thereof that are determining as regards stability evaluation of the vehicle as a whole.

TABLE I-7-2. VARIOUS FORMS OF MOTION AND VELOCITIES CORRESPONDING TO THEM

Velocity components / Form of motion	V_x	$V_y(\alpha)$	$V_z(\beta_{sl})$	Ω_x	Ω_y	Ω_z
Pitch and roll	+	+	—	+	—	+
Pitch, no roll	+	+	—	—	—	+
Roll, no pitch	+	—	—	+	—	—
No roll, no pitch	+	—	—	—	—	—

Note. The "+" denotes a nonzero velocity component and the "–" a zero velocity component.

Table I-7-2 presents certain characteristic motion forms whose investigation is of practical importance.

Investigation of a particular motion form can be simplified by excluding the effect of accelerations. This is justified in practice when the vehicle's motion develops slowly enough. If it is necessary to consider acceleration, a correction can be applied to the aerodynamic coefficient in the form of a term equal to the product of the first stability derivative with respect to the acceleration and the corresponding dimensionless acceleration parameter.

Thus, for example, we might study the stability of pitching motion, which is sometimes known as the principal motion form. Pitching-motion stability (or longitudinal stability) is determined by longitudinal damping, which, in turn, depends on the derivatives $m_z^{\dot{\alpha}}$ and $m_z^{\omega_z}$.

Sometimes, the derivatives $m_z^{\dot{\alpha}}$ and $m_z^{\omega_z}$, are confused, on the assumption that there is no difference between them. This difference can be established if we examine two motion forms, one of which is characterized by the condition $\dot{\alpha}=0, \Omega_z \neq 0$, and the other by the condition $\dot{\alpha} \neq 0, \Omega_z = 0$.

The first motion form (Fig. I-7-2) is characterized by the fact that the attack angle, which is equal to the angle between the instantaneous vector $\overline{V}_\infty$ and a body axis, does not change, so that the derivative $\dot{\alpha}=0$. In this motion, however, a variable angle ϑ forms between a certain fixed direction and the body axis. Hence $\Omega_z = d\vartheta/dt \neq 0$.

In the particular case when Ω_z = const, the trajectory in Fig. I-7-2a characterizes the motion of a vehicle executing a loop.

Figure I-7-2b shows the second motion form, which corresponds to the condition $\alpha \neq 0$, $\Omega_z = 0$. This motion may arise in free fall with constant acceleration. During fall, the angle ϑ between the fixed direction and the body axis remains constant, while the angle α between the instantaneous velocity vector and the body axis varies.

Thus, the derivative $\dot{\vartheta} = \Omega_z = 0$, and the time derivative of attack angle $\dot{\alpha} \neq 0$. In this case, this derivative $\dot{\alpha}$ = const. /43

Neither of these motion forms is often encountered in isolation. Longitudinal oscillations that represent combinations of these two motions usually occur. These oscillations are nicely described by sinusoidal relationships for the derivatives $\dot{\alpha}$ or $\dot{\vartheta} = \Omega_z$.

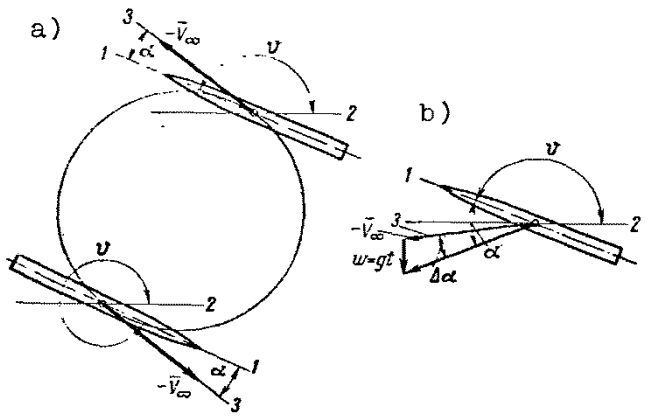

Figure I-7-2. Forms of Nonsteady Motion. /42
a) $\dot{\alpha}=0$, $\dot{\vartheta}=\Omega_z=\text{const}$; b) $\dot{\alpha}=\text{const}$, $\dot{\vartheta}=\Omega_z=0$; $\alpha=\alpha_0+\Delta\alpha=\alpha_0+$ $+gt/V_\infty$; $\dot{\alpha}=g/V_\infty$; 1) body axis; 2) fixed direction; 3) instantaneous direction of flight.

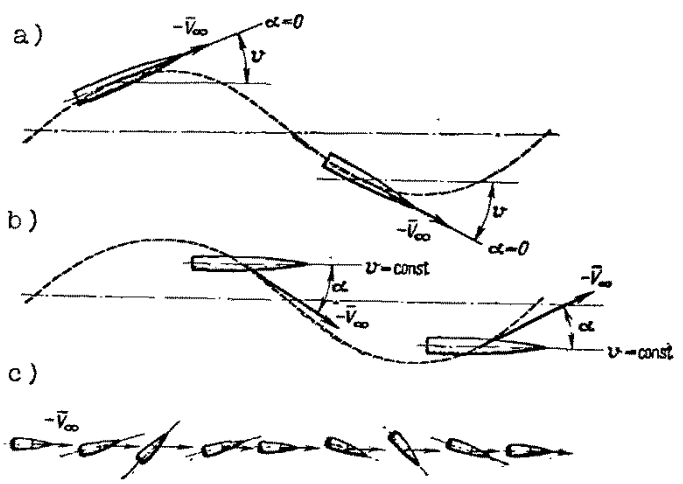

Figure I-7-3. Forms of Nonsteady Motion.
a) $\alpha=0$, $\dot{\vartheta}=\Omega_z=B\sin\varphi t$; b) $\dot{\alpha}=A\sin\omega t$, $\dot{\vartheta}=\Omega_z=0$; c) $\dot{\alpha}=\dot{\vartheta}=A\sin\omega t$

$$\dot{\alpha}=A\sin\omega t;\quad \dot{\vartheta}=\Omega_z=B\sin\varphi t, \tag{I-7-8}$$

where A and B are the amplitudes of the oscillations and ω and ϕ are their frequencies.

Equations (I-7-8) define the harmonic law of variation of the derivatives $\dot{\alpha}$, $\dot{\vartheta}$. We can consider three motion forms each of which is described by such a law. The first motion form (Fig. I-7-3a) corresponds to the condition $\alpha = 0, \dot{\vartheta} = \Omega_z = B \sin \varphi t$. In this motion form, the body axis coinciding with the direction of flight (α = 0) performs oscillations along the trajectory in accordance with the harmonic law $\dot{\vartheta} = B \sin \varphi t$.

The second motion form (Fig. I-7-3b) is characterized by absence of change in the orientation of the body axis along the trajectory, so that $\Omega_z = \dot{\vartheta} = 0$. Here, owing to the presence of a vertical velocity, the attack angle varies in accordance with the harmonic law for the derivative $\dot{\alpha}$.

Finally, the third motion form, that shown in Fig. I-7-3c, arises in the case of a rectilinear trajectory of the body's center of mass when the inclination of the body axis to the direction of flight varies harmonically. In this case, the angles α and ϑ coincide, so that $\dot{\alpha} = \dot{\vartheta}$, and the total longitudinal damping derivative is $m_z^{\dot{\alpha}} + m_z^{\omega_z}$.

If the pitching motion is accompanied by a motion in roll, the effect of the roll-damping derivative $m_x^{\dot{\alpha}} + m_x^{\omega_z}$ must be taken into consideration in investigating rolling stability.

The corresponding damping-coefficient values are found in the form of the derivatives $(m_z^{\dot{\alpha}} + m_z^{\omega_z})\bar{\dot{\alpha}}$ and $(m_x^{\dot{\alpha}} + m_x^{\omega_z})\bar{\dot{\alpha}}$, where the derivative $\bar{\dot{\alpha}}$ is determined from the harmonic law (I-7-8). Introducing the nomenclature $\alpha_0 = A/\Omega_Z$, $Sh = \Omega_Z \ell / V_\infty$, we obtain

$$\bar{\dot{\alpha}} = \frac{\alpha_0 Sh}{2} \sin \omega t. \qquad (I\text{-}7\text{-}9)$$

The dimensionless parameter $Sh = \Omega_Z \ell / V_\infty$ is known as the Strouhal number and is an important similarity criterion for nonsteady flow.

Conversion of stability derivatives with a change in reduction point position. In determining over-all nonsteady characteristics from known values of these characteristics for individual elements of a vehicle, it is necessary to reduce each of these values to a single reduction point selected for the vehicle as a whole. Thus, a stability derivative must be converted from one

reduction point to another.

Let us assume that the aerodynamic characterisiics and stability derivatives, calculated for a certain reduction point O (see Fig. I-2-2), are known for a certain lifting surface. It is required to find the corresponding characteristics with respect to another point O_1 at a distance $x = x_1'$ from point O.

To simplify the problem, let us assume that $c_{N_0} = m_{z_0} = 0$ /44 and that the aerodynamic-coefficient components governed by the variation of the translational velocity are also zero, i.e., $c_N^{\bar{u}}u = c_N^{\dot{\bar{u}}}u = m_z^{\bar{u}}u = 0$. With these assumptions,

$$c_N = c_N^{\alpha}\alpha + c_N^{\dot{\bar{\alpha}}}\dot{\bar{\alpha}} + c_N^{\bar{\omega}_z}\bar{\omega}_z + c_N^{\dot{\bar{\omega}}_z}\dot{\bar{\omega}}_z; \qquad \text{(I-7-10)}$$

$$m_z = m_z^{\alpha}\alpha + m_z^{\dot{\bar{\alpha}}}\dot{\bar{\alpha}} + m_z^{\bar{\omega}_z}\bar{\omega}_z + m_z^{\dot{\bar{\omega}}_z}\dot{\bar{\omega}}_z, \qquad \text{(I-7-11)}$$

where the derivatives are known for reference point O.

The corresponding coefficients are found for the new reduction point O_1 in the form

$$c_{N_1} = c_{N_1}^{\alpha_1}\alpha_1 + c_{N_1}^{\dot{\bar{\alpha}}_1}\dot{\bar{\alpha}}_1 + c_{N_1}^{\bar{\omega}_{z_1}}\bar{\omega}_{z_1} + c_{N_1}^{\dot{\bar{\omega}}_{z_1}}\dot{\bar{\omega}}_{z_1}; \qquad \text{(I-7-10')}$$

$$m_{z_1} = m_{z_1}^{\alpha_1}\alpha_1 + m_{z_1}^{\dot{\bar{\alpha}}_1}\dot{\bar{\alpha}}_1 + m_{z_1}^{\bar{\omega}_{z_1}}\bar{\omega}_{z_1} + m_{z_1}^{\dot{\bar{\omega}}_{z_1}}\dot{\bar{\omega}}_{z_1}. \qquad \text{(I-7-11')}$$

As we see from Fig. I-2-2,

$$\alpha_1 = \alpha + \Delta\alpha = \alpha - \frac{\Omega_z x_1'}{V_\infty} = \alpha - 2\omega_z\bar{x},$$

where $\omega_z = \Omega_z b/2V_\infty$, $\bar{x} = x_1'/b$, and then

$$\dot{\bar{\alpha}}_1 = \dot{\bar{\alpha}} - 2\dot{\omega}_z\bar{x}; \quad \omega_{z_1} = \omega_z; \quad \dot{\omega}_{z_1} = \dot{\omega}_z. \qquad \text{(I-7-12)}$$

Let us now apply the identities $c_{N_1} = c_N$ and $m_{z_1} = m_z - c_N\bar{x}$. Introducing Expressions (I-7-12) into the left members of the identities and equating the corresponding coefficients of α, $\dot{\bar{\alpha}}$, ω_z, $\dot{\omega}_z$, we obtain the following relationships for the stability derivatives:

$$
\begin{aligned}
&c_{N1}^{\alpha_1} = c_N^{\alpha}; \quad \dot{c}_{N1}^{\alpha_1} = \dot{c}_N^{\alpha}; \quad c_{N1}^{\omega_{z1}} = c_N^{\omega_z} + c_N^{\alpha}\bar{x};\\
&\dot{c}_{N1}^{\omega_{z1}} = \dot{c}_N^{\omega_z} + \dot{c}_N^{\alpha}\bar{x};\\
&m_{z1}^{\alpha_1} = m_z^{\alpha} - c_N^{\alpha}\bar{x}; \quad \dot{m}_{z1}^{\alpha_1} = m_z^{\alpha} - \dot{c}_N^{\alpha}\bar{x};\\
&m_{z1}^{\omega_{z1}} = m_z^{\omega_z} + (m_z^{\alpha} - c_N^{\omega_z})\,\bar{x} - c_N^{\alpha}\bar{x}^2;\\
&\dot{m}_{z1}^{\omega_{z1}} = \dot{m}_z^{\omega_z} + (\dot{m}_z^{\alpha} - \dot{c}_N^{\omega_z})\,\bar{x} - \dot{c}_N^{\alpha}\bar{x}^2.
\end{aligned}
\qquad \text{(I-7-13)}
$$

Chapter II /45

SHAPES OF THE VEHICLES AND THEIR ELEMENTS

The basic elements composing the modern flight vehicle are the frame, powerplant, equipment, and payload.

The frame is the basic object of aerodynamic research leading to determination of the forces exerted by the atmospheric medium. The frame of a vehicle (or simply the vehicle) incorporates its body, wings, tailplanes, controls, and certain other devices known collectively as superstructural elements.

Since the aerodynamic characteristics of a vehicle are determined to a major degree by the aerodynamic characteristics of its isolated parts – body, wings, etc. – interest attaches to consideration of the shape and certain of the most general aerodynamic properties of these parts.

§II-1. SHAPES OF VEHICLE BODIES

In most cases, the body of a vehicle is a solid of revolution and consists of three elements: nose-, mid-, and rear (or tail) sections, the latter sometimes known as the stern.

Nose section. Figure II-1-1 shows possible nose-section designs representing tapered solids of revolution, solid or with a flow passage. Nose-section shapes of this type reduce the aerodynamic drag of the body, but also reduce its useful volume. Nose sections are usually conical, ogival, or parabolic in shape, and sometimes represent combinations of these forms.

The generatrix of the ogival nose takes the form of an arc of a circle with a certain radius (Fig. II-1-2). The nose may meet the cylindrical section either tangentially or at a certain angle $\beta \neq 0$. The ogival curve is said to be tangent in the former case and secant in the latter. The equation of the ogival curve in dimensionless form is

$$\bar{r} = 2\bar{R}\{[1-\lambda_{mid}^2\bar{R}^{-2}(\bar{x}-1)^2]^{1/2}-1\}+1, \qquad \text{(II-1-1)}$$

where $\bar{R} = R/(2r_{mid})$, $\lambda_{mid} = x_{mid}/(2r_{mid})$ is the fineness ratio of /46
the nose section (x_{mid} is its absolute length), $\bar{x} = x/x_{mid}$, and $\bar{r} = r/r_{mid}$.

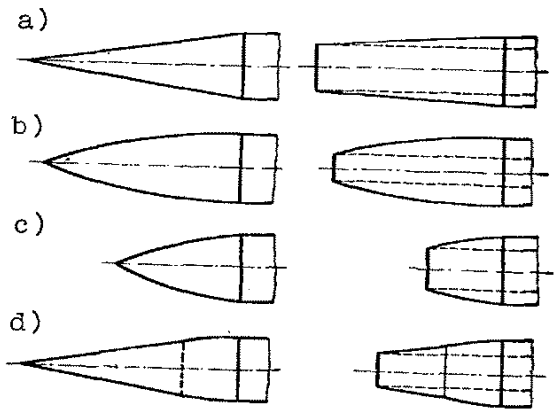

Figure II-1-1. Shapes of Tapered Nose Sections (solid and with flow passage). a) cone; b) ogival (parabolic) tangent nose section; c) ogival (parabolic) secant nose section; d) composite nose section (cone with ogive).

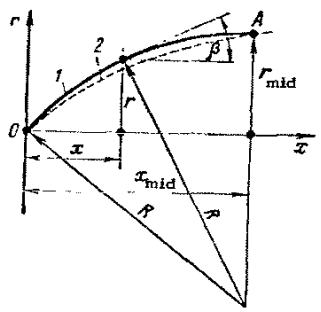

Figure II-1-2. Shape and Geometric Parameters of Ogival Nose Section of Solid of Revolution. 1) tangent ogival curve ($\beta = 0$ at point A); 2) secant ogival curve ($\beta \neq 0$ at point A).

The relation between the fineness λ_{mid} and the dimensionless radius $\bar{R}$ of the ogival generatrix can be found directly from Fig. II-1-2:

$$\lambda_{mid} = \sqrt{\bar{R} - 0.25}. \qquad \text{(II-1-2)}$$

In investigating flow over ogival surfaces, it is necessary to know how the slope of the tangent varies along the generatrix. To find the law of this variation, we differentiate (II-1-1):

$$\operatorname{tg}\beta = \frac{dr}{dx} = \frac{1}{2\lambda_{mid}}\frac{d\bar{r}}{d\bar{x}} = \\ = -\frac{\lambda_{mid}}{\bar{R}}(\bar{x}-1)\left[1-\frac{\lambda_{mid}^2}{\bar{R}^2}(\bar{x}-1)^2\right]^{-1/2}. \qquad \text{(II-1-3)}$$

This expression can be used to find, among other things, the slope of the tangent at the point of the body:

$$\operatorname{tg}\beta_0 = \left(\frac{dr}{dx}\right)_{x=0} = \frac{\lambda_{mid}}{\bar{R}}\left(1-\frac{\lambda_{mid}^2}{\bar{R}^2}\right)^{-1/2}. \qquad \text{(II-1-3')}$$

Let us examine a parabolic nose section whose characteristic geometric parameters are the same as in Fig. II-1-2. In the general case, the coordinates of points on a parabolic curve satisfy the equation

$$r = x(a + bx + cx^2 + \ldots). \qquad \text{(II-1-4)}$$

In the class of parabolic generatrices, we shall consider the particular form obtained from Eq. (II-1-1), in which the dimensionless radius $\bar{R}$ is assumed quite large. In this case, the 0.25 in (II-1-2) can be disregarded. If, for example, the permissible error does not exceed 3%, this can be done for $\bar{R} \geq 4$. As a result, we find the approximate relation $\bar{R} = \lambda^2_{mid}$. Substituting it in (II-1-1) and simplifying, we obtain the equation of a parabolic generatrix, which, in dimensionless form, takes the form

$$\bar{r} = \bar{x}(2 - \bar{x}). \qquad \text{(II-1-5)}$$

Differentiating with respect to $\bar{x}$, we find the tangent of the angle between the body axis and the tangent to the generatrix:

$$\operatorname{tg}\beta = \frac{d\bar{r}}{d\bar{x}} = \frac{1}{\lambda_{mid}}(1 - \bar{x}). \qquad \text{(II-1-6)}$$

We then have for the inclination of the tangent at the point $\tan \beta_0 = (dr/dx)_{x=0} = 1/\lambda_{mid}$. With this expression in mind, we transform Eq. (II-1-6) to

$$\frac{d\bar{r}}{d\bar{x}} = \operatorname{tg}\beta_0(1 - \bar{x}). \qquad \text{(II-1-6')}$$

Like the ogival curve, the parabolic generatrix may be tangent or secant. Bodies with parabolic generatrices have an important property that proceeds from (II-1-5) and consists in the fact that the entire infinite variety of these bodies is characterized by the same dependence of the thickness ratio r/r_{mid} on the dimensionless coordinate x/x_{mid}.

This population may include geometrically similar bodies /47
whose linear dimensions differ by the same factor. Obviously, such bodies have the same fineness ratio and can be placed in

congruence with one another by uniform deformation, i.e., deformation that is the same for all directions.

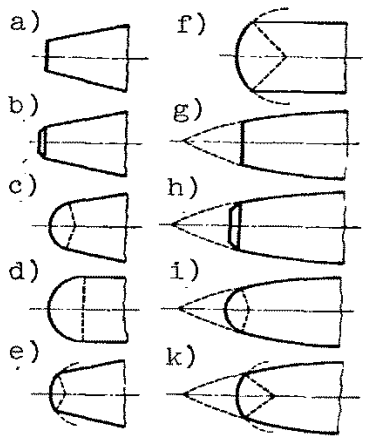

Figure II-1-3. Shapes of Blunt Nose Sections. a) truncated cone; b) stepped truncated cone; c) cone with tangent spherical nose; d) cylinder with tangent spherical nose; e) cone with secant spherical nose; f) cylinder with secant spherical nose; g) truncated ogival (parabolic) nose section; h) composite nose section (cone with ogive), truncated; i) ogival (parabolid) nose section with tangent spherical nose; k) ogival (parabolic) nose section with secant spherical nose.

However, the population of parabolic bodies also includes forms that can be brought into coincidence only by nonuniform deformation. Take, for example, bodies with different fineness ratios. Introducing a new scale for the radial coordinate, we can deform a body in the vertical direction, but this will not produce perfect congruence, which requires another scale for the axial coordinate. Such a transformation of one body into another is called affine. Accordingly, bodies with parabolic generatrices are said to be affine-transformed or affine-similar. Obviously, conical solids whose generatrices are given by the dimensionless-form equation $\bar{r} = \bar{x}$ are characterized by the same thickness-ratio distribution and, consequently, will be affine-similar.

Unlike parabolic and conical bodies, ogival nose sections have thickness ratios whose lengthwise distribution changes with a change in fineness ratio, as proceeds directly from (II-1-1). As a result, one ogival nose cannot be affinely transformed into another. Thus, bodies of ogival form are not affine-similar, except for those cases in which the nose sections have the same fineness ratio, i.e., are geometrically similar. However, in cases in which the fineness ratios are large ($\lambda_{mid} > 2$), the ogival shape differs insignificantly from the parabolic, as we have noted. Hence the change in thickness-ratio distribution over their length can be disregarded on conversion from one solid to another, and the ogival nose sections may be regarded as affine-similar.

Many vehicle designs may have blunted noses. They are used primarily at very high speeds, when the basic requirement made of the nose section is ability to withstand very high temperatures. However, vehicles capable of

moderate speeds very often have bluff shapes, perhaps because of design features, the application of the equipment, etc.

In practice, it is always necessary to deal with a bluff body, since it is impossible for technological reasons to produce an absolutely sharp nose.

Figure II-1-3 shows various shapes of blunt tips on conical nose sections and some nose sections with curvilinear form. The blunt nose tip may be made as a power-law nose section whose generatrix is given by the equation /48

$$r = r_{mid}\left(\frac{x}{x_{mid}}\right)^n, \qquad \text{(II-1-7)}$$

where the exponent $0 < n < 1$.

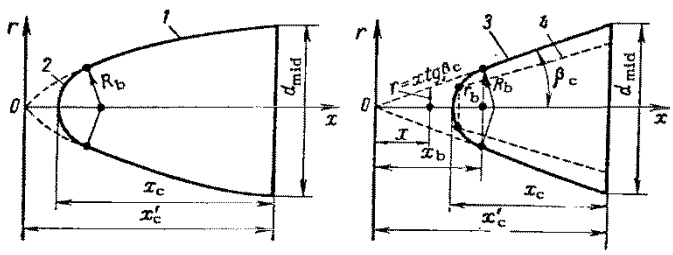

Figure II-1-4. Nose Sections with Spherical Tips. 1) Curvilinear generatrix; 2) spherical nose; 3) tangent rectilinear generatrix; 4) secant rectilinear generatrix.

The spherical body, whose generatrix equation derives from (II-1-7) with the condition that $n = 0$, is a variety of the power-law nose.

Vehicles made in the form of a sphere or having a spherical nose cap are very commonly encountered. Here the generatrix of the main section behind the spherical nose may be either curvilinear or straight (Fig. II-1-4).

Bodies with rectilinear generatrices in the form of a cone are most common. The equation of this generatrix

$$r - r_b = \operatorname{tg}\beta_c (x - x_T), \qquad \text{(II-1-8)}$$

where $r_b = R_b \cos\beta_c$, $x_b = R_b \cot\beta_c \cos\beta_c$; R_b and β_c are, respectively, the radius of the sphere and the inclination angle of the cone generatrix. If a cylindrical section follows a spherical nose (Fig. II-1-5), then $\beta_c = 0$ and $r = r_b = R_b$, i.e., the surface of the spherical nose is tangent to the cylinder.

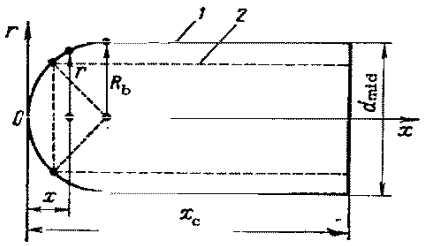

Figure II-1-5. Cylindrical Body with Spherical Nose. 1) tangent generatrix; 2) secant generatric.

The nose of a cone or cylinder may also be figured in such a way that their surfaces are not tangent to the sphere. In this case, the spherical nose is secant (Fig. II-1-5).

Investigation of flow over spherical nose tips makes use of the generatrix equation of the spherical nose, which can be derived from the ogive equation (II-1-1) by setting $r_{mid} = x_{mid} = R = R_b$. Then

$$\bar{r}^2 = 1 - (\bar{x} - 1)^2, \qquad \text{(II-1-9)}$$

where $\bar{r} = r/R_b$, $\bar{x} = x/R_b$.

The slope of the tangent to a given point of the generatrix, referred to the axis, is

$$\operatorname{tg}\beta = \frac{dr}{dx} = \frac{1-\bar{x}}{\bar{r}}. \qquad \text{(II-1-10)}$$

The spherical blunting form incorporates two families of tips made in the form of secant and tangent spheres. A tangent spherical nose is characterized by the sphere radius R_b. If it is zero, the bluntness will be "zero" and, consequently, the nose will be sharp (Fig. II-1-6). The dimensions of the nose tip increase with increasing radius. Here the maximum value of this radius for given r_{mid} and β_c is $R_b = r_{mid}/\cos\beta_c$. /49

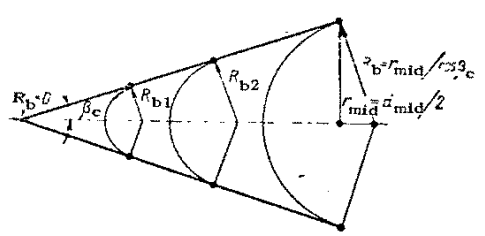

Figure II-1-6. Cone with Various Degrees of Spherical Bluntness.

If we consider a flat face on a cone or cylinder, a blunted nose constructed on this flat face with radius R_b has, in the general case, the shape of a secant sphere with various radii (Fig. II-1-7). Its smallest size is $R_b = r_b/\cos\beta_c$ or $R_b = r_b$, with the former value corresponding to a spherical nose tangent to the surface of a cone

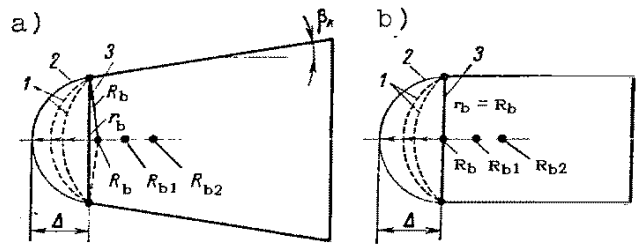

Figure II-1-7. Cone (a) and Cylinder (b) with Spherical and Flat Bluntness. 1) secant spherical nose; 2) tangent spherical nose; 3) flat face.

and the latter to a spherical nose tangent to a cylindrical surface.

If the blunt surface is flat, i.e., made in the form of a flat face (Fig. II-1-7), it can be regarded as a sphere of infinite radius.

The tangent spherical nose and the flat face are two characteristic blunt shapes that can be represented as the boundaries of the range containing the other possible shapes.

These two characteristic forms are also of interest in investigation of the aerodynamics of blunt bodies with intermediate nose shapes, since they enable us to evaluate the extreme values of the various aerodynamic parameters that they possess.

The spherical nose and the flat face may be regarded as particular cases of the elliptical surface. Figure II-1-8 represents a cone and a cylinder with this type of bluntness. The geometrical characteristics of the elliptical nose are its major and minor axes, which may be differently oriented. Figure II-1-8 shows the particular case in which the major axis is perpendicular to the axis of the body. If the two axes are equal, the elliptical bluntness becomes spherical. When the minor axis is zero, the elliptical surface degenerates into a plane.

Like a spherical bluntness, the elliptical nose may be either secant or tangent. In the latter case, the radius R_b of the smaller base of the cone is not, generally speaking, equal to the semiaxis applying to it. This equality is observed strictly when the nose is faired into the cylinder. It can also be used in approximation for a cone with a small angle β_c. /50

Yet another surface form, that shown in Fig. II-1-9, may be cited along with the bluntness forms indicated above. The bluntness shown here takes the form of a flat face with a circular bevel of radius r. When $r = r_b$, the bluntness becomes spherical; when $r = 0$, the surface becomes a flat face.

For a given nose type, the aerodynamic characteristics of a blunt body depend strongly on the bluntness ratio, a term that we shall henceforth apply to the ratio of the nose base radius r_b to the radius r_{mid} of the body's largest cross section. Also

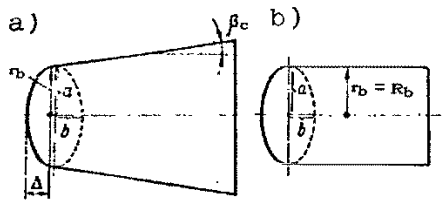

Figure II-1-8. Cone (a) and Cylinder (b) with Elliptical Bluntness.

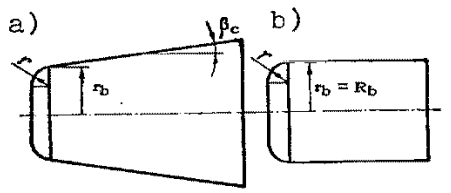

Figure II-1-9. Cone (a) and Cylinder (b) with Bluntness in the Form of a Flat Face with a Circular Bevel.

important is the geometrical parameter of the bluntness itself. For a spherical nose, this parameter is the ratio $(R_b)_{tan}$ R_b, where $(R_b)_{tan}$ is the radius of the tangent spherical nose. This parameter varies from 1 to 0. For an elliptical nose, this parameter might be the semiaxis ratio $\bar{b} = b/a$, which varies for a cylindrical body in the range $0 \leq \bar{b} \leq 1$ and for a conical body in the range $0 < \bar{b} < 1$.

For small angles β_c of conical bodies, it is convenient to take the nose height Δ (see Fig. II-1-7) as one of its characteristic dimensions and the radius r_b as the other. Then the bluntness parameter can be defined as the ratio $\bar{\Delta} = \Delta/r_b$, which can vary in the range $0 \leq \bar{\Delta} \leq 1$.

We see from Fig. II-1-9 that the quantity $\bar{r} = r/r_b$, which will vary in the range $1 \leq r \leq 0$ for cylindrical bodies and conical bodies with small β_c, can be taken as the parameter for bluntness in the form of a flat face with a circular bevel.

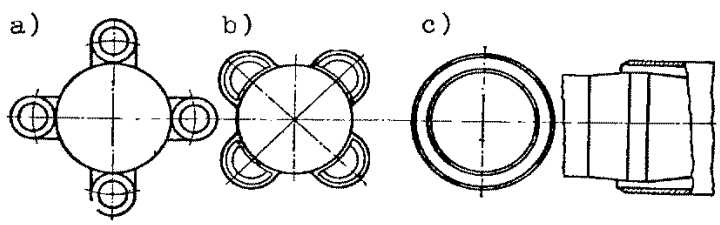

Figure II-1-10. Forms of Vehicle Bodies with Air Intakes. a) circular; b) semicircular; c) annular.

Center section. The center section of the body is usually made in the form of a cylinder. At the same time, it may be made in some cases in the form of a truncated cone with a small

generatrix inclination. On vehicles with jet engines (JE), the body center section may have either an annular shoulder or one or more sector shoulders to provide for accomodation of air intakes (Fig. II-1-10). /51

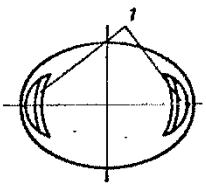

Figure II-1-11. Oval Body Form with Two Air Intakes.

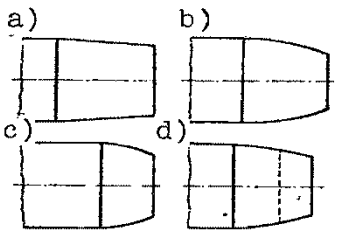

Figure II-1-12. Shapes of Tapering Tail Section. a) cone; b) tangent ogival (parabolic) tail section; c) secant ogival (parabolic) tail section; d) combination of ogive and cone.

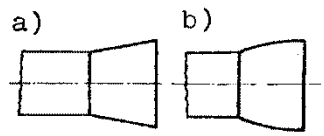

Figure II-1-13. Shape of Expanding Tail Section. a) conical; b) ogival.

The body center section need not be symmetrical. For example, a body of oval rather than circular cross section (Fig. II-1-11) is used to accomodate JE air intakes 1.

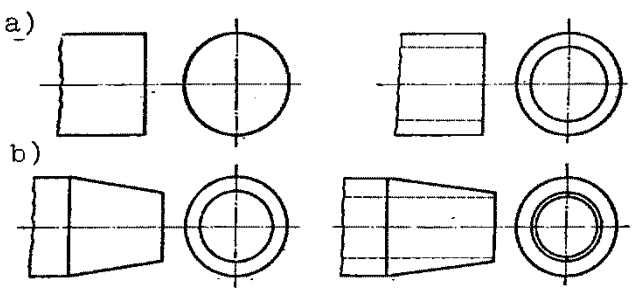

Figure II-1-14. Base-Section Shapes for Solid Bodies and Bodies with Flow Passage. a) cylindrical section; b) tapering conical section.

Tail section (stern). This section stands out from the body as the element of the body whose diameter progressively decreases (or increases) toward the base section.

The main function of the tapering tail section is to reduce total drag. Tapering tail shapes are shown in Fig. II-1-12.

In some cases, the shape of the tail section is arrived at from design considerations. It may even expand. In the latter case (Fig. II-1-13), the tail section helps improve the stability of the vehicle, although it increases drag.

The base section bounds the body or its tail section. It may be either a closed face surface or a flat ring (Fig. II-1-14). Sometimes the body is physically so designed that there is no distinct base section. In this case, the base component may present a surface of arbitrary shape. For example, the powerplant nozzle unit influences the shape of the base section. Figure II-1-15 presents certain possible forms of body base sections with nozzles. /52

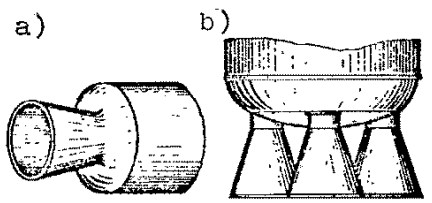

Figure II-1-15. Shapes of Body Tail Sections with Nozzles. a) single-nozzle unit; b) four-nozzle unit.

The forms of blunted and sharp nose sections and, in general, the body shapes that we have examined do not, of course, exhaust the entire variety. We have presented here only the simplest shapes, which do, to a certain degree, reflect this variety and are typical of it.

§II-2. SHAPES OF LIFTING, CONTROLLING, STABILIZING, AND AUXILIARY SURFACES

Profile. To a considerable degree, the aerodynamic properties of a wing are determined by its profile - the contour of the wing in a section passed perpendicular to its plane. The orientation of the cutting plane is to a certain degree arbitrary: it may be perpendicular to the leading edge, coincide in direction with the

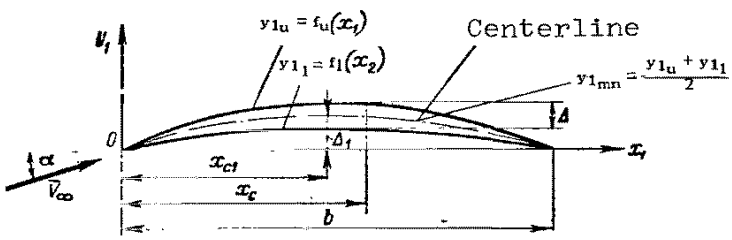

Figure II-2-1. Arbitrary Wing Profile in Uniform Undisturbed Flow at Angle of Attack α.

root chord, etc.

In general, a profile may have a curvilinear shape and no symmetry (Fig. II-2-1). The shape of a profile is given by the equations $y_{1u} = f_u(x_1)$ and $y_{1l} = f_l(x_1)$ of the upper and lower parts, respectively, of its contour.

The principal geometric parameters of the profile are indicated in Fig. II-2-1. We usually deal with dimensionless parameters: the maximum thickness ratio $\bar{\Delta} = \Delta/b$; the dimensionless distance to the point of maximum thickness $\bar{x}_c = x_c/b$; the camber $\bar{\Delta}_1 = \Delta_1/b$ and the dimensionless distance to it $\bar{x}_{c_1} = x_{c_1}/b$. /53

Figure II-2-2. Profiles of Supersonic Lifting and Stabilizing Surfaces. a) rhomboid; b) modified rhomboid; c) lenticular.

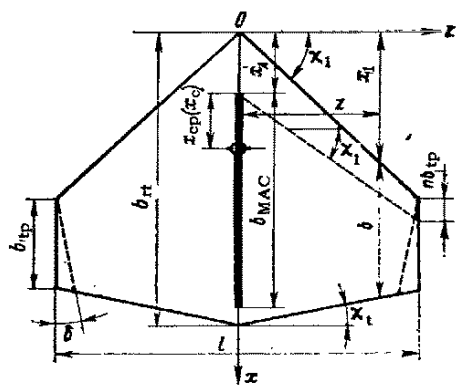

Figure II-2-3. Main Geometric Parameters of Generalized Wing Planform.

With horizontal symmetry, the equations of the upper and lower contours take the form $(y_1)_{u,l} = \pm f(x_1)$, where the plus sign applies to the upper contour and the minus sign to the lower. The centerline coincides with the chord and the camber is zero.

In modern high-speed vehicle designs, the lifting and stabilizing surfaces may have one of the following profiles: rhomboid, modified rhomboid, or lenticular (Fig. II-2-2) [23].

The first two profiles are distinguished by simplicity of manufacture. The rhomboid shape has an advantage in that it makes the wing more rigid than the modified shape. From the aerodynamic standpoint, the modified profile has some advantages, since it offers less drag and a higher lift/drag ratio at the same width as the rhomboid profile.

The lenticular profile offers even less drag than the modified rhomboid (at a given thickness ratio). The wing can be made quite rigid by adjusting the leading- and trailing-edge taper angles.

When the leading-edge taper angles are increased, the possibility of increased wave drag must be considered, as well as increased sensitivity of the flow to attack-angle variation. Thus, increasing the taper angles reduces the attack angles at which camber appears, at which point drag increases sharply, flow tends to separate, and flight stability deteriorates.

The basic difference between supersonic and subsonic profiles is that the former are symmetrical with respect to the chord while the leading edge is sharp. The nature of the flow and the pressure distribution at supersonic speeds is such that cambering of the profile centerline, which is advantageous at subsonic speeds, has no particular merit.

Planform. Modern aircraft have wings with a wide variety of planforms. Selection of this form depends on the purpose of the vehicle and its speed range. In specifying a wing planform, not only its contour, but also all geometrical parameters, both dimensional and dimensionless, are defined. A notion of the principal geometrical parameters can be obtained from Fig. II-2-3, which shows a diagram of the wing of a modern airplane. /54

The aerodynamic coefficients of a wing of specified planform and at a given flight speed depend on the sweep angles κ_l and κ_t of the leading and trailing edges, respectively; the wing aspect ratio $\lambda = \ell/b_{mn}$ or $\lambda = \ell^2/S_{wg}$ ($S_{wg} = \ell b_{mn}$ is the wing planform); the root and tip chord ratios (respectively $\bar{b}_{rt} = b_{rt}/b_{mn}$, $\bar{b}_{tp} = b_{tp}/b_{mn}$).

A most important geometrical characteristic widely used in aerodynamic research is the mean aerodynamic chord (MAC). The MAC is the chord of an equivalent wing of rectangular planform that has aerodynamic characteristics identical to those of the given wing when its planform is the same.

The moment coefficient of the equivalent wing

$$m_{z\,wg}^{e} = c_N \frac{x_A}{b_{MAC}} + m_z - c_R \frac{y_A}{b_{MAC}},$$

where x_A and y_A are the coordinates of the equivalent-wing leading edge as reckoned from a z-axis that passes across the leading edge of the given wing (Fig. II-2-3).

Equating $m_{z\,wg}^{e}$ to $m_{z\,wg}$ (I-5-16'), we obtain

$$b_{MAC} = 2\,(m_z S_{wg})^{-1} \int_0^{l/2} m_z b^2(z)\,dz;$$

$$x_A = 2\,(c_N S_{wg})^{-1} \int_0^{l/2} c_N b(z)\,x_1\,dz;$$

$$y_A = 2(c_R S_{wg})^{-1} \int_0^{l/2} c_R b(z) y_1 dz.$$

Thus, the MAC and the coordinates x_A and y_A will, strictly speaking, depend as integral quantities on the distribution of local aerodynamic parameters over the wingspan. In practice, it is assumed that the MAC and the coordinates x_A and y_A depend only on the geometrical characteristics of the wing. Accordingly, the mean aerodynamic chord

$$b_{MAC} = \frac{2}{S_{wg}} \int_0^{l/2} b^2(z) dz,$$

and the coordinates

$$x_A = \frac{2}{S_{wg}} \int_0^{l/2} b(z) x_1 dz; \quad y_A = \frac{2}{S_{wg}} \int_0^{l/2} b(z) y_1 dz.$$

For a swept wing with tip edges parallel to the root chord,

$$\frac{b_{MAC}}{b_{rt}} = \frac{2}{3} \frac{\eta^2 + \eta + 1}{\eta(1+\eta)},$$

where $\eta = b_{rt}/b_{tp}$ is the reciprocal taper of the wing.

The relative coordinate

$$\frac{x_A}{b_{MAC}} = \frac{(\eta+2)(\eta+1)}{8(\eta^2+\eta+1)} \lambda \operatorname{tg} \chi_1,$$

where λ is the wing aspect ratio.

The leading-edge sweep angle χ_1 is related as follows to the sweep angle χ_n on an nth-of-chord line (see Fig. II-2-3): /55

$$\operatorname{tg} \chi_1 = \operatorname{tg} \chi_n + \frac{4n}{\lambda} \frac{\eta - 1}{\eta + 1}.$$

The center of pressure or the wing aerodynamic center is reckoned in practice from the origin of a mean aerodynamic chord running along the wing's root chord (see Fig. II-2-3).

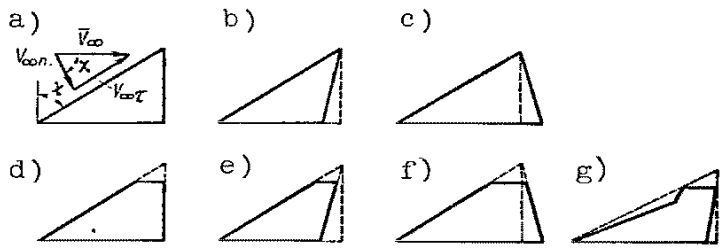

Figure II-2-4. Typical Wing Planforms of Modern High-Speed Aircraft.

Use of the mean aerodynamic chord as a characteristic geometrical parameter is convenient in that the length of this chord and the position of the aerodynamic (pressure) center with respect to its leading edge remain almost unchanged with changes in wing planform if wing area is preserved.

Typical wing planforms of modern high-speed aircraft appear in Fig. II-2-4. A characteristic feature of all wings is the presence of leading-edge sweep, whose principal purpose is to lower drag by lowering the normal velocity component of the undisturbed oncoming flow ($V_{\infty n} = V_\infty \cos \chi$).

For vehicles designed for subsonic flight, a general decrease in drag shifts shock stall (the "sound barrier") to higher speeds.

For supersonic aircraft with strongly swept wings, the passage through the sound barrier is smoother, without any substantial increase in drag; this is particularly important to preserve flight stability.

At supersonic speeds, wing aerodynamic characteristics depend strongly on whether the leading edge is subsonic or supersonic.

A leading edge is called subsonic is it lies inside a Mach cone with its apex at the forward point of the wing (Fig. II-2-5), since the oncoming-flow velocity component normal to the edge will then be smaller than the speed of sound ($V_{n\infty} < a_{n\infty}$, $M_{n\infty} < 1$).

Thus, the wing is in subsonic-flow conditions, in which a sharp leading edge is not advantageous. Flow conditions can be improved and better aerodynamic characteristics, e.g., a larger lift/drag ratio, can be obtained by rounding the leading edge slightly.

Aerodynamic characteristics will improve owing to the formation of a vacuum in the vicinity of the leading edge, leading to the formation of a suction force and, consequently, reduced drag. /56

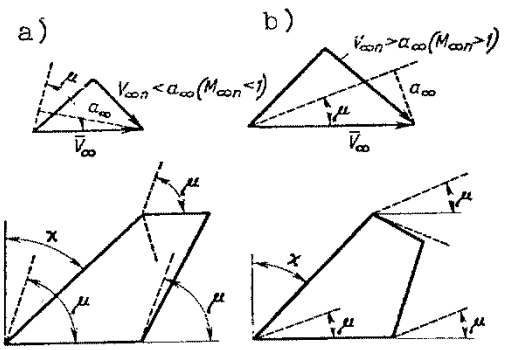

Figure II-2-5. Nature of Wing Edges in Supersonic Flight. a) leading, trailing, and lateral edges subsonic; b) same edges supersonic.

It should be remembered that drag can be lowered only if the radius of curvature, which depends on attack angle, has been properly selected. On deviation from certain optimum values of these parameters, no reduction of drag is obtained. This is because, for example, at reduced radii of curvature and larger attack angles, flow separates and drag rises.

A wing leading edge is called supersonic if it lies outside the Mach cone (see Fig. II-2-5b), since the Mach number of the flow will then be greater than unity in the direction of the normal to the edge. In view of the peculiarities of supersonic flow, it is desirable that the leading edge be sharp.

Like the leading edge, the trailing and lateral edges may also be subsonic or supersonic, with strong effects on flow over the wing.

A subsonic trailing edge forms an angle smaller than the Mach angle (see Fig. II-2-5a) with the wing's horizontal axis of symmetry. The distribution of velocity and pressure on the wing inside the Mach angle depends on the tip losses associated with flow of air across the side edge when it is subsonic (see Fig. II-2-5a, lateral subsonic edge inside Mach cone). This overflow effect reduces lift in this part of the wing.

To eliminate the unfavorable effect of the lateral edge, it is made supersonic, i.e., placed outside the Mach cone (see Fig. II-2-5b).

Another effect associated with the presence of a subsonic edge consists in its having an influence, in many cases unfavorable, over the entire section of the wing inside the Mach angle. To eliminate this effect, the trailing edge is made supersonic by giving it an inclination angle larger than the Mach angle (see Fig. II-2-5b).

We may conclude from the above that with an appropriately selected wing planform, the necessary aerodynamic characteristics can be secured. As we see from Fig. II-2-4, various wing forms with straight leading edges can be obtained by appropriate transformation of the delta wing (see Fig. II-2-4a). The delta wing has all of the desirable properties of wings with swept leading edges and, in addition, a number of advantages that become important under certain conditions of flight.

Thus, it has been established that the shift of the wing pressure center is very small in the transonic range, so that the vehicle is easier to stabilize and control. The lift/drag ratio of the delta wing at supersonic speeds is higher than those of certain other wings, and in particular that of the ordinary swept wing (Fig. II-2-4e), since there is no detrimental tip effect. Finally, the delta wing has certain design advantages that make is possible to obtain a stronger and more rigid wing and utilize the rather large internal space to accomodate equipment and fuel. Since the controls are placed along the trailing edge, which is perpendicular to the axis of the vehicle, they are more effective. /57

All of the above advantages of the delta wing and certain others naturally make their appearance under certain flight conditions. Delta wings are usually used for high-speed supersonic aircraft. With a change in flight conditions or in mission of the vehicle, delta wings may be found ineffective and other wings may be called for.

Figure II-2-4 shows possible wing designs other than the delta wing. Each of these may be regarded as an improved version of the delta.

Figures II-2-4, b and c, show tetragonal wings. The pressure center has been shifted forward in the first wing and aft in the second. The first wing has the smaller lift, and the second a somewhat larger lift.

The pentagonal wing shown in Fig. II-2-4d has properties quite similar to those of the delta if the tip rake is small. Although it does reduce the lifting-surface area slightly, this rake eliminates the sharp tip, which is not only structurally weak but is strongly affected by heating.

Two other modifications (see Figs. II-2-4, e and f) are classed as hexagonal wings, which have characteristics similar to those of the tetragon if the tip rake is small.

An important property of pentagonal and hexagonal wings with adequately developed tip chords consists in the fact that the flow over areas of the wing near the trailing edges will depend to a major degree on the flow over the lateral edges; this must

be taken into account in designing these wings.

Figure II-2-4g shows a diagram of an octagonal wing with a broken-line leading edge. This wing may be regarded as a combination of swept and delta wings. It has the property that the position of the center of pressure undergoes practically no change in transonic flight, in contrast to the case of the ordinary swept wing, in which the center of pressure shifts toward the leading edge with increasing speed.

Rectangular wings with the usual aspect ratios are not widely used. The basic reasons for this are their substantial drag, which rises sharply with the approach of the sound barrier, which is observed at comparatively low $M_\infty < 1$, plus the substantial shift of the center of pressure in the transonic speed range.

Rectangular wings of small aspect ratio have recently come into use as lifting and controlling elements in designs for high-speed aircraft. Owing to the favorable interference with the body, such wings have quite good aerodynamic characteristics.

Selection of the wing planform is one of the most critical points in elaboration of a vehicle design; it must be based on thorough theoretical and experimental studies that take account of the vehicle's mission and its specific flight conditions.

The annular wing. Annular wings are used as tail and lifting surfaces (Fig. II-2-6). Such a wing is characterized by the profile setting angle α_0 with respect to the longitudinal axis of symmetry, by the radius r_0 of the circle passing across the trailing edges of the sections (the "base" radius), and by the aspect ratio $2r_0/b$ (b is the profile chord). The vehicle can be made smaller transversely at a given lift by using the annular wing. The rigidity of the wing practically eliminates flutter. /58

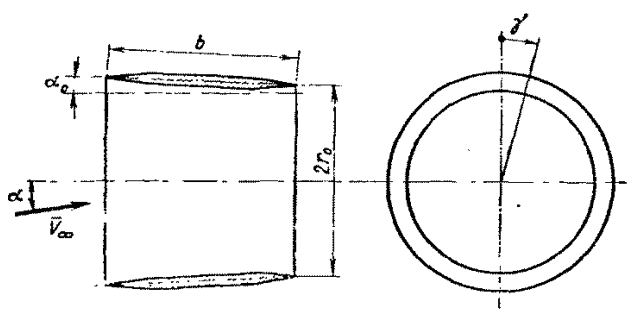

Figure II-4-6. Annular Wing.

The longitudinal symmetry of the wing makes it easy to create controlling forces in any direction with no roll, so that maneuverability is high. The large critical attack angles allow reliable performance over a broad range of attack angles. The plate (pylon) wing mounts tend to increase the lift of the annular wing. The pylons also act as stabilizers for weathercock and longitudinal static stability.

The advantages of the annular wing become particularly sensible when it is mounted on a jet-engined vehicle; it is then used simultaneously as a device to take in atmospheric air. It is also helpful for vehicles that take off vertically or from small areas.

The disadvantages of the annular wing include the weaker (by comparison with the flat wing) dependence of lift on attack angle and the drag increase from the pylons. The annular wing does not ensure transverse stability of the vehicle. Its lift is lowered owing to unfavorable interference with the body. This adverse effect becomes more pronounced the closer the wing to the body.

Wing twist. The aerodynamic characteristics of a wing may be improved with the aid of twist, which takes two forms — aerodynamic and geometric.

The aerodynamic-twist method consists in shifting the point of greatest profile thickness along the span of the wing (with respect to the leading edge), i.e., in varying the distance ratio $\bar{x}_c = x_c/b$ (see Fig. II-2-1). The wing remains flat.

In geometric twist, the relative dimensions of the profile remain constant, but the angle formed by the profile chord with the direction of the root chord is varied along the span. Thus, the wing is "twisted," acquiring the shape of a curved surface.

The basic purpose of the twist is to create better flow conditions over the tip areas of the wing, conditions that provide a more favorable pressure distribution and, as a consequence, a larger lift/drag ratio of the wing and improved stability characteristics. The same purpose is served by certain auxiliary surfaces mounted on the wing, such as the boundary-layer fence and the leading-edge dogleg. /59

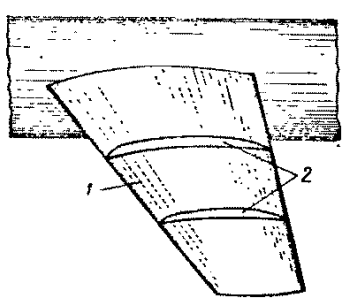

Figure II-2-7. Half-Wing (1) with Boundary-Layer Fences (2).

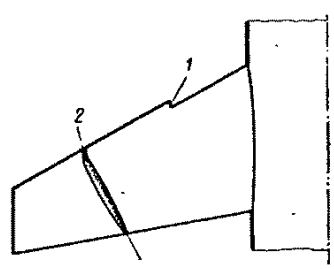

Figure II-2-8. Shape of Wing with Dogleg. 1) dogleg; 2) "bead."

Boundary-layer fences are small projections on the top of the wing, running parallel to the vehicle longitudinal axis (Fig. II-2-7). Each half of the wing carries 2-3 such fences. Their purpose is to prevent the boundary layer from overflowing spanwise and to reduce tip separation.

The boundary-layer fences may be replaced by another device, a "dogleg" on the front of the wing (Fig. II-2-8) that also prevents crossflow of the boundary layer. The front of the outboard part of the dogleg is lipped ("beaded") to provide smoother flow without boundary-layer separation at large angles of attack.

Auxiliary surfaces and aerodynamic and geometric twist may be used either independently or in combination with one another. For example, the twist may be combined — aerodynamic and geometric simultaneously. These ways to improve wing efficiency are used basically for subsonic vehicles and are not effective enough at supersonic speeds.

Supersonic wings are usually flat and may, in some cases, have a slight aerodynamic twist.

Placement of wings and tailplanes on body. On vehicles that are not designed for extensive midcourse maneuvering and have the conventional so-called airplane layout, the rule is to use the monoplane arrangement of the wings on the body (Fig. II-2-9c). The wings may be pivoted or fitted with ailerons to create controlling forces for directional maneuvering with a simultaneous rolling motion.

Of the four forms of the monoplane configuration — low-wing, mid-wind, high-wing and parasol (see Fig. II-2-9, b, c, d, e) — //60 the mid-wing configuration is most often encountered in high-speed designs. It provides better flow conditions where the wing meets the body, with less tendency to boundary-layer separation.

The monoplane configuration can be improved by introducing dihedral — positive or negative (see Fig. II-2-9, f and g). A positive dihedral aids in improving static transverse stability, while negative dihedral tends to reduce it. Negative dihedral is used for swept wings in order to bring down the high degree of transverse stability created by the wing and thus make control easier.

To permit broad maneuvering in space, vehicles are fitted with wings in the so-called normal or cross (+) and X configurations (see Fig. II-2-9, h and i). These wings act simultaneously as controls or are used to mount control surfaces. In the normal and X configurations, directional maneuvers can be executed without preliminary rolling.

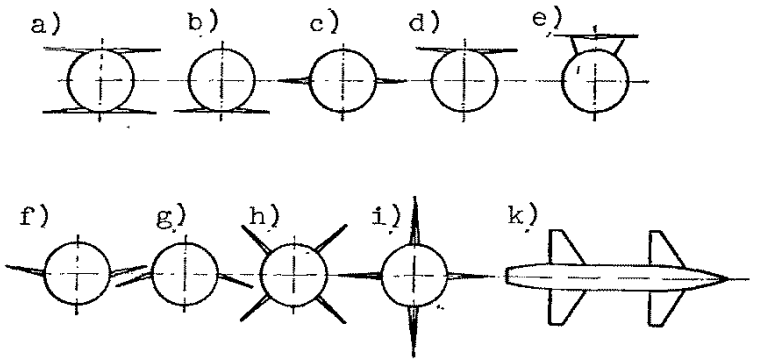

Figure II-2-9. Variants of Wing Positioning on Vehicle Body. a) biplane; b) low-wing monoplane; c) mid-wing monoplane; d) high-wing monoplane; e) parasol monoplane; f) positive dihedral; g) negative dihedral; h) X; i) cross; (k) tandem.

It must be remembered that neither scheme gives a lift advantage. However, the X-wings have certain advantages as controls. In practical cases, the configuration selected is often largely determined by structural considerations.

Usually, the wings are mounted symmetrically in these configurations and have short spans and small areas. Their small area predetermines the use of such wings for high-speed vehicles with which considerable lifting and controlling forces are generated.

When it is necessary to increase lift at a given wing area and span, the tandem arrangement of the surfaces is used (see Fig. II-2-9k). Here the rear wings may simultaneously perform the functions of tail surfaces.

The schemes of attachment of the tailplanes to the body are more varied than those for the wings. This is because of the special function of the tailplanes as stabilizing and controlling /61 elements whose shape and positioning may change substantially on even slight changes in the layout of the body, wings, engines, and other elements of the vehicle.

Of this wide variety, we might single out the two basic layouts — the normal (+) and X configurations, which are used independently and, in addition, serve as a kind of base for the construction of other schemes (Fig. II-2-10, a and i). Naturally, the general aerodynamic properties of the isolated tailplane are identical to those of wings. However, in combination with the other elements on the body, these properties of the tailplane may change substantially, and this influences selection of the specific configuration by calling for departures from the ordinary

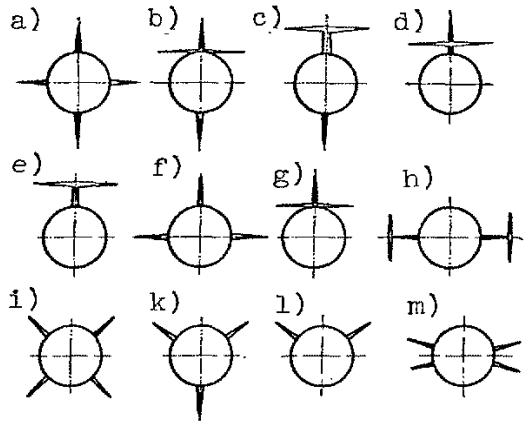

Figure II-2-10. Diagrams of Various Attachments of Tailplane to Vehicle Body.

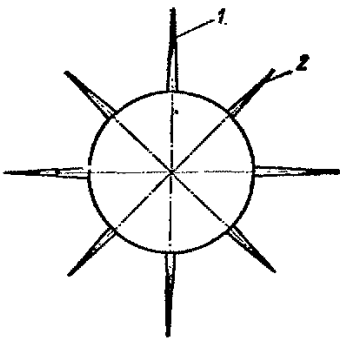

Figure II-2-11. Relative Positions of Wings (1) and tailplanes (2) on vehicle body.

normal or X configurations.

Figure II-2-10, b-h shows variations from the normal scheme that reflect the tendency to move the horizontal or vertical tailplanes upward or to the side in order to reduce the adverse effect of the disturbed flow from the wings or jet-engine exhaust. The X-configuration and its modifications (see Fig. II-2-10, i-m) may also be used for this purpose.

In many cases, a tail with vertical symmetry may not have horizontal symmetry, as we see from Fig. II-2-10, b-g. Certain inadequately effective elements of the normal or X-configuration are eliminated in the horizontally unsymmetrical tail. For example, the ventral fin is absent in diagrams d-g of Fig. II-2-10; in k, one fin is lacking and the remaining fin is oriented vertically downward; the two ventral fins are missing in diagram l.

Proper orientation of the tail with respect to the wings, as well as to the body and engine, is of great importance in securing the desired vehicle aerodynamic characteristics.

In placing the tail and its individual elements on the body, it must be made certain that the detrimental influence of the body itself, as well as that of the wings and engine, is minimal. For example, the X-configuration tail may be selected in order to reduce interference from a normal wing (Fig. II-2-11).

§II-3. CONTROLS

/62

Basic types of controls. The trajectory of an unguided vehicle acted upon only by drag and gravity is usually said to be natural or ballistic. The absence of any artificially created controlling aerodynamic or other force normal to the trajectory

is characteristic for such a trajectory. The trajectory that a guided vehicle must follow to execute a given maneuver will differ from the natural trajectory owing to an additional controlling effort that coincides with the normal to the flight-speed vector. Devices that develop the required controlling forces are known as controls. The controls are part of the system guiding the motion of the vehicle, which is understood to include the aggregate of apparatus and devices that provide for measurement of the deviations of the vehicle's actual motion from nominal, shape an appropriate signal, and generate the controlling force.

Depending on the physical nature of the controlling force, controls may be classified into three basic types: aerodynamic, gasdynamic, and combined.

Aerodynamic controls create the controlling force by changing the external-flow conditions and, consequently, producing a controlling force of aerodynamic origin. The control is a device that changes the magnitude and direction of the aerodynamic-force vector.

The action of gasdynamic controls is based on utilization of the effect produced by a change in the direction of the gas jet issuing from the nozzle of a reaction engine. The controlling force arises as a result of deflection of the thrust vector from the direction of the tangent to the trajectory.

Special thruster jet engines are used in some gasdynamic control designs.

Combined controls use the effects of aerodynamic and gasdynamic controls simultaneously in developing the controlling force.

Aerodynamic controls. Controls of this type are used for vehicles moving in rather dense layers of the atmosphere. They can be classified into the following groups: control surfaces, rollerons, spoilers, pivoting wings, and wing flaps.

Control surfaces, mounted at various locations on the vehicle, may be classified as follows (Fig. II-3-1): a) all-moving-tail controls; b) tip controls; c) controls placed along the trailing edge of a lifting surface.

In turn, tip controls can be subdivided into ordinary tip controls and compensating controls (Fig. II-3-2).

Controls situated along the trailing edge may be inboard or outboard and take up part of the edge or the entire span (Fig. II-3-3).

Vehicle control surfaces serve as rudders, elevators, ailerons and elevons.

In neutral, rudders lie along the longitudinal axes of the vehicles. Deflections from neutral cause the vehicle to turn to the right or left. /63

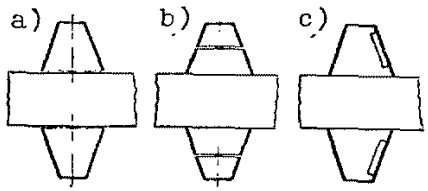

Figure II-3-1. Basic Types of Control Surfaces. a) all-moving; b) tip; c) trailing-edge.

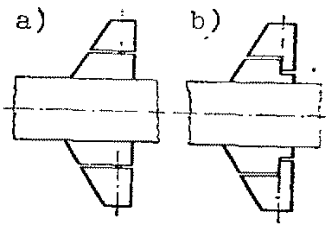

Figure II-3-2. Types of Tip Controls. a) ordinary tip controls; b) with compensation.

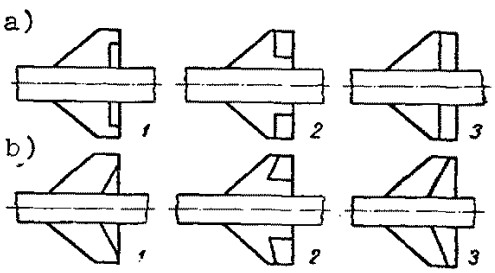

Figure II-3-3. Types of Trailing-Edge Control Surfaces. a) constant-chord; b) with inverse taper. 1) inboard control surface; 2) outboard; 3) full-span.

Elevators are perpendicular to rudders. They are deflected to change the direction of flight in the vertical plane and, consequently, altitude. The rudder-and-elevator combination makes it possible to control the vehicle simultaneously in two mutually perpendicular planes, i.e., to execute practically any maneuver in space.

There is another scheme for controlling the vehicle in space — that in which elevators and ailerons (rolling surfaces) are used. The ailerons are a pair of control surfaces that are situated on the trailing edges of the wing halves and can be deflected in either direction, thus rolling the vehicle. On simultaneous rotation of the elevator, a horizontal controlling-force component appears and turns the vehicle in the desired direction.

Unlike ailerons, elevons can be deflected in either direction independently of one another, and are therefore used simultaneously as roll controls and elevators.

Rollerons. The control device known as the rolleron is a variation of the aileron. Unlike the conventional aileron, the rolleron has a controlling plane that is rotated owing to the gyroscopic effect that arises when a disk located inside the surface rotates (Fig. II-3-4). The disk rotation axis y_1 is perpendicular to the plane of the rolleron, which turns freely about a z_1-axis rigidly bound to the wing or tail. Before flight, the disk is spun up to the required angular velocity, and this velocity is held constant during flight by the action of the slipstream on the teeth of the disk, which extend outside of the aileron. On rotation of the rolleron together with the wing about the vehicle longitudinal axis x_1 (under the action of a disturbing rolling moment), a gyroscopic torque M_g arises (Fig. II-3-4) and tends to turn the rolleron through a certain angle δ_r about the z_1-axis. Deflection of the rolleron plane out of the wing plane sets up a moment that will counter the rolling-moment disturbance. Thus, rollerons may also be used as roll stabilizers for the vehicle [81]. /64

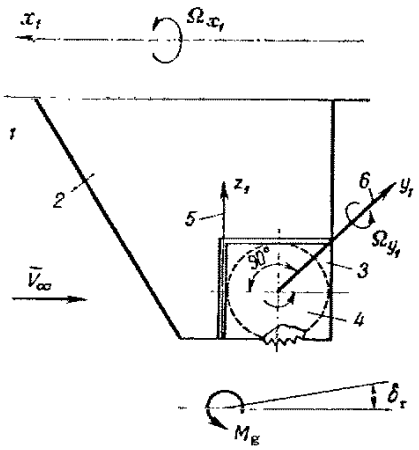

Figure II-3-4. Diagram Showing Function of Rolleron. 1) body; 2) wing; 3) rolleron; 4) disk; 5) rolleron axis; 6) disk axis.

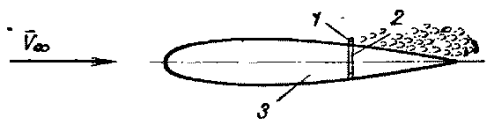

Figure II-3-5. Diagram Illustrating Function of Spoiler Control. 1) spoiler; 2) center of oscillation of spoiler; 3) wing.

An spoiler is a thin plate mounted in the wing and capable of projecting up above its surface (Fig. II-3-5). The controlling effect is due to flow stagnation when the spoiler is deployed [23].

At stagnation, the pressure on the part of the wing in front of the spoiler rises; the spoiler also tends to increase the speed of flow over the opposite side of the wing, with a consequent slight decrease in pressure, so that the resultant control effort is increased. The controlling effect of the spoiler is reduced to some degree by the lower pressure behind it that results from turbulization of the boundary layer, an increase in its thickness, and, consequently, separation, the zone of which extends to the

trailing edge when the spoiler is extended far enough. This undesirable effect is not serious when the area behind the spoiler is comparatively small.

At supersonic speeds, the pattern of flow over the deployed spoiler changes (Fig. II-3-6a) ([76], 1962, No. 4-5). Flow separates before and after the spoiler and stagnation zones form. The external flow moves around these zones like flow around impermeable wedges, forming a system of shock and expansion waves. The pressure-distribution diagram in Fig. II-3-6b indicates that, despite the vacuum behind the spoiler, a downward-directed controlling effort does appear.

To improve control effectiveness, spoilers are set in oscillatory motion whose amplitude and frequency is not usually regulated. The controlling force is adjusted by shifting the center of oscillation. The closer the center is to the wing surface, the longer is the time during which the spoiler will be "out," and, consequently, the greater will the controlling force be.

Spoilers have an advantage over control surfaces in their lower weight (including the drive mechanism). For this reason, spoilers are usually used on light aircraft.

A deficiency of spoiler control is that it does not give the aircraft a sharp maneuvering capability and increases frontal drag.

The pivoting wing is an ordinary wing that can be rotated relative to the body about the vehicle's transverse axis. Such a control has an advantage in that it delivers a large controlling effort at small deflection angles. /65

The pivoting-wing vehicle has the ability to maneuver quickly on trajectory, with the maneuver starting immediately on deflection of the wings, since it is unnecessary to turn the body with its large moment of inertia.

The pivoting wing may combine the control functions for pitch and roll of the vehicle.

The shortcomings of the pivoting wing include the large hinge moments necessary to drive it, although the drive power is not very large since the pivoting angles and speeds are small. Another shortcoming is a certain increase in the vehicle's frontal drag owing to the gaps between the pivoting wings and the body.

Wing load increases substantially on pivoting through large angles for sharp maneuvers, and this gives rise to a large bending moment applied to the body. Consequently, a pivoting-wing aircraft must have higher than normal strength.

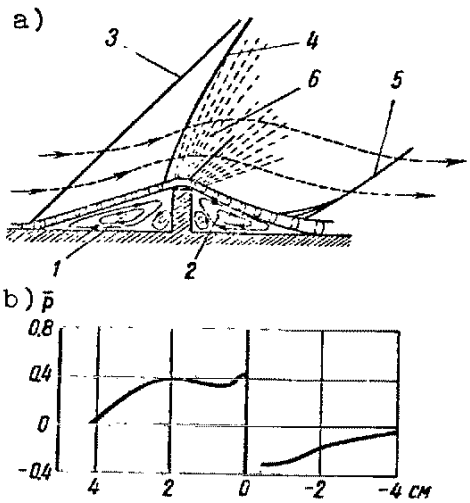

Figure II.3.6. Pattern of Supersonic Flow over Spoiler. a) pattern of flow over deployed spoiler (flow-separation zones 1 and 2, compression-shock system, 3,4,5, and expansion shock 6); b) distribution of excess pressure over wing surface around spoiler.

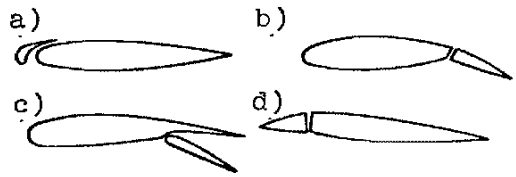

Figure II-3-7. Systems that Improve Wing Aerodynamic Characteristics. a) slat; b) plain flap; c) split flap; d) leading-edge flap.

Flaps. Various types of flaps occupy a special position among the aerodynamic controls, in that they make it possible to vary the aerodynamic characteristics of the vehicle [23].

Flaps are mounted at various points on the structure and usually serve to control a certain aerodynamic characteristic. Let us consider the group of wing flaps whose function it is to control lift. They include slats, plain flaps, split flaps, and other devices. The general effect of using these devices consists in the fact that they increase lift at large attack angles with a comparatively small increase in frontal drag.

Slats (Fig. II-3-7a) are small areas of the wing in the leading edge of the main lifting surface that can be shifted forward at large angles of attack. A stream of air tends to flow into /66
the resulting slot from bottom to top, thus ensuring smoother flow over the top side of the profile, since the kinetic energy of the air in the boundary layer is increased and separation is inhibited. Thus, flow separation is moved to attack angles larger than those at which it appears without the slats. Slats are sometimes made not over the entire length of the wing half, but only in front of the deflecting control surfaces in order to prevent detachment of flow from these surfaces and make them work more effectively at large deflection angles.

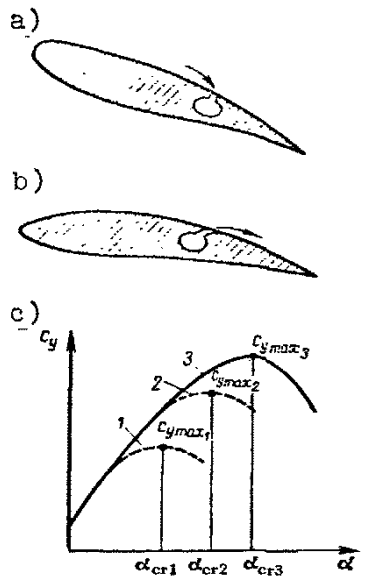

Figure II-3-8. Wing Boundary Layer Control. a) suction; b) blowing; c) increase in lift coefficient c_y and critical attack angle α_{cr} with increasing boundary layer suction [1) without suction; 2) weak suction; 3) strong suction].

Plain flaps (Fig. II-3-7b) are, like slats, small areas of the wing, but unlike the la ter they are situated at the trailing edge of the main lifting surface, as a kind of extension of it. The flaps are deflected downward, creating an additional head under the wing and thereby increasing its lift. A slot may be provided between the plain flap and the wing, making it possible to improve flow over the top of the wing and secure an additional lift increment.

Split flaps (Fig. II-3-7c) are sections of the bottom of the wing that can be deflected downward. The deflected flap creates a head under the wing and increases lift. A stagnant zone of vorticity with some underpressure forms between the deflected split flap and the wing. The result is boundary layer suction, which prevents separation of the layer and improves the characteristics of the wing at large angles of attack.

Unlike split flaps, leading-edge flaps (Fig. II-3-7d) are placed on the wing leading edges. In subsonic flight, deflection of the leading-edge flaps at large attack angles makes it possible to prevent flow separation from the sharp wing leading edges used on supersonic vehicles.

Boundary-layer suction and blowing. Boundary-layer suction and blowing devices that prevent boundary-layer separation, ensure smoother flow over the surface and, as a consequence, increase wing lift may be included among the high-lift devices.

Suction is secured using vacuum pumps working through a slot or system of holes (Fig. II-3-8a) located near the point at which boundary-layer separation would be expected.

Boundary layers are blown (Fig. II-3-8b) with discharge pumps, also working through slots and holes. The latter are placed somewhat upstream of the expected point of boundary-layer separation. The slot and hole axes should form an acute angle with the tangent to the profile contour.

The physical effect is the same for suction and blowing, and consists of an increase in kinetic energy of the air particles in the boundary layer, so that they are stagnated to a lesser degree. In the former case, this effect is achieved basically by increasing their velocity, and in the latter also by an increase in the mass of air flowing through the boundary layer. /67

The effectiveness of boundary-layer suction or blowing is evident from Fig. II-3-8c.

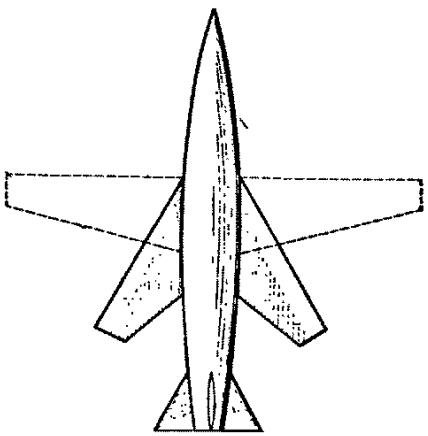

Figure II-3-9. Aircraft with Variable Geometry Wing.

Variable-sweep (swing) wing. One way to vary the lift of an aircraft is to use a device that changes the sweep of the wing or tail in flight (Fig. II-3-9). Such a device may be useful for winged vehicles with a broad range of speeds (from subsonic to high supersonic), since it provides optimum conditions for motion. For example, to break through the sound barrier with minimum drag and to prevent flutter, the wings are swept back to the maximum angle. In the ranges of high subsonic and supersonic speeds, the wings are extended to a position corresponding to a smaller sweep angle. At low speeds, as during takeoff, the vehicle is flown with the wings straight. Changing the sweep increases lift and improves the effectiveness of the aerodynamic controls. Control is made more effective owing to a certain forward shift of the center of pressure.

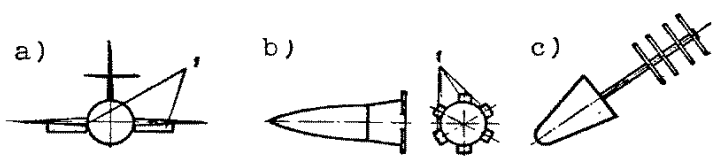

Figure II-3-10. Braking Devices. a) speed brakes on wing trailing edge; b) speed brakes on body tail section; c) strings of metal disks.

Braking flaps. Special drag-increasing devices known as braking, speed, or drag flaps are used to reduce speed. They may be mounted on the trailing edge of the aircraft's wing (Fig. II-3-10a) or at the tail of the body (Fig. II-3-10b). The large

slowing drag arises when these flaps are deflected through large angles, around 90°.

Metal disks joined by a cable (Fig. II-3-10c) and drag parachutes are also to be cited among aerodynamic braking devices.

Usually, the parachute is deployed in the final stage of the slowing process, after braking with the flaps or disks (or with flaps and disks simultaneously).

Gasdynamic controls are used under conditions in which aerodynamic controls are ineffective, as in thin layers of the atmosphere or at low speeds of the vehicle (e.g., at launch). /68

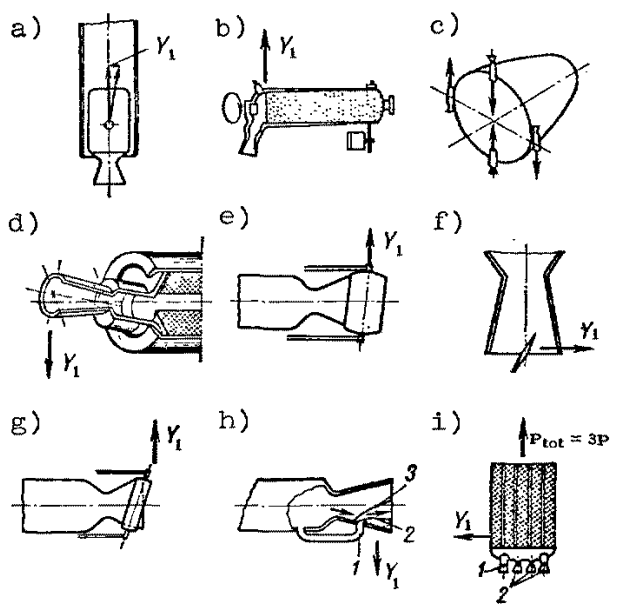

Figure II-3-11. Diagrams of Gasdynamic Controls. a) swiveled sustainer engine; b) pivoted vernier engine; c) operation of fixed thrusters; d) vectored nozzle; e) vectored hood; f) jet vanes; g) deflectors; h) injection of fluid into supersonic nozzle section; i) redistribution of thrust by nozzle closing in cluster (nozzle 1 open, nozzles 2 closed).

Figure II-3-11 shows devices that set up a controlling effort by pivoting the entire engine (Fig. II-3-11a) and by pivoting only the nozzle (Fig. II-3-11d).

Pivoting the main engine even through small angles sets up large controlling forces. However, considerable effort must be expended to turn the engine.

Use of a pivoting nozzle makes it possible to reduce the effort necessary for rotation, but this gives rise to a number of difficulties associated, in particular, with fouling and scorching of the movable joint between the nozzle and the engine chamber, with the result that the entire control is unreliable.

Simpler designs are the controls that use rotary attachments and the so-called deflectors (Fig. II-3-11, e and g). The rotary hood circles the jet of the main engine and is thus at all times being acted upon by combustion products. Such hoods

perform quite effectively, but they require frequent replacement owing to fouling and scorching. Deflectors are introduced into the gas jet only when it is necessary to develop the controlling force. Hence they are more reliable and last longer.

Jet vanes placed at the end of the sustainer nozzle (Fig. II-3-11f) can be used as controls. Deflection of the gas jet by these vanes produces rather large controlling forces. Although gas vanes are an effective control facility, they have substantial shortcomings. Since they offer substantial resistance to the stream of gases, they lower the effective thrust. They also burn out quickly under exposure to the high temperatures and velocities of the gas. /69

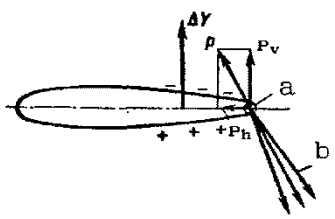

Figure II-3-12. Diagram of Combination Control. a) slotted nozzle; b) jet; P) jet reaction; P_v) vertical component of jet reaction; ΔY) additional lift of wing owing to redistribution of pressure over wing contour; P_h) horizontal component of jet reaction.

One of the modern gasdynamic-control designs is based on the principle of changing the direction of the sustainer-engine thrust vector by injecting a liquid or gas into the nozzle (Fig. II-3-11h).

The mechanism by which the controlling effort arises is as follows. The stream of liquid or gas injected into the supersonic section of the nozzle through hole 1 interacts with the supersonic flow of gaseous combustion products and is deflected from its original direction to flow in region 2.

As the main flow moves over this zone, a compression shock 3 forms, the flow is rotated behind it, and, as a consequence, the pressure is raised. The result is the lateral control force Y_1.

The magnitude of the control force can be regulated by varying the flow of injected liquid. Its direction can be changed by injecting the liquid through different holes placed around the circumference of the nozzle cross section.

It is characteristic of this control that the controlling force is generated with practically no loss of main-engine thrust. This is because the thrust loss that results from loss of mechanical energy by the gas flow as it passes through the compression shock is compensated by an increase in thrust due to the increased mass of outflowing gases. In addition, thrust may be increased slightly if the injected fluid is an oxidizer that reacts chemically with the unburned fuel to improve combustion efficiency.

Vehicles can be controlled by redistributing thrust by closing one or more of a circular cluster of sustainer-engine nozzles (Fig. II-3-11i). The result is eccentricity of the reaction force and a controlling moment.

The above gasdynamic controls can all be classed as controls based on use of the sustainer engine. A second class is that of controls that take the form of special control engines. One such device (Fig. II-3-11b) is the side-nozzle rotary ("vernier") jet engine.

A controlling force can also be created by special fixed engines with nozzles perpendicular to the vehicle axis (Fig. II-3-11c).

Combined controls. A diagram of a combined control appears in Fig. II-3-12. The basic element in the control is a rotary nozzle mounted on the trailing edge of the wing or tail and made in the form of a narrow slot of a certain length. The controlling force arises as a result of outflow of air from the nozzle, /70
which is inclined at a certain angle to the wing chord. This force has two components. One of them is equal to the normal component P_v of the thrust created by the rotary slot. The other is equal to the normal aerodynamic-force component ΔY that arises from redistribution of the pressure on the lifting surface by the interaction of the oncoming flow and the air jet issuing through the slot [80].

The so-called jet spoiler operates basically on this principle. Its gas jet is directed upward or downward through a slot in the wing. Lift is affected both by the reaction force of the spoiler and by pressure redistribution.

A shortcoming of the combined controls is inadequate effectiveness in the upper atmosphere and at low speeds. In spite of their apparent simplicity, they are actually quite complicated as regards design and are complicated to use owing to the need for a compressed-gas or liquid source.

§II-4. AERODYNAMIC CONFIGURATIONS OF AIRCRAFT

To obtain the required range, stability, and controllability and to satisfy a number of other tactical-technical requirements, an appropriate aerodynamic configuration of the aircraft must be arrived at.

By aerodynamic configuration or layout, we mean rational selection of the dimensions, external shapes, and relative positions of the vehicle's body, wings, tail, controls, and other elements.

In final elaboration of the design, these problems must be solved together in order to match dimensions, shapes, and relative positions. At the initial stage of a design, however, the layout can be selected and the calculations performed separately. Moreover, the fundamental aerodynamic layout may be outlined on the basis of tactical and technical requirements, without specific forms for the individual elements.

The proper aerodynamic layout for a vehicle can be selected with consideration of practical experience accumulated in aeronautical and rocket engineering and use of available theoretical and experimental data.

Vehicle aerodynamic configurations are divided into two classes.

Class One includes the aerodynamic configurations of tailless vehicles. The bodies of such vehicles have no conspicuous projecting surfaces. The aerodynamic layouts of tailless vehicles are classified on the basis of whether the vehicle is guided or unguided.

A long-range missile with a separating nose cone is a tailless vehicle (Fig. II-4-1a). The missile is stabilized on the powered part of its trajectory by the use of gasdynamic controls (for example, pivoting nozzles 1).

Unguided tailless vehicles include the so-called turbojet missiles (Fig. II-4-1b), which are spin-stabilized.

Class Two includes tailed vehicles, whose bodies may carry lifting and stabilizing surfaces.

The aerodynamic layouts of tailed vehicles can be classified /71
as wingless and winged or as combined wing-and-tail layouts.

Wingless tailed vehicle layouts include those of unguided and guided vehicles.

Figure II-4-1c shows a rocket with the configuration of an unguided wingless tailed vehicle. The tail on the body is fixed and acts as a stabilizer. The guided vehicle (Fig. II-4-1d) may be fitted with pivoting fins (1) or use gasdynamic controls.

Vehicles with the wing-and-tail configuration (Fig. II-4-1f) and with the combined wing and tail 1 (Fig. II-4-1g) are guided and can be classed in the same group: winged guided vehicles.

Guided winged vehicle configurations can be classified as normal, canard, and tailless, depending on the method used for guidance.

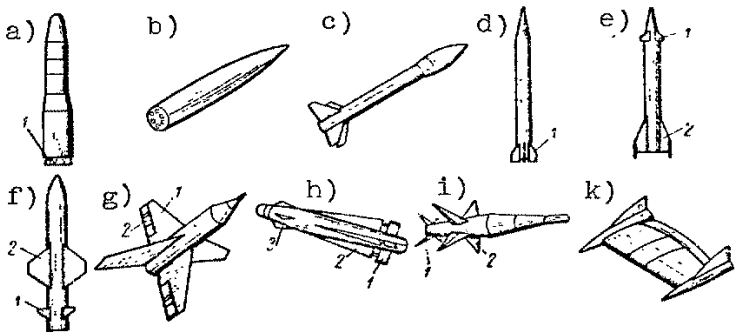

Figure II-4-1. Vehicle Aerodynamic Configurations. a) tailless guided missile; b) turbojet missile; c) wingless unguided vehicle; d) wingless guided vehicle; e) "canard" configuration; f) "normal" configuration; g) "tailless" configuration; h) "tailless" configuration with destabilizer; i) "tailless" configuration with stabilizer; k) "flying wing" configuration.

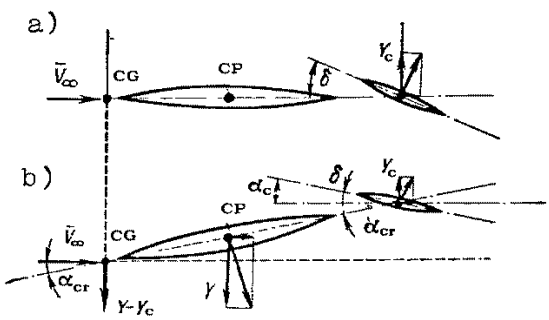

Figure II-4-2. Normal-Configuration Control of Vehicle. a) attitude prior to rotation; b) attitude after rotation of vehicle.

In the normal configuration (Fig. II-4-1f), the steering tailplanes 1 are placed behind the wing 2 on the vehicle's tail section, which endows it with a number of aerodynamic and structural advantages [80].

When the control surfaces are so positioned, the disturbances that they generate do not affect the wing and, consequently, the conditions of flow over it are more advantageous. These controls can be used for sharp maneuvering of the vehicle with retention of smooth flow over them. This is done by rotating the control surface through a rather large initial attack angle δ (Fig. II-4-2), which is then reduced in flight by the vehicle's attack angle α_{wg} to aid in preventing flow separation. /72

Tail-section control surfaces can be so designed as to provide for differential deflection of the horizontal fins as necessary to roll the vehicle.

We might consider a layout in which the rear surfaces work in pairs, like elevators and rudders, thereby providing pitch and yaw control, while a pair of surfaces on the wings acts as ailerons. A layout with fixed rear surfaces, in which pitch, yaw, and roll control is obtained by appropriate deflections of the wings, is also used. Sufficiently reliable roll stabilization is obtained in this configuration by deflecting a pair of forward control surfaces in opposite directions.

These configurations make CG trim less critical and allow much freedom in locating the aerodynamic surfaces and specifying their relative dimensions, as well as providing a wider range of guidance-system options. With the surfaces aft, a certain strength advantage is obtained, since the bending moments applied to the body are comparatively small.

The disadvantages of the normal configuration must also be considered.

1. The empennage, which is situated in a disturbed-flow zone behind the wing, is subject to the action of adverse forces, usually in the form of periodic shocks. As a result, the empennage shakes severely, in the phenomenon known as buffeting. With a view to preventing buffeting, there is a tendency to shift the empennage upward from the plane of the wing to get it outside of the disturbed-flow zone, even though this results in a loss of rigidity that may cause flutter of the tailplanes.

2. Since the wing and control-surface attack angles are of opposite signs, and, consequently, the lifting forces that they develop are oppositely directed, the over-all lift of the vehicle is somewhat lower.

3. For this reason, a destabilizing effect appears on deflection of the controls, with the result that the distance between the vehicle's centers of gravity and pressure is made shorter. This is somewhat detrimental to static stability. Further, if the control surfaces are situated at a short distance from the center of gravity, this may lower the tail damping moment and, consequently, impair dynamic stability; the periodic oscillations that arise on the trajectory will damp more slowly.

In the "canard" configuration (see Fig. II-4-1e), the steering tail 1 is forward of the wing 2 on the nose section of the vehicle and ahead of the center of gravity. The advantages of this layout are manifested in the fact that the controls are not disturbed by the wings and are therefore more effective. Because the signs of the control-surface and wing attack angles are the same and their lifts are in the same direction, the over-all vehicle lift increases [80].

Since the destabilizing moment is reduced when the control surface is deflected, static stability is somewhat improved over the normal configuration. Damping characteristics are also improved owing to the fact that the control device is usually far from the center of gravity.

Certain design advantages of the canard are associated with the fact that the control surfaces are comparatively small and therefore have small hinge moments. In addition, with the control surfaces and associated equipment forward, it is easier to accomodate fuel tanks and engines in the center and tail sections. /73

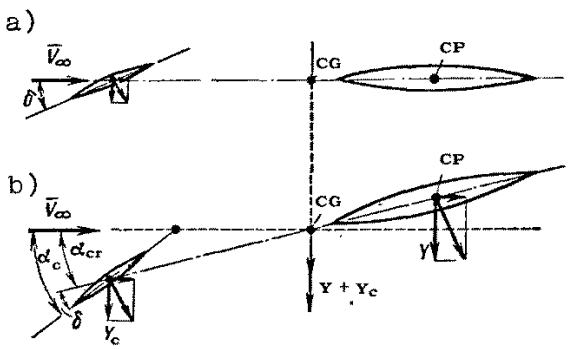

Figure II-4-3. Control of Canard-Configuration Vehicle. a) attitude prior to rotation; b) attitude after rotation of vehicle.

The deficiencies that limit practical application of this configuration are as follows.

1. The wing comes into downwash from the control surfaces, so that the true angle of attack is smaller and lift is reduced. This effect becomes stronger for small wing aspect ratios, when almost the entire wing surface is in downwash.

2. It is not convenient to use the control surfaces as ailerons for roll control, since the downwash behind them causes the wings to set up an opposed rolling moment and the ailerons are rendered practically ineffective. Moreover, because of the short arm, the aileron moment may even be smaller than the rolling moment that arises as a result of downwash. This deficiency can be corrected by providing the fixed wings with ailerons that are controlled independently of the forward surfaces, although this results in design difficulties and a weight penalty.

3. Flow conditions over the controls are unfavorable because of the large attack angles, which are equal to the sums of the wing attack angle α_{wg} and the control-surface deflection δ (Fig. II-4-3).

Flow separates from the surfaces at large angles of attack, and observations have shown that it is accompanied by pitching oscillations of the vehicle.

4. Placing the control surfaces forward of the center of gravity gives rise to a certain destabilizing effect. Here the position of the center of pressure varies as a function of surface deflection, and this makes it difficult to preserve a given range of variation of CP coordinates.

5. The loads on the controls and the bending moments applied to the body are larger than in the normal configuration, since the control surfaces have large attack angles.

6. It is difficult to provide directional stability in the canard configuration, which presupposes use of a long body nose section to carry the control surfaces. This difficulty arises from the large destabilizing moments of the nose and the need to have an expanded vertical tailplane with a long arm to the center of gravity.

In the tailless configuration, there is no sepearate controlling tail, and the controls 1 are placed on the trailing edge of lifting surface 2, which functions as a combined wing and stabilizing tailplane (see Fig. II-4-1h), whose functions may also be performed by a wing (see Fig. II-4-1i). It is also /74
possible to use gasdynamic controls at the stern of a tailless configuration. This increases the vehicle's maneuverability, since the forces applied to the control element act at the end of a long arm.

If the aerodynamic surfaces have a large area, the missile is said to be winged; if they are small, they act as stabilizers, and the vehicle becomes the ordinary ballistic missile. In the diagram of Fig. II-4-1g, the vehicle may have a fixed horizontal delta or trapazoidal wing and directional control may be obtained by deflecting the vertical surfaces. Pitch and roll control is provided by surfaces on the wing trailing edge that can be deflected in opposite directions.

Freedom from downwash, which lowers control-surface and wing effectiveness, is an advantage of this aerodynamic layout. Use of control surfaces on the horizontal wings makes roll control more dependable, since the possibility of a negative roll effect is eliminated. Static stability is quite independent of motion in pitch, yaw, and roll.

Vehicles with the tailless configuration may have a fixed fin either forward or aft of the center of mass.

Such fins are necessary to improve stability and damping characteristics. The vehicle shown in Fig. II-4-1h has fixed surfaces at its nose that act as destabilizers (3) and reduce the excessive static stability conferred by the strong expansion of the lifting surface toward the tail. The destabilizer acts simultaneously as a damper.

In Fig. II-4-1i, we see that the fixed fin 1 may be placed aft of a pivoting wing 2. It provides static stability and improves the damping properties of the vehicle.

The "flying wing" (see Fig. II-4-1k) is a variety of the tailless configuration in which the body of the vehicle is almost completely inscribed into the wing outline.

The "tailless" vehicle configuration compares favorably from the design standpoint in its compactness and the comparative simplicity of its external form. The absence of a separate controlling tail lowers frontal drag and reduces design weight. For this reason, the wing is not adversely affected by downwash.

The tailless configuration has a number of inherent disadvantages.

1. A vehicle with this configuration is not capable of sharp maneuvering, since the control surfaces are usually close to the center of gravity and cannot develop large controlling moments. A large controlling moment can be set up by increasing the control lift, which can be done by increasing the area of the surface or their deflections. However, this increases the power required to turn the controls and hence the weight of the vehicle.

2. Since the center of gravity of wing area and the design center of gravity are close together, the damping moment is small and the vehicle does not have good damping characteristics.

3. Stability and controllability deteriorate because of the /75
strong velocity dependence of the center-of-pressure coordinate. For example, for one of the tailless designs, the stability margin at $M_\infty = 1.5$ is 2.5-3 times greater than at subsonic speed, with the result that controllability deteriorates sharply, while this increase is only 1.3-1.5 for canard vehicles.

Configurations of multistage vehicles. These configurations are no different in principle from those that we have already described. Before staging, the configuration of a multistage vehicle may be regarded as guided-unfinned (see Fig. II-4-1a) or guided finned (Fig. II-4-4). The latter configuration may be used in the various modifications discussed above. The same classification can be extended to the parts of the vehicle that remain after separation.

However, certain aerodynamic-layout peculiarities are characteristic of multistaged vehicles; they arise from the tactical and technical requirements made of the vehicle as a whole (before separation) and of its individual stages.

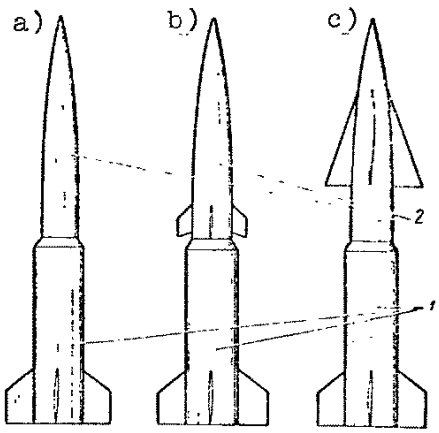

Figure II-4-4. Aerodynamic Layouts of Multistage Vehicles. a) second stage without fins; b) second stage with fins; c) second stage winged; 1) first stage; 2) second stage.

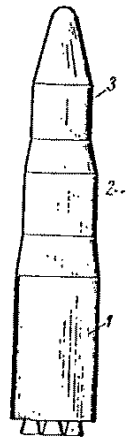

Figure II-4-5. Scheme of Multistage Rocket. 1,2,3) first, second, and third stages, respectively.

The vehicle as a whole must be stable and controllable. Gasdynamic controls are provided in the configuration of the guided unfinned vehicle (Fig. II-4-5) for this purpose. The finless body need not possess static stability in the aerodynamic sense. Figure II-4-4 shows a configuration with fins that serve to provide stability and controllability. Some designs have supplementary gasdynamic controls that function during the powered part of the flight.

The aerodynamic configuration of the vehicle that remains after separation of a stage may be the same, as shown in Fig. II-4-4, or different, depending on the purpose of the stage and the conditions of its flight. Figure II-4-4 shows how the part that remains after separation of the first stage may have unfinned (Fig. II-4-4a), finned wingless (Fig. II-4-4b), and winged (Fig. II-4-4c) configurations.

In the first case, the remaining stage may be the last stage and perform the functions of a separating nose cone. In the second case, the remainder may perform similar functions (the only difference being that the nose section is finned) or act as a second stage for an unfinned separating nose section. Finally, the remaining stage in the third case is the last stage and functions as an independent vehicle (antiaircraft rocket, lifting body). /76

An unfinned separating nose section (last stage) may be a guided or unguided vehicle and may be equipped with stabilizing devices or left statically unstable in its motion in the denser atmospheric layers.

Degree of symmetry of the vehicle about its longitudinal axis. The over-all aerodynamic layout of a vehicle is characterized by the degree of its symmetry about its longitudinal axis, i.e., the angle through which it must be turned for self-coincidence of its outlines.

Aircraft or rockets with the so-called airplane configuration have outlines that return to coincidence only on a 360° rotation. This shape corresponds to the extreme case of no symmetry about the longitudinal axis. There are vehicles for which shape coincidence occurs on rotation through 180° (configurations with 180° symmetry about the longitudinal axis).

Rocket aerodynamic layouts are characterized by higher degrees of symmetry. These vehicles have symmetry at less than 180°. Those with configurations having 120 or 90° symmetry about the longitudinal axis are typical. The configuration with 90° symmetry is particularly common (the so-called cross or X configuration). They have an aerodynamic advantage over the airplane configuration in that large lateral controlling forces can be obtained without first rolling the vehicle. This makes possible high maneuvering speeds in any plane, although it does increase the drag and weight of the structure. By virtue of symmetry, the resultant aerodynamic force on the vehicle when it is inclined to its velocity vector always lies in the plane of the longitudinal axis and the velocity vector, so that the corresponding longitudinal and lateral stability derivatives are equal.

One of the essential features of rocket layouts consists in the use of configurations with small-aspect-ratio aerodynamic surfaces. This causes nonlinearity of the aerodynamic characteristics, which is aggravated by interference between various elements of the vehicle (between the wing and tail, wing and body, etc.) and by the presence of large angular velocities.

§II-5. INFLUENCE OF MISSION AND TACTICAL-TECHNICAL REQUIREMENTS ON SELECTION OF VEHICLE AERODYNAMIC LAYOUTS

The selection of one or another aerodynamic layout is closely tied in with the mission of the vehicle and its tactical and technical specifications, in accordance with which the relative positions of the launch and target points, the shape of the trajectory, the type of powerplant and control system, and characteristic design features are established. Thus, a specific aerodynamic layout that meets tactical and technical specifications corresponds to a given vehicle. /77

Vehicle Type and Aerodynamic Layout Features

Let us examine various modern vehicle types and the corresponding aerodynamic layouts. We shall take the relative positions of the launch and target points as the factor determining vehicle type. Here, we shall use the accepted nomenclature for vehicle types, such as "space-to-space" (launch and target points in space), "space-to-ground" (launch point in space, target on ground), etc.

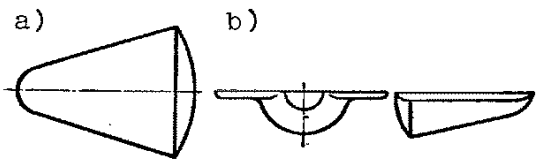

Figure II-5-1. Forms of Space-to-Ground Vehicles. a) finless; b) winged vehicle.

"Space-to-space." Since the motion takes place in airless space, the shape of the vehicle has practically no influence on its aerodynamic characteristics nor, consequently, on the parameters of the trajectory. In this case, therefore, selection of the optimum aerodynamic layout in the ordinary sense, as it applies for conditions of flight in the dense atmosphere, is meaningless. The shape of the vehicle is determined by design considerations. It may be guided or unguided. Gasdynamic controls are used to provide orientation in space and trajectory corrections.

"Space-to-ground." The distinctive property of these vehicles consists in the fact that they enter the atmosphere at very high speed and are therefore subject to severe aerodynamic heating. The basic requirement consists in reducing this heating and protecting the vehicle from destruction. For this purpose, the aerodynamic layout makes use of heat shields on the nose sections and wing edges and employs retrorockets to lower speed and, with it, heat transfer. Certain areas on the vehicle's surface are protected from overheating by providing conditions that result in premature boundary-layer separation from these areas.

The "space-to-ground" vehicle may be a guided or unguided finless (Fig. II-5-1a) or winged (Fig. II-5-1b) vehicle.

The unguided vehicles are stabilized by stabilizing skirts in the form of hollow tail sections. Gasdynamic and aerodynamic controls are used.

"Air-to-ground" and "air-to-air." The aerodynamic layouts of vehicles of these types must satisfy conditions for motion in the dense layers of the atmosphere at speeds at which all aerodynamic effects are quite strongly in evidence, except for aerodynamic heating, which is not essential in this case. Most commonly used are the single-stage finned wingless and winged guided

and unguided aerodynamic configurations. /78

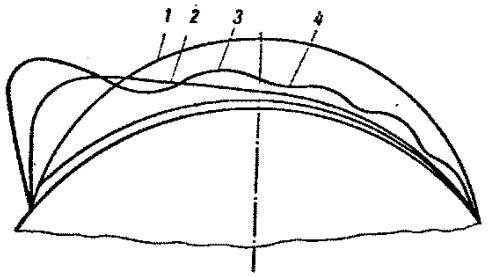

Figure II-5-2. Shapes of Intercontinental Trajectories. 1) ballistic; 2) soaring; 3) skipping; 4) grazing.

The controls are usually of the combined or aerodynamic type. Guided missiles are sometimes subject to more rigid maneuverability requirements. The aerodynamic configurations therefore provide strong control elements.

In arriving at an aerodynamic layout, consideration must be given to the conditions of launching from the carrier vehicle, which is flying at a certain speed. If the missile is launched in the direction in which the carrier is traveling, it is necessary to provide measures to prevent the missile from turning back on the carrier.

When the missile is launched at an angle to the direction of carrier flight, a crossflow effect arises from the vehicle's extra velocity component, possibly to the detriment of stability and targeting. Hence the stabilizing and control elements must be capable of eliminating the adverse consequences of this crossflow.

One of the aerodynamic-layout features may be an umbrella-type empennage used as a tail stabilizer because of the limited space available for the launcher.

"Ground-to-ground." Because of the great variety of aerodynamic layouts used in "ground-to-ground" vehicles, it will be advisable to consider these layouts after classifying them on the basis of range and trajectory type.

Intercontinental ranges. Ballistic trajectories (Fig. II-5-2, trajectory 1). As a rule, vehicles with such trajectories are multistage and finless, with a separating nose section. Control and stabilization are provided on the powered part of the trajectory by gasdynamic controls, and on the unpowered part by rocket thrusters that give the last stage (separating nose section) the necessary stability and permit correcting the trajectory.([69] 1968, No. 1) [80].

The nose-section aerodynamic layouts of these vehicles must meet the same requirements as "space-to-ground" vehicles. To reduce the drag of the blunt nose section during ascent through the dense layers of the atmosphere, these configurations may be supplemented by a sharp ballistic cap, which is jettisoned at high altitude.

When a "ground-to-ground" vehicle is made single-stage, without a separating nose section, fins are provided to give reliable stabilization on the coasting part of the trajectory. Stability and control can be provided by gasdynamic devices on the powered segment.

In some cases, the aerodynamic layout of a guided ballistic missile with a separating nose section may also be finned. Fins /79
are provided when stabilization of a statically unstable missile on its trajectory would require gasdynamic controls so large as to be impractical. The missile's tail fins make it possible to move the center of pressure closer to the center of gravity and reduce the missile's static instability. This makes it possible to design gasdynamic controls of acceptable size and weight.

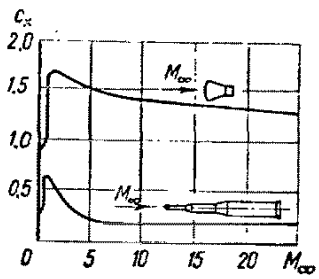

Figure II-5-3. Aerodynamic Drag of Ballistic Missile and its Nose Section.

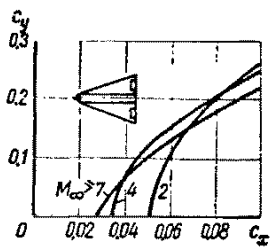

Figure II-5-4. Polar Curve of Winged Vehicle.

A ballistic missile is subject to severe aerodynamic heating. The convective heat flow to the vehicle is very large, and only a comparatively small part of it can be dissipated into the atmosphere as radiant energy. To preserve the vehicle, it is necessary that the smallest possible amount of kinetic energy be transferred to it as heat. For this purpose, the nose sections are made in the form of poorly streamlined (blunt) bodies with high pressure drag and low total friction drag, which reduces convective heat transfer.

Figure II-5-3 shows Mach-number curves of the frontal-drag coefficient of a typical ballistic missile (lower curve) and a nose section that can be used for steered decelerated reentry [78].

Soaring trajectories (Fig. II-5-2, trajectory 2). Vehicles with this trajectory move without use of thrust in the dense layers of the atmosphere. The speed of the vehicle at engine shutdown must be sufficient to produce a lift equal to the

difference between weight and centrifugal force. The aerodynamic layout must provide wings that produce the necessary lift and a maximum lift/drag ratio in order to obtain maximum range.

The vehicles are multistage or single-stage with control and stabilization elements. In the multistage layout, the wings are attached to the last stage, which executes soaring flight on the descending branch of the trajectory.

Since soaring flight in the dense layers of the atmosphere takes place at high speed, the vehicle is subject to large heat flows for considerable lengths of time. This imposes additional requirements on the aerodynamic layout in connection with reduced heat transfer and surface heating.

However, withdrawal of heat is a less complex problem for soaring rockets, since kinetic energy is converted into heat gradually during the glide and, in contrast to the ballistic missile, the rate of convective heat transfer is low. Consequently, a considerable part of the heat may be radiated into the environment at wall temperatures that are acceptable from the standpoint of material strength.

Skipping trajectories (see Fig. II-5-2, trajectory 3). Vehicles with these trajectories are intermediate between the two types discussed above. The nose section takes the form of a guided winged vehicle, so that it can skip on the unpowered part of the trajectory, alternating between dense and rarefied layers of the atmosphere. This makes it possible to obtain rather long ranges. /80

To obtain maximum range, it is necessary that the lift coefficient conform to the optimum c_y/c_x during the times in which the skipping missile is in the dense atmospheric layers.

During the motion in the thinner layers, heat transfer to the surface is reduced. The rate of heat inflow rises sharply during a skip, since the time spent in the dense layer is short. Here the heat-transfer conditions are practically the same as for a ballistic missile. To lower the maximum rate of heat transfer and the total amount of heat transmitted during entry into the dense atmospheric layers, the leading edges of the wing and body must be blunted. To avoid increasing drag, the leading edges must be sharply raked. It is therefore advisable to use the delta wing for skipping and soaring hypersonic vehicles. Figure II-5-4 [78] shows a typical polar curve for a wing of this type. For small attack angles and very large Mach numbers, the induced-drag coefficient $c_{xi} = Kc_y^n$ tends toward its limit $c_{xi} = c_y^{3/2}\sqrt{2}$.

Grazing trajectories (see Fig. II-5-2, trajectory 4). Conventional aircraft and winged missiles whose speeds may be either subsonic or supersonic are among the vehicles using this trajectory. Their aerodynamic layouts include a wing as a necessary element for compensation of gravity. Since they fly in dense layers of the atmosphere, combined or aerodynamic controls are used.

The aerodynamic layout must provide devices for stabilization and control when the missile is launched with rocket boosters. The stability necessary for in-flight refueling must be provided.

Intermediate ranges. Intermediate-range flights are made either on a ballistic trajectory (ballistic missiles) or a grazing trajectory (airplanes and winged missiles). The layout may be multistage, and in its most general form is that of the guided finned winged aerodynamic configuration. Occasional designs may be made with wide departures from this layout, e.g., the ballistic missile, which uses the simpler layouts described above.

Intermediate ranges mean additional simplification because of the lower speeds on the descending branch of the trajectory and the consequent smaller heat flows. As a result, protection from aerodynamic heating is easier and the sharp nose section can be retained.

This nose-section shape means lower drag and, consequently, higher speed and a shorter time in flight. The shorter time on trajectory increases aiming accuracy, since the time for which the vehicle is subject to the adverse effects of wind and air temperature and density variation is shorter and, consequently, the deviation from the nominal trajectory is smaller.

Short ranges. Ballistic trajectories. Vehicles describing /81
these trajectories are unguided finned wingless or unfinned types. The aerodynamic layout must provide for means to improve aiming accuracy. These devices include pitched tail fins by means of which rotation of the finned vehicle about its longitudinal axis is set up during flight and the target pattern is improved. The same effect can be produced with tangential jet-engine nozzles.

The aerodynamic forces and moments of a vehicle with this layout must be determined with consideration of spin and the design features associated with the oblique positions of the fins and the presence of tangential nozzles, and with consideration of the effect of the jet on external flow.

Grazing trajectories. Antitank rockets and artillery missiles intended for use on stationary and moving ground targets use these trajectories.

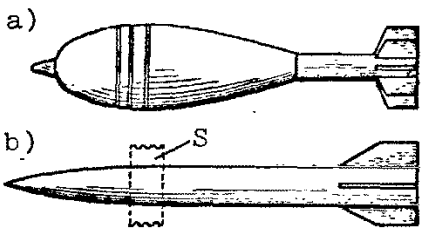

Figure II-5-5. Finned Missiles. a) mortar round; b) subcaliber missile (S is a split shackle).

Antitank rockets use the winged guided aerodynamic layout, and artillery missiles the unguided finned and finless configurations.

Unguided finned missiles (shells) may have variations defined by the span of the fins as compared to the transverse dimension of the body. If the fin span is equal to or smaller than the diameter of the largest body cross section, the configuration is said to be subcaliber (low-velocity shells, Fig. II-5-5a); if larger, the configuration is supercaliber (Fig. II-5-5b) ([69], 1960, No. 2).

"Ground-to-air" and "ground-to-space." Vehicles of these types are used for antiaircraft and antimissile defense, as well as for atmospheric and space research.

If they are to fly at high altitudes, they are made multistage. For flight over modest ranges, a single-stage version with dual-thrust engine operation is possible; here the thrust is high at the time of launch and is reduced sharply when a certain altitude (or speed) has been reached.

Space vehicles are usually of the guided finless type.

The aerodynamic layout of a "ground-to-air" missile must provide for high maneuverability. It is therefore provided with wings, fins, and powerful controls, which may be applied in the normal, canard, or tailless configuration. Pivoting wings are often used in the latter configuration.

Special research rockets (weather, geophysical, medicobiological) are used for atmospheric and space research.

Such rockets may have a wide variety of layouts depending on the specific mission for which they are designed. Figure II-5-6 shows single- and two-stage vehicles.

For single-stage rockets, a three-fin stabilizer 1 may be adequate (Fig. II-5-6a). For a two-stage rocket, the launch-engine stabilizer 1 may consist of three fins and that of the main stage 2 of four (Fig. II-5-6b). /82

Research rockets may be guided or unguided. Control can be obtained with jet vanes or by swivelling the combustion chamber. Special jet nozzles are used for angular orientation of the

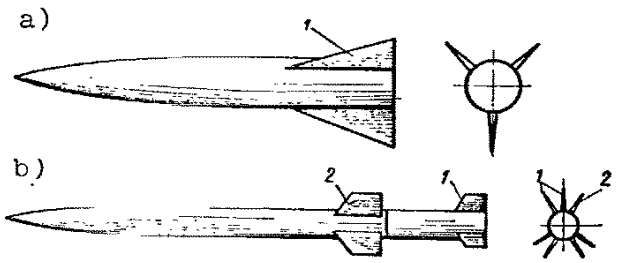

Figure II-5-6. Aerodynamic Layouts of Weather Rockets. a) single-stage; b) two-stage.

missile about its longitudinal axis.

The rockets may have specific features associated with the presence of a system for recovering the nose with its package of measuring instruments. A separating nose section is therefore included in the aerodynamic configuration (see Fig. II-3-10b). It is decelerated on reentry by special drag devices, such as string of braking disks, speed flaps that are deployed after separation, and parachutes.

"Underwater-to-underwater." Vehicles of this type are designed to move in water. However, they have the guided finned wingless aerodynamic layout. Control is aerodynamic (or, more precisely, hydrodynamic), perhaps with the controls coupled to an automatic homing system.

The layout must take account of how the aerodynamic (hydrodynamic) characteristics of the vehicle are affected by the water intakes used when water is one of the propellants.

"Air (ground)-to-underwater." Vehicles of this type must enter the water at comparatively low speed. Otherwise, the large g-forces encountered on impact would require strengthening the body and other parts of the vehicle, with the attendant weight penalty.

Drag-increasing measures are taken to reduce speed. For this purpose, the warhead is blunted and the vehicle is equipped with drag parachutes and flaps that open during the approach to the water.

The basic layout of vehicles of this type is the same as that of vehicles of the "underwater-to-underwater" type.

Powerplant Type and Aerodynamic-Layout Features

The rocket powerplant. Since the rocket engine does not use atmospheric oxygen, it does not have air intakes among the elements of its aerodynamic layout.

The engine installation is most often placed in the stern of the vehicle, a feature that influences the CG position of the vehicle, the relative positions of the gravity and pressure /83

centers, and, consequently, stability and controllability. In addition, the distribution of nozzles influences the shape of the tail section and the conditions of flow over it.

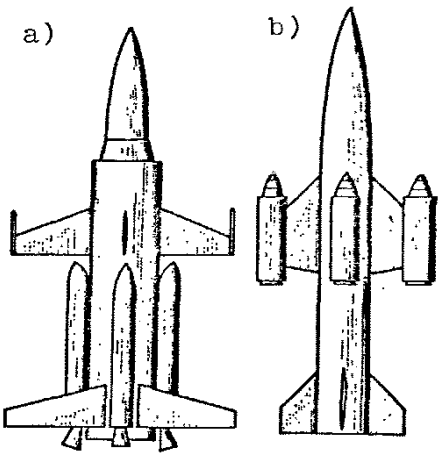

Figure II-5-7. Engine Placement on Vehicles. a) "cluster" of rocket gines around vehicle body; b) jet engines with air intakes placed in pods on pylons.

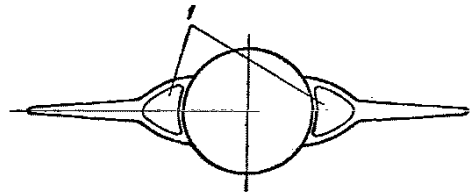

Figure II-5-8. Diagram Showing Placement of Air Intakes at Root of Wing.

Significant aerodynamic-layout peculiarities are associated with the use of several engines "clustered" around the body of the vehicle (Fig. II-5-7) and with the use of rockets as launch boosters. These engine arrangements require additional stabilization measures.

In both cases, the engines are jettisoned after burn. The aerodynamic layout must therefore provide the necessary stability and controllability at the time of separation. The frontal drag of the engine installation must be adequate to separate it quickly from the body.

Jet powerplant. Engines of this type (ramjet, turbojet) use oxygen from the air, which enters through air intakes mounted on the vehicle.

The dimensions of the air intakes, their number, their manner of placement, and their operating mode have substantial influence on the flow conditions and aerodynamic properties of the vehicle, and this, in turn, influences the thrust and economy characteristics of the engines.

To minimize total-pressure loses and thereby create better operating conditions for the engines, the air intakes should be mounted on the vehicle in such a way that they do not blanket the wings, fins, or other projecting parts, i.e., in such a way that the flow will experience as little disturbance as possible where it enters the intake.

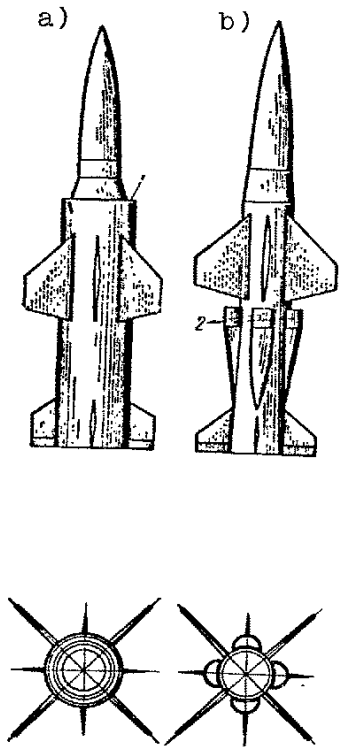

Figure II-5-9. Possible Arrangements of Air Intakes Along Length of Vehicle. a) annular air intake 1; b) four semicircular lateral air intakes 2, with entry cross sections moved outside of boundary layer.

For this purpose, it is not desirable to place the air intake near the surface of the body and far from the nose if the intake passage is found to be inside a thick boundary layer and the incoming air would lose a great deal of total pressure.

The aerodynamic-layout form of a jet-engined vehicle depends on air-intake placement. Figure II-1-10, a and b, shows configurations with lateral air intakes, and Fig. II-1-10c an annular-intake configuration; Figs. II-5-8 and II-1-11 show layouts with air intakes 1 placed at the wing root and in a body of noncircular cross section, respectively. /84

Figure II-5-9, a and b, shows the positioning of air intakes lengthwise along the vehicle. If the intake is far from the nose, boundary-layer-suction devices must be provided in front of it. It is possible to extend the entry section of the air intake outside the boundary layer (Fig. II-5-9b). All of these measures prevent airflow separation and improve the working characteristics of the intakes.

To lower the pressure losses of the air entering the engine and improve engine efficiency, the air intakes, together with the engines, may be placed in pods on the wings or on special pylons (see Fig. II-5-7). In this layout, tail fins are provided to improve stability and controllability.

A layout feature of supersonic ramjet (RJ) vehicles stems from the presence of the special booster engines used for acceleration to the speed at which the ramjet can begin to function stably. This makes the design tailheavy and requires installation of stabilizers for the necessary stability.

Chapter III /85

FUNDAMENTAL RELATIONSHIPS IN THE THEORY OF GAS FLOWS

§III-1. PECULIARITIES OF GAS FLOW AT VERY HIGH SPEEDS

Change in Physicochemical Properties and Thermodynamic Characteristics of Air with Temperature

Specific heats. Substantial increases in the speeds of aircraft have made it necessary for aerodynamic research to take account of the specific peculiarities of gas flows that result from changes in the physicochemical properties of air. While the compressibility property was considered in "conventional" supersonic aerodynamics as the most important manifestation of the peculiarities of high-speed flows, and the influence of temperature on the thermodynamic variables, especially the specific heats, was disregarded, peculiarities associated with high temperature behind shockwaves and in the boundary layer come into the foreground at hypersonic speeds. This effect increases the heat capacities of the gas as a result of excitation of vibrational internal-energy levels.

Research on shockwaves and the boundary layer has shown that all of the relationships of conventional aerodynamics are quite reliable as long as the flow conditions of the gas do not differ substantially from those for which the assumption of constant heat capacities is valid and it is possible to use the ideal-gas equation of state $p = R\rho T$, where R is the absolute gas constant and ρ and T are the gas density and temperature, respectively. It becomes necessary to consider the temperature variation of heat capacity before it is necessary to use an equation of state different from that for the ideal gas. For example, research has shown that it becomes advantageous to consider the temperature variation of specific heats on passage across a normal shock beginning at free-stream Mach numbers M_∞ of the order of 3-4. The ideal-gas equation of state can be retained up to $M_\infty = 6\text{-}7$, along with the equation for the speed of sound $a^2 = kRT$ ($k = c_p/c_v$ is the adiabatic exponent, which is equal to the ratio of the specific heat at constant pressure c_p to the specific heat at constant volume c_v).

Thermodynamic tables or interpolation formulas can be used to calculate true specific heats as functions of temperature. These formulas, derived for thermodynamic equilibrium conditions on the assumption that the specific heats are linear functions

of temperature, take the form

$$c_p = 0.2317 + 0.000221T; \quad c_v = 0.1647 + 0.000221T, \qquad \text{(III-1-1)}$$

where c_p and c_v are in kcal/kg·deg.

According to an approximate estimate of the temperature effect on specific heat at p = const,

$$\frac{c_p}{c_{p\infty}} = \left(\frac{T}{T_\infty}\right)^{\varphi}, \qquad \text{(III-1-2)}$$

where ϕ depends on temperature (Fig. III-1-1), and the subscript "∞" corresponds to the free-stream variables or any other initial conditions. /86

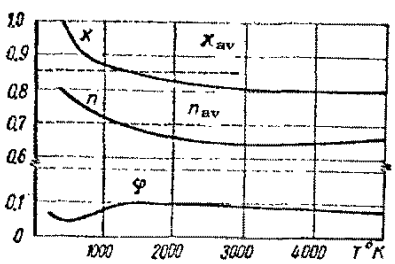

Figure III-1-1. Variation of Exponents ϕ, n, and κ in Formulas for Determination of Heat Capacity, Viscosity, and Thermal Conductivity.

the power-law relation

For T > 1000°K, we may take ϕ = = 0.1. For T_∞ = 288°K, the heat capacity $c_{p\infty}$ = 0.24 kcal/kg·deg (10^3 J/kg × × deg). Formula (III-1-2) is used up to T = 2000-2500°K, at which the vibrational degrees of freedom are found to be fully excited.

Kinetic coefficients. Friction and heat transfer in the boundary layer depend on such kinetic coefficients of the gas as its coefficients of dynamic viscosity μ and thermal conductivity λ. It has been established that in the absence of dissociation, the viscosity of air depends only on temperature and is practically independent of pressure. There are several relationships linking viscosity and temperature. For example,

$$\frac{\mu}{\mu_\infty} = \left(\frac{T}{T_\infty}\right)^{n}. \qquad \text{(III-1-3)}$$

In turn, the exponent n depends on temperature (Fig. III-1-1). For comparatively low temperature, we may take n = 0.76 (or 3/4). According to the diagram in Fig. III-1-1, n ≈ 0.7 on the average over a rather broad temperature range. Here the actual value of

μ may be put equal to $\mu_\infty = 1.82 \cdot 10^{-6}$ kg·s/m^2 ($1.79 \cdot 10^{-5}$ N·s/m^2), which corresponds to $T_\infty = 288°K$.

In approximate calculations, Formula (III-1-3) can be applied at temperatures up to the order of 2000-2300°K, i.e., until dissociation intervenes. At temperatures below 1500°K, the Sutherland formula

$$\frac{\mu}{\mu_\infty} = \left(\frac{T}{T_\infty}\right)^{\frac{1}{2}} \frac{1 + 111/T_\infty}{1 + 111/T} \qquad \text{(III-1-4)}$$

gives somewhat better results.

Like viscosity, thermal conductivity is practically independent of pressure below 2000°K and can be determined as a function of viscosity and specific heat:

$$\frac{\lambda}{\lambda_\infty} = \frac{\mu}{\mu_\infty} \frac{c_p - 0.0374}{c_{p_\infty} - 0.0374}, \qquad \text{(III-1-5)}$$

where c_p and c_{p_∞} have the dimensions kcal/kg·deg and μ and λ have the respective dimensions kg·s/m^2 and kcal/m·deg·s (or Ns/m^2 and W/m·deg).

The power-law formula

$$\frac{\lambda}{\lambda_\infty} = \left(\frac{T}{T_\infty}\right)^{\kappa}, \qquad \text{(III-1-6)}$$

is simpler; the exponent κ depends in turn (Fig. II-1-1) on temperature. For approximate calculations, we may set $\kappa = 0.85$ and $\lambda_\infty = 5.53 \cdot 10^{-3}$ kcal/m·s·deg (23.2 W/m·deg) for $T_\infty = 261°K$.

Dissociation and Ionization /87

Thermodynamic functions of air at high temperatures. With increasing flight speed, the air behind the shock wave or in the boundary layer is heated to an extent such that the vibrational degrees of freedom are fully excited. With a further temperature increase, the atoms overcome their intramolecular forces, with the result that a diatomic molecule dissociates into two separate monatomic molecules. This dissociation process is characterized by the fraction by weight of the monatomic gas, $\alpha = G_1/G$ (G_1 is the weight of that part of the gas that is in the atomic state and G is the total weight of gas). The parameter α is known as

the degree of dissociation.

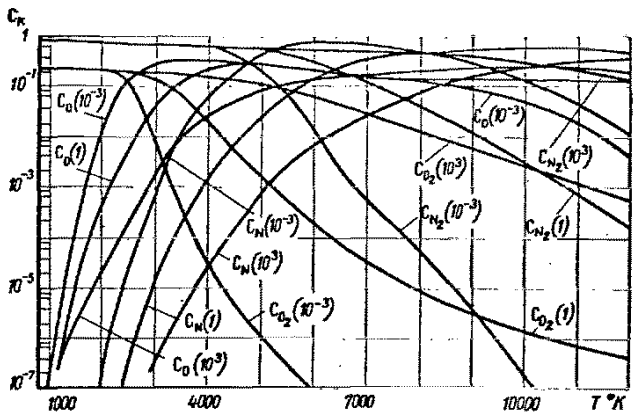

Figure III-1-2. Molar and Atomic Concentrations of Components of Air (Oxygen and Nitrogen) as Functions of Temperature and Pressure (the Pressure in Atmospheres is Indicated in the Parentheses).

At a still higher air temperature, ionization of the air takes place in addition to dissociation, which is complete at a temperature around 6000°K. The basic cause of ionization is collision between molecules in the course of their thermal motion. This process is therefore known as thermal ionization. Its rate is characterized by the degree of ionization, which is equal to the ratio of the number of ionized atoms to the total number.

Research has shown that hydrogen and nitrogen, for example, are fully thermally ionized (degree of ionization equal to unity) at temperatures of 10,000 and 17,000°, respectively, and a pressure of 1 atmosphere.

On dissociation and ionization, air departs markedly from the ideal-gas equation of state. The hypothesis of constant stagnation temperature, which is the basis, for example, for the ordinary equations of the shock wave, ceases to apply. These equations must therefore be obtained with consideration of the physicochemical transformations of air at high temperatures.

An important element in calculation of these flows is determination of the thermodynamic parameters and kinetic coefficients of dissociated and ionized air and its composition. We now have quite detailed data on these parameters and coefficients and on the composition of air at thermodynamic equilibrium at temperatures from 1000 to 20,000°K and pressures from 0.001 to 1000 atm, thanks to computer work done by a group of Soviet scientists headed by Corresponding Member of the USSR Academy of Sciences Prof. A.S. Predvoditelev [28]. The calculations have been carried out for temperatures from 1000 to 6000°K without consideration of ionization, since its influence is negligible in this temperature range. In the range from 6000 to 20,000°K, the influence of ionization was taken into account. The calculations were simplified by use of the hypothetical "single-ionization" /89

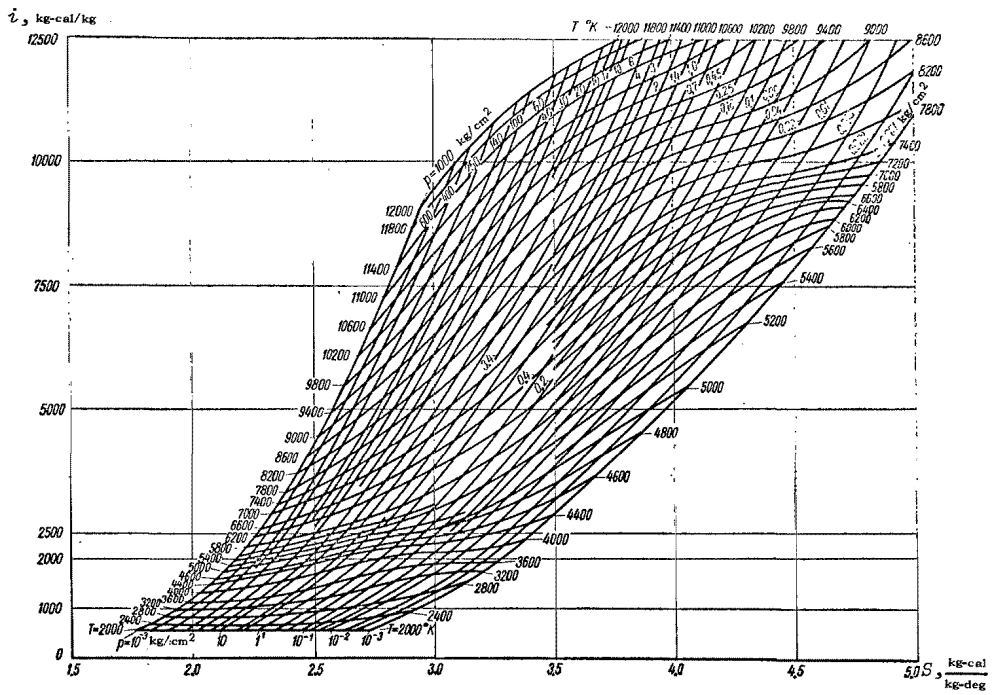

Figure III-1-3. Enthalpy-Entropy Diagram.

scheme, in which ionization is assumed to be complete at T = = 12,000°K and p = 0.001 atm.

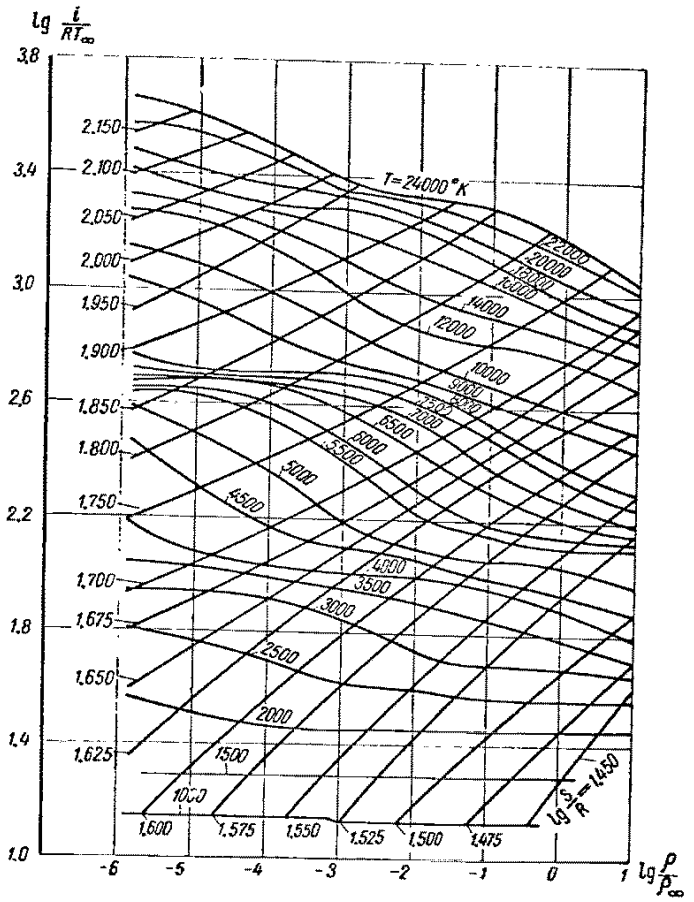

Figure III-1-4. Parameters of Air at High Temperatures Under Thermodynamic-Equilibrium Conditions. λ_∞ = 1.293 kg/m^3; T_∞ = 273.2°K; R = 29.27 kg × × m/kg·deg; $RT_\infty = 8 \cdot 10^3$ kg·m/kg.

The results obtained were used to construct curves of the atomic and molecular concentrations (Fig. III-1-2) and the i-S diagram (enthalpy-entropy diagram) shown in Fig. III-1-3, which also gives the p = const and T = const curves [28].

In Fig. II-1-4, these curves have been replotted to show density instead of pressure and the dimensionless enthalpy i/RT_∞ and entropy S/R instead of the absolute values.

Diagrams (Fig. III-1-5) that enable us to determine the molecular weight μ_{av} of dissociated and ionized air as a function of temperature and pressure are important for practical calculations. As we see from the diagrams, average molecular weight decreases with temperature. /93

Examining a model of air in the form of a homogeneous diatomic gas, we can apply the Dalton formula to determine degree of dissociation:

$$\alpha = \frac{\mu_{av\,0} - \mu_{av}}{\mu_{av}}, \qquad \text{(III-1-7)}$$

where $\mu_{av.0}$ and μ_{av} are, respectively, the average molecular

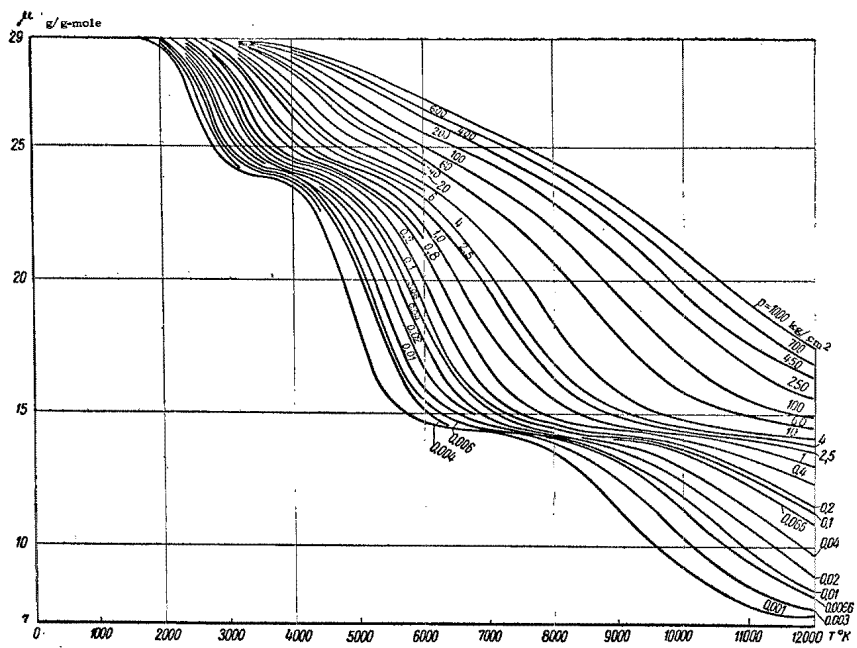

Figure III-1-5. Average Molecular Weight of Air at High Temperatures. /90

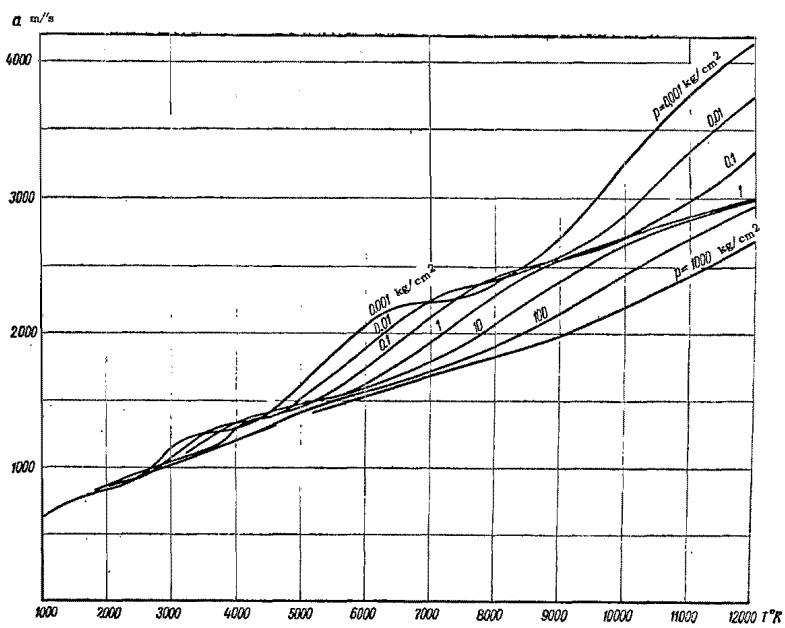

Figure III-1-6. Speed of Sound in Gas at High Temperatures. /91

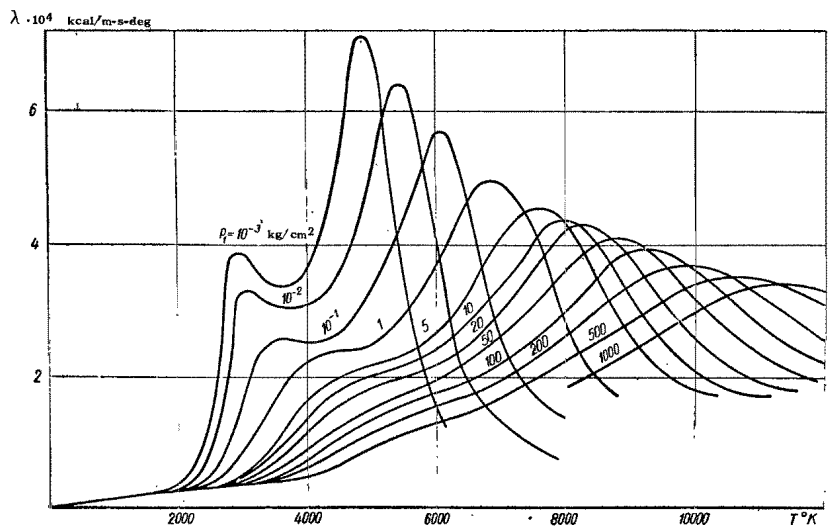

Figure III-1-7. Coefficient of Thermal Conductivity of Air at High Temperatures.

/92

weights of nondissociated air (the diatomic gas) and the dissociated medium. The value of $\mu_{av.0} = 29$, and μ_{av} is determined as a function of p and T from the diagrams in Fig. III-1-5.

The speed of sound can be found as a function of T and p by use of another family of curves, that shown in Fig. III-1-6.

Kinetic coefficients. An approximate analysis has shown that at high temperatures, the viscosity of air at equilibrium can be determined accurate to 10% up to 9000°K by use of the Sutherland formula (III-1-4). However, more exact investigations indicate that for dissociated air, μ depends not only on temperature, but also on pressure. This is taken into consideration by the improved Sutherland formula

$$\frac{\mu}{\mu_\infty} = \left(\frac{T}{T_\infty}\right)^{\frac{1}{2}} \frac{1 + 111/T_\infty}{1 + 111/T} \left(\frac{1}{1 + 0.89 c_A/c_M} + \frac{1.42}{1 + 1.26 c_M/c_A}\right), \qquad \text{(III-1-8)}$$

where c_M and c_A are the molecule and atom concentrations, respectively, with $c_M + c_A = 1$ for the binary mixture.

The degree of dissociation α can be substituted for the concentrations, namely, $c_A = \alpha$ and $c_M = 1 - \alpha$. In the absence of dissociation ($\alpha = 0$), the relation (III-1-8) becomes the ordinary Sutherland formula. At complete dissociation ($\alpha = 1$), the term in parentheses in (III-1-8) is equal to 1.42, so that the viscosity increase over the nondissociated medium is 42%.

Like the coefficient μ, the thermal conductivity coefficient depends on temperature and pressure at high temperatures. Figure III-1-7 shows the results of a theoretical investigation of the thermal conductivity coefficient on the assumption that air is a regular binary mixture of gases. The data given in [13] on the kinetic coefficients and variables of state of air may be found highly useful in study of high-velocity flows.

Basic Relationships for a Diatomic Dissociating Gas

Degree of dissociation. To simplify study of dissociation, air may be treated as a conventional diatomic gas consisting of symmetrical molecules of one type that dissociate into two atoms as a result of binary collisions. In turn, the atoms may recombine into molecules by ternary collisions. This scheme enables us to study the dissociation mechanism of a pure dissociating diatomic gas [73, 1957, No. 1].

Equilibrium dissociation is assumed. This means that in the chemical reaction defined, for example, by the elementary equation of the binary process /94

$$A_2 \underset{r_R}{\overset{r_D}{\rightleftarrows}} A + A, \qquad \text{(III-1-9)}$$

the rates of the reactions from left to right r_D and from right to left r_R (the dissociation and recombination rates, respectively) are the same.

Study of dissociating-medium flows involves determination of the equilibrium degree of dissociation α. To simplify the calculation, the air can be regarded as a mechanical mixture consisting of the pure dissociating components, namely nitrogen N_2 and oxygen O_2.

The equilibrium degree of dissociation α is determined in chemical thermodynamics by the relationship

$$\frac{\alpha^2}{1-\alpha} = \frac{\rho_d}{\rho} e^{-\frac{T_d}{T}}, \qquad \text{(III-1-10)}$$

where

$$\alpha = \frac{n_A}{n_A + 2n_{A_2}}. \qquad \text{(III-1-11)}$$

Here n_A is the number of atoms of element A in a certain volume and n_{A_2} is the number of molecules of gas A_2 in the same volume.

TABLE III-1-1. CHARACTERISTIC PARAMETERS OF DISSOCIATION

Element	p_d, atm	u_d, kcal/kg	u_d, m^2/s^2	V_d, m/s	ρ_d, g/cm^3	
					$1000<T<5000°$ K	$5000<T<7000°$ K
Oxygen	$2.3 \cdot 10^7$	$3.7 \cdot 10^3$	$1.5 \cdot 10^7$	$3.9 \cdot 10^3$	150	130
Nitrogen	$4.1 \cdot 10^7$	$8.0 \cdot 10^3$	$3.4 \cdot 10^7$	$5.8 \cdot 10^3$	130	125
Air	$3.7 \cdot 10^7$	$7.1 \cdot 10^3$	$3.0 \cdot 10^7$	$5.4 \cdot 10^3$	135	126

The quantities ρ_d and T_d, which represent the characteristic density and temperature, respectively, appear in (III-1-10). Calculations indicate that the characteristic dissociation temperature T_d = 59,000°K for oxygen and T_d = 113,000°K for nitrogen. The characteristic density varies somewhat as a function of temperature (Table III-1-1). Since this variation is small, we may use average ρ_d in approximate calculations: 150 g/cm^3 for oxygen and 130 g/cm^3 for nitrogen.

The enthalpy $\underline{i}$ [see (III-1-14') and (III-1-16')] can be used in (III-1-10) instead of temperature. Then the degree of dissociation will be determined as a function of $\underline{i}$ and ρ. Figure III-1-8 shows the corresponding relation for α vs. the dimensionless variables ρ/ρ_d and i/u_d. The variable u_d is known as the characteristic dissociation energy and is equal to the specific heat of dissociation per gram of A_2 molecules:

$$u_d = \frac{D}{2m_A}, \qquad \text{(III-1-12)}$$

where m_A is the mass of the atom and D is the dissociation energy of the A_2 molecule.

Using Dalton's formula (III-1-7), we can determine the average molecular weight μ_{av} of the mixture from the degree of dissociation α.

Together with the above variables ρ_d and u_d, Table III-1-1 /95
also lists the characteristic pressure p_d and velocity V_d, concepts that will be explained below.

Equation of state. Let us examine the equation of state of a gaseous mixture formed as a result of dissociation of diatomic molecules. This equation can be obtained using the relationships for determination of the pressure $\underline{p}$ of the mixture and the partial pressures p_i of the components:

$$p = \sum_i p_i; \quad p_i = \rho_i T \frac{k}{m_i}, \qquad \text{(III-1-13)}$$

where $\underline{k}$ is the gas constant referred to a single molecule (Boltzmann's constant) and the subscript "i" denotes the particular gaseous component.

Below, we shall identify the atomic component (i = 1) by the subscript "A" and the molecular component (i = 2) by subscript "M".

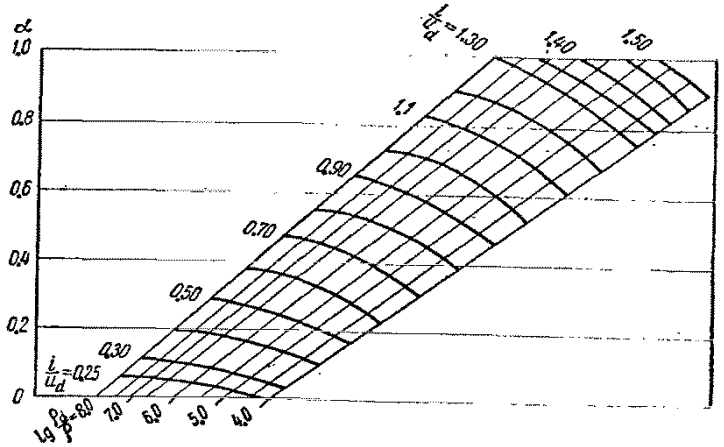

Figure III-1-8. Diagram for Determination of Degree of Dissociation of a Diatomic Gas as a Function of the Ratio i/u_d and the Parameter $\log (\rho_d/\rho)$.

Since the component concentration $c_i = \rho_i/\rho$, i.e., $c_1 = c_A = \alpha = \rho_A/\rho$, and $c_2 = c_M = 1 - \alpha = \rho_M/\rho$ for the atomic and molecular components, respectively, we find the equation of state from (III-1-13) for the condition that $m_M = 2m_A$:

$$p = \frac{k}{2m_A}\rho T(1+\alpha), \qquad \text{(III-1-14)}$$

where $k/(2m_A)$ is the gas constant for 1 gram of component A_2 in the mixture.

Applying (III-1-14) to the state defined by the characteristic parameters, we obtain the relation for the characteristic pressure $p_d = 0.5k\rho_d T_d/m_A$. Since the dissociation energy of the A_2 molecule is $D = kT_d$, it is obvious that $p_d = 0.5D\rho_d/m_A$.

The characteristic velocity that we mentioned above is determined by the formula $V_d = u_d^{1/2}$. The corresponding values of p_d and V_d for oxygen and nitrogen are given in Table III-1-1.

The equations of thermodynamics. Interest attaches to certain thermodynamic equations of the diatomic dissociating gas. In particular, the equation for the internal energy of a unit mass of the gas takes the form

$$u=\frac{3}{2}\frac{kT}{m_A}+\frac{D}{2}\frac{\alpha}{m_A}. \qquad \text{(III-1-15)}$$

We can change this equation to dimensionless form by dividing $\underline{u}$ and T by the corresponding characteristic parameters u_d and T_d: /96

$$\bar{u}=3\bar{T}+\alpha, \qquad \text{(III-1-15')}$$

where $\bar{u} = u/u_d$, $\bar{T} = T/T_d$.

Along with (II-1-15'), we can write the enthalpy equation, again in dimensionless form:

$$\bar{i}=\bar{u}+\frac{\bar{p}}{\bar{\rho}}, \qquad \text{(III-1-16)}$$

where $\bar{i} = i/u_d$, $\bar{p} = p/p_d$, $\bar{\rho} = \rho/\rho_d$.

Applying the characteristic-parameter concept, we can also reduce the equation of state (III-1-14) to dimensionless form:

$$\bar{p}=\bar{\rho}\bar{T}(1+\alpha), \qquad \text{(III-1-14')}$$

Introducing Expression (III-1-15') for $\bar{u}$ into (III-1-16) and applying (III-1-14'), we obtain for the enthalpy

$$\bar{i}=\alpha+\frac{4+\alpha}{1+\alpha}\frac{\bar{p}}{\bar{\rho}}. \qquad \text{(III-1-16')}$$

Mixture of diatomic gases. Since hydrogen and oxygen have similar molecular weights, the model of air as an additive mixture of diatomic gases may be regarded as justified to a degree. Here the difference between the characteristic temperatures of nitrogen and oxygen can be taken into consideration.

Oxygen begins to dissociate at much lower temperatures than nitrogen, and its dissociation is complete when nitrogen is entering the stage in which dissociation develops.

If we take 3500°K as the initial temperature of N_2 dissociation, the degree of dissociation of the diatomic air model will be determined at this temperature by the relative mass of oxygen

in the mixture, i.e., 0.235.

For T > 3500°K, the degree of dissociation of the air model

$$\alpha = 0.235\alpha_{O_2}, \qquad \text{(III-1-17)}$$

where α_{O_2} is the degree of dissociation of pure oxygen.

On completion of the dissociation of O_2 at temperatures T > 3500°K, $\alpha_{O_2} = 1$ and the degree of dissociation of the air

$$\alpha = 0.235 + 0.765\alpha_{N_2}, \qquad \text{(III-1-18)}$$

where α_{N_2} is the degree of dissociation of pure nitrogen and 0.765 is the fraction by volume of N_2 in air.

For fully dissociated air, $\alpha_{O_2} = \alpha_{N_2} = 1$ and, consequently, $\alpha = 1$.

Thus, a simplified mass composition of undissociated air, 76.5% N_2 and 23.5% O_2, is used in approximate calculation of the degree of dissociation and other variables (the 1% of inert gases are included arbitrarily in the atmospheric nitrogen).

Along with Formulas (III-1-17) and (III-1-18), we can make use of an approximate method based on determination of effective values of the characteristic dissociation parameters of air in accordance with the mass fractions of nitrogen and oxygen. For example, the effective characteristic dissociation pressure

$$p_d = 0.765p_{d\,N_2} + 0.235p_{d\,O_2}, \qquad \text{(III-1-19)}$$

where $p_{d\,N_2}$, $p_{d\,O_2}$ are the characteristic dissociation pressures of nitrogen and oxygen, respectively.

Effective values of other characteristic parameters can be calculated in a similar manner. /97

Effective values of p_d, u_d, and V_d calculated for air in this way are listed in Table III-1-1.

Enthalpy of equilibrium dissociation. If air is regarded as a mixture of nitrogen and oxygen, the enthalpy of the mixture

$$i_D = c_\delta \frac{\sum_{k=N,O} (ci_R)_k}{\sum_{k=N,O} c_k} = (i_R c)_{O_2} + (i_R c)_{N_2}, \qquad \text{(III-1-20)}$$

where the dissociation enthalpy of the k-th component is equal, according to (III-1-12), to $i_{Rk} = D_k/(2m_k) = u_{dk}$.

Values of i_{Rk} are given in Table III-1-1, and the concentrations on the diagram of Fig. III-1-2. For a diatomic model of the gas

$$i_D = \alpha u_d = \alpha i_R,$$

where α is the degree of dissociation of the gas model and $u_d = i_R$ is the characteristic dissociation energy of 1 gram-molecule of air. If we assume that all of the oxygen has dissociated before the nitrogen begins to dissociate, the atomic concentration is governed only by decomposition of oxygen and, consequently, $c = \alpha = 0.235$.

Accordingly,

$$i_D = 0.235\,(i_R)_{O_2}.$$

If conditions are such that the oxygen does not dissociate completely, then $i_D < 0.235(i_R)_{O_2}$ and the concentration (mixture degree of dissociation) $c = \alpha < 0.235$.

At high temperatures and low pressures, dissociation of nitrogen follows immediately upon that of the oxygen. The mixture dissociation enthalpy

$$i_R c = i_R \alpha = i_D = 0.235\,(i_R)_{O_2} + (c - 0.235)\,(i_R)_{N_2}. \qquad \text{(III-1-21)}$$

For a rough estimate of i_D, we can refer to tables or curves of the thermodynamic functions. In this case, the enthalpy i_α is found from the temperature T and pressure p with consideration of dissociation and i_D is determined as the difference

$$i_D = i_\alpha - i_{\alpha=0},$$

where $i_{\alpha=0}$ is the enthalpy at the same temperature but without considering dissociation.

For approximate calculations of the enthalpy, we can use the formula

$$i_{\alpha=0} = c_{p0}\left(\frac{T}{T_0}\right)^{\varphi} T,$$

in which the exponent $\phi = 0.1$ for $T > 1000°K$ and the specific heat c_{p_0} is taken as 0.24 kcal/kg·deg for $T_0 = 273°K$.

Determination of the characteristic parameters of air as a model of a diatomic pure dissociating gas composing a mixture of N_2 and O_2 gives rise to the peculiarity that the gaseous medium under consideration is, as it were, preheated in its initial (undissociated) state. A specific heats ratio k = 1.33 corresponds to this state with the vibrational energy levels excited.

Strictly speaking, this medium is not real for ordinary flight conditions. Nevertheless, the relationships given above have practical uses. This is because passage through the shock wave that forms ahead of the body is a nonequilibrium process.

In practice, it may be assumed that even at very high velocities and, consequently, high temperatures behind the shock, the dissociation immediately behind the wave is zero, although the vibrational levels are excited. Thus, the properties of the real and hypothetical gases agree behind the shock wave. /98

Here the accuracy of calculations increases with increasing flight speed as the gas behind the shock is heated to very high temperatures.

Relaxation Effects

Nonequilibrium flows. The above methods for computing thermodynamic variables with consideration of physicochemical transformations reflect the assumed equilibrium nature of the processes. This hypothesis consists in conformity of the internal-degree-of-freedom levels to the parameters characterizing the state of the gas. At comparatively low temperatures (low speeds), for example, equilibrium is established between temperature and the vibrational degree of freedom, and this corresponds to equilibrium between temperature and specific heat. At high temperatures (high speeds), when the gas dissociates, the equilibrium process is characterized by agreement between the degree of dissociation on the one hand, and temperature and pressure on the other.

Finally, at even higher temperatures (very high speeds), we may speak of equilibrium electron-level excitation and ionization processes.

The corresponding internal degrees of freedom are also established instantaneously on a sudden change in temperature in equilibrium flow, in which case we can regard dissociation and ionization as manifestations of new degrees of freedom. Thus, there is no lag in establishment of the degrees of freedom in these cases, i.e., the time to arrive at equilibrium is zero.

Practically equilibrium flow is observed in supersonic flow over bodies at $M_\infty > 4$-5 under conditions corresponding to altitudes of 10-15 km or less. The explanation for this is that at the maximum temperatures that arise under these conditions — of the order of 1000-1500°K — most of the internal energy goes into translational and rotational degrees of freedom, which are established practically instantaneously on sudden temperature changes, since only a few molecular collisions are enough to establish equilibrium. For this reason, the translational and rotational degrees of freedom are usually known as "active."

With increasing speed and, consequently, increasing temperature, much of the internal energy goes into vibrations, and then into dissociation, excitation of electronic levels, and ionization. The processes that actually unfold are such that these energy levels are established more slowly than the translational and rotational ones, since a substantially larger number of collisions is required. Hence the vibrational and dissociation degrees are sometimes known as "inert." Thus, a lag in arrival at equilibrium, known as relaxation, is inherent to the inert degrees. The time during which equilibrium is established, i.e., conformity is arrived at between temperature and energy level, is known as the relaxation time.

Relaxation processes are determined by the degree of freedom excited. If vibrations arise on a sudden temperature change, the corresponding nonequilibrium process is called vibrational relaxation. /99 It is characterized by the lag of heat capacity on a temperature change. If the temperature rises, heat capacity increases as a result of the change in the molecular motion from translation and rotation to translation, rotation, and vibration. The time during which the vibrational motion comes to equilibrium is known as the vibrational relaxation time. In a nonequilibrium dissociating gas, the change in degree of dissociation lags behind a sudden change in temperature. This is explained, in particular, by the fact that the rate of formation of atoms exceeds the rate of their disappearance on a rapid temperature increase, i.e., the dissociation rate is higher than the recombination rate. From the energy standpoint, a relatively small number of collisions is required to cause dissociation. And the comparatively rare three-particle collisions are required to effect recombination.

With time, the rates of the forward and reverse reactions equalize. The time required to arrive at the equilibrium concentration (or degree of dissociation) is known as the dissociation relaxation time.

At temperatures up to approximately 10,000°K, the vibrational and dissociation relaxation processes are basic. Relaxation phenomena associated with excitation of molecular and atomic electron levels and with ionization can be disregarded, since a small fraction of the internal energy falls to these degrees at these temperatures.

Nonequilibration has a substantial effect on various processes that accompany very-high-speed gas flows. For example, vibrational and dissociation relaxation changes the parameters of the gas on passage through shock waves and in flow over bodies, and this, in turn, influences processes of friction, heat transfer, and the pressure redistribution.

Chemical reaction rate equation. Study of nonequilibrium flows consists in simultaneous investigation of the motion of the medium and the chemical processes, which take place at finite rates. Formally, this has its expression in addition of an equation for the chemical-reaction rate to the usual system of gasdynamic equations.

To simplify, we can use the equation pertaining to a simple binary reaction of dissociation and recombination of a pure dissociating diatomic gas (III-1-9), in which the dissociation and recombination rates are unequal, so that there is a certain net rate of the chemical reaction. Equilibrium prevails when the rate of formation of new molecules as a result of recombination of atoms is equal to the rate of disappearance of molecules that dissociate into atoms. Thus, the true rate of the dissociation reaction

$$\frac{d\alpha}{dt} = r_D - r_R, \qquad \text{(III-1-22)}$$

where α is the present value of the degree of dissociation.

To obtain general expressions for the dissociation and recombination rates, it is necessary to apply relationships from chemical kinetics.

Recombination of two atoms of A into an A_2 molecule on collision with a third particle B is expressed by the formula $A + A + B \xrightarrow[k_R]{} A_2 + B$, where B is the particle carrying the recombination energy and k_R is the recombination rate constant. This

constant is determined from the recombination-rate equation

$$\left\{\frac{d[A]}{dt}\right\}_R = 2k_R[A]^2[B]. \qquad \text{(III-1-23)}$$

The square brackets indicate concentration in mole/cm^3 units, /100 and k_R has the dimensions cm^6/mole^2·s.

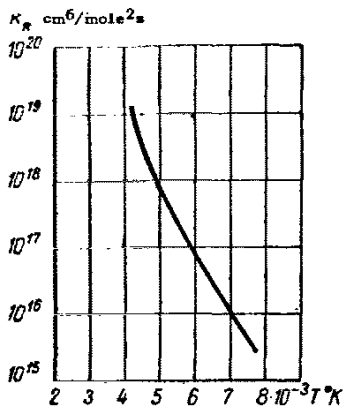

Figure III-1-9. Temperature Curve of Coefficient of Recombination Rate in Air.

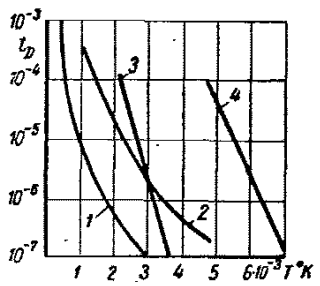

Figure III-1-10. Curves of Relaxation Time at Atmospheric Pressure. 1,2) experimental times of vibrational relaxation of O_2 and N_2, respectively; 3-4) calculated relaxation times for dissociation of O_2 and N_2, respectively.

For a binary mixture of atoms and molecules, the sum of the concentrations $c_M + c_A = 1$, so that

$$[A] = \frac{\rho c_A}{m_A}; \quad [A_2] = \frac{\rho c_M}{m_M} = \frac{\rho(1-c_A)}{2m_A}; \quad [B] = [A] + [A_2] = \frac{\rho(1+c_A)}{2m_A} \qquad \text{(III-1-24)}$$

where $c_A = \alpha$, $c_M = 1 - \alpha$. Introducing (III-1-24) into (III-1-23), we obtain a relation for the recombination rate:

$$r_R = \left(\frac{d\alpha}{dt}\right)_R = k_R\left(\frac{\rho}{m_A}\right)^2\alpha^2(1+\alpha). \qquad \text{(III-1-25)}$$

Let us consider a simple scheme of the dissociation reaction, $A_2 + B \underset{kD}{\rightarrow} A + A + B$, which reflects the process of molecule decay

resulting from pairwise collisions. Here, k_D is the dissociation rate constant and B is the second particle participating in the pairwise collision with the molecule and transmitting the dissociation energy to it.

In accordance with our scheme, the dissociation rate

$$r_D = \left(\frac{d\alpha}{dt}\right)_D = \frac{1}{2} k_D \left(\frac{\rho}{m_A}\right)^2 (1-\alpha^2). \qquad \text{(III-1-26)}$$

Substituting (III-1-25) and (III-1-26) into (III-1-22), we get

$$\frac{d\alpha}{dt} = \frac{1}{2} k_R \left(\frac{\rho}{m_A}\right)^2 (1+\alpha)[K_p(1-\alpha) - 2\alpha^2], \qquad \text{(III-1-22')}$$

where $K_p = k_D/k_R$.

For equilibrium processes, this quantity is defined as the thermodynamic equilibrium constant. With certain reservations, the constant also applies for nonequilibrium reactions.

Remembering this and setting $d\alpha/dt = 0$ in (III-1-22'), we find in the equilibrium case the value $K_p = 2\alpha_e^2/(1 - \alpha_e)$, where α_e is the equilibrium degree of dissociation. Applying (III-1-10) we obtain

$$K_p = \frac{2\alpha_e^2}{1-\alpha_e} = \frac{2\rho_d}{\rho} e^{-D/kT} = \frac{k_D}{k_R}.$$

Substituting this expression in (III-1-22'), we find

$$\frac{d\alpha}{dt} = C\bar{\rho}\rho_d[(1-\alpha)e^{-1/\bar{T}} - \bar{\rho}\alpha^2], \qquad \text{(III-1-27)}$$

where

$$C = \frac{k_R}{m_A^2}(1+\alpha)\rho_d. \qquad \text{(III-1-28)}$$

As we see from (III-1-27), it is important to know the recombination rate coefficient to investigate nonequilibrium flows. This is sufficient for determination of the dissociation rate, since the thermodynamic equilibrium constant can be used.

Figure III-1-9 shows averaged experimental values of the recombination rate coefficient obtained for a pressure of approximately one atmosphere. It is assumed that these values correspond to the lower-limit recombination rate. /101

Relaxation time. Equation (III-1-27) can be modified slightly. For this purpose, we shall use the equilibrium-constant notion, which is useful for nonequilibrium and equilibrium flow conditions. Then the ratio $e^{-1}/\overline{T}/\overline{\rho}$ can be replaced by $\alpha_e^2/(1 - \alpha_e)$ which gives after substitution into (III-1-27)

$$\frac{d\alpha}{d\bar{x}} = \alpha_e - \alpha, \qquad \text{(III-1-27')}$$

where

$$\bar{x} = \frac{x}{Vt_D}; \quad \frac{1}{t_D} = C\bar{\rho}^2\rho_d\left(\alpha + \frac{\alpha_e}{1-\alpha_e}\right). \qquad \text{(III-1-29)}$$

The parameter t_D is the relaxation time. Its determination is a major problem in the physics of relaxation processes. Certain data on the dissociation relaxation time for oxygen and nitrogen have been obtained experimentally in shock tubes (Fig. III-1-10).

Analysis shows that the calculated relaxation times for dissociation are approximately an order smaller than those for recombination. Hence the recombination time is more reliable for use in evaluating relaxation effects, although a rough estimate can also be obtained from the time for the forward reaction.

The same can be said of vibrational relaxation if we remember that the relaxation time is smaller up to a given temperature in real processes than the time for the vibrations to damp in the reverse process beginning at the same temperature.

To estimate relaxation time for recombination of oxygen or nitrogen, we may use the approximate expression

$$t_D = 7.7\cdot 10^{-7}\frac{1}{\alpha(1-0.7\alpha)}\left(\frac{T_0}{T}\right)^{\frac{1}{2}}\left(\frac{\rho_0}{\rho}\right)^2, \qquad \text{(III-1-30)}$$

where the 0 denotes the final values of the variables.

We see from (III-1-30) that the higher the initial density and temperature, the faster is the reaction and, consequently, the

shorter the relaxation time. The same formula indicates a decrease in t_D with increasing pressure, which is confirmed by the curves of Fig. III-1-11. We see that a three-order pressure increase causes an approximately tenfold decrease in relaxation time (the pressure p is referred on the diagram to the sea-level atmospheric pressure $p_{\infty g}$). Studies have shown that the relaxation times for dissociation in air are smaller than those in pure nitrogen or oxygen.

Equilibrium processes. Equilibrium flows have been studied more thoroughly than nonequilibrium flows in both their qualitative and quantitative aspects.

Because of the dissimilar relaxation times for different excitation levels, equilibrium may be established in a given flow region in some degrees of freedom while relaxation phenomena are observed in others.

As approximate model of the process can be constructed around the assumption that equilibrium is reached progressively through the degrees of freedom, i.e., if one degree of freedom is establishing equilibrium, all "lower" degrees of freedom are fully excited and the "higher" degrees are not excited at all.

The sequence of equilibrium with rising temperature can be represented in the following order of degrees of freedom: translational, rotational and vibrational degrees, dissociation, electron-level excitation, and ionization. In examining, for example, the range of establishment of vibrational equilibrium, the first two degrees of freedom may be considered fully excited and all subsequent degrees as not excited. /102

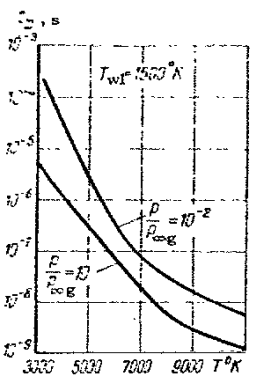

Figure III-1-11. Relaxation Time for Dissociation of Oxygen.

This scheme is not applicable to certain gases, e.g., nitrogen at high temperatures, since ionization begins before dissociation has gone to completion. This is explained by the fact that the dissociation and ionization energies of nitrogen differ by a factor of only one and a half.

A similar effect is observed in air at comparatively moderate temperatures. We see from Fig. III-1-11 that at temperatures above 3200°K, the relaxation time for the dissociation of oxygen is shorter than that for establishment of vibrations in nitrogen. Consequently, equilibrium will be reached in dissociation of oxygen before vibrations are set up in nitrogen.

Diffusion Effects in the Boundary Layer

Diffusive mass flow and heat transfer. In study of phenomena associated with high-speed flow over bodies, it is necessary to deal with nonuniform heating, which results in a three-dimensional distribution of both gas temperature and gas composition. The temperature gradients that appear give rise to a heat flow by molecular conduction. And the variable concentration of atoms from dissociated molecules results in transfer of energy by diffusion of atoms, which liberate heat on recombining into molecules. The heat flow to the surface is shaped from these basic components.

As they transfer enthalpy, the diffusing components of the gas act, in a manner of speaking, as sources of an energy flow that may even exceed the conduction flow under certain conditions.

The heat flow that arises on recombination of diffusing atoms of some component of the air

$$q_d = Qi_R, \qquad \text{(III-1-31)}$$

where Q is the diffusive mass flow and i_R is the heat of recombination of the atoms into molecules, which is obviously equal to the heat of dissociation of the air-component molecules.

Below we shall consider a simple binary mixture of atoms and molecules characterized by a binary diffusion coefficient $\overline{D}$ [m^2/s].

Assuming that $\underline{c}$ [kg/kg] signifies the mass concentration of the atomic component, we can determine its diffusive flow across the boundary layer

$$Q = -\rho\overline{D}\frac{\partial c}{\partial y}. \qquad \text{(III-1-32)}$$

Influence of reaction rate in gaseous medium. Diffusive heat transfer depends on the rate of the boundary-layer reactions. In the general case, which is characterized by finite rate values, recombination takes place in part in the gaseous medium itself, while the remaining atoms diffuse toward the wall. Thus, heat is liberated not only in the interior of the boundary layer, but also at the surface of the body.

Investigation of two extreme cases is important for analysis /103 of this process. The first is characterized by an infinite

recombination rate, so that thermodynamic equilibrium is established at each point in the flow and there is no diffusion of mass toward the wall. The chemical reaction and, consequently, the evolution of heat take place in the boundary layer itself. Here the diffusive heat transfer is governed by the equilibrium-concentration profile.

In practical cases, flow conditions similar to this hypothetical "equilibrium" boundary layer will occur when the diffusion rate is negligibly small by comparison with the dissociation and recombination rates (and, in the case of ionization, also by comparison with the rate of the electronic reactions).

In the second extreme case, recombination takes place infinitely slowly, i.e., chemical reactions do not occur. Consequently, despite the fact that the atoms do diffuse, there is no recombination and no energy is released in the boundary layer. In practice, this may occur in a flow if the chemical reaction time is great by comparison with the characteristic time of particle motion. Such flows are said to be "frozen."

In a frozen flow, the atoms formed on dissociation diffuse toward the cold wall, where they subsequently recombine. The energy liberated here depends on the catalytic properties of the wall, which manifest in various catalytic-recombination rates.

Recombination at the wall. In the general case, the catalytic effect of the wall is characterized by a finite catalytic recombination reaction rate. The properties of the wall as a catalyst are manifested most strongly in the extreme theoretical case of infinitely rapid recombination. In the other extreme case, in which the rate is vanishingly small, the wall is noncatalytic. In the general case of a finite rate, the heat liberated at the wall is determined by the steady-state mass flow

$$Q_{w1} = k_{w1}(c_{w1}\rho_{w1})^m, \qquad \text{(III-1-33)}$$

where k_{w1} is the rate constant of the catalytic reaction at the wall and m is an exponent that takes account of the nature of the catalytic reaction ($1 \leq m \leq 2$). In the particular and simplest case of a first-order reaction, we may set $m = 1$.

According to the law of conservation of mass (disregarding thermal diffusion)

$$Q_{w1} = \rho_{w1}\bar{D}_{w1}(\partial c/\partial y)_{w1}. \qquad \text{(III-1-33')}$$

It follows from (III-1-33) that in the extreme case of diffusion corresponding to an infinite recombination rate ($k_{w1} \sim \infty$), atoms reach the wall even when the concentration at the wall is zero ($c_{w1} = 0$). In the case of a noncatalytic wall ($k_{w1} = 0$), atom flow is zero, since concentration is always finite. Consequently, the heat flow due to diffusion is zero. In the first extreme case, catalysis takes place at infinitely high speed, while in the second, it is infinitesimally slow.

Existence conditions for equilibrium and "frozen" flow. These conditions are determined, on the one hand, by the average time t_{dif} for diffusion of atoms to the wall and, on the other, by the mean lifetime t_{chm} of these atoms. If t_{dif} is substantially larger than t_{chm}, the chemical reaction will take place before the atom reaches the wall, and local thermodynamic equilibrium will appear in the boundary layer. Thus, the existence condition of equilibrium will be $\bar{t}_{dif} = t_{dif}/t_{chm} \gg 1$. The relative time $\bar{t}_{dif}$ is known as the recombination rate parameter. /104

For small diffusion times ($\bar{t}_{dif} \ll 1$), the reaction takes place so slowly that for all practical purposes recombination begins only at the wall and, consequently, the gas flow is frozen.

The diffusion time t_{dif} can be calculated as the time for motion of particles through the boundary layer to the wall. As for the lifetime of the atom, difficulties arise in its evaluation owing to our inadequate knowledge of the chemical recombination processes. In approximation, t_{chm} can be determined by Formula (III-1-30), in which the variables T_0 and ρ_0 are determined for the undissociated medium and T and ρ for the gas dissociating in equilibrium at the outer limit of the boundary layer. At the same time, the following expression can be used to calculate the relative diffusion time:

$$\bar{t}_{dif} = k_1 (p_0')^2 (T_0')^{-3.5} R_0^{-2} \lambda^{-1}, \qquad \text{(III-1-34)}$$

where R_0 is the universal gas constant, p_0' and T_0' are the variables of the gas at the point of total stagnation of the body, λ is the velocity gradient at this point (it will be defined below), and k_1 is the recombination rate constant.

Very few data are available on the recombination rate constant.

It is known, for example, that the product $k_1 T^{-1.5} = 5 \cdot 10^4$ $cm^6/mole^2 \cdot s$ for the recombination of oxygen at $T = 300°K$.

The dimensionless variable $\bar{t}_{dif}$ is a similarity criterion for processes that are characterized by recombination rate and by the time for an atom to diffuse through the boundary layer.

Formula (III-1-34) indicates that frozen flows exist at high altitudes and low speeds. Here, it appears that freezing may be delayed by the increase in recombination rates that accompanies the climb.

Up to this point, we have been considering cases in which the gas is in thermodynamic equilibrium at the outer limit of the boundary layer. In a rarefied atmosphere, however, the long dissociation-relaxation times may make it impossible for a particle to reach equilibrium in its approach to the layer boundary. This complicates the analysis. The investigation can be simplified by assuming that dissociation will be inhibited at low density and moderate speeds and, consequently, the conditions of "frozen" flow will appear.

In this case, we can delay the increase in heat flow by using a wall made from noncatalytic materials. A certain rise in heat flow will occur owing to transfer of energy by molecules that have not managed to dissociate.

Criterion of the catalytic process. For this criterion, we use the so-called recombination (or catalytic) capacity $\gamma = N_r/N$, where N is the total number of atoms striking a unit area per unit time and N_r is the fraction of recombining atoms.

According to (III-1-33), the number of atoms $N_r = Q_{w1}/m_A = k_{w1} c_{w1} \rho_{w1}/m_A$ at $m = 1$. The total number of atoms $N = p_A (2\pi m_A k T_{w1})^{-1/2}$. Since $p_A = n_A k T_{w1}$ and $c_{w1}\rho_{w1} = n_A m_A$, the recombination capacity

$$\gamma = \frac{N_r}{N} = k_{w1} \left(\frac{2\pi m_A}{k T_{w1}} \right)^{1/2}. \qquad \text{(III-1-35)}$$

Figure III-1-12 presents experimental values of the catalytic capacities of a number of materials. Lines of constant k_{w1} are plotted on the same diagram. Study of oxygen recombination has shown that the catalytic capacities of the materials studied are so low that they can be used as coatings to reduce heat transfer. Here, glass is highly effective, while the chlorides /105

are less so owing to the stronger temperature dependence of their catalytic capacities.

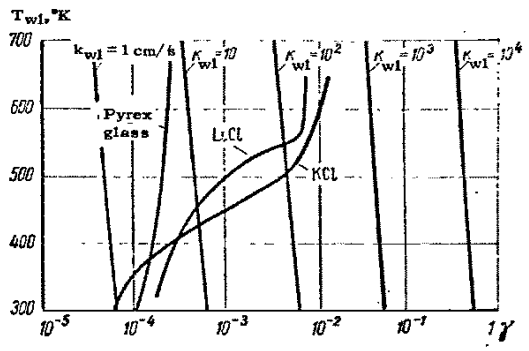

Figure III-1-12. Catalytic Capacities of Certain Materials.

Recombination of atomic nitrogen has been studied at various metallic and nonmetallic surfaces. It has been found that most metals have a strong catalytic action on atomic nitrogen. Nonmetallic materials have the opposite effect, and nitrogen shows little capacity to recombine. For example, measured at a nitrogen partial pressure of 10^{-3} atm on glass, $\gamma = 3 \cdot 10^{5}$.

Studies of the recombination of pure nitrogen and oxygen are of great practical importance, since they enable us to estimate expected catalytic effects in study of heat transfer in air. It may be assumed here that recombination of the air mixture is accelerated by intermediate reactions between oxygen and nitrogen, so that the total catalytic capacity and, consequently, heat transfer are increased.

§III-2. THE SYSTEM OF FUNDAMENTAL EQUATIONS

The problem of flow past a body contains a number of unknowns. If we take the four unknowns velocity, pressure, density, and temperature as basic, it is necessary to have a system of four independent equations (one vector and three scalar) to find them.

Here it is often found helpful to go from this number of unknowns to a larger number, with the attendant increase in the number of system equations. Thus, for example, instead of total velocity, its components in the coordinate system most convenient for solution of the particular problem are usually found. In the general case, there will be three such components and, consequently, the number of equations in the system will increase to six. The number of equations is increased by writing three equations in the projections onto the corresponding axes instead of the single equation of motion in vector form.

Along with the basic unknowns, other parameters usually appear in the equations – such as frictional stress, enthalpy, entropy, specific heat, the speed of sound, heat flow, and others. Then the equation system is complemented by appropriate equations linking these new unknowns with one another.

The resulting equation system reflects the most important laws of gas flows in their most general form. Their derivation is based on a set of premises that define the physical scheme of the particular flow.

Schematization of the flow and the processes taking place in it is the basis for any aerodynamic problem, since it enables us to obtain maximum simplicity in the equations and use a more or less complex scheme in accordance with the nature of the flow itself. /106

One of these physical schemes is based on the Prandtl theory, in which the flow past a body is regarded as inviscid (free stream) outside a thin boundary layer and viscid inside it. This scheme makes it possible to simplify the equations used to study the phenomena in both parts of the flow.

Thus, in examining particular cases of motion, we can simplify the equations describing these flows.

Below we shall consider the system of equations in its most general form and cite particular cases corresponding to free flow and flow in a boundary layer. Equations reflecting various specific peculiarities (physical schemes) of real flows will be given in each of the particular cases.

Equation of Motion

General form of the equation of motion. Let us examine the first equation of the system, namely the equation of motion of a

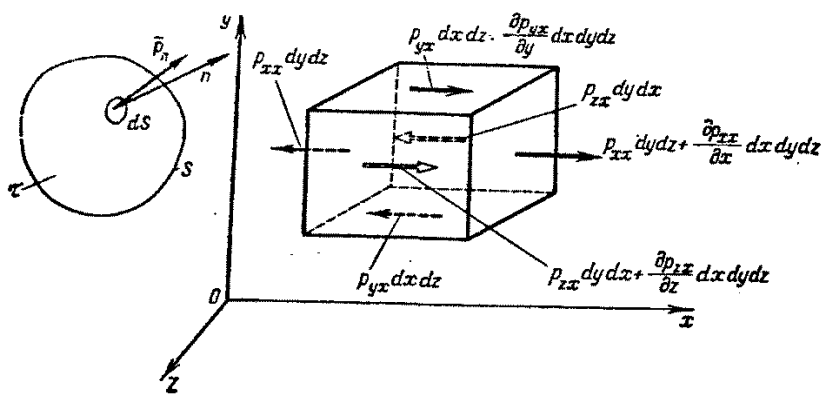

Figure III-2-1. Illustrating Derivation of Equation of Motion of a Gas. τ is the volume of the gas and S is its surface area. The mass of gas in volume τ is $\int_{(\tau)} \rho\, d\tau$.

liquid particle. It is derived from the d'Alembert principle. Applying this principle to a liquid particle in the form of an elementary parallelepiped (Fig. III-2-1) and leaving mass forces out of account, we can obtain the equation of motion in vector form [14]:

$$\frac{d\bar{V}}{dt} = \frac{1}{\rho}\left(\frac{\partial \bar{p}_x}{\partial x} + \frac{\partial \bar{p}_y}{\partial y} + \frac{\partial \bar{p}_z}{\partial z}\right). \qquad \text{(III-2-1)}$$

The surface-force vectors $\bar{p}_x$, $\bar{p}_y$, $\bar{p}_z$ can be represented in the form

$$\bar{p}_k = p_{kx}\bar{i}_1 + p_{ky}\bar{i}_2 + p_{kz}\bar{i}_3, \qquad \text{(III-2-2)}$$

where p_{kx}, p_{ky}, p_{kz} are the projections of these vectors onto the x-, y-, and z-axes, with k taking the successive values x, y, z and $\bar{i}_1$, $\bar{i}_2$, $\bar{i}_3$ are the unit vectors on the corresponding axes.

The velocity vector /107

$$\bar{V} = V_x\bar{i}_1 + V_y\bar{i}_2 + V_z\bar{i}_3,$$

where V_x, V_y, V_z are the projections of this vector onto the coordinate axes.

From (III-2-1) in vector form, we can convert to the Navier-Stokes equations:

$$\left.\begin{aligned}
\frac{dV_x}{dt} &= -\frac{1}{\rho}\frac{\partial p}{\partial x} + \frac{\nu}{3}\frac{\partial}{\partial x}(\operatorname{div}\bar{V}) + \nu\Delta V_x,\\
\frac{dV_y}{dt} &= -\frac{1}{\rho}\frac{\partial p}{\partial y} + \frac{\nu}{3}\frac{\partial}{\partial y}(\operatorname{div}\bar{V}) + \nu\Delta V_y,\\
\frac{dV_z}{dt} &= -\frac{1}{\rho}\frac{\partial p}{\partial z} + \frac{\nu}{3}\frac{\partial}{\partial z}(\operatorname{div}\bar{V}) + \nu\Delta V_z,
\end{aligned}\right\} \qquad \text{(III-2-1')}$$

where

$$\operatorname{div}\bar{V} = \frac{\partial V_x}{\partial x} + \frac{\partial V_y}{\partial y} + \frac{\partial V_z}{\partial z},$$

$$\Delta V_x = \frac{\partial^2 V_x}{\partial x^2} + \frac{\partial^2 V_x}{\partial y^2} + \frac{\partial^2 V_x}{\partial z^2},$$

$$\frac{dV_x}{dt} = \frac{\partial V_x}{\partial t} + V_x\frac{\partial V_x}{\partial x} + V_y\frac{\partial V_x}{\partial y} + V_z\frac{\partial V_x}{\partial z} \text{ etc.}.$$

These equations for Prandtl's physical scheme of the boundary layer transform to the so-called Prandtl equations for the boundary layer and, outside it, to the Euler equations for an inviscid (ideal) gas.

Equations of motion of an ideal medium. A broad class of problems involves calculation of the flow-variable distribution around various bodies in flows of inviscid (ideal) gases. The equation of motion of the ideal gas can be obtained from (III-2-1') by dropping the terms on the right that take account of viscosity. As a result, we find

$$\frac{d\bar{V}}{dt} = -\frac{1}{\rho}\operatorname{grad} p, \qquad \text{(III-2-3)}$$

where the pressure gradient

$$\operatorname{grad} p = \frac{\partial p}{\partial x}\bar{i}_1 + \frac{\partial p}{\partial y}\bar{i}_2 + \frac{\partial p}{\partial z}\bar{i}_3. \qquad \text{(III-2-4)}$$

This is the Euler equation. Applying (III-2-4) for the pressure gradient in Cartesian coordinates, the Euler equation can be written in expanded form:

$$\left.\begin{aligned}
&\frac{\partial V_x}{\partial t} + V_x\frac{\partial V_x}{\partial x} + V_y\frac{\partial V_x}{\partial y} + V_z\frac{\partial V_x}{\partial z} = -\frac{1}{\rho}\frac{\partial p}{\partial x};\\
&\frac{\partial V_y}{\partial t} + V_x\frac{\partial V_y}{\partial x} + V_y\frac{\partial V_y}{\partial y} + V_z\frac{\partial V_y}{\partial z} = -\frac{1}{\rho}\frac{\partial p}{\partial y};\\
&\frac{\partial V_z}{\partial t} + V_x\frac{\partial V_z}{\partial x} + V_y\frac{\partial V_z}{\partial y} + V_z\frac{\partial V_z}{\partial z} = -\frac{1}{\rho}\frac{\partial p}{\partial z}.
\end{aligned}\right\} \qquad \text{(III-2-5)}$$

These equations are used to study spatial (three-dimensional) nonsteady flows over bodies. Solving them, we obtain the distribution of the so-called inviscid gasdynamic variables.

In study of two-dimensional nonsteady flow (for example, in flow past profiles), two equations of System (III-2-5) must be used. If the motion is steady, the partial derivatives with respect to time are zero.

In investigation of flow over solids of revolution, it is convenient to use the Euler equation in cylindrical and spherical coordinates.

If x, r, and γ are the cylindrical coordinates (Fig. III-2-2), then the pressure gradient /108

$$\operatorname{grad} p = \frac{\partial p}{\partial x}\bar{i}_1 + \frac{\partial p}{\partial r}\bar{i}_2 + \frac{1}{r}\frac{\partial p}{\partial \gamma}\bar{i}_3.$$

Then, denoting the velocity components in cylindrical coordinates by V_x, V_r, V_γ, we obtain the equation of motion (III-2-3) in projections onto the coordinate axes in the form

$$\left.\begin{aligned}
&\frac{\partial V_x}{\partial t} + V_x\frac{\partial V_x}{\partial x} + V_r\frac{\partial V_x}{\partial r} + \frac{V_\gamma}{r}\frac{\partial V_x}{\partial \gamma} = -\frac{1}{\rho}\frac{\partial p}{\partial x};\\
&\frac{\partial V_r}{\partial t} + V_x\frac{\partial V_r}{\partial x} + V_r\frac{\partial V_r}{\partial r} + \frac{V_\gamma}{r}\frac{\partial V_r}{\partial \gamma} - \frac{V_\gamma^2}{r} = -\frac{1}{\rho}\frac{\partial p}{\partial r};\\
&\frac{\partial V_\gamma}{\partial t} + V_x\frac{\partial V_\gamma}{\partial x} + V_r\frac{\partial V_\gamma}{\partial r} + \frac{V_\gamma}{r}\frac{\partial V_\gamma}{\partial \gamma} + \frac{V_r V_\gamma}{r} = -\frac{1}{\rho r}\frac{\partial p}{\partial \gamma}.
\end{aligned}\right\} \quad \text{(III-2-6)}$$

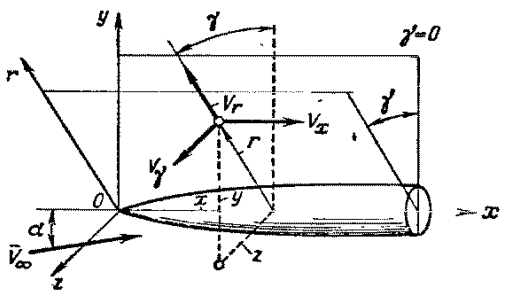

Figure III-2-2. Components of Local Flow Velocity in Cylindrical Coordinates.

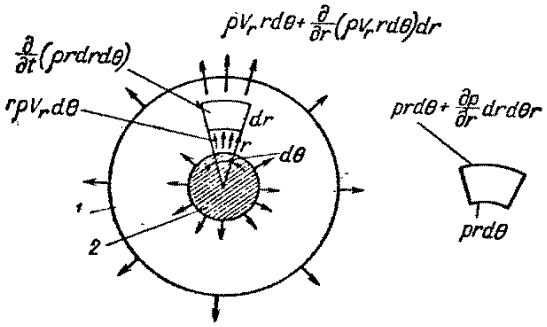

Figure III-2-3. Illustrating Derivation of Equations of Motion and Continuity for Gas Flows Behind a Cylindrical Shock Wave.

These equations are used to investigate nonsteady flow past solids of revolution of arbitrary shape under an angle of attack (unsymmetrical flow).

The system will be simplified for axisymmetric flow, when the angle of attack is zero (spatial two-dimensional flow), since the derivatives with respect to γ and the component V_γ will drop out.

A particular form of the equation of motion corresponding to purely radial flow follows from (III-2-6):

$$\frac{\partial V_r}{\partial t} + V_r\frac{\partial V_r}{\partial r} = -\frac{1}{r}\frac{\partial p}{\partial r}, \quad \text{(III-2-7)}$$

and is used to investigate nonsteady motion of a gas behind a cylindrical shock wave 1. This wave forms on expansion of piston 2, which may be regarded as a kind of impermeable moving surface (Fig. III-2-3). It will be shown below that an analogy exists between high-velocity flow past a solid of revolution and the flow of a

gas when it is displaced by the piston; it is used in solving problems in supersonic aerodynamics.

Let us now consider the equation of motion in the spherical coordinates r, θ, ψ (Fig. III-2-4), as it is used, for example, to investigate supersonic flow past cones. To obtain this equation, we write an expression for the pressure gradient in spherical coordinates: /109

$$\operatorname{grad} p = \frac{\partial p}{\partial r}\vec{i}_1 + \frac{1}{r}\frac{\partial p}{\partial \Theta}\vec{i}_2 + \frac{1}{r\sin\Theta}\frac{\partial p}{\partial \psi}\vec{i}_3.$$

Denoting further by V_r, V_θ, V_ψ the velocity components on the respective axes of our coordinate system, we obtain (III-2-3) in expanded form:

$$\left.\begin{aligned}
&\frac{\partial V_r}{\partial t} + V_r\frac{\partial V_r}{\partial r} + \frac{V_\theta}{r}\frac{\partial V_r}{\partial \Theta} + \frac{V_\psi}{r\sin\Theta}\frac{\partial V_r}{\partial \psi} - \frac{V_\theta^2 + V_\psi^2}{r} = -\frac{1}{\rho}\frac{\partial p}{\partial r};\\
&\frac{\partial V_\theta}{\partial t} + V_r\frac{\partial V_\theta}{\partial r} + \frac{V_\theta}{r}\frac{\partial V_\theta}{\partial \Theta} + \frac{V_\psi}{r\sin\Theta}\frac{\partial V_\theta}{\partial \psi} + \frac{V_r V_\theta}{r} - \\
&\qquad - \frac{V_\psi^2 \operatorname{ctg}\Theta}{r} = -\frac{1}{\rho r}\frac{\partial p}{\partial \Theta};\\
&\frac{\partial V_\psi}{\partial t} + V_r\frac{\partial V_\psi}{\partial r} + \frac{V_\theta}{r}\frac{\partial V_\psi}{\partial \Theta} + \frac{V_\psi}{r\sin\Theta}\frac{\partial V_\psi}{\partial \psi} + \frac{V_r V_\psi}{r} + \\
&\qquad + \frac{V_\theta V_\psi \operatorname{ctg}\Theta}{r} = -\frac{1}{r\rho\sin\Theta}\frac{\partial p}{\partial \psi}.
\end{aligned}\right\} \quad \text{(III-2-8)}$$

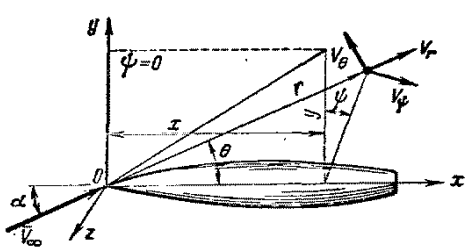

Figure III-2-4. Local Flow Velocity Components in Spherical Coordinates.

In symmetrical flow, the flow parameters are independent of the variable ψ; hence the ψ derivatives and the component V_ψ drop out of (III-2-8).

Together with the systems considered above, the normal (or natural) coordinate system (Fig. III-2-5) is commonly encountered. In the case of plane flow or with axial symmetry of the flow, one of the axes of this system coincides with the tangent to the streamline arc s, and the other along the normal n to the streamline at the particular point. The equations of motion in the axes of the normal system can be obtained by applying (III-2-3) and replacing the pressure gradient by

$$\operatorname{grad} p = \frac{\partial p}{\partial s}\bar{i}_1 + \frac{\partial p}{\partial n}\bar{i}_2,$$

and the total-acceleration vector by

$$\frac{d\bar{V}}{dt} = W_s\bar{i}_1 + W_n\bar{i}_2,$$

where the tangential component of acceleration $W_s = V_s(dV_s/ds)$ in steady-state motion and the normal component $W_n = V_s^2(d\beta/ds)$, where β is the inclination angle of the streamline. Consequently, the equations of motion will take the form

$$\left.\begin{aligned} V_s\frac{\partial V_s}{\partial s} &= -\frac{1}{\rho}\frac{\partial p}{\partial s}; \\ V_s^2\frac{\partial \beta}{\partial s} &= -\frac{1}{\rho}\frac{\partial p}{\partial n}. \end{aligned}\right\} \qquad \text{(III-2-9)}$$

A curvilinear coordinate system is usually employed in boundary-layer theory. It has also been found convenient to use the same system to study flow in a thin layer of inviscid gas between a shock wave and a curved surface at very high flight speeds. /110
The position of an arbitrary point M in this system (Fig. III-2-6) is determined by the distances y along the normal to the surface and x along the generatrix.

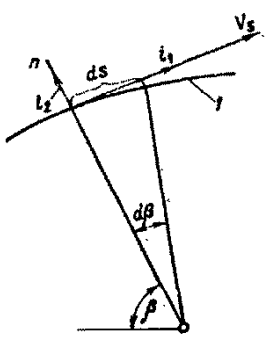

Figure III-2-5. Normal (Natural) Coordinate System. 1) streamline.

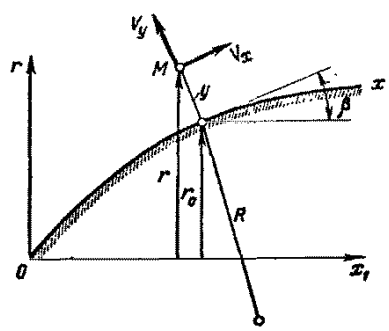

Figure III-2-6. Curvilinear Coordinate System.

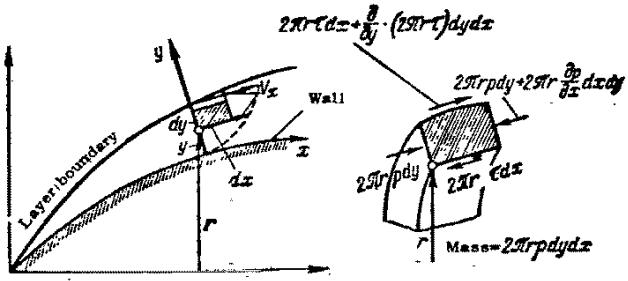

Figure III-2-7. Illustrating Derivation of Equation of Motion of Gas in Boundary Layer.

In steady flow past a flat contour or symmetrical flow past a solid of revolution, the equations of motion are

$$\left.\begin{aligned} \frac{V_x}{1+y/R}\frac{\partial V_x}{\partial x}+V_y\frac{\partial V_x}{\partial y}+\frac{V_xV_y}{R+y}&=-\frac{1}{1+y/R}\frac{1}{\rho}\frac{\partial p}{\partial x};\\ \frac{V_x}{1+y/R}\frac{\partial V_y}{\partial x}+V_y\frac{\partial V_y}{\partial y}-\frac{V_x^2}{R+y}&=-\frac{1}{\rho}\frac{\partial p}{\partial y}, \end{aligned}\right\} \qquad \text{(III-2-10)}$$

where R is the radius of curvature of the contour.

Equation of motion in the boundary layer. Figure III-2-6 shows a diagram illustrating derivation of the generalized equation of motion for the two-dimensional spatial axisymmetric and plane boundary layers. An important condition on which the derivation rests consists in a small thickness δ of the boundary layer by comparison with the linear dimensions of the body (if the characteristic linear dimension is L, the small-δ condition will be $\delta/L \ll 1$). Here $\partial p/\partial y = 0$, i.e., pressure does not change inside the boundary layer at various points along the normal to the contour of the body and is equal to the pressure at the boundary of the layer. Owing to the small thickness of the boundary layer, we can also disregard the Coriolis acceleration. Then the equation of motion in the layer will be

/111

$$V_x\frac{\partial V_x}{\partial x}+V_y\frac{\partial V_x}{\partial y}=-\frac{1}{\rho}\frac{\partial p}{\partial x}+\frac{1}{r^\varepsilon\rho}\frac{\partial (r^\varepsilon\tau)}{\partial y}, \qquad \text{(III-2-11)}$$

where $\varepsilon = 0$ if the boundary layer is plane and $\varepsilon = 1$ if it is axisymmetric.

This equation is suitable for investigation of both laminar and turbulent boundary layers in which the parameters characterizing flow in the layer are assumed to be averaged and pulsation values of the parameters are excluded. Accordingly, V_x, V_y, ρ, and p in (III-2-11) must be taken averaged and the frictional stress must be determined from the expression $\tau = (\mu + \mu_t)(\partial V_x/\partial y)$. In this expression, μ_t is the coefficient of turbulent viscosity (in distinction from μ, the coefficient of ordinary molecular viscosity in a laminar boundary layer).

In the laminary boundary layer, $\mu_t = 0$, the frictional stress $\tau = \mu \times (\partial V_x/\partial y)$, and the equation of motion is rewritten

$$V_x \frac{\partial V_x}{\partial x} + V_y \frac{\partial V_x}{\partial y} = -\frac{1}{\rho}\frac{\partial p}{\partial x} + \frac{1}{r^e \rho}\frac{\partial}{\partial y}\left(\mu r^e \frac{\partial V_x}{\partial y}\right). \qquad \text{(III-2-12)}$$

For the general case, when the gas undergoes physicochemical transformations, the coefficient μ varies across the boundary layer. When there are no such transformations or they are negligible, we can assume μ = const. Equations (III-2-11) and (III-2-12), from which the radius r must be excluded, are used to study the boundary layer about a plane contour.

Continuity Equation

Forms of the continuity equation. This equation is one of the fundamental equations of aerodynamics and is used together with the equation of motion to investigate flow past bodies.

In mathematical form, it reflects the condition that if a gas passes through a certain fixed volume τ without forming vacuums or discontinuities, the total mass of gas $\int_{(S)} \rho(\bar{V}\bar{n})\,dS$ passing per unit time across the surface S that bounds this volume is equal to the change in per-second mass in this volume $-\int_{(\tau)} \partial\rho/\partial t\,d\tau$ ($\bar{n}$ is the outer normal to the surface). Accordingly, we obtain the equation

$$\frac{\partial \rho}{\partial t} + \operatorname{div}(\rho \bar{V}) = 0. \qquad \text{(III-2-13)}$$

which is known as the continuity equation. A full derivation will be found in [2]. Factoring out the expression in (III-2-13)

for $\operatorname{div}(\rho\bar{V}) = \partial(\rho V_x)/\partial x + \partial(\rho V_y)/\partial y + \partial(\rho V_z)/\partial z$, we obtain:

$$\frac{\partial\rho}{\partial t} + \frac{\partial(\rho V_x)}{\partial x} + \frac{\partial(\rho V_y)}{\partial y} + \frac{\partial(\rho V_z)}{\partial z} = 0 \qquad \text{(III-2-14)}$$

or, remembering that $d\rho/dt = \partial\rho/\partial t + V_x(\partial\rho/\partial x) + V_y(\partial\rho/\partial y) + V_z(\partial\rho/\partial z)$, we have

$$\frac{d\rho}{dt} + \rho \operatorname{div}\bar{V} = 0.$$

To obtain the continuity equation in cylindrical coordinates, we use the expression /112

$$\operatorname{div}\bar{V} = \frac{\partial V_x}{\partial x} + \frac{\partial V_r}{\partial r} + \frac{1}{r}\frac{\partial V_\gamma}{\partial\gamma} + \frac{V_r}{r}.$$

Then the continuity equation

$$r\frac{\partial\rho}{\partial t} + \frac{\partial(\rho r V_x)}{\partial x} + \frac{\partial(\rho r V_r)}{\partial r} + \frac{1}{r}\frac{\partial(\rho r V_\gamma)}{\partial\gamma} = 0. \qquad \text{(III-2-15)}$$

From it follows the particular form

$$r\frac{\partial\rho}{\partial t} + \frac{\partial(\rho r V_r)}{\partial r} = 0. \qquad \text{(III-2-16)}$$

This equation is used to investigate nonsteady flow of a gas behind a cylindrical wave (see Fig. III-2-3).

Let us present the continuity equation in spherical coordinates. For this purpose, we use the expression for the divergence

$$\operatorname{div}\bar{V} = \frac{1}{r^2}\frac{\partial(r^2 V_r)}{\partial r} + \frac{1}{r\sin\Theta}\frac{\partial(\sin\Theta V_\Theta)}{\partial\Theta} + \frac{1}{r\sin\Theta}\frac{\partial V_\psi}{\partial\psi}.$$

After substituting this expression in (III-2-13), we obtain

$$r\frac{\partial\rho}{\partial t} + \frac{1}{r}\frac{\partial(\rho r^2 V_r)}{\partial r} + \frac{1}{\sin\Theta}\frac{\partial(\rho V_\Theta\sin\Theta)}{\partial\Theta} + \frac{1}{\sin\Theta}\frac{\partial(\rho V_\psi)}{\partial\psi} = 0. \qquad \text{(III-2-17)}$$

The equations of continuity for plane and axisymmetric flows are obtained from (III-2-14) and (III-2-15), respectively:

$$y^{\varepsilon}\frac{\partial \rho}{\partial t}+\frac{\partial (\rho y^{\varepsilon}V_x)}{\partial x}+\frac{\partial (\rho y^{\varepsilon}V_y)}{\partial y}=0, \qquad \text{(III-2-18)}$$

where $\varepsilon = 0$ for plane flow and $\varepsilon = 1$ for spatial two-dimensional flow ($y = r$, $V_y = V_r$).

The continuity equation of a spatial two-dimensional flow in spherical coordinates is obtained from (III-2-17) by dropping the fourth term in the left member.

The continuity equation for steady flow in the normal coordinate system (see Fig. III-2-5) is obtained as the condition for conservation of flow rate in flow of a gas between two closely spaced stream surfaces (spatial two-dimensional flow) or streamlines (plane two-dimensional flow).

The continuity equation

$$\frac{\partial \beta}{\partial n}+\frac{\partial \ln \rho}{\partial s}+\frac{\partial \ln V_s}{\partial s}+\frac{\sin \beta}{y}\varepsilon=0, \qquad \text{(III-2-19)}$$

where $\varepsilon = 0$ for the plane flow and $\varepsilon = 1$ for the spatial flow.

If we consider the curvilinear coordinate system (see Fig. III-2-6),

$$\frac{\partial (\rho r^{\varepsilon}V_x)}{\partial x}+\frac{\partial [\rho r^{\varepsilon}V_y (1+y/R)]}{\partial y}=0. \qquad \text{(III-2-20)}$$

In boundary-layer investigations, this equation can be simplified if we remember that the layer is thin. Dropping y/R as small compared to unity, we find

$$\frac{\partial (\rho r^{\varepsilon}V_x)}{\partial x}+\frac{\partial (\rho r^{\varepsilon}V_y)}{\partial y}=0. \qquad \text{(III-2-21)}$$

Transformation of the continuity equation. In practice, frequent use is made of an equation derived from the continuity equation by eliminating density from it with the aid of the equation of motion. Any coordinate system may be used here. /113

If we examine potential nonsteady flow in Cartesian coordinates, the transformed continuity equation will be an equation in Cartesian coordinates for the velocity potential ϕ [14]:

$$\left(1-\frac{\varphi_x^2}{a^2}\right)\varphi_{xx}+\left(1-\frac{\varphi_y^2}{a^2}\right)\varphi_{yy}+\left(1-\frac{\varphi_z^2}{a^2}\right)\varphi_{zz}-\frac{2}{a^2}\varphi_{xy}\varphi_x\varphi_y-$$
$$-\frac{2}{a^2}\varphi_{xz}\varphi_x\varphi_z-\frac{2}{a^2}\varphi_{yz}\varphi_y\varphi_z-\frac{2}{a^2}\varphi_y\varphi_{yt}-\frac{2}{a^2}\varphi_x\varphi_{xt}- \qquad \text{(III-2-22)}$$
$$-\frac{2}{a^2}\varphi_z\varphi_{zt}-\frac{1}{a^2}\varphi_{tt}=0,$$

where the derivatives $\varphi_x=\partial\varphi/\partial x$, $\varphi_{xx}=\partial^2\varphi/\partial x^2$, $\varphi_{xt}=\partial^2\varphi/\partial x\,\partial t$, $\varphi_{tt}=\partial^2\varphi/\partial t^2$ etc.

The analogous equation for the potential ϕ in cylindrical coordinates takes the form

$$\left(1-\frac{\varphi_x^2}{a^2}\right)\varphi_{xx}+\left(1-\frac{\varphi_r^2}{a^2}\right)\varphi_{rr}+\frac{\varphi_{\gamma\gamma}}{r^2}\left(1-\frac{\varphi_\gamma^2}{a^2r^2}\right)-\frac{2}{r^2}\frac{\varphi_{r\gamma}\varphi_r\varphi_\gamma}{a^2}-\frac{2}{r^2}\frac{\varphi_{x\gamma}\varphi_x\varphi_\gamma}{a^2}-$$
$$-\frac{2\varphi_{xr}\varphi_x\varphi_r}{a^2}+\frac{\varphi_r}{r}\left(1+\frac{\varphi_\gamma^2}{a^2r^2}\right)-\frac{2\varphi_x\varphi_{xt}}{a^2}-\frac{2\varphi_r\varphi_{rt}}{a^2}-\frac{2\varphi_\gamma\varphi_{\gamma t}}{a^2r^2}-\frac{\varphi_{tt}}{a^2}=0. \qquad \text{(III-2-23)}$$

An equation used to investigate two-dimensional nonsteady potential flow (plane or spatial) derives from (III-2-22):

$$\left(1-\frac{\varphi_x^2}{a^2}\right)\varphi_{xx}+\left(1-\frac{\varphi_y^2}{a^2}\right)\varphi_{yy}-\frac{2}{a^2}\varphi_{xy}\varphi_x\varphi_y-\frac{2}{a^2}\varphi_x\varphi_{xt}- \qquad \text{(III-2-24)}$$
$$-\frac{2}{a^2}\varphi_y\varphi_{yt}+\varepsilon\frac{\varphi_y}{a^2y}-\frac{\varphi_{tt}}{a^2}=0.$$

All terms containing partial time derivatives are excluded from the equations in investigation of steady flow.

Steady spatial potential flow can be studied with an equation for the velocity potential in spherical coordinates:

$$\left(1-\frac{\varphi_r^2}{a^2}\right)\varphi_{rr}+\left(1-\frac{\varphi_\theta^2}{a^2r^2}\right)\frac{\varphi_{\theta\theta}}{r^2}+\left(1-\frac{\varphi_\psi^2}{a^2r^2\sin^2\theta}\right)\frac{\varphi_{\psi\psi}}{r^2\sin^2\theta}-\frac{2\varphi_\theta\varphi_\psi\varphi_{\theta\psi}}{a^2r^4\sin^2\theta}- \qquad \text{(III-2-25)}$$
$$-\frac{2\varphi_r\varphi_\theta\varphi_{\theta r}}{a^2r^2}-\frac{2\varphi_r\varphi_\psi\varphi_{r\psi}}{a^2r^2\sin^2\theta}+\left(2-\frac{\varphi_\theta^2\sin^2\theta+\varphi_\psi^2}{a^2r^2\sin^2\theta}\right)\frac{\varphi_r}{r}+\left(1+\frac{\varphi_\psi^2}{a^2r^2\sin^2\theta}\right)\frac{\varphi_\theta\operatorname{ctg}\theta}{r^2}=0.$$

For spatial two-dimensional flow (III-2-25) is simplified in virtue of the fact that the ψ derivatives are zero.

The equations given for the velocity potential are fundamental in the aerodynamics of isentropic (irrotational) flows, a distinctive property of which is constancy of entropy over the entire region of the flow.

If we disregard the influence of viscosity, disturbed subsonic flow past a body has this property. Supersonic disturbed flow will also be isentropic if it occurs behind a normal compression shock, since the entropy behind it is everywhere the same.

In the case of smaller M_∞, the flow behind a curvilinear shock actually differs little from isentropic; we may therefore use the velocity-potential equation to study it. Solution of this equation gives better results as the body in the flow becomes more slender.

At large M_∞, supersonic flow depends substantially on the vortical nature of gas motion behind a curvilinear compression shock; in investigating it, therefore, we should proceed from a continuity equation transformed with the aid of the general-form equation of motion. /114

We indicate the form of this equation for the various coordinate systems, with a view to the case of steady two-dimensional flow.

Cartesian and cylindrical coordinates:

$$\left(1-\frac{V_x^2}{a^2}\right)\frac{\partial V_x}{\partial x}-\frac{V_xV_y}{a^2}\left(\frac{\partial V_x}{\partial y}+\frac{\partial V_y}{\partial x}\right)+\left(1-\frac{V_y^2}{a^2}\right)\frac{\partial V_y}{\partial y}+\varepsilon\frac{V_y}{y}=0. \quad \text{(III-2-26)}$$

Spherical coordinates:

$$\left(1-\frac{V_r^2}{a^2}\right)\frac{\partial V_r}{\partial r}-\frac{V_rV_\theta}{a^2}\left(\frac{\partial V_\theta}{\partial r}+\frac{1}{r}\frac{\partial V_r}{\partial\theta}\right)+\frac{1}{r}\left(1-\frac{V_\theta^2}{a^2}\right)\frac{\partial V_\theta}{\partial\theta}+\frac{2V_r}{r}+\frac{V_\theta}{r}\operatorname{ctg}\theta=0. \quad \text{(III-2-27)}$$

Normal (natural) coordinates:

$$\frac{\partial\beta}{\partial n}+\frac{\partial\ln V_s}{\partial s}\left(1-\frac{V_s^2}{a^2}\right)+\varepsilon\frac{\sin\beta}{y}=0. \quad \text{(III-2-28)}$$

Linearization of the equations. The differential equations given above are nonlinear and pertain to the general case of disturbed gas flow, whose parameters may differ substantially from the corresponding parameters of the undisturbed flow. In problems

of flow past bodies, these equations are used to study disturbed flow when the shapes of the bodies are arbitrary and flow takes place at an arbitrary angle of attack.

In many cases that are of practical interest, the bodies are slender and the attack angles small; hence the disturbed flow past such bodies differs little from the undisturbed flow. The differential equations can be linearized for weakly disturbed flow.

In accordance with the definition of the weakly disturbed or linearized flow, its parameters can be expressed in the form

$$\bar{V}=\bar{V}_\infty+\bar{V}',\ a=a_\infty+a';\ p=p_\infty+p';\ \rho=\rho_\infty+\rho';\ S=S_\infty+S',\quad \text{(III-2-29)}$$

where the subscript ∞ identifies undisturbed-flow parameters and the prime small increment parameters that appear as a result of the disturbance.

It follows from the expression $S = S_\infty + S'$ that the linearized flow is characterized by a new entropy. However, research has shown that the increment S' is so small that it may be disregarded, so that the linearized flow can be regarded as isentropic. This implies that the curvilinear compression shock degenerates into a disturbance wave of infinitesimal intensity in front of a slender tapered body.

The linearized flow may be characterized by the potential function $\varphi=\varphi_\infty+\varphi'$, which is composed of the potential ϕ_∞ of the undisturbed flow and an additional potential ϕ' of the disturbed flow (disturbance potential), which is a small quantity.

The linearized equations obtained by transforming (III-2-22) and (III-2-23) with application of (III-2-29) and the expression for $\varphi=\varphi_\infty+\varphi'$ have the form [51]:

$$(1-M_\infty^2)\varphi'_{xx}+\varphi'_{yy}+\varphi'_{zz}-\frac{2M_\infty}{a_\infty}\varphi'_{xt}-\frac{\varphi'_{tt}}{a_\infty^2}=0; \quad \text{(III-2-30)}$$

$$(1-M_\infty^2)\varphi'_{xx}+\varphi'_{rr}+\frac{\varphi'_{\gamma\gamma}}{r^2}+\frac{\varphi'_r}{r}-\frac{2M_\infty}{a_\infty}\varphi'_{xt}-\frac{\varphi'_{tt}}{a_\infty^2}=0. \quad \text{(III-2-31)}$$

As a result of simplifying (III-2-24) with exclusion of the time derivatives, we obtain a linearized equation for steady two-dimensional (plane or spatial) flow: /115

$$(1-M_\infty^2)\varphi'_{xx}+\varphi'_{yy}+\varepsilon\frac{\varphi'_y}{y}=0. \quad \text{(III-2-32)}$$

Equation for the stream function. It is more convenient to use equations transformed to the variable ψ, which is known as the stream function, instead of (III-2-26) or (III-2-27) to investigate nonisentropic flows.

To transform (III-2-26), we use the relations

$$\frac{\partial\psi}{\partial x}=-y^{\varepsilon}V_y\frac{\rho}{\rho_0};\quad \frac{\partial\psi}{\partial y}=y^{\varepsilon}V_x\frac{\rho}{\rho_0};\qquad \text{(III-2-33)}$$

and for (III-2-27)

$$\frac{\partial\psi}{\partial\theta}=-r^2V_r\sin\theta\frac{\rho}{\rho_0};\quad \frac{\partial\psi}{\partial r}=r^2V_\theta\sin\theta\frac{\rho}{\rho_0},\qquad \text{(III-2-34)}$$

where ρ_0 is the density at full isentropic stagnation.

Below, we shall use (III-2-26), transformed to the stream function ψ, to investigate bodies in supersonic flow. The form of this equation is [58]

$$\left(1-\frac{V_x^2}{a^2}\right)\psi_{xx}+\left(1-\frac{V_y^2}{a^2}\right)\psi_{yy}-\frac{2}{a^2}V_xV_y\psi_{xy}-V_x(1-\tilde{V}^2)^{\frac{1}{k-1}}\varepsilon=$$
$$=y^{2\varepsilon}\left(1-\frac{V^2}{a^2}\right)(1-\tilde{V}^2)^{\frac{k-1}{k+1}}f(\psi),\qquad \text{(III-2-35)}$$

where the derivatives $\psi_{xx}=\partial^2\psi/\partial x^2$, $\psi_{xy}=\partial^2\psi/\partial x\,\partial y$, $\psi_{yy}=\partial^2\psi/\partial y^2$, $\tilde{V}=V/V_{max}$ (V_{max} is the maximum velocity); the function

$$f(\psi)=\frac{1}{\rho_0}\frac{\partial p_0}{\partial\psi}=-\frac{1}{y^{\varepsilon}}\left(\frac{\partial V_y}{\partial x}-\frac{\partial V_x}{\partial y}\right)(1-\tilde{V}^2)^{-\frac{k}{k-1}}.\qquad \text{(III-2-36)}$$

Here p_0 is the pressure at full isentropic stagnation.

If the stagnation pressure does not vary along the shock, then $dp_0/d\psi = 0$ and, consequently, $f(\psi)=0$. In this case (III-2-35) defines the stream function for potential (isentropic) flow.

In the region behind a curvilinear compression shock, the stagnation pressure changes when we pass from one streamline to another, and, understandably, $f(\psi)\neq 0$. Consequently, (III-2-35) describes nonisentropic (vortical) flow.

Since the variation of stagnation pressure across streamlines is governed by the variation of the entropy S, (III-2-35) can be brought to a form that contains the entropy by use of the equation

$$\frac{1}{p_0}\frac{dp_0}{d\psi} = -\frac{k}{(k-1)c_p}\frac{dS}{d\psi}. \qquad \text{(III-2-37)}$$

The Diffusion Equation

Diffusion processes taking place in the boundary layer depend on the concentration distribution of the mixture components. One of the relationships that determines this distribution is the diffusion equation.

Like the continuity equation, it is also a mass-conservation equation, this time embodying the condition of conservation of the diffusing mixture component.

Let us assume that no chemical reactions take place and, consequently, that the rate W_i of formation of atoms or molecules by dissociation or recombination is zero. Then, disregarding the diffusive flow in the direction of the x-axis and thermal diffusion, we can derive the continuity equation for the i-th mixture component (the diffusion equation) from Eq. (III-2-21) by replacing $\rho r^{\varepsilon} V_x$ by $\rho r^{\varepsilon} V_x c_i$, and $\rho r^{\varepsilon} V_y$ by $\rho r^{\varepsilon} V_y c_i - Q_i$, where Q_i is the diffusion flow across the boundary layer. If, on the other hand, chemical reactions do take place in the gas and are accompanied by the formation of new particles or the disappearance of old ones, a term $r^{\varepsilon} W_i$ appears in the right member of the resulting equation to take account of the additional flow of the component. Thus, the i-th component diffusion equation will be /116

$$\frac{\partial(\rho r^{\varepsilon} V_x c_i)}{\partial x} + \frac{\partial(\rho r^{\varepsilon} V_y c_i)}{\partial y} = \frac{\partial}{\partial y}\left(\rho \bar{D} r^{\varepsilon}\frac{\partial c_i}{\partial y}\right) + r^{\varepsilon} W_i, \qquad \text{(III-2-38)}$$

where the diffusion coefficient $\bar{D}$ is assumed to be the same for each pair of diffusing components of the binary mixture.

Equation (III-2-38) is simplified if the composition of the gas is "frozen" and, consequently, no chemical reactions take place in it. In this case, we must assume $W_i = 0$.

We can convert from concentration to the degree of dissociation α of the binary mixture in the diffusion equation. For this purpose, we use the relationships $c_A = \alpha$, $c_M = 1 - \alpha$. For example,

the continuity equation for an atomic component is

$$\frac{\partial(\rho r^e V_x \alpha)}{\partial x} + \frac{\partial(\rho r^e V_y \alpha)}{\partial y} = \frac{\partial}{\partial y}\left(\rho \bar{D} r^e \frac{\partial \alpha}{\partial y}\right) + \dot{r}^e W_A. \qquad \text{(III-2-38')}$$

The above equations may refer to either laminar or turbulent boundary layers. In the former case, $\bar{D}$ is the coefficient of laminar diffusion $\bar{D} = \bar{D}_L$ and is defined as the molecular transfer parameter. In the latter case, the diffusion coefficient is composed of the coefficients of laminar $\bar{D}_L$ and turbulent $\bar{D}_t$ diffusion, i.e., $\bar{D}$ in the equation is replaced by $\bar{D}_L + \bar{D}_t$. The other gasdynamic parameters and concentration should be regarded as averaged quantities.

Equation of Momentum

General form of the equation. It is sometimes convenient in investigating gas flows to use a different form of the equation of motion that can be derived by considering the flow of a gas through some surface or section.

If we take the parallelepiped surface shown in Fig. III-2-1 as this surface and apply the momentum theorem, according to which the change in momentum is equal to the external-force impulse, we obtain the equation of momentum (equation of impulses):

$$\frac{\partial \bar{p}_x}{\partial x} + \frac{\partial \bar{p}_y}{\partial y} + \frac{\partial \bar{p}_z}{\partial z} = \frac{\partial(\rho \bar{V})}{\partial t} + \frac{\partial(\rho V_x \bar{V})}{\partial x} + \frac{\partial(\rho V_y \bar{V})}{\partial y} + \frac{\partial(\rho V_z \bar{V})}{\partial z}. \qquad \text{(III-2-39)}$$

Steady-state motion of an ideal gas. Since the partial time derivative is zero in this case, and there are no viscosity-dependent forces, (III-2-39) becomes /117

$$-\operatorname{grad} p = \frac{\partial(\rho V_x \bar{V})}{\partial x} + \frac{\partial(\rho V_y \bar{V})}{\partial y} + \frac{\partial(\rho V_z \bar{V})}{\partial z}. \qquad \text{(III-2-40)}$$

Practical interest attaches to the momentum equation of a gas in a constant-section channel, i.e., for the one-dimensional case. It follows from (III-2-40) that $dp/dx = -d(\rho V_x^2)/dx$ in these cases. Integrating over x between two arbitrary sections "1" and "2", we obtain

$$\rho_2 V_2^2 - \rho_1 V_1^2 = p_1 - p_2. \qquad \text{(III-2-41)}$$

This law, together with the other two laws of conservation of mass and energy, forms the basis of gas-flow theory.

Equation of momentum for the boundary layer. Let us examine steady motion in a two-dimensional boundary layer in which the condition of small layer thickness is satisfied.

As a result of joint transformation of the equations of motion (III-2-11) and continuity (III-2-21), in which the radius r assumes, for a given section of the layer, a constant value equal to its value r_0 at the wall, we obtain the following equation [57]:

$$\frac{d}{dx}\left[r_\delta^\varepsilon \rho_\delta V_\delta^2 \int_0^\delta \frac{\rho V_x}{\rho_\delta V_\delta}\left(1-\frac{V_x}{V_\delta}\right)dy\right]+\frac{dV_\delta}{dx}\left[r_\delta^\varepsilon \rho_\delta V_\delta \int_0^\delta \left(1-\frac{\rho V_x}{\rho_\delta V_\delta}\right)dy\right]=r_\delta^\varepsilon \tau_0, \quad \text{(III-2-42)}$$

where τ_0 is the frictional stress at the wall and V_δ and ρ_δ are the velocity and density at the layer boundary.

Physically, the left side determines the change in momentum of a certain mass of gas passing through a section of the boundary layer. Equation (III-2-42) is therefore known as the momentum equation for the boundary layer. This equation is also known as the Karman integral relationship.

The integrals in the left side of (III-2-42) are very important characteristics of the boundary layer:

$$\delta^* = \int_0^\delta \left(1-\frac{\rho V_x}{\rho_\delta V_\delta}\right)dy, \quad \delta^{**} = \int_0^\delta \frac{\rho V_x}{\rho_\delta V_\delta}\left(1-\frac{V_x}{V_\delta}\right)dy. \quad \text{(III-2-43)}$$

The parameters δ^* and δ^{**} are known, respectively, as the displacement thickness and the momentum thickness. The former characterizes the decrease in per-second flowrate and the latter the decrease in momentum (impulse) on passage of the gas through the boundary-layer section as a result of flow stagnation.

The Energy Equation

General form of the energy equation. The energy equation is one of the basic equations of aerodynamics. In mathematical form, it reflects the law of conservation of energy, according to which the change in the kinetic and internal energy of a moving particle is equal to the work done by the external forces plus the energy influx by transfer of heat from the outside.

We shall assume that the work is done by surface forces that originate from normal pressure and tangential stress. As for heat transfer, it occurs, if we disregard diffusive heat conduction, by molecular heat conduction, radiation, and diffusion of gases.

Accordingly, the energy equation for the mass of gas enclosed in an arbitrary volume τ (see Fig. III-2-1) will take the form /118

$$\frac{d}{dt}\int_{(\tau)} \rho\left(\frac{V^2}{2}+u\right)d\tau = -\int_{(S)} \bar{p}_n\bar{V}\,dS + \int_{(S)} q_c\,dS + \int_{(\tau)} \varepsilon\,d\tau + \int_{(S)} q_d\,dS, \quad \text{(III-2-44)}$$

where q_c and q_d are the respective heat flows by conduction and diffusion per unit time and through a unit surface; ε is the flow due to radiation from a unit mass per unit time; u is the internal energy of the unit mass of gas; $\bar{p}_n$ is the surface-force vector.

Energy equation for the boundary layer. Let us first examine the energy equation for a laminar boundary layer in which chemical reactions and diffusion take place. For this purpose, we shall use the general equation (III-2-44). The molecular heat-conduction flow that appears in it is determined from the formula $q_c = -\lambda(\partial T/\partial n)$.

The amount of heat transferred by the diffusing gases is

$$q_d = \sum_i Q_i i_i = -\sum_i \rho\bar{D}\frac{\partial c_i}{\partial n} i_i,$$

with the enthalpy of the i-th component

$$i_i = \int_0^T c_{pi}\,dT + (i_{chm})_i = \bar{i}_i + (i_{chm})_i,$$

where c_{pi} is the specific heat of the component, $\bar{i}_i = \int_0^T c_{pi}\,dt$ is its enthalpy as an ideal gas, and $(i_{chm})_i$ is the chemical energy of formation of the component; it may be assumed equal to zero for molecules.

For atoms, this quantity must be regarded as negative and equal to $(i_{chm})_i = -i_R$, where i_R is the dissociation energy per unit mass of the atomic components. Obviously, the enthalpy of the gas mixture $i = \sum_i c_i i_i$.

If we relate (III-2-44) to the flow conditions in a two-dimensional boundary layer and use curvilinear coordinates, the energy equation is

$$\rho r^\varepsilon \frac{d}{dt}\left(i + \frac{V^2}{2}\right) = \frac{\partial (\tau V_x r^\varepsilon)}{\partial y} + \frac{\partial}{\partial y}\left(r^\varepsilon \lambda \frac{\partial T}{\partial y}\right) - \sum_i i_i \frac{\partial (r^\varepsilon Q_i)}{\partial y}, \qquad \text{(III-2-45)}$$

where for a binary mixture of atoms and molecules

$$di = (c_p)_{av}\, dT + \sum_i i_i\, dc_i,$$

where the average heat capacity of the mixture is

$$(c_p)_{av} = \sum_i (c_p)_i c_i = (c_p)_M c_M + (c_p)_A c_A.$$

The first term on the right is the molecular component of average heat capacity, and the second is the atomic component.

Equation (III-2-45) can be transformed using the expression $i_0 = i + V^2/2$ for the stagnation enthalpy. We obtain as a result

$$\rho r^\varepsilon \frac{di_0}{dt} = V_x \rho r^\varepsilon \frac{\partial i_0}{\partial x} + V_y \rho r^\varepsilon \frac{\partial i_0}{\partial y} = \frac{\partial (\tau V_x r^\varepsilon)}{\partial y} + \\ + \frac{\partial}{\partial y}\left(r^\varepsilon \lambda \frac{\partial T}{\partial y}\right) + \sum_i \frac{\partial}{\partial y}\left(r^\varepsilon \rho \bar{D} i_i \frac{\partial c_i}{\partial y}\right). \qquad \text{(III-2-46)}$$

We transform (III-2-46) as it applies to a binary mixture of two components for which the concentration sum $c_M + c_A = 1$ and, consequently, $\partial c_M/\partial y = -\partial c_A/\partial y$. Remembering that since the enthalpy of the mixture $i = \sum_i i_i c_i$ and its average heat capacity $(c_p)_{av} = \sum_i c_i (c_p)_i$, we put for the binary composition

/119

$$di = (c_p)_{av}\, dT + (i_A - i_M)\, dc_A.$$

The partial derivative $\partial T/\partial y$ can be found from the above. Substituting it in (III-2-46) and applying the continuity equation (III-2-21) to transform the right member,

$$\frac{\partial (\rho r^{\varepsilon} V_x i_0)}{\partial x} + \frac{\partial (\rho r^{\varepsilon} V_y i_0)}{\partial y} = \frac{\partial}{\partial y}\left(\frac{r^{\varepsilon}\mu}{\mathrm{Pr}}\frac{\partial i_0}{\partial y}\right) + \\ + \frac{\partial}{\partial y}\left[r^{\varepsilon} V_x \left(1-\frac{1}{\mathrm{Pr}}\right)\frac{\partial V_x}{\partial y}\mu\right] + \frac{\partial}{\partial y}\left[r^{\varepsilon}(i_A - i_M)\rho\bar{D}\left(1-\frac{\mathrm{Sc}}{\mathrm{Pr}}\right)\frac{\partial c_A}{\partial y}\right], \quad \text{(III-2-47)}$$

where $\mathrm{Pr} = \mu(c_p)_{av}/\lambda$ is the Prandtl number and $\mathrm{Sc} = \mu/(\rho\bar{D})$ is the Schmidt number.

The ratio of these numbers, Pr/Sc = Le, is known as the Lewis-Semenov number.

These parameters are energy-transfer criteria. Pr determines the part of the kinetic energy that is converted into heat and, consequently, for gases Pr < 1. The physical significance of the Schmidt number is that it characterizes the relation between the kinetic energy of the particles and the energy transferred by diffusion. Like the Prandtl number, the parameter Sc < 1, with Sc < Pr.

The Lewis-Semenov number is the ratio of the heat transfer rates by mass transfer as a result of diffusion and heat transfer by conduction. In the general case, Le > 1.

It may be assumed that the Prandtl and Schmidt numbers are equal. Then the parameter Le = 1 and the two processes have identical rates. Formally, the last term in the right member of (III-2-47) is dropped in this case. This indicates that diffusion has no influence in the boundary layer. Since heat conduction and diffusion processes take place at the same intensity, the excess chemical energy at the boundary of the layer is converted completely into heat at the wall.

The most general case is characterized by Pr > Sc in the boundary layer and, consequently, Le > 1. This indicates that the chemical energy is converted incompletely into heat.

Along with the case Le = 1, we might examine the theoretical case in which Pr = 1. Equation (III-2-47) is then simplified even further, since the middle term on the right drops out. It follows from physical consideration that all of the external-flow kinetic energy is converted into heat at the wall in this case.

Investigation of the numerical values of the above parameters is of great practical importance. It has been established theoretically that the Schmidt number changes very little over a broad temperature range for a two-component atomic-molecular

mixture. For example, while Sc = 0.495 at T = 252°K, Sc = 0.482 at T = 3360°K. The same may also be said of the manner in which the Prandtl number varies: it remains at about 0.71. If we assume that the Schmidt number is equal to its average value Sc = = 0.49, then the Lewis number

$$\frac{\mathrm{Pr}}{\mathrm{Sc}}=\frac{c_p\mu}{\lambda}\frac{\rho\bar{D}}{\mu}=\frac{\rho\bar{D}c_p}{\lambda}=\frac{0{,}71}{0{,}49}=1{,}45.$$

According to available data, this parameter depends weakly on temperature all the way up to T = 9000°K. /120

In analyzing (III-2-47), the particular form corresponding to no diffusion must be kept in mind. In this case, the equation will not have the third term on the right, and it may be regarded as the energy equation for "frozen" flow. Here, the stagnation enthalpy i_0 that appears in it does not take account of chemical energy liberated on recombination of atoms.

We can convert from the enthalpy i_0 to the stagnation temperature, assuming that the enthalpy $i_0 = c_p T_0$. Without consideration of diffusion, therefore, the energy equation of a dissociated gas will differ from that of the ideal gas only in that the total enthalpy will figure in it instead of the stagnation temperature.

We may examine the case of low velocities, which is characterized by an insignificant compressibility effect and a negligibly small amount of heat liberated by friction and conversion of kinetic energy. Then the energy equation becomes

$$r^e V_x\frac{\partial T}{\partial x}+r^e V_y\frac{\partial T}{\partial y}=\frac{\lambda}{\rho c_p}\frac{\partial}{\partial y}\left(r^e\frac{\partial T}{\partial y}\right). \qquad \text{(III-2-48)}$$

The energy equation for a turbulent boundary layer can be obtained by applying certain formal transformations in (III-2-47) and introducing parameters characterizing transfer processes in the turbulent boundary layer. The result is

$$\begin{aligned}\rho r^e\frac{di_0}{dt}=&\frac{\partial}{\partial y}\left[r^e\left(\frac{\mu}{\mathrm{Pr}}+\frac{\mu_t}{\mathrm{Pr}_t}\right)\frac{\partial i_0}{\partial y}\right]+\frac{\partial}{\partial y}\left\{r^e\left[\mu\left(1-\frac{1}{\mathrm{Pr}}\right)+\right.\right.\\&\left.\left.+\mu_t\left(1-\frac{1}{\mathrm{Pr}_t}\right)\right]\frac{1}{2}\frac{\partial V_x^2}{\partial y}\right\}+\frac{\partial}{\partial y}\left\{r^e(i_A-i_M)\frac{\partial c_A}{\partial y}\times\right.\\&\left.\times\left[\frac{\mu}{\mathrm{Pr}}(\mathrm{Le}-1)+\frac{\mu_t}{\mathrm{Pr}_t}(\mathrm{Le}_t-1)\right]\right\},\end{aligned} \qquad \text{(III-2-49)}$$

where $Pr_t = \mu_t (c_p)_{av}/\lambda_t$ and $Le_t = \rho\bar{D}(c_p)_{av}/\lambda_t$ are the turbulent Prandtl and Lewis-Semenov numbers, respectively, and λ_t is the coefficient of turbulent thermal conductivity.

All gasdynamic and thermodynamic parameters in (III-2-49) should be regarded as averages.

Consideration of the diffusion effect necessitates solving (III-2-49). Here it is important to determine the turbulent Lewis-Semenov number. Certain studies have suggested that Le_t is approximately the same as for laminar flow, i.e., only slightly smaller.

The Equation of State

The fundamental equations of aerodynamics include the equation of state, which can be written as follows for a real medium:

$$\frac{p}{RT\rho} = \varphi(p, T), \qquad \text{(III-2-50)}$$

where R is the absolute gas constant of the ideal gas and ϕ is a function that determines the deviation of the properties of the real from the ideal gas.

If there is no such deviation and $\phi = 1$,

$$p = R\rho T. \qquad \text{(III-2-51)}$$

The inequality $\phi \neq 1$ results from the change in the physicochemical properties of air at very high pressures or on a substantial rise in temperature. In the former case, intermolecular forces are an important factor and are taken into account by the familiar van der Waals equation. /121

Processes in which dissociation and ionization occur as a result of a substantial temperature rise are also characteristic in aerodynamics. In this case, the function ϕ determines the gas constant $R_n = \phi R$ of the nonideal gas. Writing R_n as the ratio of the universal gas constant R_0 to molecular weight, we find the expression $\phi(p,T) = (\mu_{av})_0/\mu_{av}$, where the molecular weight in the numerator is that of the undissociated air and that in the denominator pertains to dissociated air. The function $\phi > 1$, since the molecular weight of air decreases on dissociation.

Remembering that the absolute gas constant $R = R_0/(\mu_{av})_0$, the equation of state of a dissociating gas can be written

$$p = \varphi R\rho T = \frac{(\mu_{av})_0}{\mu_{av}} R\rho T = \frac{R_0}{\mu_{av}} \rho T. \qquad \text{(III-2-52)}$$

In the particular case of a dissociating diatomic gas, the function ϕ can be expressed in terms of the concentration of the atomic component or, which is the same thing, in terms of the degree of dissociation α. Let the mass concentration of an arbitrary component be c_i and let its molecular weight be μ_i. Then, obviously, the average molecular weight μ_{av} of the mixture will be found from the relation $\mu_{av} \sum_i (c_i/\mu_i) = 1$, in which the summation sign determines the number of moles of the mixture. For a diatomic dissociating gas $\sum_i c_i = c_1 + c_2 = 1$. Obviously, $c_1 = c_A = \alpha$, $c_2 = c_M = 1 - \alpha$, $2\mu_A = \mu_M = (\mu_{av})_0$. Consequently, $\phi = (\mu_{av})_0/\mu_{av} = 1 + \alpha$.

On substitution of ϕ into (III-2-50), the equation of state assumes the form

$$p = (1 + \alpha) R\rho T, \qquad \text{(III-2-53)}$$

where, in accordance with (III-1-14), the gas constant $R = k/(2m_A)$.

Condition of Entropy Conservation

In study of isentropic flows, we start from the condition according to which entropy remains constant along a streamline. This condition equates to zero the scalar product of two vectors:

$$\overline{V} \operatorname{grad} S = 0, \qquad \text{(III-2-54)}$$

where the entropy gradient (the vector grad S) is normal to the tangent to the streamline at the particular point. Condition (III-2-54) can be expanded by using a specific coordinate system. Thus, for example, in the Cartesian system

$$V_x \frac{\partial S}{\partial x} + V_y \frac{\partial S}{\partial y} + V_z \frac{\partial S}{\partial z} = 0. \qquad \text{(III-2-55)}$$

If other systems are used, the vectors $\overline{V}$ and grad S are represented in appropriate form and then the scalar products are determined.

Initial and Boundary Conditions

The solution of the differential equations describing flows over bodies must satisfy certain initial and boundary conditions of this flow. The initial conditions are determined by the variables at time zero of the motion and obviously apply for nonsteady flow.

The boundary conditions are superimposed on the solution of any problem of gas motion and must be satisfied at any time during this motion; they may, moveover, take a wide variety of forms. The pressure boundary condition, for example, determines a known pressure value at some boundary surface. This may be the boundary between the disturbed and undisturbed flows, on which the free-stream pressure is known. Another boundary is the surface of the compression shock, behind which the pressure is also known. In the region between the shock and the body in the flow, this pressure determines the boundary condition in exactly the same way as the pressure boundary condition in the shock problem is determined by the free-stream pressure. /122

Solutions of the supersonic-flow equation must satisfy gas-flow conditions at the body surface and conditions in the free stream in front of the compression shock (or the conditions immediately behind the compression shock).

Let us examine boundary conditions used in solving flow problems. If nonseparation of the flow is a condition, the velocity vector $\overline{V}$ will be directed tangent to a surface with the equation $F(x,y,z) = 0$ at any of its points and, consequently, the scalar product of the vectors $\overline{V}$ and grad F will be zero, i.e.,

$$\overline{V}\,\mathrm{grad}\,F = 0. \qquad \text{(III-2-56)}$$

Resolving the vectors $\overline{V}$ and grad F, we obtain the boundary condition corresponding to nonseparating flow in Cartesian coordinates:

$$V_x\frac{\partial F}{\partial x} + V_y\frac{\partial F}{\partial y} + V_z\frac{\partial F}{\partial z} = 0. \qquad \text{(III-2-57)}$$

Analogous expressions can be obtained in other coordinate systems. For two-dimensional flow, Condition (III-2-57) becomes

$$\frac{V_y}{V_x} = -\frac{\partial F/\partial x}{\partial F/\partial y} \quad \text{or} \quad \frac{V_y}{V_x} = \frac{dy}{dx}. \qquad \text{(III-2-58)}$$

In nonseparating potential flow, the boundary condition imposed on the potential ϕ in accordance with Equality (III-2-57) assumes the form

$$\varphi_x \frac{\partial F}{\partial x} + \varphi_y \frac{\partial F}{\partial y} + \varphi_z \frac{\partial F}{\partial z} = 0. \qquad \text{(III-2-57')}$$

In the case of two-dimensional flow

$$\frac{\varphi_y}{\varphi_x} = \frac{dy}{dx}. \qquad \text{(III-2-58')}$$

Switching symbols, we obtain the condition for nonseparating flow past a solid of revolution:

$$\frac{V_r}{V_x} = \frac{dr}{dx}, \qquad \text{(III-2-59)}$$

or, for potential flow,

$$\frac{\varphi_r}{\varphi_x} = \frac{dr}{dx}. \qquad \text{(III-2-59')}$$

These boundary conditions pertain to the case of ideal flow over the bodies.

In boundary-layer research, the solutions of the various equations must satisfy conditions at the wall and at the outer limit of the layer. The conditions at the wall consist in zero flow velocity, i.e., the velocity $\overline{V} = 0$ at $y = 0$. At the outer boundary, i.e., at $y = \delta$, the velocity $\overline{V}$ is equal to its free-stream value and $\tau = 0$.

In study of thermal processes, conditions are assigned at /123
the wall and the boundary of the layer for the variables that determine heat transfer. The condition for temperature, for example, is that it be equal to the wall temperature at the boundary of the body and equal to the inviscid-flow temperature at the boundary of the layer. The heat-flow distribution over the

thickness of the layer must be such that it is zero at the layer boundary.

Boundary conditions are imposed on the concentration c_i in study of diffusion phenomena. It is usually required that concentration assume assigned values at the layer and body boundaries.

§III-3. ISENTROPIC FLOW

The case of constant heat capacities. Let us consider steady flow of a compressible medium. For this case, the differential equations (III-2-5), in which the partial time derivatives must be set equal to zero, can be integrated. This integral, which was first derived by D. Bernoulli, takes the form [2]

$$\frac{V^2}{2}+\int \frac{dp}{\rho}=c, \qquad \text{(III-3-1)}$$

where $\underline{c}$ has a constant value along a streamline.

The integral of (III-3-1) pertains to the general case of nonpotential flow. It is simplified in the case of isentropic flow, which admits of application of the adiabatic equation $dp = (kp/\rho)d\rho$, transformed with consideration of the enthalpy expression $i = Tc_p = c_p p/(\rho R)$ to the form $dp = \rho di$. After substitution in (III-3-1), integration, and determination of the constant from the total-stagnation condition, for which this constant is equal to the stagnation enthalpy i_0, we obtain the Bernoulli equation in the form

$$\frac{V^2}{2}+i=i_0. \qquad \text{(III-3-2)}$$

Relating this equation to the oncoming flow conditions, we obtain

$$\frac{V^2}{2}+i=\frac{V_\infty^2}{2}+i_\infty. \qquad \text{(III-3-2')}$$

Thus, the stagnation enthalpy i_0 is determined by the enthalpy and velocity of the oncoming flow. Substituting $i = c_p p/(\rho R)$, we obtain the Bernoulli equation in the form

$$\frac{V^2}{2}+\frac{k}{k-1}\frac{p}{\rho}=\frac{V_\infty^2}{2}+\frac{k}{k-1}\frac{p_\infty}{\rho_\infty}. \qquad \text{(III-3-3)}$$

The stagnation enthalpies correspond to definite values of the other stagnation parameters, namely the pressure p_0, density ρ_0, and temperature T_0.

The present value of one or another parameter is proportional to its value under total-stagnation conditions and depends on local velocity.

The respective formulas for calculation of pressure, density, and temperature are as follows:

$$p=p_0A^{\frac{k}{k-1}};\quad \rho=\rho_0A^{\frac{1}{k-1}};\quad T=T_0A, \qquad \text{(III-3-4)}$$

where A is determined from the expression $A = 1 - \tilde{V}^2$. In this expression, we can pass from the dimensionless velocity $\tilde{V} = V/V_{max}$ to the local Mach number $M = V/a$ or the velocity ratio $\lambda = V/a^*$, where a^* is the critical velocity and $V_{max}=a^*\sqrt{\frac{k+1}{k-1}}$. In the former case, $A=\left(1+\frac{k-1}{2}M^2\right)^{-1}$, and in the latter $A=\left(1-\frac{k-1}{k+1}\lambda^2\right)$. We see from comparison of these values that λ and M are linked as follows: /124

$$\lambda^2=\frac{k+1}{2}M^2\left(1+\frac{k-1}{2}M^2\right)^{-1}. \qquad \text{(III-3-5)}$$

The critical velocity can be determined from λ as $a^* = V/\lambda$.

By comparing the other pair of expressions for A, we can find the relation between $\tilde{V}$ and M, namely

$$\tilde{V}=\sqrt{1-\left(1+\frac{k-1}{2}M^2\right)^{-1}} \qquad \text{(III-3-6)}$$

Approximate relationships for hypersonic velocities ($M \gg 1$) can be derived from the formulas given above:

$$\frac{p}{p_\infty}=B^{\frac{2k}{k-1}},\quad \frac{\rho}{\rho_\infty}=B^{\frac{2}{k-1}},\quad \frac{T}{T_\infty}=B^2, \qquad \text{(III-3-7)}$$

where $B = M_\infty/M$.

As for Formula (III-3-6), it is also somewhat simplified:

$$\frac{\tilde{V}}{\tilde{V}_\infty}=\frac{V}{V_\infty}=1+\frac{1}{k-1}\left(\frac{1}{M_\infty^2}-\frac{1}{M^2}\right), \qquad \text{(III-3-8)}$$

where $\tilde{V}_\infty = V_\infty/V_{max}$.

The Lagrangian integral. For potential nonsteady motion of a compressible gas, the Euler differential equations can be transformed to an expression known as the Lagrangian integral [51]:

$$\frac{k}{k-1}\frac{p}{\rho}+\frac{V^2}{2}+\varphi_t=\frac{k}{k-1}\frac{p_\infty}{\rho_\infty}+\frac{V_\infty^2}{2}. \qquad \text{(III-3-9)}$$

Making the substitution $\rho = (p\rho_\infty^k/p_\infty)^{1/k}$, we find a formula for the pressure

$$\frac{p}{p_\infty}=\left[1-\frac{k-1}{2}M_\infty^2\left(\frac{V^2}{V_\infty^2}+2\frac{\varphi_t}{V_\infty^2}-1\right)\right]^{\frac{k}{k-1}}. \qquad \text{(III-3-10)}$$

Let us consider the case in which the flow disturbances are such that the second term in the square brackets is small by comparison with unity. Expanding by the binomial theorem and retaining only the first two terms, we obtain

$$\frac{p}{p_\infty}=1-\frac{kM_\infty^2}{2}\left(\frac{V^2}{V_\infty^2}+\frac{2\varphi_t}{V_\infty^2}-1\right). \qquad \text{(III-3-11)}$$

Let us present V^2 in this formula in the form $V^2 = V_\infty^2 + 2v_xV_\infty + v_y^2 + v_z^2$, where v_x, v_y, v_z are the disturbance velocity components, and substitute $\phi_t = \phi_t'$. Converting to the pressure coefficient, we get

$$\bar{p} = -\frac{2}{V_\infty}\left(v_x + \frac{v_y^2 + v_z^2}{2} + \varphi_t'\right). \qquad \text{(III-3-11')}$$

For steady flow, $\phi_t' = 0$.

The pressure coefficient can be expressed in terms of the velocity components v_{x_1}, v_{y_1}, v_{z_1} in body coordinates; this makes it possible to evaluate the influence of the attack and slip angles [51]. We use the following relationships for this purpose:

$$\begin{aligned} v_x &= v_{x1} + v_{y1}\alpha_b \cos\varphi - v_{z1}\alpha_b \sin\varphi; \\ v_y &= -v_{x1}\alpha_b + v_{y1}\cos\varphi - v_{z1}\alpha_b \sin\varphi; \\ v_z &= v_{y1}\sin\varphi + v_{z1}\cos\varphi. \end{aligned}$$

Introducing these relationships into (III-3-11') and retaining only the quadratic terms $v_{y_1}^2$ and $v_{z_1}^2$, we obtain /125

$$\bar{p} = -2(v_{x1} + v_{y1}\alpha_b \cos\varphi - v_{z1}\alpha_b \sin\varphi) - (v_{y1}^2 + v_{z1}^2) - 2\varphi_t'. \qquad \text{(III-3-12)}$$

Here the constants V_∞ and V_∞^2 are included, respectively, in the values of the velocity components and the derivative ϕ_t'. Introducing the attack and slip angles α and β_{s1}, we find

$$\bar{p} = -2(v_{x1} + v_{y1}\beta_{s1} - v_{z1}\alpha) - (v_{y1}^2 + v_{z1}^2) - 2\varphi_t'. \qquad \text{(III-3-12')}$$

We may assume for flow over thin wings that

$$\bar{p} = -2v_{x1} - 2\varphi_t'. \qquad \text{(III-3-13)}$$

For steady flow, $\phi_t' = 0$ and

$$\bar{p} = -2v_{x1}. \qquad \text{(III-3-13')}$$

In investigating flow past slender solids of revolution, it is helpful to convert to cylindrical coordinates, setting $V^2 = V_\infty^2 + 2V_\infty v_x + v_r^2 + v_\gamma^2$ in (III-3-10).

Accordingly,

$$\bar{p} = -2v_x - (v_r^2 + v_y^2) - 2\varphi_t'. \qquad \text{(III-3-14)}$$

Isentropic flow of a dissociating and ionizing gas. In studying flows of a dissociating and ionizing gas, it is necessary to take account of both the temperature and pressure dependences of the thermodynamic variables. Tables and diagrams of the thermodynamic functions of air for high temperatures are used here. Most important among them is the diagram two variations of which appear in Figs. III-1-3 and III-1-4. Equation (III-3-2), which enables us to determine the local isentropic flow velocity from a known enthalpy or, conversely, to calculate the enthalpy from the velocity, is a supplement to the tables or diagrams. In the particular case of flow of a nondissociating gas with variable heat capacities, the thermodynamic parameters depend only on local temperature.

§III-4. FUNDAMENTAL RELATIONSHIPS FOR DETERMINATION OF PARAMETERS BEHIND COMPRESSION SHOCK

Equations of the Oblique Compression Shock

Let us examine the fundamental relationships that enable us to calculate the equilibrium parameters of a dissociating and ionizing gas behind a curvilinear shock wave. The parameters subject to determination will be the pressure p_2, density ρ_2, temperature T_2, velocity V_2, enthalpy i_2, entropy S_2, the speed of sound a_2, the average molecular weights $(\mu_{av})_2$, and the shock inclination angle Θ_s (or the stream deflection angle β_s). In accordance with the number of unknown variables, it is necessary to write a system of nine equations. The parameters ahead of the shock will be the knowns in these equations.

Let us consider in Fig. III-4-1 the scheme of a curvilinear shock wave, which may be regarded as an infinite sequence of oblique shocks. For one of these shocks, whose surface coincides with the tangent to the surface of the curvilinear wave, we have constructed the velocity triangles in front of the shock (parameters with subscript 1) and behind it (parameters with subscript 2). From these triangles, we can easily determine auxiliary relationships for calculation of the normal (subscript n) and tangential (subscript τ) velocity components: /126

$$\left.\begin{aligned} V_{\tau 1} &= V_1 \cos\theta_s; \quad V_{n1} = V_1 \sin\theta_s; \\ V_{\tau 2} &= V_2 \cos(\theta_s - \beta_s); \quad V_{n2} = V_2 \sin(\theta_s - \beta_s). \end{aligned}\right\} \qquad \text{(III-4-1)}$$

When the angle ω, which is equal to the inclination of the shock radius of curvature R_s to the oncoming-flow velocity (Fig.

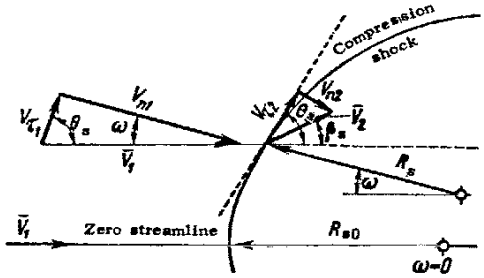

Figure III-4-1. Diagram of Curvilinear Shock Wave.

III-4-1), is used to analyze a curvilinear shock wave, the substitution $\theta_s = \pi/2 - \omega$ must be made in (III-4-1). The relation

$$\frac{V_{n1}}{V_{n2}} = \frac{\operatorname{tg}\theta_s}{\operatorname{tg}(\theta_s - \beta_s)}, \qquad \text{(III-4-2)}$$

can be derived from these relationships; it is based on the fact that the tangential velocity components before and after the shock are equal, i.e., $V_{\tau_1} = V_{\tau_2}$. This relation – the first equation of the system – enables us to find the shock inclination angle. Three other system equations are conservation equations:

for mass (flow)

$$\rho_1 V_{n1} = \rho_2 V_{n2}; \qquad \text{(III-4-3)}$$

for impulse

$$p_1 + \rho_1 V_{n1}^2 = p_2 + \rho_2 V_{n2}^2; \qquad \text{(III-4-4)}$$

and for energy

$$i_1 + \frac{V_{n1}^2}{2} = i_2 + \frac{V_{n2}^2}{2}. \qquad \text{(III-4-5)}$$

Four more equations, which enable us to determine enthalpy, entropy, average molecular weight, and the speed of sound in the dissociating gas, will be presented in the form of general relationships for these variables as functions of pressure and temperature:

$$i_2 = f_1(p_2, T_2); \qquad \text{(III-4-6)}$$

$$S_2 = f_2(p_2, T_2); \qquad \text{(III-4-7)}$$

$$(\mu_{av})_2 = f_3(p_2, T_2); \qquad \text{(III-4-8)}$$

$$a_2 = f_4(p_2, T_2). \qquad \text{(III-4-9)}$$

These parameters are found from tables or diagrams of the thermodynamic functions for air for known pressure and temperature.

The ninth equation is obtained from the equations of state related to the conditions before and after the shock:

$$p_2 - p_1 = R_0 \left[\frac{\rho_2 T_2}{(\mu_{av})_2} - \frac{\rho_1 T_1}{(\mu_{av})_1} \right]. \qquad \text{(III-4-10)}$$

Let us present the basic parameters behind the shock wave in terms of the relative change in the normal velocity components, i.e., in terms of

$$\Delta \bar{V}_n = \Delta V_n / V_{n1} = (V_{n1} - V_{n2}) / V_{n1}.$$

We find /127

$$\frac{\rho_1}{\rho_2} = 1 - \Delta \bar{V}_n; \qquad \text{(III-4-11)}$$

$$\frac{p_2}{p_1} = 1 + \frac{\rho_1 V_{n1}^2}{p_1} \Delta \bar{V}_n, \qquad \text{(III-4-12)}$$

where $\rho_1 V_{n_1}^2 / p_1 = k_1 M_{n_1}^2$ for a nondissociating oncoming flow.

The temperature and enthalpy ratios are

$$\frac{T_2}{T_1} = (1 + k_1 M_{n1}^2 \Delta \bar{V}_n)(1 - \Delta \bar{V}_n) \frac{(\mu_{av})_2}{(\mu_{av})_1}, \qquad \text{(III-4-13)}$$

$$\frac{i_2}{i_1} = 1 + \frac{V_{n1}^2}{2} \frac{\Delta \bar{V}_n}{i_1} (2 - \Delta \bar{V}_n). \qquad \text{(III-4-14)}$$

The other parameters can also be expressed interms of $\Delta \bar{V}_n$ and the known variables of the oncoming flow. Since, according to (III-4-11), this quantity is determined by the density ratio ρ_2/ρ_1, the other unknown parameter ratios, namely p_2/p_1 in (III-4-12), T_2/T_1 in (III-4-13), i_2/i_1 in (III-4-14), etc., can be represented as functions of ρ_2/ρ_1. Moreover, the values $V_{n_1} = V_1 \sin\theta_s$ and $M_{n_1} = M_1 \sin\theta_s$ can be introduced into the formulas instead of V_{n_1} and M_{n_1}, respectively. Thus, solution of the oblique-shock problem for a known inclination angle reduces to finding the density ratio ρ_2/ρ_1 or, which is the same thing, to determination of $\Delta \bar{V}_n$ with Eqs. (III-4-13) and (III-4-14):

$$\Delta \bar{V}_n = A \mp \sqrt{A^2 - B}; \qquad \text{(III-4-13')}$$

$$\Delta \bar{V}_n = 1 - \sqrt{1 - \frac{2(i_2 - i_1)}{V_{n1}^2}}, \qquad \text{(III-4-14')}$$

where

$$A=\frac{k_1M_{n1}^2-1}{2k_1M_{n1}^2};\quad B=\frac{1}{k_1M_{n1}^2}\left[\frac{T_2}{T_1}\frac{(\mu_{av})_1}{(\mu_{av})_2}-1\right]. \qquad \text{(III-4-15)}$$

Equations (III-4-13') and (III-4-14') are solved by successive approximations.

Calculation of Oblique Compression Shock with Tables or Curves of the Thermodynamic Functions for Air at Very High Temperatures

In solving the problem of a shock wave in a dissociated and ionized gas, the parameters of air at some altitude H (pressure p_1, temperature T_1, density ρ_1, etc.) and the normal velocity component V_{n_1} are taken as the initial data.

Assigning in first approximation the value $\Delta\bar{V}_n = 1$, which corresponds to the assumption of full flow stagnation behind the shock ($V_{n_2} = 0$), we find the pressure p_2 from (III-4-12) and, from (III-4-14), the enthalpy i_2, which is obviously equal to the stagnation enthalpy i_0. We then use the i-S diagram to determine the temperature T_2 and Fig. III-1-5 to find the average molecular weight $(\mu_{av})_2$. Here, instead of the diagrams and curves, we can use the corresponding tables of the thermodynamic functions of air, which will improve the accuracy of the calculations. /128

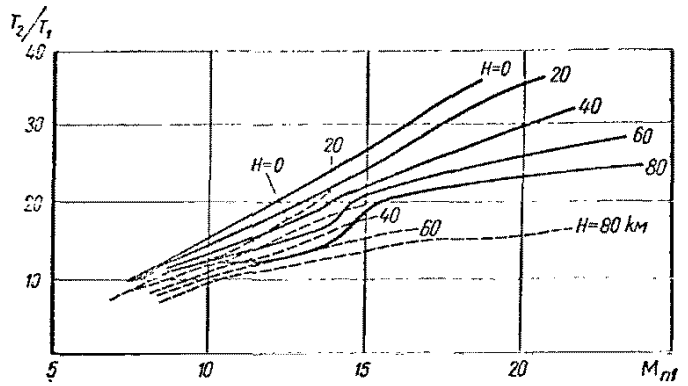

Figure III-4-2. Air Temperature Ratios After and Before Shock with Consideration of Dissociation and Ionization. Unbroken line: T_1 = = 220°K; dashed line: T_1 = 350°K.

From the values found for p_2, T_2, $(\mu_{av})_2$, we can determine the density ρ_2 with the equation of state and use (III-4-11) to improve

the value of $\Delta\bar{V}_n$. We then use this new value in the second approximation with (III-4-12) and (III-4-14) to find the pressure and enthalpy, respectively, and improve the temperature and average molecular weight with them, using the tables or diagrams. Having refined values of p_2, T_2, $(\mu_{av})_2$, we can find the density from the equation of state in the second approximation. The approximations are broken off when satisfactory accuracy is obtained.

Oblique-shock calculations can also be made when the oncoming-flow variables (including M_1) and the angle β_s are assigned.

As the first approximation, the shock angle θ_s is determined for a nondissociating gas (see below); then (III-4-11), (III-4-12), (III-4-14) are used to find the corresponding values of $\Delta\bar{V}_n$, p_2, and ρ_2. Using these values, the temperature T_2 and the average molecular weight $(\mu_{av})_2$ are calculated from tables [29] or a diagram [13].

Then $\Delta\bar{V}_n$ is improved with (III-4-13') and (III-4-15), and $\tan\theta$ and the angle θ_s with (III-4-2). The remaining parameters are refined with the above formulas.

With dissociation and ionization, the relative values of the gas parameters behind the shock depend not only on temperature, as was characteristic for the case of variable heat capacities, but also on pressure.

Figures III-4-2 through III-4-4 represent the gas parameters behind the shock as functions of M_{n_1}. Calculations of the temperature and density ratios were performed for averaged temperature values of $T_1 = 220$ and 350°K, which are the probable minimum and maximum selected in accordance with the altitude variation of air temperature for subnormal and above-normal yearly-average values.

The data obtained indicate that dissociation and ionization cause a substantial change in the equilibrium temperature and density as compared with the case of constant heat capacities ($k = 1.4 = \text{const}$).

As for pressure, it depends much less strongly on the physicochemical transformations of the air. The ratio p_2/p_1 differs little from the maximum $p_2/p_1 = 1 + k_1 M_{n_1}^2$, which is determined /129
only by the oncoming-flow conditions and not by changes in the structure and physicochemical properties of the air behind the shock.

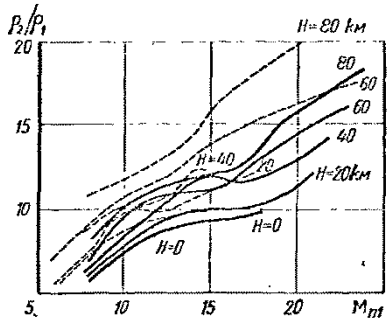

Figure III-4-3. Ratio of Densities After and Before Shock as Function of M_{n_1}, with Consideration of Dissociation and Ionization. Unbroken line: T_1 = = 220°K; dashed line: T_1 = 350°K.

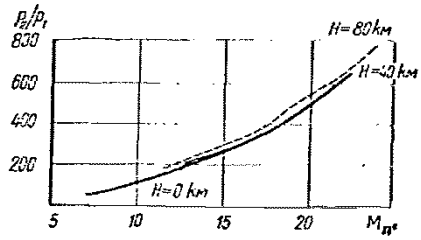

Figure III-4-4. Ratio of Pressures After and Before Shock as Function of M_{n_1} with Consideration of Dissociation and Ionization. T_1 = 220°K.

This method of calculation is equally applicable to oblique and normal compression shocks. It is simpler as applied to the normal shock, since it is known at the outset that $\theta_s = \pi/2$ and $\beta_s = 0$. Consequently, the velocity V_{n_1} must be set equal to V_1, and $M_{n_1} = M_1$. Thus, we formally dispose of the n subscripts in the relationships given above when we go to the normal shock.

Calculations of the gas parameters behind the oblique shock must be supplemented by calculation of the angle β_s (or θ_s) and the Mach number M_1 (or velocity V_1). For this purpose, it is necessary to use the relationships

$$\Delta\bar{V}_n = 1 - \frac{\operatorname{tg}(\theta_s - \beta_s)}{\operatorname{tg}\theta_s}; \quad V_1 = \frac{V_{n1}}{\sin\theta_s}; \quad M_1 = \frac{M_{n1}}{\sin\theta_s}. \tag{III-4-16}$$

The first ratio enables us to determine the angle β_s (or θ_s) from the value found for $\Delta\bar{V}_n$ provided that one of the angles is given. The velocity V_1 or M_1 is computed from the other two formulas.

For convenience in the calculations, we can calculate the angles β_s in advance for assigned θ_s and prepare the appropriate table or curve. These can then be used to find either of the angles θ_s or β_s if the other is known for any value of $\Delta\bar{V}_n$ to

which the precalculated values of the ratios p_2/p_1, ρ_2/ρ_1, etc., correspond.

Calculations indicate that the flow deflection is larger in a real gas than in an ideal gas with k = 1.4. This has as a consequence that the detached shock forms later in a heated gas than in a cold gas. Behind most of the oblique shock, M is larger than in the case of constant heat capacities, but with the approach to the normal segment, a certain decrease in this number is observed.

Calculation of flow variables at point of total stagnation. An important practical application of normal-shock theory is calculation of the variables at the total-stagnation point of a bluff body. This calculation is carried out as follows. The entropy S_2 is determined from the values found for i_2 and p_2 with consideration of dissociation and ionization from the i-S diagram or the table of thermodynamic functions for air. Taking the zero streamline and assuming that the flow along it is isentropic, an entropy S_0' equal to the value S_2 behind the shock is taken on this basis for the total-stagnation point. In addition, the enthalpy $i_0' - i_1 + 0.5V_1^2$ can be found at this point. Now, knowing S_0' and i_0', we can use the same i-S diagram or the thermodynamic tables to find the remaining parameters, namely p_0', T_0', ρ_0', etc. The results of the calculation will correspond to the assigned flight altitude. /130

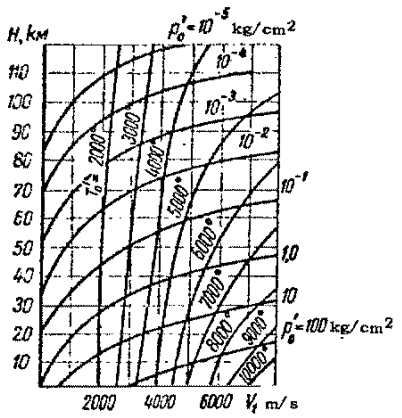

Figure III-4-5. Pressure and Temperature at Stagnation Point of Blunt Nose.

Flow conditions and, consequently, the parameters at the total-stagnation point, will change with altitude. This relation is represented graphically in Fig. III-4-5. The curves can be used to determine the temperature T_0' and pressure p_0' as functions of velocity V_1 and altitude H.

Example. Calculate the parameters of the air behind an oblique compression shock for the following conditions: M_1 = 11, angle β_s = 45°, altitude H = = 5 km. We find from the standard-atmosphere table (Appendix No. 2) for the 5-km altitude

$$p_1 = \left(\frac{p_h}{p_g}\right) p_g = 5{,}334 \cdot 10^{-1} \cdot 1{,}033 = 0{,}551 \text{ kg/cm}^2;$$

$$\rho_1 = \left(\frac{\rho_h}{\rho_g}\right) \rho_g = 6{,}012 \cdot 10^{-1} \cdot 0{,}1249 = 0{,}0751 \text{ kg-s}^2/\text{m}^4;$$

$T_1 = 255.6°K$, $a_1 = 320.5$ m/s; $\mu_{av_1} = 28.97$.

Flight speed is determined: $V_1 = M_1 a_1 = 11 \cdot 320.5 = 3526$ m/s. From [29], we find $k_1 = 1.405$, $c_{p_1} = 1002$ m^2/s^2·deg and calculate the enthalpy $i_1 = c_{p_1} T_1 = 1002 \cdot 255.6 = 0.2562 \cdot 10^6$ m^2/s^2 (61.19 kcal/kg). The angle $\theta_s = 60°$ is found from the diagram of Fig. 37 in [17] in the absence of dissociation. Remembering that the shock angle will be smaller in the presence of dissociation, we assign in first approximation $\theta_s = 55°$, for which we calculate

$$\Delta\bar{V}_n = 1 - \operatorname{tg}(\theta_s - \beta_s)/\operatorname{tg}\theta_s = 1 - \operatorname{tg}(55° - 45°)/\operatorname{tg}55° = 0.877;$$
$$p_2/p_1 = 1 + k_1 M_1^2 \Delta\bar{V}_n \sin^2\theta_s = 1 + 1.405 \cdot 11^2 \cdot 0.877 \sin^2 55° = 110;$$
$$p_2 = (p_2/p_1)\, p_1 = 110 \cdot 0.551 = 55.65 \text{ kg/cm}^2;$$
$$i_2 = i_1 + 0.5 V_1^2 \sin^2\theta_s \Delta\bar{V}_n (2 - \Delta\bar{V}_n) = 0.2562 \cdot 10^6 +$$
$$+ 0.5 \cdot 3526^2 \sin^2 55° \cdot 0.877 (2 - 0.877) = 4.36 \cdot 10^6 \text{ m}^2/\text{s}^2 \quad (1042 \text{ kcal/kg}).$$

From the tables [29] or diagram [13], knowing i_2 and p_2, we find the values $T_2 = 3357°K$ and $\mu_{av_2} = 28.7$; we then determine

$$A = \frac{k_1 M_1^2 \sin^2\theta_s - 1}{2 k_1 M_1^2 \sin^2\theta_s} = \frac{1.405 \cdot 11^2 \cdot \sin^2 55° - 1}{2 \cdot 1.405 \cdot 11^2 \sin^2 55} = 0.495;$$
$$B = \frac{1}{k_1 M_1^2 \sin^2\theta_s}\left(\frac{T_2}{T_1}\frac{\mu_{av_1}}{\mu_{av_2}} - 1\right) = \frac{1}{1.405 \cdot 11^2 \cdot \sin^2 55°}\left(\frac{3357}{255.6} \cdot \frac{28.97}{28.7} - 1\right) = 0.1074.$$

The second-approximation calculations are made with these data:

$$\Delta\bar{V}_n = A + \sqrt{A^2 - B} = 0.495 + \sqrt{0.495^2 - 0.1074} = 0.8659;$$
$$\operatorname{tg}\theta_s = \frac{\Delta\bar{V}_n - \sqrt{(\Delta\bar{V}_n)^2 - 4(1 - \Delta\bar{V}_n)}}{2(1 - \Delta\bar{V}_n)} = \frac{0.8659 - \sqrt{0.8659^2 - 4(1 - 0.8659)}}{2(1 - 0.8659)} = 1.506.$$

In the second approximation for $\theta_s = 56°25'$

$$p_2/p_1 = 1 + 1.405 \cdot 11^2 \cdot 0.8659 \cdot \sin^2 56°25' = 103.2;$$
$$p_2 = 0.551 \cdot 103.2 = 56.74 \text{ kg/cm}^2;$$
$$i_2 = 0.2562 \cdot 10^6 + \frac{1}{2} 3526^2 \cdot \sin^2 56°25' \cdot 0.8659 (2 - 0.8659) = 4.49 \cdot 10^6 \text{ m}^2/\text{s}^2 \quad (1072 \text{ kcal/kg}).$$

We determine $T_2 = 3424°K$ and $\mu_{av_2} = 28.64$ from the improved i_2 and p_2, using the tables [29] or diagram [13].

In the third approximation, the calculations give $\theta_s = 56°$.

The new value found for the angle is quite close to that found in the preceding approximation; further improvement may therefore be dispensed with. /131

Thus, we take $\theta_s = 56°$; $p_2 = 56.7$ kg/cm^2;

$$i_2 = 4.49 \cdot 10^6 \text{ m}^2/\text{s}^2; \quad T_2 = 3424° \text{K}; \quad \mu_{av2} = 28.64.$$

We find from the tables [29] or the diagram [13]

$$S_2 = 2.18 \text{ kcal/kg-deg} \quad (9.15 \cdot 10^3 \text{ m}^2/\text{s}^2\text{-deg});$$
$$S_1 = 1.77 \text{ kcal/kg-deg} \quad (7.4 \cdot 10^3 \text{ m}^2/\text{s}^2\text{-deg}); \quad a_2 = 1094 \text{ m/s}.$$

We then calculate

$$V_{2n} = V_1 (1 - \Delta\bar{V}_n) \sin\theta_s = 3526 (1 - 0.8659) \sin 56° = 383 \text{ m/s};$$
$$\rho_2 = \rho_1/(1 - \Delta\bar{V}_n) = 0.0751/(1 - 0.8659) = 0.575 \text{ kg-sec}^2/\text{m}^4$$
$$V_2 = V_{2n}/\sin(\theta_s - \beta_s) = 383/\sin(56 - 45) = 2007 \text{ m/s};$$
$$M_2 = V_2/a_2 = 2007/1094 = 1.835.$$

The air parameters at the total stagnation point behind the oblique compression shock are

$$S_0' = S_2 = 9.15 \cdot 10^3 \text{ m}^2/\text{s}^2\text{-deg};$$
$$i_0' = i_0 = i_1 + V_1^2/2 = 0.2562 \cdot 10^6 + 3526^2/2 = 6.47 \cdot 10^6 \text{ m}^2/\text{s}^2.$$

We find from the i-S diagram [13]

$$p_0' = 330 \text{ kg/cm}^2; \quad T_0' = 4490° \text{K}; \quad \rho_0' = 2.4 \text{ kg-s}^2/\text{m}^4.$$

Shock wave in a pure dissociating diatomic gas. Applying the equation system (III-4-2)-(III-4-10) and the relationships for determination of the thermodynamic functions and degree of dissociation of a pure dissociating diatomic gas, we can calculate the variables behind the shock wave with comparative ease.

Combining the impulse equations (III-4-4) and the energy equations,

$$\alpha_1+\frac{4+\alpha_1}{1+\alpha_1}\frac{\bar{p}_1}{\bar{\rho}_1}+\frac{\bar{V}_{n1}^2}{2}=\alpha_2+\frac{4+\alpha_2}{1+\alpha_2}\frac{\bar{p}_2}{\bar{\rho}_2}+\frac{\bar{V}_{n2}^2}{2}, \qquad \text{(III-4-17)}$$

in which the pressure and density relate respectively to the characteristic parameters p_d and ρ_d and the velocity to the characteristic V_d, we obtain

$$\Delta\bar{V}_n=\frac{3}{7+\alpha_2}\left(1+\sqrt{1+\frac{\bar{D}}{\bar{V}_n^2}}\right), \qquad \text{(III-4-18)}$$

where

$$\bar{D}=\frac{2}{9}(7+\alpha_2)(1+\alpha_2)\alpha_2. \qquad \text{(III-4-19)}$$

Expression (III-4-18) was derived for the following conditions: gas not dissociated in front of the shock ($\alpha_1 = 0$), velocities V_{n_1} very large, negligible undisturbed-flow enthalpy i_1, and the admissibility of dropping certain quantities of higher negative order.

Equation (III-4-18) is solved simultaneously with (III-1-10), (III-1-14'), (III-1-16'), and the enthalpy equation

$$\bar{i}_2=\frac{\bar{V}_{n1}^2}{2}\Delta\bar{V}_n(2-\Delta\bar{V}_n). \qquad \text{(III-4-20)}$$

The calculations are performed by successive approximation. Assuming the velocity V_{n_1} to be known, we assign a density ratio ρ_2/ρ_1 (or $\Delta\bar{V}_n$) in first approximation. The enthalpy $\bar{i}_2$ is determined from Expression (III-4-20) for $\Delta\bar{V}_n$, which, when ρ_2/ρ_1 is assigned, is found from (III-4-11). Then the degree of dissociation is determined in first approximation from the diagrams of Fig. III-1-8 for this value and the density ratio ρ_2/ρ_d. Then another calculation is performed to improve $\Delta\bar{V}_n$ and the other parameters with the aid of (III-4-18) and (III-4-19). /132

The above method may be used for approximate estimation of $\Delta\bar{V}_n(\alpha_2)$ and the other parameters of the air behind the shock, even though it was developed for purely dissociating diatomic gases. Here the characteristic dissociation parameters must be found for the air as for a gas model consisting of a mixture of nitrogen and oxygen in accordance with their mass composition.

The calculations show that the parameters for real air differ somewhat from those obtained by the above method for a diatomic air model. Thus, for a velocity $V_{n_1} = 1.5V_d = 8.1$ km/s, the density of real air behind the shock is $\rho_2 = 14.7\rho_1$, or approximately 5% higher than for the diatomic air model.

Compression Shock in Gas Flow with Constant Heat Capacities

Equation system. In the case of a compression shock in a gas flow with constant heat capacities, the system becomes simpler, since the average molecular weight of the air does not change and, moreover, the specific heats remain constant. Such parameters as the speed of sound and enthalpy depend only on temperature. Entropy is determined from the thermodynamics of the ideal gas. On the above basis, Eqs. (III-4-6)-(III-4-9) are written thus:

$$\left.\begin{aligned} i_2 = c_p T_2;\ S_2 = c_v \ln \frac{p_2}{\rho_2^k};\\ (\mu_{av})_2 = (\mu_{av})_1 = \mu_{av} = \text{const};\ a_2^2 = kRT_2. \end{aligned}\right\} \qquad \text{(III-4-21)}$$

Equation (III-4-10) is also simplified:

$$p_2 - p_1 = R(\rho_2 T_2 - \rho_1 T_1). \qquad \text{(III-4-22)}$$

Equations (III-4-2)-(III-4-5) are retained.

Formulas for calculation of the parameters. Solving the simplified equations (III-4-13') and (III-4-14'), we obtain an expression for the relative change in the normal velocity component:

$$\Delta\bar{V}_n = (1-\delta)[1-(M_1 \sin\theta_s)^{-2}], \qquad \text{(III-4-23)}$$

where $\delta = (k-1)/(k+1)$.

Substituting (III-4-23) into (III-4-11) and (III-4-12), we obtain the following working relationships:

$$\frac{\rho_2}{\rho_1} = \frac{M_1^2 \sin^2\theta_s}{(1-\delta)+\delta M_1^2 \sin^2\theta_s}; \qquad \text{(III-4-24)}$$

$$\frac{p_2}{p_1} = (1+\delta) M_1^2 \sin^2\theta_s - \delta, \qquad \text{(III-4-25)}$$

which can be used to find formulas for calculating the other parameters. In particular, the temperature-ratio formula is obtained with the equation of state

$$\frac{T_2}{T_1}=\frac{p_2}{p_1}\frac{\rho_1}{\rho_2}. \qquad \text{(III-4-26)}$$

The enthalpy ratio and the ratio of the squared speeds of sound after and before the shock are equal to this temperature ratio.

The parameters behind the normal shock are computed with the relationships given above, putting $\theta_s = \pi/2$. /133

Inclination angles of shock and flow velocity vector. It follows from (II-4-24) and (III-4-25) that the parameters behind the compression shock are determined not only by M_1, but also by the shock inclination angle θ_s.

The working relation for this angle is obtained from Formulas (III-4-2) and (III-4-23), and takes the form

$$\operatorname{tg}\theta_s=\frac{\rho_2}{\rho_1}\operatorname{ctg}\beta_s\left[\frac{1}{2}\left(1-\frac{\rho_1}{\rho_2}\right)\pm\sqrt{\frac{1}{4}\left(1-\frac{\rho_1}{\rho_2}\right)^2-\frac{\rho_1}{\rho_2}\operatorname{tg}^2\beta_s}\right]. \qquad \text{(III-4-27)}$$

The velocity vector inclination angle β_s can be determined by the formula

$$\operatorname{tg}\beta_s=\operatorname{ctg}\theta_s(M_1^2\sin^2\theta_s-1)\left[1+\left(\frac{1}{1-\delta}-\sin^2\theta_s\right)M_1^2\right]^{-1}. \qquad \text{(III-4-28)}$$

The manner in which β_s varies along the wave depends on whether the wave is detached or attached. In the former case, the variation of β_s begins at $\beta_s = 0$ for the "normal" segment; it then reaches a maximum (critical) value corresponding to a certain θ_s, after which it diminishes, reaching zero at infinity, where the shock degenerates into a disturbance wave. In the latter case, that of the attached wave, β_s decreases in the range from $\beta_s = \beta_{sp}$ to $\beta_s = 0$, where the initial value β_{sp} is determined by the condition of flow past the nose of the body.

Mach number and velocity behind shock wave. M_2 is determined from the expression

$$M_2^2 = \frac{1-\delta+M_1^2\delta}{(1+\delta)M_1^2\sin^2\theta_s-\delta} + \frac{(1-\delta)M_1^2\cos^2\theta_s}{1-\delta+\delta M_1^2\sin^2\theta_s}; \qquad \text{(III-4-29)}$$

The formula

$$\frac{V_2^2}{V_1^2} = \cos^2\theta_s + \left(\frac{\rho_1}{\rho_2}\right)^2\sin^2\theta_s, \qquad \text{(III-4-30)}$$

in which the density ratio can be substituted as per (III-4-24), is used to determine the velocity behind the shock.

Entropy and stagnation pressure. An important practical corollary of shock theory is calculation of entropy and stagnation pressure, which depends on entropy.

The nonisentropic nature of passage through the shock is manifested in an increase in entropy, which is determined from the expression

$$S_2 - S_1 = c_v\left(\ln\frac{p_2}{p_1} - \frac{1+\delta}{1-\delta}\ln\frac{\rho_2}{\rho_1}\right). \qquad \text{(III-4-31)}$$

A unique relation exists between the change in entropy and the decrease in stagnation pressure behind the shock:

$$\frac{p_0'}{p_0} = \exp\left[-\frac{S_2-S_1}{(k-1)c_v}\right]. \qquad \text{(III-4-32)}$$

Substituting the entropy difference according to (III-4-31),

$$\frac{p_0'}{p_0} = \delta\left[\frac{1}{\delta(1-\delta)}\right]^{\frac{1+\delta}{2\delta}} \frac{(M_1\sin\theta_s)^{\frac{1+\delta}{\delta}}}{\left(\frac{1+\delta}{\delta}M_1^2\sin^2\theta_s-1\right)^{\frac{1-\delta}{2\delta}}\left(1+\frac{\delta}{1-\delta}M_1^2\sin^2\theta_s\right)^{\frac{1+\delta}{2\delta}}}. \qquad \text{(III-4-33)}$$

Analysis of these relationships indicates that the pressure ratio p_0'/p_0 behind a compression shock is always smaller than one. Here, the larger the angle θ_s at a given M_1, i.e., the stronger the shock, the greater will be the loss of stagnation pressure and, consequently, the smaller the ratio p_0'/p_0. /134

Velocity hodograph. A solution to the problem of the flow variables behind an oblique compression shock can be obtained from the equation of the velocity hodograph, which is the geometric locus of the tips of the velocity vectors behind the compression shock. The hodograph equation derives from the general relationships for the oblique shock and has the form

$$\frac{\lambda_W^2}{(\lambda_1-\lambda_W)^2}=\frac{\lambda_1\lambda_U-1}{(1-\delta)\lambda_1^2+1-\lambda_U\lambda_1}, \qquad \text{(III-4-34)}$$

where $\lambda_W = W_2/a^*$, $\lambda_U = U_2/a^*$, $\lambda_1 = V_1/a^*$, and W_2 and U_2 denote the vertical and horizontal velocity components, respectively.

Equation (III-4-34) enables us to determine all parameters of the shock wave for a given set of free-stream conditions and given values of the flow deflection angle β_s. Since $\lambda_W = \lambda_U \tan \beta_s$, we can solve it simultaneously with (III-4-34) to find the velocity components λ_W and λ_U directly behind the shock and, consequently, the total velocity $\lambda = \sqrt{\lambda_W^2 + \lambda_U^2}$. It follows from (III-4-34) that one solution gives a larger velocity and the other a smaller one. It is then possible to state the maximum critical value of the angle $\beta_s = \beta_{cr}$, to which a unique solution for the velocity corresponds.

The higher velocity is the case in an attached shock that forms ahead of a sharp body; this velocity is reached before the turn angle at any point of the wave has passed its critical value, i.e., $\beta_s < \beta_{cr}$, so that subcritical flow is preserved.

The same velocity occurs behind that part of a detached wave on which the turn angle is less than critical. The lower velocity occurs only behind a detached shock, on the branch adjacent to the "straight" part, where there is supercritical flow.

The velocity hodograph can be used to determine the shock inclination angle by using the formula $\tan \theta_s = (\lambda_1 - \lambda_U)/\lambda_W$. A wave of infinitesimal intensity (a Mach wave) corresponds to the angle value $\theta = \arcsin (1/M_1)$, and a normal shock to $\theta = \pi/2$.

As we see from (III-4-27), there are two different solutions for the angle θ_s. The first (plus sign before the radical) corresponds to a shock wave similar in shape to the normal shock. The second solution (minus sign in front of the radical) defines the inclination of a shock wave of the same intensity and a smaller angle. The larger angle θ_s is realized for a detached compression shock and the smaller for an attached shock.

The compression shock at very high velocities (constant heat capacity). At very high velocities, the parameter $M_1 \sin \theta_s$ may be substantially greater than unity, and this enables us to simplify the relationships for calculation of flow behind compression shocks.

Formula (III-4-24) will become

$$\frac{\rho_2}{\rho_1} = \frac{k+1}{k-1} = \frac{1}{\delta}. \qquad \text{(III-4-24')}$$

Expression (III-4-25) is simplified:

$$\frac{p_2}{p_1} = (1+\delta) K_s^2, \qquad \text{(III-4-25')}$$

where $K_s = M_1 \sin \theta_s$ or, for small shock inclination angles, $K_s = M_1 \theta_s$.

The pressure coefficient behind the shock is found from (III-4-25'): /135

$$\bar{p}_2 = \frac{2(p_2 - p_1)}{kM_1^2 p_1} = 2(1-\delta)\frac{K_s^2}{M_1^2}. \qquad \text{(III-4-25")}$$

After simplification of (III-4-23),

$$\Delta \bar{V}_n = 1 - \delta. \qquad \text{(III-4-23')}$$

Approximate formulas for the other parameters can be obtained in a similar fashion.

The relationships obtained in this manner correspond to the case in which K_s is very large. It is interesting to examine the working relationships for the real cases in which M_1 influences the flow parameters. Let us assume that the shocks that have formed are inclined at small angles; we may then simplify calculation of the angles θ_s. For this purpose, applying (III-4-2), (III-4-3), and (III-4-24), we find after transformation with consideration of the fact that θ_s and β_s are small,

$$\frac{\theta_s}{\beta_s}=\frac{K_s}{K}=\frac{1}{2(1-\delta)}\left[1+\sqrt{1+4(1-\delta)^2K^{-2}}\right]. \qquad \text{(III-4-35)}$$

For $K = M_1\beta \to \infty$ the ratio θ_s/β_s tends to a limit of

$$\theta_s/\beta_s = 1/(1-\delta). \qquad \text{(III-4-35')}$$

Combining (III-4-25) and (III-4-35) with $\sin\theta_s$ assumed $\approx \theta_s$ in the former, we can find an approximate formula for the pressure coefficient:

$$\frac{\bar{p}_2}{\beta_s^2}=2\frac{\theta_s}{\beta_s}=\frac{1}{1-\delta}\left[1+\sqrt{1+4(1-\delta)^2K^{-2}}\right]. \qquad \text{(III-4-36)}$$

At the limit, as $K \to \infty$

$$\frac{\bar{p}_2}{\beta_s^2}=\frac{2}{1-\delta}. \qquad \text{(III-4-36')}$$

An expression for $\Delta\bar{V}_n$ can be obtained from (III-4-23) in the form

$$\Delta\bar{V}_n=\frac{\beta_s}{\theta_s}=2(1-\delta)\left[1+\sqrt{1+4(1-\delta)^2K^{-2}}\right]^{-1} \qquad \text{(III-4-37)}$$

It is evident from this that in the limit, as $K \to \infty$, this quantity tends to the value of (III-4-23').

We can obtain a simplified formula for determining M_2 from (III-4-29):

$$M_2^2=\left[\left(\frac{1+\delta}{1-\delta}K_s^2-\frac{\delta}{1-\delta}\right)\left(\frac{1}{K_s^2}+\frac{\delta}{1-\delta}\right)\right]^{-1}\frac{M_1^2}{(1-\delta)^2}, \qquad \text{(III-4-38)}$$

where K_s is determined as a function of the parameter K by (III-4-35).

Certain relationships for a curvilinear shock wave. A detached curvilinear wave always has at least one point at which the

tangent plane is perpendicular to the oncoming-flow velocity. This point is on the "straight" part of the wave.

The streamline passing through this point is known as the zero streamline. Along it, flow takes place without a change in direction and, consequently, the inclination angle of the radius of curvature of a shock-wave element on this line is zero.

With movement along the wave, this angle increases and, in addition, the rotation of the flow becomes more substantial.

The manner of variation of the flow rotation angle along a curvilinear shock wave is determined by the derivative /136

$$\frac{d\beta_s}{d\omega} = \frac{(1-\delta)^2 M_1^4 \cos^4\omega - (1-\delta) M_1^4 \cos^2\omega + 2(1-\delta)^2 M_1^2 \cos^2\omega - (1-\delta) M_1^2 - (1-\delta)^2}{(1-\delta+\delta M_1^2 \cos^2\omega)^2 + (M_1^2 \cos\omega \sin\omega)^2}, \quad \text{(III-4-39)}$$

which is found by differentiating (III-4-28).

Relationships that can be used to find the variations of the other parameters can be arrived at similarly. For example, the derivatives

$$\frac{d\ln p}{d\omega} = -\frac{2M_1^2 \cos\omega \sin\omega (1+\delta)}{(1+\delta) M_1^2 \cos^2\omega - \delta}; \quad \text{(III-4-40)}$$

$$\frac{d\ln \rho}{d\omega} = -\frac{1}{2}\frac{(1-\delta)\operatorname{tg}\omega}{1-\delta+\delta M_1^2 \cos^2\omega} \quad \text{(III-4-41)}$$

serve for calculation of the pressure and density variations. They indicate that with the approach to the zero streamline, the pressure and density increase monotonically, reaching their maxima at the apex of the wave, where $\omega = 0$.

Study of the geometric properties of a curvilinear shock wave is a component part of aerodynamic research, and one that is related, for example, to determination of the radius of curvature R_s of the surface and the nature of its variation along the wave.

If the equation $y = f(x)$ represents the equation of the wave generatrix in general form in a certain plane xoy, the radius of curvature of the generatrix at a given point is

$$R_s = \frac{dl}{d\omega} = -(1+y'^2)^{\frac{3}{2}} (y'')^{-1}, \quad \text{(III-4-42)}$$

where dl is an elementary arc of the generatrix; $y' = dy/dx$, $y'' = d^2y/dx^2$, with $y'' < 0$. The variation of the radius of curvature along the wave is

$$\frac{dR_s}{d\omega} = R_s (y'')^{-2} [(1 + y'^2) y''' - 3y' (y'')]^2. \qquad \text{(III-4-43)}$$

Let us assume that the wave generatrix is parabolic, $x = ay^2$.

Then

$$R_s = (2a)^{-1} (4a^2y^2 + 1)^{3/2}. \qquad \text{(III-4-44)}$$

Here, $R_s = R_{s0} = 1/(2a)$ at the point $y = 0$, through which the zero streamline passes.

For the parabolic wave, Expression (III-4-43) will be

$$\frac{dR_s}{d\omega} = 3y \frac{R_s}{R_{s0}}, \qquad \text{(III-4-43')}$$

where R_s is determined with (III-4-44).

Experimental data indicate that the generatrix of a detached curvilinear wave can also be approximated by a hyperbola near the zero streamline:

$$\frac{x^2}{a^2} - \frac{y^2}{b^2} = 1$$

where a and b are the semiaxes. Then

$$R_s = R_{s0} \left[1 + \left(1 + \frac{a}{R_{s0}}\right) \frac{y^2}{aR_{s0}}\right]^{3/2}, \qquad \text{(III-4-45)}$$

where $R_{s0} = b^2/a$ is the radius of curvature at the axis ($x = y = 0$).

In accordance with (III-4-45), the derivative

$$\frac{dR_s}{d\omega} = 3y \left(\frac{R_{s0}}{a} + 1\right) \frac{R_s}{R_{s0}} \left(1 + \frac{y^2}{aR_{s0}}\right)^{1/2}. \qquad \text{(III-4-46)}$$

The physical picture of the nonequilibrium process. As a result of passage of gas through a shock wave, some of the kinetic energy is converted into energy of active and inert degrees of freedom. Since equilibrium is established within a very short time, commensurate with the time of passage of the gas through the thickness of the shock, for the active degrees – translational and rotational – we may assume for practical purposes that equilibrium is established instantaneously. Thus, the temperature behind the shock wave will be the same as in a gas with constant specific heats.

In accordance with this scheme, the inert degrees of freedom are unexcited immediately behind the shock. Since these degrees have finite relaxation times, which are substantially longer than the time to pass through the thickness of a real shock, the initial temperature attained will diminish until the inert degrees (first vibrational, then dissociation, excitation of electron levels, and, finally, ionization) reach equilibrium. This process is accompanied by an increase in density and some increase in pressure. The degree of dissociation also rises from zero to its equilibrium value (as does the degree of ionization at very high temperatures).

Calculation of nonequilibrium flow behind a normal compression shock. The problem is one of evaluating the extent of the nonequilibrium zone or "relaxation length," and determining the nonequilibrium parameters behind the shock. For this purpose, it is necessary to solve a system consisting of an equation of one-dimensional steady motion

$$V\frac{dV}{dx}=-\frac{1}{\rho}\frac{dp}{dx},$$

and the equations of energy (III-4-17), state (III-1-14'), and chemical-reaction rate (III-1-27).

With the nomenclature introduced in §III-1, this equation system will be written as follows:

$$\begin{gathered}\frac{1}{2}\frac{d\bar{V}^2}{d\bar{x}}+\frac{1}{\bar{\rho}}\frac{d\bar{p}}{d\bar{x}}=0;\\ \alpha+\frac{4+\alpha}{1+\alpha}\frac{\bar{p}}{\bar{\rho}}+\frac{\bar{V}^2}{2}=\bar{i}_0;\\ \bar{p}=\bar{\rho}\bar{T}(1+\alpha);\end{gathered}\qquad\text{(III-4-47)}$$

$$\bar{V}\frac{d\alpha}{d\bar{x}}=\bar{\varphi}\frac{\bar{V}_1\bar{\rho}^2}{\bar{\rho}_1^2}\left[(1-\alpha)\frac{e^{-\frac{1}{\bar{T}}}}{\bar{\rho}}-\alpha^2\right], \qquad \text{(III-4-47)}$$

(Cont'd.)

where $\bar{x} = x/L$ (L is a certain characteristic linear dimension) and the parameter

$$\bar{\varphi}=\frac{c\bar{\rho}_1^2 L}{\rho_d V_1}; \qquad \text{(III-4-48)}$$

At the same time one of the equations of (III-1-27') can be used instead of the last equation of (III-4-47) system.

The above equation system reflects the case of nonequilibrium flow along an arbitrary streamline. If we consider the "zero" streamline, which passes through the straight part of the compression shock, the system is simplified to a certain degree. For example, we may use instead of the equation of motion the impulse equation for a strong shock wave: /138

$$p+\rho V^2=\rho_1 V_1^2. \qquad \text{(III-4-49)}$$

This leaves one differential equation for the chemical reaction rate in System (III-4-47).

The initial conditions are determined by integrating this equation by the variables directly behind the shock wave, which are found from the theory of the ordinary shock transition, i.e., on the assumption that there is no dissociation and, consequently, $\alpha = 0$ at $x = 0$. Pressure is assumed constant and independent of nonequilibrium along the "zero" streamline.

Figure III-4-6 shows the results of numerical integration for equilibrium of the vibrational degrees of freedom ($t_v = 0$ curve). Oxygen was chosen as the medium, with the recombination rate coefficient assumed equal to $k_R = 8.4 \cdot 10^{14}$ cm^6/mole^2·s on the basis of experimental data. The curve in Fig. III-4-6 can be used to evaluate the relaxation-zone nonequilibrium degree of dissociation, which rises from zero directly behind the shock to the equilibrium value $\alpha = \alpha_e$ at the end of the relaxation distance.

The diagram in Fig. III-4-7 illustrates the variation of density in the nonequilibrium zone. In accordance with the type of variation of the degree of dissociation, the density rises from its value for a nondissociating gas to the density at equilibrium dissociation.

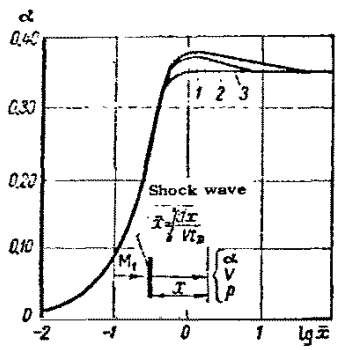

Figure III-4-6. Variation of Nonequilibrium Degree of Dissociation of Oxygen Behind Shock. 1) $t_v = 20t_D$; 2) $t_v = 4t_D$; 3) vibrations at equilibrium ($t_v = 0$); $M_1 = 13$; $p_1 = 5.65$ mmHg; $T_1 = 295°K$; t_v is the vibrational relaxation time and t_D is the dissociation relaxation time.

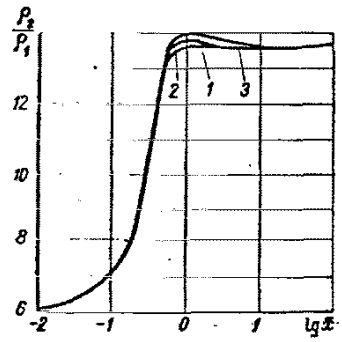

Figure III-4-7. Variation of Ratio of Oxygen Densities After and Before Compression Shock in Nonequilibrium Flow in a Compressed Layer. 1,2,3) see Fig. III-4-6.

The same Figs. III-4-6 and III-4-7 show curves ($t_v \neq 0$) that take account of the vibrational relaxation time t_v. It may be noted that atomic vibrations increase the degree of dissociation and the density ratio over their equilibrium values (for $t_v = 0$). This is because the vibrations have not reached equilibrium and the unabsorbed part of the energy is also expended on dissociation.

This increase in degree of dissociation and density in the relaxation zone occurs not only in a diatomic gas, but also in air at 4000°K. This is explained by the fact that practically no vibrations may have been excited when this temperature is reached in nitrogen behind the shock, and the unabsorbed vibrational energy may contribute to further oxygen dissociation and, consequently, to an increase in the density of the air.

Data on the degree of dissociation enable us to evaluate the nonequilibrium temperature, for example, with the approximate formula

$$\overline{T} = \frac{\bar{i} - \alpha}{4 + \alpha}, \qquad \text{(III-4-50)}$$

where it is assumed for high velocities that $\bar{i} = 0.5\bar{V}_1^2$. The equation of state (III-1-14') can also be used. According to the calculated data given in Figs. III-4-6 and III-4-7, the temperature varies from 9700°K directly behind the shock ($\bar{x} = 0$) to an equilibrium value of 3700°K. /139

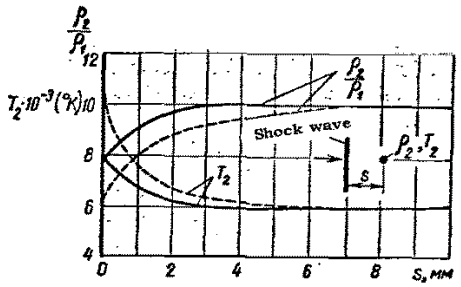

Figure III-4-8. Influence of Nonequilibrium Dissociation on Density and Temperature Behind Shock.

As we have noted, the results presented pertain to oxygen, since the recombination-rate parameter k_R is known with greatest certainty for precisely this gas. The same equation system can be used for approximate evaluation of the influence of nonequilibration on the flow of air, referring it to a diatomic air model consisting of an additive oxygen-nitrogen mixture. In this case, the coefficient $\underline{c}$ in (III-4-48) is determined for the oxygen, and all the other parameters, such as the degree of equilibrium dissociation α_e, the characteristic density, characteristic pressure, etc., are found for the diatomic air model.

Figure III-4-8 shows the density and temperature distributions in the oxygen-nitrogen air mixture in the relaxation zone behind a shock wave for $M_1 = 14.2$, $T_1 = 300°K$, and $p_1 = 1$ mmHg. The unbroken curves were plotted on the assumption of instantaneous vibrational excitation, and the dashed curve without consideration of vibrational excitation. These results indicate that the vibrations are a substantial factor. When they are not taken into account, the temperature behind the shock is 12,000°K, but it is 9770°K, i.e., much lower, for the fully excited state.

It is also evident from Fig. III-4-8 that the nonequilibrium zone is relatively small, extending over approximately 8-10 mm, with vibrational excitation practically insignificant at the end of the zone. In equilibrium-dissociation calculations, therefore, we may assume the rates of vibrational excitation to be infinite, thus regarding the gas ahead of the onset of dissociation as fully excited.

Chapter IV

/140

GENERAL METHODS OF SOLUTION OF AERODYNAMIC PROBLEMS

§IV-1. THE METHOD OF CHARACTERISTICS

General Equations for the Characteristics

The compatibility condition. The method of characteristics, which enables us to solve the equations of motion of a gas graphically or numerically and, in particular, to compute the flow behind a stationary shock wave for the condition that this flow is supersonic, occupies an important position among the methods used in supersonic aerodynamics.

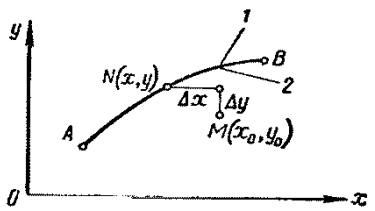

Figure IV-1-1. Method of Characteristics. AB) initial curve; 1) characteristic of first family; 2) characteristic of second family.

We shall examine the method of characteristics as it applies to steady two-dimensional supersonic rotational and irrotational gas flows. Equations (III-2-24) for the velocity potential ϕ and (III-2-35) for the stream function ψ, which can be solved by this method, are quasilinear second-order hyperbolic partial differential equations.

The solutions of these equations, $\phi = \phi(x, y)$ and $\psi = \psi(x, y)$ are represented geometrically by integral surfaces in the space defined by the x, y, ϕ or x, y, ψ coordinate systems. In these systems, the x, y-plane is regarded as the base plane and called the physical plane or the plane of independent variables.

The solutions of (III-2-24) and (III-2-35) will be unique if they are subject to certain additional conditions. These additional conditions are imposed by assigning values of the unknown function $\phi(x, y)$ or $\psi(x, y)$ and one of its first derivatives $\phi_x(\psi_x)$ or $\phi_y(\psi_y)$ on a certain initial curve AB (Fig. IV-1-1). Finding functions ϕ or ψ that satisfy the given equation and initial conditions on the basis of these initial data in the neighborhood of curve AB is the content of the Cauchy problem.

From the geometrical viewpoint, solution of the Cauchy problem consists in finding in the x, y, ϕ (or x, y, ψ) space an

integral surface that passes through a given space curve $\phi = \phi(x_{AB}, y_{AB})$ or $\psi = \psi(x_{AB}, y_{AB})$ and has the given tangent planes at points on this curve. The solution of the Cauchy problem as it applies to supersonic flows and the associated development of an appropriate method of characteristics are due to Prof. F. Frankl'.

To examine the Cauchy problem, let us represent Eqs. (III-2-24) and (III-2-35), written for steady flow, in the form

$$Au + 2Bs + Ct + H = 0, \qquad \text{(IV-1-1)}$$

where $u = \varphi_{xx} (= \psi_{xx})$, $s = \varphi_{xy} (= \psi_{xy})$, $t = \varphi_{yy} (= \psi_{yy})$ are the second partial derivatives; A, B, and C are the coefficients of the corresponding second partial derivatives in Eqs. (III-2-24) and (III-2-35), and the term H combines all of the remaining terms of these equations. /141

The solution of (IV-1-1) in the neighborhood of the initial curve AB is found as a Taylor series

$$\varphi = \varphi(x, y) + \sum_{n=1}^{\infty} \frac{1}{n!} \left[(\Delta x)^n \frac{\partial^n \varphi}{\partial x^n} + \frac{n}{1} (\Delta x)^{n-1} \Delta y \frac{\partial^n \varphi}{\partial x^{n-1} \partial y} + \right.$$
$$\left. + \frac{n(n-1)}{1 \cdot 2} (\Delta x)^{n-2} (\Delta y)^2 \frac{\partial^n \varphi}{\partial x^{n-2} \partial y^2} + \ldots + (\Delta y)^n \frac{\partial^n \varphi}{\partial y^n} \right], \qquad \text{(IV-1-2)}$$

where $\Delta x = x_0 - x$, $\Delta y = y_0 - y$ (Fig. IV-1-1); the values of the derivatives are taken at points on curve AB; the stream function ψ may appear in place of ϕ. Obviously, this expansion determines the solution that we seek if the values of the function ϕ (or ψ) and its derivatives of any order are known on the initial curve. But only the unknown function and its first derivatives $p = \varphi_x (= \psi_x)$, $q = \varphi_y (= \psi_y)$ are assigned on this curve. It is therefore necessary to indicate a method of finding derivatives of order higher than the first on curve AB.

We first find equations with which the second derivatives can be determined. Since there are three derivatives (u, s, t), it is necessary to write as many independent equations to determine them. The first of these is (IV-1-1), which we shall examine on the initial curve AB. The other two are obtained from the following relationships, which are also considered along the initial curve:

$$dp = \frac{\partial p}{\partial x} dx + \frac{\partial p}{\partial y} dy = u\,dx + s\,dy;$$

$$dq = \frac{\partial q}{\partial x}\,dx + \frac{\partial q}{\partial y}\,dy = s\,dx + t\,dy.$$

Thus, the equation system for determination of the second derivatives will be

$$\left.\begin{aligned} Au + 2Bs + Ct &= -H; \\ dxu + dys + 0 \cdot t &= dp; \\ 0 \cdot u + dxs + dyt &= dq. \end{aligned}\right\} \qquad \text{(IV-1-3)}$$

If we introduce the respective symbols Δ, Δ_u, Δ_s, Δ_t for the principal and partial determinants of the system, the second derivative on the curve will then be determined from the relationships

$$u = \frac{\Delta_u}{\Delta};\ s = \frac{\Delta_s}{\Delta};\ t = \frac{\Delta_t}{\Delta}. \qquad \text{(IV-1-4)}$$

It follows from these equalities that if the principal determinant is nonzero on AB, then the derivatives $\underline{u}$, $\underline{s}$, and $\underline{t}$ are evaluated uniquely. If, on the other hand, curve AB is such that this determinant is zero along it, i.e.,

$$\Delta = \begin{vmatrix} A & 2B & C \\ dx & dy & 0 \\ 0 & dx & dy \end{vmatrix} = 0,$$

and, consequently,

$$A\left(\frac{dy}{dx}\right)^2 - 2B\frac{dy}{dx} + C = 0, \qquad \text{(IV-1-5)}$$

then the second derivatives are either not determined at all in terms of ϕ, $\underline{p}$, and $\underline{q}$ or are determined nonuniquely.

It is readily seen that (IV-1-5), which can be rewritten /142

$$\left(\frac{dy}{dx}\right)_{1,2} = y'_{1,2} = \frac{1}{A}\left(B \pm \sqrt{B^2 - AC}\right), \qquad \text{(IV-1-5')}$$

is the differential equation of two single-parameter families of real curves provided that $B^2 - AC > 0$ ($V^2 - a^2 > 0$), i.e., if the flow is supersonic. Curves at each point of which the partial determinant of System (IV-1-3) is zero are called characteristics and Eq. (IV-1-5) a characteristic equation. Slopes calculated by (IV-1-5') define characteristic directions.

It is clear from the above that the following condition must be satisfied for unique definition of the second derivatives: the direction of the initial curve should not at any point coincide with a characteristic direction.

The same condition $\Delta \neq 0$ applies in respect to unique definition of higher derivatives appearing in the series (IV-1-2). Thus, if $\Delta \neq 0$ on the initial curve, we may write systems similar to (IV-1-3) to determine successively any of the derivatives appearing in Series (IV-1-2), and thereby find the sought solution ϕ or ψ in the neighborhood of the initial curve.

The case in which the initial curve AB coincides with one of the characteristics and not only the principal determinant of System (IV-1-3), but also the partial determinants $\Delta_u = \Delta_s = \Delta_t = 0$ on it, has a special place in supersonic-flow theory. It can be shown that if, say, the determinants Δ and Δ_t are zero, the other two determinants vanish automatically. In this case, System (IV-1-3) has solutions, although they are not unique.

On expansion, the equations

$$\Delta = 0,\ \Delta_t = \begin{vmatrix} A & 2B & -H \\ dx & dy & dp \\ 0 & dx & dq \end{vmatrix} = 0$$

have the form

$$A(y')^2 - 2By' + C = 0; \qquad \text{(IV-1-6)}$$

$$A(y'\,dq - dp) - 2B\,dq + H\,dx = 0. \qquad \text{(IV-1-7)}$$

This equation system forms the mathematical basis for the method of characteristics. Equations (IV-1-6) and (IV-1-7) are known as compatibility conditions. The former defines two families of curves (characteristics) in the physical plane, and the latter two families of curves that are known as characteristics in the p, q-plane.

We see from Eqs. (IV-1-6) and (IV-1-7) that a definite point on the corresponding characteristic in the p, q-plane corresponds to each point on the characteristic in the x, y-plane. It is this that permits use of the characteristics to calculate gas flows.

Equation (IV-1-7) is a condition that must be satisfied by the first derivatives p and q of the function ϕ or ψ on the initial curve AB when this curve is a characteristic for System (IV-1-3) to have a solution. Thus, it is a distinctive property of characteristics that while the initial conditions can be assigned arbitrarily along a curve that is not a characteristic, this can no longer be done along a characteristic.

Characteristics in the physical plane. Two families of characteristics in the physical plane are defined by the various real roots $\lambda_{1,2} = dy/dx$ of characteristic equation (IV-1-5), which may be regarded as a quadratic equation in dy/dx. After replacing the coefficients A, B, C in these equations by their values according to (III-2-24) or (III-2-35), we obtain the differential equation for the characteristics: /143

$$\lambda_{1,2} = \left(\frac{dy}{dx}\right)_{1,2} = \frac{1}{V_x^2 - a^2}\left(V_x V_y \pm \sqrt{V^2 - a^2}\right), \qquad \text{(IV-1-8)}$$

where the "1" corresponds to the first family of characteristics and the "2" to the second.

Let us find the angle μ between the characteristic direction for some point A of the flow and the direction of the velocity vector V at the same point. This angle can be found with (IV-1-8) if we refer it to the local x_1, y_1 coordinate system with its origin at point A and its x_1-axis coinciding in direction with the vector V. With this condition, $V_x = V$, $V_y = 0$ and, consequently, on the basis of (IV-1-8),

$$\left(\frac{dy_1}{dx_1}\right)_{1,2} = \operatorname{tg}\mu_{1,2} = \pm (M^2 - 1)^{-1/2}.$$

From this we see (Fig. IV-1-2), firstly, that the velocity vector bisects the angle between characteristics emanating from the same point and, secondly, that the angle between this velocity vector and the characteristic is the Mach angle. Consequently, the physical significance of the characteristic is that it is a line at each point of which the direction of the tangent coincides with the direction of one of the disturbance lines emanating from the same point.

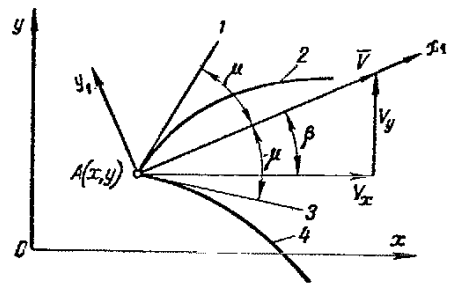

Figure IV-1-2. Determining Physical Significance of Characteristics. 1) direction of first-family characteristic at point A; 2) first-family characteristic with slope λ_1; 3) direction of second-family characteristic at point A; 4) second-family characteristic with slope λ_2.

We now note (Fig. IV-1-2) that the angle of inclination of the characteristics to the horizontal axis is $\beta \pm \mu$. Consequently, Eq. (IV-1-8) for the characteristics can also be written

$$\lambda_{1,2} = \left(\frac{dy}{dx}\right)_{1,2} = \operatorname{tg}(\beta \pm \mu), \qquad \text{(IV-1-9)}$$

where β is the angle between the velocity vector $\bar{V}$ and the x-axis.

It is essential that the characteristic equations (IV-1-8) and, consequently, the form of the characteristic curves are the same for both rotational and potential two-dimensional flows.

Characteristics in the plane of the velocity hodograph. If y' in (IV-1-7) is replaced by the first root of the characteristic equation, $y' = \lambda_1$, it will represent the first family of characteristics in the p, q-plane. A similar substitution of y' by the second root, $y' = \lambda_2$, gives the equation for the second characteristic family in the same plane. The equations thus obtained for the characteristics can be modified somewhat by using the known property of the roots of the quadratic equation (IV-1-5) according to which $2B = A(\lambda_{1,2} + \lambda_{2,1})$. Introducing this relation into (IV-1-7), we obtain it in the form

$$A(dp + \lambda_{2,1}\,dq) + H\,dx = 0, \qquad \text{(IV-1-7')}$$

where the subscript "2" corresponds to the first family of characteristics and the "1" to the second.

In contrast to (IV-1-5') for the characteristics in the physical plane, the specific form of (IV-1-7') depends on what kind of flow is being investigated: plane or spatial, rotational or potential.

Each of these types of flow has its own equation for ϕ or ψ and, consequently, its own expression for the coefficient H. /144

To obtain the equations for the characteristics in the p,q-plane in its most general form, let us examine rotational two-

dimensional supersonic flow and (III-2-35) for the stream function. We introduce the coefficients of (III-2-35) into (IV-1-7'):

$$A = 1 - \frac{V_x^2}{a^2}; \quad H = -V_x (1-\widetilde{V}^2)^{\frac{1}{k-1}} \varepsilon - y^{2\varepsilon} \left(1 - \frac{V^2}{a^2}\right) (1-\widetilde{V}^2)^{\frac{k+1}{k-1}} f(\psi).$$

Here the function $f(\psi)$ is given by Expression (III-2-36), from which we see that it is determined by the vorticity $\partial V_y/\partial x - \partial V_x/\partial y$. In turn, gasdynamics has the relation

$$\frac{\partial V_y}{\partial x} - \frac{\partial V_x}{\partial y} = \frac{a^2}{V} \frac{dS}{dn} \frac{1}{kR} \qquad \text{(IV-1-10)}$$

for vorticity, which indicates that it depends on the entropy gradient along the normal to the streamline. Consequently, the function $f(\psi)$ can be represented in the form

$$f(\psi) = -\frac{k-1}{2kR} \frac{V_{\max} (1-\widetilde{V}^2)^{-\frac{1}{k-1}}}{y^{\varepsilon} \widetilde{V}} \frac{dS}{dn}. \qquad \text{(IV-1-11)}$$

The functions p and q (IV-1-7') are replaced in accordance with (III-2-33) by the expressions

$$p = \psi_x = -y^{\varepsilon} V_y (1-\widetilde{V}^2)^{\frac{1}{k-1}}; \quad q = \psi_y = y^{\varepsilon} V_x (1-\widetilde{V}^2)^{\frac{1}{k-1}},$$

and the slopes by their values $\lambda_{2,1} = \operatorname{tg}(\beta \mp \mu)$.

Then, introducing the polar coordinates β and V, which are defined by the expressions $V_x = V\cos\beta$, $V_y = V\sin\beta$, we obtain the following equation after a number of manipulations [58]:

$$\frac{dV}{V} \mp \operatorname{tg}\mu\, d\beta - \varepsilon \frac{dx}{y} \frac{\sin\beta \sin\mu \operatorname{tg}\mu}{\cos(\beta \pm \mu)} \pm \frac{dx}{kR} \frac{\sin^3\mu}{\cos(\beta \pm \mu)} \frac{dS}{dn} = 0, \qquad \text{(IV-1-12)}$$

which is the equation for the characteristics in the velocity-hodograph plane. The upper sign corresponds to characteristics of the first family, and the lower sign to those of the second.

The stagnation pressure gradient dp_0'/dn can be introduced instead of the entropy gradient in the equations for the characteristics in the hodograph plane by applying the relation

$$\frac{dS}{dn} = -\frac{R}{p_0'}\frac{dp_0'}{dn} = -R\frac{d\ln p_0'}{dn}. \qquad \text{(IV-1-13)}$$

Characteristics of Plane Potential Flow

In this case, the equations for the characteristics in the physical plane take the form of (IV-1-9). In the hodograph plane, the corresponding equations are obtained from (IV-1-12), setting $\varepsilon = 0$ and $dS/dn = 0$:

$$\frac{dV}{V} \mp \operatorname{tg}\mu\, d\beta = 0. \qquad \text{(IV-1-14)}$$

Integrating from $V = a^*(\lambda = 1)$ to some arbitrary velocity value, we find the equation for the characteristics:

$$\beta = \pm\omega + \beta^*, \qquad \text{(IV-1-15)}$$

where β^* is the initial deflection angle of the flow; /145

$$\omega = \int_{a^*}^{V} \operatorname{ctg}\mu\frac{dV}{V} = \int_{1}^{\lambda} \operatorname{ctg}\mu\frac{d\lambda}{\lambda}. \qquad \text{(IV-1-16)}$$

In this expression, $d\lambda/\lambda$ is found with (III-3-5):

$$\frac{d\lambda}{\lambda} = \frac{dM}{M\left(1+\frac{k-1}{2}M^2\right)}.$$

After substitution, evaluation of the corresponding integral in the range from $M = 1$ to some value $M > 1$, and transformation to take account of $\cot\mu = \sqrt{M^2-1}$, we find

$$\omega = \sqrt{\frac{k+1}{k-1}}\operatorname{arctg}\sqrt{\frac{k-1}{k+1}(M^2-1)} - \operatorname{arctg}\sqrt{M^2-1}. \qquad \text{(IV-1-17)}$$

We see from this expression that the angle ω is a function only of M. If we introduce the velocity ratio $\lambda = V/a^*$, this angle can be represented as an $\omega = \omega(\lambda)$ curve. The curve constructed from (IV-1-17) is an epicycloid.

Thus, Eqs. (IV-1-15) for the characteristics of a plane flow correspond geometrically to two families of epicycloids in a ring whose internal radius is $\lambda = 1$, while its external radius is $\lambda = [(k + 1)/(k - 1)]^{1/2}$. The plus sign in front of the function $\omega(\lambda)$ corresponds to an epicycloid (characteristic) of the first family, and the minus sign to one of the second.

The physical significance of the angle ω is that it represents the deflection angle β of the flow in isentropic expansion from the direction corresponding to $M = 1$ to a direction characterized by a certain arbitrary $M > 1$ and equal to the upper limit in the integral of (IV-1-16).

The flow deflection angle at an arbitrary point can be determined as follows. Assume that we know an initial Mach number $M > 1$. As a result of flow expansion, M increases, reaching a value $M_2 > M_1$. Deflection angles ω_1 and ω_2 of the flow from the direction of flow with $M = 1$ correspond to these Mach numbers M_1 and M_2, and they can be determined from the expressions $\beta_1 = \omega(M_1)$ and $\beta_2 = \omega(M_2)$. Consequently, the angle of deflection from the original direction is $\Delta\beta = \beta_2 - \beta_1 = \omega(M_2) - \omega(M_1)$.

The flow variables can be calculated in a different procedure: the M_1 corresponding to the original direction can be determined from a known M_2 and the flow deflection angle $\Delta\beta$ from that direction. To facilitate such calculations, Table IV-1-1 gives values of the function $\omega = \omega(M)$ calculated by (IV-1-17) for various M and $k = 1.4$. The same table lists inclination angles of the disturbance line (Mach angles) calculated by the formula $\mu = \arcsin(1/M)$.

At hypersonic velocities, the equation for the function ω and consequently, calculations using the method of characteristics are simplified. Actually, for very large M, (IV-1-16) can be written

$$\omega = \frac{2}{k-1}\int_1^M \frac{dM}{M^2},$$

which gives, after integration,

$$\omega = -\frac{2}{k-1}\left(\frac{1}{M} - 1\right). \qquad \text{(IV-1-18)}$$

Equations (IV-1-17) and (IV-1-18) can be used to calculate supersonic flow over a convex angle (Fig. IV-1-3, angle ABC > > 180°). The disturbed flow past such an angle is known as Prandtl-Meyer flow. /146

TABLE IV-1-1. DEFLECTION ANGLE ω OF PLANE SUPERSONIC FLOW AND INCLINATION ANGLE μ OF DISTURBANCE LINE AS FUNCTIONS OF LOCAL M AT k = 1.4*

M	ω°	μ°	M	ω°	μ°	M	ω°	μ°
1.00	0.000	90.000	4.00	65.785	14.478	7.00	90.973	8.213
1.10	1.336	65.380	4.10	67.082	14.117	7.10	91.491	8.097
1.20	3.558	56.443	4.20	68.333	13.774	7.20	91.997	7.984
1.30	6.170	50.285	4.30	69.541	13.448	7.30	92.490	7.873
1.40	8.987	45.585	4.40	70.706	13.137	7.40	92.970	7.776
1.50	11.905	41.810	4.50	71.832	12.841	7.50	93.440	7.662
1.60	14.861	38.682	4.60	72.919	12.556	7.60	93.898	7.561
1.70	17.810	36.032	4.70	73.970	12.284	7.70	94.345	7.462
1.80	20.725	33.749	4.80	74.986	12.025	7.80	94.781	7.366
1.90	23.586	31.757	4.90	75.969	11.776	7.90	95.208	7.272
2.00	26.380	30.000	5.00	76.920	11.537	8.00	95.625	7.181
2.10	29.097	28.437	5.10	77.841	11.308	8.20	96.430	7.005
2.20	31.732	27.036	5.20	78.732	11.087	8.40	97.200	6.837
2.30	34.283	25.771	5.30	79.596	10.876	8.60	97.936	6.677
2.40	36.746	24.624	5.40	80.433	10.672	8.80	98.642	6.525
2.50	39.124	23.578	5.50	81.245	10.476	9.00	99.318	6.379
2.60	41.415	22.620	5.60	82.032	10.287	9.20	99.967	6.240
2.70	43.621	21.738	5.70	82.796	10.104	9.40	100.589	6.107
2.80	45.746	20.925	5.80	83.537	9.928	9.60	101.188	5.979
2.90	47.790	20.171	5.90	84.256	9.758	9.80	101.763	5.857
3.00	49.757	19.471	6.00	84.955	9.594	10.00	102.316	5.739
3.10	51.650	18.819	6.10	85.635	9.435	10.20	102.849	5.626
3.20	53.470	18.210	6.20	86.296	9.282	10.40	103.362	5.518
3.30	55.222	17.640	6.30	86.937	9.133	10.60	103.857	5.413
3.40	56.907	17.105	6.40	87.561	8.989	10.80	104.335	5.313
3.50	58.530	16.602	6.50	88.168	8.850	11.00	104.796	5.216
3.60	60.091	16.128	6.60	88.759	8.715	11.20	105.241	5.123
3.70	61.595	15.680	6.70	89.335	8.584	11.40	105.671	5.032
3.80	63.044	15.258	6.80	89.895	8.457	11.60	106.087	4.945
3.90	64.440	14.857	6.90	90.441	8.333	11.80	106.489	4.861
						12.00	106.879	4.780

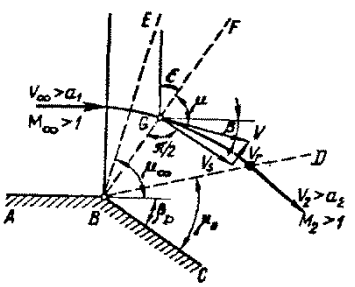

Figure IV-1-3. Supersonic Flow Past a Convex Angle (Prandtl-Meyer Flow).

In passing over angle B, the flow undergoes expansion, which begins along the Mach line BE (μ_∞ = arc sin $1/M_\infty$) and terminates on the Mach line BD(μ_0 = arc sin $1/M_0$). These Mach lines, like intermediate Mach lines such as BF, which are straight lines, correspond to characteristics of the first family, and velocities do not vary along them. Velocity changes will occur at transition from one Mach line of the first family to another. This velocity change can be analyzed with the aid of (IV-1-17) or (IV-1-18).

To find M on an intermediate characteristic BF to which a given flow deflection angle β corresponds, we first find the total angle $\omega = \omega_\infty + \beta$, where ω_∞ is found from (IV-1-17) or (IV-1-18) for the given M_∞. Knowing ω, we can use the same equations [(IV-1-17) and (IV-1-18)] to calculate the corresponding local M. The local Mach number M_0 on wall BC is determined from the angle $\omega_0 = \omega_\infty + \beta_p$. The angle ε between Mach line BF and the vertical is determined from the condition $\varepsilon = \pi/2 - (\mu - \beta)$, where $\mu = \arcsin 1/M$. /147

The properties of Prandtl-Meyer flow can be used to solve the problem of continuous supersonic flow over a convex curvilinear surface (this problem will be examined below).

Scheme of Problem Solution by the Method of Characteristics

System of equations for characteristics. Using (IV-1-16), we can transform Eq. (IV-1-12) for the characteristics in the hodograph plane and thus utilize the properties of epicycloids for calculation of two-dimensional nonisentropic flows.

As a result, the system of equations for the characteristics will be:

a) for the first family

$$dy = \operatorname{tg}(\beta + \mu)\, dx; \qquad \text{(IV-1-19)}$$

$$d(\omega - \beta) - \varepsilon \frac{dx}{y} l + \frac{dx}{kR} \frac{dS}{dn} c = 0; \qquad \text{(IV-1-20)}$$

b) for the second family

$$dy = \operatorname{tg}(\beta - \mu)\, dx; \qquad \text{(IV-1-21)}$$

$$d(\omega + \beta) - \varepsilon \frac{dx}{y} m - \frac{dx}{kR} \frac{dS}{dn} t = 0, \qquad \text{(IV-1-22)}$$

where

$$l = \frac{\sin\beta \sin\mu}{\cos(\beta + \mu)}; \quad c = \frac{\sin^2\beta \cos\mu}{\cos(\beta + \mu)}; \qquad \text{(IV-1-23)}$$

$$m = \frac{\sin\beta \sin\mu}{\cos(\beta + \mu)}; \quad t = \frac{\sin^2\beta \cos\mu}{\cos(\beta - \mu)}. \qquad \text{(IV-1-24)}$$

As we noted, the stagnation pressure gradient dp_0'/dn can be introduced instead of the entropy gradient by using the relationship between them, (IV-1-13).

For two-dimensional isentropic (potential) flow, the equations for the characteristics become:

a) for the first family

$$dy = \operatorname{tg}(\beta + \mu)\, dx; \qquad \text{(IV-1-25)}$$

$$d(\omega - \beta) - \varepsilon \frac{dx}{y} l = 0; \qquad \text{(IV-1-26)}$$

b) for the second family

$$dy = \operatorname{tg}(\beta - \mu)\, dx; \qquad \text{(IV-1-27)}$$

$$d(\omega + \beta) - \varepsilon \frac{dx}{y} m = 0. \qquad \text{(IV-1-28)}$$

We must set $\varepsilon = 0$ in the equations for plane flow and $\varepsilon = 1$ for spatial axisymmetric flow.

Method of numerical calculation. Determination of the disturbed-flow velocity field by the method of characteristics consists for the most part of solving two independent problems. The first involves determination of velocity at the intersection point of characteristics of different families emanating from two nearby points at which the velocities are known; the second consists in calculating the velocity at the intersection point of the solid wall with a characteristic if the latter is drawn from a point near the wall and if the velocity is known at this point. These problems are purely kinematic, since the method of characteristics makes it possible to find velocity directly. It must be remembered that in the general case of nonisentropic flow, velocity alone represents insufficient initial data, and other variables (entropy, stagnation pressure) must be assigned. /148

Let us examine the first problem. By its hypothesis, M_A, M_B, and other parameters, including the entropies S_A and S_B, are known at two neighboring points A and B of the physical plane (Fig. IV-1-4a), and it is necessary to find the flow variables at point C, at which elements of the first- and second-family characteristics intersect (M_C, the velocity vector inclination angle β_C, the entropy S_C, etc.). It is also required to find the coordinates x_C and y_C of point C.

All numerical calculations are based on use of the equations for the characteristics, (IV-1-19)-(IV-1-22), which are written in finite differences:

a) for the first family

$$\Delta y_B = \operatorname{tg}(\beta_B + \mu_B)\,\Delta x_B; \qquad \text{(IV-1-29)}$$

$$\Delta\omega_B - \Delta\beta_B - \varepsilon\frac{\Delta x_B}{y_B} l_B + \frac{\Delta x_B}{kR}\frac{\Delta S}{\Delta n} c_B = 0; \qquad \text{(IV-1-30)}$$

b) for the second family

$$\Delta y_A = \operatorname{tg}(\beta_A - \mu_A)\,\Delta x_A; \qquad \text{(IV-1-31)}$$

$$\Delta\omega_A + \Delta\beta_A - \varepsilon\frac{\Delta x_A}{y_A} m_A - \frac{\Delta x_A}{kR}\frac{\Delta S}{\Delta n} t_A = 0, \qquad \text{(IV-1-32)}$$

where

$$\left.\begin{aligned} &\Delta y_B = y_C - y_B;\ \Delta x_B = x_C - x_B;\ \Delta\omega_B = \omega_C - \omega_B;\ \Delta\beta_B = \beta_C - \beta_B;\\ &\Delta y_A = y_C - y_A;\ \Delta x_A = x_C - x_A;\ \Delta\omega_A = \omega_C - \omega_A;\ \Delta\beta_A = \beta_C - \beta_A;\\ &l_B = \frac{\sin\beta_B \sin\mu_B}{\cos(\beta_B + \mu_B)};\quad c_B = \frac{\sin^2\beta_B \cos\mu_B}{\cos(\beta_B + \mu_B)};\\ &m_A = \frac{\sin\beta_A \sin\mu_A}{\cos(\beta_A - \mu_A)};\quad t_A = \frac{\sin^2\beta_A \cos\mu_A}{\cos(\beta_A - \mu_A)}. \end{aligned}\right\} \qquad \text{(IV-1-33)}$$

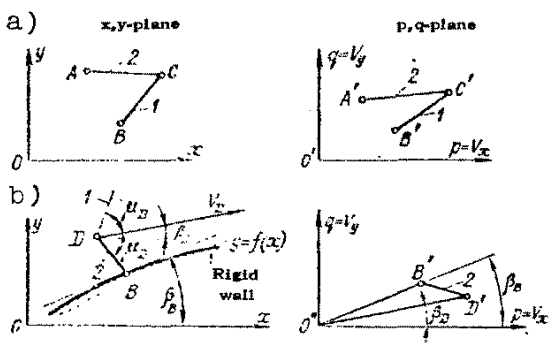

Figure IV-1-4. Illustrating Calculation of Supersonic Flow Velocity by the Method of Characteristics. 1) element of first-family characteristic; 2) element of second-family characteristic; a) first problem; b) second problem.

Thus, Eqs. (IV-1-29)-(IV-1-32) are written on the assumption that the coefficients l, m, c, and t remain constant with movement along the elements of the characteristics and are equal to their values at the initial points A and B.

To determine the coordinates x_C, y_C, it is necessary to solve the system of equations (IV-1-29) and (IV-1-31) for the elements of the conjugate characteristics in the physical plane:

$$y_C - y_B = (x_C - x_B)\operatorname{tg}(\beta_B + \mu_B);$$
$$y_C - y_A = (x_C - x_A)\operatorname{tg}(\beta_A - \mu_A).$$

Calculation of the velocity at point C and the angle β_C requires solution of equation system (IV-1-30) and (IV-1-32) for /149

the conjugate characteristics in the hodograph plane. Obviously, these parameters depend on $\Delta S/\Delta n$, which determines the change in entropy on passage along the normals to the streamlines passing through points B and A.

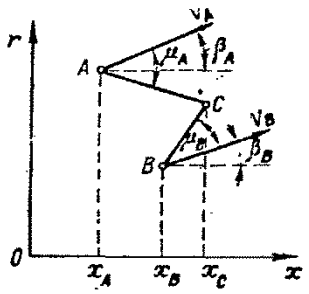

Figure IV-1-5. Illustrating Calculation of Velocity by Method of Characteristics with Consideration of Rotational Nature of Flow.

We see from Fig. IV-1-5 that

$$\frac{\Delta S}{\Delta n}=\frac{S_A-S_B}{AC\sin\mu_A+BC\sin\mu_B},$$

where

$$AC=\frac{x_C-x_A}{\cos(\beta_A-\mu_A)};\quad BC=\frac{x_C-x_B}{\cos(\beta_B-\mu_B)}.$$

Introducing the notation

$$e=(x_C-x_A)\sin\mu_A\cos(\beta_B+\mu_B);$$
$$f=(x_C-x_B)\sin\mu_B\cos(\beta_A-\mu_A),$$

we obtain

$$\frac{\Delta S}{\Delta n}=\frac{(S_A-S_B)\cos(\beta_B+\mu_B)\cos(\beta_A-\mu_A)}{f+e}. \qquad \text{(IV-1-34)}$$

The absolute value of the entropy at point C is determined from the relation

$$S_C=\Delta S_B+S_B=\frac{\Delta S}{\Delta n}BC\sin\mu_B+S_B=\frac{(S_A-S_B)f}{f+e}+S_B. \qquad \text{(IV-1-35)}$$

The stagnation pressure gradient along a streamline normal is determined with a formula similar to (IV-1-34):

$$\frac{\Delta p_0'}{\Delta n}=\frac{(p_{0A}'-p_{0B}')\cos(\beta_B+\mu_B)\cos(\beta_A-\mu_A)}{f+e}, \qquad \text{(IV-1-36)}$$

where p'_{0A} and p'_{0B} are the stagnation pressures at point A and B, respectively.

The sign of the ratio $\Delta p_0'/\Delta n$ depends on the manner of stagnation-pressure variation with movement along the streamline normal from point A to point B. In flow over bodies with a curvilinear shock, the stagnation pressure diminishes on passage to streamlines nearer the body surface. And this is understandable, since the wave becomes more intense with this transition and flow through it is accompanied by a larger entropy increase. If point B is nearer the surface, $\Delta p_0'/\Delta n - (p'_{0A} - p'_{0B})/\Delta n$ is positive, since the stagnation pressure p'_{0B} at this point is lower than that at point A. The stagnation pressure at point C on the intersection of characteristics of different families passing through points A and B is calculated by analogy with (IV-1-35) from the expression

$$p'_{0C} = p'_{0B} + \frac{(p'_{0A} - p'_{0B})f}{f+\varepsilon}. \qquad \text{(IV-1-37)}$$

The unknowns in equation system (IV-1-30) and (IV-1-32) are the increments $\Delta\omega_B$, $\Delta\omega_A$, $\Delta\beta_B$ and $\Delta\beta_A$. The number of these unknowns can be reduced to two if we remember that

$$\Delta\omega_B = \Delta\omega_A + \omega_A - \omega_B; \quad \Delta\beta_B = \Delta\beta_A + \beta_A - \beta_B.$$

Accordingly, (IV-1-32) is transformed to

$$\Delta\omega_B + \Delta\beta_B - \omega_A + \omega_B - \beta_A + \beta_B - \varepsilon\frac{\Delta x_A}{y_A} m_A - \frac{\Delta x_A}{kR}\frac{\Delta S}{\Delta n} l_A = 0. \qquad \text{(IV-1-38)}$$

Solving this equation simultaneously with (IV-1-30) for the variable $\Delta\beta_B$, we obtain /150

$$\Delta\beta_B = \frac{1}{2}\left[\left(\frac{\Delta x_A}{y_A} m_A - \frac{\Delta x_B}{y_B} l_B\right)\varepsilon + \right.$$
$$\left. + \frac{1}{kR}\frac{\Delta S}{\Delta n}(\Delta x_A l_A + \Delta x_B c_B) - (\omega_B - \omega_A) - (\beta_B - \beta_A)\right]. \qquad \text{(IV-1-39)}$$

From the value determined for $\Delta\beta_B$ from (IV-1-30) or (IV-1-38), we find the second unknown $\Delta\omega_B$. We can now calculate the angles $\beta_C = \beta_B + \Delta\beta_B$ and $\omega_C = \omega_B + \Delta\omega_B$ for point C. Then, using Table IV-1-1, we determine M_C and the Mach angle μ_C for this point from ω_C. If necessary, we can find other variables, i.e., pressure,

density, temperature, etc. The variables calculated in this way represent a first approximation, since the coefficients ℓ and m and the coordinates of the points under consideration were assumed constant along elements of the characteristics and equal to their respective values at points A and B. These variables can be improved if we substitute values calculated as means between those assigned at points A and B and those obtained at point C in the first approximation for ℓ_B, m_A, y_B, y_A in Eqs. (IV-1-30) and (IV-1-32). In performing the calculations, it must be remembered that the initial points A and B need not lie on the same characteristic.

Let us examine the second problem formulated above, which consists in determination of the velocity at point B at the intersection of element DB of the second-family characteristic with the contour of the body (see Fig. IV-1-4b). Here the magnitude and direction of the velocity at point D and the coordinates of the point are known.

The velocity at point B is determined directly with (IV-1-32), relating it to the conditions along element DB of the second-family characteristic and writing it in finite differences:

$$\Delta\omega_D = -\Delta\beta_D + \varepsilon \frac{\Delta x_D}{y_D} m_D - \frac{\Delta x_D}{k p'_{0}} \frac{\Delta p'_0}{\Delta n} t_D. \qquad \text{(IV-1-40)}$$

In this equation, the increment $\Delta\beta_D = \beta_B - \beta_D$ is the difference between the velocity-vector inclination angles at points B and D. Here, the angle β_B at point B is determined (in accordance with the condition of no flow separation from the surface) by the slope of the tangent to it at this point, i.e., $\tan \beta_B = (dy/dx)_B$. In turn, $\tan \beta_B$ is calculated from the equation of the generatrix $y = f(x)$ and the coordinates x_B and y_B, which are found by simultaneous solution of the equations

$$y_B - y_D = (x_B - x_D) \operatorname{tg} (\beta_D - \mu_D) \text{ and } y_B = f(x_B). \qquad \text{(IV-1-41)}$$

Calculating the stagnation-pressure gradient

$$\frac{\Delta p'_0}{\Delta n} = \frac{(p'_{0B} - p'_{0D}) \cos (\beta_B - \mu_B)}{(x_D - x_B) \sin \mu_B}$$

and substituting it in (IV-1-40), we can determine the increment $\Delta\omega_D$, find the angle $\omega_B = \Delta\omega_D + \omega_D$ from it, and calculate M_B and the corresponding Mach angle μ_B.

This numerical calculation method pertains to the general case of rotational two-dimensional flow. These calculations are simplified for isentropic flow. The corresponding equation system for the characteristics, written in finite differences, has the form:

a) for the first family /151

$$\Delta y_B = \operatorname{tg}(\beta_B + \mu_B)\,\Delta x_B; \qquad \text{(IV-1-42)}$$

$$\Delta\omega_B - \Delta\beta_B - \varepsilon\frac{\Delta x_B}{y_B} l_B = 0; \qquad \text{(IV-1-43)}$$

b) for the second family

$$\Delta y_A = \operatorname{tg}(\beta_A - \mu_A)\,\Delta x_A; \qquad \text{(IV-1-44)}$$

$$\Delta\omega_A + \Delta\beta_B - \varepsilon\frac{\Delta x_A}{y_A} m_A = 0. \qquad \text{(IV-1-45)}$$

We must put $\varepsilon = 0$ in (IV-1-43) and (IV-1-45) for plane potential flow and $\varepsilon = 1$ for spatial axisymmetric flow. We can also examine the case of plane nonisentropic flow. The corresponding equations for the characteristics take the form of (IV-1-30) and (IV-1-32), in which we set $\varepsilon = 0$.

Characteristics in a Dissociating Gas

The equations for the characteristics in a physical plane taken in a flow of a dissociating gas take the form of (IV-1-19) and (IV-1-21), with the provision that the local Mach numbers M and the corresponding Mach angles $\mu = \text{arc sin } (a/V)$ must be computed with consideration of both the temperature and pressure variations of the speed of sound.

To account for the influence of dissociation in determining flow variables, the latter must be considered as functions of the local Mach number M or, what is the same thing, of the Mach angle, calculated by the method indicated. With this in mind, we can use the equations for the characteristics in the hodograph plane, (IV-1-12), in the calculations after making certain modifications.

The latter proceed from the condition that $di = -VdV$ for a homogeneous oncoming flow. Moreover, the ratio of specific heats k and the gas constant are to be replaced by their values for a

nonideal gas, i.e., $k = k_n$ and $R = R_n$, where $R_n = R_0/\mu_{av}$. After making these transformations and appending (IV-1-19) and (IV-1-21), we obtain the following equation system for the characteristics of dissociating nonisentropic flow:

a) for the first family

$$dy = \operatorname{tg}(\beta+\mu)\,dx; \tag{IV-1-46}$$

$$-d\beta - f(\mu)\,d\mu - \varepsilon\frac{dx}{y}\frac{\sin\beta\sin\mu}{\cos(\beta+\mu)} + \frac{dx}{k_nR_n}\frac{\sin^2\mu\cos\mu}{\cos(\beta+\mu)}\frac{dS}{dn} = 0; \tag{IV-1-47}$$

b) for the second family

$$dy = \operatorname{tg}(\beta-\mu)\,dx; \tag{IV-1-48}$$

$$d\beta - f(\mu)\,d\mu - \varepsilon\frac{dx}{y}\frac{\sin\beta\sin\mu}{\cos(\beta-\mu)} - \frac{dx}{k_nR_n}\frac{\sin^2\mu\cos\mu}{\cos(\beta-\mu)}\frac{dS}{dn} = 0, \tag{IV-1-49}$$

where

$$f(\mu) = \frac{\sin\mu\cos\mu}{a^2}\frac{di}{d\mu}. \tag{IV-1-50}$$

In performing numerical calculations, the equations for the characteristics are represented in finite-difference form and the resulting system is solved by iteration. This system differs from the corresponding system for the ideal gas in the function $f(\mu)$ and the product k_nR_n. For an ideal gas

$$f(\mu) = f^0(\mu) = \frac{1+\cos 2\mu}{k-\cos 2\mu};\ k_nR_n = kR. \tag{IV-1-51}$$

Here we see that for the real gas, the function $f(\mu)$ cannot be presented in explicit form. In calculating flows of a real gas, it is more convenient to use instead of $f(\mu)$ the ratio $z(\mu) = f(\mu)/f^0(\mu)$, and instead of k_nR_n the ratio $\overline{kR} = k_nR_n/kR = k_n(\mu_{av})_0/k\mu_{av}$, which are equal to unity for an ideal gas. /152

An essential element in the calculation is determination of local values of the function $z(\mu)$. Knowing the conditions of the oncoming flow, we calculate the entropy behind the shock wave and, for an assigned series of possible velocity values $V_0, V_1, \ldots, V_i$, we find the corresponding series of enthalpies $i_i = i_0 + 0.5V_0^2 - 0.5V_i^2$. With the enthropy and enthalpy, we can refer to tables

or curves of the thermodynamic functions to determine pressure, temperature, and the speed of sound, and then the M_i and the Mach angle μ_i at this point. With these data, we can plot an $i(\mu)$ curve, find the derivative $di/d\mu = f(\mu)$, and calculate the function $z(\mu)$.

The equations for the characteristics, (IV-1-47) and (IV-1-49), are simplified in the case of a dissociating rotational flow, since the derivative $dS/dn = 0$. The equations for plane dissociating irrotational flow are even simpler, since the third term also drops out of the equations because $\varepsilon = 0$.

§IV-2. CONICAL FLOWS

Supersonic flows past certain sharp bodies (cone, wing with delta planform) have the property that the flow variables remain the same along every straight line passing through the apex of the body and change at passage from one straight line to another. Such a flow is said to be conical.

The equations of a conical flow can be derived from the general equations of gasdynamics. In spherical coordinates with the origin at the body apex, the flow-conicity condition is that the derivatives of the variables with respect to the coordinate r be zero. In particular, the derivatives $\partial V_r/\partial r$, $\partial V_\theta/\partial r$, $\partial V_\psi/\partial r$, $\partial p/\partial r$ are zero. Assuming also that a conical flow is steady, we obtain the equations of motion and continuity for it in the form

$$\left.\begin{aligned} V_\theta\frac{\partial V_r}{\partial\theta}+\frac{V_\psi}{\sin\psi}\frac{\partial V_r}{\partial\psi}-V_\theta^2-V_\psi^2=0;\\ V_\theta\frac{\partial V_\theta}{\partial\theta}+\frac{V_\psi}{\sin\psi}\frac{\partial V_\theta}{\partial\psi}+V_rV_\theta-V_\psi^2\operatorname{ctg}\theta=-\frac{1}{\rho}\frac{\partial p}{\partial\theta};\\ V_\theta\frac{\partial V_\psi}{\partial\theta}+\frac{V_\psi}{\sin\psi}\frac{\partial V_\psi}{\partial\psi}+V_\psi V_\theta-V_\theta V_\psi\operatorname{ctg}\theta=-\frac{1}{\rho\sin\psi}\frac{\partial p}{\partial\psi};\end{aligned}\right\} \quad \text{(IV-2-1)}$$

$$2\rho V_r\sin\psi+\frac{\partial(\rho V_\theta\sin\psi)}{\partial\theta}+\frac{\partial(\rho V_\psi)}{\partial\psi}=0. \quad \text{(IV-2-2)}$$

This equation system describes a nonisentropic conical flow.

If the flow is irrotational (or is assumed to be so with some approximation), we can use the equation for the velocity potential of the conical flow.

In accordance with the fundamental property of a conical flow, the solution for the potential function is sought in the form

$$\varphi(x, y, z)=xF\left(\frac{y}{x}, \frac{z}{x}\right). \quad \text{(IV-2-3)}$$

Calculating the derivatives, we find the velocity components /153

$$\left.\begin{aligned} \varphi_x &= F - \eta F_\eta - \varepsilon F_\varepsilon; \\ \varphi_y &= F_\eta; \\ \varphi_z &= F_\varepsilon, \end{aligned}\right\} \qquad \text{(IV-2-4)}$$

where we have introduced the nomenclature $\eta = y/x$, $\varepsilon = z/x$; $F_\eta = \partial F/\partial\eta$, $F_\varepsilon = \partial F/\partial\varepsilon$. Determining the second derivatives φ_{xx}, φ_{yy}, φ_{zz} from (IV-2-4) and introducing them into (III-2-30), which describes a weakly disturbed flow, we obtain the equation for a linearized conical flow:

$$(1-\alpha'^2\eta^2)F_{\eta\eta} + (1-\alpha'^2\varepsilon^2)F_{\varepsilon\varepsilon} - 2\varepsilon\eta\alpha'^2F_{\eta\varepsilon} = 0, \qquad \text{(IV-2-5)}$$

where

$$F_{\eta\eta} = \partial^2F/\partial\eta^2;\ F_{\varepsilon\varepsilon} = \partial^2F/\partial\varepsilon^2;\ F_{\eta\varepsilon} = \partial^2F/\partial\eta\,\partial\varepsilon.$$

Let us consider a conical irrotational flow in spherical coordinates. The general solution for the potential function of such a flow is

$$\Phi = rF(0, \psi). \qquad \text{(IV-2-6)}$$

The velocity components

$$V_r = \Phi_r = F;\ V_\theta = \frac{\Phi_\theta}{r} = F_\theta;\ V_\psi = \frac{\Phi_\psi}{r\sin\theta} = \frac{F_\psi}{\sin\theta}.$$

Hence follows a relationship important to conical-flow theory:

$$V_\theta = \frac{\partial V_r}{\partial\theta}, \qquad \text{(IV-2-7)}$$

one that enables us further to simplify System (IV-2-1) and (IV-2-2) for unsymmetrical conical potential flow. The equation system will be even simpler for a symmetrical conical flow, because the velocity component $V_\psi = 0$ and all derivatives with respect to ψ are also equal to zero. Combining the equations of motion and continuity obtained as a result of the simplification, we arrive at the following equation for a conical symmetrical flow:

$$\left(1-\frac{V_\theta^2}{a^2}\right)\frac{dV_\theta}{d\theta}+V_r\left(2-\frac{V_\theta^2}{a^2}\right)+V_\theta \operatorname{ctg}\theta=0. \qquad \text{(VI-2-8)}$$

This equation can be derived from (III-2-27) by setting $\partial V_r/\partial r=\partial V_\theta/\partial r=\bar{0}$, $\partial V_r/\partial\bar{\theta}=\bar{V}_\theta$.

§IV-3. THE METHOD OF SOURCES

The method of sources enables us to obtain the solution to (III-2-30) for the velocity potential of a weakly disturbed flow in its general form. Physically, this method is based on the possibility of substituting the flow from a unit source or from a system of sources distributed in accordance with some law for the flow represented by (III-2-30).

The source potential function can be obtained as follows. Let Q_n be the power of a point source of an incompressible fluid. Then the source potential in the coordinate system x_n, y_n, z_n will be $\phi_n = -Q_n/4\pi R_n$, where $R_n = \sqrt{x_n^2 + y_n^2 + z_n^2}$.

We usually deal with a system of continuously distributed sources whose elementary power can be represented in the form $dQ_n/f_n d\sigma$, where f_n is the density or intensity of the distributed sources and $d\sigma = d\eta d\zeta$ is an elementary area on the plane $y = 0$.

It follows from (III-2-30) for the condition $\phi_t = 0$ that the following affine relation exists between the coordinates x_n, y_n, z_n for incompressible flow and $\underline{x}$, $\underline{y}$, $\underline{z}$ for a subsonic flow: $x_n = x(1 - M^2)^{-1/2}$; $y_n = y$; $z_n = z$. Hence the elementary potential for the subsonic source is $d\phi = -f d\sigma/4\pi R$, where $R=\sqrt{x^2+(1-M^2)(y^2+z^2)}$. By direct substitution one can prove that the expression for $d\phi$ satisfies (III-2-30) for both subsonic and supersonic steady flows. /154

For supersonic velocities, the expression for $d\phi$ applies not over the entire region of the flow, but only for that part of it where $x^2 \geq (M^2 - 1)(y^2 + z^2)$. Thus, the sources influence the flow inside the space bounded by the surface described by the equation $x^2 = (M^2 - 1)(y^2 + z^2)$. This surface is a Mach cone with a generatrix inclination angle μ = arc sin (1/M). The region of integration in determining the velocity potential at the subject point (point A in Fig. IV-3-1) from sources distributed on a certain plane of the surface is found accordingly. The velocity potential

$$\varphi(x, y, z) = \iint_{\sigma} \frac{f(\varepsilon, \zeta)\, d\varepsilon\, d\zeta}{\sqrt{(x-\varepsilon)^2 - (M^2-1)\,[y^2+(z-\zeta)^2]}}, \qquad \text{(IV-3-1)}$$

where σ is the range of integration and $1/2\pi$ is a constant coefficient incorporated into the function $f(\varepsilon,\zeta)$.

For the two-dimensional case

$$\varphi(x, y) = \int_{0}^{\varepsilon} \frac{f(\varepsilon)\, d\varepsilon}{\sqrt{(x-\varepsilon)^2 - (M^2-1)\, y^2}}, \qquad \text{(IV-3-2)}$$

where the upper limit corresponds to the limit of influence of a supersonic source.

The expression found for the velocity potential forms the basis for the method of sources, according to which the body in the flow is replaced by a system of continuously distributed sources and sinks. The source-distribution law, i.e., the form of the function $f(\varepsilon,\zeta)$ must be such that the flow boundary conditions will be satisfied as a result of superimposing the undisturbed flow on the flow from these sources.

In flow over surfaces with formation of a lifting force, the disturbed flow must be replaced not only by sources and sinks, but also by dipoles. This follows from the fact that the differential equation of the flow is satisfied if the potential function is composed of sources (sinks) and a certain auxiliary function known as a dipole. Physically, a dipole is a flow formed as a result of infinitesimally close approach of a source and sink of identical intensity Q with the product Qh, where h is the distance between the source and the sink, held constant. This constant is known as the intensity or moment of the dipole.

The dipole potential can be determined from the following considerations. Let sources and sinks disposed on both sides of the plane $y = 0$ at the respective distances $y = h/2$ and $y = -h/2$ be brought toward one another, so that $h \to 0$. The resultant potential $\phi_{dip} = h(\partial\phi_{src}/\partial y$, i.e.,

$$\varphi_{dip} = \frac{\partial}{\partial y} \iint_{\sigma} \frac{hf(\varepsilon, \zeta)\, d\varepsilon\, d\zeta}{\sqrt{(x-\varepsilon)^2 - (M^2-1)\,[y^2+(z-\zeta)^2]}}, \qquad \text{(IV-3-3)}$$

where $hf = m(\varepsilon,\zeta)$ is the dipole intensity (moment) distribution function.

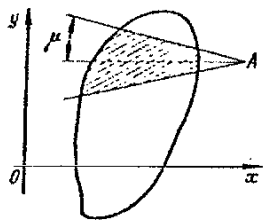

Figure IV-3-1. Region of Integration in Determining Velocity Potential by Source Method.

§IV-4. THEORY OF SUPERSONIC FLOW PAST SLENDER BODIES WITH ARBITRARY CROSS SECTION

/155

Solution of the Potential Equation

Velocity potential. The linearized potential equation, which has the form of (III-2-31) in the cylindrical coordinate system x, r, γ, forms the basis for the theory of steady supersonic flow past slender bodies.

The solution of this equation, in which it is assumed that $\phi_t = 0$, can be obtained in general form with the aid of the Laplace transformation [51]. Accordingly, the potential $\phi(x,r,\gamma)$ is transformed to the form $\Phi(p,r,\gamma)$ by means of the operator

$$L[\varphi(x, r, \gamma)] \equiv \int_0^\infty e^{-px}\varphi(x, r, \gamma)\,dx, \qquad \text{(IV-4-1)}$$

where p is the parameter of the transformation. Here $L[\phi(x,r,\gamma)] = \Phi(p,r,\gamma)$.

Applying the Laplace transformation to the individual terms in (III-2-31), we obtain

$$L[\varphi_{rr}] = \Phi_{rr};\ L[\varphi_r] = \Phi_r;\ L[\varphi_{\gamma\gamma}] = \Phi_{\gamma\gamma},\ L[\varphi_{xx}] = \Phi_{xx}p^2.$$

(Here it has been taken into account that $\phi(0,r,\gamma) = 0$, $\phi_x(0,r,\gamma) = 0$.)

As a result, the transform of (III-2-31) will be

$$\Phi_{rr} + \frac{1}{r}\Phi_r + \frac{1}{r^2}\Phi_{\gamma\gamma} = \alpha'^2 p^2 \Phi, \text{ where } \alpha'^2 = M^2 - 1. \qquad \text{(IV-4-2)}$$

The general solution of (IV-4-2) can be obtained by the Fourier method as the series

$$\Phi = \sum_{n=0}^{\infty} (C_n \sin n\gamma + D_n \cos n\gamma) I_n(\alpha' pr) + \sum_{n=0}^{\infty} (E_n \sin n\gamma + F_n \cos n\gamma) K_n(\alpha' pr). \qquad \text{(IV-4-3)}$$

In the general case, the coefficients C_n, D_n, E_n, and F_n depend on p and are so selected as to satisfy the boundary conditions.

The functions I_n and K_n are Bessel functions of an imaginary argument. Investigation has shown that only the function K_n (the MacDonald function) has physical significance for supersonic flow past sharp bodies. In (IV-4-3), therefore, we must set $C_n = 0$ and $D_n = 0$. Introducing A_n and δ_n in place of the functions E_n and F_n, we obtain the solution for Φ in the form:

$$\Phi = A_0 K_0(\alpha' pr) + \sum_{n=1}^{\infty} A_n K_n(\alpha' pr)\cos(n\gamma + \delta_n). \qquad \text{(IV-4-4)}$$

The quantity δ_n is a certain phase angle.

When the transverse dimensions of the body are very small, (IV-4-4) can be simplified. It is this case that is analyzed in the aerodynamic theory of the slender body. For small r, we have [51]:

$$K_0(\alpha' pr) = -\left(C + \ln\frac{\alpha' pr}{2}\right)[1 + O(r^2)];$$
$$K_1(\alpha' pr) = \frac{1}{\alpha' pr}[1 + O(r^2 \ln r)];$$
$$K_n(\alpha' pr) = \frac{(n-1)!}{2}\left(\frac{2}{\alpha' pr}\right)^n [1 + O(r^2)],$$

where O signifies order of magnitude and C is Euler's constant. /156

Then (IV-4-4) assumes the form

$$\Phi = -\left(C + \ln\frac{\alpha' pr}{2}\right)A_0 + \frac{1}{2}\sum_{n=1}^{\infty}(n-1)!\left(\frac{2}{\alpha' pr}\right)^n A_n \cos(n\gamma + \delta_n). \qquad \text{(IV-4-5)}$$

To convert to the potential ϕ, we must apply the inverse Laplace transformation to the terms on the right side of (IV-4-5). We introduce the notation

$$a_0(x) = L^{-1}[-A_0(p)];$$
$$b_0(x) = L^{-1}\left[-\left(C + \ln\frac{\alpha' p}{2}\right)A_0(p)\right]; \qquad \text{(IV-4-6)}$$

$$a_n(x) = A_n(x) - iB_n(x) = L^{-1}\left[\frac{(n-1)!}{2!}\left(\frac{2l}{\alpha' p}\right)^n A_{n_0}^{l}(p)\, e^{i\delta_n}\right] \qquad \text{(IV-4-6)}$$
(Cont'd.)

Then

$$\varphi = a_0 \ln r + b_0 + \sum_{n=1}^{\infty} \frac{A_n \cos n\gamma + B_n \sin n\gamma}{r^n}. \qquad \text{(IV-4-7)}$$

The potential-function component ϕ_t governed by the thickness of the body and the component ϕ_α, which characterizes the attitude of the body in the flow, can be isolated from this expression:

$$\varphi_t = a_0 \ln r + b_0; \qquad \text{(IV-4-8)}$$

$$\varphi_\alpha = \sum_{n=1}^{\infty} \frac{A_n \cos n\gamma + B_n \sin n\gamma}{r^n}. \qquad \text{(IV-4-9)}$$

Thus, the total potential

$$\varphi = \varphi_t + \varphi_\alpha. \qquad \text{(IV-4-10)}$$

Velocity potential for unsymmetrical flow past a slender solid of revolution. For a slender solid of revolution, the potential function can be obtained in a simpler and more concrete form. For this purpose, we start with the equation of motion written for the body axes x_1, y_1, z_1 (Fig. IV-4-1). The equation will be analogous in cylindrical coordinates (III-2-31) with x_1, $\underline{r}$, and γ substituted for $\underline{x}$, $\underline{r}$, γ, respectively.

The flow past a slender solid of revolution may be regarded as consisting of two superimposed flows (see Fig. IV-4-1): a longitudinal (symmetrical) flow with velocity $V_\infty \cos\alpha \approx V_\infty$ and a transverse flow with velocity $V_\infty \sin\alpha \approx V_\infty\alpha$. The longitudinal flow governs the potential component ϕ_t that depends on the thickness of the body, and the transverse flow, i.e., the component ϕ_α, which is related to angle of attack.

We may convince ourselves by direct substitution that the expression

$$\varphi = \varphi_t + \varphi_\alpha = \int_0^{x_1-\alpha' r} \frac{f(\varepsilon)\,d\varepsilon}{\sqrt{(x_1-\varepsilon)^2-\alpha'^2 r^2}} + \frac{\cos\gamma}{x_1}\frac{\partial}{\partial x_1}\int_0^{x_1-\alpha' r} \frac{m(\varepsilon)(x_1-\varepsilon)\,d\varepsilon}{\sqrt{(x_1-\varepsilon)^2-\alpha'^2 r^2}} \qquad \text{(IV-4-11)}$$

does indeed satisfy (III-2-31).

The function $f(\varepsilon)$ determines the distribution intensity of the sources (sinks), and $m(\varepsilon)$ the dipole distribution intensity.

Expression (IV-4-11) is the potential function corresponding to the linear theory of flow over solids of revolution. A further simplification can be obtained within the framework of flow theory for very slender solids in which the radius r_0 is small by comparison with the distance x_1 and $(x_1 - \varepsilon)/\alpha' r$ is large (with the exception of a small neighborhood around the nose, but this is not essential). /157

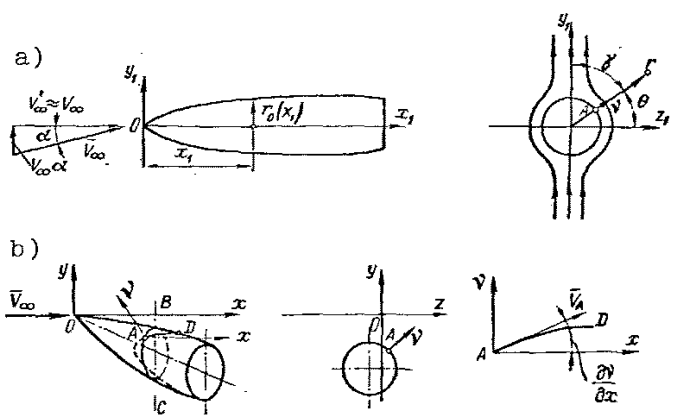

Figure IV-4-1. Unsymmetrical Flow Past Solid of Revolution. a) body coordinate system; b) wind system.

With this condition, the component

$$\varphi_t = \frac{\partial}{\partial x_1}\int_0^{x_1-\alpha' r} f(\varepsilon)\ \text{arc cosh}\ \frac{x_1-\varepsilon}{\alpha' r}\,d\varepsilon. \qquad \text{(IV-4-12)}$$

For a slender body, the inverse hyperbolic cosine can be represented approximately in the form $\text{arc cosh}\,[(x_1-\varepsilon)/\alpha' r] \simeq \ln[2(x_1-\varepsilon)/\alpha' r]$. As a result, we obtain the equation $\partial\varphi_t/\partial r = -f(x_1-\alpha' r)/r$.

Since on the surface of the body

$$\frac{1}{V_\infty}\frac{\partial \varphi_t}{\partial r}=\frac{V_r}{V_{\infty i}}=\frac{dr}{dx_1}=\frac{S'(x_1)}{2\pi r}, \qquad \text{(IV-4-13)}$$

where $S(x_1)$ is the law of variation of the body's cross-sectional area over its length

$$f(x_1-\alpha' r)=-\frac{V_\infty S'(x_1)}{2\pi}. \qquad \text{(IV-4-14)}$$

Consequently,

$$\varphi_t=\frac{S'(x_1)}{2\pi}\ln r+\frac{S'(x_1)}{2\pi}\ln\frac{\alpha'}{2}-\frac{1}{2\pi}\frac{\partial}{\partial x_1}\int_0^{x_1}S'(\varepsilon)\ln(x_1-\varepsilon)\,d\varepsilon. \qquad \text{(IV-4-15)}$$

In this expression, the velocity V_∞ is incorporated into ϕ_t.

To obtain the function ϕ_α for a slender body, it is necessary to pass to the limit as $r \to 0$ in the second term on the right in (IV-4-11). As a result, we find $\varphi_\alpha=(\cos\gamma/r)\,m(x_1)$, where the function $m(x_1)$ is determined from the condition for nonseparation of flow:

$$\frac{1}{V_\infty}\left[\frac{\partial \varphi_t}{\partial r}+\alpha V_\infty\cos\gamma-\frac{\cos\gamma}{r^2}m(x_1)\right]=\frac{dr}{dx_1}. \qquad \text{(IV-4-16)}$$

But the condition $(1/V_\infty)\,\partial\varphi_t/\partial r=dr/dx_1$ is satisfied in symmetrical flow. Consequently, $m(x_1)=\alpha V_\infty r^2$. Accordingly,

$$\varphi_\alpha=\frac{\cos\gamma_1}{r}r^2\alpha, \qquad \text{(IV-4-17)}$$

where ϕ_α is a function that includes the constant V_∞.

The complex potential. Studies have shown that in flow of a compressible fluid over a slender body, density varies extremely slightly, so that the ratio $\rho/\rho_\infty=1+O(t^2)$, where t is the body's thickness ratio. Accurate to $O(t^2)$, we may assume that $\rho/\rho_\infty\simeq 1$, so that /158

$$V_r = \frac{1}{r}\frac{\partial\psi}{\partial\gamma}, \quad V_\gamma = -\frac{\partial\psi}{\partial r}; \qquad \text{(IV-4-18)}$$

or

$$\frac{\partial\varphi}{\partial r} = -\frac{1}{r}\frac{\partial\psi}{\partial\gamma}; \quad \frac{1}{r}\frac{\partial\varphi}{\partial\gamma} = -\frac{\partial\psi}{\partial r}. \qquad \text{(IV-4-18')}$$

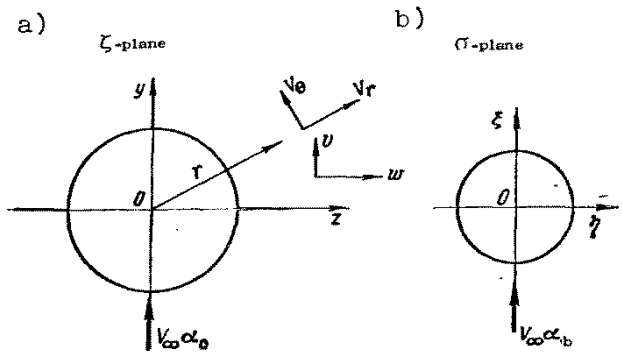

Figure IV-4-2. The Physical Plane $\zeta = z + iy$ (a) and the Transformed Plane $\sigma = \eta + i\xi$ (b).

In the theory of functions of the complex variable, these equations are known, of course, as the Cauchy-Riemann equations; they express the condition that the function

$$W(\zeta) = \varphi(r, \gamma) + i\psi(r, \gamma) \qquad \text{(IV-4-19)}$$

is an analytic function of the complex variable $\zeta = re^{-i\gamma} = z + iy$. The function (IV-4-19) is known as the complex potential.

Thus, the flow of a compressible fluid past a slender body can be characterized by the complex potential. The plane in which the flow is defined is known as the physical plane of the complex variable $\zeta = z + iy$ (Fig. IV-4-2a).

The potential ϕ can be regarded as the real part of the function $W(\zeta)$. Having (IV-4-7) for ϕ, an expression for the complex potential $W(\zeta)$ can be obtained as follows. In (IV-4-7), we substitute $\ln\zeta$ for $\ln r$, and a_n/ζ^n for the expression under the summation sign, obtaining as a result

$$W(\zeta) = a_0 \ln\zeta + b_0 + \sum_{n=1}^{\infty}\frac{a_n}{\zeta^n}. \qquad \text{(IV-4-20)}$$

In accordance with the formula $\phi = \phi_t + \phi_\alpha$, we can write a similar expression for the complex potential

$$W(\zeta) = W_t(\zeta) + W_\alpha(\zeta). \qquad \text{(IV-4-21)}$$

The boundary condition. The coefficients that appear in (IV-4-20) are determined from a boundary condition according to which the direction of the velocity at a certain point on the washed surface must coincide with the tangent to the surface at the same point. Let the subject point A (see Fig. IV-4-1) be situated in the transverse flow plane BC perpendicular to the flow axis $\underline{x}$, and let it simultaneously lie in the flow plane (the longitudinal plane containing the normal ν to the contour of the body in the transverse plane at point A and parallel to the flow axis $\underline{x}$). Curve AD in Fig. IV-4-1, which passes through point A, is the intersection of the body's surface with the flow plane. The inclination of this curve to the $\underline{x}$-axis at point A is determined by the derivative $\partial\nu/\partial x$. According to the condition of non-separating flow, the ratio of the velocity components $V_\nu/V_x = \partial\nu/\partial x$ or $(\partial\phi/\partial\nu)/(V_\infty + \partial\phi/\partial x) = \partial\nu/\partial x$. Since the disturbed axial velocity component $\partial\phi/\partial x \ll V_\infty$, the boundary condition

/159

$$\frac{\partial\varphi}{\partial\nu} = \frac{\partial\nu}{\partial x}, \qquad \text{(IV-4-22)}$$

in which the velocity V_∞ has been incorporated into the potential function ϕ.

Determination of the coefficients $a_0(x)$ and $b_0(x)$. To determine $a_0(x)$, let us examine an arbitrary neighborhood of a certain radius $\underline{r}$ in the transverse flow plane of the body and evaluate the integral over this contour:

$$\oint \frac{\partial\varphi}{\partial\nu}\,ds = \int_0^{2\pi} \frac{\partial\varphi}{\partial r}\,r\,d\gamma = \int_0^{2\pi} \left(\frac{a_0}{r} - \sum_{n=1}^{\infty} \frac{nA_n}{r^{n+1}}\cos n\gamma\right) r\,d\gamma = 2\pi a_0.$$

The integral over the same contour can be evaluated using boundary condition (IV-4-22),

$$\oint \frac{\partial\varphi}{\partial\nu}\,ds = \oint \frac{\partial\nu}{\partial x}\,ds = \int_0^{2\pi} \frac{dr}{dx}\,r\,d\gamma = \frac{1}{2}\,\frac{d}{dx}\int_0^{2\pi} r^2\,d\gamma = \frac{dS(x)}{dx} = S'(x),$$

where S(x) is the cross-sectional area of the body. Thus,

$$a_0(x)=\frac{S'(x)}{2\pi}. \qquad \text{(IV-4-23)}$$

To determine the coefficient $b_0(x)$, we use (IV-4-6). Applying the theorem of convolution of originals [51], we obtain

$$b_0(x)=\frac{1}{2\pi}\left[S'(x)\ln\frac{\alpha'}{2}-\int_0^x \ln(x-\varepsilon)S''(\varepsilon)\,d\varepsilon\right]. \qquad \text{(IV-4-24)}$$

Aerodynamic Forces and Moments

Lift and lateral force. The lift Y can be determined by calculating the change in the momentum of the fluid on passage across a reference cylindrical surface S_2 of a certain radius r in the direction of the y-axis and across the base surface S_3 in the same direction (Fig. IV-4-3a):

$$Y=-\int_{(S_2)}\left(\rho V_\infty^2\frac{\partial\varphi}{\partial r}\frac{\partial\varphi}{\partial y}+p\cos\gamma\right)dS_2-\int_{(S_3)}\rho V_\infty^2\left(1+\frac{\partial\varphi}{\partial x}\right)\frac{\partial\varphi}{\partial y}\,dS_3. \qquad \text{(IV-4-25)}$$

Calculating the change in momentum on passage in the direction of the z axis, we find the lateral force

$$Z=-\int_{(S_2)}\left(\rho V_\infty^2\frac{\partial\varphi}{\partial r}\frac{\partial\varphi}{\partial z}+p\sin\gamma\right)dS_2-\int_{(S_3)}\rho V_\infty^2\left(1+\frac{\partial\varphi}{\partial x}\right)\frac{\partial\varphi}{\partial z}\,dS_3. \qquad \text{(IV-4-26)}$$

The flow of fluid through surface S_1 does not yield lift and lateral-force components, since this surface is in an undisturbed region where $\partial\phi/\partial y = \partial\phi/\partial z = 0$ and the change in momentum in the transverse direction is zero. /160

In flow past a slender body, the density change is small; we may therefore set $\rho = \rho_\infty$ in (IV-4-25) and (IV-4-26).

It is convenient to examine the complex variable F = Z + iY instead of the forces Z and Y.

After substitution of Y and Z, we obtain the following expression for this quantity:

$$\frac{F}{q} = -2\int\limits_{(S_2)}\left[\frac{\partial\varphi}{\partial r}\left(\frac{\partial\varphi}{\partial z}+i\frac{\partial\varphi}{\partial y}\right)+\frac{\bar{p}}{2}e^{i\nu}\right]dS_2 - \\ -2\int\limits_{(S_3)}\left(1+\frac{\partial\varphi}{\partial x}\right)\left(\frac{\partial\varphi}{\partial z}+i\frac{\partial\varphi}{\partial y}\right)dS_3, \qquad \text{(IV-4-27)}$$

where $q = \rho_\infty V_\infty^2/2$, $\bar{p} = (p-p_\infty)/q$.

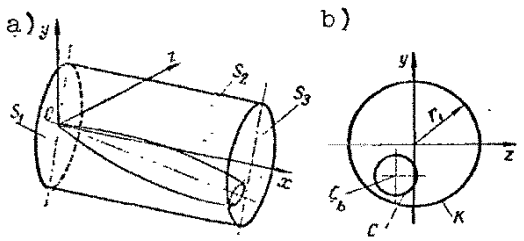

Figure IV-4-3. Cylindrical Reference Surface (a) with Two Contours (b).

Formula (IV-4-27) can be transformed by applying the relationships

$$\frac{dW}{d\zeta} = \frac{\partial\varphi}{\partial z} - i\frac{\partial\varphi}{\partial y}; \quad \frac{d\overline{W}}{dy} = \frac{\partial\varphi}{\partial z} + i\frac{\partial\varphi}{\partial y},$$

and the expression for the pressure coefficient

$$\bar{p} = -2\frac{\partial\varphi}{\partial x} - \left[\left(\frac{\partial\varphi}{\partial z}\right)^2 + \left(\frac{\partial\varphi}{\partial y}\right)^2\right] = -2\frac{\partial\varphi}{\partial x} - \frac{dW}{d\zeta}\cdot\frac{d\overline{W}}{dy}$$

As a result,

$$\frac{F}{q} = -2\int\limits_{(S_2)}\frac{\partial\varphi}{\partial r}\cdot\frac{d\overline{W}}{dy}\,dS_2 + \int\limits_{(S_2)}\left(2\frac{\partial\varphi}{\partial x} + \frac{dW}{\partial\zeta}\cdot\frac{d\overline{W}}{\partial y}\right)e^{i\nu}\,dS_2 - \\ -2\int\limits_{(S_3)}\left(1+\frac{\partial\varphi}{\partial x}\right)\left(\frac{\partial\varphi}{\partial z}+i\frac{\partial\varphi}{\partial y}\right)dS_3. \qquad \text{(IV-4-27')}$$

The first two integrals can be evaluated by the Stokes formula for a certain arbitrary circular contour K of radius r_1 that encloses the reference surface S_2 (see Fig. IV-4-3b). Since

$dS_2 = r_1\,d\gamma\,dx$, the Stokes formula indicates that the integral is of the form $\int\limits_{(S_2)} f\,dS_2 = \int\limits_0^{2\pi}\int\limits_0^1 f r_1\,d\gamma\,dx$. Let us also examine contour C, which coincides with the base-section contour. According to the Stokes formula

$$\int\limits_{(S_3)} \left(\frac{\partial\varphi}{\partial z} + i\frac{\partial\varphi}{\partial y}\right) dS_3 = i\oint\limits_K \varphi\,(dz + i\,dy) - i\oint\limits_C \varphi\,(dz + i\,dy).$$

Since $dz + i\,dy = d\zeta$ and $d\zeta = r_1\,de^{i\gamma} = r_1 ie^{i\gamma}\,d\gamma$, and the contour coincides with our circle of radius r_1,

$$\int\limits_{S_3)} \left(\frac{\partial\varphi}{\partial z} + i\frac{\partial\varphi}{\partial y}\right) dS_3 = i\oint\limits_C \varphi\,d\zeta + \int\limits_0^{2\pi}\int\limits_0^1 r_1 e^{i\gamma}\frac{\partial\varphi}{\partial x}\,d\gamma\,dx.$$

With the above transformations, /161

$$\frac{F}{q} = -2i\oint\limits_C \varphi\,d\zeta - \int\limits_0^{2\pi}\int\limits_0^1 \left(2\frac{\partial\varphi}{\partial r}\frac{d\overline{W}}{dy} - \frac{dW}{d\zeta}\frac{d\overline{W}}{dy}e^{i\gamma}\right) r_1\,d\gamma\,dx.$$

With increasing contour radius r_1, which can be chosen arbitrarily, the disturbances diminish. At the limit, as $r \to \infty$, the disturbed-velocity components $\partial\phi/\partial r$, $d\overline{W}/dy$ and $dW/d\zeta$ and, consequently, the double integral vanish. With this in mind, we obtain $F = -2qi\oint\varphi\,d\zeta$ for the complex force. With additional transformation [51], we can find the more workable formula

$$\frac{F}{q} = \frac{Z + iY}{q} = 4\pi a_1(1) + 2[S'(1)\zeta_b + S(1)\zeta_b'], \qquad \text{(IV-4-28)}$$

where $\zeta_b = z_b + iy_b$; z_b, y_b are the coordinates of the center of gravity of the body's base plane S(1); the derivative $\zeta_b' = d\zeta_b/dx$.

Separating the real and imaginary parts from (IV-4-28), we obtain the lateral force and lift, respectively.

Moment. In complex form,

$$M = M_z + iM_y = i\int_0^x x\,\frac{dF}{dx}\,dx.$$

Integrating by parts and setting x = 1, we obtain after certain transformations

$$\frac{M}{q} = \frac{M_z + iM_y}{q} = 4\pi i a_1(1) + 2i\left[S'(1)\,\zeta_д + S(1)\,\zeta_д'\right] - 4\pi i\int_0^1 a_1\,dx - 2\pi S(1)\,\zeta_д. \qquad \text{(IV-4-29)}$$

The real part of this complex function gives the moment about the z-axis (pitching moment M_z), and the imaginary part the moment about the y-axis (the yawing moment M_y).

Drag. The drag, which is determined by the momentum change on passage of the fluid across the reference surface shown in Fig. IV-4-3a in the direction of the x-axis, is

$$X = \int_{(S_1)} (p_\infty + \rho_\infty V_\infty^2)\,dS_1 - \int_{(S_3)} \left[p + \rho V_\infty^2\left(1 + \frac{\partial\varphi}{\partial x}\right)^2\right] dS_3 - \int_{(S_2)} \rho V_\infty^2 \frac{\partial\varphi}{\partial r}\left(1 + \frac{\partial\varphi}{\partial x}\right) dS_2.$$

Certain simplifications can be managed in this expression by using the equation of conservation of flowrate:

$$\int_{(S_1)} \rho_\infty V_\infty\,dS_1 - \int_{(S_2)} \rho V_\infty \frac{\partial\varphi}{\partial r}\,dS_2 - \int_{(S_3)} \rho V_\infty\left(1 + \frac{\partial\varphi}{\partial x}\right) dS_3 = 0$$

and the pressure-coefficient formula

$$\bar{p} = \frac{p - p_\infty}{q} = -2\,\frac{\partial\varphi}{\partial x} - \left[\left(\frac{\partial\varphi}{\partial r}\right)^2 + \frac{1}{r^2}\left(\frac{\partial\varphi}{\partial\gamma}\right)^2\right].$$

Setting $\rho = \rho_\infty$ and disregarding $\partial\phi/\partial x$ as small by comparison with unity, we obtain the following drag formula after substitution of ϕ from (IV-4-7) and rearranging: /162

$$\frac{X}{q} = -\frac{1}{2\pi}\int_0^1\int_0^1 \ln\frac{1}{|x-\varepsilon|}S''(x)\,S''(\varepsilon)\,dx\,d\varepsilon - \frac{S'(1)}{2\pi}\int_0^1 \ln\frac{1}{|1-\varepsilon|}S''(\varepsilon)\,d\varepsilon - \oint_C \varphi\frac{\partial\varphi}{\partial\nu}\,dS. \qquad \text{(IV-4-30)}$$

This formula determines the wave drag of slender elongated bodies, including solids of revolution and bodies with arbitrary cross sections. The first two terms give the drag due to distribution of thickness over the length of the body independently of the shape and inclination of the cross section. This drag is independent of angle of attack and, consequently, also of lift.

The third term determines the drag that depends on cross-section inclination. Since $\phi = \phi_t + \phi\alpha$, where $\phi\alpha$ is the potential governed by transverse flow, part of the drag will depend on lift. Research has shown that this part of drag is equal to $0.5\alpha Y$. Thus, the total drag

$$X = X_0 + 0.5\alpha Y, \qquad \text{(IV-4-31)}$$

where X_0 is the drag at zero lift.

The Method of Conformal Transformation

It was shown above (IV-4-18) that for high-velocity flow over a slender body, the flow in the cross section (normal to the body's longitudinal axis) may be regarded as potential and independent of Mach number. Such a flow can be studied with the aid of the complex potential (IV-4-19), which depends on the shape of the body's cross-sectional contour.

In many problems with complex contour shapes, the complex potential is determined indirectly, using the method of conformal transformation. To use this method, it is necessary to know the complex potential of flow past a circular cylinder. The conformal transformation method enables us to pass from this particular case to construction of complex potentials for flows over contours of arbitrary shape.

The essentials of the conformal-transformation method are set forth rather exhaustively in [1]. We briefly recall certain basic propositions of this method. Assume that in a certain region S in the plane of the complex variable $\zeta = z + iy$ we have given an analytic function $\sigma = f(\zeta) = \eta + i\xi$, i.e., a function that is single-valued and differentiable at each point in the region under consideration. The aggregate of points $\sigma = f(\zeta)$

corresponding to points of region S forms a new region S_1 in the σ-plane (transformed plane). Consequently, the single-valued analytic function $\sigma = f(\zeta)$ maps region S of the $\zeta = z + iy$ plane onto region S_1 of the transformed plane $\sigma = \eta + i\xi$.

Thus, we can accomplish this mapping if we know the transformation formula $\sigma = f(\zeta)$ (mapping function), which establishes the relation between the complex variables σ and ζ. By way of example, let us consider the transformation of N.Ye. Zhukovskiy:

$$\zeta = \sigma + \frac{r^2}{\sigma}.$$

Let us assume that $\zeta = z_1 + iy_1$ (z_1 and y_1 are bound coordinates for the washed surface) and $\sigma = \eta + i\xi$. Then /163

$$z_1 + iy_1 = \eta + i\xi + \frac{r_0^2}{\eta + i\xi}.$$

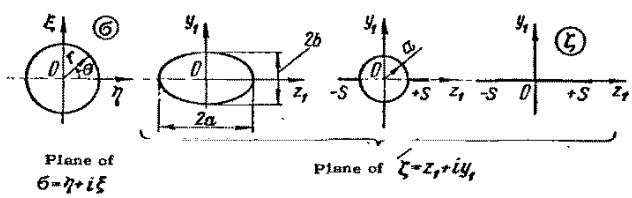

Figure IV-4-4. Conformal Transformations of a Circle onto Regions with Different Boundaries.

The quantity $r_0^2/(\eta + i\xi)$ is equal to $r_0^2(\eta - i\xi)/(\xi^2 + \eta^2)$. Suppose that a circle of radius r_0 with its center at the origin, the equation of which is $r_0^2 = \xi^2 + \eta^2$ (Fig. IV-4-4), is given in the plane of the complex variable $\sigma = \eta + i\xi$. The transformation formula will then be

$$z_1 + iy_1 = 2\eta.$$

From this we find that $z_1 = 2\eta_1$; $y_1 = 0$. This result indicates that for points on the circle, the coordinate z_1 is real and varies from $+2r_0$ to $-2r_0$ (as η varies from $+r_0$ to $-r_0$) and from $-2r_0$ to $+2r_0$ (as η varies from $-r_0$ to $+r_0$). Consequently, the Zhukovskiy formula transforms a circle of radius r_0 into a line segment on the axis of reals with length $4r_0$ (see Fig.

IV-4-4, where we have introduced the nomenclature s = $2r_0$). This segment may be regarded as a flat wing of span 2s.

By specific selection of the conformal-transformation formula, we can transform the circle into another figure whose shape coincides with the cross section of the body in flow. Selection of this formula is one of the problems of the theory of flow past slender bodies with given cross-section configurations.

Conformal-transformation formulas have been derived [51] for the cross-section configurations of air vehicles of the body-and-flat-wing, isolated-flat-wing, and prolate-ellipsoid types (see Fig. IV-4-4); they can be presented in the general form

$$\sigma=\zeta+\sum_{n=0}^{\infty}\frac{c_n}{\zeta^n} \quad \text{or} \quad \zeta=\sigma+\sum_{n=0}^{\infty}\frac{k_n}{\sigma^n}, \qquad \text{(IV-4-32)}$$

where the coefficients c_n and k_n are complex numbers.

Formulas (IV-4-32), whose particular forms for these configurations are given in Table IV-4-1, accomplish transformations that preserve the direction and magnitude of the flow velocity at infinity.

From Table IV-4-1, we can determine potentials in transverse flow over an ellipsoid, a combined body and wing, and a flat wing if we know the potential function for a circular cylinder.

Let us examine two cases of cylinder flow that have been investigated in the theory of incompressible plane flows. In the first case, a cylinder with a fixed contour of radius r_0 is in a homogeneous transverse flow at velocity V_0 (Fig. IV-4-5a) at an angle ϕ to the vertical axis ξ. The complex potential of this disturbed flow is /164

$$W(\sigma)=-iV_0e^{-i\varphi}\left(\sigma-\frac{r_0^2e^{2i\varphi}}{\sigma}\right). \qquad \text{(IV-4-33)}$$

In the second case, there is no homogeneous transverse flow, and expansion of the contour of a cylinder of radius r_0 causes disturbed flow in the transverse direction with uniform radial velocity V_r (Fig. IV-4-5b). This flow is similar to the flow from a point source, whose complex potential is

$$W(\sigma)=r_0V_r\ln\sigma. \qquad \text{(VI-4-34)}$$

TABLE IV-4-1. CONFORMAL TRANSFORMATION FORMULAS

Type of conformal transformation	Transformation formula
Transformation of circle to ellipse	$\zeta=\sigma+\frac{a^2-b^2}{4\sigma}$; $\sigma=\frac{1}{2}[\zeta+(\zeta^2-a^2+b^2)]^{1/2}$; $r_0=\frac{a+b}{2}$;
Transformation of circle into combination of body and flat wing	$\zeta=\frac{A}{4}\left(\frac{\sigma}{r_0}+\frac{r_0}{\sigma}\right)\pm$ $\pm\left[\left(\frac{A}{4}\right)^2\left(\frac{\sigma}{r_0}+\frac{r_0}{\sigma}\right)^2-a^2\right]^{1/2}$; $\frac{\sigma}{r_0}=\frac{1}{A}\left(\zeta+\frac{a^2}{\zeta}\right)\pm\left[\frac{(\zeta+a^2/\zeta)^2}{A^2}-1\right]^{1/2}$; $A=2r_0=s+\frac{a^2}{s}$, $\sigma-\frac{r_0^2}{\sigma}=\left[\left(\zeta+\frac{a^2}{\zeta}\right)^2-\left(s+\frac{a^2}{s}\right)^2\right]^{1/2}$;
Transformation of circle into flat wing	$\zeta=\sigma+\frac{s^2}{4\sigma}$; $\frac{\sigma}{r_0}=\frac{\zeta}{s}\pm\left(\frac{\zeta^2}{s^2}-1\right)^{1/2}$; $s=2r_0$.

Note: "+" for the upper half-plane; "-" for the lower half-plane.

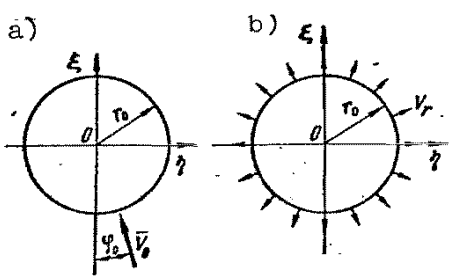

Figure IV-4-5. Flow Past Circular Cylinder. a) cylinder in homogeneous flow; b) flow past uniformly expanding cylinder.

If we examine an elongated body whose cross sectional area varies over its length and which is placed in axial flow, the velocity potential can be determined in each cross section with the aid of (IV-4-34). In the simultaneous presence of a transverse flow, such as exists in flow at an angle of attack over an elongated body, it is necessary to add the complex potential (IV-4-33).

The complex potential is constructed for the given configuration in the $\zeta = z + iy$ plane by substituting ζ for the function σ in (IV-4-33) and (IV-4-34) in accordance with the conformal-transformation formulas.

§IV-5. FLOW-REVERSIBILITY METHOD

This method is applicable to the calculation of aerodynamic characteristics for thin isolated wings and for such wings in combination with a slender body under conditions such as the flow disturbances are small and, therefore, the angles of attack are also small. Here the oncoming flow may be either supersonic or subsonic.

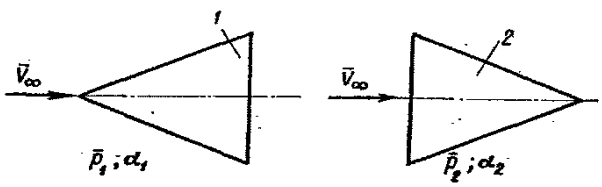

Figure IV-5-1. Forward and Reverse Flows of Wings 1 and 2.

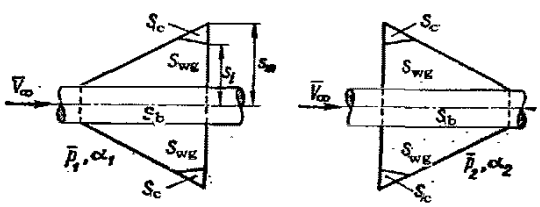

Figure IV-5-2. Forward and Reverse Flows of Body-Wing-Control Surface Combination.

Let us examine the basic relationship of the reversibility method as it applies to flow conditions over two thin wings of the same planform but with different lifting-surface curvatures [6], [41]. Suppose that an oncoming flow with a certain velocity $\bar{V}_\infty$, passing over wing 1 in the direction indicated in Fig. IV-5-1, is characterized by the distribution of the pressure coefficient $\bar{p}_1$ and the corresponding local angle of attack α_1. Flow at the same velocity over the second wing in the opposite direction is characterized by $\bar{p}_2$ and α_2. The method of reversibility establishes the following integral relationship:

$$\iint_{(S)} \Delta\bar{p}_1 \alpha_2 \, dS = \iint_{(S)} \Delta\bar{p}_2 \alpha_1 \, dS, \qquad \text{(IV-5-1)}$$

in which $\Delta\bar{p}_1$, α_1, $\Delta\bar{p}_2$, α_2 are measured at the same point, and $\Delta\bar{p}_1$, $\Delta\bar{p}_2$ are the pressure-coefficient drops across the lower and upper sides of the wing in the forward and reverse flows.

In using (IV-5-1), it must be remembered that it is applicable for any distribution of the local angles of attack over the wing surfaces in forward and reverse flow. For example, if

$\alpha_1 = \alpha_2 = \text{const}$, we obtain from (IV-5-1) that the two wings have identical lifts.

Relation (IV-5-1) can be used in the more general case in which we have a certain combination consisting of a body and wing. Here the wing may be fitted with control elements (Fig. IV-5-2). In this case, (IV-5-1) becomes /166

$$\iint\limits_{(S_c+S_{wg}+S_b)} \Delta\bar{p}_1\alpha_2\, dS = \iint\limits_{(S_c+S_{wg}+S_b)} \Delta\bar{p}_2\alpha_1\, dS. \qquad \text{(VI-5-2)}$$

To illustrate application of the flow-reversibility method and (IV-5-2), let us examine a particular case in which there is no body ($S_b = 0$). Let it be required to find the lift of the undeflected wing with the condition of a small control rotation angle $\alpha_1 = \delta$. Thus, the local attack angle $\alpha_1 = 0$ on the wing, while $\alpha_1 = \delta$ on the control. We shall assume that when the flow over the wing and control is reversed, the angle of attack will be the same over the entire surface at $\alpha_2 = \delta$.

Introducing the attack-angle values into (IV-5-2), we obtain

$$\iint\limits_{(S_c+S_{wg})} \Delta\bar{p}_1\, dS = \iint\limits_{(S_c)} \Delta\bar{p}_2\, dS.$$

Here the left member determines the unknown wing lift with the control deflected through an angle δ. It follows from the expression obtained that it can be determined as the lift set up by the undeflected control with the wing in reversed flow at the total angle of attack δ.

Thus, the flow-reversibility method enables us to reduce the more complex problem of flow over a wing with a deflected control surface to the substantially simpler problem of the aerodynamic characteristics of a surface with the control surface undeflected.

§IV-6. GENERAL EXPRESSIONS FOR THE STABILITY DERIVATIVES OF A FINNED SOLID OF REVOLUTION. THE METHOD OF ATTACHED MASSES

An effective method of determining stability derivatives has been developed for application to slender finned bodies; it is known as the method of attached masses or the method of inertia coefficients [14], [51].

This method is applicable when there is interaction only between the body and the wing (fins), and no effect of vortices from the wing on the fins. The influence of interference between

the wing and fins is taken into consideration by special methods.

Let us consider a finned body (Fig. IV-6-1) moving at a certain velocity $\bar{V}_\infty$ and at the same time rotating at an angular velocity $\bar{\Omega}$. The origin of the body axes x, y, z coincides with the center of gravity, the ξ-, η-, and ζ-axes are put parallel to the x-, y-, and z-axes, and the origin O' of the ξηζ system is placed at an arbitrary point on the x-axis.

In the transverse-flow plane, which coincides with the ηO'ζ-plane, the velocity potential

$$\varphi = u\varphi_1 + v\varphi_2 + \Omega_x\varphi_3, \qquad \text{(IV-6-1)}$$

where u and v are the components of the body's translational velocity in the plane under consideration and Ω_x is the angular velocity about the longitudinal axis.

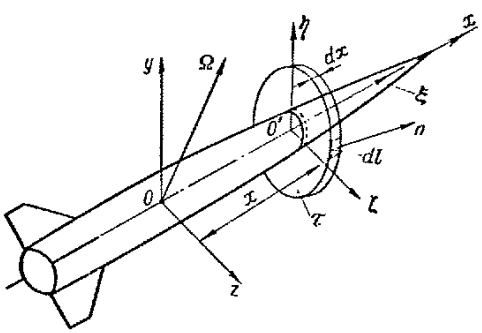

Figure IV-6-1. Illustrating Determination of Stability Derivatives for Finned Solid of Revolution.

The potentials ϕ_1 and ϕ_2 define the flows that arise in motion of a flat contour with unit velocities parallel to the O'η and O'ζ axes, while ϕ_3 characterizes the flow due to rotation of the contour about the longitudinal axis at unit angular velocity. /167

Since a moving coordinate system that is rigidly bound to the body has been selected, the potentials ϕ_1, ϕ_2, and ϕ_3 are independent of time. The time dependence of the total potential ϕ is governed by the time variation of the velocities u, v, and Ω_x. The potential ϕ determines flow in the transverse plane, which influences the stability derivatives. The potential component for longitudinal flow is of no importance, since it does not influence these derivatives.

If we have determined the function ϕ and its components, we can find the transverse-flow velocity distribution and the kinetic energy of the gas enclosed in a certain volume τ (Fig. IV-6-1), which is equal to

$$T=\frac{1}{2}\int\limits_{(\tau)}\rho_\infty\left[\left(\frac{\partial\varphi}{\partial\eta}\right)^2+\left(\frac{\partial\varphi}{\partial\zeta}\right)^2\right]d\tau. \qquad \text{(IV-6-2)}$$

Applying Green's transformation to this equation, we obtain an expression for the kinetic energy of the gas per unit length in the direction of the x-axis:

$$T=-\frac{\rho_\infty}{2}\oint\limits_C\varphi\frac{\partial\varphi}{\partial n}dl=-\frac{\rho_\infty}{2}\oint\limits_C(\varphi_1u+\varphi_2v+\varphi_3\Omega_x)\frac{\partial}{\partial n}(\varphi_1u+\varphi_2v+\varphi_3\Omega_x)\,dl, \qquad \text{(IV-6-3)}$$

where C is a contour consisting of the outline of the body in cross section and the outer boundary of the subject volume τ; n is the exterior normal; l is an arc of contour C.

We see from (IV-6-3) that the kinetic energy is determined by nine terms, each of which incorporates a coefficient of the form

$$\lambda_{ik}=-\rho_\infty\oint\limits_C\varphi_i\frac{\partial\varphi_k}{\partial n}dl, \qquad \text{(IV-6-4)}$$

which is known as the coefficient of attached masses or the cross-section inertia coefficient.

Formula (IV-6-4) can be modified by applying the Cauchy-Riemann conditions $\partial\varphi/\partial n=\partial\psi/\partial l$, $\partial\varphi/\partial l=-\partial\psi/\partial n$. After simple rearrangement, we obtain

$$\lambda_{ik}=-\rho_\infty\oint\limits_C\varphi_i\,d\psi_k, \qquad \text{(IV-6-4')}$$

where, by analogy with the velocity potential, the stream function is represented as the sum of three components:

$$\psi=u\psi_1+v\psi_2+\Omega_x\psi_3. \qquad \text{(IV-6-5)}$$

We apply to (IV-6-4) the partial Green's formula, which is valid for the potential functions ϕ_1, ϕ_2, and ϕ_3: /168

$$\oint\limits_C\varphi_i\frac{\partial\varphi_k}{\partial n}dl=\oint\limits_C\varphi_k\frac{\partial\varphi_i}{\partial n}dl.$$

Thus, $\lambda_{ik} = \lambda_{ki}$ and, consequently, six of the nine terms in (IV-6-3) remain. Then for the kinetic energy

$$2T = \lambda_{11}u^2 + \lambda_{22}v^2 + \lambda_{33}\Omega_x^2 + 2\lambda_{12}uv + 2\lambda_{13}u\Omega_x + 2\lambda_{23}v\Omega_x. \qquad \text{(IV-6-3')}$$

where u and v are velocities that can be replaced by the values

$$u = \beta_{s1}V_\infty + \Omega_z x; \quad v = \alpha V_\infty - \Omega_y x. \qquad \text{(IV-6-6)}$$

The lift and lateral force and the rolling moment acting on the body are determined from the known kinetic energy:

$$\frac{dZ}{dx} = -\frac{d}{dt}\left(\frac{\partial T}{\partial u}\right) + \Omega_x \frac{\partial T}{\partial v}; \qquad \text{(IV-6-7)}$$

$$\frac{dY}{dx} = -\frac{d}{dt}\left(\frac{\partial T}{\partial v}\right) - \Omega_x \frac{\partial T}{\partial u}; \qquad \text{(IV-6-8)}$$

$$\frac{dM_x}{dx} = -\frac{d}{dt}\left(\frac{\partial T}{\partial \Omega_x}\right) + v\frac{\partial T}{\partial u} - u\frac{\partial T}{\partial v}. \qquad \text{(IV-6-9)}$$

The total derivative d/dt is determined with consideration of variation of the parameters for a fixed cross section. For a given arbitrary parameter f that is a function of time t and the distance x to the origin (Fig. IV-6-1),

$$\frac{df(t, x)}{dt} = \frac{\partial f}{\partial t} + \frac{dx}{dt}\cdot\frac{\partial f}{\partial x},$$

where $dx/dt = -V_\infty$,

$$\frac{d}{dt} = \frac{\partial}{\partial t} - V_\infty \frac{\partial}{\partial x}.$$

The pitching M_z and yawing M_y moments are found from the equations

$$\frac{dM_z}{dx} = x\frac{dY}{dx}; \quad \frac{dM_y}{dx} = x\frac{dZ}{dx}. \qquad \text{(IV-6-10)}$$

Integration extends from the base of the body with coordinate $x = -x_b$ to the nose, with the coordinate $x = x_n$. Thus, all moments are calculated with respect to axes passing through the center of gravity.

It is more convenient to convert to aerodynamic coefficients. For this purpose, the expressions obtained for the forces must be divided by $0{,}5\rho_\infty V_\infty^2 S$, and the moments by $0{,}5\rho_\infty V_\infty^2 Sl$. Determination of the stability derivatives requires appropriate differentiation of the expressions for the coefficients $c_y \simeq c_N$, c_z, m_x, m_y, m_z. Differentiating successively with respect to α, β, ω_x $\bar{\Omega}_x l/2V_\infty$, $\omega_y = \Omega_y l/2V_\infty$, $\omega_z = \Omega_z l/2V_\infty$, we obtain the static and rotary derivatives; differentiating with respect to $\dot{\bar{\alpha}} = \dot{\alpha} l/2V_\infty$, $\dot{\bar{\beta}} = \dot{\beta} l/2V_\infty$, $\dot{\bar{\omega}}_x = \dot{\omega}_x l^2/2V_\infty^2$, $\dot{\bar{\omega}}_y = \dot{\omega}_y l^2/2V_\infty^2$, $\dot{\bar{\omega}}_z = \dot{\omega}_z l^2/2V_\infty^2$, $\dot{\bar{V}}_\infty = \dot{V}_\infty l/2V_\infty^2$, we find the stability derivatives with respect to the accelerations.

The static stability derivatives have the form

$$c_N^\alpha = -4\dot{\bar{V}}_\infty B_{22} - 2\bar{A}_{22} - 4\omega_x B_{12}; \quad \text{(IV-6-11)}$$

$$c_N^\beta = -4\dot{\bar{V}}_\infty B_{12} - 2\bar{A}_{12} - 4\omega_x B_{11}; \quad \text{(IV-6-12)}$$

$$c_z^\alpha = -4\dot{\bar{V}}_\infty B_{12} - 2\bar{A}_{12} + 4\omega_x B_{22}; \quad \text{(IV-6-13)}$$

$$c_z^\beta = -4\dot{\bar{V}}_\infty B_{11} - 2\bar{A}_{11} + 4\omega_x B_{12}; \quad \text{(IV-6-14)}$$ /169

$$m_x^\alpha = -4\dot{\bar{V}}_\infty B_{23} - 2\bar{A}_{23} + 4\alpha B_{12} + 2\beta(B_{11} - B_{22}) + 4\omega_x B_{13} - 8\omega_z C_{12} + 4\omega_y (C_{11} - C_{22}); \quad \text{(IV-6-15)}$$

$$m_x^\beta = -4\dot{\bar{V}}_\infty B_{13} - 2\bar{A}_{13} + 2\alpha(B_{11} - B_{22}) - 4\beta B_{12} - 4\omega_x B_{23} - 4\omega_z (C_{11} - C_{22}) - 8\omega_y C_{12}; \quad \text{(IV-6-16)}$$

$$m_y^\alpha = -4\dot{\bar{V}}_\infty C_{12} - 2\left[B_{12} + \bar{A}_{12}\left(\frac{x}{l}\right)_{\text{bse}}\right] + 4\omega_x C_{22}; \quad \text{(IV-6-17)}$$

$$m_y^\beta = -4\dot{\bar{V}}_\infty C_{11} - 2\left[B_{11} + \bar{A}_{11}\left(\frac{x}{l}\right)_{\text{bse}}\right] + 4\omega_x C_{12}; \quad \text{(IV-6-18)}$$

$$m_z^\alpha = +4\dot{\bar{V}}_\infty C_{22} + 2\left[B_{22} + \bar{A}_{22}\left(\frac{x}{l}\right)_{\text{bse}}\right] + 4\omega_x C_{12}; \quad \text{(IV-6-19)}$$

$$m_z^\beta = 4\dot{\bar{V}}_\infty C_{12} + 2\left[B_{12} + \bar{A}_{12}\left(\frac{x}{l}\right)_{\text{bse}}\right] + 4\omega_x C_{11}. \quad \text{(IV-6-20)}$$

The rotary derivatives are determined by the expressions:

$$c_N^{\omega_x} = -4\bar{A}_{23} - 4\alpha B_{12} - 4\beta B_{11} - 16\omega_x B_{13} + 8\omega_z C_{12} - 8\omega_y C_{11}; \quad \text{(IV-6-21)}$$

$$c_N^{\omega_y} = -4\bar{A}_{12}\left(\frac{x}{l}\right)_{\text{bse}} - 8\omega_x C_{11}; \quad \text{(IV-6-22)}$$

$$c_N^{\omega_z} = 4\bar{A}_{22}\left(\frac{x}{l}\right)_{\text{bse}} + 8\omega_x C_{12}; \quad \text{(IV-6-23)}$$

$$c_z^{\omega_x} = -4\bar{A}_{13} + 4\alpha B_{22} + 4\beta B_{12} + 16\omega_x B_{23} - 8\omega_z C_{22} + 8\omega_y C_{12}; \quad \text{(IV-6-24)}$$

$$c_z^{\omega_y} = -4\bar{A}_{11}\left(\frac{x}{l}\right)_{\text{bse}} + 8\omega_x C_{12}; \quad \text{(IV-6-25)}$$

$$c_z^{\omega_z} = 4\bar{A}_{12}\left(\frac{x}{l}\right)_{bse} - 8\omega_x C_{22}; \quad \text{(IV-6-26)}$$

$$m_x^{\omega_x} = -4\bar{A}_{33} + 4\alpha B_{13} - 4\beta B_{23} - 8\omega_z C_{13} - 8\omega_y C_{23}; \quad \text{(IV-6-27)}$$

$$m_x^{\omega_y} = -4\bar{A}_{33}\left(\frac{x}{l}\right)_{bse} + 4\alpha(C_{11} - C_{22}) - 8\beta C_{12} - 8\omega_x C_{23} - 8\omega_z(D_{11} - D_{22}) - 16\omega_y D_{12}; \quad \text{(IV-6-28)}$$

$$m_x^{\omega_z} = 4\bar{A}_{23}\left(\frac{x}{l}\right)_{bse} - 8\alpha C_{12} - 4\beta(C_{11} - C_{22}) - 8\omega_x C_{13} + 16\omega_z D_{12} - 8\omega_y(D_{11} - D_{22}); \quad \text{(IV-6-29)}$$

$$m_y^{\omega_x} = -4\left[B_{13} + \bar{A}_{13}\left(\frac{x}{l}\right)_{bse}\right] + 4\alpha C_{22} + 4\beta C_{12} + 16\omega_x C_{23} - 8\omega_z D_{22} + 8\omega_y D_{12}; \quad \text{(IV-6-30)}$$

$$m_y^{\omega_y} = -\left[\bar{A}_{11}\left(\frac{x}{l}\right)_{bse} + C_{11}\right] + 8\omega_x D_{12}; \quad \text{(IV-6-31)}$$

$$m_y^{\omega_z} = 4\left[\bar{A}_{12}\left(\frac{x}{l}\right)_{bse} + C_{12}\right] - 8\omega_x D_{22}; \quad \text{(IV-6-32)}$$

$$m_z^{\omega_x} = 4\left[B_{23} + \bar{A}_{23}\left(\frac{x}{l}\right)_{bse}\right] + 4\alpha C_{12} + 4\beta C_{11} + 16\omega_x C_{13} - 8\omega_z D_{12} + 8\omega_y D_{11}; \quad \text{(IV-6-33)}$$

$$m_z^{\omega_y} = 4\left[\bar{A}_{12}\left(\frac{x}{l}\right)_{bse}^2 + C_{12}\right] + 8\omega_x D_{11}; \quad \text{(IV-6-34)} \quad /170$$

$$m_z^{\omega_z} = -4\left[\bar{A}_{22}\left(\frac{x}{l}\right)_{bse}^2 + C_{22}\right] - 8\omega_x D_{12}. \quad \text{(IV-6-35)}$$

The acceleration derivatives are

$$c_N^{\dot{\alpha}} = -4B_{22};\ c_N^{\dot{\beta}} = 4B_{12};\ c_N^{\dot{V}_\infty} = -4\alpha B_{22} - 4\beta B_{12}; \quad \text{(IV-6-36)}$$

$$c_N^{\dot{\omega}_x} = -4B_{23};\ c_N^{\dot{\omega}_y} = -4C_{12};\ c_N^{\dot{\omega}_z} = 4C_{22}; \quad \text{(IV-6-37)}$$

$$c_z^{\dot{\alpha}} = -4B_{12};\ c_z^{\dot{\beta}} = -4B_{11};\ c_z^{\dot{V}_\infty} = -4\alpha B_{12} - 4\beta B_{11}; \quad \text{(IV-6-38)}$$

$$c_z^{\dot{\omega}_x} = -4B_{13};\ c_z^{\dot{\omega}_y} = -4C_{11};\ c_z^{\dot{\omega}_z} = 4C_{12}; \quad \text{(IV-6-39)}$$

$$m_x^{\dot{\alpha}} = -4B_{23};\ m_x^{\dot{\beta}} = -4B_{13};\ m_x^{\dot{V}_\infty} = -4\alpha B_{23} - 4\beta B_{13}; \quad \text{(IV-6-40)}$$

$$m_x^{\dot{\omega}_x} = -4B_{33};\ m_x^{\dot{\omega}_y} = -4C_{13};\ m_x^{\dot{\omega}_z} = 4C_{23}; \quad \text{(IV-6-41)}$$

$$m_y^{\dot{\alpha}} = -4C_{12};\ m_y^{\dot{\beta}} = -4C_{11};\ m_y^{\dot{V}_\infty} = -4\alpha C_{12} - 4\beta C_{11}; \quad \text{(IV-6-42)}$$

$$m_y^{\dot{\omega}_x} = -4C_{13};\ m_y^{\dot{\omega}_y} = -4D_{11};\ m_y^{\dot{\omega}_z} = 4D_{12}; \quad \text{(IV-6-43)}$$

$$m_z^{\dot{\alpha}} = 4C_{22};\ m_z^{\dot{\beta}} = 4C_{12};\ m_z^{\dot{V}_\infty} = 4\alpha C_{22} + 4\beta C_{12}; \quad \text{(IV-6-44)}$$

$$m_z^{\dot{\omega}_x} = 4C_{23};\ m_z^{\dot{\omega}_y} = 4D_{12};\ m_z^{\dot{\omega}_z} = -4D_{22}. \quad \text{(IV-6-45)}$$

The dimensionless parameters B_{ik}, C_{ik}, D_{ik} have been introduced into the expressions for the stability derivatives; they are determined for $\underline{i}$ and $\underline{k}$ of 1, 2, and 3 by the relationship

$$E_{ik} = \int_{\bar{x}_{base}}^{\bar{x}_n} A_{ik} \bar{x}^n \, d\bar{x}. \qquad \text{(IV-6-46)}$$

Here

$$\bar{x} = x/l, \quad \bar{x}_{base} = x_{base}/l, \quad \bar{x}_n = x_n/l.$$

The parameters A_{ik} are the dimensionless attached-mass coefficients, which are related to the dimensional coefficients λ_{ik} by

$$\left.\begin{aligned} A_{11} &= \frac{\lambda_{11}}{\rho_\infty S}, \quad A_{12} = A_{21} = \frac{\lambda_{12}}{\rho_\infty S}, \quad A_{22} = \frac{\lambda_{22}}{\rho_\infty S}, \\ A_{13} &= A_{31} = \frac{\lambda_{13}}{\rho_\infty l S}, \quad A_{23} = A_{32} = \frac{\lambda_{23}}{\rho_\infty l S}, \quad A_{33} = \frac{\lambda_{33}}{\rho_\infty l^2 S}. \end{aligned}\right\} \qquad \text{(IV-6-47)}$$

Unlike A_{ik}, the parameters $\bar{A}_{ik}$ that appear in the expressions for the stability derivatives determine the dimensionless attached-mass coefficients found for the cross section of the body at the base with contour C, over which the integration extends in Formula (IV-6-4).

Determination of the stability derivatives requires calculation of the attached-mass coefficients by Formulas (IV-6-4) or (IV-6-4'). We see from (IV-6-4) that the coefficients λ_{ik} can be found for a given body shape if we know the velocity potentials in transverse flow ϕ_1, ϕ_2, and ϕ_3 and the derivatives with respect to the normal to the cross-section contour.

These derivatives can be determined directly by examination of the conditions on the contour boundary. Since the derivative $\partial\phi/\partial n$ is the velocity of a point of the contour in the direction of the normal, /171

$$\frac{\partial \varphi_1}{\partial n} = \frac{\partial y}{\partial t}, \quad \frac{\partial \varphi_2}{\partial n} = -\frac{\partial z}{\partial t}, \quad \frac{\partial \varphi_3}{\partial n} = -\frac{1}{2}\frac{dr^2}{dt} = -\frac{1}{2}\frac{d(y^2+z^2)}{dt}. \qquad \text{(IV-6-48)}$$

We can convert from the potentials ϕ_i to the complex potentials $W_i = \phi_i + i\psi_i$. With (IV-6-48), the expressions for the

attached-mass coefficients are

$$\lambda_{1k} + i\lambda_{2k} = i\rho_\infty \oint (W_k - i\psi_k)\, d\zeta, \qquad \text{(IV-6-49)}$$

where $\zeta = z + iy$, and the coefficient k assumes the successive values 1, 2, 3. The attached-mass coefficient

$$\lambda_{33} = \frac{\rho_\infty}{2} \oint (W_3 - i\psi)\, d(\zeta\bar{\zeta}), \qquad \text{(IV-6-50)}$$

where $\bar{\zeta} = z - iy$.

The integrals containing the stream function are evaluated from the boundary conditions on the contour. For this purpose, (IV-6-48) and the Cauchy-Riemann conditions must be used to find contour stream-function values ψ_1, ψ_2, ψ_3. After substituting them in the integrals $\oint_C \psi_k\, d\zeta$, we find for k = 1 and 2 the respective values S_s and $-iS_s$, which are determined by the cross-sectional area, and obtain a zero value of the integral for k = 3, provided that the section is symmetrical in form.

The complex potential W_k is found by conformal transformation of the given cross section in the plane $\zeta = z + iy$ into a circle with a certain radius r_0 in the plane $\sigma = \eta + i\xi$, using the general formula (IV-4-32). If the potential $W_k(\sigma)$ is known for the circle, we can obtain the complex potential $W_k(\zeta)$ in the physical plane ζ by making the substitution $\sigma = \sigma(\zeta)$.

The potentials W_1 and W_2, which characterize the flow over the body in its motion along the z- and y-axes, respectively, are easiest to obtain. Expression (IV-4-33) can be used for this purpose. Setting $V_\infty = 1$ and $\phi = 0$ in this formula, we obtain $W = \sigma - r_0^2/\sigma$, which determines the complex potential for a stationary cylinder with a unit-velocity oncoming flow passing over it in the direction of the y-axis.

Comparing with Formula (IV-4-33), the minus sign in front of the i has been changed to a plus sign, since in our case positive values of the coordinate y are reckoned downward.

The potential obtained is equal to $W_2(\zeta) + i\zeta$, which characterizes transverse flow over a stationary body in the ζ-plane, with $W_2[\zeta(\sigma)]$ representing the complex potential for a moving cylinder in the σ-plane. Substituting ζ in accordance with (IV-4-32),

$$W_2[\zeta(\sigma)] = i(\sigma - \zeta) - i\frac{r_0^2}{\sigma} = -i_0\frac{r_0^2}{\sigma} - i\sum_{n=0}^{\infty}\frac{k_n}{\sigma^n}. \qquad \text{(IV-6-51)}$$

Similarly, we obtain the complex flow potential in the σ-plane with the flow direction along the z-axis:

$$W_1[\zeta(\sigma)] = -\frac{r_0^2}{\sigma} + \sum_{n=0}^{\infty}\frac{k_n}{\sigma^n}. \qquad \text{(IV-6-52)}$$

In determining the complex potential W_3, we can proceed from /172
the expression $\operatorname{Im} W_3 = \operatorname{Im}(i\psi_3)$, which indicates that W_3 is the imaginary part of potential ψ_3. Here, the potential ψ_3 must satisfy the condition for the stream function at the boundary of the moving body $\partial\phi_3/\partial n = \partial\psi/\partial\ell$, in accordance with which

$$\psi_3 = -\frac{1}{2}(z^2 + y^2) = -\frac{1}{2}(z + iy)(z - iy) = -\frac{1}{2}\zeta\bar{\zeta}. \qquad \text{(IV-6-53)}$$

Thus, finding the potential W_3 requires solution of the Dirichlet problem of determining the function ψ_3 in a certain region from the boundary condition (IV-6-53).

The general expression for W_3 may take the form

$$\operatorname{Im} W_3 = \operatorname{Im}\left(-\frac{1}{2}\zeta\bar{\zeta}\right). \qquad \text{(IV-6-54)}$$

The ζ from (IV-4-32) and the series

$$\bar{\zeta} = \bar{\sigma} + \sum_{n=0}^{\infty}\frac{\bar{k}_n}{\bar{\sigma}^n}, \qquad \text{(IV-6-55)}$$

where $\bar{\sigma} = c^2/\sigma$, must be introduced into this expression. As a result of these substitutions, the complex potential

$$W_3 = -i\sum_{n=1}^{\infty}\frac{b_n}{\sigma^n}. \qquad \text{(IV-6-56)}$$

The coefficient of attached masses can be calculated directly from (IV-6-4). Here the potential ϕ_i and the stream function ψ_k

are found from the expression for the complex potential, $W = \phi + i\psi$.

Example. Determine the attached-mass coefficients for an ellipse with semiaxes a and b. For this purpose, we find the complex potentials W_1 and W_2 by the conformal formula (see Table IV-4-1)

$$\zeta = \sigma + \frac{a^2 - b^2}{4\sigma}, \qquad \text{(IV-6-57)}$$

which maps the exterior of an ellipse in the ζ-plane onto the exterior of a circle of radius $r_0 = 0.5(a + b)$.

The potential W_1 is determined from (IV-6-52). To determine the series coefficients k_n, it is necessary to use (IV-6-57) and (IV-4-32). Comparing them, we find that $k_1 = (a^2 - b^2)/4$, and the other coefficients of the series are zero.

Introducing the value for k_1, we obtain

$$W_1 = -\frac{br_0}{\sigma}. \qquad \text{(IV-6-58)}$$

Similarly, we find the equation

$$W_2 = -\frac{iar_0}{\sigma}. \qquad \text{(IV-6-59)}$$

The complex potentials can also be determined from the boundary conditions for the stream functions. Let us illustrate this in the example of the complex potential W_1.

From the condition $\psi_1 = y$ at the contour boundary, we obtain the relation $\operatorname{Im} W_1 = \operatorname{Im} \zeta$. Introducing (IV-6-57) in place of ζ under the Im sign in this relationship, we obtain, after several rearrangements, the formula $\operatorname{Im} W_1 = \operatorname{Im} (-r_0 b/\sigma)$, which is valid on the circle. Generalizing this formula, we get (IV-6-58).

We find an expression for W_2 in a similar manner. For this purpose, we start from the boundary condition $\psi_2 = -x$ or $\operatorname{Im} W_2 = \operatorname{Im} (-i\zeta)$. After substituting ζ from (IV-6-57), we arrive at (IV-6-59).

To determine the potential W_3, we use (IV-6-56). Introducing the ζ from (IV-6-57) and /173

$$\bar{\zeta} = \bar{\sigma} + \frac{a^2 - b^2}{4\bar{\sigma}},$$

we obtain, after rearrangement, the complex potential

$$W_3 = -\frac{i(a^2 - b^2) r_0^2}{4\sigma^2}. \qquad \text{(IV-6-60)}$$

The attached-mass coefficients are calculated by (IV-6-4'). It is helpful to convert to the polar coordinates r_0 and θ for the calculation. For example, the complex potential W_1 is written in the form $W_1 = -(r_0 b)/\sigma = -be^{-i\theta}$. Then the velocity potential $\phi_1 = -b \cos\theta$ and the stream function $\psi_1 = b \sin\theta$. W_2 and W_3 are represented similarly, and the corresponding expressions found for the potentials and stream functions.

Introducing the expressions for ϕ_i and ψ_k into (IV-6-4') and integrating from 0 to 2π, we obtain the following values for the attached-mass coefficients:

$$\lambda_{11} = \pi\rho_\infty b^2;\ \lambda_{22} = \pi\rho_\infty a^2;\ \lambda_{33} = \frac{1}{8}\pi\rho_\infty (a^2 - b^2)^2;\ \lambda_{12} = \lambda_{13} = \lambda_{23} = 0. \qquad \text{(IV-6-61)}$$

We see from this example that the attached-mass coefficients λ_{ik} are zero for the ellipse if $i \neq k$. This feature is preserved for all bodies whose cross sections have symmetry.

§IV-7. APPROXIMATE METHODS OF CALCULATION OF FLOW OVER SURFACES

The Newton method. This method is used for approximate calculations of the pressure at very high flow velocities. It is based on Newton's corpuscular theory (or the theory of "Newtonian deceleration"), according to which gas particles experience disturbances only when they strike a solid wall and lose their entire momentum components normal to the wall. The excess pressure is determined by this loss of momentum in accordance with the formula $p - p_\infty = \rho_\infty V_n^2$, where V_n is the component of undisturbed velocity normal to the wall. Dividing by the velocity head $q = 0.5\rho_\infty V_\infty^2$ we obtain Newton's formula for the pressure coefficient:

$$\bar{p} = \frac{p - p_\infty}{q} = 2\frac{V_n^2}{V_\infty^2}. \qquad \text{(IV-7-1)}$$

This formula can also be presented in the form

$$\bar{p} = 2\cos^2\eta, \qquad \text{(IV-7-1')}$$

where η is the angle between the velocity vector $\bar{V}_\infty$ and the surface normal.

Let us relate (IV-7-1') to some fixed point of a surface whose inclination is determined by the angle η^*. For this point, the local pressure coefficient $\bar{p}_0 = 2\cos^2\eta^*$. Appending (IV-7-1') we obtain an improved Newtonian formula for the pressure coefficient at an arbitrary point of the surface:

$$\frac{\bar{p}}{\bar{p}_0} = \frac{\cos^2\eta}{\cos^2\eta^*}. \qquad \text{(IV-7-2)}$$

This formula gives a better approximation than (IV-7-1'), since $\bar{p}_0$ is calculated quite accurately for an initial point of the surface, such as the conical tip of a sharp body or the total-stagnation point on a blunted surface. In the latter case, $\cos\eta^* = 1$ and /174

$$\bar{p} = \bar{p}_0\cos^2\eta. \qquad \text{(IV-7-3)}$$

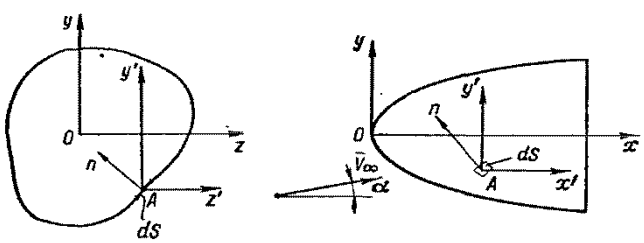

Figure IV-7-1. Illustrating Determination of Velocity Component Normal to Washed Surface y = f(z,x).

The above formulas determine the pressure that arises in translational motion of the body. At the same time, translational motion may be accompanied by rotation about the center of gravity, and this may have a substantial pressure-redistribution effect.

Formula (IV-7-1) must be used to take account of this effect, with V_n determined as the sum of two components, namely the normal component of undisturbed velocity and the normal component

of the velocity induced at the particular point in the presence of rotation.

Thus, determination of pressure by the Newtonian method involves calculation of the over-all velocity component normal to the body's surface.

Let us consider an arbitrary surface (Fig. IV-7-1) with the equation $y = f(z,x)$ situated in a flow of high velocity $\bar{V}_\infty$. The angle of attack measured in the yOx-plane is formed by the vector $\bar{V}_\infty$ and the positive direction of the x-axis. To find the velocity component $V_{n\infty}$ of the translational flow normal to element dS at point A, we must calculate the scalar product of vector $\bar{V}_\infty$ and the unit vector $\bar{n}$ of the interior normal to the surface element under consideration. We see from Fig. IV-7-1 that the vector $\bar{V}_\infty = V_\infty \cos \alpha \bar{i} + V_\infty \sin \alpha \bar{j}$. The unit vector $\bar{n}$ can be presented in the form $\bar{n} = \cos \alpha_x \bar{i} + \cos \alpha_y \bar{j} + \cos \alpha_z \bar{k}$, where $\bar{i}$, $\bar{j}$, $\bar{k}$ are the unit vectors and α_x, α_y, α_z are the angles formed by vector $\bar{n}$ with the directions of the coordinate axes.

The cosines of these angles

$$\cos\alpha_x = \frac{\partial y/\partial x}{\sqrt{(\partial y/\partial x)^2 + (\partial y/\partial z)^2 + 1}}; \quad \cos\alpha_y = \frac{-1}{\sqrt{(\partial y/\partial x)^2 + (\partial y/\partial z)^2 + 1}};$$

$$\cos\alpha_z = \frac{\partial y/\partial z}{\sqrt{(\partial y/\partial x)^2 + (\partial y/\partial z)^2 + 1}}. \qquad \text{(IV-7-3')}$$

In accordance with the values of vectors $\bar{V}_\infty$ and $\bar{n}$, the normal velocity component of the translational flow

$$V_{n\infty} = V_\infty \cos\alpha \cos\alpha_x + V_\infty \sin\alpha \cos\alpha_y. \qquad \text{(IV-7-4)}$$

Let us assume that the body in the flow is rotating at a certain angular velocity $\bar{\Omega} = \Omega_x \bar{i} + \Omega_y \bar{j} + \Omega_z \bar{k}$. /175

The additional velocity induced at point A under consideration is equal to the vector product $\bar{v} = \bar{\Omega} \times \bar{R}$, where $\bar{R}$ is the radius vector for point A. If v_x, v_y, v_z are the components of vector $\bar{v}$, the component $V_{n\Omega}$ of velocity normal to the surface element dS is

$$V_{n\Omega} = v_x \cos\alpha_x + v_y \cos\alpha_y + v_z \cos\alpha_z. \qquad \text{(IV-7-5)}$$

The radius vector $\bar{R}$ can be presented in the form $\bar{R} = x_A\bar{i} + y_A\bar{j} + z_A\bar{k}$, where x_A, y_A, z_A are the distances from the center of rotation to point A. Thus, the induced-velocity vector

$$\bar{v} = v_x\bar{i} + v_y\bar{j} + v_z\bar{k} = (\Omega_y z_A - \Omega_z y_A)\bar{i} - (\Omega_x z_A - \Omega_z x_A)\bar{j} + (\Omega_x y_A - \Omega_y x_A)\bar{k}. \quad \text{(IV-7-6)}$$

The components v_x, v_y, and v_z that appear in (IV-7-5) for $V_{n\Omega}$ are determined directly from this expression. Having determined $V_{n\infty}$, $V_{n\Omega}$ we can find the resultant normal velocity component $V_n = V_{n\infty} + V_{n\Omega}$ and, consequently, the pressure coefficient (IV-7-1). Its magnitude can be presented as the sum of two components:

$$\bar{p} = \bar{p}_V + \bar{p}_\Omega, \quad \text{(IV-7-7)}$$

where the first term

$$\bar{p}_V = 2\frac{V_{n\infty}^2}{V_\infty^2} \quad \text{(IV-7-8)}$$

characterizes the pressure increment from the translational motion and the second term

$$\bar{p}_\Omega = \frac{2}{V_\infty^2}(2V_{n\infty}V_{n\Omega} + V_{n\Omega}^2) \quad \text{(IV-7-9)}$$

gives the component governed by the rotational motion.

The aerodynamic characteristics (forces, moments, and their coefficients) can be determined from the known external form of the washed surface and the pressure distribution.

Application of the Newtonian method is obviously limited to the zones of the body's surface that face the oncoming flow and collide with gas particles. These zones are limited by a certain curve along which the normal velocity component $V_{n\infty}$ and, consequently, the pressure coefficient $\bar{p}_V$ are equal to zero. It follows from (IV-7-4) that the equation of this curve is

$$\cos\alpha\cos\alpha_x + \sin\alpha\cos\alpha_y = 0. \quad \text{(IV-7-10)}$$

Beyond this curve, in the so-called "shaded" zone, the pressure in which we shall denote by p_e, we may start from various considerations in evaluating the coefficient $\bar{p}_e = (2/kM_\infty^2) \times \times (p_e/p_\infty - 1)$. Assuming, for example, that $M \to \infty$, we obtain $\bar{p}_e = 0$. We can also adopt the condition that the speeds are finite, even though they are very large, so that $M_\infty >> 1$ and a total vacuum is formed in the "shaded" zone ($p_e = 0$). The corresponding pressure coefficient will be $\bar{p}_e = -2/kM_\infty^2$.

In principle, the Newtonian method is applicable for arbitrary flows — plane or spatial. However, experimental data have shown that it gives less satisfactory results for plane than for spatial flows. This means, for example, that the pressure distribution determined by this method for a wing profile will be less accurate than one determined for a solid of revolution.

Method combining compression-shock and expansion-flow theories. This method, by which the parameters of supersonic flow over a sharp surface can be determined, consists in the following. First the parameters on the sharp nose are computed by compression-shock theory, and then those on the remaining downstream zones, on which the flow expands, are found with the aid of the Prandtl-Meyer theory. /176

It is assumed in this method that supersonic flow over the sharp nose ("point") may be plane (flow past a wedge) or spatial (flow past a cone). As for supersonic flow over the remainder of the surface, it is regarded as plane.

The analytical relationships for the characteristic epicycloids of two-dimensional flow can be used to calculate a plane supersonic flow of this type. A definite local M and a definite flow deflection angle correspond to each point of an epicycloid as the flow expands isentropically from the initial state with M = 1 and the critical pressure p*. Hence it follows that at the same time a definite pressure-ratio value

$$\frac{p}{p^*} = \left(\frac{k+1}{2}\right)^{\frac{k}{k-1}} \left(1 + \frac{k-1}{2} M^2\right)^{-\frac{k}{k-1}} \qquad \text{(IV-7-11)}$$

corresponds to each point of the epicycloid.

This formula enables us to calculate the pressure at those points of the flow at which the state of the gas has changed as a result of isentropic expansion or compression. Here the initial isentropic-flow parameters are determined immediately behind the

compression shock, where the flow has been deflected through a certain angle β_p and where the local M is equal to some value $M_2 > 1$.

Assume that it is required to find the pressure at a certain point of a surface the tangent to which forms an angle β with the vector $\overline{V}_\infty$. For this purpose, we use (IV-1-17) or Table IV-1-1 to find for M_2 the angle ω_2, which is equal to the rotation angle of the flow expanding from M = 1 to $M = M_2 > 1$. We then find the total rotation angle $\omega = \omega_2 + \beta_p - \beta$, for which Table IV-1-1 gives us the local M. Introducing this number into (IV-7-11), we calculate the ratio p/p^* and then the pressure coefficient

$$\bar{p} = 2\left(\frac{p}{p^*} - \frac{p_\infty}{p^*}\right)\left(kM_\infty^2 \frac{p_\infty}{p^*}\right)^{-1}. \qquad \text{(IV-7-12)}$$

When this method is used to calculate hypersonic flow past slender sharpened bodies, we can use the simplified equation (IV-1-18) for the epicycloids. If this equation is referred to the flow conditions immediately behind the compression shock,

$$\omega_2 = -\frac{2}{k-1}\left(\frac{1}{M_2} - 1\right). \qquad \text{(IV-7-13)}$$

For an arbitrary point on the controur $\omega = \omega_2 + \beta_p - \beta$.

As a result, the relation between the angle ω and M assumes the extremely simple form

$$\Delta\beta = \omega - \omega_2 = -\frac{2}{k-1}\left(\frac{1}{M} - \frac{1}{M_2}\right). \qquad \text{(IV-7-14)}$$

The remaining parameters, such as the pressure, density, temperature, and flow velocity, are calculated by (III-3-7) or (III-3-8) from the value found for M.

For example, we can obtain a relation from (III-3-7) for calculation of the pressure coefficient: /177

$$\frac{\bar{p}}{\beta_p^2} = \left(\frac{M_2}{M}\right)^{\frac{2k}{k-1}}\left(\frac{\bar{p}_k}{\beta_p^2} + \frac{2}{kK_1^2}\right) - \frac{2}{kK_1^2}. \qquad \text{(IV-7-15)}$$

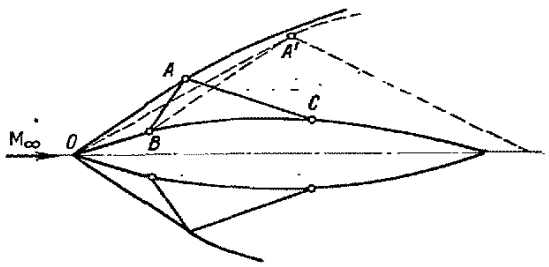

Figure IV-7-2. Interaction of Waves in Supersonic Flow over Flat Contour.

The Mach number M_2 in this formula and (IV-7-14) is also determined from simplified relationships for a wedge or cone.

The expression for the pressure coefficient at an arbitrary point of a curved surface can be presented in the general form

$$\bar{p} = \bar{p}_2 + \frac{\rho_2 V_2^2}{\rho_1 V_1^2} f_p(M_2, \beta_p - \beta), \quad \text{(IV-7-16)}$$

where f_p is a certain function that depends on M_2 behind the shock at the sharp nose and on the flow rotation angle $\beta_p - \beta$.

This function is independent of surface for a given M_2. Parameters with the subscript 2 are determined in accordance with whether the flow in front of the sharp nose is plane (wing) or spatial (body).

Application of the above method is better justified for calculation of plane supersonic flows, e.g., over wings. Its inaccuracy is due to failure to take account of the interaction between the washed surface and the compression shock (Fig. IV-7-2) in the region to the right of the reflected wave AC.

In investigation of flows over sharp bodies, an error arises from substitution of plane flow for spatial behind the shock wave.

Calculations by this method give more satisfactory results as the velocities increase. For wings, it may be regarded as accurate when the simple expansion wave reflected from the shock wave at point A' does not intersect the surface (Fig. IV-7-2).

For slender bodies, accuracy increases with increasing parameter $K = M_\infty \beta_p$. Experimental studies indicate that good results are obtained when $K > 1$ and the attack angles are not large.

For large attack angles, substantial deviations from experimental results are observed on the windward side of the surface; this is associated with a strong influence of viscosity, which is not taken into account by this method.

Unlike the Newton method, this method can be used to calculate flow over those zones of a surface that have negative inclinations to the velocity vector $\bar{V}_\infty$, i.e., zones in the "shaded"

region. It follows from the very content of the method that it can give the experimentally observed negative pressure coefficients in a certain region. Here, the agreement with experimental data may be satisfactory when a "shaded" zone comes directly behind the "shock" region. Some caution should be exercized in applying the method to evaluate supersonic-flow variables for tapering tail regions of the body remote from the nose, since it does not take account of all of the complex processes of flow past the upstream zones. /178

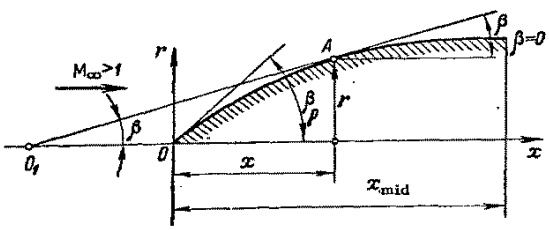

Figure IV-7-3. Diagram Illustrating Method of "Tangent" Cones.

One of the peculiarities of these processes is that they involve interaction between the flow and the shock wave, and this exerts a substantial influence on the variation of the gas parameters.

Also among the deficiencies of the method is the fact that it does not consider the prior history of gas-particle motion. It is unimportant for this method how the particle moved to its present position, and only its position is regarded as essential. Thus, the variables at any given point will be the same regardless of the shape of the surface on the preceding segment, provided that constant taper angles β_p and inclination angles β of the surface at the particular point are preserved.

The above applies to both the nose and tail zones of the body. However, while experimental data indicate that there are practically no manifestations of these deficiencies around the bow, the deviation from the true picture may be more substantial at the stern.

Method of "tangent surfaces." To illustrate this method, let us consider solution of the problem of symmetrical supersonic flow past a tapered solid of revolution. The pressure coefficient at a certain point A of the surface of a body in flow with $M_\infty > 1$ is assumed to be of the same magnitude as on a conical surface tangent to this point and washed by a flow with the same M_∞ (Fig. IV-7-3). Such is the content of the "tangent cone" method, which, as we see, makes it possible to investigate the flow over a surface with a curvilinear generatrix by use of data on supersonic flow over a simpler conical surface.

This method can be extended to sharp surfaces of arbitrary shape by setting the pressure coefficient at any point of the surface equal to its value at the same point on an appropriate

tangent surface (the "tangent surface" method).

In selecting the shape of the tangent surface, which is an essential point in the calculation, the shape of the washed surface under investigation must be taken into account (Fig. IV-7-4). For example, the tangent surface for a wing is a plane with a leading edge having the same sweep as line AB, at point on which the pressure is determined. For a tapered solid of revolution, the tangent surface will be a circular cone. /179

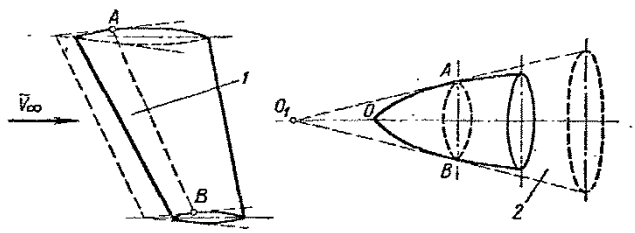

Figure IV-7-4. Construction of Tangent Surface on Wing and Body. 1) plane tangent surface to wing; 2) conical tangent surface to body.

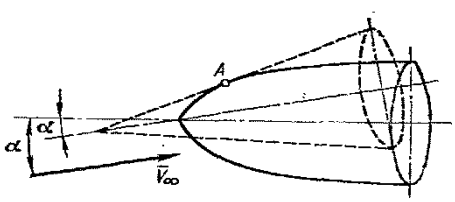

Figure IV-7-5. Tangent Surface in the Presence of an Attack Angle.

The taper angle of the tangent surface is equal to the angle formed by the tangent to the particular surface point with the vector $\bar{V}_\infty$. In the presence of an attack angle, the tangent surface must be so constructed that flow will strike it at zero angle of attack (Fig. IV-7-5). Thus, the pressure at a point on a tapered surface in flow at an angle of attack is assumed to be the same as on the corresponding tangent surface with the condition that $\alpha = 0$ for the latter.

We might examine another variety of the tangent-surface method based on the hypothesis of equal velocities at the point of tangency of the real and tangent surfaces. According to this hypothesis, the pressure coefficient is determined by the formula $\bar{p}_v = [2/(kM_\infty^2)]\,(p_v/p_\infty - 1)$, in which the absolute pressure

$$p_v = p_0' \left(1 - \frac{V_c^2}{V_{max}^2}\right)^{\frac{k}{k-1}} \qquad \text{(IV-7-17)}$$

is calculated from the velocity V_v and the stagnation pressure p_0'. This pressure is determined for a given M_∞ from the angle of the shock at the point of the body (the subscript "v" pertains to quantities calculated by the equal-velocity hypothesis).

The calculation based on the equal-velocity hypothesis can be simplified by use of results obtained with an equal-pressure hypothesis. Since the velocities calculated on the basis of the two hypotheses are the same, we can find the relation

$$\bar{p}_v = \bar{p}_p \bar{\nu} + \frac{2(\bar{\nu}-1)}{kM_\infty^2}, \qquad \text{(IV-7-18)}$$

where $\bar{p}_p$ is the pressure coefficient corresponding to the equal-pressure hypothesis; $\bar{\nu}$ is equal to the ratio ν_0/ν, in which the coefficient $\nu = p''/p_0$ is calculated from the stagnation pressure p_0'' for the local tangent surface inclined at β to the vector $\bar{V}_\infty$, and the quantity $\nu_0 = p_0'/p_0$ is determined from the stagnation pressure p_0' for the tangent surface with inclination angle β_0.

Thus, in order to calculate the pressure coefficient $\bar{p}_v$, it /180
is first necessary to find the value of $\bar{p}_p$ on the local tangent surface and determine the ratio $\bar{\nu} = \nu_0/\nu$. At the point, this ratio is unity, and for points where $\beta < \beta_p$, the quantity $\bar{\nu} < 1$. As follows from (IV-7-18), therefore, the coefficient $\bar{p}_v$ assumes a zero value in a certain section and then becomes negative downstream.

The possibility of obtaining negative pressure coefficients is the fundamental difference between the "tangent surface" method, which is based on the equal-velocity hypothesis, and the method based on the hypothesis of equal pressures, in which the pressure coefficient may be either greater than or equal to zero.

Experimental data and certain theoretical investigations indicate that distinct regions of rarefaction arise on areas remote from the nose at moderate Mach numbers M_∞. This confirms that the equal-velocity hypothesis is more realistic for such velocities than the equal-pressure hypothesis.

At very large M_∞, almost all of the positive-slope surface comes under a positive excess pressure; this is at variance with the equal-velocity hypothesis, which gives improbably low pressure values.

The sense of this method makes it applicable for calculation of flow at points at which the tangent-surface inclination to the

vector $\overline{V}_\infty$ forms an angle $\beta \geq 0$. Here, at the point where $\beta = 0$, the pressure p_p is assumed equal to the pressure p_∞ of the undisturbed flow and, consequently, the pressure coefficient at this point $\overline{p}_p = 0$. Thus, this method is not, strictly speaking, applicable to surface elements with negative slope ($\beta < 0$).

However, the "tangent surface" method can be used for rough estimation of the pressure coefficient in the "shaded" zone. It is assumed here that the pressure coefficient will be negative on a surface elements with angle $\beta < 0$, but equal in absolute magnitude to the pressure coefficient on an element with a positive inclination angle ($\beta > 0$).

The Busemann formula. According to the Newtonian corpuscular theory, an aerodynamic force arises as a result of collision of gas particles with the surface. Thus, the fundamental conception of this theory consists precisely in the impact effect.

The conclusions of the Newtonian theory can be obtained from shock-wave theory by making the limit transition in the appropriate expressions for $k \to 1$, $M_\infty \to \infty$, which corresponds to full application of the shock wave to the surface and, consequently, an infinitesimally thin compressed layer.

Under real flow conditions, the shock wave cannot approach flush to the surface. Hence, as they impact on passage across the compression shock, the particles continue to move on curved trajectories. As a consequence, the pressure on the surface of the body differs from the pressure immediately behind the shock.

The phenomenon will be fundamentally the same in a hypothetical flow with $M_\infty \to \infty$, $k \to 1$. Crossing a shock wave in coincidence with the surface, the gas particles continue their motion in an infinitesimally thin layer along geodesic lines of the surface.

The velocity V_2 of this motion, calculated from compression-shock theory for $k \to 1$, $M_\infty \to \infty$, is $V_2 = V_1 \cos \beta$ (the subscripts 1 and 2 pertain to the flow variables before and after the shock, respectively).

The motion along the curved trajectory will result in the appearance of a centrifugal force, which will change the pressure on the body's surface from the value obtained by Newton's theory.

The magnitude of this force, which is determined by the mass per unit volume of the particles that have passed through the shock (density ρ_2) and by the centrifugal acceleration V_2^2/R, where R is the radius of curvature of the washed contour, is $\rho_2 V_2^2/R$. Consequently, the elementary pressure value created by this force in a thin layer of thickness dn will be $dp_{cf} = (\rho_2 V_2^2/R)dn$. /181

The product $\rho_2 V_2^2 dn$ can be replaced by an expression obtained from the flow rate equation $\rho_2 V_2^2 f(x) dn = \rho_1 V_1 dS$, in which $f(x) = 1$ for plane and $f(x) = 2\pi r(x)$ for spatial symmetrical flows; S is cross-sectional area. Then the elementary centrifugal pressure

$$dp_{cf} = \frac{\rho_1 V_1^2 \cos\beta}{Rf(x)} dS.$$

Integrating this relationship over S and remembering that the pressure $\rho_1 V_1^2 \sin^2\beta$ behind the shock wave, we find [38]

$$p = \rho_1 V_1^2 \left[\sin^2\beta - \frac{1}{f(x) R} \int_0^S \cos\beta \, dS \right]. \qquad \text{(IV-7-19)}$$

This formula, which was derived by Busemann, determines the pressure not only as a function of the local inclination of the elementary surface with respect to the vector $\bar{V}_\infty$, but also as a function of the shape of the surface over the entire zone between the surface element and the forward point.

For slender bodies for which the angles β are everywhere small ($\cos\beta \approx 1$, $\sin\beta \approx \beta$), the influence of surface shape on the preceding segment is found to be negligible. Formula (IV-7-19) becomes

$$p = \rho_1 V_1^2 \left[\beta^2 - \frac{S}{f(x) R} \right]. \qquad \text{(IV-7-20)}$$

Substituting the slender-body value $R = -(d^2y/dx^2)^{-1}$ for the radius of curvature and converting to the pressure coefficient, we obtain

$$\bar{p} = 2\left[\beta^2 + \frac{S}{f(x)} \frac{d^2y}{dx^2} \right], \qquad \text{(IV-7-21)}$$

where y is the coordinate of a point on the wing surface (plane flow) or body surface (spatial flow).

In the latter case, y is equal to the radius r of the solid-of-revolution generatrix.

As in the case of the improved Newton formula, we can write the Busemann formula for the pressure coefficient

$$\bar{p}=\frac{\bar{p}_0}{\sin^2\beta}\left[\sin^2\beta-\frac{1}{f(x)R}\int_0^S\cos\beta\,dS\right]. \qquad \text{(IV-7-22)}$$

For a slender body

$$\bar{p}=\frac{\bar{p}_0}{\beta_0^2}\left[\beta^2+\frac{S}{f(x)}\frac{d^2y}{dx^2}\right] \qquad \text{(IV-7-23)}$$

or

$$\bar{p}=\frac{\bar{p}_0}{\beta_0^2}\left(\beta^2+\frac{y}{\nu}\frac{d^2y}{dx^2}\right), \qquad \text{(IV-7-24)}$$

where $\nu = 1$ for plane flows and $\nu = 2$ for symmetrical spatial flows.

The above relationships differ from the corresponding Newtonian formulas in having a second term in the brackets that characterizes the influence of contour curvature and, consequently, takes account of the centrifugal-force influence on pressure.

Studies have shown that this effect will be real for flow over concave surfaces with $k = 1.4$.

For bodies with convex surfaces, correction for the influence of centrifugal forces is physically meaningless; hence it is better to use the Newtonian formula for the calculations. However, it gives high values of the pressure for thin surfaces when $M_\infty \to \infty$, $k \to 1$, and, consequently, preference should be given in this case to the Busemann formula. /182

§IV-8. AERODYNAMIC HEATING

Flight in the atmosphere is accompanied by transfer of heat from the environment to the vehicle when the gas temperature near its surface rises above that of the body. The high-temperature regions arise as a result of flow stagnation in the shock waves and boundary layer, with the resulting increase in the static enthalpy of the air.

The heat-transfer calculation consists in determining: a) the rate of heat transfer at the total-stagnation point; b) the rate of heat transfer at any other point on the wall; c) the total heat flow to the surface. Solution of the first problem makes possible proper design of the cooling system or selection of other means of protecting the surface from overheating. Solution of the other two makes it possible to identify zones at which excessive thermal stressing occurs and surface damage is possible, with a view

to adopting practical precautionary measures.

Let us examine certain general concepts of aerodynamic-heating theory.

The Parameters of Heat Transfer

Temperature and enthalpy in the boundary layer. Let us examine expressions that define the temperature and enthalpy for the conditions of total stagnation in the boundary layer.

If no energy transfer occurs at all, i.e., the viscosity forces do no work, heat conduction is absent, and there are no diffusive or radiative heat flows, the stagnation temperature is

$$T_0 = T + \frac{V_x^2}{2(c_p)_{av}}, \qquad \text{(IV-8-1)}$$

where V_x is the velocity at a certain point in the cross section of the boundary layer, T is the static temperature at this point, and $(c_p)_{av}$ is the average specific heat for the temperature range T_0 - T.

The temperature T_0, a measure of total energy, does not change over the thickness of the layer and is determined by the parameters T_δ and V_δ on the outer edge of the boundary layer in accordance with the expression

$$T_0 = T_\delta + \frac{V_\delta^2}{2(c_p)_{av}}. \qquad \text{(IV-8-1')}$$

Substituting in this expression

$$V_\delta^2 = M_\delta^2 \bar{k} R T_\delta \quad \text{and} \quad (c_p)_{av} = R\bar{k}/(\bar{k}-1),$$

where M_δ is the Mach number at the outer edge and $\bar{k}$ is the average ratio of specific heats for the temperature range T_0 - T_δ, we obtain the approximate relation /183

$$T_0 = T_\delta \left(1 + \frac{\bar{k}-1}{2} M_\delta^2\right); \qquad \text{(IV-8-1")}$$

with constant heat capacities, it is necessary to set $\bar{k} = k =$ = const. When heat capacity varies strongly with temperature as a result of dissociation and ionization, and it cannot be replaced by an average value, it is advisable to use instead of T_0 the stagnation enthalpy, which is determined by the expressions

$$i_0 = i + \frac{V_x^2}{2} = i_\delta + \frac{V_\delta^2}{2}, \qquad \text{(IV-8-2)}$$

where i and i_δ are the respective enthalpies at an arbitrary point in the boundary layer and on its outer edge.

By analogy with (IV-8-1"), we can use the following formula to calculate i_0 for constant heat capacities:

$$i_0 = i_\delta \left(1 + \frac{k-1}{2} M_\delta^2\right). \qquad \text{(IV-8-2')}$$

Let us now consider the case in which the wall is heat-insulated (adiabatic) and the processes taking place in the boundary layer are characterized by energy transfer. Here, owing to the work of friction, the wall heats up, and this is accompanied by conductive heat transfer into its deeper layers. Heating will increase until equilibrium is reached between the heat transfer from the inner layers to the outer layers, and the inflow of heat due to the work of the viscosity forces. The corresponding wall temperature T_r is known as the equilibrium or recovery temperature and is obviously lower than the stagnation temperature T_0. This drop in wall temperature can be characterized by the recovery coefficient

$$r = \frac{T_r - T_\delta}{T_0 - T_\delta}, \qquad \text{(IV-8-3)}$$

which indicates how close the recovery temperature is to the stagnation temperature.

With dissociation and ionization, it is preferable to convert to the recovery enthalpy i_r and the corresponding recovery coefficient

$$r = \frac{i_r - i_\delta}{i_0 - i_\delta}. \qquad \text{(IV-8-4)}$$

According to (IV-8-3) and (IV-8-4), the expressions for the recovery temperature and enthalpy take the forms

$$T_r = T_\delta + r\frac{V_\delta^2}{2(c_p)_{av}}; \quad T_r = T_\delta\left(1 + r\frac{\bar{k}-1}{2}M_\delta^2\right), \qquad \text{(IV-8-5)}$$

$$i_r = i_\delta + r\frac{V_\delta^2}{2}; \quad i_r = i_\delta\left(1 + r\frac{\bar{k}-1}{2}M_\delta^2\right), \qquad \text{(IV-8-6)}$$

where $(c_p)_{av}$ and $\bar{k}$ are the average values for the temperature range $T_r - T_\delta$.

The recovery coefficient is determined from the general formula $r - Pr^m$, in which $m = 1/2$ for a laminary boundary and $M = 1/3$ for a turbulent one. The Prandtl number Pr and hence the coefficient r depend on physicochemical transformations in the gas. However, this dependence is weak, and in approximate calculations we may assume the recovery coefficient to be constant at $r_l = 0.85$ for a laminar boundary layer and $r_t = 0.88$-0.9 for a turbulent layer.

Determining parameters. Flow in a compressible boundary layer at high velocities is characterized by a certain law of variation of temperature, enthalpy, and other thermodynamic and kinetic variables of the gas over the thickness of the layer. In practice, flow in the layer is characterized by determining parameters, which represent certain averaged values of temperature, enthalpy, density, etc., that are constant for the cross section under consideration. /184

A boundary layer with such parameters is calculated with the relationships for an incompressible gas. The data obtained on friction and heat transfer are in very good agreement with experimental results found in the absence of diffusion for flow along a surface with constant pressure (for example, past a plate or cone) in a broad range of velocities (V_δ = 300-7000 m/s), temperatures (T_δ = 450-6500°K; T_{w1} = 300-3000°K), and pressures (p_δ = = 0.1-10 atm).

The parameters on which the properties of such an arbitrary incompressible boundary layer depend are calculated as functions of temperature for a certain enthalpy i* between the extreme values of i obtaining in the boundary layer. According to Eckert [50],

$$i^* = 0{,}5\,(i_{w1} + i_\delta) + 0{,}22\,(i_r - i_\delta), \qquad \text{(IV-8-7)}$$

where i_{w1} and i_δ are the enthalpies of the gas at the wall and at the layer outer edge, respectively; i_r is the recovery enthalpy.

Relation (IV-8-7) can also be represented in another form:

$$\frac{i^*}{i_\delta} = \frac{1}{2}\left[\left(1 + \frac{V_\delta^2}{2i_\delta}\right)\bar{i}_{w1} + 1\right] + 0.22r^*\frac{V_\delta^2}{2i_\delta}, \qquad \text{(IV-8-7')}$$

where

$$\bar{i}_{w1} = i_{w1}/i_0.$$

The determining enthalpy depends on the structure of the boundary layer and on M_∞. There are a number of relationships that can be used to calculate i* separately for laminar and turbulent boundary layers and for various M_∞ ranges. Formula (IV-8-7) compares favorably with these relationships by virtue of its universality and the fact that it can be applied with a certain approximation for both laminar and turbulent flows in a rather broad range of M_∞.

As we see from (IV-8-7), it is necessary to know the wall enthalpy i_{w1} to calculate i*. In the practically most important case in which the surface temperature is held at a required level, the wall enthalpy will be known. If, however, heating is spontaneous, the determination of i_{w1} requires solving the problem of heat transfer between the wall and the gas.

Of the two parameters that appear in (IV-8-7), the enthalpy i_δ at the outer boundary of the layer is usually known. As for the recovery enthalpy, it is determined from the expression

$$i_r = i_\delta + r^*\frac{V_\delta^2}{2}. \qquad \text{(IV-8-8)}$$

in which the recovery coefficient r* can generally be calculated as a determining parameter with the expression $r^* = (Pr^*)^m$, where the Prandtl number $Pr^* = c_p^*\mu^*/\lambda^*$ (the symbol "*" signifies the determining values of all quantities).

Relation (IV-8-7) is used in the general case of a dissociating gas and when the gas in the boundary layer is heated to a temperature at which dissociation does not yet occur but the heat capacities change.

In the former case, the determining temperature is found as a function of p and i*. Tables or diagrams of state for air at very high temperatures can be used for the calculations. /185

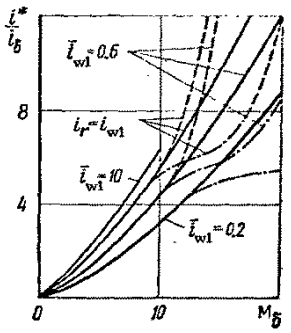

Figure IV-8-1. Determining Enthalpy (broken lines without consideration of dissociation; solid lines with dissociation taken into account at a pressure p = 100 kg/cm^2; dot-dash lines for p = = 0.001 kg/cm^2).

In the latter case, (IV-8-7) can be used to find the determining temperature, with the enthalpy replaced by temperature in accordance with the expression

$$i_k - i_\delta = (c_p)_{av.}(T_k - T_\delta), \qquad \text{(IV-8-9)}$$

where the enthalpy i_k may assume the values of i_r, i_{w1}, or i* and the temperature T_k the respective values T_r, T_{w1}, or T*. The average heat capacity $(c_p)_{av}$ is calculated for the temperature range $T_k - T_\delta$. As a result of substitution, we obtain instead of (IV-8-7) a relation for the determining temperature T*, with the recovery temperature found by (IV-8-5), in which r* is substituted for r.

When the specific heats to not depend on temperature (at temperatures of approximately 700-800°C or lower),

$$T^* = \frac{1}{2}(T_\delta + T_{w1}) + 0.22(T_r - T_\delta).$$

Introducing the values for T_r and T_0 into this relation, we obtain

$$\frac{T^*}{T_\delta} = \frac{1}{2}\left[1 + \left(1 + \frac{k-1}{2}M_\delta^2\right)\bar{T}_{w1}\right] + 0.22\frac{k-1}{2}rM_\delta^2,$$

where $\bar{T}_{w1} = T_{w1}/T_0$.

For a heat-insulated wall, it is necessary to take $T_{w1} = T_r$ in the relationships given above for the determining values of enthalpy and temperature.

Figure IV-8-1 shows determining-enthalpy values calculated by (IV-8-7) for undissociated and dissociated gases.

The thermodynamic functions and kinetic coefficients are calculated in dependence on the determining temperature by the formulas

$$\frac{c_p^*}{c_{p\infty}} = \left(\frac{T^*}{T_\infty}\right)^\varphi; \quad \frac{\mu^*}{\mu_\infty} = \left(\frac{T^*}{T_\infty}\right)^n; \quad \frac{\lambda^*}{\lambda_\infty} = \left(\frac{T^*}{T_\infty}\right)^\varkappa. \qquad \text{(IV-8-10)}$$

The heat-balance equation. In its general form, this equation determines the over-all heat flow q_{wl} going to heat the wall. It is equal to the difference between the heat inflow q_i to the surface and the heat flow q_w withdrawn from it, i.e., $q_{wl} = q_i - q_w$.

The heat inflow arises as a consequence of: heating of the boundary layer due to friction (convective q_c and radiative q_{rad} heat flows); radiation from the sun q_s and earth q_e; transfer of heat from the equipment, q_{eq}. Thus,

$$q_i = q_c + q_{rad} + q_s + q_e + q_{eq} \qquad \text{(IV-8-11)}$$

The heat withdrawn is composed of the thermal energy emitted by the heated surface (q_{em}), that absorbed by the wall material and dissipated into the environment during ablation (q_{ab}), and the heat withdrawn by various cooling systems (q_{cs}).

Consequently,

$$q_w = q_{em} + q_{ab} + q_{cs}. \qquad \text{(IV-8-12)}$$

The heat flow from the equipment and the heat withdrawn by the cooling system may have large specific weights in the heat balance. Problems involving the permissible q_{eq} and the required q_{cs} are primarily of a structural-engineering nature. /186

Convective heat flow. At flow velocities at which there are no chemical reactions in the boundary layer, the specific convective heat flow is determined with a modification of Newton's law:

$$q_c = \alpha_{w1}(T_r - T_{w1}). \qquad \text{(IV-8-13)}$$

Chemical processes become essential at very high velocities, and the change in enthalpy must be taken into account in calculating heat transfer in accordance with the formula

$$q_c = \frac{\alpha_{w1}}{(c_p)_{w1}}(i_r - i_{w1}), \qquad \text{(IV-8-14)}$$

where α_{w1} is the heat output coefficient and $(c_p)_{w1}$ is the specific heat capacity for the conditions of the gas at the wall.

To characterize heat flow, it is convenient to use dimensionless heat-transfer criteria instead of the dimensional heat output coefficient, namely, the Stanton number

$$St = \frac{q_c}{\rho_\delta V_\delta (i_r - i_{w1})} = \frac{\alpha_{w1}}{\rho_\delta V_\delta (c_p)_{w1}} \qquad \text{(IV-8-15)}$$

and the Nusselt number

$$Nu = \alpha_{w1}\ell/\lambda_{w1}. \qquad \text{(IV-8-16)}$$

where ℓ is an arbitrary linear dimension and λ_{w1} is the thermal conductivity coefficient of the gas at the wall.

The relation between these two numbers is established by the relation

$$Nu = StRePr, \qquad \text{(IV-8-17)}$$

where the Reynolds number $Re = V_\delta \rho_\delta \ell/\mu_\delta$; the Prandtl number $Pr = (c_p)_{w1}\mu_\delta/\lambda_{w1}$.

The basic problem of aerodynamic heat-transfer theory consists in determining α_{w1} or the dimensionless heat-transfer coefficients.

Radiative heat flux. As a result of the sharp rise in temperature behind the shock wave or in the boundary layer, the nitric oxide concentration in the air rises substantially, with the result that the air ceases to be optically transparent and becomes a source of radiative flux.

The optical properties of air are characterized by a certain parameter ε, which is the emissivity of a unit length of radiating layer and has the dimensions $1/\ell$. For a radiating layer s_0 thick, the dimensionless characteristic of emissivity will be εs_0, which is known as the effective emissivity of the gas.

According to the Stefan-Boltzmann law, the heat radiated by an absolutely black body is $q_{rad} = \sigma T^4$. To take account of transparency, this formula must include a certain function $f(\varepsilon s_0)$ that depends on effective emissivity and characterizes the "blackness" of the gas. Thus, the radiative heat flux to the wall is

$$q_{rad} = f(\varepsilon s_0)\sigma T^4, \qquad \text{(IV-8-18)}$$

where $\sigma = 5.85 \cdot 10^{-9}$ kg·m/m^2·s·deg^4 is the emission coefficient of the absolutely black body and T is the temperature of the radiating gas.

Formula (IV-8-18) pertains to the case in which the wall does not radiate and its temperature $T_{w1} < 3000°K$.

Figure IV-8-2 shows a curve characterizing the variation of the function $f(\varepsilon s_0)$ with effective emissivity. This curve can be approximated by the equation /187

$$f = 1 - \exp(-\varepsilon s_0), \qquad \text{(IV-8-19)}$$

which gives an error no greater than 20%.

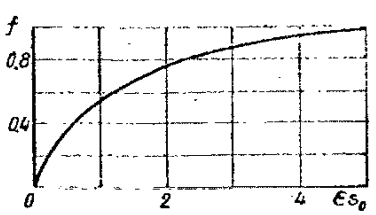

Figure IV-8-2. Variation of Function $f(\varepsilon S_0)$ Which Characterizes Radiative Flux at the Critical Point.

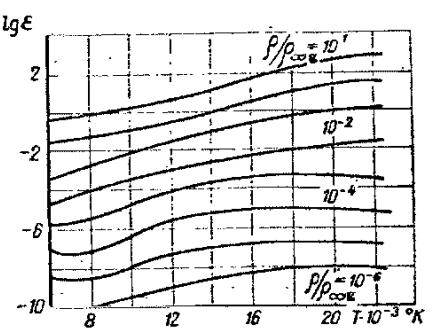

Figure IV-8-3. Experimental Data on Gas Emissivity.

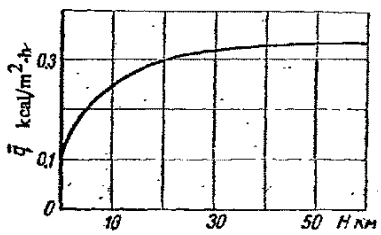

Figure IV-8-4. Radiative Power of Sun as a Function of Altitude.

We see from Fig. IV-8-3 [11], which presents the results of experimental studies, that the parameter ε depends on air temperature and density. In the temperature range 8000°K $\leq$ T $\leq$ 16,000°K, the family of curves in Fig. IV-8-3 is closely approximated by the formula

$$\varepsilon = 0.138 \left(\frac{\rho}{\rho_{\infty g}}\right)^{1.28} \left(\frac{T\,^\circ K}{10^4}\right)^{6.54} cm^{-1}, \quad \text{(IV-8-20)}$$

where $\rho_{\infty g}$ is the density of the air at the ground.

Solar and ground radiation. The radiant heat flux from the sun

$$q_s = \bar{q}\beta_s \cos\psi, \quad \text{(IV-8-21)}$$

where ψ is the angle between the direction of the sunlight and the normal to the body's surface; $\bar{q}$ is the radiative power of the sun, which depends basically on altitude, weather conditions, and the zenith distance of the sun.

Figure IV-8-4 shows values of $\bar{q}$ for the sun at the zenith for average geographic conditions but without consideration of absorption by the atmosphere. Data on the coefficient β_s, which takes account of the absorptivities of matter, are given in Table IV-8-1 [6].

The specific heat flux from the ground is very small. For convenience, it may be regarded as the sum of two components: $q_{i.e}$, the intrinsic radiative flux from the earth, and the heat flow $q_{r.e}$, composed of sunlight reflected from the earth's surface and from clouds.

Research has shown [11] that for the conditions of flight at 500 km, $q_{i.e}$ can be found in approximation by the formula

$$q_{i.e.} = 0.007\,(1 + 2\cos\varphi)\,\beta_e, \quad \text{(IV-8-22)}$$

where ϕ is the angle between the normal to the surface and the vehicle-ground line.

Available experimental data indicate the possibility of calculating the maximum ground radiant flux by the formula /188

$$(q_e)_{max} = \bar{q}_e \beta_e. \qquad \text{(IV-8-23)}$$

TABLE IV-8-1. ABSORPTIVITIES OF MATERIALS (Values of the Coefficients β_s and β_e)

Material \ Type of radiation	From earth (β_e)	From sun (β_s)
Al	0.04—0.10	0.10—0.49
Fe	0.06—0.74	0.45
Ni	0.01—0.39	0.40
Alloys:		
Duralumin type	0.04—0.55	0.53
Alloy steels	0.12—0.62	0.60
Insulating materials:		
Plexiglas	0.89	—
Glass	0.85	—
Painted surfaces		
Dark	0.80—0.99	0.97
Light	0.80—0.90	0.14—0.18

Note: The data on the coefficients β_e and β_s are given for the wall-temperature range 200-600°C.

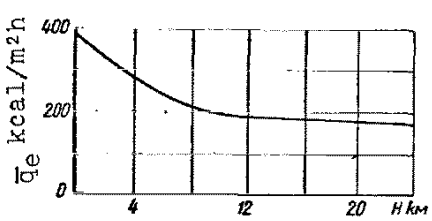

Figure IV-8-5. Curve of $\bar{q}_e$ as a Function of Altitude H.

Values of $\bar{q}_e$ and β_e are given in Fig. IV-8-5 and Table IV-8-1, respectively.

Data on the specific heat flow $q_{r.e}$ are also experimental and have been obtained for a body at an altitude of 500 km on the earth-sun line [11]. According to this source,

$$q_{r.e} = 0.016(1 + 2\cos\varphi)\beta_e. \qquad \text{(IV-8-24)}$$

Radiant heat flow from the wall surface. The heat flow emitted by a unit area of the wall is determined by the Stefan-Boltzmann law

$$q_{em} = \varepsilon\sigma T^4, \qquad \text{(IV-8-25)}$$

where ε is the blackness of the surface or the emission coefficient, and depends on the material, the method of surface preparation, and surface temperature.

Data on the emission coefficient are given in [11].

The emission coefficient rises with increasing surface roughness. If the height of surface prominences is several times the wavelength of the radiation, the dependence of the emission coefficient ε_r of the rough surface on the emission coefficient ε of the smooth surface can be expressed by the formula

$$\varepsilon_r = \varepsilon[1 + 2.8(1-\varepsilon)^2]. \qquad \text{(IV-8-26)}$$

Here the wavelength of the maximum-intensity radiation depends on temperature:

$$\lambda = \frac{2898}{T}\mu k. \qquad \text{(IV-8-27)}$$

Equation for calculation of temperature of a thin skin. Let us assume that the skin of a vehicle is a thin wall and is heated instantaneously throughout its entire thickness. In this case, the specific heat flow absorbed by the wall is /189

$$q_{w1} = c\gamma\delta\frac{dT_{w1}}{dt}, \qquad \text{(IV-8-28)}$$

where c, γ, and δ are the heat capacity, specific gravity, and thickness of the skin material.

After substituting q_{w1} into the heat-balance equation $q_{w1} = q_i - q_w$, we obtain an equation for calculation of the temperature of a thin skin:

$$c\gamma\delta\frac{dT_{w1}}{dt} = \alpha_{w1}(T_r - T_{w1}) + q_{rad} + q_s + q_e + q_{eq} - \varepsilon\sigma T_{w1}^4 - q_{cs}. \qquad \text{(IV-8-29)}$$

This equation is solved by numerical methods if the flight trajectory, the initial skin temperature, its material, and its thickness are known. The result is T_{w1} as a function of time t. The following fundamentally possible ways to lower wall temperature proceed from (IV-8-29): 1) reducing the convective heat flow

by reducing α_{w1}. The heat output coefficient is lowered under the conditions of flight in a thin atmosphere. The coefficient α_{w1} is substantially lower for a laminar boundary layer; 2) use of artificial cooling. For example, cooling by evaporation of a liquid through pores in the skin is highly effective; 3) increasing the roughness of the surface; 4) use of heat-insulating coatings with large heat capacities.

Equilibrium radiation temperature. Let us assume that the thermal conditions, which are characterized solely by convective inflow from the boundary layer to the wall and withdrawal of heat energy from it by radiation are steady, i.e., that the wall temperature does not change with time and that $dT_{w1}/dt = 0$. Then (IV-8-29) becomes

$$\alpha_{w1}(T_r - T_{w1}) = \varepsilon\sigma T_{w1}^4 \qquad \text{(IV-8-30)}$$

The wall temperature determined by this equation is known as the equilibrium radiation temperature and is denoted by T_e.

This concept differs from that of the recovery temperature, which is by definition the temperature of the surface in the absence of radiation and any internal dissipation or supply of heat. Hence the temperature T_r is sometimes known as the adiabatic-wall temperature.

The temperature T_e represents a kind of upper limit for the radiating surface, one that is reached when the heated wall radiates all of the energy that it receives. This temperature is not realistic at very high heat flows, since it is so high that it cannot be reached before destruction of the material (melting, sublimation, combustion) occurs. In certain cases, however, the equilibrium radiation temperature may be found realistic — as on the surface of a soaring vehicle. In soaring, kinetic energy is converted into heat gradually, and the intensity of convective heat flow may be comparatively moderate, so that emission of all of the absorbed energy becomes quite possible at the structurally acceptable equilibrium temperature.

Equation (IV-8-30) contains the unknowns α_{w1}, T_{w1}, and T_r. Hence it must be supplemented by two independent relationships for these parameters from boundary-layer theory. Solution of the equation system enables us to find the temperature $T_{w1} = T_e$.

The equilibrium radiation temperature can be determined directly from (IV-8-30) by assigning values to T_r and α_{w1}/ε. Then the recovery temperature can be calculated from the enthalpy i_r, /190

which is equal to $i_r = 0.5V_\infty^2$ at high velocities. The solution of (IV-8-30) is given in Fig. IV-8-6 and permits the conclusion that the principal way to lower the equilibrium radiation temperature is to reduce the ratio α_{w1}/ε.

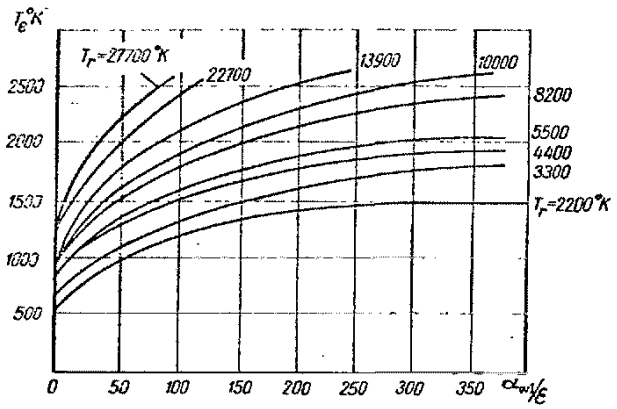

Figure IV-8-6. Equilibrium Radiation Temperature T_e as a Function of the Parameters α/ε and T_r.

The concept of equilibrium radiation temperature can be generalized for the case in which other forms of energy inflow are taken into consideration, as is withdrawal of heat by cooling, specifically q_s, q_e and q_{cs}. In this case, the equation for T_{w1} will be

$$\alpha_{w1}(T_r - T_{w1}) + q_s + q_e = \varepsilon\sigma T_{w1}^4 + q_{cs}. \qquad \text{(IV-8-31)}$$

Relation between friction and heat transfer. The heat transfer coefficient α_{w1} in the heat-balance equation can, with certain simplifying assumptions, be linked by comparatively simple relationships to the variables characterizing friction between the gas and the wall. These relationships appear in the system of equations for determination of aerodynamic heating.

To derive these relationships, let us examine the equations of motion (III-2-12) and energy (III-2-46) for flow conditions in a laminar boundary layer. If p = const in these equations, they will describe the supersonic boundary layer around a cone or plate or, with a certain approximation, around a slightly curved surface. If it is further assumed that the Prandtl and Schmidt

numbers are equal to unity,

$$\rho r^{\varepsilon} V_x \frac{\partial V_x}{\partial x} + \rho r^{\varepsilon} V_y \frac{\partial V_x}{\partial y} = \frac{\partial}{\partial y}\left(r^{\varepsilon}\mu \frac{\partial V_x}{\partial y}\right); \qquad \text{(IV-8-32)}$$

$$\rho r^{\varepsilon} V_x \frac{\partial i_0}{\partial x} + \rho r^{\varepsilon} V_y \frac{\partial i_0}{\partial y} = \frac{\partial}{\partial y}\left(r^{\varepsilon}\mu \frac{\partial i_0}{\partial y}\right). \qquad \text{(IV-8-33)}$$

On converting to the variables $\overline{V}_x = V_x/V_\delta$; $\theta = (i_0 - i_{w1})/(i_{0\delta} - i_{w1})$ in the equations, we note that $\overline{V}_x$ and θ satisfy the same equation and the same boundary conditions: V_x and θ are zero at the wall and one at the layer boundary. Consequently, according to the uniqueness theorem of the solution, the functions $\overline{V}_x$ and θ must be the same, i.e.,

$$\frac{i_0 - i_{w1}}{i_{0\delta} - i_{w1}} = \frac{V_x}{V_\delta}.$$

Considering the conditions at the wall, where $(\partial i_0/\partial y)_{w1} = (\partial i/\partial y)_{w1} = \frac{/191}{}$ $= [c_p(\partial T/\partial y)]_{w1}$, and remembering that the specific heat flow at the surface $q = -(\lambda \partial T/\partial y)_{w1}$, while the frictional stress $\tau_{w1} = [\mu(\partial V_x/\partial y)]_{w1}$, we obtain an expression for the heat flow

$$q = \frac{i_{0\delta} - i_{w1}}{(c_p)_{w1}}\left[\left(\frac{\lambda\tau}{\mu}\right)_{w1}\frac{1}{V_\delta}\right].$$

The quantity in the square brackets represents the local heat-output coefficient α_x. On the other hand, we know that the local coefficient of friction $c_{fx} = 2\tau_{w1}/\rho_\delta V_\delta^2$. Consequently, we have the following relation between these two coefficients:

$$\alpha_x = \frac{c_{fx}}{2}\frac{\rho_\delta V_\delta \lambda_{w1}}{\mu_{w1}}. \qquad \text{(IV-8-34)}$$

Relationships for the local Nusselt number

$$\mathrm{Nu}_x = \frac{\alpha_x x}{\lambda_{w1}} = \frac{c_{fx}}{2}\mathrm{Re}_x, \qquad \text{(IV-8-35)}$$

where $\mathrm{Re}_x = \rho_\delta V_\delta x/\mu_{w1}$, and for the local Stanton number

$$St_x = \frac{c_{fx}}{2} \qquad \text{(IV-8-36)}$$

follow from this expression.

The relation established between the friction and heat-transfer parameters is approximate, since Pr and Sc actually differ from unity. The influence of these numbers can be taken into account if the expressions for the Nusselt and Stanton numbers are written

$$Nu_x = \frac{1}{2} c_{fx} Re_x f_1(Pr, Sc); \quad St_x = \frac{1}{2} c_{fx} f_2(Pr, Sc), \qquad \text{(IV-8-37)}$$

where f_1 and f_2 are certain functions of Pr and Sc.

Physically, consideration of the influence of these nonunity numbers means that the excess chemical and kinetic energies are not converted completely into heat at the surface. The specific forms of the functions f_1 and f_2 are determined by solving the boundary-layer equations for the condition that $Pr \neq 1$, $Sc \neq 1$ ($Le \neq 1$). Research has shown that if the influence of diffusion is disregarded ($Le = 1$), then $f_1 = Pr^{1/3}$, and $f_2 = Pr^{-2/3}$. Thus, we have for the local Stanton number

$$St_x = \frac{c_{fx}}{2} f_2 = \frac{c_{fx}}{2} Pr^{-2/3}. \qquad \text{(IV-8-38)}$$

We can convert from the local Stanton number to its average value by dropping the subscript x. Here it may be assumed that the local and average Prandtl numbers are the same.

Formula (IV-8-38) is of great practical importance and reflects the Reynolds analogy, according to which the heat-transfer criterion depends basically on the same parameter as the coefficient of friction — on Re_x. Accordingly, $f_2 = Pr^{-2/3}$ is known as the Reynolds analogy factor.

Studies have shown that Formula (IV-8-38) is also applicable for a turbulent boundary layer, the only difference being that the coefficient of friction and the parameter f_2 must be calculated from the corresponding relationships for a turbulent boundary layer. In particular, f_2 can be determined by the formula

$$f_2 = [1 + 2.135 Re_x^{-0.1} (Pr - 1)]^{-1}. \qquad \text{(IV-8-38')}$$

In calculating the average Stanton number, the parameter f_2 is found to be equal to

$$f_2 = [1 + 2.2\,\mathrm{Re}_x^{-0.1}(\mathrm{Pr} - 1)]^{-1}. \qquad \text{(IV-8-38")}$$

The calculations show that, as for laminar flow, f_2 in the absence of diffusion in a turbulent boundary layer can be set equal to $f_2 = \mathrm{Pr}^{-2/3}$ with a certain approximation. To account for the influence of Pr, it is advisable to convert from the enthalpy $i_{0\delta} = i_\delta + 0.5V_\delta^2$ to the recovery enthalpy i_r. Then we obtain for the local heat flow /192

$$q_x = \frac{\alpha_x}{(c_p)_{w1}}(i_r - i_{w1}), \qquad \text{(IV-8-39)}$$

where

$$\alpha_x = \mathrm{St}_x \rho_\delta V_\delta (c_p)_{w1}. \qquad \text{(IV-8-40)}$$

Calculation of heat transfer from the determining parameters. The influence of physicochemical processes on heat transfer in the boundary layer at high temperatures can be taken into account with the determining parameters. For example, by applying the Reynolds analogy, we obtain for the determining Stanton number

$$\mathrm{St}^* = \frac{c_{fx}^*}{2} f_{2x}^*, \qquad \text{(IV-8-40')}$$

where the local coefficient of friction c_{fx}^*, like the Prandtl number, is calculated from the determining parameters.

Accordingly, the heat flow to the wall is

$$q_x = \mathrm{St}_x^* \rho_\delta V_\delta (i_r - i_{w1}),$$

from which the coefficient of heat transfer

$$\alpha_x^* = \mathrm{St}^* \rho_\delta V_\delta (c_p)_{w1}.$$

We determine the Nusselt number in the form

$$\mathrm{Nu}_x^* = \frac{q_x c_{p\delta} x}{\lambda_\delta (i_r - i_{w1})}.$$

Consequently,

$$\mathrm{Nu}_x^* = \mathrm{St}_x^* \mathrm{Re}_x \mathrm{Pr}, \qquad \text{(IV-8-35')}$$

where

$$\mathrm{Re}_x = V_\delta \rho_\delta x/\mu_\delta; \quad \mathrm{Pr} = c_{p\delta}\mu_\delta/\lambda_\delta.$$

The generalized criterial relationships can be used for laminar and turbulent boundary layers.

Heat Transfer in the Laminar Boundary Layer on a Curved Surface

Total heat flow. In the general case of flow over a surface at very high speed in the presence of temperature and concentration gradients, the heat flow from a dissociating gas to the wall can be regarded, disregarding convection, as the sum of two components, namely the heat flow by conduction q_c and diffusive heat transfer q_d, i.e., $q = q_c + q_d$.

The relationships for the heat-transfer components can be obtained in their simplest form if we examine a model of air as a binary mixture of atoms and molecules characterized by an atomic diffusion coefficient $\bar{D}$. If we disregard the influence of ionization on heat transfer, the total heat flow /193

$$q = q_c + q_d = -\left(\lambda \frac{\partial T}{\partial y} + \rho \bar{D} i_A \frac{\partial c_A}{\partial y}\right) = -\frac{\lambda}{c_p}\frac{\partial i_A}{\partial y} \times \times \left\{\left[1 - \frac{i_A (\partial c_A/\partial y)}{\partial i/\partial y}\right] + \mathrm{Le}\frac{i_A (\partial c_A/\partial y)}{\partial i/\partial y}\right\}, \qquad \text{(IV-8-41)}$$

where $\mathrm{Le} = \rho \bar{D} c_p/\lambda$ is the Lewis-Semenov number; i_A and c_A are the enthalpy (energy of dissociation per unit mass) and concentration of the atomic component; c_p is the average specific heat of the mixture.

In (IV-8-41), c_p and λ are taken for "frozen" flow in the boundary layer.

If there is no dissociation in the boundary layer, as is the case at moderate flow velocities, the heat flow is determined by conduction in accordance with the formula $q_c = -(\lambda/c_p)(\partial i/\partial y)$. Such also will be the heat transfer in a "frozen" boundary layer in the presence of a noncatalytic wall on whose surface no recombination reactions take place, so that the concentration $c_A = \alpha$ in

the layer does not change.

Interest attaches to the theoretical case of hypersonic flow when Le = 1 and, according to (IV-8-41), the heat flow $q = -(\lambda/c_p)(\partial i/\partial y)$, i.e., is determined by the enthalpy gradient and does not depend on the heat-transfer mechanism. Atoms striking a cold catalytic surface recombine instantaneously on it, releasing the same energy as on instantaneous recombination in the boundary layer. The specific heat flow corresponds to thermodynamic equilibrium in the boundary layer.

To obtain a more accurate value of the heat flow, it is necessary to know the real value of Le $\neq$ 1; this enables us to take account of diffusion effects and conductive heat transfer.

The extreme case characterized by diffusive heat transfer can occur at very high speeds, when, as research has shown, $i_A(\partial c_A/\partial y)/(\partial i/\partial y)$ is close to unity. As we see from (IV-8-41), only the second, diffusive component of heat transfer remains in it.

Heat transfer at thermodynamic equilibrium. To determine equilibrium heat transfer, it is necessary to solve a laminar-boundary-layer equation system incorporating the equations of continuity (III-2-21), motion (III-2-12), and energy (III-2-47) with the condition that Sc = Pr(Le = 1) is assumed in the latter equation. If, moreover, we set $r = r_0 = \text{const}$ in (III-2-12) and (III-2-47) (r_0 is the coordinate of a point on the contour of the body), the equation system becomes

$$\frac{\partial(\rho V_x r^{\varepsilon})}{\partial x}+\frac{\partial(\rho V_y r^{\varepsilon})}{\partial y}=0;$$

$$\rho\left(V_x\frac{\partial V_x}{\partial x}+V_y\frac{\partial V_x}{\partial y}\right)=-\frac{dp_\delta}{dx}+\frac{\partial}{\partial y}\left(\mu\frac{\partial V_x}{\partial y}\right);$$

$$\rho\left(V_x\frac{\partial i_0}{\partial x}+V_y\frac{\partial i_0}{\partial y}\right)=\frac{\partial}{\partial y}\left(\frac{\mu}{\mathrm{Pr}}\frac{\partial i_0}{\partial y}\right)+\frac{\partial}{\partial y}\left[\frac{\mu}{2}\left(1-\frac{1}{\mathrm{Pr}}\right)\frac{\partial V_x^2}{\partial y}\right].$$

Following Lees [50], we introduce the Dorodnitsin variables

$$\eta=\frac{\rho_\delta V_\delta}{(2\tilde{x})^{1/2}}\int_0^y r^{\varepsilon}\frac{\rho}{\rho_\delta}\,dy;\quad \tilde{x}=\int_0^x \rho_\delta V_\delta\mu_\delta r^{2\varepsilon}\,dx, \tag{IV-8-42}$$

from which

$$\frac{\partial\eta}{\partial y}=\frac{\rho V_\delta r^{\varepsilon}}{(2\tilde{x})^{1/2}};\quad \frac{\partial\tilde{x}}{\partial x}=\rho_\delta V_\delta\mu_\delta r^{2\varepsilon}. \tag{IV-8-42'}$$

For subsequent transformations, we use the stream function, which is defined by (III-2-33). In the new variables η, $\tilde{x}$, the expression for the stream function can be presented in the form $\psi(\tilde{x}, \eta) = (2\tilde{x})^{1/2} f(\eta)$. Accordingly, the velocity ratio is written $V_x/V_\delta = \partial f(\eta)/\partial\eta = f'(\eta)$. Then, introducing the function $g(\eta) = i_0/i_{0\delta}$ ($i_{0\delta} = i_\delta + 0{,}5V_\delta^2$), which determines the enthalpy ratio, we can obtain the equations of motion and energy converted to the new variables: /194

$$(\overline{\rho\mu} f'')' + ff'' + \bar{\beta}\left[\frac{\rho_\delta}{\rho} - (f')^2\right] = 0; \qquad \text{(IV-8-43)}$$

$$\left(\frac{\overline{\rho\mu}}{\mathrm{Pr}} g'\right)' + fg' + \frac{V_\delta^2}{2i_{0\delta}}\left[2\overline{\rho\mu}\left(1 - \frac{1}{\mathrm{Pr}}\right) f'f''\right]' = 0. \qquad \text{(IV-8-44)}$$

where the partial derivatives, which are indicated by the primes, are computed with respect to η and the parameter $\overline{\rho\mu} = \rho\mu/\rho_\delta\mu_\delta$.

The functions $f(\eta)$ and $g(\eta)$, the solutions to this equation system, must satisfy the conditions

$$\left.\begin{aligned} &f(0) = f'(0) = 0;\ f'(\eta) \to 1 \text{ as } \eta \to \infty; \\ &g(0) = g_w(\tilde{x});\ g'(0) = 0;\ g(\eta) \to 1 \text{ as } \eta \to \infty \end{aligned}\right\} \qquad \text{(IV-8-45)}$$

The system can be solved by numerical methods. Here, further simplifications can be introduced for the conditions of hypersonic flow. For example, we can set $\rho\mu = 1$. Moreover, since the Prandtl number is a weak function of temperature, it may be considered constant and equal to a certain average value for a given boundary-layer cross section. At high supersonic velocities, it is assumed that the enthalpy ratio is approximately $i_0/i_{0\delta} = \rho_\delta/\rho = g(\eta)$.

The solutions obtained give the values of the functions g and f as they depend on the boundary-layer coordinate η. Since the free-stream variables, including the velocity gradient $\bar{\beta}$, generally vary along the surface, g and f will also depend on $\tilde{x}$. Thus, the solutions are not similar (self-similar).

However, research has shown that self-similar solutions suitable for any boundary-layer section can be obtained for certain flow conditions. This will be the case when $V_\delta^2/2i_r = \rho\mu = 1$, the velocity gradient $\bar{\beta}$ = const, and the Prandtl number is equal to a certain constant value for the particular conditions. With these conditions, the equations become self-similar:

$$f''' + ff'' + \bar{\beta}[g - (f')^2] = 0; \qquad \text{(IV-8-43')}$$

$$\mathrm{Pr}^{-1} g'' + fg' + 2(1 - \mathrm{Pr}^{-1})(f'f')' = 0. \qquad \text{(IV-8-44')}$$

By numerical integration of these equations, we can find values of f' and g' as functions of Pr, the density ratio $\rho_\delta/\rho_{w1} = g_{w1}$, and the velocity gradient $\bar{\beta} = (2i_0/i_\delta)\, d\ln V_\delta / d\ln \tilde{x}$.

Particular interest attaches to the case of a strongly cooled wall, when the density ratio $\rho_\delta/\rho_{w1} \ll 1$. The calculations indicate that while the derivative f' and, consequently, the frictional stress depend essentially on the velocity gradient, the quantity g', which determines heat transfer, is a weak function of the parameter $\bar{\beta}$.

Thus the derivative g' can be calculated for a zero pressure gradient. These calculations indicate that the derivative $g'(0) = (\partial g/\partial \eta)_{w1}$ at the wall can be assumed equal to $0.47\mathrm{Pr}^{1/3}$ for the entire blunted surface.

The specific heat flow at thermodynamic equilibrium is determined from the derivative $g'(0) = 0.47\mathrm{Pr}^{1/3}$: /195

$$q_c = \frac{\lambda_{w1}}{(c_p)_{w1}} \left(\frac{\partial i}{\partial y}\right)_{w1} = \frac{1}{2} \frac{\lambda_{w1} i_\delta}{(c_p)_{w1}} \mathrm{Pr}^{1/3} \left(\frac{\partial \eta}{\partial y}\right)_{w1}. \qquad \text{(IV-8-46)}$$

Introducing the value of the derivative $(d\eta/dy)_{w1}$ found with (IV-8-42), assuming further that $\rho_{w1}\mu_{w1} = \rho_\delta \mu_\delta$, and substituting $i_r = i_{0\delta}[1 + (\sqrt{\mathrm{Pr}} - 1) \times V_\delta^2/2i_{0\delta}]$ for $i_{0\delta}$, we find

$$q_c = 0.47\mathrm{Pr}^{-2/3} \sqrt{\rho_0' \mu_0' V_\infty} i_r F(x), \qquad \text{(IV-8-47)}$$

where the function

$$F(x) = \frac{\sqrt{2}}{2} \frac{p}{p_0'} \frac{\omega_\delta}{\omega_0'} \frac{V_\delta}{V_\infty} r^\varepsilon \left[\int_0^x \frac{p}{p_0'} \frac{V_\delta}{V_\infty} \frac{\omega_\delta}{\omega_0'} r^{2\varepsilon} dx\right]^{-1/2}. \qquad \text{(IV-8-48)}$$

Here $\omega_\delta = \mu_\delta/R_\delta T_\delta$ [$R_\delta = R_0/(\mu_{av})_\delta$], and the subscript 0 signifies the parameter at the total-stagnation point.

For the heat flow at the total-stagnation point, the working relationship is obtained from the condition that $p/p_0' = 1$, $\omega_\delta/\omega_0' = 1$; $r \simeq x$; $V_\delta = \bar{\lambda} x$ ($\bar{\lambda} = dV_\delta/dx = \mathrm{const}$). This relation takes the form

$$q_{c.0} = 0.47\mathrm{Pr}^{-2/3} \sqrt{\rho_0' \mu_0' \bar{\lambda}} i_r \sqrt{\varepsilon + 1}. \qquad \text{(IV-8-49)}$$

Heat flow governed by diffusion. For quantitative evaluation of the diffusion-governed heat transfer, we can examine a "frozen" boundary layer for the condition that the thermodynamic equilibrium is reached at its edge. In this case, the effect of diffusion is manifested in a thin layer next to the catalytic wall, since the recombination rates are so small that the atoms reach the surface without recombining in the boundary layer.

In accordance with this scheme, the heat flow due to molecular heat transfer is determined separately by solving the equations for an equilibrium boundary layer.

The second component of the total heat flow that arises because of diffusion must be determined on the basis of the diffusion equation (III-2-38). Solving it, we find the concentration gradient of the atomic component at the wall, on which the diffusive mass flow depends in accordance with (III-1-32).

To find the solution, we transform this equation to the new variables η and $\tilde{x}$, obtaining as a result

$$2\varepsilon \frac{\partial z}{\partial \tilde{x}} f' - fz' - \left(\frac{\overline{\rho\mu}}{\mathrm{Sc}} z'\right)' = 0, \qquad \text{(IV-8-50)}$$

where $\underline{z}$ is a variable that determines dimensionless concentration in accordance with the expression $z = c/c_\delta$; the prime denotes derivatives with respect to η.

Equation (IV-8-50) can be simplified by setting Sc equal to a certain constant value for the particular conditions and the parameter $\overline{\rho\mu} = 1$ and by assuming that the concentration profile remains the same along the boundary layer, i.e., $\partial z/\partial \tilde{x} = 0$.

With the above, the equation for $\underline{z}$ becomes

$$\mathrm{Sc}\, fz' + z'' = 0. \qquad \text{(IV-8-50')}$$

It follows from this equation that the solution obtained is self-similar.

Equation (IV-8-50') is solved simultaneously with (IV-8-43') and (IV-8-44') with the appropriate boundary conditions. These conditions were stated previously for the functions $\underline{g}$ and $\underline{f}$. The solution for the function $\underline{z}$ must satisfy the condition $z(\infty) = 1$ on the outer boundary ($\eta \sim \infty$); on the wall, the boundary condition has the form (III-1-33). In the new variables $\tilde{x}$ and η, this condition is written on the assumption that $m = 1$, /196

$$z'(0) = \left(\frac{\partial z}{\partial \eta}\right)_{w1} = \frac{\sqrt{2\varepsilon}}{r^{\varepsilon} V_\delta} \frac{k_{w1}}{\rho_{w1} \bar{D}} z(0). \qquad \text{(IV-8-51)}$$

Since Solution (IV-8-50') does not depend on the coordinate $\tilde{x}$, we can consider the cross-section of the boundary layer at the total-stagnation point.

Near the critical point, the variable $\tilde{x}$ can be calculated by (IV-8-42) with the condition that $r \sim x$, $V_\delta = \bar{\lambda} x$, and $\rho_\delta V_\delta = \text{const}$. Assuming further that $\rho_\delta \mu_\delta = \rho_0' \mu_0'$, we find the boundary condition

$$z'(0) = \sqrt{\frac{\rho_0' \mu_0'}{(\varepsilon+1)\bar{\lambda}}} \frac{k_{w1}}{\rho_{w1} \bar{D}} z(0). \qquad \text{(IV-8-51')}$$

Integrating (IV-8-50') twice, we obtain

$$z(\eta) - z(0) = z'(0) \int_0^\eta e^{-\int_0^\eta \mathrm{Sc}\, f(\eta)\, d\eta} d\eta.$$

Numerical calculations showed that for $\eta \sim \infty$, the integral is approximately $(0.47\ \mathrm{Sc}^{1/3})^{-1}$. Therefore

$$z'(0) = 0.47\, \mathrm{Sc}^{1/3} [1 - z(0)]. \qquad \text{(IV-8-52)}$$

Introducing z'(0) from (IV-8-51'), we find the dimensionless concentration at the wall

$$z(0) = \frac{c_{w1}}{c_\delta} = \left[\left(\frac{\rho_0' \mu_0'}{(\varepsilon+1)\bar{\lambda}}\right)^{1/2} \frac{k_{w1}}{0.47\, \mathrm{Sc}^{1/3} \rho_{w1} \bar{D}} + 1\right]^{-1}. \qquad \text{(IV-8-53)}$$

It follows from (IV-8-53) and (IV-8-52) that for infinitely fast catalysis ($k_{w1} \sim \infty$), the dimensionless concentration at the wall $z(0) = 0$, and the derivative $z'(0) = 0.47\mathrm{Sc}^{1/3}$. In the other extreme case of infinitesimally slow catalytic reaction ($k_{w1} = 0$), the concentration at the wall remains the same as at the layer outer edge, i.e., $z(0) = 1$ and the derivative $z'(0) = 0$.

The heat flow liberated on recombination at the wall at the total-stagnation point can be obtained by substituting the concentration gradient (IV-8-52) into (III-1-32) with z(0) substituted in accordance with (IV-8-53). This relation takes the form

$$q_d = 0.47\sqrt{\varepsilon+1}\,(\rho_0'\mu_0'\tilde{\lambda})^{1/2}\,\mathrm{Sc}^{-2/3}\,i_R c_\delta \varphi, \qquad \text{(IV-8-54)}$$

where i_R is the average dissociation energy per atom and the catalytic coefficient

$$\varphi = \left[1 + \frac{0.47\sqrt{\varepsilon+1}\,\mathrm{Sc}^{-2/3}\,(\rho_0'\mu_0'\tilde{\lambda})^{1/2}}{\rho_{w1}k_{w1}}\right]^{-1}. \qquad \text{(IV-8-55)}$$

The sense of this coefficient is to take account of the influence of the finite recombination rate, since the parameter k_{w1} appears in the expression for it.

In one of the extreme cases, when $k_{w1} \sim \infty$, the coefficient $\phi = 1$, which corresponds to liberation of the maximum amount of heat at recombination. In the other extreme case of infinitesimally slow reaction ($k_{w1} = 0$), the coefficient $\phi = 0$. Here the physical process takes place in a manner such that no additional heat is liberated. /197

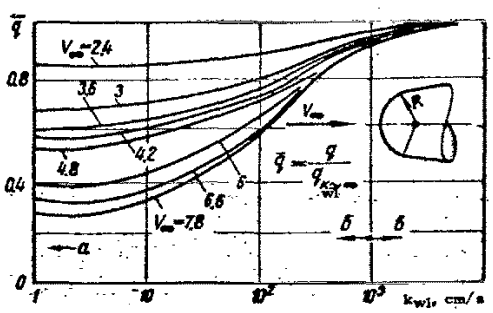

Figure IV-8-7. Variation of Heat Transfer as a Function of Flight Speed (V_∞, km/s) and Recombination rate (H = 60 km, R_b = 0.3 m, T_{w1} = 700°K). a) noncatalytic wall (glass); b) intermediate surface (oxides); c) catalysts (metals).

The total heat flow to the wall will be determined by adding the heat from diffusion to the heat from conduction.

In the presence of a concentration gradient, the heat transfer by molecular conductivity will be

$$q_c = q_c^0\left(1 - \frac{i_D}{i_r}\right), \qquad \text{(IV-8-56)}$$

where $i_D = i_R c_\delta$ is the average dissociation energy per atom multiplied by the mass concentration of the atoms ($c_\delta = \alpha_\delta$) at the outer edge of the layer and q_c^0 is the heat

transfer in the absence of a concentration gradient.

By adding q_c and q_d, we obtain

$$q = q_c^0 [1 + (\mathrm{Le}^{2/3}\varphi - 1)\tilde{i}_D], \qquad \text{(IV-8-57)}$$

where $\tilde{i}_D = i_D/i_r$.

Introducing the Nusselt and Reynolds numbers

$$\mathrm{Nu}_{w1} = \frac{\dot{q}(c_p)_{w1}x}{\lambda_{w1}(i_r - i_{w1})}; \quad \mathrm{Re}_{w1} = \frac{V_\delta \rho_{w1} x}{\mu_{w1}},$$

we obtain for the dimensionless heat-transfer criterion

$$\frac{\mathrm{Nu}_{w1}}{\sqrt{\mathrm{Re}_{w1}}} = 0{,}47\sqrt{\varepsilon + 1}\,\mathrm{Pr}_{w1}^{-2/3}[1 + (\mathrm{Le}^{2/3}\varphi - 1)\tilde{i}_D]. \qquad \text{(IV-8-58)}$$

Formulas (IV-8-57) and (IV-8-58) can be used to calculate heat transfer both at the total-stagnation point and at an arbitrary point on the wall. Here Le and the coefficient ϕ are determined for the conditions at the total-stagnation point and are assumed constant for the entire surface.

The values of q_c^0 and i_D are calculated as functions of the position of the particular point on the wall.

For more detailed study of the influence of recombination, it is helpful to consider the ratio of the amount of heat q liberated at a finite recombination rate to the heat flow $q_{k_{w1}\sim\infty}$ in the case of infinitely fast catalysis

$$\bar{q} = \frac{q}{q_{k_{w1}\sim\infty}} = 1 - \frac{\mathrm{Le}^{2/3}\tilde{i}_D}{1 + (\mathrm{Le}^{2/3} - 1)\tilde{i}_D}(1 - \varphi). \qquad \text{(IV-8-59)}$$

We see from (IV-8-55) that the catalytic coefficient ϕ depends not only on recombination rate, but also on flight speed. This relation is shown in Fig. IV-8-7. The data given indicate the importance of taking the finite recombination rate into account, as well as the possibility of reducing heat transfer by

using a skin made from a noncatalytic material. Since recombination does not occur near the surface of such a skin, the entire heat flow will be governed by nonequilibrium dissociation, which absorbs considerable heat energy. This is why the heat flow is reduced. In the limiting case with $\phi = 0$, the heat flow is determined by (IV-8-56). /198

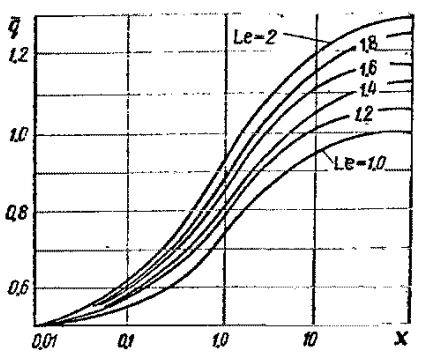

Figure IV-8-8. Heat Transfer as a Function of Parameter of Recombination at the Wall and the Lewis-Semenov Number.

The heat transfer governed by diffusion can be characterized by the catalytic parameter

$$\chi = \rho_{w1} k_{w1} \left[0{,}47 \sqrt{\varepsilon + 1}\, S_c^{-2/3} (\rho_0' \mu_0' \tilde{\lambda})^{1/2}\right]^{-1}, \qquad \text{(IV-8-60)}$$

which is related to the coefficient ϕ by

$$\chi = \frac{\varphi}{1-\varphi}. \qquad \text{(IV-8-60')}$$

Figure IV-8-8 shows the results of a calculation by Formulas (IV-8-57) and (IV-8-60') to determine values of $\bar{q} = q/q_c$ as a function of the parameter χ for the case in which the ratio $i_D/i_r = 0.5$ and the nose surface is vigorously cooled, so that the concentration on it $c_{w1} = 0$.

If the wall remains hot enough, chemical reactions will take place until thermodynamic equilibrium with a final concentration $c_{w1} = 0$ is established; this will reduce the heat flow. The corresponding value of the catalytic coefficient in (IV-8-59) will be determined by

$$\varphi = \frac{\chi}{1+\chi+c_{w1}} \left(1 - \frac{c_{w1}}{c_\delta}\right). \qquad \text{(IV-8-61)}$$

In (IV-8-59), the quantity

$$\tilde{i}_D = i_R (c_\delta - c_{w1})/i_r,$$

and we may assume for a binary mixture that $c_\delta = \alpha_\delta$ and $c_{w1} = \alpha_{w1}$.

For more accurate calculations by (IV-8-59), $i_r - i_{wl}$ must be substituted for i_r in the expression $\tilde{i}_D = i_D/i_r$.

Factors lowering diffusive heat transfer. Together with the rate constant of catalytic recombination, we shall examine a number of other factors by clever utilization of which we can reduce diffusive mass and heat transfer.

1. It follows from (IV-8-54) and (IV-8-55) that diffusive heat transfer can be lowered by increasing the velocity gradient $\lambda = V_\delta/x$. For example, if we take a spherical nose section, heat flow can be reduced by reducing the radius of the nose, since λ varies in inverse proportion to the radius of the sphere.

2. As we see from Fig. IV-8-7, the heat flow from diffusion decreases with increasing flight speed in the real case of finite recombination rates. This is because the fraction of the heat expended on dissociation increases along with the increase in total heat transfer. As a result, the fraction of energy liberated as a result of chemical reaction at the wall becomes smaller.

3. Wall temperature is also of importance for the heat-transfer effect. It is evident from (IV-8-55) that the coefficient ϕ depends basically on the product $\rho_{wl}k_{wl}$, which, in turn, is determined by T_{wl}. Here, if the recombination rate is a strong function of wall temperature (for example, $\rho_{wl}k_{wl} \approx T^{3/2}$ for one glass type), the density varies somewhat more weakly. /199

Thus, $\rho_{wl}k_{wl}$ is approximately proportional to wall temperature. Among other things, it follows from this that the coefficient ϕ will decrease with decreasing T_{wl}. This means that low surface temperatures prevent liberation of a large amount of chemical energy. This is, of course, associated with another effect, namely a large inflow of heat to the wall by convection.

The quasiequilibrium boundary layer. As a supplement to the "frozen-flow" scheme, we can examine a quasiequilibrium boundary layer, which is characterized by a local equilibrium concentration distribution. The local equilibrium concentration can be found from the distribution of enthalpy across the boundary layer by reference to tables or diagrams of the thermodynamic functions for air at thermodynamic equilibrium.

In turn, the enthalpy distribution is found by solving the equations of motion and energy, retaining the diffusion term in the latter. With the variables $\tilde{x}$ and η, this equation will be

$$\frac{\partial}{\partial\eta}\left[\frac{\overline{\rho\mu}}{\mathrm{Pr}}(1+\tilde{d})\frac{\partial g}{\partial\eta}\right]+f\frac{\partial g}{\partial\eta}=0, \qquad \text{(IV-8-62)}$$

where the parameter

$$\tilde{d}=(\mathrm{Le}-1)(i_A-i_M)\left(\frac{\partial c_A}{\partial i_0}\right)_p;$$

the Lewis-Semenov number is assumed constant, and the subscript p denotes differentiation at constant pressure.

The equation system is solved with the following boundary conditions:

$$f(0)=0,\quad \frac{\partial f(0)}{\partial\eta}=0,\quad \frac{\partial f(\infty)}{\partial\eta}=1,\quad g(0)=g_{w1},\quad g(\infty)=1.$$

The parameters Pr, $\overline{\rho\mu}$ and $\tilde{d}$ are determined in first approximation for a given cross section with the aid of thermodynamic tables or diagrams for air at thermodynamic equilibrium, from the known conditions at the wall and at the layer boundary. After solving the equations and determining the functions g and f, these parameters can be taken into account. Having determined the enthalpy and concentration gradients, we can calculate heat transfer with consideration of diffusion. The calculations indicate that the heat flow in the quasiequilibrium boundary layer is determined by the approximate formula

$$q=q_c^0\left[1+(\mathrm{Le}^{0.52}-1)\frac{i_D}{i_r}\right]. \qquad \text{(IV-8-63)}$$

The slightly larger exponent of the Lewis-Semenov number in (IV-8-57) as compared with the value of this exponent in the case of the equilibrium boundary layer is explained physically by the fact that diffusion through the thickness of a "frozen" layer has a stronger influence on heat transfer. Here, despite this difference in the values of the exponent, the total heat flows still differ little.

To determine whether the flow in the boundary layer in the neighborhood of the stagnation point is equilibrium or "frozen," we can use an empirical relationship for the recombination-rate parameter [47]: /200

$$C=4000\left(\frac{\rho_{\infty H}}{\rho_{\infty g}}\right)^2(15\bar{\rho})^{-2.5}\left(\frac{5000^\circ\mathrm{K}}{T_0'}\right)^{0.2}\frac{R_b}{V_\infty}, \qquad \text{(IV-8-64)}$$

where R_b is the radius of the sphere [m]; V_∞ is the flight speed [m/s]; $\bar{\rho}$ is the ratio of the density $\rho_{\infty H}$ to the density ρ_0' at the stagnation point; T_0' is the temperature at the stagnation point.

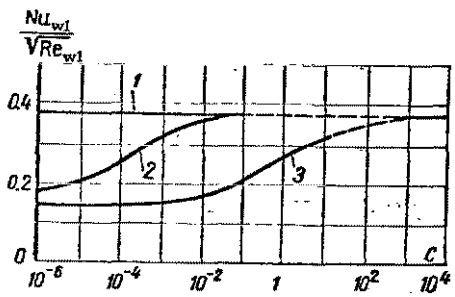

Figure IV-8-9. Heat-Transfer Parameter as a Function of Recombination Rate (T_{w1} = 300°K; Le = 1.4; Pr = 0.7; i_{w1}/i_r = 0.0123; α = 0.5310). 1) catalytic surface; 2) noncatalytic surface; 3) catalytic surface (heat flow by conduction).

A value of $C > 0.1$ corresponds to the equilibrium boundary layer, while $C < 10^{-5}$ corresponds to a "frozen" layer. We see from (IV-8-64) that the deviation from equilibrium increases with altitude. This formula can also be used for approximate evaluation of the recombination rate parameter around a blunt two-dimensional body (wedge).

The "frozen" boundary-layer flow that arises around the stagnation point is also preserved on more distant segments of the washed surface. While the flow is equilibrium in the neighborhood of the stagnation point of a cold wall, deviation from equilibrium is observed downstream in inviscid gas owing to increased expansion. Knowing the density ρ_δ of the inviscid flow at the surface, we can evaluate the deviation from equilibrium for this flow by the formula

$$\frac{C_\delta}{C_0} = \left(\frac{\rho_\delta}{\rho_\delta'}\right)^2, \qquad \text{(IV-8-65)}$$

where C_0 is the recombination rate parameter (IV-8-64) calculated for the stagnation point.

"Freezing" gradually extends through the thickness of the boundary layer, and if the inequality

$$\left(\frac{T_\delta}{T_{w1}}\right)^{3.5} C_\delta < 0.01 \qquad \text{(IV-8-66)}$$

is satisfied, the boundary layer is completely "frozen."

Influence of recombination rate in the gas. The case of finite recombination rate in the boundary layer is closest to

reality, since neither "frozen" nor equilibrium flows will occur in reality.

Figure IV-8-9 shows the results of calculation of the heat-exchange factor

$$\frac{\mathrm{Nu}_{w1}}{\sqrt{\mathrm{Re}_{w1}}} = \frac{0.71q}{(i_r - i_{w1})\sqrt{\bar{\lambda}\mu_{w1}\rho_{w1}}} \qquad \text{(IV-8-67)}$$

for various values of the recombination rate parameter C given by (III-1-28). Here the wall was catalytic in one case and noncatalytic in the other.

Curve 1 in Fig. IV-8-9 characterizes the total heat flow to a catalytic surface. As we see, it is practically independent of the recombination rate parameter.

This equalization of the heat flows at low recombination rates ("frozen" flow) is explained by the catalytic action of the wall and, at higher speeds, by the opposite effect associated with a small catalytic influence of the surface (equilibrium boundary layer). In the latter case, the process consists in the fact that the atoms do not have time to reach the wall by diffusion and recombine in the boundary layer itself. Thus, the heat flow in the presence of a catalytic wall can be calculated in practice without considering dissociation. /201

Comparing curve 1 in Fig. IV-8-9 with curve 3, which characterizes the conductive heat flow to a catalytic wall, we can determine the part of the heat flow that approaches the catalytic surface as a result of diffusion. For large parameters C, which correspond to high recombination rates, the process in the boundary layer is a nearly equilibrium process, and the effect of diffusion in the direction toward the wall becomes weaker. In this case, most of the heat is supplied by conduction.

Curve 2 represents the heat flow toward a noncatalytic wall. We see that much smaller values of C are required to "freeze" the boundary layer than in the case of a catalytic wall. This is because a large number of atoms piles up near a noncatalytic surface, increasing the rate of recombination in the boundary layer. To "freeze" the flow, therefore, it is necessary to prevent such high concentrations, and this is possible with smaller values of C.

The parameter C varies in proportion to the square of density at a given temperature. This means that while the flow in the boundary layer will be equilibrium for atmospheric conditions near the ground, where C is quite large, it may be "frozen" at high altitude.

If it is assumed that these two extreme states are separated by a range of C-values equal to about 10^4, the density must be reduced by a factor of 100 for transition to the "frozen" state. This corresponds to a 30-km altitude change. It also follows from (IV-8-64) that the smaller the radius of a spherical nose, the lower will be the altitudes necessary to attain the "frozen" state.

Thus, the heat flow to a surface washed by a dissociating gas with formation of a laminar boundary layer can be calculated by (IV-8-63) for the equilibrium layer and by (IV-8-57) for a "frozen" one. Here the heat flow depends mainly on the product $\rho_\delta \mu_\delta$ at the outer edge of the boundary layer. If the wall is catalytic, dissociation does not influence the heat flow, which remains practically the same as in an undissociated boundary layer.

If the wall is not a catalyst, heat transfer must be calculated with dissociation taken into account. Then the total heat flow will be smaller than that to a catalytic wall, when the diffusion rate exceeds the recombination rate in the boundary layer by a substantial margin.

§IV-9. INFLUENCE OF VISCOUS INTERACTION ON FLOW PARAMETERS

As long as the thickness of the boundary layer around the body in flow is small by comparison with the transverse dimensions of the body and the thickness of the shock layer, investigation of the dissociation processes governed by viscosity and conduction of heat can be limited to the region of flow inside the boundary layer, and it can be assumed that the boundary layer has no influence on free inviscid flow. According to this hypothesis of /202
no reciprocal effect of the boundary layer on the free flow, the same pressure as in the free inviscid flow is established on the surface of the body. This implies that the pressure can be calculated without reference to the viscosity properties of the gas.

The longer the body, the thicker will be the boundary layer and the less reliable the hypothesis of no reciprocal effect of the layer on the free flow, and the stronger will be the interaction between the boundary layer and the free flow. Layer thickness increases at high flow velocities owing to the high temperature, and this will also strengthen the viscous-interaction effect. In such cases, the pressure on the surface, like the other flow variables, must be calculated with viscosity taken into account. The viscous interaction will have an additional influence on dissociation processes.

To take account of viscous interaction, we can use the equations of motion in the general form derived with consideration of the real properties of the gas instead of the Euler equations.

In practice, however, this calculation is difficult. Experimental studies have shown that good results as regards the viscous-interaction correction can be obtained if we proceed from the assumption that there is a physical boundary between the free inviscid flow and the boundary layer in interaction with it. The reciprocal effect of the thickened boundary layer consists in a certain pressure increase of the gas in the inviscid-flow region due to deflection of the streamlines. The pressure and other variables at the wall will be the same as in inviscid flow over an equivalent body with its cross section increased by the displacement thickness. In turn, the "inviscid" parameters induced by the boundary layer influence the increase in its thickness [59].

In the case of hypersonic flow past slender sharpened bodies, the viscous interaction can be calculated starting from the dependence of the local "inviscid" variables on the inclination of the tangent plane to the equivalent-body surface:

$$\beta^* = \beta + \frac{d\delta^*}{dx}. \qquad \text{(IV-9-1)}$$

In investigating viscous hypersonic interaction for slender bodies [59], two regions are arbitrarily distinguished: regions of weak and strong interaction, for which rather simple analytic working relationships have been derived. In the region of strong interaction, the streamline deflection and, consequently, the induced pressure are small. The effect of strong interaction manifests in a larger streamline deflection and, accordingly, in a more substantial pressure increase. For a flat plate, the region of strong interaction is near the leading edge, while the region of weak interaction is remote from it.

For both of these regions of interaction, the induced pressure on a slender sharp body can be calculated by the tangent-surface method, using the hypersonic similarity parameter

$$M_\infty \beta^* = K^* = M_\infty \left(\beta + \frac{d\delta^*}{dx}\right) = K + M_\infty \frac{d\delta^*}{dx}, \qquad \text{(IV-9-2)}$$

where $K = M_\infty \beta$.

Extreme values of the parameters $K^* \ll 1$ and $K^* \gg 1$ correspond to the regions of weak and strong interaction.

In addition to the basic form of interaction considered above, which was governed by the deflection of the inviscid-flow streamlines, there is another type known as vortex interaction.

It consists in the fact that the processes taking place in the boundary layer are influenced not only by the velocity distribution, but also by the vortex distribution in the external flow. The vortex distribution arises in the presence of a boundary layer whose thickness is commensurate with that of the shock layer and when there is a sharply curved compression shock. Behind such a shock, the vorticity in a layer of inviscid gas is of the same order as the average vorticity in the boundary layer, which is governed by the action of tangential stresses. /203

As a parameter for evaluation of vortex interaction, we can take

$$\Omega = \frac{\xi_i \delta}{V_\delta}, \qquad \text{(IV-9-3)}$$

which is the ratio of the vorticity ξ_i in inviscid flow to the average vorticity V_δ/δ in the boundary layer at low velocity. If $\Omega \ll 1$, the vortex interaction can be disregarded, but with $\Omega \sim 1$, this interaction must be taken into account, since it increases friction and heat transfer.

Calculations indicate that vortex interaction is insignificant in the regions of weak and strong interaction and may be of substantial importance in the neighborhood of the total-stagnation point on a bluff body.

§IV-10. PECULIARITIES OF FLOW PAST BODIES WITH BLUNTED NOSE SECTION

A practically important aerodynamic property of bluff bodies is that they are heated and damaged to a lesser degree than sharp bodies in motion through the atmosphere at very high speeds.

Let us consider which gasdynamic phenomena govern this property of bluff bodies. Figure IV-10-1 presents a diagram of the flow past a bluff body of arbitrary shape. A detached curvilinear shock wave with variable intensity at different points on its surface forms in front of the body. At a distance from the nose, the shock wave degenerates into an ordinary interference wave with infinitesimal intensity and an inclination angle $\theta_s = \mu_\infty = \text{arc sin } 1/M_\infty$. The maximum intensity will occur at the apex of the wave, where $\theta_s = \pi/2$.

Since the angle θ_s differs little from $\pi/2$ in the neighborhood of the nose, the corresponding wave segment will consequently have a rather high intensity, approaching that of the normal shock.

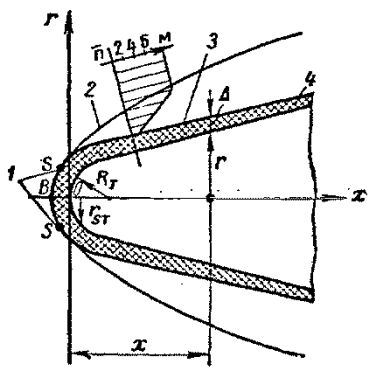

Figure IV-10-1. Diagram of Flow Past Blunt Body. 1) "sonic" points; 2) shock wave; 3) sonic streamline; 4) high-entropy layer.

Passage of gas particles through such a strong compression shock will be accompanied by substantial losses of total head and an increase in entropy. As a result, the surface of the body will be covered by a layer of a certain thickness in which the gas has high entropy.

Strictly speaking, owing to the differing degrees of stagnation at different points of the shock wave, the flow in such a layer will be characterized by a certain velocity gradient in the direction of the normal, as shown in Fig. IV-10-1. However, if the boundary layer is substantially thinner and if the shock wave inclination angle is near normal on the zone through which the layer of diminished velocities passes, the velocity gradient can be disregarded in this layer and this will simplify the calculations. The velocity in this layer is lower than on a sharpened body or wedge. Near the surface, the flow region characterized by low velocities (and, consequently, low Mach and Reynolds numbers) is a decisive factor in shaping the boundary-layer processes. /204

An essential feature of the flow is a change in flow conditions in the boundary layer as a result of blunting. Owing to the decrease in the local Reynolds numbers computed from the velocity at the layer boundary, the laminar boundary layer becomes turbulent much farther downstream and, consequently, the extent of the laminar boundary layer increases. This helps reduce friction and the heat flows to the wall.

The decrease in heat flow that results from the increase in the entropy of the gas on passage through the compression shock is known as the entropy effect. Here it must be remembered that the entropy effect embodies not only a decrease in velocity at the outer boundary of the boundary layer, but also a decrease in gas density, i.e., lower Reynolds numbers. At the same time, the increase in entropy causes an increase in the temperature at the boundary layer outer edge over that for a sharp body. This is the contrary effect of the high-entropy layer, which results in a certain increase in the heat flow from the boundary layer to the wall. However, with appropriate selection of the degree and form of the blunting, calculations and experimental studies indicate that the over-all entropy effect reduces the heat flows.

As a rule, the wave drag of a bluff body is higher than that of a sharp one. However, for certain slender bodies with small bluntings (for example, cones), a decrease in drag is observed; this is explained by the appearance of a lower pressure over a substantial part of the body in spite of the pressure increase in the neighborhood of the blunt nose. The drag of a cone or wedge with half-angle β and length x_c becomes commensurate with that of a nose of small diameter (thickness) D_b only if $x_c/D_b \sim [\beta(\varepsilon + 3)/(\varepsilon + 1)]^2$ ($\varepsilon = 0$ for a wedge and $\varepsilon = 1$ for a cone). Thus, slight blunting has a much greater effect on the total drag of a wing than on that of a slender body. Downstream from the nose, the shock wave moves comparatively far away from the body's surface. In this region, the pressure distribution depends on the decay of the wave and is not greatly influenced by the prior history of the flow. The pressure established on elongated sections of the bluff surface is the same as that on a sharp surface.

The chief effect of blunting consists not in the change in drag, which is comparatively minor for small degrees of blunting, but in a substantial decrease in heat transfer.

The great practical importance of aerodynamic research on bluff bodies should be clear from the above. However, the use of intentionally blunted bodies is not the sole reason for the importance of this research. The fact is that in reality, all solids of revolution are blunted to one degree or another, since it is technologically impossible to make an ideally sharp nose. The blunting is increased by accidental mechanical disturbances; moreover, the nose may be blunted by melting in the case of motion of the body at very high velocity in a dense gas. Many vehicles and individual elements of these vehicles may have blunted shapes because of design considerations. Thus, we deal in practice with blunted bodies instead of bodies with absolutely sharp tips. /205

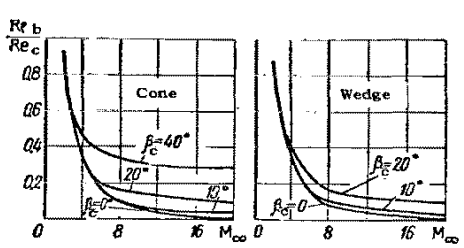

Figure IV-10-2. Influence of Bluntness on Reynolds Number for Cone and Wedge.

Let us evaluate the relative displacement of the laminar-to-turbulent transition of the boundary layer owing to bluntness, on the assumption that the critical Reynolds numbers will be the same for the sharp and blunt bodies. For these bodies (subscripts sh and b, respectively), we have the equality

$$\left(\frac{V\rho x}{\mu}\right)_{sh} = \left(\frac{V\rho x}{\mu}\right)_{b}.$$

The following formula follows from this equality for the relative shift of the transition point:

$$\frac{x_b}{x_{sh}} = \left(\frac{V\rho}{\mu}\right)_{sh.} \left(\frac{\mu}{\rho V}\right)_b .$$

All parameters in this formula refer to the transition point.

If we consider conical or wedge-shaped bodies, we can write, since the flow variables are constant along the generatrix of either,

$$\frac{x_b}{x_c} = \left(\frac{V\rho x}{\mu}\right)_c \left(\frac{\mu}{V\rho x}\right)_b = \frac{Re_c}{Re_b} . \qquad \text{(IV-10-1)}$$

Here the subscripts "c" and "b" now refer respectively to sharp and blunted cones or wedges, and all quantities appearing in the middle and right-hand members of (IV-10-1) pertain to arbitrary sections through both cones with the same coordinate x. We obtain from (IV-10-1)

$$\frac{Re_c}{Re_b} = \frac{V_c}{V_b} \frac{\rho_c}{\rho_b} \frac{\mu_b}{\mu_c} .$$

Assume that $\mu_b/\mu_c = (T_b/T_c)^n$ and that the pressures on the sharp and blunt bodies are the same. Then $\rho_c/\rho_b = T_b/T_c$. Remembering that

$$T = T_0 \left(1 + \frac{k-1}{2} M^2\right)^{-1},$$

we obtain for the Reynolds-number ratio

$$\frac{Re_c}{Re_b} = \left(\frac{1 + \frac{k-1}{2} M_c^2}{1 + \frac{k-1}{2} M_b^2}\right)^{n+\frac{1}{2}} \frac{M_c}{M_b} . \qquad \text{(IV-10-2)}$$

The numbers M_c and M_b are calculated from the respective formulas /206

$$p_c = p'_{0c}\left(1+\frac{k-1}{2}M_c^2\right)^{-\frac{k}{k-1}};\quad p_c = (p_0)_{\theta_s=\pi/2}\left(1+\frac{k-1}{2}M_b^2\right)^{-\frac{k}{k-1}},$$

where p_c is the pressure on the sharp body, p'_{0c} is the stagnation pressure behind the oblique shock in front of a sharp wedge or cone, and $(p'_0)_{\theta_s=\pi/2}$ is the stagnation pressure behind the normal compression shock.

The ratio Re_b/Re_c is given in Fig. IV-10-2 for the cone and wedge. We see that a substantial decrease in the Reynolds numbers and, consequently, a substantial shift in the transition point are characteristic for slender cones and wedges, while the influence of bluntness is more marked with increasing M_∞.

Part Two /207

AERODYNAMICS OF LIFTING, STABILIZING, AND CONTROL SURFACES

/208

Chapter V /209

CALCULATION OF THE AERODYNAMIC COEFFICIENTS

§V-1. SUBSONIC AND TRANSONIC SPEEDS

Influence of Compressibility on Pressure

The Khristianovich method. The problem of potential flow around a given profile at a certain Mach number $M_\infty < M_{\infty cr}$ ($M_{\infty cr} < 1$ is the critical Mach number) involves solution of Eq. (III-2-24), in which ε is set equal to zero and the velocities are expressed in terms of the velocity potential. As a result of solution, the velocity and pressure distributions are found with consideration of the compressibility effect.

The problem is found to be very complex in this formulation. It is simplified by breaking it into two simpler problems. The first involves determination of pressure distribution $\bar{p}_{ic}$ for incompressible flow around the profile, and the second calculation of a correction to $\bar{p}_{ic}$ to take compressibility into account.

We shall examine the second problem, i.e., we shall assume that the pressure distribution in the incompressible flow is known and that it is required to find the distribution with compressibility considered.

In 1902, S.A. Chaplygin introduced the new independent variables V and β (V is the absolute value of velocity and β is the inclination angle of the velocity vector to the $\bar{x}$-axis) to transform the nonlinear equation of gas dynamics for the potential ϕ and stream function ψ exactly into linear equations. Academician S.A. Khristianovich [37], using these equations, originated a rigorous theory for calculation of pressure with consideration of compressibility at subcritical velocities of flow over profiles.

In this theory, the problem of subsonic flow of gas around the profile is reduced to the problem of flow of an incompressible fluid around a profile of modified shape. Consequently, to use the Khristianovich method, it is necessary to know the relative velocity $\lambda_\infty = V_\infty/a^*$ of the oncoming compressible flow, the shape of the particular profile, a rule for conversion from the particular profile to a fictitious profile, and from the true compressible flow to a fictitious incompressible flow, and the distribution of the coefficient $\bar{p}_{ic}$ over the fictitious profile in incompressible flow.

If the given profile is sufficiently extended, there is almost no change in the shape of the modified profile. We may therefore regard the actual and fictitious profiles as identical. Then the Khristianovich method enables us to convert the pressure $\bar{p}_{1c}$ quite easily to any value $\bar{p}$ corresponding to a given M_∞.

A relation between the relative velocity λ of the compressible flow and the velocity Λ of the fictitious incompressible flow serves for this purpose (Table V-1-1). Λ is determined from the formula

$$\bar{p}_{1c} = 1 - \frac{\Lambda^2}{\Lambda_\infty^2}, \qquad \text{(V-1-1)}$$

in which the velocity Λ_∞ of the fictitious oncoming flow is regarded as known and determined from Table V-1-1 from the given λ_∞. Having determined Λ, we can use the same Table V-1-1 to find λ, (III-3-4) to calculate the true pressure $\bar{p}$, and then find the pressure coefficient $\bar{p} = (p - p_\infty)/q$. /210

TABLE V-1-1. THE RELATION $\lambda = \lambda(\Lambda)$

λ	0	0.05	0.10	0.15	0.20	0.25	0.30	0.35	0.40	0.45
Λ	0	0.0500	0.0998	0.1493	0.1983	0.2467	0.2943	0.3410	0.3862	0.4307
λ	0.50	0.55	0.60	0.625	0.650	0.675	0.700	0.725	0.750	0.775
Λ	0.4734	0.5144	0.5535	0.5722	0.5904	0.6080	0.6251	0.6413	0.6568	0.6717
λ	0.800	0.825	0.850	0.875	0.900	0.925	0.950	0.975	1.000	
Λ	0.6857	0.6988	0.7110	0.7223	0.7324	0.7413	0.7483	0.7546	0.7577	

Conversion of pressure from one M_∞ to another. Let us assume that the distribution of the pressure coefficient $\bar{p}_1$ of a compressible fluid is known for a certain $M_{\infty 1}$. The Khristianovich theory enables us to convert this coefficient to another Mach number $M_{\infty 2}$ and obtain the corresponding values $\bar{p}_2$.

The calculations are performed as follows. We first determine the pressure ratio p_1/p_∞ at a certain point at which $\bar{p}_1$ is known:

$$\frac{p_1}{p_\infty} = \bar{p}_1 \frac{kM_{\infty 1}^2}{2} + 1.$$

Then we use the formula

$$\frac{p_1}{p_\infty} = \left(1 - \frac{k-1}{k+1}\lambda_1^2\right)^{\frac{k}{k-1}} \left(1 - \frac{k-1}{k+1}\lambda_{\infty 1}^2\right)^{-\frac{k}{k-1}}$$

to find λ_1. From λ_1 and $\lambda_{\infty 1}$, we refer to Table V-1-1 to determine Λ_1 and $\Lambda_{\infty 1}$, respectively. From these data and Formula (V-1-1),

$$\bar{p}_{ic_1} = 1 - \frac{\Lambda_1^2}{\Lambda_{\infty 1}^2} \qquad \text{(V-1-1')}$$

we calculate $\bar{p}_{ic}$. Then the compressible-flow pressure coefficient is determined by the procedure indicated above. The value of $\Lambda_{\infty 2}$ is determined for $\lambda_{\infty 2}$ from Table V-1-1, and then Λ_2 is found from the formula $\bar{p}_{ic} = 1 - (\Lambda_2/\Lambda_{\infty 2})^2$. Returning to Table V-1-1, we determine λ_2 from Λ_2, calculate p_2, and, finally, find the coefficient $\bar{p}_2$.

The critical Mach number. The critical Mach number is determined as follows in this method.

It is assumed that the local speed of sound, which corresponds to the critical free-stream Mach number $M_{\infty cr}$, occurs at the point of greatest vacuum on the profile in the case of incompressible flow around it, i.e., where the pressure coefficient $\bar{p}_{ic} = \bar{p}_{ic\ min}$.

Knowing $\bar{p}_{ic\ min}$, we can calculate Λ_∞ from (V-1-1), where we must set $\Lambda = 0.7577$ according to Table V-1-1. Thus, the velocity of the fictitious oncoming flow /211

$$\Lambda_\infty = \frac{0.7577}{\sqrt{1 - \bar{p}_{ic\,min}}}. \qquad \text{(V-1-2)}$$

Then the critical velocity $\lambda_{\infty cr}$ is determined from Table V-1-1 and the formula

$$M_{\infty cr} = \lambda_{\infty cr}\left(\frac{k+1}{2} - \frac{k-1}{2}\lambda_{\infty cr}^2\right)^{-1/2} \qquad \text{(V-1-3)}$$

is used to find the critical Mach number.

Approximate relationships. An approximate relation corresponding to a certain simplified model of the actual connection between the pressures given by the Khristianovich method can be established between the pressure coefficients $\bar{p}$ and $\bar{p}_{ic}$. This relationship, which is known in the literature as the Karman-Tsiang formula, is

$$\bar{p}=\bar{p}_{ic}\left(\sqrt{1-M_\infty^2}+\frac{1}{2}\frac{M_\infty^2}{1+\sqrt{1-M_\infty^2}}\bar{p}_{ic}\right)^{-1}. \qquad (V\text{-}1\text{-}4)$$

Prof. G.F. Burago proposed an approximate method for conversion of pressure with consideration of compressibility [6] that gives practically the same results as the Khristianovich method.

An important corollary of the Burago method is establishment of a highly effective and simple relationship between $\bar{p}_{ic\ min}$ and $M_{\infty cr}$:

$$\bar{p}_{ic\ min}=1-\frac{1}{8M_{\infty cr}^2}\left[\sqrt{1+0.2M_{\infty cr}^2}+(1+0.2M_{\infty cr}^2)^3\right]^2. \qquad (V\text{-}1\text{-}5)$$

Linearized flow. The above method for calculation of pressure with consideration of compressibility takes account of large disturbances that arise in flow around profiles.

When these disturbances are weak (thin profile), the relation between the pressures in compressible and incompressible flows can be obtained in very simple form.

For this purpose, we use the linearized equation (III-2-30) for the velocity potential. It is simplified for steady flow:

$$(1-M_\infty^2)\varphi'_{xx}+\varphi'_{yy}=0. \qquad (V\text{-}1\text{-}6)$$

If we introduce the new variables

$$x_1=x;\ y_1=y\sqrt{1-M_\infty^2};\ \varphi'_1=\gamma\varphi'\frac{V_{1\infty}}{V_\infty}, \qquad (V\text{-}1\text{-}7)$$

where $V_{1\infty}$ and V_∞ are the respective velocities of the fictitious incompressible and the real compressible flows and γ is an arbitrary constant, then (V-1-6) becomes $(\varphi'_1)_{x_1x_1}+(\varphi'_1)_{y_1y_1}=0$, which describes the flow of an incompressible fluid. Thus, the problem of compressible flow around a given profile reduces to the problem

of flow of an incompressible fluid around some other profile.

It follows from (V-1-7) that the relation $\bar{p}_{ic} = \bar{p}$ exists between the pressure coefficients at corresponding points. The relation between the profile shapes is established with the aid of their nonseparating-flow conditions: $V_{y_1}/V_{1\infty} = dy_1/dx_1$ and $V_y/V_\infty = dy/dx$, from which we find $y_1 = y\gamma(1-M_\infty^2)^{-1/2}$. Setting $\gamma = (1-M_\infty^2)^{1/2}$, we arrive at the conclusion that both profiles – in compressible and incompressible flows – are identical in shape and have identical attack angles. Consequently, we have the following relation between the pressure coefficients at corresponding points: /212

$$\bar{p} = \frac{\bar{p}_{ic}}{\sqrt{1-M_\infty^2}}. \qquad \text{(V-1-8)}$$

This relation is known as the Prandtl-Glauert formula. It is quickly noted that it can be derived from (V-1-4) by setting $\bar{p}_{ic}$ sufficiently small.

Example. Let the pressure coefficient $\bar{p}_{ic} = 0.5$ at a certain point on a profile in an incompressible-fluid flow. Determine $\bar{p}$ at the same point on the profile in a compressible fluid flow at a velocity $\lambda_\infty = 0.5$ ($M_\infty = 0.4663$).

From the value $\lambda_\infty = 0.5$, we find from Table V-1-1 the quantity $\Lambda_\infty = 0.4734$ and the corresponding value $\Lambda = 0.3348$ from (V-1-1) for the point selected. From the value found for Λ, we determine $\lambda = 0.3434$ from the same Table V-1-1.

The pressure at the point in question on the profile

$$p = p_\infty \left[\left(1-\frac{k-1}{k+1}\lambda^2\right)\Big/\left(1-\frac{k-1}{k+1}\lambda_\infty^2\right)\right]^{\frac{k}{k-1}} = 1.082\,p_\infty.$$

Knowing p/p_∞, we can calculate the pressure coefficient

$$\bar{p} = \frac{2(p/p_\infty - 1)}{kM_\infty^2} = \frac{2\cdot 0.082}{1.4\cdot 0.4663^2} = 0.539.$$

Calculation by the approximate relation (V-1-4) gives $\bar{p} = 0.547$, while (V-1-8) of the linearized theory gives the less accurate result $\bar{p} = 0.565$.

We convert the pressure coefficient $\bar{p}_1 = 0.539$ obtained for the velocity $\lambda_{\infty 1} = 0.5$ to another free-stream velocity $\lambda_{\infty 2} = 0.7$.

We determine the pressure ratio p_1/p_∞ at the point at which $\bar{p}_1 = 0.539$ is known:

$$\frac{p_1}{p_\infty} = \bar{p}_1 \frac{kM_{\infty 1}^2}{2} + 1 = 0.539 \frac{1.4 \cdot 0.4663^2}{2} + 1 = 1.08.$$

From

$$p_1/p_{01} = \left(1 - \frac{k-1}{k+1}\lambda_1^2\right)^{\frac{k}{k-1}},$$

in which

$$p_1/p_{01} = (p_1/p_{\infty 1})\left(1 - \frac{k-1}{k+1}\lambda_{\infty 1}^2\right)^{k/(k-1)},$$

we find

$$\lambda_1 = 0.3434.$$

From λ_1 and $\lambda_{\infty 1}$, we refer to Table V-1-1 to determine $\Lambda_1 = 0.3348$ and $\Lambda_{\infty 1} = 0.4734$, respectively, and use (V-1-1') to calculate $\bar{p}_{ic} = 0.5$ — the pressure coefficient at the point under consideration on the given profile in incompressible flow.

The rest of the calculation merely repeats the beginning of this example. We find $\Lambda_{\infty 2} = 0.6251$ from $\lambda_{\infty 2} = 0.7$ in Table V-1-1, $\Lambda_2 = 0.442$ from (V-1-1), and $\lambda_2 = 0.4632$ from Table V-1-1. The pressure at the point under consideration $p_2 = 1.187p_\infty$, and the pressure coefficient $\bar{p}_2 = 2(p_2/p_\infty - 1)/kM_{\infty 2}^2 = 0.6$. To determine the critical Mach number $M_{\infty cr}$, we assign the minimum value of $\bar{p}_{ic}$ for incompressible flow around the profile, $\bar{p}_{ic\ min} = -1.17$, and use (V-1-2) to calculate

$$\Lambda_\infty = \Lambda(1 - \bar{p}_{ic\ min})^{-1/2} = 0.7577(1 + 1.17)^{-1/2} = 0.5144.$$

Referring to Table V-1-1, we determine $\lambda_{\infty cr} = 0.55$ from the value found for Λ_∞, and then use (V-1-3) to find $M_{\infty cr} = 0.515$.

Lift [6]

Unswept wings. In an incompressible flow, the lift coefficient of a wing with unsymmetrical profile can be determined by the formula

$$c_{y\,ic} = \frac{a_0(\alpha - \alpha_0)}{1 + \frac{a_0}{\pi\lambda_{wg}}(1+\tau)}, \qquad \text{(V-1-9)}$$

where α is the attack angle, α_0 is the attack angle at zero lift, /213
λ_{wg} is the wing aspect ratio, and $a_0 = dc_{y\,ic}/d\alpha$ is a coefficient calculated for the profile. The theoretical a_0 for a thin plate is 2π.

TABLE V-1-2. THE COEFFICIENTS δ AND τ [6]

Rectangular wings (η = 1)

λ_{wg}/a_0	1/2	3/4	1	1.25	1.5	1.75
δ	0.019	0.034	0.049	0.063	0.076	0.088
τ	0.10	0.14	0.17	0.20	0.22	0.24

Trapezoidal wings

η	1	4/3	2	4	∞
δ	0.049	0.026	0.011	0.016	0.141
τ	0.17	0.10	0.03	0.01	0.17

Note: The data from trapezoidal wings were obtained for the condition that $\lambda_{wg} = a_0$.

For symmetrical-profile thickness ratios $\bar{c} \leq 0.2$, this coefficient depends little on form and varies linearly with $\bar{c}$ in accordance with the formula [61]

$$a_0 = 2\pi + 5\bar{c}. \qquad \text{(V-1-10)}$$

An experimental check indicates that the actual values a_{0e} are somewhat smaller than the theoretical a_0 and depend on the trailing-edge angle β_e, $Re = bV_\infty/\nu_\infty$, and the position of the transition point on the profile. If the transition point lies at 0.5b, the real value a_{0e} for $Re = 10^8$ and $\beta_e = 0$ (plate) is $0.97a_0$, and for $\tan \beta_e = 0.2$, $a_{0e} = 0.85a_0$; for $Re = 10^6$, these coefficients are, respectively, $a_{0e} = 0.9a_0$ and $a_{0e} = 0.74a_0$. If the transition point is on the leading edge (boundary layer fully turbulent) and $Re = 10^8$, then $a_{0e} = 0.97a_0$ ($\beta_e = 0$) and $a_{0e} = 0.82a_0$ ($\tan \beta_e = 0.2$). If $Re = 10^6$, then $a_{0e} = 0.9a_0$ ($\beta_e = 0$) and $a_{0e} = 0.68a_0$. In evaluating a_{0e} for the ranges $10^6 \leq Re \leq 10^8$, $0 \leq \tan \beta_e \leq 0.2$, linear interpolation is acceptable.

The parameter τ in (V-1-9) takes account of wing planform and can be presented as a $\tau = \tau(m,\eta)$ relationship, where $m = \lambda_{wg}/a_0$ and η is the taper. The approximate relation for τ takes the form

$$\tau = 5.88\tau_1(m)\tau_2(\eta), \qquad \text{(V-1-11)}$$

where the functions $\tau_1(m)$ and $\tau_2(\eta)$ are given in Table V-1-2.

The influence of compressibility on the lift coefficient can be taken into account in quite simple form for wings with thin profiles at small attack angles, the flow around which will be weakly disturbed. To obtain the working relationships, let us examine the linearized equation (III-2-30) for the velocity potential with the condition that the time derivatives in it are zero. We introduce the variables /214

$$x_1 = \frac{x}{\sqrt{1-M_\infty^2}}; \quad y_1 = y; \quad z_1 = z \qquad \text{(V-1-12)}$$

and convert (III-2-30) to them.

As a result, we obtain the Laplace equation

$$\frac{\partial^2\varphi'}{\partial x_1^2} + \frac{\partial^2\varphi'}{\partial y_1^2} + \frac{\partial^2\varphi'}{\partial z_1^2} = 0,$$

which may be regarded as the equation for the velocity potential of a disturbed incompressible fluid flow in the coordinates x_1, y_1, z_1. On converting to the new variables, the wing chord becomes larger by a factor $\sqrt{1 - M_\infty^2}$, but the span does not change, since $z_1 = z$.

Let us consider the profile thickness. From the conditions for nonseparating flow $(\partial\varphi'/\partial y_1)/V_\infty = \partial y_1/\partial x_1$ (incompressible flow) and $(\partial\varphi'/\partial y)/V_\infty = \partial y/\partial x$ (compressible flow), we have

$$\frac{dy_1}{dx_1} = \frac{dy}{dx}.$$

In incompressible flow, therefore, the shape of sections taken downstream does not change and, consequently, neither do the section attack angles. The pressure coefficient on the wing $\bar{p}_1 = -2(\partial\varphi'/\partial x_1) = -2(\partial\varphi'/\partial x)\sqrt{1-M_\infty^2}$, i.e., will be smaller by a factor $\sqrt{1-M_\infty^2}$ than on the profile in compressible flow. Hence the lift coefficients for the two wings will be connected by the relationship $c_{y\,ic} = c_y\sqrt{1-M_\infty^2}$.

For the wing in incompressible flow, the lift coefficient

$$c_{y\,ic} = \frac{a_0(\alpha' - \alpha_0')}{1 + \frac{a_0}{\lambda'_{wg}\pi}(1+\tau')}. \qquad \text{(V-1-13)}$$

From the conditions $x_1 = x/\sqrt{1-M_\infty^2}$ and $z_1 = z$, we obtain a relation for the wing aspect ratios in incompressible and compressible flows:

$$\lambda'_{wg} = \lambda_{wg}\sqrt{1-M_\infty^2}. \qquad \text{(V-1-14)}$$

Since the lift coefficients of the fictitious wing in incompressible flow and of the given wing in compressible flow are related by $c_{y\,ic} = c_y\sqrt{1-M_\infty^2}$ and $\alpha' = \alpha$, we have on the basis of (V-1-13) and (V-1-14) for the wing in compressible flow

$$c_y = \frac{a_0(\alpha - \alpha_0)}{\sqrt{1-M_\infty^2} + \frac{a_0}{\lambda_{wg}\pi}(1+\tau')}, \qquad \text{(V-1-15)}$$

where τ' is calculated by (V-1-11), in which the parameter $\underline{m}$ should be set equal to $m = \lambda_{wg}\sqrt{1-M_\infty^2}/a_0$.

Specifically, for a wing of elliptical planform with a thin symmetrical profile ($a_0 = 2\pi$, $\alpha_0 = 0$), /215

$$c_y = \frac{2\pi\lambda_{wg}\alpha}{2 + \lambda_{wg}\sqrt{1 - M_\infty^2}}. \qquad \text{(V-1-16)}$$

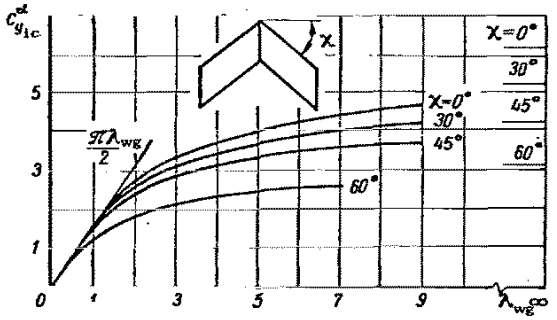

Figure V-1-1. Derivative $c^{\alpha}_{y\ ic}$ for Swept Wing with Taper $\eta = 1$.

Swept wings and wings of small aspect ratio. For swept wings, a formula simpler than (V-1-9) should be used to compute the incompressible-fluid lift coefficient:

$$c_{y\ ic} = \frac{\pi\lambda_{wg}(\alpha - \alpha_0)}{1 + \tau + \sqrt{(1+\tau)^2 + (\pi m)^2}}, \qquad \text{(V-1-17)}$$

where $m = \lambda_{wg}/(a_0 \cos\chi)$; τ is a parameter calculated by (V-1-11) using the new m.

For a wing with given parameters λ_{wg}, a_0, η, and χ, the calculation is performed as follows. The parameter $m = \lambda_{wg}/(a_0 \cos\chi)$ is calculated, and then Table V-1-2 is used to find τ_1. Then, having used Table V-1-2 to find τ_2 for the given η, we find τ and, finally, $c_{y\ ic}$. Figure V-1-1 shows the results of a calculation by (V-1-17).

For wings of small aspect ratio, the order of the terms in the denominator of (V-1-17) is found to be such that this formula can be simplified, with the result

$$c_{y\ ic} = \frac{\pi\lambda_{wg}}{2}(\alpha - \alpha_0). \qquad \text{(V-1-18)}$$

If the wing is thin, the influence of compressibility should be taken into account with (V-1-14) and the expression

$$\operatorname{tg}\chi' = \frac{\operatorname{tg}\chi}{\sqrt{1 - M_\infty^2}}, \qquad \text{(V-1-19)}$$

which gives the relation between the sweep angles χ' and χ of the wings in incompressible and compressible flows, respectively.

The wing taper η remains the same for both wings.

To determine the lift coefficient with consideration of compressibility, we use the values given for M_∞, λ_{wg}, and χ to calculate the parameters tan χ', λ'_{wg}, τ', and m' and apply (V-1-17):

$$c_y = \frac{\pi\lambda_{wg}(\alpha-\alpha_0)}{1+\tau'+\sqrt{(1+\tau')^2+(m'\pi)^2}}. \qquad \text{(V-1-20)}$$

The quantity τ' is usually small by comparison with unity, but it becomes more important with increasing aspect ratio and sweep angle and with decreasing M_∞. The incompressible-flow τ can be used in approximate lift calculations. Then the working formula for the lift coefficient with consideration of compressibility becomes /216

$$c_y = \frac{\pi\lambda_{wg}(\alpha-\alpha_0)}{1+\tau+\sqrt{(1+\tau)^2+\frac{\pi^2\lambda^2_{wg}}{a_0^2}(1+\operatorname{tg}^2\chi-M^2_\infty)}}. \qquad \text{(V-1-21)}$$

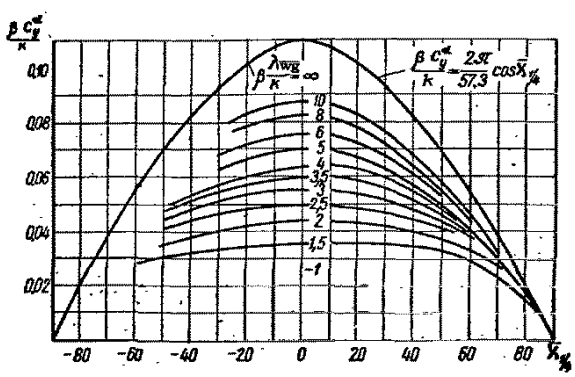

Figure V-1-2. Inclination of Lift Coefficient Curves for Swept Wings ($\beta = \sqrt{1-M^2_\infty}$; $k = a_{0e}\times\sqrt{1-M^2_\infty}/2\pi$; $\bar{\chi}_{1/4} = \arctan[\tan\chi_{1/4}(1-M^2_\infty)^{-1/2}]$).

For wings of small aspect ratio, the lift coefficient can, as we have noted, be calculated by (V-1-18).

The derivative $c_y^\alpha = \partial c_y/\partial\alpha$ can be presented in the form [61]

$$c_y^\alpha = \frac{a_{0e}}{2\pi} f(\eta, \bar{\chi}_{1/4}),$$

where f is a certain function of the taper $\eta = b_{rt}/b_{tp}$ and of the parameter

$$\bar{\chi}_{1/4} = \arctan\left(\frac{\operatorname{tg}\chi_{1/4}}{\sqrt{1-M^2_\infty}}\right),$$

determined from the sweep angle $\chi_{1/4}$ of the wing at the 1/4-chord line. Research has shown that the function $f(\eta, \bar{\chi}_{1/4})$ can be set

approximately equal to $f(\chi_{1/4})$. Figure V-1-2 shows theoretical c_y^α-curves constructed for $\eta = 2$. These curves enable us to find with a certain approximation the value of c_y^α for arbitrary values of η if we have experimental values $a_{0e} = (\partial c_y/\partial\alpha)_e$ for the profile at $M_\infty < M_{\infty cr}$. The data of Fig. V-1-2 are applicable to large angles of attack if the flow does not separate. Here a_{0e} can be determined from the Prandtl-Glauert rule $a_{0e} = a_{0e}^\circ(1 - M_\infty^2)^{-1/2}$, where a_{0e}° is the experimental value of c_y^α for the profile in incompressible flow.

Effectiveness of controls. A control occupying all or part of the wingspan at the trailing edge changes the wing's lift as a function of the control deflection angle δ_c. The effectiveness of the control on the profile is determined by the derivative $a_{0c} = \partial c_y/\partial\delta_c$ of profile lift with respect to the control angle δ_c. The theoretical a_{0c} obtained for the linear range of the profile lift coefficient (at $M_\infty = 0$) as a function of attack angle α and deflection angle δ_c are given in Fig. V-1-3a [61]. At small angles of attack, these curves should be used for $\delta_c \leq 15°$. The correction to the a_{0c} found from experimental data for $a_{0c} = a_{0ce}$ is given in Fig. V-1-3b. The value of a_{0e}/a_0 for a given profile can be determined with the aid of (V-1-10) and linear interpolation from the data on page 286. /217

For $M_\infty \leq M_{cr}$, the effectiveness $a_{0c.m} = c_{y\ cm}^\alpha$ of controls extending along the entire span of tapered wings with straight edges, tip chords parallel to the root chord, and a constant ratio b_c/b can be evaluated by the parameter /218

$$\frac{a_{0c.m}/a_{0c.e}}{a_{0m}/a_{0e}} = f\left(\frac{b_c}{b},\ \lambda_{we}\sqrt{1-M_\infty^2}\right), \qquad \text{(V-1-22)}$$

where $a_{0m} = c_{ym}^\alpha$, the slope of the wing lift curve, is determined from Fig. V-1-2. This effectiveness parameter can be determined from the data of Fig. V-1-4, which are applicable for linear variation of the coefficient c_y with α and δ_c.

The effectiveness $a_{0c.m}$ of a control occupying part of the wingspan and extending to the wing tip chord can be determined with the semiempirical relation

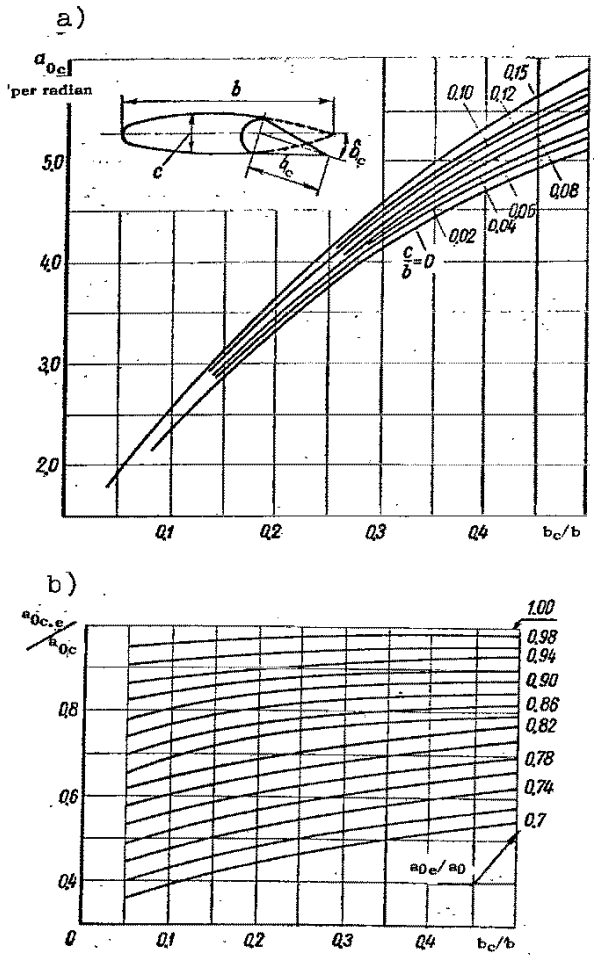

Figure V-1-3. Effectiveness of Control Surface on Profile in Incompressible Flow. a) theoretical value $a_{0c} = \partial c_y/\partial \delta_c$; b) ratio $a_{0ce}/a_{0c} = (\partial c_y/\partial \delta_{ce})/(\partial c_y/\partial \delta_c)$ from experimental data.

$$a'_{0c.m} = a_{0c.m}K, \quad \text{(V-1-23)}$$

where

$$K = k_1\{1 + k_2(\lambda_{wg}\sqrt{1-M_\infty^2} - 6) + k_3 \sin[\operatorname{arctg}(\operatorname{tg}\chi_{1/2}\sqrt{1-M_\infty^2})]\}. \quad \text{(V-1-24)}$$

The coefficients k_n are functions of the wing taper η and of the ratio $\ell_c/\ell = \bar{\ell}_c$, where ℓ_c is the distance between the outboard edges of the control surfaces and ℓ is the wingspan. The coefficient k_1 is a weak function of taper and approximately equal to

$$k_1 = \bar{l}_c(1 - \sqrt{\bar{l}_c}). \quad \text{(V-1-25)}$$

The linear relation

$$k_2 = a(1 - \bar{l}_c), \quad \text{(V-1-26)}$$

can be used to calculate the coefficient k_2; here $a = -0.017$, -0.007, and 0.015 for $\eta = 1$, 2, ∞, respectively.

The coefficient k_2 is approximately equal to

$$k_3 = b(1 - \bar{l}^{5/4}), \quad \text{(V-1-27)}$$

where $b = 0.088$, 0.112, and 0.129 for $\eta = 1$, 2, ∞, respectively. The coefficients k_2 and k_3 for intermediate η can be determined by linear interpolation. For cases in which the root chord of

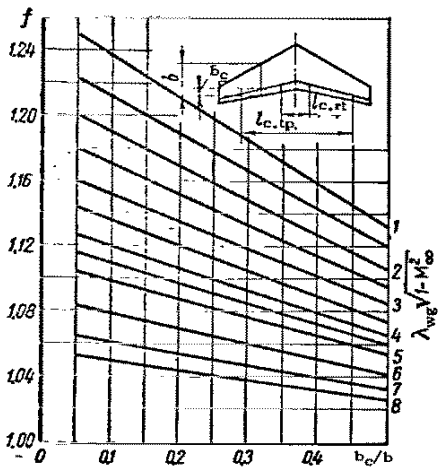

Figure V-1-4. Effectiveness of Controls on Swept Wings; Value of

$$f = \frac{a_{0cm}/a_{0ce}}{a_{0m}/a_{0e}} = \frac{(\partial c_y/\partial\delta_{cm})/(\partial c_y/\partial\delta_{ce})}{(\partial c_y/\partial\alpha)_m/(\partial c_y/\partial\alpha)_e}$$

the control does not coincide with the root chord of the wing, $a^{!}_{0\,c.m}$ is equal to the effectiveness difference between two control surfaces whose spans $\ell_{c.tp}$ and $\ell_{c.rt}$ are respectively equal to the distances between the outboard (tip) and inboard (root) chords of the controls.

Maximum lift coefficient. The lift coefficient can be calculated approximately by the relation

$$c_{y\,max} = c_{y\,max\,pr} K_\eta \frac{1+\cos\chi}{2}, \qquad \text{(V-1-28)}$$

where $c_{y\ max\ pr}$ is the maximum profile lift coefficient, χ is the sweep angle, and K_η is a taper-dependent coefficient. Values of this coefficient appear in Table V-1-3.

The $c_{y\ max}$ of the wing with the control surface deflected can be determined from the approximate formula /219

$$c_{y\,max\,\delta} = c_{y\,max} + 0{,}075\bar{S}_c\bar{\delta}\cos^2\chi_{av}, \qquad \text{(V-1-29)}$$

where $\bar{S}_c = S_c/S_{wg}$ is the ratio of the part of the wing area that serves as a control to the total area and χ_{av} is the average sweep angle determined by the formula

$$\operatorname{tg}\chi_{av} = \operatorname{tg}\chi - \frac{2}{\lambda_{wg}}\frac{\eta-1}{\eta+1}. \qquad \text{(V-1-30)}$$

The parameter $\bar{\delta}$, which depends on the deflection angle and relative chord of the control surface, can be determined with the aid of Fig. V-1-5, with the relative chord taken as the average over the length of the control surface.

Example. Compute the lift coefficient of a wing with a control surface at a flight speed $M_\infty = 0.6$ at an angle of attack $\alpha = 5°$. The geometrical characteristics of the wing are

TABLE V-1-3. VALUES OF COEFFICIENT K_η $\lambda_{wg}=8/3$; $\eta=2$; $\chi_1=45°$; $\bar{c}=0.1$.

η	1	2	3	4
K_η	0.90	0.94	0.93	0.93

The attack angle corresponding to zero lift is $\alpha_0 = -2°$.

The effective values of the parameters are

$$\lambda'_{wg}=\lambda_{wg}\sqrt{1-M_\infty^2}=\frac{8}{3}\sqrt{1-0.6^2}=2.136;$$

$$\operatorname{tg}\chi'_1=\operatorname{tg}\chi_1(1-M_\infty^2)^{-1/2}=1\,(1-0.6^2)^{-1/2}=1.25\;(\chi'_1=51°\,20');$$

$$m'=\lambda_{wg}\sqrt{1-M_\infty^2}/(a_0\cos\chi')=2.136/(6.28\cdot0.6246)=0.545,$$

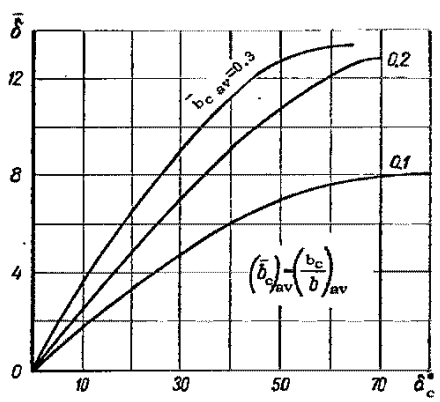

Figure V-1-5. Diagram for Determination of Parameter $\bar{\delta}$.

where the parameter a_0 is set equal to 2π.

From (V-1-11), we determine t' using m' and η:

$$\tau'=5.88\cdot0.107\cdot0.03=0.0189.$$

Applying (V-1-20),

$$c_y=\frac{3.14\cdot2.67\,(0.0873+0.0349)}{1+0.0189+\sqrt{(1+0.0189)^2+(0.513\cdot3.14)^2}}=0.341.$$

We calculate the maximum lift coefficient from (V-1-28), setting $c_{y\ max\ pr} = 0.9$ for the profile.

Remembering also that according to Table V-1-3, $K_\eta = 0.94$,

$$c_{y\ max}=0.9\cdot0.94\,\frac{1+0.7071}{2}=0.722.$$

We determine the $c_{y\ max}$ of the wing with the control from (V-1-29). Let $\bar{S}_c = 0.4$ in this formula. Setting the value of the relative control-surface chord averaged over the span equal to $\bar{b}_{c\ av} = 0.2$, and the deflection angle $\delta_c^0 = 60°$, we refer to /220

Fig. V-1-5 to find the parameter $\bar{\delta} = 12$. Then, using

$$\operatorname{tg}\chi_{av} = \operatorname{tg}\chi_1 - \frac{2}{\lambda_{wg}}\frac{\eta-1}{\eta+1} = 1 - \frac{2}{8/3}\frac{2-1}{2+1} = \frac{3}{4}$$

to calculate $\cos\chi_{av} = 0.80$, we calculate

$$c_{y\max\delta} = 0.722 + 0.075 \cdot 0.4 \cdot 12 \cdot 0.8^2 = 0.95.$$

Similarity rules for transonic flows. These rules enable us to unify calculations of the aerodynamic characteristics of wings in flows at M_∞ around unity. With the similarity rules, we can start from a known aerodynamic-coefficient value for a wing at a given M_∞ and obtain the corresponding aerodynamic coefficient for another Mach number M'_∞ and a modified (deformed) wing.

The approximate equation for the velocity potential in the transonic region should be used to establish the similarity rule:

$$(1-M_\infty^2)\bar{\varphi}_{xx} + \bar{\varphi}_{yy} + \bar{\varphi}_{zz} = (k+1)M_\infty^2\bar{\varphi}_x\bar{\varphi}_{xx}, \qquad \text{(V-1-31)}$$

where $\bar{\varphi} = \varphi/V_\infty$. Equation (V-1-31), the derivation of which is given in [6], differs from the corresponding equation of linear theory in the presence of a nonlinear right member. We introduce the new variables (denoted by the primes)

$$x(1-M_\infty^2)^{-1/2} = x'(1-M_\infty'^2)^{-1/2};\ y = y';\ z = z';\ \bar{\varphi}\bar{c}^{-1} = \bar{\varphi}'(\bar{c}')^{-1}, \qquad \text{(V-1-32)}$$

where $\bar{c}$ is the profile thickness ratio.

Substituting these variables into (V-1-31) and introducing the additional condition

$$\frac{(1-M_\infty^2)^{3/2}}{(k+1)M_\infty^2\bar{c}} = \frac{(1-M_\infty'^2)^{3/2}}{(k_1+1)M_\infty'^2\bar{c}'}, \qquad \text{(V-1-33)}$$

we obtain an equation in the new variables whose superficial form is exactly the same as that of (V-1-31). This equation describes similar flow around a wing of modified form. Relationships describing the deformation of the wing are easily obtained from (V-1-32):

$$\left.\begin{aligned}&\lambda_{wg}\sqrt{1-M_\infty^2}=\lambda'_{wg}\sqrt{1-M_\infty'^2};\ \eta=\eta';\\&\operatorname{tg}\chi\,(1-M_\infty^2)^{-1/2}=\operatorname{tg}\chi'\,(1-M_\infty'^2)^{-1/2}.\end{aligned}\right\}\qquad\text{(V-1-34)}$$

Formulas (V-1-33) and (V-1-34) are known as criterial [dimensionless] relationships.

Applying (III-1-13') and the criterial relationships, we can establish the relation between the aerodynamic characteristics of similar wings in similar flows.

For example, the relationships between the pressure and lift coefficients will be

$$\left.\begin{aligned}&\bar{p}\bar{c}^{-1}\sqrt{1-M_\infty^2}=\bar{p}'\,(\bar{c}')^{-1}\sqrt{1-M_\infty'^2};\\&c_y\bar{c}^{-1}\sqrt{1-M_\infty^2}=c_y'\,(\bar{c}')^{-1}\sqrt{1-M_\infty'^2};\\&\alpha\bar{c}^{-1}=\alpha'\,(\bar{c}')^{-1}.\end{aligned}\right\}\qquad\text{(V-1-35)}$$

Thus, calculation of the wing aerodynamic characerristics in transonic flow at arbitrary M_∞ can be reduced to calculation for some single Mach number M_∞ and subsequent conversion by the above formulas to any other M_∞.

These similarity-theory relationships can be extended to low supersonic velocities. This requires replacing $\sqrt{1-M_\infty^2}$ by $\sqrt{M_\infty^2-1}$ in all expressions. /221

The similarity rules enable us to establish certain relationships by which experimental data can be systematized. Let us take, for example, single-profile rectangular wings with thickness ratio $\bar{c}$. According to similarity theory, the general relation for the derivative c_y^α takes the form

$$c_y^\alpha\bar{c}^{1/3}=f\left(\frac{M_\infty^2-1}{\bar{c}^{2/3}},\ \lambda_{wg}\bar{c}^{1/3}\right).\qquad\text{(V-1-36)}$$

In the particular case with $M_\infty = 1$, the first similarity criterion in the parentheses is zero and

$$c_y^\alpha\bar{c}^{1/3}=f(\lambda_{wg}\bar{c}^{1/3}).\qquad\text{(V-1-37)}$$

Thus, $c_y^\alpha\bar{c}^{1/3}$ is a function of only the variable $\lambda_{wg}\bar{c}^{1/3}$ and can therefore be represented graphically as a single curve.

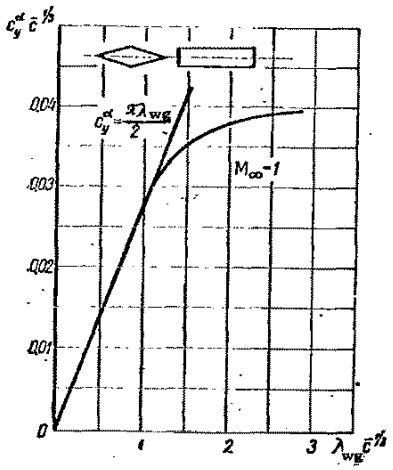

Figure V-1-6. Lift of Rectangular Wing at $M_\infty = 1$.

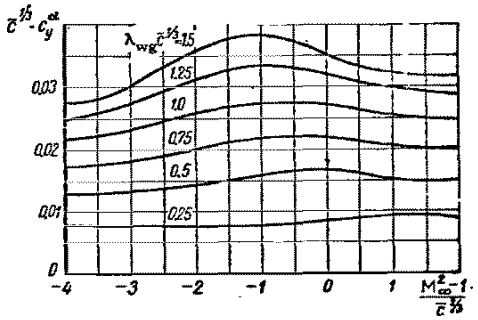

Figure V-1-7. Lift of Rectangular Wings at Transonic Speeds.

To calculate the derivatives c_y^α of rectangular wings for various transonic M_∞, we now need the family of curves defined by (V-1-36).

Figure V-1-6 presents experimental data for rectangular wings with rhomboid profiles at $M_\infty = 1$. These data indicate that with $\lambda_{wg}\bar{c}^{1/3} < 1$ the relation for c_y^α can be represented in the form $c_y^\alpha = \pi\lambda_{wg}/2$.

Figure V-1-7 shows more complete experimental data for rectangular wings with various profiles. These data can also be used for approximate evaluation of aerodynamic characteristics for slightly tapered trapezoidal wings.

For swept wings of small aspect ratio ($\lambda_{wg} \leq 3$), the derivative c_y^α can be determined by the methods established for subsonic flows.

Example. Calculate the lift coefficient of an isolated wing (see example on page 293) with a symmetrical profile whose thickness ratio $\bar{c} = c/b = 0.04$ at $M_\infty' = 0.95$ if the wing lift coefficient is known to be $c_y = 0.295$ at $M_\infty = 0.9$.

We determine the thickness ratio of the modified-wing profile by (V-1-33): /222

$$\frac{(1-0.9^2)^{3/2}}{0.9^2 \cdot 0.04} = \frac{(1-0.95^2)^{3/2}}{0.95^2 \bar{c}'},$$

whence $\bar{c}' = 0.013$.

Using Formulas (V-1-34) for the modified wing,

$$\eta' = 2:$$

$$\lambda'_{wg} = 2.67 \frac{\sqrt{1-0.9^2}}{\sqrt{1-0.95^2}} = 3.727;$$

$$\operatorname{tg} \chi' = 1 \frac{\sqrt{1-0.95^2}}{\sqrt{1-0.9^2}} = 0.7162 \qquad (\chi' = 35°36').$$

From (V-1-35), we calculate

$$c'_y = \frac{\bar{c}'}{\bar{c}} \frac{\sqrt{1-M_\infty^2}}{\sqrt{1-M_\infty^2}} c_y = \frac{0.013}{0.04} \frac{\sqrt{1-0.9^2}}{\sqrt{1-0.95^2}} 0.295 = 0.134.$$

The corresponding attack angle is

$$\alpha' = \alpha \frac{\bar{c}'}{\bar{c}} = 5 \frac{0.013}{0.04} = 1.63°.$$

Frontal Drag

Subcritical velocities ($M_\infty < M_{\infty cr}$). According to (I-3-1), the frontal drag coefficient is defined as the sum of the profile and induced drag coefficients. The profile drag coefficient can be calculated from the formula [26]

$$c_{x\,pr} = 2c_{xf}(0.93 + 2.8\bar{c})\,(1 + 5\bar{c}M_\infty^4), \qquad \text{(V-1-38)}$$

where $2c_{xf}$ is the coefficient of friction of a flat plate of length equal to the wing mean chord and with the same position of the laminar-to-turbulent boundary-layer transition as the wing. Its value is calculated in the general case with consideration of compressibility (see Chapter VI).

For straight (unswept) wings, the transition point can be regarded in first approximation as coinciding with the abscissa of maximum profile thickness. At low speeds, the boundary layer can be regarded as completely turbulent for swept wings with large enough sweep angles.

The induced drag of the wing in incompressible flow

$$c_{xi} = \frac{c_y^2}{\pi \lambda_{wg}} (1 + \delta), \qquad \text{(V-1-39)}$$

where

$$\delta = 20.41 \delta_1 (m) \delta_2 (\eta). \qquad \text{(V-1-40)}$$

In this formula, δ_1 is found from Table V-1-2 as a function of the parameter $m = \lambda_{wg}/a_0$, and δ_2 from the same table as a function of the taper η. In the particular case of an elliptical-planform wing, $\delta = 0$.

For a swept wing, the coefficient δ is calculated by Formula (V-1-40) and Table V-1-2 for the condition $m = \lambda_{wg}/(a_0 \cos \chi)$.

The effect of compressibility on the induced drag coefficient is taken into account by the formula

$$c_{xi} = \frac{c_{xi0}}{\sqrt{1 - M_\infty^2}}, \qquad \text{(V-1-41)}$$

where c_{xi_0} is found from (V-1-39).

Under conditions approaching those of flow separation, the drag is approximately equal to the theoretical minimum [41]: /223

$$c_x = c_{x\,pr} + \frac{c_y^2}{\pi \lambda_{wg}}, \qquad \text{(V-1-42)}$$

and at large angles of attack it approaches

$$c_x = c_{x\,pr} + c_y \operatorname{tg} \alpha. \qquad \text{(V-1-42')}$$

Supercritical velocities ($M_\infty > M_{\infty cr}$). It may be assumed in approximate calculations that the drag of a wing at supercritical velocities is governed basically by local shock waves. The wave-drag coefficient of an unswept wing can be calculated by the formula [26]

$$c_{xw} = (0.25x + 1.2x^2 - 0.45x^5)\, c_{xw\,max}, \qquad \text{(V-1-43)}$$

where $c_{x\ w\ max}$ is the maximum value of the wave-drag coefficient, which is reached at $M_\infty = 1$ and $\underline{x}$ is a parameter equal to

$$x = \frac{M_\infty - M_{\infty\,cr}}{1 - M_{\infty\,cr}}. \qquad \text{(V-1-44)}$$

The critical Mach number $M_{\infty\ cr}$ is determined by the approximate formula

$$M_{\infty\,cr} = 1 - 0.7\bar{c}^{1/2} - 3.2\bar{c}c_y^{3/2}. \qquad \text{(V-1-45)}$$

The quantity $c_{x\ w\ max}$ can be regarded with a certain approximation as a function of the profile thickness ratio $\bar{c}$:

$$c_{xw\,max} = -0.017 + 0.008\bar{1}c, \qquad \text{(V-1-46)}$$

where $\bar{c}$ is taken in percent.

The drag calculated by (V-1-43) corresponds to the range $M_{\infty cr} \leq M_\infty \leq 1$.

Equation (V-2-9) should be used to find the segment of the wave-drag curve between $M_\infty = 1$ and an M_∞ slightly larger than unity.

The third term in (V-2-9), which does not depend on attack angle, must be replaced by the coefficients of (V-1-46) at the speed of sound. Having calculated $c_{x\ w_0}$ from (V-2-11), we can construct the intermediate segment of the curve, which enables us to find an approximate value of $c_{x\ w_0}$ in the transonic range between $M_\infty = 1$ and an M_∞ somewhat greater than unity.

It is now necessary to find that part of the wave drag in this range that depends on attack angle. For $M_\infty \leq M_{\infty cr}$, there is no wave drag, and for $M_\infty > 1$, when the flow around the wing is completely supersonic, this part of the drag is determined by the first two terms in (V-2-9). We interpolate to find intermediate values of the wave drag coefficient increment.

Thus, the total drag coefficient is

$$c_{x\ w} = c_{x\ w0} + \Delta c^2, \qquad \text{(V-1-47)}$$

where Δ is a parameter determined by interpolation between the values

$$\Delta = 0 \,(M_\infty = M_{\infty\,cr}) \quad \text{and} \quad \Delta = \frac{\sqrt{M_\infty^2 - 1}}{4} \,(M_\infty > 1).$$

Figure V-1-8 shows an example of calculation of Δ.

The total frontal-drag coefficient of the wing at Mach numbers in the range $M_{\infty cr} \leq M_\infty \leq 1$ can be obtained by adding the wave, profile, and induced drag coefficients. Theoretical and experimental studies indicate that wave drag is considerably greater than the profile and induced drags. /224

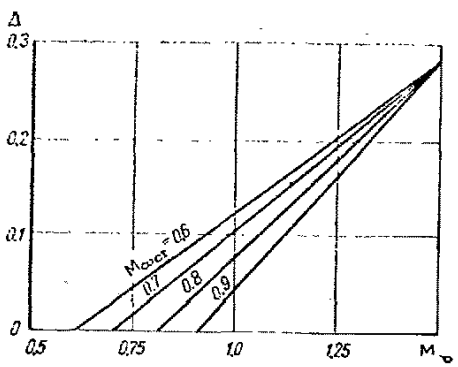

Figure V-1-8. Diagram for Determination of Parameter Δ.

For $M_\infty > 1$ in the transonic range, profile drag can be determined as the frictional drag. The induced drag for a straight wing is small in this case and can be disregarded with a certain approximation.

Swept wings. The wave drag coefficient component $c_{x\,w_0}$, which does not depend on α, is

$$c_{xw0} = \frac{1}{2}[(1-\bar{S}_{sl})\,c_{xw0\,pr} + (1+\bar{S}_{sl})\,c_{xw0\,sl}\cos^3\chi]. \qquad \text{(V-1-48)}$$

The $\bar{S}_{sl}$ in this formula represents the ratio of the area of the part of the wing working as a slipping wing to the total area, and is determined from the expression

$$\bar{S}_{sl} = \frac{S_{sl}}{S_{wg}} = 1 - \left(\frac{1.23\eta}{1+\eta}\right)^2 \frac{\sin 2\chi}{\lambda_{wg}} \left(2 - 1.5\frac{\sin 2\chi}{\lambda_{wg}}\frac{\eta-1}{\eta+1}\right). \qquad \text{(V-1-49)}$$

The quantity $c_{x\,w\,0\,pr}$ is equal to the wave-drag coefficient of the part of the wing that is arbitrarily assumed to be working as a straight wing and is determined from the actual M_∞, the actual c_y, and the profile thickness ratio $\bar{c}$ in a section parallel to the plane of symmetry.

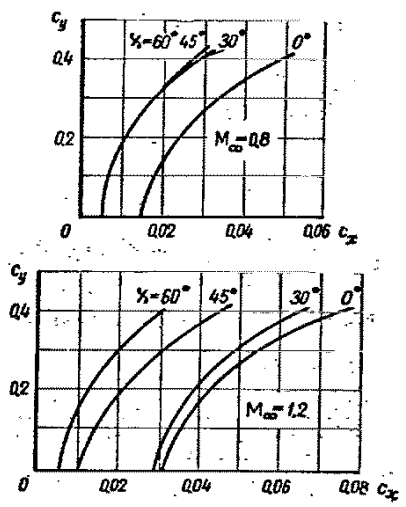

Figure V-1-9. Polars of Wings with Various Sweep Angles (λ_{wg} = 4; η = 2; $\bar{c}$ = 0.06. At M_∞ = $= M_{\infty cr} c_{x\ pr}$ = 0.005).

The coefficient $c_{x\ w\ 0\ sl}$ pertains to the part of the wing working as a slipping wing and is determined by the methods set forth above from the effective values $M_{\infty ef} = M_\infty \cos\chi$, the lift coefficient $c_{y\ ef} = c_y/\cos\chi$ and the profile thickness ratio $\bar{c}_{ef} = \bar{c}/\cos\chi$.

An approximate expression for the second drag coefficient component, which does depend on α, takes the form

$$c_{x\ w\ i} = \Delta_{swp} c_y^2, \qquad \text{(V-1-50)}$$

where

$$\Delta_{swp} = \frac{1}{2}\left[\frac{1-\bar{S}_{sl}}{\cos^2\chi}\Delta_{pr} + (1+\bar{S}_{sl})\cos\chi\Delta_{sl}\right]. \qquad \text{(V-1-51)}$$

In this formula, Δ_{pr} pertains to the part of the wing working as a straight wing and is determined for the actual values of M_∞, $\bar{c}$, and c_y; the parameter Δ_{sl} pertains to the part of the wing working as a slipping wing, and is determined for $M_{\infty ef}$, $\bar{c}_{ef}$, $c_{y\ ef}$ (see Fig. V-1-8). /225

Figure V-1-9 presents the results of a calculation by the above method for specified conditions.

Example. Calculate the wave-drag coefficient of a swept wing whose geometric characteristics are defined by the following parameters: λ_{wg} = 8/3; η = 2; χ_1 = 45°; $\bar{c}$ = 0.1. The wing is moving at an angle of attack α = 5° at the velocity corresponding to M_∞ = 0.8. The attack angle at which c_y = 0 is α_0 = -2°.

Assume that the wing's lift coefficient is 0.382 for M_∞ = = 0.8 and α = 5°. The following critical Mach number correponds to this value [see (V-1-45)]:

$$M_{\infty cr} = 1 - 0.7\sqrt{0.1} - 3.2\cdot 0.1\cdot 0.382^{1.5} = 0.703.$$

Since the given Mach number $M_\infty = 0.8 > M_{\infty cr}$, the flight corresponds to supercritical flow.

The wave drag coefficient

$$c_{xw} = c_{xw0} + c_{xwi},$$

where $c_{x\,w_0}$ is calculated with (V-1-48). Let us calculate certain parameters appearing in this expression. The dimensionless quantity

$$\bar{S}_{s1} = 1 - \left(\frac{1.23 \cdot 2}{2+1}\right)^2 \frac{3}{8}\left(2 - 1.5\,\frac{3}{8}\,\frac{1}{3}\right) = 0.544.$$

The parameter $c_{x\,w_0\,pr}$ is found with (V-1-43) from the value of (V-1-44):

$$x = \frac{0.8 - 0.703}{1 - 0.703} = 0.327$$

and from (V-1-46)

$$c_{x\,w\,max} = -0.017 + 0.0081 \cdot 10 = 0.064.$$

Applying (V-1-43), we get

$$c_{x\,w0\,pr} = (0.25 \cdot 0.327 + 1.2 \cdot 0.327^2 - 0.45 \cdot 0.327^5)\,0.064 = 0.013.$$

We then compute the coefficient $c_{x\,w_0\,sl}$ [see (V-1-43)].

For this purpose, we determine

$$M_{\infty ef} = M_\infty \cos\chi_1 = 0.8 \cdot 0.7071 = 0.57;$$
$$c_{y\,ef} = c_y/\cos\chi_1 = 0.382/0.7071 = 0.54;$$
$$\bar{c}_{ef} = \bar{c}/\cos\chi_1 = 0.1/0.7071 = 0.141;$$
$$c_{x\,w\,max\,ef} = -0.017 + 0.0081 \cdot 14.1 = 0.097;$$
$$M_{\infty cr\,ef} = 1 - 0.7\sqrt{0.141} - 3.2 \cdot 0.141 \cdot 0.54^{1.5} = 0.558;$$
$$x_{ef} = (M_{\infty ef} - M_{\infty cr,ef})/(1 - M_{\infty cr\,ef}) = (0.57 - 0.558)/(1 - 0.558) = 0.027;$$

and then calculate

$$c_{x\,w0\,sl}=(0.25\cdot0.027+1.2\cdot0.027^2-0.45\cdot0.027^3)\,0.097=0.0074.$$

Applying (V-1-48),

$$c_{x\,w0}=\frac{1}{2}\left[(1-0.544)\,0.013+(1+0.544)\,0.0074\cdot0.7071^3\right]=0.005.$$

We calculate the induced drag component $c_{x\,w\,i}$. For this purpose, we find the coefficient Δ_{swp} in (V-1-50). Δ_{pr} and Δ_{sl} are the unknown variables in this formula. If we know M_∞, $\bar{c}$, and c_y, the value of Δ_{pr} can be found from Fig. V-1-8 or from the interpolation formula

$$\Delta_{pr}=0.2795\frac{M_\infty-M_{\infty\,cr}}{1.5-M_{\infty\,cr}}.$$

Calculations give $\Delta_{pr}=0.034$.

In a similar manner, we determine $\Delta_{sl}=0.003$ from the values of $M_{\infty ef}$, $\bar{c}_{ef}$, and $c_{y\,ef}$. With the data obtained, /226

$$\Delta_{swp}=\frac{1}{2}\left[\frac{1-0.544}{0.7071^2}\,0.034+(1+0.544)\,0.7071\cdot0.003\right]=0.0017;$$

$$c_{x\,w\,i}=\Delta_{swp}c_y^2=0.017\cdot0.382^2=0.0025.$$

Consequently,

$$c_{x\,w}=0.005+0.0025=0.0075.$$

Similarity rules. Along with the relationships cited above, those that proceed from similarity theory can be used in calculating drag for the conditions of transonic flight:

$$\left.\begin{aligned}c_x\bar{c}^{-5/3}&=c_{x_1}(\bar{c}')^{-5/3};\\ c_xc_y^{-2}\bar{c}^{-1/3}&=c_{x_1}c_{y_1}^{-2}(\bar{c}')^{-1/3}.\end{aligned}\right\}\qquad\text{(V-1-52)}$$

For a rectangular wing, the drag similarity rule has the following functional dependence:

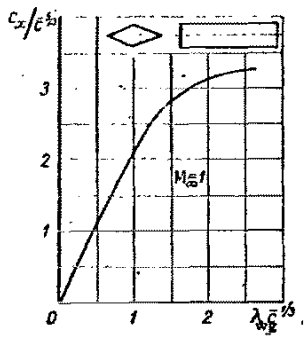

Figure V-1-10. Drag of Rectangular Wing at $M_\infty = 1$.

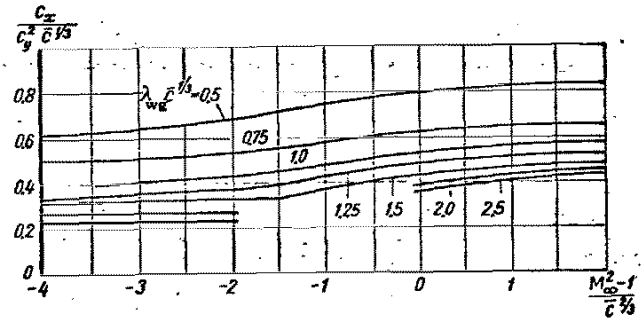

Figure V-1-11. Drag of Rectangular Wings at Transonic Speeds.

$$\frac{c_x}{c_y^2\bar{c}^{1/3}} = f\left(\frac{M_\infty^2-1}{\bar{c}^{2/3}},\ \lambda_{wg}\bar{c}^{1/3}\right). \qquad \text{(V-1-53)}$$

For $\alpha = 0$,

$$\frac{c_x}{\bar{c}^{5/3}} = f_0\left(\frac{M_\infty^2-1}{\bar{c}^{2/3}},\ \lambda_{wg}\bar{c}^{1/3}\right). \qquad \text{(V-1-54)}$$

At $M_\infty = 1$, (V-1-53) and (V-1-54) simplify:

$$\frac{c_x}{c_y^2\bar{c}^{1/3}} = f(\lambda_{wg}\bar{c}^{1/3}); \qquad \text{(V-1-53')}$$

$$\frac{c_x}{\bar{c}^{5/3}} = f_0(\lambda_{wg}\bar{c}^{1/3}). \qquad \text{(V-1-54')}$$

The curve representing (V-1-54') is shown in Fig. V-1-10. It was plotted on the basis of experimental data for a rectangular wing with rhomboid profile.

Experimental data on the drag of rectangular wings at transonic speeds are also given in Figs. V-1-11 and V-1-12. These data can be used in approximate calculations of the drag of wings with various types of profiles. Here the wings need not be rectangular; they may also be slightly trapezoidal. /227

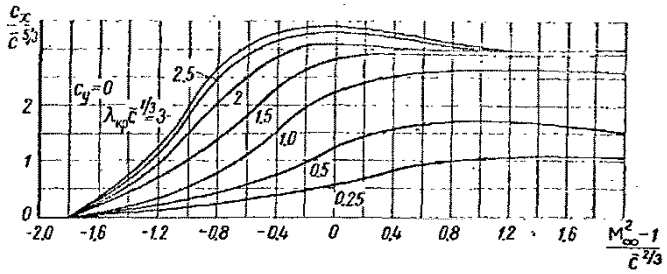

Figure V-1-12. Drag of Rectangular Wings at Transonic Speeds.

Moment and Aerodynamic Center (Center of Pressure)

Research has shown that the aerodynamic focus (center of pressure) of a modern symmetrical profile with a thickness ratio

TABLE V-1-4. VALUES OF THE FUNCTION F(η) OF TAPER EFFECT ON CENTER OF PRESSURE POSITION

η	1.0	1.5	1.7	2.0	2.5	3.0	4.0	5.0	6.0
$F(\eta)$	−0.022	−0.005	0	0.006	0.012	0.016	0.022	0.024	0.025

of the order of $\bar{c} = 0.04$ in incompressible flow is situated at 22-25% of chord behind the nose; on the wing, this point lies on the mean aerodynamic chord and is at the same relative distance from its leading edge.

To compute the position of the center of pressure (aerodynamic center) at subsonic speeds, we may make use of the approximate formula

$$c_{c.p} = \frac{x_{c.p}}{b_{MAC}} = c_{c.p\ pr} + \left(\lambda_{wg} \operatorname{tg} \chi_{1/2} + \frac{\eta-1}{\eta+1}\right) F(\eta), \qquad \text{(V-1-55)}$$

where $c_{c.p\ pr}$ is the distance to the profile center of pressure, expressed as a fraction of the mean aerodynamic chord and F(η) is a function characterizing the influence of taper on the center of pressure position. Values of this function are given in Table V-1-4.

As we have noted, the quantity $c_{c.p\ pr}$ in (V-1-55) can be set equal to 0.22-0.25 for profiles with thicknesses $\bar{c}$ of the

order of 0.04.

The relative distance of the center of pressure (aerodynamic center) $x_{c.p}/b_{MAC}$ from the beginning of the mean aerodynamic chord for swept wings at low velocities and small angles of attack can be determined from the curves in Fig. V-1-13 [61]. The dashed lines indicate $x_{c.p}/b_{MAC}$ for wings with unswept trailing edges. /228

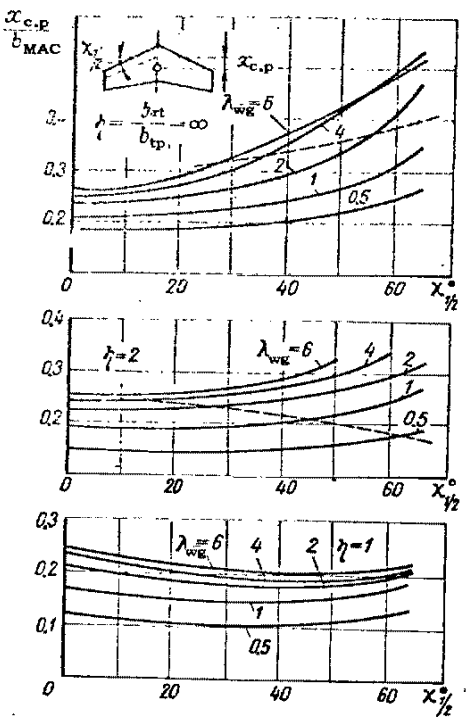

Figure V-1-13. Position of Wing Center of Pressure (Aerodynamic Center) at Low Flow Velocities and Small Angles of Attack. The Dashed Lines Characterize the Center of Pressure Position for a Wing with an Unswept Trailing Edge.

Figure V-1-14 shows the influence of compressibility on the center of pressure position for swept wings in linearized subsonic flow. The dashed curves were obtained by extrapolating data from a theoretical calculation.

Research has shown that in the transonic speed range ($M_{\infty cr} < M_\infty < 1$), the pressure center shifts slightly aft with increasing M_∞. From the value found for the lift coefficient and the center of pressure indicated above, we can determine the profile or wing moment coefficient for a subcritical flow velocity.

Similarity theory implies the following relation between the moment coefficients of thin wings in compressible and incompressible flows at identical attack angles:

$$m_z = \frac{m_{z\,ic}}{\sqrt{1-M_\infty^2}}. \qquad \text{(V-1-56)}$$

The coefficient m_{zic} is determined for a wing in incompressible flow and deformed in accordance with the similarity formulas (V-1-14) and (V-1-19).

Let us consider how the moment is determined for a wing with deflected flaps. If the calculation is performed about an axis passing through the center of gravity, the pitching-moment coefficient is

$$m_{z\,\mathrm{fps}} = m_{z\,0} + \Delta m_{z\,0\,\mathrm{fps}} - (\bar{x}_F - \bar{x}_g)(c_y + \Delta c_{y\,\mathrm{fps}}), \qquad \text{(V-1-57)}$$

where $\bar{x}_g$ and $\bar{x}_F$ are the respective coordinates of the center of gravity and the aerodynamic center, reckoned from the leading edge; m_{z_0} is the moment coefficient for $c_y = 0$;

$$\Delta m_{z\,0\,\mathrm{fps}} = -0.25\Delta c_{y\,\mathrm{fps}}; \qquad \text{(V-1-58)}$$

the quantity

$$\Delta c_{y\,\mathrm{fps}} = 0.075\bar{S}_{\mathrm{fps}}\bar{\delta}\cos^2\chi_{\mathrm{av}}. \qquad \text{(V-1-59)}$$

Example. Calculate the coefficient of center of pressure and moment for a wing with the following geometry:

$$\lambda_{wg} = 8/3; \quad \eta = 2; \quad \bar{c} = 0.04; \quad \mathrm{tg}\,\chi_1 = 1; \quad \mathrm{tg}\,\chi_t = 0.5.$$

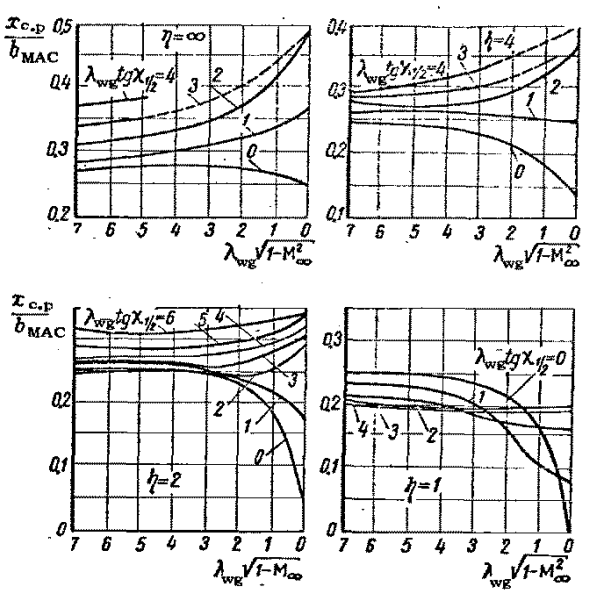

Figure V-1-14. Influence of Compressibility on Position of Center of Pressure (Focus) for Swept Wings.

Let us assume that the wing, which has a symmetrical rhomboid profile ($\alpha_0 = 0$ for such a wing), is in motion at an angle $\alpha = 5°$ at a speed corresponding to $M_\infty = 0.6$. For these conditions, the lift coefficient $c_y = 0.255$. /229

We assume that $c_{c.p\ pr}$ is 0.25 for this profile.

We calculate $c_{c.p}$ from (V-1-55), in which $F(\eta) = 0.006$ (see Table V-1-4) and

$$\mathrm{tg}\,\chi_{1/2} = \frac{1}{2}(\mathrm{tg}\,\chi_1 + \mathrm{tg}\,\chi_t) = \frac{1}{2}(1 + 0.5) = \frac{3}{4}.$$

We calculate the center of pressure coefficient

$$c_{c.p} = 0.25 + \left(\frac{8}{3}\cdot\frac{3}{4} + \frac{2-1}{2+1}\right) 0.006 = 0.264$$

and the moment coefficient

$$m_z = c_y c_{c.p} = 0.255 \cdot 0.264 = 0.0673.$$

§V-2. SUPERSONIC SPEEDS

Flow Around a Thin Plate

Applying the method of characteristics for plane two-dimensional flows and compression-shock theory, we can calculates supersonic flow past a thin plate (Figs. V-2-1 and V-2-2).

The calculation is performed separately for the upper and lower surfaces. To investigate the flow over the upper surface, which is characterized by additional expansion, we use the general relation (IV-1-17) of the nethod of characteristics, which enables us to calculate the flow for arbitrary M_∞ and attack angle. This relationship is simplified in two particular cases. /230

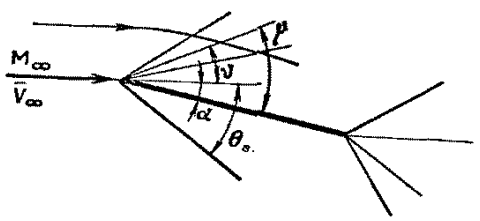

Figure V-2-1. Thin Plate in Supersonic Flow.

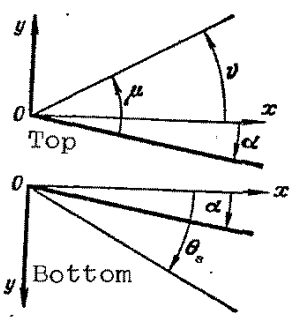

Figure V-2-2. Diagram of Supersonic Flow Past a Plate at an Angle of Attack.

The first pertains to linearized flow (small M_∞ and angle α). From (III-2-30), we find formulas for the additional disturbance velocity and the pressure coefficient on the upper surface:

$$V'_{x\,u} = \frac{\alpha V_\infty}{\sqrt{M_\infty^2 - 1}}, \quad \bar{p}_u = \frac{-2\alpha}{\sqrt{M_\infty^2 - 1}}. \qquad \text{(V-2-1)}$$

The second case is characterized by hypersonic flow ($M_\infty >> 1$, arbitrary α). The local Mach numbers M should be determined by

TABLE V-2-1. PARAMETERS OF FLOW AROUND A THIN PLATE AT AN ANGLE OF ATTACK /231

Flow conditions	Flow variable	Formula	Remarks
Linearized flow at $M_\infty > 1$ (small attack angle α)	Pressure coefficient	$\bar{p}=\frac{-2\alpha}{\sqrt{M_\infty^2-1}}$	Upper surface (vacuum)
			Lower surface (compression)
		$\bar{p}=\frac{2\alpha}{\sqrt{M_\infty^2-1}}$	Angles α assumed positive
	Coefficient of wave drag	$c_{xw}=\frac{4\alpha^2}{\sqrt{M_\infty^2-1}}$	
	Lift coefficient	$c_y=\frac{4\alpha}{\sqrt{M_\infty^2-1}}$	
Very high speeds $M_\infty >> 1$ (attack angle α arbitrary)	Angle between Mach wave and $\bar{V}_\infty$	$\vartheta=\alpha-\frac{1}{M}$	Upper surface
	Mach number M	$\frac{M_\infty}{M}=1-\frac{k-1}{2}M_\infty\alpha$	$M>M_\infty$
	Pressure	$\frac{p}{p_\infty}=\left(1-\frac{k-1}{2}M_\infty\alpha\right)^{\frac{2k}{k-1}}$	As $\alpha > \frac{2}{(k-1)M_\infty}$
	Pressure coefficient	$\bar{p}=\frac{2}{kM_\infty^2}\times$ $\times\left[\left(1-\frac{k-1}{2}M_\infty\alpha\right)^{\frac{2k}{k-1}}-1\right]$	flow separates from leading edge and formula does not apply
	Density	$\frac{\rho}{\rho_\infty}=\left(\frac{M_\infty}{M}\right)^{\frac{2}{k-1}}$	
	Temperature	$\frac{T}{T_\infty}=\left(\frac{M_\infty}{M}\right)^2$	
	Velocity	$\frac{V}{V_\infty}=1+\frac{k-1}{2}\left(\frac{1}{M_\infty^2}-\frac{1}{M^2}\right)$	
Arbitrary $M_\infty > 1$ (attack angle also arbitrary)	Horizontal velocity component	$V_x=V_\infty+V'_x=$ $=V_\infty\left[1-\frac{2}{k+1}(\sin^2\theta_s-M_\infty^{-2})\right]$	Lower surface
	Vertical velocity component	$V_y=\frac{2V_\infty}{k+1}\operatorname{ctg}\theta_s\times$ $\times(\sin^2\theta_s-M_\infty^{-2})$	
	Pressure coefficient	$\bar{p}=\frac{4}{k+1}(\sin^2\theta_s-M_\infty^{-2})$	

TABLE V-2-1 (Cont'd.)

Flow conditions	Flow variable	Formula	Remarks
	Density	$\frac{\rho}{\rho_\infty}=\frac{k+1}{k-1}\times$ $\times\left(1+\frac{2}{k-1}\frac{1}{M_\infty^2\sin^2\theta_s}\right)^{-1}$	
	Inclination angle of compression shock	$\operatorname{tg}\alpha=\frac{2}{k+1}\operatorname{ctg}\theta_s\times$ $\times(\sin^2\theta_s-M_\infty^{-2})\times$ $\times\left[1-\frac{2}{k+1}(\sin^2\theta_s-M_\infty^{-2})\right]^{-1}$	
$M_\infty >> 1$ (attack angle arbitrary)	Same parameters as for $M_\infty > 1$	$V_x=V_\infty+V_x'=$ $=V_\infty\left(1-\frac{2}{k+1}\sin^2\theta_s\right)$ $V_y=\frac{2V_\infty}{k+1}\sin\theta_s\cos\theta_s$ $\bar{p}=\frac{4}{k+1}\sin^2\theta_s$ $\frac{\rho}{\rho_\infty}=\frac{k+1}{k-1}$ $\operatorname{tg}\alpha=\frac{2}{k+1}\sin\theta_s\cos\theta_s\times$ $\times\left(1-\frac{2}{k+1}\sin^2\theta_s\right)^{-1}$	
$M_\infty >> 1$ (attack angles small)	Horizontal velocity component increment	$\frac{V_x'}{V_\infty\alpha^2}=-\frac{2}{k+1}\frac{K_s^2-1}{K^2}$	Lower surface $K_s = M_\infty\theta_s$ $K = M_\infty\alpha$
	Vertical velocity component	$\frac{V_y}{V_\infty\alpha}=1$	
	Pressure	$\frac{p}{p_\infty}=1+\frac{2k}{k+1}(K_s^2-1)$	
	Density	$\frac{\rho}{\rho_\infty}=\frac{k+1}{k-1}\left(1+\frac{2}{k-1}K_s^{-2}\right)^{-1}$	
	K_s	$K_s=\frac{k+1}{4}K+$ $+\left[\left(\frac{k+1}{4}K\right)^2+1\right]^{1/2}$	
	Pressure coefficient	$\bar{p}=\frac{4}{k+1}\frac{K_s^2-1}{K^2}\alpha^2$	
	Mach number M	$M^2=M_\infty^2\left(\frac{2k}{k+1}K_s^2-\frac{k-1}{k+1}\right)^{-1}\times$ $\times\left(\frac{k-1}{k+1}+\frac{2}{k+1}K_s^{-2}\right)^{-1}$	
		$M\to\frac{1}{\alpha}\left[\frac{2}{k(k-1)}\right]^{1/2}$	$K_s\to\infty$

TABLE V-2-1 (Cont'd.)

Flow conditions	Flow variable	Formula	Remarks
Total aerodynamic coefficients	Wave drag coefficient	$c_{x\,w}=\alpha^3\left\{\frac{k+1}{2}+\right.$ $+\left[\left(\frac{k+1}{2}\right)^2+4K^{-2}\right]^{1/2}+$ $+\frac{2}{kK^2}\left[1-\right.$ $\left.\left.-\left(1-\frac{k-1}{2}K\right)^{\frac{2k}{k-1}}\right]\right\}$	For $K \leq 1$
	Lift coefficient	$c_y=\frac{c_{x\,w}}{\alpha}$	
		$c_y=(k+1)\alpha^2$	$M_\infty \to \infty$
		$c_y=2\pi\alpha$	$M_\infty = 0$

(IV-1-18) and the pressure by (IV-7-12).

In investigating the flow on the lower surface of the plate, where the stream is compressed, we can examine the general case, which is characterized by arbitrary M and attack angle. In this case, the variables should be calculated from the general relationships of compression-shock theory. In particular, the pressure on the lower surface is determined from (III-4-25).

As for the upper surface, we can examine two particular cases of flow: linearized (M_∞ and α small) and hypersonic ($M_\infty >> >> 1$, arbitrary attack angles).

In the case of linearized flow, the case of weak compression on the lower surface can be calculated by the method of characteristics, using formulas analogous to (V-2-2):

$$V'_{x1}=\frac{-\alpha V_\infty}{\sqrt{M_\infty^2-1}};\quad \bar{p}_1=\frac{2\alpha}{\sqrt{M_\infty^2-1}}. \qquad \text{(V-2-2)}$$

Hypersonic flows are calculated from the theory of the strong shock wave. For example, pressure is determined by (III-4-19).

The results of a calculation of the flow variables for a thin plate at an angle of attack and the wave-drag and lift coefficients appear in Table V-2-1.

At hypersonic flow velocities, the gas undergoes chemical transformations on the side of the plate with the compression shock. In the general case, the flow along the streamline from the compression shock to the plate will move at variable density. If, however, the shock wave is thin, the change in density can be disregarded, and we can assume for the wall that the relative quantity $\bar{\rho} = \rho_\infty/\rho_s = \rho_1/\rho_2$. For this case, the pressure coefficient on the plate is /233

$$\bar{p} = \frac{2\sin^2\alpha}{(1-\bar{\rho})\cos^2(\theta_s-\alpha)}. \qquad \text{(V-2-3)}$$

For a fixed α, we can assign, for example, $\bar{\rho}$ and determine the angle θ_s of an attached shock by using the hypersonic-theory formulas

$$\operatorname{tg}\theta_s = \bar{\rho}^{-1/2} f(\eta); \quad f(\eta) = 2\eta\left(1 \pm \sqrt{1-4\eta^2}\right)^{-1}, \qquad \text{(V-2-4)}$$

where

$$\eta = \bar{\rho}^{1/2}(1-\bar{\rho})^{-1}\operatorname{tg}\alpha. \qquad \text{(V-2-5)}$$

The range of variation of the function $f(\eta)$: $0 \leq f(\eta) \leq 1$ corresponds to the interval $0 \leq \eta \leq 0.5$. The value of $\cos^2(\theta_s - \alpha)$ is determined from the difference $\theta_s - \alpha$. Applying (III-4-14), in which $\Delta\bar{V}_n = 1 - \bar{\rho}$, we can, assigning $V_{n_1}^2/2$, determine the enthalpy i_2 and, knowing i_2 and $\rho = \rho_\infty/\bar{\rho}$, refer to the thermodynamic tables to calculate the pressure p_2. From p_2, using (III-4-12), we can improve V_{n_1} and then find the oncoming-flow velocity $V_\infty = V_{n_1}/\sin\theta_s$. For high velocities, at which the wave touches the wall, $\cos(\theta_s - \alpha) \approx 1$ and the pressure coefficient

$$\bar{p} = 2\sin^2\alpha\,(1+\bar{\rho}). \qquad \text{(V-2-5')}$$

Profile in Supersonic Flow

Pressure distribution. Let us examine a sharp-edged profile in a supersonic flow at an angle of attack (Fig. V-2-3). The problem of flow around the profile can be solved by the method of characteristics. In approximate form, this problem can be solved using a method that combines the theory of plane flows (Prandtl-Meyer theory) and compression-shock theory. Here, /234 Prandtl-Meyer flow can be investigated with the relationships

of the characteristics method for plane flows.

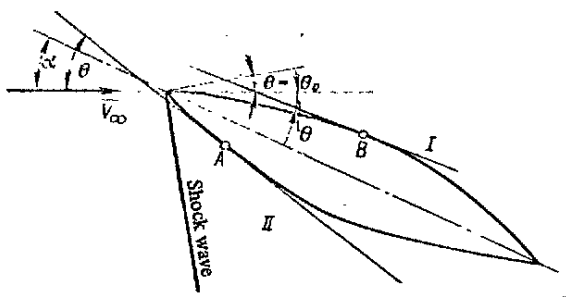

Figure V-2-3. Thin Profile in Flow at Angle of Attack. I) region of flow with expansion; II) region of flow with compression.

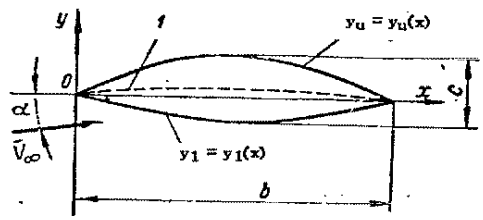

Figure V-2-4. Geometry of Profile with Curved Contour (1 is the profile centerline).

For thin profiles and small attack angles, an approximate solution can be obtained in explicit form. For this purpose, the function $\bar{p} = f(\theta)$, where θ is the angle between the tangent to the profile at a given point and the vector $\bar{V}_\infty$, is represented in the form of a series in powers of the small parameter θ. The coefficients of θ^n are the corresponding derivatives $\partial\bar{p}^n/\partial\theta^n$ and are determined from the epicycloid equation $\theta = \omega(M) + \text{const}$ and the expression for pressure in an isentropic flow.

Since the profile is thin, we can limit ourselves to the term in θ^2 in the expansion to obtain

$$\bar{p} = 2(c_1\theta + c_2\theta^2), \qquad \text{(V-2-6)}$$

where

$$c_1 = (M_\infty^2 - 1)^{-1/2}; \quad c_2 = \frac{1}{4}(M_\infty^2 - 1)^{-2}[(M_\infty^2 - 2)^2 + kM_\infty^4]. \qquad \text{(V-2-7)}$$

Formula (V-2-6) applies to expansion flow for $\theta < 0$ and to compression flow for $\theta > 0$. Here, compression flow can be regarded as isentropic or be associated with passage through a shock. Formula (V-2-6) corresponds to the second-approximation theory elaborated by Prof. Busemann and, in the USSR, by Prof. A.A. Lebedev. It is assumed in first-approximation theory that $\bar{p} = 2c_1\theta$.

Aerodynamic coefficients in linearized flow. The thickness of a profile can be made so small as to permit setting $c_2 = 0$ in (V-2-6) and, consequently, to permit use of the first-approximation theory. Assuming that $\theta = y' \mp \alpha$, we obtain linearized relationships for calculation of pressure on the upper and lower

profile surfaces:

$$\bar{p}_u = \frac{2(y'_u - \alpha)}{\sqrt{M_\infty^2 - 1}}; \quad \bar{p}_l = \frac{2(-y'_l + \alpha)}{\sqrt{M_\infty^2 - 1}};$$

where the derivatives

$$y'_u = \frac{dy_u}{dx}; \quad y'_l = \frac{dy_l}{dx}$$

are calculated from the familiar expressions $y_u = y_u(x)$ for the upper and $y_l = y_l(x)$ for the lower contour (Fig. V-2-4). If the profile is symmetrical, $|y'_u| = |y'_l|$.

Using the formulas for the pressure coefficients $\bar{p}_u$ and $\bar{p}_l$, /235 we can derive the following relation for the lift of a sharp thin profile with arbitrary cross section:

$$c_y = \frac{4\alpha}{\sqrt{M_\infty^2 - 1}}. \qquad \text{(V-2-8)}$$

For a thin profile of a swept infinite-span wing, the lift coefficient

$$c_y = \frac{4\alpha \cos \chi}{\sqrt{M_\infty^2 \cos^2 \chi - 1}}. \qquad \text{(V-2-8')}$$

It is remembered that the leading edge is supersonic, so that $M_\infty \cos \chi > 1$.

The wave drag coefficient

$$c_{xw} = \frac{4\alpha^2}{\sqrt{M_\infty^2 - 1}} - \frac{4\alpha}{\sqrt{M_\infty^2 - 1}} \int_0^1 (y'_u + y'_l)\, d\bar{x} + \frac{2}{\sqrt{M_\infty^2 - 1}} \int_0^1 (y'^2_u + y'^2_l)\, d\bar{x}, \qquad \text{(V-2-9)}$$

where $\bar{x} = x/b$.

At zero angle of attack

$$c_{xw} = c_{xw0} = \frac{2}{\sqrt{M_\infty^2 - 1}} \int_0^1 (y'^2_u + y'^2_l)\, d\bar{x}. \qquad \text{(V-2-10)}$$

In this formula

$$\int_0^{\bar{1}} (y_u'^2 + y_l'^2)\, d\bar{x} = k_1 \bar{c}^2,$$

so that

$$c_{x_{w0}} = \frac{2k_1\bar{c}^2}{\sqrt{M_\infty^2 - 1}}. \qquad \text{(V-2-11)}$$

where k_1 is a coefficient that depends on the shape and dimensions of the profile or, more precisely, on the parameter $\bar{x}_c$, which is the ratio of the distance from the nose to the point of greatest thickness to the chord (Fig. V-2-5).

Values of this coefficient are given in Table V-2-2 [6]. It is assumed in the table that $\bar{x}_c$ is the same for the bottom and top surfaces.

The coefficient $c_{x\,w_0}$ determines the drag governed by the thickness and shape of the profile and is independent of attack angle.

The first two terms in (V-2-9) determine that part of the total profile drag that depends on attack angle.

The component governed by lift

$$c_{x_{w1}} = \frac{4\alpha^2}{\sqrt{M_\infty^2 - 1}} = \alpha c_y, \qquad \text{(V-2-12)}$$

is independent of the dimensions and shape of the profile.

The second component, which does depend on attack angle and profile shape,

$$c_{x_{w2}} = -\frac{4\alpha}{\sqrt{M_\infty^2 - 1}} \int_0^{\bar{1}} (y_u' + y_l')\, d\bar{x} \qquad \text{(V-2-13)}$$

can also be written /236

$$c_{x_{w2}} = -\frac{8\alpha}{\sqrt{M_\infty^2 - 1}} \int_0^{\bar{1}} \left(\frac{d\bar{y}}{d\bar{x}}\right) d\bar{x}, \qquad \text{(V-2-14)}$$

where $d\bar{y}/dx$ is a derivative calculated from the equation $\bar{y} = \frac{1}{2}(y_u + y_l)$ of the profile centerline. The second component is associated with the simultaneous effect of attack angle and profile shape. This component is zero when the trailing edge is sharp or, if it is not, when the profile is symmetrical.

TABLE V-2-2. VALUES OF THE COEFFICIENT k_1 AND RELATIVE DISTANCE $\bar{x}_c$ TO THE POINT OF MAXIMUM THICKNESS

Profile form	$\bar{x}_c$	$2k_1$
Rhomboid	0.5	4
Wedge	0.4	4.16
"	0.3	4.76
Parabolic symmetrical	0.5	5.33
Wedge with one flat side	0.5	8
Same	0.4	8.32
"	0.3	9.52
Parabolic with one flat side	0.5	10.67
Formed by two circular arcs	0.5	16/3

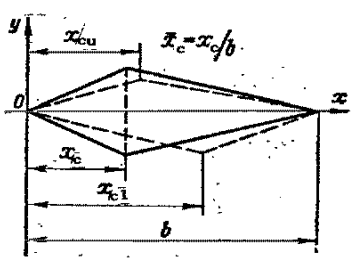

Figure V-2-5. Geometry of Profile with Straight-Line Walls.

For the most commonly encountered symmetrical profiles or profiles that are sharp at both ends,

$$c_{xw} = \frac{2k_1\bar{c}^2}{\sqrt{M_\infty^2 - 1}} + \frac{\sqrt{M_\infty^2 - 1}}{4} c_y^2. \qquad \text{(V-2-15)}$$

The above formulas can be used for slightly curved wings set at a small angle of attack.

Flow around profile with consideration of nonlinear effect. This flow is calculated using (V-2-6) for the pressure coefficients. For the top of the profile,

$$\bar{p}_u = c_1(y'_u - \alpha) + c_2(y'_u - \alpha)^2, \qquad \text{(V-2-16)}$$

and for the bottom

$$\bar{p}_l = c_1(-y'_l + \alpha) + c_2(-y'_l + \alpha)^2. \qquad \text{(V-2-17)}$$

Integrating over the surface of a profile of assigned form, we can obtain relationships for the lift and wave-drag coefficients:

$$c_y = 4c_1(\alpha - \alpha_0), \qquad \text{(V-2-18)}$$

$$c_{xw} = \alpha c_y - 8c_2\alpha A_2 + 2c_1 B_2 - 2c_2 A_3, \qquad \text{(V-2-19)}$$

where α_0 is the attack angle at which $c_y = 0$ (angle of zero lift), /237 and is calculated by the formula

$$\alpha_0 = -\frac{c_2}{2c_1} A_2. \qquad \text{(V-2-20)}$$

TABLE V-2-3. VALUES OF THE COEFFICIENTS A_2, B_2, AND A_3 FOR CALCULATION OF THE AERODYNAMIC COEFFICIENTS

Profile form	Formulas for Coefficients A_2, B_2, A_3	Remarks
Profile formed by arcs of circles; profile has vertical symmetry (Fig. V-2-6a)	$A_2 = \frac{16}{3}(\bar{c}_1^2 - \bar{c}_u^2)$ $B_2 = \frac{16}{3}(\bar{c}_1^2 + \bar{c}_u^2)$ $A_3 = 0$	$\bar{c}_1 = c_1/b$; $\bar{c}_u = c_u/b$. With horizontal symmetry, $\lvert c_1\rvert = c_u$
Profile formed by two trapezoids (Fig. V-2-6b) Same formulas apply to rhomboid profile ($b_{2u} = b_{2l} = 0$)	$A_2 = \bar{c}_1^2\left(\frac{1}{\bar{b}_{11}} + \frac{1}{\bar{b}_{31}}\right) - \bar{c}_u^2\left(\frac{1}{\bar{b}_{1u}} + \frac{1}{\bar{b}_{3u}}\right)$ $B_2 = \bar{c}_1^2\left(\frac{1}{\bar{b}_{11}} + \frac{1}{\bar{b}_{31}}\right) + \bar{c}_u^2\left(\frac{1}{\bar{b}_{1u}} + \frac{1}{\bar{b}_{3u}}\right)$ $A_3 = \bar{c}_1^3\left(\frac{1}{\bar{b}_{11}} - \frac{1}{\bar{b}_{31}}\right)\left(\frac{1}{\bar{b}_{11}} + \frac{1}{\bar{b}_{31}}\right) - -\bar{c}_u^3\left(\frac{1}{\bar{b}_{1u}} - \frac{1}{\bar{b}_{3u}}\right)\left(\frac{1}{\bar{b}_{1u}} + \frac{1}{\bar{b}_{3u}}\right)$	$\bar{b}_1 = b_1/b$, $\bar{b}_u = b_u/b$ $c_1 < 0$ $c_u > 0$ For symmetrical profile $\lvert c_1\rvert = c_u$; $b_{1l} = b_{1u}$ $b_{3l} = b_{3u}$
Profile formed by arcs of circles with different radii (Fig. V-2-6b)	$A_2 = \frac{4}{3}\left[\bar{c}_1^2\left(\frac{1}{\bar{b}_{11}} + \frac{1}{\bar{b}_{21}}\right) - \bar{c}_u^2\left(\frac{1}{\bar{b}_{1u}} + \frac{1}{\bar{b}_{2u}}\right)\right]$ $B_2 = \frac{4}{3}\left[\bar{c}_1^2\left(\frac{1}{\bar{b}_{11}} + \frac{1}{\bar{b}_{21}}\right) + \bar{c}_u^2\left(\frac{1}{\bar{b}_{1u}} + \frac{1}{\bar{b}_{2u}}\right)\right]$ $A_3 = -2\left[\bar{c}_1^3\left(\frac{1}{\bar{b}_{11}^2} - \frac{1}{\bar{b}_{21}^2}\right) - \bar{c}_u^3\left(\frac{1}{\bar{b}_{1u}^2} - \frac{1}{\bar{b}_{3u}^2}\right)\right]$	For profile with horizontal symmetry $\lvert c_1\rvert = c_u$

The quantities A_2, B_2, and A_3, which depend on profile form, are determined as follows:

$$\left.\begin{aligned} A_2 &= \int_0^1 [(y_1')^2 - (y_u')^2]\, d\bar{x}; \quad B_2 = \int_0^1 [(y_1')^2 + (y_u')^2]\, d\bar{x}; \\ A_3 &= \int_0^1 [(y_1')^3 - (y_u')^3]\, d\bar{x}. \end{aligned}\right\} \qquad \text{(V-2-21)}$$

Combining (V-2-18) and (V-2-19) and dropping terms of higher orders from the resulting expression, we find the polar equation of the profile:

$$c_x = \frac{c_y^2}{4c_1} - \alpha_0 c_y + c_{x\,w0}. \qquad \text{(V-2-22)}$$

where $c_{x\,w_0}$ is the wave-drag coefficient at zero lift and is equal to

$$c_{x\,w0} = 2c_1 B_2 - 2c_2 A_3. \qquad \text{(V-2-23)}$$

Values of the coefficients A_2, B_2, and A_3 for certain profile types are given in Table V-2-3.

Profile with minimum drag. Having determined the minimum of the drag function expressed by (V-2-23), we can find the profile shape corresponding to $c_{x\,w_0\,min}$ for a given thickness ratio. Research has shown that this profile is a wedge with a relative distance to the point of maximum thickness /238

$$\bar{b}_1 = \frac{b_1}{b} = \frac{1}{2}\left(1 + \frac{c_2}{c_1}\bar{c}\right), \text{ where } \bar{c} = \frac{c}{b}. \qquad \text{(V-2-24)}$$

The coefficient of minimum wave drag is

$$c_{x\,w0\,min} = 4c_1\bar{c}^2\left(1 - \frac{c_2^2}{c_1^2}\bar{c}^2\right). \qquad \text{(V-2-25)}$$

By determining drag as a function of the dimensions of a profile with a given shape, we can establish that $c_{x\,w_0}$ reaches its smallest value (provided that the maximum thickness ratio is given) when the thicknesses of the upper and lower parts of the profile are the same, i.e., when the profile has horizontal symmetry. For example, for a profile formed by arcs of circles

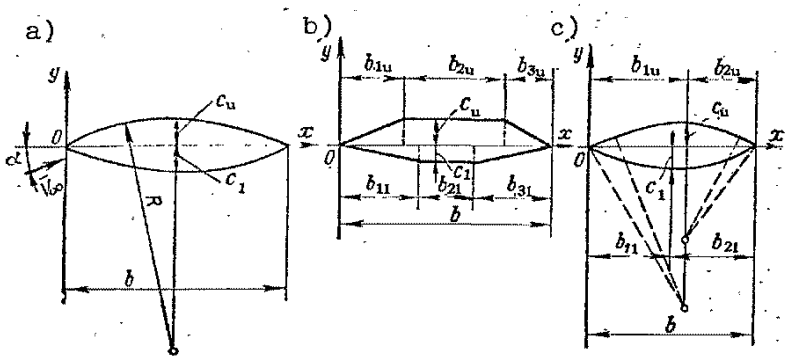

Figure V-2-6. Profile Geometries. a) profile formed by two circular arcs (profile has vertical symmetry); b) profile formed by two trapezoids; c) profile formed by arcs of circles of different radii.

$$c_{x\,w0}=\frac{16}{3}c_1\bar{c}^2\left(1-\frac{9}{4}\frac{c_2^2}{c_1^2}\right). \qquad \text{(V-2-26)}$$

The point of maximum profile thickness, which corresponds to the value of the coefficient $c_{x\,w_0}$ in (V-2-26), is determined by the distance ratio

$$\bar{b}_1=\frac{b_1}{b}=\frac{1}{2}\left(1+\frac{3c_2}{c_1}\bar{c}\right). \qquad \text{(V-2-27)}$$

For a symmetrical profile formed by two trapezoids with given distances b_1, b_3, and $\underline{c}$, the minimum drag

$$c_{x\,w0}=\frac{4c_1\bar{c}^2}{\bar{b}_1+\bar{b}_3}\left[1-\frac{\bar{c}^2}{(\bar{b}_1+\bar{b}_3)^2}\frac{c_2^2}{c_1^2}\right] \qquad \text{(V-2-28)}$$

is reached when

$$\frac{\bar{b}_1}{\bar{b}_1+\bar{b}_3}=\frac{1}{2}\left(1+\frac{c_2}{c_1}\frac{\bar{c}}{\bar{b}_1+\bar{b}_3}\right). \qquad \text{(V-2-29)}$$

When the wing is mounted on a vehicle with a specific design, importance attaches to its strength characteristics, which depend /239 in many respects on the shape of the profile and its moment of

inertia with respect to the chord. It is therefore important to determine the minimum profile drag at a given moment of inertia. Calculations show that this drag for a profile formed by two trapezoids is

$$c_{x\,w0}=5c_1\bar{c}^2\left(1-\frac{25}{16}\frac{c_2^2}{c_1^2}\bar{c}^2\right). \qquad \text{(V-2-30)}$$

The moment of inertia corresponding to this drag

$$J=\frac{1}{30}\bar{c}^3\bar{b}^4; \qquad \text{(V-2-31)}$$

the other profile dimensions are

$$\bar{b}_1+\bar{b}_3=\frac{4}{5},\ \bar{b}_2=\frac{1}{5}. \qquad \text{(V-2-32)}$$

Profile with maximum lift/drag ratio. Analyzing (V-2-22) and (V-2-23), we can establish that the maximum lift/drag ratio,

$$\left(\frac{c_y}{c_{x\,w}}\right)_{max}=\left(\frac{c_2}{2c_1}A_2+\left[\frac{c_{x\,w0}}{c_1}\right]^{1/2}\right)^{-1} \qquad \text{(V-2-33)}$$

occurs when

$$c_y=2\left[c_1c_{x\,w0}\right]^{1/2}. \qquad \text{(V-2-34)}$$

For a fixed thickness ratio, the profile with maximum lift/drag ratio will be rhomboid with a relative distance to the point of maximum thickness determined by (V-2-24). The thicknesses of the top and bottom parts of the profile are

$$\bar{c}_u=-\bar{c}_1\left(1+\frac{2c_2}{c_1}\bar{c}\right);\quad \bar{c}_1=\frac{1}{2\bar{c}}\left(1-\frac{c_2}{c_1}\bar{c}\right). \qquad \text{(V-2-35)}$$

Accordingly, the formula for the maximum lift/drag ratio

$$\left(\frac{c_y}{c_{x\,w}}\right)_{max}=\left(2\bar{c}-\frac{2c_2}{c_1}\bar{c}^3\right)^{-1} \qquad \text{(V-2-36)}$$

Lift and drag of swept infinite-span wing. For a swept infinite-span wing with a supersonic leading edge ($M_\infty \cos \chi > 1$), the aerodynamic coefficients and the corresponding forces can be determined from the values of c_y^0 and $c_{x\,w}^0$ for a straight-wing profile with the condition that $M_{\infty s} = M_\infty \cos \chi$ is taken as the free-stream Mach number. Thus, $M_\infty \cos \chi$ must be substituted for M_∞ in all of the above formulas for c_y and $c_{x\,w}$ in converting to the profile of the infinite-span swept wing.

The lift and drag of the profile in the direction of the velocity $\bar{V}_\infty$ are calculated by the formulas

$$Y = \frac{1}{2} c_y^0 \rho_\infty V_\infty^2 S_{wg} \cos^2 \chi; \qquad \text{(V-2-37)}$$

$$X_w = \frac{1}{2} c_{xw}^0 \rho_\infty V_\infty^2 S_{wg} \cos^3 \chi, \qquad \text{(V-2-38)}$$

whence it follows that for a swept wing

$$c_y = c_y^0 \cos^2 \chi; \qquad \text{(V-2-37')}$$

$$c_{xw} = c_{xw}^0 \cos^3 \chi. \qquad \text{(V-2-38')}$$

For symmetrical profiles /240

$$c_y^0 = \frac{4\alpha \cos \chi}{\sqrt{M_\infty^2 \cos^2 \chi - 1}}; \qquad \text{(V-2-39)}$$

$$c_{xw}^0 = \alpha c_y^0 + \frac{2B_2}{\sqrt{M_\infty^2 \cos^2 \chi - 1}}. \qquad \text{(V-2-40)}$$

For a wing with a subsonic leading edge ($M_\infty \cos \chi < 1$), the methods of subsonic- or transonic-flow aerodynamics should be used in calculating the aerodynamic coefficients of the profile placed in the direction of the velocity component $M_\infty \cos \chi$.

Center of pressure. In the case of linearized flow around a thin profile, the pressure center lies aft the center of the chord and, consequently, the center of pressure coefficient $c_{c.p} = x_{c.p}/b = 1/2$. A deviation from this figure results from the nonlinear effect governed by profile thickness and shape. This effect manifests in a redistribution of pressure, which is calculated by (V-2-3).

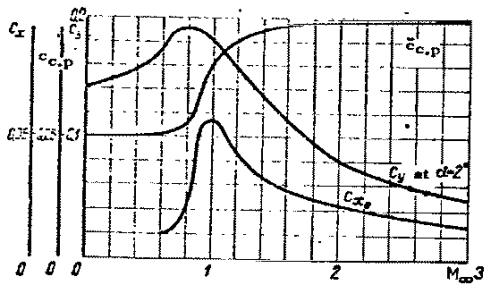

Figure V-2-7. Aerodynamic Coefficients of Rectangular Wing of Infinite Span.

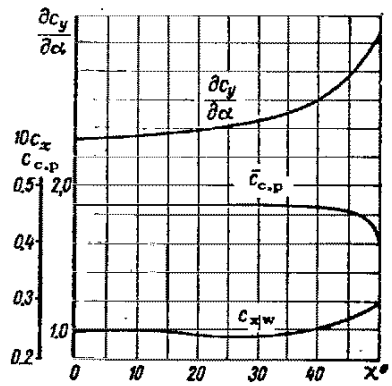

Figure V-2-8. Influence of Sweep on Aerodynamic Characteristics of Infinite-Span Wing (M_∞ = 2, $\bar{c}$ = 0.08).

If we examine the symmetrical profile normally used, the expression for the center of pressure coefficient will be [26]

$$c_{c.p} = \frac{x_{c.p}}{b} = \frac{1}{2}[1 - k_2 \bar{c} F(M_\infty)], \qquad \text{(V-2-41)}$$

where

$$F(M_\infty) = \frac{(M_\infty^2 - 2)^2 + 0.7M_\infty^4}{4(M_\infty^2 - 1)^{1.5}}. \qquad \text{(V-2-42)}$$

Coefficient k_2 depends on profile shape. For a rhomboid profile, k_2 = 1; for a profile formed by two circles, k_2 = 4/3.

The center of pressure coefficient of a swept-wing profile is

$$c_{c.p} = \frac{1}{2}\left[1 - \frac{k_2 \bar{c}}{\cos\chi} \frac{(M_\infty^2 \cos^2\chi - 2)^2 + 0.7M_\infty^4 \cos^4\chi}{4(M_\infty^2 \cos^2\chi - 1)^{1.5}}\right]. \qquad \text{(V-2-43)}$$

Figure V-2-7 and V-2-8 show curves of the aerodynamic coefficients of infinite-span wings in the range from sonic to supersonic speeds.

§V-3. LIFT AND MOMENT OF THIN FINITE-SPAN WINGS. DRAG DEPENDENT ON LIFT

/241

Let us examine the aerodynamic characteristics of finite-span wings with small but finite thickness for small attack

angles. In other words, let us seek a linearized solution of (V-1-6) for the velocity potential.

The unknown velocity potential ϕ' can be presented as the sum $\phi_1' + \phi_2'$, where ϕ_1' is the potential of the flow around a wing of given thickness at zero angle of attack; ϕ_2' is the potential function obtained from the condition of flow around an infinitesimally thin plate of the same planform as the wing at the given angle of attack.

Accordingly, the wing's lift is equal to the lift of the plate, and its drag will be composed of two parts: the drag of a wing of the given thickness at $\alpha = 0$ ($c_y = 0$; profile assumed symmetrical) and the plate drag for $\alpha \neq 0$.

Delta wing. Consider a wing of delta planform with supersonic leading edges. To calculate the pressure distribution and aerodynamic coefficients, we can use the method of sources, which Prof. N.A. Krasil'shchikov used in 1947 as a basis for solution of the problem of supersonic flow over a finite-span wing.

In the general case, the velocity potential from the system of sources and sinks by which the given surface is replaced is given by (IV-3-1). For a flat plate, the function $f(\varepsilon,\xi)$ is to be set equal to a certain constant f_0. Then the velocity potential at a certain point A from the source system is

$$\varphi = -f_0 \int_{\varepsilon_1}^{\varepsilon_2} d\varepsilon \int_{\xi_1}^{\xi_2} \frac{d\xi}{\sqrt{(x-\varepsilon)^2 - (M_\infty^2 - 1)[y^2 + (z-\xi)^2]}}. \qquad \text{(V-3-1)}$$

The range of integration is determined by the area obtained by intersecting the $y = 0$ plane with the surface of the Mach cone (disturbance cone) and bounded, consequently, by the equation of a parabola

$$(x-\varepsilon)^2 = \alpha'^2 [y^2 + (z-\xi)^2], \qquad \text{(V-3-2)}$$

where x, y, z are the coordinates of point A. The integral of (V-3-1) can be evaluated directly. Remembering (V-3-2), we find that the first definite integral is π. Since, moreover, $\varepsilon_1 = x_{A_1}$ and $\varepsilon_2 = x_A - \alpha' y_A$, where x_{A_1} is the intersection point of the Mach cone with the $y = 0$ plane, which corresponds to $z = z_A$, then the unknown potential at point A is

$$\varphi = -\frac{\pi f_0}{\alpha'}(x_A - \alpha' y - x_{A_1}), \qquad \text{(V-3-3)}$$

The vertical velocity component

$$v_y = \frac{\partial \varphi}{\partial y} = \pi f_0. \qquad \text{(V-3-4)}$$

The same velocity value will obtain when the point is on the y = 0 plane.

If the surface is in flow at an attack angle α, we have from the condition of nonseparating flow $f_0 = \alpha V_\infty / \pi$.

Assume that a wing in the form of a thin triangular plate has an infinite span (Fig. V-3-1). In zone I between the supersonic leading edge and the generatrix of the Mach cone with apex at O, the components of the axial disturbance velocity and the pressure coefficient are determined by the ordinary theory of linearized flow: /242

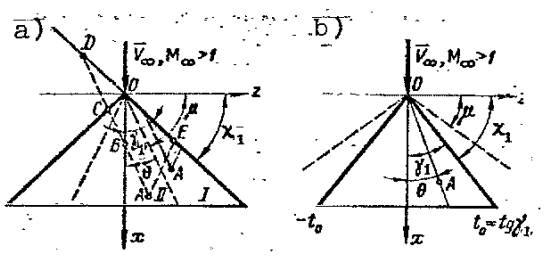

Figure V-3-1. Flow Around Delta Wing. a) with supersonic leading edges; b) with subsonic leading edges.

$$v_x = \varphi_x = \pm \frac{\alpha V_\infty \cos\chi}{\sqrt{M_\infty^2 \cos^2\chi - 1}} = \pm \frac{\pi f_0 \cos\chi}{\sqrt{M_\infty^2 \cos^2\chi - 1}}; \qquad \text{(V-3-5)}$$

$$\bar{p} = \mp \frac{2\alpha \cos\chi}{\sqrt{M_\infty^2 \cos^2\chi - 1}}. \qquad \text{(V-3-6)}$$

Consider region II, which lies inside the Mach cone. The added velocity component at point A results from the action of sources in regions ADE, BCO and BDO. Here the source intensity in region BDO is equal but opposite in sign to the intensity in region ADE.

Sources in region ADE induce a velocity determined by (V-3-5). The velocity corresponding to region BDO is

$$v_x = f_0 \int_{z_D}^{\bar{0}} \frac{d\xi}{\sqrt{(x_A - \varepsilon)^2 - \alpha'^2 (z_A - \xi)^2}}, \qquad \text{(V-3-7)}$$

where

$$z_D = (x_A - \alpha' z_A)/(\operatorname{tg}\chi - \alpha');$$
$$\varepsilon = \xi \operatorname{tg}\chi.$$

Integrating,

$$v_x = \frac{f_0}{\alpha' \sqrt{1-n^2}} \arccos \frac{\sigma - n^2}{n(1-\sigma)}, \qquad \text{(V-3-8)}$$

where $n = \tan\chi/\alpha'$, $\sigma = \tan\chi z_A/x_A$, with $0 < \sigma < n < 1$.

The velocity induced by sources in region BCO is found from an expression analogous to (V-3-7) and can be presented in the form

$$v_x = -\frac{f_0}{\alpha' \sqrt{1-n^2}} \arccos \frac{\sigma + n^2}{n(1+\sigma)}, \qquad \text{(V-3-9)}$$

where $|n| < 1$, $|n| > \sigma > 0$.

Summing (V-3-5), (V-3-8) and (V-3-9), we obtain the axial velocity component at point A for region II:

$$v_x = -\frac{f_0}{\alpha' \sqrt{1-n^2}} \left(\pi - 2\arcsin \sqrt{\frac{n^2-\sigma^2}{1-\sigma^2}}\right). \qquad \text{(V-3-10)}$$

In this region, therefore, the pressure coefficient [58] is

$$\bar{p} = \pm \frac{2\alpha}{\alpha' \sqrt{1-n^2}} \left(1 - \frac{2}{\pi} \arcsin \sqrt{\frac{n^2-\sigma^2}{1-\sigma^2}}\right), \qquad \text{(V-3-11)}$$

where the "-" pertains to the upper surface and "+" to the lower surface of the wing.

The lift coefficient /243

$$c_y = \frac{1}{S_{wg}} \int_{(S_{wg})} (\bar{p}_l - \bar{p}_u)\, dS,$$

where

$$dS = \frac{1}{2} x^2 \operatorname{ctg}\chi\, d\sigma; \quad S_{wg} = \frac{1}{2} x^2 \operatorname{ctg}\chi.$$

Introducing $\bar{p}_l$ and $\bar{p}_u$ from (V-3-11), we obtain for c_y a formula from which it follows that the lift coefficient for a delta wing with a supersonic leading edge is independent of sweep angle and is determined in the same way as for a flat unswept plate.

The drag coefficient governed by wave losses is

$$c_{x\,w} = c_y \alpha = \frac{\sqrt{M_\infty^2 - 1}}{4} c_u^2. \qquad \text{(V-3-12)}$$

This lift-dependent drag can be determined in the same way as the induced drag of a delta wing with supersonic leading edges. Since the conditions of conical flow are satisfied, the center of pressure is at a distance from the apex equal to 2/3 of the root chord.

The pressure distribution and, consequently, the aerodynamic coefficients for a delta wing with subsonic leading edges (see Fig. V-3-1) will be different owing to the subsonic nature of the flow over the surface.

The flow around a wing set at an angle of attack α is equivalent to the flow from continuously distributed dipoles, the potential function for which is given by Formula (IV-4-4).

Since the flow around the wing is conical, all variables depend on $t = \xi/\varepsilon$ and the dipole distribution function can be presented in the form $m(\varepsilon,\xi) = \varepsilon f(t)$. Thus the expression for the dipole potential will be

$$\varphi_{dip} = \int_{-t_0}^{t_0} f(t)\, dt \frac{\partial}{\partial y} \int_0^{\varepsilon_1} \frac{\varepsilon^2\, d\varepsilon}{\sqrt{(x-\varepsilon)^2 - \alpha'^2\,[(z-t\varepsilon)^2 + y^2]}}, \qquad \text{(V-3-13)}$$

where t_0 and $-t_0$ are the values of $t = \tan \gamma_1$ corresponding to the leading edges; ε_1 is determined from the condition that the supersonic disturbances propagate within the Mach cone.

Accordingly, the radicand in (V-3-13) vanishes for $\varepsilon = \varepsilon_1$.

We obtain by integration

$$\varphi_{dip} = \int_{-t_0}^{t_0} F f(t)\, dt, \qquad \text{(V-3-14)}$$

where

$$F = y\bar{n}^{-3/2}\alpha'^2\left(\frac{\xi}{1-\xi^2} + \operatorname{arcth}\xi\right); \qquad \text{(V-3-15)}$$

$$\bar{n} = 1-(\alpha' t)^2;\ \xi = -\frac{\alpha'^2\frac{z}{x}t-1}{\sqrt{\bar{n}\left[1-\alpha'^2\left(\frac{z^2}{x^2}+\frac{y^2}{x^2}\right)\right]}}. \qquad \text{(V-3-16)}$$

According to (V-3-16), the function F depends on the variables y/x, z/x, ε/ξ.

The function f(t), which represents the intensity of the distributed sources, is found from the condition of nonseparating flow over the wing, according to which $(V_y)_{y=0} = V_\infty\alpha = (\partial\varphi_{dip}/\partial y)_{y=0}$. Consequently, /244

$$V_\infty\alpha = \int_{-t_0}^{t_0}\left(\frac{\partial F}{\partial y}\right)_{y=0} f(t)\,dt. \qquad \text{(V-3-17)}$$

Research has shown that the function f(t) can be presented in the form $f(t) = f_0\sqrt{t_0^2-t^2}$, where f_0 is a constant. The value of this constant can be found from (V-3-17) by substituting the given function f(t) in it. Integrating,

$$f_0 = \frac{\alpha V_\infty}{\pi E(\sqrt{1-\alpha'^2 t_0^2})}; \qquad \text{(V-3-18)}$$

where $E(\sqrt{1-\alpha'^2 t_0^2})$ is a complete elliptic integral of the second kind with parameter $k = \sqrt{1-\alpha'^2 t_0^2}$;

$$E = \int_0^{\pi/2}(1-k^2\sin^2\psi)^{1/2}\,d\psi. \qquad \text{(V-3-18')}$$

Passing to $y \to 0$,

$$\varphi_{dip} = \pi m(\varepsilon, \xi) = \frac{\varepsilon\alpha V_\infty\sqrt{t_0^2-t^2}}{E(k)}, \qquad \text{(V-3-19)}$$

from which the axial component

$$v_x = \frac{\partial\varphi_{dip}}{\partial x} = \frac{\alpha V_\infty t_0^2}{E(k)\sqrt{t_0^2-t^2}}. \qquad \text{(V-3-20)}$$

The pressure coefficients on the upper (-) and lower (+) wing surfaces are determined in accordance with the v_x:

$$\bar{p} = \pm \frac{2\alpha t_0^2}{E(k)\sqrt{t_0^2 - t^2}} = \pm \frac{2\alpha \operatorname{tg}\gamma_1}{E(k)\sqrt{1-(\operatorname{tg}\theta/\operatorname{tg}\gamma_1)^2}}, \qquad \text{(V-3-21)}$$

where the absolute value of α is used.

The lift and moment coefficients can be found from the pressure. For wings of arbitrary planform

$$c_y = \frac{\eta}{\eta+1} \iint_{(S_{wg})} (\bar{p}_l - \bar{p}_u)\, d\bar{x}\, d\bar{z}; \qquad \text{(V-3-22)}$$

$$m_z = \frac{\eta}{\eta+1} \iint_{(S_{wg})} (\bar{p}_l - \bar{p}_u)\, \bar{x}\, d\bar{x}\, d\bar{z}, \qquad \text{(V-3-23)}$$

where the moment coefficient is computed for the root chord b_{rt};

$$\bar{x} = x/b_{rt}; \quad \bar{z} = 2z/l; \quad \eta = b_{rt}/b_{tp}.$$

Remembering that $\eta = \infty$ for a delta wing and rearranging, we obtain

$$c_y = \frac{2}{\operatorname{tg}\gamma_1} \int_0^1 \bar{x}\, d\bar{x} \int_0^{\operatorname{tg}\gamma_1} (\bar{p}_l - \bar{p}_u)\, dt; \qquad \text{(V-3-24)}$$

$$m_z = \frac{2}{\operatorname{tg}\gamma_1} \int_0^1 \bar{x}^2\, d\bar{x} \int_0^{\operatorname{tg}\gamma_1} (\bar{p}_l - \bar{p}_u)\, dt. \qquad \text{(V-3-25)}$$

Introducing $\bar{p}_l$ and $\bar{p}_u$ from (V-3-21), /245

$$c_y = \frac{1}{E(k)} 2\pi \operatorname{tg}\gamma_1 \alpha; \qquad \text{(V-3-26)}$$

$$m_z = \frac{1}{E(k)} \frac{4}{3} \pi \operatorname{tg}\gamma_1 \alpha. \qquad \text{(V-3-27)}$$

It follows from these expressions that the center of pressure coefficient of a delta wing is 2/3.

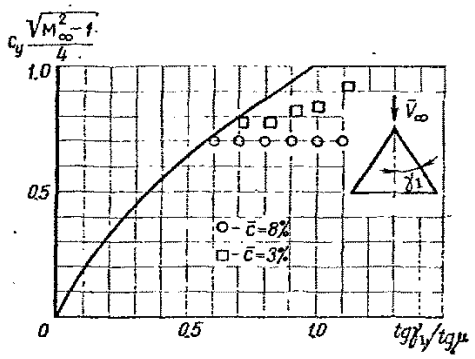

Figure V-3-2. Theoretical Curve for Lift Coefficient of Delta Wing. Experimental Data: ○ — $\bar{c}$ = 8%, □ — $\bar{c}$ = 3%

The formulas given for c_y and m_z can be simplified for the particular case of a wing with very small aspect ratio. Letting $\alpha' t_0 \to 0$, we find that $E(k) \to 1$ and, consequently,

$$c_y = 2\pi \operatorname{tg}\gamma_1 \alpha, \quad m_z = \frac{4}{3}\pi \operatorname{tg}\gamma_1 \alpha. \qquad \text{(V-3-28)}$$

Introducing the aspect ratio $\lambda_{wg} = 4 \tan \gamma_1$, we obtain

$$c_y = \frac{1}{2}\pi\lambda_{wg}\alpha, \quad m_z = \frac{1}{3}\pi\lambda_{wg}\alpha. \qquad \text{(V-3-29)}$$

If $\alpha' t_0 \to 1$, then $E(k) \to \pi/2$ and the formula for c_y assumes a form reminiscent of the case of a supersonic-edged wing.

Values of the derivative c_y^α calculated for delta wings with sub- and supersonic leading edges are given in Fig. V-3-2 as functions of $\tan \gamma_1 / \tan \mu = \alpha' t_0$.

The same figure shows experimental data for wings with a symmetrical profile formed by arcs of circles. The largest difference between the experimental and theoretical results occurs for $\alpha' t_0$ near unity, i.e., when the leading edge becomes almost sonic.

Drag of wings with subsonic leading edge. When wings have sharp subsonic leading edges, vortices detach from the edge and drag increases as a result. To prevent vortex detachment, the leading edge is made slightly rounded. Since the velocities on the edge remain quite high, the pressure will be very small and a suction force will appear and reduce drag. If the coefficient of suction force is denoted by $c_{x\,s}$, the total drag coefficient of a wing with a subsonic leading edge will be

$$c_x = c_y\alpha - c_{x\,s}. \qquad \text{(V-3-30)}$$

Research has shown that

$$c_{x\,s} = \frac{c_y^2}{\pi\lambda_{wg}}\sqrt{1-(\alpha' t_0)^2}. \qquad \text{(V-3-31)}$$

Accordingly,

$$c_x = \frac{c_y^2}{\pi\lambda_{wg}}\left[2E(k) - \sqrt{1-(\alpha' t_0)^2}\right]. \qquad \text{(V-3-30')}$$

If $\alpha' t_0 = 1$ (sonic leading edge), then $c_x = c_y^2/\lambda_{wg}$. For wings of very small aspect ratio $(\alpha' t_0 \to 0)$ $c_x = c_y^2/\pi\lambda_{wg}$, which is consistent with the expression for the induced-drag coefficient in the case of an incompressible fluid. /246

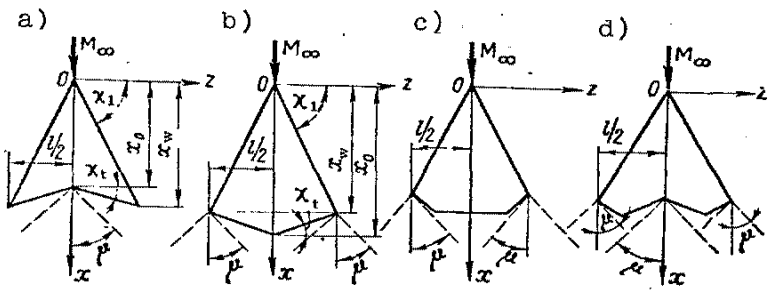

Figure V-3-3. Wings with Supersonic Trailing and Lateral Edges. a) tetragonal wing with sweptback trailing edge; b) tetragonal wing with sweptforward leading edge; c) pentagonal wing; d) hexagonal wing.

Wings in the form of tetragonal, pentagonal, and hexagonal plates [58]. The methods of flow theory for delta wings can be used in calculating the aerodynamic characteristics of tetragonal, pentagonal, and hexagonal-plate wings with supersonic trailing and lateral edges (Fig. V-3-3). Flow over such wings is characterized by the absence of zones of interference between the aft and lateral areas bounded by the intersections of Mach cones with wing, i.e., the flow at the lateral and trailing edges will be purely supersonic.

The formulas for the surface pressure on wings of these shapes will be the same as those for the triangular plate and are selected with consideration of the leading-edge form — sub- or supersonic. The lift, moment, and drag coefficients can be determined by integration over the pressure pattern.

We cite results obtained for a tetragonal wing. In the case of a subsonic leading edge

$$c_y = \frac{4\alpha \operatorname{tg}\gamma_1}{(1-\varepsilon)E(k)}\left[(1-\varepsilon^2)^{-1/2}\arccos\varepsilon - \varepsilon\right]; \qquad \text{(V-3-32)}$$

$$m_z = \frac{4\alpha \operatorname{tg}\gamma_1}{3(1-\varepsilon)E(k)}\left[\frac{2+\varepsilon^2}{(1+\varepsilon)^{3/2}}\arccos\varepsilon - \frac{\varepsilon(4-\varepsilon^2)}{1-\varepsilon^2}\right]. \qquad \text{(V-3-33)}$$

For wings with supersonic leading edges

$$c_y = \frac{8\alpha}{(1-\varepsilon)\sqrt{M_\infty^2-1}}\left(\frac{-\varepsilon}{\sqrt{1-n^2}}\arccos n + \frac{1}{\sqrt{1-n_1^2}}\arccos n_1\right); \qquad \text{(V-3-34)}$$

$$m_z = \frac{8\alpha}{3(1-\varepsilon)\sqrt{M_\infty^2-1}}\left[\frac{2-n_1^2(1+\varepsilon^2)}{(1-\varepsilon^2)(1-n_1^2)^{3/2}}\arccos n_1 - \right.$$
$$\left. - \frac{\varepsilon(3-\varepsilon^2)}{(1-\varepsilon^2)\sqrt{1-n^2}}\arccos n - \frac{n}{1-n^2}\right], \qquad \text{(V-3-35)}$$

where $n = \tan\chi_1 \tan\mu$, $n_1 = \tan\chi_t \tan\mu$.

Calculations by these formulas can be simplified if the tetragonal wings differ little in shape from deltas. In this case, with the condition that $|\varepsilon| \ll 1$,

$$c_y = \frac{c_{y\Delta}}{1-\varepsilon}; \quad m_z = \frac{m_{z\Delta}}{1-\varepsilon}, \qquad \text{(V-3-36)}$$

where $c_{y\Delta}$ and $m_{z\Delta}$ are the lift and moment coefficients of the delta wing and the quantity /247

$$\varepsilon = \frac{x_w - x_0}{x_w} = \frac{\operatorname{tg}\chi_t}{\operatorname{tg}\chi_1} = 1 - \frac{4}{\lambda \operatorname{tg}\chi_1}, \qquad \text{(V-3-37)}$$

where χ_1 and χ_t are the sweep angles of the leading and trailing edges and x_0 and x_w are the wing dimensions indicated in Fig. V-3-3.

For wings of the "dovetail" type (Fig. V-3-3a), ε is positive, but it is negative for rhomboid plates (Fig. V-3-3b).

In the particular case when $\tan\gamma_1/\tan\mu \gg 1$ for a wing with a supersonic leading edge, the parameter ε has practically no influence on c_y, and the dovetail or boattail will change lift almost in proportion to the change in plate area.

Figure V-3-4 shows curves of

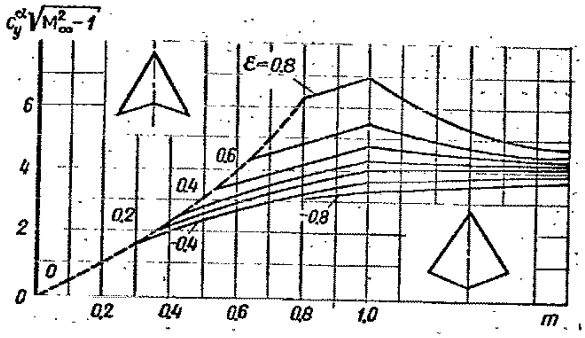

Figure V-3-4. Diagrams for Calculation of Lift of Tetragonal Plates ($m = \tan\gamma_1/\tan\mu$).

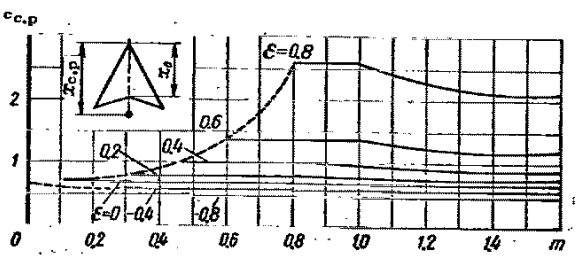

Figure V-3-5. Diagrams for Calculation of Center of Pressure Coefficient for Tetragonal Wings ($m = \tan\gamma_1/\tan\mu$).

$$c_y^\alpha\sqrt{M_\infty^2-1} = f(m, \varepsilon), \quad \left(m = \frac{\operatorname{tg}\gamma_1}{\operatorname{tg}\mu}\right)$$

obtained by the linear theory for tetragonal plates with the condition that the trailing edges are supersonic. Figure V-3-5 shows calculated results characterizing the center of pressure position on these plates.

Similar curves plotted for a pentagonal plate appear in Figs. V-3-6-V-3-8.

The frontal drag of the wings is calculated as follows. If the edge is supersonic, then, irrespective of plate shape

$$c_x = c_y\alpha = \frac{c_y^2}{c_y^\alpha} \quad (m \geqslant 1). \quad \text{(V-3-38)}$$

If the leading edge /248
is subsonic, this coefficient must be reduced by the suction-force coefficient, i.e., the calculation must be performed by (V-3-30). The suction force is

$$F = \frac{1}{2}\rho_\infty V_\infty^2\alpha^2\sqrt{1-(\alpha' l)^2}\,\frac{l^2}{4\pi E^2(k)}, \quad \text{(V-3-39)}$$

where l is the span (see Fig. V-3-3).

Dividing F by the product qS_{wg}, where S_{wg} is the area of the given plate form, we obtain $c_{x\ s}$.

For a tetragonal wing differing slightly from the delta, the calculation can be performed by the formula

$$c_{x_s} = \frac{(c_{x_s})_\Delta}{1-\varepsilon}, \quad \text{(V-3-40)}$$

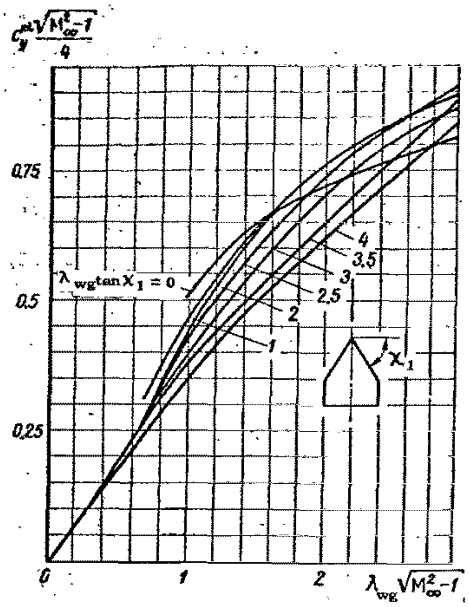

Figure V-3-6. Diagrams for Calculation of Lift Coefficients of Pentagonal Wings of Small Aspect Ratio.

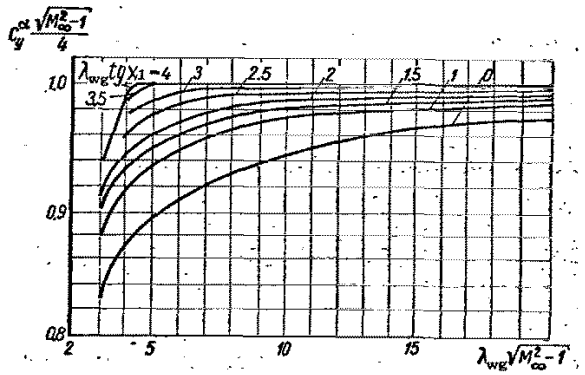

Figure V-3-7. Curves for Calculation of Lift Coefficients for Pentagonal Wings of Large Aspect Ratio.

where $(c_{x\ s})_{\Delta}$ is calculated by (V-3-31) for a triangular plate.

Let us examine wings with subsonic trailing edges, assuming that, as is the case in practice, the trailing edges are supersonic. Flow calculations for such wings are more complicated owing to the formation of interference zones at the lateral edges and the necessity of accounting for gas overflow into these zones from one side of the plate to the other.

Zones of influence inside the Mach cones are shown in Fig. V-3-9 for a hexagonal wing. In zone I, the flow is determined by the subsonic leading edges and their influence on overflow from the bottom to the top surface (or vice versa) must be taken into account in the flow calculation. In zone II, flow is influenced by the right lateral edge, and in zone III also by the left edge. /249

Since the flow is symmetrical with respect to the x-axis, we can regard zones I, II, and III as situated on the same side of the x-axis.

At a given free-stream velocity, the variables at a given point on the surface of the hexagonal wing (Fig. V-3-10) or its resultant aerodynamic characteristics depend in the most general case on the set of dimensionless geometrical characteristics of the plate, namely, the aspect ratio λ_{wg}, the taper $\eta = b_{rt}/b_{tp}$, and the angles χ_1 and χ_t (or the corresponding γ_1 and γ_t).

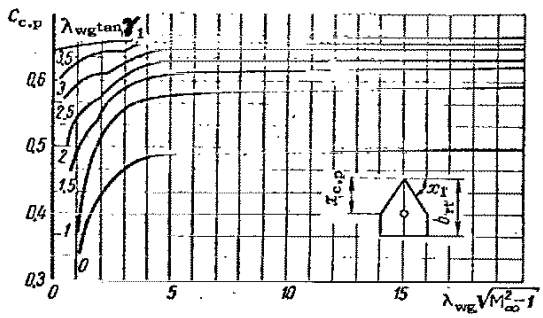

Figure V-3-8. Center of Pressure Coefficient of Pentagonal Wing ($c_{cp} = x_{cp}/b_{rt}$).

In zone I behind the subsonic leading edge, the pressure coefficient is determined by (V-3-21). The characteristic parameter for this zone is the leading-edge inclination γ_1 (or the sweep angle χ_1).

Applying the method of sources and sinks, we can determine the pressure in zones II and III. Studies have shown that the pressure coefficient in zone II is

$$\bar{p} = \pm \frac{2\alpha \operatorname{tg}\gamma_1}{E(k)} \sqrt{\frac{1+\operatorname{tg}\mu/\operatorname{tg}\gamma_1}{\operatorname{tg}\mu}} \sqrt{\frac{1-\bar{z}}{\bar{z}} \frac{\operatorname{tg}\theta}{1-\operatorname{tg}\theta/\operatorname{tg}\gamma_1}}, \qquad \text{(V-3-41)}$$

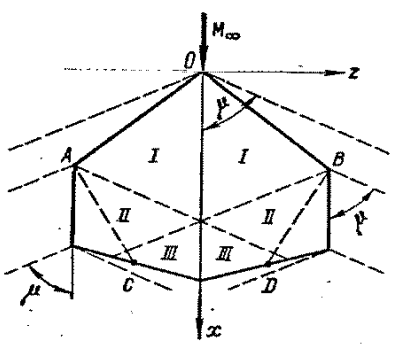

Figure V-3-9. Diagram of Flow Around Hexagonal Wing With Subsonic Leading and Lateral Edges and Supersonic Trailing Edges.

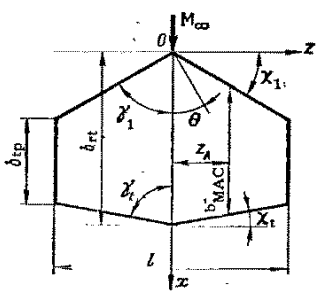

Figure V-3-10. Geometry of Hexagonal Wing.

where $\bar{z} = 2z/\ell$, and $\tan\theta = z/x$. The excess pressure in zone III is zero, since the effects of the leading and lateral edges on flow in this zone are opposed, with the result that the additional axial velocity component vanishes. /250

Introducing the values of $\bar{p}_l$ and $\bar{p}_u$ from (V-3-41) into (V-3-22) and (V-3-23), we can compute the lift and moment coefficients. In the case most frequently encountered, in which zone

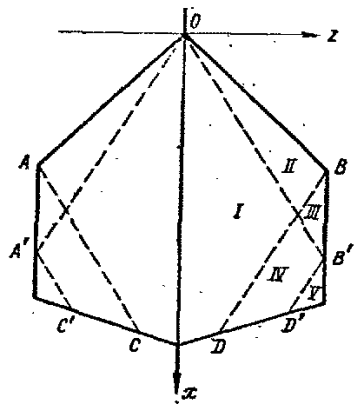

Figure V-3-11. Diagram of Flow Over Hexagonal Wing with Supersonic Leading and Trailing Edges and Subsonic Lateral Edges.

III is absent and only zones I and II remain (Mach waves AC and BD, which originate at the forward corners of the lateral edges, as shown in Fig. V-3-11, cross at a point off the wing).

To determine the aerodynamic coefficients for a pentagonal wing, we must set $\tan \chi_t = 0$. For tetragonal wings, $\eta = \infty$.

Let us consider the aerodynamic characteristics of hexagonal wings with supersonic leading and trailing edges and subsonic lateral edges (Fig. V-3-11).

The flow over such a wing is complex in nature and is characterized by the influence of the lateral edges on the variables in zones III, IV, and V. In zones I and II, the flow will be the same as on a delta wing with supersonic leading edges.

In zone I, the added axial velocity component and the pressure coefficient are determined by (V-3-5) and (V-3-6), respectively, and in zone II by (V-3-10) and (V-3-11).

Using the method of sources, we can determine the analogous quantities in the remaining zones. Let us present the coefficient values in zones III, IV, and V. In zone III, the pressure coefficient

$$\bar{p} = \pm \frac{a\lambda_{wg}\alpha}{\pi \sqrt{1-n^2}} A_1; \qquad \text{(V-3-42)}$$

in zone IV

$$\bar{p} = \pm \frac{a\lambda_{wg}\alpha}{\pi \sqrt{1-n^2}} (A_1 + A_2 - A_3); \qquad \text{(V-3-43)}$$

and in zone V

$$\bar{p} = \pm \frac{2a\lambda_{wg}\alpha}{\pi \sqrt{1-n^2}} \left\{ A_1 - A_2 - A_3 + \arccos \frac{2n\bar{x} - [(2+n)\,z + 2(1+n)]\, a\lambda_{wg} \operatorname{tg} \chi_1}{2(\bar{x} + 0{,}5a\lambda_{wg}\bar{z} \operatorname{tg} \chi_1)\, n} \right\}, \qquad \text{(V-3-44)}$$

where

$$A_1 = \arccos \frac{2n\bar{x} + [(2+n)\bar{z} - 2(1+n)]\, a\lambda_{wg} \operatorname{tg}\chi_1}{2n(\bar{x} - 0.5a\lambda_{wg}\bar{z}\operatorname{tg}\chi_1)};$$

$$A_2 = \arccos \frac{n^2\bar{x} + 0.5a\lambda_{wg}\bar{z}\operatorname{tg}\chi_1}{n(\bar{x} + 0.5a\lambda_{wg}\bar{z}\operatorname{tg}\chi_1)}; \qquad \text{(V-3-45)}$$

$$A_3 = \arccos \frac{n^2\bar{x} - 0.5a\lambda_{wg}\bar{z}\operatorname{tg}\chi_1}{n(\bar{x} - 0.5a\lambda_{wg}\bar{z}\operatorname{tg}\chi_1)}.$$

In these formulas, the parameter $a = S_{wg}/(lb_{rt}) = (\eta + 1)/(2\eta)$.

Using (V-3-22) and (V-3-23), we can determine the lift and moment coefficients for the hexagonal wing. To convert to the pentagonal wing, we set tan χ_t = 0. /251

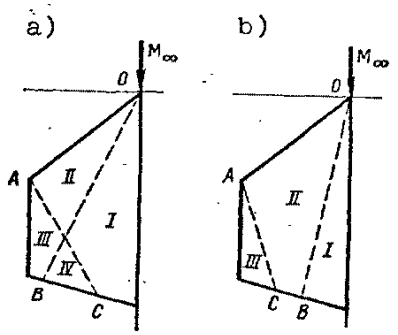

Figure V-3-12. Hexagonal Wings with Supersonic Leading and Trailing Edges and Subsonic Lateral Edges.

Practical interest attaches to the case of flow in which the Mach lines OB and AC intersect on the wing (Fig. V-3-12a) or when these lines intersect off the wing (Fig. V-3-12b). The pressure distribution must be calculated with consideration of the number and conventional numeration of the influence zones. We see from Fig. V-3-12a that there are four such zones (I-IV), and three (I-III) in Fig. V-3-12b.

Applying (V-3-22) and (V-3-23), we can satisfy ourselves that although the pressure distributions differ, the aerodynamic coefficients corresponding to the two flow schemes are the same.

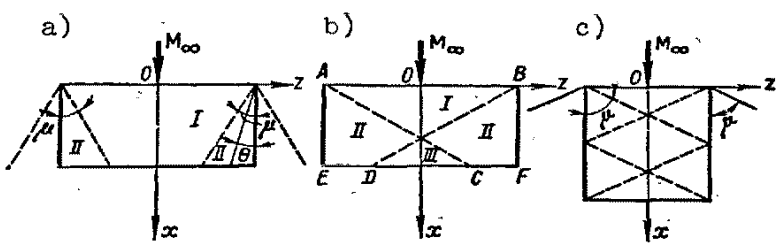

Figure V-3-13. Diagram of Flow Over Rectangular Wing. a) zones II to not intersect; b) flow with formation of zone III; c) multiple intersection of wave zones.

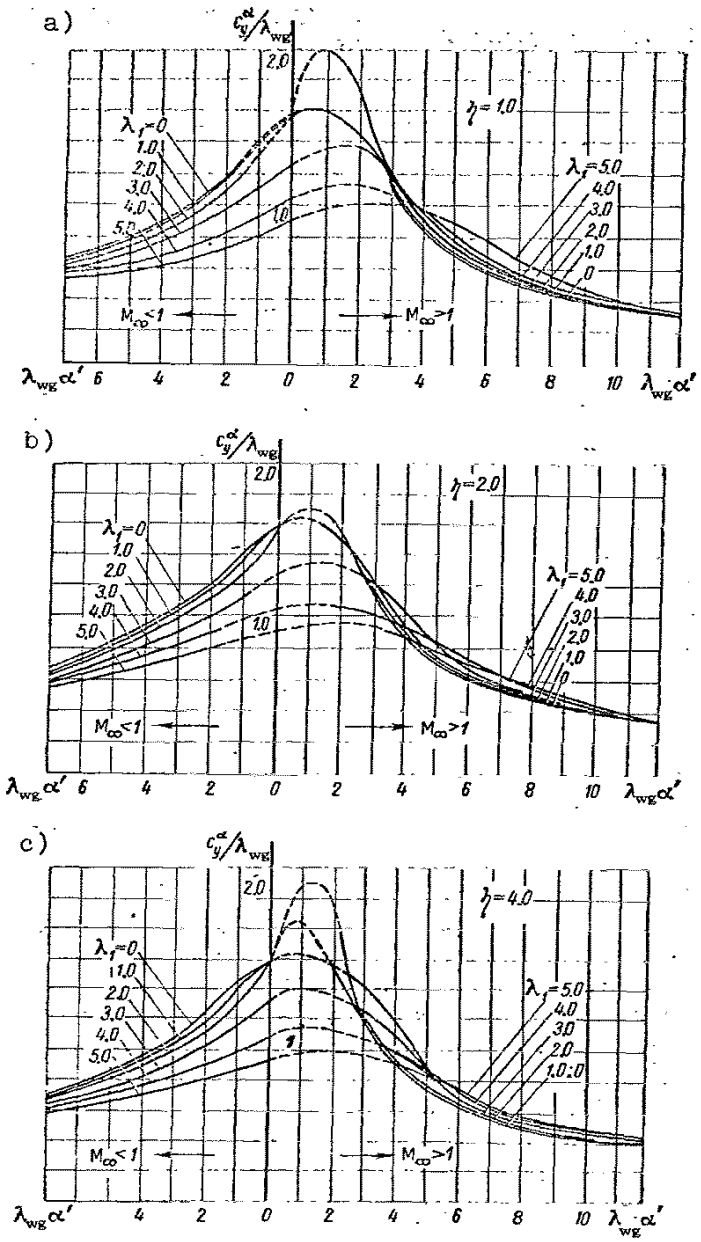

Figure V-3-16.* Variation of c_y^α/λ_{wg} of Isolated for Various η.

*Translator's Note: Figure numbering follows the same order as in the original Russian text. Figures V-3-14 and V-3-15 are on page 343.

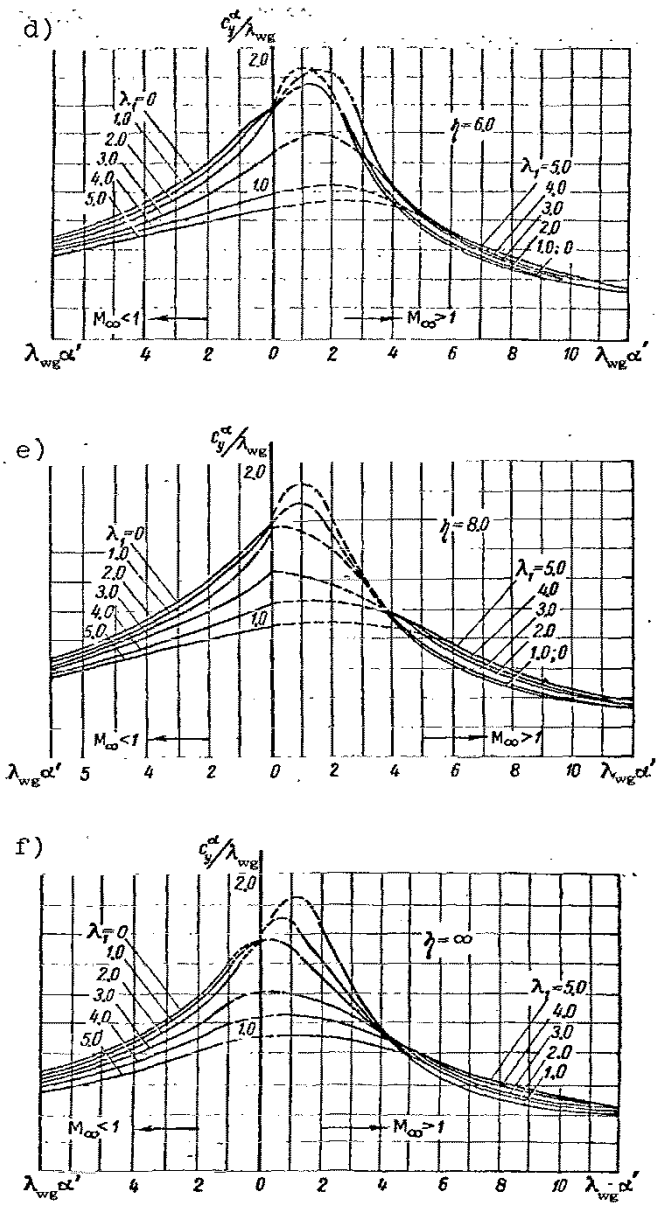

Wing as Function of Parameters $\lambda_{wg}\alpha' = \lambda_{wg}\sqrt{M_\infty^2 - 1}$; $\lambda_1 = \lambda_{wg}|\tan \chi_{1/2}$

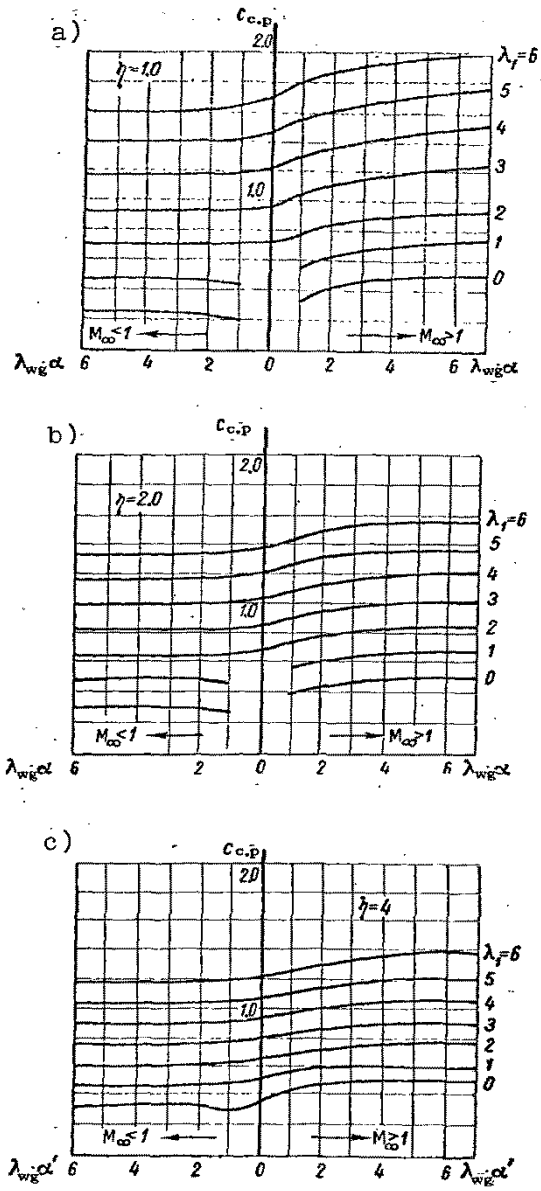

Figure V-3-17. Variation of $c_{c.p}$ of Isolated $=\lambda_{wg}\tan\chi_{1/2}$ for various η.

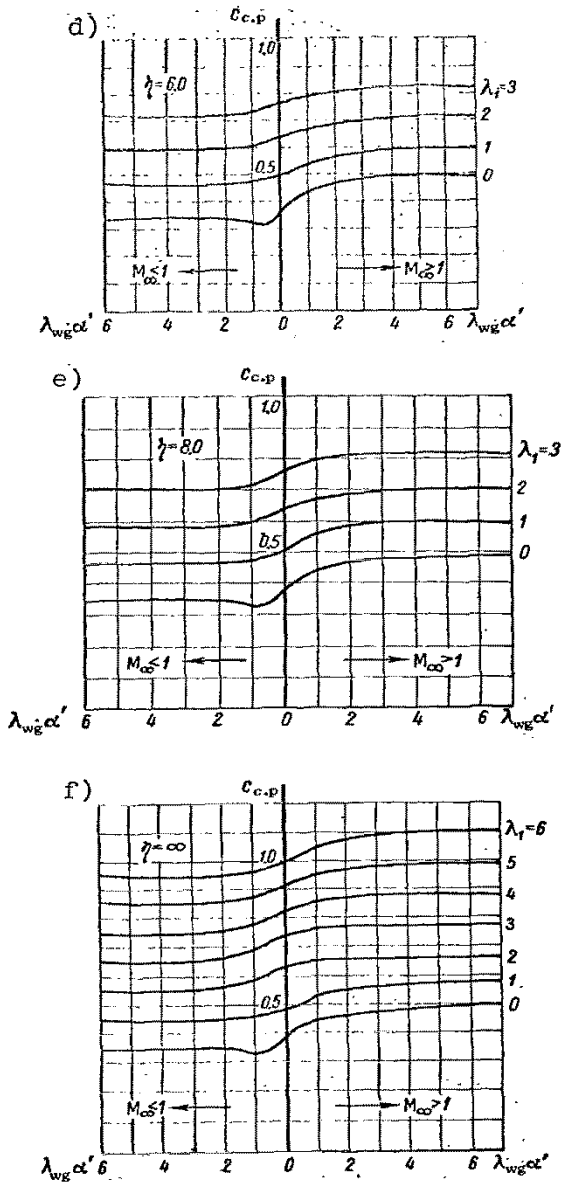

Wing as a Function of Parameters $\lambda_{wg}\alpha'$, $\lambda_1 =$.

Rectangular wing. Figure V-3-13 shows a rectangular wing whose leading and trailing edges are supersonic while its lateral edges are subsonic. Ordinary supersonic flow prevails in zone I, and the pressure is determined by (V-3-6) for a thin plate with the condition cos $\chi = 1$.

In zone II, where the lateral edge influences flow,

$$\bar{p} = \pm \frac{4\alpha}{\pi \sqrt{M_\infty^2 - 1}} \arcsin \sqrt{\frac{\operatorname{tg}\theta}{\operatorname{tg}\mu}}. \qquad \text{(V-3-46)}$$

If the right- and left-lateral-edge zones II intersect, the pressure coefficient in the resulting intersection zone III is $\bar{p}_{III} = (\bar{p}_{II})_{lft} + (\bar{p}_{II})_{rght} - \bar{p}_I$.

For the cases of flow shown schematically in Fig. V-3-13, which correspond to the condition $\lambda_{wg}\sqrt{M_\infty^2 - 1} \geqslant 1$, with which the Mach lines BD and AC intersect at points E and F, respectively, on the wing trailing edge (Fig. V-3-13b),

$$c_y = 4\alpha \operatorname{tg}\mu \left(1 - \frac{\operatorname{tg}\mu}{2\lambda_{wg}}\right); \qquad \text{(V-3-47)}$$

$$m_z = 2\alpha \operatorname{tg}\mu \left(1 - \frac{2\operatorname{tg}\mu}{3\lambda_{wg}}\right). \qquad \text{(V-3-48)}$$

The flow is more complex if $\lambda_{wg}\sqrt{M_\infty^2 - 1} < 1$. In this case (Fig. V-3-13c), new wave regions arise as a result of intersection of the incident Mach waves and those reflected from the lateral edges. The data in Fig. V-3-14 can be used to determine the coefficient c_y for the wing. /256

The results given for c_y and m_z can be used to find the center of pressure coefficient $c_{c.p} = x_{c.p}/b_{rt} = m_z/c_y$ (Fig. V-3-15).

The drag coefficient of the rectangular wing is

$$c_x = \alpha c_y = 4\alpha^2 \operatorname{tg}\mu \left(1 - \frac{\operatorname{tg}\mu}{2\lambda_{wg}}\right). \qquad \text{(V-3-49)}$$

In practical calculations of aerodynamic coefficients, it is more convenient to use the curves shown in Figs. V-3-16, a-f and V-3-17, a-f, which characterize the variation of c_y^α/λ_{wg} and the

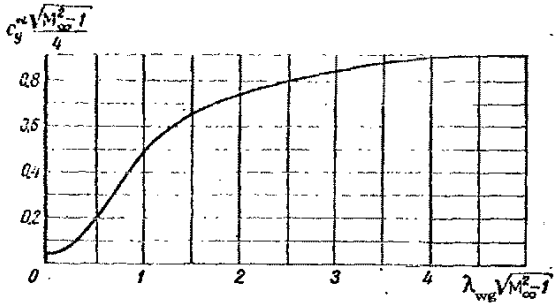

Figure V-3-14. Curve for Calculation of Lift of Finite-Span Rectangular Wing.

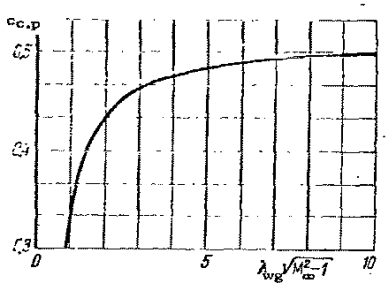

Figure V-3-15. Center of Pressure Coefficient of Finite-Span Rectangular Wing.

coefficient $c_{c.p}$ as function of the parameters $\lambda_{wg}\sqrt{M_\infty^2-1}$, $\lambda_1 = \lambda_{wg} \tan \chi_{1/2}$, [$\tan \chi_{1/2} = 0.5 (\tan \chi_1 + \tan \chi_t)$] and η.

From $c_{c.p}$, which is equal to the ratio of the center of pressure distance to the root chord b_{rt}, we can determine the distance to the center of pressure as a fraction of mean aerodynamic chord:

$$c_{c.p} = \frac{x_{c.p}}{b_{MAC}} = \left(\frac{3}{2}c_{c.p} - \frac{\lambda \operatorname{tg} \chi_1}{8} \cdot \frac{\eta+2}{\eta}\right) \frac{\eta(\eta+1)}{1+\eta(\eta+1)}. \qquad \text{(V-3-50)}$$

§V-4. DRAG OF WINGS OF FINITE THICKNESS

Wing of delta planform. To determine the drag due to thickness, it is necessary to investigate flow around the wing at zero attack angle (zero lift). The investigation can be carried out with the method of sources.

Let us consider a thin wing of delta planform [58]. From the gasdynamic standpoint, this wing is equivalent to a system of distributed sources (sinks), whose velocity potential is determined by (IV-3-1). /257

The function $f(\varepsilon, \xi)$, which determines the source intensity, is found from the condition of nonseparating flow. With (V-3-4) in mind,

$$f = f_0 = \frac{y' V_\infty}{\pi}, \qquad \text{(V-4-1)}$$

where y' is the slope of the profile at the point under consideration.

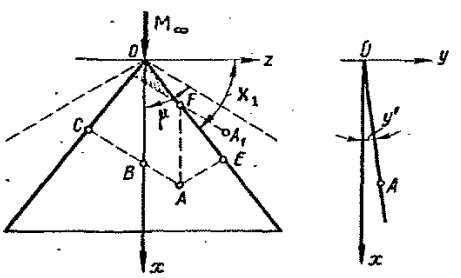

Figure V-4-1. Delta Wing of Finite Thickness with Subsonic Leading Edge in Supersonic Flow.

Formulas (V-3-5) and (V-3-9) with (V-4-1) substituted for f_0 can be used to determine the added axial velocity component on a wing with a supersonic leading edge. Accordingly, we obtain the following relationships for the pressure coefficient. In the zone between the Mach wave and the leading edge

$$\bar{p}=\frac{2y'}{\alpha'\sqrt{1-n^2}}; \qquad \text{(V-4-2)}$$

and in the region within the Mach cone

$$\bar{p}=\frac{2y'}{\alpha'\sqrt{1-n^2}}\times \qquad \text{(V-4-3)}$$
$$\times\left(1-\frac{2}{\pi}\arcsin\sqrt{\frac{n^2-\sigma^2}{1-\sigma^2}}\right).$$

To calculate the flow around a wing with a subsonic leading edge, (IV-3-1) should be used with the condition that the limits of integration are determined with consideration of the source distribution in the region between Mach lines AC and AE and the corresponding segments of the leading edges (Fig. V-4-1).

The velocity potential for point A can be presented in the form of three components determined by the action of the sources in zones OCB, OBAF and FAE. Accordingly, (V-3-1) becomes

$$\varphi=\frac{-y'V_\infty}{\pi}\Bigg[\int_{-z_C}^{0}d\xi\int_{-\xi\operatorname{tg}\chi_1}^{x_A-\operatorname{tg}\mu(z_A-\xi)}F(\varepsilon,\xi)\,d\varepsilon+\int_{0}^{z_A}d\xi\int_{\xi\operatorname{tg}\chi_1}^{x_A-\operatorname{tg}\mu(z_A-\xi)}F(\varepsilon,\xi)\,d\varepsilon+$$
$$+\int_{z_A}^{z_E}d\xi\int_{\xi\operatorname{tg}\chi_1}^{x_A-\operatorname{tg}\mu(\xi-z_A)}F(\varepsilon,\xi)\,d\varepsilon\Bigg]. \qquad \text{(V-4-4)}$$

If the sources are distributed in the y = 0 plane, the function

$$F(\varepsilon, \xi) = [(x_A - \varepsilon)^2 - \alpha'^2 (z_A - \xi)^2]^{-1/2}.$$

The coordinates z_C and z_E, which are determined by the position of point A, can be found directly from Fig. V-4-1. Differentiating with respect to $\underline{x}$ in (V-4-4), we find the additional axial velocity component, and then determine the expression for the pressure coefficient

$$\bar{p} = \frac{4y'}{\pi\alpha' \sqrt{n^2-1}} \operatorname{arch} \sqrt{\frac{n^2-\sigma^2}{1-\sigma^2}}. \qquad \text{(V-4-5)}$$

If point A_1 lies between the wing leading edge and the Mach wave, calculations analogous to those given for point A with consideration of the fact that the sources in the shaded region of Fig. V-4-1 act on point A give for the pressure coefficient /258

$$\bar{p} = \frac{-4y'}{\pi\alpha' \sqrt{n^2-1}} \operatorname{arch} \sqrt{\frac{n^2-1}{\sigma^2-1}}. \qquad \text{(V-4-6)}$$

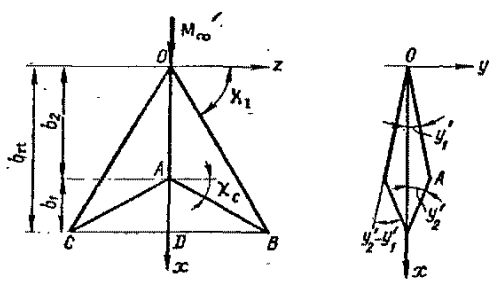

Figure V-4-2. Delta Wing with Rhomboid Profile.

Delta wing with rhomboid profile. Figure V-4-2 presents a diagram of this wing. The drag due to wing thickness can be calculated using the results given above for the delta wing with constant profile contour inclination.

Three design cases should be considered in determining the aerodynamic characteristics (Fig. V-4-3):

a) leading edges and lines AB and AC of maximum profile thickness supersonic ($1 > n > n_C$, where $n = \tan \chi_1 \tan \mu$, $n_C = \tan \chi_C \tan \mu$);

b) leading edges subsonic, and lines AB and AC supersonic ($n > 1 > n_C$);

c) lines AB and AC subsonic ($n > n_C > 1$).

Let us consider the case $1 > n > n_C$. The pressure distribution on zone OBA is calculated by (V-4-2) in the region between the boundary of the Mach wave and the leading edge and by (V-4-3)

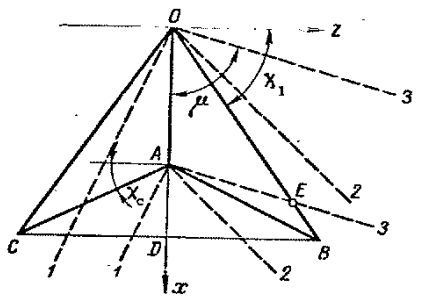

Figure V-4-3. Design Cases of Flow Around Delta Wing. 1-1) edges OB (OC) and AB (AC) supersonic ($1 > n > n_c$); 2-2) edge OB subsonic, edge AB supersonic ($n > 1 > n_c$); 3-3) edges OB and AB subsonic ($n > n_c > 1$).

in the zone inside the Mach angle. Integrating over area OBA, we obtain the component of total drag coefficient

$$c_{x1} = \frac{8(y_1')^2}{\alpha'\pi} F(n, \bar{b}_1), \qquad \text{(V-4-7)}$$

where $\bar{b}_1/b_{rt}$ (see Fig. V-4-2); F is a function equal to

$$F(n, \bar{b}_1) = \frac{1-\bar{b}_1}{1+\bar{b}_1}\left\{\frac{\bar{b}_1}{1-n^2}\arccos n + \right. \qquad \text{(V-4-8)}$$
$$\left. + \frac{1}{\sqrt{1-\bar{b}_1^2 n^2}}\left[\frac{\pi}{2} + \arcsin(\bar{b}_1 n)\right]\right\}.$$

The second drag component is governed by the action of the sources that give rise to the vertical velocity component $v_y = y_1' V_\infty$ and influence flow in region ABD with inclination y_2'. The pressures in the zones of wing area ABD outside and inside the Mach angle are calculated by (V-4-2) and (V-4-3), respectively. Integrating over surface ABD, we obtain

$$c_{x2} = \frac{8y_1'y_2'}{\alpha'\pi}\left[\frac{\pi}{2} - F(n, \bar{b}_1)\right]. \qquad \text{(V-4-9)}$$

To calculate the third drag component, it is necessary to take account of sources on area ABD with intensity $f_0 = V_\infty(y_2' - y_1')/\pi$. /259 Using this intensity, the pressures in the corresponding zones are determined by (V-4-2) and (V-4-3) with y_1' in these formulas replaced by $y_2' - y_1'$.

Integrating over area ABD,

$$c_{x3} = \frac{4y_2'(y_2' - y_1')}{\alpha'} \frac{S_{\triangle BC}}{S_{wg}}. \qquad \text{(V-4-10)}$$

Summing the components, we find the total wing drag coefficient $c_x = c_{x_1} + c_{x_2} + c_{x_3}$.

In the second case, $n > 1 > n_c$, drag is calculated similarly with the condition that the pressure on the leading part

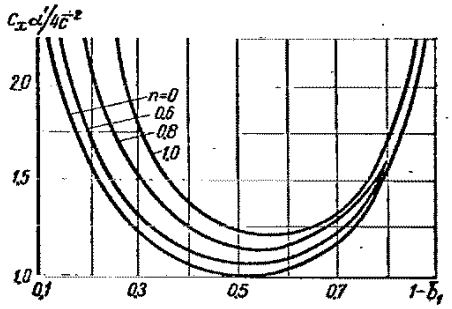

Figure V-4-4. Variation of Drag Coefficient of Delta Wing with Rhomboid Profile and Supersonic Leading Edge as a Function of Position of Maximum Thickness for Various Sweep Angles.

of the wing is found by (V-4-6). The first drag component is found accordingly for zone AOB, and the second component from the sources $f_0 = y_1' V_\infty/\pi$ distributed on region ABD. The quantity c_{x_3}, which corresponds to supersonic edge AB and depends on sources in region ABD with intensity $f_0 = (y_2' - y_2')V_\infty/\pi$, is determined by (V-4-10).

For the third case, which is characterized by subsonic edges OB and AB and, consequently, $n > n_C > 1$, the three drag components are calculated in the same way as in the preceding case, except that edge AB is subsonic and therefore $\bar{b}_1 n > 1$.

To these three components, we must add the drag due to the influence exerted on region AEB by sources with intensity $f_0 = (y_2' - y_1')V_\infty/\pi$, on region ABD. Since the pressure is found from (V-4-6) in region AEB, the third part of the drag is expressed by

$$c_{x4} = \frac{8y_1'(y_2'-y_1')}{\pi\alpha'} \frac{2S_{ABE}}{S_{wg}} \frac{(1-\bar{b}_1)^2}{\sqrt{n_C^2-1}} \int_1^{n_C} \frac{1}{(\sigma-\bar{b}_1)^2} \operatorname{arch} \sqrt{\frac{n_C^2-1}{\sigma^2-1}}\, d\sigma. \quad \text{(V-4-11)}$$

Summing the components, we find the total drag coefficient $c_x = \sum_{k=1}^{4} c_{xk}$.

Figures V-4-4 and V-4-5 show results from a calculation of the drag parameter $c_x\alpha'/4\bar{c}^2$ for delta wings with supersonic (Fig. V-4-4) and subsonic (Fig. V-4-5) leading edges as a function of $1 - \bar{b}_1$ for various $n = \tan\chi_1 \tan\mu$.

Tetragonal wing with rhomboid profile. The scheme set forth above for calculation of flow around a delta wing by the source method can be used to calculate the drag of a wing of arbitrary planform.

Let us consider a tetragonal wing with a rhomboid profile (Fig. V-4-6). The flow around the wing can be presented as the resultant flow from three source systems having a triangular distribution. The first source system is distributed in triangle OBL (we are considering half of the wing) and has the intensity /260

$f_0 = y'V_\infty/\pi$; the sources of the second system with intensity $f_0 = (y_2' - y_1')V_\infty/\pi$ are distributed in triangle ABD and, finally, those of the third system, which have the negative intensity $f_0 = -y_2'V_\infty/\pi$, are distributed in region DBL.

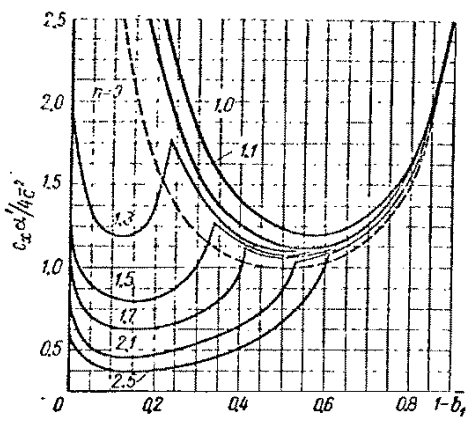

Figure V-4-5. Variation of Drag Coefficient of Delta Wing with Subsonic Leading Edge as a Function of Maximum-Thickness Position.

In the most general case, the additional axial velocity component at a certain point on the wing surface and, consequently, the pressure will be determined as a result of addition of components obtained from each source distribution. Depending on sweep angle or the position of each of the three source distributions relative to the surface point under consideration, the pressure coefficient will be determined by Eqs. (V-4-2), (V-4-3), (V-4-5), and (V-4-6).

Let wing edges OB, AB, and DB be subsonic. We can then examine the four regions oz_{D_1}, $z_{D_1}z_{A_1}$, $z_{A_1}z_{D_2}$, and $z_{D_2}z$, each of which is characterized by the same

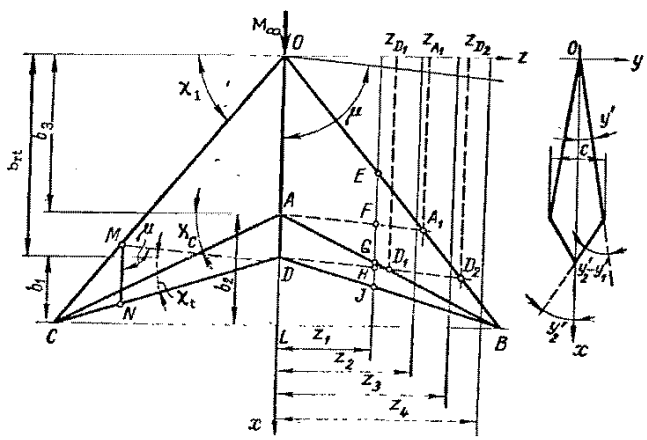

Figure V-4-6. Tetragonal Wing with Rhomboid Profile.

positions of the source-distribution zones. Consequently, the pressure distribution will be identical within the zone

around each section, and the profiles will have identical local drag coefficients.

The flow around profile EGJ with coordinate $z_1 (0 \leq z_1 \leq z_{D_1})$ is calculated as follows. The pressure coefficient on segment EF with inclination y_1', which depends on the source distribution in triangle OBL, is calculated from (V-4-5). For segment FG, which has the same inclination, it is also necessary to consider the influence of sources in zone ABL. Consequently, the coefficient calculated by (V-4-6) with $y_2' - y_1'$ substituted for y_1' and σ calculated with respect to point B at the origin must be added to (V-4-5). /261

The second pressure component on profile segment GH with inclination y_2' must be calculated by (V-4-5) with $y_2' - y_1'$ substituted for y_1'.

Finally, on the fourth profile segment HJ, it is necessary to add to the above two components a third governed by the action of sources in triangle DBL and determined by (V-4-6) with $-y_2'$ substituted for y_1'.

Flow over the wing in sections with the coordinates z_2, z_2, z_4 is investigated similarly. Four segments must also be examined in the z_2 section. On the first segment, which lies between the leading edge and Mach line AA_1, we have one pressure-coefficient component determined from (V-4-5). On the second segment, which is bounded by the Mach lines AA_1 and DD_2, we must add a component calculated by (V-4-6) with y_1' replaced by $y_2' - y_1'$. The third profile segment lies between line DD_2 and edge AB. To the two preceding pressure-coefficient components, we add a third found from (V-4-6) with $-y_2'$ substituted for y_1' and the apex D regarded as being at the origin. On the fourth segment, which extends to the trailing edge, the pressure components are determined in the same way as for the third.

Three profile segments must be examined in the z_3 section and two in the z_4 section. Since the z_4 section lies behind wave DD_2, three source distributions will influence flow simultaneously at each point of this section.

If the wing edges are supersonic, (V-4-3) must be used instead of (V-4-5) to determine the pressure coefficients.

Calculation of the flow over a symmetrical rhomboid-profile wing by the above method indicates that the drag coefficient governed by thickness can be presented in the form

$$c_x = \frac{2\bar{c}^2}{\pi\alpha'} f(n, \bar{b}_1, \bar{b}_2), \qquad \text{(V-4-12)}$$

where $\bar{b}_1 = b_1/b_{rt}$, $\bar{b}_2 = b_2/b_{rt}$, $\underline{f}$ is a function that depends on the parameters n, $\bar{b}_1$, $\bar{b}_2$, and takes various forms, depending on the relationships between the values of these parameters.

The forms of the function $\underline{f}$ are obtained for the following three cases as a result of the investigation: $n < \bar{b}_2$, $\bar{b}_2 < n < \bar{b}_1$ and $n > \bar{b}_1$.

Figure V-4-7, a and b, shows calculations of $\alpha' c_x/\bar{c}^2$ by (V-4-12) as a function of $\bar{n} = 1/n$ for various $\bar{b}_1$ and $\bar{b}_2$.

Swept wing with curved profile. The flow over a thin swept wing with a curvilinear profile can be calculated by the method of sources.

Let us assume that a thin profile is symmetrical and formed by arcs of circles (Fig. V-4-8). The source-method formulas given above should be used to determine the pressure coefficient at a certain surface point A, followed by summing of the pressure components induced by the various source distributions.

It is first necessary to inspect the distribution of sources with intensity $f_0 = y_0' V_\infty/\pi$, which is determined by the initial slope of the profile. Assuming that the leading edge is subsonic and applying (V-4-5), we obtain for the pressure coefficient /262

$$\bar{p} = -\frac{4y_0'}{\pi\alpha' \sqrt{n^2-1}} \operatorname{arch} \sqrt{\frac{n^2-\sigma_1^2}{1-\sigma^2}}, \qquad \text{(V-4-13)}$$

where

$$n = \operatorname{tg}\chi_1 \operatorname{tg}\mu;\ \sigma_1 = \frac{z_A}{x_A} \operatorname{tg}\chi_1.$$

A pressure is induced at point A by sources with intensity dy' distributed in a triangle with an apex at point C (Fig. (V-4-8):

$$d\bar{p} = \frac{-4dy'}{\pi\alpha' \sqrt{n^2-1}} \operatorname{arch} \sqrt{\frac{n^2-\sigma_2^2}{1-\sigma_2^2}}, \qquad \text{(V-4-14)}$$

where /263

$$\sigma_2 = \frac{z_A \operatorname{tg}\chi_1}{x_A - x_C}.$$

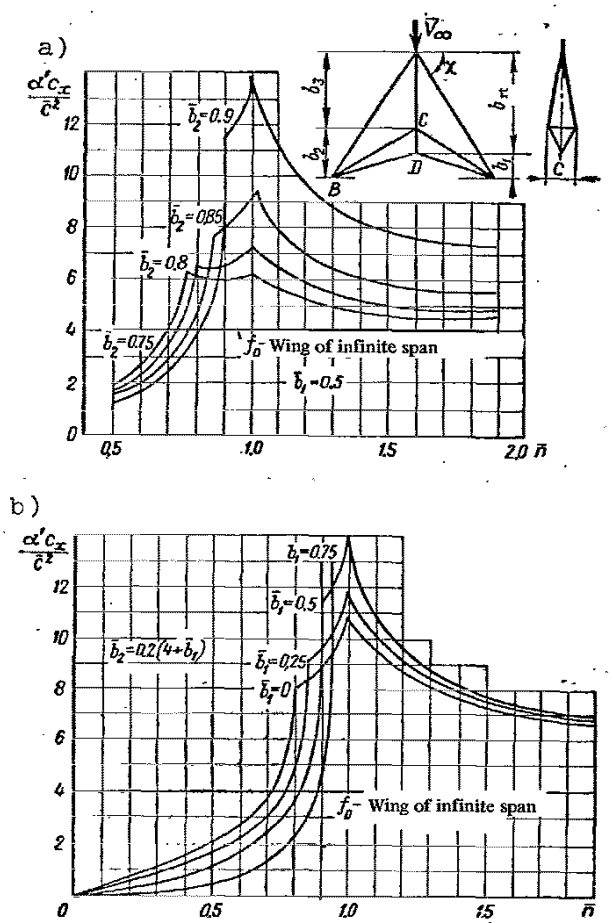

Figure V-4-7. Wave Drag Coefficient of Wing as a Function $\bar{n} = 1/n$ for Various $\bar{b}_1$ and $\bar{b}_2$.

If $\sigma > 1$, the pressure coefficient increment is calculated in accordance with (V-4-6):

$$d\bar{p} = \frac{-4dy'}{\pi\alpha' \sqrt{n^2-1}} \operatorname{arch} \sqrt{\frac{n^2-1}{\sigma_2^2-1}}. \qquad \text{(V-4-15)}$$

We can convert from the differential dy' to $dy' = (dy'/dx)\,dx = [(dy'/dx)\operatorname{tg}\chi_1 y_A/\sigma_2^2]\,d\sigma_2$, where $dy'/dx = -2y_0'/b$ for the circular arc.

To obtain the total pressure component, (V-4-14) must be integrated from $\sigma_2 = \sigma_1$ to $\sigma_2 = 1$, and (V-4-15) from $\sigma_2 = 1$ to $\sigma_2 = n$. If the position of point A is such that it is influenced by sources with intensity $f_0 = y_0' V_\infty/\pi$ in a triangle with apex B, the limit of integration $\sigma_2 = n$ for (V-4-15) should be replaced by $\sigma_2 = \sigma_B$, where $\sigma_B = [\operatorname{tg}\chi_1 z_A/(x_{A_1} - x_D)] < n$.

The third component of pressure at point A will be determined by the indicated source distribution $f_0 = -y_0' V_\infty/\pi$

$$\bar{p} = \frac{-4y_0'}{\pi\alpha' \sqrt{n^2-1}} \operatorname{arch} \sqrt{\frac{n^2-1}{\sigma_B^2-1}}. \qquad \text{(V-4-16)}$$

The total pressure coefficient for the particular point can be found by summing the components obtained.

The pressure distribution around a profile with a circular-arc contour, computed by the above method for $M_\infty = 1.4$ and

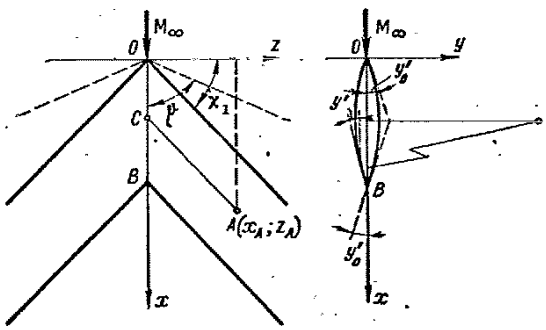

Figure V-4-8. Swept Wing with Curvilinear Profile.

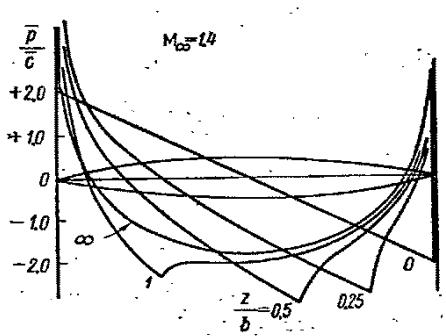

Figure V-4-9. Chordwise Pressure Distribution on Wing with 60° Sweep Angle.

$\chi_1 = 60°$ as a function of the ratio z/b appear in Fig. V-4-9. The spanwise variation of the local drag coefficient is shown in Fig. V-4-10.

Wings of arbitrary planform. The problem of flow around a wing of arbitrary planform can be reduced by the method of sources to a problem of flow over triangular surfaces. In this method, the given surface is filled out in plan to form a triangle. It can then be assumed that the flow around the given surface is induced by sources with positive intensity distributed on the triangular surface and by sources of the opposite sign on the added part of the surface, which is also dismembered into individual zones of triangular form. /264

By way of example, let us consider a hexagonal wing as a triangular wing with a tip rake of chord MN (see Fig. V-4-6).

The flow past such a wing is calculated as follows. Filling out the wing to the triangular form ODC, we calculate the flow from sources distributed on area ODC. Here the flow on area OMD (MD is a Mach line) remains the same as for the original wing. The parameters obtained for the tip MDN must be improved, since it will be influenced by sources of the opposite sign in triangle MNC.

General relationship for drag of finite-span swept wing. The total drag of an aerodynamically flat wing is

$$c_x = c_{xf} + c_{xw0} + Ac_y^2, \qquad \text{(V-4-17)}$$

where A is a certain coefficient.

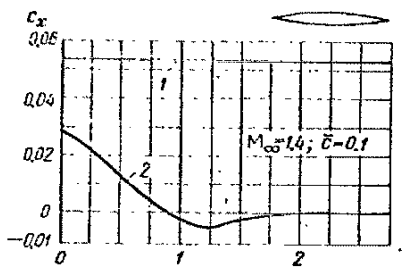

Figure V-4-10. Spanwise Distribution of Profile Drag on Wing with 60° Sweep and a Symmetrical Profile Formed by Arcs of Circles (1) straight wing; 2) swept wing); the abscissa is distance from the root section in fractions of root chord.

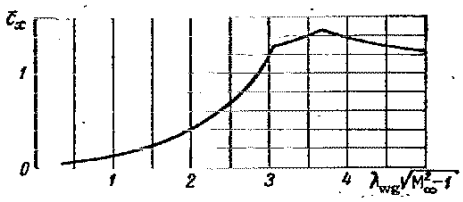

Figure V-4-11. Variation of Proportionality Coefficient $\bar{c}_x$ in (V-4-20) According to Linear Theory ($\eta = 2$, $x_c = 0.5$; $\lambda_{wg} \tan \chi = 3.67$).

The value of this coefficient is determined by the type of leading edge. If the leading edge is supersonic, $A = (c_y^\alpha)^{-1}$; if subsonic, $A < (c_y^\alpha)^{-1}$. The quantity $c_{x\,w_0}$ is the wave-drag coefficient of the wing at $\alpha = 0$. This quantity is conveniently expressed in terms of the profile wave drag coefficient $c_{x\,w}$, using the relation

$$c_{x\,w\,0} = \bar{c}_x c_{x\,w}, \qquad \text{(V-4-18)}$$

where

$$c_{xw} = \frac{2k_1\bar{c}^2}{\sqrt{M_\infty^2-1}}. \qquad \text{(V-4-19)}$$

The proportionality coefficient $\bar{c}_x$ can be represented within the framework of the linear theory as a function [6]

$$\bar{c}_x = \frac{c_{xw0}}{c_{x\,w}} = f(\lambda_{wg}\sqrt{M_\infty^2-1},\ \lambda_{wg}\operatorname{tg}\chi,\ \eta,\ \bar{x}_c). \qquad \text{(V-4-20)}$$

As an example, Fig. V-4-11 shows a $\bar{c}_x$ curve for a swept wing with taper $\eta = 2$, the abscissa $\bar{x}_c = 0.5$, and $\lambda_{wg} \tan \chi = 3.67$. /265
Here the angle χ (Fig. V-4-12) is measured with respect to the leading edge.

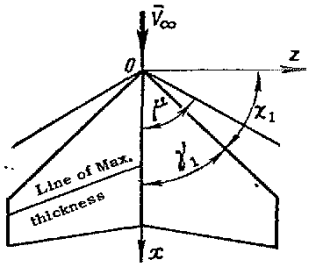

Figure V-4-12. Geometry of Swept Wing.

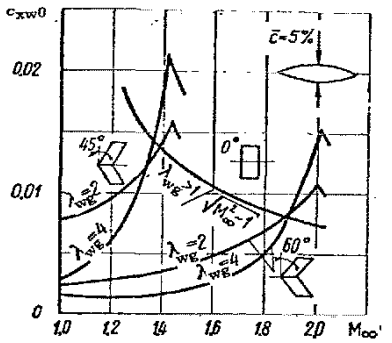

Figure V-4-13. Wave Drag of Wings

When the wing has an unsymmetrical profile (see Fig. V-2-5) with different maximum-thickness positions x_{c_l} and x_{c_u} on the lower and upper surfaces, the coefficient $c_{x\,w_0}$ should be determined as the sum

$$c_{x\,w_0} = c_{x\,w_0\,l} + c_{x\,w_0\,u}, \qquad \text{(V-4-21)}$$

where the first term applies to the lower surface and the second to the upper surface.

By way of illustration, Fig. V-4-13 shows curves of the wave drag $c_{x\,w_0}$ for wings of various planforms. All wings have lenticular profiles with a thickness ratio $\bar{c} = 0.05$.

Similarity. Let us use the subscript "*" to denote the parameters (geometric and aerodynamic) of a swept wing at $M_\infty = \sqrt{2}$.

It can be shown that the geometric parameters of wings will be interrelated as follows for any $M_\infty > 1$ and at $M_\infty = \sqrt{2}$:

$$\left.\begin{aligned} \alpha' &= \alpha'_*; \\ \eta &= \eta_*; \\ \lambda_{wg}\sqrt{M_\infty^2-1} &= \lambda_*; \\ \lambda_{wg}\operatorname{tg}\chi &= \lambda_*\operatorname{tg}\chi_*; \\ \operatorname{tg}\chi &= \operatorname{tg}\chi_*\sqrt{M_\infty^2-1}. \end{aligned}\right\} \qquad \text{(V-4-22)}$$

The corresponding relation between the aerodynamic coefficients of these wings and their sections will be as follows:

$$\left.\begin{aligned} \bar{p}\sqrt{M_\infty^2-1}&=\bar{p}_*;\\ c_y\sqrt{M_\infty^2-1}&=c_{y*};\\ c_x\sqrt{M_\infty^2-1}&=c_{x*};\end{aligned}\right\} \qquad \text{(V-4-23)}$$

$$\left.\begin{aligned} m_z\sqrt{M_\infty^2-1}&=m_{z*};\\ c_{c.p}&=c_{c.p\ *}.\end{aligned}\right\} \qquad \text{(V-4-24)}$$

Thus, to calculate the parameters at a certain $M_\infty > 1$, it is necessary that they be known for wings with several other tapers η_* and aspect ratios λ_* but the same section shape and attack angles as the original wing. /266

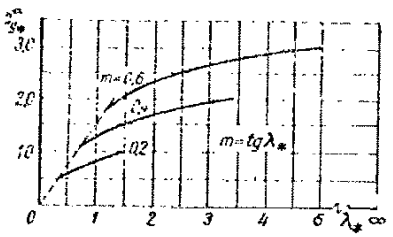

Figure V-4-14. $c_y^\alpha = f(\lambda_*)$ for Swept Wings with Various tan χ_* and a Taper $\eta_* = 1$.

By way of example, Fig. V-4-14 shows theoretical $c_{y*}^\alpha = f(\lambda_*)$ curves for swept wings for various tan χ_* and a taper of $\eta_* = 1$.

To use these curves for other $M_\infty > 1$, it is sufficient to substitute $c_y^\alpha\sqrt{M_\infty^2-1};\lambda_{wg}\sqrt{M_\infty^2-1};\operatorname{tg}\chi/\sqrt{M_\infty^2-1}$ for c_{y*}^α, λ_*, tan χ_* in Fig. V-4-14 in accordance with the given transformation formulas.

§V-5. THE NONLINEAR PROBLEM OF SUPERSONIC FLOW AROUND WINGS

Application of the Method of Characteristics

Calculation of flow past sharp profile. In the general case of supersonic flow around a sharpened curvilinear profile of arbitrary thickness, the M_∞ of which can also be arbitrary, the local aerodynamic parameters of the gas can be calculated by the method of characteristics.

The calculation is performed as follows. A rather small wedge surface OA (Fig. V-5-1) is taken in the neighborhood of the sharpened leading edge and the flow variables calculated for it by the theory of the oblique compression shock. The result is construction of the rectilinear shock segment OC and determination of its intersection point C with the simple straight wave drawn from point A. This wave AB coincides with a characteristic that might conventionally be called the first-family characteristic.

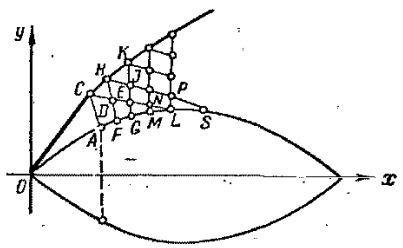

Figure V-5-1. Diagram Illustrating Calculations of Supersonic Flow Around Profile by Method of Characteristics.

The flow over the curvilinear contour downstream from point A depends on the shape of this contour, the values of the gas parameters at points on characteristic AC, and the interaction with the shock wave, as the result of which the shock wave itself acquires a curvilinear form. Here we can isolate a contour segment AL where the curvilinear shock has no influence. This segment can be determined by drawing rectilinear first-family characteristics from closely spaced points F, G, etc., to their intersections at points D, E, etc., with the corresponding elements of second-family characteristics. The second-family characteristic element NL drawn from point N intersects the profile contour at a point L, which will be the boundary of the sought potential (irrotational) flow segment, which is independent of flow behind the curvilinear wave. /267

On this segment, the local M is determined from the theory of the simple wave, which is known as the theory of Prandtl-Meyer potential expansion flows (see page 190). In this theory, for example, the expansion angle of a flow with the initial condition $M = 1$ for point F will be $\omega_F = \beta_A - \beta_F + \omega_A$. The corresponding M_F at point F is found from Table IV-1-1. The calculation for other points of this contour, including point L, is analogous.

Pressure must be determined by the formula

$$p = p_0' \left(1 + \frac{k-1}{2} M^2\right)^{-\frac{k}{k-1}},$$

where M is the local Mach number and p_0' is the flow stagnation pressure behind shock OC. This pressure is assumed to be the same both for points A, F, ..., L and for all other points downstream from L.

The pressure coefficient is calculated by (IV-7-12). The flow will be rotational in the region between the second-family characteristic CL and the curvilinear wall, and will depend on flow conditions immediately behind the curvilinear shock wave, which takes the form of a broken line that is extended out stepwise in the course of solving the problem. The appropriate method of characteristics must be used for the flow calculation in combination with shock-wave theory.

Let us examine calculation of the flow in triangle CDH. It will be determined if the flow variables are found at points C, D, and H. At point C, the gas variables are found as the parameters immediately behind the shock. At point D, the parameters will be the same as at point F; in particular, $\mu_D = \mu_F$, $\beta_D = \beta_F$. Hence the inclination of characteristic DH to the $\underline{x}$-axis can be found; it will be defined by the angle $\beta_D + \mu_D$.

To determine the flow at point H, which lies on the compression shock and characteristic DH, it is necessary to examine the shock and characteristic equations simultaneously. Here the equation for the characteristic must be written with consideration of flow vorticity. As a result of solving the corresponding equation system, we determine the angle difference

$$\Delta\beta_D = \beta_H - \beta_D = \left[\left(\frac{d\omega}{d\beta}\right)_{\beta_D} - 1\right]\left(\omega_D - \omega_C - \frac{x_H - x_D}{kp'_{0D}}\frac{\Delta p'_0}{\Delta n}c_D\right), \qquad \text{(V-5-1)}$$

where

$$c_D = \frac{\sin^2\mu_D\cos\mu_D}{\cos(\beta_D+\mu_D)}, \quad \Delta p'_0 = p'_{0H} - p'_{0D}, \quad \Delta n = DH\sin\mu_D.$$

From $\Delta\beta_D$, we can find

$$\Delta\omega_D = \omega_H - \omega_D = \Delta\beta_D - \frac{x_H - x_D}{kp'_{0D}}\frac{\Delta p'_0}{\Delta n}c_D, \qquad \text{(V-5-2)}$$

and then determine ω_H and the corresponding M_H. The shock inclination θ_{sH} at point H is determined from the values of M_H and the angle $\beta_H = \Delta\beta_D + \beta_D$. The gas variables at this point can be refined by repeating the calculation using the new p'_H corresponding to the parameters M_H and θ_{sH}.

We can now find the variables at point J, which lies at the intersection of the two characteristics HJ and EJ of the second and first families, respectively. For this purpose, we use for the characteristics the equations that take account of flow vorticity. By solving them simultaneously, we obtain

$$\Delta\beta_E = \beta_J - \beta_E = \frac{1}{2}\left(-\frac{x_J - x_H}{kp'_{0H}}\frac{\Delta p'_0}{\Delta n}t_H - \frac{x_J - x_E}{kp'_{0E}}\frac{\Delta p'_0}{\Delta n}c_E - \omega_E + \omega_H - \beta_E + \beta_H\right), \qquad \text{(V-5-3)}$$

where

/268

$$c_H = \frac{\sin^2 \mu_H \cos \mu_H}{\cos (\beta_H - \mu_H)}; \quad c_E = \frac{\sin^2 \mu_E \cos \mu_E}{\cos (\beta_E + \mu_E)};$$
$$p'_0 = p'_{0H} - p'_{0E};$$
$$\Delta n = HJ \sin \mu_H + BC \sin \mu_E.$$

The difference

$$\Delta\omega_E = \omega_J - \omega_E = \Delta\beta_E + \frac{x_J - x_E}{k p'_{0E}} \frac{\Delta p'_0}{\Delta n} c_E \qquad \text{(V-5-4)}$$

corresponds to this $\Delta\beta_E$.

Thus, the angles β_J, ω_J, μ_J and the number M_J can be calculated for point J.

The variables of the gas at other points of this region that lie on the curvilinear shock or at the nodes of conjugate characteristics are determined in a similar manner.

The last element in the calculation is determination of the rotational-flow parameters at points on the contour. By way of example, let us consider point S. Since it lies on the contour and, simultaneously, on the second-family characteristic PS, we can use the equation for this characteristic,

$$\Delta\omega_P = \omega_S - \omega_P = -\Delta\beta_P + \frac{x_S - x_P}{k p'_{0P}} \frac{\Delta p'_0}{\Delta n}, \qquad \text{(V-5-5)}$$

where

$$\Delta p'_0 = p'_{0P} - p'_{0S};$$
$$\Delta n = PS \sin \mu_P.$$

The $\Delta\beta_P$ in this equation is equal to the difference $\beta_S - \beta_P$, in which angle β_S is known by hypothesis. Calculating $\Delta\omega_P$, we find the values of ω_S, μ_S, and M_S at point S.

Determination of the coordinates of points at the nodes of the characteristic net, on the compression shock or on the contour, is a component part of the calculations.

As an example, let us consider the intersection point J of the two conjugate characteristics HJ and EJ. Its coordinates y_J

and x_J are determined by solving the equations

$$\left.\begin{aligned} y_J - y_E &= (x_J - x_E)\,\mathrm{tg}\,(\beta_E + \mu_E);\\ y_J - y_H &= (x_J - x_H)\,\mathrm{tg}\,(\beta_H - \mu_H). \end{aligned}\right\} \qquad \text{(V-5-6)}$$

By way of illustration, let us calculate the coordinates of points H and S. The former is situated on the shock and a first-family characteristic. Its coordinates y_H and x_H are therefore determined by solving the equations

$$\left.\begin{aligned} y_H - y_C &= (x_H - x_C)\,\mathrm{tg}\,\theta_{CH};\\ y_H - y_D &= (x_H - x_D)\,\mathrm{tg}\,(\beta_D + \mu_D). \end{aligned}\right\} \qquad \text{(V-5-7)}$$

The second point S is located simultaneously on the contour and on the second-family characteristic PS. Its coordinates y_S and x_S are therefore determined by the equations

$$\left.\begin{aligned} y_S &= f(x_S);\\ y_S - y_P &= (x_S - x_P)\,\mathrm{tg}\,(\beta_P - \mu_P). \end{aligned}\right\} \qquad \text{(V-5-8)}$$

The coordinates of other points are determined in a similar manner.

The above method of flow calculation can also be used when the profile is set at an angle of attack. If the attack angle is such that the angle between the tangent to the contour at the point and the vector $\bar{V}_\infty$ is smaller than 180°, the calculation must consider formation of a shock wave above and below the profile in accordance with the hypothesis for which the calculation was set forth. /269

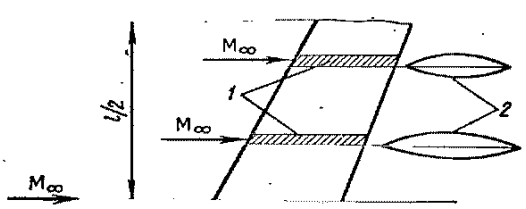

Figure V-5-2. Calculation of Supersonic Flow Around Profile by Strip Method. 1) strips; 2) local profiles.

If one of the tangents is inclined to the vector $\bar{V}_\infty$ by 180° or more, no shock is formed on the corresponding side and the flow must be calculated by the Prandtl-Meyer theory, i.e., by the simple-wave formulas.

This method of calculation enables us to find the M distribution over the profile. The pressure can be found from M and then the

aerodynamic coefficients can be calculated by Formulas (I-3-20), (I-4-16) and (I-5-12).

Swept wing. The "method of strips," in which the surface of the swept wing is represented in the form of a set of narrow strips oriented in the direction of the oncoming-flow velocity vector (Fig. V-5-2), can be used for approximate determination of the aerodynamic characteristics of a wing with a swept leading edge. The basic premise is that the supersonic flow is regarded as two-dimensional for each strip and there is no interaction between strips. The flow can therefore be calculated, for example, by the method of characteristics for two-dimensional flows. the strip method gives good results for high velocities, but it can also be used for small supersonic speeds to obtain estimates.

If the profile is thin and the M_∞ are small, the local flow can be calculated in accordance with the linearized theory.

The aerodynamic force, moment, or corresponding coefficient can be evaluated by summing the aerodynamic characteristics spanwise for each strip. Formulas (I-3-28), (I-4-22) and (I-5-16) should be used for this purpose.

Aerodynamic Characteristics at Very High (Hypersonic) Speeds

Application of Newton's method. The basis of the Newtonian method, which is used for approximate determination of profile aerodynamic characteristics for hypersonic speeds, is the working relationship (IV-7-2). The quantity $\bar{p}^*$ that appears in it — the pressure coefficient on the corresponding side at the sharp forward point of the profile — is calculated by the exact theory of flow around a plate. The angle between the profile normal and vector $\bar{V}_\infty$ is η^*. This angle is equal to η at an arbitrary point of the profile where the pressure coefficient is $\bar{p}$.

The cosines of the angles η^* and η are determined from (IV-7-4) by calculating the ratio $Vn_\infty/V_\infty = \cos\eta$, in which the values of $\cos\alpha_x$ and $\cos\alpha_y$ are found by Formulas (IV-7-3). Since $\partial y/\partial x = \tan\beta$, where β is the angle between the tangent to the profile and the chord, and $\partial y/\partial z = 0$, $\cos\alpha_x = \sin\beta$, $\cos\alpha_y = -\cos\beta$.

Consequently /270

$$\cos\eta = \frac{V_{n\infty}}{V_\infty} = \cos\alpha\sin\beta - \sin\alpha\cos\beta = \sin(\beta-\alpha). \qquad \text{(V-5-9)}$$

At the nose point, where $\beta = \beta_p$,

$$\cos\eta^* = -\cos\alpha\sin\beta_p - \sin\alpha\cos\beta_p = \sin(\beta_p - \alpha). \qquad \text{(V-5-9')}$$

Thus, (IV-7-2) can be written

$$\bar{p} = \bar{p}^* \frac{(\cos\alpha\sin\beta - \sin\alpha\cos\beta)^2}{(\cos\alpha\sin\beta_p - \sin\alpha\cos\beta_p)^2} = \bar{p}^* \frac{\sin^2(\beta-\alpha)}{\sin^2(\beta_p-\alpha)}. \qquad \text{(V-5-10)}$$

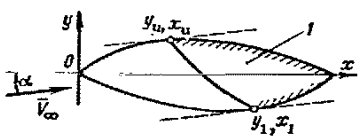

Figure V-5-3. Boundaries of "Shaded" Zone on Profile (1 is the Shaded Zone).

This formula applies for a positive inclination of the local surface element, i.e., for cases in which the values of $\bar{p}$ are themselves positive, with the limit $\bar{p} = 0$. At contour points where this value is realized, the condition $\alpha = \beta$, from which the coordinates of points on the boundaries of the "shaded zone" can be found, must be satisfied (Fig. V-5-3). The respective equations for determination of these coordinates on the upper and lower parts of the profile have the form

$$\left(\frac{dy}{dx}\right)_u = \operatorname{tg}\alpha; \quad \left(\frac{dy}{dx}\right)_l = \operatorname{tg}\alpha. \qquad \text{(V-5-11)}$$

At points in the "shaded zone," the coefficient $\bar{p} = 0$ is to be taken in accordance with Newton's theory.

The pressure distributions are found separately for the top of the profile, where the contour equation $y_u = y_u(x)$, and on the bottom, where $y_l = y_l(x)$. The corresponding formulas for the pressure coefficient are

$$\bar{p}_u = \bar{p}_u^* \frac{\sin^2(\beta_u-\alpha)}{\sin^2(\beta_{pu}-\alpha)}; \quad \bar{p}_l = \bar{p}_l^* \frac{\sin^2(\beta_l-\alpha)}{\sin^2(\beta_{pl}-\alpha)}. \qquad \text{(V-5-12)}$$

The coefficient $\bar{p}^*$ is determined from the theory of oblique compression shock in the general case for arbitrary angles β_{pu} and β_{pl}. The formulas are accordingly suitable for both thin and thick profiles in flows at high M_∞ at arbitrary α. If the profiles are thin and the attack angles small, Formulas (V-5-12) simplify:

$$\bar{p}_u = \bar{p}_u^* \frac{(\beta_u-\alpha)^2}{(\beta_{pu}-\alpha)^2}; \quad \bar{p}_l = \bar{p}_l^* \frac{(\beta_l-\alpha)^2}{(\beta_{pl}-\alpha)^2}. \qquad \text{(V-5-12')}$$

In using the formula for $\bar{p}_1$, it should be remembered that the angle β_1 is calculated from the contour equation $y_1 = y_1(x)$ on the assumption that the coordinates y_1, like y_u, are positive. Consequently, the angles $\beta_1 = (dy/dx)_1$ are positive at the beginning of the profile, but may become negative at the trailing edge.

We have from the theory of the oblique compression shock for the pressure coefficient $\bar{p}^*$

$$\bar{p}^* = \frac{k+1}{2}\left\{1 + \sqrt{1 + \left[\frac{4}{(k+1)M_\infty \Theta_0}\right]^2}\right\}\Theta_0^2, \qquad \text{(V-5-13)}$$

where $\Theta_{0u} = \beta_{pu} - \alpha$ for the top and $\Theta_{0l} = \beta_{pl} - \alpha$ for the bottom. In the extreme case of $M_\infty \Theta_0 \to \infty$,

$$\left.\begin{aligned}\bar{p}_u^* &= (k+1)(\beta_{pu}-\alpha)^2;\\ \bar{p}_l^* &= (k+1)(\beta_{pl}-\alpha)^2.\end{aligned}\right\} \qquad \text{(V-5-14)}$$

The value k = 1 corresponds to the so-called pure Newtonian theory; then /271

$$\left.\begin{aligned}\bar{p}_u^* &= 2(\beta_{pu}-\alpha)^2;\\ \bar{p}_l^* &= 2(\beta_{pl}-\alpha)^2.\end{aligned}\right\} \qquad \text{(V-5-15)}$$

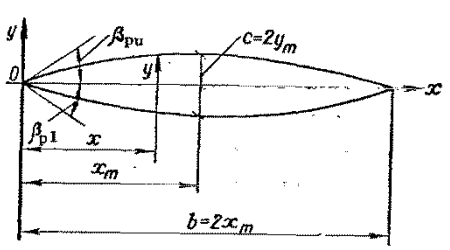

Figure V-5-4. Profile with Parabolic Contour.

The aerodynamic coefficients can be calculated from the pressure distribution. The lift coefficient

$$c_y = \int_0^1 (\bar{p}_l - \bar{p}_u)\, d\bar{x}, \qquad \text{(V-5-16)}$$

where $\bar{x} = x/b$, or, remembering that $\bar{p} = 0$ in the "shaded zone," we can write

$$c_y = \int_0^{\bar{x}_l} \bar{p}_l\, d\bar{x} - \int_0^{\bar{x}_u} \bar{p}_u\, d\bar{x}, \qquad \text{(V-5-16')}$$

where $\bar{x}_1$ and $\bar{x}_u$ are dimensionless coordinates of points on the boundary of the "shaded zone" for the lower and upper surfaces of the profile, respectively, and $\bar{p}_1$ and $\bar{p}_u$ are the pressure coefficients calculated by (V-5-12) and (V-5-12').

The wave drag coefficient

$$c_x = \int_0^1 (-\bar{p}_1\Theta_1 + \bar{p}_u\Theta_u)\, d\bar{x}. \qquad \text{(V-5-17)}$$

After substituting $\Theta_1 = \beta_1 - \alpha$ and $\Theta_u = \beta_u - \alpha$, we find

$$c_x = \alpha c_y - \int_0^{\bar{x}_1} \bar{p}_1\beta_1 d\bar{x} + \int_0^{\bar{x}_u} \bar{p}_u\beta_u d\bar{x}. \qquad \text{(V-5-17')}$$

The moment coefficient about the leading edge is

$$m_z = -\int_0^1 (\bar{p}_1 - \bar{p}_u)\bar{x}\, d\bar{x} \qquad \text{(V-5-18)}$$

or

$$m_z = -\int_0^{\bar{x}_1} \bar{p}_1\bar{x}\, d\bar{x} + \int_0^{\bar{x}_u} \bar{p}_u\bar{x}\, d\bar{x}. \qquad \text{(V-5-18')}$$

As an example, consider calculation of the aerodynamic characteristics of a symmetrical profile whose contour is formed by a second-order parabolic curve $\bar{y} = 4\bar{x}(1 - \bar{x})$, where $\bar{y} = y/y_m$, $\bar{x} = x/2x_m$ (Fig. V-5-4).

The respective contour equations for the lower and upper surfaces are

$$y_1 = -2c\bar{x}(1 - \bar{x}); \quad y_u = 2c\bar{x}(1 - \bar{x}),$$

where

$$\bar{c} = 2y_m/b = 2y_m/2x_m.$$

We determine the angles β_1 and β_u:

$$\beta_1 = -2\bar{c}(1 - 2\bar{x}_1); \quad \beta_u = 2\bar{c}(1 - 2\bar{x}_u).$$

We find the coordinates of points on the "shaded zone" boundary from the conditions /272

$$\alpha = -2\bar{c}(1 - 2\bar{x}_1); \quad \alpha = 2\bar{c}(1 - 2\bar{x}_u),$$

from which we see that

$$\bar{x}_1 = \frac{x_1}{b} = \frac{1}{2\bar{c}}(\alpha + 2\bar{c}); \quad \bar{x}_u = \frac{x_u}{b} = \frac{1}{2\bar{c}}(2\bar{c} - \alpha).$$

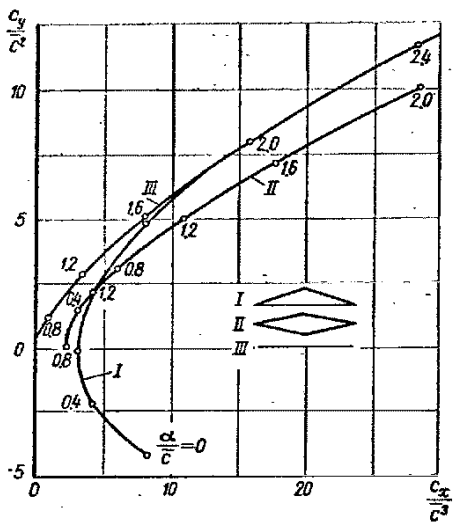

Figure V-5-5. Polars for a Plate and Two Thin Profiles.

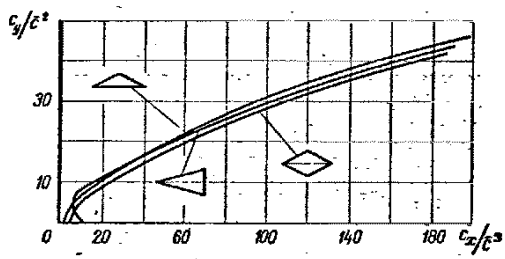

Figure V-5-6. Polars for Wing Profiles as Found with the Newtonian Formula.

Integrating in (V-5-16') and (V-5-17') for $\alpha < 2\bar{c}$ and $\bar{p}_u^*$ and $\bar{p}_1^*$ determined from (V-5-14), we obtain expressions for the lift and drag coefficients:

$$c_y = \bar{p}^* \left(2\alpha\bar{c} + \frac{1}{6}\frac{\alpha^3}{\bar{c}}\right); \qquad \text{(V-5-19)}$$

$$\bar{c}_{x\,w} = \bar{p}^* \left(2\bar{c}^3 + 3\alpha^2\bar{c} + \frac{1}{8}\frac{\alpha^4}{\bar{c}^3}\right), \qquad \text{(V-5-20)}$$

where

$$\bar{p}^* = k + 1. \qquad \text{(V-5-21)}$$

The moment coefficient is determined similarly by (V-5-18).

Formulas (V-5-19) and (V-5-20) do not apply for the case $\alpha \geq 2\bar{c}$, i.e., when the attack angles are equal to or greater than the inclination of the profile at the leading edge. In this case,

the entire upper surface will be in the "blanketed zone," and, consequently, the limits of integration will be $\bar{x}_l = 1$ and $\bar{x}_u = 0$. Accordingly, we obtain for the lift and drag coefficients

$$c_y = \tilde{p}^* \left(\alpha^2 + \frac{4}{3}\bar{c}^2\right); \qquad \text{(V-5-22)}$$

$$c_{xw} = \tilde{p}^* (4\alpha\bar{c}^2 + \alpha^3). \qquad \text{(V-5-23)}$$

The aerodynamic coefficients for various profiles can be calculated in the same way if their forms are given.

As we have noted, $k = 1$ corresponds to "pure" Newtonian theory and, consequently, $\tilde{p}^* = 2$. Profile polars corresponding to (V-5-19) and (V-5-20) have been plotted in Figs. V-5-5 and V-5-6 for this value. Analysis of the curves shows, for example, that a delta profile has lift/drag-ratio advantages over rhomboid profiles at large enough angles of attack.

Method using the theory of compression shocks and expansion flows. Calculation of pressure by this method requires Formula (IV-7-16) with the parameters indexed 2 and the function $\tilde{c}_p$ in the following form (provided that the wing is thin and the M_∞ are very large): /273

$$\bar{p}_2 = \frac{4}{k+1}\frac{K_0^2 - 1}{M_\infty^2} \qquad (K_0 = M_\infty \theta_0);$$

$$\frac{\rho_2}{\rho_\infty} = \left(\frac{k-1}{k+1} + \frac{2}{k+1}K_0^{-2}\right)^{-1}, \quad \frac{V_2}{V_1} = 1;$$

$$M_2 = M_\infty \left[\left(\frac{2k}{k+1}K_0^2 - \frac{k-1}{k+1}\right)\left(\frac{k-1}{k+1} + \frac{2}{k+1}K_0^{-2}\right)\right]^{-1/2};$$

$$\tilde{c}_p = \frac{2}{kM_\infty^2}\left\{\left[1 - \frac{k-1}{2}M_2(\Theta_0 - \Theta)\right]^{\frac{2k}{k-1}} - 1\right\};$$

$$K_0 = \frac{k+1}{4}K_1 + \sqrt{\left(\frac{k+1}{4}K_1\right)^2 + 1},$$

where $K_1 = M_\infty \Theta_0$.

After transformations, Formula (IV-7-16) can be brought to the form

$$\bar{p} = \frac{2}{kM_\infty^2}\left\{g\left[1 - f\left(1 - \frac{\Theta}{\Theta_0}\right)\right]^{\frac{2k}{k-1}} - 1\right\}, \qquad \text{(V-5-24)}$$

where

$$g = \frac{2k}{k+1}K_0^2 - \frac{k-1}{k+1}; \qquad \text{(V-5-25)}$$

$$f=\frac{k-1}{2}K_1\left[\left(\frac{2k}{k+1}K_0^2-\frac{k-1}{k+1}\right)\left(\frac{k-1}{k+1}+\frac{2}{k+1}K_0^{-2}\right)\right]^{-1/2}. \qquad \text{(V-5-26)}$$

If the attack angle is large enough, no shock forms on the top of the profile and the pressure distribution can be found by the simple-wave formula

$$\bar{p}=\frac{2}{kM_\infty^2}\left[\left(1+\frac{k-1}{2}M_\infty\Theta\right)^{\frac{2k}{k-1}}-1\right], \qquad \text{(V-5-27)}$$

where the angle Θ is reckoned from the direction of vector $\bar{V}_\infty$.

For $|M_\infty\Theta|\leqslant\frac{2}{k-1}$ the pressure coefficient is set equal to zero.

It must be remembered in calculations with (V-5-24) that it applies when the disturbances reflected from point C of the shock wave do not reach the contour. If, however, the surface of the profile is curved, disturbances reflected from the shock wave must, generally speaking, be taken into consideration in determining pressure. However, study has shown that these disturbances are of low intensity even at high supersonic speeds.

Formula (V-5-24) can be used with an error of less than 10% for $M_\infty > 3$ and $\Theta < 25°$. Its accuracy improves for k close to unity (see Fig. V-5-12).

Influence of physicochemical transformations. A method of flow calculation applicable to an ideal gas was considered earlier. In hypersonic flows in which the properties of the gas differ from those of the ideal gas, the disturbed flow can be determined by the method of characteristics, which takes account of equilibrium chemical reactions [Eqs. (IV-1-46)-(IV-1-50)].

To simplify the problem, we can examine, instead of flow at thermodynamic equilibrium, a "frozen" flow in which the gas has the same equilibrium composition as at a certain point or on a certain zone behind the shock. This flow will correspond to chemical-reaction times longer than the characteristic particle-translation time. /274

For the "frozen" state of a dissociated gas that originally consisted of diatomic molecules, we have the equation $p=\rho(1+\alpha)RT=\rho R_f T$, where $R_f=R(1+\alpha)$ is the gas constant for the "frozen" state. The degree of dissociation α is determined for equilibrium conditions directly behind the shock and assumed constant for the entire flow. The "frozen" gas will be characterized, apart from the modified gas constant R_f, by the effective isentropic specific-heat ratio $k_f=(c_p/c_v)_f$.

For the "frozen" state, in which the rates of all chemical reactions are very low and the vibrational energy levels do not excite owing to the long relaxation time, the isentropic exponent $k_f = (7+3\alpha)/(5+\alpha)$. Another "frozen" state is characterized by chemical-recombination relaxation times that are substantially greater than the relaxation time for vibrational degrees of freedom, which are fully excited behind the shock. For this state, $k_f = (9+\alpha)/(7-\alpha)$. The difference between these two kinds of "frozen" state can be brought out by consideration of the $\alpha = 0$ case. Then the "frozen" gas has $k_f = 7/5$ for the first state and $k_f = 9/7$ for the second with the fully excited vibrational levels.

"Frozen" disturbed flow around a profile can be calculated by the method of characteristics, using (IV-1-17) or (IV-1-18) with the effective value of k_f. To find this value when the type of "frozen" state is known, the equilibrium degree of dissociation α should be determined behind the shock wave. To establish the type of "frozen" flow, it is necessary to know the corresponding gas relaxation times.

Solution for thermodynamic equilibrium conditions. Reference [18] examines a method for solution of the problem of flow of an equilibrium-dissociating gas around a convex surface (see Fig. IV-1-3); it is based on use of diagrams of the thermodynamic functions of air at high temperatures [13]. This flow is described by the differential equation

$$\frac{d\beta}{\sqrt{1+2c_1}} = \frac{dV_r}{-F+\sqrt{F^2+A-V_r^2}},$$

where V_r is the radial velocity component, which coincides in direction with a ray drawn from the vertex of the convex angle and the parameters $F = c_1/\sqrt{1+2c_2}$; $A = 2(i_0 - c_0)$.

The coefficients c_n are determined from the isentropic-flow condition, which takes the form $i = c_0 + c_1 a + c_2 a^2$, using tables or i-a (enthalpy-speed of sound) diagrams for a certain range of enthalpy variation. By solving the differential equation, we obtain the relation between the rotation angle and gas parameters with consideration of dissociation.

For given initial flow conditions, these parameters, as in the case of constant heat capacities, depend on the total rotation angle $\omega = \omega_\infty + \beta$, where ω_∞ is the initial rotation angle reckoned from the direction of the velocity vector that corresponds to M = 1.

Reference [18] presents tables of the angle ω_∞ calculated for various entropies S and enthalpies of stagnation $i_0 = i_\infty + 0{,}5V_\infty^2$. Adding the given flow angle of turn β to ω_∞ and determining $\omega = \omega_\infty + \beta$, we can use the same tables to find the local gas parameters (i, V, a, M). The corresponding pressure and temperature are determined from tables or diagrams of the thermodynamic functions of air for the known i and S. /275

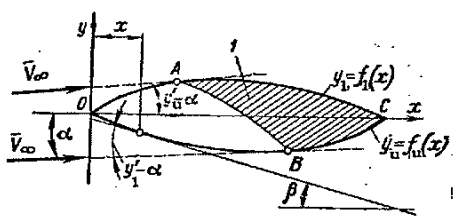

Figure V-5-7. Profile of Arbitrary Form with "Shaded Zone" 1.

As an example [18], let us calculate the variables of an air flow (with the initial conditions V_∞ = 2500 m/s, S = $= 1.4 \cdot 10^4$ m^2/s^2·deg, i = $= 28.87 \cdot 10^6$ m^2/s^2) when it turns through an angle $\beta = 20°$. The stagnation enthalpy $i_0 = 28.87 \cdot 10^6 + 0.5 \cdot 2500^2 = 31.995 \cdot 10^6$ m^2/s^2. From the table [18], we find the angle $\omega_0 = 4.19°$ for this value of i_0 and the given entropy S = $= 1.4 \cdot 10^4$ m^2/s^2·deg and calculate $\omega = 4.19° + 20° = 24.19°$. We find the disturbed parameters for this angle from the same table: V = 3472 m/s, a = 1955 m/s, M = 1.776, and i = 25.973 × $\times 10^6$ m^2/s^2. The following approach should be taken to find the distribution of the parameters of a dissociating gas over the convex surface of a sharp profile. First the dissociating-gas parameters are determined directly behind the shock on the profile nose. These parameters are regarded as initial data for solution of the flow-turn problem. Knowing, for example, the initial enthalpy i_s and speed of sound a_s, we can refer to the i-a diagram [13] to find the entropy S and, with consideration of the total enthalpy $i_0 = i_\infty + 0.5V_\infty^2$, determine the initial angle of turn ω_∞ from the table [18]. Assigning the local inclination angle β of the tangent to the profile contour, we can find the angle $\omega = \omega_\infty + \beta$ and then use the table [18] to determine the gas variables at this point.

The method of "tangent surfaces." For a sharp profile of arbitrary form (Fig. V-5-7, the pressure coefficient can be calculated by the "tangent surface" method. In this method, the pressure at a certain point of the profile is assumed to be the same as on a flat plate inclined to the direction of the oncoming flow at an angle equal to the angle between the tangent to the contour at the particular point and vector $\bar{V}_\infty$.

The initial expressions for the calculation are the formulas for a flat plate. If the attack angle is α, the pressure coefficient on the lower plate surface according to (V-5-13), in which we set $\theta_0 = \alpha$, will be

$$\bar{p}_1 = \frac{k+1}{2}\alpha^2\left\{1+\sqrt{1+\left[\frac{4}{(k+1)M_\infty\alpha}\right]^2}\right\}. \qquad \text{(V-5-28)}$$

Formula (V-5-27) can be used for the top surface with α substituted for θ. Practically the same results are obtained with the expression [6]

$$\bar{p} = -\frac{k+1}{2}\alpha^2\left\{\sqrt{1+\left[\frac{4}{(k+1)M_\infty\alpha}\right]^2}-1\right\}. \qquad \text{(V-5-29)}$$

These formulas give good results when $M_\infty\alpha > 0.5$. Let us use θ to denote the local attack angle for the tangent plane. Then with θ positive, the pressure coefficient at the corresponding point will be

$$\bar{p} = \frac{k+1}{2}\left\{1+\sqrt{1+\left[\frac{4}{(k+1)M_\infty\theta}\right]^2}\right\}\theta^2; \qquad \text{(V-5-30)}$$

for a negative angle /276

$$\bar{p} = -\frac{k+1}{2}\left\{\sqrt{1+\left[\frac{4}{(k+1)M_\infty\theta}\right]^2}-1\right\}\theta^2. \qquad \text{(V-5-31)}$$

The local attack angle

$$\theta = y_1' - \alpha \text{ (on lower surface)};$$

$$\theta = y_u' - \alpha \text{ (on upper surface)},$$

with

$$y_1' = dy_1/dx \text{ (on lower surface)},$$

$$y_u' = dy_u/dx \text{ (on upper surface)},$$

where $y_1 = f_1(x)$ and $y_u = f_u(x)$ are the equations of the lower and upper contours respectively.

In the extreme case with $M_\infty \to \infty$

$$\left.\begin{aligned}\bar{p} &= (k+1)\,\Theta^2 \quad (\Theta > 0);\\ \bar{p} &= 0 \qquad\quad (\Theta \leqslant 0).\end{aligned}\right\} \tag{V-5-32}$$

We can find the other aerodynamic coefficients from the known pressure coefficient.

At small angles of attack, the lift coefficient is calculated by (V-5-16).

This formula can be written

$$c_y = c_{y\infty} + \Delta c_y, \tag{V-5-33}$$

where

$$c_{y\infty} = \int_0^1 (\bar{p}_{1\infty} - \bar{p}_{u\infty})\, d\bar{x} - \tag{V-5-34}$$

is the profile lift coefficient for $M_\infty \to \infty$, and the added term

$$\Delta c_y = \int_0^1 (\Delta\bar{p}_1 - \Delta\bar{p}_u)\, d\bar{x} \tag{V-5-35}$$

accounts for the influence of M_∞. The respective pressure coefficients are

$$\left.\begin{aligned}\bar{p}_\infty &= (k+1)\,\Theta^2 \quad (\Theta > 0);\\ \bar{p}_\infty &= 0 \qquad\quad (\Theta \leqslant 0),\end{aligned}\right\} \tag{V-5-36}$$

and $\Delta\bar{p}$ is determined by the expressions

$$\left.\begin{aligned}\Delta\bar{p} &= \frac{k+1}{2}\left\{1 + \sqrt{1 + \left[\frac{4}{(k+1)\,M_\infty\Theta}\right]^2}\right\}\Theta^2 \quad (\Theta > 0);\\ \Delta\bar{p} &= -\frac{k+1}{2}\left\{\sqrt{1 + \left[\frac{4}{(k+1)^2\,M_\infty\Theta}\right]^2} - 1\right\}\Theta^2 \quad (\Theta \leqslant 0).\end{aligned}\right\} \tag{V-5-37}$$

Formula (V-5-18) for the moment coefficient about the leading edge can be written

$$m_z = m_{z\infty} + \Delta m_z, \tag{V-5-38}$$

where

$$m_{z_\infty} = -\int_0^1 (\bar{p}_{1\infty} - \bar{p}_{u\infty})\,\bar{x}\,d\bar{x}; \qquad \text{(V-5-39)}$$

$$\Delta m_z = -\int_0^1 (\Delta\bar{p}_1 - \Delta\bar{p}_u)\,\bar{x}\,d\bar{x}. \qquad \text{(V-5-40)}$$

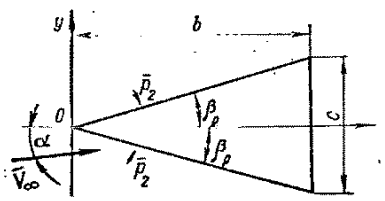

Figure V-5-8. Wedge Profile.

The frontal-drag coefficient of a profile with the local attack angles Θ_l and Θ_u on the lower and upper surfaces is determined by (V-5-17').

Since

$$c_y = c_{y\infty} + \Delta c_y, \quad \bar{p} = \bar{p}_\infty + \Delta\bar{p},$$

then

$$c_{xw} = (c_{xw})_\infty + \Delta c_{xw}, \qquad \text{(V-5-41)}$$

where

$$(c_{xw})_\infty = c_{y\infty}\alpha - \int_0^1 (\bar{p}_{1\infty}y'_l - \bar{p}_{u\infty}y'_u)\,d\bar{x}; \qquad \text{(V-5-42)}$$

$$\Delta c_{xw} = -\int_0^1 (\Delta\bar{p}_1 y'_l - \Delta\bar{p}_u y'_u)\,d\bar{x} + \Delta c_y\alpha. \qquad \text{(V-5-43)}$$

As an example, let us examine a wedge profile (Fig. V-5-8). The local attack angles on the lower and upper surfaces, respectively, are

$$\Theta_l = -\left(\alpha + \frac{\bar{c}}{2}\right); \quad \Theta_u = \alpha - \frac{\bar{c}}{2},$$

where $\bar{c} = c/b$.

If the attack angles $\alpha < \bar{c}/2$,

$$\bar{p}_{1\infty} = (k+1)\left(\alpha + \frac{\bar{c}}{2}\right)^2; \quad \bar{p}_{u\infty} = (k+1)\left(\alpha - \frac{\bar{c}}{2}\right)^2;$$

$$\Delta\bar{p}_l = K_1 M_\infty^2; \quad \Delta\bar{p}_u = K_2 M_\infty^2,$$

where

$$K_{1,2}=\frac{k+1}{2}\left\{\sqrt{1+\left[\frac{4}{(k+1)\,M_\infty\Theta_{1,2}}\right]^2}+1\right\}M_\infty^2\Theta_{1,2}^2,$$

and $\Theta_1 = \Theta_l$ corresponds to K_1 and $\Theta_2 = \Theta_u$ to K_2.

In accordance with the values obtained,

$$\frac{c_{y\infty}}{\bar{c}^2}=2(k+1)\frac{\alpha}{\bar{c}};\quad \frac{\Delta c_y}{\bar{c}^2}=\frac{1}{M_\infty^2\bar{c}^2}(K_1-K_2); \tag{V-5-44}$$

$$\frac{m_{z\infty}}{\bar{c}^2}=-(k+1)\frac{\alpha}{\bar{c}};\quad \frac{\Delta m_z}{\bar{c}^2}=-\frac{1}{2M_\infty^2\bar{c}^2}(K_1-K_2); \tag{V-5-45}$$

$$\frac{(c_{xw})_\infty}{\bar{c}^2}=(k+1)\left(3\frac{\alpha^2}{\bar{c}^2}+\frac{1}{4}\right);\quad \frac{\Delta c_{xw}}{\bar{c}^2}=\frac{1}{M_\infty^2\bar{c}^2}\left[K_1\left(\frac{\alpha}{\bar{c}}+\frac{1}{2}\right)+K_2\left(\frac{1}{2}-\frac{\alpha}{\bar{c}}\right)\right]. \tag{V-5-46}$$

If $\alpha > \bar{c}/2$

$$\left.\begin{aligned}&\bar{p}_{1\infty}=(k+1)\left(\alpha+\frac{\bar{c}}{2}\right)^2;\quad \bar{p}_{u\infty}=0;\\&\Delta\bar{p}_1=\frac{K_1}{M_\infty^2};\quad \Delta\bar{p}_u=-\frac{K_2}{M_\infty^2},\end{aligned}\right\} \tag{V-5-47}$$

where /278

$$\left.\begin{aligned}K_1&=\frac{k+1}{2}\left\{\sqrt{1+\left[\frac{4}{(k+1)\,M_\infty\Theta_1}\right]^2}+1\right\}M_\infty^2\Theta_1^2;\\K_2&=\frac{k+1}{2}\left\{\sqrt{1+\left[\frac{4}{(k+1)\,M_\infty\Theta_u}\right]^2}-1\right\}M_\infty^2\Theta_u^2.\end{aligned}\right\} \tag{V-5-48}$$

In the particular case of a thin plate, we must set $\bar{c} = 0$. Accordingly,

$$c_y=(k+1)\alpha^2\sqrt{1+\left[\frac{4}{(k+1)\,M_\infty\alpha}\right]^2}; \tag{V-5-49}$$

$$c_{xw}=\alpha c_y=(k+1)\alpha^3\sqrt{1+\left[\frac{4}{(k+1)\,M_\infty\alpha}\right]^2}. \tag{V-5-50}$$

At the limit, as $M_\infty\alpha \to \infty$

$$c_y=(k+1)\alpha^2; \tag{V-5-49'}$$

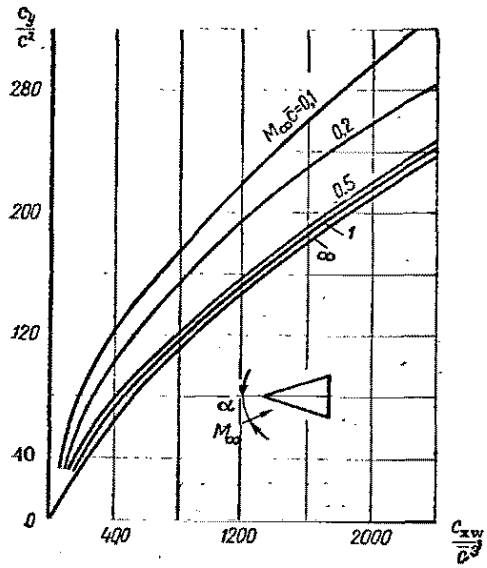

Figure V-5-9. Polars for Wedge Profile.

$$c_{x\,w} = (k+1)\alpha^3. \qquad \text{(V-5-50')}$$

Profile of arbitrary form. Using the above method, we can calculate aerodynamic coefficients for profiles of arbitrary form. It is necessary to know the equations for the lower and upper contours, i.e., the functions $y_l(x)$ and $y_u(x)$.

Calculations indicate that, as in the case of the wedge profile, the coefficients of lift (moment) and wave drag of the profile of arbitrary form, referred respectively to $\bar{c}^2$ and $\bar{c}^3$, are functions of the ratio $\alpha/\bar{c}$.

The corresponding formulas for the three profile types are given in Table V-5-1 [6]. Analysis of these formulas indicates that the polar of the profile expressed by $c_y/\bar{c}^2 = f(c_{x\,w}/\bar{c}^3)$ is a weak function of the ratio $\alpha/\bar{c}$. For approximate determination of $c_y/\bar{c}^2$ as a function of $c_{x\,w}/\bar{c}^3$ in the case of an arbitrary profile, therefore, we can use, for example, the curves for the wedge profile (Fig. V-5-9).

The center of pressure coefficient

$$c_{c.p} = \frac{x_{c.p}}{b} = \frac{m_{z\infty} + \Delta m_z}{c_{y\infty} + \Delta c_y} \qquad \text{(V-5-51)}$$

can be determined from the data in Table V-5-1.

Figure V-5-10 presents curves characterizing the variation of the center of pressure coefficient for the three profiles. The pressure center for the flat plate occurs at half chord of the plate, so that $c_{c.p} = 1/2$.

The lift/drag ratio is to be calculated by the equality

$$K = \frac{c_y}{c_{x\,w}} = \frac{c_{y\infty} + \Delta c_y}{c_{x\infty} + \Delta c_x}. \qquad \text{(V-5-52)}$$

TABLE V-5-1. AERODYNAMIC COEFFICIENTS OF PROFILE AT VERY LARGE M_∞

No.	Profile type	Lift coefficient $c_y/\bar{c}^2 = c_{y\infty}/\bar{c}^2 + \Delta c_y/\bar{c}^2$				Parameter $M_\infty\vert\Theta\vert$ determining coefficient K_n	
		$c_{y\infty}/\bar{c}^2$		$\Delta c_y/\bar{c}^2$			
		$\alpha/\vert\nu'\vert \leq 1$	$\alpha/\vert\nu'\vert > 1$	$\alpha/\vert\nu'\vert \leq 1$	$\alpha/\vert\nu'\vert > 1$		
1	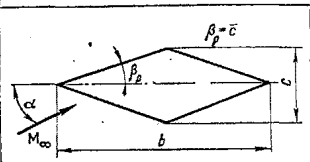	$2(k+1)\frac{\alpha}{\bar{c}}$	$(k+1)\left(\frac{\alpha^2}{\bar{c}^2}+1\right)$	$\frac{1}{M_\infty^2\bar{c}^2}(K_1-K_2)$	$\frac{1}{M_\infty^2\bar{c}^2}(K_1+K_2)$	K_1 K_2	$M_\infty(\alpha+\bar{c})$ $M_\infty(\alpha-\bar{c})$
2	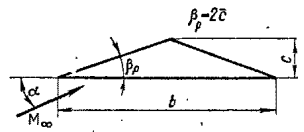	$\frac{1}{2}(k+1)\left(\frac{\alpha^2}{\bar{c}^2}+4\frac{\alpha}{\bar{c}}-4\right)$	$(k+1)\frac{\alpha^2}{\bar{c}^2}$	$\frac{1}{2M_\infty^2\bar{c}^2}\times(2K_1+K_2-K_3)$	$\frac{1}{2M_\infty^2\bar{c}^2}\times(2K_1+K_2+K_3)$	K_1 K_2 K_3	$M_\infty\alpha$ $M_\infty(\alpha-2\bar{c})$ $M_\infty(\alpha+2\bar{c})$
3	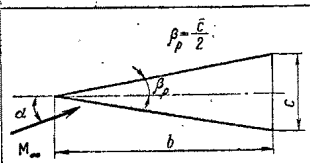	$2(k+1)\frac{\alpha}{\bar{c}}$	$(k+1)\left(\frac{\alpha}{\bar{c}}+\frac{1}{2}\right)^2$	$\frac{1}{M_\infty^2\bar{c}^2}(K_1-K_2)$	$\frac{1}{M_\infty^2\bar{c}^2}(K_1+K_2)$	K_1 K_2	$M_\infty\left(\alpha+\frac{\bar{c}}{2}\right)$ $M_\infty\left(\alpha-\frac{\bar{c}}{2}\right)$

No.	Profile type	Drag coefficient $c_{xw}/\bar{c}^3 = (c_{xw})_\infty/\bar{c}^3 + \Delta c_{xw}/\bar{c}^3$				Parameter $M_\infty\lvert\vartheta\rvert$, determining coefficient K_n	
		$(c_{xw})_\infty/\bar{c}^3$		$\Delta c_{xw}/\bar{c}^3$			
		$\alpha/\lvert\nu'\rvert \leq 1$	$\alpha/\lvert\nu'\rvert > 1$	$\alpha/\lvert\nu'\rvert \leq 1$	$\alpha/\lvert\nu'\rvert > 1$		
1	See Profile type 1, page 374	$(k+1)\times$ $\times\left(3\frac{\alpha^2}{\bar{c}^2}+1\right)$	$(k+1)\frac{\alpha}{\bar{c}}\times$ $\times\left(3+\frac{\alpha^2}{\bar{c}^2}\right)$	$\frac{1}{M_\infty^2\bar{c}^2}\times$ $\times\left[K_1\left(\frac{\alpha}{\bar{c}}+1\right)-\right.$ $\left.-K_2\left(\frac{\alpha}{\bar{c}}-1\right)\right]$	$\frac{1}{M_\infty^2\bar{c}^2}\times$ $\times\left[K_1\left(\frac{\alpha}{\bar{c}}+1\right)+\right.$ $\left.+K_2\left(\frac{\alpha}{\bar{c}}-1\right)\right]$	K_1 K_2	$M_\infty(\alpha+\bar{c})$ $M_\infty(\alpha-\bar{c})$
2	See profile type 2, page 374	$(k+1)\frac{1}{2}\left(\frac{\alpha^3}{\bar{c}^3}+\right.$ $+6\frac{\alpha^2}{\bar{c}^2}-$ $\left.-12\frac{\alpha}{\bar{c}}+8\right)$	$(k+1)\frac{\alpha^3}{\bar{c}^3}$	$\frac{1}{M_\infty^2\bar{c}^2}\left[K_1\frac{\alpha}{\bar{c}}+\right.$ $+\frac{1}{2}K_2\left(\frac{\alpha}{\bar{c}}+2\right)-$ $\left.-\frac{1}{2}K_3\left(\frac{\alpha}{\bar{c}}-2\right)\right]$	$\frac{1}{M_\infty^2\bar{c}^2}\left[K_1\frac{\alpha}{\bar{c}}+\right.$ $+\frac{1}{2}K_2\left(\frac{\alpha}{\bar{c}}+2\right)+$ $\left.+\frac{1}{2}K_3\left(\frac{\alpha}{\bar{c}}-2\right)\right]$	K_1 K_2 K_3	$M_\infty\alpha$ $M_\infty(\alpha-2\bar{c})$ $M_\infty(\alpha+2\bar{c})$
3	See profile type 3, page 374	$(k+1)\times$ $\times\left(3\frac{\alpha^2}{\bar{c}^2}+\frac{1}{4}\right)$	$k(k+1)\times$ $\times\left(\frac{\alpha}{\bar{c}}+\frac{1}{2}\right)^3$	$\frac{1}{M_\infty^2\bar{c}^2}\times$ $\times\left[K_1\left(\frac{\alpha}{\bar{c}}+\frac{1}{2}\right)-\right.$ $\left.-K_2\left(\frac{\alpha}{\bar{c}}-\frac{1}{2}\right)\right]$	$\frac{1}{M_\infty^2\bar{c}^2}\times$ $\times\left[K_1\left(\frac{\alpha}{\bar{c}}+\frac{1}{2}\right)+\right.$ $\left.+K_2\left(\frac{\alpha}{\bar{c}}-\frac{1}{2}\right)\right]$	K_1 K_2	$M_\infty\left(\alpha+\frac{\bar{c}}{2}\right)$ $M_\infty\left(\alpha-\frac{\bar{c}}{2}\right)$

No.	Profile type	Moment coefficient $m_z/\bar{c}^2 = m_{z0}/\bar{c}^2 + \Delta m_z/\bar{c}^2$				Parameter $M_\infty\lvert\Theta\rvert$, determining coefficient K_n	
		$m_{z0}/\bar{c}^2$		$\Delta m_z/\bar{c}^2$			
		$\alpha/\lvert\nu'\rvert \leqslant 1$	$\alpha/\lvert\nu'\rvert > 1$	$\alpha/\lvert\nu'\rvert \leqslant 1$	$\alpha/\lvert\nu'\rvert > 1$		
1	See profile type 1, page 374	$-\frac{1}{2}(k+1)\frac{\alpha}{\bar{c}}$	$-\frac{1}{2}(k+1)\times$ $\times\left(\frac{\alpha^2}{\bar{c}^2}-\frac{\alpha}{\bar{c}}+1\right)$	$-\frac{1}{2M_\infty^2\bar{c}^2}\times$ $\times(K_1-K_2)$	$-\frac{1}{2M_\infty^2\bar{c}^2}\times$ $\times(K_1-K_2)$	K_1 K_2	$M_\infty(\alpha+\bar{c})$ $M_\infty(\alpha-\bar{c})$
2	See profile type 2, page 374	$-\frac{1}{2}(k-1)\times$ $\times\left(\frac{3}{4}\frac{\alpha^2}{\bar{c}^2}+\right.$ $\left.+\frac{3}{2}\frac{\alpha}{\bar{c}}-1\right)$	$-\frac{1}{2}(k+1)\frac{\alpha^2}{\bar{c}^2}$	$-\frac{1}{M_\infty^2\bar{c}^2}\times$ $\times\left(K_1+\frac{3}{4}K_2-\right.$ $\left.-\frac{1}{4}K_3\right)$	$-\frac{1}{2M_\infty^2\bar{c}^2}\times$ $\times\left(K_1+\frac{3}{4}K_2+\right.$ $\left.+\frac{1}{4}K_3\right)$	K_1 K_2 K_3	$M_\infty\alpha$ $M_\infty(\alpha-2\bar{c})$ $M_\infty(\alpha+2\bar{c})$
3	See profile type 3, page 374	$-(k+1)\frac{\alpha}{\bar{c}}$	$-\frac{1}{2}(k+1)\times$ $\times\left(\frac{\alpha}{\bar{c}}+\frac{1}{2}\right)^2$	$-\frac{1}{2M_\infty^2\bar{c}^2}\times$ $\times(K_1-K_2)$	$-\frac{1}{2M_\infty^2\bar{c}^2}\times$ $\times(K_1+K_2)$	K_1 K_2	$M_\infty\left(\alpha+\frac{\bar{c}}{2}\right)$ $M_\infty\left(\alpha-\frac{\bar{c}}{2}\right)$

For very large M_∞, this quantity can be evaluated by the formula $K = c_{y_\infty}/c_{x_\infty}$. /282

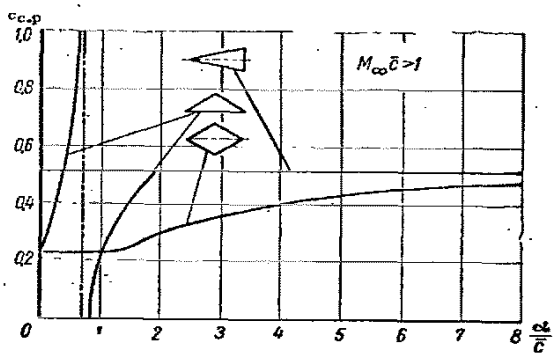

Figure V-5-10. Center of Pressure Coefficient for Profiles at Very Large M_∞.

If we introduce the nomenclature $c_{y_\infty}/\bar{c}^2 = \bar{c}_{y_\infty}$; $(c_{xw})_\infty/\bar{c}^2 = (\bar{c}_{xw})_\infty$,

$$K\bar{c} = \frac{\bar{c}_{y_\infty}}{(\bar{c}_{xw})_\infty}. \qquad \text{(V-5-53)}$$

Figure V-5-11 presents values of $K\bar{c}$ for three profiles with rectilinear contours.

Variable heat capacities. Let us consider a very-high-velocity flow of an ideal gas over a profile when the isentropic specific-heat ratio behind the shock varies and a certain fixed value of $k_2 < k_\infty$ is preserved. According to the method of tangent wedges, the pressure coefficient at a certain point on a thin profile with angle $\Theta > 0$ is

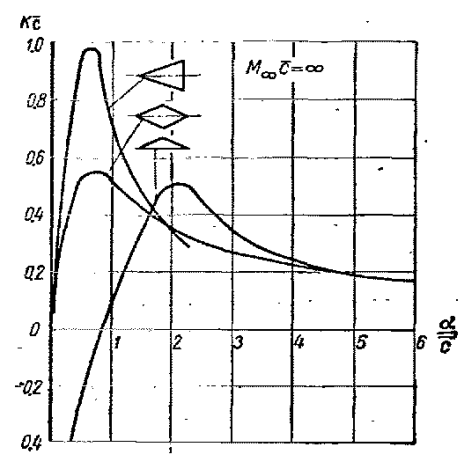

Figure V-5-11. Curves for Calculation of Lift/Drag Ratios of Profiles with Rectilinear Contours.

$$\bar{p} = 2\Theta^2(1-\bar{\rho})^{-1} = \frac{2\Theta^2}{1-\bar{\rho}_c}\left[1 + \frac{\bar{\rho}_c(\bar{\rho}_\infty - \bar{\rho}_c)}{k_\infty K_1^2}\right], \qquad \text{(V-5-54)}$$

where

$$\bar{\rho} = \rho_\infty/\rho_2;\ \bar{\rho}_c = (k_2-1)/(k_2+1);$$
$$\rho_\infty = (k_\infty - 1)/(k_\infty + 1);$$
$$K_1 = M_\infty\Theta \gg 1.$$

The tangent-wedge method can be improved by considering the effect of the curvature resulting from centrifugal forces. The corresponding formula, derived for very small $1/\bar{\rho}$, takes the form

$$\bar{p} = 2\Theta^2(1-\bar{\rho})^{-1} - \frac{2y}{R}, \qquad \text{(V-5-54')}$$

where y is the coordinate of the profile point reckoned along the normal to vector $\bar{V}_\infty$ and R is the profile radius of curvature.

Calculation by the Busemann formula. The Busemann formula (IV-7-22) gives better results than the Newton method in the pressure calculation for concave profiles with k = 1.4 and for convex profiles as k → ∞. /283

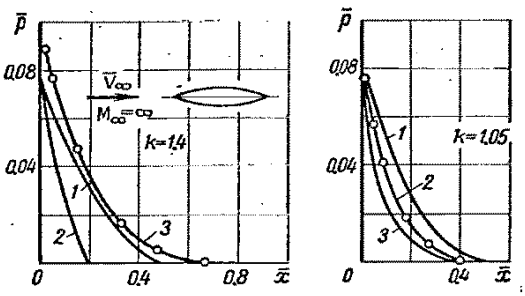

Figure V-5-12. Pressure Distribution over Profile ($M_\infty = \infty$, $\bar{c} = 0.1$). 1) According to Newton formula; 2) according to Busemann formula; 3) according to method using relationships on the shock and in a simple wave; o) according to the method of characteristics.

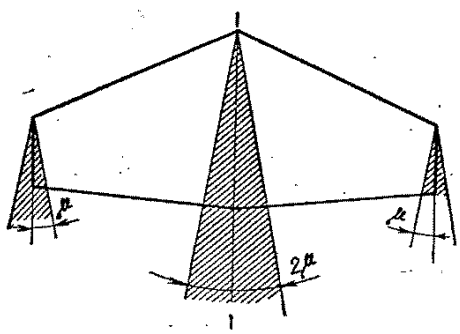

Figure V-5-13. Zones of Influence at Very Large M_∞.

Setting f(x) = 1 in this formula, we obtain the following working relation for the profile:

$$\bar{p} = \frac{\bar{p}^*}{\sin^2\beta_p}\left(\sin^2\beta - \frac{1}{R}\int_0^S \cos\beta\, dS\right). \qquad \text{(V-5-55)}$$

For a thin profile, we can use (IV-7-21), setting ν = 1:

$$\bar{p} = \frac{\bar{p}^*}{\beta_p^2}\left(\beta^2 + y\frac{d^2y}{dx^2}\right), \qquad \text{(V-5-55')}$$

where y = y(x) is the equation of the profile contour.

For comparison, Fig. V-5-12 presents results of pressure calculations by the Newton and Busemann formulas and by the method of characteristics. We see that for k = 1.05, the Busemann formula gives results close to those obtained by the method of characteristics.

Similarity law for flow around profiles. Research has established that $K = M_\infty\bar{c}$ and $\alpha/\bar{c}$ are similarity parameters for

flow around thin profiles. This follows, for example, from the "tangent-surface" method. The general form of the similarity formulas for drag and lift is as follows:

$$\frac{c_{xw}}{\bar{c}^3} = F_1\left(K, \frac{\alpha}{\bar{c}}\right); \frac{c_y}{\bar{c}^2} = F_2\left(K, \frac{\alpha}{\bar{c}}\right). \qquad \text{(V-5-56)}$$

For $K \to \infty$. the ratios $c_{x\,w}/\bar{c}^3$ and $c_y/\bar{c}^2$ become functions of only the one parameter $\alpha/\bar{c}$, as is confirmed by calculations using the Newton method and the Busemann formula.

Wings of finite span. Flow over finite-span wings can be calculated by the "method of strips." This method gives better results at very high speeds than at moderate M_∞.

This is because the zones of influence of the lateral edges narrow considerably at high speeds, as does the zone of influence exerted on the wing around the root section by disturbances originating from the vertex (Fig. V-5-13), so that they become very small by comparison with the total wing area.

One of the methods set forth above can be used to calculate hypersonic flow over the profile (strip), and the over-all aerodynamic coefficients of a wing of given planform can be found by spanwise integration of the aerodynamic characteristics obtained for the strip. /284

The similarity formulas (V-5-56), which should be regarded as expressions for the local aerodynamic coefficients, can be used to calculate the total characteristics. When the profile thickness ratio does not change along the span, Formulas (V-5-56) will give the aerodynamic-coefficient values for the entire wing.

§V-6. WAKE DRAG. VISCOUS INTERACTION

Wake drag. A wake drag is added to the drag components due to friction and pressure on the forward surface for wings with blunt trailing edges. Research has shown that the wake pressure, which determines wake drag, depends substantially on the structure of the boundary layer on the area between the trailing edge (point of separation) and the sticking point on the axial line at which the boundary layer detached from the trailing edge converges.

Purely turbulent and purely laminar flows. If the point of transition of a laminar boundary layer to turbulent lies upstream of the detachment point (base section), the flow will be purely turbulent on the segment between this point and the sticking point. Figure V-6-1 shows the variation of wake pressure for this case. The curve characterizing the ratio of the wake pressure

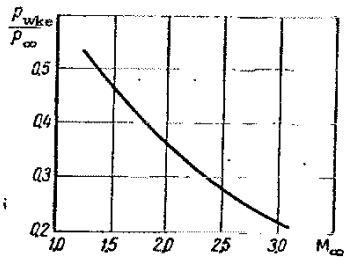

Figure V-6-1. Variation of Wake Drag Behind a Profile with Relatively Thin Boundary Layer.

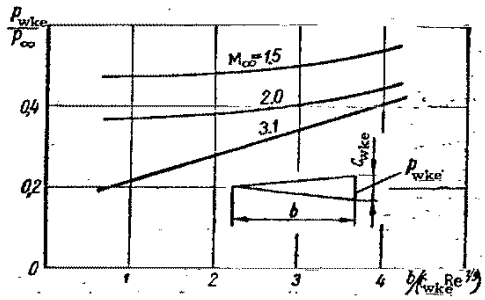

Figure V-6-2. Influence of Reynolds Number on Wake Pressure for Turbulent Boundary Layer.

behind the bluff base of the profile to the free-stream pressure determines the wake pressure for profiles with relatively thin turbulent layers in accordance with the formula $p_{wke}/p_\infty = f_t(M_\infty)$. In a more general case, the formula should also reflect the dependence of wake pressure on boundary-layer thickness. Available experimental data point to the more general relation

$$\frac{p_{wke}}{p_\infty} = f_t\left(M_\infty, \frac{\delta}{c_{wke}}\right), \qquad \text{(V-6-1)}$$

where c_{wke} is the thickness of the trailing edge.

Introducing the Reynolds number, we obtain

$$\frac{p_{wke}}{p_\infty} = f_t\left(M_\infty, \frac{b}{c_{wke}\,Re^{1/5}}\right), \qquad \text{(V-6-2)}$$

where b is the profile chord.

A similar relation can also be obtained for purely laminar boundary layers in which the transition point is downstream of the sticking point: /285

$$\frac{p_{wke}}{p_\infty} = f_1\left(M_\infty, \frac{b}{c_{wke}\,Re^{1/2}}\right). \qquad \text{(V-6-3)}$$

Experimental curves corresponding to (V-6-1) appear in Fig. V-6-2.

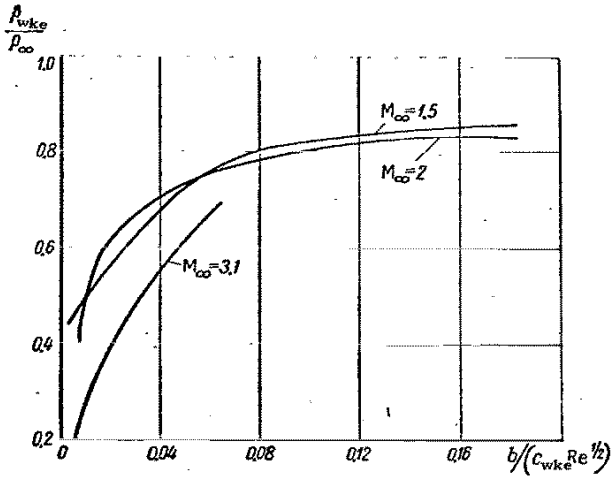

Figure V-6-3. Variation of Wake Pressure Behind Profile with Mixed Boundary Layer.

Mixed flow. A mixed boundary layer forms when the transition point lies between the detachment and sticking points. Under this flow condition, study of the wake pressure becomes particularly difficult, primarily because of unclear definition of the transition point. Wake pressure in the presence of a mixed bounary layer has been studied by wind-tunnel testing of wing models. The results of these measurements permit the conclusion that the relative wake pressure can be represented by (V-6-1) and plotted graphically in the form of a family of curves, as shown in Fig. V-6-3. The wake pressure behind the profile increases with increasing parameter $b/(c_{wke}Re^{1/2})$. At small Reynolds numbers (large values of this parameter), a laminar boundary layer is observed in practice between the detachment and sticking points, and the wake pressure is found to be higher than is characteristic for a purely laminar flow.

Wake pressure is also influenced by other parameters, such as the attack angle and heating or cooling of the boundary layer.

Viscous interaction. Let us consider the change in pressure on the surface of a sharpened profile owing to interaction of a hypersonic boundary layer with an inviscid flow.

Weak interaction. In weak interaction, the pressure varies only moderately from the original conditions. Values of $K^* \leq 1$ or $d\delta^*/dx < \beta$ with arbitrary $K = M_\infty\beta$ correspond to weak interaction [see Formula (IV-10-2)]. Such interactions arise on thin wedges at small angles of attack and large Re and M, or at moderate supersonic speeds and small Re. Weak interaction occurs on thick /286
wedges at large angles of attack on the side of the wedge at which the compression occurs.

Applying the theory of the oblique compression shock and the tangent-wedge method, we arrive at the following relationship for induced pressure [59] for a wedge with a laminar boundary layer and a wall inclination angle $\beta^* = \beta + d\delta^*/dx$:

$$\frac{p}{p_i} = 1 + kE_1\bar{\chi}_i + \frac{k(k+1)}{4}E_2\bar{\chi}_i^2 + \ldots, \qquad \text{(V-6-4)}$$

where

$$E_1 = \frac{M_\infty}{M_i}J_1 d_i; \quad E_2 = \left(\frac{M_\infty}{M_i}\right)^2 J_2 d_i^2. \qquad \text{(V-6-5)}$$

The quantity $\bar{\chi}_i$ is a hypersonic interaction parameter defined by the relation

$$\bar{\chi}_i = M_i^3 c_i^{1/2}\,\mathrm{Re}_{xi}^{-1/2}. \qquad \text{(V-6-6)}$$

The subscript i pertains to initial conditions in a homogeneous flow of inviscid gas around the wedge. The other parameters are:

$$J_1 = \frac{p_\infty}{p_i}\left[\frac{k+1}{2}K + \sqrt{1+\left(\frac{k+1}{4}\right)^2 K^2}\right]; \qquad \text{(V-6-7)}$$

$$J_2 = \frac{p_\infty}{p_i}\left\{1 + \frac{\frac{k+1}{4}K\left[\left(\frac{k+1}{4}\right)^2 K^2 - \frac{3}{2}\right]}{\left[1+\left(\frac{k+1}{4}\right)^2 K^2\right]^{3/2}}\right\}; \qquad \text{(V-6-8)}$$

$$c_i = \frac{\mu_{wi}}{\mu_i}\frac{T_i}{T_{wi}}; \quad d_i = \frac{A}{M_i^2}\frac{T_{wi}}{T_i} + (k-1)B; \quad \mathrm{Re}_{x\,i} = \frac{xV_{\delta i}}{\nu_i}. \qquad \text{(V-6-9)}$$

The coefficients A and B are functions of Prandtl number. For Pr = 1, A = 0.865, B = 0.166; for Pr = 0.725 the coefficients A = 0.968 and B = 0.145. We may assume for a heat-insulated wall

$$\frac{T_{wi}}{T_i} = 1 + \sqrt{\mathrm{Pr}}\,\frac{k-1}{2}M_i^2; \quad d_i = (k-1)D, \qquad \text{(V-6-10)}$$

where D = 0.599 for Pr = 1 and D = 0.556 for Pr = 0.725. For a very cold wall, $T_{wi}/T_i \ll 1$ and, in approximation,

$$d_i = (k-1)B. \qquad \text{(V-6-11)}$$

In both particular cases, the induced pressure is determined only by the parameters K and χ_i. If we introduce the interaction parameter

$$\bar{\chi} = M_\infty^3 c_\infty^{1/2} \mathrm{Re}_{x\infty}^{-1/2},$$

which is determined for the conditions in undisturbed flow, the ratio $\bar{\chi}_1/\bar{\chi}$ will depend only on $K = M_\infty \cdot \beta$. For $K >> 1$,

$$p_1/p_\infty = \frac{k(k+1)}{2} K^2; \quad J_1 = \frac{2}{kK}; \quad J_2 = \frac{4}{k(k+1)K^2}; \quad M_1\beta = \sqrt{\frac{2}{k(k-1)}}.$$

Since $\mu_1 \sim M_\infty^2 \beta^2$ for $\mu \sim T$, we have $(M_\infty/M_1)(\bar{\chi}_1/K) \sim \bar{\chi}/K^2$.

Consequently, the order of magnitude of the pressure change is

$$\frac{p}{p_1} - 1 \sim d_1 \frac{\bar{\chi}}{K^2}. \qquad \text{(V-6-12)}$$

For a flat plate at zero attack angle $K = 0$, $J_1 = J_2 = 1$. /287
Experimental data obtained for a heat-insulated plate confirm the results obtained from (V-6-4) for $k = 1.4$ and $Pr = 0.725$ for the pressure ratio

$$\frac{\bar{p}}{p_\infty} = 1 + 0.31\bar{\chi} + 0.05\bar{\chi}^2. \qquad \text{(V-6-13)}$$

Good agreement is observed between experiment and the weak-interaction formula up to values of the hypersonic parameter $\bar{\chi} = 3\text{-}4$.

Research has shown that the local heat flow and equilibrium wall temperature depend very little on induced pressure. The local coefficient of friction varies more extensively in accordance with the relation

$$c_{fx}^{(p)} = c_{fx} + \frac{2J_1^2}{M_1^2}\left(M_\infty \frac{d\delta^*}{dx}\right)^2, \qquad \text{(V-6-14)}$$

where $c_{fx}^{(p)}$, c_{fx} are the local coefficients of friction with and without an induced pressure, respectively; the derivative

$$\frac{d\delta^*}{dx} = d_1 \frac{\bar{\chi}_1}{M_1} = d_1 \sqrt{c_1}\, \frac{M_1^2}{\sqrt{\mathrm{Re}_{w1}}}. \qquad \text{(V-6-15)}$$

Strong interaction. The region of strong interaction is characterized by $d\delta^*/dx > \beta$ and $K^* >> 1$. This region is formed in flow around a plate at a small angle of attack when the Mach

numbers are quite large and the local Reynolds numbers are not large.

TABLE V-6-1. PARAMETERS FOR CALCULATION OF VISCOUS INTERACTION

g_{w1}	c	s	p_0
0	0.208	0.0788	0.149
0.2	0.279	0.105	0.232
0.6	0.412	0.155	0.377
1.0	0.549	0.187	0.514

The strong interaction can be analyzed by the method of tangent wedges, which gives the following relationship for the induced pressure:

$$\frac{p}{p_\infty}=\frac{k(k+1)}{2}K^{*2}+\frac{3k+1}{k+1}\frac{8k}{(k+1)^3}K^{*-2}, \quad \text{(V-6-16)}$$

where $K^*=M_\infty(\beta+d\delta^*/dx)$.

The expression for p/p_∞ can be written

$$\frac{p}{p_\infty}=p_0\bar{\chi}\left(1+\frac{p_1K}{\bar{\chi}^{1/2}}+\frac{p_2+p_3K^2}{\bar{\chi}}\right). \quad \text{(V-6-17)}$$

Here p_0 depends on the wall cooling $g_{w1}=i_{w1}/i_{0\delta}$. Table V-6-1 gives values of p_0 for $k = 1.4$ and $Pr = 1$. The coefficients p_1, p_2, and p_3 are determined experimentally or from hypersonic boundary-layer theory. For a plate, $K = M_\infty\beta = 0$ and

$$\frac{p}{p_\infty}=p_0\bar{\chi}+p_2. \quad \text{(V-6-18)}$$

For a heat-insulated wall at $Pr = 1$ and $k = 1.4$, calculations give $p_2 = 0.759$. Consequently,

$$\frac{p}{p_\infty}=0.514\bar{\chi}+0.759. \quad \text{(V-6-18')}$$

This formula agrees with experimental data for $\bar{\chi}=M_\infty^3c_\infty^{1/2}\mathrm{Re}_{x\infty}^{-1/2}=3.5$-7.

To estimate the variation of the coefficients of friction and heat transfer at strong interaction, we can use the relationships

$$c_{fx}=c\bar{\chi}^{-1/2};\quad \mathrm{St}_x=s\bar{\chi}^{1/2}=\frac{q}{\rho_\infty V_\infty c_p(T_r-T_{w1})}. \quad \text{(V-6-19)}$$

Table V-6-1 gives the coefficients c and s for k = 1.4 and Pr = 1.

§V-7. AERODYNAMICS OF BLUNT WEDGES AT HIGH SUPERSONIC SPEEDS /288

Flow Around Blunt Profile Leading Edge

Separation and shape of shock wave. Let us consider flow around the front of a profile whose contour has an arbitrary curvilinear shape (Fig. V-7-1).

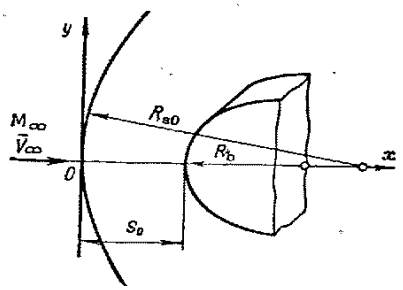

Figure V-7-1. Blunt Leading Edge of Profile in Supersonic Flow.

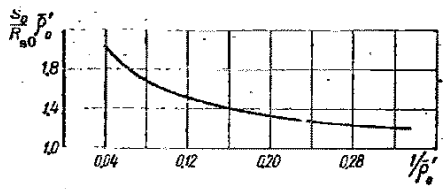

Figure V-7-2. Parameter Characterizing Distance to Shock Wave from Total-Stagnation Point of a Cylinder.

The flow around the blunt edge is characterized by formation of a detached curvilinear shock wave. Research has shown that the distance s_0 from the shock wave to the critical point depends on the radius of curvature of the wave on the axis, R_{s_0}, and on M_∞. The ratio s_0/R_{s_0} is determined by the expression

$$\frac{s_0}{R_{s0}} = \frac{k+1}{2}\,\frac{M_\infty^2-1}{kM_\infty^2-\frac{k-1}{2}}\left(\sqrt{1+2\,\frac{1+\frac{k-1}{2}M_\infty^2}{M_\infty^2-1}}-1\right). \qquad \text{(V-7-1)}$$

In the limit as $M_\infty \to \infty$ at k = 1.4, the ratio $s_0/R_{s0} = 0.1586$. At very high speeds, it is necessary to consider the influence of dissociation and ionization of the gas in the shock layer. In this case, the following expression [59] should be used instead of (V-7-1):

$$\frac{s_0}{R_{s0}} = \frac{1}{2\bar{\rho}_2}\left[\ln\frac{4\bar{\rho}_2}{3}\left(1+\frac{1}{2\bar{\rho}_2}\right)+\frac{1}{2\bar{\rho}_2}\right], \qquad \text{(V-7-2)}$$

Practical interest attaches to calculation of the wave-drag coefficient of a blunt nose. Let the segment length of this nose (along the chord) be x_e, and let the nose be symmetrical about the chord. The drag coefficient referred to the total length of the nose (its chord) is

$$c_{x\,w}=\frac{2\bar{p}_0}{x_e}\int_0^{x_e}\frac{\sin^3\beta}{\cos\beta}\,dx. \qquad \text{(V-7-4)}$$

In the particular case in which the nose contour is a circular arc, the expression for $c_{x\,w}$ will be

$$c_{x\,w}=2\bar{p}_0\frac{\cos\beta}{1-\sin\beta}\left(1-\frac{\cos^2\beta}{3}\right). \qquad \text{(V-7-5)}$$

For a semicircular contour ($\beta = 0$),

$$c_{x\,w}=\frac{4}{3}\bar{p}_0. \qquad \text{(V-7-5')}$$

Calculation of flow around profile with blunt curvilinear contour using Newtonian theory. When the Newton formula is used, the pressure distribution for a profile with a blunt nose is calculated in the same way as that for a profile with a sharp leading edge.

In the general case, such profiles may have "blanketed zones" with zero excess pressure on both the top and bottom surfaces when local areas of the contour have a negative inclination to the oncoming-flow velocity vector.

The calculations are simplified to a degree when there are no such areas and, consequently, the entire contour interacts with gas particles. In this case, the excess pressure will be positive everywhere on the contour. For convenience in the calculations, we can arbitrarily isolate the blunt nose and peripheral parts from the total contour. The aerodynamic coefficient is calculated as the sum of two components for each of these parts.

Consider, for example, the expression for the frontal drag of a profile in the form of a symmetrical wedge with a rounded nose in flow at zero angle of attack. If the nose length is x_e, the profile length is x_p, and the inclination angle of the wedge plane is β, then the drag coefficient calculated for length x_p is

$$c_{xw}=2\bar{p}_0\left[\frac{\cos\beta}{1-\sin\beta}\left(1-\frac{\cos^2\beta}{3}\right)\frac{x_e}{x_p}+\frac{\sin^3\beta}{\cos\beta}\left(1-\frac{x_e}{x_p}\right)\right]. \qquad \text{(V-7-6)}$$

This value of $c_{x\,w}$ may be set equal to the axial-force coefficient in considering flow around the profile at an angle of attack when the velocity head is calculated by the expression $0.5\rho_\infty V_\infty^2 \cos^2\beta$. The axial force

$$R_p=c_{xp}\frac{\rho_\infty V_\infty^2\cos^2\beta}{2}x_p.$$

Consequently, the axial-force coefficient, referred to the velocity head $\rho_\infty V_\infty^2/2$, is

$$c_{xp}=c_{xw}\cos^2\beta. \qquad \text{(V-7-7)}$$

Bluntness in the Form of a Flat Plate /291

Flow scheme and equation system [47]. Let us examine the flow scheme in the coordinates X, Y around the leading edge of a profile in the form of a flat plate of width 2b (Fig. V-7-5). A curvilinear wave forms in front of the plate, at a distance s_0 from the critical point. The velocity components referred to V_∞ will be denoted for an arbitrary streamline point by $\bar{V}_Y = V_Y/V_\infty$; $\bar{V}_X = V_X/V_\infty$.

To calculate inviscid two-dimensional flow around a plate when a curvilinear shock forms, it is necessary to use a system of gasdynamic equations including an equation of continuity, equations of motion in the projections onto the Y- and X-axes, and an entropy equation.

In the general case, solution of this system is a highly complex problem. The system can be simplified on the basis of a model of two-dimensional Newtonial flow when $1/\bar{\rho}_2 = \rho_\infty/\rho_2$ is zero and the wave applies directly to the surface of the plate. Assuming the flow velocity to be large enough and the flow to be close to the limiting Newtonian case, we can treat $\bar{\rho} = \delta_0$ as a small parameter ($\bar{\rho} = \delta_0$ is the density ratio for the normal compression shock) and present the variables characterizing the flow in the form of a series in this small parameter. The expansion is based on determination of the order of the gasdynamic variables behind the shock by use of the following relationships:

$$\frac{1}{\bar{\rho}_2}=\delta_0\left(1+\frac{\bar{i}_\infty}{1+\bar{i}_\infty}\operatorname{tg}^2\Theta_s\right); \qquad \text{(V-7-8)}$$

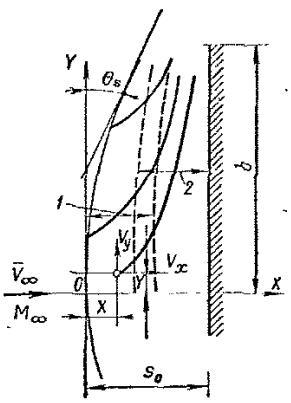

Figure V-7-5. Two-Dimensional Plane Supersonic Flow Around a Blunt Nose. 1) region of external series expansion; 2) region of internal series expansion.

$$\bar{\bar{p}}_2 - \bar{\bar{p}}_\infty = 1 - \delta_0 - \operatorname{tg}^2\Theta_s; \qquad \text{(V-7-9)}$$

$$\bar{V}_{X_2} = (\delta_0 + \operatorname{tg}^2\Theta_s)(1 - \operatorname{tg}^2\Theta_s); \qquad \text{(V-7-10)}$$

$$\bar{V}_{Y_2} = (1 - \delta_0 - \operatorname{tg}^2\Theta_s)\operatorname{tg}\Theta_s; \qquad \text{(V-7-11)}$$

$$\bar{i}_2 = 1 + \bar{i}_\infty - \operatorname{tg}^2\Theta_s, \qquad \text{(V-7-12)}$$

where $\bar{\bar{p}}_2 = p_2/\rho_\infty V_\infty^2$; $\bar{\bar{p}}_\infty = p_\infty/\rho_\infty V_\infty^2$; $\bar{i}_2 = i_2/(0{,}5V_\infty^2)$, $\bar{i}_\infty = i_\infty/(0{,}5V_\infty^2)$, and

$$\delta_0 = \frac{k-1}{k+1} + \frac{2}{(k+1)\,M_\infty^2}. \qquad \text{(V-7-13)}$$

When $\delta_0 \to 0$ and the shock applies to the nose, the slope of the shock with respect to the vertical axis is of the order $\delta_0^{1/2}$, i.e., $\tan\Theta_s = O(\delta_0^{1/2})$. The orders of magnitude of the other parameters are determined accordingly, namely:

$$\frac{1}{\bar{\rho}_2} = \delta_0 + O(\delta_0^2), \quad \bar{\bar{p}}_2 - \bar{\bar{p}}_\infty = 1 + O(\delta_0), \quad \bar{V}_{X2} = O(\delta_0), \quad \bar{V}_{Y2} = O(\delta_0^{1/2}).$$

Let us introduce the new coordinate $x = X\delta_0^{-1/2}$, but keep the old content of the variable Y, which we shall denote by $y = Y$ for the sake of tidiness. Taking account of the orders of magnitude of the variables behind the shock, we can express the quantities characterizing the flow in the disturbed flow region next to the shock in the form of expansions in powers of the small parameter δ_0: /292

$$\bar{V}_x = \delta_0 u(x, y) + \ldots; \qquad \text{(V-7-14)}$$

$$\bar{V}_y = \delta_0^{1/2} v(x, y) + \ldots; \qquad \text{(V-7-15)}$$

$$\bar{\bar{p}} - \bar{\bar{p}}_\infty = 1 + \delta_0 p(x, y) + \ldots; \qquad \text{(V-7-16)}$$

$$\bar{\rho} = \delta_0^{-1} + \rho(x, y) + \ldots, \qquad \text{(V-7-17)}$$

where u, v, p, and ρ are certain dimensionless functions of the variables $x = X\delta_0^{-1/2}$, $y = Y$.

Considering the form of Expansions (V-7-14)-(V-7-17) and using the new coordinate $x = X\delta_0^{-1/2}$, we can obtain the equations for the disturbed flow in a simplified (limit) form. Take, for example, the continuity equation $\partial(\rho V_X)/\partial X + \partial(\rho V_Y)/\partial Y = 0$. After appropriate substitutions

$$\delta_0 u \frac{\partial \rho}{\partial X} + (\delta_0^{-1} + \rho)\,\delta_0 \frac{\partial u}{\partial X} + \delta^{1/2} v \frac{\partial \rho}{\partial Y} + (\delta_0^{-1} + \rho)\,\delta_0^{1/2} \frac{\partial v}{\partial Y} = 0.$$

Comparing the terms in the left member of the equation, we note that the first and third are of higher negative order and can be disregarded. The equation then becomes

$$(\delta_0^{-1} + \rho)\,\delta_0 \frac{\partial u}{\partial X} + (\delta_0^{-1} + \rho)\,\delta_0^{1/2} \frac{\partial v}{\partial Y} = 0.$$

Substituting the values $\partial u/\partial X = (\partial u/\partial x)\,\delta_0^{-1/2}$, $\partial v/\partial Y = \partial v/\partial y$, of the derivatives, we obtain $\partial u/\partial x + \partial v/\partial y = 0$. In the coordinates $\underline{x}$, $\underline{y}$, therefore, the continuity equation has been brought to the form for an incompressible fluid. Simplified forms of the other system equations can be obtained similarly. As a result, the equation system will be

$$\frac{\partial u}{\partial x} + \frac{\partial v}{\partial y} = 0; \qquad \text{(V-7-18)}$$

$$u \frac{\partial v}{\partial x} + v \frac{\partial v}{\partial y} = 0; \qquad \text{(V-7-19)}$$

$$u \frac{\partial u}{\partial x} + v \frac{\partial u}{\partial y} = -\frac{\partial p}{\partial x}; \qquad \text{(V-7-20)}$$

$$u \frac{\partial (p-\rho)}{\partial x} + v \frac{\partial (p-\rho)}{\partial y} = 0. \qquad \text{(V-7-21)}$$

Equation (V-7-19) has been obtained for the condition that in the equation

$$\bar{V}_X (\partial \bar{V}_Y/\partial X) + \bar{V}_Y (\partial \bar{V}_Y/\partial Y) = -(1/\bar{\rho})\,\partial \bar{\bar{p}}/\partial Y,$$

transformed to the variables $y = Y$, $x = X\delta_0^{-1/2}$ with application of Expansions (V-7-14)-(V-7-17), the term $\partial \bar{\bar{p}}/\partial Y$ is negligibly small and that we can set $\partial p/\partial y = 0$.

It follows from this that the pressure does not change in the direction of the axis $Y = y$. The first two equations of the system enable us to determine the velocity field. The third and fourth serve for calculation of the pressure and correction of the density.

The boundary conditions are determined by the conditions of flow immediately behind the compression shock and on the surface of the nose. It follows from (V-7-9)-(V-7-11), (V-7-14)-(V-7-16), and the relation $(dX/dY)_2 = \tan \Theta_s$ that the functions $\underline{u}$, $\underline{v}$, and $\underline{p}$ must satisfy the following conditions on the shock wave: /293

$$v_2 = \left(\frac{dx}{dy}\right)_2; \qquad \text{(V-7-22)}$$

$$u_2 = 1 + v_x^2 = -p_2. \qquad \text{(V-7-23)}$$

Investigation shows that the condition u/v → 0 cannot be satisfied on the surface, since the two-dimensional flow described by equation system (V-7-18)-(V-7-21) does not occur near this surface. More precisely, the velocities here are different in order of magnitude from those near the shock, although the orders of magnitude of the pressure and density remain the same over the entire flow region between the shock and the nose. Hence the region of flow between the curvilinear wave and the plate must be resolved into two parts: external and internal expansion regions (see Fig. V-7-5). The flow in the outer region is described by System (V-7-18)-(V-7-21) and by conditions (V-7-22)-(V-7-23). As concerns the internal region, where the nonseparating-flow condition u/v → 0 must be satisfied, the flow parameters can be presented in the form of the expansions

$$\bar{V}_x = \delta_0^{3/2}\tilde{u}(\tilde{x}, y) + \ldots; \qquad \text{(V-7-24)}$$

$$\bar{V}_y = \delta_0\tilde{v}(\tilde{x}, y) + \ldots; \qquad \text{(V-7-25)}$$

$$\bar{\bar{p}} - \bar{\bar{p}}_\infty = 1 + \delta_0\tilde{p}(\tilde{x}, y) + \ldots; \qquad \text{(V-7-26)}$$

$$\bar{\rho} = \rho_0^{-1} + \tilde{\rho}(\tilde{x}, y) + \ldots, \qquad \text{(V-7-27)}$$

where $\tilde{x}$ is the variable corresponding to the inner region and is determined by the equality $\tilde{x} = \delta_0^{-1/2}(X - s_0)$; $\tilde{u}$, $\tilde{v}$, $\tilde{p}$, $\tilde{\rho}$ are variables analogous to u, v, p and ρ in the internal expansion region.

After substituting Expansions (V-7-24)-(V-7-27) into the continuity, motion and entropy equations,

$$\frac{\partial\tilde{u}}{\partial\tilde{x}} + \frac{\partial\tilde{v}}{\partial y} = 0; \qquad \text{(V-7-28)}$$

$$\frac{\partial\tilde{p}}{\partial\tilde{x}} = 0; \qquad \text{(V-7-29)}$$

$$\tilde{u}\frac{\partial\tilde{v}}{\partial\tilde{x}} + \tilde{v}\frac{\partial\tilde{v}}{\partial y} = -\frac{\partial\tilde{p}}{\partial y}; \qquad \text{(V-7-30)}$$

$$\tilde{u}\frac{\partial(\tilde{p}-\tilde{\rho})}{\partial\tilde{x}} + \tilde{v}\frac{\partial(\tilde{p}-\tilde{\rho})}{\partial y} = 0. \qquad \text{(V-7-31)}$$

We see from the second equation that the pressure is independent of $\tilde{x}$ and depends only on y.

The solution of this equation system must satisfy the boundary conditions at the wall

$$\tilde{u}(o, y) = 0; \quad \tilde{v}(o, y) = V_\delta(y), \tag{V-7-32}$$

where V_δ is the velocity at the wall found by integration of (V-7-30) with the condition that $\tilde{u} = 0$, and is related to pressure by the formula

$$p_\delta(y) + \frac{V_\delta^2(y)}{2} = \text{const}. \tag{V-7-33}$$

For a given y, this quantity will determine the pressure throughout the inner region. Consequently, $\partial\tilde{p}/\partial y = -2V_\delta (dV_\delta/d\tilde{y})$ and (V-7-30) becomes a purely kinematic relation. Solving Eqs. (V-7-28) and (V-7-30), we can find the velocity values $\tilde{u}(\tilde{x},\tilde{y})$ and $\tilde{v}(\tilde{x},\tilde{y})$, which satisfy the boundary conditions at the wall (V-7-32). /294

The solutions of the equations for the outer and inner regions, which satisfy the boundary conditions on the shock and on the wall, respectively, are also subject to conjugation conditions at the boundary between the two regions, so that the flow in the region under consideration can be determined uniquely.

Results of solution of the equations. Without dwelling on the method of solving the equations or conjugating the resulting solutions, we present only the basic results that are of practical importance for aerodynamic calculations.

Separation and shape of shock wave. The distance to the shock wave in dimensionless form is

$$\bar{s}_0 = \frac{s_0}{b} = -1.23\delta_0^{1/2} \ln \delta_0^{1/2}. \tag{V-7-34}$$

The equation of the shock wave curve can be given in the following approximate form:

$$\bar{y} = 1.32\bar{x}^{0.46}\delta_0^{-0.23}, \tag{V-7-35}$$

where $\bar{y} = y/b$, $\bar{x} = x/b$.

Pressure and velocity. The working formula for the pressure coefficient is

$$\bar{p}_\delta = \frac{p_\delta - p_\infty}{q} = 2[1 + \delta_0 p_\delta(\bar{y})]. \tag{V-7-36}$$

The function $p_\delta(\bar{y})$ can be approximated by

$$p_\delta(\bar{y}) = -\frac{1}{2}\left[1+\bar{y}^2\left(\frac{2}{5}\bar{y}+\frac{4}{3}\right)^2\right]. \qquad \text{(V-7-37)}$$

Consequently, the pressure coefficient

$$\bar{p}_\delta = 2-\delta^0\left[1+\bar{y}^2\left(\frac{2}{5}\bar{y}+\frac{4}{3}\right)^2\right]. \qquad \text{(V-7-38)}$$

The velocity at the wall is calculated by the formula $V_{y\delta}/V_\infty = \delta_0 V_\delta$, where V_δ is calculated by (V-7-33). Introducing the value of $p_\delta(\bar{y})$ from (V-7-37) into (V-7-33), we find an approximate relation for use in calculating velocity:

$$\frac{V_{y\delta}}{V_\infty} = \delta_0\bar{y}\left(\frac{2}{5}\bar{y}+\frac{4}{3}\right). \qquad \text{(V-7-39)}$$

From this, we determine the velocity gradient at the critical point:

$$\bar{\lambda} = \frac{1}{V_\infty}\left(\frac{dV_\delta}{d\bar{y}}\right)_{y=0} = \frac{4}{3}\delta_0. \qquad \text{(V-7-40)}$$

Drag. The drag of a plate is determined by integrating over its surface. Using (V-7-38), we can obtain a relation for the drag coefficient referred to the plate's span 2b:

$$c_{x|w} = \frac{X_w}{q2b} = \int_0^1 \bar{p}_\delta\, d\bar{y} = 2(1-0.95\delta_0). \qquad \text{(V-7-41)}$$

Aerodynamic calculation of the wing. Methods of calculating hypersonic flow around a plate placed crosswise in the flow can be used to determine the aerodynamic characteristics of a wing in the following cases. /295

These methods are used to calculate the flow around a flat-blunted wing-profile leading edge at a near-zero angle of attack.

The flow over the peripheral part of the profile can be determined, for example, by the Newtonian corpuscular theory, and the over-all aerodynamic characteristics of the wing by the "method of strips."

We might examine another case of motion of a wing that is characterized by attack angles near 90°. This type of motion may occur when a vehicle reenters the atmosphere at hypersonic speeds and the wing is used as a brake offering the highest possible frontal drag.

The "method of strips," in which the flow along the plate (strip) is assumed plane, is used to calculate flow around a wing. This flow is approximated with a series of plates, each of which is considered to be set perpendicular to the direction of the oncoming flow. Here the over-all aerodynamic coefficient of the wing will be the same as for an isolated plate. For example, the over-all drag coefficient will be given by (V-7-41).

It must be remembered in using the "method of strips" that it gives better results for parts of the wing that are quite far from both the tip and root chords and where the flow is nearly plane.

The over-all aerodynamic characteristics of a finite-span wing, as calculated by the "method of strips," must be regarded as tentative and requiring verification and improvement either by more rigorous theoretical methods or by experiment.

Profile with Small Bluntness

Research has shown that the drag of a profile with a small bluntness at moderate supersonic speeds can be obtained by summing the drag of the blunt nose and that of the rest of the profile, which is calculated in accordance with the theory of flow around bluff bodies without consideration of the small influence exerted on this drag by disturbances emanating from the subsonic region.

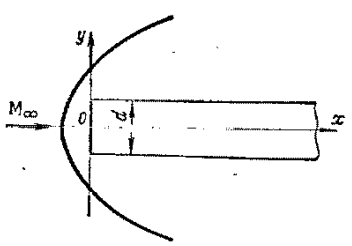

Figure V-7-6. Plate of Finite Thickness in Supersonic Flow.

At very high supersonic speeds, this effect may become substantial. To evaluate the length L of the profile segment on which a small blunting of thickness $\bar{d}$ exerts an influence, we can use the expression $L/d \sim \beta^{-3}$, where β is the characteristic inclination angle of the surface. For example, if $\beta = 0.1$, a small bluntness changes the flow pattern and the pressure distribution on a length $L \sim 1000d$ substantially.

Plate of finite thickness. Let us consider a plate of small thickness $\bar{d}$ in a flow at very high supersonic velocity (Fig. V-7-6). The studies of Prof. G.G. Chernyy [38] have shown that the pressure distribution over the surface of the plate is characterized by the general relation

$$\frac{\Delta p}{p_\infty} = P_1\left(k,\ \frac{1}{c_x M_\infty^2}\cdot\frac{x}{d}\right), \qquad \text{(V-7-42)}$$

where P_1 is a certain function of the parameters k, $(c_x M_\infty^2)^{-1} x/d$; c_x is the drag coefficient of the bluntness. /296

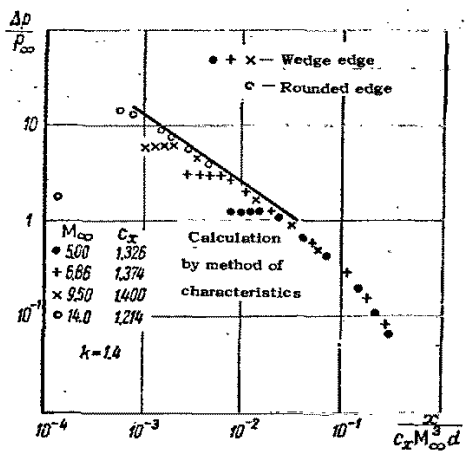

Figure V-7-7. Pressure Distributions on Plates with Wedge (● + ×) and Rounded (o) Edges. The Drag of the Rounded Edge was Calculated by the Formula $c_x = \frac{2}{3}\overline{p}_0$. The Unbroken Line Represents Formula (V-7-44).

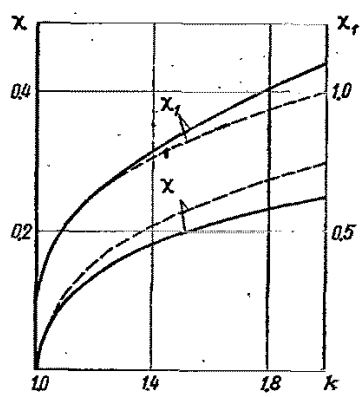

Figure V-7-8. Functions χ and χ_1 used in Calculating Flow Around a Plate of Finite Thickness and a Blunted Wedge.

The equation of the bow compression shock curve is

$$\frac{1}{c_x M_\infty^2}\frac{y}{d} = R_1\left(k,\ \frac{1}{c_x M_\infty^2}\frac{x}{d}\right), \qquad \text{(V-7-43)}$$

where R_1 is a certain function of the same parameters, which are to be regarded as similarity parameters for hypersonic flow around a blunted plate.

Formulas (V-7-42) and (V-7-43) agree well with calculations by the method of characteristics for a plate with a rounded flat bluntness or a wedge-shaped leading edge so selected that the sonic velocity occurs on it (Fig. V-7-7).

At very high flight speeds, the pressure p_∞ is small by comparison with the pressure behind the shock. In this case, the parameter p_∞ and, with it, M_∞ exert little influence, and (V-7-42) and (V-7-43) assume the simpler forms

$$\frac{2\Delta p}{\rho_\infty V_\infty^2} = \chi(k)\, c_x^{2/3} \left(\frac{x}{d}\right)^{-2/3}; \qquad \text{(V-7-44)}$$

$$\frac{y}{d} = \chi_1(k)\, c_x^{1/3} \left(\frac{x}{d}\right)^{2/3}. \qquad \text{(V-7-45)}$$

where χ and χ_1 are functions that depend only on the ratio of specific heats.

Values of these functions are represented by the solid lines in Fig. V-7-8. The approximating relationships for the function $\chi(k)$ and $\chi_1(k)$ (dashed curve in Fig. V-7-8) take the form

$$\chi = \left[\frac{\sqrt{2}}{3}\frac{(k+1)^{1/2}(k-1)}{3k-1}\right]^{2/3}; \qquad \text{(V-7-46)}$$

$$\chi_1 = \left[\frac{9}{16}\frac{(k+1)^2(k-1)}{3k-1}\right]^{1/3}. \qquad \text{(V-7-47)}$$

The quantities defined by (V-7-44) and (V-7-45) should be regarded as the principal terms of the series obtained by expanding the functions P_1 and R_1 with the condition that the parameter $x/(c_x M_\infty^3 d)$ is small. /297

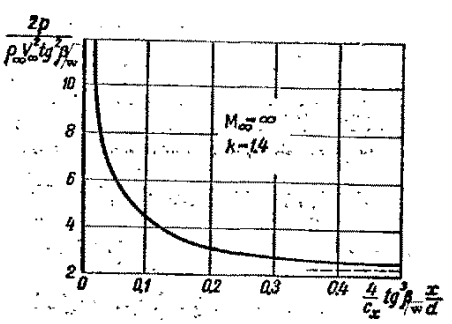

Figure V-7-9. Pressure Distribution on Wedge with Small Bluntness. The Dashed Line Represents a Sharp Wedge.

In the calculations, it must be remembered that these formulas give satisfactory results when the Reynolds numbers computed from plate thickness exceed 2000.

Thin wedge with small bluntness. Hypersonic flow theory gives the following general formula for the pressure distribution over the surface of a blunted wedge with a semivertex angle β_w:

$$\frac{2p}{\rho_\infty V_\infty^2 \operatorname{tg}^2 \beta_w} = P_2\left(\frac{4 \operatorname{tg}^2 \beta_w}{c_x}\cdot\frac{x}{d}\right). \qquad \text{(V-7-48)}$$

The shape of the shock wave is characterized by the relation

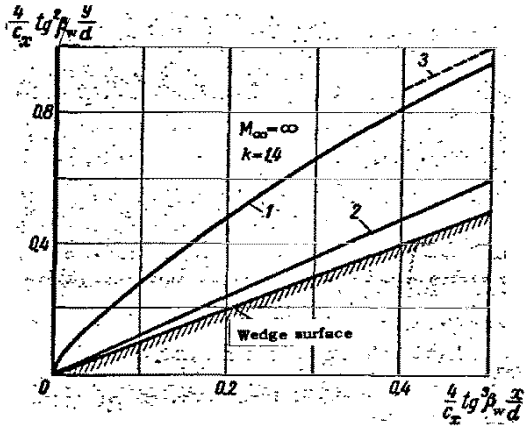

Figure V-7-10. Shape of Bow Wave in Front of Wedge. 1) with bluntness; 2) sharp wedge; 3) shock coinciding far from the nose with the shock in front of the sharp wedge.

$$\frac{y}{d} = \frac{c_x}{4\operatorname{tg}^2\beta_w} R_2\left(\frac{4\operatorname{tg}^3\beta_w}{c_x}\frac{x}{d}\right). \quad \text{(V-7-49)}$$

In these expressions, P_2 and R_2 are certain functions of the parameter $4\tan^3\beta_w x/(c_x d)$; c_x is the drag coefficient of the blunt nose. Relationships (V-7-48) and (V-7-49), which were derived without consideration of the initial pressure, are represented graphically in Figs. V-7-9 and V-7-10.

The quantity $4\tan^3\beta_w x/(c_x d)$ is a similarity parameter for hypersonic flow around a blunt wedge. At lower velocities, when back pressure is taken into account, it is necessary to introduce one more parameter $M_\infty \bar{c}$ ($\bar{c}$ is the wedge thickness ratio $2\tan\beta_w$), and, in the general case, also the specific-heat ratio k, which takes account of the properties of the gas.

The total drag X_{we} of a wedge of length x_w with a blunted leading edge is /298

$$X_{we} = 2X + 2\int_0^{x_w} p\operatorname{tg}\beta_w dx = 2X\left[1 + P_2\left(\frac{4\operatorname{tg}^3\beta_w}{c_x}\frac{x_w}{d}\right)\right], \quad \text{(V-7-50)}$$

where X is half the drag of the bluntness.

The drag coefficient of the wedge is

$$c_{xwe} = \frac{2}{t}[1 + P_2(t)]\operatorname{tg}^2\beta_w, \quad \text{(V-7-51)}$$

where $t = 4\tan^3\beta_w x_w/c_x d)$.

Figure V-7-11 presents a diagram of (V-7-51) for small t. The approximate relation

$$c_{xwe} = \left(k + 1 + \frac{2k}{t}\right)\operatorname{tg}^2\beta_w, \quad \text{(V-7-52)}$$

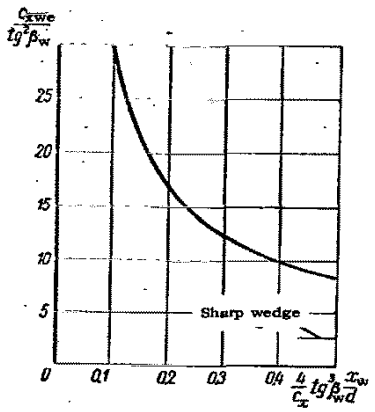

Figure V-7-11. Drag Coefficient of Blunted Wedge.

corresponds to large $\underline{t}$.

If the drag of the blunt surface is calculated as the sum of the drags of the bluntness and a sharpened wedge, we can use (V-7-52) with 2/t substituted for 2k/t.

Pressure center of blunted profile. The center of pressure of a blunted profile is shifted forward from its position for the same profile with a sharp edge.

This shift may be substantial. Thus, for example, for a profile in the form of a blunted plate, the center of pressure is located at 1/4 of the plate length from the leading edge at very high speeds, and not at the center, as in the case of an infinitesimally thin plate.

Law of similarity. The variation of the drag coefficient of a blunt wedge is characterized by a similarity law for which the general experssion is

$$c_{xwe} = \bar{c}^2 F(k, K, K^*), \qquad \text{(V-7-53)}$$

or, at very high speed

$$c_{xwe} = \bar{c}^2 F_\infty(k, K^{**}), \qquad \text{(V-7-54)}$$

where the similarity parameters are

$$K = M_\infty \bar{c}; \quad K^* = c_x M_\infty^2 d; \quad K^{**} = \frac{c_x d}{\bar{c}^3}. \qquad \text{(V-7-55)}$$

In (V-7-53), (V-7-54) the functions F and F_∞ are determined respectively by the parameters $\underline{k}$, K, K* and $\underline{k}$, K**. The dimension $\underline{d}$ is given as a fraction of wedge length.

The pressure distribution over the surface of the wedge and the coordinates of points on the bow shock wave are determined by the general relationships of similarity theory

$$\frac{\Delta p}{\rho_\infty V_\infty^2 \bar{c}^2} = P_3(K^{*-1}x, k, K); \quad \text{(V-7-56)}$$

$$K^{*-1}\frac{y}{\bar{c}} = R_3(K^{*-1}x, k, K), \quad \text{(V-7-57)}$$

which become for very high supersonic speeds /299

$$\frac{\Delta p}{\rho_\infty V_\infty^2 \bar{c}^2} = P_\infty[(K^{**})^{-1}x, k]; \quad \text{(V-7-58)}$$

$$(K^{**})^{-1}\frac{y}{\bar{c}} = R_\infty[(K^{**})^{-1}x, k]. \quad \text{(V-7-59)}$$

The functions P_3 and R_3 are determined by the parameters K*x, $\underline{k}$, K, and P_∞, R_∞ by the parameters k**x, $\underline{k}$; $\underline{x}$ and $\underline{y}$ are measured as fractions of wedge length.

Effect of sweep on drag. The drag increase caused by blunting the leading edge is mitigated for swept wings. Studies have shown [55] that the drag of a cylindrical swept wing can be found in approximation by the formula

$$c_{x\chi} = c_{x\chi=0}(1 - \sin\chi). \quad \text{(V-7-60)}$$

§V-8. ANNULAR WINGS

Incompressible flow. The lift of an annular wing at zero angle of attack can be determined by the formula [6]:

$$c_y = \frac{\pi}{2}\alpha a_0\left(1 + \frac{a_0}{\lambda_{wg}}\right)^{-1}, \quad \text{(V-8-1)}$$

in which $\lambda_{wg} = 2r/b$ is the aspect ratio and $a_0 = c_{y0}^{\alpha} = \partial c_{y0}/\partial\alpha$ is a parameter of the wing profile.

The lift is calculated from the expression $Y = 2c_y qrb$, where $2rb$ is the area of the wing's horizontal projection.

The induced drag coefficient of an annular wing

$$c_{xi} = \frac{c_y^2}{2\pi\lambda_{wg}}. \quad \text{(V-8-2)}$$

Let c_{x_0} be the wing's drag coefficient at $c_y = 0$, referred to the area 2rb. The frontal drag is therefore

$$X_0 = 2c_{x0}qrb. \qquad \text{(V-8-3)}$$

The same force can be determined from the expression

$$X_0 = c_{xp}qS = 2c_{xp}q\pi rb, \qquad \text{(V-8-3')}$$

where $S = 2\pi rb$ is the area of a cylinder of radius r and length b equal to the profile chord and c_{xp} is the profile drag coefficient for $c_y = 0$.

Comparing the two expressions for x_0, we find

$$c_{x0} = \pi c_{xp}. \qquad \text{(V-8-4)}$$

Accordingly, the total frontal drag coefficient, calculated as a lift coefficient from the area of the wing horizontal projection is

$$c_x = c_{x0} + c_{xi} = \pi c_{xp} + \frac{c_y^2}{2\pi\lambda_{wg}}. \qquad \text{(V-8-5)}$$

The pitching moment, which is usually determined with respect to the coordinate axis z, is created solely by lift. To determine it, we can proceed from the fact that the center of pressure of the wing (or the aerodynamic center for an unsymmetrical profile) will occupy the same axial position relative to the leading edge as does the profile center of pressure, i.e., we can assume that

$$c_{c.p.wg} = c_{c.p.pr}. \qquad \text{(V-8-6)}$$

Thus, /300

$$M_z = Yc_{c.p.pr}b,$$

and its coefficient

$$m_z = \frac{M_z}{2qrb^2} = c_y c_{\text{c.p.pr}} \qquad \text{(V-8-7)}$$

Effect of compressibility. For subsonic speeds, this effect can be taken into account with the formulas

$$c_y = \frac{c_{y\,ci}}{\sqrt{1-M_\infty^2}}; \qquad \text{(V-8-8)}$$

$$c_{xi} = \frac{c_{xi\,ci}}{\sqrt{1-M_\infty^2}}. \qquad \text{(V-8-9)}$$

Here the coefficient $c_{y\ ci}$ and $c_{xi\ ci}$ for a wing in incompressible flow are calculated for the aspect ratio $\lambda_{0wg} = \lambda_{wg}\sqrt{1-M_\infty^2}$.

Studies have shown that the center of pressure (aerodynanic center) position does not change in linearized compressible flow.

Supersonic speeds. The reciprocal effects between sections are weaker in supersonic than in subsonic flow. This influence decreases with increasing M_∞.

If the Mach cone originating at the leading edge of a section does not intersect the chord of the diametrially opposite section, the interaction between sections may be disregarded in first approximation.

In this case, it may be assumed that each section in the plane γ = const will be at an angle of attack $\alpha_\gamma = \alpha \cos \gamma$. Consequently, the section lift coefficient in the same plane will be

$$c_y' = c_y^{0\alpha}\alpha_\gamma = c_y^{0\alpha}\alpha\cos\gamma = c_y^0\cos\gamma, \qquad \text{(V-8-10)}$$

where c_y^0 is the lift coefficient of the profile at angle of attack α.

Assuming that the lift dY' in the plane γ = const is determined for a wing element with area dS = brdγ by the equality

$$dY' = c_y' \frac{\rho_\infty V_\infty^2}{2} br\, d\gamma,$$

we find the actual lift of the element

$$dY = dY'\cos\gamma = c_y' \frac{\rho_\infty V_\infty^2}{2} br\cos\gamma\, d\gamma = c_y^0 \frac{\rho_\infty V_\infty^2}{2} br\cos^2\gamma\, d\gamma.$$

The wing lift

$$Y = c_y^0 q b r \int_0^{2\pi} \cos^2\gamma \, d\gamma = c_y^0 q \pi b r.$$

Consequently, the lift coefficient

$$c_y = \frac{Y}{2qbr} = \frac{\pi}{2} c_y^0. \qquad \text{(V-8-11)}$$

Since there is no suction force on the leading edge of an annular wing in supersonic flow, the frontal drag coefficient due to lift

$$c_{xi} = c_y \alpha. \qquad \text{(V-8-12)}$$

The frontal drag coefficient for $c_y = 0$ is found from (V-8-5), with c_{xp} set equal to the profile drag coefficient at $c_y = 0$ and the given M_∞.

The wing aerodynamic center will occupy the same position relative to the leading edge as the aerodynamic center of the section profile at the same M_∞.

The frontal drag due to lift does not cause a pitching moment owing to the symmetrical distribution of the lift with respect to the z-axis. The coefficient m_z will also be zero by virtue of the wing's axial symmetry. /301

§V-9. CRUCIFORM WINGS

Figure V-9-1 is a diagram of flow past cruciform wings. In calculating aerodynamic characteristics for such wings, we can proceed from the fact that the influence of the slip of each plane on the coefficient c_y, c_x, and m_z can be disregarded with $2\psi = 90°$ (ψ is the inclination of the plane to the z_1-axis) and a small attack angle.

At supersonic speeds, because each plane is in the plane of symmetry of the other, the assumption that there is practically no mutual influence between them will be justified with a certain approximation.

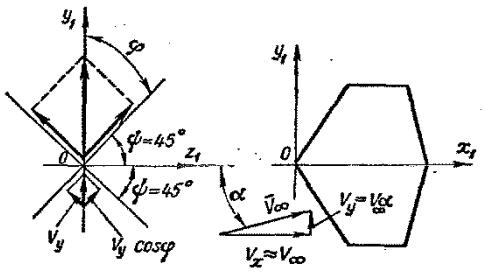

Figure V-9-1. Diagram of Flow Around Cruciform Wing.

In view of the above, each plane of a cruciform wing with the angle ψ = 45° will have the same aerodynamic characteristics as it would have in isolated form at the same flow velocity.

The effective attack angle of each plane of a cruciform wing at an angle of attack α (Fig. V-9-1) will be

$$\alpha_{p1}=\frac{V_y}{V_\infty}\cos\psi=\alpha\cos\psi=\frac{\alpha\sqrt{2}}{2}. \qquad \text{(V-9-1)}$$

Setting the attack-angle derivative of the isolated-plane lift coefficient equal to $c_y^{0\alpha}$, we find the lift coefficients c_{y_1} and c_{y_2} of the two planes of the cruciform wing:

$$c_{y1}=c_{y2}=c_y^{0\alpha}\alpha_{p1}=\alpha c_y^{0\alpha}\frac{\sqrt{2}}{2}=c_y^0\frac{\sqrt{2}}{2},$$

where c_y^0 is the lift coefficient of an isolated plane at an angle of attack α.

The lift coefficient of the entire cruciform wing, referred to the area of one plane, is

$$c_y=(c_{y1}+c_{y2})\cos\psi=c_y^0\cos\psi\sqrt{2}=c_y^0, \qquad \text{(V-9-2)}$$

i.e., it is equal to the lift coefficient of an isolated plane at the same angle of attack α.

The drag coefficient governed by lift and referred to the area of one plane is found, as for an ordinary wing, in the form

$$c_{xi}=Ac_y^2. \qquad \text{(V-9-3)}$$

At subsonic speeds, $A \approx 1/(\pi\lambda_{wg})$, where λ_{wg} is the aspect ratio of the individual wing; at supersonic speeds, $A = 1/c_y^{0\alpha}$ (if there is no suction force on the wing leading edges).

The frontal drag of a cruciform wing at $c_y = 0$ will be twice the frontal drag of the ordinary wing; consequently, $c_x = 2c_x^0$, where the coefficients c_x anc c_x^0 are referred to the area of one plane.

In attaching a cruciform wing to a body (see Fig. XV-1-3), it is necessary to consider the reciprocal effects between the planes and the body. In first approximation, this effect can be considered separately for each plane. The coefficients c_y^0, c_x^0, $c_y^{0\alpha}$ found in this manner for an individual plane are then substituted into the formula given above to obtain the characteristics of the cruciform wing with consideration of the body effect. /302

§V-10. NONSTATIONARY WING AERODYNAMICS

Plate in Supersonic Flow

If a wing is in nonstationary flow, which corresponds to conditions under which it executes an oscillatory motion, the aerodynamic characteristics also depend on the parameters that determine this motion.

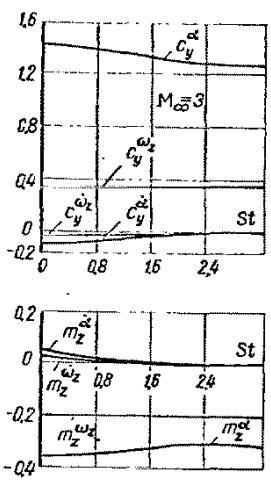

Figure V-10-1. Nonstationary Aerodynamic Characteristics of Rectangular Plate of Infinite Span (axis of rotation at 1/4 chord; $\bar{x}_{ro} = x_{ro}/b = 0.25$).

As an example for the most commonly encountered form of harmonic oscillations, Figs. V-10-1 and V-10-2 [6] show the theoretical curves of the nonsteady characteristics of an infinite-span flat plate at $M_\infty = 0$ and $M_\infty = 3$. The moment coefficients shown in Figs. V-10-1 and V-10-2 correspond to a reduction point situated at a distance $x_{ro} = 0.25b$ from the leading edge.

Figures V-10-3 – V-10-8 show the stability derivatives as functions of aspect ratio for rectangular and delta wings in subsonic flow. These data indicate that the effect of the Strouhal number St on the nonsteady characteristics decreases at small λ_{wg}. The same effect is observed at supersonic speeds. The influence of St also diminishes with increasing M_∞ (Figs. V-10-9 and V-10-10).

In solving practical problems, it is necessary to deal with St of the order of 0.05-0.07. With a certain accuracy, therefore, we can use the nonstationary characteristics for St → 0, i.e., assume that

the stability derivatives do not depend on the frequency of the oscillations. According to this hypothesis and for $x_{ro} = 0.25b$, we obtain the following values of the stability derivatives for an infinite-span plate in supersonic flow under harmonic-oscillatory conditions:

$$c_y^{\alpha} = \frac{4}{\sqrt{M_\infty^2 - 1}}; \qquad c_y^{\dot{\alpha}} = -\frac{2}{(M_\infty^2 - 1)^{3/2}}; \tag{V-10-1}$$

$$c_y^{\omega_z} = \frac{1}{\sqrt{M_\infty^2 - 1}}; \qquad c_y^{\dot{\omega}_z} = -\frac{1}{6}\frac{1}{(M_\infty^2 - 1)^{3/2}}; \tag{V-10-2}$$

$$m_z^{\alpha} = \frac{1}{\sqrt{M_\infty^2 - 1}}; \qquad m_z^{\dot{\alpha}} = \frac{5}{6}\frac{1}{(M_\infty^2 - 1)^{3/2}}; \tag{V-10-3}$$

$$m_z^{\omega_z} = -\frac{7}{12}\frac{1}{\sqrt{M_\infty^2 - 1}}; \qquad m_z^{\dot{\omega}_z} = \frac{1}{8}\frac{1}{(M_\infty^2 - 1)^{3/2}}. \tag{V-10-4}$$

/303

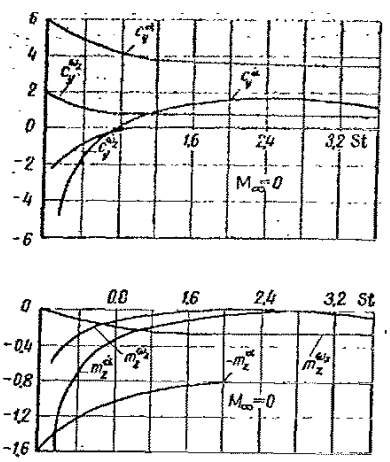

Figure V-10-2. Nonstationary Aerodynamic Characteristics of Infinite-Span Rectangular Plate ($\bar{x}_{ro} = 0.25$).

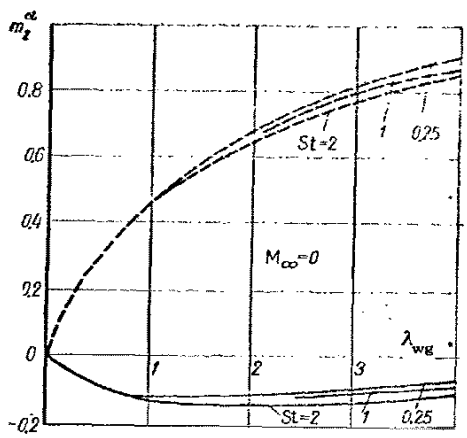

Figure V-10-3. Coefficient m_z^{α} (Solid Lines for Rectangular wings, Dashed Lines for Delta Wings). λ_{wg} is the Aspect Ratio. The Wing Rotation Axis is at 1/4 Root Chord, i.e., $\bar{x}_{ro} = 0.25$.

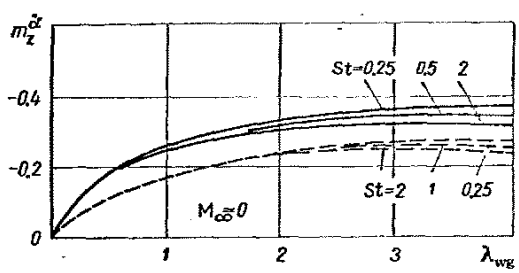

Figure V-10-4. Coefficient $m_z^{\dot{\alpha}}$ (Solid Lines for Straight Wings, Dashed Lines for Delta Wings); λ_{wg} is the Aspect Ratio; $\bar{x}_{ro} = 0.25$.

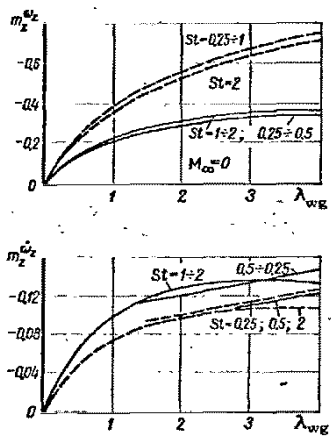

Figure V-10-5. Coefficients $m_z^{\omega_z}$ and $m_z^{\dot{\omega}_z}$ (Solid Lines for Rectangular Wings, Dashed Lines for Delta Wings); λ_{wg} is the Aspect Ratio; $\bar{x}_{ro} = 0.25$.

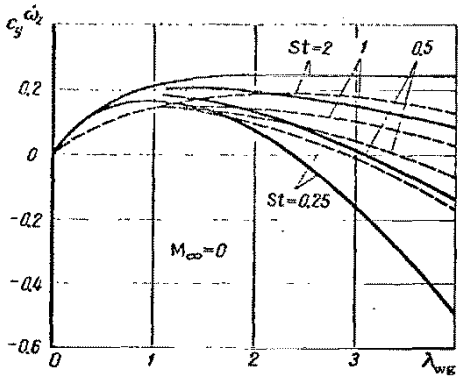

Figure V-10-7. Coefficient $c_y^{\dot{\omega}_z}$ (Solid Lines for Rectangular Wings, Dashed Lines for Delta Wings); λ_{wg} is the Aspect Ratio and $\bar{x}_{ro} = 0.25$.

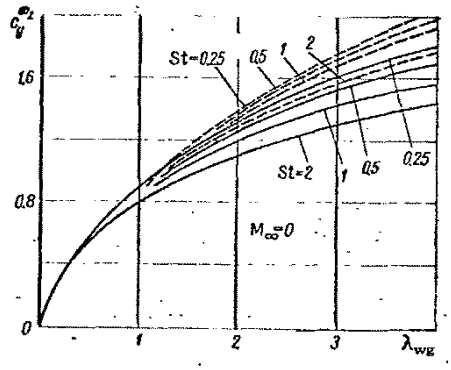

Figure V-10-6. Coefficient $c_y^{\omega_z}$ (Solid Lines for Rectangular Wings, Dashed Lines for Delta Wings); λ_{wg} is the Aspect Ratio; $\bar{x}_{ro} = 0.25$.

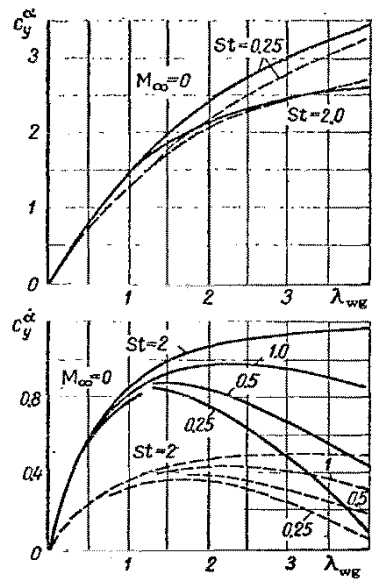

Figure V-10-8. Coefficients c_y^{α} and $c_y^{\dot{\alpha}}$ (Solid Lines for Rectangular Wings, Dashed Lines for Delta Wings); λ_{wg} is the Aspect Ratio; $\bar{x}_{ro} = 0.25$.

/304

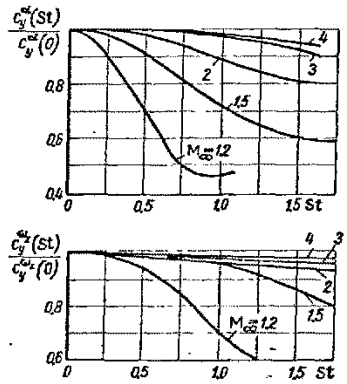

Figure V-10-9. Nonstationary Aerodynamic Characteristics of Rectangular Wing as Functions of M_∞ ($\lambda_{wg} = 1$, $\bar{x}_{ro} = 0.25$).

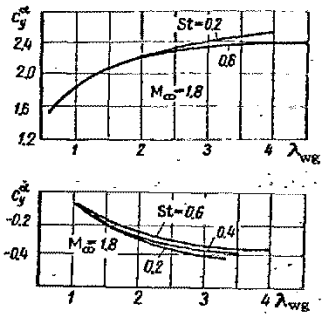

Figure V-10-10. Coefficients c_y^{α} and $c_y^{\dot{\alpha}}$ as Functions of Aspect Ratio of Rectangular Wing.

The relationships given here /305 can be used with a certain approximation in practical calculations for any other law of variation of the kinematic parameters in time if the condition $St \to 0$ is satisfied. This is the "harmonicity" hypothesis.

Wings in Subsonic Flow

In practical cases, we can disregard the influence of velocity variation on the aerodynamic characteristics (except for motions with very large accelerations). Assuming further that the slip angle $\beta_{sl} = 0$, we obtain for the aerodynamic coefficients

$$c_y = c_{y0} + c_y^{\alpha}\alpha + c_y^{\dot{\alpha}}\dot{\alpha} + c_y^{\omega_z}\omega_z + c_y^{\dot{\omega}_z}\dot{\omega}_z; \qquad \text{(V-10-5)}$$

$$m_z = m_{z0} + m_z^{\alpha}\alpha + m_z^{\dot{\alpha}}\dot{\alpha} + m_z^{\omega_z}\omega_z + m_z^{\dot{\omega}_z}\dot{\omega}_z. \qquad \text{(V-10-6)}$$

The curves of Figs. V-10-3 – V-10-8, which correspond to an incompressible medium ($M_\infty = 0$), can be used to compute the stability derivatives.

Compressibility (for $M_\infty \leq M_{\infty cr}$) can be taken into consideration using the similarity theory of subsonic flows. Here the corresponding relationships will pertain only to the static stability derivatives and to the rotary derivatives with respect to ω_z.

The method of the calculation is as follows. The geometrical parameters of a fictitious wing in incompressible flow are determined from the given wing form, its aspect ratio, and M_∞:

$$\lambda_{icwg}=\lambda_{wg}\sqrt{1-M_\infty^2};\ \eta_{ic}=\eta;\ \operatorname{tg}\chi_{ic}=\frac{\operatorname{tg}\chi}{\sqrt{1-M_\infty^2}}, \qquad \text{(V-10-7)}$$

where the parameters subscripted "ic" pertain to incompressible flow. Then the appropriate diagrams or formulas are used to find the stability derivatives for the fictitious wing. The corresponding coefficients for the wing in compressible flow are calculated from the results:

$$c_y^\alpha=\frac{c_{y\,ic}^\alpha}{\sqrt{1-M_\infty^2}};\qquad c_y^{\omega_z}=\frac{c_{y\,ic}^{\omega_z}}{\sqrt{1-M_\infty^2}}; \qquad \text{(V-10-8)}$$

$$m_z^\alpha=\frac{m_{z\,ic}^\alpha}{\sqrt{1-M_\infty^2}};\qquad m_z^{\omega_z}=\frac{m_{z\,ic}^{\omega_z}}{\sqrt{1-M_\infty^2}}. \qquad \text{(V-10-9)}$$

Rolling-moment derivatives.[61]. The theoretical values of the roll-damping derivative $m_x^{\omega_x}=\partial m_x/\partial\omega_x$ ($\omega_x=\Omega l/2V_\infty$, where l is the wingspan) are given in Fig. V-10-11 for straight-edged tapered wings in subsonic flow ($M_\infty < M_{\infty cr}$). It follows from this figure that the derivative $m_x^{\omega_x}$ depends on the parameter $\underline{k}$, which represents the ratio of the actual (experimental) slope of the profile lift curve to the theoretical value, and on the taper $\eta = b_{rt}/b_{tp}$ and the angle $\bar{\chi}_{1/4}=\operatorname{arctg}[(1-M^2)^{1/2}\operatorname{tg}\chi_{1/4}]$ in degrees. Like all subsequent derivatives, $m_x^{\omega_x}$ is determined for coordinates bound to the wing (Fig. V-10-11).

When the vehicle slips, another transverse moment whose magnitude is $(\partial m_x/\partial\beta)\beta_{sl}=m_x^\beta\beta_{sl}$ at small slip angles makes its appearance. The static transverse stability derivative m_x^β depends in the general case on wing planform and M_∞. Experimental values of m_x^β are given in Fig. V-10-12 as functions of aspect ratio λ_{wg} for $\eta = 1$ and $\eta = 2$ and small flow velocities ($M_\infty = 0$). The derivatives m_x^β depend weakly on the taper η, so that we may assume in approximation that m_x^β is a function only of the aspect ratio λ_{wg} and the sweep angle. /307

The rolling moment changes as the vehicle rotates about its vertical axis at angular velocity Ω_y. This change is equal to $m_x^{\omega_y}/\omega_y$, where $\omega_y = \Omega_y l/2V_\infty$. The theoretical values of the cross

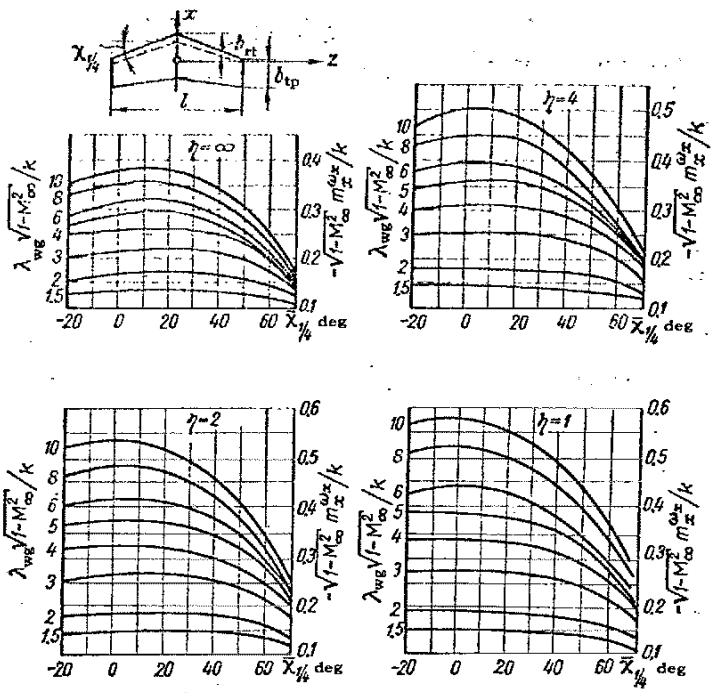

Figure V-10-11. Roll-Damping Derivatives for Swept Wing at Subsonic Speeds.

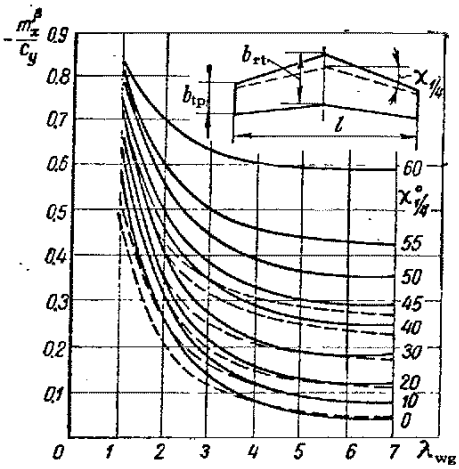

Figure V-10-12. Static Transverse Stability Derivative for Swept Wings at Low Speeds (Solid Lines for $\eta = 1$, Dashed Lines $\eta = 2$).

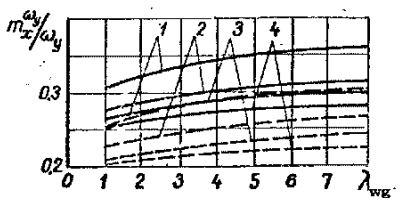

Figure V-10-13. Variation of Cross Rotary Derivative $m_x^{\omega_y}$ of Swept Wing in Incompressible Flow: Solid Lines for $\eta = 1$, Dashed Lines for $\eta = 2$.

1 – $\chi_{1/4} = \pm 60°$; 2 – $\chi_{1/4} = \pm 50°$; 3 – $\chi_{1/4} = \pm 40°$; 4 – $\chi_{1/4} = 0°$

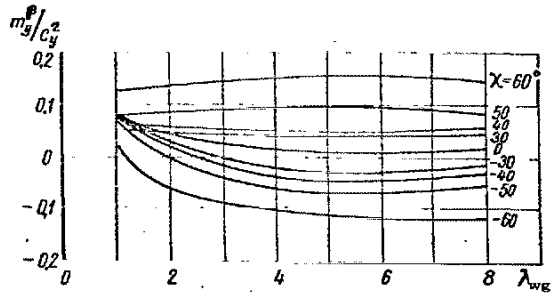

Figure V-10-14. Variation of Ratio of Weathercock Statility Derivative m_y^β to c_y^2 as Function of Wing Sweep Angle and Aspect Ratio.

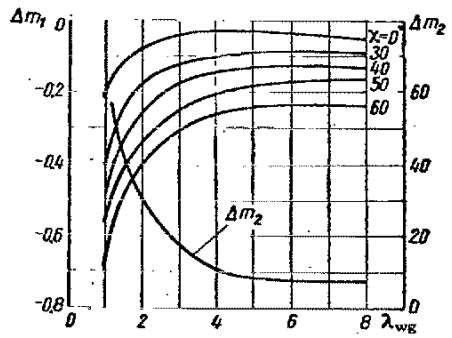

Figure V-10-15. Variation of Coefficients Δm_1 and Δm_2 Which Determine Static Derivative of Directional Moment (Center of Rotation Coincides with Wing Aerodynamic Center).

rotary stability derivative $m_x^{\omega_y}$ for swept wings with taper and straight edges are shown in Fig. V-10-13 for incompressible flow. To account for the influence of compressibility on the derivatives m_x^β and $m_x^{\omega_y}$ it is necessary to use the transformations (V-10-7)-(V-10-9).

Derivatives of directional moment [61]. The variation of the directional moment is governed by slip and rotation about the longitudinal and vertical axes at the respective angular velocities ω_x and ω_y. The directional-moment increments that result are equal to $m_y^\beta \beta_{sl}$ (for slip), $m_y^{\omega_x}\omega_x$ (for rotation about the x-axis), and $m_y^{\omega_y}\omega_y$ (for rotation about the y-axis). Theoretical values of the weathercock-moment derivative for swept wings without taper, which has no substantial influence, can be determined from Fig. V-10-14 for subsonic flow ($M_\infty = 0$). The directional-moment derivative $m_y^{\omega_x}$ (cross derivative of angular velocity of transverse motion) can be determined with the auxiliary coefficients Δm_1 and Δm_2 by the formula

$$m_y^{\omega_x} = \Delta m_1 c_y + \Delta m_2 (c_x^\alpha)_{pr}, \qquad \text{(V-10-10)}$$

where c_y is the wing lift coefficient and the derivative

$$(c_x)_{pr}^\alpha = \frac{\partial}{\partial \alpha}\left[c_x - c_y^2/(\pi \lambda_{wg})\right],$$

i.e., it is equal to the derivative of profile drag. The coefficients Δm_1 and Δm_2 are represented in Fig. V-10-15 for swept wings without taper, which has practically no influence on the values of these coefficients. According to Fig. V-10-15, the coefficient Δm_1 depends in incompressible flow on the sweep angle χ and the aspect ratio λ_{wg}, while the coefficient Δm_2 depends only on aspect ratio. /308

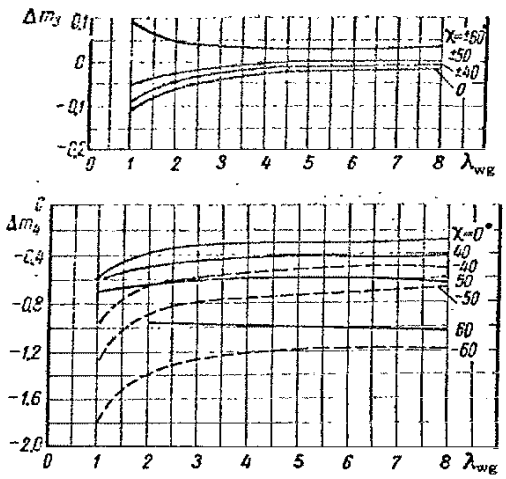

Figure V-10-16. Variation of Coefficients Δm_3 and Δm_4, which Determine Directional Damping Derivative (Center of Rotation Coincident with Wing Aerodynamic Center).

The directional damping derivative

$$m_y^{\omega_y} = \Delta m_3 c_y^2 + \Delta m_4 (c_x)_{pr}, \quad \text{(V-10-11)}$$

where the profile drag coefficient

$$(c_x)_{pr} = c_x - \frac{c_y^2}{\pi\lambda_{wg}}. \quad \text{(V-10-12)}$$

The coefficients Δm_3 and Δm_4 are given for swept wings in incompressible flow in Fig. V-10-16. With a certain approximation, these coefficients may be considered independent of taper. The effect of compressibility on the directional-moment derivative can be taken into account with the transformations (V-10-7)-(V-10-9).

Wings in Supersonic Flow (Slender-Body Theory

General relationships for stability derivatives of wings of arbitrary form. If $\alpha'\lambda_{wg}$ is near zero, the stability derivatives can be calculated according to the slender-body theory. Studies have shown that they are independent of M_∞ and are determined by wing geometry.

Let us examine wings of arbitrary configuration but with the same positioning of the cantilevers (Fig. V-10-17). We shall determine the derivatives in the body coordinate system x, y, z, whose origin need not coincide with the center of gravity of the area.

Motion of the wing is characterized by the attack angle α and slip angle β_{sl}, and by the angular velocity components Ω_x,

Ω_y, and Ω_z. The translational displacement at velocity V_∞ may be nonuniform.

The stability derivatives for wings are determined in the slender-body theory by Expressions (IV-7-11)-(IV-7-45). The quantities B_{ik}, C_{ik}, D_{ik}, $\bar{A}_{ik}$ that appear here depend on the attached-mass coefficients, which, in turn, are determined by the cross-sectional form of the wings. These coefficients have been found for several wing configurations, of which we shall examine the two-, three-, and four-cantilever configurations. Here, the two-cantilever wing appears in cross section as a straight-line segment in the ζ-plane on the horizontal axis. Let the wingspan (i.e., the segment length) be 2ℓ. This segment is transformed into a circle of radius r_0 in the σ-plane by the conformal formula (see Table IV-4-1) /309

$$\zeta = \sigma + \frac{r_0^2}{\sigma}, \qquad \text{(V-10-13)}$$

where $r_0 = \ell/2$.

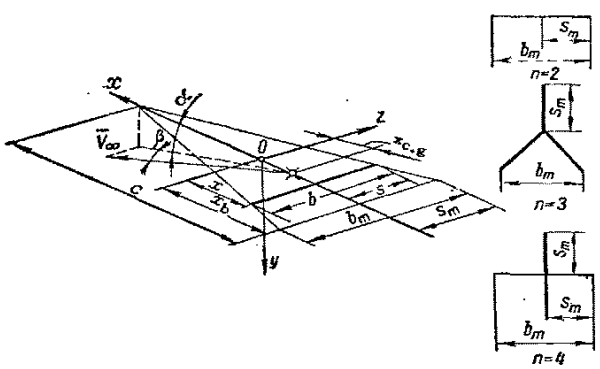

Figure V-10-17. Nomenclature for Wing in Determination of Stability Derivatives (n is the Number of Cantilevers).

Applying (IV-6-51) and (IV-6-52), we can find the complex potentials W_2 and W_1, and with (IV-6-53) and (IV-6-54) we can determine potential W_3. The attached-mass coefficients are found by (IV-6-4) or (IV-6-4').

In performing the calculations, it must be remembered that the velocity component V_z in the direction of the z-axis does not cause disturbances, so that it can be stated at once that the attached-mass coefficients

$$\lambda_{11} = \lambda_{12} = \lambda_{13} = 0.$$

Formula (IV-6-4) should be used to calculate the attached-mass coefficients for other wing cross-section shapes, with appropriate modification for the shapes of three- or four-cantilever wings.

In examining a cantilever inclined to the y- or z-axis, the velocities V_y and V_z must be resolved into components in the direction of the cantilever and normal to it.

Calculations indicate that the attached-mass coefficients λ_{12}, λ_{13}, λ_{23} are zero for all three configurations. As for the other coefficients, they have the following values [51]: two-cantilever wing (plane configuration)

$$\lambda_{11}=0;\ \lambda_{22}=\pi\rho_\infty l^2;\ \lambda_{33}=\frac{1}{8}\pi\rho_\infty l^4; \qquad \text{(V-10-14)}$$

three-cantilever wing

$$\lambda_{11}=\lambda_{22}=0.793\pi\rho_\infty l^2;\ \lambda_{33}=0.533\rho_\infty l^4; \qquad \text{(V-10-14')}$$

four-cantilever wing (cruciform configuration)

$$\lambda_{11}=\lambda_{22}=\pi\rho_\infty l^2;\ \lambda_{33}=\frac{2}{\pi}\rho_\infty l^4. \qquad \text{(V-10-14")}$$

Knowing the attached-mass coefficients, we can use (IV-6-47) to find the ooefficients A_{ik}. Since the attached-mass coefficients $\lambda_{12}=\lambda_{13}=\lambda_{23}=0$, the corresponding coefficients A_{ik} are also equal to zero, i.e., $A_{12}=A_{13}=A_{23}=0$.

Taking the wing area ($S=S_{wg}$) and $2l_m=b_m$ as characteristic parameters in (IV-6-47), we obtain the following expressions for the coefficients A_{11}, A_{22}, A_{33} on the trailing edge: /310

two-cantilever wing

$$A_{11}=0;\quad A_{22}=\frac{\pi l^2}{S_{wg}};\quad A_{33}=\frac{\pi}{8}\frac{l^4}{b_m^2 S_{wg}}; \qquad \text{(V-10-15)}$$

three-cantilever wing

$$A_{11}=A_{22}=0.793\pi\frac{l^2}{S_{wg}};\quad A_{33}=0.533\frac{l^4}{b_m^2 S_{wg}}; \qquad \text{(V-10-15')}$$

four-cantilever wing

$$A_{11}=A_{22}=\frac{\pi l^2}{S_{wg}};\quad A_{33}=\frac{2l^4}{\pi b_m^2 S_{wg}}. \qquad \text{(V-10-15")}$$

Setting $\ell = \ell_m = b_m/2$ in these formulas, we obtain the values of the coefficients $\overline{A}_{11}$, $\overline{A}_{22}$, $\overline{A}_{33}$ for the conditions on the trailing edge. It must be remembered that the coefficients $\overline{A}_{12}$, $\overline{A}_{13}$, $\overline{A}_{23}$ are equal to zero.

From the coefficients A_{ik}, we can calculate the coefficients B_{ik}, C_{ik}, D_{ik} from (IV-6-46). Nine of these coefficients, those corresponding to the indices ik = 12, 13, 23, are equal to zero because $A_{12} = A_{13} = A_{23} = 0$. This simplifies Formulas (IV-6-11)-(IV-6-45) substantially.

Determination of the other values of the coefficients B_{ik}, C_{ik}, D_{ik} from (IV-6-46) requires knowledge of the cantilever planform. Here the cantilevers may differ in form from conventional deltas; for example, they may have curvilinear edges.

By way of example, let us consider calculation of the stability derivatives for a thin flat delta wing and a four-cantilever (cruciform) configuration.

Delta wing. The fundamental nomenclature for this wing is shown in Fig. V-10-17. As our characteristic area, we shall take the wing area $S_{wg} = 0.5b_m c$ and as our characteristic linear dimension the span $2\ell_m = b_m$.

After substituting the values A_{ii} (V-10-14) into (IV-6-46) and integrating on the assumption that the coordinate origin coincides with the center of gravity ($x_{c.g} = c/3$), we obtain

$$B_{11}=0;\quad B_{22}=\frac{\pi}{6};\quad B_{33}=\frac{\pi}{320}; \tag{V-10-16}$$

$$C_{11}=0;\quad C_{22}=-\frac{\pi}{36\lambda_{wg}} \tag{V-10-17}$$

$$D_{11}=0;\quad D_{22}=\frac{4\pi}{135\lambda_{wg}^2}, \tag{V-10-18}$$

where the wing aspect ratio

$$\lambda_{wg}=b_m^2/S_{wg}=2b_m/c. \tag{V-10-19}$$

Introducing A_{ii}, B_{ii}, C_{ii}, and D_{ii} into the general expressions for the stability derivatives, (IV-6-11)-(IV-6-45), we obtain their values for the delta wing.

The static stability derivatives take the form

$$c_N^{\alpha} = -\frac{2\pi}{3}\dot{\bar{V}} - \frac{\pi\lambda_{wg}}{2}; \quad c_N^{\beta} = 0; \tag{V-10-20}$$

$$c_z^{\alpha} = \frac{2}{3}\pi\omega_x; \quad c_z^{\beta} = 0; \tag{V-10-21}$$

$$m_x^{\alpha} = -\frac{\pi}{3}\beta + \frac{\pi}{9}\frac{\omega_y}{\lambda_{wg}}; \quad m_x^{\beta} = -\frac{\alpha\pi}{3} - \frac{\pi\omega_z}{9\lambda_{wg}}; \tag{V-10-22}$$

$$m_y^{\alpha} = -\frac{\pi}{9}\frac{\omega_x}{\lambda_{wg}}; \quad m_y^{\beta} = 0; \tag{V-10-23}$$

$$m_z^{\alpha} = -\frac{\pi}{9}\frac{\dot{\bar{V}}}{\lambda_{wg}}; \quad m_z^{\beta} = 0. \tag{V-10-24}$$

The rotary derivatives /311

$$c_N^{\omega_x} = 0; \quad c_N^{\omega_y} = 0; \quad c_N^{\omega_z} = -\frac{2}{3}\pi; \tag{V-10-25}$$

$$c_z^{\omega_x} = -\frac{2}{3}\alpha\pi + \frac{2}{9}\frac{\omega_x\pi}{\lambda_{wg}}; \quad c_z^{\omega_y} = 0; \quad c_z^{\omega_z} = \frac{2}{9}\frac{\omega_z\pi}{\lambda_{wg}}; \tag{V-10-26}$$

$$\left.\begin{aligned} m_x^{\omega_x} &= -\frac{1}{32}\pi\lambda_{wg}; \quad m_x^{\omega_y} = \frac{1}{9}\frac{\pi}{\lambda_{wg}} + \frac{32}{135}\frac{\omega_x\pi}{\lambda_{wg}^2}; \\ m_x^{\omega_z} &= -\frac{1}{9}\frac{\pi\beta}{\lambda_{wg}} + \frac{32}{135}\frac{\omega_y\pi}{\lambda_{wg}^2}; \end{aligned}\right\} \tag{V-10-27}$$

$$m_y^{\omega_x} = -\frac{1}{9}\frac{\pi\alpha}{\lambda_{wg}} - \frac{32}{135}\frac{\pi\omega_z}{\lambda_{wg}^2}; \quad m_y^{\omega_y} = 0; \quad m_y^{\omega_z} = -\frac{32}{135}\frac{\pi\omega_x}{\lambda_{wg}^2}; \tag{V-10-28}$$

$$m_z^{\omega_x} = 0; \quad m_z^{\omega_y} = 0; \quad m_z^{\omega_z} = -\frac{1}{3}\frac{\pi}{\lambda_{wg}}. \tag{V-10-29}$$

The acceleration derivatives

$$c_N^{\dot{\alpha}} = -\frac{2}{3}\pi; \quad c_N^{\dot{\bar{V}}} = -\frac{2}{3}\pi\alpha; \quad c_N^{\dot{\omega}_z} = -\frac{\pi}{9\lambda_{wg}}; \tag{V-10-30}$$

$$m_x^{\dot{\omega}_x} = -\frac{\pi}{80}; \tag{V-10-31}$$

$$m_z^{\dot{\alpha}} = -\frac{\pi}{9\lambda_{wg}}; \quad m_z^{\dot{\bar{V}}} = -\frac{\pi\alpha}{9\lambda_{wg}}; \quad m_z^{\dot{\omega}_z} = -\frac{16\pi}{135\lambda_{wg}^3}. \tag{V-10-32}$$

The remaining derivatives with respect to the accelerations are zero. In using the expressions for the derivatives, it must be remembered that all parameters were calculated for the characteristic length b_m. For example, $\omega_x = \Omega_x b_m/2V_\infty$, $\dot{\bar{V}} = \dot{V}_\infty b_m/2V_\infty^2$, where the derivative $\dot{\bar{V}} = d\bar{V}/dt$.

A number of stability derivatives depend on the translational acceleration. If the influence of this acceleration is nil or negligibly small, we must set $\dot{\bar{V}} = 0$.

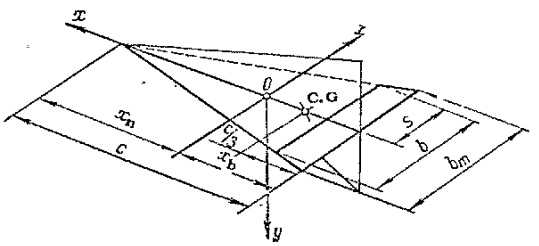

Figure V-10-18. Nomenclature for Cruciform Wing in Determination of Stability Derivatives.

The relationships given here can be used to analyze specific forms of motion, e.g., rolling motion, motion in the presence of only longitudinal damping, etc. In performing the analysis, it must be remembered that these relationships are suitable only for wings of small aspect ratio with the condition that the product $\alpha'\lambda_{wg}$ be small.

When this condition is met, the wing is situated near the axis of the Mach cone. At large M_∞ or with an increase in aspect ratio, these relationships give increasingly unsatisfactory results. The influence of aspect ratio and M_∞ will be examined below.

Four-cantilever (cruciform) wing. The basic dimensions of a wing whose four cantilevers are identical are shown in Fig. V-10-18. Introducing (V-10-15) for A_{ii} into (IV-6-46), we obtain the following relationships for B_{ii}, C_{ii}, D_{ii}

$$B_{11}=B_{22}=\frac{\pi}{6};\quad C_{11}=C_{22}=\frac{\pi}{\lambda_{wg}}\left[\frac{1}{3}\left(1+\frac{x_{c.g}}{C}\right)-\frac{1}{4}\right];\quad B_{33}=\frac{1}{20\pi}; \tag{V-10-33}$$

$$D_{11}=D_{22}=\frac{\pi}{\lambda_{wg}^2}\left[\frac{2}{5}-\left(1+\frac{x_{c.g}}{c}\right)+\frac{2}{3}\left(1+\frac{x_{c.g}}{c}\right)^2\right]. \tag{V-10-34}$$

The formulas for C_{ii} and D_{ii} are suitable for any position of the coordinate origin of the body system chosen. If the origin is placed at the wing-area center of gravity, it is necessary to set $x_{c.g}/c = -1/3$. In this case, $C_{11} = C_{22} = -\pi/(36\lambda_{wg})$, $D_{11} = D_{22} = 4\pi/(135\lambda_{wg}^2)$. /312

The stability derivatives (IV-6-11)-(IV-6-45) are written as follows.

Static stability derivatives:

$$c_N^\alpha=-\frac{\pi}{2}\lambda_{wg}-\frac{2}{3}\pi\dot{\bar{V}};\quad c_N^\beta=-\frac{2}{3}\pi\omega_x; \tag{V-10-35}$$

$$c_z^\alpha=\frac{2}{3}\pi\omega_x;\quad c_z^\beta=-\frac{\pi}{2}\lambda_{wg}-\frac{2}{3}\pi\dot{\bar{V}}; \tag{V-10-36}$$

$$m_x^\alpha=m_x^\beta=0;\quad m_y^\alpha=-\frac{\pi\omega_x}{9\lambda_{wg}};\quad m_y^\beta=\frac{\pi}{9\lambda_{wg}}\dot{\bar{V}}; \tag{V-10-37}$$

$$m_z^{\alpha} = -\frac{\pi\dot{\bar{V}}}{9\lambda_{wg}}; \quad m_z^{\beta} = -\frac{\pi\omega_x}{9\lambda_{wg}}; \qquad \text{(V-10-38)}$$

rotary derivatives:

$$c_N^{\omega_x} = -\frac{2\pi}{3}\beta + \frac{2\pi}{9\lambda_{кр}}\omega_y; \quad c_N^{\omega_y} = \frac{2\pi}{9\lambda_{wg}}\omega_x; \quad c_N^{\omega_z} = -\frac{2\pi}{3}; \qquad \text{(V-10-39)}$$

$$c_z^{\omega_x} = \frac{2\pi}{3}\alpha + \frac{2\pi}{9\lambda_{wg}}\omega_z; \quad c_z^{\omega_y} = \frac{2\pi}{3}; \quad c_z^{\omega_z} = \frac{2\pi}{9\lambda_{wg}}\omega_x; \qquad \text{(V-10-40)}$$

$$m_x^{\omega_x} = -\frac{\lambda_{wg}}{2\pi}; \quad m_x^{\omega_y} = m_x^{\omega_z} = 0; \qquad \text{(V-10-41)}$$

$$m_y^{\omega_x} = -\frac{\pi}{9\lambda_{wg}}\alpha - \frac{32\pi}{135\lambda_{wg}^2}\omega_z; \quad m_y^{\omega_y} = -\frac{\pi}{3\lambda_{wg}}; \quad m_y^{\omega_z} = -\frac{32\pi}{135\lambda_{wg}^2}\omega_x; \qquad \text{(V-10-42)}$$

$$m_z^{\omega_x} = -\frac{\pi}{9\lambda_{wg}}\beta + \frac{32\pi}{135\lambda_{wg}^2}\omega_y; \quad m_z^{\omega_y} = \frac{32\pi}{135\lambda_{wg}^2}\omega_x; \qquad \text{(V-10-43)}$$

$$m_z^{\omega_z} = -\frac{\pi}{3\lambda_{wg}}; \qquad \text{(V-10-44)}$$

acceleration derivatives:

$$c_N^{\dot{\alpha}} = -\frac{2}{3}\pi; \quad c_N^{\dot{\bar{V}}} = -\frac{2}{3}\pi\alpha; \quad c_N^{\dot{\omega}_z} = -\frac{\pi}{9\lambda_{wg}}; \qquad \text{(V-10-45)}$$

$$c_z^{\dot{\beta}} = -\frac{2}{3}\pi; \quad c_z^{\dot{\bar{V}}} = -\frac{2}{3}\pi\beta; \quad c_z^{\dot{\omega}_y} = \frac{\pi}{9\lambda_{wg}}; \qquad \text{(V-10-46)}$$

$$m_x^{\dot{\omega}_x} = -\frac{1}{5\lambda_{wg}}; \qquad \text{(V-10-47)}$$

$$m_y^{\dot{\beta}} = \frac{\pi}{9\lambda_{wg}}; \quad m_y^{\dot{\bar{V}}} = \frac{\pi}{9\lambda_{wg}}\beta; \quad m_y^{\dot{\omega}_y} = -\frac{16\pi}{135\lambda_{wg}^2}; \qquad \text{(V-10-48)}$$

$$m_z^{\dot{\alpha}} = -\frac{\pi}{9\lambda_{wg}}; \quad m_z^{\dot{\bar{V}}} = -\frac{\pi}{9\lambda_{wg}}\alpha; \quad m_z^{\dot{\omega}_z} = -\frac{16\pi}{135\lambda_{wg}^2}. \qquad \text{(V-10-49)}$$

$S_{wg} = b_m c/2$ is taken as the characteristic area in calculating the derivatives, and the span of the wing at the base $2\ell_m = b_m$ as the characteristic length. The parameters ω_x, ω_y, ω_z, $\bar{V}$ and their derivatives are determined, as for a plane wing, from the characteristic length b_m.

Influence of Wing Aspect Ratio and M_∞ on Stability Derivatives

Delta wing. Slender-body theory gives stability derivatives that are independent of M_∞. Nor does this theory permit establishing the effect of aspect ratio on the derivatives, though it might appear, that the corresponding expressions convey it. This /313 is because the appearance of λ_{Wg} in these expressions arises not from the physical process but from the formal selection of the characterisitc geometrical parameters.

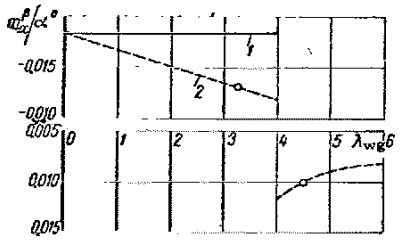

Figure V-10-19. Relation for Transverse Stability Derivative of Delta Wing for $M_\infty = \sqrt{2}$: 1) according to slender-body theory; 2) according to linearized theory; o) angle $\beta = 5°$ for wing with subsonic leading edge.

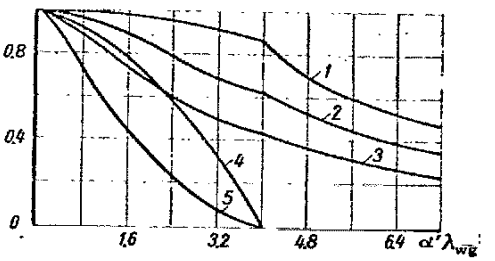

Figure V-10-20. Ratios of Delta-Wing Stability Derivatives Calculated by Linearized Theory and Slender-Body Theory:

$1 - \bar{m}_x^{\omega_x}$; $2 - \bar{c}_N^{\alpha}$; $3 - \bar{m}_z^{\omega_z}$; $4 - \bar{c}_z^{\alpha\omega_x}$; $5 - \bar{c}_N^{\omega_z}$

The results of supersonic linearized theory should be used to establish the stability derivatives as functions of M_∞ and λ_{wg}. Let us consider a delta wing. The independent variable for the stability derivatives is $\alpha'\lambda_{wg} = 4\alpha' \tan \gamma_1$, where γ_1 is the semivertex angle of the wing. The wing area S_{wg} is the characteristic area for calculation of the derivatives, and the span b_m is the characteristic length.

To ascertain the influence of aspect ratio and M_∞, let us compare the most important stability derivatives as obtained by the slender-body and linearized theories. This comparison will also enable us to establish the possibility of using the slender-body theory and the accuracy that can be expected. We shall examine the case in which there is no longitudinal acceleration and $\dot{\bar{V}} = 0$.

Static stability derivatives. We shall analyze the stability derivatives for the moments with consideration of the fact that the moments are calculated with respect to the wing's center of gravity, about which the rotation takes place. Special mention will be made of a different positioning of the centers of moment and rotation. Calculations by the aerodynamic theory of the slender body give $m_z^{\alpha} = 0$, i.e., the same value as the linearized theory. This indicates that the slender-body theory gives a rather good approximation. At the same time, the result $m_z^{\alpha} = 0$ indicates that the influence of M_∞ on the static stability derivative cannot be determined within the framework of the linear theory.

If the center of moments does not coincide with the center of gravity, $m_z^\alpha \neq 0$. Figure V-10-25 shows a pitching-moment curve calculated in the linearized theory for an axis of rotation passing through the origin of the chord and a supersonic leading edge. Investigations have established that the derivative m_z^α does not depend on the aspect ratio of a delta wing.

There are differences in the results for the transverse stability derivative m_x^β. In Fig. V-10-19, which shows computed data for the case $M_\infty = \sqrt{2}$, we see that the values of m_x^β given by the two theories for the delta wing are similar until the leading edge becomes sonic ($\alpha'\lambda_{wg} = 4$). Here the derivative m_x^β remains negative (stabilizing) according to the linearized theory for the subsonic edge, but becomes positive (destabilizing) for a supersonic edge. In the zone of transition from the sub- to the supersonic edge, the difference between the theories becomes especially pronounced. /314

Slip angle influences sweep angle and, consequently, the value of the rolling moment. With increasing angle β_{sl}, the leading edge becomes sonic and the destabilizing effect appears sooner. When the edge passes from sub- to supersonic, the dependence of m_x on β_{sl} deviates from linearity.

Let us consider the derivatives of the normal-force coefficient, introducing the notation

$$\bar{c}_N^\alpha = \frac{c_{N1}^\alpha}{c_{Nt}^\alpha}. \qquad \text{(V-10-50)}$$

Here the numerator is the derivative obtained from the linearized theory, which is equal to

$$c_{N1}^\alpha = \begin{cases} \pi\lambda_{wg}/(2E) & \text{for } \alpha'\lambda_{wg} < 4 \\ 4/\alpha' & \text{for } \alpha'\lambda_{wg} > 4; \end{cases} \qquad \text{(V-10-51)}$$

and the denominator is the derivative found from slender-body theory, $c_{Nt}^\alpha = \pi\lambda_{wg}/2$. The function E in (V-10-51) is a complete elliptic integral of the second kind with the parameter $k = [1 - (\alpha\lambda_{wg}/2)^2]^{1/2}$.

Figure V-10-20 shows a curve of $\bar{c}_N^\alpha$ constructed as a function of the parameter $\alpha'\lambda_{wg}$. The break in the curve occurs at $\alpha'\lambda_{wg} = 4$, when the edge becomes sonic. With increasing aspect ratio or

M_∞, slender-body theory gives increasingly understated values. Figure V-10-20 shows a $\bar{c}_N^{\alpha}$ curve for a delta wing with a supersonic leading edge.

Rotary derivatives and derivatives with respect to the accelerations. One of the rotary derivatives, namely the roll-damping derivative, is determined in linearized theory by the expressions

$$\left.\begin{aligned} m_{x1}^{\omega_x} &= -\frac{\pi\lambda_{wg}k^2}{16[(1+k^2)E-(1-k^2)K]} \text{ for } \alpha'\lambda_{wg}<4; \\ m_{x1}^{\omega_x} &= -\frac{1}{3\alpha'} \text{ for } \alpha'\lambda_{wg}>4, \end{aligned}\right\} \qquad \text{(V-10-52)}$$

where K is a complete elliptic integral of the first kind:

$$K=\int_0^{\pi/2}(1-k^2\sin^2\psi)^{-1/2}d\psi \qquad \text{(V-10-52')}$$

with the parameter $k = [1 - (\alpha'\lambda_{wg}/2)^2]^{1/2}$.

In slender-body theory, the same derivative $m_{xt}^{\omega_x} = -\pi\lambda_{wg}/32$. The derivative ratio $\bar{m}_x^{\omega_x} = m_{x1}^{\omega_x}/m_{xt}^{\omega_x}$ is shown in Fig. V-10-20. Slender-body theory gives smaller values of the derivatives than does the linearized theory, although the difference is smaller than for the derivative c_N^{α}.

Longitudinal damping depends on the derivatives of m_z with respect to $\dot{\alpha}$ and ω_z, which are determined differently in the two theories. According to the linearized theory,

$$\left.\begin{aligned} m_{z1}^{\omega_z} &= \frac{-\pi k^2}{3\lambda_{wg}[(2k^2-1)E+(1-k^2)K]} \text{ for } \alpha'\lambda_{wg}<4; \\ m_{z1}^{\omega_z} &= -\frac{16}{9\alpha'\lambda_{wg}^2} \text{ for } \alpha'\lambda_{wg}>4; \end{aligned}\right\} \qquad \text{(V-10-53)}$$

$$\left.\begin{aligned} m_{z1}^{\dot{\alpha}} &= -\frac{\pi}{9\alpha'^2\lambda_{wg}}\left[\frac{3k^2(\alpha'^2+1)}{(2k^2-1)E+(1-k^2)K}-\frac{2\alpha'^2+3}{E}\right] \text{ for } \alpha'\lambda_{wg}<4; \\ m_{z1}^{\dot{\alpha}} &= \frac{8}{9\alpha'^2\lambda_{wg}^2} \text{ for } \alpha'\lambda_{wg}>4. \end{aligned}\right\} \qquad \text{(V-10-54)}$$

In the slender-body theory, the derivatives are $m_z^{\omega_z} = -\pi/(3\lambda_{wg})$, $m_z^{\dot{\alpha}} = -\pi/9\lambda_{wg}^2$. The ratios $\bar{m}_Z^{\omega_x}$ and $\bar{m}_z^{\dot{\alpha}}$ can be calculated from the known derivative values, and are plotted in Fig. V-10-20 and V-10-21, respectively. /315

According to the linearized theory, the derivatives of the normal-force coefficients are determined as follows:

$$\left.\begin{aligned} c_{N\,1}^{\omega_z} &= \frac{2\pi}{3}\left[\frac{3k^2}{(2k^2-1)E+(1-k^2)K}-\frac{2}{E}\right] \text{ for } \alpha'\lambda_{wg}<4;\\ c_{N\,1}^{\omega_z} &= 0 \text{ for } \alpha'\lambda_{wg}>4; \end{aligned}\right\} \qquad \text{(V-10-55)}$$

$$\left.\begin{aligned} c_{N\,1}^{\dot{\alpha}} &= \frac{2\pi}{3\alpha'^2}\left[\frac{3k^2(\alpha'^2+1)}{(2k^2-1)E+(1-k^2)K}-\frac{2\alpha'^2+3}{E}\right] \text{ for } \alpha'\lambda_{wg}<4;\\ c_{N\,1}^{\dot{\alpha}} &= \frac{-16}{3\alpha'^2\lambda_{wg}} \text{ for } \alpha'\lambda_{wg}>4. \end{aligned}\right\} \qquad \text{(V-10-56)}$$

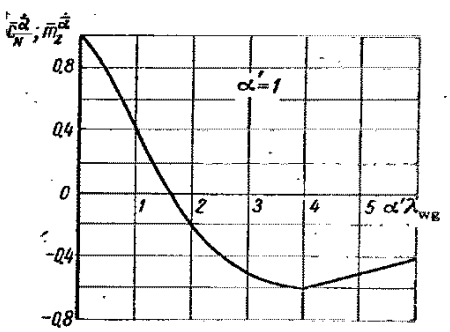

Figure V-10-21. Ratio of Delta-Wing Stability Derivatives Calculated by Linearized and Slender-Body Theories.

In the slender-body theory, the derivatives are defined by the expressions $c_{N\,t}^{\omega_z}=2\pi/3$, $c_{N\,t}^{\dot{\alpha}}=2\pi/3$. According to both theories, the corresponding derivatives with respect to ω_z and $\dot{\alpha}$ determine the ratios $\bar{c}_N^{\omega_z}$ and $\bar{c}_N^{\dot{\alpha}}$. Figure V-10-20 shows a curve of $\bar{c}_N^{\omega_z}$, and Fig. V-10-21 $\bar{c}_N^{\dot{\alpha}}$.

Figures V-10-24 and V-10-27 show curves of $\bar{c}_N^{\dot{\alpha}}$, $\bar{c}_N^{\omega_z}$ constructed by the linearized theory for a supersonic wing edge (the axis of rotation passes through the root-chord origin).

Analysis of available data indicates that slender-body theory can be used quite confidently to calculate the derivatives at very small aspect ratios. For large aspect ratios, however, this theory is suitable only for qualitative estimates, for example, of the center-of-pressure position and the stabilizing effects of damping.

At small aspect ratios, the center of pressure coordinate in the case of rotation about the center of gravity is determined as follows by the slender-body theory:

$$\frac{m_z^{\omega_z}}{c_N^{\omega_z}} = -\frac{\pi}{3\lambda_{wg}}\cdot\frac{3}{2\pi} = -\frac{c}{4b_m}. \qquad \text{(V-10-57)}$$

Thus, the center of pressure lies behind the center of gravity and, consequently, the damping moment is a stabilizing moment. For $\alpha'\lambda_{wg} > 4$, the linearized theory indicates $c_N^{\omega_z}=0$,

while $m_z^{\omega_z}$ is nonzero and negative. This means that the center of pressure has moved to an infinite distance behind the wing. Consequently, the qualitative picture of damping stabilization predicted by slender-body theory is preserved.

However, qualitative analyses by the slender-body theory must be made with caution. For example, in a motion that involves a time change in the attack angle ($\dot{\bar{\alpha}} \neq 0$), the center of pressure coefficient is determined in the slender-body theory by /316

$$\frac{m_z^{\dot{\bar{\alpha}}}}{c_N^{\dot{\bar{\alpha}}}} = -\frac{\pi}{9\lambda_{wg}} \cdot \frac{3}{2\pi} = -\frac{1}{12}\frac{e}{b_m}. \qquad \text{(V-10-58)}$$

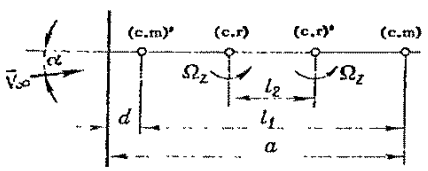

Figure V-10-22. Illustrating Conversion of Stability Derivative from One Center of Rotation (Center of Moments) to Another.

Consequently, the normal force $c_N^{\dot{\bar{\alpha}}}\dot{\bar{\alpha}}$ is always stabilizing. It follows from the linearized theory that the center of pressure coordinate will be the same as that given by slender-body theory. But, as we see from Fig. V-10-21, the normal force $c_N^{\dot{\bar{\alpha}}}\dot{\bar{\alpha}}$ becomes negative at certain values of $\alpha'\lambda_{wg}$. This means that a destabilizing effect not predicted by the slender-body theory makes its appearance.

In the general case, the center of rotation need not coincide with the center of moments, i.e., with the point about which the moments are determined. Then it is sometimes necessary to convert the derivatives from one center of rotation (or one center of moments) to another. The conversion formulas are:

$$c_N^{\dot{\bar{\alpha}}} = (c_N^{\dot{\bar{\alpha}}})'; \qquad \text{(V-10-59)}$$

$$m_z^{\dot{\bar{\alpha}}} = (m_z^{\dot{\bar{\alpha}}})' + \frac{l_2}{l}(c_N^{\dot{\bar{\alpha}}})'; \qquad \text{(V-10-60)}$$

$$c_N^{\omega_z} = (c_N^{\omega_z})' - 2c_N^{\alpha}\frac{l_2}{l}; \qquad \text{(V-10-61)}$$

$$m_z^{\omega_z} = (m_z^{\omega_z})' - 2(m_z^{\alpha})'\frac{l_2}{l} + (c_N^{\omega_z})'\frac{l_1}{l} - 2\frac{l_1}{l}\frac{l_2}{l}c_N^{\alpha}. \qquad \text{(V-10-62)}$$

In these formulas, the primed coefficients are the values of the derivatives for the given rotation or moment center (in

the general case, these centers do not coincide); the other coefficients correspond to the new positions of these centers. Here, the new centers of moments and rotation are located at the respective distances l_1 and l_2 aft of the old ones (Fig. V-10-22). A certain length l, which is set equal to the span b_m for a wing, is the characteristic dimension.

The rolling moments caused by rotation about the y-axis are determined in the linearized theory by the formula

$$m_{x1}^{\omega_y} = \frac{\pi(1+9\lambda_{wg}^2/16)\alpha}{9\lambda_{wg}E}, \qquad \text{(V-10-63)}$$

while in the slender-body theory $m_{x1}^{\omega_y} = \pi\alpha/(9\lambda_{wg})$. The difference is substantial. The ratio of the corresponding derivatives is

$$\overline{m}_x^{\omega_y} = \left(1 - \frac{9\lambda_{wg}^2}{16}\right)\frac{1}{E}. \qquad \text{(V-10-64)}$$

As $\lambda_{wg} \to 0$, this ratio $\overline{m}_x^{\omega_y} \to 1$.

Forces and moments of the Magnus effect. The forces and moments of the Magnus effect arise from oblique flow around a wing in rotation about the longitudinal axis. These forces are proportional to the products $\alpha\omega_x$ or $\beta_{s1}\omega_x$. In particular, the lateral force $Z \sim \alpha\omega_x$, and the yawing moment $M_y \sim \alpha\omega_x$. In the wind axes, the stability derivatives for lateral force and yawing moment are determined as follows in the linearized theory: /318

$$c_{z1}^{\alpha\omega_x} = -\frac{4\pi k^3}{3E[(k^2+1)E-(1-k^2)K]}; \qquad \text{(V-10-65)}$$

$$m_{y1}^{\alpha\omega_x} = -\frac{2\pi k^3[\lambda_{wg}/16+1/(9\lambda_{wg})]}{E[(k^2+1)E-(1-k^2)K]}. \qquad \text{(V-10-66)}$$

For $\alpha'\lambda_{wg} \geq 4$, both derivatives are zero.

In the slender-body theory, the expressions $c_{z1}^{\alpha\omega_x} = -\frac{2\pi}{3}$, $m_{y1}^{\alpha\omega_x} = -\frac{\pi}{9\lambda_{wg}}$ correspond to the coefficients in (V-10-65) and (V-10-66). Figure V-10-20 shows the curve of the ratio $\frac{c_z^{\alpha\omega_x}}{\alpha\omega_x}$. As we see, the two theories differ qualitatively for $\alpha'\lambda_{wg} = 4$.

Rectangular wing. Figures V-10-23 through V-10-30 present certain data on the stability derivatives for a rectangular wing,

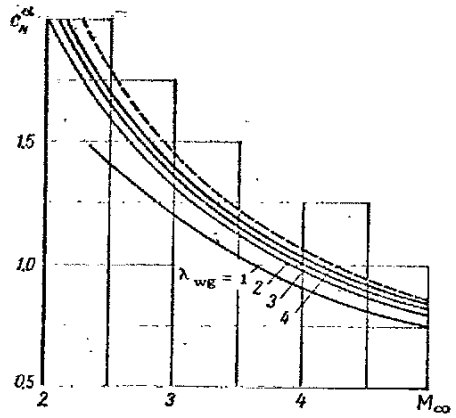

Figure V-10-23. Dependence of c_N^α on Aspect Ratio and M_∞ at Supersonic Speeds (St = 0).

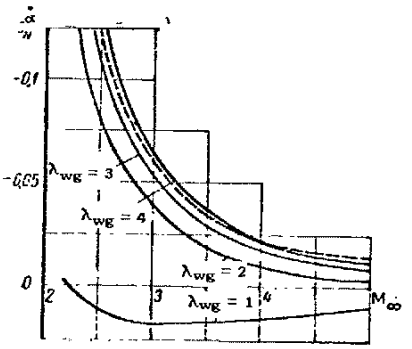

Figure V-10-24. Dependence of $c_N^{\dot{\alpha}}$ on Aspect Ratio and M_∞ at Supersonic Speed (St = 0).

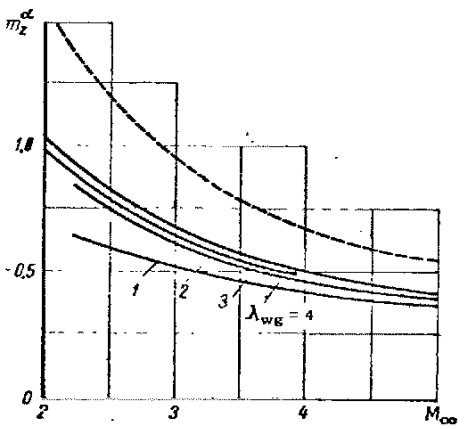

Figure V-10-25. Dependence of m_z^α on Aspect Ratio and M_∞ at Supersonic Speeds (St = 0).

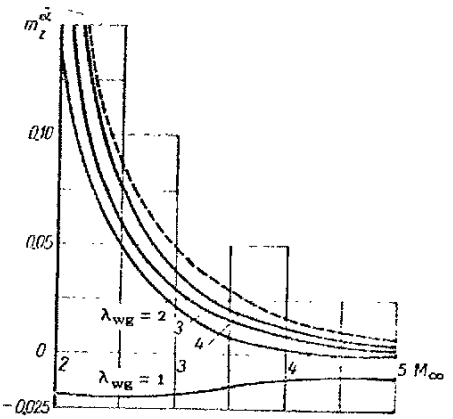

Figure V-10-26. Dependence of $m_z^{\bar{\alpha}}$ on Aspect Ratio and M_∞ at Supersonic Speeds (St = 0).

as obtained in the linearized theory. In contrast to the case of delta wings, the stability derivatives depend on aspect ratio (the solid lines in the figures represent the characteristics for the rectangular wing, and the dashed lines those of the delta).

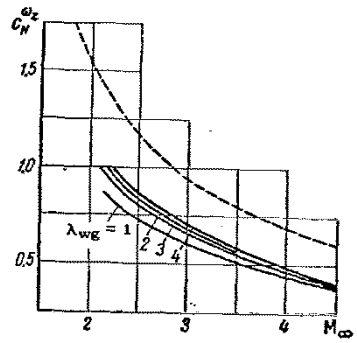

Figure V-10-27. Dependence of $c_N^{\omega_z}$ on Aspect Ratio and M_∞ at Supersonic Speeds (St = 0).

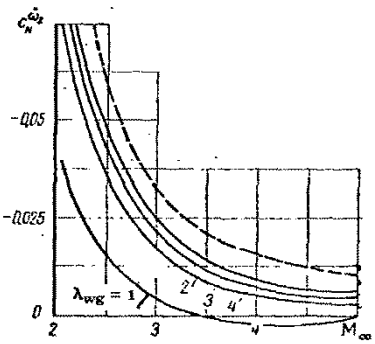

Figure V-10-28. Dependence of $c_N^{\dot{\omega}_z}$ on Aspect Ratio and M_∞ at Supersonic Speeds (St = 0).

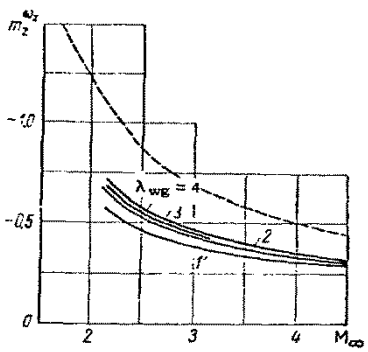

Figure V-10-29. Dependence of $m_z^{\omega_z}$ on Aspect Ratio and M_∞ at Supersonic Speeds (St = 0).

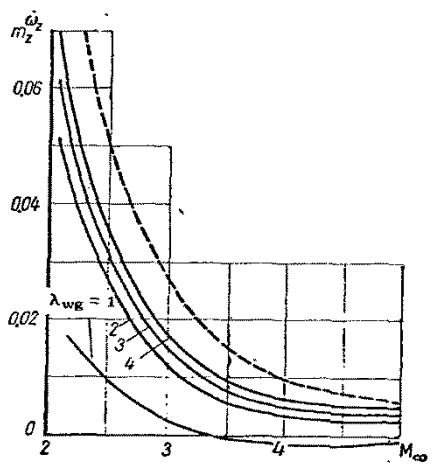

Figure V-10-30. Dependence of $m_z^{\dot{\omega}_z}$ on Aspect Ratio and M_∞ at Supersonic Speeds (St = 0).

Research has shown that at supersonic speeds, the rotary derivatives depend less on Strouhal number the smaller that number and the smaller the wing aspect ratio. Here, the aerodynamic-characteristic values obtained for St → 0 can be used with adequate accuracy in the range of St encountered in practice.

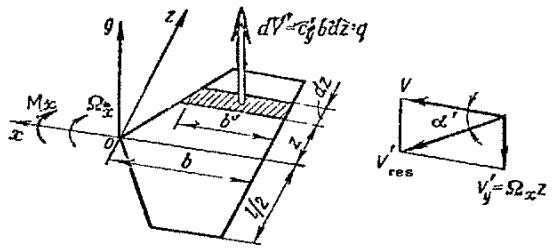

Figure V-10-31. Illustrating Determination of Roll Damping Moment.

Figures V-10-23 through V-10-30 present the corresponding data for the coefficients of the rotary derivatives calculated for axes of rotation and moments that pass through the origin of the wing root chord.

Damping characteristics of rolling motion. We shall investigate separately the rotation of a wing about the x-axis at angular velocity Ω_x (Fig. V-10-31), which results in the appearance of a roll damping moment M_x opposed to the direction of rotation and equal to $M_x = m_x S_{wg} \ell q$.

In the general case, the damping-moment coefficient is /319

$$m_x = m_x^{\omega_x}\omega_x + m_x^{\dot{\omega}_x}\dot{\omega}_x. \qquad \text{(V-10-67)}$$

In practical cases, the accelerations $\dot{\omega}_x$ are small, so that we can write

$$m_x = m_x^{\omega_x}\omega_x. \qquad \text{(V-10-67')}$$

Using the "method of strips," we find for the wing as a whole

$$m_x^{\omega_x} = -\frac{b_{mn}l}{2S_{wg}}\int_0^1 c_y'^{\alpha}\bar{z}^2\frac{b}{b_{mn}}d\bar{z}, \qquad \text{(V-10-68)}$$

where $\bar{z} = 2z/\ell$; $c_y'^{\alpha}$ is the derivative for a given section, determined from the condition

$$c_y' = c_y'^{\alpha}\frac{\Omega_x z}{V_\infty} = c_y'^{\alpha}\omega_x\bar{z}, \qquad \text{(V-10-69)}$$

in which

$$\omega_x = \frac{\Omega_x l}{2V_\infty}.$$

The other nomenclature is evident from Fig. V-10-31.

The damping-coefficient derivative can be calculated by (V-10-68) for $b\bar{z}^2/b_{mn}$, and $c_y'^{\alpha}(\bar{z},M_\infty)$, which for the given wing are known as functions of the coordinate $\bar{z}$ and M_∞.

Chapter VI /320

FRICTION AND HEAT TRANSFER ON WINGS

§VI-1. PARAMETERS OF FRICTION IN FLOW AROUND A FLAT PLATE

Homogeneous Boundary Layer

Incompressible boundary layer. Let us examine calculation of the friction parameters for a plate in incompressible flow. The result of this calculation is the determination of such boundary-layer variables as thickness and the conventional displacement and momentum thicknesses. As we shall show, these parameters can be used to calculate more complex cases of gas flow in the boundary layer, those characterized by compressibility and high-temperature effects and curvilinear shape of the washed surface.

Let us consider the basic relationships for an incompressible boundary layer around a plate on the assumption that the boundary layer has a certain small finite thickness δ_{ic} and that the velocity distributions across the sections of the laminar and turbulent boundary layers are characterized respectively by the parabolic law proposed by Pohlhausen

$$\frac{V_x}{V_\delta} = \frac{3}{2}\frac{y}{\delta_{ic}} - \frac{1}{2}\frac{y^3}{\delta_{ic}^3} \qquad \text{(VI-1-1)}$$

and the "seventh root" law (according to Karman)

$$\frac{V_x}{V_\delta} = \left(\frac{y}{\delta_{ic}}\right)^{1/7}, \qquad \text{(VI-1-2)}$$

which is a particular case of the more general "$\overline{k}$th-root" law

$$\frac{V_x}{V_\delta} = \left(\frac{y}{\delta_{ic}}\right)^{1/\overline{k}}. \qquad \text{(VI-1-3)}$$

Introducing (VI-1-1) and VI-1-2) into integral relationship (III-2-42), we find the thickness of the boundary layer:

$$\frac{\delta_{ic}}{x_w} = A\bar{x}^m \mathrm{Re}^n, \qquad \text{(VI-1-4)}$$

where x_w is the length of the plate; $x = x/x_w$ is a dimensionless coordinate; $Re = V_\delta x_w/\nu$.

The friction stress $\tau_{wl.ic}$ on the wall is determined by substituting Expression (VI-1-4) for the layer thickness into the formulas

$$\tau_{wl,ic} = \mu\left(\frac{\partial V_x}{\partial y}\right)_{y=0};\ \tau_{wl,ic} = 0.0225\rho_\delta V_\delta^2\left(\frac{\nu}{V_\delta\delta_{ic}}\right)^{1/4}, \qquad \text{(VI-1-5)}$$

the first of which pertains to a laminar boundary layer and the second to a turbulent boundary layer. As a result,

$$\tau_{wl.ic} = B\rho_\delta V_\delta^2\,\mathrm{Re}_x^n, \qquad \text{(VI-1-6)}$$

where $Re_x = V_\delta x/\nu$ is the local Reynolds number.

From the stress $\tau_{wl.ic}$, we can find the local coefficient of friction /321

$$c_{fx\ ic} = \frac{\tau_{wl.ic}}{q} = C\,\mathrm{Re}_x^n, \qquad \text{(VI-1-7)}$$

where $q = (\rho_\delta V_\delta^2)/2$.

TABLE VI-1-1. VALUES OF COEFFICIENTS AND EXPONENTS IN FORMULAS FOR BOUNDARY-LAYER PARAMETERS

Boundary layer	A	B	C	D	m	n
Laminar	5.8	0.332	0.664	1.33	$\frac{1}{2}$	$-\frac{1}{2}$
Turbulent	0.37	0.0289	0.0578	0.074	$\frac{1}{5}$	$-\frac{1}{5}$

Applying (VI-1-7), we determine the average value of this coefficient:

$$c_{f\ ic} = \int_0^1 c_{fx\,ic}\,d\bar{x} = D\,\mathrm{Re}^n. \qquad \text{(VI-1-8)}$$

Values of the coefficients A, B, C, and D and the exponents m and n are given in Table VI-1-1.

Other results for the turbulent boundary layer. Formula (VI-1-8) for the turbulent friction coefficient $c_{f\,t\,ic}$ can be used with greater confidence if Re does not exceed 10^6. Other relationships give better results for larger values. For example, for Re in the range $10^6 < Re < 10^9$

$$c_{f\,t.ic} = 0.427\,(\lg \mathrm{Re} - 0.407)^{-2.46}. \qquad \text{(VI-1-9)}$$

The following formula can also be used for the interval $5 \cdot 10^6 < Re < 10^{10}$:

$$c_{f\,t.ic} = 0.043\,\mathrm{Re}^{-0.167}. \qquad \text{(VI-1-10)}$$

For Reynolds numbers in the range $2 \cdot 10^6 < Re < 10^{10}$ we have

$$c_{f\,t.ic} = 0.032\,\mathrm{Re}^{-0.145}. \qquad \text{(VI-1-11)}$$

For larger Reynolds numbers, we can consider the universal Prandtl-Schlichting formula for calculation of the average turbulent-friction coefficient:

$$c_{f\,t.ic} = \frac{0.455}{(\lg \mathrm{Re})^{2.58}}. \qquad \text{(VI-1-12)}$$

The Schultz-Grünow formula for calculation of the local turbulent friction coefficient may be regarded as equally universal:

$$c_{fx\,t.ic} = \frac{0.37}{(\lg \mathrm{Re}_x)^{2.584}}; \qquad \text{(VI-1-13)}$$

here, Re_x can vary up to 10^9.

The thickness of a boundary layer with a velocity profile characterized by the power law (VI-1-3) can be determined from the expression

$$\delta_{t.ic} = \bar{B}\left(\frac{V_\delta x}{\nu_\delta}\right)^{-\frac{2}{\bar{n}+3}} x, \qquad \text{(VI-1-14)}$$

where

$$\bar{B} = \left[\frac{\bar{k}}{(\bar{k}+3)(\bar{k}+2)}\right]^{-\frac{\bar{k}+1}{\bar{k}+3}} \bar{C}^{-\frac{2\bar{k}}{\bar{k}+3}},$$

and, according to Wishard, the coefficient $\bar{C}$ equals

$$\bar{C} = 0.917\bar{k} + 2.343.$$

TABLE VI-1-2. VALUES OF THE PARAMETERS $\bar{B}$ AND $\bar{C}$

$\bar{k}$	5	6	7	8	9	10
$\bar{C}$	6.93	7.84	8.74	9.71	10.6	11.5
$\bar{B}$	0.544	0.445	0.370	0.311	0.274	0.261

Values of $\bar{B}$ and $\bar{C}$ are given in Table VI-1-2.

The exponent $\bar{k}$ can be determined by the formula

$$\bar{k} = 2.35(\lg \mathrm{Re}^{**} - 1), \qquad \text{(VI-1-15)}$$

where $\mathrm{Re}^{**} = V_\delta \delta^{**}/\nu_\delta$.

The following relationship exists between the conventional displacement and momentum thicknesses δ^* and δ^{**} and the thickness δ_{1c} of the boundary layer in an incompressible fluid:

$$\delta^*_{t.ic} = \frac{1}{\bar{k}+1}\delta_{t.ic}, \quad \delta^{**}_{t.ic} = \frac{\bar{k}}{(\bar{k}+1)(\bar{k}+2)}\delta_{t.ic} \qquad \text{(VI-1-16)}$$

Example. Determine the parameters of a boundary layer on a plate for the conditions

$V = 200$ m/s; $H = 2000$ m; $\nu_\delta = 0.1715 \cdot 10^{-4}$ m^2/s^2; $x = 1$ m.

Solution is by the method of successive approximations. We take the exponent in the velocity-distribution law $\bar{k} = 7.46$ as our first approximation and calculate the corresponding

coefficients $\overline{B}$ and $\overline{C}$

$$\overline{C}=0.917\overline{k}+2.343=9.18;$$

$$\overline{B}=\left[\frac{\overline{k}}{(\overline{k}+3)(\overline{k}+2)}\right]^{\frac{\overline{k}+1}{\overline{k}+3}}\overline{C}^{-\frac{2\overline{k}}{\overline{k}+3}}=$$

$$=\left[\frac{7.46}{(7.46+3)(7.46+2)}\right]^{\frac{7.46+1}{7.46+3}}9.18^{-\frac{2\cdot 7.46}{7.46+3}}=0.343.$$

From (IV-1-14) we determine the layer thickness:

$$\delta_{t.lc}=\overline{B}\left(\frac{V_\delta x}{\nu_\delta}\right)^{\frac{2}{\overline{k}+3}}x=0.343\left(\frac{200\cdot 1}{0.1715\cdot 10^{-4}}\right)^{\frac{2}{7.46+3}}1=0.0153\text{ m}.$$

From (VI-1-16), we find

$$\delta^{**}_{t.lc}=\frac{\overline{k}}{(\overline{k}+1)(\overline{k}+2)}\delta_{t.lc}=\frac{7.46}{(7.46+1)(7.46+2)}0.0153=0.0014\text{ m}.$$

We then determine

$$\mathrm{Re}^{**}=\frac{V_\delta(\delta^{**}_t)_{t.c}}{\nu_\delta}=\frac{200\cdot 0.0014}{0.1715\cdot 10^{-4}}=16\,300$$

and calculate $\overline{k}$ in the second approximation: /323

$$\overline{k}=2.35(\lg \mathrm{Re}^{**}-1)=2.35(\lg 16\,300-1)=7.55.$$

Using this $\overline{k}$, we improve the boundary-layer parameters:

$$\overline{C}=0.917\cdot 7.55+2.343=9.266;\quad \overline{B}=0.338;$$

$$\delta_{t.lc}=0.01545\text{ m};\qquad \delta^{**}_{t.lc}=0.00143\text{ m};$$

$$\mathrm{Re}^{**}=\frac{200\cdot 0.00143}{0.1715\cdot 10^{-4}}=16\,680.$$

These data correspond to

$$\overline{k}=2.35(\lg 16\,680-1)=7.57.$$

Since the resulting $\bar{k}$ differs insignificantly ($\sim$0.2%) from the value in the preceding approximation, we may regard $\bar{k} = 7.57$ and the boundary-layer parameters corresponding to it as final.

Influence of altitude. This effect manifests in an altitude variation of Reynolds number. If $Re_g = M_\infty a_g x_w/\nu_g$ near the ground (a_g and ν_g are the speed of sound and the kinematic viscosity coefficient, respectively, near the ground) and $Re = M_\infty a x_w/\nu$ at a certain altitude, we can write for it

$$Re = Re_g f_1(H) f_2(H) f_3(H), \qquad \text{(VI-1-17)}$$

where

$$f_1(H) = \frac{\rho}{\rho_g}; \quad f_2(H) = \frac{a}{a_g}; \quad f_3(H) = \frac{\mu_g}{\mu}$$

are functions that determine the variation of density, the speed of sound, and the dynamic viscosity coefficient with altitude. The values of these functions are found from the appropriate tables (see Appendix No. 2).

Influence of compressibility (in the absence of heat transfer). The boundary-layer parameters, and especially the frictional stress and coefficient of friction, will differ substantially from the values for incompressible flow at high velocities owing to the action of such factors as compressibility, heating, and heat transfer.

These parameters can be calculated by various methods with consideration of the above factors, depending on the nature of the thermal processes that take place. Let us examine a calculation based on the assumption that there is no heat transfer (although aerodynamic heating of the boundary layer does take place) and without taking any of the possible physicochemical processes into account.

If we assume that heating takes place with no change whatever in internal energy (we shall disregard the work of viscous forces and conduction or radiation of heat), then the influence of heating on the boundary-layer parameters will manifest in a dependence of these parameters on M_∞.

The corresponding relation for a laminar boundary layer takes the form

$$\frac{c_{f\,1}}{c_{f\,1.ic}} = (1+0.03M_\delta^2)^{-1/3}. \qquad \text{(VI-1-18)}$$

For a turbulent boundary layer, the form of the ratio $c_{f\ t}/c_{f\ t.ic}$ as a function of M_δ will generally be determined by the exponent in the law of velocity variation, i.e., by $\bar{k}$ or, which is the same thing, by the Reynolds number. However, as we see from Fig. VI-1-1, variation of $\bar{k}$ from 5 to 9, which corresponds to a change in Reynolds number from 10^6 to 10^8, has practically no effect on the ratio $c_{f\ t}/c_{f\ t.ic}$.

We may therefore assume for practical purposes that this ratio is independent of $\bar{k}$ (of Reynolds number). According to Fig. VI-1-1, the ratio of the coefficients of friction is presented as a function of M_δ for a turbulent layer in the form /324

$$\frac{c_{f\,1}}{c_{f\,t.ic}} = \left(1+\frac{\bar{k}-1}{2}M_\delta^2\right)^t, \qquad \text{(VI-1-19)}$$

where $t = -0.43$ for $6 < M_\delta < 15$ and $t = -0.39$ for $0 < M_\delta < 6$.

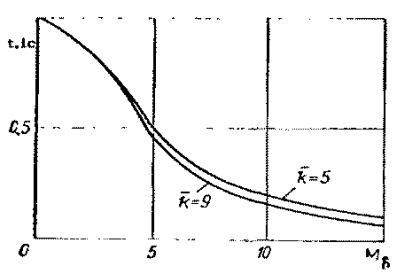

Figure VI-1-1. Ratio $c_{f\ t}/c_{f\ t.ic}$ for a Turbulent Boundary Layer as a Function of M_δ for Various $\bar{k}$.

An experimental study of the influence of wall temperature on the ratio $c_{f\ t}/c_{f\ t.ic}$ showed that this effect is minor in a turbulent flow and need not be taken into account in practical calculations if the coefficients of friction are calculated for the parameters at the outer boundary of the layer. Here the formula will be more exact for a heat-insulated (adiabatic) wall.

Apart from (VI-1-19), we can use a relationship found by Acad. A.A. Dorodnitsin

$$c_{f_t} = 0.472\,(1+0.1M_\delta^2)^{-0.1} \times \\ \times\,[\lg \mathrm{Re}\,(1+0.2M_\delta^2)^{-1.76}]^{-2.58} \qquad \text{(VI-1-20)}$$

or the Luter formula

$$c_{f\,t} = 0.0631 \exp(-0.172M_\delta^2)\,\mathrm{Re}^{-0.182}, \qquad \text{(VI-1-21)}$$

which give better results for Reynolds numbers in the range $10^6 < Re < 10^{10}$.

Boundary-layer thicknesses can be calculated with (VI-1-4) with consideration of compressibility and wall temperature by converting in that formula to determining parameters. The displacement and momentum thicknesses can be determined by (VI-1-16) from the layer thickness found in this manner. A correction for the Mach-number effect must be applied to $\bar{k}$ in calculations with (VI-1-14). This can be done by applying (VI-1-15), in which

$$\mathrm{Re}^{**} = 0.036\,\mathrm{Re}_x^{0.8}\left(1+\frac{k-1}{2}M_\delta^2\right)^t. \qquad \text{(VI-1-22)}$$

The quantities δ^{**} and δ^* can be calculated directly with the expressions

$$\frac{\delta^{**}}{\delta}=\int_0^1 \frac{\rho V_x}{\rho_\delta V_\delta}\left(1-\frac{V_x}{V_\delta}\right)d\left(\frac{y}{\delta}\right);\quad \frac{\delta^*}{\delta}=\int_0^1\left(1-\frac{\rho V_x}{\rho_\delta V_\delta}\right)d\left(\frac{y}{\delta}\right), \qquad \text{(VI-1-23)}$$

in which it is assumed that $V_x/V_\delta=(y/\delta)^{1/\bar{k}}$; $V_x/V_\delta=(T_0-T_{w1})/(T_{0\delta}-T_{w1})$, where T_0 and $T_{0\delta}$ are the respective stagnation temperatures in the boundary layer and the free stream. Here density is determined from the equation $p = \rho RT$ for the condition that $\partial p/\partial y = 0$ in the boundary layer.

The momentum and displacement thicknesses, referred to the boundary-layer thickness and calculated for the "seventh root" law, are expressed as follows:

$$\frac{\delta_t^{**}}{\delta_t}=\frac{85.2\,[1-0.038\,(3-b)]\,(1-0.78G)}{\left(1+\frac{k-1}{2}M_\delta^2\right)\bar{T}_{w1}}, \qquad \text{(VI-1-24)}$$

where /325

$$G=\frac{\frac{k-1}{2}M_\delta^2}{1+\frac{k-1}{2}M_\delta^2}+0.197\left\{1-\left[1+\frac{k-1}{2}(M_\delta-2)^2\right]^{-0.15}\right\};$$

$$b=\frac{1}{\bar{T}_{w1}}-1; \qquad \text{(VI-1-25)}$$

$$\frac{\delta_t^*}{\delta_t}=\left\{\frac{16}{7}\left[1+0.465\,(k-1)\,M_\delta^2\right]\left[1+0.54\,(\bar{T}_{w1}-1)\right]-1\right\}\frac{\delta_t^{**}}{\delta_t}.$$

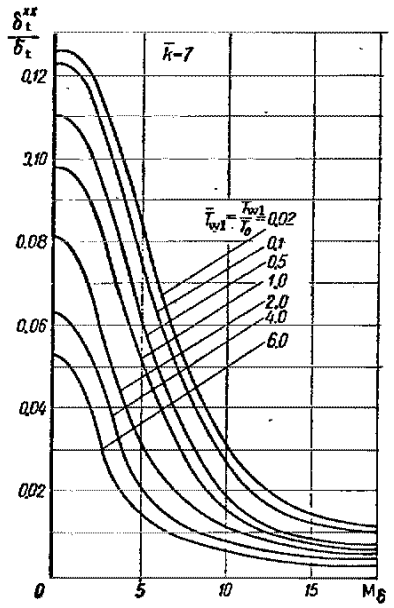

Figure VI-1-2. Ratio δ_t^{**}/δ_t as a Function of M_δ and the Relative Wall Temperature $\bar{T}_{w1}$.

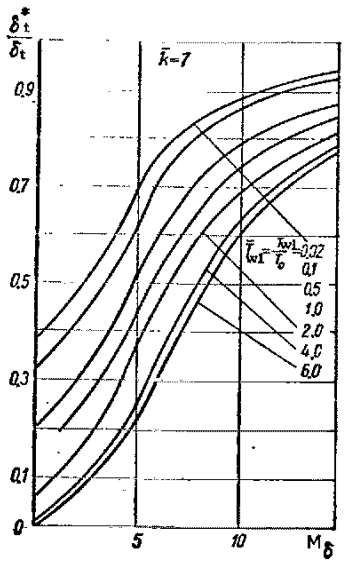

Figure VI-1-3. Ratio δ_t^{*}/δ_t as a Function of M_δ and Relative Wall Temperature $\bar{T}_{w1}$.

Figures VI-1-2 and VI-1-3 present the results of calculation of δ_t^{**}/δ_t and δ_t^{*}/δ_t as functions of M_δ and the relative wall temperature $\bar{T}_{w1} = T_{w1}/T_0$.

With the values of δ_t^{**}/δ_t, we can use the formula $\delta_t^{**} = (1/2)c_{fx\ t}x$ to calculate the boundary-layer thickness.

$$\frac{\delta_t}{\delta_{t.ic}} = \frac{c_{ft}}{c_{f\,t.ic}} \frac{\delta_{t.ic}^{**}/\delta_{t.ic}}{\delta_t^{**}/\delta_{t.ic}}. \qquad \text{(VI-1-26)}$$

The ratios δ_t^{**}/δ_t and δ_t^{*}/δ_t were obtained for conditions under which the influence of the laminar sublayer is not taken into account. Studies have shown that this effect on δ_t^{*}/δ_t is small and may be disregarded.

As for the momentum thickness, the laminar sublayer may have a substantial influence, and one that increases with decreasing Re_δ and with increasing M_δ. The quantity δ_t^{**}/δ_t can be /326

represented by the general relationship

$$\frac{\delta_t^{**}}{\delta_t} = \left(\frac{\delta_t^{**}}{\delta_t}\right)_{Re_\delta=\infty} N_1(\bar{T}_{w1}, Re_\delta, M_\delta) N_2(M_\delta, Re_\delta), \qquad (VI\text{-}1\text{-}27)$$

where $(\delta_t^{**}/\delta_t)_{Re_\delta=\infty}$ is the ratio of the momentum thickness to the layer thickness when there is no laminar sublayer (see Fig. VI-1-2); $Re_\delta = V_\delta \delta/\nu_\delta$. For the particular case of a heat-insulated wall ($\bar{T}_{w1} = 1$), the function

$$N_1 = 1 + 0.004(M_\delta - 10)(1 - 0.125\,Re_\delta).$$

The function N_2 is calculated by the formula

$$N_2 = 1 - 0.848\left(\frac{M_\delta - 1}{10}\right)^2 (8 - \lg Re_\delta)^h,$$

where $h = 3.9 - 0.6\sqrt{M_\delta - 3}$ for $M_\delta > 3$ and $h = 3.9$ for $1 < M_\delta \leq 3$. For $M_\delta \leq 1$, $N_2 = 1$.

Influence of high temperatures on flow in the boundary layer. Owing to flow stagnation in the boundary layer and the temperature rise, the density of the gas changes, and this influences the boundary-layer parameters. The property of compressibility and the dependence of the boundary-layer variables on Mach number are manifested here.

With increasing velocity, temperature increases and the boundary layer is heated to such a degree that chemical reactions may take place in it. As a result, other physical parameters of the gas also change along with density. These effects are of decisive importance in shaping the friction and heat-exchange processes in the boundary layer. However, quite major difficulties are encountered in taking them into consideration. For this reason, attempts have been made to find comparatively simple approximate methods for calculation of the boundary layer at very high flow velocities. One of them, which will be examined below, is based on the use of relationships derived from investigation of the boundary layer in an incompressible medium. Near the surface, there are always regions in which the flow is extensively stagnated and, consequently, the properties of the gas make a close approach to those in an incompressible medium. If we consider flow in this region to have the basic influence on friction and heat-transfer processes, we can investigate the boundary layer by relationships that are superficially similar

to those for the incompressible medium. The difference will be that parameters determined in accordance with the local temperature values in the boundary layer will appear in these relationships. Here, as research has shown, satisfactory results are obtained if the calculation is made for a determining temperature T* and the determining enthalpy i*, density ρ*, coefficients μ*, ν*, etc. that correspond to it.

Let us examine certain relationships for calculation of the boundary layer from determining parameters.

Laminar boundary layer. In introducing the determining parameters, we can use relationships that take account of the influence of high temperature. For example, in accordance with (VI-1-4), the thickness of the high-temperature boundary layer is

$$\delta_1 = \delta_{1.ic} \left(\frac{\mu^*}{\mu_\delta}\frac{\rho_\delta}{\rho^*}\right)^{1/2}. \qquad \text{(VI-1-4')}$$

In the general case, the displacement and momentum thicknesses can be determined similarly with consideration of dissociation and the wall temperature. In addition to calculation by the determining-temperature method, the thicknesses can also be computed with the ordinary boundary-layer equations. If c_p = = const and Pr = 1, solution of these equation gives relationships that enable us to determine boundary-layer parameters close to the true ones as functions of wall temperature and M_δ. These relationships have the form

/327

$$\bar{\delta}_1 = \frac{\delta_1}{x_k} = 4K\,[0.4\,(\bar{T}_{w1} + 1.5)\,(1 + 0.2M_\delta^2) - 0.09M_\delta^2]; \qquad \text{(VI-1-28)}$$

$$\bar{\delta}_1^* = \frac{\delta_1^*}{x_k} = 1.6K\left(\bar{T}_{w1} + 0.18\frac{V_\delta^2}{i_0}\right)\left(1 - \frac{V_\delta^2}{2i_0}\right)^{-1}; \qquad \text{(VI-1-29)}$$

$$\bar{\delta}_1^{**} = \frac{\delta_1^{**}}{x_k} = 0.57K, \qquad \text{(VI-1-30)}$$

where $\bar{T}_{w1} = T_{w1}/T_0$; the coefficient

$$K = \sqrt{\frac{\bar{x}}{\mathrm{Re}}\frac{\lambda_{w1}}{\lambda_\delta}}.$$

Here $\bar{x} = x/x_k$, $\mathrm{Re} = V_\delta x_k/\nu_\delta$; the coefficient λ_{w1} is found from one of Formulas (VI-3-2).

We can calculate the coefficient λ_δ on substituting T_δ for T_{w1} in these formulas.

Taking (VI-1-5) as the starting formula, we find the relation for the friction stress

$$\tau_{w1.1} = \tau_{w1.1.ic}\frac{\delta_1}{\delta_{1.ic}}\frac{\rho^*}{\rho_\delta} \qquad \text{(VI-1-5')}$$

The ratio of friction stresses is equal to the ratio of the local and mean coefficients of friction:

$$\frac{\tau_{w1.1}}{\tau_{w1.1.ic}} = \frac{c_{fx\ 1}}{c_{fx\ 1.ic}} = \frac{c_{f\ 1}}{c_{f\ 1.ic}} \qquad \text{(VI-1-31)}$$

We see from (VI-1-4') that the thickness of a laminar boundary layer increases with rising temperature. Despite the increase in viscosity, friction stress decreases because of the lower density, which has the dominating effect on friction. The relationships for the boundary-layer parameters simplify in the absence of dissociation, when we can set $\rho_\delta/\rho^* = T^*/T_\delta$, $\mu^*/\mu_\delta = (T^*/T_\delta)^n$.

The following procedure is used in calculating friction stress by the determining-temperature (enthalpy) method for given stream parameters on the outer and inner boundaries of a laminar boundary layer.

First, the determining enthalpy is found. This can be done by (IV-8-7) or a relation derived for a laminar boundary layer

$$i^* = \frac{0.363\,\mathrm{Pr}^*}{0.126 + \mathrm{Pr}^*} i_\delta + \frac{0.126 + 0.437\,\mathrm{Pr}^*}{0.126 + \mathrm{Pr}^*} i_{w1} + \frac{0.211\,\mathrm{Pr}^*}{1.53 + \mathrm{Pr}^*} V_\delta^2. \qquad \text{(VI-1-32)}$$

Here, the i* calculated from the $Pr^* = Pr_{w1}$ at the wall is determined as the first approximation. Then this i* is used to find the second-approximation Pr*, and so forth.

In practice, we can limit ourselves to calculation of the determining enthalpy in first approximation, i.e., calculate i* by (VI-1-32), setting $Pr^* = Pr_{w1}$ in it.

Here the largest possible deviation of the friction coefficient or heat transfer from the true values does not exceed 10%. /328

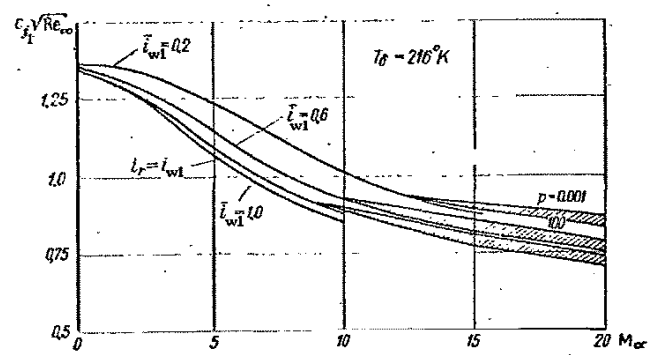

Figure VI-1-4. $c_{f1}\sqrt{Re_\infty}$ ($Re_\infty = Re = V_\delta x_k/\nu_\delta$) as a Function of M_∞ and the Enthalpy Ratio $\bar{i}_{w1} = i_{w1}/i_0$ (Laminar Boundary Layer).

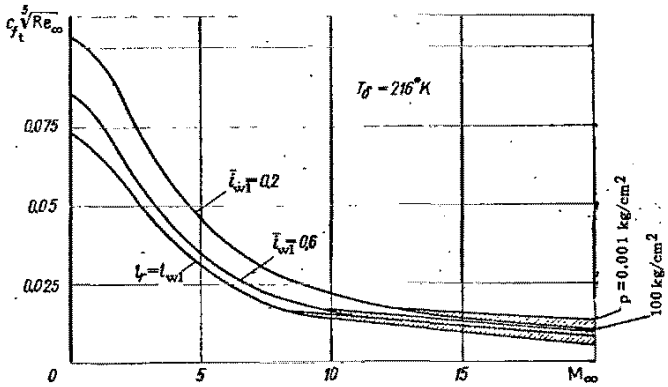

Figure VI-1-5. $c_{f_t}\sqrt[5]{Re_\infty}$ as a Function of M_∞ and the Enthalpy Ratio $\bar{i}_{w1} = i_{w1}/i_0$ (Turbulent Boundary Layer).

The determining temperature is found for the determining enthalpy by reference to tables or diagrams of the thermodynamic functions of air; then $c = \rho^*\mu^*/\rho_\delta\mu_\delta$ is calculated and the local and average coefficients of friction are found:

$$\left.\begin{aligned} c_{fx\,1} &= \frac{2\tau_{w1.1}}{\rho_\delta V_\delta^2} = 0.664\sqrt{\frac{c}{Re_x}}, \text{ where } Re_x = \frac{V_\delta x}{\nu_\delta}; \\ c_{f\,1} &= \frac{2X_{f\,1}}{\rho_\delta V_\delta^2 S} = 1.33\sqrt{\frac{c}{Re}}, \text{ where } Re = \frac{V_\delta x_k}{\nu_\delta}. \end{aligned}\right\} \qquad \text{(VI-1-33)}$$

If the coefficient of friction is determined for both sides of the plate, the result obtained must be doubled.

Turbulent boundary layer. If we start with the power law (VI-1-2) for the velocity distribution and the corresponding expression (VI-1-4) for the incompressible boundary layer, we can introduce defining parameters to find a formula for the boundary-layer thickness: /329

$$\delta_t = \delta_{t,ic} \left(\frac{\mu^*}{\mu_\delta}\frac{\rho_\delta}{\rho^*}\right)^{1/5}. \qquad \text{(VI-1-4")}$$

The formulas for the stress and coefficient of friction have the same superficial form as (Vi-1-5') and (VI-1-31). The difference is that the layer thickness must be taken according to (VI-1-4"). Applying (VI-1-8) to calculate the coefficient of friction of a flat plate in incompressible flow, we can obtain a generalized expression for the coefficient of friction:

$$c_f \mathrm{Re}_\infty^{-n} = D \left(\frac{\mu^*}{\mu_\delta}\right)^{-n} \left(\frac{\rho^*}{\rho_\delta}\right)^{1+n}, \qquad \text{(VI-1-34)}$$

in which n = - 1/2 for a laminar boundary layer and n = -1/5 for a turbulent layer. Figures VI-1-4 and VI-1-5 show how the product $c_f \mathrm{Re}_\infty^{-n}$ depends on a number of parameters when it is calculated with dissociation taken into account.

To calculate the coefficient of friction in a dissociated boundary layer, we can also use the formula

$$c_{fxt} = c_{f0t}\left[2\left(\frac{1+\alpha_\delta}{1+\alpha_{wl}}\right)^{1/7} - 1\right], \qquad \text{(VI-1-35)}$$

which is derived from the general equations of the turbulent boundary layer. In this formula, $c_{f\,0t}$ is the coefficient of friction calculated for the corresponding local M_∞, T_{wl}/T_δ and $\mathrm{Re}_\delta = V_\delta \delta/\nu_\delta$, but in the absence of dissociation; α_δ and α_{wl} are the degrees of dissociation at the outer layer boundary and at the wall, respectively, and can be determined for air on the assumption that air is a diatomic gas model.

The local coefficient of friction

$$c_{f\,0t} = 0.058\,\mathrm{Re}_x^{-0.27}\left(\frac{T_{wl}}{T_r}\right)^{-0.27}\left(1+\frac{k-1}{2}r\mathrm{M}_\delta^2\right)^{-0.55} = c_{f\,0t,ic}\left(\frac{T_{cr}}{T_r}\right)^{-0.27}\left(1+\frac{k-1}{2}r\mathrm{M}_\delta^2\right)^{-0.55}, \qquad \text{(VI-1-36)}$$

where $\mathrm{Re}_x = V_\delta x/\nu_\delta$.

The calculations are performed for a given wall temperature. Certain data on the coefficient $c_{f\,0t}$ are given in Figs. VI-1-6 through VI-1-8.

The variation of $c_{fxt}/c_{f\,0t}$ calculated from VI-1-35 is shown graphically in Fig. VI-1-9. It follows from Fig. VI-1-9 that dissociation makes itself felt either in a 22% increase in friction coefficient if $\alpha_\delta = 1$, $\alpha_{wl} = 0$, the surface is catalytic, and the atoms all recombine at the wall, or in an equal decrease if $\alpha_\delta = 0$, $\alpha_{wl} = 1$ and the surface is not a catalyst.

The formula given above for the calculation of the boundary layer in terms of determining parameters can be applied to any case of flow. An example is a flow over an adiabatic wall, i.e., an unheated and uncooled wall. If there is no heat exchange in the gas, the variation of the thermodynamic parameters across the layer will be adiabatic. Then the above formulas will reflect the influence of compressibility (M_∞) on the boundary-layer parameters.

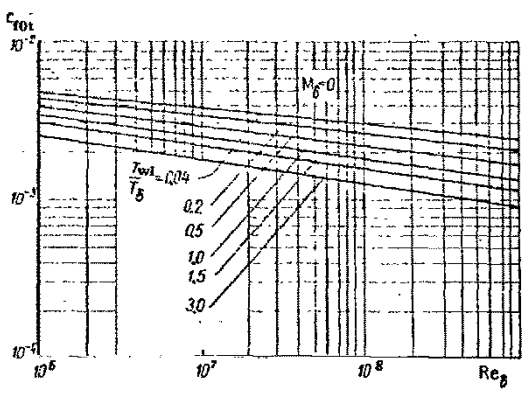

Figure VI-1-6. Local Friction Coefficient on a Plate in an Incompressible Turbulent Flow.

The qualitative pattern of this effect can be inspected quite easily with the formulas. Compressibility will dominate at moderate flow velocities when there is little heating. As a result, the gas will be "softer" and more compliant to density change. This implies that the premise of incompressibility of the gas in the boundary layer is less reliable at moderate speeds than at high speeds, when the gas becomes harder as a result of a substantial temperature rise and behaves as an incompressible medium. Thus, these formulas with the determining parameters are more reliable in application to calculation of the boundary layer for very high velocities. It is always important that the

/330-
/331

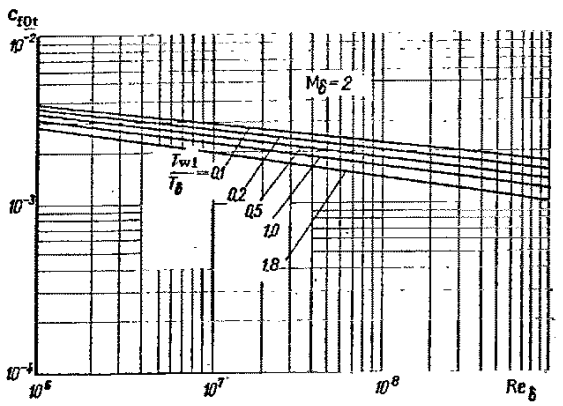

Figure VI-1-7. Local Friction Coefficient on a Plate in Compressible Flow in the Absence of Dissociation ($\alpha_\delta = \alpha_{w1} = 0$).

determining parameters are calculated with consideration of the gas temperature (enthalpy) at the wall, which participates in shaping the friction and heat-transfer processes.

The procedure for calculating the parameters of a turbulent boundary layer by the determining-enthalpy method for given conditions on the outer boundary of the layer and the wall will be the same as for a laminar layer.

When the parameters are not given for the wall, but must be determined by calculation, the friction parameters for both laminar and turbulent boundary layers are computed jointly with the heat flows and surface temperature, using the appropriate heat-transfer equations.

Approximate calculation of turbulent friction on plate.(after V.M. Iyevlev). The local frictional stress

$$\tau_{w1} = A_1 \rho_x V_\delta^2, \qquad \text{(VI-1-37)}$$

where

$$A_1 = 0.03327 z^{-0.224} + 3.966 \cdot 10^{-4}; \qquad \text{(VI-1-38)}$$

$$z = 1.175\,\mathrm{Re}_x; \qquad \text{(VI-1-39)}$$

$$\mathrm{Re}_x = \frac{\rho_x V_\delta x}{\mu_1}. \qquad \text{(VI-1-40)}$$

The parameter ρ_x is a certain density determined by the relation

$$\rho_x = \rho_1^{0.817} \rho_2^{0.183}, \qquad \text{(VI-1-41)}$$

where ρ_1 and ρ_2 are the respective densities at the enthalpies i_1 and i_2:

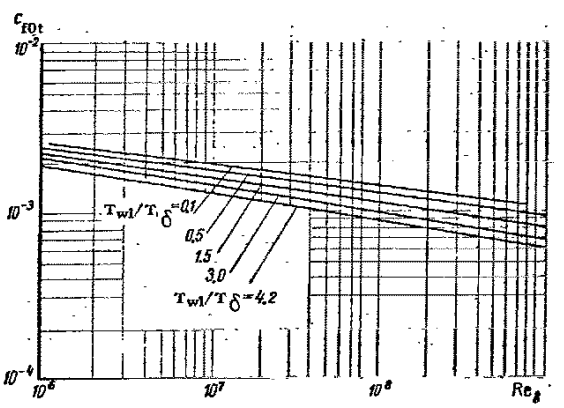

Figure VI-1-8. Local Friction Coefficient on a Plate in Compressible Flow in the Absence of Dissociation ($\alpha_\delta = \alpha_{w1} = 0$), $M_\delta = 4$.

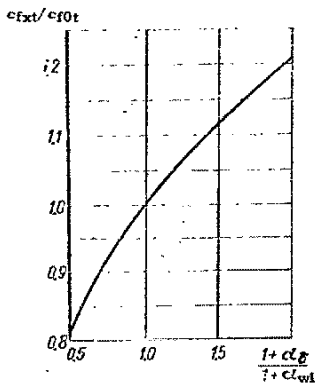

Figure VI-1-9. Ratio of Friction Coefficient on a Plate with Consideration of Dissociation to its Value in the Absence of Dissociation.

$(10^5 \leqslant \mathrm{Re}_\delta \leqslant 10^8;\ 0 \leqslant M_\delta \leqslant 4;$
$0{,}04 \leqslant T_{w1}/T_\delta \leqslant 1{,}0)$

$$\left.\begin{aligned} i_1 &= \frac{1}{2}(i_\delta + i_{w1}) + \frac{1}{8} V_\delta^2 ; \\ i_2 &= \frac{1}{4}(3i_\delta + i_{w1}) + \frac{3}{32} V_\delta^2. \end{aligned}\right\} \qquad \text{(VI-1-42)}$$

In (VI-1-40), μ_1 is defined as the viscosity at enthalpy i_1.

Mixed Boundary Layer /332

Transition point. Critical Reynolds number. In addressing ourselves to calculation of the boundary layer, we must analyze the nature of that layer on a plate and establish whether it is laminar, mixed, or purely turbulent. If the boundary layer is mixed, it is necessary to determine the position of the transition point x_t (Fig. VI-1-10).

Strictly speaking, the transition from the laminar to the turbulent boundary layer takes place gradually, but it is still possible to mark the beginning and end of the transition region clearly.

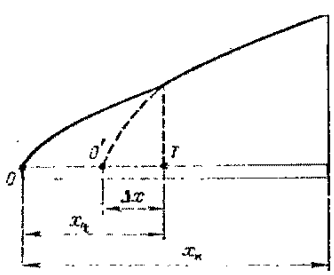

Figure VI-1-10. Mixed Boundary Layer on Plate.

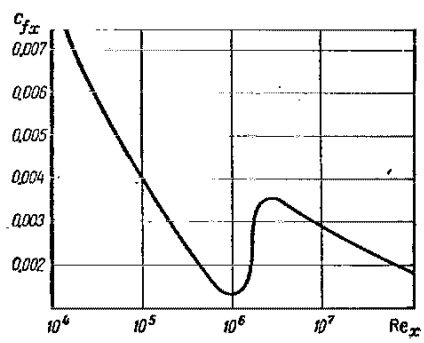

Figure VI-1-11. Variation of Friction-Drag Coefficient in Incompressible Flow as a Function of Re_x.

We may therefore speak of critical Reynolds numbers, one of which corresponds to the beginning of the transition and the other to its end.

The minimum critical Reynolds number, below which all vibrations damp out in a laminar boundary layer, corresponds to the beginning of the transition region. Figure VI-1-11, which

shows the variation of friction-drag coefficient in an incompressible flow as a function of $Re_x = V_\delta x/\nu_\delta$, indicates that the minimum critical number is approximately 10^6.

The c_{fx} minimum is followed by a sharp, almost stepwise increase in the local friction coefficient, which reaches a maximum value, corresponding to the boundary of the transition region and the maximum critical Reynolds number, of about $5 \cdot 10^6$. The turbulent boundary layer will be stable to the right of this boundary.

Experimental data indicate that the presence of a laminar segment and a transition region does not influence the development of the turbulent boundary layer beyond the transition point. Beyond that point, therefore, we can use relationships derived on the assumption that the flow in the boundary layer is fully turbulent.

The position of the transition point on the surface of a body depends on many factors, principal among which are the turbulence of the flow, the condition of the surface, the temperature factor, and M_δ.

Below we shall examine the transition point corresponding to a critical Reynolds number defined as the mean between its values for the beginning and end of the transition.

Thus, the scheme adopted here corresponds to an infinitesimally small transition region.

The influence of turbulence in an incompressible fluid on Re_{cr} at the transition point is illustrated in Fig. VI-1-12 [the degree of turbulence, which is plotted against the axis of abscissas, is measured in percent and is equal to $(1/V) \times \sqrt{(1/3)(\overline{u'^2} + \overline{v'^2} + \overline{w'^2})} \cdot 100$, where u', v', and w' are the pulsation velocity components and V is the average flow velocity].

With increasing M_δ, the influence of turbulence on Re_{cr} diminishes, and the effect can be disregarded for $M_\delta > 4$-5 (Fig. VI-1-13). /333

The influence of surface condition on Re_{cr}, which is characterized by the parameter Δ/δ^* (Δ is the roughness height and δ^* is the displacement thickness), is shown in Fig. VI-1-14 for various M_δ. We note that with increasing M_δ, roughness has less and less influence on the critical Reynolds number, which can be disregarded at $M_\delta > 4$-5.

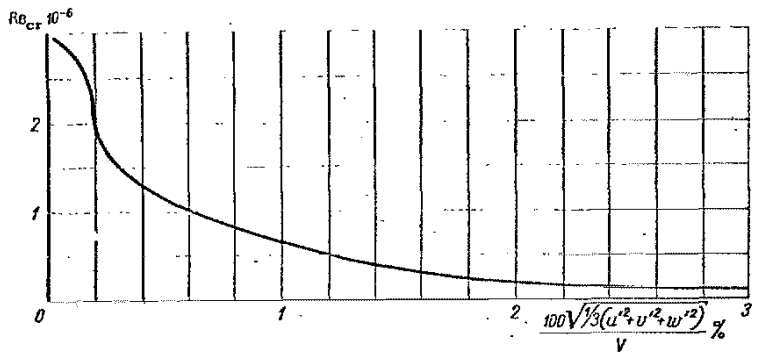

Figure VI-1-12. Influence of the Degree of Turbulence in Incompressible Fluid on Reynolds Number at the Transition Point.

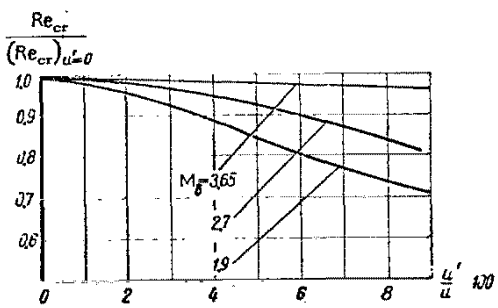

Figure VI-1-13. Influence of Degree of Turbulence on Critical Reynolds Number at Various M_δ (According to Van Dreest).

Cooling of the washed surface contributes to stabilization of the boundary layer and raises the critical Re_{cr}. The flow-stability criterion in the boundary layer is the temperature factor $\overline{T}_{wl} = T_{wl}/T_r$, which is the argument of $Re_{cr}/(Re_{cr})_{\overline{T}_{wl}=1}$ in Fig. VI-1-15.

When the surface is cooled, the boundary-layer displacement thickness becomes smaller, so that when a certain $\delta^* < \Delta$ is reached, the cooling effect will be reduced owing to the influence of roughness on the critical Reynolds number.

The data of Fig. VI-1-15 were used to plot a universal curve (Fig. VI-1-16) that characterizes $Re_{cr}/(Re_{cr_{\overline{T}_{wl}=1}})$ as a function of the parameter $(\overline{T}_{wl} - 1)/M_\delta^2$, which includes, as we see, the temperature factor and M_δ.

Analysis of the data given here indicates that the effect of such factors as degree of turbulence, roughness, and wall cooling on the laminar-to-turbulent transition of the boundary layer decreases with increasing M_δ.

Theoretical and experimental data on the critical Reynolds numbers can be used to construct diagrams that define regions of stable laminar boundary layers. One such diagram is shown in Fig. VI-1-17, where the regions inside curves 1 and 2 correspond to a stable laminary boundary layer observed in plate experiments. /335

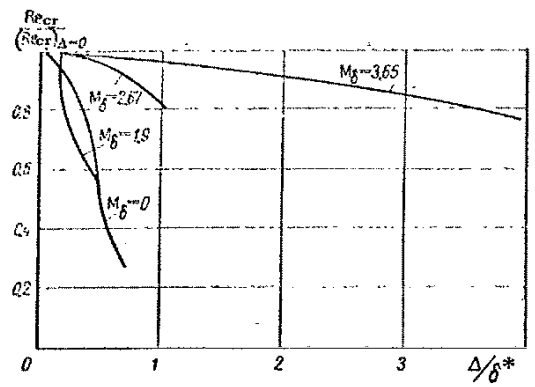

Figure VI-1-14. Influence of Surface Condition on Critical Reynolds Number.

Having determined the transition point, we can calculate the boundary-layer parameters separately for the pure laminar and pure turbulent regions. Beyond point T (see Fig. VI-1-10), however, the relationships for calculating the turbulent boundary layer cannot be applied directly, since the layer begins not at zero thickness, but at a certain finite thickness. To eliminate this mismatch, it is necessary to find a conventional origin of the turbulent boundary layer, which is defined in Fig. VI-1-10 by point O'. One of the two following schemes can be used for this purpose. /334

In the first, it is assumed that the distance Δx to point O', which is the origin of a conventional plate with a completely turbulent layer, must be such as to ensure a turbulent-boundary-layer thickness δ_t at the transition point equal to the thickness of the boundary layer at length x_t. At low velocities, this gives the condition

$$A_1 x_t \mathrm{Re}_{x_t\,cr}^{-1/2} = A_2 \Delta x \mathrm{Re}_{\Delta x}^{-1/5}, \qquad \text{(VI-1-43)}$$

where $A_1 = 5.8$; $A_2 = 0.37$; the Reynolds numbers

$$\mathrm{Re}_{x_t\,cr} = \frac{V_\delta x_t}{\nu_\delta}, \quad \mathrm{Re}_{\Delta x} = \frac{V_\delta \Delta x}{\nu_\delta}.$$

Here the critical Reynolds number $\mathrm{Re}_{x_t cr}$ can be found from the data given above. At the same time, determining parameters can be used to take approximate account of the effect of high

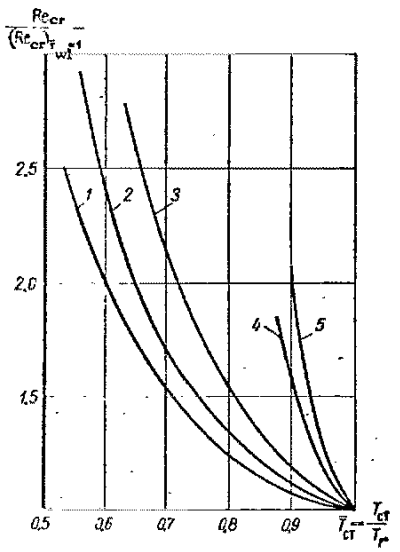

Figure VI-1-15. Influence of Temperature Factor $\overline{T}_{w1} = T_{w1}/T_r$ on the Ratio $Re_{cr}/(Re_{cr})_{\overline{T}_{w1}=1}$: 1) Van Dreest, $M_\delta = 3.65$; 3) Van Dreest, $M_\delta = 2.7$; 2) Jane, $M_\delta = 3.0$; 4) Browning, $M_\delta = 1.85$; 5) Zanesskiy, $M_\delta = 1.67$.

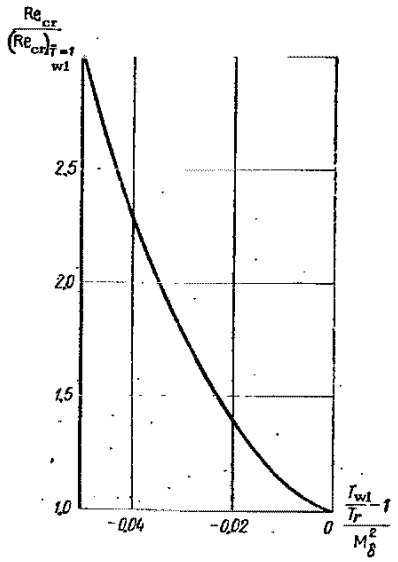

Figure VI-1-16. Experimental Curve Characterizing Variation of $Re_{cr}/(Re_{cr})_{\overline{T}_{w1}=1}$ as a Function of the Parameter $(\overline{T}_{w1} - 1)/M_\delta^2$.

velocities. For this purpose, the Reynolds-number expressions can be written in the form

$$Re_{x_t\,cr} = \frac{V_\delta x_1}{\nu^*}; \quad Re_{\Delta x} = \frac{V_\delta \Delta x}{\nu^*},$$

where $Re_{x_t cr}$ for the incompressible boundary layer can be assumed equal to $(2\text{-}5)\cdot 10^6$. Since the coordinate x_t is known, we can find Δx.

It is assumed in the second scheme that the momentum thicknesses δ^{**} rather than the boundary-layer thicknesses are the same for the laminar and turbulent layers at the transition point, and Δx is calculated from this condition. The working formula will be similar to (VI-1-43), with the difference that the coefficients A_1 and A_2 must be assumed equal to 0.808 and 0.036, respectively. In the second scheme, the values for Δx will be somewhat larger than in the first. It can be assumed that the mean between the Δx

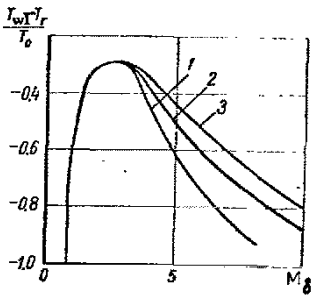

Figure VI-1-17. Determination of Region of Stable Laminar Boundary Layer.
1) plate (tunnel);
2) plate (flight;
3) cone (flight).

values given by these two schemes will be a better approximation of reality.

When we have found O', we can proceed to calculate the boundary-layer thicknesses, the tangential-stress distribution, and the local coefficients of friction, using, if necessary, relationships that incorporate determining parameters.

The average friction coefficient for a plate of length x_w washed by a mixed boundary layer is determined in accordance with Fig. VI-1-10 by the formula /336

$$c_{fic} = c_{f\,1.ic}\frac{x_t}{x_w} + c'_{ft.ic}\frac{x'}{x_w} - c''_{ft.ic}\frac{\Delta x}{x_w}, \quad \text{(VI-1-44)}$$

where $x' = x_w = x_t + \Delta x$.

The Reynolds number for the first coefficient $c_{fl.ic}$ is computed from length x_t, that for the second coefficient $c'_{ft.ic}$ from length x', and that for the third coefficient $c''_{ft.ic}$ from length Δx.

Friction on a Plate Set at an Angle of Attack

Let us consider a plate in a supersonic flow with an attached compression shock. The friction is calculated separately for each side with the condition that the flows over the top and bottom are independent. One of them arises as a constant-velocity flow behind an oblique compression shock, and the other also with constant velocity as an expansion flow behind a simple shock.

The relationships given above are therefore used to determine the local and average friction coefficients. Here, the parameters calculated by compression-shock and Prandtl-Meyer expansion-flow theories on the upper and lower surfaces of the plate are given.

In the general case, the calculation can be performed by the determining-enthalpy method. The frictional forces acting on the lower and upper plate surfaces are respectively equal to

$$R_{fl} = c_{fl}q_l x_w; \; R_{fu} = c_{fu}q_u x_w,$$

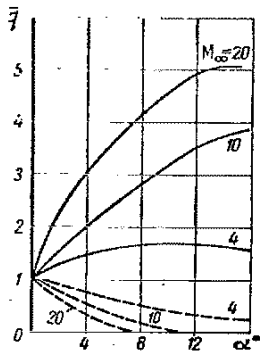

Figure VI-1-18. Ratio $\bar{q}$ of Velocity Heads on Lower (Solid Lines) and Upper (Dashed Lines) Surfaces of Plate to the Velocity Head $q_\infty = \rho_\infty V_\infty^2/2$.

where $q_l = \rho_l V_l^2/2$, $q_u = \rho_u V_u^2/2$ are the velocity heads; $c_{f\,l}$ and $c_{f\,u}$ are the average friction coefficients on the bottom and top, respectively.

The total friction of a plate inclined at an angle α is

$$R_\alpha = R_{f\,l} + R_{f\,u} = 2c_{f\alpha} q x_w, \qquad \text{(VI-1-45)}$$

where $q = \rho_\delta V_\delta^2/2$, and the coefficient

$$c_{f\alpha} = \frac{1}{2}(c_{f\,l}\bar{q}_l + c_{f\,u}\bar{q}_u), \qquad \text{(VI-1-46)}$$

where

$$\bar{q}_l = \frac{q_l}{q}; \quad \bar{q}_u = \frac{q_u}{q}.$$

In the case of a zero attack angle, $R_{f\alpha=0} = 2d_{f\alpha=0} q x_w$.

Consequently,

$$\frac{R_{f\alpha}}{R_{f\alpha=0}} = \frac{c_{f\alpha}}{c_{f\alpha=0}} = k_\alpha = \frac{k_{\alpha l} + k_{\alpha u}}{2}, \qquad \text{(VI-1-47)}$$

where

$$k_{\alpha l} = \frac{c_{f\,l}}{c_{f\alpha=0}}\bar{q}_l; \quad k_{\alpha u} = \frac{c_{f\,u}}{c_{f\alpha=0}}\bar{q}_u. \qquad \text{(VI-1-48)}$$

Figure VI-1-18 shows the ratios of the velocity heads $\bar{q}_l$ and $\bar{q}_u$, and Fig. VI-1-19 the values of the coefficients $k_{\alpha l}$ and $k_{\alpha u}$ for laminar and turbulent boundary layers.

Figure VI-1-20 shows diagrams for the resultant k_α plotted for $\bar{i}_{wl} = i_{wl}/i_r = 0.2$ at the wall. /338

Figure VI-1-21 shows the friction coefficient as a function of transition-point coordinates for various M_∞ and $Re = 10^6$ and 10^7. As follows from Fig. VI-1-21, this dependence weakens with increasing M_∞ and decreasing Re.

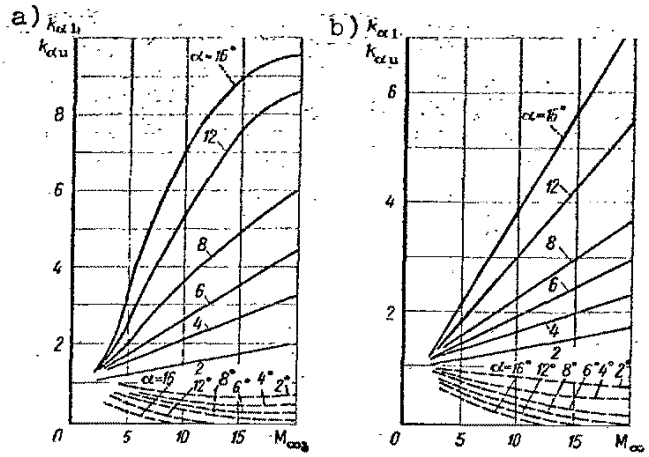

Figure VI-1-19. Coefficients $k_{\alpha l}$ on Lower Surface (Solid Lines) and $k_{\alpha u}$ on Upper Surface (Dashed Lines). a) turbulent layer; b) laminar layer. Enthalpy ratio at wall $\bar{i}_{wl} = 0.2$.

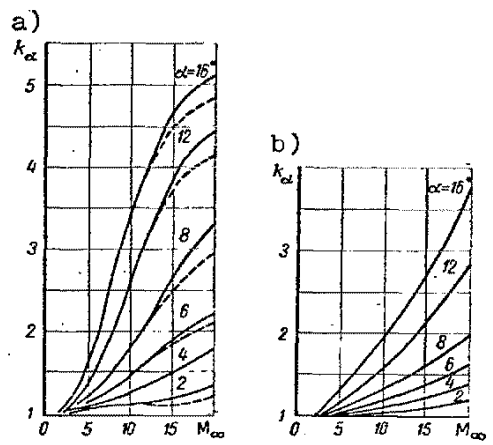

Figure VI-1-20. Over-All Values of Coefficient k_{α} for a Plate. Solid Lines Represent Altitude H = 0 km, Dashed Lines H = 60 km. a) turbulent layer; b) laminar layer. Enthalpy ratio at wall $\bar{i}_{wl} = 0.2$.

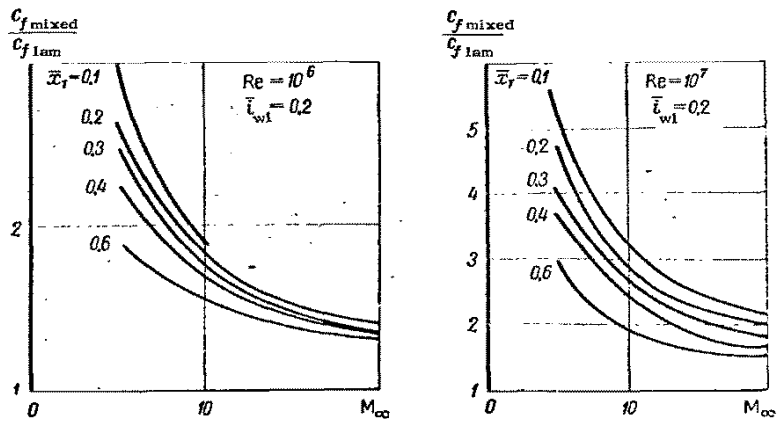

Figure VI-1-21. Influence of Transition Point on Friction Coefficients at Very High Velocities.

§VI-2. HEAT TRANSFER ON A FLAT PLATE

Incompressible Flow

The heat transfer from an incompressible boundary layer to a flat wall can be characterized at any point by the local Stanton number, defined in accordance with Formulas (IV-8-38) and (VI-1-7) in the form

$$\mathrm{St}_x = \frac{c_{fx}}{2} f_{2x} = \frac{1}{2} C \,\mathrm{Re}_x^n f_{2x}. \qquad \text{(VI-2-1)}$$

The average Stanton number over the length of the plate is

$$\mathrm{St}_{av} = \frac{1}{2} D \,\mathrm{Re}^n f_{2av}. \qquad \text{VI-2-2)}$$

The values of the coefficients C and D and the exponent n are given in Table VI-1-1.

For a laminar boundary layer, the local and average values of the parameter f_2 (f_{2x} and f_{2av}, respectively) are the same and are calculated by the formula $f_{2x} = f_{2av} = \mathrm{Pr}^{-2/3}$. For a turbulent boundary layer, the values of f_{2x} and f_{2av} can be assumed the same as for the laminar layer, although f_{2x} should be

calculated by (IV-8-38') and f_{2av} by (IV-8-38") for greater accuracy.

Influence of High Velocities

Formulas (VI-2-1) and (VI-2-2) are applicable for calculation of heat flows not only at low speeds, but also at high speeds when compressibility has a substantial influence and the parameters on which heat transfer depends undergo changes owing to kinetic heating.

In this case, heat transfer can be calculated from the determining enthalpy, using (IV-8-7). In the general case, dissociating laminar or turbulent boundary layers can be calculated.

It is preferable to determine the specific heat flow from the expression

$$q_{w1} = St^*_x \rho_\delta V_\delta (i_r - i_{w1}). \qquad \text{(VI-2-3)}$$

Laminar flow. Research has shown that f^*_{2x} is best set equal to $0.437(1.3 + Pr^*)/Pr^*$ for laminar flows. Accordingly, the Stanton number in (VI-2-3) is

$$St^*_x = \frac{q_{w1}}{\rho_\delta V_\delta (i_r - i_{w1})} = 0.145 \frac{1.3 + Pr^*}{Pr^*} \sqrt{\frac{C}{Re_x}}, \qquad \text{(VI-2-4)}$$

where $C = \rho^*\mu^*/\rho_\delta\mu_\delta$; $Re_x = V_\delta\rho_\delta x/\mu_\delta$.

The Nusselt number, calculated from the determining parameters, is

$$Nu^*_x = \frac{q_{w1} c_{p\delta} x}{\lambda_\delta (i_r - i_{w1})} = 0.145 (1.3 + Pr^*) \sqrt{C Re_x}. \qquad \text{(VI-2-4')}$$

It follows from these relationships that the variation of $\rho\mu$ through the boundary layer thickness is an important factor influencing friction and heat transfer. /339

In approximate evaluation of the local Nusselt number, we can proceed from experimental data [46], according to which

$$Nu^*_x = 0.33 (Re^*_x)^{0.5} (Pr^*)^{0.33}. \qquad \text{(VI-2-4")}$$

where $Re^*_x = V_\delta x/\nu^*$.

If we set Pr* constant at 0.74, then $Nu^* = 0.3(Re^*_x)^{0.5}$.

When the wall temperature is below the dissociation limit, the specific heat flow $q_{wl} = \alpha_x(T_r - T_{wl})$, where

$$\alpha_x = 0.3\frac{\lambda_\delta}{x}(Re^*_x)^{0.5}. \qquad \text{(VI-2-4'')}$$

The average Stanton number

$$St^*_{av} = 0.29\frac{1.3 + Pr^*}{Pr^*}\sqrt{\frac{C}{Re}}, \qquad \text{(VI-2-5)}$$

where $Re = V_\delta x_w/\nu_\delta$.

The following formula can be used to calculate laminar heat flows without taking dissociation into account and with $c_{p\delta}$ = = const:

$$q_{wl} = \alpha_x(T_r - T_{wl}) = 0.332\left(\frac{\mu_\delta\rho_\delta}{\mu_{wl}\rho_{wl}}\right)^{\overline{T}_{wl}/15} \times \times \left(\frac{\mu^*\rho^*}{\mu_{wl}\rho_{wl}}\right)^{1/3}\lambda_{wl}\sqrt{\frac{V_\delta}{\nu_{wl}x}}(1 - \overline{T}_{wl})\,Pr^{1/3}\overline{T}_{wl}, \qquad \text{(VI-2-6)}$$

where $\overline{T}_{wl} = T_{wl}/T_r$.

The values of μ* and ρ* are calculated from the temperature T*, which, in turn, must be selected with consideration of the state of the wall.

If $T_{wl} < T_r$ (wall heated), T* is found from the formula

$$\frac{T^* - T_{wl}}{T_0 - T_{wl}} = \frac{1}{4}\left[\left(1 - \frac{T_{wl}}{T_\delta}\right)\left(\frac{k-1}{2}M^2_\delta\right)^{-1} + 1\right], \qquad \text{(VI-2-7)}$$

where T_0 is the stagnation temperature of the oncoming flow.

If $T_{wl} \geq T_r$ (wall cooled), we must set $T^* = T_{wl}$. At low flow velocities around the plate, the determining temperature $T^* = T_\delta$.

Approximate calculation of turbulent heat transfer on a plate (after V.M. Iyevlev). The specific heat flow can be

calculated by the formula

$$q_{w1} = A_2 \rho_x V_\delta \tilde{i}, \qquad \text{(VI-2-8)}$$

where

$$A_2 = 0.9 A_1 [1.1 + 2.58 (1 - \mathrm{Pr})^3 z^{0.075}]; \qquad \text{(VI-2-9)}$$

$$\tilde{i} = i_1 - i_\delta + B \frac{V_\delta^2}{2}; \qquad \text{(VI-2-10)}$$

$$B = 0.9 - \frac{2.4}{z^{0.24}} (\mathrm{Pr} - 0.9); \qquad \text{(VI-2-11)}$$

$$\mathrm{Pr} = \frac{c_p \mu_\delta}{\lambda_\delta}. \qquad \text{(VI-2-12)}$$

The ρ_x, i_1, and z that appear in these relationships are determined with the formulas on pages 444-445.

An empirical relation [46] for the Nusselt number may be used for approximate evaluation of heat transfer:

$$\mathrm{Nu}_x^* = \frac{q_{w1} c_{p\delta} r}{\lambda_\delta (i_r - i_{w1})} = 0.029 (\mathrm{Re}_x^*)^{0.8} (\mathrm{Pr}^*)^{0.4}. \qquad \text{(V-2-13)}$$

If we set Pr* = 0.74, then /340

$$\mathrm{Nu}_x^* = 0.026 (\mathrm{Re}_x^*)^{0.8}. \qquad \text{(VI-2-14)}$$

For a cold wall and no dissociation at the wall, the heat transfer $q_{w1} = \alpha_x (T_r - T_{w1})$, where

$$\alpha_x = 0.026 \frac{\lambda_\delta}{x} (\mathrm{Re}_x^*)^{0.8}. \qquad \text{(VI-2-15)}$$

For a plate at an angle of attack, the heat transfer is determined separately for each side and the results are added. This calculation involves determination of the parameters of an inviscid disturbed flow. The inviscid parameters are determined according to compression-shock theory for the supersonic flow with an attached shock, and by the Prandtl-Meyer theory on the side on which no shock forms.

Heat Transfer on a Plate Set Perpendicular to the Oncoming Flow (Laminar Boundary Layer)

Let us examine the heat flow to a plate whose angle of attack is $\alpha = 90°$ (see Fig. V-7-5). In this case, a detached curvilinear shock wave forms ahead of the plate. In view of the severe flow stagnation behind the shock, the boundary layer around the plate can be regarded as laminar over the entire surface.

On the assumptions that the wall is vigorously cooled and the ratio $\overline{\rho\mu} = \rho\mu/\rho_{w1}\mu_{w1} = 1$, the specific heat flow at thermodynamic equilibrium is calculated by (IV-8-42) and (IV-8-46). Setting $\omega_\delta = \omega_0'$, $k = 0$, $x = y$ in these formulas, we obtain the following working relationships [47]:

$$q_c = 0.47\,\mathrm{Pr}^{-2/3}(\rho_\delta\mu_\delta)^{1/2}V_\infty^{1/2}i_r F(y), \qquad \text{(VI-2-16)}$$

where

$$F(y) = \frac{\sqrt{2}}{2}\frac{p_\delta}{p_0'}\frac{V_\delta}{V_\infty}\left[\int_0^y \frac{p_\delta}{p_0'}\frac{V_\delta}{V_\infty}dy\right]^{-1/2}. \qquad \text{(VI-2-17)}$$

The value of the function F(y) can be found with the extrapolation formulas (V-7-38) and (V-7-39), which are used to compute the pressure p_δ/p_0' and velocity V_δ/V_∞ ratios. According to (V-7-39), the pressure ratio

$$\frac{p_\delta}{p_0'} = \frac{2-\delta_0\left[1+\bar{y}^2\left(\frac{2}{5}\bar{y}+\frac{4}{3}\right)^2\right]}{2-\delta_0}.$$

Introducing the value of p_δ/p_0' and the V_δ/V_∞ determined by (V-7-39), we obtain

$$F(y) = \frac{\sqrt{\delta_0}}{\sqrt{b(2-\delta_0)}}\frac{f_1(\bar{y})}{f_2(\bar{y})} = \bar{F}(\bar{y})\,b^{-1/2}, \qquad \text{(VI-2-18)}$$

where

$$f_1(\bar{y}) = \left\{2-\delta_0\left[1+\bar{y}^2\left(\frac{2}{5}\bar{y}+\frac{4}{3}\right)^2\right]\right\}\left(\frac{2}{5}\bar{y}+\frac{4}{3}\right);$$

$$f_2(\bar{y}) = \left\{\frac{4}{3}\left[2\left(\frac{1}{5}\bar{y}+1\right)-\delta_0\left(1+\frac{1}{5}\bar{y}+\frac{8}{9}\bar{y}^2+\frac{16}{25}\bar{y}^3+\frac{4}{25}\bar{y}^4\right)\right]\right\}^{1/2} \qquad \text{(VI-2-19)}$$

$$\bar{F}(\bar{y}) = \sqrt{\frac{\delta_0}{2-\delta_0}}\frac{f_1(\bar{y})}{f_2(\bar{y})}. \qquad \text{(VI-2-20)}$$

At the point of total stagnation /341

$$f_1(0) = \frac{4}{3}(2-\delta_0);\ f_2(0) = \left[\frac{4}{3}(2-\delta_0)\right]^{1/2}. \qquad \text{(VI-2-21)}$$

Applying (VI-2-20), we obtain the following expression for F(0):

$$F(0) = \frac{\bar{F}(0)}{\sqrt{\bar{b}}} = \sqrt{\frac{(4/3)\delta_0}{b}} \text{ or } F(0) = \sqrt{\frac{\bar{\lambda}}{\bar{b}}}, \qquad \text{(VI-2-20')}$$

since $(4/3)\delta_0 = \bar{\lambda}$ according to (V-7-40). The values of $f_1(\bar{y})$ and $f_2(\bar{y})$ will be as follows at the edge of the plate ($\bar{y} = 1$):

$$f_1(1) = 3.46(1-2\delta_0);\ f_2(1) = 1.79(1-1.2\delta_0)^{1/2}. \qquad \text{(VI-2-21')}$$

Dropping small quantities of order δ_0^2,

$$F(1) = 1.2(1-1.15\delta_0)F(0), \qquad \text{(VI-2-20")}$$

where F(0) is determined with (VI-2-20').

The density ρ_δ and the dynamic viscosity coefficient μ_δ in (VI-2-16) are generally variable over the span of the plate.

Their values can be determined as follows. First the entropy S_0' is determined from i_0 and p_0' for the total-stagnation point; this can be done by reference to tables or diagrams of the thermodynamic functions that take dissociation and ionization into account for the general case. Then, assuming the flow along the wall to be isentropic, the local density ρ_δ and the temperature T_δ are found from the local pressure p_δ and the entropy S_0'. Viscosity can be determined, for example, by the Sutherland formula from T_δ.

Calculations indicate that the changes in density and viscosity coefficient from their values at the total stagnation point are small and of the order of δ_0^2.

Hence the parameters ρ_δ and μ_δ can be assumed, correct to δ_0^2, to be constant, and equal to the respective values ρ_0' and μ_0' at the total-stagnation point. Pr can also be assumed constant and equal to its value at the same total-stagnation point.

Thus, the change in heat transfer will be determined by the function $\bar{F}(\bar{y})$. For an arbitrary point

$$\frac{q_c}{q_{c0}} = \frac{\bar{F}(\bar{y})}{\bar{F}(0)}, \qquad \text{(VI-2-22)}$$

where q_{c0} is the heat transfer at the critical point, which is equal to

$$q_{c0} = 0.47\,\mathrm{Pr}^{-2/3}(\rho_0'\mu_0')^{1/2}V_\infty^{1/2}i_r\sqrt{\frac{\bar{\lambda}}{b}}. \qquad \text{(VI-2-23)}$$

At hypersonic velocities, the stagnation enthalpy can be determined by the formula $i_0 = 0.5V_\infty^2$.

It follows from (VI-2-20") that the heat flow at the edge of the plate ($\bar{y} = 1$) is

$$q_c = 1.2q_{c0}(1 - 1.15\delta_0). \qquad \text{(VI-2-24)}$$

Depending on δ_0, q_c may be larger or smaller than at the total-stagnation point.

Instead of the dimensional variable, we can use the dimensionless heat-transfer number

$$\mathrm{Re}_b^{1/2}\mathrm{St}_x = 0.47\,\mathrm{Pr}^{-2/3}\left(\frac{\rho_\delta}{\rho_\infty}\frac{\mu_\delta}{\mu_\infty}\right)^{1/2}\bar{F}(\bar{y}), \qquad \text{(VI-2-25)}$$

where $\mathrm{Re}_b = V_\infty\rho_\infty b/\mu_\infty$; $\mathrm{St}_x = \alpha_x/(\rho_\infty V_\infty c_p) = q_c/\rho_\infty V_\infty i_r$). /342

To determine the dimensionless heat-transfer number at the critical point, the function $\bar{F}(\bar{y})$ in (VI-2-25) must be set equal to $\bar{F}(0)$ (VI-2-20'). Thus, the ratio of the Stanton coefficients for an arbitrary point and the total-stagnation point will be analogous to (VI-2-22), i.e., equal to $\bar{F}(\bar{y})/\bar{F}(0)$.

Heat transfer on an inclined plate. The method of heat transfer calculation set forth above pertains to the case in which the flow strikes the plate at an angle of attack $\alpha = 90°$. At deviation of the flow from this direction, i.e., for $\alpha < 90°$, we may assume that the spanwise distribution of the heat flows will be determined by the same relationships as for $\alpha = 90°$, in which V_∞ is replaced by the component $V_\infty \sin \alpha°$.

Accordingly, the heat transfer at the critical point for $\alpha < 90$ is

$$q_{c0} = (q_{c0})_{\alpha=90} \sin^{5/2}\alpha. \qquad \text{(VI-2-26)}$$

For the dimensionless heat-transfer number at the critical point, we obtain

$$\mathrm{Re}_b^{1/2}(\mathrm{St})_0 = [\mathrm{Re}_b^{1/2}(\mathrm{St})_0]_{\alpha=90} \sin^{5/2}\alpha. \qquad \text{(VI-2-27)}$$

Formula (VI-2-22) is used to calculate the spanwise distribution of heat transfer on the inclined plate.

Average heat transfer. We determine the average specific heat flow by integrating over the surface:

$$q_{w1} = \int_0^1 q_c \, d\bar{y}.$$

Substituting the value for q_c from (VI-2-16) and the function $\bar{F}(\bar{y})$ in the form of (VI-2-20) in the integrand, we obtain

$$q_{av} = 1.13(1 - 0.75\delta_0) q_{c0}. \qquad \text{(VI-2-28)}$$

Depending on the density ratio, the average heat flow on the plate may be greater or smaller than the value at the total-stagnation point. For example, for $\delta_0 = 0.2$, $q_{av} = 0.96q_{c0}$, and for $\delta_0 = 0.05$ we obtain $q_{av} = 1.09q_{c0}$.

Influence of diffusion. The following result has been obtained experimentally for the parameter of total specific heat flow at the stagnation point in the presence of diffusion [59]:

$$\frac{\mathrm{Nu}}{\sqrt{\mathrm{Re}}} = 0.54\mathrm{Pr}^{0.4}\left(\frac{\rho_{w1}\mu_{w1}}{\rho_0\mu_0}\right)^{-0.4}\left[1 + (\mathrm{Le}^{0.52} - 1)\frac{i_D}{i_r}\right]. \qquad \text{(VI-2-29)}$$

This relationship takes account of the variation of $\rho\mu$ over the thickness of the boundary layer and is suitable for wall temperatures not in excess of the stagnation temperature.

The specific heat flow is determined by the relationships

$$\mathrm{Nu}=\frac{q_0 (c_p)_{w1} y}{\lambda_{w1} (i_r - i_{w1})}; \quad \mathrm{Re}=\frac{\rho_{w1} y^2}{\mu_{w1}} \left(\frac{\partial V_\delta}{\partial y}\right)_0. \qquad \text{(VI-2-30)}$$

To find the heat-flow distribution on a plate with consideration of diffusion, we may start with the hypothesis that the influence of the Lewis-Semenov number will be the same at various points as at the total-stagnation point. Thus we can use formula (VI-2-22), which is applicable for a strongly cooled surface and does not take account of the velocity gradient. To allow for this effect, we can use the relation /343

$$\frac{q}{q_0}=\frac{\bar{F}(\bar{y})}{\bar{F}(0)} \frac{g'_{w1}}{g'_{w10}}, \qquad \text{(VI-2-31)}$$

in which the ratio g'_{w1}/g'_{w10} is determined by the empirical formula

$$\frac{g'_{w1}}{g'_{w10}}=0.82\,(1+0.096\beta^{1/2}) \frac{1-i_{w1}}{1-i_{w10}} \qquad \text{(VI-2-32)}$$

The coefficient

$$\beta=2\frac{i_0}{i_\delta} \frac{d \ln V_\delta}{d \ln \bar{x}}=-2\frac{i_0}{i_0 \rho_\delta} \int_0^y (\rho_\delta V_\delta\, dy) \frac{dp_\delta}{dy} (\rho_\delta V_\delta^3)^{-1}. \qquad \text{(VI-2-33)}$$

§VI-3. FRICTION AND HEAT TRANSFER ON WINGS OF FINITE THICKNESS

Wing with Sharp Leading Edge

In examining the boundary layer around a flat plate, we assumed the velocity to be constant along the x-axis outside the boundary layer. The pressure would therefore also be constant, and the pressure gradient dp/dx = 0. In contrast to the case of the straight wall, the velocity at the outer boundary of the boundary layer on a curved surface is a variable that depends on the x-coordinate. At this boundary, the pressure will vary along the x-axis, so that the pressure gradient dp/dx ≠ 0 and this must be taken into account in calculating the boundary layer.

Let us consider the influence of the pressure gradient on laminar friction. The results to be given below are based on the assumptions that Pr = 1 and the dynamic viscosity coefficient is proportional to temperature. Research has shown that for constant heat capacities, these assumptions introduce a small error into the calculated boundary-layer parameters.

To determine flow in the boundary layer, we can use the equations of motion (III-2-11), continuity (III-2-21), and energy (III-2-47), provided that the flow under consideration is plane two-dimensional. Moreover, the last term in the right member of (III-2-47) is set equal to zero, and the stagnation enthalpy i_0 is replaced by the stagnation temperature $T_0 = T + V_x^2/(2c_p)$.

The equation system is converted to Dorodnitsin variables, which take the form

$$\xi = \int_0^x \frac{p}{p_0}\,dx; \quad \eta = \int_0^y \frac{\rho}{\rho_0}\,dy = \frac{p}{p_0}\int_0^y \frac{T_0}{T}\,dy,$$

where

$$\frac{p}{p_0} = \left(1 - \frac{V_\delta^2}{2i_0}\right)^{\frac{k}{k-1}}; \quad \frac{\rho}{\rho_0} = \frac{T_0}{T}\frac{p}{p_0}.$$

The dynamic viscosity coefficient, which appears in the equation of motion, is determined from the expression

$$\frac{\mu}{\mu_0} = \lambda\,\frac{T}{T_0}, \qquad \text{(VI-3-1)}$$

where, according to (III-1-5) or (III-1-6), λ is determined by /344

$$\lambda = \left(\frac{T_{w1}}{T_0}\right)^{n-1} \text{ or } \lambda = \sqrt{\frac{T_{w1}}{T_0}}\,\frac{T_0 + 111}{T_{w1} + 111}, \qquad \text{(VI-3-2)}$$

provided that the wall temperature is given.

As a result of the transformation, the equation system assumes a form similar to the system for an incompressible fluid. It is solved with boundary conditions at the wall ($T = T_{w1}$, $V_x = V_y = 0$) and at the layer boundary [$(\partial V_x/\partial\eta)_{\eta=\delta} = 0$], where δ is the value of the variable η at the layer boundary.

The parabolic relationship $V_x = a_1\eta + a_2\eta^2 + a_3\eta^3 + \ldots$ is taken as the law of velocity variation across the section of the boundary layer. The local frictional stress

$$\tau_{w1} = \mu_{w1}\left(\frac{\partial V_x}{\partial y}\right)_{y=0} = \mu_{w1}\frac{p}{p_0}\frac{T_0}{T_{w1}}\left(\frac{\partial V_x}{\partial\eta}\right)_{\eta=0}.$$

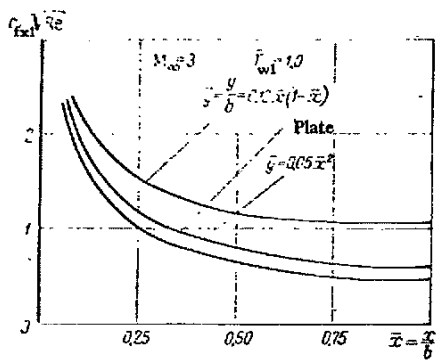

Figure VI-3-1. Values of $c_{f_{x1}}\sqrt{Re}$ for Various Profiles as Calculated by (VI-3-3).

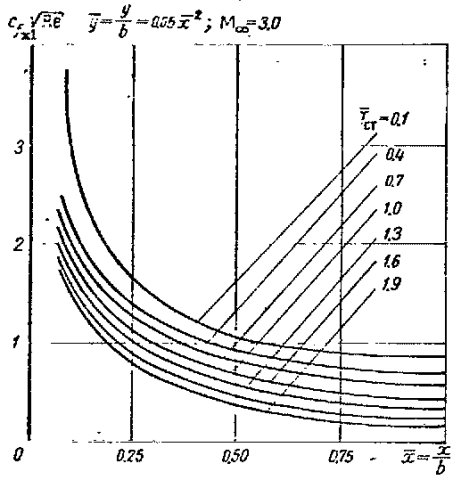

Figure VI-3-2. Values of $c_{f_{x1}}\sqrt{Re}$ for a Parabolic Wall with the Equation $\bar{y} = 0.05\bar{x}^2$ for Various $\bar{T}_{w1}$ ($M_\infty = 3.0$).

Without setting the solution forth in detail, we present the basic results. The local friction coefficient

$$c_{fx} = \frac{2\tau_{w1}}{\rho_\delta V_\delta^2} = \frac{2}{3}\sqrt{\frac{\lambda_{w1}/\lambda_\delta}{\mathrm{Re}\,k(\bar{x})}} \times \left[1 + \frac{2}{3}\frac{\bar{V}_\delta' k(\bar{x})(5\bar{T}_{cr}+1)}{\bar{V}_\delta(1-\bar{V}_\delta^2/2i_0)}\right], \qquad \text{(VI-3-3-)}$$

where λ_δ is calculated by one of the formulas of (VI-3-2), in which T_{w1} is replaced by T_δ; $\bar{T}_{w1}/T_0$; $\mathrm{Re} = V_\delta b/\nu_\delta$; $\bar{V}_\delta = V_\delta/V_\infty$; $\bar{V}_\delta' = d\bar{V}_\delta/d\bar{x}$. The coefficient

$$k(\bar{x}) = \frac{1}{f(\bar{V}_\delta)}\int_0^{\bar{x}} f(\bar{V}_\delta)\,d\bar{x}, \qquad \text{(VI-3-4)}$$

where

$$f(\bar{V}_\delta) = \bar{V}_\delta^{\frac{7+8\bar{T}_{w1}}{3}} \cdot \left(1 - \frac{\bar{V}_\delta^2}{2i_0}\right)^{\frac{k}{k-1}\frac{2+4\bar{T}_{w1}}{3}}.$$

Setting $\bar{V}_\delta' = 0$ and $k(\bar{x}) = \bar{x}$ in (VI-3-3), we obtain the formula for the friction coefficient on a flat plate on which the pressure gradient is zero.

As an example, (VI-3-3) was used to calculate values of $c_{f_x}\sqrt{Re}$ for a parabolic profile with the equation $y/b = 0.12(x/b)(1 - x/b)$, a parabolic wall with the equation $y/b = 0.05(x/b)^2$, and a plate at temperature $\bar{T}_{w1} = 1$ (heat-insulated wall) set in a flow with $M_\infty = 3$. It follows from the calculated results, which are presented in Fig. VI-3-1, that the presence of a negative pressure gradient increases friction, while a positive gradient lowers it vis-a-vis the plate ($\bar{V}'_\delta = 0$). /345

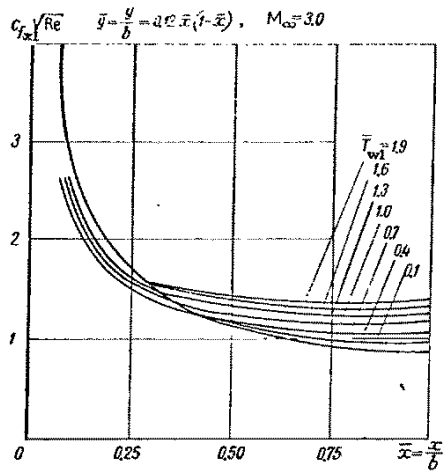

Figure VI-3-3. Values of $c_{f_{x1}}\sqrt{Re}$ for a Parabolic Profile with the Equation $y = 0.12\bar{x}(1 - \bar{x})$ at Various $\bar{T}_{w1}$ ($M_\infty = 3.0$).

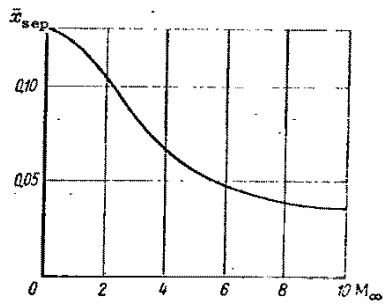

Figure VI-3-4. Coordinate of Detachment Point for Velocity Varying Linearly on Profile ($\bar{V}_\delta = 1 - \bar{x}$) and Heat-Insulated Wall.

Figures VI-3-2 and VI-3-3 show curves plotted by (VI-3-3) and characterizing the simultaneous effects of wall temperature and pressure gradient. Cooling the wall increases friction with a positive pressure gradient (Fig. VI-3-2) as it does in its absence (plate). As for the effect of a negative pressure gradient (Fig. VI-3-3), it is different in nature for different segments of the profile. At the beginning of the profile with a cooled wall, friction becomes greater, but it is smaller on peripheral segments.

Setting the local coefficient of friction (VI-3-3) equal to zero, we can determine the separation-point coordinate of a laminar boundary layer. More exact studies indicate that this coordinate is best determined from the equation

$$\frac{\bar{V}'_\delta k(\bar{x})}{\bar{V}_\delta(1-\bar{V}_\delta^2/2i_0)} = -\frac{1.2}{5\bar{T}_{w1}+1}. \qquad \text{(VI-3-5)}$$

Figure VI-3-4 shows results calculated by (VI-3-5) for the separation-point coordinate $\bar{x} = \bar{x}_{sep}$ for the conditions that velocity varies linearly along the profile $\bar{V}_\delta = 1 - \bar{x}$ and the wall is heat-insulated ($\bar{T}_{w1} = 1$).

Approximate calculation of friction and heat transfer on profile. This calculation is based on use of solutions for a compressible boundary layer with no gradient, i.e., on the use of the corresponding relationships obtained for a flat plate.

The method set forth below gives satisfactory results for slightly curved contours, flow over which is characterized by small longitudinal pressure gradients that have almost no influence on the velocity profile. The effect of a pressure gradient can be taken into account by appropriate selection of the effective length in determination of the Reynolds number.

In the method, the contour of the sharpened profile, which is in flow with an attacked shock wave, is broken up into a series of small rectilinear segments. Thus, the calculation scheme examines a unit-span wing profile that consists of a set of short plates (Fig. VI-3-5). /346

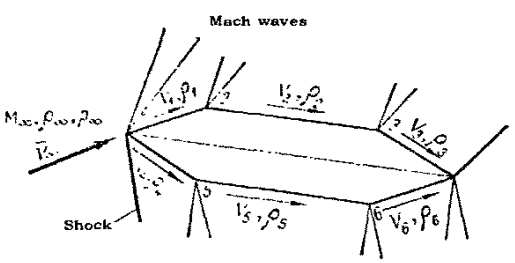

Figure VI-3-5. Diagram of Supersonic Flow Around Profile with Straight Walls and Attached Shock Wave.

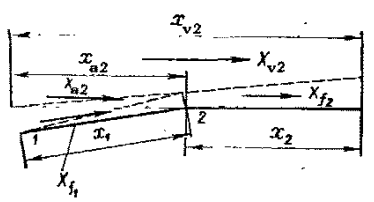

Figure VI-3-6. Illustrating Calculation of Friction and Heat Transfer on Profile.

The inviscid-flow parameters are determined at the start of the calculation. The compression-shock and Prandtl-Meyer theories can be used here. It is assumed that the "inviscid" parameters are constants on each plate (face).

We shall examine two variations of the method, one of which is based on the assumption of equal layer thicknesses at the transition from one plate to another, while the other assumes equal momentum thicknesses.

Hypothesis of equal boundary-layer thicknesses. Friction can be calculated by the universal formulas for both laminar and turbulent boundary layers. The "seventh-root" law is used for the turbulent layer.

Considering face 1 on the upper surface, where the free (inviscid) flow parameters are known, we can find $Re_1 = \rho_1 V_1 x_1/\mu_1$ from the face length x_1 and the values of ρ_1, V_1, and μ_1.

A friction coefficient that may be regarded as an average for the face is found from the formulas for a plate, using determining parameters with consideration of the boundary-layer structure or using the diagrams in Figs. VI-1-4 and VI-1-5 as functions of M_1 and the enthalpy ratio $\bar{i}_{w1}$. The quantity $(C_f Re^{-n})_1$, is found from Figs. VI-1-4 and VI-1-5, and this is followed by calculation of the coefficient

$$c_{f1} = (c_f \mathrm{Re}^{-n})_1 \mathrm{Re}_1^n.$$

Passing to face 2 (Fig. VI-3-6), we assume that the thickness of the boundary layer at the beginning of this face is the same as that at the end of face 1. But a layer of this thickness at the beginning of face 2 can be regarded as a result of flow over a virtual plate of length $x_{v2} = x_2 = x_{a2}$ at M_2. The length x_{a2} of the virtual added segment can be found from the condition indicated above - equality of the boundary-layer thicknesses —, i.e., from the expression

$$x_1 \mathrm{Re}_1^n = x_{a2} \mathrm{Re}_{a2}^n,$$

where the Reynolds numbers Re_1 and Re_{a_2} are calculated from the local velocities V_1 and $V_{a2} = V_2$, the lengths x_1 and x_{a2}, and, in the general case, from the determining values of the kinematic viscosity coefficients ν_1^* and $\nu_{a_2}^* = \nu_2^*$.

The average coefficient of friction on length x_{v_2}, which corresponds to the friction X_{v_2}, will be

$$c_{f\,v2} = (c_f \mathrm{Re}^{-n})_{v2} \mathrm{Re}_{v2}^n.$$

Since the friction coefficient $c_{f\,a2} = (c_f Re^{-n})_{a2} Re_{a2}^n$ on the virtual segment of length x_{a_2}, which is acted upon by

friction X_{a2}, the friction on face 2 is

$$X_{f2} = q_2 (c_{f\,v2} x_{v2} - c_{f\,a2} x_{a2}) = c_{f2} q_2 x_2.$$

Remembering that $(c_f \mathrm{Re}^{-n})_{a2} = (c_f \mathrm{Re}^{-n})_{v2} = (c_f \mathrm{Re}^{-n})_2$, we obtain for the coefficient of friction on face 2 /347

$$c_{f2} = (c_f \mathrm{Re}^{-n})_2 \left[\mathrm{Re}_{v2}^n \left(\frac{x_{a2}}{x_2} + 1 \right) - \mathrm{Re}_{a2}^n \frac{x_{a2}}{x_2} \right].$$

Accordingly, for any ith segment,

$$c_{fi} = (c_f \mathrm{Re}^{-n})_i \left[\mathrm{Re}_{vi}^n \left(\frac{x_{ai}}{x_i} + 1 \right) - \mathrm{Re}_{ai}^n \frac{x_{ai}}{x_i} \right]. \qquad \text{(VI-3-6)}$$

Here the total length of the virtual element $x_{vi} = x_{ai} + x_i$, where the length x_i is determined by the recurrent equation system

$$x_{ai}\, \mathrm{Re}_{ai}^n = x_{v,\,i-1}\, \mathrm{Re}_{v,\,i-1}^n, \qquad \text{(VI-3-7)}$$

in which the Reynolds numbers are generally calculated from the determining parameters.

Having thus calculated the coefficients of friction and the corresponding forces on the lower surface, an analogous calculation is made for the top. Summing, we find the profile friction

$$X_f = \sum_{i=1}^{N} X_{fi} \cos \theta_i,$$

where the X_{fi} are the friction forces on the lower and upper faces; the θ_i are the inclination angles of the faces to vector $\overline{V}_\infty$; i is the number of the face; N is the total number of faces on the bottom and top.

The general expression for the friction on any given face is

$$X_{fi} = (c_f \mathrm{Re}^{-n})_i \cdot q_i \cdot (\mathrm{Re}_{vi}^n x_{vi} - \mathrm{Re}_{ai}^n x_{ai}),$$

where the velocity head $q_i = \rho_i V_i^2/2$ is determined from the corresponding inviscid parameters on the face under consideration.

The Stanton number can be calculated and the specific heat flow determined from the known coefficients of friction on the local plates, using the Reynolds analogy.

Hypothesis of equal momentum thicknesses. As in the preceding case, calculations can be made with this hypothesis for both laminar and turbulent boundary layers. We assume here that the boundary layer is undissociated, the specific heats are constant, and the compressibility effect on the coefficient of friction manifests in its dependence only on Mach number.

For face 1, the coefficient of friction is determined as for an ordinary plate from $Re_1 = V_1 x_1/\nu_1$ and M_1. On transition to the second segment, the virtual additional length x_{a2}, which takes account of the prior history of boundary-layer development, must be known in order to determine the Reynolds number from the parameters on this segment. This length is calculated from the hypothesis that the momentum thickness remains unchanged at the boundary between the first and second segments. Accordingly,

$$\frac{1}{(\rho_\delta V_\delta^2)_1}\left[\int_0^\delta \rho V_x (V_\delta - V_x)\, dy\right]_1 = \frac{1}{(\rho_\delta V_\delta^2)_2}\left[\int_0^\delta \rho V_x (V_\delta - V_x)\, dy\right]_2,$$

where the left member is $(1/2)(c_f x)_1$, and the right member $(1/2)(c_f x)_{a2}$. We may therefore write the following expression for determination of length x_{a2} with consideration of c_{f1} and c_{fa2} as functions of compressibility:

$$\frac{x_{a2}}{x_1} = \left[\frac{(c_f/c_{f\,ic})_1}{(c_f/c_{f\,ic})_2}\right]^{\frac{1}{n+1}} \cdot \left[\frac{(\mu_\delta/\rho_\delta V_\delta)_1}{(\mu_\delta/\rho_\delta V_\delta)_2}\right]^{-\frac{n}{n+1}},$$

where n is determined in accordance with the type of boundary layer from Table VI-1-1.

The $c_f/c_{f\,ic}$ ratios for the first and second segments are determined as functions of the corresponding M_1 and M_2 on these segments, using (VI-1-18) for a laminar boundary layer and (VI-1-19)-(VI-1-21) for a turbulent layer. /348

For an arbitrary ith segment, the virtual length is determined from the condition

$$\frac{x_{ai}}{x_{i-1}+x_{ai-1}}=\left[\frac{(c_f c_{f\,ic})_{i-1}}{(c_f c_{f\,ic})_i}\right]^{\frac{1}{n+1}}\cdot\left[\frac{(\mu_\delta\rho_\delta V_\delta)_{i-1}}{(\mu_\delta\rho_\delta V_\delta)_i}\right]^{-\frac{n}{n+1}}. \qquad \text{(VI-3-8)}$$

If we assume that the turbulent-layer velocity profile varies in accordance with the more general "kth-root" law, then (VI-3-8) assumes the form

$$\frac{x_{ai}}{x_{i-1}+x_{ai-1}}=\left[\frac{(c_f c_{f\,ic})_{i-1}}{(c_f c_{f\,ic})_i}\right]^{\frac{k+3}{k+1}}\left[\frac{(\mu_\delta\rho_\delta V_\delta)_{i-1}}{(\mu_\delta\rho_\delta V_\delta)_i}\right]^{\frac{2}{k+1}}. \qquad \text{(VI-3-9)}$$

Having determined the virtual plate lengths $x_{v\,i}$, we can go on to calculate the friction coefficients and forces on the face.

The friction coefficient on the first face is

$$c_{f1}=(c_{f\,ic})_1\left(\frac{c_f}{c_{f\,ic}}\right)_1.$$

For the second segment

$$c_{f2}=\left(\frac{c_f}{c_{f\,ic}}\right)_2\left[(c_{f\,ic})_{v2}\left(\frac{x_{a2}}{x_2}+1\right)-(c_{f\,ic})_{a2}\frac{x_{a2}}{x_2}\right],$$

where $(c_{f\,ic})_{v2}$ and $(c_{f\,ic})_{a2}$ are determined by the incompressible-fluid formulas and for Reynolds numbers calculated respectively from lengths x_{v2} and x_{a2} and from the second-segment parameters.

For an arbitrary ith segment,

$$c_{fi}=\left(\frac{c_f}{c_{f\,ic}}\right)_i\left[(c_{f\,ic})_{vi}\left(\frac{x_{ai}}{x_i}+1\right)-(c_{f\,ic})_{ai}\frac{x_{ai}}{x_i}\right]. \qquad \text{(VI-3-10)}$$

Knowing the Reynolds numbers $Re_i = V_i\rho_i x_{v\,i}/\mu_i$ and the values of $(x_{a\,i}+x_i)/x_i$, we can determine the boundary-layer thicknesses at the end of each face.

Having determined the friction coefficients, we can calculate the specific heat transfer with consideration of the pressure gradient on a curved surface.

For this purpose, we can use Formulas (VI-2-1) and (VI-2-2), which proceed from the Reynolds analogy.

Heat Transfer on Blunt Wing Surface

The total-stagnation point. The leading edge may have a flat blunting. In this case, the heat flow at the total-stagnation point is calculated by (VI-2-23) for a flat plate in hypersonic flow.

For a total-stagnation point on a blunted curvilinear nose surface, the thermodynamic-equilibrium heat transfer must be calculated by (IV-8-47) and (IV-8-48). Assuming $\varepsilon = 0$ in these formulas, we obtain

$$q = q_{c0} = 0.47 \Pr^{-2/3} \sqrt{\rho_0' \mu_0' \tilde{\lambda}} i_r. \qquad \text{(VI-3-11)}$$

Here the velocity gradient $\tilde{\lambda}$ is determined at very large Mach numbers from the expression

$$\tilde{\lambda} = \left(\frac{\partial V_\delta}{\partial x}\right)_{x=0} = \frac{V_\infty}{R_r} \sqrt{\frac{k_2 - 1}{k_2}\left(1 + \frac{2}{k_\infty - 1} M_\infty^2\right)\left[1 - (k_\infty M_\infty^2)^{-1}\right]}. \qquad \text{(VI-3-12)}$$

At moderate supersonic speeds, $\tilde{\lambda}$ can be obtained from the Newton formula for the velocity distribution /349

$$\left(\frac{\partial V_\delta}{\partial x}\right)_{x=0} = \frac{V_\infty}{2R_b}\left\{\frac{8[(k-1)M_\infty^2 + 2]}{(k+1)M_\infty^2}\left[1 + \frac{k+1}{2}\frac{(k-1)M_\infty^2 + 2}{2kM_\infty^2 (k-1)}\right]^{-\frac{1}{k-1}}\right\}^{1/2}. \qquad \text{(VI-3-13)}$$

Formulas (VI-2-29) and (VI-2-30) can be used to calculate heat transfer with consideration of diffusion and the variation of $\rho\mu$ across the boundary layer, and for arbitrary T_{w1}.

If the wing is swept, the heat transfer at the leading-edge critical point will be smaller than for a straight wing. The decrease in heat transfer can be estimated from the diagram in Fig. VI-3-7.

Distribution of heat flow over nose surface. At hypersonic velocities of flow past a nose with a strongly cooled surface, and with the condition that the product $\rho\mu$ remain unchanged across the layer, the distribution of equilibrium heat flow is calculated by (IV-8-47), in which the function F(x) is determined by (IV-8-48). If $\varepsilon = 0$; $\omega_\delta = \omega_0'$, it assumes the form

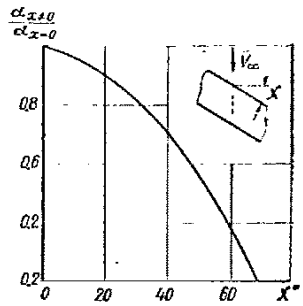

Figure VI-3-7. Influence of Wing Sweep on Heat Transfer at Leading-Edge Total-Stagnation Point.

$$F(x)=\frac{\sqrt{2}}{2}\frac{p}{p_0'}\frac{V_\delta}{V_\infty}\left[\int_0^x \frac{p}{p_0'}\frac{V_\delta}{V_\infty}\,dx\right]^{-1/2}. \quad \text{(VI-3-14)}$$

According to the improved Newtonian formula, the pressure on the curvilinear nose surface

$$\frac{p}{p_0'}=\cos^2\eta+\frac{1}{k_\infty M_\infty^2}\sin^2\eta, \quad \text{(VI-3-15)}$$

where η is the angle between the tangent to the contour and the direction of the radius of curvature.

The local-velocity distribution

$$\frac{V_\delta}{V_\infty}=\left\{\left(1+\frac{2}{k_\infty-1}\frac{1}{M_\infty^2}\right)\left[1-\left(\frac{p}{p_0'}\right)^{\frac{k_2-1}{k_2}}\right]\right\}^{1/2}. \quad \text{(VI-3-16)}$$

For a curvilinear contour of arbitrary shape, the function F(x) is found by numerical integration.

In the particular case in which the contour is an arc of a circle with a certain radius R_b, the determination of heat transfer can be simplified by using a linear law of velocity variation instead of (VI-3-16):

$$\frac{V_\delta}{V_\infty}=\left(\frac{\partial V_\delta}{\partial x}\right)_{x=0}x=\bar{\lambda}x=\bar{\lambda}R_b\varphi. \quad \text{(VI-3-16')}$$

$R_b d\varphi$ must be substituted for dx in (VI-3-14). As a result of simple transposition, we obtain for the ratios of the heat flows at an arbitrary point and at the total-stagnation point

$$\frac{q_c}{q_{c0}}=\sqrt{2}\varphi\left(\cos^2\varphi+\frac{1}{k_\infty M_\infty^2}\sin^2\varphi\right)D^{-1/2}(\varphi), \quad \text{(VI-3-17)}$$

where the function

$$D(\varphi)=\varphi^2\left(1+\frac{1}{k_\infty M_\infty^2}\right)+\sin\varphi\,(2\varphi\cos\varphi-\sin\varphi)\left(1-\frac{1}{k_\infty M_\infty^2}\right). \quad \text{(VI-3-18)}$$

In the limit as $\phi \to 0$, the ratio $q_c/q_{c0} \to 1$; at the end of the nose, where $\phi = \pi/2$, this ratio $q_c/q_{c0} = 1.8/k_\infty M_\infty^2$.

At moderate supersonic velocities, the heat-transfer distribution over a flat contour can be calculated approximately by the expression /350

$$q = A \Pr^{-2/3} \mathrm{Re}_x^{-1/n} \rho_\delta V_\delta (i_r - i_{w1}), \qquad \text{(VI-3-19)}$$

where A = 0.57 and 0.042 for laminar and turbulent flows, respectively, and n = 2 and 5, respectively. The enthalpy difference can be calculated with consideration of some heating

$$i_r - i_{w1} = c_p \Big|_{T_{w1}}^{T_r} (T_r - T_{w1}), \qquad \text{(VI-3-20)}$$

where $c_p \Big|_{T_{w1}}^{T_r}$ is the heat capacity calculated as the average for the temperature range $T_r - T_{w1}$.

The Reynolds number is determined from the expression $\mathrm{Re} = \rho_\delta V_\delta x/\mu_\delta$.

In addition to cases of supersonic flow, Formula (VI-3-19) can be used for subsonic flows, when heat transfer is found to be relatively minor. With increasing velocity, the temperature in the boundary layer rises, and this must be taken into consideration in calculating heat transfer. For this purpose, (VI-3-19) must be converted to determining parameters.

In performing the calculations, it must be remembered that the flow will always be laminar near the critical point. The boundary of the laminar region is determined by the critical Reynolds number, which is usually established by experiment.

Influence of diffusion and wall heating. If we assume that the influence of diffusion at an arbitrary surface point is the same as at the total-stagnation point and take an arbitrary wall temperature (wall not necessarily strongly cooled), the ratio of heat flows is

$$\frac{q}{q_0} = \frac{\rho_\delta \mu_\delta V_\delta}{\sqrt{2\tilde{x}\rho_0' \mu_0' (dV_\delta/dx)_0}} \frac{g_{w1}'}{g_{w10}'}, \qquad \text{(VI-3-21)}$$

where $\tilde{x}$ is determined from (IV-8-42) and the ratio g_{w1}'/g_{w10}' by (VI-2-32). The specific heat flow q_0 at the total-stagnation

point is calculated by (VI-2-30).

Influence of sweep. For a wing with a leading edge rounded with a certain radius and with a sweep angle χ, the heat transfer at the stagnation point or its average value for the blunted edge surface can be determined according to [55] by the formula

$$q_\chi = q_{\chi=0} \cdot \cos^{4/3}\chi. \qquad \text{(VI-3-22)}$$

§VI-4. WALL TEMPERATURE

Steady-State Heating

Equilibrium radiation temperature of wall in the absence of internal cooling. In the absence of internal cooling, radiative flow to the wall, and the miscellaneous heat leakages, the equilibrium temperature is determined from (IV-8-30). Figure IV-8-6 shows the variation of this temperature as a function of T_r and α/ε. However, this diagram cannot be used to determine $T_{w1} = T_e$, since T_r and α are unknown and are themselves determined in the course of solving (IV-8-30) simultaneously with the temperature T_e.

Solution is by the method of successive approximations, using the appropriate relationships for friction and heat transfer. M_∞, altitude and angle of attack are given and are used to find the distribution of the "inviscid" flow variables on the wing surface. /351

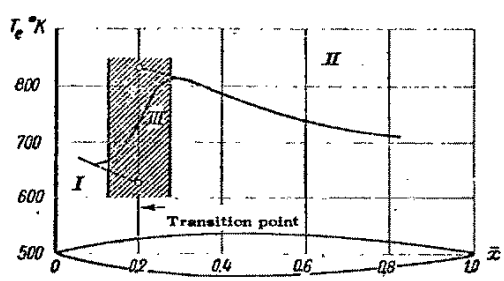

Figure VI-4-1. Nature of Distribution of Equilibrium Radiation Temperature over Surface of Profile. I) Laminar layer; II) turbulent layer; III) transition region.

To find the equilibrium temperature at a given point on the surface, the temperature $T_r = T_\delta + r(V_\delta^2/2)$, where $r = \sqrt{Pr}$ (laminar boundary layer) or $r = \sqrt[3]{Pr}$ (turbulent boundary layer) is determined as the first approximation. Then several values of the temperature T_{w1}, which must be somewhat lower than T_r, are assigned.

The difference $q_{w1} = \alpha_x(T_r - T_{w1}) - \varepsilon\sigma T_{w1}^4$ is found for each T_{w1} and a curve of q_{w1} as a function of T_{w1} is plotted.

Setting $q_{w1} = 0$, we determine the equilibrium temperature $T_{w1} = T_e$ on the diagram. From the condition of equal convective and radiant heat flows, we can improve the heat-transfer coefficient α_x and the coefficient of friction on the basis of $T_{w1} = T_e$.

The recovery temperature can be improved from the equilibrium temperature thus found by determining the second-approximation recovery coefficient $\underline{r}$ and then repeating calculation of the temperature T_e.

T_{w1} can be obtained by direct numerical calculations. In this case, it is necessary to know at least two values q_{w11} and q_{w12}, the first of which is positive, while the second is negative. Knowing the temperatures T_{w11} and T_{w12} that correspond to them and using linear interpolation, we find the value $T_{w1} = T_e$ that corresponds to $q_{w1} = 0$:

$$T_e = T_{w11} + q_{w11}\frac{T_{w12} - T_{w11}}{q_{w11} - q_{w12}}. \qquad \text{(VI-4-1)}$$

The equilibrium temperature must be calculated with consideration of the presence of a mixed boundary layer on the washed surface, using the appropriate relationships to determine the friction and heat-transfer variables. In connection with this, the critical Reynolds numbers must be found and the transition points determined.

At high speeds, the equilibrium temperature and the other parameters associated with its determination are calculated by the determining-enthalpy (temperature) method.

By way of illustration, the diagram of Fig. VI-4-1 presents results of an equilibrium-temperature calculation for a parabolic profile at a supersonic flow velocity. The calculation was performed without consideration of the longitudinal pressure gradient for fixed values of $r = \sqrt{0.71} = 0.84$ and $r = \sqrt[3]{0.71} = 0.89$ and $Pr = 0.71$.

In constructing diagrams similar to Fig. VI-4-1, it is necessary to remember the transitional region, in whose neighborhood the heat flows vary along a certain curve. There may be no breaks on the curve, since longitudinal heat flows arise in reality and equalize the temperatures.

Equilibrium temperature of internally cooled wall. Let us consider a case in which a certain amount of heat q_{cs} is /352

withdrawn from the wall with some sort of cooling system in the absence of an inflow of external radiant heat. With steady-state heat transfer, the heat-balance equation will be $q_c - q_{em} - q_{cs} = 0$ or

$$\sigma T_{wl}^4 = \frac{\alpha_x}{\varepsilon}(T_r' - T_{wl}), \qquad \text{(VI-4-2)}$$

where T_r' is the reduced recovery temperature, determined from the condition $T_r' = T_r[1 - q_{cs}/(\alpha_x T_r)]$.

Since the specific heat flow q_{cs} is usually given, the problem of determining the equilibrium wall radiation temperature T_{wl} is solved in principle in the same way as in the absence of cooling. The difference is that the reduced value T_r' is determined instead of the recovery temperature.

We see from (VI-4-2) that the equilibrium wall temperature $T_{wl} = T_e$ is lowered by cooling.

From the value found for T_{wl}, we can determine the outside T_{sk} and inside T_{in} wall temperatures on the assumption that the insulation (if present) and the skin are heated to the temperature corresponding to steady heat exchange and, consequently, that the same amount of heat passes through them:

$$\lambda_{insl}\left(\frac{\partial T}{\partial y}\right)_{insl} = \lambda_{sk}\left(\frac{\partial T}{\partial y}\right)_{sk} = q_{cs} \qquad \text{(VI-4-3)}$$

which depends on the thermal conductivity coefficients of the insulation and skin materials. If we assume that they are constant, integration over the integration thickness δ_{insl} (in this case external) and the skin thickness δ_{sk} gives

$$T_{sk} = T_{wl} - \frac{q_{cs}\delta_{insl}}{\lambda_{insl}}, \quad T_{in} = T_{sk} - \frac{q_{cs}\delta_{sk}}{\lambda_{sk}}. \qquad \text{(VI-4-4)}$$

Nonsteady Heating

In the case of nonsteady heating, the wall temperature varies in time. If we take thin-walled metal skins with high thermal conductivity, we can disregard the effect of the thickness temperature gradient on heating and assume that the wall is heated instantaneously. Equation (VI-8-29), in which we may

assume for simplicity that only the outer surface emits, should be used to calculate wall temperature.

In integrating differential equation (VI-8-29), a certain initial temperature is assigned; it might be, for example, the equilibrium radiation temperature established in motion of the body at constant speed and altitude. This motion preceeds the point in time at which the nonsteady process begins (acceleration or deceleration of the vehicle).

Having assigned an arbitrary time interval Δt and knowing the M_∞ corresponding to $t + \Delta t$ from the trajectory calculation, we can determine the inviscid-flow parameters and the values of α_{1x} and T_{r1} at a certain point on the surface for steady heat transfer. The derivative

$$\left(\frac{dT_{w1}}{dt}\right)_1 = \{\alpha_{1x}[T_{r1} - T_{w11}] + \varepsilon\sigma T_{w11}^4\}(c\gamma\delta)_{sk} \qquad \text{(VI-4-5)}$$

is determined in first approximation from these data, and then the wall temperature is improved:

$$T_{w12} = \Delta T + T_{w11} = \left(\frac{dT_{w1}}{dt}\right)_1 \Delta t + T_{w11}.$$

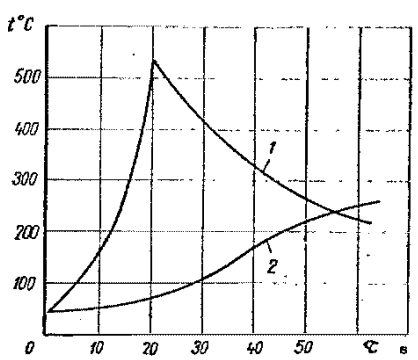

Figure VI-4-2. Skin Temperature for Variable Flight Speed. 1) adiabatic wall temperature T_r; 2) actual skin temperature.

The values of α_2, T_{r2}, and T_{w12} are determined in second approximation for this temperature, and then the derivative (VI-4-5) and, finally, the temperature T_{w13} are found. Here, if the time interval is taken small enough, we can stop at the first approximation in calculating the derivative of (VI-4-5). /353

Figure VI-4-2 shows a typical time variation of the temperature of a thin wall at a certain point on the surface of a body moving in flow first with acceleration (up to time τ = 20 s, as the diagram shows), and then with deceleration. Calculations indicate that the skin temperature lags behind the rise in the adiabatic wall temperature and that we have a thermal

inertia governed by the heat capacity of the skin.

In the case of flight at high altitudes, where aerodynamic heating can be disregarded, the equation for the nonsteady thin-skin temperature will be

$$\frac{dT_{w1}}{dt} = \frac{\varepsilon\sigma}{(c\gamma)_{sk}}\left[\left(\frac{q_1}{\varepsilon\sigma}\right) - T_{w1}^4\right], \qquad \text{(VI-4-5')}$$

where q_r is the radiant flux supplied to the surface.

In the general case of variable q_r, the equation given above is solved by numerical integration.

At moderate flight speeds in the dense atmosphere, the radiant heat flow into the environment may be neglected. Disregarding also the radiant energy supplied to the wall and assuming that the amount of heat absorbed by the thin skin is equal to the amount of heat transmitted to it by the boundary layer, we can write

$$(c\gamma\delta)_{sk}\, dT_{w1} = \alpha\,(T_r' - T_{w1})\, dt.$$

Remembering that $(c\gamma\delta)_{sk}$, α, and T_r are weak functions of time, and assuming these parameters constant, we find after integration with the initial conditions $t = 0$, $T_{w1} = T_0$

$$T_{w1} = T_r - (T_r - T_0)\, e^{-\bar{t}}, \qquad \text{(VI-4-6)}$$

where $\bar{t} = -\alpha t/(c\gamma\delta)_{sk}$.

The above scheme for calculation of nonsteady heat transfer is not applicable to materials with low thermal conductivities (protective coatings) or to thick metal skins, which are characterized by heating that is nonuniform over their thickness, with the result that the outer surface may be substantially hotter than the inner surface. Calculation of the temperature distribution through the thickness of such a skin is discussed in [11], which also submits a method of determining the required thickness of the heat-insulating coating.

Wall Temperature in the Presence of Solar Heating

At high altitudes (of the order of 100-150 km and up), the aerodynamic heat flow is insignificant by comparison with the

amount of radiant energy. Disregarding dissipation of heat along the surface, we may assume that the heat-balance equation for the steady process takes the form

$$q_s + q_e + q_{rf} = q_{em}.$$

In practice, the thermal emission from the earth and the solar energy q_{rf} reflected from it can be disregarded. Accordingly, $q_s = q_{em}$ and, consequently, /354

$$T_{wl} = \left(\frac{\beta_a}{\varepsilon}\frac{\bar{q}_a}{\sigma}\cos\psi\right)^{1/4}, \qquad \text{(VI-4-7)}$$

from which we see that the maximum temperature will occur at $\psi = 0$. In practice, we can use the constant value $\bar{q}_s = 0.332$ kcal/m^2·s, to which the wall temperature

$$T_{wl} = 395\left(\frac{\beta_a}{\varepsilon}\right)^{1/4} \qquad \text{(VI-4-7')}$$

corresponds.

For a rotating spherical vehicle, the averaged surface temperature is

$$T_{av} = 280\left(\frac{\beta_a}{\varepsilon}\right)^{1/4}. \qquad \text{(VI-4-8)}$$

§VI-5. WING LEADING EDGE BLUNTNESS FOR MAXIMUM REDUCTION OF HEAT-FLOWS

The effect of bluntness is manifested in smaller local Re, so that the point of the turbulent transition of a laminar boundary layer is shifted and, as a result, friction and the heat flows are reduced. This decrease will be largest when the bluntness shifts the transition point to the trailing edge. Consequently, the degree of bluntness must be so large that the Reynolds number on the outer edge of the boundary layer will approach the value of this number computed from the lower velocity V_δ of high-entropy inviscid flow for the entire laminar-flow segment. The position of the transition point is determined by the critical Reynolds number Re_{cr}, which is computed for the velocity V_δ. Hence the bluntness must be sufficient for the flow, which has been retarded in the high-entropy "inviscid" layer covering the

boundary layer, to have the necessary velocity V_δ at the end of the body.

Research [50] has shown that the streamline passing through the "sonic" point with coordinate y_S on a separated shock wave (see Fig. IV-10-1) may be taken as the upper boundary of this layer. The gas flow across a section of area $y_S \cdot 1$ will be $\rho_\infty V_\infty y_S$. The same amount will pass through a layer of smaller Re that has a certain thickness Δ corresponding to an arbitrary section of the body at coordinate $\underline{x}$. Consequently, $\rho_\infty V_\infty y_S = \rho_\delta V_\delta \Delta$, from which the "inviscid"-layer thickness is

$$\frac{\Delta}{y_s} = \frac{\rho_\infty V_\infty}{\rho_\delta V_\delta}, \qquad \text{(VI-5-1)}$$

where ρ_δ and V_δ are the density and velocity in the particular section, respectively, as calculated for inviscid flow over the surface with consideration of the effect of bluntness. In determining these parameters, we can start from the condition that the pressure established at a certain distance from the blunt nose is the same as that for a sharp body. Curves or tables of the thermodynamic functions of air are used in calculating "inviscid" parameters with dissociation taken into account. Knowing the pressure and the calculated average entropy S_0 (between the apex of the wave and the "sonic" point or, in simplified calculations, the value of S_0 behind the normal part of the shock), we use these tables to find the density ρ_δ and enthalpy i_δ in a given section. Then V_δ is calculated from the equation $I_0 = i_\delta + 0.5V_\delta^2$. The velocity and density of the gas in flow sections remote from the nose can be calculated for constant heat capacities by the respective formulas

/355

$$\frac{V_\delta^2}{V_\infty^2} = \left\{\left[1 - \left(\frac{p_\infty}{p_0}\right)^{\frac{k-1}{k}}\right] \times \left(1 + \frac{k-1}{2} M_\delta^2\right)\right\}^{-1} \frac{k-1}{2} M_\delta^2; \qquad \text{(VI-5-2)}$$

$$\frac{\rho_\delta}{\rho_\infty} = \frac{\rho_0}{\rho_\infty} \frac{p_0'}{p_0} \left(1 + \frac{k-1}{2} M_\delta^2\right)^{-\frac{1}{k-1}}, \qquad \text{(VI-5-3)}$$

where the local Mach number

$$M_\delta^2 = \frac{2}{k-1}\left[\left(\frac{p_0'}{p}\right)^{\frac{k-1}{k}} - 1\right]. \qquad \text{(VI-5-4)}$$

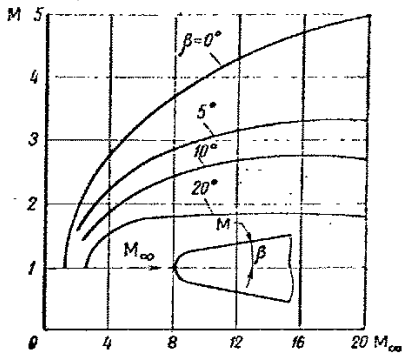

Figure VI-5-1. Local Mach Number on Surface of Blunt Wedge.

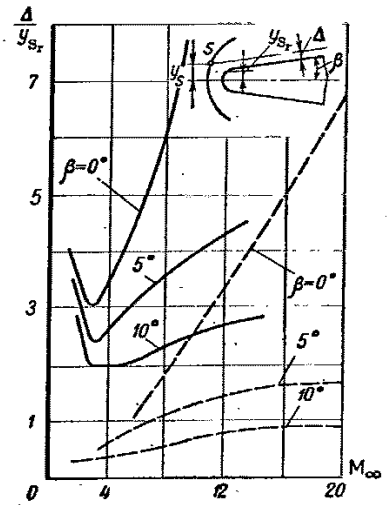

Figure VI-5-2. Ratio of Thickness Δ of "Inviscid" Layer on Blunt Wedge to Coordinate of "Sonic" Point on Spherical Nose (The Solid Curve was Computed for the Exact Value of y_S/y_{S_r}, the Dashed Curve for $y_S/y_{S_r} = 0.5$).

The values of M calculated by this formula for a blunt wedge appear in Fig. VI-5-1. The stagnation pressure p_0' is determined to refine the calculations as the mean between the corresponding values at points B and S (see Fig. IV-10-1), of which the former is situated directly behind the normal part of the shock, while the latter is on the curvilinear segment and is "sonic."

Knowing the parameters ρ_δ and V_δ and the coordinate y_S of the "sonic" point on the shock wave, we can determine the thickness of the "inviscid" layer.

Figure VI-5-2 presents the results of a calculation by this method to determine Δ, referred to the coordinate y_{S_r} of the "sonic" point on a spherically blunted wedge,

$$\frac{\Delta}{y_{S_r}} = \frac{y_S}{y_{S_r}} \frac{\rho_\infty V_\infty}{\rho_\delta V_\delta}. \qquad \text{(VI-5-5)}$$

To calculate the required bluntness (y_{S_r}), we set up the condition that the thickness of the boundary layer at the transition point must be equal to the thickness of the low-velocity layer.

Consequently, the conditions from which y_{S_r} can be determined will be

$$\delta_1 = y_S \frac{\rho_\infty V_\infty}{\rho_\delta V_\delta} \quad \text{or} \quad \delta_1 = y_{S_r}\left(\frac{\Delta}{y_{S_r}}\right). \qquad \text{(VI-5-6)}$$

It follows from the second formula (VI-5-6) that if $\Delta/y_{S_r} \simeq 1$, the "sonic-point" coordinate $y_{S_r} \simeq \delta_1$. To determine the laminar-layer thickness at the transition point on the surface of a blunt wedge, we can use the corresponding relation for a flat plate with the condition that the parameters appearing in it are the same as on a blunt wedge. The laminar-layer thickness at the transition point is

/356

$$\frac{\delta_1}{x_t} = 5.8\,(\mathrm{Re}^*_{cr})_{we}^{1/2}, \qquad \text{(VI-5-7)}$$

where x_t is the distance to the transition point.

The critical Reynolds number can be calculated from the determining parameters for a blunt wedge, i.e., $(\mathrm{Re}^*_{cr})_{we} = (V_\delta x_t \rho^*/\mu^*)_{we}$. Since the critical Reynolds number is assumed to be known, we can determine the length of the laminar segment

$$x_t = \left(\frac{\mu^*_\delta \mathrm{Re}^*_{cr}}{V_\delta \rho^*}\right)_{we},$$

and then the thickness of the boundary layer at the transition point:

$$\delta_1 = x_t\left(\frac{\delta_1}{x_t}\right)_{we}. \qquad \text{(VI-5-8)}$$

The required bluntness becomes smaller if we consider the influence of the conventional displacement thickness, which increases the effective wedge thickness and, consequently, the thickness of the inviscid layer of diminished Reynolds numbers. Accordingly, the coordinate of the "sonic" point is

$$y_{S_r} = (\delta_1 - \delta^*)\left(\frac{\Delta}{y_{S_r}}\right)^{-1}. \qquad \text{(VI-5-9)}$$

If we assume that $\delta^* = 0.125\delta_1$ (the conventional thickness, like the layer thickness, is calculated in the general case from the determining parameters on the blunt wedge), then

$$\delta_1 = \delta^* = 0.875\delta_1. \qquad \text{(VI-5-10)}$$

Part Three

/357

BODY AERODYNAMICS

/358

AERODYNAMIC COEFFICIENTS AT SUBSONIC AND TRANSONIC SPEEDS

§VII-1. SUBSONIC SPEEDS

Friction drag. The flat-plate relationships can be used in simplified calculations of body friction drag. The results must be regarded as highly approximate, since they do not take account of the spatial nature of the flow and the shape of the washed surface.

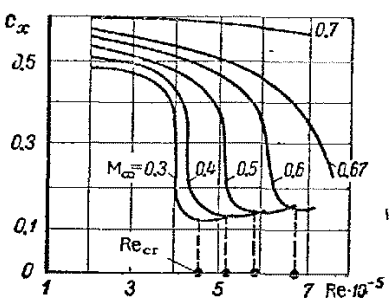

Figure VII-1-1. Influence of Compressibility on the Critical Reynolds Number Re_{cr} of a Solid of Revolution.

If $c_{x\,f}$ is the friction-drag coefficient of a plate whose length is equal to the length of the body, the friction drag force $X_f = c_{xf}qS_{sde}$, where S_{sde} is the area of the side of the body.

The boundary layer around a body is mixed under real conditions: it is laminar on the forward section and turbulent on the rest. Accordingly, the average body drag coefficient calculated for the midships section is

$$c_{xf} = c''_{xf\,b}\frac{S_{sde}}{S_{mid}} - c''_{xf\,l}\frac{S_l}{S_{mid}} + c'_{xf\,l}\frac{S_l}{S_{mid}}, \qquad \text{(VII-1-1)}$$

where $c''_{xf\,b}$ and $c''_{xf\,l}$ are the turbulent-friction coefficients of the plate; the former is found from the Reynolds number calculated for the length of the body, and the latter from the Reynolds number calculated for the laminar length; $c'_{xf\,l}$ is the average laminar friction coefficient of a plate whose length is equal to that of the laminar layer on the body. The quantities S_{sde} and S_l are, respectively, the total lateral area of the body and the part of this area that corresponds to the length of the laminar layer.

In the general case, the laminar-segment length depends on the shape of the body, M_∞, the wall temperature, and the roughness of the wall surface. In the simplest case, that of an absolutely smooth surface in incompressible flow in the presence of a negative pressure gradient, the critical Reynolds number for an elongated body may be set equal to $Re_{cr} = 10^6$. The diagrams in Fig. VII-1-1 permit inferences as to the effect of compressibility on the critical Reynolds number of a solid of revolution.

Data pertaining to plane two-dimensional flows may be used to evaluate Re_{cr} if it is remembered that the actual Re_{cr} for bodies are somewhat larger. Below we shall set forth more detailed data on critical Reynolds numbers for bodies.

Pressure drag. At subsonic speeds, the pressure distribution, which must be known to calculate the corresponding drag components, can be found dependably enough only by experiment. /360
Here, studies have shown that the difference between the pressures in incompressible and subsonic compressible flows is small for elongated bodies.

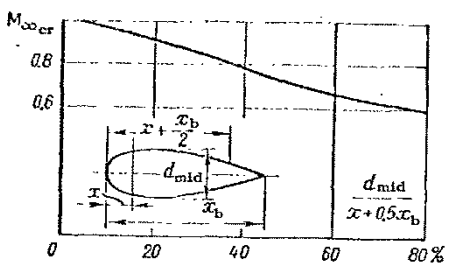

Figure VII-1-2. Critical Mach Number $M_{\infty cr}$ of Solid of Revolution.

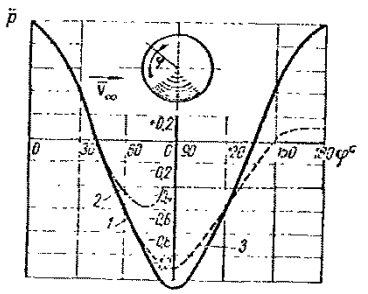

Figure VII-1-3. Pressure Distribution over a Sphere. 1) potential flow; 2) $Re > Re_{cr}$; 3) $Re < Re_{cr}$.

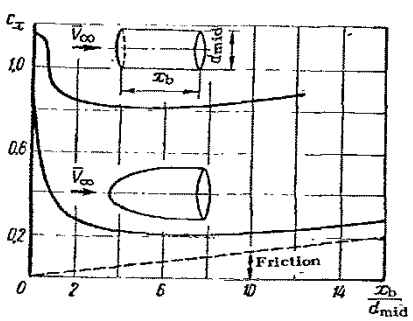

Figure VII-1-4. Drag of Solids of Revolution.

The pressure coefficient $\bar{p}$ for a subcritical Mach number can be found by use of the pressure-coefficient values $\bar{p}_{ic}$ for an incompressible flow and the conversion formula

$$\bar{p} = \bar{p}_{ic}(1 - M_\infty^2)^{-0,5}. \qquad \text{(VII-1-2)}$$

The diagram in Fig. VII-1-2 can be used for approximate evaluation of the critical Mach number. For a strongly curved surface, the pressure distribution depends on the Reynolds numbers — subcritical or supercritical — of the flow. This is seen from Fig. VII-1-3, which shows the pressure distribution over a sphere.

The coefficient of the nose drag that arises from pressure and friction on the front of the body (profile drag) is determined by the empirical formula [26]

$$c_{x\,\mathrm{pr}} = k_s c_{xf}, \qquad \text{(VII-1-3)}$$

in which the shape factor

$$k_s = 1.86 - 0.175\lambda_s + 0.01\lambda_s^2. \qquad \text{(VII-1-4)}$$

The parameter λ_s is known as the reduced aspect ratio and is determined by the expression

$$\lambda_s = \lambda_b \sqrt{1 - M_\infty^2}. \qquad \text{(VII-1-5)}$$

The friction drag coefficient c_{xf} referred to the midship section is calculated with consideration of compressibility and as a function of the nature of the flow in the boundary layer.

Total drag. It should be regarded as the sum of the nose (profile) and wake drags (see §XIV-2). Experimental data on total-drag coefficients for certain solids of revolution in incompressible flow are shown in Fig. VII-1-4 [16]. According to these data, the friction drag coefficient /361

$$c_{xf} = 0.014 \frac{x_b}{d_{\mathrm{mid}}}. \qquad \text{(VII-1-6)}$$

Compressibility influences the drag of bodies in high-velocity flow. At subcritical Mach numbers, however, this effect, as we see from the experimental data in Fig. VII-1-5, is small and is usually manifested in a slight increase in the drag coefficient.

Body drag depends substantially on the shape of the nose section (Fig. VII-1-6). The following empirical relation for the drag coefficient of an elongated solid of revolution with a flat

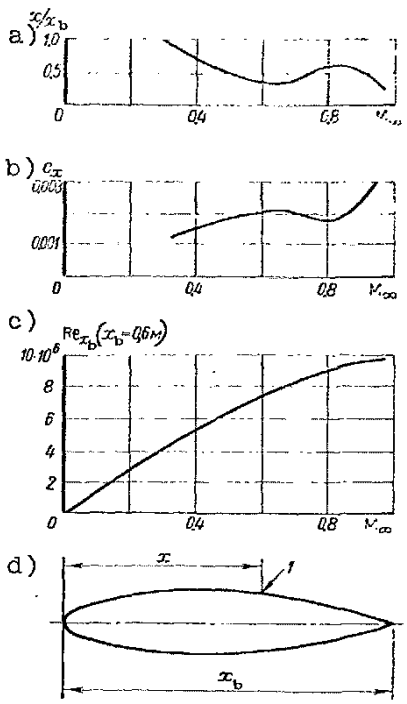

Figure VII-1-5. Transition Point (a), Drag (b) and Reynolds Number (c) for Solid of Revolution (d) at Various M_∞; 1) transition point.

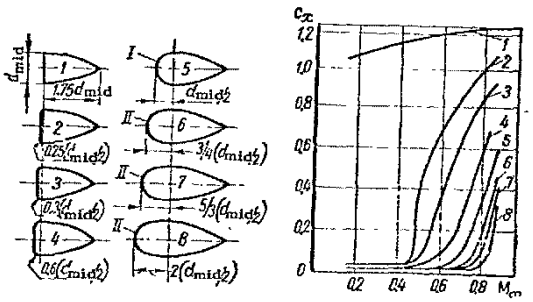

Figure VII-1-6. Influence of Nose-Section Shape of Solid of Revolution on Frontal-Drag Coefficient. I) circle; II) ellipse.

nose corresponds to the experimental data in Fig. VII-1-6 [16] (model 1):

$$c_x = 0.5 + 0.645\left(1 + \frac{M_\infty^2}{4}\right). \qquad \text{(VII-1-7)}$$

Flight tests of spherical missiles have shown that up to $M_\infty \leq 0.5$, the total drag coefficient can be assumed constant at $c_x = 0.4923$ ([72], No. 4, 1945).

Normal force, moment. Research has shown that at subsonic speeds, the normal force and moment of slender bodies can be determined from the same relationships as in the case of supersonic flow. The normal-force and moment coefficients can be calculated by Formulas (XI-3-31) and (XI-3-40), which take account of flow separation as it influences the aerodynamic characteristics. /362

§VII-2. TRANSONIC SPEEDS

Similarity of Transonic Flows

Equation of symmetrical transonic flow. The linearized equations of motion of a gas are not applicable in the case of transonic flow velocities around a solid of revolution, even if it is slender. This becomes understandable when we remember that

the difference between the squared velocities $a^2 - V_x^2$ was replaced by the approximate value $a^2 - V_\infty^2$ in linearization of the equations. This substitution is not admissible under transonic speed conditions. In fact, the difference $a^2 - V_x^2$ in the linearized flow, which is equal to $a_\infty^2 - V_\infty^2 - V_x' V_\infty (k + 1)$ can be replaced by the approximate expression $a_\infty^2 - V_\infty^2$ because the term $V_x' V_\infty (k + 1)$ is small by comparison with $a_\infty^2 - V_\infty^2$.

At the same time, under transonic-flow conditions, when the flow velocity is near sonic, the quantity $V_x' V_\infty (k + 1)$, which is determined by the additional disturbance-velocity component V_x', will be commensurate with the difference $a_\infty^2 - V_\infty^2$ and, consequently, linearization of the equations is impossible. Although the basic equations cannot be linearized, they can nevertheless be simplified with certain assumptions. Simplified equations that have been derived [43] facilitate investigation of transonic symmetrical flows substantially.

Let us consider the equation for the velocity potential of a steady symmetrical transonic flow, as derived by simplifying (III-2-22).

Let us define the disturbance potential ϕ' by the relationships

$$\frac{\partial \varphi'}{\partial x} = \varphi_x' = V_x - a^*; \quad \frac{\partial \varphi'}{\partial r} = \varphi_r' = V_r. \qquad \text{(VII-2-1)}$$

The disturbance potential corresponds to a type of flow around a slender solid of revolution in which the local velocity differs little from the critical velocity a^* and, consequently, the derivative $\partial \phi'/\partial x$ is small.

The potential ϕ' must obviously satisfy the conditions "at infinity":

$$\left(\frac{\partial \varphi'}{\partial x}\right)_\infty = V_\infty - a^*; \quad \left(\frac{\partial \varphi'}{\partial r}\right)_\infty = 0. \qquad \text{(VII-2-2)}$$

Introducing the potential ϕ' into (III-2-22) and remembering that the square of ϕ_x'/a can be disregarded at near-sonic velocities V_∞, we obtain the differential equation for the potential of steady transonic flow:

$$\frac{k+1}{a^*} \varphi_x' \varphi_{xx}' + \frac{2}{a^*} \varphi_r' \varphi_{rx}' = \varphi_{rr}' + \frac{\varphi_r'}{r}. \qquad \text{(VII-2-3)}$$

This equation is nonlinear in ϕ'; it is more complex than the linearized equation, but at the same time simpler than the general equation (III-2-22) for velocity potential.

Law of flow similarity. The similarity law for transonic flows around solids of revolution with different slenderness ratios but similar thickness distributions (for example, conical and parabolic) is derived by supplementing the simplified equation (VII-2-3) with boundary conditions (VII-2-2) and the nonseparating-flow conditions /363

$$\frac{dr}{dx} = \frac{V_r}{V_x} = \frac{\varphi_r'}{a^*}. \qquad \text{(VII-2-4)}$$

Substituting $dr/dx = s(x/x_b)/\lambda_b$ for the derivative dr/dx in (VII-2-4), where $s(x/x_b)$ is a certain function that characterizes the slope of the generatrix and $\lambda_b = x_b/d_{mid}$ is the slenderness ratio of the body, we obtain

$$\varphi_r' = \frac{a^*}{\lambda_b} s\left(\frac{x}{x_b}\right). \qquad \text{(VII-2-5)}$$

Relation (VII-2-5) indicates that the order of magnitude of the potential on the body's surface is $\phi' \sim ra^*/\lambda_b$. On the basis of this evaluation, we can introduce the affine variables ξ and η, which are related by

$$x = x_b\xi; \quad r = \frac{x_b\lambda_b}{\sqrt{\Gamma}}\eta, \qquad \text{(VII-2-6)}$$

and represent the potential ϕ' in the form

$$\varphi' = x_b a^* \frac{1-\lambda_\infty}{\Gamma} F(\xi, \eta), \qquad \text{(VII-2-7)}$$

where $\Gamma = (k + 1)/2$ takes account of the influence of the gas properties, defined by the ratio of specific heats, on flow similarity and $\lambda_\infty = V_\infty/a^*$ is the relative velocity of the oncoming flow.

Introduction of the multiplier $1 - \lambda_\infty$ is dictated by the infinity condition, and the function $F(\xi,\eta)$ is subject to determination.

After conversion to the new variables and simplification (certain terms are small enough to be dropped), Eq. (VII-2-3) will be

$$2K\frac{\partial F}{\partial \xi}\frac{\partial^2 F}{\partial \xi^2}=\frac{\partial^2 F}{\partial \eta^2}+\frac{1}{\eta}\frac{\partial F}{\partial \eta}, \qquad \text{(VII-2-8)}$$

where

$$K=\lambda_b^3\frac{1-\lambda_\infty}{\Gamma}. \qquad \text{(VII-2-9)}$$

For given values of the parameter K, Eq. (VII-2-8) describes a whole class of flows around solids of revolution with large slenderness ratios and the same thickness distribution. Thus, the parameter K expresses the law of similarity for flows at transonic velocity. Here, similarity must be understood in the sense that the flows are described by the same form of (VII-2-8).

Pressure and drag coefficients. We first find a general formula for the pressure coefficient. For this purpose, we use the relation

$$p=p_0\left(1-\frac{V_x^2+V_r^2}{V_{max}^2}\right)^{\frac{k}{k-1}} \qquad \text{(VII-2-10)}$$

and substitute V_x^2 therein by the approximate expression

$$V_x^2=(a^*)^2+2\varphi_x' V_\infty.$$

Here, $(a^*)^2$ is defined as follows in terms of the oncoming-flow velocity in accordance with the "infinity" condition $\phi'_{x\infty} = V_\infty - a^*$:

$$(a^*)^2=V_\infty^2-2V_\infty\varphi'_{x\infty},$$

where $\phi'_{x\infty}$ is calculated from (VII-2-2).

Expanding our expression in series and keeping only two terms, /364

$$p-p_\infty=-\rho_\infty(\varphi'_x-\varphi'_{x\infty})V_\infty-\frac{1}{2}\rho_\infty\varphi_r'^2,$$

whence the pressure coefficient

$$\bar{p} = -\frac{2(v_x - v_{x\infty})}{V_\infty} - \frac{v_r^2}{V_\infty^2} = -\frac{2(V_x - V_\infty)}{V_\infty} - \frac{V_r^2}{V_\infty^2}. \qquad \text{(VII-2-11)}$$

We then find the axial velocity component

$$V_x = a^* + \frac{\partial \varphi'}{\partial x} = a^* \left(1 - \frac{V_\infty}{a^*} + \frac{1-\lambda_\infty}{\Gamma} \frac{\partial F}{\partial \xi}\right) + V_\infty. \qquad \text{(VII-2-12)}$$

Applying the approximate relation $1 - V_\infty/a^* = (1 - \lambda_\infty)/\Gamma$, and (VII-2-5) and (VII-2-12), we can bring (VII-2-11) to the form

$$\bar{p} = -\frac{1}{\lambda_b^2} P(K, \xi), \qquad \text{(VII-2-13)}$$

where the function

$$P(K, \xi) = -2K\left(1 + \frac{\partial F}{\partial \xi}\right) - s^2(\xi) \qquad \text{(VII-2-14)}$$

depends only on the similarity parameter K for a given point with the dimensionless coordinate ξ.

We now find a general expression for the pressure drag coefficient. For this purpose, we substitute the coefficient $\bar{p}$ defined by (VII-2-13) into (I-3-14). As a result,

$$c_{xp} = \frac{1}{\lambda_b^2} D(K), \qquad \text{(VII-2-15)}$$

where D(K) is a function of the similarity parameter K and is determined from the expression

$$D = 4\int_0^1 \lambda_b P\left(K, \frac{x}{x_b}\right) \bar{r} \operatorname{tg} \beta \, d\bar{x}. \qquad \text{(VII-2-16)}$$

The relationships found for the coefficients $\bar{p}$ and c_{xp} indidate that at a given K, transonic flows around solids of revolution are simpler in the sense that $\lambda_b^2 \bar{p}$ and $\lambda_b^2 c_{xp}$ are the same.

Thus, K is the basic parameter characterizing transonic flows. Hence the law of flow similarity with respect to the

parameter K can be used as a basis for experimental and theoretical study of the transonic aerodynamic characteristics of bodies. A relation for the parameter K that differs slightly from (VII-2-9) may be used:

$$K = \frac{(M_\infty^2 - 1)\lambda_b^2}{M_\infty^2 (k+1)}; \qquad \text{(VII-2-17)}$$

which reflects similarity more exactly.

A more rigorous approach leads us to the conclusion that the similarity laws are somewhat more complex than (VII-2-13) and (VII-2-15), namely: /365

$$\bar{p} = \frac{B(K, \xi)}{\lambda_b^2} + E(M_\infty, \lambda_b, k, \xi); \qquad \text{(VII-2-18)}$$

$$c_{xp} = \frac{C(K)}{\lambda_b^2} + G(M_\infty, \lambda_b, k), \qquad \text{(VII-2-19)}$$

where B, C, E, and G are certain functions.

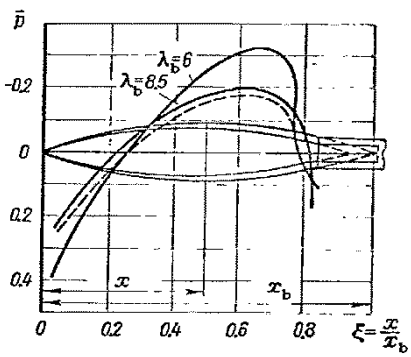

Figure VI-2-1. Illustrating Conversion of Pressure Coefficient for a Parabolic Solid of Revolution. ——— experiment; ----- according to Formula (VII-2-18).

The variables on which they depend are indicated in (VII-2-18) and (VII-2-19).

According to these formulas, similarity will pertain not to the functions $\bar{p}\lambda_b^2$ and $c_{xp}\lambda_b^2$, but to the products respectively.

$$(\bar{p} - E)\lambda_b^2; \quad (c_{xp} - G)\lambda_b^2.$$

Sharp slender body with curvilinear generatrix. Research has shown that for a family of affinely similar slender sharp solids of revolution, the second term in (VII-2-18) takes the form

$$E = -\frac{1}{\pi} S''(x) \ln\left[\frac{M_\infty}{\lambda_b^2}(k+1)^{1/2}\right]. \qquad \text{(VII-2-20)}$$

Together with (VII-2-18), Formula (VII-2-20) enables us to generalize isolated experimental data for a given M_∞ and a given model with a given slenderness ratio for various values of λ_b.

Figure VII-2-1 shows, for example, an experimental pressure distribution for $M_\infty = 1$ around a parabolic solid of revolution with a slenderness ratio $\lambda_b = 6$. Using this distribution and the value $\lambda_b = 6$, the functions $B(\xi)$ were calculated at each point with a given coordinate $\xi = x/x_b$ with the aid of similarity rule (VII-2-18). Then, using the same Formula (VII-2-18) and having values of the function $B(\xi)$ for $\lambda_b = 6$, the pressure coefficients were calculated at the corresponding points on a more slender solid of revolution with $\lambda_b = 8.5$. The results are in good agreement with experimental data [16].

Introducing Expression (VII-2-18) for $\bar{p}$ into (I-3-14), we can obtain the following similarity law for the drag coefficient:

$$c_{xp} = \frac{4}{\pi}\frac{C(K)}{\lambda_b^2} - \frac{1}{2\pi}\frac{[S'(x_b)]^2}{S_{mid}}\ln\left[\frac{M_\infty}{\lambda_b^2}(k+1)^{1/2}\right], \qquad \text{(VII-2-21)}$$

from which the function G that appears in (VII-2-19) can be found.

Similarity law (VII-2-21) is simplified if the body's base section coincides with its midships section or if it terminates in a sharp tail, since the derivative of the cross-sectional area $S'(x_b) = 0$ in either case.

The relationships given above as reflecting the similarity law are applicable for M_∞ in the neighborhood of unity; the calculated results are in good agreement with experimental data for sonic or slightly supersonic flows. /366

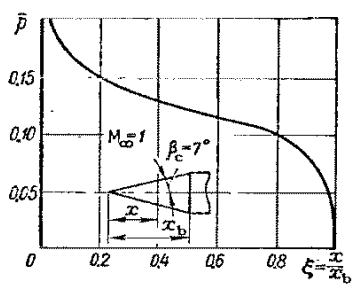

Figure VII-2-2. Pressure Coefficient on Sharp Cone ($M_\infty = 1$).

Slender sharp cone with cylindrical tail section. A peculiarity of flow around such a body at transonic or sonic velocity is that the velocity of sound is always established at the point of the angle. Hence the pressure at this point can be calculated in advance. At other points on the cone, the flow variables are found theoretically by solving (VII-2-8) or experimentally.

This solution results in the following relationship, which we can use to compute the pressure coefficient for $M_\infty = 1$:

$$\frac{\bar{p}}{\beta_c^2} = -2\ln(\beta_c\xi) + \ln A - B, \qquad \text{(VII-2-22)}$$

where

$$\left.\begin{aligned} A &= \frac{8.96\xi(1-\xi)}{(k+1)\beta_c^2},\quad B = \frac{1}{2}\frac{1+\xi}{1-\xi} \text{ for } 0 < \xi \leqslant \frac{1}{3};\\ A &= \beta_c^2 + \frac{2.24(1-\xi^2)}{(k+1)\beta_c^2},\quad B = 1 \text{ for } 0 < \xi \leqslant 1. \end{aligned}\right\} \qquad \text{(VII-2-23)}$$

Figure VII-2-2 shows a curve computed by (VII-2-22) for a cone with $\beta_c = 7°$. It agrees closely with experiment.

Using available data — theoretical or experimental — obtained for conditions characterized by specific values of M_∞ and β_c, and knowing the similarity rule (VII-2-22), we can calculate the distribution of pressure around a family of slender cones. This distribution will correspond to flow around conical bodies at various M_∞, but with the parameter K remaining constant.

A similarity rule similar to (VII-2-22) can also be obtained for $M_\infty \neq 1$. For this purpose, we use Formulas (VII-2-18)-(VII-2-20). Since $S(x) = \pi x\beta_c^2$; $S''(x) = 2\pi\beta_c^2$; $\lambda_c = 0.5/\beta_c$ for a cone, the pressure coefficient (VII-2-18) will be

$$\bar{p} = 4\beta_c^2 B(K, \xi) - 2\beta_c^2 \ln[4\beta_c^2 M_\infty (k+1)^{1/2}]. \qquad \text{(VII-2-24)}$$

The drag-coefficient expression that corresponds to (VII-2-21) is

$$c_{xp} = \frac{8\beta_c^2}{\pi} C(K) - 2\beta_c^2 \ln[4\beta_c^2 M_\infty (k+1)^{1/2}]. \qquad \text{(VII-2-25)}$$

For $M_\infty = 1$, (VII-2-24) and (VII-2-25) simplify, since the parameter $K = 0$. In particular, the expression by which we can determine the drag coefficient will be

$$(c_{xp})_{M_\infty = 1} = -\beta_c^2(1.09 + 4\ln\beta_c). \qquad \text{(VII-2-26)}$$

When M_∞ differs from unity and we have a slender body, we can use instead of the general formula (VII-2-25) the more concrete relationship

$$c_{xp} = -\beta_c^2(1.09 - 8K + 4\ln\beta_c). \qquad \text{(VII-2-27)}$$

Application of this formula is limited to values of the parameter K that satisfy the inequality /367

$$K = \frac{M_\infty^2 - 1}{4M_\infty^2 (k+1)\beta_c^2} \ll 1. \qquad \text{(VII-2-28)}$$

Total Drag of Various Solids of Revolution at Transonic Speeds

Experimental data [16] on the nose drag of a sharp solid of revolution with a tail are given in Fig. VII-2-3. These data indicate that the drag coefficient rises sharply beginning at M_∞ = = 0.8 and reaches a maximum at approximately M_∞ = 1.1.

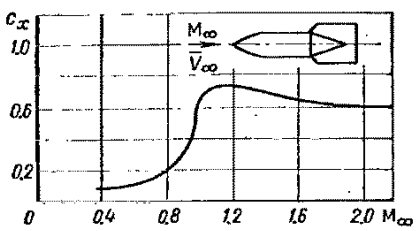

Figure VII-2-3. Drag Coefficient of Bomb.

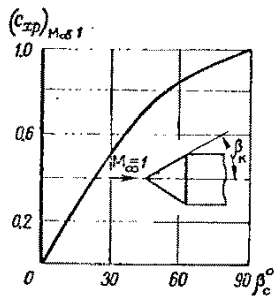

Figure VII-2-4. Drag of Conical Nose Sections at M_∞ = 1 (Experiment).

Experimental data [16] on the drag of sharp conical and ogival nose sections at the speed of sound (M_∞ = 1) are given in Figs. VII-2-4 and VII-2-5, respectively.

Nose blunting causes an increase in drag in both sub- and supersonic zones, but the increase in drag on passage through the transonic region is less sharp than for pointed bodies.

This is evident from Figs. VII-2-6 and VII-2-7, which present the results of experiments for a sphere and a flat-faced cylinder, respectively. Drag increases by a factor of two for the sphere and about 2.3 for the cylinder, while the corresponding factor for the sharp body (Fig. VII-2-3) is greater than 7.

The following conclusions can be drawn from analysis of these and other experimental data:

1) the frontal-drag coefficient reaches its maximum $c_{x\,max}$ at M_∞ somewhat larger than unity and lying in a range whose approximate limits are M_∞ = 1.1 and M_∞ = 1.5;

2) the shape of the body's nose section has the dominant influence on $c_{x\ max}$.

These conclusions can be used as a practical guide in approximate evaluation of the maximum value of the frontal drag coefficient. The experimental curve shown in Fig. VII-2-8 and representing $c_{x\ max}$ as a function of the nose slenderness ratio λ_{mid} can be used for the same purpose. This relation can be represented by the interpolation formula

/368

$$c_{x\,max} = \frac{0.8}{\lambda_{mid}} + 0.014\lambda_{mid}. \qquad \text{(VII-2-29)}$$

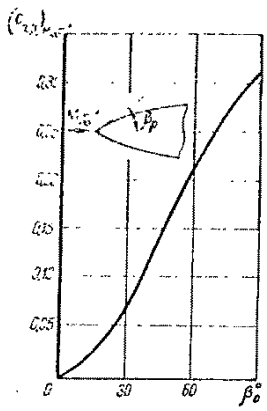

Figure VII-2-5. Drag of Ogival Nose Sections at $M_\infty = 1$ (Experiment).

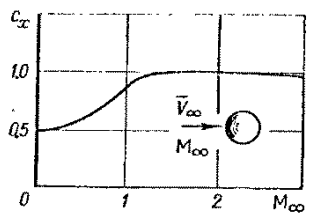

Figure VII-2-6. Frontal Drag Coefficient of Sphere (Experimental Data).

The second term on the right in this formula is an estimate of the friction drag coefficient.

The optimum slenderness ratio of the nose section, which, according to (VII-2-29), determines the smallest value of the coefficient $c_{x\ max}$, is nine. This slenderness ratio is that of a very slender body whose friction drag is largest as regards specific weight in the over-all balance of forces that compose total drag.

Analysis of theoretical and experimental data on flow around a hemisphere at various velocities, including transonic velocities, has established that the pressure drag coefficient can be calculated by the formula [16]

$$c_{xp} = 0{,}46 - \frac{1}{\pi}\operatorname{arctg}[1{,}61\,(1{,}2 - M_\infty)]. \qquad \text{(VII-2-30)}$$

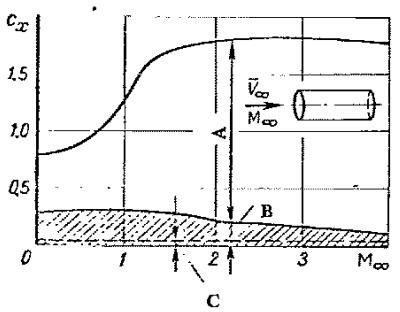

Figure VII-2-7. Drag of Cylindrical Solid of Revolution with Flat Face. A) drag of nose section; B) wake drag; C) friction drag.

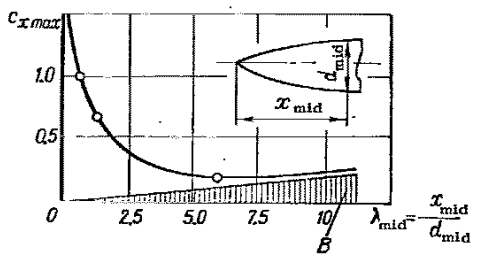

Figure VII-2-8. Maximum Value of Drag Coefficient for Solids of Revolution ($1.1 < M_\infty < 1.5$). B) frictional drag.

This "arc-tangent" law can also be applied to calculation of the pressure coefficient at the critical point of a sphere: /369

$$\bar{p}_0 = 1.35 - \frac{1}{\pi}\operatorname{arctg}[1.96(1 - M_\infty)]. \qquad \text{(VII-2-31)}$$

Formulas (VII-2-30) and (VII-2-31) give satisfactory results both for transonic speeds, including $M_\infty = 1$, and for a broader range extending from $M_\infty = 0$ to M_∞ of the order of 7-8.

Calculation of drag of sharp bodies based on the principle of "steady" local Mach number. It is assumed in accordance with this principle that the derivative $(\partial M/\partial M_\infty)_{M_\infty = 1} = 0$, i.e., the local M, does not vary and remains "frozen" as the oncoming-flow M_∞ passes through unity.

The range of M_∞ in which the distribution of local M is "frozen" is relatively narrow. Thus, for example, for a cone with the angle $\beta_c = 25°$, this range is 0.9-1.1, and for $\beta_c = 7°$, the M_∞ range from 0.99-1.01.

Using the principle of "steady" local M, we can derive a relationship by which we can calculate the drag of a sharp nose section at transonic speeds. Let us assume that we know the local M distribution. Then the corresponding velocity is

$$\frac{V^2}{V_\infty^2} = \left(\frac{M}{M_\infty}\right)^2 \frac{2 + (k-1)M_\infty^2}{2 + (k-1)M^2}, \qquad \text{(VII-2-32)}$$

and the pressure coefficient

$$\bar{p}=\frac{2}{kM_\infty^2}\left\{\left[\left(1+\frac{k-1}{2}M_\infty^2\right)\left(1-\frac{\bar{r}^2}{\bar{r}_{max}^2}\right)\right]^{\frac{k}{k-1}}-1\right\}. \qquad \text{(VII-2-33)}$$

Applying this relationship for the pressure coefficient and Expression (VII-2-32), we find after appropriate substitution into (I-3-14) a relationship by which we can compute the drag of a conical nose section:

$$c_{xp}=\frac{2}{kM_\infty^2}\left\{\int_0^1\left[\frac{2+(k-1)M_\infty^2}{2+(k-1)M^2}\right]^{\frac{k}{k-1}}d\bar{r}^2-1\right\}. \qquad \text{(VII-2-34)}$$

Expanding the expression in square brackets in series and dropping terms containing the second and higher powers of the difference $M_\infty - 1$, we obtain

$$c_{xp}=\frac{2}{kM_\infty^2}\left\{\left[1+\frac{k}{k+1}(M_\infty^2-1)\right]\int_0^1\left[\frac{k+1}{M^2(k-1)+2}\right]^{\frac{k}{k-1}}d\bar{r}^2-1\right\}. \qquad \text{(VII-2-35)}$$

Setting $M_\infty = 1$, we find from this expression a formula that defines the drag in sonic flight:

$$(c_{xp})_{M_\infty=1}=\frac{2}{k}\left\{\int_0^1\left[\frac{k+1}{M^2(k-1)+2}\right]^{\frac{k}{k-1}}d\bar{r}^2-1\right\}. \qquad \text{(VII-2-36)}$$

If we now assume in accordance with the steady Mach number principle that the local M is invariant with respect to M_∞ around unity, the integral in (VII-2-35) can be substituted in accordance with (VII-2-36). The result is a formula for the drag coefficient at transonic speeds:

$$c_{xp}=\frac{kM_\infty^2+1}{(k+1)M_\infty^2}(c_{xp})_{M_\infty=1}+\frac{2(M_\infty^2-1)}{(k+1)M_\infty^2}, \qquad \text{(VII-2-37)}$$

where the values of $(c_{xp})_{M_\infty=1}$ can be determined for conical and ogival nose sections from the experimental curves in Figs. VII-2-4 and VII-2-5 [16]. /370

With the relationships for c_{xp}, we can find the slope of the drag curve at the point corresponding to $M_\infty = 1$. Differentiating c_{xp} with respect to M_∞ and setting $M_\infty = 1$, we obtain

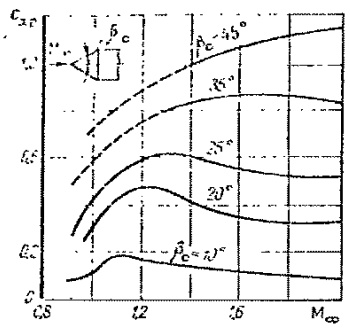

Figure VII-2-9. c_{xp} of Conical Nose Sections as Functions of M_∞. ——— experiment; ----- extrapolation.

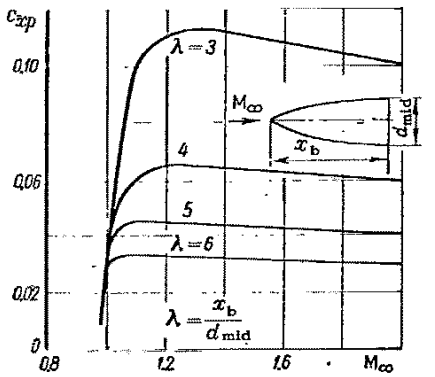

Figure VII-2-10. Drag of Ogival Nose Sections at Trans- and Supersonic Speeds.

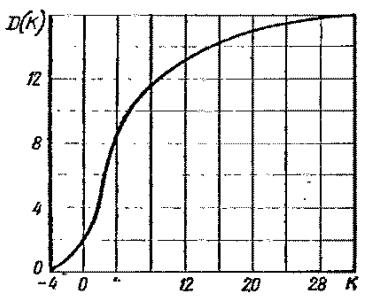

Figure VII-2-11. Function Defining Wave Drag of Solid of Revolution at Transonic Speeds.

$$\left(\frac{\partial c_{xp}}{\partial M_\infty}\right)_{M_\infty=1} = \frac{4}{k+1}\left[1 - \frac{(c_{xp})_{M_\infty<1}}{2}\right]. \qquad \text{(VII-2-38)}$$

It has been established in tests with cones that rough estimation of $(c_{xp})_{M_\infty = 1}$ by extrapolation of the drag curve constructed for $M_\infty < 1$ gives good results in determination of the slope of c_{xp} for M_∞.

Figures VII-2-9 and VII-2-10 present experimental data on the drag of a cone and an ogival nose section at transonic speeds. These data are in satisfactory agreement with the results of a drag-coefficient calculation for the transonic range and the slope of the c_{xp} curve at $M_\infty = 1$.

According to wind-tunnel measurements on solid-of-revolution models with curved nose and tail sections, the wave drag coefficient is

$$c_{xw} = \frac{1}{\lambda_{ef}^2} D(K), \qquad \text{(VII-2-39)}$$

where $\lambda_{ef} = \lambda_n + \lambda_{tl} + \Delta\lambda_C$ is the effective slenderness ratio, which is equal to the sum of the slenderness ratios of the nose λ_n and tail λ_{tl} sections of the body and a certain quantity $\Delta\lambda_C$ that takes account of the influence of the intermediate cylinder on the flow over the forward and aft segments of the surface. The quantity $\Delta\lambda_C$ is usually set equal to three. The function D(K) is found from the diagram of Fig. VII-2-11 as a function of the parameter

$$K = \lambda_{ef}^2 (M_\infty^2 - 1). \qquad \text{(VII-2-40)}$$

Normal force and center of pressure. It has been established by observation that the coefficient of normal force of a slender solid of revolution in the neighborhood of the speed of sound may reach a maximum value 25-35% greater than the value of the coefficient c_N at subsonic speeds. /371

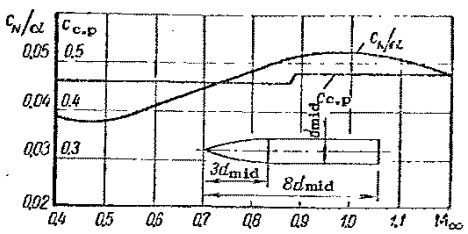

Figure VII-2-12. Variation of c_N/α and $c_{c.p}$ of Solid of Revolution with Parabolic Generatrix.

This conclusion may be illustrated with the data in Fig. VII-2-12, which indicate c_N/α as a function of M_∞ for small attack angles of the order of α = 0-3°. According to these data, the ratio c_N/α reaches its maximum at M_∞ = = 1.0, where it is about 35% larger than the c_N/α corresponding to M_∞ = 0.4.

The moment also increases with increasing normal force. As a result, the center of pressure position may undergo practically no change. This is seen in Fig. VII-2-12, which shows the results of measurement of the center of pressure coefficient of a cylindrical body with a parabolic nose section. The registered change in this coefficient on passage through the speed of sound is only about 2%.

A similar picture is also observed in experimental studies of flow around cones. It is known that the center of pressure coefficient of a cone is about 0.667 at supersonic speeds. At subsonic speeds, experiment indicates that it is, for example, 4% smaller for a cone with a semivertex angle β_c = 15°, i.e., the center of pressure is located nearer the point. On passage through the speed of sound, the center of pressure coefficient of a cone increases insignificantly, reaching 0.65 at M_∞ = 1.0.

In bodies formed by combining a nose cone and cylindrical tail section, experimental data indicate that the cylindrical segment bordering directly on the cone shifts the center of pressure toward the base of the cone. This effect is observed both at subsonic speeds and during passage through the speed of sound. The size of the shift depends on the length of the cylindrical segment bordering on the cone. However, this effect manifests in practice only up to certain values of the relative length of the cylindrical segment.

For slender cones, the increase in the center of pressure coefficient, in the range of $M_\infty = 0.7\text{-}1.2$ owing to the influence of a cylindrical section of $0.5d_{mid}$ approximate length, is 5-7%.

At a cylindrical-section length of $0.75d_{mid}$, this increase reaches 7-13%, and $c_{c.p}$ is found to be close to its maximum. At a further increase in cylinder length, the center of pressure position undergoes practically no change.

To obtain an idea of the variation of the center of pressure coefficient for an entire body consisting of a cone and a cylinder, it is necessary to consider the lifting capacity not only of the nose section, but also that of the cylindrical part. The presence of this part results in an additional rearward shift of the center of pressure.

When the body has a parabolic nose section, the center of pressure remains virtually stationary during passage through the speed of sound.

Chapter VIII /372

THE CONE IN SUPERSONIC FLOW

§VIII-1. AXISYMMETRIC SUPERSONIC FLOW PAST A CONE

Equation System

Let us consider a sharp circular cone with a half-angle β_c at the vertex in an axial supersonic flow. The problem is to calculate the flow of gas between this cone and the compression shock that forms ahead of it and has the shape of a conical surface. It is also necessary here to determine the inclination angle θ_s of the conical-shock generatrix (Fig. VIII-1-1). For this purpose, we shall examine the equation system applying to a case of flow in which the gas undergoes physicochemical changes behind the shock under the influence of high temperatures.

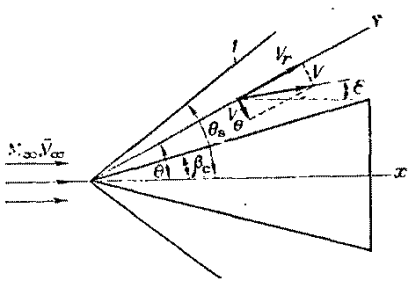

Figure VIII-1-1. Diagram of Supersonic Gas Flow Around a Sharp Cone. 1) compression shock.

Let us assume that thermodynamic equilibrium is established in the disturbed region. Let us assume further that the solution sought for the cone must have the property that the gas variables remain constant on the surface of any intermediate cone (including cones with angles $\theta = \theta_s$ and $\theta = \beta_c$) and change on passage from one surface to the other. The flow that corresponds to this solution is said to be conical. With consideration of this property, the partial derivative of any variable with respect to the r-coordinate (Fig. VIII-1-1) is zero, and we can then obtain the first two system equations from (III-2-8):

$$\frac{dV_r}{d\theta} = V_\theta; \qquad \text{(VIII-1-1)}$$

$$\rho V_\theta \frac{dV_\theta}{d\theta} + \rho V_r V_\theta + \frac{dp}{d\theta} = 0. \qquad \text{(VIII-1-2)}$$

According to the number of unknown parameters to be determined, it is necessary to add the continuity equation (III-2-17)

to these two equations, written in the form

$$2\rho V_r + V_\theta \frac{d\rho}{d\theta} + \rho \frac{dV_\theta}{d\theta} + \rho V_\theta \operatorname{ctg}\theta = 0, \qquad \text{(VIII-1-3)}$$

and also the equation

$$\frac{p}{p_s} = \frac{(\mu_{av})_s}{\mu_{av}} \frac{\rho}{\rho_s} \frac{T}{T_s}, \qquad \text{(VIII-1-4)}$$

which is derived from the equation of state (III-2-52), and the energy equation

$$i + \frac{V^2}{2} = i_s + \frac{V_s^2}{2}. \qquad \text{(VIII-1-5)}$$

In these equations, the subscript s identifies the parameters immediately behind the compression shock. The general relationships (III-4-6)-(III-4-9) for calculating of the enthalpy, entropy, average molecular weight, and the speed of sound must also be included in this system. 373

Constant Heat Capacities

Let us examine the solution for the particular case in which there is no dissociation and the specific heats do not change on passage through the shock wave.

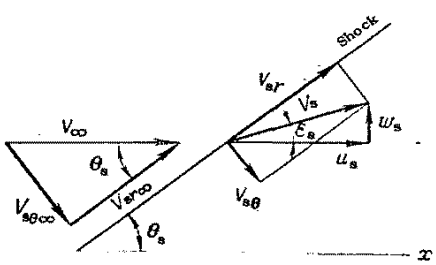

Figure VIII-1-2. Illustrating Determination of Boundary Conditions on Compression Shock Around a Sharp Cone.

For this case, the system consists of (VIII-1-1) and the equation

$$\frac{dV_\theta}{d\theta} = \left[-V_\theta \operatorname{ctg}\theta + V_r\left(\frac{V_\theta^2}{a^2} - 2\right)\right]\left(1 - \frac{V_\theta^2}{a^2}\right)^{-1}, \qquad \text{(VIII-1-6)}$$

obtained by combining (VIII-1-2) and (VIII-1-3) with consideration of the fact that $dp/d\theta = a^2(d\rho/d\theta)$, where the square of the speed of sound $a^2 = [(k-1)/2](V_{max}^2 - V^2)$.

The distribution of the velocities V_r and V_θ can be found by simultaneous solution of these two differential equations. This

is sufficient for complete solution of the problem, since the remaining gasdynamic variables (pressure, temperature, etc.) can be found from the velocities by the Bernoulli equation.

Numerical integration of the differential equations to find V_r and V_θ uses the following boundary conditions on the cone and the shock. The condition on the cone is that on its surface the normal velocity component $V_\theta = 0$, i.e., $dV_r/d\theta = V_\theta = 0$ for $\varepsilon = \beta_c$ (see Fig. VIII-1-1).

Applying Eq. (III-4-34) for the shock polar, we can obtain the condition on the compression shock:

$$\operatorname{tg}\theta_s = -\frac{k-1}{k+1}\left(1-\tilde{V}_{sr}^2\right)\left(\tilde{V}_{sr}\tilde{V}_{s\theta}\right)^{-1}, \qquad \text{(VIII-1-7)}$$

where

$$\tilde{V}_{sr} = V_{sr}/V_{max}; \quad \tilde{V}_{s\theta} = V_{s\theta}/V_{max};$$

V_{sr} and $V_{s\theta}$ are the radial and normal components, respectively, of the velocity on the compression shock.

The equation was derived with consideration of the fact that (Fig. VIII-1-2)

$$V_{sr} = V_{sr\infty} = V_\infty \cos\theta_s. \qquad \text{(VIII-1-8)}$$

The calculations begin with calculation of the parameters V_{sr} and $V_{s\theta}$ and the speed of sound a_s behind the shock for a given angle θ_s from the known oncoming-flow velocity. Then, knowing these boundary conditions, we find the parameters on a series of intermediate conical surfaces by successive numerical integration. The calculations are broken off when the boundary conditions on the cone are satisfied: the corresponding angle θ equal to the cone angle β_c, the value of $\tilde{V}_r = \tilde{V}_c$ equal to the total relative velocity on its surface.

The calculations can also be performed in reverse order, by assigning the conditions on the cone (angle β_c, velocity V_c). The gas variables and the inclination angle of the shock that forms ahead of the particular cone are the results. /374

Solution in Taylor-series form. The Taylor-series expansion can be used for numerical calculation of flow past a cone.

Let us present the expression for the radial velocity component, referred to its maximum value, in the form of such a series:

$$\tilde{V}_r = \tilde{V}_c + \tilde{V}'_{c\,r}(\theta - \beta_c) + \ldots + \tilde{V}^{(n)}_{c\,r}\frac{(\theta-\beta_c)^n}{n!} + \ldots, \qquad \text{(VIII-1-9)}$$

where the $\tilde{V}^{(n)}_{c\,r}$ are the values of the derivatives $d^n\tilde{V}_r/d\theta^n$ on the cone surface.

These derivatives are determined from the known velocity on the cone, with the first derivative $\tilde{V}'_{c\,r}$ equal to zero, since the normal velocity component on it $\tilde{V}_{c\theta} = \tilde{V}'_{c\,r} = 0$. For the second derivative, we obtain from (VIII-1-6)

$$\tilde{V}''_r = \left[\tilde{V}_r\left(\frac{\tilde{V}'^2_r}{\tilde{a}^2} - 2\right) - \tilde{V}'_r \operatorname{ctg}\theta\right]\left(1 - \frac{\tilde{V}'^2_r}{\tilde{a}^2}\right), \qquad \text{(VIII-1-10)}$$

where $\tilde{a} = a/V_{max}$.

If we consider the surface of the cone, $\theta = \beta_c$, $\tilde{V}_r = \tilde{V}_c$, $\tilde{V}'_r = \tilde{V}'_{c\,r} = 0$ and, consequently, $\tilde{V}''_{c\,r} = -2\tilde{V}_c$.

The third and higher derivatives are determined by successive differentiation of (VIII-1-6). Series (VIII-1-9) can then be written

$$\frac{\tilde{V}_r}{\tilde{V}_c} = 1 - h^2 + a_3h^3 - a_4h^4 + \ldots, \qquad \text{(VIII-1-11)}$$

where $k = \theta - \beta_c$, and the coefficients a_3 and a_4 are given for $k = 1.4$ by the relationships

$$a_3 = \frac{\operatorname{ctg}\beta_c}{3}; \quad a_4 = \frac{1}{12}\left(3\operatorname{ctg}^2\beta_c + \frac{20\tilde{V}^2_c}{1-\tilde{V}^2_c}\right). \qquad \text{(VIII-1-12)}$$

Differentiating (VIII-1-11) with respect to θ, we find the series representing the normal velocity component

$$\frac{\tilde{V}_\theta}{\tilde{V}_c} = -2h + 3a_3h^2 - 4a_4h^3 + \ldots. \qquad \text{(VIII-1-13)}$$

With Formulas (VIII-1-11) and (VIII-1-13), we can calculate the velocity components near the cone and then successively (stepwise) determine the velocity components on intermediate conical surfaces. The series

$$\tilde{V}_{rh} = \tilde{V}_{rh-1} + h\tilde{V}'_{rh-1} + \ldots, \qquad \text{(VIII-1-14)}$$

is used for this purpose; here, $\tilde{V}_{rh}$ is the radial velocity component at the conical surface with generatrix inclination angle $\theta + h$; $\tilde{V}_{rh-1}$ is the same component on the next intermediate cone with angle θ; $\tilde{V}'_{rh-1}$ is the value of the first derivative on the same cone.

In practical calculations, it is better to take the mean

$$\tilde{V}'_{rh-1} = \tilde{V}_{0h-1} = \frac{1}{2}(\tilde{V}_{0h} + \tilde{V}_{0h-1}).$$

By analogy with (VIII-1-14), we can write an expression for the derivative:

$$\tilde{V}'_{rh} = \tilde{V}'_{rh-1} + h\tilde{V}''_{rh-1} + \ldots . \qquad \text{(VIII-1-15)}$$

Here the first and second derivatives in the right member are found with (VIII-1-6). Formula (VIII-1-15) enables us to compute the normal velocity component on an intermediate conical surface: /375

$$\tilde{V}_{0h} = \tilde{V}_{0h-1} + h\tilde{V}'_{rh-1} + \ldots . \qquad \text{(VIII-1-16)}$$

The basic operation in performing these calculations is to use (VIII-1-10) to determine the second derivative on the preceding conical surface.

As the calculations move from one surface to another, they terminate when the angle θ obtained by adding β_c and all given intervals $h = \Delta\theta$ is found to be equal to the $\theta = \theta_s$ calculated by (VIII-1-7). This figure determines the shock inclination angle and the values $\tilde{V}_r = \tilde{V}_{s\,r}$, $\tilde{V}_\theta = \tilde{V}_{s\theta}$ will be the radial and normal velocity components behind it, respectively. Having determined the component $\tilde{V}_{s\,r}$ and the angle θ_s from (VIII-1-8), we can find the oncoming-flow velocity.

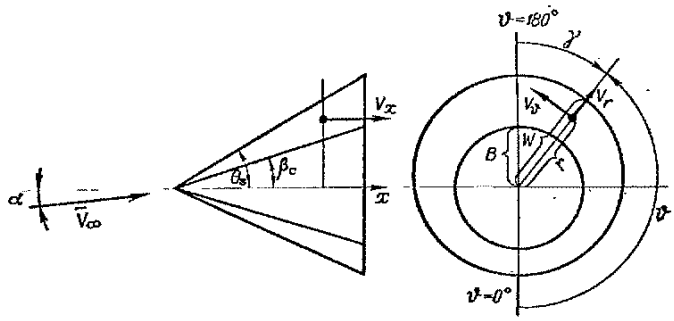

Figure VIII-1-3. Illustrating Determination of Gas Variables Around a Cone.

Tables, diagrams, approximate formulas. It is shown in [4] that in supersonic flow over a cone, the gasdynamic variables are functions of M_∞, β_c, and the coordinate $\xi = (r - B)/(W - B)$, where B and W are the respective distances from the axis to the surface of the cone and to the shock wave (Fig. VIII-1-3).

The results of numerical calculations of axisymmetric flow around cones are presented in Appendix No. 1 (Tables VIII-1-1 and VIII-2-2).

Table VIII-1-1 gives values of the gasdynamic functions V_x, V_r, p, and ρ, which are dimensionless and referred to the following qualtities: the axial and radial velocity components (in cylindrical coordinates) are referred to the critical speed of sound a^*, the density to ρ_∞, and the pressure to $\rho_\infty a^{*2}$. The same table gives W_x, which is equal to the slope of the shock wave with respect to the cone axis.

Table VIII-2-2 presents values of the wave drag coefficient $c_{x\,w} = c_{Rp}$ for a cone, as calculated from the data of Table VIII-1-1. The quantity $c_{x\,w}$ is equal to the pressure coefficient on the cone.

The formulas to be used in calculating the flow variables from tabular data (subscript $\underline{t}$) are $V_x = V_{x\,t} a^*$, $V_r = V_{r\,t} a^*$, $p = p_t \rho_\infty a^{*2}$, $\rho = \rho_t \rho_\infty$, where $a^{*2} = [2/(k + 1)]a_\infty^2 + [(k - 1)/(k + 1]V_\infty^2$. The slope of the intermediate-cone generatrix is found from the given coordinate ξ with the formula $\tan \theta = r/x = \tan \beta_c + \xi(W_x - \tan \beta_c)$.

The temperature, pressure, and density can be determined from the known velocity by Formulas (III-3-4), which are more

conveniently presented in the form

$$\frac{p}{p_\infty} = \left(\frac{T}{T_\infty}\right)^{\frac{k}{k-1}} \nu_0, \quad \frac{\rho}{\rho_\infty} = \left(\frac{T}{T_\infty}\right)^{1/(k-1)} \nu_0; \qquad \text{(VIII-1-17)}$$
$$\frac{T}{T_\infty} = (1 - \tilde{V}^2)\left(1 + \frac{k-1}{2} M_\infty^2\right),$$

where $\tilde{V}^2 = (V_r^2 + V_x^2)/V_{max}^2$; the parameter $\nu_0 = p_0'/p_0$ is the ratio of the stagnation pressure behind and in front of the shock and is determined as a function of M_∞ and θ_s by Formula (III-4-33).

TABLE VIII-1-2. MINIMUM VALUES OF M_∞ FOR WHICH CONICAL FLOW IS POSSIBLE (THEORETICAL DATA)

β_c^0	5	7.5	10	12.5	15	17.5	20
$M_{\infty\,min}$	1.0129	1.0294	1.0528	1.0828	1.1193	1.1622	1.2115

22.5	25	30	35	40
1.2673	1.3301	1.4820	1.6814	1.9582

On the basis of calculation processing, we can recommend the following approximate formulas for calculating the pressure coefficient and the compression-shock inclination angle:

$$\bar{p}_c = c_{x\,w} = (0.0016 + 0.002 M_\infty^{-2})(\beta_c)^{1.7}; \qquad \text{(VIII-1-18)}$$
$$M_\infty \sin\theta_s = 1 - \cos\beta_c + \left(1 + \frac{k+1}{2} M_\infty^2 \sin^2\beta_c\right)^{1/2}, \qquad \text{(VIII-1-19)}$$

where β_c is the cone angle in degrees.

In practice, this formula is used for calculations in a broad range of β_c and M_∞ with errors as small as 5%. The permissible lower limits for β_c and M_∞ are determined by the values at which the flow between the cone and the shock remains supersonic. The error of Expression (VIII-1-19) increases with increasing M_∞ and β_c as the effect of dissociation becomes significant (M_∞ > 10-15, β_c > 30-40°).

Studies have shown that the speed of sound varies so weakly in the disturbed region that it may be assumed constant and equal to the corresponding value directly behind the shock. Calculations carried out on this assumption have shown good results. For example, at $M_\infty = 3$ and $\theta_s = 25°11'$, the error in determining the cone angle by comparison with the exact theory was 0.08%, and the error of the velocity on its surface was about 0.2%.

The cone-flow calculations give satisfactory results as long as conical flow is preserved between the cone and the compression shock. The smallest M_∞ at which conical flow is possible according to theory are given in Table VIII-1-2.

Hypersonic velocities. A comparatively simple approximate solution of the problem of a cone flow at very high M_∞ can be found from the expressions for the velocity components in the form of Taylor series.

At these velocities, the shock makes a rather close approach to the surface of the cone and the angle difference $\theta_s - \beta_c$ becomes so small that the following relationships can be written for the flow velocity components on the compression shock by use of Series (VIII-1-11) and (VIII-1-13): /377

$$\tilde{V}_{sr} = \tilde{V}_c\left[1 - (\theta_s - \beta_c)^2 + \frac{1}{3}(\theta_s - \beta_c)^3 \operatorname{ctg}\beta_c - \ldots\right]; \qquad \text{(VIII-1-20)}$$

$$\tilde{V}_{s\theta} = \tilde{V}_c\left[-2(\theta_s - \beta_c) + (\theta_s - \beta_c)^2 \operatorname{ctg}\beta_c - \ldots\right]. \qquad \text{(VIII-1-21)}$$

These relationships can be used to calculate the inclination angle of the compression shock. For this purpose, we write the flowrate equation (III-4-3) in the form

$$-\frac{\tilde{V}_{\infty\theta}}{\tilde{V}_{s\theta}} = \frac{k+1}{2} M_\infty^2 \sin^2\theta_s \left(1 + \frac{k-1}{2} M_\infty^2 \sin^2\theta_s\right)^{-1}. \qquad \text{(VIII-1-22)}$$

Since the oncoming-flow velocity component normal to the compression shock is $\tilde{V}_{\infty\theta} = \tilde{V}_\infty \sin\theta_s$, (VIII-1-22) is transformed with consideration of (VIII-1-8) to

$$-\frac{\tilde{V}_{sr}}{\tilde{V}_{s\theta}} = \frac{k+1}{4} M_\infty^2 \sin 2\theta_s \left(1 + \frac{k-1}{2} M_\infty^2 \sin^2\theta_s\right)^{-1}. \qquad \text{(VIII-1-22')}$$

If we are considering flow at very high velocities with the condition that the shock inclination angle θ_s and the difference $\theta_s - \beta_c$ are small, we can derive the following formula from

(VIII-1-20), (VIII-1-21), and (VIII-1-22') for the compression-shock inclination angle:

$$K_0 = \frac{k+1}{k+3} K_1 + \sqrt{\left(\frac{k+1}{k+3}\right)^2 K_1^2 + \frac{2}{k+3}}, \qquad \text{(VIII-1-23)}$$

where

$$K_0 = M_\infty \theta_s; \; K_1 = M_\infty \beta_c.$$

We see from (VIII-1-23) that K_0 will be the same for all cones with different relationships between the angle β_c and M_∞ provided that constancy of K_1 is observed.

Let us find expressions for determining the parameters on the cone and its wave drag. For this purpose, we use the relation $p_c/p_\infty = (p_c/p_s)(p_s/p_\infty)$ where p_s/p_∞ is found from (III-4-25) and the value of p_c/p_s with the aid of the adiabatic equation $p_c/p_s = (a_c/a_s)^{2k/(k-1)}$.

For the speeds of sound on the cone and the shock, we have the formulas

$$a_c^2 = \frac{k-1}{2}(V_{max}^2 - V_c^2); \quad a_s^2 = \frac{k-1}{2}[V_{max}^2 - (V_{s\theta}^2 + V_{sr}^2)],$$

on the basis of which

$$\frac{a_c^2}{a_s^2} = 1 + \frac{k-1}{2}\frac{V_{sr}^2}{a_s^2}\left(1 + \frac{V_{s\theta}^2}{V_{sr}^2} - \frac{V_c^2}{V_{sr}^2}\right), \qquad \text{(VIII-1-24)}$$

where V_{sr} and $V_{s\theta}$ are determined with (VIII-1-20) and (VIII-1-21).

Calculating the speed of sound a_s with (III-1-26), remembering that the M_∞ ahead of the shock are very large and certain simplifications can be adopted, and determining the pressure p_s from (III-4-25), we obtain a formula for the pressure on the cone:

$$\frac{p_c}{p_\infty} = \frac{2k}{k+1}(K_0^2 - 1) + (K_0 - K_1)^2 \frac{kK_0(k+1)}{2 + (k-1)K_0^2} + 1. \qquad \text{(VIII-1-25)}$$

With this formula, it is easy to calculate the pressure coefficient on the cone, $\bar{p}_c = (2/kM_\infty^2)(p_c/p_\infty - 1)$, which is equal to its wave drag coefficient.

The drag function is determined from the pressure coefficient: /378

$$\bar{p}_c M_\infty^2 = c_{xw} M_\infty^2 = \frac{4}{k+1}(K_0^2 - 1) + (K_0 - K_1)^2 \frac{2(k+1)K_0^2}{2 + (k-1)K_0^2}. \quad \text{(VIII-1-26)}$$

Actually, this formula determines the drag function only as it depends on the single parameter K_1, because K_0 depends in turn on this parameter, as we see from (VIII-1-23).

Thus, flows around cones at very high M_∞ are found to be similar in the sense that if the similarity parameters K_1 are the same, the drag functions will also be the same.

Formula (VIII-1-26) is inconvenient to use, since it is necessary to determine the intermediate parameter K_0. In practice, the approximating relation

$$\bar{p}_c M_\infty^2 = c_{xw} M_\infty^2 = \frac{2(k+1)(k+7)}{(k+3)^2} K_1^2 \left(1 + \frac{1}{3k} K_1^{-3/2}\right) \quad \text{(VIII-1-27)}$$

is more convenient; for $k = 1.4$, it takes the form

$$\bar{p}_c M_\infty^2 = c_{xw} M_\infty^2 = 2.091 K_1^2 (1 + 0.143 K_1^{-3/2}). \quad \text{(VIII-1-27')}$$

It follows from the very derivation of (VIII-1-23) and (VIII-1-26) that they will be more exact the larger M_∞ and, consequently, the closer the compression shock is to the surface of the slender cone. Those values of $c_{x\,w} = \bar{p}_c$ that correspond to values of the parameter $K_1 >> 1$ agree better with the exact theory and with experiment.

Limiting case. In the limiting case when $M_\infty \to \infty$, Formula (VIII-1-23) for the compression shock inclination assumes the form

$$\theta_s = \frac{2(k+1)}{k+3}\beta_c. \quad \text{(VIII-1-28)}$$

The corresponding value for the pressure coefficient is obtained from (VIII-1-26) in the form

$$\bar{p}_c = \frac{4}{k+1}\theta_s^2 + (\theta_s^2 - \beta_c^2)\frac{2(k+1)}{k-1}, \quad \text{(VIII-1-29)}$$

or, applying (VIII-1-28),

$$\bar{p}_c = \frac{2(k+1)(k+7)}{(k+3)^2}\beta_c^2. \qquad \text{(VIII-1-30)}$$

By comparing this expression with (VI-7-3), in which $\cos^2\eta$ is replaced by the squared cone angle β_c^2 in the case of a slender cone, we see that the difference between them is in the values of the coefficient of β_c^2. Obviously, Formula (VIII-1-30), which takes account of the peculiarities of flow around the cone, is more exact than (IV-7-3). Formula (VIII-1-30) agrees with (IV-7-3) if we set K = 1.

Formula (VIII-1-30) can be extended to cones of arbitrary thickness, for which the pressure coefficient

$$\bar{p}_c = \frac{2(k+1)(k+7)}{(k+3)^2}\sin^2\beta_c. \qquad \text{(VIII-1-30')}$$

This formula is known as the improved Newton formula for the cone.

Evaluation of disturbances in flow around a slender cone. The relationships derived above can be used to evaluate the disturbances that arise in the flow around a cone at very high velocities. First we determine the velocity on the cone from (VIII-1-20). Setting $V_{s\theta} = V_\infty(1 - 0.5\beta_c^2)$, we find

$$V_c = V_\infty\left[1 + (\theta_s - \beta_c)^2 - \frac{\beta_c^2}{2}\right]. \qquad \text{(VIII-1-31)}$$

This expression implies that the vertical velocity component $V_r = V_c \sin\beta_c \sim V_c\beta_c$, and the horizontal component $V_x = V_c \cos\beta_c \sim V_c$. /379

Thus, the axial disturbance-velocity component, which is equal to $V_\infty[(\theta_s - \beta_c)^2 - 0.5\beta_c^2]$, will be an order smaller than the vertical component. Consequently, the process in which the gas is compressed in flow around the cone is governed basically by the displacement of air particles across the flow, while the nature of the flow in the longitudinal direction is subject to very minor changes. Disregarding this velocity change, i.e., setting the longitudinal component equal to the oncoming-flow velocity, we assume that the particle-displacement process takes place only in the plane normal to the cone axis. This process

is one of the particular examples of application of the law of plane sections.

If we examine the extreme case to which shock angles θ_s = $= 1.093\beta_c$ correspond with $k = 1.4$, then the limiting values of the disturbance velocity on the cone will be $V_c = V_\infty(1 - 0.5\beta_c^2)$. Consequently, the longitudinal disturbance can be evaluated by $- 0.5V_\infty\beta_c^2$.

As we see, this quantity is determined by a square-law dependence on the small parameter β_c^2. Here the reciprocal of cone slenderness ratio, i.e., $1/\lambda_c$, which represents its thickness ratio, can be taken as the small parameter instead of the angle.

If we introduce the symbol τ for the small parameter of the general case, the longitudinal disturbance at an arbitrary point in the flow is evaluated on the basis of the disturbance estimate obtained for the conditions on the cone by the quantity $V_\infty\tau^2$, and the transverse disturbance by $V_\infty\tau$.

Expression (VIII-1-27) can be used to evaluate the pressure disturbances; we find from it that the pressure coefficient on the cone is of the order of $\overline{p}_c \sim \beta_c^2$, and, consequently, the absolute pressure is estimated at $p_c \sim p_\infty M_\infty^2\beta_c^2$. On the basis of this estimate, the pressure at any point in the flow around the cone can be evaluated by $p \sim p_\infty M_\infty^2\tau^2$, which, as we see, will be considerably higher than the free-stream pressure.

As for density, we can proceed from (III-4-24) to evaluate the disturbances. Since we are concerned with very high velocities, when $M_\infty\theta_s = K_0 >> 1$, we can conclude that the density in the disturbed flow is approximately an order higher than in the undisturbed stream. Thus, the disturbances are also found to be larger in respect to density.

In spite of the large pressure and density disturbances, it has nevertheless been possible, as we noted, to simplify the problem of very-high-velocity flow around cones and to obtain quite simple working relationships. This has been made possible by the smallness of the velocity disturbances.

It should be noted here that the disturbance estimates examined above can be extended to the case of flow around any slender body with an arbitrary generatrix. Thus, solution of the problem of flow around such a slender body at high supersonic velocity can be simplified mathematically as in the case of a cone.

Influence of Dissociation and Ionization

Some of the system equations, namely, (VIII-1-1), (VIII-1-4)-(VIII-1-6) are used in their original form in calculating flow with consideration of changes in air composition. The difference consists in the use of more general relationships for determination of the speed of sound, enthalpy, entropy, and average molecular weight. The calculation begins with determination of the gas variables behind an oblique shock for a given angle θ_s and known values of p_∞, T_∞, V_∞. Then Eqs. (VIII-1-1) and (VIII-1-6) are used to calculate the first derivatives for the conditions at the shock, the velocity components V_r and V are calculated, /380 and the enthalpy difference $i - i_s$ on the next conical surface with angle $\theta_s - \Delta\theta$ is found. Assuming that the flow behind the

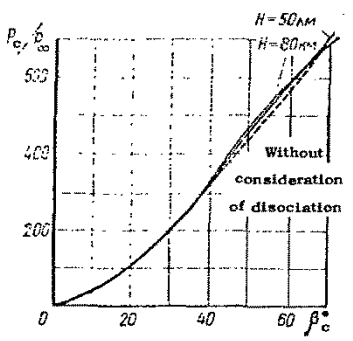

Figure VIII-1-4. Pressure on Cone with Dissociation Taken into Account. T_∞ = 222°K; M_∞ = 23.5.

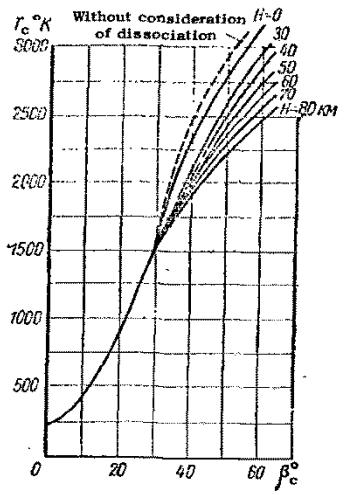

Figure VIII-1-5. Temperature on Cone with Dissociation Taken into Account. T_∞ = 222°K; M_∞ = 10.

shock is isentropic throughout the region and that its entropy S = S_s = const, we can use the entropy diagram or tables to determine the pressure on this surface from the known i and S. The speed of sound, average molecular weight, and density are determined from the values found for T and p. Then we shift to the next intermediate conical surface for analogous calculations, and so forth. The process is broken off when the normal velocity component is found to be zero on one of these surfaces. The variables obtained will pertain to the surfaces of the cone.

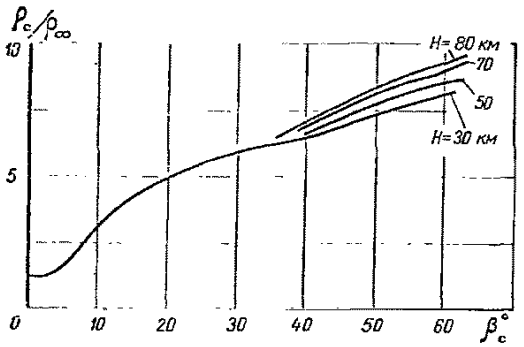

Figure VIII-1-6. Density on Cone with Dissociation Taken into Account. T_∞ = 222°K; M_∞ = = 10.

As we see, these parameters depend on the temperature and pressure of the oncoming flow, while in the absence of dissociation in the case of flow of a heated gas with variable heat capacity, they depended on T_∞ and not on p_∞. Certain results from calculation of the variables of flow over a cone at high speeds are presented in Figs. VIII-1-4 through VIII-1-6. These parameters vary in the same manner in the presence of dissociation and ionization as they do directly behind the shock. For example, the pressure change is found to be just as small. As for temperature and density, they vary quite substantially. This variation is greater the thicker the cone.

If the cone angles are small, these parameters on the cone are only slightly affected by physicochemical transformations even at rather high speeds. For example, calculations indicate that /381
at M_∞ = 24, density undergoes almost no change with altitude up to β_c = 15°, and up to β_c = 35° at M_∞ = 10 (Fig. VIII-1-6). Thus, the range of angles within which high temperatures have no manifest influence broadens with decreasing speed. The same effect is observed with decreasing altitude.

Thickening the cone causes more intensive heating and, consequently, dissociation and ionization, which may have a substantial influence on the flow variables. By way of illustration, Fig. VIII-1-7 shows this effect on the variation of shock inclination angle in front of a 40-degree cone. The shock inclination angle becomes smaller than at constant heat capacities (k = 1.4). Figure VIII-1-7 also shows the variation of θ_s as calculated for a hypothetical ideal gas with a specific-heats ratio k = 1.2. We see that at very high velocities, the hypothetical-gas scheme gives satisfactory results. It follows that the disturbed-flow variables for a cone at these velocities are determined basically by the physicochemical properties of the gas heated behind the shock wave, and primarily by the ratio of specific heats.

The above pertains to such variables as density, temperature, and shock angle. As for pressure, we have noted that it undergoes practically no change from the ideal-gas values. It depends almost entirely on the oncoming-flow conditions. Here the maximum excess pressure cannot exceed $\rho_\infty V_\infty^2$. On the other

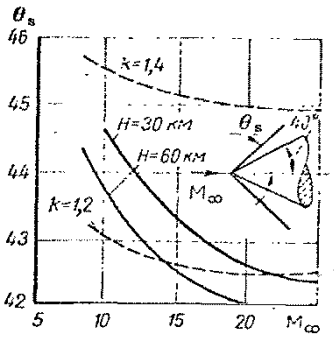

Figure VIII-1-7. Variation of Compression-Shock Inclination Angle Ahead of Cone. ——— real gas; ----- ideal gas.

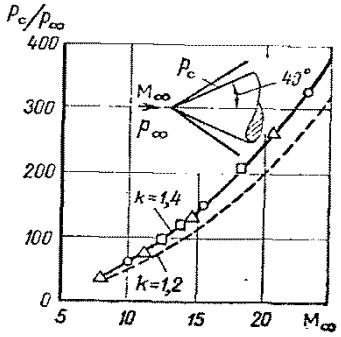

Figure VIII-1-8. Pressure on Cone in Dissociated Gas. o) H = 0 km; □) H = 30 km; Δ) H = 60 km; the solid and dashed lines represent ideal gases with constant heat capacities.

hand, calculations made with the fictitious specific-heats ratio k = 1.2 give lower pressure values, as we see from Fig. VIII-1-8.

Studies of flow of a real gas around a cone can be simplified if the speed of sound is assumed constant behind the shock. It was indicated above that at constant heat capacities, this assumption leads to insignificant deviations from the exact results.

Numerical integration of (VIII-1-6) with $a = a_s = \text{const}$ has shown that the accuracy of the calculation is higher in the presence of dissociation. For example, for standard conditions (T_∞ = = 288°K, p_∞ = 1kg/cm^2 = 9.807·10^4 N/m^2) in front of a shock with the angle $\theta_s = 14°$ and $M_\infty = 14$, the error in determining β_c is 0.06%, and the velocity error 0.002%.

Given constant sonic velocity, the problem consists basically in determining the velocities on intermediate conical surfaces. As for such variables as enthalpy, pressure, density, and temperature, they can be calculated independently even after the velocity field has been found.

At very high velocities, the flow calculation is simplified /382
by the fact that owing to the proximity of the shock to the cone and, consequently, the small thickness of the disturbed flow region, the derivative $dV_\theta/d\theta$ can be assumed constant in this region and equal to its value directly behind the shock, while the

derivative $dV_r/d\theta$ is equal to $0.5V_{s\theta}$, i.e., the mean between the values on the shock and cone.

The angle of flow over the cone and the velocity on it can be determined directly with these premises:

$$\beta_c = \theta_s - |\Delta\theta|; \quad V_c = V_{cr} = V_{sr} - 0{,}5V_{s\theta}|\Delta\theta|, \qquad \text{(VIII-1-32)}$$

where $|\Delta\theta| = V_{s\theta}(dV_\theta/d\theta)_s^{-1}$.

Solution with constant density. At very high flow velocities around a cone, the shock layer is found to be quite thin, with the result that pressure varies little in it and density can be assumed practically constant along a streamline. Thus, the value $\bar{\rho} = \rho_\infty/\rho_s = \rho_1/\rho_2$ directly behind the shock will determine density on the cone.

Solution of the equations of motion of a gas around a cone gives an approximate relation for the pressure coefficient [59]:

$$\bar{p}_c = 2\sin^2\beta_c\,[(1-0.25\bar{\rho})\cos^2(\theta_s-\beta_c)]^{-1}. \qquad \text{(VIII-1-33)}$$

Calculations indicate that this formula gives good results for $\bar{\rho}$ of approximately 0.1 and smaller.

To calculate the pressure coefficient by (VIII-1-33), it is necessary to know the shock angles θ_s, the density ratio $\bar{\rho}$ at the given oncoming-flow parameters, and the cone angle β_c. The calculations may proceed as follows. Assigning $\bar{\rho}$, determine the angle of the attached shock from the formula of hypersonic flow around a cone:

$$\operatorname{tg}\theta_s = \left(\frac{\bar{\rho}}{2}\right)^{-\frac{1}{2}} f(\eta), \qquad \text{(VIII-1-34)}$$

where

$$f(\eta) = 2\eta\left(1 + \sqrt{1-4\eta^2}\right)^{-1}; \quad \eta = \left(\frac{\bar{\rho}}{2}\right)^{1/2}\left(1-\frac{\bar{\rho}}{2}\right)^{-1}\operatorname{tg}\beta_c. \qquad \text{(VIII-1-35)}$$

The values of η vary from 0 to 0.5, and the corresponding values of the function $f(\eta)$ from 0 to 1. From the angle difference $\theta_s - \beta_c$, we calculate $\cos^2(\theta_s - \beta_c)$. Here we can assume $\cos(\theta_s - \beta_c) \approx 1$ for small values of $\theta_s - \beta_c$.

The enthalpy i_2 and pressure p_2 are calculated from (III-4-14) and (III-4-12), respectively, and then the known i_2 and p_2 are used with the thermodynamic tables to find ρ_2 and the angle θ_s and the pressure coefficient are improved.

The calculations are simplified if an empirical relationship is used to determine the shock inclination angle ahead of the cone ([70], No. 12, 1964):

$$10^2 M_\infty \sin\theta_s = 39 - \lg p_\infty + 0.5\,(206 + \lg p_\infty)\, M_\infty \sin\beta_c, \qquad \text{(VIII-1-36)}$$

where p_∞ is the atmospheric pressure in kg/cm^2.

With $M_\infty \sin\theta_s > 6$ this formula is accurate to about 1%. Calculations by (VIII-1-34)-(VIII-1-36) do not require reference to thermodynamic function tables. The known M_∞, β_c, and ρ_∞ are used with (VIII-1-36) to determine θ_s, and then (VIII-1-34) and (VIII-1-35) are used in one or two approximations to find $\bar{\rho}$; then p_c is calculated by (VIII-1-33).

Example. Calculate the flow around a sharp cone with the angle $\beta_c = 45°$ with the condition that $M_\infty = 20$ and the free-stream parameters correspond to an altitude H = 5 km. Referring to the standard-atmosphere tables, we find for these parameters /383

$$p_\infty = p_1 = 0.56\ \frac{\text{kg}}{\text{cm}^2};\quad T_\infty = T_1 = 255.7°;\quad a_\infty = a_1 = 320.5\ \frac{\text{m}}{\text{s}};\quad \rho_\infty = \rho_1 = 0.0733\ \frac{\text{kg}\cdot\text{s}^2}{\text{m}^4}.$$

For convenience in subsequent calculations, we use (VIII-1-35) to reduce (VIII-1-34) to the form

$$\operatorname{tg}\theta_s = 2\operatorname{tg}\beta_c\left\{\left(1-\frac{\bar{\rho}}{2}\right)\left[1+\sqrt{1-\frac{2\bar{\rho}\,(\mu^2\beta_c}{\left(1-\frac{\bar{\rho}}{2}\right)^2}}\right]\right\}^{-1}. \qquad \text{(VIII-1-37)}$$

We determine the enthalpy and pressure behind the compression shock from the equalities

$$i_2 = i_1 + \frac{V_{n1}^2}{2}(1-\rho^2);\quad p_2 = p_1\left[1 + k_1\frac{V_{n1}^2}{a_1^2}(1-\bar{\rho})\right].$$

As our first approximation, we take $\bar{\rho} = 0.108$ and find for this value

$$\operatorname{tg}\theta_s = 1.1298\ (\theta_s = 48°29').$$

Consequently, considering that $V_{n1} = V_\infty \sin\theta_s$ and $i_1 = c_p T_1$, the enthalpy

$$i_2 = 1002 \cdot 255.7 + \frac{20^2 320.5^2 \sin^2 48°29'}{2}(1 - 0.108^2) = 1.387 \cdot 10^7\ \text{м}^2/\text{с}^2$$

and the pressure

$$p_2 = 5.5 \cdot 10^4 \left[1 + 1.4\,\frac{20^2 320.5^2 \sin^2 48°29'}{320.5^2}(1 - 0.108)\right] = 1.6475 \cdot 10^6\ \text{кг/м}^2.$$

From the i-p diagram [13], we determine $\rho_2 = 0.67\ \text{кг}\cdot\text{с}^2/\text{м}^4$, and then calculate the corresponding parameter $\bar{\rho} = 0.1095$.

The second approximation gives $\theta_s = 48°32'$.

With these values of $\bar{\rho}$ and θ_s, (VIII-1-33) gives the pressure coefficient on the cone:

$$\bar{p}_c = 2 \cdot 0.7072^2 \left[\left(1 - \frac{0.25 \cdot 0.1095}{}\right)\cos^2(48°32' - 45°)\right]^{-1} = 1.032.$$

With Formula (VIII-1-36), we find for the assigned flow conditions

$$\sin\theta_s = \frac{1}{10^2 \cdot 20}[39 - \lg 0.56 + 0.5\,(206 + \lg 0.56)\,20 \sin 45°] =$$
$$= 0.7456 \text{ and } \theta_s = 48°13'.$$

To find the density, we use (VIII-1-34), which is transformed to

$$\bar{\rho} = 2\left\{1 - \operatorname{tg}\theta_s\left[1 + \sqrt{1 - \frac{2\bar{\rho}\operatorname{tg}^2\beta_c}{\left(1 - \frac{\bar{\rho}}{2}\right)^2}}\right]\right\}. \qquad \text{(VIII-1-38)}$$

After a series of approximations, we find $\bar{\rho} = 0.1$. The pressure coefficient corresponding to this value is practically the same as the value obtained above.

Self-similar solutions. It is shown in [4] that the solution of the problem of flow around a circular cone in the presence of chemical reactions is self-similar with regard to the parameter $\xi = (r - B)/(W - B)$ (see Fig. VIII-1-3). At a given flight speed, the gasdynamic variables at a point with coordinate ξ depend on the cone angle β_c and the pressure, density, and temperature of the oncoming flow.

Table VIII-1-3 compares the results of calculation of flow around a cone with $\beta_c = 20°$ at $M_\infty = 15$ and 20, respectively, for cases in which chemical reactions are taken into account and the air does not undergo physicochemical changes ($k = 1.4$). These tables give the dimensionless variables V_x/a^*, V_r/a^*, $p/\rho_\infty a^{*2}$, ρ/ρ_∞, calculated for the free-stream conditions $M_\infty = 15$ for $a^* = 1962$ m/s, $\rho_\infty a^{*2} = 0.1567$ atm ($0.1537 \cdot 10^5$ N/m^2) and at $M_\infty = 20$ for $a^* = 2604$ m/s, $\rho_\infty a^{*2} = 0.2759$ atm ($0.2706 \cdot 10^5$ N/m^2). The values $T_\infty = 250°$, $p_\infty = 0.292 \cdot 10^{-2}$ atm ($0.2864 \cdot 10^3$ N/m^2), $\rho_\infty = 0.412 \cdot 10^{-2}$ kg/m^3 correspond approximately to atmospheric conditions at the 40-km altitude. /384

Solution by means of series [18]. We present the solutions for the component V_r and V_θ [see Fig. (VIII-1-1)] in the form of the series

$$V_r = A_0 + A_1 H + \frac{1}{2} A_2 H^2 + \frac{1}{6} A_3 H^3 + \ldots; \qquad \text{(VIII-1-39)}$$

$$-V_\theta = A_1 + A_2 H + \frac{1}{2} A_3 H^2 + \ldots, \qquad \text{(VIII-1-40)}$$

where $H = \theta_s - \theta$.

To determine the coefficient A_i, we shall use equation system (VIII-1-1)-(VIII-1-5) and boundary conditions. On the shock surface

$$\left.\begin{aligned} V_r = V_{sr}; \quad \frac{dV_r}{d\theta} = V_{s\theta}; \\ \frac{d^2V_r}{d\theta^2} = -V_{sr} - (V_{s\theta} \operatorname{ctg} \theta_s + V_{sr}) \left(1 - \frac{V_{s\theta}^2}{a_s^2}\right)^{-1}; \end{aligned}\right\} \qquad \text{(VIII-1-41)}$$

on the surface of the body in the flow

$$V_{c\theta} = \left(\frac{dV_r}{d\theta}\right)_c = 0; \quad \left(\frac{d^2V_r}{d\theta^2}\right)_c = -2V_{cr}. \qquad \text{(VIII-1-42)}$$

TABLE VIII-1-3. GASDYNAMIC PARAMETERS ON CIRCULAR CONE WITH SEMIVERTEX ANGLE $\beta_c = 20°$, CALCULATED WITH CONSIDERATION OF CHEMICAL REACTIONS AND FOR k = 1.4 = const

$\bar{\xi}$	M_∞ / Parameter	$M_\infty = 15$ with consideration of chemical reactions	$M_\infty = 15$ $k = 1.4$	$M_\infty = 20$ with consideration of chemical reaction	$M_\infty = 20$ $k = 1.4$
0	V_x	2.113	2.109	2.127	2.121
	V_r	0.769	0.768	0.774	0.772
	p	0.738	0.742	0.732	0.739
	ρ	6.022	5.410	7.031	5.727
0.2	V_x	2.118	2.116	2.132	2.127
	V_r	0.754	0.751	0.762	0.756
	p	0.737	0.741	0.730	0.737
	ρ	6.012	5.401	7.021	5.718
0.4	V_x	2.124	2.122	2.136	2.133
	V_r	0.740	0.735	0.749	0.741
	p	0.732	0.736	0.727	0.733
	ρ	5.985	5.375	6.992	5.692
0.6	V_x	2.129	2.128	2.141	2.139
	V_r	0.726	0.719	0.737	0.726
	p	0.725	0.727	0.721	0.725
	ρ	5.940	5.332	6.945	5.649
0.8	V_x	2.135	2.134	2.146	2.145
	V_r	0.711	0.702	0.725	0.711
	p	0.715	0.716	0.712	0.714
	ρ	5.877	5.274	6.879	5.591
1.0	V_x	2.140	2.141	2.150	2.151
	V_r	0.697	0.687	0.713	0.696
	p	0.703	0.702	0.702	0.701
	ρ	5.797	5.199	6.794	5.516
	$\theta_s = \partial W/\partial x$	0.405	0.410	0.398	0.407

In accordance with the boundary conditions /385

$$\left.\begin{aligned} A_0 &= V_{sr} = V_\infty \cos\theta_s; \\ A_1 &= -V_{s0}; \\ A_2 &= -V_{sr} - (V_{s0}\operatorname{ctg}\theta_s + V_{sr})\left(1 - \frac{V_s^2\theta}{a_s^2}\right)^{-1}; \end{aligned}\right\} \qquad \text{(VIII-1-43)}$$

$$A_3 = -\frac{2}{H_c^2}(A_1 + A_2 H_c), \qquad \text{(VIII-1-44)}$$

where $H_c = \theta_s - \beta_c$.

H_c is found by solving the equation

$$H_c = 2A_1\left(1 - \frac{2}{3}H_c^2\right)\left[2A_0 - A_2\left(1 - \frac{H_c^2}{3}\right)\right]^{-1}. \qquad \text{(VIII-1-45)}$$

The coefficient A_n is determined from the given shock angle θ_s and the values of $V_{s\theta}$ and a_s calculated for this shock with consideration of dissociation. The A_n are used to determine the flow field around the cone with the angle $\beta_c = \theta_s - H_c$ corresponding to the given θ_s.

Influence of Nonequilibrium

We have examined two cases of inviscid flow around a cone. In one of them, the heat capacities were constant, and in the other equilibrium dissociation and ionization occurred in the zone between the wave and the body. These two cases may be regarded as extremes and on the boundaries of the range within which nonequilibrium gas flows obtain in the disturbed region.

The first case is characterized by the chemical and physical properties of the gas remaining the same in the disturbed region as directly behind the shock wave, with the passage across the wave effected at constant heat capacities. Thus, the gas is regarded as "frozen" throughout the disturbed region. This extreme state is characterized by the absence of energy-level excitation. It may be assumed as a further approximation that the vibrational degrees of freedom arrive at equilibrium directly behind the wave front and then remain "frozen." If we consider a gas consisting entirely of diatomic molecules, the exponent for the "frozen" state $k = 9/7$.

The other case has the peculiarity that the dissociating gas is at equilibrium throughout the disturbed region, including the zone directly behind the shock front. Research has shown that there are differences in the flow-variable values in the two extreme cases. In "frozen" flow, for example, the shock angle and the temperature at the surface are greater than the corresponding values in an equilibrium dissociating flow, while the density and pressure on the other hand, are smaller. Here the "frozen" flow can be examined with unexcited or excited vibrational levels.

If the temperatures are not high enough for dissociation to develop, the limiting cases will be characterized on the one hand by "frozen" flow with constant heat capacities and, on the other, by flow with vibrational levels excited throughout the entire region. Thus, the second limiting case will be characterized, depending on temperature, by equilibrium excitation of vibrations or by equilibrium dissociation.

If the first extreme case is regarded as "frozen" flow at very high temperatures, this premise is found to be better justified when the vibration relaxation time is smaller than that of dissociation relaxation. The two limiting cases are regarded as conical flows. The intermediate nonequilibrium flow is not /386

conical. Understandably, investigation of the flow variables is a more complex problem.

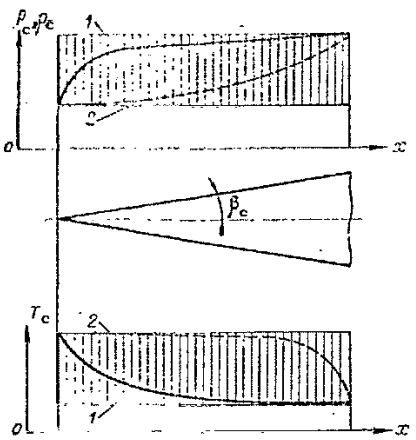

Figure VIII-1-9. Nonequilibrium Parameters on Cone.

It can be assumed for tentative evaluation that they change from the values at the nose for "frozen" flow to the equilibrium values at the end of the relaxation length, i.e., where the equilibrium degree of dissociation (or vibrational equilibrium) is attained. Figure VIII-1-9 shows a diagram of this effect. The unbroken curves correspond to a case that approaches the equilibrium case 1 over almost the entire region, while the dashed curves correspond to the "frozen" case 2. Here the first case is more probable at low altitudes and the second at high altitudes.

If follows from this qualitative evaluation that nonequilibrium flows affect aerodynamic characteristics. For example, drag is found to be greater than in the "frozen" case and smaller than in the equilibrium case. However, the difference is small. If, however, we consider the influence of nonequilibrium on lift, it may be found to be more substantial.

§VIII-2. CONE AT ANGLE OF ATTACK

Certain Results from Calculation of Supersonic Conical Flows

Let us examine the results obtained by a scientific team headed by Prof. K.I. Babenko [4] in a calculation of supersonic conical flows by the method of finite differences. The solution of the problem of flow around an infinite cone at an angle of attack is self-similar. The corresponding gasdynamic variables depend only on two variables, which represent certain combinations of the initial variables. The angle γ and the variable $\xi = (r - B)/(w - B)$ may be taken as these variables.

Tables VIII-2-1 and VIII-2-2 present the results of a calculation of supersonic flow of an ideal gas with a constant ratio of specific heats $k = 1.4$ around a cone (see Appendix No. 1). The flow fields shown in Table VIII-2-1 were calculated in the cylindrical coordinate system x, r, ϑ ($\vartheta = \pi/2 - \gamma$), with the $\vartheta = 0$ ($\gamma = \pi$) half-plane on the windward side (see Fig. VIII-1-3).

M_∞, the cone angles β_c and the attack angles α were taken as the parameters, while the independent variables were ϑ and $\xi = (r - B)/(W - B)$. The values of the velocity components V_x, V_r, V_ϑ were referred to the critical speed of sound a^*, the density to ρ_∞, and the pressure to $\rho_\infty a^{*2}$. For each value of ϑ, Table VIII-2-1 gives the value of $\bar{W}_x = \partial W/\partial x$, which is equal to the tangent of the angle between the x-axis and the shock-wave generatrix in the corresponding meridional plane. /387

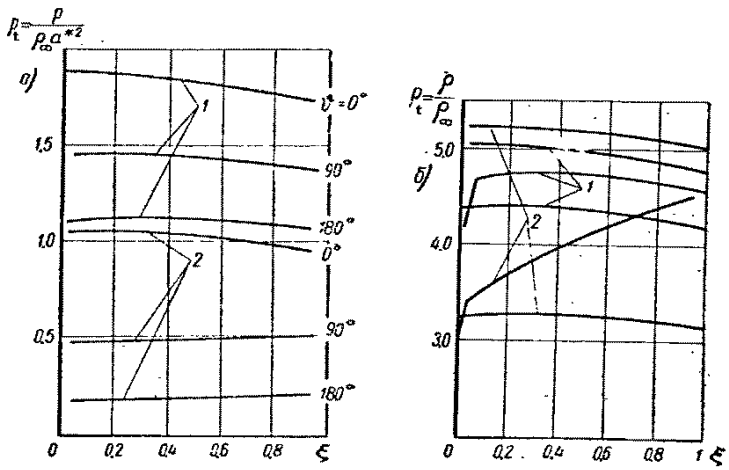

Figure VIII-2-1. Pressure and Density Around a Cone as a Function of the ξ-Coordinate.
a) 1) $M_\infty = 5$; $\beta_c = 30°$; $\alpha = 5°$; 2) $M_\infty = 5$; $\beta_c = 15°$, $\alpha = 10°$; b)1) $M_\infty = 7$, $\beta_c = 30°$, $\alpha = 5°$; ($\vartheta = 0.90°$; 180°); 2) $M_\infty = 7$, $\beta_c = 30°$, $\alpha = 15°$ ($\vartheta = 0.90°$; 180°).

Values of the aerodynamic coefficients in the body coordinate system, calculated by the formulas

$$c_{Rp} = \frac{1}{\pi}\int_0^\pi \bar{p}\,d\vartheta; \quad c_{Np} = \frac{\operatorname{ctg}\beta_c}{\pi}\int_0^\pi \bar{p}\cos\vartheta\,d\vartheta, \qquad \text{(VIII-2-1)}$$

are given in Table VIII-2-2. The same table lists values of the moment coefficient m_{zp}.

The wave-drag $c_{x\,w}$ and lift $c_{y\,p}$ coefficients are determined in the wind system by the conversion formulas

$$c_{x\,w} = c_{Rp}\cos\alpha + c_{Np}\sin\alpha;$$
$$c_{yp} = c_{Np}\cos\alpha - c_{Rp}\sin\alpha.$$

The formulas $V_x = V_{xt}a^*$ (the other components V_r and $V_\#$ are found similarly), $\rho = \rho_t\rho_\infty$; $p = p_t\rho_\infty a^{*2}$ should be used to calculate the flow variables from the tabular data (with subscript t).

The distance r from the cone axis for given x, ξ, ϑ is determined by the formula $r/x = \tan\beta_c + \xi(W_x - \tan\beta_c)$.

Analysis of Calculated Results for Flow Around Cones

The data given in Table VIII-2-1 permit certain general conclusions regarding nonaxisymmetric flow around circular cones and bring out certain characteristic features of conical flow.

Form of shock waves. The shock waves, whose traces in the transverse plane may differ markedly from circular, are classified into two types on the basis of shape. The first type is characterized by a smaller distance from the wave to the cone on the windward side ($\vartheta = 0$) than on the leeward ($\vartheta = 180°$) side. The second type, which is observed at large cone angles and M_∞, is characterized by a smaller distance on the leeward side. Thus, we can find specific values of β_c and M_∞ and the corresponding angles ϑ other than 0 and π at which the wave is farthest from the cone surface. Usually, the greatest distance to the shock corresponds to $\vartheta = 180°$.

Gas variables as functions of ξ-coordinate. At small angles of attack, this relation is nearly linear, derivating from linearity with increasing α.

The gas density, like the pressure, is usually higher near /388
the surface of the cone than at a distance from it (Fig. VIII-2-1). At large α, however, density increases in certain meridional planes right up to the shock wave.

The gas variables (except for pressure) may differ sharply on the cone surface ($\xi = 0$) from their values at the ξ of the next point ($\xi = 0.05$); this is explained by the difference between the entropy function p/p^k on the cone and at the nearby point.

Variation of gasdynamic functions with angle ϑ. This dependence is essentially nonlinear, with the gas parameters varying more sharply with decreasing ϑ the larger the attack angle. The velocity component V_ϑ has a distinct maximum, which is reached for small α at a value of ϑ near 90°. With increasing M_∞ and

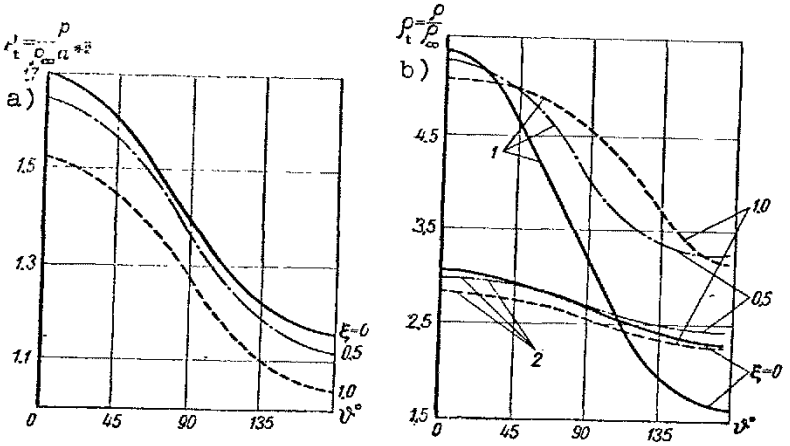

Figure VIII-2-2. Pressure and Density Around Cone as Functions of Angle ϑ. a) $M_\infty = 3$, $\beta_c = 30°$, $\alpha = 5°$; b) 1) $M_\infty = 7$, $\beta_c = 30°$, $\alpha = 15°$; 2) $M_\infty = 3$, $\beta_c = 30°$, $\alpha = 5°$.

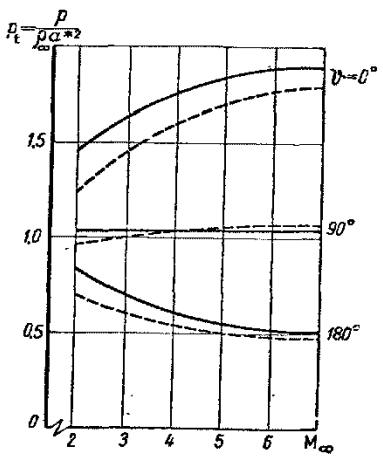

Figure VIII-2-3. Pressure as a Function of M_∞ at $\beta_c = 25°$, $\alpha = 10°$. Solid Line Represents Surface of Cone, Dashed Line Surface of Shock Wave.

decreasing difference $\beta_c - \alpha$, the maximum is shifted toward larger angles ϑ. Figure VIII-2-2 is a graphical representation of pressure and density as functions of the angle ϑ.

Variation of gas variables as functions of M_∞. All gasdynamic functions vary monotonically with Mach number and their derivatives decrease in absolute value.

Regardless of the angle ϑ, the circumferential velocity component decreases on the cone, but increases with increasing M_∞ directly behind the shock.

The nature of the pressure variation changes substantially with changing angle ϑ and depends weakly on ξ (Fig. VIII-2-3).

Influence of cone angle β_c and attack angle α. The gasdynamic functions depend essentially nonlinearly on β_c. Here the /389

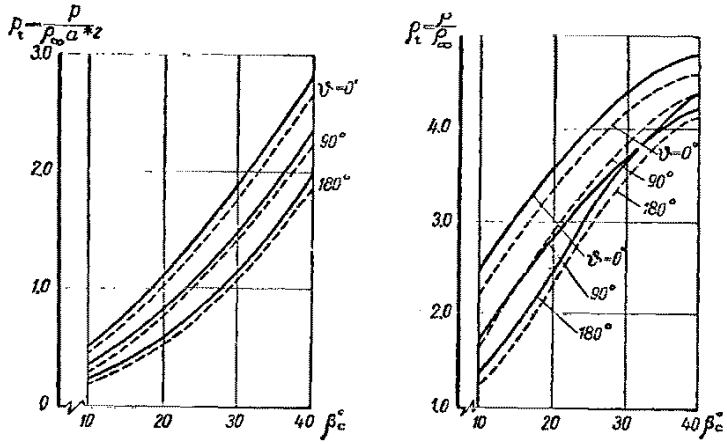

Figure VIII-2-4. Pressure and Density as Functions of Cone Angle: Solid Line Represents Cone Surface, Dashed Line Shock Surface ($M_\infty = 5$, $\alpha = 5$).

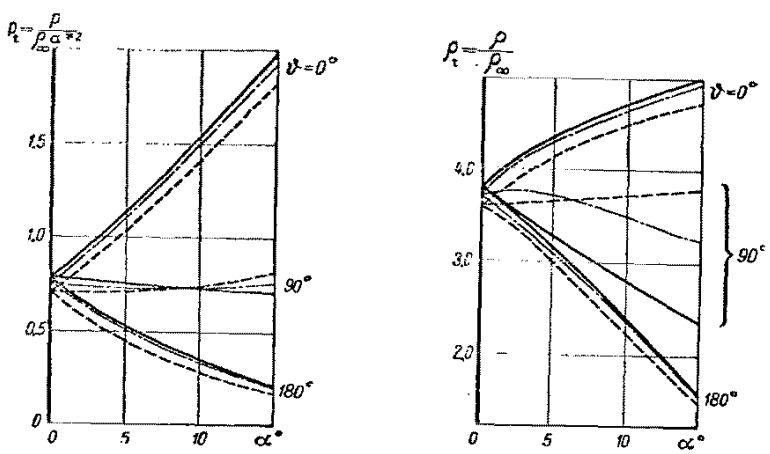

Figure VIII-2-5. Pressure and Density as Functions of Cone Attack Angle α at $M_\infty = 7$, $\beta_c = 20°$, ——— $\xi = 0$, -•-•- $\xi = 0.5$, ----- $\xi = 1$.

behavior of each gasdynamic function with respect to β_c (except for V_ϑ) depends weakly on ξ and ϑ. The V_ϑ decreases with increasing β_c on the cone, but increases behind the shock wave.

At small angles of attack ($\alpha < 5°$) we may assume in approximation that the gasdynamic functions depend linearly on α. The relationship becomes nonlinear at large α. The behavior of the gasdynamic functions with varying α is little affected by the coordinate ξ, but depends substantially on the ϑ-coordinate.

Figures VIII-2-4 and VIII-2-5 present curves characterizing pressure and density as functions of β_c and α, respectively.

Kopal's Tables /390

Certain data on supersonic flow around circular cones were obtained by Z. Kopal and published in the form of special tables ([62]-[64]). The tabular data were obtained using Stone's solution for the conical-flow equations. Later, A. Ferri pointed out an error allowed in Stone's solution and proposed a simple way to improve this solution.

Let us examine certain working relationships used to determine the aerodynamic coefficients of a circular cone with the aid of Kopal's tables.

The axial-force coefficient

$$c_{Xp} = -\frac{8}{\pi} K_D + \alpha^2 \left\{ \left(\frac{8}{\pi} K_D + \frac{2}{kM_\infty^2} \right) \left[K_{D2} - \frac{k\tilde{V}_c^0 x_c d}{2(\tilde{a}_c^0)^2 (k-1)} + \frac{1}{2} \right] - \frac{8}{\pi} K_N \right\}, \quad \text{(VIII-2-2)}$$

and the normal-force coefficient /391

$$c_{Xp} = -\frac{8\alpha K_N}{\pi}. \quad \text{(VIII-2-3)}$$

The coefficients K_D, K_{D2}, x_c, $\underline{d}$, K_N are listed in Table VIII-2-3. The functions $\tilde{V}_c^0$, V_c^0/V_{max}, $(a_c^0)^2$, $(a_c^0)^2 V_{max}^2$ are calculated accordingly from the flow velocity V_c^0 and the speed of sound a_c^0 on the cone in flow at a zero attack angle. For symmetrical flow around the cone, $K_D = \pi p_c^0/8$.

The inclination angle of the shock generatrix is

$$\theta = \theta_s^0 - \alpha\varepsilon\cos\gamma + \alpha^2 \left[\mu_0 + \mu_2 \cos 2\gamma + \frac{\varepsilon}{2} \operatorname{ctg}\beta_c (1 - \cos 2\gamma) \right], \quad \text{(VIII-2-4)}$$

where μ_0, μ_2, and ε are found from Table VIII-2-3 and θ_s^0 is the generatrix angle of the compression shock ahead of the cone at $\alpha = 0$.

TABLE VIII-2-3. VALUES OF COEFFICIENTS NEEDED TO CALCULATE FLOW VARIABLES FOR SUPERSONIC FLOW AROUND A CONE AT AN ANGLE OF ATTACK (k = 1.4)*

$\bar{r}_c^0$	θ_s^0	M_∞	K_D	K_N	ε	K_{D2}	μ_0	μ_2	d	x_c
				$\beta_c = 10°$						
0.40	68.653	1.0901	0.07243	0.7151	0.0884	0.28	0.25	0.03	0	—0.1406
0.45	55.162	1.2330	0.05784	0.7195	0.0753	0.53	0.14	0.06	0	—0.1523
0.50	46.309	1.4028	0.05113	0.7188	0.0886	0.91	0.15	0.10	0	—0.1635
0.55	39.708	1.5956	0.04666	0.7171	0.1140	1.43	0.23	0.16	0.0001	—0.1737
0.60	34.452	1.8165	0.04318	0.7152	0.1508	2.11	0.33	0.24	0.0002	—0.1825
0.65	30.091	2.0750	0.04028	0.7138	0.2001	3.04	0.43	0.34	0.0008	—0.1898
0.70	26.363	2.3869	0.03772	0.7132	0.2630	4.30	0.53	0.44	0.0027	—0.1951
0.75	23.101	2.7794	0.03539	0.7139	0.3408	6.10	0.61	0.55	0.0089	—0.1983
0.80	20.181	3.3041	0.03319	0.7168	0.4354	8.68	0.66	0.66	0.0295	—0.1990
0.85	17.518	4.0748	0.03101	0.7224	0.5495	12.34	0.71	0.77	0.1011	—0.1971
0.95	12.566	9.0999		0.7518	0.8791					
0.97	11.568	15.146		0.7650	0.9815					
				$\beta_c = 15°$						
0.40	61.679	1.1916	0.12292	0.6682	0.2337	0.37	0.48	0.09	0.0004	—0.2101
0.45	51.757	1.3382	0.10428	0.6731	0.2408	0.64	0.39	0.15	0.0007	—0.2217
0.50	44.559	1.5144	0.09362	0.6752	0.2772	1.04	0.41	0.21	0.0016	—0.2327
0.55	39.013	1.7178	0.08614	0.6769	0.3287	1.57	0.45	0.28	0.0038	—0.2423
0.60	34.620	1.9541	0.08034	0.6793	0.3899	2.26	0.48	0.34	0.0091	—0.2503
0.65	30.959	2.2345	0.07557	0.6827	0.4585	3.13	0.50	0.40	0.0214	—0.2566
0.70	27.854	2.5787	0.07148	0.6874	0.5331	4.16	0.48	0.45	0.0492	—0.2614
0.75	25.163	3.0217	0.06785	0.6933	0.6130	5.33	0.42	0.51	0.1113	—0.2651
0.80	22.784	3.6345	0.06455	0.7009	0.6992	6.31	0.32	0.57	0.2521	—0.2684
0.85	20.639	4.5010		0.7107	0.7939					
0.95	16.805	16.855		0.7416	1.0309					
				$\beta_c = 20°$						
0.35	68.507	1.2175	0.21723	0.6152	0.4748	1.34	2.66	0.04	0.0042	—0.2761
0.40	58.043	1.3144	0.17594	0.6238	0.4251	0.75	0.72	0.11	0.0046	—0.2786
0.45	50.281	1.4672	0.15498	0.6297	0.4444	0.69	0.55	0.17	0.0079	—0.2873
0.50	44.424	1.6531	0.14162	0.6348	0.4680	1.05	0.50	0.22	0.0152	—0.2967
0.55	39.835	1.8714	0.13199	0.6401	0.5422	1.50	0.47	0.27	0.0301	—0.3057
0.60	36.124	2.1297	0.12650	0.6459	0.6017	2.01	0.43	0.31	0.0587	—0.3141
0.65	33.045	2.4431	0.11841	0.6524	0.6642	2.50	0.37	0.35	0.1120	—0.3222
0.70	30.435	2.8387	0.11325	0.6596	0.7288	2.82	0.29	0.40	0.2099	—0.3305
0.75	28.180	3.3694		0.6675	0.7952					
0.85	24.433	5.5457		0.6862	0.9375					
0.90	22.834	9.5928		0.6978	1.0161					

Special interest attaches to shock-surface generatrices that lie in the vertical plane of symmetry ($\gamma = 0$ and π). The inclination angles of these generatrices

$$\theta^{\gamma=0} = \theta_s + \alpha\varepsilon + \alpha^2(\mu_0 + \mu_2); \quad \theta^{\gamma=\pi} = \theta_s^0 - \alpha\varepsilon + \alpha^2(\mu_0 - \mu_2 + \varepsilon \operatorname{ctg}\beta_c), \text{(VIII-2-5)}$$

where α is the attack angle in radians and in absolute value.

The first relationship in (VIII-2-5) pertains to a generatrix lying on the downwind ($\gamma = 0$) side and the second to a generatrix

on the windward side ($\gamma = \pi$).

Approximate Calculation of Flow at High Velocities

The "tangent-surface" method can be used for this calculation of pressure on a circular cone in the presence of an attack angle. The local tangent cone constructed about the generatrix on which the pressure is sought is taken as the tangent surface. The local-cone angle is

$$\beta_c' = \beta_c - \alpha \cos\gamma + \frac{\alpha^2}{2} \operatorname{ctg}\beta_c \sin^2\gamma. \qquad \text{(VIII-2-6)}$$

The value of this angle is used with the appropriate formulas, tables and diagrams to find the pressure and other parameters of symmetrical flow around the cone, which are assumed to be equal to their values on the generatrix of the actual conical surface. The pressure coefficient is determined in this manner, for example, as a function of the angle γ for given M_∞, α, and β_c.

For the limiting case $M_\infty \to \infty$ the pressure coefficient can be calculated by combining the "tangent-cone" and Newton methods. Formula (VIII-1-30) is used here with the angle β_c' instead of β_c.

Chapter IX /392

APPLICATION OF DIFFERENCE METHODS TO CALCULATE FLOW AROUND BODIES WITH CURVED GENERATRICES

§IX-1. CALCULATION OF AXISYMMETRIC SUPERSONIC FLOW AROUND A SHARP SOLID OF REVOLUTION BY THE METHOD OF CHARACTERISTICS [17]

Potential flow. Potential flow around a sharp solid of revolution at zero angle of attack (Fig. IX-1-1)is calculated by the system of difference equations for the characteristics (IV-1-25)-(IV-1-28) with the condition that $\varepsilon = 1$.

The calculation usually starts with determination of the conical flow around the sharp tip, which can be replaced by a cone in a small neighborhood of the nose (the cone boundary is point K in Fig. IX-1-1). As a result, the velocities and the angles ω, μ, and β are determined on the generatrices OD and OA and other intermediate conical surfaces (including the cone generatrix OK and the shock generatrix OS). Here the angles θ of the intermediate cones are selected arbitrarily, but such that the interval $\Delta\theta$ will be small enough to ensure the required accuracy.

As the calculations are performed, it is helpful to construct the net of characteristics shown in Fig. IX-1-1. First, element KD of the first-family characteristic is plotted, using as data the angles μ_K and β_K, which are known at point K. The terminal D of the element is the point at which it intersects the next generatrix OD. Its coordinates x_D and r_D are found by simultaneous solution of the equations

$$r_K - r_D = (x_K - x_D)\operatorname{tg}(\beta_K + \mu_K);\ r_D = x_D \operatorname{tg}\theta_D. \qquad \text{(IX-1-1)}$$

The coordinates of the remaining points on the first-family characteristic, which is the boundary of the conical flow, are found similarly; to obtain more accurate data, the coordinates can be calculated from the mean values of angles β and μ between the neighboring points K and D, D and A, and so forth.

In addition to the coordinates at each point on this characteristic, including the point S where it intersects the shock, the magnitudes and directions of the velocities and M and the angles ω, μ, and β will be known. The problem now reduces to finding the velocity field in the region between the characteristic

and the generatrix of the body.

The parameters are first calculated at point B, which lies at the intersection of the body's generatrix and element DB of the second-family characteristic. Then, using the velocity found for point B and the parameters at point A, which are known from the solution of the cone problem, the parameters are calculated for point C, which lies at the intersection of element AC of the second-family characteristic and element BC of the first-family characteristic. During the calculations, the angles β and ω are determined, and ω is used to find M and the angle μ; these calculations can be performed with the aid of Table IV-1-1. Similar calculations determine the parameters at all other points of the second row, including point N. The subsequent calculation involves finding the gas variables at the intersection point of the characteristic element drawn through point N with the shock. Here, the shock inclination at the intersection point must also be calculated. In practice, the characteristic is drawn not from /393
point M but from point F, which lies between points N and S, in order to obtain a better approximation. In this construction of the characteristic, that element next to the shock becomes quite small.

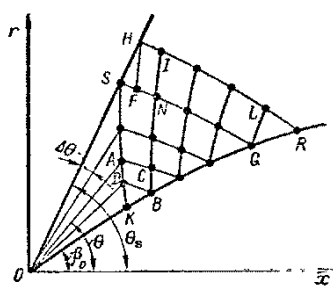

Figure IX-1-1. Diagram for Calculation of Flow Around Solid of Revolution by the Method of Characteristics.

The coordinates of point F and the other parameters corresponding to it (M, ω, μ, β) are calculated from the known values for points S and N by linear interpolation. Equations can then be written for element FH of the first-family characteristic of the physical plane, as well as for the element of the corresponding characteristic of the same family in the hodograph plane.

Solving the equation for the characteristic in the $\bar{x}$, $\bar{r}$-plane simultaneously with the equation of the rectilinear shock generatrix, we find the coordinate of point H in first approximation. To determine the velocity at this point, it is necessary to consider the conditions on the shock as well as the conditions on the characteristic, since point H is also on the shock surface. Characteristic FH, which extends to the shock, is by nature an expansion wave that arises on the surface of the body. On encountering the compression shock, this wave decreases in intensity and, consequently, in its inclination, the angle of which must be determined.

One of the unknown parameters at point H is the velocity vector inclination angle β_H, which is determined by the increment

$\Delta\beta_F$ in the angle β along element FH : $\beta_H = \Delta\beta_F + \beta_F$. Let us assume that the angle β changes by $\Delta\beta_F$ along shock element SH. An increment in M equal to $\Delta M_{\beta_F} = (dM/d\beta)_{\beta_F} \Delta\beta_F$ will correspond to this change.

If we assume that the flow deflection behind the shock at point S is the same as at F, i.e., that it is determined by the angle β_F, we can calculate the corresponcing M_S from this deflection and then find M at H in first approximation:

$$M_H = M_S + \left(\frac{dM}{d\beta}\right)_{\beta_F} \Delta\beta_F. \qquad \text{(IX-1-2)}$$

The derivative $(dM/d\beta)_{\beta_F}$ that appears in (IX-1-2) can be calculated by compression-shock theory, using the formula

$$\frac{dM}{d\beta} = \frac{dM}{d\beta_s} = -M\left[\operatorname{ctg}(\theta_s - \beta_s)\left(\frac{d\theta_s}{d\beta_s} - 1\right) + M^2 \sin^2(\theta_s - \beta_s)\frac{k+1}{4}\frac{d}{d\beta_s}\left(\frac{\rho_2}{\rho_1}\right)\right]. \qquad \text{(IX-1-3)}$$

The two derivatives in the right side of this expression are in turn determined by the formulas

$$\frac{d}{d\beta_s}\left(\frac{\rho_2}{\rho_1}\right) = 2\operatorname{ctg}\theta_s \frac{\rho_2}{\rho_1}\left(1 - \frac{k-1}{k+1}\frac{\rho_2}{\rho_1}\right)\frac{d\theta_s}{d\beta_s}; \qquad \text{(IX-1-4)}$$

$$\frac{d\theta_s}{d\beta_s} = -\frac{\rho_2}{\rho_1}\left[\frac{\cos^2(\theta_c - \beta_c)}{\cos^2\theta_s} - \frac{\rho_2}{\rho_1} - 2\cos^2(\theta_s - \beta_s)\left(1 - \frac{k-1}{k+1}\frac{\rho_2}{\rho_1}\right)\right]^{-1}. \qquad \text{(IX-1-5)}$$

Then the change in M on passage along the characteristic from point F to point H, i.e., $\Delta M_F = M_H - M_F$, is determined. For this purpose, Expression (IX-1-2) is substituted in the above for M_H, with the result

$$\Delta M_F = M_S + \left(\frac{dM}{d\beta}\right)_{\beta_F} \Delta\beta_F - M_F. \qquad \text{(IX-1-6)}$$

Passing from M to the angle ω, we obtain /394

$$\Delta\omega_F = \omega_S + \left(\frac{d\omega}{d\beta}\right)_{\beta_F} \Delta\beta_F - \omega_F, \qquad \text{(IX-1-7)}$$

where

$$\frac{d\omega}{d\beta} = g(M)\frac{dM}{d\beta}, \qquad \text{(IX-1-8)}$$

and the function g(M) is determined in turn by the expression

$$g(M) = \frac{d\omega}{dM} = \sqrt{M^2-1}\left[M\left(1+\frac{k-1}{2}M^2\right)\right]^{-1} \qquad \text{(IX-1-9)}$$

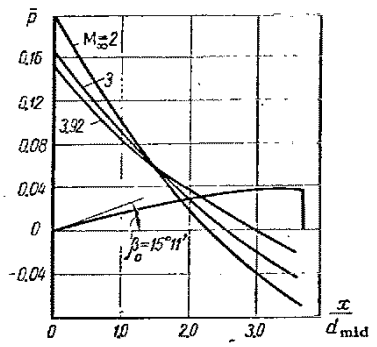

Figure IX-1-2. Distribution of Pressure Coefficient on Surface of Parabolic Nose Section, as Calculated by the Method of Characteristics.

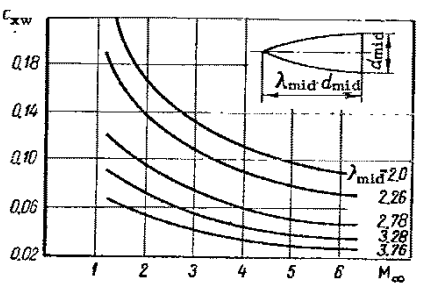

Figure IX-1-3. Wave Drag Coefficients of Parabolic Nose Section as Calculated by Method of Characteristics.

Referring Eq. (IV-1-26) for the first-family characteristic to element FH and solving it simultaneously with (IX-1-6), we find

$$\Delta\beta_F = \left(\omega_F - \omega_S + \frac{x_H - x_F}{r_F}l_F\right)\left[\left(\frac{d\omega}{d\beta}\right)_{\beta_F} - 1\right]^{-1}; \qquad \text{(IX-1-10)}$$

$$\Delta\omega_F = \Delta\beta_F + \frac{x_H - x_F}{r_F}l_F. \qquad \text{(IX-1-11)}$$

From $\Delta\omega_F$, we can calculate the angle ω_H at point H and then find M_H and the Mach angle μ_H. The angle $\beta_H = \Delta\beta_F + \beta_F$ is calculated for the same point and used to improve the shock inclination angle. It will be smaller than for the conical shock, and the decrease, as we have noted, will be due to the decline in shock intensity.

Terminating the calculation for point H, we proceed with calculations for the next row of points, and so forth. The

result is determination of a velocity (M) field for flow around a sharp solid of revolution with any generatrix assigned in the form of a smooth curve.

Other parameters, namely temperature, density, and pressure, can be found from the values of M at the intersections of the characteristics with the body's generatrix. For example, at point B

$$\frac{T_B}{T_0}=\left(1+\frac{k-1}{2}M_B^2\right)^{-1};\quad \frac{\rho_B}{\rho_0}=\left(\frac{T_B}{T_0}\right)^{\frac{1}{k-1}}\nu_0;\quad \frac{p_B}{p_0}=\left(\frac{T_B}{T_0}\right)^{\frac{k}{k-1}}\nu_0, \qquad \text{(IX-1-12)}$$

where T_0, ρ_0, and p_0 are the parameters of the isentropically frozen flow and are determined by the formulas

$$\frac{T_0}{T_\infty}=1+\frac{k-1}{2}M_\infty^2;\quad \frac{\rho_0}{\rho_\infty}=\left(\frac{T_0}{T_\infty}\right)^{\frac{1}{k-1}};\quad \frac{p_0}{p_\infty}=\left(\frac{T_0}{T_\infty}\right)^{\frac{k}{k-1}}. \qquad \text{(IX-1-13)}$$

The coefficient $\nu_0 = p_0'/p_0$, which is the ratio of the stagnation pressures after and before the shock, can be found by (III-4-33) as a function of M_∞ and the angle θ_s of the conical shock at the point. The absolute value found for the pressure is used to calculate the pressure coefficient $\bar{p}_B = (1/kM_\infty^2)[(p_B/p_0)(p_0/p_\infty) - 1]$. The pressure-coefficient distribution calculated by the method of characteristics for a parabolic solid of revolution with a slenderness ratio $\lambda_{mid} = 3.8$ for $M_\infty = 2$, 3, and 3.92 is shown in Fig. IX-1-2. Figure IX-1-3 presents data on the wave-drag coefficient obtained from the known pressure distribution around bodies of the same parabolic shape (after Frankl'). /395

Rotational flow. With increasing M_∞ of supersonic flow, the intensity of the curved shock in front of a solid of revolution increases to the extent that it becomes necessary to take account of the rotational nature of the flow. In this case, the equation system (IV-1-19)-(IV-1-22) should be used for the characteristics, since it enables us to solve differential equation (III-2-35) numerically for the stream function and thus to calculate the rotational flow in the zone between the shock and the solid of revolution.

In the example of flow around a solid of revolution with a conical element (see Fig. IX-1-1), rotational flow will be observed behind the shock beginning at a point S at the end of its conical segment. The lower boundary of the vortical region coincides with the second-family characteristic SG emanating from the same point. The flow on the segment bounded by this characteristic and the conical shock will be potential. Consequently, the

velocity field is calculated here by the method of characteristics for potential flow.

In the zone above curve SG, it is necessary to proceed from the theory of characteristics as it applies to vortical motion. As an example, let us calculate the velocity at point H (see Fig. IX-1-1), which lies on the curvilinear branch of the compression shock.

We must first find $(1/p_0')\Delta p_0'/\Delta n$, which takes account of the change in stagnation pressure on passage from point F to point H, assuming that this change will be the same as along the curved shock segment SH. Here the stagnation pressure p_{0S}' at point S will be determined with (III-4-33) from the values of M_∞ and the conical-shock angle.

Assuming further that the deviation of the flow behind the compression shock at point H is equal to the velocity vector inclination at point F, we find the shock inclination angle θ_{sH} and then compute the stagnation pressure p_{0H}'.

We now determine the distance along the normal to the characteristic between point F and H:

$$\Delta n = (FH)\sin\mu_F = \frac{x_H - x_F}{\cos(\beta_F + \mu_F)}\sin\mu_F \qquad \text{(IX-1-14)}$$

and the stagnation-pressure change on this segment:

$$\frac{1}{p_{0F}'}\frac{\Delta p_0'}{\Delta n} = \frac{1}{p_{0S}'}\frac{p_{0H}' - p_{0S}'}{\Delta n}. \qquad \text{(IX-1-15)}$$

Since point H lies on the compression shock, Condition (IX-1-6) on the shock must be considered along with the equation for the first-family characteristics in order to find the flow variables in the compression shock. Thus, to find the angle increment $\Delta\beta_F$, we arrive at an expression similar to (IX-1-10), differing from it in having a term governed by the vortex effect:

$$\Delta\beta_F = \left[\left(\frac{d\omega}{d\beta}\right)_{\beta_F} - 1\right]^{-1}\left(\omega_F - \omega_H + \frac{x_H - x_F}{r_F}l_F - \frac{x_H - x_F}{p_{0F}'k}\frac{\Delta p_0'}{\Delta n}c_F\right). \qquad \text{(IX-1-16)}$$

Then, using (IX-1-11), we can calculate the increment $\Delta\omega_F$, /396
the angle ω_H, and M_H. Having then determined the angle $\beta_H = \Delta\beta_F + \beta_F$, we find the shock inclination angle θ_{sH} at point H from the

values of this angle and M_H. We can then improve the stagnation-pressure ratio for this point.

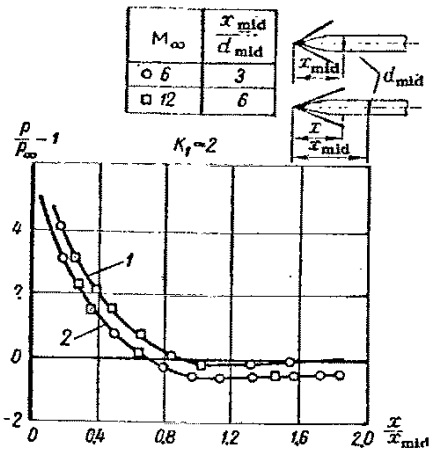

Figure IX-1-4. Pressure Distribution Around Solids of Revolution with Parabolic Nose Section ($\alpha = 0$). 1) with consideration of vortical motion behind shock; 2) for potential motion behind shock.

We then pass to calculation of the parameters at the next point I (see Fig. IX-1-1); this is done in the same way as for point C of the earlier example (see Fig. IV-1-5). The relationships given in this example will be valid if they are converted from the nomenclature for points A, B, and C to the corresponding nomenclature for points H, N, and I.

Thus, the coordinates of points H, I, ..., L of the second-family characteristic are determined step by step, along with the gasdynamic variables at these points. The velocity and other variables at point R on the contour of the body can be determined from the values found for point L. Here, the geometrical coordinates of the former point are calculated by simultaneous solution of the equations of the body's generatrix and the line drawn through point L at an angle $\beta_L - \mu_L$. Also among the known parameters is the velocity vector inclination angle at point R, where it is equal to the inclination angle of the tangent to the contour. Further, we know the stagnation pressure p'_{0R}, which will be the same as at points K, B, ..., G, which belong to the same streamline. We can therefore find the change in stagnation pressure along characteristic LR:

$$\left(\frac{1}{p'_0}\frac{\Delta p'_0}{\Delta n}\right)_L = \left(\frac{p'_0}{p_0}\right)_z^{-1}[(x_R - x_L)\sin\mu_L]^{-1}\left[\left(\frac{p'_0}{p_0}\right)_L - \left(\frac{p'_0}{p_0}\right)_R\right]\cos(\beta_L - \mu_L). \quad \text{(IX-1-17)}$$

We then apply the equation of the second-family characteristic to find

$$\Delta\omega_L = -\Delta\beta_L + \frac{x_R - x_L}{r_L}m_L - \frac{x_R - x_L}{kr_z}\left(\frac{1}{p'_0}\frac{\Delta p'_0}{\Delta n}\right)_L. \quad \text{(IX-1-18)}$$

Since the increment $\Delta\beta_L$ in this expression is assumed to be known and equal to $\Delta\beta_L = \beta_R - \beta_L$, we can calculate the difference $\Delta\omega_L$, the angle $\omega_R = \Delta\omega_L + \omega_L$ at point R, and M_R, as well as the pressure and other parameters with consideration of the rotational nature of the flow.

As we have noted, this effect is substantial at high velocities. Calculations have shown that, for example, for a parabolic nose with a slenderness ratio $\lambda_{mid} = 5$ at the value $K_1 = M_\infty/\lambda_{mid} = 1$ for which $M_\infty = 5$, the wave drag increased by only 5% over its value in potential flow as a result of the vortex effect. At the same time, it increased by more than 25% at $K_1 = 4$ ($M_\infty = 20$). The effect of increasing drag is explained from the physical standpoint by the fact that more of the flow's kinetic energy is expended irreversibly on formation of the vortices.

Figure IX-1-4 shows the pressure distributions found by the method of characteristics for two bodies with parabolic nose sections with the condition that the parameter $K_1 = M_\infty \tan\beta_0 = M_\infty/\lambda_{mid} = 2$. The rise in pressure over that of the potential flow can be seen in the diagram. This must be taken into account in practical cases beginning at about $K_1 = 1.2$-1.5. For smaller values of this parameter, the vortex effect can be disregarded. /397

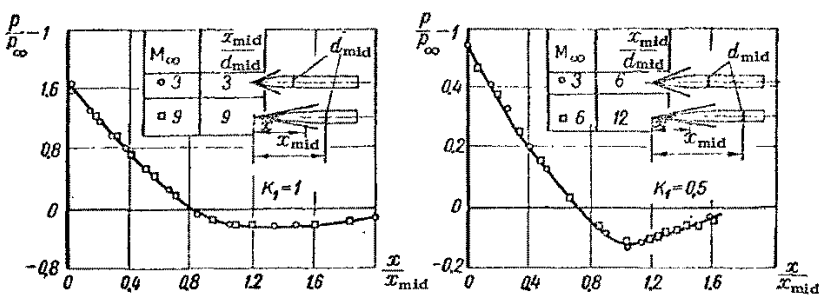

Figure IX-1-5. Pressure Distribution over Surfaces of Parabolic Solids of Revolution.

The diagram of Fig. IX-1-4 confirms the effect of the similarity law with respect to parameter K_1 not only for cones, but also for affinely similar solids of revolution with curvilinear generatrices, such as bodies of parabolic shape. We see that the flows around two different bodies with the same K_1 are characterized by the same pressure-function curve.

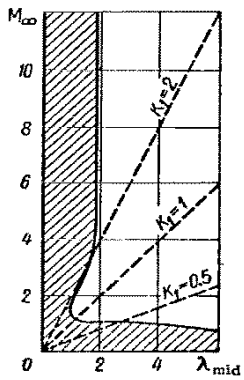

Figure IX-1-6. Range of Application of Similarity Law for Ogival Bodies (Similarity is Doubtful in the Shaded Region).

The range of application of the similarity law can be broadened by using experimental or theoretical data for various K_1. By way of illustration, Fig. IX-1-5 shows such data as obtained by the method of characteristics for slender cylindrical bodies with parabolic nose sections for $K_1 = 1$ and 0.5.

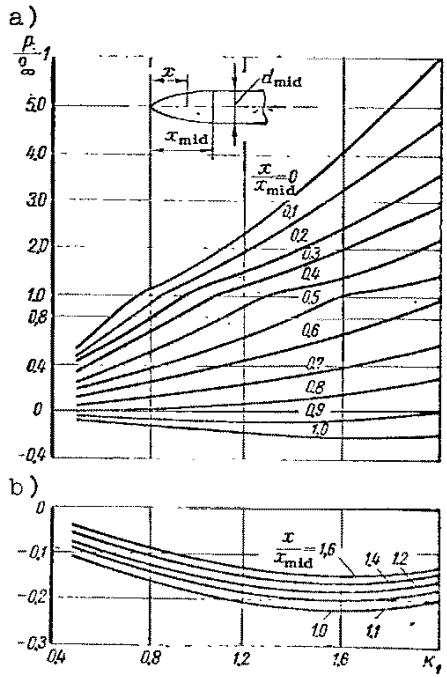

Figure XI-1-7. Diagrams for Determination of Pressure on Surfaces of Bodies with Ogival Nose Sections. a) for nose section; b) for cylindrical section.

/398

There is a limiting value of K_1 below which the similarity law for the curvilinear nose does not apply. This value is established from analysis of the possible use of the similarity law for a conical point (Fig. IX-1-6).

In accordance with the limits of applicability of the similarity law, which are established by the diagram in Fig. IX-1-6, calculations were carried out by the method of characteristics to determine the pressure distributions about slender cylindrical solids of revolution with parabolic (or ogival) nose sections. The results of these calculations are presented in generalized form in Fig. IX-1-7.

The wave drag coefficient can be obtained by integrating the pressure over the surface. As a result of reduction of data that were obtained by the method of characteristics and improved

experimentally, the following relationship was found for the wave drag coefficient of ogival nose sections with semivertex angles $10° \leq \beta \leq 45°$ at M_∞ in the range $1.5 \leq M_\infty \leq 3.5$:

$$c_{xw} = \bar{p}_c \left[1 - \frac{196\lambda_{mid}^2 - 16}{11 (M_\infty + 18) \lambda_{mid}^2} \right], \qquad \text{(IX-1-19)}$$

where $\bar{p}_c$ is the pressure coefficient at the cone vertex and λ_{mid} is the slenderness ratio of the solid of revolution as determined by (II-1-2) or from the expression $\lambda_{mid} = 1/[2 \tan (0.5\beta_0)]$.

Pressure on cylindrical section at very high flow velocities. The method of characteristics was used to calculate the flow past cylindrical surfaces of bodies with ogival and conical nose sections for velocities corresponding to $M_\infty = 20$. The results indicate that the conical head produces larger changes in the pressure on the cylinder.

Results obtained by the following empirical formula are in good agreement with pressures calculated by the method of characteristics:

$$\frac{p}{p_\infty} = 0.55 + 0.061 k^2 M_\infty^2 \sqrt{c_{xw}} \frac{r_{mid}}{x}, \qquad \text{(IX-1-20)}$$

where $c_{x\,w}$ is the drag coefficient of the nose section and x is distance measured from the point at which the nose section meets the cylinder.

The compression-shock generatrix is approximated satisfactorily by

$$\frac{r_s}{r_{mid}} = 1.31 k^{1/4} \left(\frac{x}{r_{mid}} \sqrt{c_{xw}} \right)^{0.46}. \qquad \text{(IX-1-21)}$$

Relationships (IX-1-20) and (IX-1-21) are valid for $0.4 < \lambda_{mid} < 4$ and $x > 4d_{mid}$.

The "local cone" method. The results of flow calculation by the method of characteristics are to a certain extent standard and are used as a criterion in evaluating data obtained by the various approximate methods. A comparison shows that the "local-cone" (or "tangential-cone") method (see §IV-7) gives results that come especially close to the method of characteristics in calculation of flows around sharp solids of revolution with unbroken generatrices.

The satisfactory agreement of the results indicates that the "local-cone" method makes it possible, in some degree, to take the vortex effect that occurs behind a curvilinear shock wave into consideration.

If the "equal-pressure" hypothesis is used in the "local-cone" method, the pressure at a given point of the generatrix is determined as the pressure on a cone with a semi-vertex angle equal to the inclination angle of the tangent. With the "equal-velocity" hypothesis, the pressure should be calculated by Formula (IV-7-17) and the pressure coefficient from (IV-7-18). /399

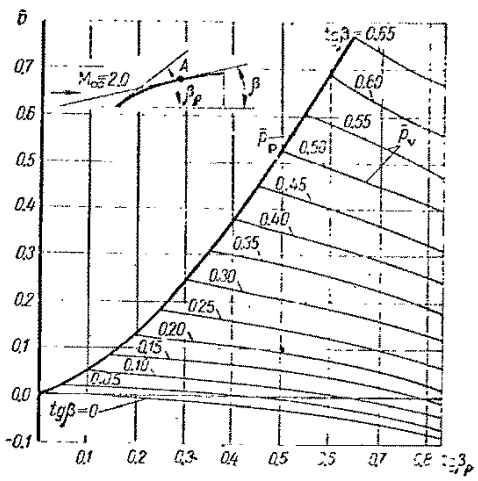

Figure IX-1-8. Diagram of Pressure Distribution about a Solid of Revolution as Constructed on the Basis of the "Equal-Pressures" and "Equal-Velocities" Hypotheses ($M_\infty = 2$).

Curves characterizing the variation of the coefficient $\bar{p}_v$ as a function of $\tan\beta_p$ and $\tan\beta$ are shown for the two values M_∞ = = 2 and 5 in Figs. IX-1-8 and IX-1-9. Knowing the distribution of the pressure $\bar{p}_v$, we can determine the corresponding wave drag coefficient $c_{x\ w.v}$. At the same time, its value can be calculated in approximation by using (IV-7-18) which relates the coefficients $\bar{p}_v$ and $\bar{p}_p$ with one another. The corresponding working relationship is obtained by application of (I-3-14) and (IV-7-18):

$$c'_{x\,w.v} = 2\int_0^1 \left[\bar{p}_p\bar{\nu} + \frac{2(\bar{\nu}-1)}{kM_\infty^2}\right]\bar{r}\,d\bar{r}, \quad \text{(IX-1-22)}$$

where $\bar{r} = r/r_{bse}$.

This formula determines the drag coefficient referred to the base-section area of the secant body with radius r_{bse}, which may differ from the radius of the midships section of the tangent nose section. Formula (IX-1-22) can be simplified if we consider cases of flow in which the function ν varies little along the solid of revolution. With this condition, it becomes possible to take $\bar{\nu}$ and $\bar{\nu} - 1$ out from under the integral sign as the corresponding average values, and Formula (IX-1-22) becomes

$$c'_{x\,w.v} = c'_{x\,w.p}\bar{\nu}_{av} + \frac{2(\bar{\nu}_{av}-1)}{kM_\infty^2}, \quad \text{(IX-1-23)}$$

where $c'_{x\ w.p}$ is the drag coefficient referred to the base-section area πr^2_{bse} and calculated on the equal-pressure hypothesis. This coefficient is determined by (I-3-14), in which we must set $\bar{p} = \bar{p}_p$.

Calculations by (IX-1-23) are made up to values of $\bar{\nu}$ in the interval $0.8 \leq \bar{\nu} \leq 1$. If this condition is not satisfied, it is necessary to use the general formula (IX-1-22). In this case, however, the calculation can also be simplified. Studies have shown that the distribution of the function $\bar{\nu}$ along a parabolic or ogival nose section can be approximated by the equation

$$\bar{\nu} = \nu_0 + (1 - \nu_0)(1 - \bar{x}^2), \qquad \text{(IX-1-24)}$$

where $\bar{x} = x/x_{mid}$.

It has also been established that the pressure coefficient $\bar{p}_p$ can be estimated from the expression $\bar{p}_p = \bar{p}_c(1-\bar{x})^{1.47}$, where $\bar{p}_c$ is the pressure coefficient at the tip of the solid of revolution. /400
With these approximate relationships, Formula (IX-1-22) becomes after calculation of the integral

$$c'_{x\,w.v} = c'_{x\,w.p} - 0.667\bar{r}_{bse}(1-\nu_0)\left[(1 - 0.552\bar{r}_{bse} + 0.068\bar{r}_{bse} - 0.189\bar{r}^3_{bse})\bar{p}_s + \frac{1.43}{M^2_\infty}\right], \qquad \text{(IX-1-25)}$$

where $\bar{r}_{bse} = r_{bse}/r_{mid}$.

For a nose section with $r_{bse} = r_{mid}$, this formula becomes

$$c_{x\,w.v} = c_{x\,w.p} - 0.667\left(0.327\bar{p}_c + \frac{1.43}{M^2_\infty}\right)(1-\nu_0). \qquad \text{(IX-1-26)}$$

Here the coefficients $c_{x\ w.v}$ and $c_{x\ w.p}$ refer to the area πr^2_{mid}.

For a parabolic nose section, the coefficient

$$c_{x\,w.p.} = 0.415\bar{p}_c. \qquad \text{(IX-1-27)}$$

If its value is referred to the area πr^2_{bse} of some arbitrary cross section, then

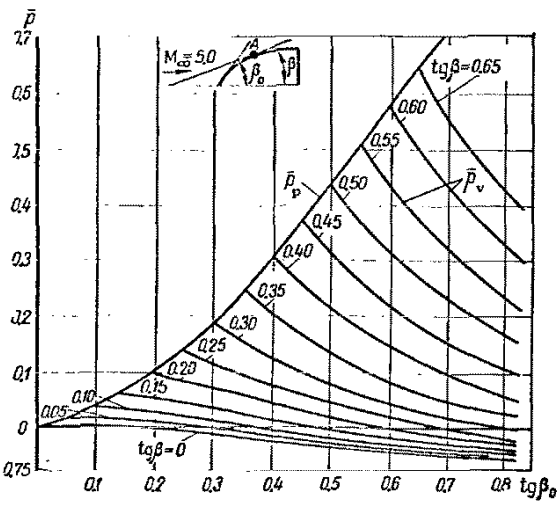

Figure IX-1-9. Diagram of Pressure Distribution Around a Solid of Revolution as Constructed on the "Equal Pressures" and "Equal Velocities" Hypotheses ($M_\infty = 5$).

$$c'_{xw.p} = \bar{p}_c(1 - 0{,}49\bar{r}_{base} + 0{,}056\bar{r}^2_{base} - 0{,}151\bar{r}^3_{base}). \qquad \text{(IX-1-28)}$$

Comparison with the method of characteristics and experimental data indicates that Formula (IX-1-26) can be used for M_∞ in the range $2 < M_\infty \leq (6\text{-}7)$ and the slenderness ratios satisfying the inequality $\lambda_{mid} \leq (2\text{-}2.2)$. These are the slenderness ratios of rather thick solids of revolution. Formula (IX-1-27) gives results on the high side for these conditions. For example, for a parabolic head with the slenderness ratio $\lambda_{mid} = 2$, the $c_{x\,w}$ calculated by this formula for $M_\infty = 2$ is almost twice that obtained by the method of characteristics. Formula (IX-1-27) gives more satisfactory results by substituting the parameter dependent on M_∞ for the numerical coefficient 0.415. The corresponding expression for the wave drag coefficient is /401

$$c_{xw} = \frac{0{,}08(15{,}7 + M_\infty)\bar{p}_c}{3 + M_\infty}, \qquad \text{(IX-1-29)}$$

and is applicable for slenderness ratios $\lambda_{mid} \geq 2.5$ and the range $1.5 \leq M_\infty \leq 6$.

§IX-2. THE NET-POINT METHOD

Experiment and theory indicate that it is necessary to take account not only of the vortical nature of the flow at high M_∞, but also such factors as the boundary layer and the various effects observed in it (compressibility, dissociation, heat transfer between the wall and the gas). Vibrational excitation and air dissociation, which may occur at very high flow velocities owing to the substantial temperature rise in the inviscid flow region between the shock wave and the surface of the body, are also of substantial influence.

This region can be calculated by the method of characteristics when the gas undergoes physicochemical changes. The equation system (IV-1-29)-(IV-1-32) for the characteristics, written in finite differences, should be used. The fundamental scheme of the calculation is the same as for a flow with constant heat capacities. There will be a difference in the calculations of the conical flow around the tip and in determination of the gas variables in the rest of the flow, which must be performed with consideration of dissociation and ionization of the gas. Tables or diagrams of the equilibrium thermodynamic functions of air at high temperatures may be used.

In Reference [4], the difference method known as the net-point method was used to calculate flow around bodies with consideration of equilibrium chemical reactions between the components of air and ionization reactions; with it, the ordinary equations of gasdynamics and the equations of chemical kinetics were solved jointly. The flow variables and thermodynamic functions were determined for dissociating and ionizing air whose original composition by volume was placed at 78.08% nitrogen, 20.95% oxygen, and 0.97% argon. Let us examine certain results of these calculations.

Axisymmetric flow. The solids of revolution for which the calculations were made had a nose cone that met the basic cone or cylinder on a fourth-order curve. The calculated results given in the tables (see Appendix No. 1) and diagrams were obtained for $M_\infty = 15$ and 20, a temperature $T_\infty = 250°K$, and a pressure $p_\infty = 0.292 \cdot 10^{-2}$ atm ($0.2864 \cdot 10^3$ N/m^2). For $M_\infty = 15$ the value $a^* = 1962$ m/s, $\rho_\infty a^{*2} = 0.1567$ atm ($0.1537 \cdot 10^3$ N/m^2), and for $M_\infty = 20$ $a^* = 2604$ m/s, $\rho_\infty a^{*2} = 0.2759$ atm ($0.2706 \cdot 10^5$ N/m^2). The density of the oncoming flow was set equal to $\rho_\infty = 0.412 \cdot 10^{-5}$ g/cm^3.

The gasdynamic functions, which are given for certain values of $\underline{x}$ and ξ, are the axial and radial velocity components V_x and V_r referred to a^*, the pressure $\underline{p}$ referred to $\rho_\infty a^{*2}$, and the parameter ρ, which is the ratio of the density to ρ_∞. The value $x = 1$ corresponds to the length of the nose cone to the point at which it meets the transitional curve. Table IX-2-1 (see Appendix No. 1) presents the gasdynamic functions of flow around a body with a nose cone ($\beta_c = 40°$) and a base cone ($\beta_c = 20°$ and 10°) at M_∞ = /402
= 20 and 15. Table IX-2-2 (see Appendix No. 1) presents the results of flow calculation for a body consisting of a nose cone with a semivertex angle $\beta_c = 40°$ fitted to a cylinder at $M_\infty = 20$, with consideration of equilibrium chemical reactions, and with $k = 1.4$. The studies indicate that downstream, the layer of high function gradients becomes thicker and is "squeezed" directly against the wall, while the flow regions of conical nature become larger. At a nose distance of the order of $x = 20$-30, the gasdynamic functions for $\xi = 0.05$ are close to their values in the conical flow.

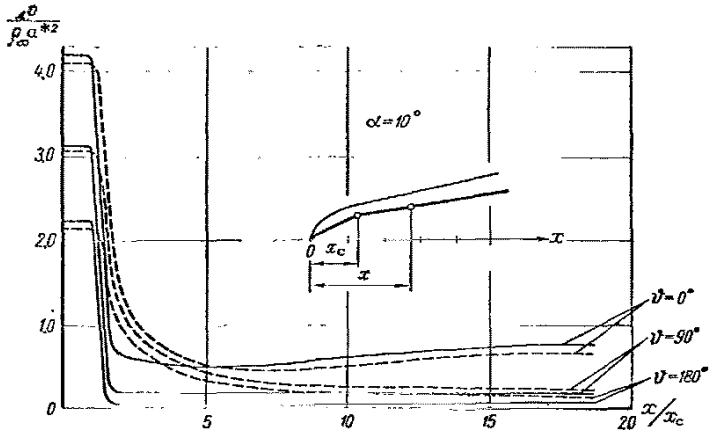

Figure IX-2-1. Variation of Pressure on Surface of Body (Solid Lines) and on Surface of Shock Wave (Dashed Lines).

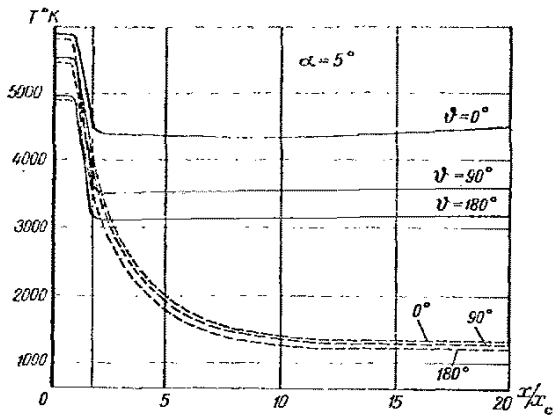

Figure IX-2-2. Variation of Temperature on Surface of Body (Solid Lines) and on Surface of Shock Wave (Dashed Lines).

In the region of rapid flow expansion, the influence of equilibrium chemical reactions is felt most strongly in the density and pressure.

Unsymmetrical flow. Table IX-2-3 (see Appendix No. 1) presents the results of a calculation of the variables V_x, V_r, V_ϑ, $\underline{p}$ and ρ for $\alpha = 5°$ and $M_\infty = 20$ for a body consisting of a nose cone with a semivertex angle of 46.9° and a cylindrical tail. The values of V_x, V_r, V_ϑ are referred to a^*, $\underline{p}$ to $\rho_\infty a^{*2}$, and ρ to the free-stream density ρ_∞.

The gasdynamic functions are given for a series of values of $\vartheta = (\pi/2) - \lambda$, $\underline{x}$, and ξ. The $\underline{x}$-coordinate is dimensionless and referred to the nose-cone length, while the variable ξ is determined from the expression

$$\tilde{\xi} = \frac{r-B}{W-B}\left\{\Phi + (1-\Phi)\frac{r-B}{W-B}\right\}, \qquad \text{(IX-2-1)}$$

where $\Phi = \Phi(x, \vartheta)$ is a certain function whose values are given in Table IX-2-4 (see Appendix No. 1).

From the data of this table, we can convert from the $\tilde{\xi}$ - coordinate to ξ for $1.4 \leq x \leq 2.4$ by the formula

$$\xi = 2\tilde{\xi}\{[\Phi^2 + 4(1-\Phi)\tilde{\xi}]^{1/2} + \Phi\}^{-1}. \qquad \text{(IX-2-2)}$$

For $x < 1.4$ and $x > 2.4$, the value of $\xi = \tilde{\xi}$.

Figures IX-2-1 and IX-2-2 present diagrams constructed from the results of calculation of the air pressure and temperature with consideration of the equilibrium chemical reactions at $M_\infty = 20$ for a body consisting of two cones (the forward cone is sharp). A very strong variation of pressure and density occurs on the segment from x = 1 to x = 2, especially on the surface of the body ($\xi = 0$). The changes are also quite substantial, but smoother, directly behind the shock wave ($\xi = 1$). At the surface of the body at x > 3, the gasdynamic functions, like the values of the thermodynamic parameters, practically cease to depend on x. The same effect is observed behind the shock wave at x > 15. /403

§IX-3. INFLUENCE OF ATTACK ANGLE ON FRONTAL DRAG

Experimental studies have shown that the frontal drag coefficients of sharp solids of revolution vary in accordance with the formula

$$c_x = c_{x0}(1 + \varepsilon z), \qquad \text{(IX-3-1)}$$

in which c_{x_0} is the frontal drag coefficient at zero angle of attack;

$$z = \sin^2(\alpha/2);$$

ε is a certain coefficient that depends basically on the shape of the solid of revolution.

For example, $\varepsilon \approx 87$ for a sharp-nosed 12.7-mm bullet in the range $1.5 \leq M_\infty \leq 2.2$, and $\varepsilon \approx 80$ for a 20-mm projectile in the same Mach-number range.

Relation (IX-3-1) was confirmed after reduction of the results of experimental firings at velocities above 450 m/s and values of $0 \leq z \leq 0.1$ ($0 \leq \alpha \leq 37°$). At lower speeds, it was found that the linear relation does not apply and the more

general relation

$$c_x = c_{x0}(1 + a_1 z + a_2 z^2 + \ldots) \qquad \text{(IX-3-2)}$$

should be used; here, depending on flow conditions, it is necessary to include terms in the second and even higher powers of z. /404

The formulas given above for the frontal-drag coefficient pertain to the case of rather large attack angles. If, on the other hand, the attack angles are small (of the order of 0-5°), we may start approximate calculations with Expression (I-2-5), which gives $c_x = c_R + c_N|\alpha|$ for small attack angles. Experimental and theoretical studies have shown that the axial-force coefficient in this formula varies insignificantly as a function of attack angle. For example, it was established by wind-tunnel tests that as the attack angle was changed from 0 to 5°, the c_R of a model in the form of a cylinder with a conical nose rose by approximately 2-2.5%. In first approximation, therefore, the axial-force coefficient may be assumed constant and equal to the corresponding value c_{R_0} for zero attack angle. Then the working formula for the drag coefficient is simplified:

$$c_x = c_{R0} + c_N|\alpha|. \qquad \text{(IX-3-3)}$$

According to this formula, calculation of c_x for an unsymmetrical flow involves preliminary calculation of the axial-force coefficient for $\alpha = 0$ and of the normal-force coefficient for the given attack angle.

Chapter X

HYPERSONIC VELOCITIES

§X-1. FLOW AROUND SLENDER BODIES AT VERY HIGH SPEEDS

The Equation System

Simplification of the equations. Solution of the hypersonic-flow problem for slender solids of revolution is based on simplified aerodynamic equations derived for small velocity disturbances.

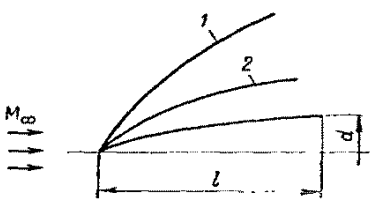

Figure X-1-1. Position of Compression Shock at Moderate (1) and Very High (2) M_∞.

Simplification of the equations differs substantially from linearization of the equations for small M_∞, although linearization is also brought about on the basis of the small-disturbance hypothesis. Since the M_∞ are small, simplification (linearization) is obtained by dropping terms containing the first and higher powers of the disturbances, i.e., having the respective orders τ, τ^2, etc. (for example, $M_\infty\tau < 1$, $M_\infty^2\tau^2 \ll 1$).

The flow pattern corresponding to this case appears in Fig. X-1-1. A feature of this flow linearization is that the thickness of the body is small by comparison with the distance between the body and the shock.

At very high velocities, on the other hand, the shock comes very close to the body (Fig. X-1-1), whose influence on the disturbed flow is stronger than in the linearized flow.

Although the disturbances are small, the product $M_\infty\tau$ may be of the order of unity. In this case, terms in the first power of the disturbance may not be disregarded if they contain the parameter $M_\infty\tau$, since they are of the same order as the other terms in the equation. Simplification is obtained by dropping terms of order τ^2 and higher if the small parameter τ appears independently and not together with M_∞.

Despite the simplifications, the system of flow equations remains nonlinear and, consequently, nonlinearity is an essential property of the equations for gas flows with large M_∞.

Let us transform the equations of symmetrical steady flow ([71], No. 3, 1954). For this purpose, we shall introduce the dimensionless coordinates ξ and η, defined by the conditions

$$x = x_b\xi; \quad r = \tau r_b\eta. \tag{X-1-1}$$

Since $\tau \ll 1$ (by the hypothesis of small thickness of the body), $r \ll x$, and this corresponds to the conclusion drawn above as to the existence of a thin supersonic layer in which all flow parameters change at very high flow speeds around the body. Relations (X-1-1) are affine transformation formulas.

Similarly, we may write in accordance with the estimates made earlier of the changes in velocity, pressure, and density in conical flow

/406

$$V_x = V_\infty[1 + \tau^2\bar{V}_\xi(\xi, \eta)]; \quad V_r = V_\infty\tau\bar{V}_\eta(\xi, \eta); \tag{X-1-2}$$

$$p = p_\infty kM_\infty^2\tau^2\bar{p}(\xi, \eta); \quad \rho = \rho_\infty\bar{\rho}(\xi, \eta), \tag{X-1-3}$$

where $\bar{V}_\xi$, $\bar{V}_\eta$, $\bar{p}$, $\bar{\rho}$ are the new dimensionless variables on which the actual velocity, pressure, and density depend.

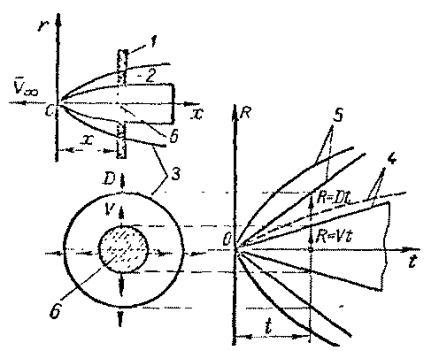

Figure X-1-2. Illustrating Law of "Plane Sections." 1) undisturbed gas particles; 2) disturbed particles; 3) shock wave; 4) path of piston; 5) path of shock wave; 6) piston.

Substituting Expressions (X-1-1) -(X-1-3) into the equations of motion (III-2-5) and continuity (III-2-15) for the case of steady symmetrical flow, together with the entropy-conservation condition (III-2-54), and dropping terms of the order of τ^2 by comparison with unity, we obtain

$$\frac{\partial\bar{V}_\eta}{\partial\xi} + \bar{V}_\eta\frac{\partial\bar{V}_\eta}{\partial\eta} = -\frac{1}{\bar{\rho}}\frac{\partial\bar{p}}{\partial\eta}; \tag{X-1-4}$$

$$\frac{\partial\bar{p}}{\partial\xi} - \frac{\partial(\bar{\rho}\bar{V}_\eta)}{\partial\eta} + \frac{\bar{\rho}\bar{V}_\eta}{\eta} = 0; \tag{X-1-5}$$

$$\frac{\partial}{\partial\xi}\left(\frac{\bar{p}}{\bar{\rho}^k}\right) + \bar{V}_\eta\frac{\partial}{\partial\eta}\left(\frac{\bar{p}}{\bar{\rho}^k}\right) = 0. \tag{X-1-6}$$

These equations, which form the basis of small-disturbance theory, are used in investigating isentropic (nonpotential) flow around slender solids of revolution at hypersonic velocities.

Law of plane sections. The essence of this law is that a body moving at very high speed causes only transverse displacement of air particles. This motion of the gas arises when it is displaced by a flat cylindrical piston. Consequently, we can draw an analogy between plane nonsteady motion of a gas behind an expanding piston and steady flow around a cone.

Suppose that at time $t = 0$, a piston (Fig. X-1-2) starts in motion instantaneously at an initial velocity V, setting up ahead of itself a plane cylindrical shock wave whose front advances at velocity D. The distances $R = Vt$ and $R = Dt$ covered by the piston and shock wave, respectively, are represented in the (R, t) plane by a straight line to which the generatrices of the cone and compression shock correspond in the physical (r, x) plane. Thus, nonsteady plane flow behind a uniformly expanding piston corresponds to stationary flow around a cone.

When this analogy is used, the physical coordinate is found to be similar to the time t. If the piston expands nonuniformly in accordance with some arbitrary law $R(t)$, the traces of the piston and shock-front motions are mapped in the (R, t) plane by curves to which the curvilinear generatrices of the solid of revolution and the shock will correspond in the (r, x) plane (Fig. X-1-2).

Consequently, the nonsteady plane gas flow behind a nonuniformly expanding piston is analogous to steady flow around a body with a curvilinear generatrix. This is the generalized law of plane sections, which, as we see, proceeds directly from the analogy with piston motion. In flow calculation by this law, the flow variables are obtained accurate to τ^2 by comparison with unity. /407

The law of plane sections, which is represented schematically in Fig. X-1-2, becomes more palpable if we examine the uninverted system consisting of a stationary medium and moving body. From this medium, we isolate a layer of particles in a certain section perpendicular to the direction of motion. Then an observer in this section will see that the body, in its motion through the layer of particles, moves them aside, forcing particle displacement only in the given plane section. We can now understand that the surface of the body, which is a moving boundary through which gas particles cannot pass, acts as a piston.

If the generatrix of this body is assigned with an equation $r = f(x)$, we can interpret time as $t = x/V_\infty$ to find the relation for the variation of piston radius in the form $R = f(tV_\infty)$ that corresponds to this equation. Differentiating with respect to t, we find the piston's expansion rate $V_r = \partial R/\partial t$.

If we are concerned with flow around a cone, then $r = x\beta_c$, and, consequently, $R = V_\infty \beta_c t$ and $V_r = dR/dt = V_\infty \beta_c$. This last

expression permits the conclusion that the similarity law for flows at very high velocities proceeds directly from the law of plane sections.

Actually, the disturbed particle velocity on the cone surface, which coincides in the equivalent piston problem with the rate of piston expansion, will be the same if the product $V_\infty \beta_c$ is preserved. Then steady flows around the cone (or the equivalent nonsteady gas motions at a flat cylindrical piston) will differ at different values of V_∞ and β_c only in the linear scale. Since conical bodies are affinely similar, it is obvious that analogous conclusions can be extended to other affine-similar bodies, including bodies with parabolic generatrices.

Boundary conditions. The solutions of (X-1-4)-(X-1-6) must satisfy boundary conditions at the surface of the body and in the undisturbed stream.

If the equation $r = \tau b(x)$ of the solid-of-revolution generatrix is known, the condition at the boundary of the body is written

$$\overline{V}_\eta = \frac{db(\xi)}{d\xi} = b'(\xi) \quad \text{for} \quad \eta = b(\xi); \tag{X-1-7}$$

and the undisturbed-stream conditions

$$\overline{V}_\xi \to 0, \ \overline{V}_\eta \to 0; \ \overline{p} \to (kM_\infty^2\tau^2)^{-1}; \ \overline{\rho} \to 1 \quad \text{as} \quad \xi \to \infty. \tag{X-1-8}$$

In addition, conditions on the compression shock, whose surface may be described by an equation $r = \tau s(x)$, must also be satisfied. For example, the condition that the function $\overline{V}_\eta$ must satisfy can be determined from (III-4-2) for an oblique shock.

For this purpose, a formula is found from the above relationship for the variation of the normal velocity component on passage across the shock. Then, remembering that $V_{n_1} = V_{n\infty} = V_\infty \sin \theta_s$; $V_{n_2} = V_\tau \tan(\theta_s - \beta_s)$, and that the $M_1 = M_\infty$ are so large that we may assume $V_\tau = V_\infty \cos \theta_s \simeq V_\infty$ and substitute the angles for the sine and tangent, we obtain

$$\frac{V_\infty \theta_s - V_\infty(\theta_s - \beta_s)}{V_\infty \theta_s} = \frac{2}{k+1}\left(1 - \frac{1}{K_\delta^2}\right).$$

We note at once that $V_\infty\theta_s$ in this expression is the radial velocity component V_r immediately behind the shock. We replace this component with its value /408

$$V_r = V_\infty\tau\bar{V}_\eta = -\frac{V_\infty\theta_*\bar{V}_\eta}{s'(x)},$$

where, according to the equation of the shock generatrix r = ts(x), the small parameter

$$\tau = \frac{dr}{dx}\left[\frac{ds(x)}{dx}\right]^{-1} = \frac{\theta_*}{s'(x)}.$$

Then, introducing $K_0 = M_\infty\theta_s$ and substituting the new variable ξ for $\underline{x}$, we obtain

$$\bar{V}_\eta = \frac{2}{k+1}\frac{K_0^2-1}{K_0^2}s'(\xi). \qquad \text{(X-1-9)}$$

The conditions on the compression shock for the functions ρ and $\bar{p}$ are obtained from (III-4-24) and (III-4-25), by replacing p_2/p_1 in the former by the expression

$$\frac{p_2}{p_1} = kM_\infty^2\tau^2\bar{p} = \bar{p}\frac{kK_0^2}{[s'(x)]^2},$$

which is obtained from the conditions

$$\tau = \frac{\frac{dr}{dx}}{\frac{ds(x)}{dx}} = \frac{\theta_*}{s'(x)},$$

$$K_0 = M_\infty\theta_*,$$

and substituting in the latter

$$\frac{\rho_2}{\rho_1} = \frac{\rho}{\rho_\infty} = \bar{\rho}.$$

Then, converting from $\underline{x}$ to the variable ξ, we find after elementary manipulation

$$\left.\begin{aligned}\bar{p} &= \frac{2kK_0^2 - (k-1)}{k(k+1)K_0^2}[s'(\xi)]^2,\\ \bar{\rho} &= \frac{(k+1)K_0^2}{2+(k-1)K_0^2}.\end{aligned}\right\} \qquad \text{(X-1-10)}$$

Solution of Eqs. (X-1-4)-(X-1-6) for a given surface shape of a sharp solid of revolution and a given M_∞ gives the gas variables in the region of disturbed flow between this surface and the compression shock. The shape of the compression-shock surface is found simultaneously by solving these equations.

Equation for the stream function. Solution of problems of flow around solids of revolution with curvilinear generatrices requires consideration of the change in entropy behind the shock on passage from one streamline to another.

To make this solution easier, the equations described above are transformed to the stream function ψ, which is defined by (III-2-33).

/409

If we convert in these relationships to the variables ξ and η, including V_∞, τ, and x_b, which are constant for given conditions, in the value of the stream function $\psi = \Psi$, we obtain in the subject case of small disturbances

$$\Psi_\eta = \frac{\partial\Psi}{\partial\eta} = \eta\bar{\rho}; \quad \Psi_\xi = \frac{\partial\Psi}{\partial\xi} = -\eta\bar{\rho}\bar{V}_\eta, \qquad \text{(X-1-11)}$$

whence it follows that

$$\bar{V}_\eta = -\frac{\Psi_\xi}{\Psi_\eta}; \quad \bar{\rho} = \frac{\Psi_\eta}{\eta}. \qquad \text{(X-1-12)}$$

To transform (X-1-4)-(X-1-6) to the variable Ψ, we present the derivative $\partial\bar{p}/\partial\eta$ in the form

$$\frac{\partial\bar{p}}{\partial\eta} = \frac{\partial}{\partial\eta}(\omega\bar{\rho}^k) = \frac{\partial\omega}{\partial\eta}\bar{\rho}^k + k\omega\bar{\rho}^{k-1}\frac{\partial\bar{\rho}}{\partial\eta} = \frac{d\omega}{d\Psi}\frac{d\Psi}{\partial\eta}\bar{\rho}^k + k\omega\bar{\rho}^{k-1}\frac{\partial\bar{\rho}}{\partial\eta}, \qquad \text{(X-1-13)}$$

where $\omega = \bar{p}/\bar{\rho}^k$ is a function that depends on the change in entropy on passage from one streamline to another and is consequently determined by the function Ψ.

Denoting the derivative $d\omega/d\Psi$ by ω' and substituting (X-1-10) for $\bar{\rho}$, we obtain the stream-function equation

$$\Psi_\eta^2\Psi_{\xi\xi}-2\Psi_\xi\Psi_\eta\Psi_{\xi\eta}+\Psi_\xi^2\Psi_{\eta\eta}=\frac{\Psi_\eta^{k+1}}{\eta^{k-1}}\left[k\omega\left(\Psi_{\eta\eta}-\frac{\Psi_\eta}{\eta}\right)+\omega'\Psi_\eta^2\right]. \qquad \text{(X-1-14)}$$

The pressure in our nomenclature is

$$\bar{p}=\omega\bar{\rho}^k=\omega\left(\frac{\Psi_\eta}{\eta}\right)^k. \qquad \text{(X-1-15)}$$

Flow Calculation

Let us consider the solution of (X-1-14) for the stream function, which enables us to calculate the gas variables in the neighborhood of the point.

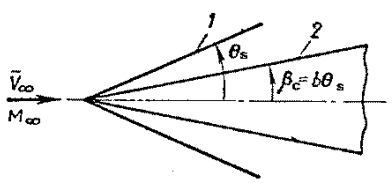

Figure X-1-3. Working Diagram of Flow Around a Cone. 1) compression shock; 2) cone. The arrows indicate the directions in which the angles are measured.

The procedure of the solution is as follows. First, the solution is found for flow past a conical point with the angle β_p. In this case, the solution is exact. Then, considering a small neighborhood of the curvilinear surface and correcting the stream function for flow around a cone, we find a new solution for the same Eq. (X-1-14), which will take account, in first approximation, of the effect of surface curvature near the nose on the stream function. The solution of the problem can then be obtained in a second approximation.

Solution of Eq. (X-1-14) for a cone (Fig. X-1-3). Flow around a cone is characterized by constant entropy throughout the region behind the compression shock. Hence the derivative ω' in (X-1-14) is zero. By virtue of the conical character of the flow, the stream function

$$\Psi(\xi,\eta)=\xi^2 f(\theta), \qquad \text{(X-1-16)}$$

where θ is the relative angle of the intermediate conical surface defined by the condition $\theta = r/(\theta_s x) = \eta/\xi$.

The shock inclination angle θ_s is to be regarded as the small parameter previously denoted by τ.

Introducing Expression (X-1-16) into (X-1-14), we obtain the ordinary nonlinear differential equation /410

$$4f^2f''-2f(f')^2=k\omega_0\frac{(f')^{k+1}}{\theta^{k-1}}\left(f''-\frac{f'}{\theta}\right); \qquad \text{(X-1-17)}$$

where f' and f" are the first and second derivatives with respect to θ, respectively; ω_0 is the ratio $\bar{p}/\bar{\rho}^k$ behind the compression shock, which is constant for given conditions. This ratio is determined in the following form from (III-4-24) and (III-4-25):

$$\omega_0=\frac{2kK_0^2-(k-1)}{k(k+1)K_0^2}\left[\frac{2+(k-1)K_0^2}{(k+1)K_0^2}\right]^k. \qquad \text{(X-1-18)}$$

The solution of (X-1-17) must satisfy the boundary conditions on the compression shock, which are obtained from (X-1-10), (X-1-11), (X-1-16) and (X-1-18). For example, the conditions for the function $f(\theta)$ and its derivative $f'(\theta)$ are found as follows. First general expressions $f'(\theta)$ and $f(\theta)$ are determined. For this purpose, (X-1-10) and (X-1-11) are used to calculate the derivative $\Psi_\eta=\xi f'(\theta)=\eta\bar{\rho}$, from which $f'(\theta)=(\eta/\xi)\bar{\rho}$ is found.

The function $f(\theta)$ is found from (X-1-10), (X-1-12), and (X-1-16) in the form

$$f(0)=-\frac{1}{2}f'(0)\left(\frac{\Psi_\xi}{\Psi_\eta}+0\right)=\frac{\theta}{2}\bar{\rho}(\theta-\bar{V}_\eta). \qquad \text{(X-1-19)}$$

If we now set $\theta=1$ in the expressions obtained for $f'(\theta)$ and $f(\theta)$ and use (X-1-12) for $\bar{V}_\eta$ and $\bar{\rho}$, we can arrive at the following conditions on the compression shock:

$$f'(1)=\frac{(k+1)K_0^2}{2+(k-1)K_0^2};\quad f(1)=\frac{1}{2}. \qquad \text{(X-1-20)}$$

The nonseparation condition requires that the stream functions be zero on the surface of the body. If the equation of the cone generatrix is assigned in the form $r=\theta_s bx$, this condition will be $f(b)=0$.

Equation (X-1-17) is integrated numerically for the given boundary conditions. It is convenient to extend this integration from the conditions on the compression shock to those on the cone surface. The resulting value $\beta_c=b\theta_s$ will be the angle of the cone in flow around which a compression shock with angle θ_s corresponding to the given parameter K_0 is formed.

In addition to the angle β_c, the value of the derivative f' is found on the surface of the cone, so that we can calculate the

pressure coefficient

$$\frac{\bar{p}_c}{\beta_c^2} = \frac{2(p_c - p_\infty)}{kK_1^2 p_\infty} = 2\left[\frac{\omega_0}{b^2}\left(\frac{f'}{b}\right)^k - \frac{1}{kK_1^2}\right], \qquad \text{(X-1-21)}$$

where $K_1 = M_\infty \beta_c$.

The results found by the method of small disturbances agree closely with the exact theory.

Consideration of the effect of curvature in first approximation. Let us assume that the generatrices of the solid of revolution and the compression shock are represented by the respective equations

$$r = \theta_0\left(bx + \frac{1}{2}cx^2\right); \quad r = \theta_0\left(x + \frac{1}{2}lcx^2\right); \qquad \text{(X-1-22)}$$

where θ_0 is the compression shock inclination angle at the point (Fig. X-1-4).

In solving (X-1-17) for the case of a curvilinear surface, the conditions for the functions Ψ and ω immediately behind the compression shock are determined by relationships found from (X-1-10), (X-1-11), and (X-1-18). These conditions will depend on the local shock inclination. /411

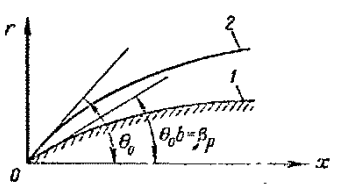

Figure X-1-4. Nomenclature for Angles of Inclination of Tangent to Generatrix of Solid of Revolution (1) and Generatrix of Compression Shock (2).

Since we are examining a small neighborhood of the nose, we can simplify determination of the conditions on the shock for Ψ and ω, by using the series expansion of the functions under consideration in this neighborhood in the parameter $K = M_\infty \theta_s$, which is calculated from the local shock inclination. The parameter K_0, a constant for the conditions, calculated from the shock angle θ_0 at the point ($x = r = 0$) will be $K_0 = M_\infty \theta_0$.

The conditions for the stream function directly behind the compression shock will be determined in terms of the conditions for its derivatives Ψ_ξ and Ψ_η.

We shall consider how the condition for the derivative Ψ_ξ is found, remembering that the condition on the shock will be

found similarly for the other derivative Ψ_η. First, we note that Expressions (X-1-9)-(X-1-11) indicate that the function Ψ_ξ depends on the parameter K. Expanding this function in series in the parameter K in the neighborhood of the point and breaking the expansion off at two terms, we find

$$\Psi_\xi = \Psi_\xi(K_0) + \left.\frac{\partial \Psi_\xi}{\partial K}\right|_{K=K_0}(K - K_0). \qquad \text{(X-1-23)}$$

Here the value of the function $\Psi_\xi(K_0)$ is determined with (X-1-9)-(X-1-11). Since

$$s'(\xi) = \frac{1}{\theta_0}\frac{dr}{dx} = \frac{K}{K_0},$$

the function Ψ_ξ takes the form

$$\Psi_\xi = -\frac{2}{k+1}\eta\frac{K^2-1}{2+K^2(k-1)}\frac{K}{K_0}. \qquad \text{(X-1-24)}$$

Setting $K = K_0$ in the above, we find $\Psi_\xi(K_0)$.

To find the derivative $\partial\Psi_\xi/\partial K|_{K=K_0}$, it is necessary to differentiate (X-1-24) with respect to K and set $K = K_0$ in the resulting expression.

Then the difference

$$K - K_0 = M_\infty\left(\frac{dr}{dx} - \theta_0\right) = M_\infty(\theta_s - \theta_0) = K_0 l c_\xi^s$$

is determined from (X-1-22) for the shock generatrix.

With consideration of expressions found from the function Ψ_ξ and its derivative with respect to K with $K = K_0$, and the difference $K - K_0$, the condition for the derivative Ψ_ξ on the compression shock will be

$$\Psi_\xi = -\eta\frac{2(K_0^2-1)}{2+(k-1)K_0^2}\left\{1 + \frac{(k-1)K_0^4 + (k+5)K_0^2 - 2}{(K_0^2-1)[2+(k-1)K_0^2]} l c_\xi^s\right\}. \qquad \text{(X-1-25)}$$

The condition for the derivative Ψ_η is found similarly:

$$\Psi_\eta = \eta \frac{(k+1)K_0^2}{2+(k-1)K_0^2}\left[1+\frac{4}{2+(k-1)K_0^2} lc\xi\right]. \qquad \text{(X-1-26)}$$

The condition for the function ω will be

$$\omega = \frac{\bar{p}}{\bar{\rho}^k} = \frac{2kK_0^2-(k-1)}{k(k+1)K_0^2}\left[\frac{2+(k-1)K_0^2}{(k+1)K_0^2}\right]^k \left\{1+\frac{4(k-1)k(K_0^2-1)^2}{[2kK_0^2-(k-1)][2+(k-1)K_0^2]} lc\xi\right\}. \qquad \text{(X-1-27)}$$

As in the cone problem, it is necessary to assign the form of the sought solution (stream function). Let us assume that this solution is basically determined by the value of the stream function for a cone at the point of a body with a generatrix inclined at an angle $\beta_p = \theta_0 b$, and assume that curvature can be allowed for in first approximation by a linear correction. Accordingly, the solution will be sought in the form /412

$$\Psi(\xi, \eta) = \xi^2 f(0) - lc\xi^2 g(\theta), \qquad \text{(X-1-28)}$$

where $g(\theta)$ is a certain function that takes account of generatrix curvature.

Obviously, this solution must also satisfy a condition on the conical shock surface at the point, which can be defined, assuming $g(\theta) = 0$ and $f(\theta) = 0.5$, in the form $\Psi = 0.5\eta^2 = 0.5\xi^2$.

The entropy function $\omega(\Psi)$ is determined by the stream function and can be represented in series form, keeping only the second term:

$$\omega(\Psi) = \omega_0\left(1+\omega_1 lc\sqrt{2\Psi}\right), \qquad \text{(X-1-29)}$$

where ω_0 is given by (X-1-18) and

$$\omega_1 = \frac{4k(k-1)(K_0^2-1)^2}{[2kK_0^2-(k-1)][2+(k-1)K_0^2]}. \qquad \text{(X-1-30)}$$

Introducing (X-1-28) and (X-1-29) into (X-1-14) and grouping terms in equal powers of ξ, we obtain two equations. One of them is a nonlinear equation for the function $f(\theta)$ and is identical with (X-1-17) for a cone, while the other is a linear equation for the function $g(\theta)$ and has the form

$$Dg'' = A + Bg + Cg', \qquad \text{(X-1-31)}$$

where g' and g" are the first and second total derivatives of the function $g(\theta)$ with respect to θ.

The coefficients in the last equation are

$$\left.\begin{aligned} A &= \omega_0\omega_1 \frac{(f')^{k+1}}{\theta^{k-1}}\left[\frac{(f')^2}{\sqrt{2f}} - k\sqrt{2f}\left(\frac{f'}{\theta} - f''\right)\right]; \\ B &= 12ff''; \; C = k\omega_0 \frac{(f')^{k+1}}{\theta^{k-1}}\left[\frac{k+1}{\theta} - (k+1)\frac{f''}{f'}\right] - 8ff'; \\ D &= k\omega_0 \frac{(f')^{k+1}}{\theta^{k-1}} - 4f^2. \end{aligned}\right\} \qquad \text{(X-1-32)}$$

Differential equation (X-1-31) can be integrated numerically. Here, the conditions on the shock that the functions $g(\theta)$ and $g'(\theta)$ found from this equation must satisfy are obtained with the aid of (X-1-25), (X-1-26), (X-1-28) for $\theta = 1$:

$$\begin{aligned} g(1) &= \frac{K_0^2 - 1}{2 + (k-1)K_0^2}; \\ g'(1) &= -K_0^2 \frac{(k-1)K_0^2 + 2(2k+3)}{[2 + (k-1)K_0^2]^2}. \end{aligned} \qquad \text{(X-1-33)}$$

In the numerical calculations, the assigned parameters may be the values of K_0 that were taken in calculating flow around the cone. The integration proceeds stepwise from the known conditions on the compression shock, using the same intervals as in the cone problem. The result is the function g and its derivative g' for each value of the angle θ, including $\theta = b$, which corresponds to the conditions on the conical nose section.

After the functions f and g and their derivatives have been determined, we can find the shape of the compression shock and calculate the pressure in first approximation. /413

As we see from (X-1-22), the shape of the compression shock is determined by the coefficient ℓ, which is equal to the ratio of the shock curvature to the curvature of the body's generatrix. This coefficient is found from (X-1-28) with the condition that the stream function on the surface is zero:

$$l = \frac{f'(b)}{2g(b)}. \qquad \text{(X-1-34)}$$

The pressure will be equal to its value on the cone plus a certain correction that is linear with respect to x and depends on the initial pressure gradient

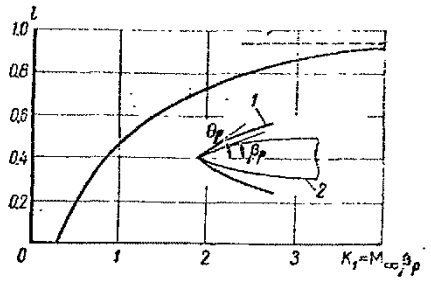

Figure X-1-5. Coefficient ℓ as a Function of K_1. ----- asymptotic value as $K_1 \to \infty$; 1) compression shock; 2) solid of revolution.

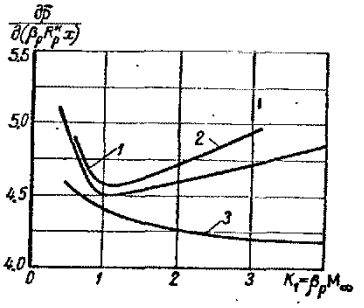

Figure X-1-6. Initial Pressure Gradient as a Function of Similarity Criterion K_1. 1) according to small-disturbance theory; 2) by method of conical flows and expansion flows; 3) by method of "local" cones ("equal pressure" hypothesis).

$$\left.\frac{\partial\bar{p}}{\partial x}\right|_b = \frac{[f'(b)]^k}{M_\infty^2 b^{k-1}\beta_p^2}\cdot\frac{-g'(b)}{g(b)}\beta_p R''_p, \quad \text{(X-1-35)}$$

where the parameter R''_p can be regarded for practical purposes as the generatrix curvature at the point of a sufficiently slender body.

The results of integration of (X-1-31) are presented in the diagrams of Figs. X-1-5 and X-1-6 and in Table X-1-1. The results for the coefficient ℓ can be approximated by

$$l = 0.959 - 0.515K_1^{0.4K_1^{-1}-1.5}. \quad \text{(X-1-36)}$$

The initial pressure gradient can be approximated by the formula

$$\frac{\partial\bar{p}}{\partial(\beta_p R''_p x)} = 4.929 - 0.429K_1^{-3/2} - 0.645(K_1-1)K^{-2}. \quad \text{(X-1-37)}$$

Both formulas give satisfactory approximations in the interval $0.5 \leq K_1 \leq \infty$.

The pressure-distribution calculation starts from the formula obtained by series expansion in powers of the small parameter $\underline{x}$, with the series limited to the linear term:

$$\bar{p} = \bar{p}_c + \frac{\partial\bar{p}}{\partial x}x \quad \text{or} \quad \bar{p} = \bar{p}_c + \beta_p R''_p \frac{\partial\bar{p}}{\partial(\beta_p R''_p x)}x, \quad \text{(X-1-38)}$$

where $\bar{p}_c$ is the pressure coefficient on the conical nose.

The curvature R''_p is found from the generatrix equation written in the form

$$r = \beta_p x + \frac{1}{2} R''_p x^2. \qquad \text{(X-1-39)}$$

The shape of the compression-shock surface generatrix is determined by (X-1-22), which can be written somewhat differently, namely: /414

$$r = 0_p x + \frac{1}{2} R''_p x^2. \qquad \text{(X-1-22')}$$

TABLE X-1-1. RESULTS OF CALCULATION OF FUNCTIONS g(b), g'(b), ℓ AND THE INITIAL PRESSURE GRADIENT

K_1	$g(b)$	$g'(b)$	l	$\frac{1}{\beta_p R''_p}\frac{\partial \bar{p}}{\partial x}\Big\|_b$
0.3765	5.170	—8.502	0.0426	5.532
0.6599	1.800	—3.040	0.2346	4.662
1.150	1.573	—4.073	0.5106	4.514
2.469	2.101	—6.820	0.8039	4.684
3.988	2.487	—8.638	0.8921	4.802
∞	2.931	—10.76	0.9586	4.929

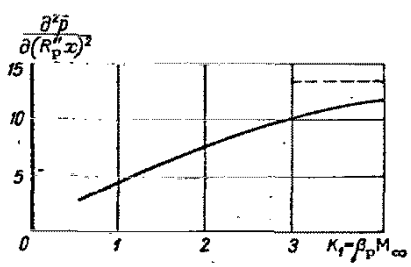

Figure X-1-7. Nature of Variation of Derivative $\partial^2 p/\partial(R''_p x)^2$ as a Function of K . -----asymptotic value as $K_1 \to \infty$.

As an example, let us find the shape of the compression-shock curve and the pressure distribution in the neighborhood of the tip of a solid of revolution with a parabolic generatrix.

From the equation of the parabola, we can find the cone angle $\beta_p = \lambda_{mid}^{-1}$ and the generatrix curvature at point x = r = 0:

$$R''_p = \frac{d^2 r}{dx^2} = -(\lambda_{mid} x_{mid})^{-1}.$$

Then the shock-generatrix equation will be written

$$\bar{r} = \bar{x}\left(2\frac{K_0}{K_1} - l\bar{x}\right).$$

We use (X-1-38) to determine the form of the pressure-distribution curve. Substituting the value $R''_p = \beta_p / x_{mid}$ found for the curvature,

$$\frac{\bar{p}}{\beta_p^2} = \frac{\bar{p}_c}{\beta_p^2} - \frac{\partial \bar{p}}{\partial(\beta_p R''_p x)}\bar{x}.$$

It is quickly noted that the specific form of the compression shock and the value of the pressure coefficient at a particular point on a given body are determined only by the parameter $K_1 = M_\infty \beta_p$, since the parameter K_0 and the coefficient ℓ are in turn functions of it.

Second approximation. The second-approximation solution of the flow problem involves finding an expression for the stream function that is more exact thatn (X-1-28). Analysis of the results of this solution indicates that for slender sharp nose sections, the pressure coefficient can be calculated in the second approximation by the formula

$$\bar{p} = (R'_p)^2 \frac{\bar{p}_c}{(R'_p)^2} + R'_p R''_p \frac{\partial \bar{p}}{\partial(R'_p R''_p x)} \times x + \frac{1}{2}(R''_p)^2 \frac{\partial^2 \bar{p}}{\partial(R''_p x)^2} x^2, \qquad \text{(X-1-40)}$$

in which $\bar{p}_c/(R'_p)^2 = \bar{p}_c/\beta_p^2$ and $\partial\bar{p}/\partial(R'_p R''_p x)$ are determined by (X-1-21) and (X-1-35) and the approximating expressions (VIII-1-27') and (X-1-37). The relation for the second derivative $\partial^2 p/\partial(R''_p x)^2$ given in Fig. X-1-7 can be determined with the formula /415

$$\frac{\partial^2 \bar{p}}{\partial(R''_p x)^2} = 13{,}7 - (K_1^{3/2} + 30K_1^{1/2} - b)K_1^{-2}, \qquad \text{(X-1-41)}$$

which gives satisfactory results for K_1 in the interval $1 \leq K_1 \leq \infty$ when the coefficient b = 22.5 and in the interval $0.5 \leq K_1 < 1$ when b = 19.2.

Here, determination of the second derivative with (X-1-41) enables us to calculate the pressure distribution in a somewhat broader range. However, this calculation does not give a complete picture of the pressure distribution over the entire surface of the body.

To complement the results obtained by the theory of small disturbances, let us examine certain approximate methods for calculation of flow around bodies.

§X-2. USE OF APPROXIMATE METHODS TO CALCULATE FLOW AROUND SOLIDS OF REVOLUTION AT VERY HIGH SPEEDS

"Local Cone" Method

Symmetrical flow. We shall examine a variation of this method based on the equal-pressure hypothesis. Consequently, Formula (XIII-1-27') can be used to calculate the pressure distribution around a solid of revolution with arbitrary generatrix if the parameter K_1 in that formula is determined from the local cone angle β.

For a slender solid of revolution with a parabolic generatrix and a local tangent inclination angle $\beta = \beta_p(1 - \bar{x})$, we obtain the distribution-curve equation

$$\frac{\bar{p}}{\beta_p^2} = 2.091\,[(1-\bar{x})^2 + 0.143K_1^{-3/2}(1-\bar{x})^{1/2}], \qquad (X\text{-}2\text{-}1)$$

where $K_1 = M_\infty\beta_p$ is determined from the local-cone angle at the point.

Interest attaches to comparison of the first derivatives of the pressure coefficient at the point found with (X-2-1) and by the theory of small disturbances, e.g., from (X-1-37). Calculating the derivative with (X-2-1), we find

$$\frac{\partial\bar{p}}{\partial(\beta_p^2\bar{x})} = -4.182\,(1 + 0.036K_1^{-3/2}). \qquad (X\text{-}2\text{-}2)$$

The diagram in Fig. X-1-6 shows the variation of the initial pressure gradient calculated by this formula and the corresponding results from the theory of small disturbances. We see that the accuracy of the calculation by the local-cone method decreases with increasing parameter K_1.

Comparing the pressures in the neighborhood of the point as computed by the small-disturbance theory and the "local-cone" method, we may conclude that a certain exaggeration of the pressure is inherent to the latter method, although the difference in the results is small.

The same conclusion can also naturally be drawn for the wave drag coefficient. An approximate relation for this coefficient can be obtained by introducing (X-2-1) into (I-3-14) and

integrating. We obtain as a result

$$\frac{c_{xw}}{\beta_p^2} = 0.697 + 0.213K_1^{-3/2}. \qquad \text{(X-2-3)}$$

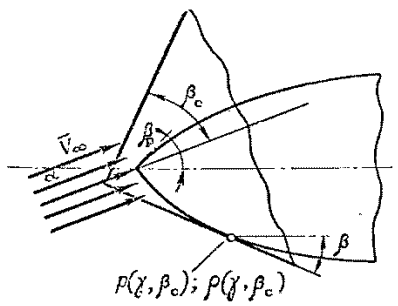

Figure X-2-1. Construction of "Local Cone."

If we use another variation of the "local-cone" method based on the equal-velocity hypothesis, a comparison shows that the pressures obtained are strikingly low for large M_∞.

Consideration of variable heat capacity effect. Let us examine a particular case of hypersonic flow around a slender solid of revolution in which an ideal gas has a fixed isentropic exponent $k_2 < k_\infty$ behind the shock wave. The pressure on the local cone can be calculated by the formula [59]

$$\frac{p}{p_\infty} = 1 + k_\infty K_1^2(1-0.25\bar{\rho})^{-1} - \frac{k_\infty M_\infty^2}{2}\frac{r}{R}, \qquad \text{(X-2-4)}$$

where $K_1 = M_\infty\beta > 1$; $\bar{\rho} = \rho_\infty/\rho_2 << 1$; r is the radial coordinate of a point on the body; R is the generatrix radius of curvature at that point. Thus, this formula takes account of the surface curvature.

Flow at an angle of attack. Applied to calculated unsymmetric flow around a solid of revolution with an arbitrary generatrix, the "local cone" method consists in the following. It is assumed that a line tangent to the body contour at a certain point on the surface (Fig. X-2-1) is simultaneously the generatrix of a cone around which the undisturbed stream moves symmetrically. The angle of this "local cone" can be determined from the expression

$$\beta_c = \beta - \alpha\cos\gamma + \frac{\alpha^2}{2}\operatorname{ctg}\beta\sin^2\gamma, \qquad \text{(X-2-5)}$$

where β is the angle between the tangent to the generatrix and the axis of the body.

If the parameters are determined on this cone for $\alpha = 0$, they will be, in accordance with the notion of the "local cone" method, precisely the parameters that characterize the real flow at the particular surface point and the given attack angle.

Calculations and a comparison with experimental data indicate that for M_∞ of the order of 3-4 or lower and small attack angles, it is necessary to use the equal-velocity hypothesis in the "local-cone" method to calculate the variables on the surfaces of sharp solids of revolution with moderate nose-section slenderness ratios. Using the velocity obtained on the basis of this hypothesis, the pressure and density are calculated with consideration of the entropy of the filament flowing in the particular meridional plane across the compression shock directly at the tip.

The equal-pressure hypothesis gives better results at high velocities. The velocity and density are calculated with consideration of the same entropy from the pressure found on the basis of this hypothesis.

Application of the "local cone" method is limited to points at which the tangents to the surface are parallel to the oncoming flow. Obviously, the "local-cone" angles are zero in this case. Here, the values of the corresponding inclination angles of these tangents to the body axis can be obtained from the condition $\beta_c = 0$. Indeed, setting $\beta_c = 0$, we find from (X-2-5) that /417

$$\beta = \alpha\cos\gamma - \frac{\alpha^2}{2}\operatorname{ctg}\beta\sin^2\gamma. \qquad \text{(X-2-6)}$$

At the surface points whose positions are determined by these angles, the pressure will be equal, according to the equal-pressure hypothesis, to the static free-stream pressure. If, on the other hand, the calculation is based on the other hypothesis — that of equal velocities — the velocity will remain the same as that of the undisturbed flow at the same point.

However, the "local cone" method can also be used to evaluate flow variables outside of this boundary, in the so-called "shadow" zone. For this purpose, it is necessary to examine an arbitrary "local cone" with a "negative" angle β_c computed by the same Formula (X-2-5).

Then the pressure coefficient found for the absolute value of β_c must be regarded as negative for the given point of the "shadow" zone.

Method Combining Conical and Expansion Flows

Axisymmetric flow. The content of the method of conical and expansion flows was set forth in §IV-7. The working formula for the pressure coefficient is

$$\frac{\bar{p}}{\beta_p^2} = \left(\frac{\bar{p}_c}{\beta_p^2} + \frac{2}{kK_1^2}\right)\left[1 - \frac{k-1}{2} M_s \left(\frac{p_s}{p_c}\right)^{\frac{k-1}{2k}} (\beta_p - \beta)\right]^{\frac{2k}{k-1}} - \frac{2}{kK_1^2}, \qquad (X\text{-}2\text{-}7)$$

where $K_1 = M_\infty \beta_p$; M_s and p_s are the Mach number M and the pressure directly behind the compression shock at the point; $\bar{p}_c$ is the pressure coefficient on the conical nose.

$M_s = M_2$ is found from (III-4-29) or (III-4-38), and the pressure $p_s = p_2$ is determined with Formula (III-4-36). The pressure coefficient $\bar{p}_c$ and the absolute pressure p_c on the conical nose are calculated from (VIII-1-27).

Let us illustrate application of this formula with the specific example of a symmetrical flow around a sharp solid of revolution with a conical-nose angle $\beta_p = 0.2$ with the condition that $M_\infty = 10$ ($K_1 = 2$).

First of all, we find $M_s = M_2$ on the conical nose. For this purpose, setting $K = 1.4$, we first use Formula (VIII-1-23) to determine $K_0 = M_\infty \theta_s = 2.38$. We then use (III-4-29) to compute $M_2 = 6.73$. At very large M_∞, the pressures p_s and p_c differ only slightly, so that we may set $(p_s/p_c)^{(k-1)/2k} \simeq 1$ in (X-2-7), thus assuming that M_s is approximately equal to the M_c on the conical nose. For a given value of $K_1 = 2$, we use (X-1-21) to determine $\bar{p}_c/\beta_p^2 = 2.2$ on the conical nose. We calculate the pressure at the point where the tangent inclination $\beta = 0.1$. In this case, the flow is deflected, starting at the apex, through an angle $\Delta\beta = \beta_p - \beta = 0.1$. Introducing the resulting data into (X-2-7), we find $\bar{p}/\beta_p^2 = 0.543$ for the selected point. If we take a more remote point for which $\beta = 0$, then $\bar{p}/\beta_p^2 = -0.085$. The corresponding M calculated by (IV-7-14) will be 7.83 and 9.27.

A comparison (see Fig. X-1-6) indicates that the initial inclination of the pressure distribution curve calculated by combining conical and expansion flows agrees more closely with the results of small-disturbance theory than with the "local-cone" method. The results of a calculation by the method of characteristics confirm this.

The axial-force coefficient is calculated from the pressure distribution using (I-3-14'). /418

For a given shape of the solid of revolution, the drag coefficient is presented in general form as the function

$$c_{Rp} = f_R(K_1)/M_\infty^2,$$

where $K_1 = M_\infty \beta_p$.

By way of example, let us consider a solid of revolution with a parabolic generatrix whose equation in dimensionless form is $\bar{r} = \bar{x}(2 - \bar{x})$. Introducing $\bar{r}$ and the value of $\bar{p}$ from (X-2-7) into the integrand of (I-3-14') and integrating from zero to 1 (numerically or graphically), we can determine c_{Rp} as a function of K_1 and M_∞^2. Calculations indicate that $c_{Rp}M_\infty^2$ is an increasing function of the parameter $K_1 = M_\infty \beta_p$. For the value $K_1 = 2$ chosen for the above example, $c_{Rp}M_\infty^2 = 2.86$, and for $K_1 = 3$, this quantity $c_{Rp}M_\infty^2 = 6.09$. Specific values of c_{Rp} for a body with a given slenderness ratio $\lambda_{mid} = 1/\beta_p$ correspond to a definite M_∞, which can be calculated from the condition $M_\infty = K_1\lambda_{mid}$. For example, for $\lambda_{mid} = 3$, $M_\infty = 6$; the corresponding value of $c_{Rp} = 2.86/36 = 0.079$. This method can be used to calculate flow around bodies with consideration of the change in the properties of the gas behind the shock at very high temperatures. For this purpose, as we noted in our investigation of flow around profiles, we can start with "frozen" flow behind the shock and a gas with a constant exponent k_2 determined for the conditions directly behind the shock.

Instead of k, it is necessary to use k_2 in the corresponding formulas of the method of characteristics.

Evaluation of flow parameters for tapering body tail section. M can be evaluated on this section in the same way as on the nose section.

Let us assume that the tail section of a solid of revolution is tapered and has an arbitrary shape with a smooth contour. Since the inclination angle β^t of the generatrix of this section is known at each point, the flow rotation angle can be determined rrom the conditions on the nose. It is $\Delta\beta = \beta_p - \beta^t$. Here the angle β^t is negative. Suppose, for example, that $\beta^t = -0.1$. Then $\Delta\beta = 0.2 - (-0.1) = 0.3$ and, consequently, M is 11.4 at the point under consideration according to (IV-7-14). Using (IV-7-15), we find $\bar{p}/\beta_p^2 = -0.293$. As we see, the taper has resulted in increased expansion.

Having thus computed the pressure distribution, we can apply the formula $c_{xw}^{u}=\int_{1}^{\bar{r}_{bse}^2}|\bar{p}|\,d\bar{r}^2$, to calculate the added wave drag due to the tail section. If the tail in our example has the form of a truncated cone with the angle $\beta^t = -0.1$ and the pressure coefficient is constant over its surface at $\bar{p} = -0.293\beta_p^2$, then

$$c_{xw}^{u}=0.293\beta_p^2(1-\bar{S}_{bse}). \qquad \text{(X-2-8)}$$

The deficiencies of the method, of which we spoke in §IV-7, render the calculation inaccurate for the flows around the nose and especially the tail section of a solid of revolution, where the deviation from the true picture may be more substantial. If we consider an intermediate cylindrical section, the method has, by its very content, no way of reflecting, even approximately, the possible pattern of the flow around it. Hence it can be used only for rough calculation of the parameters of flow around the body.

Nonaxisymmetric flow. As applied to nonaxisymmetric flow around a sharp solid of revolution, the method consists in taking M and other parameters on the nose in each meridional plane from the solution of the problem of flow around a cone at an attack angle, and calculating the flow behind the nose in the corresponding meridional plane as the two-dimensional supersonic expansion flow known as Prandtl-Meyer flow. /419

In solving the problem of nonaxisymmetric flow around a cone, we find the M_2 on the cone for a selected angle γ, and find the corresponding angle ω_2 from (IV-1-17) or Table IV-1-1. Thereafter, the calculation is the same as for the symmetrical case, i.e., the total rotation angle ω, understood as the sum of the rotation angle ω_2 and the local (or absolute) deflection angle $\beta_p - \beta$, is found, and the local M is determined from Table IV-1-1 for the value $\omega = \omega_2 + (\beta_p - \beta)$. Knowing the local Mach number, we can calculate the absolute pressure and the pressure coefficient. A formula similar to (X-2-7) can be used at very high M_∞ to calculate the pressure distribution around thin sharp solids of revolution:

$$\frac{\bar{p}}{(\beta_p')^2}=\left[\frac{\bar{p}_c}{(\beta_p')^2}+\frac{2}{k(K_1')^2}\right]\left[1-\frac{k-1}{2}M_c\beta_p\left(1-\frac{\beta}{\beta_p}\right)\right]^{\frac{2k}{k-1}}-\frac{2}{k(K_1')^2}, \qquad \text{(X-2-9)}$$

where the parameter K_1', which is equal to $M_\infty\beta_p'$, is determined from the "local cone" angle at the point, $\beta_p' = \beta_p - \alpha\cos\gamma$, for the

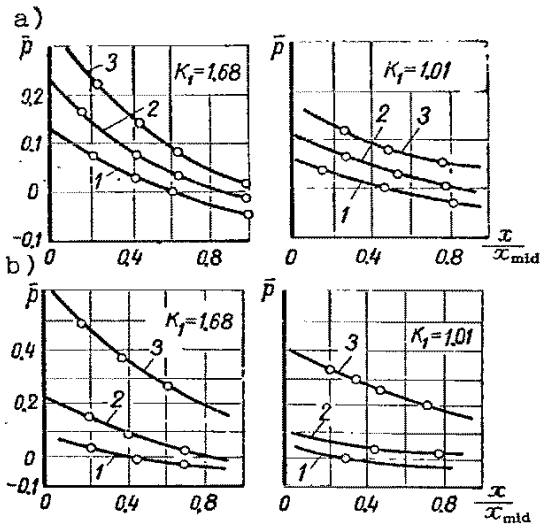

Figure X-2-2. Distribution of Pressure Coefficient over Surface of Ogival Solid of Revolution. a) $\alpha = 5°$; b) $\alpha = 15°$. generatrices: 1) downwind; 2) crosswind; 3) upwind.

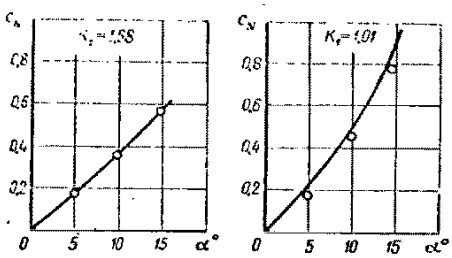

Figure X-2-3. Normal Force Coefficient of Ogival Nose Section as a Function of Attack Angle, $M_\infty = 5.05$. o) experiment; ———) calculation.

given meridional-plane angle γ. M_c and the pressure coefficient $\bar{p}_c$ are determined from the parameter K_1' for the "local cone." Formula (VIII-1-27) is used to calculate $\bar{p}_c$. M_c may be assumed equal to the M_s directly behind the shock, which can be calculated by (III-4-38) from the parameter $K_p' = M_\infty \beta_s'$, which, in turn, is found from (VIII-1-23) for $K' = M_\infty \beta_p'$.

By using (X-2-9) for given body shape, M_∞, and α, we find the distribution of the pressure coefficient over the surface of the body, i.e., the function $\bar{p} = \bar{p}(x,\gamma)$. The data obtained are the more accurate the larger M_∞ and the values of the similarity parameter $K_1 = M_\infty/\lambda_{mid}$. This is evident from Fig. X-2-2, which presents the results of studies of the pressure distributions around ogival nose sections with fineness ratios $\lambda_{mid} = 3$ and 5 for $M_\infty = 5.05$ and attack angles $\alpha = 5$ and 15°. Closer approximation of theory to experiment is observed for the larger parameter value $K_1 = 1.68$, i.e., for a body with $\lambda_{mid}' = 3$. For a nose section with $\lambda_{mid} = 5$ ($K_1 = 1.01$), an approximate calculation gives values on the top of the body that are somewhat lower than the experimental results. This effect is observed at practically all values of $K_1 > 1$, although the accuracy of the calculation falls off as the similarity parameter becomes smaller. If this parameter is smaller than unity, the rule is that approximate calculations are unacceptable.

/420

We may also conclude from comparison of the data that the approximate method gives better results as the angle of attack becomes smaller. Here the deviation of the theoretical pressure distribution from experiment at large α is explained by the viscosity of the transverse flow, especially on the top of the body — an effect not taken into account by the approximate theory. This effect increases with increasing M_∞.

The aerodynamic coefficients for nonaxisymmetric flow around the body are determined from the established pressure distribution with the aid of (I-3-14), (I-4-11), and (I-5-8) by numerical or graphical integration. Here, the second term in (I-5-8) for the moment coefficient can be disregarded in view of the small thickness of the body. Calculations of the axial-force coefficient by (I-3-14) indicate that because of the small attack angles, c_{Rp} is practically no different at $\alpha \neq 0$ from the corresponding value at $\alpha = 0$, so that $c_{Rp} \simeq c_{x\,w}$.

Calculations of the normal-force and moment coefficients indicate that for a given body shape, the expressions for them can be written in the general case in the respective forms

$$c_{Np} = f_N\left(\frac{\alpha}{\beta_p},\ K_1\right)\frac{1}{M_\infty} \quad \text{and} \quad m_{zp} = f_M\left(\frac{\alpha}{\beta_p},\ K_1\right)\frac{1}{M_\infty}.$$

For a parabolic generatrix $\bar{r} = \bar{x}(2 - \bar{x})$, the values found for $C_{n_p M_\infty}$ are as follows:

α/β_p \ $M_\infty\beta_p$	0.6	1.0	1.6	2.5	4.0
0	0	0	0	0	0
0.2	0.393	0.600	0.793	1.00	1.36
0.6	1.22	1.79	2.42	3.30	4.74
1.0	2.46	3.32	4.33	5.79	8.20

The calculated normal-force coefficients are compared with experimental figures in Fig. X-2-3. As we see, the agreement of the results is satisfactory. However, better agreement between theory and experiment is observed for the larger value of the similarity parameter. /421

The studies indicate that for hypersonic flow around slender sharp bodies with parabolic ogival generatrices, the center of pressure coefficient can be calculated by the approximate formula

$$c_{c.p} = \frac{x_{c.p}}{x_{mid}} = \frac{1}{10}\left[7 - K_1\left(1 - \frac{K_1}{8}\right)\right], \qquad \text{(X-2-10)}$$

where $K_1 = M_\infty \beta_p$.

This formula gives satisfactory results for $K_1 \leq 0.5$-0.6. Knowing the center of pressure coefficient, we can use the formula $m_{zp} = x_{c.p} c_{Np}$ to find the coefficient of the moment about the nose of the body.

§X-3. THE NEWTON METHOD

Pressure

In this method, pressure is calculated by (IV-7-2), in which the values of $\cos^2 \eta$ and $\cos^2 \eta^*$ are determined with (IV-7-4).

Since we are concerned with a solid of revolution, (IV-7-2) becomes

$$\bar{p} = \bar{p}^* \left(\frac{\sin\beta\cos\alpha - \sin\alpha\cos\beta\cos\gamma}{\sin\beta_p\cos\alpha - \sin\alpha\cos\beta_p\cos\gamma} \right)^2, \qquad \text{(X-3-1)}$$

where $\bar{p}^*$ is the pressure coefficient on a conical nose and is calculated by the ordinary theory of supersonic nonaxisymmetric flow around a cone and, for given values of the angle β_p and M_∞, is a function of the angles α and γ.

In the case of zero attack angle (X-3-1) simplifies:

$$\bar{p} = \bar{p}^* \frac{\sin^2\beta}{\sin^2\beta_p}, \qquad \text{(X-3-2)}$$

where $\bar{p}^*$ no longer depends on α and γ and is constant for given axisymmetric-flow conditions.

When the velocities are so high that pressure practically ceases to depend on M_∞, the parameter $\bar{p}^*/\cos^2 \eta^*$ in (X-3-1) can be replaced by $\tilde{p}(k) = \bar{p}_c/\sin^2 \eta_c$, which is determined from (VIII-1-30') in the form

$$\tilde{p}(k) = \frac{2(k+1)(k+7)}{(k+3)^2}. \qquad \text{(X-3-3)}$$

We may therefore write

$$\bar{p} = \tilde{p}(k)(\sin\beta\cos\alpha - \sin\alpha\cos\beta\cos\gamma)^2. \qquad \text{(X-3-4)}$$

Coefficient of Axial Force

Introducing (X-3-1) into (I-3-14), we find a relation for the axial-force coefficient:

$$c_{xp} = 4\int_0^{\bar{x}'_b} \lambda_{mid}\,\frac{A(\gamma_c)}{\pi}\,\bar{r}\,\mathrm{tg}\,\beta\,d\bar{x}, \qquad \text{(X-3-5)}$$

where /422

$$A(\gamma_c) = \int_{\gamma_c}^{\pi} \frac{\bar{p}^*\,(\sin\beta\cos\alpha - \sin\alpha\cos\beta\cos\gamma)^2}{(\sin\beta_p\cos\alpha - \sin\alpha\cos\beta_p\cos\gamma)^2}\,d\gamma. \qquad \text{(X-3-6)}$$

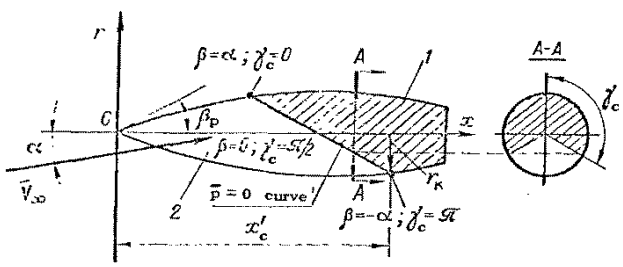

Figure X-3-1. Formation of "Shaded" Region in Flow Around a Solid of Revolution at an Attack Angle.

When (X-3-4) is used,

$$A(\gamma_c) = \bar{p}(k)\int_{\gamma_c}^{\pi} (\sin\beta\cos\alpha - \sin\alpha\cos\beta\cos\gamma)^2\,d\gamma$$

and after integration

$$A(\gamma_c) = \bar{p}(k)\left[(\pi - \gamma_c)\left(\cos^2\alpha\sin^2\beta + \frac{1}{2}\sin^2\alpha\cos^2\beta\right) + \right.$$
$$\left. + \frac{\sin\gamma_c}{2}\left(\sin 2\alpha\sin 2\beta - \sin^2\alpha\cos^2\beta\cos\gamma_c\right)\right]. \qquad \text{(X-3-7)}$$

The limits of integration γ_c and $\bar{x}'_c$ (or, in dimensional form, x'_c) depend on the geometrical shape of the body and the attack angle. To establish them, it is necessary to start from the feature of "Newtonian flow" around the body, which, as we have noted,

consists in the formation of a certain "shaded" zone on its surface in which particle collisions do not occur.

The boundary of this region (Fig. X-3-1) is determined by a curve on and everywhere behind which the pressure is zero. Hence the values of the limits γ_c and x_c' (or the corresponding coordinate r_c) are defined as functions of the position of the boundary of the "shaded" region. In accordance with (IV-7-10), the angle γ_c is found from the condition $\tan \beta/\tan \alpha = \cos \gamma_c$ or, for small α and β, from the condition $\beta/\alpha = \cos \gamma_c$.

In calculating x_c', which is the distance from the tip to the most remote point at which the pressure is zero, we proceed from the condition $\beta = -\alpha$. Accordingly, the equation for x_c' (or r_c) becomes

$$\left(\frac{dr}{dx}\right)_{x=x_c'} = -\operatorname{tg}\alpha. \qquad \text{(X-3-8)}$$

Two possible cases of flow must be kept in mind in calculating the limits. In the first, the attack angle α is smaller than the cone angle β_p at the point of the body (see Fig. X-3-1). In this case, as long as the present value of the generatrix inclination angle β is greater than or equal to α, the limit $\gamma_c = 0$. When β becomes smaller than the attack angle, γ_c will be greater than zero. For example, at $\beta = 0$, the angle $\gamma_c = \pi/2$, and in the case of $\beta = -\alpha$, $\gamma_c = \pi$.

Obviously, $\gamma_c = \pi/2$ is always the case for a cylinder, since /423
$\beta = 0$. The form of the function $A(\gamma_c)$ represented by (X-3-7) is simplified substantially for these two values of β. With $\beta = 0$, $\gamma_c = \pi/2$, for example, Formula (X-3-7) assumes the form $A(\gamma_c) = \frac{\pi}{4}\tilde{p}(k)\sin^2\alpha$, while in the case $\beta = -\alpha$, $\gamma_c = \pi$, $A(\gamma_c) = 0$.

The limit x_c' is determined by the position of the point on the lower generatrix where the "shaded" zone begins. Here, as we see from Fig. X-3-1, x_c' differs from the total length of the body in the general case.

With $\alpha \ll \beta_p$, a small "shaded" zone forms on a curvilinear nose section, and we may assume in approximation that $x_c' = x_{mid}$ and $\bar{x}_c' = 1$. Since $\gamma_c = 0$ in this case,

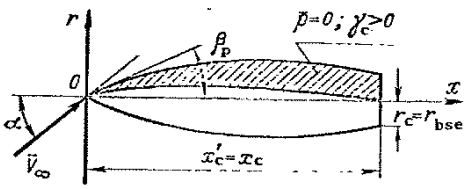

Figure X-3-2. Formation of "Shaded" Zone (Crosshatched) on Solid of Revolution at $\alpha > \beta_0$.

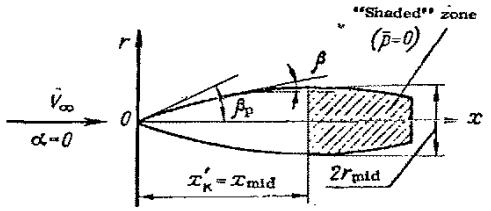

Figure X-3-3. Diagram of Flow Around Solid of Revolution with $\alpha = 0$.

$$A(\gamma_c) = \pi\bar{p}(k)\left(\cos^2\alpha\sin^2\beta + \frac{1}{2}\sin^2\alpha\cos^2\beta\right). \qquad \text{(X-3-9)}$$

Consequently,

$$c_{Rp} = \lambda_{mid}\bar{p}(k)\int_0^1\left(\cos^2\alpha\sin^2\beta + \frac{1}{2}\sin^2\alpha\cos^2\beta\right)\bar{r}\,\mathrm{tg}\,\beta\,d\bar{x}. \qquad \text{(X-3-10)}$$

Let us assume that we have a given parabolic nose section with the equation $\bar{r} = \bar{x}(2 - \bar{x})$. For it, $\tan\beta = \tan\beta_p(1 - \bar{x})$, where $\tan\beta_p = 1/\gamma_{mid}$ and $\sin^2\beta = \tan^2\beta/(1 + \tan^2\beta)$. After appropriate substitution in (X-3-10) and calculation of the integral, we can determine c_{Rp}.

The distinctive feature of the second case is that the attack angle is larger than or equal to the angle of the cone at the tip (Fig. X-3-2). In this case, if $\alpha = \beta_p$, the value $\gamma_c = 0$ obviously corresponds to the tip position. A "blanketed" region in which $\gamma_c > 0$ everywhere begins immediately behind it. This region, as is indicated on Fig. X-3-2, extends to the base, so that the coordinate $x'_c = x_c$.

The pressure coefficient $\bar{p}^*$ on the nose cone can be determined by the "local cone" method in either case.

At zero angle of attack, the function $A(\gamma_c) = (\pi\bar{p}^*/\sin^2\beta_p)\sin^2\beta$ in Expression (X-3-5), so that the formula for the axial-force coefficient, which is equal to the coefficient of wave drag, assumes the form

$$c_{Rp} = c_{xw} = \frac{2\bar{p}^*}{\sin^2\beta_p}\int_0^1\sin^2\beta\bar{r}\,d\bar{r}. \qquad \text{(X-3-11)}$$

In this formula, the upper limit $\bar{r} = 1$ of the integral is determined by the fact that the "shaded" zone (Fig. X-3-3) begins where the body has its largest cross section. Considering a parabolic body for which $\tan\beta = \tan\beta_p \sqrt{1-\bar{r}}$, and substituting $\sin^2\beta$ accordingly, we obtain after integration

$$c_{Rp} = \frac{\bar{p}^*}{\sin^2\beta_p}\left[1 + 2\lambda_{mid}^2 - 2\lambda_{mid}^2(1+\lambda_{mid}^2)\ln\frac{1+\lambda_{mid}^2}{\lambda_{mid}^2}\right]. \qquad (X\text{-}3\text{-}12)$$

When $\delta_{mid} > 2$, this formula can be presented in a simpler form: /424

$$c_{Rp} \approx \frac{\bar{p}^*}{3\sin^2\beta_p}\frac{1}{\lambda_{mid}^2}\left(1 - \frac{2}{\lambda_{mid}^2}\right). \qquad (X\text{-}3\text{-}13)$$

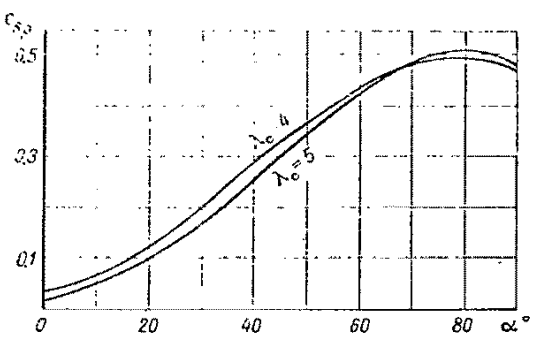

Figure X-3-4. Axial Force Coefficient for Parabolic Nose Section as a Function of Attack Angle.

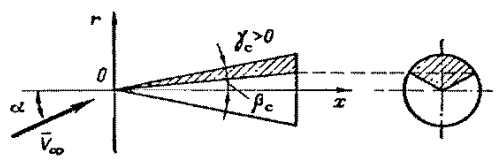

Figure X-3-5. "Shaded" Zone on Cone.

If the solid of revolution is slender, then $\gamma_{mid} \approx 1/\beta_p$ and $c_{Rp} \approx \bar{p}^*/3$.

Thus, the drag coefficient of a parabolic nose section is found to be half as large as for a conical nose. Setting $\bar{p}^* = p(k)\beta_p^2$, we find, for example, that at $k = 1.4$, $c_{Rp} = 0.697\beta_p^2$. Figure X-3-4 shows how c_{Rp} varies as a function of α for a parabolic nose section with $\tilde{p}(k) = 2$.

Axial force coefficient of a cone. Since $\beta = \beta_c = \text{const}$ for a cone, it follows that the function $A(\gamma_c)$ defined by (X-3-6) will be constant. Hence

$$c_{Rp} = \frac{A(\gamma_c)}{\pi}. \qquad (X\text{-}3\text{-}14)$$

If the cone angle is larger than the angle of attack, as corresponds to the first case, there is no "shaded" zone, the angle $\gamma_c = 0$, and, consequently $A(\gamma_c) = A(0)$ (see X-3-9), where $\beta = \beta_c$. For a slender cone

$$A(\gamma_c) = A(0) = \pi \tilde{p}(k) \left(\beta^2 + \frac{\alpha^2}{2}\right). \qquad \text{(X-3-15)}$$

If the cone angle is smaller than the attack angle (second case considered above), a "shaded" zone forms on top (Fig. X-3-5) and the function $A(\gamma_c)$ must be determined by (X-3-7).

At zero angle of attack, the axial-force coefficient $c_{Rp} = c_{x\,w} = \tilde{p}(k) \sin^2 \beta_c$, which gives $2.091 \sin^2 \beta_c$ for $k = 1.4$.

To take account of the Mach number, we can use the approximate relation

$$\bar{p}_c = c_{Rp} = \tilde{p}(k) \left(\sin \beta_c + \frac{0{,}38}{\sqrt{M_\infty^2 - 1}}\right) \sin \beta_c. \qquad \text{(X-3-16)}$$

Influence of flow expansion in the "shaded" zone. Up to this point, we have been concerned with a pure "Newtonian flow," in which the pressure coefficient for the "shaded" zone was assumed equal to zero. The axial force coefficient in this extreme case is determined by (X-3-5).

In fact, at a deviation from the extreme case, when the M_∞ remain finite though very large, c_{Rp} will differ from the value obtained from (X-3-5). One of the reasons is that this formula does not consider the influence of expansion in the "shaded" zone.

The results can be improved if the axial force coefficient is evaluated by the more general expression /425

$$c_{Rp} = \frac{2}{\pi r_{mid}^2} \int_0^{x_c} \int_0^{\pi} \bar{p} r \operatorname{tg} \beta \, dx \, d\gamma, \qquad \text{(X-3-17)}$$

which takes account of the "shaded" region's influence.

For convenience, let us present this coefficient as a sum of two components:

$$c_{Rp} = c_{Rp\,s} + \Delta c_{Rp}, \qquad \text{(X-3-18)}$$

where $c_{Rp\ s}$ is the axial force coefficient that arises as a result of stagnation and Δc_{Rp} is the additional coefficient due to expansion in the "shaded" zone.

The value of $c_{Rp\ s}$ is calculated by (X-3-17), and Δc_{Rp} from the expression

$$\Delta c_{Rp} = \frac{2}{\pi r_{mid}^2} \int_{x_c'}^{x_c} \int_{0}^{\gamma_c} \bar{p}_e r \operatorname{tg}\beta \, dx \, d\gamma, \qquad \text{(X-3-19)}$$

which derives from extending the integration into the "shaded" zone in determining the axial force coefficient. In this expression, the lower limit x_c' is equal to the distance from the tip to the beginning of the "shaded" zone on the top of the body.

The pressure coefficient $\bar{p}_e$ in this zone is determined by the formula $\bar{p}_e = (2/kM_\infty^2)(p_e/p_\infty - 1)$ and will obviously be variable in the general case.

For approximate evaluation of the influence of the "shaded" zone, the pressure coefficient is assumed constant at all points and equal to $\bar{p}_e = -2/(kM_\infty^2)$. Here we proceed from the assumption that a vacuum forms in the "shaded" zone at very high speeds ($p_e = 0$). Then

$$\Delta c_{Rp} = \frac{-4}{kM_\infty^2 r_{mid}^2 \pi} \int_{x_c'}^{x_c} \gamma_c r \operatorname{tg}\beta \, dx. \qquad \text{(X-3-20)}$$

In the case of a cone, for example, integration is extended from 0 to x_c when a "shaded" zone forms; as a result,

$$\Delta c_{Rp} = \frac{-2}{kM_\infty^2} \frac{\gamma_c}{\pi}, \qquad \text{(X-3-21)}$$

i.e., the over-all axial force is somewhat smaller. If no blanketing occurs ($\gamma_c = 0$), the additional negative axial force disappears.

On solids of revolution with curvilinear generatrices, the "shaded" zone covers the entire tail section at zero attack angle. Then, since $x_c' = x_c = x_{mid}$, $\gamma_c = \pi$,

$$\Delta c_{xp} = \frac{2}{k M_\infty^2}(1 - \bar{r}_{base}^2) \qquad \text{(X-3-22)}$$

so that the axial force becomes somewhat larger.

Shape of Nose Section with Minimum Drag

Application of the Newton formula. The Newton formula $p = \rho_\infty V_\infty^2 \sin^2 \beta$ can be used to determine the shape of the generatrix of a solid of revolution with minimum drag at very high speeds. For this purpose, bearing Formula (I-3-14) and $p = \rho_\infty V_\infty^2 (dr/ds)^2$ in mind, we write an expression for the drag in symmetrical flow: /426

$$R_p = 2\rho_\infty V_\infty^2 \pi \int_0^r r \left(\frac{dr}{ds}\right)^2 dr. \qquad \text{(X-3-23)}$$

The problem is to determine the generatrix equation $r = f(x)$ to which the minimum of function R_p corresponds. In solving this problem, we can assume ([72], 1962, No. 1), that the drag minimum is determined for constant lateral area S and volume W of the body, i.e.,

$$S = 2\pi \int_0^s r\,ds = \text{const}; \quad W = \pi \int_0^x r^2\,dx = \text{const}. \qquad \text{(X-3-24)}$$

The solution of this isoparametric variational problem reduces to investigation of the functional

$$\int_0^s \left[r \left(\frac{dr}{ds}\right)^3 + \lambda_1 r + \lambda_2 r^2 \frac{dx}{ds} \right] ds$$

or

$$\int_0^s \left[r \left(\frac{dr}{ds}\right)^3 + \lambda_1 r + \lambda_2 r^2 \sqrt{1 - \left(\frac{dr}{ds}\right)^2} \right] ds,$$

for its unconditional extremum; here, λ_1 and λ_2 are certain constants known as Lagrangian multipliers.

Writing the Euler equation for the last functional,

$$\frac{d}{ds}\left(\frac{\partial F}{\partial r'}\right) - \frac{\partial F}{\partial r} = 0, \qquad \text{(X-3-25)}$$

where r' = dr/ds and

$$F\left(r, \frac{dr}{ds}\right) = r\left(\frac{dr}{ds}\right)^3 + \lambda_1 r + \lambda_2 r^2 \sqrt{1 - \left(\frac{dr}{ds}\right)^2}, \qquad \text{(X-3-26)}$$

we obtain the equation which the minimizing function must satisfy. After substitution of Expression (X-3-26) into (X-3-25), applying $\partial F/\partial s = 0$, this equation assumes the form

$$-\left(\frac{dr}{ds}\right)^3 + \frac{1}{2}\lambda_2 r\left[1 - \left(\frac{dr}{ds}\right)^2\right]^{-1/2} + \frac{1}{2}\lambda_1 = 0.$$

The constants λ_1 and λ_2 can be determined from the condition that for r = 0 the derivative $(dr/ds)_0 = \sin \beta_p$, and for $r = r_{mid}$ this derivative is zero. As a result, the equation of the minimizing function becomes

$$\left(\frac{dr}{ds}\right)^3 = -\sin^3\beta_0 \left\{1 - \frac{r}{r_{mid}}\left[1 - \left(\frac{dr}{ds}\right)^2\right]^{-1/2}\right\}. \qquad \text{(X-3-27)}$$

We take the local slope u = dr/ds as the parameter in this equation. Then the equation itself gives an expression for the coordinate r of points on the generatrix:

$$\frac{r}{r_{mid}} = \sqrt{1 - u^2}\left(1 - \frac{u^3}{\sin^3\beta_0}\right). \qquad \text{(X-3-27')}$$

The equation for the x-coordinate is

$$\frac{dx}{dr} = \sqrt{\left(\frac{ds}{dr}\right)^2 - 1} = \frac{1}{u}\sqrt{1 - u^2}. \qquad \text{(X-3-28)}$$

Let us integrate this equation, applying (X-3-27'), in the range from $r = r_{mid}$, $x = x_c$ to current values of r and x. We obtain /427

$$\int_{x_c}^{x} dx = \int_{r_{mid}}^{r} \frac{1}{u}\sqrt{1 - u^2}\, dr,$$

from which

$$x = -r_{mid}\left(u + \frac{3u^2}{2\sin^3\beta_p} - \frac{u^4}{\sin^3\beta_p}\right) + x_c. \qquad \text{(X-3-29)}$$

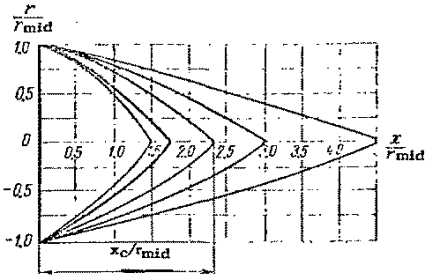

Figure X-3-6. Family of Generatrices for Bodies of Minimum Drag.

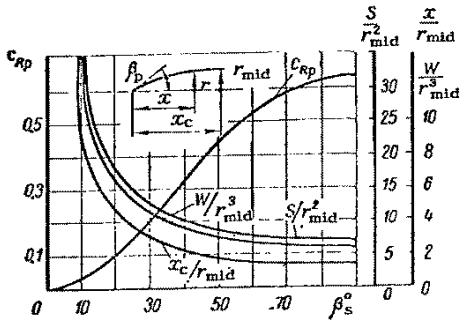

Figure X-3-7. Parameters of Minimum-Drag Nose Sections.

From this, setting x = 0 and u = sin β_p, we find the length of the nose section:

$$x_c = \frac{3}{2}\frac{r_{mid}}{\sin\beta_p}. \qquad \text{(X-3-30)}$$

Equations (X-3-27) and (X-3-29) present the generatrices of minimum-drag solids of revolution in parametric form. A family of such generatrices, constructed for various values of the angle β_p, is shown in Fig. X-3-6. The generatrix of the minimum-drag body is approximated satisfactorily by a curve with the equation

$$\frac{r}{r_{mid}} = \left(\frac{x}{x_{mid}}\right)^{3/4}. \qquad \text{(X-3-31)}$$

Using the parametric equations of the minimizing curve, we can obtain expressions for the drag, lateral area, and volume of the solid of revolution. Introducing (X-3-27') into (X-3-23), we find

$$R_p = \frac{9}{10}\rho_\infty V_\infty^2 \pi r_{mid}^2 \sin^2\beta_p\left(\frac{1}{2} - \frac{1}{7}\sin^2\beta_p\right), \qquad \text{(X-3-32)}$$

from which the drag coefficient

TABLE X-3-1a. WAVE DRAG OF OPTIMUM-SHAPE NOSE SECTIONS

1	2	3	4	5	6
Parameter	d_{mid}	x_{mid}	λ_{mid}^{-1}	S_{sde}	$c_{x\,w}$
x_{mid}, d_{mid}	d_{mid}	x_{mid}	d_{mid}/x_{mid}	$1.091x_{mid}$, d_{mid}	$0.288\lambda_{mid}^{-2}$
S_{sde}, d_{mid}	d_{mid}	$0.598\frac{S_{sde}}{d_{mid}}$	$1.67\frac{d_{mid}^2}{S_{sde}}$	S_{sde}	$0.340\lambda_{mid}^{-2}$
W_b, d_{mid}	d_{mid}	$4.5\frac{W_b}{d_{mid}^2}$	$0.222\frac{d_{mid}^3}{W_b}$	$6.05\frac{W_b}{d_{mid}}$	$0.564\lambda_{mid}^{-2}$
W_b, x_{mid}	$1.60\sqrt{\frac{W_b}{x_{mid}}}$	x_{mid}	$1.60\sqrt{\frac{W_b}{x_{mid}}}$	$3.28\sqrt{W_b x_{mid}}$	$0.321\lambda_{mid}^{-2}$
W_b, S_{sde}	$5.33\frac{W_b}{S_{sde}}$	$0.098\frac{S_{sde}^2}{W_b}$	$5.44\frac{W_b^2}{S_{sde}^3}$	S_{sde}	$0.307\lambda_{mid}^{-2}$

Note: Column 1 contains given geometrical parameters of the nose section; Columns 2-5 contain the calculated geometrical parameters of the optimum solid of revolution; Column 6 lists calculated values of the minimum wave drag coefficient.

$$c_{Rp} = \frac{2R_p}{\rho_\infty V_\infty^2 \pi r_{mid}^2} = \frac{9}{10} \sin^2 \beta_p \left(1 - \frac{2}{7} \sin^2 \beta_p\right). \qquad \text{(X-3-33)}$$

The formulas for calculation of lateral area and volume are

$$S = \frac{9\pi r_{mid}^2}{70 \sin \beta_p} (14 + 5 \sin^2 \beta_p); \quad W = \frac{27\pi r_{mid}^3}{\sin \beta_p} (7 + 2 \sin^2 \beta_p). \qquad \text{(X-3-34)}$$

Figure X-3-7 shows how the values of minimum drag vary with the nose tip angle β_p. The same figure shows curves characterizing the variation of the dimensionless quantities x_c/r_{mid}, S/r_{mid}^2, and W/r_{mid}^2. These curves, and the diagrams in Fig. X-3-6, indicate that the generatrix shapes come very close to the ogival curve. At the same time, we discern a tendency toward lengths exceeding that of the ogival head for a given β_p, and to more pronounced taper of the forward section.

TABLE X-3-1b. SHAPE OF OPTIMUM-NOSE-SECTION GENERATRIX

Given Parameters	Coordinates of Transition Point $\xi_0 = x_0/x_{mid}$, $\eta_0 = d_0/d_{mid}$	Equation of First Generatrix Segment
x_{mid}, d_{mid}	$\xi_0 = 0.6$, $\eta_0 = 0.736$	$\frac{\eta}{\eta_0} = \left(\frac{\xi}{\xi_0}\right)^{3/4}$
S_{sde}, d_{mid}	$\xi_0 = 0.704$, $\eta_0 = 0.76$	$\frac{\eta}{\eta_0} = \frac{\xi}{\xi_0}$
W_b, d_{mid}	$\xi_0 = 0.802$, $\eta_0 = 0.778$	$\frac{\eta}{\eta_0} = \left(\frac{\xi}{\xi_0}\right)^{3/2}$
W_b, x_{mid}	$\xi_0 = 0.385$, $\eta_0 = 0.617$	$\frac{\xi}{\xi_0} = \frac{h(\eta) - h(0)}{h(\eta_0) - h(0)}$, where $h(\eta) = \frac{2\eta^2 - 1}{2.73 - \sqrt{4\eta^2(1-\eta^2)}} - F(\varphi, k) + \sqrt{3}E(\varphi, k)$, $\varphi = \arccos[0.73 + \sqrt{4\eta^2(1-\eta^2)}] \times [2.73 - \sqrt{4\eta^2(1-\eta^2)}]^{-1}$; $k = 0.696$
W_b, S_{sde}	$\xi_0 = 0.463$, $\eta_0 = 0.637$	$\frac{\xi}{\xi_0} = [1 - (1-\eta)^{2/3}][1 - (1-\eta_0)^{2/3}]^{-1}$

Note: The functions F and E are incomplete elliptic integrals of the first and second kinds, respectively.

Use of the Busemann formula. The optimum shapes found for the nose sections are somewhat different if they are determined by the Busemann formula (IV-7-19). Solution of the variational problem ([68], 1960, No. 6; 1963, No. 3; [70], 1963, No. 1) leads us to the conclusion that the generatrix of the minimum-drag nose section consists of two successive curve branches. On the first, the excess pressure is always positive, while on the second it is zero. /429

Tables X-3-1, a and b, present the results of solution of six problems in which the minimum wave-drag coefficient and the generatrix equation of the corresponding nose section were determined. The initial conditions were the nose-section length x_{mid}, the midships-section diameter d_{mid}, the volume W_b, and the lateral area S_{sde}, assigned pairwise in various combinations. The relative coordinates $\xi_0 = x_0/x_{mid}$, $\eta_0 = d_0/d_{mid}$ of the points of transition of the first branch of the curve into the second were determined for each given combination of parameters. The generatrix equation on the second segment is found to be the same in each case,

$$\eta = \frac{d}{d_{mid}} = \left[1 - \frac{1-\eta_0^3}{1-\xi_0}(1-\xi)\right]^{1/3}, \qquad \text{(X-3-35)}$$

where $1 \leq \xi = x/x_{mid} \leq \xi_0$.

Normal-Force Coefficient

Solid of revolution with arbitrary generatrix. The working relation for the normal-force coefficient is obtained after substitution of (X-3-1) for the pressure coefficient into (I-4-11):

$$c_{xp} = \frac{-2}{\pi r_{mid}^2} \int_0^{x_c'} B(\gamma_c)\, r\, dx, \qquad \text{(X-3-36)}$$

where the function

$$B(\gamma_c) = \int_{\gamma_c}^{\pi} \bar{p}^* \frac{(\sin\beta\cos\alpha - \sin\alpha\cos\beta\cos\gamma)^2\cos\gamma}{(\sin\beta_p\cos\alpha - \sin\alpha\cos\beta_p\cos\gamma)^2}\, d\gamma, \qquad \text{(X-3-37)}$$

and the upper limit x_c' is the distance from the tip to the most distant point on the surface of the body beyond which the "shaded" zone begins.

If Formula (X-3-4) is used for the pressure coefficient, we can calculate the integral of (X-3-37) and find the function $B(\gamma)$ in explicit form:

$$B(\gamma_c) = -\tilde{p}(k)\left\{\frac{1}{4}(\pi-\gamma_c)\sin 2\alpha \sin 2\beta + \right.$$
$$\left. + \sin\gamma_c\left[\cos^2\alpha\sin^2\beta - \frac{1}{4}\sin 2\alpha \sin 2\beta\cos\gamma_c + \frac{1}{3}\sin^2\alpha\cos^2\beta(\cos^2\gamma_c + 2)\right]\right\}. \quad \text{(X-3-38)}$$

The limit x_c' is calculated in accordance with the possible working cases presented above.

Expression (X-3-38) for the function $B(\gamma_c)$ is greatly simplified for the first of these cases. It was stated above that as long as the condition $\alpha \leq \beta$ is satisfied, $\gamma_c = 0$ and, consequently,

$$B(\gamma_c) = B(0) = -\frac{1}{4}\pi\tilde{p}(k)\sin 2\alpha \sin 2\beta.$$

But when the present value of the angle β becomes smaller than α, we have $\gamma_c > 0$. In particular, if $\beta = 0$, then $\gamma_c = \pi/2$ and

$$B(\gamma_c) = B(\pi/2) = -\frac{2}{3}\sin^2\alpha\cos^2\beta\tilde{p}(k).$$

If $\beta = -\alpha$, then $\gamma_c = \pi$ and $B(\gamma_c) = B(\pi) = 0$.

For our case with $\alpha \leq \beta_p$, we can disregard the "shaded" zone; then /430

$$c_{xp} = \tilde{p}(k)\lambda_{mid}\sin 2\alpha\int_0^1 \sin 2\beta\bar{r}\,d\bar{x}. \quad \text{(X-3-39)}$$

The function in the integrand depends on the shape of the generatrix. In the particular case of a parabolic nose section,

$$\bar{r} = \bar{x}(2-\bar{x}) \quad \text{and} \quad \sin 2\beta = \frac{2\operatorname{tg}\beta_0(1-\bar{x})}{1+\operatorname{tg}^2\beta_0(1-\bar{x})^2},$$

where $\tan\beta_p = 1/\lambda_{mid}$.

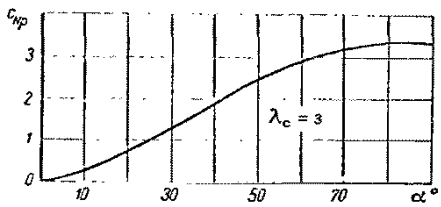

Figure X-3-8. Normal Force Coefficient for a Parabolic Nose Section as a Function of Attack Angle.

In the second case, the "shaded" zone, to which values of $\gamma_c > 0$ correspond, begins directly behind the forward point and, consequently, the function $B(\gamma_c)$ must be calculated from (X-3-38).

If the attack angles are small, the "shaded" zone has negligible influence. In this case, by introducing the expression for $B(\gamma_c) = -\tilde{p}(k)\alpha\beta\pi$ into (X-3-36), we obtain

$$c_{Np} = \tilde{p}(k)\,\alpha. \qquad \text{(X-3-40)}$$

Figure X-3-8 presents the results of calculation of the normal force coefficient by (X-3-36) for a parabolic nose section.

We note at once that a constant value of the integrand in (X-3-36) corresponds to a cylindrical segment ($\bar{x} \geq 1$) following a curvilinear nose section. It follows from (X-3-38) that, since $B(\gamma_c) = -(2/3)\tilde{p}(k)\sin^2\alpha$ the normal force coefficient of the cylindrical segment is

$$c_{Np}^{c} = \frac{8}{3\pi}\,\tilde{p}(k)\,\lambda_c \sin^2\alpha. \qquad \text{(X-3-41)}$$

Normal force coefficient of a slender cone. Since the function $B(\gamma_c)$ = const for a cone, (X-3-36) gives

$$c_{Np} = -\frac{B(\gamma_c)}{\pi \operatorname{tg}\beta_c}. \qquad \text{(X-3-42)}$$

Applying (X-3-38) for the function $B(\gamma_c)$, we can present (X-3-42) in more concrete form by examining the particular cases of flow.

Since $\alpha \leq \beta_c$ in the first case, $\gamma_c = 0$, $B(\gamma_c) = B(0) = -\pi\tilde{p}(k) \sin 2\alpha \sin 2\beta/4$, and, consequently,

$$c_{Np} = \frac{1}{2}\,\tilde{p}(k)\cos^2\beta_c \sin 2\alpha. \qquad \text{(X-3-43)}$$

For small angles α and β_c

$$c_{Np} = \tilde{p}(k)\alpha. \qquad \text{(X-3-44)}$$

From (X-3-43), we can find the initial slope of the $c_{Np}(\alpha)$ curve, which is determined by the derivative

$$\left(\frac{\partial c_{Np}}{\partial \alpha}\right)_{\alpha=0} = \tilde{p}(k)\cos^2\beta_k. \qquad \text{(X-3-45)}$$

For a slender cone at small angles of attack and k = 1, this last formula gives $(\partial c_{Np}/\partial\alpha)_{\alpha=0} = 2$, which, as will be shown below, corresponds exactly to linearized flow.

We may therefore conclude that the slope of the curve and c_{Np} depend weakly on M_∞ throughout the entire range from small to very large values of this Mach number. This conclusion is confirmed by the results of an exact calculation of $(\partial c_{Np}/\partial\alpha)_{\alpha=0}\cos^{-2}\beta_c$ as a function of M_∞ for cones with various values of the angle β_c. /431

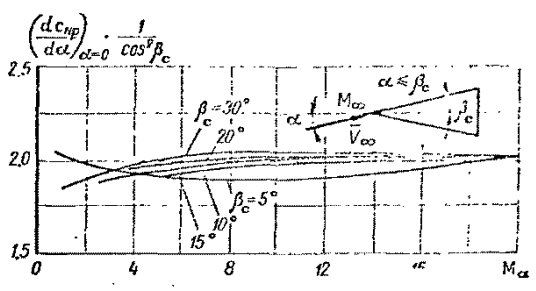

Figure X-3-9. Initial Slope Variation of the Cone Normal Force Coefficient Curve as a Function of M_∞ and the Angle β_c.

In Fig. X-3-9, which presents these results, we also see that the influence of M_∞ is also weaker the thicker the cone and the larger M_∞. At the same time, a comparison shows that the Newton theory agrees better with the exact data in evaluations of the normal force coefficient if we set k = 1 in the calculation of $B(\gamma_c)$.

In the second case, with $\alpha > \beta_c$, the quantity $\gamma_c > 0$ and $B(\gamma_c)$ must be calculated by Formulas (X-3-37) and (X-3-38).

Influence of flow expansion in the "shaded" zone. To evaluate the normal force coefficient with consideration of expansion in the "shaded" zone, it is necessary to use a more general expression instead of (X-3-36):

$$c_{xp} = -\frac{2}{\pi r_{mid}^2} \int_0^{x_c} \int_0^{\pi} \bar{p} \cos\gamma r \, dx \, d\gamma. \qquad \text{(X-3-46)}$$

Here the normal force coefficient can be presented as the sum of two components:

$$c_{xp} = c_{xp\,s} + \Delta c_{xp}, \qquad \text{(X-3-47)}$$

where $c_{Np\ s}$ is calculated by Formula (X-3-36) from the stagnation condition and Δc_{Np} is determined for the "shaded" region with (X-3-46).

Let us examine determination of Δc_{Np} in greater detail. We shall assume, as before, that the pressure coefficient $\bar{p}_e = (2/kM_\infty^2)(p_e/p_\infty - 1)$ is the same everywhere in the "shaded" zone. With this in mind, we find after substitution of $\bar{p}_e$ in (X-3-46)

$$\Delta c_{xp} = -\frac{4}{kM_\infty^2 \pi r_{mid}^2} \left(\frac{p_e}{p_\infty} - 1\right) \int_{x_c}^{x_c} \int_0^{\gamma_c} r \cos\gamma \, d\gamma \, dx. \qquad \text{(X-3-48)}$$

Knowing the shape of the body in the "shaded" zone and the boundaries of this zone, we can determine Δc_{Np}. For a slender cone, for example, the absolute value

$$|\Delta c_{xp}| = \frac{2}{kM_\infty^2 \beta_c \pi} \left(1 - \frac{p_{eC}}{p_\infty}\right) \sqrt{1 - \frac{\beta_c^2}{\alpha^2}}, \qquad \text{(X-3-49)}$$

and for a cylinder, for which $r = r_{mid}$, $\gamma_c = \pi/2$,

$$|\Delta c_{xp}| = \frac{8\lambda_C}{kM_\infty^2 \pi} \left(1 - \frac{p_{eC}}{p_\infty}\right). \qquad \text{(X-3-50)}$$

The greatest effect of expansion in the "shaded" zone will correspond to a total vacuum, i.e., the case in which $p_e = p_{ec} = p_{eC}$ everywhere in this zone and, consequently, $\bar{p}_e = \bar{p}_{ec} = \bar{p}_{eC} = -2/(kM_\infty^2)$.

Figure X-3-10 shows the results of a calculation of the normal force coefficient of a solid of revolution composed of a /432

cone and a cylinder at $\alpha = 5$ and $10°$, with the corrections calculated by Formulas (X-3-49) and (X-3-50), and with the pressure coefficient $\bar{p}_e$ in the "shaded" zone assumed equal to zero. We see that the experimental data fit into the interval between the results obtained with and without the corrections. It can also be noted that the effect of "shading" also becomes weaker with decreasing attack angle.

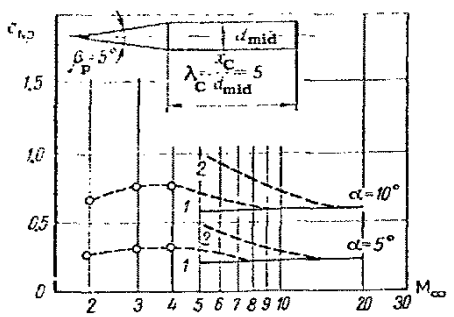

Figure X-3-10. Calculation of Influence of Flow Expansion in "Shaded" Zone on Normal Force Coefficient According to Newton Theory. 1) $\bar{p}_e = 0$; 2) $\bar{p}_e = -2/kM^2$; o) experiment.

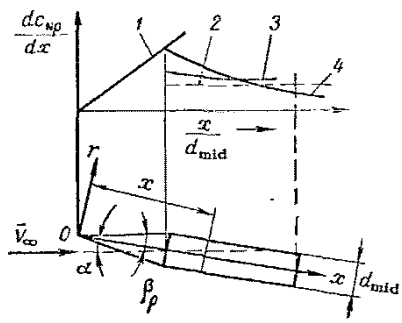

Figure X-3-11. Variation of $\partial c_{Np}/\partial x$ Along Lontitudinal Axis. 1) for cone; 2) for cylinder according to Newton theory; 3) at high supersonic speeds; 4) at low supersonic speeds.

It also follows from Fig. X-3-10 that at an angle of attack $\alpha = 5°$, i.e., the same as the cone angle, the experimental curve is quite close to the curve found from the "Newtonian stagnation" theory without correction. This is explained by the absence of a "shaded" zone on the cone and by the weak "shading" effect on the cylinder.

Influence of cylindrical section of body on normal force coefficient. Calculations and experimental studies indicate that this effect depends on the shape of the nose section and on M_∞.

Figure X-3-11 shows the distribution curve of the normal force coefficient on a cylindrical body section following a conical nose section. This diagram enables us to evaluate the importance of the cylindrical section in creating normal force at various velocities.

At relatively low supersonic speeds ($M_\infty = 2$-3), the coefficient of local normal force decreases downstream and vanishes approximately at a distance of $(2\text{-}2.5)d_{mid}$ from the joint between

the cylindrical and conical sections. At larger M_∞ in the range $3 < M_\infty < 6$, the distribution of the local normal force coefficient is found to be such as to give it the largest average value.

A further increase in M_∞ is accompanied by steadily smaller changes in the normal force coefficient, and it quite clearly tends to a certain constant value determined by the Newtonian-theory approximation.

To establish quantitative characteristics for evaluation of the effect of the cylindrical section at large M_∞, let us first examine certain general considerations pertaining to the variation of the initial slope of the c_{Np} curve.

For the body whose shape is represented in Fig. X-3-12, the normal force coefficient can be presented in the form of the general relationship /433

$$c_{Np} = f\left(\beta_p, \frac{x_a}{d_{mid}}, \frac{d_{bse}}{d_{mid}}, M_\infty, \alpha\right). \qquad (X\text{-}3\text{-}51)$$

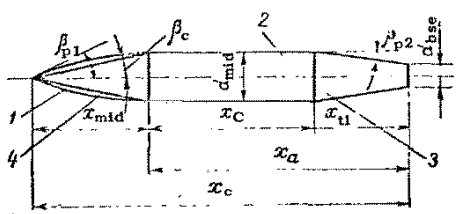

Figure X-3-12. Working Diagram for Solid of Revolution. 1) nose section with arbitrary generatrix; 2) cylindrical section; 3) conical stern; 4) conical nose section.

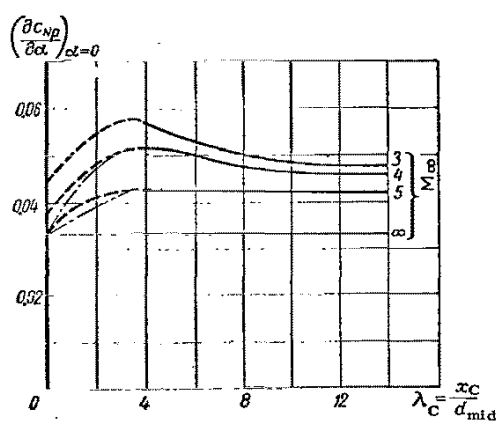

Figure X-3-13. $(\partial c_{Np}/\partial\alpha)_{\alpha=0}$ as a Function of λ_C for a Cylindrical Body with Slender Nose Sections: -·-·- conical nose section; ----- ogival nose section; ——— conical and ogival nose sections.

When the entire tail section is cylindrical, i.e., $x_a = x_C$ and $d_{bse} = d_{mid}$ this relationship becomes

$$c_{Np} = f\left(\beta_p, \frac{x_C}{d_{mid}}, M_\infty, \alpha\right). \qquad (X\text{-}3\text{-}51')$$

If the attack angles are small, c_{Np} can be regarded as a linear function of α and, consequently, the expression for the normal-force coefficient will be written in the form $c_{Np} = (\partial c_{Np}/\partial\alpha)_{\alpha=0}\alpha$, where the derivative

$$\left(\frac{\partial c_{Np}}{\partial\alpha}\right)_{\alpha=0} = \varphi\left(\beta_p, \frac{x_c}{d_{mid}}, M_\infty\right) \qquad \text{(X-3-52)}$$

is a certain function ϕ of the variables β_p, x_c/d_{mid}, and M_∞.

Examining Formula (X-3-45) and Fig. X-3-9, we may conclude that the normal force coefficient varies approximately in proportion to $\cos^2\beta_p$. However, if we examine slender bodies with angles β_p no greater than 10-15°, the influence of the taper angle will be slight and we can then assume that

$$\left(\frac{\partial c_{Np}}{\partial\alpha}\right)_{\alpha=0} = \varphi\left(\frac{x_c}{d_{mid}}, M_\infty\right). \qquad \text{(X-3-52')}$$

This relationship was used as a basis for an experiment with two body models with cylindrical tail elements. One of them has a conical nose section, and the other an ogival nose.

The results, which are presented in Fig. X-3-13 [16], indicate that when the length of the cylindrical section becomes of the order of $3d_{mid}$, the slope of the normal force coefficient curve is practically the same for both models.

With a large length ratio of the cylinder, of the order of λ_c = 8-9 and higher, the initial slope of the c_{Np} curve is practically independent of λ_c.

As the experimental data indicate, the slope of the curve decreases with increasing M_∞, becoming equal at $M_\infty > 8$-9 to the angle obtained for the cone by the "Newtonian flow" theory. This is in agreement with a conclusion that follows from (X-3-41): /434
As $M_\infty \to \infty$, the cylindrical section does not produce an initial-slope component.

Nonlinear dependence of normal force on attack angle. If the inclination of the normal force coefficient curve is independent of attack angle, then we can calculate c_{Np}, for example, with the diagram in Fig. X-3-13, from which data are taken for the initial derivative, and the linear relationship $c_{Np} = (\partial c_{Np}/\partial\alpha)_{\alpha=0}\alpha$.

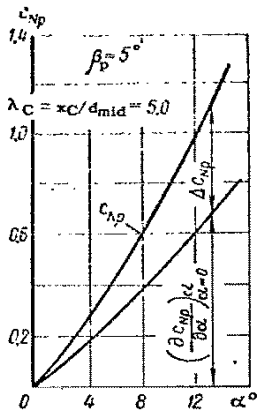

Figure X-3-14. Variation of Normal Force Coefficient and its Components for a Cylindrical Body with a Slender Sharp Nose Section ($M_\infty = 4$).

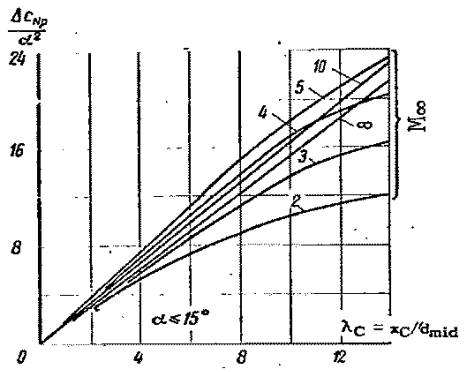

Figure X-3-15. Variation of $\Delta c_{Np}/\alpha^2$ as a Function of Cylinder Length Ratio and M_∞.

With increasing attack angle, however, the dependence of the normal force coefficient on α deviates from linearity:

$$c_{Np} = \left(\frac{\partial c_{Np}}{\partial \alpha}\right)_{\alpha=0}\alpha + \Delta c_{Np}, \qquad \text{(X-3-53)}$$

where the additional term Δc_{Np} reflects the nonlinearity of the normal force coefficient as a function of attack angle.

Figure X-3-14 shows a graphical interpretation of Formula (X-3-53) on the basis of experimental data. As we should expect, Δc_{Np} is proportional to α^2 for angles $\alpha < 15^\circ$, at which the experiments were conducted, i.e., the additional term characterizes a square-law relationship. Consequently, the parameter $\Delta c_{Np}/\alpha^2$ is independent of attack angle and is obviously determined in the general case by the geometrical dimensions of the cylinder and the flow velocity, as can be established in concrete terms by experiment. Curves characterizing the variation of $\Delta c_{Np}/\alpha^2$ as a function of M_∞ and the relative length of the body's cylindrical section were plotted from the results of studies with attack angles $\alpha \leq 15^\circ$ (Fig. X-3-15). The same figure shows the limiting straight line constructed on the basis of (X-3-41).

Having curves of $(\partial c_{Np}/\partial\alpha)_{\alpha=0}$ and c_{Np}/α^2 (see Figs. X-3-13 and X-3-15), we can make an approximate evaluation of the normal force coefficient for very large M_∞. To do this, it is necessary to assign the attack angle and find, for several M_∞, the values of the initial slope of the normal force coefficient curve in Fig. X-3-13 and Δc_{Np} in Fig. X-3-15, and then calculate c_{Np} by (X-3-53). These values can be used to plot a curve, which is then extrapolated so that at M_∞ of the order of 15-20 it reaches the value determined from the "Newtonian stagnation" theory (line 1 in Fig. X-3-10). The extrapolation curve can be used for approximate evaluation of the normal force coefficient for intermediate M_∞.

Influence of tapering tail section of solid of revolution. /435
This effect can be evaluated for large M_∞ by use of the experimental curve (Fig. X-3-16) characterizing the variation of the initial derivative of normal force coefficient as a function of base taper and M_∞.

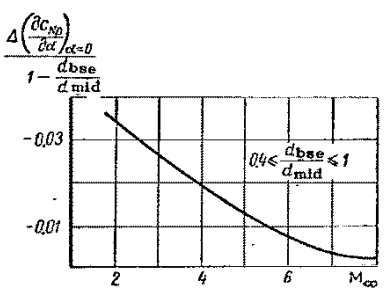

Figure X-3-16. Initial Slope of c_{Np} Curve as a Function of M_∞ for a Body with a Tapered Tail.

The experimental curve is a graphical representation of the function

$$f(M_\infty)=\Delta\left(\frac{\partial c_{Np}}{\partial\alpha}\right)_{\alpha=0}\left(1-\frac{d_{bse}}{d_{mid}}\right)^{-1}, \quad \text{(X-3-54)}$$

where $\Delta(\partial c_{Np}/\partial\alpha)_{\alpha=0}$ is the change in the initial derivative. Physically, the curve reflects the experimentally observed phenomenon in which $f(M_\infty)$ decreases approximately linearly with decreasing ratio d_{bse}/d_{mid} in the range $0.4 \leq d_{bse}/d_{mid} \leq 0.1$.

It has also been established by experiment that the shape of the tail-section generatrix is a less important factor in the variation of c_{Np} than is the base taper.

It follows from analysis of the data in Fig. X-3-16 that the tail-taper effect becomes substantial at low speeds. This is consistent with the known conclusion of the linearized theory to the effect that the normal lift coefficient vanishes at zero taper ($d_{bse}/d_{mid} = 0$).

As for large M_∞, we see from Fig. X-3-16 that the stern effect has already vanished at M_∞ = 8-9. The same effect occurs in

the approximation by the Newton theory when the tail section is in a "shaded" zone; as a result, the attack angle is equal to or smaller than the generatrix inclination angle of this part of the body. Otherwise a stabilizing effect appears, since the tail section leaves the "shaded" zone, forming a stagnation zone.

Coefficients of Moment and Center of Pressure

Approximate evaluation of moment coefficient. Substituting the expression for the pressure coefficient into (I-5-8), we find

$$m_{zp}=\frac{-4\lambda_{mid}^2}{\pi\lambda_c}\int_0^{\bar{x}_c'}\bar{x}\bar{r}B(\gamma_c)\,d\bar{x}-\frac{2\lambda_{mid.}}{\pi\lambda_c}\int_0^{\bar{x}_c'}\bar{r}^2\operatorname{tg}\beta B(\gamma_c)\,d\bar{x}, \qquad \text{(X-3-55)}$$

where the function $B(\gamma_c)$ is found from (X-3-37) or (X-3-38). If the body is slender, the second term in (X-3-55) can be dropped.

In determining the integral in (X-3-55), we can use values of $B(\gamma_c)$ obtained during the preceding calculations of the normal force coefficient. The moment coefficient calculated by this formula refers to the length x_b of the body.

The calculation by (X-3-55) with numerical or graphical integration is expedient only for the nose section. As for the cylindrical section, a formula for determining the moment coefficient m_{zp}^c of the cylinder can be obtained directly by substituting the expression found above, $B(\gamma_b) = -(2/3)\tilde{p}(k)\sin^2\alpha$, into (X-3-55). Remembering that $\lambda_{mid} = \lambda_c$, $\bar{r} = 1$, $\bar{x}_c = 1$ in this case, we find /436

$$(m_{zp}')^c=\frac{4\tilde{p}(k)}{3\pi}\lambda_c\sin^2\alpha. \qquad \text{(X-3-56)}$$

Here the characteristic dimension is the length of the cylindrical section. The value of the coefficient $(m_{zp}')^c$ obtained from this formula corresponds to the moment calculated with respect to a point on the front face of the cylinder. If the moment of the forces acting on the cylindrical section is calculated with respect to another point on the face at a distance $\bar{x}$, the corresponding value of the coefficient, referred to length $\bar{x}_c$, will be

$$m_{zp}^c=\frac{8\tilde{p}(k)}{3\pi}\frac{\bar{x}+0.5\bar{x}_c}{\bar{x}_c}\lambda_c\sin^2\alpha. \qquad \text{(X-3-57)}$$

The appropriate substitution must be made in the denominator of (X-3-57) in referring the moment coefficient to any other characteristic length. For example, if the length of the nose section or the total length of the body is taken as the characteristic dimension, the respective substitutions for x_c are x_{mid} and $x_b = x_{mid} + x_c$.

Taking the dimension corresponding to the total length x_b for a body with a curvilinear nose-section generatrix and a cylindrical tail and calculating the moment about the tip, we obtain for the moment coefficient

$$m_{zp}^{c} = \frac{8\tilde{p}(k)}{3\pi}\lambda_c \sin^2\alpha\left(1 + 0.5\frac{\lambda_c}{\lambda_{mid}}\right)\frac{\lambda_{mid}}{\lambda_c}. \qquad \text{(X-3-58)}$$

Adding this figure to the moment coefficient for the nose section referred to the total body length, we find the over-all coefficient

$$m_{zp} = m_{zp}^{c} + m_{zp}^{n}\frac{\lambda_{mid}}{\lambda_c}. \qquad \text{(X-3-59)}$$

Calculation of the nose-section moment coefficient m_{zp}^{n} can be simplified if we assume that the "shaded" zone has negligible influence. In this case, we have for a slender nose section

$$m_{zp}^{n} = \tilde{p}(k)\left(1 - \frac{W_b}{x_c S_{mid}}\right)\alpha, \qquad \text{(X-3-60)}$$

where W_b is the volume occupied by the body.

Coefficient of moment of forces for a cone. Remembering that the function $B(\gamma_c)$ is a constant for a cone, we have for the moment coefficient

$$m_{zp} = -\frac{2}{3}\frac{B(\gamma_c)}{\pi \operatorname{tg}\beta_c}(1 + \operatorname{tg}^2\beta_c). \qquad \text{(X-3-61)}$$

The function $B(\gamma_c)$ calculated by (X-3-38) is simplified in the first case of flow ($\alpha \leq \beta_c$, $\gamma_c = 0$), and the moment coefficient

$$m_{zp} = -\frac{\tilde{p}(k)}{3}\sin 2\alpha\cos^2\beta_c(1+\operatorname{tg}^2\beta_c). \qquad \text{(X-3-62)}$$

In the second case ($\alpha > \beta_c$, $\gamma_c > 0$) the value of $B(\gamma_c)$ calculated by the same Formula (X-3-38) retains its more complex form and the moment coefficient is found from (X-3-55).

Solid of revolution consisting of a cone and a cylinder. It is quite easy to obtain an expression for the moment coefficient of the forces acting on such a body, since the separate moment coefficients are known for the cone and the cylinder. If the body length x_b is taken as the characteristic dimension and we proceed from (X-3-38) for the function $B(\gamma_c)$, then /437

$$m_{zp} = -\tilde{p}(k)\left[\frac{2}{3}\frac{B(\gamma_c)}{\tilde{p}(k)}\frac{1+\operatorname{tg}^2\beta_p}{\operatorname{tg}\beta_p}+\frac{8}{3\pi}\lambda_c\sin^2\alpha\left(1-0.5\frac{\lambda_c}{\lambda_{mid}}\right)\right]\frac{\lambda_{mid}}{\lambda_c}. \qquad \text{(X-3-63)}$$

When $\alpha \leq \beta_p$, it is necessary to set $B(\gamma_c) = -\tilde{p}(k)\pi \sin 2\alpha \sin 2\beta_p/4$ in this formula.

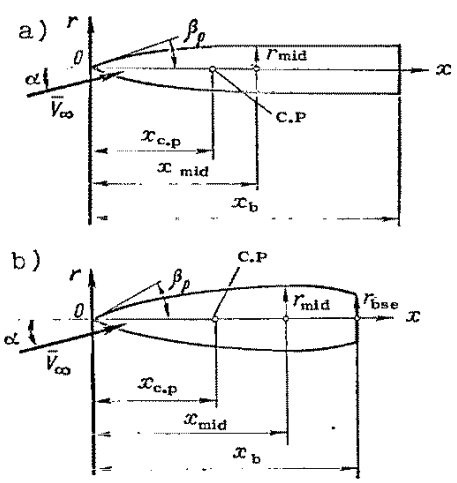

Figure X-3-17. Diagrams for Calculating Center of Pressure Positions for Various Bodies.

Approximate evaluation of center of pressure coefficient. Remembering that the center of pressure coefficient is equal to the ratio of the moment coefficient to the normal-force coefficient and applying Formulas (X-3-36) and (X-3-55), we obtain an expression for a slender body that does not take the "shaded" zone into account:

$$c_{c.p} = \int_0^{\tilde{x}_b'} \tilde{x}\tilde{r}B(\gamma_b)\,d\tilde{x}\left(\int_0^{\tilde{x}_b'}\tilde{r}B(\gamma_b)\,d\tilde{x}\right)^{-1}, \qquad \text{(X-3-64)}$$

where $\tilde{x}_b' = x_b'/x_b$.

The center of pressure coefficient can be calculated in each specific case by evaluating the integrals in (X-3-64). If, however, the coefficients m_{zp} and c_{Np} have first been calculated, the value of $c_{c.p}$ referred to the body length x_b is calculated by the formula $c_{c.p} = m_{zp}/c_{Np}$.

Formulas for approximate evaluation of center of pressure coefficient. Approximate relationships other than those examined above can be recommended for evaluation of the $c_{c.p}$ limit. One of them can be obtained from Formulas (X-3-40) and (X-3-60):

$$c_{c.p.} = 1 - \frac{W_b}{x_b S_{mid}}. \qquad \text{(X-3-65)}$$

This formula should be used for the conditions of flow around a slender curvilinear nose section, to which (X-3-40) and (X-3-60) correspond; the nose section length $x_b = x_{mid}$.

For a solid of revolution with a nearly ogival or parabolic generatrix (Fig. X-3-17b), study has shown that the center of pressure coefficient can be determined in approximation by the formula

$$c_{c.p} = \frac{x_{c.p}}{x_b} = \frac{0.67 - 0.75\bar{x}_b + 0.2\bar{x}_b^2}{1 - \bar{x}_b - 0.25\bar{x}_b^2}, \qquad \text{(X-3-66)}$$

which can be used when $\alpha < \beta_p$, and the dimensionless length $0 \leq \bar{x}_b < (1.1\text{-}1.2)$. Thus, the body under consideration may have a short tapering tail.

If this section is replaced by a cylinder (Fig. X-3-17a), the center of pressure coefficient of the resulting body is to be calculated by another formula:

$$c_{c.p} = \frac{0.73 + 0.67\alpha\lambda_{mid}(\bar{x}_b^2 - 1)}{\bar{x}_b[1.57 + 1.33\alpha\lambda_{mid}(\bar{x}_b - 1)]}. \qquad \text{(X-3-67)}$$

In using this formula, it is necessary to observe the conditions $\alpha < \beta_p$ and $\bar{x}_b \geq 1$. /438

Analyzing (X-3-67), we may conclude that the center of pressure shifts toward the base as the length of the body increases and as $\bar{x}_b \to \infty$ tends to a limiting position $c_{c.p} = 0.5$.

We shall use (X-3-64) to determine the cone center of pressure coefficient. Since $B(\gamma_c)$ is constant for a cone, it can be cancelled. After integration, we find the coefficient value $c_{c.p} = 2/3$. The same value is obtained if we consider the limiting position of the center of pressure for a curvilinear nose section of infinitesimally short length, in which case its shape is that of a cone. We find from (X-3-67) that $\lim_{\bar{x}_b \to 0} c_{c.p} = 2/3 \approx 0.667$. If

a cylinder is attached to the conical nose section, we have for the resulting body

$$c_{c.p} = \frac{0.667\lambda_{mid} + 0.81\lambda_c\alpha\,(\lambda_{mid} + 0.5\lambda_c)}{(1 + 0.81\lambda_c\alpha)\,\lambda_c}. \qquad \text{(X-3-68)}$$

For $\lambda_c = 0$, i.e., in the absence of a cylindrical section, this formula gives $c_{c.p} = 0.667$ for the pure cone. If, on the other hand, the cylinder is very long, the center of pressure coefficient tends toward the limit $c_{c.p} = 0.5$.

Comparing two bodies with the same slenderness ratio and conical and parabolic (or ogival) nose sections, we may conclude from the results obtained by Formula (X-3-67) and (X-3-68) that a more rearward position of the center of pressure is characteristic for the conical body.

Center of pressure coefficient as a function of M_∞. Calculations by the formulas given above yield limits of the center of pressure coefficients that are practically identical to those for realistic but quite large M_∞ of the order of 15-20. The center of pressure coefficient can be calculated as follows for smaller M_∞.

Assuming that the given body consists of several elements, we use Formula (XI-3-45) to calculate $c^n_{c.p}$. The nose-section coefficient c^n_{Np} that appears in it is determined from the diagram in Fig. X-3-13 by the formula $c^n_{Np} = (\partial c_{Np}/\partial\alpha)_{\alpha=0}\alpha$, and the coefficient c^c_{Np} is found from Fig. X-3-15 with the condition that c^c_{Np} is equal to the correction Δc_{Np} that takes the influence of the cylindrical section into account.

Finally, the component c^{tl}_{Np} for the tail section can be found with Fig. X-3-16. It is used to determine $\Delta(\partial c_{Np}/\partial\alpha)_{\alpha=0}$ as a function of M_∞ and of the ratio d_{bse}/d_{mid}; then the component $c^{tl}_{Np} = \Delta(\partial c_{Np}/\partial\alpha)_{\alpha=0}\alpha$ is calculated.

According to Formula (XI-3-45), it is necessary to determine the center of pressure coordinate for each element. In approximate calculations, the center of pressure may be assumed to lie at a distance $x_{c.p} \approx 0.5x_{mid}$ for a nose section with a curvilinear generatrix, and at $x_{c.p} \approx 0.667x_{mid}$ for a conical nose section. As for the centers of pressure of the cylindrical and tail sections, they may be assumed to lie at the centers of these segments of the body.

The normal-force coefficients and center of pressure coordinates that have been found are used to calculate the sum of their products $\Sigma(c_{Np})_i(\bar{x}_{c.p})_i$, the value of $\Sigma(c_{Np})_i$, and then the coefficient $c_{c.p}$ is determined in accordance with (XI-3-46).

A curve can be plotted with the values of this coefficient calculated for a series of M_∞. If the curve is extrapolated in such a way that it indicates the result that follows from the Newton theory at an M_∞ of the order of 15-20, it can be used to find the $c_{c.p}$ for intermediate M_∞, as well as for larger values. /439
Analysis of the influence of M_∞ indicates that transition to smaller values is accompanied by a decrease in the center of pressure coefficient, since the center of pressure moves closer to the tip as compared to the limiting case with $M_\infty \to \infty$.

The increase in the center of pressure coefficient with increasing velocity is due to the fact that, as we see from Fig. X-3-11, the stabilizing moment of the cylinder is increased by the increasingly large contribution of the positive force. In the limiting case with $M_\infty \to \infty$, the entire cylindrical section is "working". Here the center of pressure is situated quite far from the tip. At smaller M_∞, on the other hand, a significant part of the cylinder will be nonlifting.

Up to M_∞ of the order of 2-3, normal force is created only on a length of about $(2\text{-}2.5)d_{mid}$. In this case, we observe a weaker stabilizing effect of the cylindrical section, on the one hand because of the smaller normal force and, on the other, because of the greater forward shift of the center of pressure. It may therefore be found that with a given center of gravity position, a solid of revolution with a well-developed cylindrical section will be statically stable at very high speeds and unstable at lower speeds.

The problems examined above were associated with the determination, for very large M_∞, of aerodynamic coefficients that depend on the normal pressure distribution over the lateral surface. The over-all values of these coefficients will also depend on wake pressure.

If the "Newtonian stagnation" theory is followed rigorously, the wake pressure coefficient must, as we have noted, be set equal to zero for $M_\infty \to \infty$.

Accordingly, the base section lies in a "shaded" zone, and, consequently, has no influence on the aerodynamic coefficients. But when the coefficients are determined for realistic large M_∞, the influence of wake pressure can be estimated, as was recommended in considering flow expansion in a "shaded" zone on the body's lateral surface, i.e., it can be assumed that

the pressure behind the base is zero at large [Mach] numbers and, consequently, that $\bar{p}_{bse} = -2/(kM_\infty^2)$. Accordingly, the axial force coefficient $c_{Rbse} = (2/kM_\infty^2)\bar{S}_{bse}$.

Application of the Busemann formula. The Busemann formula (IV-7-22) should be used to consider the influence exerted on pressure by the centrifugal forces that arise in motion of the gas particles along curved trajectories. Setting $f(x) = 2\pi r$ in this formula, we obtain the following expression for the pressure coefficient on the surface of a solid of revolution:

$$\bar{p} = \frac{\bar{p}^*}{\sin^2\beta_p}\left(\sin^2\beta - \frac{1}{2\pi rR}\int_0^S \cos\beta\, dS\right). \qquad \text{(X-3-69)}$$

Formula (IV-7-24) can be used for a slender body. Setting $\nu = 2$ in this formula, we find

$$\bar{p} = \frac{\bar{p}^*}{\beta_p^2}\left(\beta^2 + \frac{r}{2}\frac{d^2r}{dx^2}\right). \qquad \text{(X-3-70)}$$

In the particular case of a slender body with a parabolic generatrix

$$R = -(\lambda_{mid}r_{mid})^{-1}\quad r = r_{mid}\bar{x}(2-\bar{x}),\ \beta = \beta_p(1-\bar{x}),\ \beta_p = \lambda_{mid}^{-1}.$$

Consequently, setting $\bar{p}^* = \bar{p}_b$, we obtain /440

$$\bar{p} = \bar{p}_c\left[(1-\bar{x})^2 - \frac{\bar{x}}{4}(2-\bar{x})\right]. \qquad \text{(X-3-71)}$$

We see from this expression that the centrifugal forces tend to lower the pressure.

As a result, the curve calculated by (X-3-71) shows significant expansion at the end of the body. However, experimental data and theoretical analyses by the method of characteristics do not confirm these results. In fact, the expansion practically vanishes at large M_∞ and the pressure that is set up is found to be very close to that obtained by the improved Newton theory.

Thus, correcting for centrifugal forces lowers the accuracy of the calculation for solids of revolution with convex surfaces. Hence the Newton theory should be used for such bodies at $k = 1.4$ without consideration of centrifugal forces. On the other hand, this theory gives poorer results for concave-surfaced bodies and,

as we have noted, the flow calculation requires the Busemann formula. The pressures obtained by the Newton formula are exaggerated. This formula may lead to such overstatement when the pressure behind the shock wave and that calculated by the Newton theory are the same, so that only the pressure-lowering effect of the centrifugal forces remains. This effect will occur as $M_\infty \to \infty$ and $k \to 1$, when the wave coincides with the body's surface at the limit. In flow of hot air ($k < 1.4$) around convex bodies at very high M_∞, therefore, the Busemann formula will become more accurate. In the limit with $M_\infty \to \infty$ and $k \to 1$, when the density in the layer becomes infinite, the Busemann formula will give exact pressure values.

Similarity Law for Nonaxisymmetric Flow

It was established above that at very high speeds and zero angle of attack, the similarity law for slender solids of revolution is determined by the parameter $K_1 = M_\infty \beta_p$, where the small parameter β_p may be the cone angle, the generatrix angle at the tip, or the body's thickness ratio.

For example, the pressure coefficient at an arbitrary point on the body's surface is $\bar{p} = \beta_p^2 f(K_1, \bar{x})$, where $f(K_1, \bar{x})$ is a certain function of K_1 and the dimensionless coordinate of the point. The drag coefficient of the same body $c_{x\,w} = \beta_p^2 F(K_1)$, where $F(K_1)$ is a certain function determined by the parameter K_1.

In nonaxisymmetric flow, the aerodynamic coefficients depend on attack angle. Let us show that the flows around bodies will be similar and, consequently, their aerodynamic coefficients will remain the same, if together with a constant parameter K_1 we have the equality $K_2 = \alpha/\beta_p$. For this purpose, we use Expression (X-3-1), in which we express the pressure coefficient $\bar{p}^*$ on the slender conical tip in accordance with the "local cone" method in the form $\bar{p}^* = \theta_c^2 \phi_p(K_1)$, where $\phi_p(K_1)$ is a certain function that depends on the parameter K_1. If the angle of the "local cone" is presented for small attack angles as $\theta_c = \beta_p - \alpha \cos \gamma$, then it is obvious that

$$\bar{p} = (\beta_p - \alpha \cos \gamma)^2 \varphi_p(K_1).$$

Consequently,

$$\frac{\bar{p}}{\beta_p^2} = \varphi_p(K_1) \left(\frac{\beta}{\beta_p} - K_2 \cos \gamma\right)^2. \qquad \text{(X-3-72)}$$

Thus, if equality of the parameters K_2 and K_1 is observed for two affinely similar bodies, the values of $\bar{p}/\beta_p^2$ will be the same at corresponding points on the surface with the same values of γ and β/β_p. /441

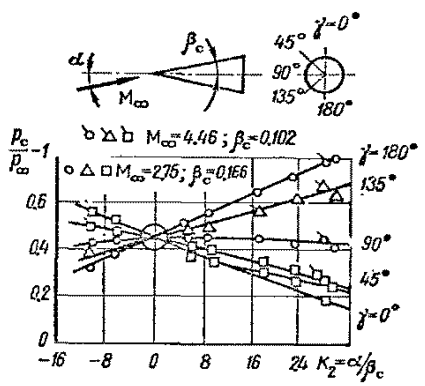

Figure X-3-18. Pressure Distribution on Surface of Cone in Nonsymmetrical Flow.

Substituting our relationship (X-3-72) into Formula (I-3-14), we obtain a general expression for the axial force coefficient:

$$\frac{c_{Rp}}{\beta_p^2}=\varphi_R(K_1, K_2). \qquad \text{(X-3-73)}$$

To obtain the corresponding expression for the normal force coefficient, we make a similar substitution in (I-4-11). Here we bear in mind that the coordinate $\underline{r}$ that appears in this formula will be an order smaller than $\underline{x}$, i.e., $r \sim \beta_p x$, just as $r_{mid} \sim \beta_p x_{mid}$ or $r_{mid} \sim \beta_p x_b$. After integration, we arrive at a general relationship for the normal force coefficient:

$$\frac{c_{Np}}{\beta_p}=\varphi_N(K_1, K_2). \qquad \text{(X-3-74)}$$

Thus, a family of affinely similar bodies in flows for which both the K_1 and the K_2 are the same is characterized by constant values of c_{Rp}/β_p^2, c_{Np}/β_p.

In the limiting case with $M_\infty \to \infty (K_1 \to \infty)$, only K_2 remains as a similarity parameter for the aerodynamic coefficients. This is evident, for example, in the example of a cone, for which the pressure coefficient

$$\bar{p}_c=\frac{\tilde{p}(k)}{\beta_c^2}\left(1-\frac{\alpha}{\beta_c}\cos\gamma\right)^2, \qquad \text{(X-3-75)}$$

and, according to (X-3-14) and (X-3-42),

$$\frac{c_{Rp}}{\beta_c^2}=\tilde{p}(k)\left(1+\frac{\alpha^2}{\beta_c^2}\right);\quad \frac{c_{Np}}{\beta_c}=\tilde{p}(k)\frac{\alpha}{\beta_c}. \qquad \text{(X-3-76)}$$

The law of similarity with respect to the parameters K_1 and K_2 is quite nicely confirmed by calculations and experimental data. These data bring out an important feature: the similarity law remains in force even at small values of K_1, although it was derived on the assumption of M_∞ large enough so that the condition $K_1 > 1$ would be satisfied for small β_p.

This is clearly seen in Fig. X-3-18, which presents experimental data on the pressure distribution as a function of attack angle on the surfaces of two cones with angles $\beta_c = 0.166$ and 0.102 for $M_\infty = 2.75$ and 4.46. The product $M_\infty\beta_c$ gives the same value, $K_1 = 0.455$, for both bodies. In the experiment, the pressure was measured at points corresponding to the angles $\gamma = 0$, 45°, 90°, 135°, and 180°. The function $p_b/p_\infty - 1$ found as a result of the measurements was plotted for each of the cones and a fixed angle γ as a function of K_2.

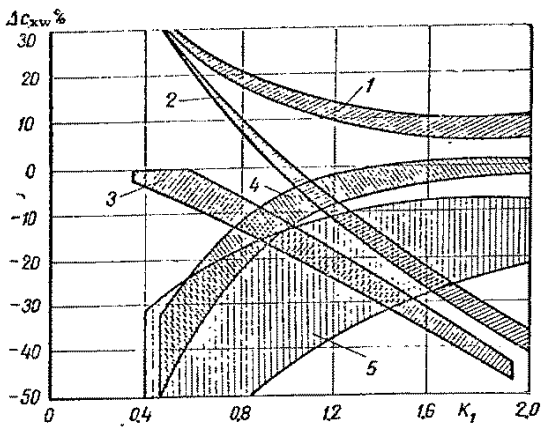

Figure X-3-19. Accuracy of Approximate Methods of Calculating Wave Drag at Zero Angle of Attack as Compared with Method of Characteristics. 1) method of "local" cones (equal-pressure hypothesis); 2) method of "local" cones (equal-velocity hypothesis); 3) linearized theory; 4) combination of conical and expansion flows; 5) Newtonian theory.

As we see from this diagram, the values of the pressure function for corresponding points on the two cones are determined by practically the same curve. Some deviation is observed at large values of the parameter K_2 on the top of the cone. This is explained by the flow separation that appears with increasing attack angle which is not taken into account by the K_2 similarity law. /442

Thus, in using the K_2 similarity law for practical purposes, it must be remembered that it is restricted to small attack angles. As for the M_∞, the K_1 similarity law is practically useful for a rather broad range of values.

Estimation of Error of Approximate Methods

Figure X-3-19 [51] is a graphical representation of data that enable us to establish, as a function of the similarity parameter $K_1 = M_\infty/\lambda_{mid}$, the errors of the various approximate

methods of calculating flow around ogival nose sections as compared with the method of characteristics. We note that the linearized theory (see §XI-2) gives small errors with similarity-parameter values smaller than unity.

In contrast to this method, the accuracy of the Newtonian theory, the first "tangent cone" method (equal-pressure hypothesis), and the method that combines conical and expansion theories increases with increasing similarity parameter K_1. The errors of the second "local cone" method, which is based on the hypothesis of equal velocities, are smaller than those of the first method for similarity parameters not exceeding $K_1 = 1.2$. Thus, at moderate supersonic speeds, when $K_1 \leq 1.2$, better results are obtained when the flow is calculated by the "local cone" method based on the equal-velocity hypothesis. When the parameter $K > 1.2$, preference should be given to the first "tangent cone" method, although its accuracy is poorer than that of the combined conical-and-expansion-flow method. We see from Fig. X-3-19 that the Newtonian theory gives the widest scattering, although the range of dispersion narrows with increasing parameter K_1.

Chapter XI

AERODYNAMICS OF SLENDER BODIES IN LINEARIZED FLOW

§XI-1. APPLICATION OF THE METHOD OF SOURCES

Equations of linearized flow. The aerodynamic characteristics of slender bodies in linearized flow are investigated with Eq. (III-2-31), which reads for steady-state flow conditions

$$(1-M_\infty^2)\varphi'_{xx}+\varphi'_{rr}+\frac{1}{r^2}\varphi'_{\gamma\gamma}+\frac{1}{r}\varphi'_r=0. \qquad \text{(XI-1-1)}$$

For symmetrical flow, this equation is simplified:

$$(1-M_\infty^2)\varphi'_{xx}+\varphi'_{rr}+\frac{1}{r}\varphi'_r=0. \qquad \text{(XI-1-2)}$$

Boundary conditions. Equations (XI-1-1) and (XI-1-2) form the theoretical foundation of linearized-flow aerodynamics. By solving these equations, we find the disturbance potential ϕ', which must satisfy Condition (III-2-58') at the boundary of the body. This condition, which pertains to the general case of flow with strong disturbances, can be modified. For this purpose, we find expressions for the oncoming-flow velocity components in cylindrical coordinates:

$$V_{x\infty}=V_\infty\cos\alpha;\ V_{r\infty}=V_\infty\sin\alpha\cos\gamma;\ V_{\gamma\infty}=-V_\infty\sin\alpha\sin\gamma. \qquad \text{(XI-1-3)}$$

Accordingly, the potential function for the oncoming flow is

$$\Phi_\infty=\varphi_\infty=xV_\infty\cos\alpha+rV_\infty\sin\alpha\cos\gamma. \qquad \text{(XI-1-4)}$$

This expression represents a condition that the disturbed-flow velocity potential must satisfy in addition to the body-boundary condition. A counterpart of this requirement is that the solutions for the velocity components must satisfy Conditions (XI-1-3) in undisturbed flow.

If the sought potential function

$$\Phi = xV_\infty \cos\alpha + rV_\infty \sin\alpha \cos\gamma + \varphi'(x, r, \gamma), \qquad \text{(XI-1-5)}$$

then according to Condition (XI-1-4), the added potential $\phi'(x,r,\gamma)$ in the undisturbed stream must be zero. At the very surface of the body, it must satisfy the nonseparating-flow condition

$$\frac{\Phi_r}{\Phi_x} = \frac{V_\infty \sin\alpha\cos\gamma + \varphi'_r(x, r, \gamma)}{V_\infty \cos\alpha + \varphi'_x(x, r, \gamma)} = \frac{dr}{dx}. \qquad \text{(XI-1-6)}$$

This condition is simplified for linearized flow, since, setting $\cos\alpha \approx 1$ and $\sin\alpha \approx \alpha$, the sought potential function Φ (XI-1-5) can be written in the form

$$\Phi = xV_\infty + rV_\infty \alpha\cos\gamma + \varphi'(x, r, \gamma). \qquad \text{(XI-1-7)}$$

Calculating the derivatives of the total potential function Φ, we find the disturbed-flow velocity components:

$$V_x = V_\infty + \varphi'_x; \; V_r = \alpha V_\infty \cos\gamma + \varphi'_r; \; V_\gamma = -\alpha V_\infty \sin\gamma + \frac{\varphi'_\gamma}{r}. \qquad \text{(XI-1-8)}$$

With these relationships in mind, we obtain the nonseparating-flow condition (XI-1-6) in the presence of an attack angle: /444

$$[V_\infty + \varphi'_x(x, r, \gamma)]\frac{dr}{dx} = \alpha V_\infty \cos\gamma + \varphi'_r(x, r, \gamma). \qquad \text{(XI-1-9)}$$

If the flow is axisymmetric (XI-1-9) is simplified:

$$[V_\infty + \varphi'_x(x, r)]\frac{dr}{dx} = \varphi'_r(x, r). \qquad \text{(XI-1-10)}$$

The velocity potential of a linearized flow around a solid of revolution at an attack angle can be presented as the sum of three components: the free-stream potential ϕ_∞, the potential $\phi_1'(x,r)$ of the disturbed axisymmetric flow, and the potential from disturbance of symmetry $\phi_2'(x,r,\gamma)$.

In linearized-flow theory, ϕ_1' and ϕ_2' are regarded as functions that define mutually independent streams. Hence each of these functions, as a solution of the equation of motion, must satisfy certain boundary conditions. In particular, ϕ_1' must satisfy the axisymmetric-flow condition (XI-1-10). As for the potential ϕ_2', the corresponding condition on the boundary of the

body can be obtained from (XI-1-9). For this purpose, we rewrite (XI-1-9) as follows:

$$(V_\infty + \varphi'_{1x} + \varphi'_{2x})\frac{dr}{dx} = \alpha V_\infty \cos\gamma + \varphi'_{1r} + \varphi'_{2r}, \qquad \text{(XI-1-11)}$$

where $\varphi'_{1x} = \partial\varphi'_1/\partial x$, $\varphi'_{2x} = \partial\varphi'_2/\partial x$ etc.

Applying Equality (XI-1-10), in which ϕ'_x and ϕ'_r are replaced by ϕ'_{1x} and ϕ'_{2r}, respectively, and dropping the lower-order term $(dr/dx)\phi'_{2x}$, we obtain the nonseparating-flow condition from (XI-1-11):

$$V_{2r} = -\alpha V_\infty \cos\gamma. \qquad \text{(XI-1-11')}$$

General expressions for the potential function and the pressure. Calculation of the distribution of the gasdynamic variables around a slender solid of revolution in linearized flow is based in the case of steady flow at an angle of attack on differential equation (XI-1-1) for the disturbance potential ϕ'. It was indicated above that the solution of this equation is sought as the sum of the potentials $\phi = \phi_\infty + \phi'_1 + \phi'_2$, which apply respectively for the undisturbed stream, axisymmetric flow $\phi'_1(x,r)$, and flow with disturbed symmetry $\phi'_2(x,r,\gamma)$.

On the basis of (XI-1-2) and (XI-1-1), we obtain for ϕ'_1 and ϕ'_2

$$(1-M_\infty^2)\varphi'_{1xx} + \varphi'_{1rr} + \frac{\varphi'_{1r}}{r} = 0; \qquad \text{(XI-1-12)}$$

$$(1-M_\infty^2)\varphi'_{2xx} + \varphi'_{2rr} + \frac{1}{r^2}\varphi'_{2\gamma\gamma} + \frac{1}{r}\varphi'_{2r} = 0. \qquad \text{(XI-1-13)}$$

Thus,,the parameters of nonaxisymmetric flow around a solid of revolution will be found if we solve two independent problems: the problem of flow around the body at zero angle of attack and the problem of the additional flow that arises from disturbance of symmetry. Here the solution of the second problem is obtained with the solution to the first, and it can be shown that a definite relation exists between ϕ'_1 and ϕ'_2.

For this purpose, we differentiate the equation of the axisymmetric disturbed flow with respect to r:

$$(1-M_\infty^2)\frac{\partial^2}{\partial r^2}\left(\frac{\partial\varphi'_1}{\partial r}\right) + \frac{\partial^2}{\partial r^2}\left(\frac{\partial\varphi'_1}{\partial r}\right) - \frac{1}{r^2}\frac{\partial\varphi'_1}{\partial r} + \frac{1}{r}\frac{\partial^2\varphi'_1}{r^2} = 0.$$

Comparison of this equation with (XI-1-13) and application of boundary condition (XI-1-11') indicates that /445

$$\varphi_2' = -\frac{\partial \varphi_1'}{\partial r}\cos\gamma. \qquad \text{(XI-1-14)}$$

Consequently, the total disturbance potential for nonaxisymmetric flow is

$$\varphi' = \varphi_1' - \frac{\partial \varphi_1'}{\partial r}\cos\gamma. \qquad \text{(XI-1-15)}$$

We have examined the case of steady flow. However, Expression(XI-1-14) for ϕ_2' can also be extended to nonsteady flow, as we can see if we use the more general equation (III-2-31) as our point of departure.

Having determined the total additional potential ϕ' with consideration of the boundary conditions, we calculate the velocities and then the pressures with (III-3-14). Substituting the approximate value $V_r = V_\infty(dr/dx)$ for the radial velocity component in accordance with the nonseparating-flow condition and replacing V_x' and V_γ by their expressions in terms of the added potential ϕ', which in this case is a function of the coordinates x, r, γ and time t, we find

$$\bar{p} = \frac{-2}{V_\infty^2}\left[V_\infty\varphi_x' + \frac{V_\infty^2}{2}\left(\frac{dr}{dx}\right)^2 + \frac{1}{2}\left(\frac{\varphi_\gamma'}{r} - \alpha V_\infty \sin\alpha\right)^2 + \varphi_t' - \frac{\alpha^2 V_\infty^2}{2}\right]. \qquad \text{(XI-1-16)}$$

The pressure coefficient can be presented as the sum of two components, namely $\bar{p} = \bar{p}_1 + \bar{p}_2$. One of the components, $\bar{p}_1$, is determined from the conditions of longitudinal axisymmetric flow with the aid of the formula

$$\bar{p}_1 = \frac{-2}{V_\infty^2}\left[V_\infty\varphi_{1x}' + \frac{V_\infty^2}{2}\left(\frac{dr}{dx}\right)^2 + \varphi_{1t}'\right], \qquad \text{(XI-1-17)}$$

while the other, $\bar{p}_2$, is found from the transverse-flow conditions as a function of attack angle:

$$\bar{p}_2 = \frac{-2}{V_\infty^2}\left[V_\infty\varphi_{2x}' + \frac{1}{2}\left(\frac{\varphi_{2\gamma}'}{r} - \alpha V_\infty \sin\gamma\right)^2 + \varphi_{2t}' - \frac{\alpha^2 V_\infty^2}{2}\right]. \qquad \text{(XI-1-18)}$$

If the flow condition is steady, the partial time derivatives ϕ'_{1t} and ϕ'_{2t} in these expressions are zero. We can also present the case in which the axisymmetric flow component is steady and the pressure coefficient

$$\bar{p}_1 = -2\left[\varphi'_{1x} + \frac{1}{2}\left(\frac{dr}{dx}\right)^2\right], \qquad \text{(XI-1-19)}$$

where the derivative ϕ'_{1x} is a dimensionless quantity referred to V_∞.

If the transverse flow is nonsteady, the pressure coefficient must be calculated by (XI-1-18). If, on the other hand, the transverse flow is also steady, we have

$$\bar{p}_2 = -2\left[\varphi'_{2x} + \frac{1}{2}\left(\frac{\varphi'_{2x}}{r} - \alpha\sin\gamma\right)^2 - \frac{\alpha^2}{2}\right]; \qquad \text{(XI-1-20)}$$

where the constant V_∞ is included in the value of potential ϕ'_2.

Formula (XI-1-18) for $\bar{p}_2$ can be simplified if we apply (XI-1-14) for ϕ'_2 and Condition (XI-1-1'), which we use to evaluate the ratio $\phi'_{2\gamma}/r$.

Let us present (XI-1-14) in the form $\varphi_2 = -(1/r)[r(\partial\varphi'_1/\partial r)]\cos\gamma$. As will be shown (see page 612), the quantity $\partial\phi'_1/\partial r = V_{1r}$ as $r \to 0$ has the structure $f(x)/r$ and, consequently, the product rV_{1r} as $r \to 0$ tends to the limit $f(x)$. We shall use this as a point of departure in evaluating the ratio $\phi'_{2\gamma}/r$. Differentiating (XI-1-14) with respect to γ, we find that for small enough r /446

$$V_\gamma = -\frac{\varphi'_{2\gamma}}{r} = -\frac{1}{r^2} f(x)\sin\gamma,$$

while differentiation of the r derivative gives the additional radial velocity component (also for $r \to 0$):

$$V_{2r} = \varphi'_{2r} = -\frac{1}{r^2} f(x)\cos\gamma.$$

By Condition (XI-1-11'), this component is $-\alpha V_\infty \cos\gamma$ on the surface of the body. Consequently, the function $f(x) = -\alpha V_\infty r^2$, so that $\phi'_{2\gamma}/r = -\alpha V_\infty \sin\gamma$. After substituting this expression into

(XI-1-18) we obtain

$$\bar{p}_2 = -2\left[\varphi'_{2x} + \frac{\alpha^2}{2}(4\sin^2\gamma - 1) + \varphi'_{2t}\right], \qquad \text{(XI-1-21)}$$

where the derivative ϕ'_{2t} is a dimensionless variable referred to the squared velocity V_∞^2.

The total pressure coefficient for nonsteady flow at an angle of attack is

$$\bar{p} = -2\left[\varphi'_{1x} + \frac{1}{2}\left(\frac{dr}{dx}\right)^2 - \varphi'_{1rx}\cos\gamma + \frac{\alpha^2}{2}(4\sin^2\gamma - 1) + \varphi'_{2t}\right], \qquad \text{(XI-1-22)}$$

where the second derivative ϕ'_{1rx} is a dimensionless quantity referred to the squared velocity V_∞^2.

In steady flow

$$\bar{p}_2 = -2\left[-\varphi'_{1rx}\cos\gamma + \frac{\alpha^2}{2}(4\sin^2\gamma - 1)\right]. \qquad \text{(XI-1-23)}$$

Consequently, the total pressure coefficient is

$$\bar{p} = -2\left[\varphi'_{1x} + \frac{1}{2}\left(\frac{dr}{dx}\right)^2 - \varphi'_{1rx}\cos\gamma + \frac{\alpha^2}{2}(4\sin^2\gamma - 1)\right], \qquad \text{(XI-1-24)}$$

where the derivatives ϕ'_{1x} and ϕ'_{1rx} in (XI-1-24) depend only on the variables $\underline{x}$ and $\underline{r}$.

Substituting this expression into (I-3-14), we note that the basic axial-force-coefficient component is independent of attack angle and is determined by the conditions of axisymmetric flow. The increment is due to disturbance of symmetry and depends on the square of the attack angle.

The influence of α can be disregarded accurate to terms of the second negative order, and it can be assumed that it is sufficient to determine the pressure distribution around a solid of revolution in axisymmetric flow in order to calculate the axial-force coefficient. The wave-drag coefficient found as a result of the calculation will also be equal to the axial-force coefficient.

The method of sources. It follows from the relationships obtained above that the problem of linearized flow around a slender

body will have been solved if we find the additional velocity potential ϕ_1' of the axisymmetric stream. Its value is then used directly to calculate the velocity and pressure distributions and the wave drag at zero angle of attack.

Let us use the method of sources to determine ϕ_1'. In this method, the added velocity potential is sought with (IV-3-3). Setting y = r in this expression and including the minus sign in the value of the function f(ε), we obtain

$$\varphi_1' = -\int_0^{x-\alpha' r} \frac{f(\varepsilon)\,d\varepsilon}{\sqrt{(x-\varepsilon)^2-(\alpha')^2 r^2}}, \qquad \text{(XI-1-25)}$$

where $\alpha' = \sqrt{M_\infty^2 - 1}$.

The source-distribution law, i.e., the form of the function f(ε), must be such that one of the streamlines of the resultant flow will coincide with the generatrix of the solid of revolution when we superimpose the undisturbed stream on the flow from these sources. In other words, the potential function ϕ_1' must satisfy the nonseparating-flow condition. /447

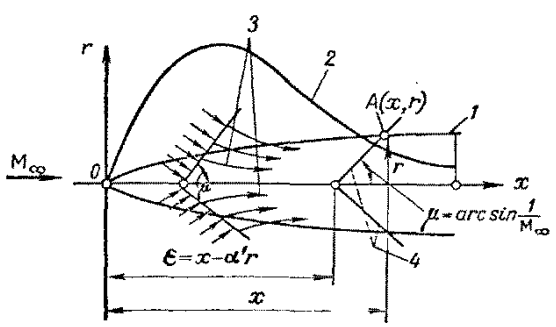

Figure XI-1-1. Distribution of Supersonic Sources Along Axis of a Solid of Revolution. 1) generatrix of body; 2) source intensity distribution curve; 3) streamlines from sources; 4) Mach line.

In using the method of sources, it must be remembered that in supersonic flow, the source disturbances are propagated only inside Mach cones with their apices at the sources.

Thus, if we take a system of sources that are continuously distributed along the axis of the body (Fig. XI-1-1), the velocity and other parameters at any point A(x,r) will be determined by the disturbances emanating from sources situated upstream, beginning at point ε = x - α'r and extending to point ε = x = 0. At point ε = x = 0, the source intensity is zero, since it is assumed that there are no disturbances at ε ≤ 0. This means that the vertex of the body is at point x = 0.

The values of the integration limits in (XI-1-25) will be understood on this basis. The form of the f(ε) [or f(x)] curve

representing the source-distribution law for a slender body with arbitrary generatrix is represented in Fig. XI-1-1. This curve determines the continuous nature of small disturbances in linearized flow.

To find general relationships for velocity and pressure, we transform (XI-1-25) with the new variable

$$z = \operatorname{arch} \frac{x-\varepsilon}{\alpha' r}. \qquad \text{(XI-1-26)}$$

Remembering that

$$\operatorname{ch} z = \frac{x-\varepsilon}{\alpha' r}; \quad \varepsilon = x - \alpha' r \operatorname{ch} z; \quad d\varepsilon = -\alpha' r \operatorname{sh} z \, dz,$$

we find by substituting this expression into the integrand in (XI-1-25)

$$\varphi_1' = \int_0^{\operatorname{arch}(x/\alpha' r)} f(x - \alpha' r \operatorname{ch} z) \, dz. \qquad \text{(XI-1-25')}$$

We have (XI-1-14) for the disturbance potential in flow at an angle of attack. Using it and differentiating (XI-1-25') with respect to r, we find /448

$$\varphi_2' = \alpha' \cos\gamma \int_0^{\operatorname{arch}(x/\alpha' r)} m(x - \alpha' r \operatorname{ch} z) \operatorname{ch} z \, dz, \qquad \text{(XI-1-27)}$$

where m is the derivative of the function f with respect to the argument x - α'r cosh z, i.e., m = f'(x - α'r cosh z).

Converting in (XI-1-27) from the variable z to the variable ε = x - α'r cosh z and remembering that m(ε) = f'(ε), we obtain

$$\varphi_2' = \frac{\cos\gamma}{r} \int_0^{x-\alpha' r} \frac{m(\varepsilon)(x-\varepsilon) \, d\varepsilon}{\sqrt{(x-\varepsilon)^2 - (\alpha')^2 r^2}}. \qquad \text{(XI-1-27')}$$

The integral ϕ_2' represents the dipole potential, and the function m(ε) describes their distribution. Consequently, the additional disturbance from the dipoles is equivalent to the disturbance that the body introduces into the stream in nonaxisymmetric flow.

In substituting axially distributed dipoles for the body, it must be remembered that, like the disturbances from the sources, those from dipoles are propagated in supersonic flow only downstream and within Mach cones.

§XI-2. AXISYMMETRIC FLOW

Calculation of Velocity and Pressure

Differentiating the function ϕ_1' defined by (XI-1-25') with respect to $\underline{x}$ and $\underline{r}$ and setting the source intensity at the point of the body $f(\varepsilon) = f(0) = 0$, we obtain for the velocity components

$$\varphi'_{1x} = V'_x = \int_0^{\operatorname{arch}(x/\alpha' r)} \dot{f}(x - \alpha' r \operatorname{ch} z)\, dz; \qquad \text{(XI-2-1)}$$

$$\varphi'_{1r} = V_r = -\alpha' \int_0^{\operatorname{arch}(x/\alpha' r)} \dot{f}(x - \alpha' r \operatorname{ch} z) \operatorname{ch} z\, dz. \qquad \text{(XI-2-2)}$$

To use these formulas to calculate the velocity components, we must know the function $f(\varepsilon)$. To determine the form of this function, we transform (XI-2-2) to the variable ε in accordance with the condition (XI-1-26)

$$V_r = \frac{1}{r} \int_{x-\alpha' r}^{0} \frac{\dot{f}(\varepsilon)(x-\varepsilon)\, d\varepsilon}{\sqrt{(x-\varepsilon)^2 - (\alpha' r)^2}}. \qquad \text{(XI-2-2')}$$

We shall assume that the value of the integral for surface points differs little from its limiting value on the axis, i.e., as $r \to 0$. Accordingly,

$$V_r = -\frac{1}{r} f(x). \qquad \text{(XI-2-3)}$$

This expression has already been used in determining the order of magnitude of rV_r near the axis (page 608).

Assuming that the component V_r is determined on the surface of a very slender body by Expression (XI-2-3) and using the approximate nonseparating-flow condition $V_r \approx dr/dx$ (which is obtained from the exact relation $V_r/(1 + V'_x)$ with $1 + V'_x \approx 1$), we find the equation of the source-distribution curve for such a body: /449

$$f(x) = -r\frac{dr}{dx}. \qquad \text{(XI-2-4)}$$

Differentiating this function with respect to x, we find the derivative

$$\dot{f}(x) = -\left[\left(\frac{dr}{dx}\right)^2 + r\frac{d^2r}{dx^2}\right]. \qquad \text{(XI-2-5)}$$

Let us assume that the generatrix is given in the form of a parabolic curve:

$$r = \sum_{n=0}^{t} e_n x^{n+1}. \qquad \text{(XI-2-6)}$$

If this expression for r is introduced into (XI-2-5) and the terms in the resulting relationship are arranged by powers of x, we arrive at the following general form of the derivative:

$$\dot{f}(x) = -\sum_{m=0}^{k} d_m x^m. \qquad \text{(XI-2-7)}$$

Expression (XI-2-7) is an approximate one for the derivative of the source distribution function in the case of an arbitrary solid of revolution, since an approximate nonseparating-flow condition was used in deriving it. To improve this relationship, we can introduce into (XI-2-7) the correction factors a_0 and a_1, which will be determined in the course of solving the problem itself. Then, introducing the variable ε instead of x, we find the function $\dot{f}(\varepsilon)$ in the form

$$\dot{f}(\varepsilon) = -\left(a_0 + a_1\sum_{m=1}^{k} d_m\varepsilon^m\right). \qquad \text{(XI-2-8)}$$

Now let us substitute Expression (XI-2-8), setting ε = $= x - \alpha' r \cosh z$, in Eq. (XI-2-2) for the derivative $\dot{f}(\varepsilon)$. As a result of simple manipulation, we obtain for the radial velocity component

$$\dot{V}_r = \alpha'(a_0 i_r^0 + a_1\eta), \qquad \text{(XI-2-9)}$$

where

$$i_r^0 = \int_0^{\operatorname{arch} u} \operatorname{ch} z\, dz; \quad \eta = \int_0^{\operatorname{arch} u}\sum_{m=1}^{k} d_m(x - \alpha' r\operatorname{ch} z)^m \operatorname{ch} z\, dz; \quad u = \frac{x}{\alpha' r}. \qquad \text{(XI-2-10)}$$

A similar relation can be found for the axial velocity component. For this purpose, we introduce Expression (XI-2-8) for the derivative $\dot{f}$ into (XI-2-1), with the result that

$$-V'_x = a_0 i^0_x + a_1 \psi, \qquad \text{(XI-2-11)}$$

where

$$i^0_x = \int_0^{\operatorname{arch} u} dz; \quad \psi = \int_0^{\operatorname{arch} u} \sum_{m=1}^{k} d_m (x - \alpha' r \operatorname{ch} z)^m dz. \qquad \text{(XI-2-12)}$$

It is easily seen that in Expressions (XI-2-10) and (XI-2-12), we must evaluate integrals of the form

$$I_n = \int_0^{\operatorname{arch} u} (\operatorname{ch} z)^n dz, \qquad \text{(XI-2-13)}$$

and that if we limit ourselves to k = 3, each of Eqs. (XI-2-9) and (XI-2-11) contains functions i^n_r and i^n_x, whose values are determined from the expressions /450

$$\left.\begin{aligned} &i^0_r = I_1; \quad i'_r = uI_1 - I_2; \\ &i^2_r = u^2 I_1 - 2uI_2 + I_3; \quad i^3_r = u^3 I_1 - 3u^2 I_2 + 3uI_3 - I_4; \\ &i^0_x = I_0; \quad i'_x = uI_0 - I_1; \\ &i^2_x = u^2 I_0 - 2uI_1 + I_2; \quad i^3_x = u^3 I_0 - 3u^2 I_1 + 3uI_2 - I_3. \end{aligned}\right\} \qquad \text{(XI-2-14)}$$

It proceeds from (XI-2-13) and (XI-2-14) that the functions i^n_r and i^n_x depend only on the parameter u. These functions, calculated for values of the parameter u from 1 to 12.2, are given in Table XI-2-1.

To determine the coefficients a_0 and a_1, it is better to use the nonseparating-flow condition

$$\frac{dr}{dx} = \frac{V_r}{1 + V'_x} = \frac{\alpha' (a_0 i^0_r + a_1 \eta)}{1 - (a_0 i^0_x + a_1 \psi)}; \qquad \text{(XI-2-15)}$$

Let us refer this condition to a conical forward element of a solid of revolution. Then, remembering that k = m = 1 and, consequently, $\eta = \psi = 0$, we obtain

$$a_0 = \left(\frac{dr}{dx}\right)_0 \left[\left(\frac{dr}{dx}\right)_0 (i^0_x)_0 + \alpha' (i^0_r)_0\right]^{-1}, \qquad \text{(XI-2-16)}$$

where $(i_r^0)_0$ and $(i_x^0)_0$ are determined from Expressions (XI-2-10) and (XI-2-12) with the condition that the parameter $u = u_0 = 1/(\alpha'\beta_0)$ on the point of the cone ($x = r = 0$). Consequently,

$$(i_r^0)_0 = \sqrt{u_0^2 - 1}, \quad (i_x^0)_0 = \operatorname{arch} u_0. \tag{XI-2-17}$$

The coefficient a_0 is assumed constant for the entire body. Coefficient a_1 is calculated each time on the basis of the non-separating-flow condition (XI-2-15) for the particular surface point:

$$a_1 = \left[\frac{dr}{dx} - a_0\left(\frac{dr}{dx} i_x^0 + \alpha' i_r^0\right)\right]\left(\alpha'\eta + \frac{dr}{dx}\psi\right)^{-1}. \tag{XI-2-18}$$

The values of the functions i_x^0 and i_r^0 and of η and ψ are found for the $\underline{u}$ at the same point.

Substituting the values found for the coefficients a_0 and a_1 into Formulas (XI-2-9) and (XI-2-11), we can determine the added velocity components. Then, using (XI-1-19), we calculate the pressure coefficient.

By way of illustration, let us consider application of this method to calculation of flow around a solid of revolution with a parabolic generatrix of the form $\bar{r} = \bar{x}(2 - \bar{x})$. In this case,

$$\dot{f}(\varepsilon) = -\left[a_0 + a_1\left(\varepsilon - \frac{\varepsilon^2}{2}\right)\right]. \tag{XI-2-19}$$

Comparing (XI-2-19) and (XI-2-8), we see that $\sum_{m=1}^{k} d_m \varepsilon^m \cdots \varepsilon - \varepsilon^2/2$. Assuming further that the variable $\varepsilon = x - \alpha' r \cosh z$ in (XI-2-19), we obtain on substituting $\dot{f}$ in the integrands of the functions η (XI-2-10) and ψ (XI-1-12) the following expressions for these functions:

$$\eta = \bar{m}\left(i_r' - \frac{\bar{m} i_r^2}{2}\right), \quad \psi = \bar{m}\left(i_x' - \frac{\bar{m} i_x^2}{2}\right), \tag{XI-2-20}$$

where $\bar{m} = \frac{\alpha' r}{2\lambda_{mid}}$, $\bar{r} = \frac{r}{r_{mid}}$.

The functions i_x^2 and i_r^2 are found from the parameter $\underline{u}$ or with Formulas (XI-2-10) and (XI-2-12), or from Table XI-2-1.

TABLE XI-2-1. VALUES OF THE FUNCTIONS $i_x^n(u)$ and $i_r^n(u)$*

/451

u	i_x^0	i_x^1	i_x^2	i_x^3	i_r^0	i_r^1	i_r^2	i_r^3
1.0	0	0	0	0	0	0	0	0
1.1	0.4435	0.0298	0.0019	0.0001	0.4582	0.0303	0.0026	0.0004
1.2	0.6223	0.0838	0.0149	0.0071	0.6633	0.0856	0.0109	0.0015
1.3	0.7567	0.1527	0.0392	0.0095	0.8312	0.1256	0.0383	0.0096
1.4	0.8673	0.2342	0.0753	0.0254	0.9804	0.2526	0.0794	0.0231
1.6	1.047	0.4205	0.2068	0.2412	1.249	0.4756	0.2230	0.1124
1.8	1.177	0.6690	0.4875	0.4631	1.450	0.7166	0.4137	0.2349
2.0	1.317	0.9024	0.7314	0.6332	1.732	1.073	0.8296	0.6956
2.2	1.426	1.177	1.146	1.260	1.960	1.443	1.332	1.318
2.4	1.522	1.472	1.675	2.030	2.182	1.857	1.990	2.326
2.6	1.610	1.785	2.326	3.230	2.400	2.316	2.823	3.776
2.8	1.690	2.116	3.107	4.854	2.615	2.816	3.846	5.946
3.0	1.763	2.461	4.022	7.584	2.828	3.361	5.080	8.422
3.2	1.831	2.820	5.076	9.701	3.040	3.948	6.543	11.90
3.4	1.895	3.193	6.278	13.09	3.250	4.578	8.247	16.32
3.6	1.954	3.578	7.634	17.28	3.458	5.247	10.21	21.84
3.8	2.011	3.975	9.148	22.29	3.666	5.955	12.45	28.63
4.0	2.064	4.382	10.81	28.28	3.873	6.714	14.98	36.84
4.2	2.114	4.800	12.65	37.31	4.079	7.509	17.82	46.59
4.4	2.162	5.227	14.65	43.46	4.286	8.348	21.00	58.31
4.6	2.208	5.665	16.84	52.94	4.490	9.223	24.51	71.98
4.8	2.251	6.111	19.19	63.76	4.694	10.14	28.37	87.74
5.0	2.293	6.565	21.72	75.99	4.899	11.10	32.63	108.1
5.2	2.333	7.028	24.44	89.85	5.103	12.10	37.26	127.0
5.4	2.371	7.498	27.35	105.5	5.306	13.14	42.30	150.9
5.6	2.408	7.976	30.44	122.7	5.510	14.22	47.78	177.9
5.8	2.444	8.462	33.73	141.9	5.713	15.35	53.70	208.3
6.0	2.478	8.953	37.21	163.2	5.916	16.51	60.07	242.4
6.2	2.511	9.452	40.89	186.5	6.119	17.71	66.91	280.3
6.4	2.544	9.958	44.77	212.3	6.322	18.96	74.25	322.8
6.6	2.575	10.47	48.86	240.4	6.524	20.24	82.08	369.8
6.8	2.605	10.99	53.17	271.1	6.726	21.56	90.44	421.4
7.0	2.634	11.51	57.66	304.2	6.928	22.93	99.34	478.4
7.2	2.663	12.04	62.37	340.2	7.130	24.34	108.8	540.7
7.4	2.690	12.58	67.29	379.1	7.332	25.78	118.8	608.8
7.6	2.717	13.12	72.43	421.0	7.534	27.27	129.4	683.4
7.8	2.744	13.66	77.78	466.2	7.736	28.80	140.6	764.9
8.0	2,769	14.22	83.37	514.5	7.937	30.36	152.5	852.2
8.2	2.794	14.49	89.17	566.3	8.138	31.97	165.2	947.8
8.4	2.818	15.33	95.18	621.4	8.341	33.62	178.1	1050.4
8.6	2.842	15.90	101.4	680.7	8.540	35.30	191.8	1161.4
8.8	2.865	16.47	107.9	743.3	8.743	37.04	206.3	1280.6
9.0	2.888	17.05	114.6	810.0	8.944	38.80	221.4	1409.0
9.4	2.932	18.21	128.7	955.8	9.348	42.47	253.6	1694.5
9.8	2.974	19.39	143.7	1119.1	9.751	46.29	289.5	2020.4
10.2	3.014	20.59	159.7	1301.3	10.15	50.26	328.0	2389.8
10.6	3.052	21.80	176.7	1503.4	10.53	54.40	369.8	2807.8
11.0	3.089	23.03	194.7	1726.4	10.95	58.68	415.0	3277.7
11.4	3,126	24.27	213.5	1969.6	11.36	63.19	464.0	3808.3
11.8	3.160	25.53	233.4	2238.2	11.76	67.80	516.4	4394.4
12.2	3.194	26.80	254.4	2530,8	12.16	72,59	572.4	5047.2

The values found for η and ψ enable us to determine the coefficient a_1 for a given point and then to use it to find the disturbance velocity component $V'_x = \phi'_{ix}$. The pressure coefficient can be computed by substituting the latter into (XI-1-19). It must be remembered here that the pressure coefficient component $\Delta\bar{p} = -(dr/dx)^2$ can be found in advance if we know the shape of the body. For example, for a parabolic nose section $\Delta\bar{p}_1 = -\beta_0^2(1 - \bar{x})^2$. /452

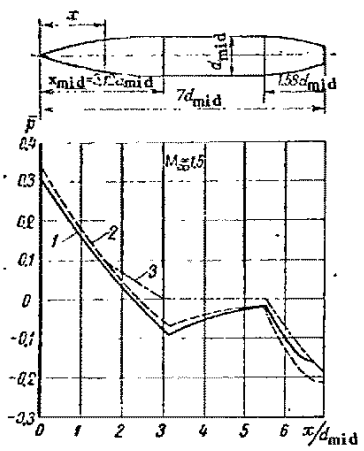

Figure XI-2-1. Pressure on Surface of Body with Parabolic Nose and Tail Sections. 1) by method of characteristics; 2) linearized theory; 3) "local cone" method.

This method can be used for approximate calculation of flow around solids of revolution that represent combinations of elements. For example, we might consider a body consisting of a nose section and a cylindrical part. A tapering tail surface element or a segment with any other shape may be attached at the rear.

Figure XI-2-1 shows the pressure distribution calculated for the cylindrical and tail segments of a solid of revolution for $M_\infty = 1.5$. As we see, the pressure increases downstream along the cylindrical section beginning at the end of the nose section, while the flow around the tapering tail section is accompanied by a drop in pressure over most of its length.

For comparison, Fig. XI-2-1 also shows curves calculated by the method of characteristics and by the "local cone" method.

Flow around the cylindrical section is characterized by recovery of the pressure to atmospheric; this takes place almost entirely on a length of slightly more than two diameters, measured from the end of the nose section. The pressure decrease on the tapering tail section does not continue over its entire length. We see some pressure increase in the vicinity of the base section or the point of the tail.

The accuracy of this method of calculating linearized flow increases with increasing taper. It may become unnecessary to introduce the correction factors a_0 and a_1 into (XI-2-7) for very slender bodies. In this case, it is necessary to proceed from (XI-2-4), which can be rewritten $f(x) = \frac{-1}{2\pi}\frac{dS(x)}{dx} = -S'(x)/2\pi$, where $S(x) = \pi r^2$ is the current value of the slender body's cross-sectional area. Then

$$f(x) = -\frac{1}{2\pi}\frac{d^2S(x)}{dx^2} = -\frac{S''(x)}{2\pi}. \qquad \text{(XI-2-21)}$$

Converting in this expression to the variable ε, substituting ε = x - α'r cosh z, and then substituting the value found for the derivative f(ε) under the integral in (XI-2-11), we obtain

$$V'_x = -\frac{1}{2\pi}\int_0^{\operatorname{arch} u} S''(x-\alpha' r\operatorname{ch} z)\,dz. \qquad \text{(XI-2-22)}$$

If the shape of the body is given, we can find the function S, determine its second derivative S", and then evaluate the integral of (XI-2-22); this will enable us to calculate the additional velocity component.

Suppose, for example, that we have a given parabolic nose section whose generatrix equation is /453

$$r = (x/2\lambda_{\text{mid}})(2 - x/x_{\text{mid}}).$$

Consequently, the cross-sectional area and the second derivative of the function S will be, respectively (with ε substituted for x),

$$S(\varepsilon) = \frac{\pi}{4\lambda^2_{\text{mid}}}\left(4\varepsilon^2 - \frac{4\varepsilon^3}{x_{\text{mid}}} + \frac{\varepsilon^4}{x^2_{\text{mid}}}\right); \quad S''(\varepsilon) = \frac{2\pi}{\lambda^2_{\text{mid}}}\left(1 - \frac{6\varepsilon}{x_{\text{mid}}} + \frac{3\varepsilon^2}{x^2_{\text{mid}}}\right). \qquad \text{(XI-2-23)}$$

Substituting x - α'r cosh z for ε in the expression for the second derivative and substituting it into the integrand of (XI-1-22), we obtain on integration

$$V'_x = -\frac{\Omega_1}{2\pi}, \qquad \text{(XI-2-24)}$$

where

$$\Omega_1 = \int_0^{\operatorname{arch} u} S''(x-\alpha' r\operatorname{ch} z)\,dz = \frac{\pi}{\lambda^2_{\text{mid}}}\left(2i^0_x - \frac{6\bar{x}i'_x}{u} + \frac{3\bar{x}^2 i^2_x}{u^2}\right).$$

A difference in the results of the above two methods can be brought out by comparing, for example, the axial velocity components on the point of a cone. In the first method [Formula (XI-2-11)] and in the second (XI-2-24), these components are defined by the respective relationships

$$V'_x = -\beta_p (i^{(1)}_x)_0 [\beta_p (i^0_x)_0 + \alpha' (i^0_r)_0]^{-1}; \quad V'_x = -\frac{(i^0_x)_0}{\lambda^2_{\text{mid}}} = -\beta^2_p (i^0_x)_0. \qquad \text{(XI-2-24')}$$

It is easily seen that the second expression can be obtained from the first if the cone is very slender. In fact, the term $\beta_p(i_x^0)_0$ in the square brackets is of higher negative order in this case and can be disregarded. As for the remaining term, it is reduced to the form $\alpha'(i_r^0)_0 \approx \beta_p^{-1}$ at small β_p.

Formulas (XI-2-24') enable us to estimate the order of magnitude of the disturbance in a flow around a slender cone. As we see, the added disturbance velocity component is of the order of the square of the small cone angle. In the general case of an arbitrary generatrix, this component is of the order of τ^2. According to the nonseparating-flow condition, the radial disturbance velocity component is $V_r = dr/dx$ and consequently of the order of τ. Thus, the disturbances in the longitudinal direction are an order smaller than those in the transverse direction. For this reason, terms containing the squares of the disturbances in the transverse direction were retained in (XI-1-19) for the pressure.

Similarity law for pressure function and drag coefficient. Let us examine the pressure-coefficient relation

$$\bar{p} = \frac{\Omega_1}{\pi} - \left(\frac{dr}{dx}\right)^2. \qquad \text{(XI-2-25)}$$

We see from (XI-2-24) that the function Ω_1 depends for a given point with coordinate $\bar{x}$ on the parameter $u = x/(\alpha' r)$ and the slenderness ratio λ_{mid}, which, in turn, determines the point angle β_p ($\beta_p = 1/\lambda_{mid}$). The parameter u can be presented in general form as $u = u_0 h(\bar{x})$, where, e.g., the function $\bar{h}(x) = 2(2 - \bar{x})^{-1}$ for a parabolic generatrix.

On the basis of the above, the pressure coefficient in general form is

$$\bar{p} = \beta_p^2 N(u_0, \bar{x}), \qquad \text{(XI-2-26)}$$

where N is a certain function of the parameter u and the dimensionless coordinate $\bar{x}$.

Applying (I-3-14), we find a general relation for the wave drag coefficient: /454

$$c_{xw} = \beta_p^2 D(u_0), \qquad \text{(XI-2-27)}$$

where D is a certain function of the parameter u_0.

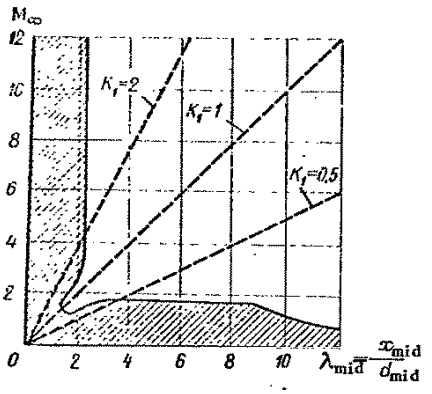

Figure XI-2-2. Region of Possible Application of Similarity Law for Conical Nose Sections (Similarity is Doubtful in the Shaded Area).

Formulas (XI-2-26) and (XI-2-27) permit the following inference as to similarity of flows around solids of revolution. If these flows are characterized by equal parameters u_0, the ratios p/β_p^2 will be the same at corresponding points; this follows directly from (XI-2-26). It follows from another formula (XI-2-27) that solids of revolution in gasdynamically similar flows experience axial forces such that the ratios $c_{x\,w}/\beta_p^2$ will be the same for these bodies. Thus, the flow-similarity criterion in this case is the parameter

$$u_0 = (\alpha'\beta_p)^{-1} = (\beta_p\sqrt{M_\infty^2 - 1})^{-1}. \qquad \text{(XI-2-28)}$$

Relation (XI-2-26) can be presented in a somewhat different form for cases in which the M_∞ are quite large and we can set $\sqrt{M_\infty^2 - 1} \simeq M_\infty$. For this purpose, we introduce the similarity parameter $K_1 = M_\infty/\lambda_{mid} = M_\infty\beta_p$. Multiplying (XI-2-26) by M_∞^2 and applying the expression for the similarity parameter, we obtain a relation for the pressure function:

$$\frac{p}{p_\infty} - 1 = N_1(K_1, \bar{x}). \qquad \text{(XI-2-29)}$$

Thus, the pressure function at a given point $\bar{x}$ depends only on the similarity parameter $K_1 = M_\infty\beta_p$.

The law of similarity in this parameter is confirmed by a calculation of the pressure distribution by the method of characteristics. Satisfactory results are obtained only for K_1 smaller than unity.

The law of similarity in the parameter K_1 (or u_0) is found to be doubtful for certain combinations of M_∞ and fineness ratio λ_{mid}.

Physically, this occurs on deviation of the real from the linearized flow for thick bodies with small slenderness ratios or at very large M_∞. To preserve the linearized nature of the flow, it is necessary to taper the body more strongly as the M_∞ increase. Here, as follows from (XI-2-24), the inequality $u_0 > 1$ must be observed.

It follows from the expression $u_0 = (\alpha'\beta_p)^{-1}$ that if a solid of revolution is sufficiently slender, i.e., its slenderness ratio is large, the condition $M_\infty > 1$ must be satisfied to preserve the inequality $u_0 > 1$. If, however, $M_\infty \to 1$ (XI-2-28) indicates that the absolute value of the disturbance velocity becomes infinite, and this is physically impossible. Thus, the theory of linearized flows and their similarity laws are applicable when the two inequalities $\lambda_{mid} > \sqrt{M_\infty^2 - 1}$ and $M_\infty > 1$ are observed simultaneously.

The regions of possible application of linearized-flow theory and the corresponding similarity laws are shown in Fig. IX-1-6 (for an ogival nose section) and Fig. XI-2-2 (for a cone), where the shaded region corresponds to doubtful similarity. Accordingly, /455 it is not recommended that calculations be made for small fineness ratios $\lambda_{mid} < 2$ and moderate M_∞. In practical cases, the M_∞ selected should be at least 1.3-1.5.

If in Figs. IX-1-6 and XI-2-2 we draw $K_1 = \text{const}$ lines corresponding to parameter values smaller than unity, for which similarity gives satisfactory results, we can find the corresponding nose-section slenderness ratio from these lines for a given M_∞.

Similarity in parameter K_1 also defines similarity for the wave drag function $M_\infty^2 c_{x\,w}$.

Multiplying both sides of (XI-2-27) by M_∞^2, we obtain a general expression for this function: $M_\infty^2 c_{x\,w} = H(K_1)$.

The Wave Drag Coefficient

Wave drag of a slender cone. The relation found for the additional axial disturbance velocity component on a cone, (XI-2-24), can be used to determine the pressure coefficient on it and, consequently, its coefficient of wave drag.

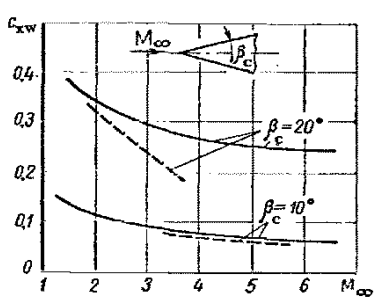

Figure XI-2-3. Wave Drag Coefficient for a Sharp Cone. ——— exact theory; -----linearized theory.

In accordance with (XI-1-19), we find

$$\bar{p}_c = c_{xw} = 2(i_x^0)_c A - \beta_c^2, \qquad \text{(XI-2-30)}$$

where

$$A = [(i_x^0)_c + (\alpha'/\beta_c)(i_r^0)_c]^{-1};$$

$(i_x^0)_c$ and $(i_r^0)_c$ are the functions calculated from Expressions (XI-2-17) after substituting the parameter $u_0 = (\alpha'\beta_c)^{-1}$.

This formula can be simplified slightly for values of $u_0 > 3$:

$$\bar{p}_c = c_{xw} = \beta_c^2 (4.606 \lg 2u_0 - 1). \qquad \text{(XI-2-31)}$$

A comparison of the results of calculation of the wave drag coefficient by (XI-2-30) and by the exact theory is given in Fig. XI-2-3. Up to large M_∞, the agreement is good for slender cones. A substantial discrepancy appears between the results for moderate M_∞ and thicker cones, as we see from Fig. XI-2-3 in the example of the cone with $\beta_c = 20°$. Obviously, the flow around this cone deviated substantially from the linearized flow. In using the flow calculation methods set forth above, therefore, it is necessary to hold strictly to the indicated rules for determining the permissible M_∞ and angles β_c for which the linearized flow is not disturbed.

Wave drag of solids of revolution composed of conical elements. Figure XI-2-4 shows several possible schemes of solids of revolution that incorporate individual conical elements. In the general case, it is necessary to know the pressure distribution over the surface of the bodies in order to calculate their wave-drag coefficients. Figure XI-2-5 presents experimental data on this distribution for $M_\infty = 2$, as obtained by wind-tunnel tests on a model solid of revolution consisting of a conical nose section, a cylindrical part, and a truncated tail cone. Calculation by the linearized theory gives about the same results.

Calculation of the flow around the tail segment encounters certain difficulties owing to the fact that, strictly speaking, this flow can be calculated if the flow parameters have been found on the section of the surface in front of the tail and including the cylindrical section. /456

This complete calculation can be performed either by the linearized theory or by the method of characteristics. However, it requires a great deal of time. At the same time, there is a practical need for simple method of approximate determination of the flow parameters on the stern, and pressure in particular; this would enable us to find the component of total drag and take the influence of the tail section into consideration.

For this purpose, we can use (VIII-1-18), which, as we have noted, gives an almost exact value of the wave drag coefficient for a nose cone. Here, as we see from (XI-2-5), the actual value of the pressure coefficient on a conical stern element is found to be smaller than that obtained by Formula (VIII-1-18). Hence the pressure distribution found by this formula must be regarded as an approximate evaluation of the true picture. Use of Formula (VIII-1-18) enables us to find a comparatively simple but very close approximate relation for the wave-drag coefficients of

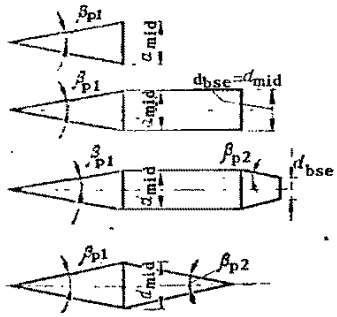

Figure XI-2-4. Shapes of Solids of Revolution.

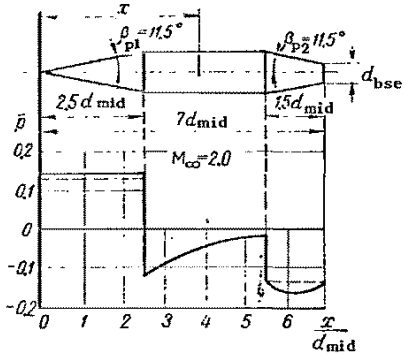

Figure XI-2-5. Pressure Distribution Curves for a Body Composed of Conical Elements. ——— experiment; ----- according to cone formula.

solids of revolution that consist of conical elements.

Let us assume that $\bar{p}_1$ and $\bar{p}_2$ are the respective coefficients of pressure on the forward and aft cones, and that the dimensionless quantity $\bar{S}_{bse}$ defines the tail taper, which is equal to $\bar{S}_{bse} = S_{bse}/S_{mid} = (d_{bse}/d_{mid})^2$. Then, applying (I-3-14), we obtain

$$c_{xw} = \bar{p}_1 + \bar{p}_2 (1 - \bar{S}_{bse}). \qquad \text{(XI-2-32)}$$

Here the first term gives the nose-cone drag $c^{n}_{x\,w} = \bar{p}_1$, while the second gives the tail (stern) drag $c^{tl}_{x\,w} = \bar{p}_2 (1 - \bar{S}_{bse})$.

Replacing $\bar{p}_1$ and $\bar{p}_2$ in Formula (XI-2-32) by their expressions according to (VIII-1-18), we find

$$c_{xw} = 0.002\,(0.8 + M_\infty^2)\,[(\beta_{p1})^{1.7} + (\beta_{p2})^{1.7}]\,(1 - \bar{S}_{bse}), \qquad \text{(XI-2-33)}$$

where β_{p1} and β_{p2} are the angles of the nose and tail cones in degrees.

The part of the drag /457

$$c^{tl}_{xw} = 0.002\,(0.8 + M_\infty^2)\,(\beta_{p2})^{1.7}\,(1 - \bar{S}_{bse}) \qquad \text{(XI-2-34)}$$

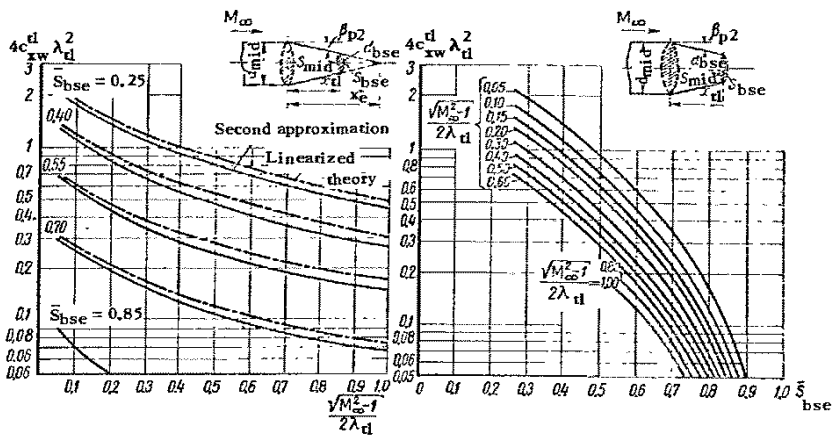

Figure XI-2-6. Curves for Determination of Wave Drag Coefficients of Conical Tail Sections.

belonging to the tail element can be separated from the expression in the right member of this formula. This part can be determined by using the results given in Fig. XI-2-6. Some of these results were obtained from the linearized theory, and others by a more exact theory with a second approximation and all results found for conical tail sections on the assumption that they are quite far from the nose. In this case, pressure recovers fully in front of the tail section, so that the velocity is equal to its value for the oncoming flow.

In calculations using the curves in Fig. XI-2-6, the slenderness ratio of the tail section is first determined from the known data by the formula $\lambda_{tl} = x_{tl}/d_{mid}$ or from the expression $\lambda_{tl} = (1 - \bar{S}^{1/2}_{bse})(2\beta^\circ_{p_2})^{-1}$, followed by calculation of the parameter $(M^2_\infty - 1)^{1/2}(2\lambda_{tl})^{-1}$. The product $4c^{st}_{x\,w}\lambda^2_{st}$ is found for this parameter from the diagram and used to determine $c^{st}_{x\,w}$.

Calculations made with the data in Fig. XI-2-6 indicate that it gives better results than Formula (XI-2-34) if the approximating relationship

$$c^{d}_{xw} = 0.002\,(0.8 + M^2_\infty)\,(\beta^\circ_{p2})^{1.7}\sqrt{1 - \bar{S}_{bse}} \qquad \text{(XI-2-35)}$$

is used.

Then, adding the nose-cone drag

$$c_{xw}^{n} = 0.002\,(0.8 + M_{\infty}^{2})\,(\beta_{01}^{\circ})^{1.7}. \qquad \text{(XI-2-36)}$$

to this component, we obtain a formula for the total drag coefficient:

$$c_{xw} = c_{xw}^{n}\left[1 + \left(\frac{\beta_{p2}}{\beta_{p1}}\right)^{1.7}\sqrt{1 - \bar{S}_{bse}}\right]. \qquad \text{(XI-2-37)}$$

If the angles β_{p1} and β_{p2} of the nose and tail cones are equal, (XI-2-37) becomes

$$c_{xw} = 0.002\,(0.8 + M_{\infty}^{2})\,(\beta_{p1}^{\circ})^{1.7}\,(1 + \sqrt{1 - \bar{S}_{bse}}). \qquad \text{(XI-2-38)}$$

The tail section may expand instead of tapering. In the latter case, the base section is larger than the midships section. As a result, the drag coefficient of the solid of revolution becomes even larger. Here the drag will be larger the larger the taper angle and slenderness ratio of the tail cone. /458

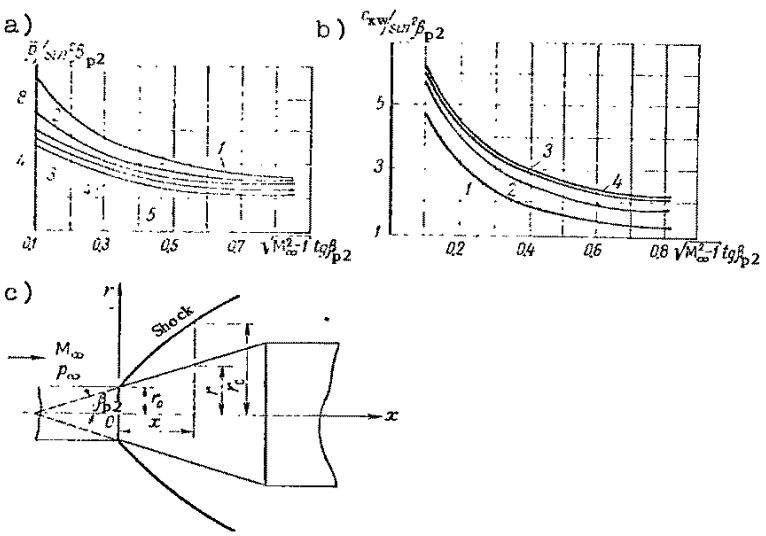

Figure XI-2-7. Diagrams (a and b) for Determination of Pressure and Wave Drag of Expanding Body Section (c) ($1.5 < M_\infty < 3.5$; $5^\circ < \beta_{p2} < 20^\circ$). Curves 1, 2, 3, 4, and 5 Correspond to r/r_0 Ratios of 1.25, 1.5, 1.75, 2, and 3; $c_{x\,w}$ is Referred to the Maximum Area of the Expanding Part.

Investigation of the drag component produced by an expanded tail cone is a complex problem. It is simpler if the taper angle is small. In this case, the method of characteristics could be used. If, on the other hand, the angles are large, only experimental investigation gives reliable enough results.

However, the method of "local cones" can be used for rough estimation of the flow-variable values, on the assumption that the gas moves at the free-stream velocity in front of an expanding conical stern.

In this method, drag is determined as a part of the drag of the full cone with the same generatrix inclination angle. Consequently, the wave drag coefficient of a conical stern will depend on the tail-cone slenderness ratio $\lambda_{tl} = x_{tl}/d_{mid}$ (or on the taper angle β_{p_2}), $\bar{S}_{bse}$, and M_∞.

Figure XI-2-7, a and b ([70], 1963, No. 41) presents diagrams with which the pressure and the coefficient $c_{x\,w}^{tl}$ can be determined.

Wave drag of a slender solid of revolution with an arbitrary generatrix. The general case of calculation of the wave-drag coefficient requires calculation of the pressure distribution followed by application of (I-3-14).

This general method enables us to obtain the necessary results with sufficient accuracy for an arbitrary solid of revolution, for which possible shapes are shown in Fig. XI-2-8.

At the same time, as in the case of flow calculations for solids of revolution composed of conical elements, we can consider approximate relationships by which we can evaluate the wave-drag coefficient comparatively easily for arbitrary solids of revolution. /459

Nose sections of various shapes. We see from Fig. XI-2-8 that the nose sections have a dual role. They may be independent vehicles (Fig. XI-2-8, models Nos. 1 and 2) or component forward elements of solids of revolution (Fig. XI-2-8, models Nos. 3-6). In the latter case, the nose-section drag is part of the total drag of the body as a whole.

The flow around the nose section can be calculated by the "local-cone" method, using Formula (XI-2-31).

For a slender nose section with a parabolic generatrix and a local inclination angle $\beta = \beta_p(1 - \bar{x})$ of the tangent at an arbitrary point, the approximate relation for pressure takes the form

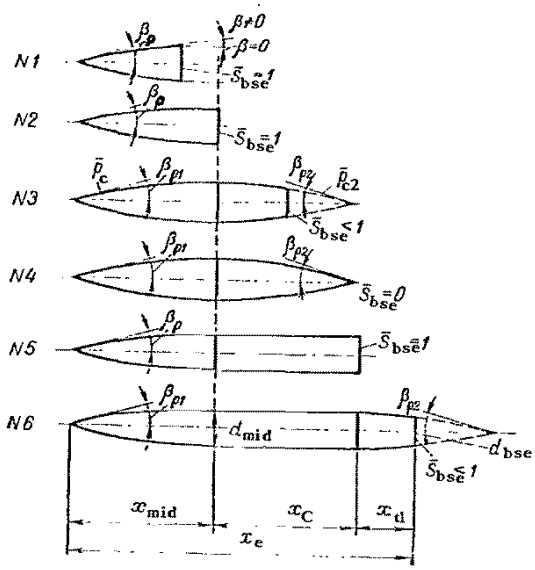

Figure XI-2-8. Certain Shapes of Bodies with Arbitrary Generatrices.

$$M_\infty^2 \bar{p} = 2K_1^2 (1-\bar{x})^2 \ln \times \times \{2[K_1(1-\bar{x})]^{-1}\} - K_1^2 (1-\bar{x})^2, \quad \text{(XI-2-39)}$$

where $K_1 = M_\infty \beta_p$.

The wave drag coefficient of the nose section can be calculated by this relationship, using (I-3-14'):

$$M_\infty^2 c_{xw} = K_1^2 \left(\frac{2}{3} \ln \frac{2}{K_1} + \frac{5}{18} \right). \quad \text{(XI-2-40)}$$

In using this formula, it must be remembered that it was derived for the complete nose section (Fig. XI-2-8, Model No. 2). A similar relationship is easily obtained for the truncated nose section (Fig. XI-2-8, Model No. 1).

In addition to (XI-2-40), the wave drag of a slender parabolic or ogival nose section can be calculated by the somewhat more general expressions (XI-1-26) and (XI-1-27). However, the latter formula gives overstated values of the wave drag coefficient for the full nose section. Better results are obtained if 0.332 is used instead of the coefficient 0.415:

$$c_{x\ w} = 0.332 \bar{p}_c. \quad \text{(XI-2-41)}$$

Tapered tail section. The distribution around a tapered tail section can be calculated by the method of characteristics. Here, if the cylindrical section is long enough, the calculation begins from the joint between the cylinder and the stern, where the local velocity can be set equal to the free-stream value.

The results obtained on this assumption indicated that the pressure coefficient at a certain point on the surface of the tail element depends on tan β and the coordinate ratio r/x. The angle β defines the inclination of the tangent to the generatrix at a particular point to the axis of the body, while the coordinate x is equal to the distance from this point to the intersection of the Mach line drawn through the origin of the tail section with the axis of the body. Curves characterizing the /460

variation of the pressure coefficient on the tail section as a function of the parameters tan β and r/x are given in Fig. XI-2-9 for various M_∞.

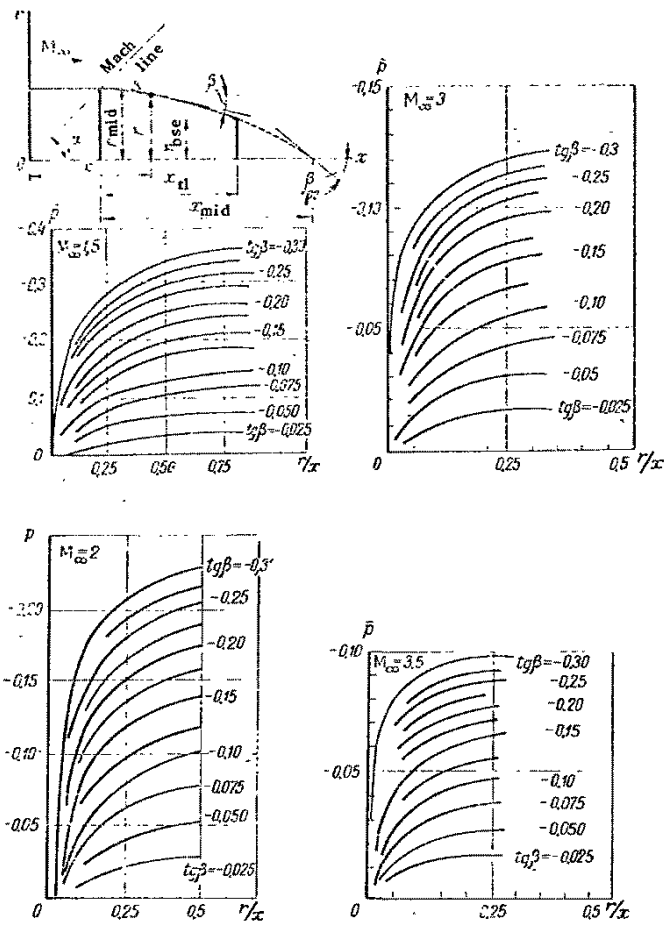

Figure XI-2-9. Curves Characterizing Variation of Pressure Coefficient on Stern Surface at Various M_∞.

The added drag coefficient $c_{x\,w}^{tl}$ that results from the influence of the stern can be calculated from the pressure distribution. Such data, obtained for a tail element made in the form of a parabolic solid of revolution, appear in Fig. XI-2-10.

It is clear from these diagrams that $c_{x\,w}^{tl}$ depends on the stern slenderness ratio $\lambda_{tl} = x_{tl}/d_{mid}$ (x_{tl} is the length of the

tail segment), the base taper $\bar{S}_{bse}$, and M_∞. Here, the diagrams themselves reflect the law of variation of $4\lambda_{tl}^2 c_{x\,w}^{tl}$ as a function of the parameters $(2\lambda_{tl})^{-1}\sqrt{M_\infty^2 - 1}$ and $\bar{S}_{bse}$. We can easily satisfy ourselves that the latter parameter depends on the slenderness ratio λ_{tl} of the real tail section and the ratio $\lambda_{mid} = \tan^{-1}\beta_{02} = x_{mid}/d_{mid}$ of a certain virtual parabolic solid obtained by grafting the tail section to the full nose section, as shown in Fig. XI-2-9. The corresponding relationships for $\bar{S}_{bse}$ has the form $\bar{S}_{bse} = (1 - \lambda_{tl}^2/\lambda_{mid}^2)^2$. /461

Figure XI-2-11 presents curves calculated by the method of characteristics for determination of the wave drag of an expanding parabolic tail section.

In addition to the method of characteristics, the "local cone" method can be used for approximate evaluation of the influence of the stern on wave drag.

Let us consider application of this method for a tail section made in the form of a parabolic solid with taper $\bar{S}_{bse}$. We shall assume that the fineness ratio of the virtual nose section constructed on the basis of the given tail element is λ_{mid}, and that the corresponding angle of the cone at the point is β_{p_2} (Fig. XI-2-8, Models Nos. 3, 4, and 6). Then if $\bar{p}_{c_2}$ is the (negative) pressure coefficient on the tail cone, we find with (I-3-14) that /462

$$c_{xw}^{tl} = \int_{\bar{S}_{bse}}^{1} \bar{p}_{c2}\, d\bar{r}^2. \qquad \text{(XI-2-42)}$$

Substituting $\bar{p}_{c_2}$ from (VIII-1-18) into this formula with $\beta = 57.3\beta_p(1 - \bar{x})$ substituted for β_c and then improving the resulting relationship by use of the characteristic-method data, we obtain the approximate formula

$$c_{xw}^{tl} = 0.4\bar{p}_{c2}\left[1 - 2.41\bar{S}_{bse}^{4/3}\left(1 - 0.49\bar{S}_{bse}^{1/2} + 0.056\bar{S}_{bse} - 0.151\bar{S}_{bse}^{3/2}\right)\right], \qquad \text{(XI-2-43)}$$

where $\bar{p}_{c_2}$ is the pressure coefficient on a cone with angle β_{p_2}.

Applying (XI-2-43) and Expression (XI-2-41), we obtain for the total wave-drag coefficient of a body with parabolic nose and tail sections:

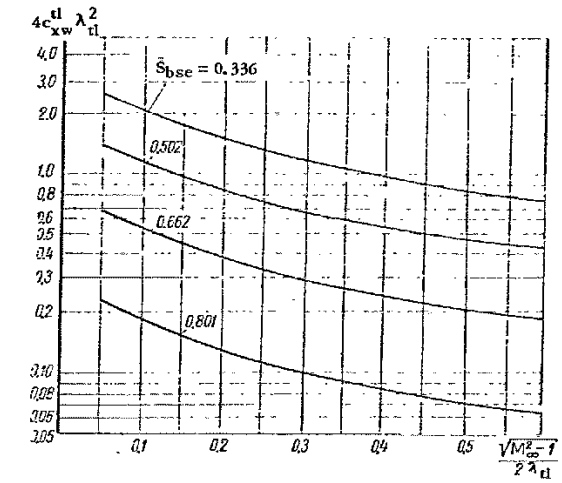

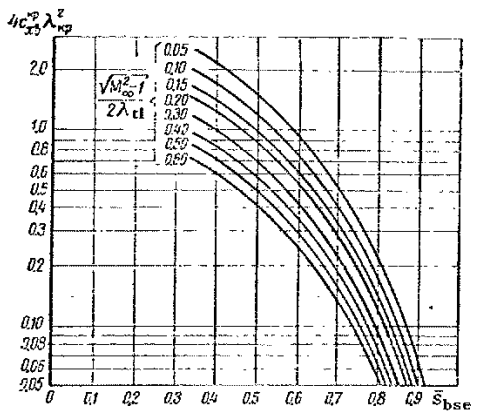

Figure XI-2-10. Drag of Tapering Tail Section with Parabolic Generatrix. $\lambda_{tl} = x_{tl}/x_{mid}$ (Diagrams Obtained by the Method of Characteristics).

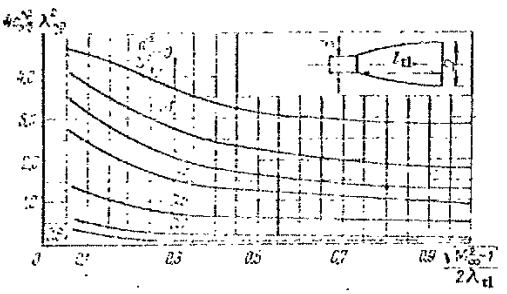

Figure XI-2-11. Illustrating Calculation of Wave Drag of Expanding Parabolic Tail Section. $\lambda_{tl} = \ell_{tl}/D$.

$$c_{xw} = 0.332\bar{p}_{c1} + 0.4\bar{p}_{c2}\,[1 - 2.41\bar{S}_{bse}^{4/3}\,(1 - 0.49\bar{S}_{bse}^{1/2} + 0.056\bar{S}_{bse} - 0.151\bar{S}_{bse}^{3/2})], \quad \text{(XI-2-44)}$$

where $\bar{p}_{c1}$ is the pressure coefficient calculated for a cone with angle β_{p1}.

When the body's stern is a cone with base taper $\bar{S}_{bse}$, the total wave drag coefficient is calculated by the simpler formula

$$c_{xw} = 0.332\bar{p}_{c1} + \bar{p}_{c2}\sqrt{1 - \bar{S}_{bse}}, \quad \text{(XI-2-45)}$$

where $\bar{p}_{c2}$ is found from the known angle β_{p2} of the conical element.

Very Slender Body

The relationships presented above for wave drag pertained to slender bodies for which the flow parameters depend more or less substantially on M_∞; here, the investigations showed that this dependence becomes weaker as the body becomes more slender. In the theoretical limiting case with $r \to 0$, supersonic disturbed flow will no longer depend on compressibility. In practice, this corresponds to a very slender body with a large slenderness ratio.

The above limiting case is examined in aerodynamics in a special department known as the "aerodynamics of slender bodies."

According to this theory, the relation for the wave-drag coefficient is found from the general expression (IV-5-30). Its specific form depends on the shape of the slender body.

Body tapered at both ends. For such a body, S'(1) = 0. /463
Moreover, the last term in (IV-4-30) is also zero, since the contour C over which the integral is evaluated shrinks to a point. Hence the wave-drag coefficient is

$$c_{xw} = \frac{X_w}{qS_{mid}} = -\frac{1}{2\pi S_{mid}} \int_0^1 \int_0^1 S''(x) S''(\xi) \ln|x-\xi| \, dx \, d\xi. \qquad \text{(XI-2-46)}$$

The same relationship will also obtain when $\alpha = 0$ and the body has a cylindrical base. In fact, the derivative $S'(1) = 0$ in this case. In addition, the radial velocity component $\partial\phi_0/\partial\nu$ also vanishes at the end of the body by the nonseparating-flow condition. Hence the second and third terms on the right side of (IV-4-30) are zero, and the drag coefficient formula assumes the form (XI-2-46).

Nonaxisymmetric body with circular base. Attack angle $\alpha = 0$. For a body lacking axial symmetry in the general case but having a circular base, the drag formula (IV-4-30) can be presented in a more concrete form. For this purpose, we write an expression for the function dr/dx, determined for points of the base section, in series form [51]:

$$\left(\frac{dr}{dx}\right)_{x=1} = \sum_{m=0}^{\infty} f_{2m} \cos 2m \left(\frac{\pi}{2} - \gamma\right), \qquad \text{(XI-2-47)}$$

where the f_{2m} are certain dimensionless quantities.

Calculating the derivative $(\partial\phi_0/\partial r)_{x=1}$ by (IV-4-7) and remembering that $(\partial\phi_0/\partial r)_{x=1} = (dr/dx)_{x=1}$, we find the coefficients A_n and B_n and then determine the integral $\oint_C \varphi_0 (\partial\varphi_0/\partial\nu) \, d\tau = \int_0^{2\pi} \varphi_0 (\partial\varphi_0/dr) \, r_0 \, d\theta$. Introducing the value found for the integral into (VI-4-30), we find for the wave-drag coefficient

$$c_{xw} = \frac{X_w}{qS_{mid}} = -\frac{1}{2\pi S_{mid}} \int_0^1 \int_0^1 \ln|x-\xi| S''(x) S''(\xi)\, dx\, d\xi + \\ + \frac{S'(1)}{2\pi S_{mid}} \int_0^1 \ln(1-\xi) S''(\xi)\, d\xi - \frac{1}{2\pi S_{mid}} [S''(1)]^2 \ln\frac{\alpha' r_{bse}}{2} + \\ + \frac{\pi}{S_{mid}} \sum_{m=1}^{\infty} \frac{f_{2m}^2 r_{bse}^2}{2m}. \qquad \text{(XI-2-48)}$$

For an axisymmetric solid of revolution, Formula (XI-2-48) is simplified, since the last term vanishes. In its simplified form, the formula determines the drag of a body whose tail section tapers in the general case. At the end of such a body, the derivative $S'(1) = 0$.

Shape of Solid of Revolution with Minimum Wave Drag

Total drag can be minimized for certain conditions (flight speeds, attack angle, volume and length of body, etc.) by appropriate adaptation of the shape of the body. We shall consider bodies offering minimum wave drag: optimum nose sections obtained in the aerodynamic theory of the slender body for zero attack angle. The shapes of these nose sections are found by calculating the function (XI-2-46), which determines wave drag.

Body symmetrical about center point of axis, with zero cross-sectional area at the ends. This body, which has come to be known as the Sears-Haak body [51], has a minimum wave drag of /464

$$c_{xw} = \frac{24V_b}{x_e^3} \qquad \text{(XI-2-49)}$$

for an assigned body volume. The distribution of area along the axis is given by the formulas

$$S(0) = \frac{16V_b}{3\pi x_e} \sin^3\theta; \; S\left(\frac{x_e}{2}\right) = S_{mid} = \frac{16V_b}{3\pi x_e}, \qquad \text{(XI-2-50)}$$

where the angle θ is related to the x-coordinate by

$$x = \frac{1}{2} x_e (1 + \cos\theta). \qquad \text{(XI-2-51)}$$

We see from this relation that the forward point ($x = 0$) corresponds to an angle $\theta = \pi$, while the end point ($x = x_e$) corresponds to $\theta = 0$. For the center point with its coordinate $x = x_e/2$ (the point of largest cross section), $\theta = \pi/2$.

Optimum nose section with base section S_{mid}. Karman derived the shape of the optimum nose section. It gives minimum wave drag for given body length x_e and base-section area $S(x_e) = S_{bse}$ if $S'(x_e) = 0$ at the end point. For this body, therefore, $S(x_e) = S_{bse} = S_{mid}$. The drag coefficient of this nose section is

$$c_{xw} = \frac{4S_{mid}}{\pi x_e^2}. \qquad \text{(XI-2-52)}$$

The distribution of areas along the axis is given by the equation

$$S(x) = \frac{S_{mid}}{\pi}\left(\pi - \theta + \frac{1}{2}\sin 2\theta\right), \qquad \text{(XI-2-53)}$$

where $S_{mid} = 2W_b/x_e$ and the angle θ is related to x by (XI-2-51). In contrast to the Sears-Haak body, for which an angle $\theta = \pi/2$ corresponds to the maximum-section point ($x = x_e/2$), the Karman nose section has $\theta = 0$ corresponding to this cross section ($x = x_e$).

Equation (XI-2-53) describes the generatrix of a slightly blunted slender solid of revolution. Despite the blunting, the drag nevertheless remains very small, since the tail sections of the body are situated in a zone of reduced pressure owing to the nose effect.

The drag of bodies of optimum shape shows little dependence on flow conditions. This means that if, for example, a Karman nose section is placed in a flow at very high velocity, its shape will remain close to optimum even under these conditions. Thus, the optimum nose-section shape from the standpoint of minimum drag under a given set of conditions depends little on the law used in calculating the pressure distribution.

§XI-3. FLOW AROUND SOLIDS OF REVOLUTION AT AN ANGLE OF ATTACK

Pressure Distribution in Nonaxisymmetric Flow

Basic relationships. The nonaxisymmetric-flow problem reduces to determination of the added pressure coefficient $\bar{p}_2$ that appears as a result of disturbance of flow symmetry. This pressure depends on the disturbance potential ϕ_2' in transverse flow, which is the integral of differential equation (XI-1-13) and can be expressed in general form by (XI-1-14). The total pressure coefficient in nonaxisymmetric flow is $\bar{p} = \bar{p}_1 + \bar{p}_2$, where $\bar{p}_1$ /465

depends only on the variables $\underline{x}$ and $\underline{r}$, but $\bar{p}_2$ also depends on the variable γ.

In the linearized flow, the normal-force coefficient is determined in accordance with (I-4-11) as

$$c_{Np} = -\frac{4\lambda_b}{\pi}\int_0^1 \bar{r}\,d\tilde{x}\int_0^{\pi}\bar{p}_2\cos\gamma\,d\gamma. \qquad \text{(XI-3-1)}$$

Thus, the normal-force coefficient depends only on the non-axisymmetric-flow conditions. To evaluate this coefficient, it is necessary to find the distribution of the coefficient $\bar{p}_2$, calculation of which requires calculation of the added potential ϕ_2' defined by (XI-1-27) or (XI-1-27').

The nonseparating-flow condition (XI-1-11') must be attached to the equation for ϕ_2'. Including the constant V_∞ in the values of the added axial V_x' and radial V_r' disturbance-velocity components for simplicity and differentiating (XI-1-27) with respect to first $\underline{x}$ and then $\underline{r}$, we find

$$\varphi'_{2x} = V'_x = \alpha'\cos\gamma\int_0^{\operatorname{arch} u}\dot{m}\,(x-\alpha' r\operatorname{ch} z)\operatorname{ch} z\,dz; \qquad \text{(XI-3-2)}$$

$$\varphi'_{2r} = V'_r = -(\alpha')^2\cos\gamma\int_0^{\operatorname{arch} u}\dot{m}\,(x-\alpha' r\operatorname{ch} z)\operatorname{ch}^2 z\,dz, \qquad \text{(XI-3-3)}$$

where the derivative

$$\dot{m} = m'(\varepsilon)\big|_{\varepsilon=x-\alpha' r\operatorname{ch} z}$$

Equating the right members of (XI-3-3) and (XI-1-11'), we obtain the equation

$$\alpha = (\alpha')^2\int_0^{\operatorname{arch} u}\dot{m}\,(x-\alpha' r\operatorname{ch} z)\operatorname{ch}^2 z\,dz \qquad \text{(XI-3-4)}$$

for determination of the function $m(\varepsilon)$.

On the basis of our expression (XI-3-2) for the additional axial velocity component, we find the pressure coefficient

$$\bar{p}_2 = -2\alpha'\cos\gamma\int_0^{\operatorname{arch} u}\dot{m}\,(x-\alpha' r\operatorname{ch} z)\operatorname{ch} z\,dz - \alpha^2(4\sin^2\gamma - 1). \qquad \text{(XI-3-5)}$$

As we see, a quadratic term has appeared in this expression; it enables us to improve the pressure-coefficient value. If the attack angles are very small, this term can be disregarded; then

$$\overline{p}_2 = -2\alpha' \cos\gamma \int_0^{\operatorname{arch} u} \dot{m}(x - \alpha' r \operatorname{ch} z) \operatorname{ch} z \, dz. \qquad \text{(XI-3-6)}$$

Calculation of flow variables. We shall examine a calculation method based on the law of dipole distribution along the axis of a very slender body as the first approximation. The form of the function m(x) that corresponds to this law can be found from (XI-3-4) if we set $\varepsilon = x - \alpha' r \cosh z$ in it:

$$\int_0^{x-\alpha' r} \frac{\dot{m}(\varepsilon)(x-\varepsilon)^2 \, d\varepsilon}{\sqrt{(x-\varepsilon)^2 - (\alpha' r)^2}} = \alpha r^2. \qquad \text{(XI-3-7)}$$

For a very slender body (r very small), αr^2 can be assumed equal in first approximation to its value for $r \to 0$. Then $\alpha r^2 \int_0^x \dot{m}(\varepsilon)(x-\varepsilon) \, d\varepsilon$. Setting $u = x - \varepsilon$, $dv = \dot{m} \, d\varepsilon$ and integrating by parts, remembering that m(0) = 0 at the tip, we obtain $\int_0^x m(\varepsilon) \, d\varepsilon = \alpha r^2$. /466

From this we find the law of dipole distribution along the axis of a very slender body: $m = 2\alpha r(dr/dx)$. It is interesting to note that this law is of the same type as the law of source distribution.

The relationship given above for the function m can be used to calculate flow around other than very slender bodies in much the same way as was done in §XI-2 in connection with use of the first approximation for the source distribution function f of the symmetrical case. As an illustration, let us consider a specific case of flow around a body with a parabolic generatrix.

Bearing in mind the expression obtained for the function m, we find the derivative $\dot{m}(\varepsilon)$. Correcting the distribution law thus found for this derivative by introducing the constant coefficients a_0 and a_1, we obtain

$$\dot{m}(\varepsilon) = \alpha\left[a_0 + a_1\left(\varepsilon - \frac{\varepsilon^2}{2}\right)\right]. \qquad \text{(XI-3-8)}$$

Converting in this equation from ε to the variable z and including the constant α' in the coefficients a_0 and a_1,

$$\dot{m}(x - \alpha' r \operatorname{ch} z) = \alpha\{a_0 + a_1(u - \operatorname{ch} z)\overline{m}[1 - 0.5\overline{m}(u - \operatorname{ch} z)]\}. \qquad \text{(XI-3-9)}$$

Introducing this expression for the function $\dot{m}$ into (XI-3-4), we obtain the nonseparating-flow condition by integrating:

$$a_0 j_r^0 + a_1(j_r^1 - 0.5\overline{m} j_r^2) = (\alpha')^{-1}. \qquad \text{(XI-3-10)}$$

From this we can find the two coefficients a_0 and a_1. To determine the former, it is necessary to refer Condition (XI-3-10) to the point of the cone ($x = \varepsilon = 0$); the second coefficient is found from the same condition written for an arbitrary surface point. The result is

$$a_0 = [\alpha'(j_r^0)_0]^{-1}; \quad a_1 = [(\alpha')^{-1} - a_0 j_r^0](j_r^1 - 0.5\overline{m} j_r^2)^{-1}. \qquad \text{(XI-3-11)}$$

In Expressions (XI-3-10) and (XI-3-11), j_r^n is a certain function that depends only on the parameter $u = x/(\alpha' r)$. In particular cases, the function $(j_r^0)_0$ depends on the parameter $u = u_0 = (\alpha'\beta_p)^{-1}$ at the point of the cone.

To obtain a relationship for the additional axial disturbance-velocity component in transverse flow, we introduce (XI-3-9) into (XI-3-2) and integrate:

$$V_x' = \alpha \cos\gamma \left\{ \frac{j_x^0}{\alpha'(j_r^0)_0} + \frac{j_x' - 0.5\overline{m} j_x^2}{j_r' - 0.5\overline{m} j_r^2}\left[1 - \frac{j_r^0}{(j_r^0)_0}\right]\frac{1}{\alpha'} \right\}, \qquad \text{(XI-3-12)}$$

where j_x^n is a certain function of the same parameter u.

The functions j_r^n and j_x^n introduced here are analogous to the i_r^n and i_x^n examined in our study of axisymmetric flow.

If we are concerned with the somewhat more general case of assignment of the derivative $\dot{m}(\varepsilon)$, as in the form of a third-degree parabola [a term in ε^3 appears in (XI-3-8)], substituting it into (XI-3-2) and (XI-3-3) leads us to relationships that incorporate the functions: /467

$$\left.\begin{aligned} j_x^0 &= I_1; \; j_x' = uI_1 - I_2; \; j_x^2 = u^2 I_1 - 2uI_2 + I_3; \\ j_x^3 &= u^3 I_1 - 3u^2 I_2 + 3uI_3 - I_4; \\ j_r^0 &= I_2; \; j_r' = uI_2 - I_3; \; j_r^2 = u^2 I_2 - 2uI_3 + I_4; \\ j_r^3 &= u^3 I_2 - 3u^2 I_3 + 3uI_4 - I_5, \end{aligned}\right\} \qquad \text{(XI-3-13)}$$

where the I_n are functions representing integrals of the form (XI-2-13). We might point out that the functions j_x^n repeat the corresponding functions i_r^n that were introduced in the axisymmetric case. Values of the other functions j_r^n defined by (XI-3-13) have been computed for various parameters $\bar{u}$ and are presented in Table XI-3-1. In using this table, as for Table XI-2-1 for axisymmetric flow, it must be remembered that they were drawn up for $\bar{u}$ ranging from 1 to 12.2. If necessary, when it is found in the course of the calculation that the values of $\bar{u}$ are not covered by the table, the corresponding values of the functions i^n and j^n must be calculated by Formulas (XI-2-14) and (XI-3-13) to supplement the table. This may become necessary in investigating flows around long slender solids at small M_∞.

As we see, determination of the additional velocity component V_x' for given α and cos γ by Formula (XI-3-12) necessitates calculation of the values of the functions j_x^n and j_r^n and the parameter $\bar{m}$ at the point under consideration, as well as $(j_r^0)_0$ for the cone at the tip.

Having found this component, we can use (XI-1-23) to compute the additional pressure coefficient:

$$\bar{p}_2 = -2\alpha\cos\gamma\left(\frac{V_x'}{\alpha\cos\gamma}\right) - \alpha^2(4\sin^2\gamma - 1), \qquad \text{(XI-3-14)}$$

where the ratio $V_x'/(\alpha\cos\gamma)$ is independent of α cos γ and is determined from (XI-3-12).

This method of calculating nonaxisymmetric flow can be simplified. For this purpose, we shall use results from the theory of flow around slender bodies. In determining the law of dipole distribution with this theory, e.g., in the form of (XI-3-8), it is unnecessary to correct with the coefficients a_0 and a_1.

For a very slender solid of revolution, the function $\bar{m}$ can be presented in the form $m = (\alpha/\pi)S'(x)$ and its derivative as $\dot{m} = (\alpha/\pi)S''(x)$. Accordingly, the added axial velocity component is

$$V_x' = \frac{\alpha\alpha'}{\pi}\cos\gamma\int_0^{\operatorname{arch} u} S''(x-\alpha' r\operatorname{ch} z)\operatorname{ch} z\,dz. \qquad \text{(XI-3-15)}$$

As an example, let us consider application of this relation for calculation of flow around a solid of revolution with a

TABLE XI-3-1. VALUES OF THE FUNCTIONS $j_r^n(u)$*

/468

u	j_r^0	j_r^1	j_r^2	j_r^3
1	0	0	0	0
1.1	0.4736	$0.3090 \cdot 10^{-1}$	$0.2300 \cdot 10^{-2}$	$0.1173 \cdot 10^{-3}$
1.2	7090	8394	$0.1450 \cdot 10^{-1}$	$0.3326 \cdot 10^{-2}$
1.3	8824	$0.1719 \cdot 10^{0}$	4021	$0.1031 \cdot 10^{-1}$
1.4	$0.1120 \cdot 10$	2688	8462	2862
1.6	1523	5378	$0.2416 \cdot 10^{0}$	$0.1191 \cdot 10^{0}$
1.8	1894	8758	5519	4109
2.0	$0.2391 \cdot 10$	$0.1317 \cdot 10$	$0.9632 \cdot 10^{0}$	$0.7850 \cdot 10^{0}$
2.2	2869	1813	$0.1599 \cdot 10$	$0.1490 \cdot 10$
2.4	3380	2467	2450	2740
2.6	3925	3197	3579	4536
2.8	4506	4039	5024	7103
3.0	$0.5124 \cdot 10$	$0.5001 \cdot 10$	$0.6827 \cdot 10$	$0.1086 \cdot 10^{2}$
3.2	5780	6092	9040	1538
3.4	6472	7316	$0.1172 \cdot 10^{2}$	2158
3.6	7202	8682	1491	2954
3.8	7966	$0.1020 \cdot 10^{2}$	1868	3939
4.0	$0.8778 \cdot 10$	$0.1187 \cdot 10^{2}$	$0.2309 \cdot 10^{2}$	$0.5209 \cdot 10^{2}$
4.2	9623	1371	2821	6745
4.4	$0.1051 \cdot 10^{2}$	1573	3409	8609
4.6	1143	1792	4081	$0.1085 \cdot 10^{3}$
4.8	1239	2030	4844	1330
5.0	$0.1339 \cdot 10^{2}$	$0.2288 \cdot 10^{2}$	$0.5703 \cdot 10^{2}$	$0.1669 \cdot 10^{3}$
5.2	1443	2566	6678	2040
5.4	1551	2865	7763	2472
5.6	1663	3187	8974	2974
5.8	1779	3531	$0.1032 \cdot 10^{3}$	3552
6.0	$0.1899 \cdot 10^{2}$	$0.3899 \cdot 10^{2}$	$0.1180 \cdot 10^{3}$	$0.4214 \cdot 10^{3}$
6.2	2022	4291	1344	4971
6.4	2150	4708	1524	5831
6.6	2282	5151	1721	6803
6.8	2417	5621	1936	7899
7.0	$0.2556 \cdot 10^{2}$	$0.6118 \cdot 10^{2}$	$0.2171 \cdot 10^{3}$	$0.9130 \cdot 10^{3}$
7.2	2700	6644	2426	$0.1051 \cdot 10^{4}$
7.4	2847	7198	2703	1204
7.6	2999	7783	3002	1376
7.8	3154	8399	3326	1565
8.0	$0.3313 \cdot 10^{2}$	$0.9045 \cdot 10^{2}$	$0.3674 \cdot 10^{3}$	$0.1779 \cdot 10^{4}$
8.2	3476	9723	4049	1997
8.4	3644	$0.1044 \cdot 10^{3}$	4453	2262
8.6	3814	1118	4884	2541
8.8	3990	1196	5348	2849
9.0	$0.4169 \cdot 10^{2}$	$0.1278 \cdot 10^{3}$	$0.5842 \cdot 10^{3}$	$0.3189 \cdot 10^{4}$
9.4	4540	1452	6935	3950
9.8	4927	1642	8171	4855
10.2	5327	1846	9563	5916
10.6	5747	2067	$0.1112 \cdot 10^{4}$	7154
11.0	$0.6177 \cdot 10^{2}$	$0.2305 \cdot 10^{3}$	$0.1287 \cdot 10^{4}$	$0.8592 \cdot 10^{4}$
11.4	6631	2563	1483	$0.1026 \cdot 10^{5}$
11.8	7096	2837	1698	1216
12.2	7578	3130	1937	1437

parabolic generatrix. For this body, the second derivative S" is given by (XI-2-23). Substituting it into the integrand of (XI-3-15), we obtain

$$V'_x = \frac{\alpha\alpha'}{\pi}\cos\gamma\Omega_2, \qquad \text{(XI-3-16)}$$

where

$$\Omega_2 = \int_0^{\operatorname{arch} u} S''(x-\alpha' r\operatorname{ch} z)\operatorname{ch} z\,dz = \frac{\pi}{\lambda_{\text{mid}}^2}\left(2i_r^0 - \frac{6\bar{x}i_r'}{u} + \frac{3\bar{x}^2 i_r^2}{u^2}\right). \qquad \text{(XI-3-17)}$$

The above methods can be used to evaluate velocity and, consequently, pressure on the cylindrical and tail sections of a body. Here the tail section must taper or expand slightly to preserve the linearized character of the flow. /469

Law of flow similarity. According to (XI-3-16), the function $V'_x/(\alpha\cos\gamma)$ at a given point depends on $\underline{u}$. It was shown in §XI-2 that this parameter is determined in turn by its value u_0 on the cone at the tip and by a certain function $\underline{h}$ of the variable $\bar{x}$, i.e., $u = u_0 h(\bar{x})$. Consequently, if we take into account that the function $(j_r^0)_0$ depends on the same parameter u_0, we can write the following general expression for the added pressure coefficient in accordance with (XI-3-16):

$$\bar{p}_2 = -2\alpha\beta_p G(u_0, \bar{x})\cos\gamma - \alpha^2(4\sin^2\gamma - 1), \qquad \text{(XI-3-18)}$$

where G is a certain function that depends on u_0 for a given surface point.

Let us examine cases in which M_∞ is large and the solid of revolution has a parabolic generatrix, so that its slenderness ratio $\lambda_{\text{mid}} = 1/\beta_0$. Then, multiplying (XI-3-18) by M_∞^2, we find

$$\frac{p_2}{p_1} - 1 = -\alpha\lambda_{\text{mid}}K_1^2 B_1(K_1, \bar{x})\cos\gamma - (\alpha\lambda_{\text{mid}})^2 K_1^2(4\sin^2\gamma - 1), \qquad \text{(XI-3-19)}$$

where B_1 is a certain function defined at a given point by the parameter $K_1 = M_\infty\beta$.

Denoting the parameter $\alpha\lambda_{\text{mid}}$ by K , we write (XI-3-19) in general form:

$$\frac{p_2}{p_1} - 1 = B(K_1, K_2, \bar{x}, \gamma). \qquad \text{(XI-3-20)}$$

We see from this expression that the pressure function at a given point depends on K_1 and K_2, which are the similarity parameters of flows around slender solids of revolution at an angle of attack.

In accordance with (I-4-11) and (I-5-8), the normal-force and moment coefficients will depend on the same parameters:

$$M_\infty^2 c_{Np} = E(K_1, K_2); \quad M_\infty^2 m_{zp} = F(K_1, K_2), \tag{XI-3-21}$$

where E and F are certain functions of the parameters K_1 and K_2.

Normal-Force Coefficient

Solid of revolution with arbitrary generatrix. If we know the distribution of the additional coefficient $\bar{p}_2$ in nonaxisymmetric flow, we can calculate the normal-force coefficient. We use Formula (I-4-11) for this purpose. Remembering that

$$\int_0^\pi (4\sin^2\gamma - 1)\cos\gamma\, d\gamma = 0,$$

we obtain

$$c_{Np} = 4\lambda_{mid}\alpha \int_0^{\bar{x}_b} \frac{V'_x}{\alpha\cos\gamma}\bar{r}\, d\bar{x}; \quad \bar{x} = \frac{x}{x_{mid}}. \tag{XI-3-22}$$

For the particular case of a parabolic-generatrix solid of revolution, this formula can be transformed to

$$c_{Np} = 4\lambda_{mid}\alpha \int_0^{t_b} \frac{V'_x}{\alpha\cos\gamma}\, dt, \tag{XI-3-23}$$

where $t = \bar{x}^2[1 - (\bar{x}/3)]$.

Practical interest attaches to study of the function $V'_x/(\alpha\cos\gamma)$ as it varies along the body. This function determines the element of normal-force coefficient referred to a unit length of the body, in accordance with the formula /470

$$\frac{V'_x}{\alpha\cos\gamma} = \frac{1}{4\alpha\lambda_{mid}} \frac{dc_{Np}}{d\bar{x}} \frac{1}{\bar{r}}. \tag{XI-3-24}$$

We see from Fig. XI-3-1 that the normal force coefficient element vanishes at a length of approximately $2d_{mid}$ measured from

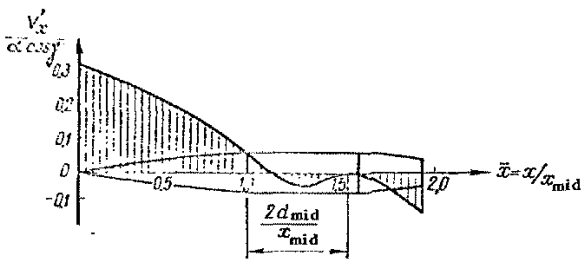

Figure XI-3-1. Variation of Function $V'_x/(\alpha \cos \gamma)$ Along Composite Solid of Revolution.

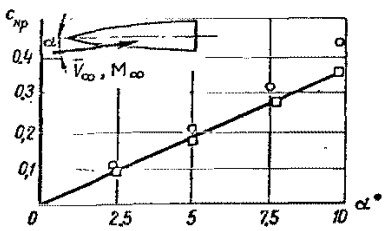

Figure XI-3-2. Variation of Normal Force Coefficient as a Function of Attack Angle for Two Solids of Revolution. $M_\infty = 5.05$; solid line from Formula (XI-3-25); oo) experimental data for $\lambda_{mid} = 5$; □) same for $\lambda_{mid} = 3$.

the end of the nose section, and then acquires increasing negative values on the tail section with the approach to the base. In practice, the cylindrical center section of the body has little influence on normal force. As for the tail section, its influence may be substantial when the length and taper are sufficiently large.

Studies have shown that the normal force coefficients of slender bodies are practically independent of M_∞ and slenderness ratio at small angles of attack. For example, Fig. XI-3-2 shows that the coefficients c_{Np} are practically the same for two solids of revolution with slenderness ratios $\lambda_{mid} = 3$ to 5 up to attack angles of the order of 4-5° at $M_\infty = 5.05$, although a trend to increasing normal force coefficient values is observed with increasing slenderness ratios.

The data given in Fig. XI-3-2 indicate a nearly linear dependence of the coefficient c_{Np} on attack angle, of the approximate form

$$c_{Np} = 2\alpha. \qquad \text{(XI-3-25)}$$

It is remarkable that the linearized theory for very slender solids of revolution gives this value of the normal-force coefficient. To demonstrate this, it is necessary to find the pressure coefficient distribution in the extreme case of an infinitesimally slender body, i.e., for $r \to 0$. This limiting case is examined, as we have noted, in slender-body aerodynamics. According to this theory, the pressure coefficient can be found by converting in (XI-3-5) to the variable $\varepsilon = x - \alpha' r \cosh z$ and finding

the limit of $\bar{p}_2$ as $r \to 0$. Calculation of the limit gives /471

$$\bar{p}_2 = \frac{-2\cos\gamma}{r} m - \alpha^2 (4\sin^2\gamma - 1). \qquad \text{(XI-3-26)}$$

Since the function $m = 2\alpha r(dr/dx)$, the added pressure coefficient in this case will be

$$\bar{p}_2 = -4\alpha\cos\gamma \frac{dr}{dx} - \alpha^2 (4\sin^2\gamma - 1). \qquad \text{(XI-3-27)}$$

If we introduce this expression into (XI-3-1), evaluation of the integral yields the relation

$$c_{Np} = 2\alpha\bar{S}_{bse}, \qquad \text{(XI-3-28)}$$

which agrees with (XI-3-25) in the absence of tail taper ($\bar{S}_{bse} = 1$).

Thus, slender-body aerodynamics establishes the same linearity of the normal-force coefficient as a function of attack angle that was observed previously in experiments. Physically, this theory also reflects correctly the effect of tail-section shape, which consists in diminishing c_{Np} in the presence of stern taper ($\bar{S}_{bse} < 1$).

It should be noted here that the same experimental studies indicate that for real bodies other than very slender ones, c_{Np} is proportional to the relative base diameter $\bar{d}_{bse}$ rather than to the taper $\bar{S}_{bse}$. However, while bearing this in mind, we shall use the theoretical result (XI-3-28) in the material that follows. Studies have shown that Formula (XI-3-25) can be used for approximate evaluation of the normal force coefficients of comparatively short slender solids of revolution with slenderness ratios of the order of 3-5.

Most interesting for practical problems is determination of the normal-force coefficient for solids of revolution that represent, in the general case, a combination of a nose section with a certain shape, an intermediate cylinder, and a tail section. If the body has a cylindrical stern, its basic lifting element will be the nose section; hence the normal force coefficient will change when its geometry is changed.

Experiments have shown that the normal force coefficient increases, for example, with increasing slenderness ratio of the

nose section. It must be noted, however, that the change in the normal force coefficient is small for a small change in the geometry of a sufficiently tapered nose section.

The dependence of this coefficient on tapered-nose shape for bodies with equal relative cylindrical-section lengths was also tested experimentally. It was found that, for example, for a body with a parabolic nose section, the normal force coefficient is somewhat greater than for a body with a conical nose section with the same slenderness ratio.

It was established that this relationship is also affected by the nose section's effect on flow over the adjacent cylindrical section. For example, an additional negative normal force may be created by this effect on a cylinder length of $2\text{-}3d_{mid}$ in the case of a parabolic or ogival nose section at small M_∞.

For a conical nose section, on the other hand, an additional positive normal force arises on the same length, as we see clearly in Fig. XI-3-3. This force appears on the cylinder because a positive excess pressure is created on the bottom and a negative one on the top.

It is easily seen that the pressure drop practically vanishes at a section situated at a distance of about $3d_{mid}$. Here /472
the lifting part of the cylinder creates an additional normal force larger than in the case in which the cylinder is preceded by a parabolic nose. Moreover, this additional force is so small in the latter case that it can be disregarded in practice. At the same time, it may be advisable to take it into account for a body with a conical nose.

Starting with the above and using available experimental data, we can find the normal-force coefficient by Formula (XI-3-25) as it depends on pressure for cylindrical bodies with parabolic or ogival noses. We find that the calculation can be performed in the same way for bodies with nose cones. The agreement between the coefficients is probably due to masking of the increase in the cone normal force that results from the cylindrical segment next to the nose section by the decrease as compared with the parabolic nose.

If a cylindrical body terminates in a tail section of some shape other than cylindrical, the redistribution of pressure on it gives rise to an additional normal-force component. This component reduces the over-all normal force if the tail is tapered ($\bar{S}_{bse} < 1$) and increases it if it expands. In either case, experimental studies indicate that the normal force of the body together with its tail section can be evaluated approximately by Formula (XI-3-28), which does not take account of the dependence

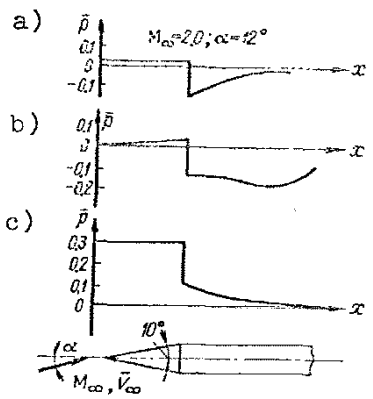

Figure XI-3-3. Pressure Distribution over Cone and Adjacent Cylindrical Segment (Experiment). Generatrices: a) upper; b) side; c) lower.

of c_{Np} on M_∞, although research has established that this dependence, although weak, does exist. Here we observe a tendency to a slight increase in c_{Np} with increasing M_∞.

Influence of flow separation. The normal-force evaluation given above does not take flow separation into account. While this is justified for short bodies, the flow around which is practically nonseparating, it must be taken into account in evaluating normal force for long bodies, for which it is observed in transverse flow of a viscous medium around a body at velocity $V_\infty \sin\alpha$ (Fig. XI-3-4).

For a surface element of length dx (Fig. XI-3-4), the additional normal force governed by separation is

$$dN_f = c\frac{\rho_\infty (V_\infty \sin\alpha)^2}{2} 2r\,dx = dc_{Nf}\frac{\rho_\infty V_\infty^2}{2}\pi r_{mid}^2,$$

where c is a certain coefficient determined by the flow conditions in the boundary layer.

Accordingly,

$$dc_{Nf} = c\frac{2}{\pi}\frac{r}{r_{mid}^2}\sin^2\alpha\,dx.$$

Integrating in the range from x_{se} to x_b, we obtain /473

$$c_{Nf} = c\frac{2}{\pi}\frac{\sin^2\alpha}{r_{mid}^2}\int_{x_{se}}^{x_b} r\,dx; \qquad \text{(XI-3-29)}$$

the coordinate x_{se} is equal to the distance to the cross section on the cylinder where flow separation begins.

Studies have shown that this distance is not constant and depends on attack angle, M_∞, Reynolds number, and the shape of the body. Figure XI-3-5 shows an approximate curve of x_{se} as a

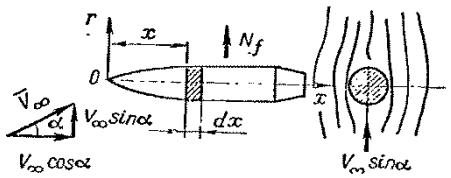

Figure XI-3-4. Influence of Normal Velocity Component $V_\infty \sin\alpha$ on Flow Around Solid of Revolution.

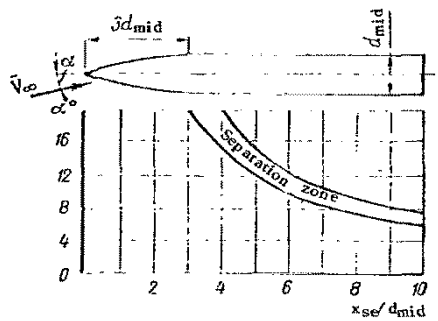

Figure XI-3-5. Distance to Boundary-Layer Separation Region on Lee Side of Solid of Revolution.

function of attack angle at $M_\infty = 2$ for an ogival-nosed cylinder. It is readily seen that $x_{se} > x_{mid}$ in the general case, and that a trend to initial formation of vortices and separation in the transitional zone between the ogival part and the cylinder is observed with increasing attack angle. We may assume for tentative calculations that the beginning of separation coincides with the beginning of the cylindrical section, i.e., take $x_{se} = x_{mid}$ as the lower limit in (XI-3-29). Data similar to the plot in Fig. XI-3-5 should be used to correct the calculated results.

In the presence of a tail section, it is unnecessary to evaluate the integral in (XI-3-29). In this case, it is quite permissible to substitute a cylinder with the slenderness ratio $\lambda_{tl} = x_{tl}/d_{mid}$ for the stern. Accordingly,

$$c_{Nf} = c\frac{4}{\pi}(\lambda_C + \lambda_d)\sin^2\alpha, \qquad \text{(XI-3-30)}$$

where $\lambda_C = (x_c - x_{mid} - x_{tl})/d_{mid}$ is the slenderness ratio of the body's cylindrical part.

At small angles of attack

$$c_{Nf} = c\frac{4}{\pi}(\lambda_C + \lambda_d)\alpha^2. \qquad \text{(XI-3-30')}$$

Experimental studies have shown that the coefficient $\underline{c}$ depends on whether the boundary layer is turbulent of laminar. For laminar flow in the range of Reynolds numbers $Re = V_\infty d_{mid}/\nu$ from $2\cdot10^4$ to $2\cdot10^5$, $\underline{c}$ is approximately 1.2. Lacking other data, this

value can be used for other Re in approximate calculations. For turbulent flow, we may assume $c \approx 0.3$-0.4. With the additional normal force taken into account, the over-all normal-force coefficient becomes

$$c_N = 2\alpha \bar{S}_{bse} + c\frac{4}{\pi}(\lambda_C + \lambda_n)\alpha^2. \qquad \text{(XI-3-31)}$$

/474

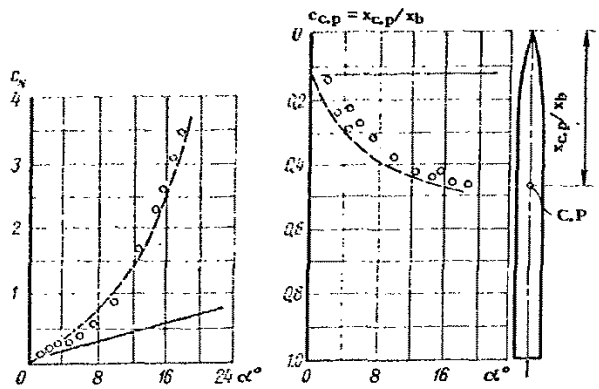

Figure XI-3-6. Coefficients of Normal Force and Center of Pressure for Tapered Solid of Revolution. Total Slenderness Ratio of Body 21, Nose-Section Slenderness $\lambda_{mid} = 4.75$. ——— slender-body theory; ----- with boundary-layer separation in transverse flow considered; o) experiment at M = 2.

Figure XI-3-6 presents experimental data, which are compared with the results of calculation by slender-body theory (XI-3-28) and by (XI-3-31), which takes separation into account. The normal force determined from slender-body theory acts only on the expanding part of the body in front of the separation region, while viscous transverse forces act behind this region. As the attack angle increases, these forces increase in proportion to α^2, while the normal force computed by slender-body theory increases in proportion to α. Formula (XI-3-31) gives results that agree satisfactorily with experiment. /475

Figure XI-3-7 presents certain experimental results on the coefficient c_N for cylindrical bodies with conical and ogival nose sections.

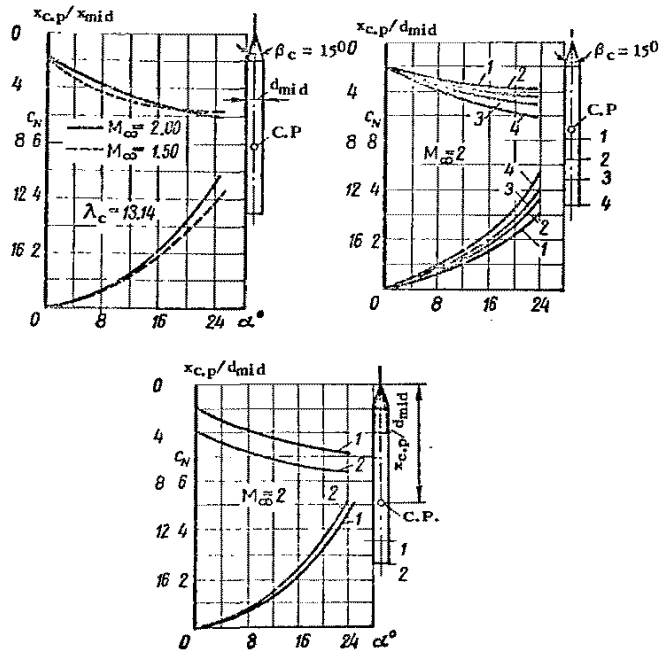

Figure XI-3-7. Variation of c_N and $c_{c.p}$ for Cylindrical Bodies with Conical and Ogival Nose Sections. The numerals 1, 2, 3, 4 on the curves correspond to those on the diagram of the body and represent reference lengths.

Normal-force coefficient of slender cone. To calculate this coefficient, it is necessary to know the distribution of the additional pressure coefficient. To find it, let us use Expressions (XI-3-14) and (XI-3-16), which we combine to obtain

$$\bar{p}_2 = -\frac{2\alpha}{\alpha'}\frac{(i_r^0)_c}{(i_r^0)_c}\cos\gamma - \alpha^2(4\sin^2\gamma - 1), \qquad \text{(XI-3-32)}$$

where the subscript c replaces the 0.

Substituting the value of $\bar{p}_2$ into (XI-3-1), we find

$$c_{Np} = \frac{\alpha}{\alpha'\beta_c}\frac{(i_r^0)_c}{(i_r^0)_c}. \qquad \text{(XI-3-33)}$$

For a very slender cone ($\beta_c \to 0$), we can find $c_{Np} = 2\alpha$ from this formula.

Coefficient of Moment of Forces

Solid of revolution of arbitrary shape. Leaving aside the influence of separation, we shall assume that the moment coefficient depends on the distribution of the added pressure and on the position of the reduction point about which the moment is calculated. We shall also assume that this point is the tip of the body.

The moment coefficient is determined by Expression (I-5-8), which gives m_{zp} referred to the total body length x_b. At the same time, we can obtain a relation for the moment coefficient m'_{zp} referred to any other characteristic length, such as the nose-section length x_{mid}. The relation to be used for this purpose is

$$m'_{zp} = m_{zp}\frac{x_b}{x_{mid}} = m_{zp}\frac{\lambda_b}{\lambda_{mid}}. \qquad \text{(XI-3-34)}$$

An expression for the moment coefficient referred to the total body length can be obtained from (I-5-8) by applying (XI-1-24) for p_2:

$$m_{zp} = \frac{-4\lambda_{mid}^2\alpha}{\lambda_b}\int_0^{\bar{x}_b}\frac{V'_x}{\alpha\cos\gamma}\bar{r}\,\bar{x}\,d\bar{x}. \qquad \text{(XI-3-35)}$$

In the particular case of a parabolic generatrix, this formula can be written somewhat differently:

$$m_{zp} = \frac{-4\lambda_{mid}^2\alpha}{\lambda_b}\int_0^{l_b}\frac{V'_x}{\alpha\cos\gamma}\,dl, \qquad \text{(XI-3-35')}$$

where $l = \bar{x}^3(2/3 - \bar{x}/4)$.

To calculate the moment coefficient with Formula (XI-3-35'), it is first necessary to find values of $V'_x/(\alpha\cos\gamma)$ as a function of l and then to integrate numerically or graphically (Fig. XI-3-8). /476

Moment coefficient of cone. Applying (XI-3-32) for the additional pressure coefficient on a cone, we can obtain a formula for the moment coefficient from (XI-3-35):

$$m_{zp} = -\frac{2}{3}\frac{\alpha}{\alpha_c^0}\frac{(i_\gamma^0)_c}{(i_y^0)_c}. \qquad \text{(XI-3-36)}$$

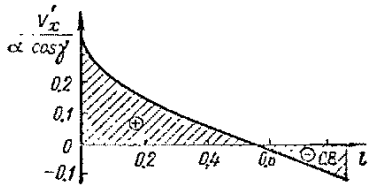

Figure XI-3-8. Graphical Determination of Moment Coefficient.

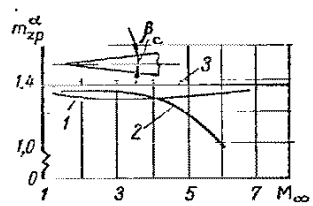

Figure XI-3-9. Angle Derivative of Moment Coefficient of Slender Cone. 1) exact theory; 2) calculation by method of sources; 3) by slender-body theory.

Moment coefficient of very slender solids of revolution. By introducing (XI-3-27) into Formula (I-5-8), we obtain

$$m_{zp} = -2\alpha\left(\bar{S}_{bse} - \frac{W_b}{W_C}\right), \qquad \text{(XI-3-37)}$$

where W_b is the volume of the solid of revolution and $W_C = x_b S_{mid}$ is the volume of a cylinder whose base is equal to the largest cross section area and whose height is equal to the length of the body.

If the moment is determined with respect to a point situated at a distance $x_{c.g}$ from the nose,

$$m_{zp} = 2\alpha\left[\left(\frac{x_{c.g}}{x_c} - 1\right)\bar{S}_{bse} + \frac{W_b}{W_C}\right]. \qquad \text{(XI-3-37')}$$

For real slender solids of revolution, Formula (XI-3-37) is valid only as far as the order of magnitude of the moment coefficient. More satisfactory results are obtained by this formula for slender bodies of arbitrary shape without tail taper. It also gives a fair approximation for slender conical nose sections. For example, for a cone with $\bar{S}_{bse} = 1$ and $W_b/W_C = 1/2$, the value of $m_{zp} = -1.33\alpha$ is close to the rather good value -1.27α obtained for m_{zp} from (XI-3-36) at $M_\infty = 1.87$ for a cone with the angle $\beta_c = 0.1$.

The data given in Fig. XI-3-9 also indicate that the results of a calculation of the derivative $m^{\alpha}_{zp} = \partial m_{zp}/\partial\alpha$ by Formula (XI-3-37) for the same cone are in good agreement with the exact

theory. We see from the results of the exact-theory calculation that the derivative m_{zp}^{α} is almost independent of M_∞ for slender cones.

Influence of separation. Flow separation on the top of the washed surface results in the appearance of an additional pitching moment. The element of this moment (Fig. XI-3-10) is

$$dM_{zf} = -x\,dN_f = -c\,\frac{\rho_\infty (V_\infty \sin\alpha)^2}{2}\,2rx\,dx = -dm_{zf}\,\frac{\rho_\infty V_\infty^2}{2}\,\pi r_{\text{mid}}^2\,x_c,$$

whence

/477

$$m_{zf} = -\frac{2}{\pi}\,\frac{c\sin^2\alpha}{r_{\text{mid}}^2 x_k}\int_{x_{\text{mid}}}^{x_c} rx\,dx. \qquad \text{(XI-3-38)}$$

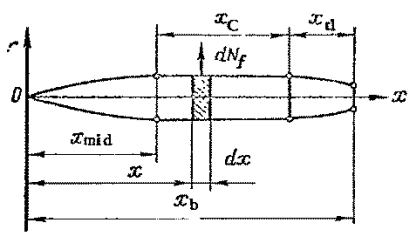

Figure XI-3-10. Illustrating Determination of Friction Moment.

If the body has a short tail section, this part can be replaced by a cylinder in calculating the moment coefficient from the forces due to flow separation, and then the formula can be simplified for small attack angles:

$$m_{zf} = \frac{2}{\pi}\,c\left(\lambda_b - \frac{\lambda_{\text{mid}}^2}{\lambda_b}\right)\alpha^2. \qquad \text{(XI-3-39)}$$

The total moment coefficient is the sum of the component due to pressure, which is determined by (XI-3-37), and the component that appears at flow separation and calculated from (XI-3-39), i.e.,

$$m_z = 2\alpha\left(\bar{S}_{\text{bse}} - \frac{W_b}{W_C}\right) + \frac{2}{\pi}\,c\alpha^2\left(\lambda_b - \frac{\lambda_{\text{mid}}^2}{\lambda_b}\right). \qquad \text{(XI-3-40)}$$

This formula gives better results for a cylindrical body with a conical nose section than for the same body when it has a tapering or expanding tail section.

Data more reliable than those of Formula (XI-3-40) can be obtained by experiment.

If the coefficient of normal force and center of pressure are determined first, the moment coefficient

$$m_z = c_N c_{c.p}. \qquad \text{(XI-3-41)}$$

Center of Pressure Coefficient

Cone and solid of revolution of arbitrary shape. It follows from Formulas (I-4-11) that the center of pressure of a slender cone at small attack angles is situated in the absence of a viscosity effect at 2/3 of its length, so that $c_{c.p} = 2/3$. In practice, the influence of viscosity on the coefficient is negligible.

For a solid of revolution of arbitrary shape, the center of pressure coefficient is determined by (I-4-11) or (I-5-8) if we consider only the pressure distribution. In linearized flow, this coefficient is

$$c_{c.p} = \frac{\lambda_{mid}}{\lambda_b}\left[\int_0^{\bar{x}_b} \frac{V'_x}{\alpha \cos\gamma}\bar{r}\,d\bar{x}\right]^{-1} \int_0^{\bar{x}_b} \frac{V'_x}{\alpha \cos\gamma}\bar{r}\bar{x}\,d\bar{x}. \qquad \text{(XI-3-42)}$$

This formula does not take account of separation, and is therefore suitable for bodies with comparatively short cylindrical sections.

The function $V'_x/(\alpha \cos \gamma)$ and, consequently, the center of pressure coefficient are independent of attack angle. For slender solids of revolution with parabolic generatrices and slenderness ratios ranging up to about 5, $c_{c.p}$ can be calculated by the approximate formula

$$c_{c.p} = \frac{2}{3} - 10^{-2}(11 + u_0)\,\bar{x}, \qquad \text{(XI-3-43)}$$

where $u_0 = (\alpha'\beta_p)^{-1}$.

The center of pressure coefficient calculated by this formula is referred to the length of the nose section, i.e., $c_{c.p} = x_{c.p}/x$ and corresponds to the linearized-flow conditions. The dimensionless variable $\bar{x}$ in (XI-3-43) is determined by the ratio $\bar{x} = x/x_{mid}$ and must satisfy the condition $(1.1\text{-}1.15) \geq \bar{x} \geq 0$ (Fig. XI-3-11). /478

We see from (XI-3-43) that the center of pressure coefficient is a weak function of M_∞. With increasing M_∞, the center of pressure shifts slightly toward the base of the body. This is because the expansion at the end of the nose section decreases with increasing speed and, consequently, the destabilizing effect

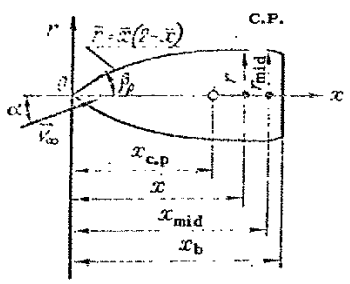

Figure XI-3-11. Geometrical Parameters of Body Necessary for Calculation of Center of Pressure Coefficient.

of the tail section becomes weaker. At M_∞ = 2.5-3, the expansion practically vanishes, and a positive excess pressure even appears at large Mach numbers, so that the rear of the nose section begins to act as a kind of stabilizer.

At moderate speeds ($M_\infty \leq 1.5$), the center of pressure may shift toward the point of the body, since the increase in the normal force is larger at the front of the nose than at the rear.

Stabilization of nose sections. A conical nose section or a nose section of arbitrary generatrix will possess static stability if the center of pressure is behind the center of gravity, i.e., nearer the base of the body. Here the stability margin in percent is determined from the relation

$$Y = \frac{x_{c.p} - x_{c.g}}{x_{mid}} 100\%.$$

To ensure a positive stability margin for a given nose-section shape and hence a given value of the coefficient $c_{c.p}$, we can obviously weight the forward part and thereby shift the center of gravity toward the tip.

A positive stability margin can also be secured by shifting the body's center of pressure towards its base. Various stabilizing measures are taken for this purpose. They include, for example, stabilization by the use of tail fins. Other aerodynamic devices are also employed.

Fin stabilization is most commonly encountered. It is based on the fact that fins at the end of the body set up a positive force, so that the center of pressure is shifted toward the base.

The same effect is obtained by the use of so-called stabilizing skirts. Let us explain this stabilization method with reference to a nose-cone solid of revolution. Assume that we have a solid cone. Since its center of gravity is at 3/4-height from the nose (Fig. XI-3-12a) and its center of pressure is at 2/3-height, the body will clearly be statically unstable in flight, since its stability margin is negative and equal to

$$Y = (c_{c.p} - \bar{x}_{c.g}) 100 = \left(\frac{2}{3} - \frac{3}{4}\right) 100 = -8.34\%.$$

Let us now attach a stabilizing skirt to the base of the conical body. This may be either a truncated hollow cone that forms an extension of the main body (Fig. XI-3-12b) or has a smaller generatrix inclination angle (Fig. XI-3-12c) or a hollow cylinder (Fig. XI-3-12d). All of these stabilizer variations are determined basically by design configurations. /479

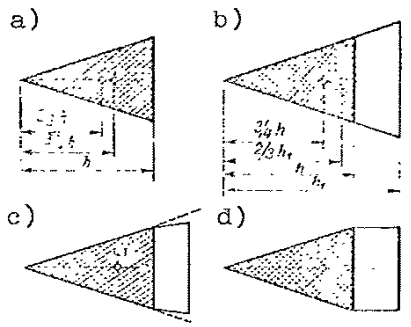

Figure XI-3-12. Diagram Showing Relative Positions of Centers of Pressure and Gravity of a Conical Body.

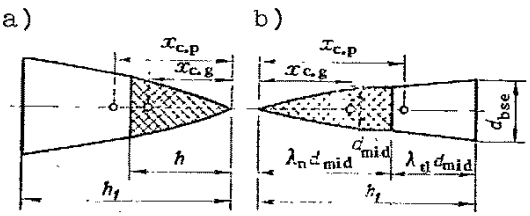

Figure XI-3-13. Diagram Showing Relative Positions of Centers of Pressure and Gravity for Nose Sections of Arbitrary Shape.

The version in which a conical skirt forms an extension of the main cone is simplest for calculation of the stability margin. In this case, we may assume if the skirt weight is negligible that the center of pressure of the entire stabilized body remains in position and that its dimensionless coordinate

$$\bar{x}_{c.p} = \frac{x_{c.g}}{h_1} = \frac{3}{4}\frac{h}{h_1},$$

where h is the height of the main nose section and h_1 is the height of the entire body with the stabilizing skirt.

The center of pressure of such a body will lie at a distance $2/3h_1$ from the point. Consequently, the center of pressure coefficient is 2/3 and the stability margin $Y = \frac{2}{3}[1-(9/8)(h/h_1)]\,100\%$.

The value of h can be adjusted in such a way that the center of pressure will fall between the base and the center of gravity and the stability margin will be positive. In practice, the stability margin is usually placed between 8 and 10%. The required h/h_1 ratio is determined on the basis of the selected margin.

A similar method of stabilization using a conical skirt can be used when the main nose section has a curvilinear generatrix (Fig. XI-3-13). Experiments have shown that the center of pressure

coefficient of the body shown in Fig. XI-3-13a, which is an incomplete nose section with a conical skirt and h_1 of the order of (1.5-2)h, is approximately 0.5-0.55. It depends weakly on M_∞, attack angle, and the length of the stabilizing skirt, although a trend toward a slight increase in $c_{c.p}$ is observed with increasing attack angle or on passage to a greater skirt length.

Interest attaches to analysis of the manner in which the normal force coefficient of such a body varies. It is practically independent of M_∞. The influence of attack angle is represented by the linear relation

$$c_N \quad (2.5 \cdots 3)\alpha.$$

Figure XI-3-13b shows another shape of a full (or tangent) /480
nose with a stabilizing skirt.

Studies have shown that such nose sections with slenderness ratios λ_n = 3.5-5 and stabilizing skirts having slenderness ratios λ_{tl} = 1.5-2.5 and base-section relative diameters $\bar{d}_{bse}$ = $= d_{bse}/d_{mid}$ = 1.5-1.8 have center of pressure coefficients $c_{c.p}$ = $= x_{c.p}/h_1$ of approximately 0.55-0.60, with the smaller value corresponding to shorter and narrower stabilizing skirts.

The length h_1 of a body with a stabilizing skirt is chosen in the same way as in the conical-body example for the known length $\underline{h}$ and a given center of gravity position.

Center of pressure coefficient of long bodies. When a rather long segment is attached to a nose cone, the center of pressure position of the resulting body will be influenced to some degree by flow separation. This effect, which increases with attack angle, shifts the center of pressure toward the base and, consequently, increases static stability.

Let us consider a case in which a nose cone with slenderness ratio λ_n terminates in a cylinder with a certain length $\lambda_C d_{mid}$ which, in turn, is fitted with a tapering or expanding tail section with a length ratio $\lambda_{tl} = x_{tl}/d_{mid}$. With the condition $\lambda_C > 1.5\text{-}2$ the center of pressure coefficients of slender solids of revolution with small taper ($\bar{S}_{bse} \approx 0.9\text{-}1.1$) can be determined approximately by the formula

$$c_{c.p} = \frac{2\left(\bar{S}_{bse} - \frac{W_b}{W_C}\right) + c\frac{2}{\pi}\left(\lambda_b - \frac{\lambda_{mid}^2}{\lambda_b}\right)\alpha}{2\bar{S}_{bse} + c\frac{4}{\pi}(\lambda_C + \lambda_{tl})\alpha}. \qquad \text{(XI-3-44)}$$

This formula can be used for tentative evaluation of $c_{c.p}$ if it is remembered that the actual center of pressure will be situated closer to the point than indicated by the calculation. This is evident, for example, from Fig. XI-3-6, which shows experimental data for a long tapered solid of revolution. Figure XI-3-7 shows analogous results obtained for cylindrical bodies with conical and ogival tapered noses.

With increasing M_∞, a body with an expanding stern shows a tendency toward smaller $c_{c.p}$. Thus, for one of the solids of revolution with a conical expanding stern, the center of pressure coefficient was about 7% smaller at $M_\infty = 4$ than at $M_\infty = 2$. Thus, the increase in M_∞ resulted in some destabilization.

Formula (XI-3-44) gives more satisfactory results when the end of the body is not tapered or expanded and, consequently, we must set $\bar{S}_{bse} = 1$ and $\lambda_{tl} = 0$ in this formula.

Apart from the formulas given above, the center of pressure coefficient of a body of arbitrary shape can be approximated with the aid of the aerodynamic coefficients known for the individual elements of this body. Let us illustrate this using as an example the solid of revolution diagramed in Fig. XI-3-14.

We dismember this body into elements each of which creates a known normal force whose point of application is also known. We calculate the sum of the force moments about point O; it is equal to the produce of the total normal force by its arm $x_{c.p}$, which is the distance from the nose to the unknown center of pressure of the body as a whole:

$$Nx_{c.p} = N_n x_{c.p}^n + N_C x_{c.p}^C \pm N_{tl} x_{c.p}^{tl},$$

where the subscripts n, C, and tl denote the normal forces and the respective coordinates of application for the nose section, the cylinder, and the tail section, with N_C understood as the normal force arising as a result of flow separation and acting on the cylindrical section of the body, i.e., $N_C = N_f$. /481

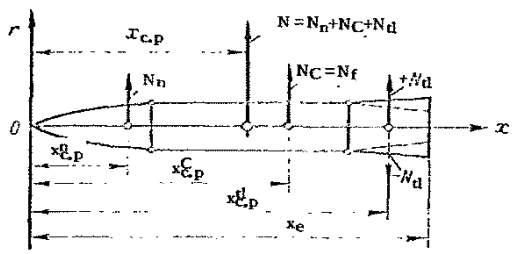

Figure XI-3-14. Diagram for Calculation of Center of Pressure Coefficient of Body.

Considering that $N = N_n + N_C \pm N_{tl}$ and substituting the force coefficients for the forces both for the entire body and for each of its elements, we obtain an equation for the center of pressure coefficient of the entire body:

$$c_{c.p} = \frac{1}{c_N}(c_N^n \bar{x}_{c.p}^n + c_N^C \bar{x}_{c.p}^C \pm c_N^d \bar{x}_{c.p}^d), \quad \text{(XI-3-45)}$$

where the over-all normal-force coefficient is $c_N = c_N^n + c_N^C \pm c_N^{tl}$. The plus sign corresponds to an expanding stern, which gives rise to a stabilizing effect, and the minus sign to a tapering tail element, which creates a negative normal force. Expression (XI-3-45) also contains the dimensionless coordinates $\bar{x}^n_{c.p} = x^n_{c.p}/x_b$, $\bar{x}^C = x^C/x_b$ and $\bar{x}^{tl} = x^{tl}/x_b$.

Generally, if the solid of revolution consists of several elements, the formula for the center of pressure coefficient becomes

$$c_{c.p.} = \frac{x_{c.p}}{x_b} = \frac{\sum (c_{Nf})_i (\bar{x}_{c.p})_i}{\sum (c_{Np})_i}. \quad \text{(XI-3-46)}$$

Let us consider how the individual quantities in the formula for the center of pressure coefficients are determined. The normal-force coefficient c_N of the entire body is calculated by (XI-3-31). The value of c_N^n for the nose section must be calculated with consideration of the cylinder that follows it. In this case, it is recommended that the calculation be performed by the formula $c_N = 3\alpha$. The coordinate $x^n_{c.p}$ of the center of pressure of this part of the body will also be influenced by the cylinder, and since the part of the cylinder adjacent to the nose cone is a lifting element, it shifts the center of pressure of the nose section slightly backward from its position for the isolated nose. For a conical nose and cylinder, this shift might be about 5-10%. In calculating the coordinate $x^n_{c.p}$ for a nose section of this type with an attached cylindrical section, we can assume its value equal to $x^n_{c.p} = (2/3)(1.05\text{-}1.10)x_{mid}$, i.e., the dimensionless coordinate in this case

$$\bar{x}^{n}_{c.p} = \frac{x^{n}_{c.p}}{x_b} = \frac{2}{3}\frac{\lambda_{mid}}{\lambda_b}(1.05 \div 1.10). \qquad \text{(XI-3-47)}$$

For a parabolic nose section, the calculation is performed by the usual formula $\bar{x}^{n}_{c.p} = c_{c.p}(\lambda_{mid}/\lambda_b)$, and if the head meets the cylindrical section at a tangent, the coefficient $c_{c.p}$ is taken from Formula (XI-3-43). If, on the other ahnd, the nose section is cut off, the value of this coefficient obtained from (XI-3-43) should be increased by about 5-10%. This is because the cylindrical segment adjoining the nose is a lifting element in this case, like a cylindrical segment adjacent to a conical nose section. /482

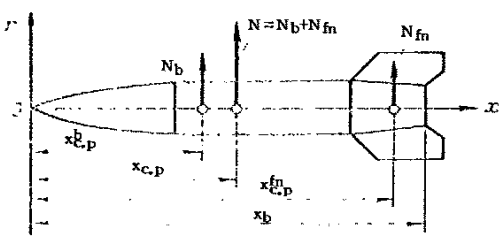

Figure XI-3-15. Diagram for Calculation of Center of Pressure Coefficient of a Finned Solid of Revolution.

Let us now examine that part of the normal-force coefficient and the corresponding dimensionless center of pressure coordinate that are governed by transverse flow. The normal-force coefficient of the cylindrical section can be determined by the formula

$$c^{C}_{N} = c_{N\beta} \cdot c\alpha^2 \frac{4}{\pi}(\lambda_b - \lambda_{mid}), \qquad \text{(XI-3-48)}$$

on the assumption that the stern gives the same separation-controlled component as a cylindrical segment of equal length.

The dimensionless coordinate $\bar{x}^{C}_{c.p}$ of the center of pressure will be found on the assumption that the normal force in transverse flow around the body is distributed uniformly over a segment of length $\lambda_b - \lambda_{mid}$ and, consequently, that the center of pressure is located in the middle, i.e.,

$$\bar{x}^{C}_{c.p} = \frac{x^{C}_{c.p}}{x_b} = \frac{1}{2}\left(1 + \frac{\lambda_{mid}}{\lambda_b}\right). \qquad \text{(XI-3-49)}$$

The absolute value of the normal-force coefficient created on a tapering or expanding tail section as a result of pressure redistribution in inviscid flow can be computed according to (XI-3-28) by the formula

$$c_N^{tl} = 2\alpha(\bar{S}_{bse} - 1). \qquad \text{(XI-3-50)}$$

In the first approximation, the application point of the normal force may be assumed to be at the middle of the tail section. Accordingly, the dimensionless coordinate

$$\bar{x}_{c.p}^{tl} = \frac{x_{tl}}{x_b} = 1 - \frac{1}{2}\frac{\lambda_{tl}}{\lambda_b}. \qquad \text{(XI-3-51)}$$

Stabilization of long solids of revolution. Like short ones, long solids of revolution can be stabilized with fins or special aerodynamic devices. Fin stabilization is most commonly encountered.

Here, if we know the normal-force coefficient c_N^{fn} of the fins referred to the midships section of the body and the dimensionless coordinate $\bar{x}_{c.p}^{fn} = x_{c.p}^{fn}/x_b$ of the fin center of pressure, we find the following expression for the center of pressure coefficient of the finned body in accordance with the diagram shown in Fig. XI-3-15:

$$c_{c.p} = \frac{c_N^b c_{c.p}^b + c_N^{fn}\bar{x}_{c.p}^{fn}}{c_N^b + c_N^{fn}}. \qquad \text{(XI-3-52)}$$

Here c_N^b and c_N^{fn} are the respective normal force coefficients of the body and fins and $c_{c.p}^b$ and $\bar{x}_{c.p}^{fn}$ are the body center of pressure coefficient and the dimensionless coordinate of the fin center of pressure.

The body's normal-force coefficient is determined by the formula $c_N^b = c_N^n + c_N^c \pm c_N^{tl}$ as the sum of the three components for the nose, cylinder, and stern, respectively. Recommendations /483
for their calculation were set forth above. The body center of pressure coefficient $c_{c.p}^b$ is found from Expression (XI-3-45).

In computing the aerodynamic characteristics of the body, it is necessary to take the fins on the solid of revolution into account. The same applies to calculation of the fin characteristics, which will be influenced by the body. Thus, it is necessary that the calculations be performed with consideration of the interference between the body and the fins. In estimating the static stability margin of a finned solid of revolution, the normal force coefficients of the body and fins, as well as the center of pressure coordinates can be calculated separately for each of these elements, i.e., without consideration of

interference. The accuracy of these calculations improves with increasing flow velocities. The fin center of pressure coordinate can be assumed to lie at the middle of the mean aerodynamic chord.

By appropriate adjustment of the fin area, we can place the center of pressure of the finned body aft of its center of gravity and thereby obtain a positive stability margin. If the margin is assigned, the plan area of the stabilizer can be determined for a selected stabilizer shape.

In fact, since the stability margin $Y = (c_{c.p} - \bar{x}_{c.g})100\%$ where $c_{c.p}$ and $\bar{x}_{c.g}$ are the center of pressure coefficient and the dimensionless center of gravity coordinate of the finned body, respectively, it is obvious that $c_{c.p} = \bar{x}_{c.g} + Y/100\%$.

Thus, the general expression for the coefficient c_N^{fn} can be written $c_N^{fn} = (c_N^{fn})'(S_{fn}/S_{mid})$, where $(c_N^{fn})'$ is the fin normal force coefficient referred to the plan area of the stabilizers. In approximate calculations in which interference is considered, the part of the body area between the fins (center section) is included in the area S_{fn}.

We can use Expression (XI-3-52) to find the ratio of fin area, including the center section, to the largest cross-sectional area of the solid of revolution:

$$\bar{S}_{fn} = \frac{S_{fn}}{S_{mid}} = \frac{c_N^b(\bar{x}_{c.g} + 0{,}01Y - c_{c.p}^b)}{(c_N^{fn})'(\bar{x}_{c.p}^{fn} - 0{,}01Y - \bar{x}_{c.g})}. \qquad \text{(XI-3-53)}$$

Assigning a stability margin of 8-10%, we can use this formula to find the required relative fin area $\bar{S}_{fn}$ at which this stability margin is ensured.

Another highly effective stabilization method involves the use of an expanding tail cone. Like fins, it creates a positive lifting force and thus shifts the center of pressure toward the base of the body.

Formula (XI-3-45) can be used to determine the center of pressure coefficient in this stabilization method. Replacing the coefficients c_N^n and c_N^{tl} in this formula by their values, which might be obtained from the formulas $c_N^n = 2\alpha$ and $c_N^{tl} = 2\alpha(\bar{S}_{bse} - 1)$, we obtain

$$c_{c.p} = \frac{2\alpha\bar{x}_{c.p}^n + c_N^C\bar{x}_{c.p}^C + 2\alpha(\bar{S}_{bse} - 1)\bar{x}_{c.p}^{tl}}{2\alpha\bar{S}_{bse} + c_N^{tl}}. \qquad \text{(XI-3-54)}$$

This expression can be used to find the required expansion of the tail section for a given stability margin and a specified tail-section length, i.e., it gives the dimensionless area

$$\bar{S}_{bse} = \frac{2\alpha(\bar{x}^{d}_{c.p} - \bar{x}^{n}_{c.p}) + c^{C}_{N}(\bar{x}_{c.g} + 0.01Y - \bar{x}^{C}_{c.p})}{2\alpha(\bar{x}^{d}_{c.p} - \bar{x}_{c.g} - 0.01Y)}. \qquad \text{(XI-3-55)}$$

It can be established by analysis of this expression that, other conditions being the same, $\bar{S}_{bse}$ reaches its largest value at very small angles of attack ($\alpha \to 0$). The largest cone generatrix inclination angle will obviously correspond to this value at a given tail-section length. /484

Drag Due to Lift

A body in flow at an angle of attack experiences an additional drag governed by the generation of lift. This drag can be regarded as resulting from vortices that trail from the body and change the pressure distribution on its surface. The drag due to lift is equivalent to the induced drag of finite-span wings. It can be determined [51] by analyzing the contour integral in Formula (IV-3-30). Let us introduce the value $\phi_0 = \phi_t + \phi_\alpha$ into the integrand; here, ϕ_t and ϕ_α are given, respectively by (IV-4-15) and (IV-4-17). Then the terms that contain ϕ_α will give the unknown drag component X_1. Assuming $\partial\phi_\alpha/\partial r = -\alpha \sin\theta$ in accordance with the nonseparating-flow condition, we find

$$X_i = \pi r^2_{bse} q \alpha^2.$$

The corresponding drag coefficient is

$$c_{xi} = \frac{X_i}{S_{mid} q} = \bar{S}_{bse}\alpha^2, \qquad \text{(XI-3-56)}$$

where $\bar{S}_{bse} = S_{bse}/S_{mid}$. The above formulas can be expressed in terms of the lift $Y = 2\pi r^2_{bse} q\alpha$ or the coefficient of the lifting force

$$c_y = \frac{Y}{S_{mid} q} = 2\bar{S}_{bse}\alpha. \qquad \text{(XI-3-57)}$$

In fact, $X_i = \frac{1}{2}Y\alpha$ or

$$c_{xi} = \frac{1}{2} c_y \alpha. \qquad \text{(XI-3-58)}$$

Drag due to flow separation. By its nature, this drag is a pressure drag. It is unrelated to surface-friction forces and appears as a result of flow separation from the top of a body at an angle of attack and, consequently, from vortex formation. Thus, the drag in the presence of transverse flow arises from forces normal to the axis of the body. If the total normal force that appears in such a flow has been found, we can multiply it by the angle α to determine the additional drag. According to (XI-3-30'), the coefficient of this drag is

$$c_{xf} = c \frac{4}{\pi} (\lambda_c + \lambda_{tl}) \alpha^3. \qquad \text{(XI-3-59)}$$

It must be remembered in calculating c_{xf} that the transverse-flow drag, like the additional lift, appears beginning at certain attack angles at which flow separation occurs with its consequent pressure redistribution on the upper surface.

In a more exact analysis of separation, it must be remembered that the position of the laminar-to-turbulent boundary layer transition influences the length of the separation zone. The transition point shifts forward with increasing attack angle, causing earlier separation and vortex formation. It may be assumed to simplify the calculations that the additional drag appears at all small attack angles and that the length of the separation zone, which begins at the end of the nose section, is $\lambda_c + \lambda_{tl}$.

Chapter XII /485

AERODYNAMICS OF BLUNT SOLIDS OF REVOLUTION

§XII-1. INVISCID FLOW AROUND A BLUNTED NOSE

General Solution for a Nose of Arbitrary Shape

Study of the aerodynamics of the whole blunt body involves investigation of the flow around its forward section, which is a blunted nose of some particular shape. The results of these investigations form the basis for calculation of the flow variables on the rest of the body. On the other hand, these results are of independent importance, since they enable us to determine the aerodynamic characteristics of the blunt nose. The over-all aerodynamic characteristics of the body can be determined by adding the components for the nose and the remainder.

Here it must be noted that if the flow around the peripheral part of the body depends on the blunting, the flow conditions around the nose itself are determined only by its shape, or, more precisely, by the shape of the part of the nose forward of the "sonic" point on its surface. This implies that the problem of flow around a blunt nose is autonomous, i.e., it is solved independently.

Inviscid flow will be examined below. Nevertheless, the solution found is of great practical importance, since it permits determination of the basic flow conditions outside the boundary layer, conditions that must be known to investigate the friction and heat-transfer processes that are shaped in the boundary layer itself.

At the present time, a number of methods have been devised for solving the problem of flow around a blunt nose. Some authors have based their methods on assignment of the shape and position of the shock wave as found, for example, from experiment. Then they solved the inverse problem: the system of nonlinear partial differential equations was integrated approximately for known boundary conditions on a curvilinear shock wave and the flow around the blunting calculated in this manner. The actual nose shape was determined in this process.

Academician A.A. Dorodnitsin proposed an integration method that reduces to numerical solution of an approximating system of ordinary differential equations in a certain region [10]. This method can be used, for example, when the boundary of the region,

which might be a curvilinear shock wave ahead of the blunting, is known in advance. Consequently, its shape and position can be determined in the process of solving the problem of flow around the nose. Using this method, O.M. Belotserkovskiy computed flows around blunt symmetrical bodies with separated curvilinear shock waves ([68], 1960, XXIV, No. 3).

Let us examine the equation system for solution of this problem. In the calculation of mixed (subsonic, sonic, and supersonic) rotational flow of a gas between a curvilinear shock and a blunt nose of arbitrary shape, it is more convenient to use an equation system written in spherical coordinates (Fig. XII-1-1). Since we are concerned with axisymmetric flow, the equations of motion (III-2-8) and continuity (III-2-17) appear in this system in simplified form, as does Condition (III-2-54) for isentropic gas flow. /486

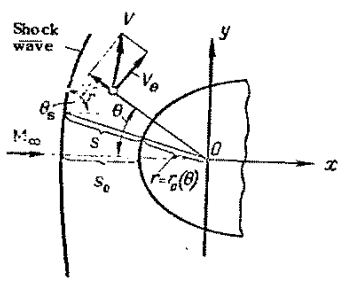

Figure XII-1-1. Working Diagram of Flow Around Bluntness.

For greater convenience in the calculations, it is helpful to transform the equation of motion with the Bernoulli equation and to introduce the stream function Ψ. Then the complete equation system will be

$$\left.\begin{aligned}
&\frac{\partial[\bar{r}^2(\bar{p}+\bar{\rho}\bar{V}_r^2)\sin\Theta]}{\partial\bar{r}}+\frac{\partial(\bar{r}\bar{\rho}\bar{V}_\Theta\bar{V}_r\sin\Theta)}{\partial\Theta}=\bar{r}(2\bar{p}+\bar{\rho}\bar{V}_\Theta^2)\sin\Theta;\\
&\frac{\partial(\bar{r}\bar{V}_r\sin\Theta)}{\partial\bar{r}}+\frac{\partial(\bar{r}\bar{V}_\Theta\sin\Theta)}{\partial\Theta}=0;\\
&\frac{\partial\Psi}{\partial\Theta}=\bar{r}\bar{\rho}\left(\bar{V}_\Theta\frac{d\bar{r}}{d\Theta}-\bar{r}\bar{V}_r\right)\sin\Theta;\quad f=f(\Psi),
\end{aligned}\right\} \qquad \text{(XII-1-1)}$$

where

$$\bar{p}=\frac{k-1}{2k}\bar{\rho}(1-\bar{V}^2);\quad \bar{\rho}=\tau^{\frac{1}{k-1}};\quad \tau=\left[\frac{k-1}{2k}(1-\bar{V}^2)\right]^{\frac{1}{k-1}},\quad f=\frac{\bar{p}}{\bar{\rho}^k}. \qquad \text{(XII-1-2)}$$

Here we have introduced the dimensionless parameters $\bar{V} = V/V_{max}$, $\bar{\rho} = \rho/\rho_\infty$, $\bar{p} = p/(\rho_\infty V_{max}^2)$, $\bar{r} = r/\ell$, where ℓ is a certain characteristic linear dimension of the body.

The entropy function f, which changes as we pass from one streamline to another, i.e., depends on the stream function ψ, is defined by the relation $S = c_v \ln f$.

The four-equation system (XII-1-1) can be used to calculate the unknowns $\tilde{V}_r$, $\tilde{V}_\theta$, $\underline{f}$ and ψ. Its solution must satisfy boundary conditions on the surface of the nose section and on the shock wave. The following equalities must be satisfied on the surface of a blunt nose whose generatrix equation is $r = r_0(\theta)$:

$$\tilde{V}_r = \frac{\tilde{V}_\theta}{r_0}\frac{dr_0}{d\theta};\ \psi = 0;\ f = f(0) = \text{const}, \qquad \text{(XII-1-3)}$$

with the entropy function found for the conditions of passage through the vertex of the shock wave, which are written in the form

$$f(0) = \frac{2}{k+1}\left(\frac{k-1}{k+1}\right)^k \tilde{V}_\infty^{-2k}\left[\tilde{V}_\infty^2 - \frac{(k-1)^2}{4k}(1-\tilde{V}_\infty^2)\right]. \qquad \text{(XII-1-4)}$$

The boundary conditions on a shock wave with the generatrix $r = r_0(\theta) + s(\theta)$, where s is radial distance and θ = const from the contour of the body to the wave, are found from the theory of the curvilinear compression shock and take the form

$$\left.\begin{gathered}
\tilde{V}_r = \tilde{V}_y \sin\theta_s + \tilde{V}_x \cos\theta_s;\quad \tilde{V}_\theta = \tilde{V}_x \sin\theta_s + \tilde{V}_y \cos\theta_s;\\
\tilde{V}_x = \tilde{V}_\infty\left[1 - \frac{2}{k+1}(\sin^2\theta_s - M_\infty^{-2})\right];\quad \tilde{V}_y = (\tilde{V}_\infty - \tilde{V}_x)\operatorname{ctg}\theta_s;\\
\bar{p} = \frac{2}{k+1}\left[\tilde{V}_\infty^2 \sin^2\theta_s - (1-\tilde{V}_\infty^2)\frac{(k-1)^2}{4k}\right];\\
\bar{\rho} = \frac{k+1}{k-1}\frac{\tilde{V}_\infty^2 \sin^2\theta_s}{1-\tilde{V}_\infty^2\cos^2\theta_s};\quad \psi = \psi_\infty = \frac{(r_0+s)^2}{2}\tilde{V}_\infty \sin^2\theta_s.
\end{gathered}\right\} \qquad \text{(XII-1-5)}$$

The boundary condition for the entropy function is found from the expressions for $\bar{p}$ and $\bar{\rho}$.

The reader can consult the specialized literature ([68], 1960, No. 3) for the solution of equation system (XII-1-1) by the Dorodnitsin method. An electronic computer can be used for numerical integration. The result is calculation of flows around bodies with detached shock waves; the bodies may have various blunting shapes, including the sphere, the flat face, curvilinear surfaces with inflection points, etc. It is the possibility of using high-speed electronic computers that makes this method effective; the final results are obtained on the machine with the required accuracy. /487

The calculated results permit inferences as to the shape and position of the shock wave and the magnitudes and manner of distribution of the flow variables between the wave and the blunt nose.

§XII-2. APPROXIMATE METHODS OF CALCULATING FLOW AROUND NOSES WITH VARIOUS SHAPES

Spherical Nose

Equation system and solution for the neighborhood of the total stagnation point (critical point). One of the most characteristic points on a spherical nose is its point of total stagnation. Study of the flow in its neighborhood is of interest primarily because it is related to a problem of such practical importance as that of determining the heat flows, which may reach their largest values here. It is shown below that this value depends on the initial velocity gradient along the spherical surface. The initial velocity gradient can be found by investigating inviscid flow around the blunt nose. At the same time, solution of the problem of flow near the critical point enables us to determine the distance from the wave to the body and the distribution of the gasdynamic variables in this small region; the solution can be obtained in the general case with consideration of physicochemical changes in the gas.

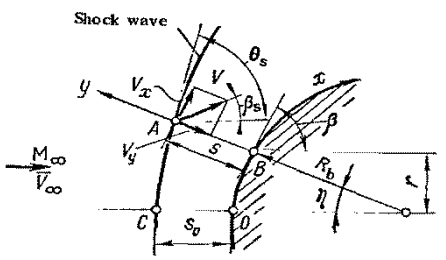

Figure XII-2-1. Components of Flow Velocity Around a Blunted Nose in Curvilinear Coordinates.

Let us consider the solution of the problem formulated ([72], 1957, No. 1). For this purpose, we shall use the equations of motion (III-2-10) and continuity (III-2-20) in a curvilinear orthogonal system. The system origin coincides with the critical point, the x-coordinate is reckoned along the surface, and y along the normal to it (Fig. XII-2-1).

If we assume that a region in the neighborhood of the critical point is to be investigated and that the oncoming flow has a very high supersonic velocity, the complex initial equations can be simplified. In fact, the flow behind the shock wave has practically incompressible properties under these conditions, since M_2 differs little from the value $[(k - 1)/2k]^{1/2}$ in the limiting case of flow (as $M_\infty \to \infty$, at $k = \text{const}$) behind a normal shock. In the neighborhood under consideration, therefore, density may be assumed constant at $\rho = \rho_\infty/\bar{\rho}$, where $\bar{\rho} = \rho_\infty/\rho_s$, and ρ_s is the density behind the shock at the critical point. Thus, we may substitute the constant $\rho_\infty/\bar{\rho}$ for the variable density ρ in the motion and continuity equations. /488

Since we are concerned with high velocities, the shock wave will make a close approach to the surface of the body in this

case. Here the region of disturbed flow lies in a thin layer of a certain thickness $\bar{s}$ that is very small by comparison with the radius of curvature $\bar{R}$ of the surface near the critical point.

Thus, if we assume that $s/R \ll 1$, then obviously $y/R \ll 1$, since $0 \leq y \leq x$. In the equations for the gasdynamic flow, therefore, $y/\bar{R}$ can be disregarded as small by comparison with unity. Moreover, the third terms on the left can be disregarded in Eqs. (III-2-10), since they are of lower order, again because $y \ll R$ and $x \ll R$. Finally, the continuity equation can be simplified for the conditions around the critical point by setting $r \approx x$.

With the above simplifications, the system of equations (III-2-10) and (III-2-20) assumes the form

$$V_x \frac{\partial V_x}{\partial x} + V_y \frac{\partial V_x}{\partial y} = -\frac{\bar{\rho}}{\rho_\infty} \frac{\partial p}{\partial x}; \qquad \text{(XII-2-1)}$$

$$V_x \frac{\partial V_y}{\partial x} + V_y \frac{\partial V_y}{\partial y} = -\frac{\bar{\rho}}{\rho_\infty} \frac{\partial p}{\partial y}; \qquad \text{(XII-2-2)}$$

$$\frac{\partial (V_x r)}{\partial x} + \frac{\partial (V_y r)}{\partial y} = 0. \qquad \text{(XII-2-3)}$$

The solution of this system must satisfy the conditions at the surface of the body at an arbitrary point, where the normal velocity component $V_y = 0$ at $y = 0$, and then at the critical point, at which the components $V_x = V_y = 0$, at $y = x = 0$. In addition, the solution must satisfy the flow conditions directly behind the shock wave. These conditions, written for the velocity components at point A at a distance $\bar{s}$ from the surface of the nose, take the form (Fig. XII-2-1)

$$V_x = V \cos(\beta - \beta_s); \qquad \text{(XII-2-4)}$$

$$V_y = -V \sin(\beta - \beta_s). \qquad \text{(XII-2-5)}$$

According to Expressions (III-4-24) and (III-4-12) and considering that $\rho = \rho_\infty/\bar{\rho}$ directly behind the shock, we shall have the following conditions for the total velocity $\bar{V}$ and the pressure $\bar{p}$ at the particular point A:

$$\frac{V}{V_\infty} = (\bar{\rho}^2 \sin^2 \theta_s + \cos^2 \theta_s)^{1/2}; \qquad \text{(XII-2-6)}$$

$$\frac{p}{p_\infty} = 1 + kM_\infty^2 (1 - \bar{\rho}) \sin^2 \theta_s. \qquad \text{(XII-2-7)}$$

Pressure and density can be excluded from (XII-2-1) and (XII-2-2). For this purpose, we differentiate these equations with respect to y and x, respectively. Then, equating the results of differentiation and applying (XII-2-3),

$$\frac{\omega_z V_x}{x} = V_x \frac{\partial \omega_z}{\partial x} + V_y \frac{\partial \omega_z}{\partial y}, \qquad \text{(XII-2-8)}$$

where the function (vorticity expression)

$$\omega_z = \partial V_x/\partial y - \partial V_y/\partial x. \qquad \text{(XII-2-9)}$$

Thus, the problem consists in finding solutions for Eqs. (XII-2-3) and (XII-2-8) that satisfy the above boundary conditions.

Let us assume that the solution for V_x in the neighborhood of the axis x = 0 can be found in series form: /489

$$V_x = a_0(y) + a_1(y)x + a_2(y)x^2 + a_3(y)x^3 + \ldots, \qquad \text{(XII-2-10)}$$

where x is a small parameter. The structure of this series can be simplified to some degree. By the oddness condition, according to which equal but opposite velocity components V_x correspond to equal to opposite x, only the terms with odd powers are retained in the expansion:

$$V_x = a_1(y)x + a_3(y)x^3 + \ldots. \qquad \text{(XII-2-11)}$$

Since a small neighborhood around the critical point is being considered, we shall disregard terms containing x in the third and higher powers. We therefore arrive at the expression $V_x = a_1(y)x$.

We introduce the function

$$F(y) = \int_0^y a_1(y)\,dy, \qquad \text{(XII-2-12)}$$

so that

$$F'(y) = a_1(y) \quad \text{and} \quad F(0) = 0. \qquad \text{(XII-2-13)}$$

Then

$$V_x = xF'(y). \qquad \text{(XII-2-14)}$$

Substituting this expression for V_x in the continuity equation (XII-2-3), we find the expression for the other velocity component:

$$V_y = -2F(y) + f(x). \qquad \text{(XII-2-15)}$$

But according to the nonseparating-flow condition $V_y(x,0) = 0$, i.e., $-2F(0) + f(x) = 0$, and since $F(0) = 0$, $f(x) = 0$.

Consequently,

$$V_y = -2F(y). \qquad \text{(XII-2-16)}$$

Introducing the relationships for V_x and V_y into (XII-2-8), we obtain

$$F'''(y) = 0, \qquad \text{(XII-2-17)}$$

which has the general solution

$$-\frac{V_y}{2} = F(y) = C_0 + C_1 y + C_2 y^2. \qquad \text{(XII-2-18)}$$

Since $F(0) = 0$, $C_0 = 0$. The other two coefficients can be determined from the conditions on the shock wave near the critical point as $x \to 0$. Specifically, since the velocity $V_y = V_C = -2(C_1 s_0 + C_2 s_0^2)$ at point C and the angle $\theta_s = \pi/2$, we find on the basis of (XII-2-6) with consideration of the y-axis direction that $V_C = -\bar{\rho} V_\infty$ and, consequently,

$$C_1 s_0 + C_2 s_0^2 = \frac{\bar{\rho} V_\infty}{2}. \qquad \text{(XII-2-19)}$$

On the other hand,

$$V_x = xF'(y) = x(C_1 + 2C_2 y). \qquad \text{(XII-2-20)}$$

Equating this velocity to its value on the shock wave according to (XII-2-4) and going to the limit as $x \to 0$, we obtain

$$\lim_{x \to 0} \frac{\cos(\beta - \beta_s)}{x} = C_1 + 2C_2 y.$$

The limit on the left can be calculated as follows. We see from Fig. XII-2-1 that the angle $\beta - \beta_s = \frac{\pi}{2} - (\eta + \beta_s)$ at an arbitrary point. Consequently, $\cos(\beta - \beta_s) = \sin(\eta + \beta_s)$, and for small η and β_s we can assume $\sin(\eta + \beta_s) \approx \eta + \beta_s$. Then /490

$$\lim_{x \to 0} \frac{\cos(\beta - \beta_s)}{x} = \lim_{x \to 0} \frac{\eta + \beta_s}{x} = \frac{1}{R_b} + \left(\frac{\beta_s}{\omega}\right)_{x \to 0} \frac{1}{R_{s0}},$$

where ω is the angle of inclination of the shock radius of curvature to the flow axis and R_{s_0} is the shock radius of curvature on this axis.

The ratio

$$\left(\frac{\beta_s}{\omega}\right)_{x \to 0} = \left(\frac{d\beta_s}{d\omega}\right)_{\beta_s \to 0}$$

is equal to $1/\bar{\rho} - 1$. This value can be obtained from (III-4-23), in which we must substitute $\Delta V_n/V_{n1} = 1 - \bar{\rho}$, $\theta_s = \pi/2 - \omega$ and pass to the limit as $\omega \to 0$. Setting the ratio R_{s0}/R_b approximately equal to unity, we find

$$C_1 + 2C_2 s_0 = \frac{V_\infty}{R_{s0}}. \qquad \text{(XII-2-21)}$$

We add one more relation to Eqs. (XII-2-19) and (XII-2-21) (since they contain the three unknown constants C_1, C_2, and s_0). This relationship proceeds from the expression for vorticity behind the shock. According to (XII-2-20), we obtain the relation $\omega_z = \partial V_x/\partial y = 2C_2 x$ for the conditions on the body's surface. On the other hand, we know from curvilinear-shock theory that the vorticity

$$\omega_z = 2C_2 x = \frac{V_\infty (1-\bar{\rho})^2 \sin\theta_s \cos\theta_s}{\sin(\theta_s - \beta_s)\left[\bar{\rho}^2 \sin^2\theta_s + \cos^2\theta_s\right]} \frac{d\theta_s}{dx}.$$

Passing to the limit in this expression as $x \to 0$, we obtain

$$C_2 = \frac{(1-\bar{\rho})^2}{2}\frac{V_\infty}{\bar{\rho}R_{s0}^2}; \qquad \text{(XII-2-22)}$$

Substituting C_2 into Eqs. (XII-2-19) and (XII-2-21) and solving them jointly, we find the coefficient C_1 and the detachment distance S_0:

$$C_1 = \mp\sqrt{1-\Delta^2}\frac{V_\infty}{R_{s0}}; \qquad \text{(XII-2-23)}$$

$$s_0 = (1 \pm \sqrt{1-\Delta^2})\,\Delta^{-2}\bar{\rho}R_{s0}, \qquad \text{(XII-2-24)}$$

where $\Delta = 1 - \bar{\rho}$.

Another expression for s_0 can also be obtained. Thus, it is shown in [59] that at high flow velocities and a constant density behind a shock that is concentric with respect to a spherical surface, the separation

$$s_0 = -\bar{\rho}\left(1 - \sqrt{\frac{8\bar{\rho}}{3} + \frac{13}{5}\bar{\rho}}\right)R_{s0}. \qquad \text{(XII-2-24')}$$

This solution is valid for small $\bar{\rho}$ (of the order of 0.1 and smaller).

Initial gradient and distribution of velocity. It follows from (XII-2-20) that the velocity $V_x = C_1 x$ on the contour of the body, where $y = 0$, i.e., with (XII-2-23)

$$V_x = \mp\sqrt{1-\Delta^2}\frac{V_\infty}{R_{s0}}x. \qquad \text{(XII-2-25)}$$

Since $V_x > 0$ and $V_x < 0$ must apply for $x > 0$ and $x < 0$, respectively, it is clear that the lower sign must be taken in this formula and hence also in Equalities (XII-2-23) and (XII-2-24). In view of the above, we can determine the velocity components in the disturbed stream from the values found for the coefficients C_1 and C_2: /491

$$\frac{V_y}{V_\infty} = -2\bar{\rho}y\left(\frac{\sqrt{1-\Delta^2}}{\bar{\rho}R_{s0}} + \frac{\Delta^2}{2\bar{\rho}^2R_{s0}^2}y\right); \qquad \text{(XII-2-26)}$$

$$\frac{V_x}{V_\infty} = \bar{\rho}x\left(\frac{\sqrt{1-\Lambda^2}}{\bar{\rho}R_{s0}} + \frac{\Lambda^2}{\bar{\rho}^2R_{s0}^2}y\right), \qquad \text{(XII-2-26)}$$
(Cont'd.)

where $\bar{\rho}R_{s0}$ is expressed in terms of s_0 by Formula (XII-2-24).

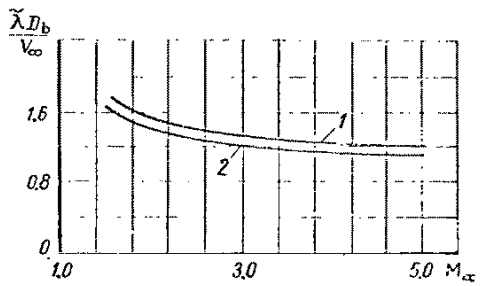

Figure XII-2-2. Velocity Gradient at Critical Point of Body. 1) theory; 2) experiment.

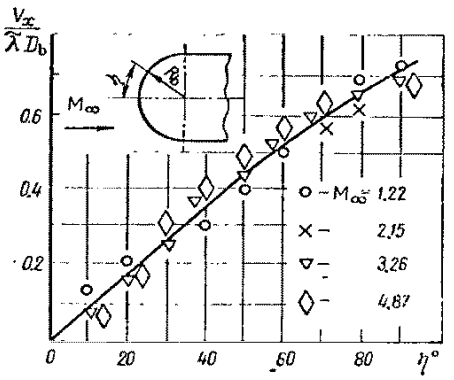

Figure XII-2-3. Velocity Distribution Over Spherical Nose Section.

As we have already noted, it is necessary to know the critical-point velocity gradient in order to determine heat transfer. According to (XII-2-25),

$$\left(\frac{\partial V_x}{\partial x}\right)_{y=0} = \tilde{\lambda} = \frac{V_\infty}{R_{s0}}\sqrt{1-\Lambda^2}. \qquad \text{(XII-2-27)}$$

Experimental studies have shown that this relationship, which has been derived for cases of flow at very high velocities, can also be used in approximate calculations at comparatively moderate speeds. This follows, for example, from Fig. XII-2-2, which shows experimental values of the dimensionless velocity gradient $\tilde{\lambda}D_b/V_\infty$ ($D_b = 2R_b$).

In Formula (XII-2-25), which we rewrite in the form $V_x = \tilde{\lambda}x$, we can replace x by the central angle η determined from the expression $x = \lambda R_b$. Then $V_x = \tilde{\lambda}R_b\eta$, which indicates that V_x depends linearly on η. It will be recalled that this relation was obtained from analysis of flow at very high velocity in a small neighborhood of the nose. However, experimental studies have shown that the linear velocity variation applies on a substantially larger area of the curvilinear surface and at comparatively small M_∞.

This is confirmed by the data in Fig. XII-2-3, which shows values of the dimensionless velocity $V_x/(\tilde{\lambda}D_b)$ on a hemispherical nose as calculated from wind-tunnel measurements for four different M_∞. It can be noted that linearity is well preserved up to values of the angle η = 45-50° and persists with small deviations at larger η.

The formula $V_x = \tilde{\lambda}R_b\eta$ that corresponds to this law can be represented in the form $V_x = \bar{\lambda}V_\infty\bar{x}$, where $\bar{x} = x/D_b$, and the dimensionless velocity gradient $\bar{\lambda} = D_b\tilde{\lambda}/V_\infty$. Experimental and theoretical data for this gradient are shown in Fig. XII-2-4, with the velocity gradient determined from the approximate relationship /492

$$\left(\frac{\partial V_x}{\partial x}\right)_{x=0} = \frac{1}{R_b}\sqrt{\frac{2(p_0' - p_\infty)}{\rho_0'}}. \qquad \text{(XII-2-27')}$$

which is derived from the improved Newton formula $\bar{p} = \bar{p}_0\cos^2\eta$. This formula can be used to evaluate the velocity distribution over a spherical nose. An expression obtained from the condition of isentropic flow behind the shock should be used for this purpose:

$$\frac{V_x^2}{V_\infty^2} = \left(1 + \frac{2}{k_\infty - 1}\frac{1}{M_\infty^2}\right)\left[1 - \left(\frac{p}{p_0'}\right)^{\frac{\bar{k}-1}{\bar{k}}}\right], \qquad \text{(XII-2-28)}$$

where k_∞ is the ratio of heat capacities in the free stream and $\bar{k}$ is the average ratio of heat capacities behind a bow compression shock and may reach $\bar{k}$ = 1.1-1.2 at very high temperatures.

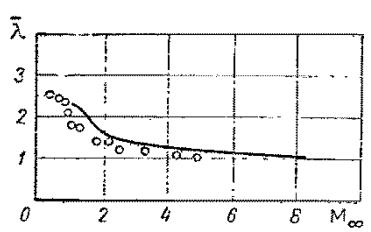

Figure XII-2-4. Velocity Gradient at Critical Point of Sphere. o) experiment.

According to the Newton formula, the pressure ratio that appears in (XII-2-28) is equal to

$$\frac{p}{p_0'} = \cos^2\eta + \frac{p_\infty}{p_0'}\sin^2\eta, \qquad \text{(XII-2-29)}$$

and p_∞/p_0' can be set approximately equal to $(kM_\infty^2)^{-1}$ at sufficiently large M_∞.

Expression (XII-2-28) easily yields simplified relationships for velocity and its gradient in the neighborhood of the critical point:

$$\frac{V_x}{V_\infty} = \bar{K}\eta; \quad \left(\frac{1}{V_\infty}\frac{dV_x}{d\eta}\right)_{\eta=0} = \bar{K}. \qquad \text{(XII-2-30)}$$

where

$$\bar{K} = \left[\frac{\bar{k}-1}{\bar{k}}\left(1 + \frac{2}{k_\infty - 1}\frac{1}{M_\infty^2}\right)\left(1 - \frac{1}{k_\infty M_\infty^2}\right)\right]^{1/2}. \qquad \text{(XII-2-31)}$$

This expression for $\bar{K}$ and, consequently, Formulas((XII-2-30) themselves, can be simplified if we are concerned with very high velocities. Then the quantities that are inversely proportional to M_∞ in (XII-2-31) can be set equal to zero. Further simplification results from assuming the flow in the neighborhood of the tip to be incompressible. Accordingly, we can write $p_0' = p + \frac{1}{2}\rho_0' V_x^2$. Here the pressure can be substituted in accordance with (XII-2-29), in which we set $\cos\eta \simeq 1$, $\sin\eta \simeq \eta = xR_b$ in view of the smallness of η. Then, differentiating V_x with respect to x, we arrive at Formula (XII-2-27') for the velocity gradient. The p_∞/p_0' under the radical can be disregarded at high velicities.

For a certain range of velocities from subsonic to medium supersonic, we have in the neighborhood of the critical point

$$V_x = \chi V_\infty \frac{x}{R_b}. \qquad \text{(XII-2-32)}$$

In this formula, $\chi = 1.5$ for incompressible flow, so that the velocity gradient

$$\frac{dV_x}{dx} = \frac{3V_\infty}{D_b}. \qquad \text{(XII-2-33)}$$

The value of χ becomes smaller with increasing M_∞. For $M_\infty >$ /493
> 1, it can be found from the empirical expression

$$\chi = 0{,}8M_\infty^{-0{,}232}. \qquad \text{(XII-2-34)}$$

It is interesting to evaluate the dimensions of the incompressible-flow region and the distance to the sonic point on the sphere. We can use (XII-2-28) for isentropic flow, assuming that this flow begins at the critical point. With a certain approximation, the conditions at this point may be assumed the same as those directly behind the normal part of the shock wave.

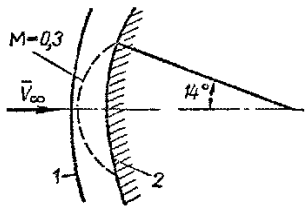

Figure XII-2-5. Position of Incompressible-Flow Region ($M \leq 0.3$) in the Neighborhood of the Critical Point of a Sphere. $M_\infty = 5.1$; $\rho_\infty/\rho_2 = 0.2$; $k = 1.4$. 1) shock wave; 2) surface of body.

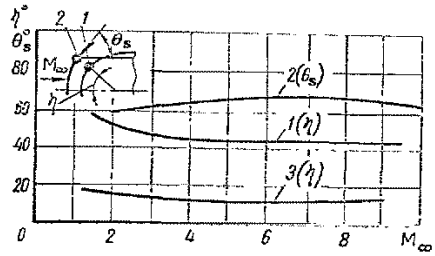

Figure XII-2-6. Position of "Sonic" Points on Sphere (1) and on Shock Wave (2). Angular Distance (3) to Boundary of Incompressible Region on Sphere (to the Point at Which $M = 0.3$).

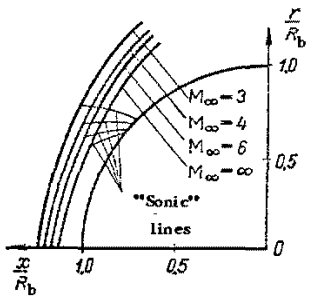

Figure XII-2-7. Positions of Shock Waves and "Sonic" Lines Around a Spherical Surface at Various M_∞.

For example, the region of undissociated incompressible flow at $k = 1.4$ was determined in this way on the assumption that the local $M > 0.3$ outside of it. This region is shown schematically in Fig. XII-2-5. Figure XII-2-6 shows the angular distance to points on the sphere at which the local Mach numbers are $M = 0.3$ and $M = 1$, as found by the same method and for the same conditions.

These results are in good agreement with the data in Fig. XII-2-7 on the positions of "sonic" points on a sphere as obtained on an electronic computer by the Dorodnitsyn method. Figure XII-2-7 also gives an idea of the shape of the "sonic" lines for various M_∞ and the positions of the "sonic" points on the shock wave. The shock inclination angles corresponding to these points are shown in Fig. XII-2-6. Under real conditions, the regions of incompressible and subsonic compressible flows will be smaller than indicated by this calculation. This is because vibrational excitation of molecules or dissociation behind the shock wave at high velocities results in a temperature decrease. This tends to lower the speed of sound. Consequently, the local M increases and the $M = 0.3$ and $M = 1$ points are shifted on the sphere at the same velocity.

Pressure distribution and drag coefficient. The results obtained for the velocity enable us to find the pressure distribution in a thin shock layer in the neighborhood of the axis and on

the body surface near the critical point. For this purpose, we can use the Bernoulli equation for an incompressible medium, from which it is easy to obtain an expression for the pressure coefficient at an arbitrary point of the shock layer: /494

$$\bar{p}=\frac{2(p-p_\infty)}{\rho_\infty V_\infty^2}\quad \bar{p}_A+\frac{1}{\bar{\rho}}\left[\left(\frac{V_A}{V_\infty}\right)^2-\left(\frac{V_y}{V_\infty}\right)^2-\left(\frac{V_x}{V_\infty}\right)^2\right]. \qquad \text{(XII-2-35)}$$

Since the layer is thin, the pressure coefficient $\bar{p}_A$ and the velocity directly behind the shock at a point on its curvilinear surface can be replaced in approximation by the values $\bar{p}_C$ and V_C behind the normal part at point C. As is indicated by (XII-2-7) and (XII-2-6), these values are respectively

$$\bar{p}_C=2(1-\bar{\rho})=2\Delta;\quad V_C=V_\infty\bar{\rho}.$$

Clearly, $\bar{p}_A = \bar{p}_C$ and $V_A = V_C$ for the conditions on the axial (zero) streamline. Then the pressure coefficient at an arbitrary point on this line is

$$\bar{p}=2\Delta+\bar{\rho}\left[1-\left(\frac{V_y}{\bar{\rho}V_\infty}\right)^2\right], \qquad \text{(XII-2-35')}$$

where $V_y/(\bar{\rho}V_\infty)$ is calculated by (XII-2-26).

Assigning various values to y/s_0, we can compute the pressure coefficient at each point on the axial streamline. For example, at the critical point on the surface, where $V_y = 0$, this coefficient is

$$\bar{p}_0=2-\bar{\rho}. \qquad \text{(XII-2-36)}$$

The pressure distribution on the body's surface in the neighborhood of the critical point can be calculated by (XII-2-35), in which we must set $V_y = 0$ and $V_x = \lambda x$. Then

$$\bar{p}=2\Delta+\bar{\rho}\left[1-\left(\frac{\tilde{\lambda}x}{\bar{\rho}V_\infty}\right)^2\right]. \qquad \text{(XII-2-37)}$$

Substituting the gradient $\tilde{\lambda}$ according to (XII-2-27) into the above equation and setting $R_{s_0} = R_b$, we obtain

$$\bar{p} = (2-\bar{\rho})\left[1-\left(\frac{x}{R_b}\right)^2\right] = \bar{p}_0\left[1-\left(\frac{x}{R_b}\right)^2\right]. \qquad \text{(XII-2-38)}$$

This formula was derived for small x. However, studies have shown that Formula (XII-2-38) can be extended after a simple transformation to a substantially larger area of the body's surface. In fact, since $x/R_b \simeq \eta \simeq \sin\eta$, it is obvious that $\bar{p} = (2 - \bar{\rho})\cos^2\eta$ and, consequently, $\bar{p} = \bar{p}_0\cos^2\eta$. We have thus obtained the improved Newton formula. Experimental studies indicate that this formula can be used for highly accurate calculations of pressure distribution over practically the entire surface of a hemisphere, although the error rises somewhat at the end of a blunt nose, where the Newtonian theory gives results somewhat higher than those from experiments.

According to (I-3-14), the working formula for the wave drag of a spherical nose has the form $c_{xw} = \int_0^{\sin^2\eta} \bar{p}\, d\sin^2\eta$. Introducing $\bar{p} = \bar{p}_0\cos^2\eta$ into this formula and integrating, we find

$$c_{xw} = \bar{p}_0\sin^2\eta\left(1-\frac{\sin^2\eta}{2}\right). \qquad \text{(XII-2-39)}$$

Specifically, for a hemisphere ($\eta = \pi/2$), the coefficient $c_{x\,w} = 0.5\bar{p}_0$.

Experiments in which the drag of a hemisphere was measured without consideration of wake pressure (Fig. XII-2-8) confirm Formula (XII-2-39), indicating that its accuracy increases with velocity. For angles near $\eta = \pi/2$, the Newton formula gives incorrect results. /495

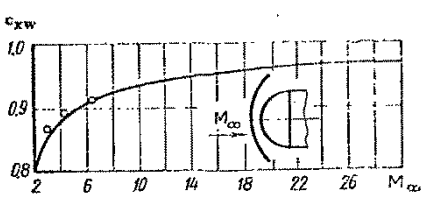

Figure XII-2-8. Wave Drag Coefficient of Hemisphere.

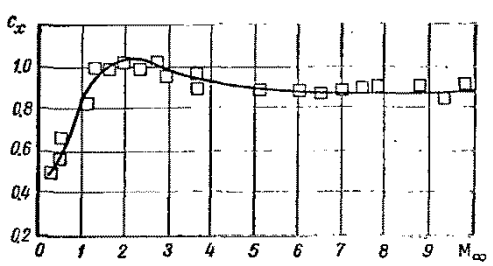

Figure XII-2-9. Frontal Drag Coefficient of a Sphere (Experiment).

Research has shown that under the conditions of an equilibrium-dissociating gas at flight speeds $V_\infty \geq 3000$ m/s, the pressure distribution is

approximated closely over the entire forward surface of the sphere by the equation ([77], 1966, No. 1)

$$\frac{p}{p_0'} = 1 - 1.17\sin^2\eta + 0.225\sin^6\eta. \qquad \text{(XII-2-39')}$$

In the range $10 \leq M_\infty \leq 40$, the pressure distribution is practically independent of Mach number. For $M_\infty > 3$ and $k = 1.4$ (dissociation disregarded)

$$\frac{p}{p_0'} = 1 - (1.525 - 1.85\bar{\rho})\sin^2\eta + (0.487 - 1.32\bar{\rho})\sin^4\eta, \qquad \text{(XII-2-39")}$$

where

$$\bar{\rho} = \frac{k-1}{k+1} + \frac{2}{(k+1)M_\infty^2}.$$

The wave drag coefficients calculated from the pressure distributions (XI-2-39') and (XII-2-39") for a spherical segment with the semivertex angle $\eta > \eta^*$ (η^* is the central angle corresponding to the "sonic" point on the sphere) are respectively equal to

$$c_{xw} = \frac{1}{kM_\infty^2}\left[\frac{p_0'}{p_\infty}(2 - 1.17\sin^2\eta + 0.113\sin^6\eta) - 2\right]; \qquad \text{(XII-2-40)}$$

$$c_{xw} = \frac{1}{kM_\infty^2}\left\{\frac{p_0'}{p_\infty}[2 - (1.525 - 1.85\bar{\rho})\sin^2\eta + (0.325 - 0.885\bar{\rho})\sin^4\eta] - 2\right\}. \qquad \text{(XII-2-40')}$$

To determine the drag coefficient of a hemisphere or part of one, it is necessary to find the pressure p_0' at the total-stagnation point. To do so, we can determine (with consideration of physicochemical transformations) the density ratio $\bar{\rho} = \rho_\infty/\rho^2$ behind the normal part of the wave and then use (XII-2-36) to calculate the pressure coefficient and the corresponding p_0'. The formula $p_0'/p_\infty = kM_\infty^2$ can be used for approximate evaluation of the stagnation pressure at very large M_∞.

The effect of pressure on the aft part of the surface must be considered in determining the drag of a sphere. As we see from the experimental data in Fig. XII-2-9, this effect will be substantial at moderate supersonic velocities. For $M_\infty > 5$ this effect can for all practical purposes be disregarded, assuming that $c_{x\,w} = 0.5\bar{p}_0$. At $k = 1.4$, $c_{x\,w} = 0.92$; this agrees well with the data of Fig. XII-2-9, which were obtained for a "cold" stream.. We note that the drag of the sphere reaches its /496

maximum at about $M_\infty \simeq 1$. It decreases up to $M_\infty \simeq 4$ and remains almost unchanged with further velocity increase. In the presence of dissociation and ionization, drag increases slightly with increasing M_∞ (see Fig. XII-2-8).

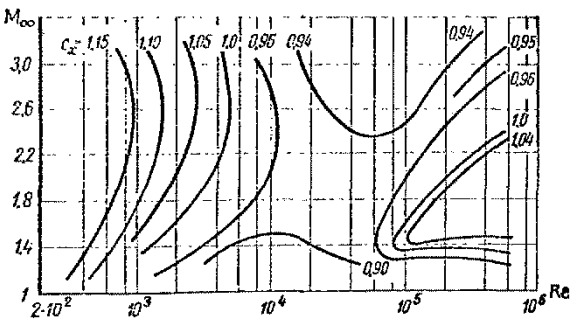

Figure XII-2-10. Drag of a Sphere as a Function of M_∞ and $Re = 2R_b V_\infty/\nu_\infty$.

Research has shown that the total drag of a sphere depends not only on M_∞, but also on Reynolds number. This is evident from Fig. XII-2-10, which shows the results of experimental determination of the total drag coefficient of a sphere as a function of M_∞ and $Re = 2V_\infty R_b/\nu_\infty$ [55]. The dependence of drag on M_∞ and Re becomes weaker with increasing flow velocity.

Detachment distance and shape of shock wave. The detachment distance s_0 can be determined from (XII-2-24), which was derived for very high velocities, in which case we may set $R_{s_0} = R_b$, for which experiments indicate that $\bar{\rho} \leq 0.1$. But the same formula can also be used for lower velocities (larger $\bar{\rho}$), when $R_{s_0} > R_b$. The only difference is that in this case (XII-2-24) yields the relative detachment distance $\tilde{s}_0 = s/R_{s_0}$. To determine the absolute value s_0, it is necessary to find R_{s_0}. For a given oncoming flow, R_{s_0} is determined by the sphere radius R_b, and research has shown that the wave radius of curvature depends linearly on R_b.

If, with this in mind, we proceed from the assumption that the wave is concentric with the sphere on the axis, then $\bar{R}_{s_0} = R_{s_0}/R_b = (1 - \tilde{s}_0)^{-1}$. Experiments indicate that the violation of concentricity is greater the smaller the M_∞. Better results are obtained with the relationship

$$\bar{R}_{s0} = \frac{R_{s0}}{R_b} = (1 - \tilde{s}_0)^{-2}. \qquad \text{(XII-2-41)}$$

Then the detachment distance, referred to the radius of a spherical nose, is

$$\bar{s}_0 = \frac{s_0}{R_\tau} = \tilde{s}_0 R_{s0} = \tilde{s}_0 (1 - \tilde{s}_0)^{-2}. \qquad \text{(XII-2-42)}$$

Figure XII-2-11 presents results of a calculation by (XII-2-42) and (XII-2-24).

For $\bar{\rho} < 0.5$, the empirical relation /497

$$\bar{s}_0 = \frac{2}{3} \frac{\bar{\rho}}{1 - \bar{\rho}} \qquad \text{(XII-2-42')}$$

gives relative detachment distances that agree quite well with these results.

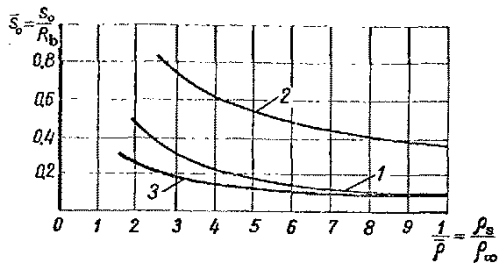

Figure XII-2-11. Relative Detachment Distance of Shock Wave in Front of Sphere (1) and Flat Truncation (2). Calculation by Formula (XII-2-42) (3).

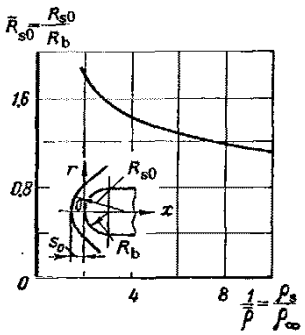

Figure XII-2-12. Radius of Curvature of Shock Wave in Front of a Sphere.

To construct the shock wave in front of a blunt nose, it is necessary to know not only the distance s_0, but also the shape of the wave's generatrix. It can be assumed with adequate approximation that the wave is parabolic

$$x = -s_0 + \frac{r^2}{2R_{s0}}$$

or hyperbolic

$$\frac{(x + a)^2}{a^2} - \frac{y^2}{b^2} = 1.$$

The semiaxes a and b of the hyperbola are determined from the conditions

$$R_{s0}=\frac{b^2}{a};\quad \frac{b}{a}=(M_\infty^2-1)^{-1/2}.$$

The shock-wave generatrix constructed in this manner agrees closely with the experimental wave for practically all M_∞, and the approximation improves as the Mach number increases. Figure XII-2-12 presents a curve characterizing the variation of radius R_{s_0} in accordance with Formula (XII-2-41) and (XII-2-24).

According to ([77] 1966, No. 1), the wave radius of curvature on the axis at very high flow velocities is

$$R_{s0} = (0.935 - 1.05\bar{\rho})^{-1}R_b, \qquad \text{(XII-2-41')}$$

where $0.06 \leq \bar{\rho} \leq 0.2$.

Knowing the shape of the shock wave, we can determine the variables directly behind it at any point on its surface. For example, we can find the M_2 distribution and the point at which $M_2 = 1$. For this purpose, the following approach should be taken in the case of a dissociating gas. After assigning a series of values of $\omega = \pi/2 - \theta_s$, the oblique-compression-shock problem is solved for each of them with consideration of dissociation. Local values of V_2 and a_2 and hence also of M_2 are determined in this process. $M_2 = 1$ will correspond to one of the assigned angles $\omega = \omega^{(1)}$. The distance from the axis to the point on the shock wave at which $M_2 = 1$ is approximately

$$r = R_{s0}\sin\omega^{(1)}.$$

Ordinary oblique-shock theory, and Formula (III-4-29) in particular, can be used to evaluate r.

Assigning a series of angles θ_s, we can find the value of an angle to which corresponds $M_2 = 1$ for a known $M_1 = M_\infty$. Figure XII-2-6 shows the variation of the angles θ_s calculated by this method for $k = 1.4$.

Flat Face /498

Pressure distribution and drag coefficient. The solid curve in Fig. XII-2-13 is a graphical representation of the pressure

distribution over a flat face in axisymmetric flow as calculated on an electronic computer for one of the M_∞. Experimental results are shown on this figure along with those from theory.

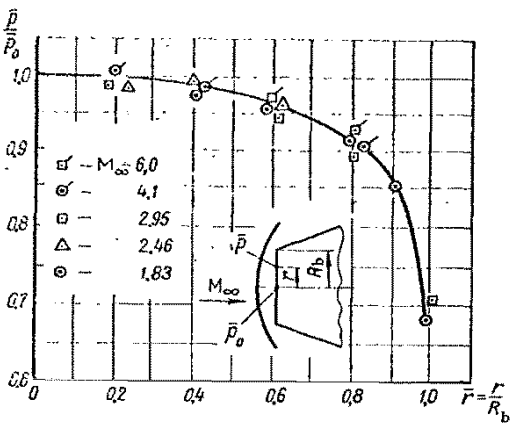

Figure XII-2-13. Pressure Distribution over Flat Face.

Analysis of the results obtained establishes a general relation for the pressure-coefficient variation in the form $\bar{p} = \bar{p}_0 f(\bar{r})$, where the dimensionless variable $\bar{r}$ is equal to the ratio of the distance r to an arbitrary point on the surface of the face to its radius R_b; $f(\bar{r})$ is a certain "universal" function that depends only on $\bar{r}$, and $\bar{p}_0$ is the pressure coefficient at the center of the face, which coincides with the total-stagnation point.

Accordingly, the wave drag coefficient of the face is

$$c_{xw} = \bar{p}_0 \int_0^1 f(\bar{r})\, d\bar{r}^2.$$

Assuming that the diagram in Fig. XII-2-13 gives a "universal" function $f(\bar{r})$ that can be used for all velocities, we can calculate the integral and obtain

$$c_{xw} = 0.915\bar{p}_0. \qquad \text{(XII-2-43)}$$

As we see, the drag coefficient of the flat face is almost twice that of a hemisphere. Available experimental data confirm this result.

Detachment distance and shape of bow shock wave. Detachment-distance measurements made in various wind tunnels have indicated that this distance is proportional to the face radius R_b but also depends on the velocity of the oncoming flow and the state of the gas. As we know, these latter factors determine the variation of density behind the shock.

If we take the general case of a dissociating and ionizing gas, we can assume that the distance from the wave to the body, referred to the radius R_b, will depend, as in the case of a

spherical nose, on the density ratio $\bar{\rho} = \rho_\infty/\rho_s$ behind the normal part of the shock.

It is also noted that the separation of the wave from a flat face is greater than that from a sphere. A rough calculation leads us to the conclusion that while $\bar{s}_0 = s_0/R_b$ is of the order of the density ratio $\bar{\rho} = \rho_\infty/\rho_s$ for a spherical nose, it is $\bar{s}_0 \sim \sqrt{\bar{\rho}}$ for a flat bluntness.

The expression for the relative detachment distance found from experimental data can be represented by /499

$$\bar{s}_0 = \frac{s_0}{R_b} = 1.03\sqrt{\frac{\bar{\rho}}{1-\bar{\rho}}}. \qquad \text{(XII-2-44)}$$

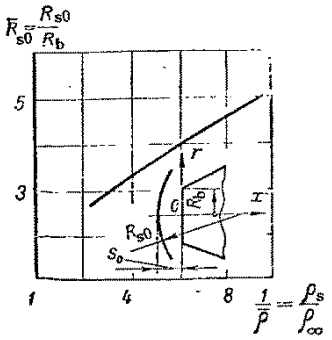

Figure XII-2-14. Shock Wave Radius of Curvature in Front of Critical Point of Flat Face.

The radius of curvature of the wave on the axis, which determines its shape near the face, is found, like the detachment distance, to be proportional to the radius of the bluntness. Here we can write for the relative radius of curvature $\bar{R}_{s0} = R_{s0}/R_b$ the obvious expression $(\bar{R}_{s0})_f = (\bar{s}_0/\tilde{s}_0)_f$ in which, as before, $\tilde{s}_0 = s_0/R_{s0}$, and the subscript f identifies the parameters for the flat face.

A similar relationship, $(R_{s0})_{sp} = (\bar{s}_0/\tilde{s})_{sp}$, can be applied to the sphere. Here, experiment has shown that the relative detachment distances $\tilde{s}_0$ for the sphere and the flat face are approximately the same. Accordingly, the ratios $\bar{s}_0/\bar{R}_{s0}$ will also be the same. We may therefore write for the relative radius of the wave's curvature in front of the flat face

$$(\bar{R}_{s0})_f = \frac{(\bar{s}_0)_f}{(\bar{s}_0)_{sp}}(\bar{R}_{s0})_{sp}. \qquad \text{(XII-2-45)}$$

The relative detachment distance $(\bar{s}_0)_f$ for the flat face and the $(\bar{s}_0)_{sp}$ and $(\bar{R}_{s0})_{sp}$ for the sphere are determined by Formulas (XII-2-42') and (XII-2-41), respectively.

Relation (XII-2-45) can be presented in a simpler form if we assume that the wave is concentric with the sphere. In this case,

$$(\bar{R}_{s0})_{sp} = 1 + (\bar{s}_0)_{sp}. \qquad \text{(XII-2-46)}$$

Then, applying (XII-2-42') and (XII-2-44), we find for the flat face

$$\bar{R}_{s0} = 0.52\,(3-\bar{\rho})\,[\bar{\rho}\,(1-\bar{\rho})]^{-1/2}. \qquad \text{(XII-2-47)}$$

Figure XII-2-14 presents a curve of this relationship for $\bar{R}_{s_0}$.

It is easily seen that according to (XII-2-47), $R_{s_0} \to \infty$ as $\bar{\rho} \to 0$, since the wave touches the flat surface at the limit.

The position of the "sonic" point on the shock wave is determined by the methods that were indicated in our study of flow around a sphere.

As concerns the washed surface, the "sonic" point coincides with the sharp edge of the face; this is confirmed by experimental data.

Since the velocity is sonic at the edge of the face and, consequently, the local Mach number M = 1 is known, the pressure can be determined at this point.

Regarding the flow as isentropic along the streamline between the total-stagnation and "sonic" points, we can write for the pressure

$$\frac{p_{sn}}{p_0} = \left(\frac{2}{k_2+1}\right)^{\frac{k_2}{k_2-1}},$$

where k_2 is the ratio of heat capacities calculated for the conditions on the normal part of the shock. For moderate velocities, $k_2 = k_1$, so that the pressure p_{sn} at the "sonic" point is determined by the usual formula. /500

At high velocities, it is necessary to consider the variation of the heat capacities. If we assume that $\bar{\rho} = (k_2 - 1)/(k_2 + 1)$, we have in approximation

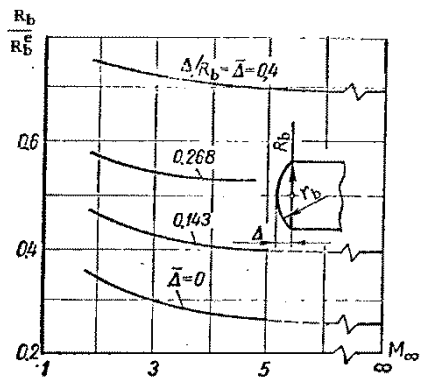

Figure XII-2-15. Illustrating Determination of Equivalent Radius ($\bar{\Delta} = \Delta/R_b$).

$$\frac{\bar{p}_{sn}}{\bar{p}_0} = 0.5(1 + \bar{\rho}). \qquad \text{(XII-2-48)}$$

According to this formula, the pressure at the inflection point of the flat face is approximately half that at the total-stagnation point.

Velocity gradient at critical point. It has been shown that the velocity gradient for a sphere is inversely proportional to the surface radius R_b. As this radius increases, therefore, the velocity gradient decreases and vanishes at the limit as $R_b \to \infty$, i.e., for a flat bluntness.

This conclusion follows from (XII-2-27'). Studies indicate that the velocity gradient at the critical point on a flat face differs from zero. It may be assumed on this basis that a flat face influences the flow in much the same way as a spherical surface with a certain radius R_b^e. This conclusion is confirmed by observations of shock-wave shape.

It is possible to find an equivalent sphere radius R_b^e at which the axial curvature of the wave will be approximately the same as its curvature in front of a flat face. Then

$$(\bar{R}_{s_0})_f R_b = (\bar{R}_{s_0})_{sp} R_b^e.$$

Hence the equivalent radius

$$R_b^e = R_b[(\bar{R}_{s_0})_f]/[(\bar{R}_{s_0})_{sp}], \qquad \text{(XII-2-49)}$$

where $R_b = D_b/2$ is the radius of the flat face.

Applying (XII-2-27'), we can determine the velocity gradient at the critical point of a sphere of the equivalent radius:

$$\left(\frac{\partial V_x}{\partial x}\right)_{\substack{x=0\\y=0}} = \frac{1}{J}\frac{R_b}{R_b^e}, \qquad \text{(XII-2-50)}$$

where

$$J = R_b\left[\frac{2p_0'}{\rho_0'}\left(1-\frac{p_\infty}{p_0'}\right)\right]^{-1/2}.$$

The velocity gradient determined by (XII-2-50) is assumed to be the same as that at the total stagnation point on the flat face. This assumption is naturally not rigorous and requires supplementary experimental verification. The data available in Fig. XII-2-15 indicate that Formula (XII-2-50) gives an approximately correct solution at high velocities.

Other Blunted Nose Shapes

Pressure distribution and drag. Let us consider a flat blunting with a circular bevel (rounded edge) (Fig. XII-2-16, curve 2) and a spherical-segment bluntness with a radius larger than that of the hemisphere (Fig. XII-2-16, curve 3).

Studies have shown ([72] 1961, No. 11) that in the subsonic range, the pressure distribution is influenced somewhat farther upstream, beginning at the total-stagnation point, by the shape and radius of curvature of the contour near its sharp inflection point. /501

The determining parameter for flat noses with rounded edges is the radius of curvature ratio $\bar{r} = r/R_b$; for noses with a spherical segment, it is the dimensionless radius $\bar{r} = r/R_b$ of the sphere (or the dimensionless segment height $\bar{\Delta} = \Delta/R_b$), with the influence of the inflection point coming into play for the latter nose shape if sonic flow is established at that point.

Experimental studies at $M_\infty = 5.8$ showed that the sonic-velocity condition is preserved at the inflection point up to values of the spherical-surface inclination angle $\beta_{br} \geq 45°$ at that point. For $67° \leq \beta_{br} \leq 90°$, the shape of the shock wave near the nose is practically independent of the nose curvature radius. The "sonic" point on the shock wave lies at the intersection of the wave with a normal drawn from the inflection point. For $\beta_{br} \to 67°$, the surfaces of the nose and the shock wave are almost concentric. For generatrix inclination angles of $45° \leq \beta_{br} \leq 67°$ at the inflection point, the flow condition is characterized by shifting of the "sonic" point on the shock wave toward the axis of the body as the segment radius increases, while the "sonic" point on the body remains at the inflection point. The shape of the wave becomes more and more divergent from the shape of the nose, and the pressure distribution approaches that obtained on a hemisphere.

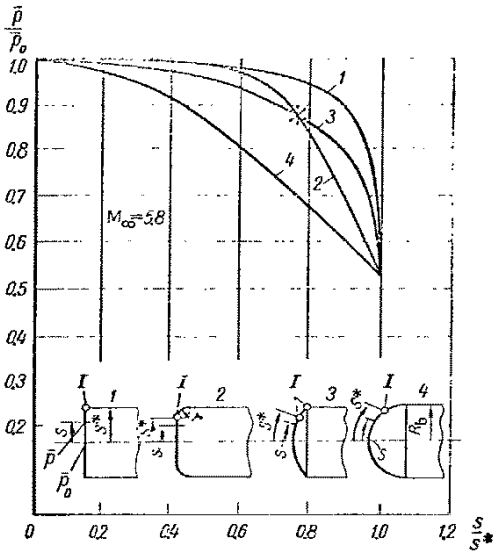

Figure XII-2-16. Distribution of Pressure Over Variously Shaped Blunted Surfaces. S* is the coordinate of the "sonic"point on the blunt surface; I is the possible position of the "sonic" point; * indicates the point at which the circular chamfer meets the flat face.

The pressures are equalized when the contour at the inflection point is inclined at the same angle as at the "sonic" point on the hemisphere. In particular, this occurs at $M_\infty = 5.8$ when $0 \leq \beta_{br} \leq 45°$ at the inflection point. In this flow regime, a decrease in the nose radius of curvature causes a shift of the "sonic" point on the body surface from the inflection toward the axis. The pressure distribution does not change, since disturbances do not penetrate into the subsonic region from the inflection point, where velocity is supersonic.

The manner of variation of $\bar{p}/\bar{p}_0$ in Fig. XII-2-16 depends relatively weakly on M_∞, as is confirmed by the data of Fig. XII-2-17, which shows the experimental distribution of $\bar{p}/\bar{p}_0$ near the surface of a spherical segment with the angle $\eta = 20°.21$ for two Mach numbers: $M_\infty = 2.01$ and 4.76. For this nose, the inflection and "sonic" points coincide.

Experimental studies made at moderate M_∞ brought out a linear relation between the wave drag coefficient of a rounded nose and the dimensionless parameter $\bar{r}$, which is presented in the form /502

$$c_{x\,w} = (c_{x\,w})_f - [(C_{x\,w})f - (c_{x\,w})_{sp}]\bar{r}. \qquad \text{(XII-2-51)}$$

It may be assumed that this relationship will also be preserved at higher velocities.

With a certain approximation, Formula (XII-2-51) can be extended to bodies with blunted noses made in the form of spherical segments with increased radius $R_{sp} > R_b$ or in the form of an

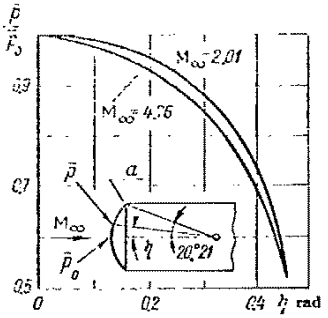

Figure XII-2-17. Pressure on Blunted Surface at Various M. a) "sonic" point.

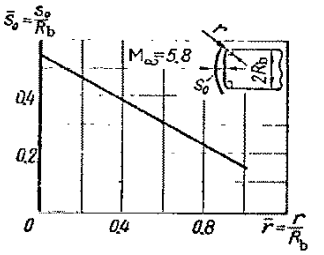

Figure XII-2-18. Detachment Ratio of Shock Wave at Flat Bluntness with Circular Bevel (Experiment).

ellipse, although, strictly speaking, experiments indicate a certain deviation from linearity.

When Formula (XII-2-51) is used in these two cases, the parameter $\bar{r}$ must be replaced by $\bar{b}$ and $\bar{\Delta}$, respectively.

Detachment distance and radius of curvature of wave. A similar linear relation is also observed for the relative detachment distance of the shock wave in front of a rounded nose.

Figure XII-2-18 shows an experimentally obtained diagram of $\bar{s}_0 = s_0/R_b$ as a function of the bluntness parameter $\bar{r} = r/R_b$ for $M_\infty = 5.8$. As we see, the shape of the body's surface in the "sonic" region has a strong influence on the separation and curvature of the wave.

Assuming that this law is preserved for arbitrary M_∞, we write, by analogy with (XII-2-51), a general experssion for the relative detachment distance:

$$\bar{s}_0 = (\bar{s}_0)_f - [(\bar{s}_0)_f - (\bar{s}_0)_{sp}]\bar{r}. \qquad \text{(XII-2-52)}$$

Experimental data obtained on nose models with spherical segments indicate nearly linear variation of $\bar{s}_0$ as a function of segment height ratios in the range $-0.1 \leq \bar{\Delta} \leq 0.45$.

The corresponding approximate relation for the relative detachment distance is

$$\bar{s}_0 = (\bar{s}_0)_f + \frac{20}{9}[(\bar{s}_0)_f - A]\bar{\Delta}, \qquad \text{(XII-2-53)}$$

where A is the detachment distance ratio for $\bar{\Delta} = 0.45$. According to certain experimental data, this value may be set approximately equal to $2(\bar{s}_0)_{sp}$. /503

Experiments have also established the approximate nature of the relationship for the relative curvature radius of the shock wave on the axis. For rounded bodies, it is hyperbolic in nature over the entire range $0 \leq \bar{r} \leq 1$, with the radius of curvature decreasing with decreasing rounding radius. The corresponding empirical relation is

$$\bar{R}_{s0} = \frac{R_{s0}}{R_b} = \frac{(\bar{R}_{s0})_f (\bar{R}_{s0})_{sp}}{(\bar{R}_{s0})_{sp} + [(\bar{R}_{s0})_f - (\bar{R}_{s0})_{sp}]\bar{r}}. \qquad \text{(XII-2-54)}$$

For roundings in the form of spherical segments, the relative radius, like the separation, is an almost linear function of $\bar{\Delta}$ for the case of a nearly flat nose ($-0.1 \leq \bar{\Delta} \leq 0.45$). In this range of $\bar{\Delta}$, the relative curvature radius

$$\bar{R}_{s0} = \frac{9(\bar{R}_{s0})_f B}{9B + 20[(\bar{R}_{s0})_f - B]\bar{\Delta}}, \qquad \text{(XII-2-55)}$$

where B is the value of $\bar{R}_{s_0}$ that corresponds to $\bar{\Delta} = 0.45$. Experimental data indicate in approximation that $B = (1.8\text{-}2)(\bar{R}_{s_0})_{sp}$.

Equivalent radius of sphere and velocity gradient at critical point. The premises for calculation of these parameters are the same as those adopted in study of flow around a flat face. The equivalent sphere radius corresponding to a given nose is determined from (XII-2-49), in which the numerator must be calculated by (XII-2-54) or (XII-2-55).

The velocity gradient at the critical point will be determined by (XII-2-50) after the equivalent radius is found. According to our premises, the values obtained are tentative, and it is recommended that they be verified and refined experimentally in each case.

The results of such studies at lowered M_∞ are shown in Fig. XII-2-15. Here we see that Formula (XII-2-50) agrees well with the experimental data for the spherical segment with $\bar{\Delta} = 0.4$, although the corner point is "sonic" in this case (the largest value of $\bar{\Delta}$, which corresponds to the speed of sound, is $\bar{\Delta} = 0.45$).

Available data indicate that (XII-2-50) can be used to calculate the velocity gradient at the critical point of segment noses even for $\bar{\Delta}$ somewhat smaller than 0.4, beginning at about 0.3-0.35. For a body with a nearly flat nose (rounding radius

large enough so that $\bar{\Delta} \to 0$), the approximate value of the velocity gradient at the total-stagnation point [55] is

$$\left(\frac{\partial V_x}{\partial x}\right)_{\substack{x=0\\y=0}} = \frac{4}{3\tau}\frac{V_\infty}{R_b}\sqrt{\bar{\rho}(2-\bar{\rho})}. \qquad \text{(XII-2-50')}$$

Spherical Surface with "Blunted" Forward End

Pressure can be calculated for very-high-velocity circular airflow around a "blunted" sphere formed by combining part of a sphere with an arbitrarily shaped surface (Fig. XII-2-19) by the improved Newton formula

$$\bar{p} = \bar{p}_0(\cos\alpha\sin\beta - \sin\alpha\cos\beta\cos\gamma)^2. \qquad \text{(XII-2-56)}$$

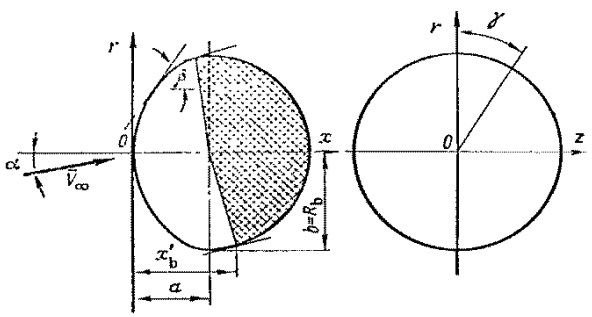

Figure XII-2-19. Working Diagram for "Blunted" Sphere.

Setting the pressure coefficient $p_e = 0$ in the "shaded" zone, we determine the axial-force coefficient c_{Rp} in accordance with (X-3-5) by the formula /504

$$c_{Rp} = \frac{2}{\pi R_b^2}\int_0^{x'_b} A(\gamma_b)\, r \operatorname{tg}\beta\, dx, \qquad \text{(XII-2-57)}$$

where x'_b is the coordinate of the point corresponding to the beginning of the "shaded" zone on the bottom of the surface and $A(\gamma_b)$ is the function defined by (X-3-6).

The normal-force coefficient is determined by Formula (X-3-36)

$$c_{Np} = -\frac{2}{\pi R_b^2}\int_0^{x'_b} B(\gamma_b)\, r\, dx, \qquad \text{(XII-2-58)}$$

where $B(\gamma_b)$ is the function calculated from Expression (X-3-37).

The moment coefficient is determined with (X-3-55):

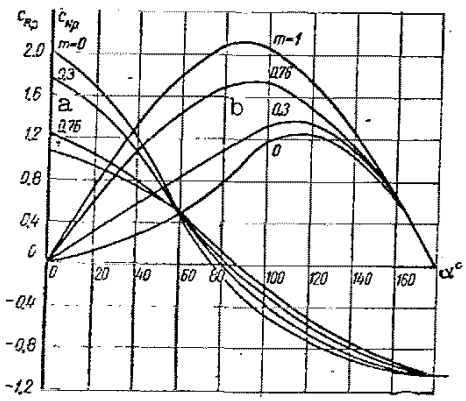

Figure XII-2-20. Coefficients of Axial (a) and Normal (b) Forces for "Blunted" Sphere.

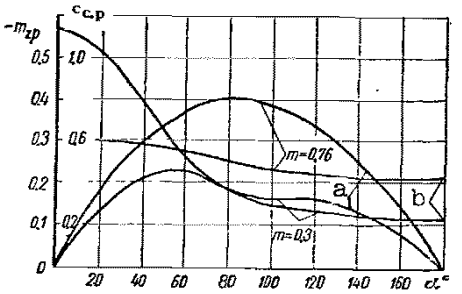

Figure XII-2-21. Coefficients of Moment (a) and Center of Pressure (b) for "Blunted" Sphere.

$$m_{zp} = \frac{-2}{\pi R_b^2 (a + R_b)} \int_0^{x'_b} xrB(\gamma_b)\, dx - \frac{2}{\pi R_b^2 (a + R_b)} \int_0^{x'_b} r^2 \operatorname{tg}\beta\, B(\gamma_b)\, dx. \quad \text{(XII-2-59)}$$

Knowing the coefficients m_{zp} and c_{Np}, we can determine the center of pressure coefficient $c_{c.p} = m_{zp}/c_{Np}$. The above formulas can be used for attack angles varying from 0 to π, i.e., for the circular-onflow case. Figures XII-2-20 and XII-2-21 show the results of a flow calculation for a sphere joined to a half-ellipsoid for various semiaxis ratios $m = a/b = a/R_b$. The value m = 1 corresponds to a spherical surface, and m = 0 to a flat face. Qualitatively, these results agree well with experimental data. Less satisfactory agreement of the quantitative characteristics is explained by the imprecision of the method, which, for example, does not take account of the pressure in the "shaded" zone. /505

§XII-3. FLOW AT HIGH VELOCITIES AROUND CYLINDRICAL AND CONICAL BODIES WITH SMALL BLUNTNESS

Analogy with Nonsteady Motion of Piston

Influence of a small bluntness. Studies have shown that the influence of a small bluntness on the flow around the entire body is not the same for different sets of conditions and depends, for example, on the velocity of the oncoming flow. Thus, it has been established by experiments that at moderate M_∞, this effect is

insignificant and affects only a small neighborhood around the nose of the body.

The influence of bluntness increases substantially at very high velocities. A blunted nose changes the nature of the flow in a disturbed region whose length ranges to tens and hundreds of bluntness diameters; the more slender the body, the larger this region and, consequently, the more effective the bluntness. To the above, we should add that the bluntness effect also depends on the shape of the blunted body; e.g., it is substantially greater for a profile than for a solid of revolution.

For example, the drag of a blunted profile is always greater than that of a sharp one, and the increase may be very large. For a solid of revolution, however, it may not only not increese, but even become smaller.

The nature of the flow around the body will depend on the degree of bluntness, which we can define by the ratio $2R_b/L$. The degree of bluntness and the flow effect corresponding to it are definitely consistent with the research methods of bluff-body aerodynamics. For example, if the bluntness dimension is small ($2R_b/L \ll 1$), the investigation may be carried out on the assumption that the body has remained sharp and the bluntness effect may be replaced by the effect of concentrated forces exerted by the bluntness on the moving flow.

The problem has been solved in this formulation by Prof. G.G. Chernyy [38]. To obtain a clearer conception of the proposed method, let us recall the analogy between steady flow around a cone and unsteady motion of a gas behind a cylindrical shock wave that forms in front of a piston. In this analogy, the disturbed flow around the cone is equivalent in a transverse plane stationary with respect to the body to the gas flow that arises in front of a cylindrical piston. For an observer in this plane, the flow is analogous to the flow that arises during propagation of an explosion wave.

Thus, the disturbed flow around the cone is analogous to the /506
flow formed when a long concentrated cylindrical charge explodes at $t = 0$. The initial energy of the gas is assumed equal to its value in the undisturbed flow owing to the absence of a strong effect of a sharp nose on the gas in front of the explosion (or the piston).

In the presence of bluntness, however, the force acting on the gas is not zero. This force, which is equal to the frontal drag X of the blunt nose, acts on the gas, performing a work that imparts a certain energy E to it. Thus, the initial energy per unit length of the concentrated charge is identified with the nose drag.

Limiting ourselves to symmetrical flow, we can now formulate the problem of motion of a cylindrical piston that is equivalent to the problem of flow around a bluff body. In a gas at rest lying along a certain straight line, an explosion takes place at the initial point in time, with the result that a specific energy E is imparted to the gas. At the same instant, a flow similar to the flow in front of a cylindrical piston moving at velocity V arises in the gas at the point of the explosion.

Solution of the problem consists in determining the motion that appears ahead of the piston. In the equivalent problem of stationary flow, this solution will enable us to find the shape of the shock wave ahead of the blunt cone and the pressure distribution over its surface. By passing to this problem, we must set

$$E = X = c_x \frac{\rho_\infty V_\infty^2}{2} \pi R_b^2; \; t = \frac{x}{V_\infty}; \; V = V_\infty \operatorname{tg} \beta_c, \qquad \text{(XII-3-1)}$$

where c_x is the drag coefficient of the bluntness.

In the general case, therefore, the problem of flow around a blunt cone reduces to the problem of an explosion with subsequent piston expansion. It must be noted that this analogy pertains to a flow region not too close to the nose of the body, where the velocity disturbance in the longitudinal direction is small and, consequently, the law of plane sections applies.

The equation system. Problems of this type involving analysis of motion at a piston are conveniently solved by use of equations in a form proposed by Lagrange instead of in the Euler form (see Chapter III). Written in this form, the equations reflect individual-particle motion. If, as in our case, the concern is one-dimensional radial motion around a cylindrical piston, the solution of these equations will determine the r-coordinates and the variables of state of the particle for any time t.

If at t = 0, the particle coordinate is r_1, then its present coordinate r will be a function of time t and the initial coordinate r_1, i.e., $r = f(r_1, t)$. The variables of state are also functions of the initial coordinate r_1 and time t when their initial values are known (for example, the density β_∞, pressure p_∞, entropy S_∞, etc).

Referring to Fig. III-2-3, let us briefly set forth the derivation of the fundamental equations in the Lagrangian form. Equating to zero the sum of the inertia forces $(\partial V_r/\partial t)\rho \times$ $\times (2\pi r \, dr \cdot 1)$ and pressure forces $(\partial p/\partial r)(2\pi r \cdot 1)dr$ acting on a particle of volume $2\pi r \, dr \cdot 1$, we obtain the equation of motion

$$\frac{\partial V_r}{\partial t} = \frac{\partial^2 r}{\partial t^2} = -\frac{\partial p}{\partial r}\frac{1}{\rho}. \qquad \text{(XII-3-2)}$$

The continuity equation is obtained from the condition of particle-mass conservation during the motion. According to this condition, if the mass was $\rho_\infty(2\pi r_1 dr_1 \cdot 1)$ at the initial point in time, it will remain the same after a time t. Consequently,

$$2\pi r\, dr\rho = 2\pi r_1\, dr_1 \rho_\infty.$$

Since this condition is in effect at any point in time, the total derivative dr/dr_1 can be replaced by the partial derivative $\partial r/\partial r_1$. Then the continuity equation assumes the form /507

$$\frac{\partial r}{\partial r_1} = \frac{\rho_\infty r_1}{\rho r}. \qquad \text{(XII-3-3)}$$

If we introduce the new Lagrangian variable $m = \rho_\infty r_1^2/2$, the equations of motion and continuity, written in this variable, will be

$$\frac{\partial V_r}{\partial t} = -r\frac{\partial p}{\partial m}; \qquad \text{(XII-3-2')}$$

$$\frac{\partial r}{\partial m} = \frac{1}{\rho r}. \qquad \text{(XII-3-3')}$$

These equations are solved for isentropic flow at the piston. In mathematical form, the condition of time constancy of particle entropy is

$$\frac{\partial S}{\partial t} = 0 \quad \text{or} \quad \frac{\partial}{\partial t}\left(\frac{p}{\rho^k}\right) = 0. \qquad \text{(XII-3-4)}$$

The first expression applies for the more general case in which physicochemical transformations may occur in the gas, while the latter corresponds to isentropic flow with constant heat capacities.

Let us supplement our equation system with an energy equation referred to the same conditions behind the cylindrical shock wave. If we are concerned with piston-impelled motion of a gas that has started after an explosion, then according to this law the total (kinetic and internal) energy of the moving gas is equal at any point in time to the energy E liberated per unit length by the explosion, the initial energy E_1, and the work of

expansion of the piston. Consequently,

$$2\pi \int_{r_0}^{r} \left(\frac{V_r^2}{2} + u\right) \rho r\, dr = E + 2\pi \int_0^r u_\infty \rho r\, dr + 2\pi \int_0^r pr\, dr, \qquad \text{(XII-3-5)}$$

where u and u_∞ are the specific internal energies and have the dimensions of velocity squared; p is the gas pressure on the piston; r_0 and r are the distances to the piston and the shock wave, respectively.

Examining the case of constant heat capacities, when $u = c_r T = [1/(k-1)]p/\rho$, and remembering that $V_r = \partial r/\partial t$ and $r_1 \rho_\infty dr_1 = r\rho dr$, we find

$$\int_{r_0}^{r} \left[\frac{1}{2}\left(\frac{\partial r}{\partial t}\right)^2 + \frac{1}{k-1}\frac{p}{\rho}\right] \rho r\, dr = \frac{E}{2\pi} + \frac{p_\infty r^2}{2(k-1)} + \int_0^r pr\, dr. \qquad \text{(XII-3-5')}$$

Finally, we obtain the equation of momentum, which, together with the energy equation, is most convenient for solution of problems of gas motion around a cylindrical piston. The momentum equation can be obtained from the equation of motion when the latter is written in the form

$$\rho r \frac{\partial V_r}{\partial t} dr = -\frac{dp}{dr} r\, dr.$$

After integrating over the thickness of the disturbed layer, we find

$$\int_{r_1}^{r} \frac{\partial V_r}{\partial t} \rho r\, dr = -\int_{p_\infty}^{p} r\, dp. \qquad \text{(XII-3-6)}$$

Flow Around a Blunted Cylinder

/508

Solution of the equivalent problem of nonsteady motion of a cylindrical piston enables us to calculate the flow around a blunted cylinder. It is assumed here that a charge distributed along a certain straight line imparts an initial energy E to the gas as it explodes.

The gas motion that results from this explosion corresponds to the condition of velocity V = 0 at the piston. In the general case, the parameters that determine this motion behind the shock wave are the initial pressure p_∞ and the density ρ_∞, the explosion energy E (work per unit length), the heat-capacity ratio

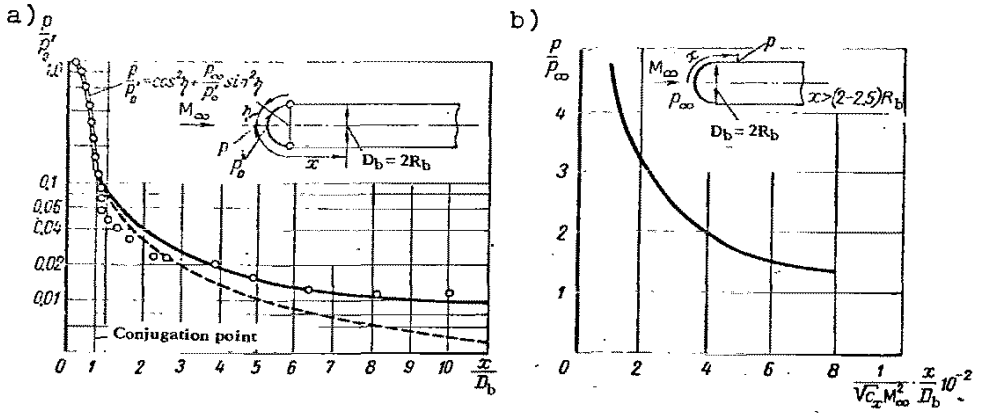

Figure XII-3-1. Pressure Distribution on Generatrix of Cylindrical Body with Spherical Nose. o) experiment; ———) according to (XII-3-12); -----) according to (XII-3-10').

k, the distance r from the line of the explosion, and the time t. If we calculate the dimensionless characteristics of the disturbed flow, e.g., the relative pressure, they will also be functions of dimensionless combinations derived from the determining parameters named above.

Since one of these parameters, namely, the ratio of specific heats k, is dimensionless, the additional dimensionless combinations must, according to dimensionality theory [31], be composed of the remaining five parameters. Since three of them have independent dimensions, we can obviously write two more independent dimensionless combinations, namely $p_\infty^{1/2} r/E^{1/2}$, $p_\infty t/(\rho_\infty E)^{1/2}$.

After they have been reduced to dimensionless form, therefore, the unknowns behind the shock will depend on these three dimensionless parameters. The latter two can be transformed by the substitution with (XII-3-1). Then the system of dimensionless parameters takes the form

$$k;\ \frac{1}{M_\infty \sqrt{c_x}} \frac{r}{D_b};\ \frac{1}{M_\infty^2 \sqrt{c_x}} \frac{x}{D_b}. \qquad \text{(XII-3-7)}$$

It follows from the above that the shape of the bow shock in front of a blunted cylinder is determined by the general functional relation

$$\frac{1}{M_\infty \sqrt{c_x}} \frac{r_c}{D_b} = R\left(k, \frac{1}{M_\infty^2 \sqrt{c_x}} \frac{x}{D_b}\right). \qquad \text{(XII-3-8)}$$

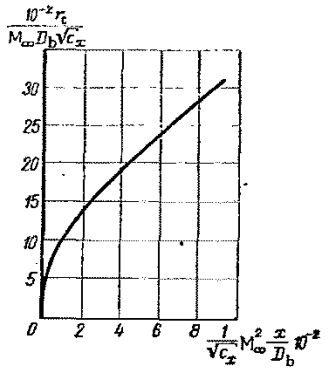

Figure XII-3-2. Curve for Determination of Shape of Bow Wave in Front of a Cylindrical Body with a Spherical Nose.

The general relation for the pressure distribution on the surface of the cylinder is found from the condition r = 0 and has the form /509

$$\frac{\Delta p}{p_\infty} = P\left(k, \frac{1}{M_\infty^2 \sqrt{c_x}} \frac{x}{D_b}\right). \qquad \text{(XII-3-9)}$$

In (XII-3-8) and (XII-3-9), the functions R and P depend on $\frac{1}{M_\infty^2 \sqrt{c_x}} \frac{x}{D_b}$ and k, which are similarity parameters. The existence of these parameters enables us to generalize isolated experimental results into a group of similar flows around blunted cylindrical bodies. By way of illustration, let us examine experimental data on the pressure distribution obtained for $M_\infty = 7.7$ and $k = 1.4$ in wind-tunnel tests of a cylinder model with a hemispherical nose (Fig. XII-3-1a). To generalize these data, values of the parameter $(x/D_b)/(M_\infty^2\sqrt{c_x})$, in which the coefficient c_x was found for $M_\infty = 7.7$ in accordance with the experimental conditions, were calculated. The ratios x/D_b were the same as in the experiment. The diagram constructed with this parameter in Fig. XII-3-1b (experimental data [16]) can be used to calculate pressure for arbitrary M_∞. Figure XII-3-2 shows a similar diagram that generalizes experimental results obtained under the same conditions ($k = 1.4$, $M_\infty = 7.7$) in a study of shock-wave shape.

In certain cases, the general relationships (XII-3-8) and (XII-3-9) can be converted to a more concrete form. This is possible, for example, at very high flow velocities, when the initial gas pressure p_∞ is negligible as compared with the pressure behind a very strong shock wave. In this case, the pressure p_∞ is dropped from the determining parameters listed above. Consequently, the pressure on the cylinder can be presented by the relation

$$\Delta p \simeq p = P(k, \rho_\infty, E, t).$$

The last three parameters under the sign of the function P have independent dimensions and cannot form a dimensionless combination. Consequently, according to the basic theorem of dimensionality theory, Δp must be determined by the expression

$$\Delta p = f_1(k)\,\rho_\infty^x E^y t^z,$$

where $f_1(k)$ is a certain function that depends on the ratio of heat capacities. After substituting Expressions (XII-3-1) for E and t, we can write

$$\Delta p = f_1(k)\,\rho_\infty^x \left(c_x \frac{\rho_\infty V_\infty^2}{2} \frac{\pi D_b^2}{4}\right)^y \left(\frac{x}{V_\infty}\right)^z.$$

The exponents are determined with the basic formula of dimensional analysis, which takes the form of a power monomial:

$$ML^{-1}T^{-2} = [ML^{-3}]^x [MLT^{-2}]^y [T]^z,$$

where M, L, and T are the independent dimensions of mass, length, and time, respectively. From this we find that x = y = 1/2, z = 1. Consequently, /510

$$\frac{2\Delta p}{\rho_\infty V_\infty^2} = \bar{p} = f(k)\sqrt{c_x}\frac{D_b}{x}. \qquad \text{(XII-3-10)}$$

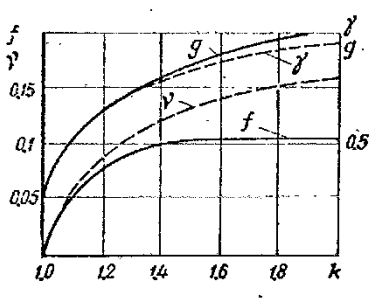

Figure XII-3-3. Curves for Determination of Working Coefficients in Formulas (XII-3-10) and (XII-3-11).

A similar relationship can be obtained for the coordinates of shock-wave points. Let us first write a general expression for the wave radius in the form $r_s = R(k, \rho_\infty, E, t)$ where R is a certain function of the parameters in the parentheses, and then apply dimensionality theory, which was used in deriving the general relation for the pressure function, i.e., present r_s in the form

$$r_s = g_1(k)\,\rho_\infty^x E^y t^z,$$

where $g_1(k)$ is a certain function of the specific heats ratio k, to obtain a formula for the dimensionless coordinate

$$\frac{r_s}{D_b} = g(k)\,c_x^{1/4}\left(\frac{x}{D_b}\right)^{1/2}. \qquad \text{(XII-3-11)}$$

In (XII-11), the functions f(k) and g(k), which depend on the adiabatic gas ratio $k = c_p/c_v$, are determined by exact solution of the problem of a strong linear-charge explosion. The values obtained for these functions are presented graphically in Fig. XII-3-3. In accordance with these values and with the expression from (XII-3-10), we can obtain the expressi

$$\frac{p}{p_\infty} = 0.066 M_\infty^2 \frac{D_b}{x}. \qquad \text{(XII-3-10')}$$

It must be remembered that this formula, like the more general relationship (XII-3-11), is a first approximation, since it does not take account of the initial pressure.

Attempts were made to take account of this pressure. The result was the more exact formula

$$\frac{p}{p_\infty} = 0{,}066 M_\infty^2 \frac{D_b}{x} + 0.405 + \frac{0.155}{M_\infty^2} \frac{x}{D_b}. \qquad \text{(XII-3-12)}$$

As we see from Fig. XII-3-1, the results calculated from this formula agree better with experiment. Formula (XII-3-12), which applies to a cylinder with a spherical nose, can be extended to cylindrical bodies with arbitrary blunted shapes. For the case k = 1.4, the generalized formula takes the form

$$\frac{p}{p_\infty} = 0.069 M_\infty^2 \sqrt{c_x} \frac{D_b}{x} + 0.405 + 0.15 \frac{1}{M_\infty^2 \sqrt{c_x}} \frac{x}{D_b}. \qquad \text{(XII-3-13)}$$

If the cylinder is fitted with a spherical nose, for which we assume $c_x = 0.94$, this formula becomes (XII-3-12) with the same condition k = 1.4.

Similar relationships have been derived for determination of shock-wave shape. Finding the values of g(k) for k = 1.4 on the diagram of Fig. XII-3-3 and assuming, as before, that $c_x = 0.94$, we obtain, in accordance with (XII-3-11), the following formula for first-approximation calculation of the radius of a point on the shock wave around a cylinder with a sphere: /511

$$\frac{r_s}{D_b} = 0.78 \sqrt{\frac{x}{D_b}}. \qquad \text{(XII-3-11')}$$

A more exact relationship that takes counterpressure into consideration is

$$\frac{r_s}{D_b} = 0.78\sqrt{\frac{x}{D_b}}\left[1 + \frac{1.62}{M_\infty^2}\frac{x}{D_b} - \frac{6.17}{M_\infty^4}\left(\frac{x}{D_b}\right)^2\right]. \qquad \text{(XII-3-14)}$$

This relationship, extended to the general case in which the cylinder has a bluntness of arbitrary shape at its forward end, is

$$\frac{r_s}{D_b} = 0.795\,(c_x)^{1/4}\left(\frac{x}{D_b}\right)^{1/2}\left[1 + \frac{1.57}{M_\infty^2\sqrt{c_x}}\frac{x}{D_b} - \frac{5.8}{M_\infty^4 c_x}\left(\frac{x}{D_b}\right)^2\right]. \qquad \text{(XII-3-15)}$$

In using (XII-3-10)-(XII-3-15), it must be remembered that they give satisfactory results for zones of the body approximately one nose radius distant from the base of the nose. The corresponding values of x, reckoned from the critical point of the nose (see Fig. XII-3-1), should be taken from the condition $x > (2\text{-}2.5)R_b$ in practical calculations.

Flow Around a Slender Cone with a Small Bluntness

General equations and method of solution. Case of $K_1 = \infty$. To calculate the flow around a slender cone at very high supersonic velocity, we shall use the analogy with the problem of unsteady gas motion with cylindrical waves.

Assuming that the layer of gas between the piston and the shock wave is very thin at high velocities, we can simplify the energy equation (XII-3-5'):

$$\frac{r^2}{4}\rho_\infty\left(\frac{\partial r}{\partial t}\right)^2 + \frac{r^2 - r_0^2}{2(k-1)}p = \frac{E}{2\pi} + \frac{p_\infty r^2}{2(k-1)} + \int_0^r p r_0\, dr_0. \qquad \text{(XII-3-5")}$$

The momentum equation (XII-3-6) can also be simplified. Since the layer of disturbed gas is considered thin, this equation will be

$$\rho_\infty \frac{\partial r}{\partial t}\frac{r^2}{2} = \int_0^t (p - p_\infty)\, r\, dt. \qquad \text{(XII-3-6')}$$

In these equations, we shall assume $\partial r/\partial t = \dot{r}$ to be constant throughout the disturbed region and equal to the velocity of particles immediately behind the shock wave, bearing in mind that velocity can be determined from compression-shock theory. In the theory of the steady shock, the relative velocity change is given

by

$$\frac{V_\infty - V_2}{V_\infty} = \frac{2}{k+1}\left(1 - \frac{a_\infty^2}{V_\infty^2}\right).$$

Inverting the motion, so that a shock wave moves at velocity $V_\infty = D = \dot{r}_s$ in a stationary flow, we find the particle velocity behind the shock:

$$\dot{r} = V_\infty - V_2 = \frac{2}{k+2}\left(\dot{r}_s - \frac{a_\infty^2}{\dot{r}_s^2}\right). \qquad \text{(XII-3-16)}$$

As we know, this formula takes account of the initial gas pressure.

Further, remembering that the disturbed layer is thin, we take the coordinate r equal to the distance to the shock wave and the piston radius r_0 equal to Ut, where U is the speed of piston expansion. We now introduce Expression (XII-3-16) for $\dot{r}$ and the values $r = r_s$ and $r_0 = Ut$ into Eqs. (XII-3-5") and (XII-3-6') and convert to dimensionless variables in the resulting equations by means of the length $L = E/(\pi\rho_\infty U^2)$ and time L/U scales. The result is /512

$$\frac{1}{2}r_s^2\left(\frac{2}{k+1}\dot{r}\right)^2\left(\dot{r}_s - \frac{1}{K_1^2\dot{r}_s}\right) + \frac{r_s^2 - t^2}{k-1}\left(\Delta p + \frac{1}{kK_1^2}\right) =$$

$$= \frac{r_s^2}{k-1}\frac{1}{kK_1^2} + 2\int_0^t \left(\Delta p + \frac{1}{kK_1^2}\right) t\,dt; \qquad \text{(XII-3-17)}$$

$$r_s^2\frac{2}{k+1}\left(\dot{r}_s - \frac{1}{K_1^2\dot{r}_s}\right) = 2\int_0^t \Delta p r_s\,dt, \qquad \text{(XII-3-18)}$$

where $\Delta p = (p - p_\infty)/(\rho_\infty U^2)$, and $K_1 = U(kp_\infty/\rho_\infty)^{-1/2} = M_\infty \operatorname{tg}\beta_c$ is a similarity parameter.

In the general case, these solutions can be solved for arbitrary t by numerical integration.

Let us consider the limiting case when $K_1 \to \infty$. We shall assume further that the time t is small, so that the initial energy of the gas in the disturbed region and the work of piston expansion will also be small by comparison with the energy released in the explosion. Equations (XII-3-17) and (XII-3-18) then become substantially simpler:

$$\frac{1}{2} r_s^2 \left(\frac{2}{k+1}\right)^2 \dot{r}_s^2 + \frac{r_s^2}{k-1} \Delta p = 1; \qquad \text{(XII-3-17')}$$

$$r_s^2 \dot{r}_s \frac{2}{k+1} = 2 \int_0^t \Delta p r_s \, dt. \qquad \text{(XII-3-18')}$$

Excluding Δp from these equations, we obtain

$$\frac{1}{2} \left(\frac{2}{k+1}\right)^2 r_s^2 \dot{r}_s^2 + \frac{r_s}{k^2-1} \frac{d(r_s^2 \dot{r}_s)}{dt} = 1. \qquad \text{(XII-3-19)}$$

This equation has a unique solution for $r_s(t)$ that satisfies the condition $r_s(0) = 0$, and which exists at all $t \geq 0$. For small t, the solution takes the form

$$r_s = \left[\frac{4(k+1)^2(k-1)}{3k-1}\right]^{1/4} t^{1/2}. \qquad \text{(XII-3-20)}$$

The coordinates of shock-wave points can be calculated by this formula

Substitution of the value for r_s from (XII-3-20) into (XII-3-17') enables us to find the pressure

$$\Delta p = \left[\frac{k-1}{4(3k-1)}\right]^{1/2} t^{-1}. \qquad \text{(XII-3-21)}$$

Converting to dimensional parameters and bearing (XII-3-1) in mind, we find relationships for the shock-wave shape and the pressure distribution on the surface of a cone:

$$\frac{r_s}{D_b} = \gamma c_x^{1/4} \left(\frac{x}{D_b}\right)^{1/2}; \qquad \text{(XII-3-20')}$$

$$\bar{p} = \frac{2(p-p_\infty)}{\rho_\infty V_\infty^2} = \nu c_x^{1/2} \frac{D_b}{x}, \qquad \text{(XII-3-21')}$$

in which the coefficients

$$\gamma = \frac{1}{2}\left[\frac{8(k+1)^2(k-1)}{3k-1}\right]^{1/4}; \quad \nu = \left[\frac{k-1}{8(3k-1)}\right]^{1/2}.$$

It is readily seen that (XII-3-20') and (XII-3-21') differ from the corresponding relationships for a cylindrical body only in the values of the coefficients γ and ν. These values are represented graphically in Fig. XII-3-3. /513

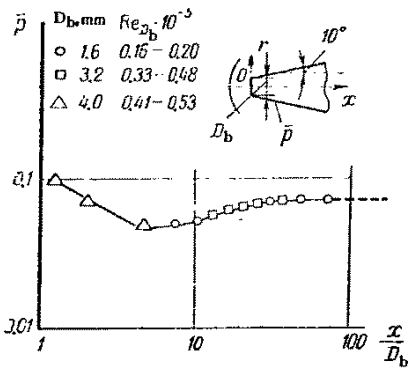

Figure XII-3-4. Pressure Coefficient on Surface of Cone with Flat Bluntness at $M_\infty = 6.85$. ----- conical theory.

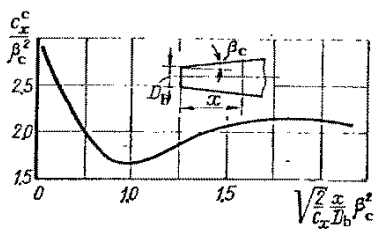

Figure XII-3-5. Drag Coefficieint of Slender Cone with Flat Bluntness.

According to (XII-3-21'), the pressure coefficient, which increases without limit at the forward critical point, decreases rapidly with increasing distance from the nose. Its values are substantially smaller on a certain segment than on the sharp cone.

This effect is observed, for example, on a cone with a spherical nose. For comparison, let us assume that the pressure coefficient on the sharp cone is $\bar{p}_c = 2\beta_c^2$ in accordance with the Newton theory and that the drag coefficient of the spherical nose is $c_x = 1$. For $k = 1.4$, the coefficient $\nu = 0.125$. In this case,

$$\frac{\bar{p}}{\bar{p}_c} = \frac{0.0625}{\beta_c^2}\frac{D_b}{x}.$$

If, for example, the cone angle $\beta_c = 0.1$, then $\bar{p}/\bar{p}_c = 6.25(D_b/x)$. It is now clear that the pressure on the blunt cone is below that on a sharp cone at distances $x > 6.25D_b$ from the nose.

Investigation shows that this qualitative peculiarity, which we have established for the limiting case $K_1 = \infty$, also persists at finite values of K_1, and in particular when it is of the order of unity.

Formula (XII-3-21') cannot be used to ascertain the type of pressure variation over the entire surface of the cone, but is suitable only for comparatively small $\underline{x}$.

Experimentally confirmed investigations indicate that the pressure coefficient, like the shock inclination angles, tends at greater distances from the nose to values determined by the conditions of flow around a sharp cone.

These peculiarities of the pressure distribution are clearly evident in Fig. XII-3-4, which shows the results of wind-tunnel tests on a flat-blunted cone with the angle $\beta_c = 10°$ at $M_\infty = 6.85$. We note that the pressure minimum is reached at a distance of about 10 blunting diameters, and that pressure recovers to its value for the sharp cone on a length about 10 times greater. The lower pressure over a substantial part of the blunt cone may have as a consequence that it offers less drag than a sharp one.

Figure XII-3-5 presents a diagram that can be used to calculate the drag of a blunt cone. We see from this diagram that the drag of the cone reaches a minimum at a certain cone length. /514

According to the diagram of Fig. XII-3-5, the drag-coefficient minimum is reached at a cone length ratio

$$\frac{x}{D_b} = \frac{0{,}96}{\beta_c^2}\sqrt{\frac{c_x}{2}}.$$

For example, $x/D_b = 68$ for a cone with a spherical nose ($c_x = 1$) and an angle $\beta_c = 0.1$.

The minimum drag of a blunt cone is approximately 10% smaller than that of a sharp one. When the optimum length is not observed, the drag of slightly blunted cones at very high velocities is practically the same as that of sharp cones.

Studies have shown that for slightly blunted slender bodies, the pressure on the conical part is substantially smaller than its value on a sharp cone, and that it recovers to the sharp-cone value comparatively slowly with increasing distance from the nose. However, the difference between the pressures decreases sharply for flow around a thick cone, and the recovery process is practically complete near the blunting. Experiments indicate that for a spherically blunted 40-degree cone at $M_\infty = 6$, the pressure on the conical part is practically equal to its value on a sharp cone at a distance of little more than one blunting diameter from the total-stagnation point. This indicates a practical possibility of evaluating pressure on the conical part of a body on the basis of sharp-cone flow theory.

As for the spherical nose and a small neighborhood around it, including the conical part, we see from Fig. XII-3-1 that the improved Newton formula $\bar{p} = \bar{p}_0 \cos^2 \eta$ gives a good approximation of the experimental data.

Similarity law. Arbitrary M_∞. The above considerations as to the nature of flow around blunted bodies enable us to derive a similarity law to which the flow around a blunt cone is subject.

It was established in deriving general relationships to characterize flow around a blunted cylinder that this flow is determined by the dimensionless parameters of (XII-3-7). If we take a slender blunted cone, we must add the angle β_c to the set of parameters that determine pressure. Then, as in the case of flow around a sharp cone, the similarity parameter $K_1 = M_\infty \beta_c$ must also be included among the dimensionless parameters on which the flow depends.

These dimensionless parameters must determine the dimensionless flow characteristics. If we consider pressure, Newton's theory indicates that the excess on the cone $p - p_\infty \sim \rho_\infty V_\infty^2 \beta_c^2$. On the basis of this estimate, the excess pressure can be determined as $p - p_\infty = \rho_\infty V_\infty^2 \beta_c^2 \tilde{p}$, where $\tilde{p}$ is a certain dimensionless characteristic for the pressure.

Consequently, the pressure coefficient on the cone surface is

$$\frac{\bar{p}}{\beta_c^2} = \frac{2(p - p_\infty)}{\rho_\infty V_\infty^2 \beta_c^2} = P(x_*^{-1}, K_1, k), \qquad \text{(XII-3-22)}$$

where the function P, which is equal to $2\tilde{p}$, is determined, with the parameter K_1, by the dimensionless quantity

$$x_* = \frac{x}{D_b} \frac{1}{M_\infty^2 \sqrt{c_x}} = \frac{x}{K_3}, \qquad \text{(XII-3-23)}$$

which can be regarded as a certain conventional relative coordinate. Here, as we have noted, the section under investigation must be at least one radius R_b from the base of the blunting. For blunted conical bodies, we shall henceforth measure the coordinate $\underline{x}$ along the axis of the body from the base of the nose, so that $x > R_b$ in the calculations. /515

By analogy with (XII-3-8), the similarity law for the coordinates of shock-wave points is

$$\frac{1}{M_\infty^2}\frac{1}{\sqrt{c_x}}\frac{1}{\beta_c}\frac{r}{D_b} = \vartheta(x_*^{-1},\ K_1,\ \underline{k}), \qquad \text{(XII-3-24)}$$

where ϑ is a certain function of the parameters x_*^{-1}, K_1, $\underline{k}$.

We can broaden the range of applicability of the similarity law by substituting $\tan \beta_c$ for the angle β_c. According to this law, the dimensionless quantities defined by (XII-3-22) and (XII-3-24) will be the same at equal relative coordinates x/D_b in flow around slightly blunted cones that have different angles β_c and nose diameters D_b if $\underline{k}$ and the similarity parameters

$$K_1 = M_\infty \operatorname{tg}\beta_c;\ K_3 = M_\infty^2 D_b \sqrt{c_x}$$

remain the same.

The parameter K_3 reflects the specific peculiarities of flow around the blunted cone.

The above similarity law can be extended to blunt bodies of arbitrary shape but with affinely modified generatrices. In this case, it is necessary to replace the angle β_c with another parameter τ that characterizes the body's thickness ratio.

§XII-4. APPLICATION OF METHOD OF CHARACTERISTICS TO CALCULATION OF FLOW AROUND BLUNT SOLIDS OF REVOLUTION

System of equations for the characteristics. The theoretical methods set forth above are applicable to investigation of very-high-speed flows around blunt bodies. In practical cases, it may be necessary to calculate the flow in the zone behind a blunt nose also for relatively low supersonic speeds. This calculation can be made by the method of characteristics in the region of purely supersonic flow between the shock wave and the body's surface. Here, since the shock wave is curvilinear in front of a blunt body, a method that takes account of vorticity must be used.

Consequently, Eqs. (IV-1-20) and (IV-1-22) for the conjugate characteristics of rotational supersonic flow can be used as the working relationships. With them, we can calculate the flow variables numerically for assigned conditions in a certain region including the surface of the body and the shock wave.

However, the method of characteristics involves extremely cumbersome calculations. They required a great deal of time, and this discouraged extensive practical use of the method.

With the advent of the high-speed electronic computer, this deficiency of the method of characteristics ceased to be substantial. At the same time, it was found that utilization of the machines to solve the conventional characteristic equations (IV-1-20) and (IV-1-22) is inefficient. These equations do not adapt for machine computation, since they include a whole series of functions (including exponential and trigonometric) that require additional machine time for calculation. /516

Thus it became necessary to improve the method of characteristics and adapt it for calculations on the electronic computer. This was done by P.I. Chushkin ([68], 1960, No. 5), who also used a computer to calculate supersonic flow around a number of conical bodies with spherical noses.

In order to improve the equations for the characteristics, (IV-1-20) and (IV-1-22), it is helpful to convert them to the unknown functions $\alpha' = \operatorname{ctg}\mu = \sqrt{M_\infty^2 - 1}$, $\xi = \operatorname{tg}\beta$, $S = \ln \bar{p}\bar{\rho}^k$, $\bar{\rho} = \rho/\rho_\infty$, $\bar{p} = p/(\rho_\infty a^{*2})$.

Then, after transformation to these new variables, equation system (IV-1-20) and (IV-1-22) for the conjugate characteristics in the physical and hodograph planes is written as follows:

first family

$$\frac{dx}{dr} = \frac{\alpha' - \xi}{\alpha'\xi + 1} \equiv m; \qquad \text{(XII-4-1)}$$

$$d\xi + K\,d\alpha' + L\,dr - P\,dS = 0; \qquad \text{(XII-4-2)}$$

second family

$$\frac{dr}{dx} = \frac{\alpha'\xi - 1}{\alpha' + \xi} \equiv n; \qquad \text{(XII-4-3)}$$

$$d\xi - K\,d\alpha' - N\,dx + P\,dS = 0, \qquad \text{(XII-4-4)}$$

where

$$K = \frac{-2(\alpha')^2(\xi^2+1)}{(k+1)[(\alpha')^2+1][\delta(\alpha')^2+1]}; \quad L = \frac{\xi(\xi^2+1)}{r(\alpha'\xi+1)};$$
$$N = \frac{\xi(\xi^2+1)}{r(\alpha'+\xi)}; \quad P = \frac{\alpha'(\xi^2+1)}{k(k-1)[(\alpha')^2+1]}.$$

To calculate entropy, it is helpful to express it in terms of the stream function ψ if (III-2-23) and the relation for entropy are transformed jointly with consideration of the new variables α' and ξ; here it is more convenient to replace the function ψ by its modification Ψ in accordance with

$$d\Psi = (ke^S)^{\frac{1}{k-1}} d\psi.$$

Writing the differential $d\psi$ in the form

$$d\psi = \psi_x dx + \psi_r dr$$

and replacing the partial derivatives ψ_x and ψ_r in accordance with (III-2-33), we find an equation for the modified stream function after introducing the variables α' and ξ:

$$\frac{d\Psi}{dx} = -\frac{r\sqrt{[(\alpha')^2+1](\xi^2+1)}}{(\alpha'+\xi)[\delta(\alpha')^2+1]^{1/2\delta}} \equiv q. \qquad \text{(XII-4-5)}$$

The entropy S can be found from our function Ψ. Since we are concerned with isentropic flow and, consequently, the entropy is constant on a given streamline Ψ = const, we can do this by using the relation between Ψ and S that was obtained from the conditions on the shock wave.

The system composed of Eqs. (XII-4-1)-(XII-4-5) and the equation linking S and Ψ is solved numerically. For this purpose, each of the equations is presented in finite-difference form.

The solution procedure for the two problems represented graphically in Fig. IV-1-4 is the same as in the ordinary method of characteristics, which was set forth in Chapter IV. The third problem, which involves calculation of the point H on the shock wave (see Fig. IX-1-1), can be solved here as follows. /517

At point H, whose position is not yet known, we assign an arbitrary value of the wave inclination angle θ_{sH} that is somewhat smaller than at a neighboring point F. From the relationships on the shock wave, we then determine

$$\bar{\rho}_H^2 = \frac{\bar{\rho}_0^2 \operatorname{tg}^2\theta_{sH}}{1-\delta\bar{\rho}_0^2+\operatorname{tg}^2\theta_{sH}}; \quad \bar{\rho}_0^2 = \frac{(k+1)M_\infty^2}{2+(k-1)M_\infty^2};$$

$$\alpha'_H = \left[\frac{\bar{\rho}_0^2(\operatorname{tg}^2\theta_{sH}+\bar{\rho}_H^2)-\bar{\rho}_H^2(1+\operatorname{tg}^2\theta_{sH})}{\bar{\rho}_H^2(1+\operatorname{tg}^2\theta_{sH})-\delta\bar{\rho}_0^2(\operatorname{tg}^2\theta_{sH}+\bar{\rho}_H^2)}\right]^{1/2};$$

$$\xi = \frac{\operatorname{tg}\theta_{sH}(\bar{\rho}_H-1)}{\operatorname{tg}^2\theta_{sH}+\bar{\rho}_H}, \quad S = \ln\left[\frac{2}{k+1}\frac{\bar{\rho}_0^2\operatorname{tg}^2\theta_{sH}}{1+\operatorname{tg}^2\theta_{sH}}\left(\frac{k+1}{2k}(1-\delta\bar{\rho}_0^2)\bar{\rho}_0^{-k}\right)\right].$$

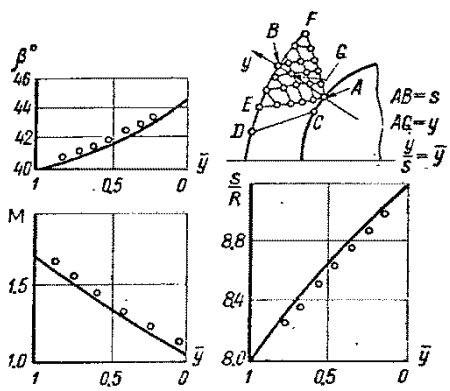

Figure XII-4-1. Distribution of Variables Over Thickness of Shock Layer. ———) exact solution; ooo) Formula (XII-4-7); S/R is the ratio of entropy to the gas constant.

The coordinates x_H and r_H of point H are found by iterative solution of a system consisting of an equation in the form $\Delta x = m\Delta r$ for the first-family characteristic and the equation of a parabola representing wave segment FH.

The approximations are broken off when the equation for the second-family characteristic is satisfied:

$$\xi_H - \xi_N + K_N(\alpha'_H - \alpha'_N) + L_N(r_H - r_N) - P_N(S_H - S_N) = 0.$$

The modified stream function

$$\Psi_H = \Psi_F + K^{\frac{1}{k-1}} \frac{\bar{\rho}_0}{4} \left(\exp \frac{S_F}{k-1} + \exp \frac{S_N}{k-1}\right)(r_H^2 - r_F^2)$$

is determined from the parameters found at point H.

Boundary conditions. To apply the above method of characteristics for calculation of the supersonic part of flow around a blunted solid of revolution, it is necessary to know the parameters on some boundary curve. If they are known, we can determine the parameter field in the region between this curve, the surface of the body, and the compression shock; the compression-shock generatrix is plotted progressively during the solution. If we are considering a body with a spherical nose, the initial data may be known on the normal segment AB to the spherical surface, which is situated in the completely supersonic layer near the "sonic" line CD (Fig. XII-4-1). These data are determined by various methods. One of the most exact, for example, is the method of integral relations set forth earlier.

The following approximate method may also be used. First, a shock-wave generatrix is constructed around the spherical nose in accordance with the equation $r^2 = 2R_{s_0}(x + s_0)$. Then an arbitrary point A is selected near the "sonic" point on the sphere, and normal AB to the nose surface is drawn through it (Fig. /518

XII-4-1). Now the distribution of a certain parameter along the normal can be assigned by the polynomial

$$\Pi = \sum_{n=0}^{n} a_n \bar{y}^n, \qquad \text{(XII-4-6)}$$

where $\bar{y} = y/s$ and s is the thickness of the shock layer in the section considered. The independent variable $\bar{y}$ varies from zero at the wall to unity on the shock wave.

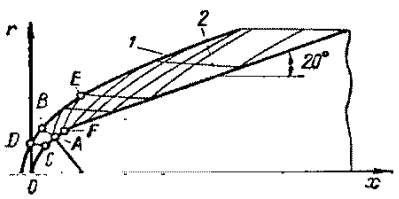

Figure XII-4-2. Net of Characteristics for Blunted Cone.

For high enough velocities and, consequently, small shock-layer thicknesses, we may limit the polynomial to three terms and take

$$\Pi = a_0 + a_1\bar{y} + a_2\bar{y}^2.$$

The unknown coefficient a_0 is determined from the condition at the wall at $\bar{y} = 0$. Here the parameters on the wall are calculated approximately by the improved Newton theory or are found experimentally.

The other two coefficients are determined by using the shock-wave condition for $\bar{y} = 1$, where the parameters are found from the angle θ_s of its inclination at point B and from M_∞, as well as the known value of the derivative $\partial\Pi/\partial\bar{y}$ at the point $B(\bar{y} = 1)$ or $A(\bar{y} = 0)$. Knowledge of this derivative enables us to find the coefficient a_1 in the form $a_1 = (\partial\Pi/\partial\bar{y})_{\bar{y}=0}$.

Figure XII-4-1 shows the results of an exact calculation of the distribution of certain parameters, including M, β, and the dimensionless entropy S/R; as we see, data obtained with the parabolic relation (XII-4-7) agree with them closely.

The method of characteristics can be used directly to determine the initial data along the selected normal. For this purpose, a tight row of points is taken along an arbitrary arc EF of the assigned shock wave (Fig. XII-4-1). Since the parameters are known at each of these points, the equations for the characteristics can be used. By solving them, we find a net of characteristics at whose points the flow variables have become known in the region between arc EF and the conjugate characteristics EA and FA. The parameters can be found along the normal from these data. The results shown in Fig. XII-4-1 were obtained in precisely this manner.

Calculation procedure and certain results. Now that a row of points at which the parameters are known has been established along our selected normal, we can use the equations for the characteristics in finite-difference form. As a result of successive application of these equations, the parameters are calculated by iteration at points of the row next to the normal. Here, one of the points of the row, the uppermost one, lies at the intersection of the first-family characteristic and the shock-wave surface, and another, the lowermost, at the intersection of the second-family characteristic and the body's generatrix. All other points lie at the intersections of conjugate characteristics emanating from adjacent points on the normal.

Then the coordinates of points in the next row are found in a similar fashion, the parameters at these points are calculated, and so forth. This method was used on a computer to calculate flows around a series of spherical-nosed cones at various velocities. The cone angles were β_c = 0, 20, 30, and 40°, and the M_∞ = 3, 4, 6, 10, and ∞. Normal segment AB was broken up into 48 intervals. In Fig. XII-4-2, we have constructed the scheme of the flow around a blunted cone with angle β_c = 20° at M_∞ = = 6; this will give an idea of the shape of the shock-wave generatrix 1 and the characteristic net 2. Also shown is the first-family characteristic FE emanating from the point at which the sphere meets the cone and bounding the part of the flow that is shaped in flow around the spherical nose and behind which flow governed not only by the sphere, but also by the main part of the body begins. /519

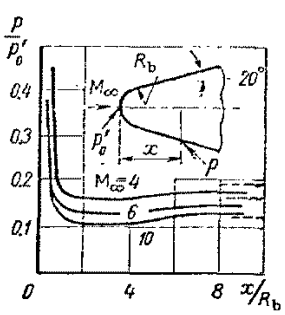

Figure XII-4-3. Pressure Distribution on Generatrix of Blunted Cone. ----- pressure on sharp cone.

Thus, characteristic FE is analogous to KS (see Fig. IX-1-1), which separates conical flow from the flow that arises around a curvilinear surface.

Figure XII-4-3 shows the pressure distribution on a spherically blunted cone with the angle β_c = 20° as computed by the method of characteristics on an electronic machine for three M_∞. The dashed lines indicate the pressures on sharp cones for comparison. As we see, bluntness lowers the pressure on a certain length, with the relative change increasing with M_∞.

At moderate velocities, therefore, the flow around the peripheral part of a blunt body is practically no different from the flow around a sharp cone. This indicates the possibility of calculating the drag of a blunt cone in approximation by adding the drags of the

nose and the peripheral part of the cone, on which the pressure is assumed to be the same as on the sharp-cone surface.

The same inference can also be drawn with respect to a thickened blunt body, on which the pressure distribution at any speed differs little on the main segment from the corresponding distribution on the sharp body. Needless to say, a small neighborhood of the peripheral surface directly adjacent to the nose, where the pressure may vary substantially, must be excluded from this analysis.

§XII-5. INFLUENCE OF ATTACK ANGLE

Investigation of nonaxisymmetric flow around blunt cones indicates that the basic pecularities associated with the pressure change along generatrices lying in different meridional planes are the same as at zero angle of attack. This is evident, for example, from the experimental results obtained for a cone with a spherical nose at $M_\infty = 5.8$ and attack angles $\alpha = 4$ and 8° (Fig. XII-5-1). The pressure decreases gradually after the critical point on the lower and upper generatrices, reaching a minimum at a certain distance from the nose. It then increases to values near those observed in flow around a sharp cone. Experimental investigations have shown that for $\alpha \leq 4$-5°, the pressure distribution can be approximated rather well by the equation

$$\bar{p} = \bar{p}_{\alpha=0} - \alpha B \cos\gamma + \alpha^2 (C \cos 2\gamma + D) \qquad \text{(XII-5-1)}$$

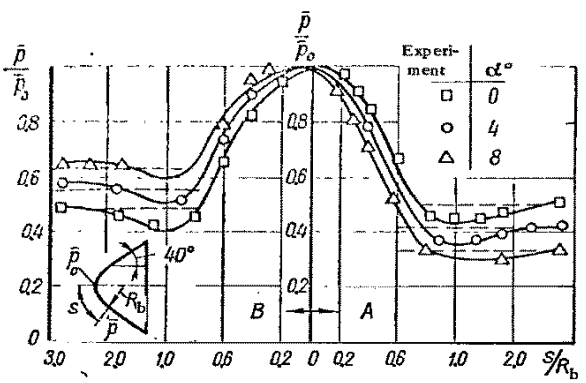

Figure XII-5-1. Pressure on Spherically Blunted Cone in Flow at an angle of attack.------) sharp cone (theory); A) for upper generatrix; B) for lower generatrix.

Here the coefficients B, C, and D are independent of attack angle, and hence the results of measurement or calculation of /520 the pressure distribution along three arbitrary generatrices of the body at a given angle of attack can be used to determine them.

Equation (XII-5-1) is simplified if the attack angles are so small that the term $\alpha^2 D$ can be disregarded. Then the two coefficients B and C in (XII-5-1) must be determined, and this can be done by using data for the pressure on

generatrices in the $\gamma = 0$ and $\gamma = \pi$ planes. For very small α, we can limit (XII-5-1) to the second term and assume

$$\bar{p} = \bar{p}_{\alpha=0} - \alpha B \cos\gamma. \qquad \text{(XII-5-2)}$$

§XII-6. THE NEWTON METHOD

Calculation of the aerodynamic coefficients of solids of revolution with blunt curvilinear noses in hypersonic flow can

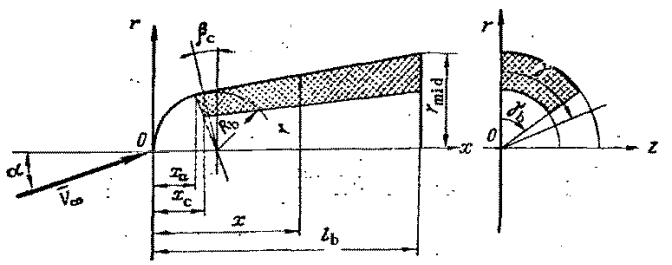

Figure XII-6-1. Scheme of Flow Calculation for Blunt Cone by Newton Method.

be based on the improved Newton formula (X-3-1) for the pressure.

Determination of the boundaries of the "shaded" zone for a given body shape is an essential element in the calculation. Let us consider a body in the form of a spherical-nosed cone (Fig. XII-6-1). The generatrix takes the form of an arc of a circle on segment $0 \leq x \leq x_c$, and on segment $x_c \leq x \leq l_c$ is a straight line with the equations /521

$$r^2 + (R_b - x)^2 = R_b^2; \quad x = x_c + \frac{r - r_b}{\operatorname{tg}\beta_c}, \qquad \text{(XII-6-1)}$$

where x_c and r_c are the coordinates of the joint between the sphere and the cylinder.

We see from Fig. XII-6-1 that $r_c = R_b \cos\beta_c$; $x_c = R_b(1 - \sin\beta_c)$. As a characteristic of the bluntness, we can introduce the ratio $\bar{l} = l_c/l_c'$, where $l_c' = r_{mid}/\tan\beta_c$ is the length of the unblunted cone. As another bluntness parameter, it is helpful to consider the radius ratio $\bar{R}_b = R_b/r_{mid}$, which, as we see from Fig. XII-6-1, is equal to

$$\bar{R}_b = \frac{R_b}{r_{mid}} = \frac{\cos\beta_c}{1-\sin\beta_c}(1-\bar{l}). \qquad \text{(XII-6-2)}$$

Assume that we are concerned with the most general case of flow, in which the "shaded" zone covers part of the conical surface and the sphere. Its boundary is determined from the condition $\bar{p}_e = 0$, which gives $\cos\gamma_c = \tan\beta/\tan\alpha$. On the sphere, the boundary curve is a circle of radius R_b, whose plane is inclined to the $\bar{r}$-axis at an angle α (see Fig. XII-6-1). On the cone, the boundary of the "shaded" zone is determined by the equation $\cos\gamma_c = \tan\beta_c/\tan\alpha = \text{const}$. The part of the sphere in front of the point with coordinate $x_a = R_b(1 = \sin\alpha)$ is completely inside the flow, and, consequently, $\gamma_c = 0$.

The axial-force coefficient is determined as follows with Formula (X-3-5):

$$c_{Rp} = \frac{2}{\pi r_{mid}^2}\left\{\int_0^{x_a} A_1(\gamma_c)\, r\,\mathrm{tg}\,\beta\, dx + \int_{x_a}^{x_c} A_2(\gamma_c)\, r\,\mathrm{tg}\,\beta\, dx + \int_{x_c}^{l_c} A_3(\gamma_c)\, r\,\mathrm{tg}\,\beta\, dx.\right. \qquad \text{(XII-6-3)}$$

The function A_1 corresponds to the full-flow zone at the spherical nose and is determined from (X-3-6) for $\gamma_c = 0$. The value of $\tan\beta = dr/dx = (R_b - x)/r$. To evaluate the second integral in (XII-6-3), Expression (X-3-6), in which we set $\gamma_c =$ $= \text{arc cos}\,(\tan\beta/\tan\alpha)$ and $\tan\beta = (R_b - x)/r$ should be substituted for $A_2(\gamma_c)$, thereby taking the influence of the "shaded" zone on the spherical nose into account. The third integral is simplest to evaluate; it corresponds to the conical segment, for which we must set $\gamma_c = \text{arc cos}\,\tan\beta_c/\tan\alpha$; $A_3(\gamma_c) = \text{const}$; $\tan\beta = \tan\beta_c = \text{const}$ and substitute for $\bar{r}$ in accordance with the second relation of (XII-6-1). Having evaluated the integrals in (XII-6-3), we obtain for the axial-force coefficient

$$c_{Rp} = c_1 + \bar{R}_b^2 \Delta c_1, \qquad \text{(XII-6-4)}$$

where c_1 is the coefficient of the axial force acting on the unblunted cone:

$$c_1 = \left(1 - \frac{\gamma_c}{\pi}\right)\left[2\sin^2\beta_c + \sin^2\alpha\,(1 - 3\sin^2\beta_c)\right] + \frac{3}{4}\,\frac{\sin\gamma_c}{\pi}\sin 2\alpha \sin 2\beta_c. \qquad \text{(XII-6-5)}$$

The parameter Δc_1 determines the additional component of the axial-force coefficient due to bluntness:

$$\Delta c_1 = \frac{1}{2}\cos^4\beta_c\left(1-\frac{\gamma_c}{\pi}\right)(2-3\sin^2\alpha) - \frac{\cos\alpha}{2}\left[1-\frac{2}{\pi}\operatorname{arctg}\left(\frac{\operatorname{ctg}\gamma_c}{\cos\alpha}\right)\right] - \frac{\sin\gamma_c}{8\pi}\sin 2\alpha\sin 2\beta_c(2+3\cos^2\beta_c). \quad \text{(XII-6-6)}$$

The angle γ_c is determined from the taper angle by the formula $\cos\gamma_c = \tan\beta_c/\tan\alpha$. If $\beta_c \geq \alpha$, there is no "shaded" zone on the body, and hence the angle $\gamma_c = 0$ and the axial-force coefficient is /522

$$c_{Rp} = 2\sin^2\beta_c + \sin^2\alpha(1-3\sin^2\beta_c) + \bar{R}_b^2\frac{\cos^4\beta_c}{2}(2-3\sin^2\alpha). \quad \text{(XII-6-7)}$$

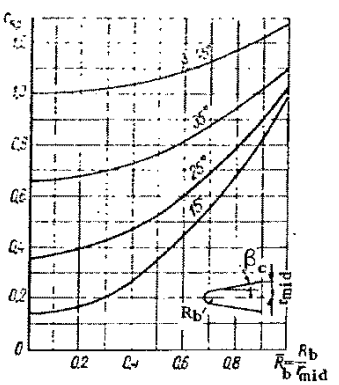

Figure XII-6-2. Axial-Force Coefficient of Blunted Cone, Calculated by Newtonian Theory (zero attack angle).

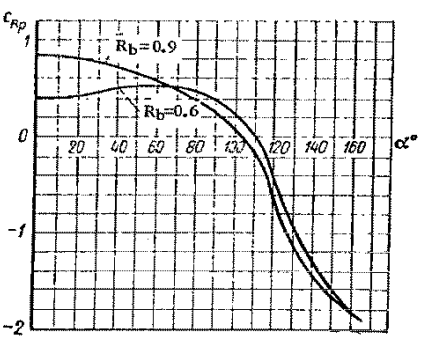

Figure XII-6-3. Axial-Force Coefficient of Blunted Cone Calculated by Newtonian Theory (circular onflow).

For axisymmetric flow, it is necessary to set $\alpha = 0$ and $\gamma_c = 0$ in the above expressions. Figure XII-6-2 shows the results of calculation of c_{Rp} for this case. For the unblunted cone, $R_b = 0$. Formula (XII-6-4) enables us to determine the axial-force coefficient for circular-onflow conditions. Figure XII-6-3 shows the corresponding calculated results for $\beta_c = 15°$

and $\bar{R}_b$ = 0.9 and 0.6. c_{Rp} was assumed equal to 2 for $\alpha = 180°$, i.e., on a flat face (at the total-stagnation point).

The normal-force coefficient is determined by analogy with (XII-6-3) also as the sum of three components. Remembering (X-3-36), we write

$$c_{Np} = \frac{-2}{\pi r_{mid}^2}\left\{\int_0^{x_a} B(\gamma_c)\, r\, dx + \int_{x_a}^{x_b} B(\gamma_c)\, r\, dx + \int_{x_b}^{l_b} B(\gamma_c)\, r\, dx\right\}. \quad \text{(XII-6-8)}$$

The function $B(\gamma_c)$ for each of the three integration segments is determined from (X-3-37), using the respective values $\gamma_c = 0$, $\gamma_c = \arccos(\tan\beta/\tan\alpha)$ and $\gamma_c = \arccos(\tan\beta_c/\tan\alpha)$. After evaluating the integrals and rearranging, we obtain

$$c_{Np} = c_2 - \bar{R}_b^2 \Delta c_2, \quad \text{(XII-6-9)}$$

where c_2 is the normal-force coefficient of a sharp cone;

$$c_2 = \cos^2\beta_c \sin 2\alpha\left[\left(1 - \frac{\gamma_c}{\pi}\right) + \frac{1}{3\pi}\sin\gamma_c\,(\operatorname{tg}\beta_c \operatorname{ctg}\alpha + 2\operatorname{ctg}\beta_c \operatorname{tg}\alpha)\right]. \quad \text{(XII-6-10)}$$

The quantity Δc_2 determines the decrease in normal force coefficient owing to the spherical nose:

$$\Delta c_2 = c_2 \cos^2\beta_c + c_3, \quad \text{(XII-6-11)}$$

where

$$c_3 = -\frac{1}{2}\cos^4\beta_c \sin 2\alpha\left(1 - \frac{\gamma_c}{\pi}\right) - \frac{\sin\alpha}{2}\left[1 - \frac{2}{\pi}\operatorname{arctg}\left(\frac{\operatorname{ctg}\gamma_c}{\cos\alpha}\right)\right] + \frac{1}{6}\frac{\sin\gamma_c}{\pi}\sin 2\beta_c\,[5\sin^2\alpha + \sin^2\beta_c\,(1 - 3\sin^2\alpha)]. \quad \text{(XII-6-12)}$$

In the absence of a "shaded" zone ($\alpha \leq \beta_c$), the angle $\gamma_c = 0$ and /523

$$c_{Np} = \cos^2\beta_c \sin 2\alpha\left(1 - \frac{\bar{R}_b^2}{2}\cos^2\beta_c\right). \quad \text{(XII-6-13)}$$

The influence of a cylindrical segment on the coefficient c_{Np} is taken into account by adding $\Delta c_{Np} = (16/3\pi)\lambda_c \sin^2\alpha$. Figure XII-6-4 shows calculated results for the normal force

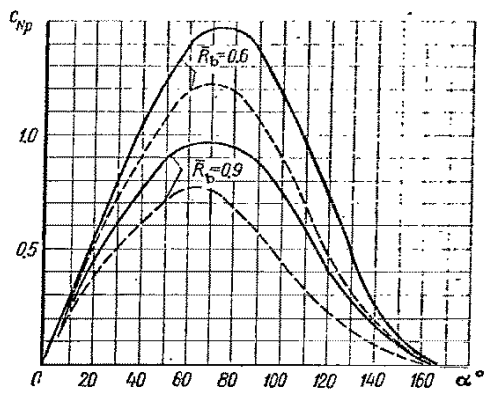

Figure XII-6-4. Normal-Force Coefficient of Blunted Cone (β_c = 15°). ——— without cylindrical part; ----- with cylindrical part of length $0.33 4 d_{mid}$.

coefficient according to (XII-6-9). It is noted that the cylindrical segment increases the maximum of c_{Np}.

Using (X-3-55), we can calculate the moment coefficient by representing each integral in this formula as a sum of three integrals: the first corresponding to the surface zone from 0 to x_a, the second extending from x_a to x_b, and the third from x_b to ℓ_b. The $\pi R_b^2(a + R_b)$ in the denominator should be replaced by $\pi r_{mid}^2 \ell_b$.

After the calculation, we have

$$m_{zp} = -\frac{2}{3}\frac{\sin 2\alpha}{\bar{l}}\frac{1-\bar{l}}{\bar{l}}c_2 + \bar{R}_b^3 c_4. \qquad \text{(XII-6-14)}$$

Here

$$c_4 = \frac{1}{3}\frac{\cos\beta_c}{\bar{l}} \times (1 - 3\sin\beta_c)c_2 - \frac{\operatorname{tg}\beta_c}{\bar{l}}c_3. \qquad \text{(XII-6-15)}$$

The parameter $\bar{l} = \ell_b/\ell_b'$ and the coefficients c_2 and c_3 are given by (XII-6-10) and (XII-6-12), respectively. In the absence of a "shaded" zone, $\gamma_c = 0$ and

$$m_{zp} = \frac{1}{\bar{l}}\cos^2\beta_c \sin 2\alpha\left[\frac{2}{3\cos^2\beta_c} - (1-\bar{l}) + \bar{R}_b^3\frac{\cos^3\beta_c}{6}(2 - 3\sin\beta_c)\right]. \qquad \text{(XII-6-16)}$$

From the values of m_{zp} and c_{Np}, we find the center of pressure coefficient $c_{c.p} = x_{c.p}/\ell_b = m_{zp}/c_{Np}$. In the particular case in which there is no "shaded" zone ($\gamma_c = 0$), we find from (XII-6-16) and (XII-6-13)

$$c_{c.p} = \frac{\frac{2}{3\cos^2\beta_c} - (1-\bar{l}) + \bar{R}_b^3\frac{\cos^3\beta_c}{6}(2 - 3\sin\beta_c)}{\bar{l}\left(1 - \frac{\bar{R}_b^2}{2}\cos^2\beta_c\right)}. \qquad \text{(XII-6-17)}$$

For a sharp cone ($\bar{R}_b = 0$), we obtain the expression $c_{c.p} = 2/(3\cos^2\beta_c)$.

Cylinder with hemispherical nose. In the case of flow around a cylinder with a nose of a given shape, e.g., a hemisphere, the "shaded" zone will always cover half of the cylindrical surface at any attack angle, and, consequently, $\gamma_c = \pi/2$. At the nose, the "shaded" zone begins at the point (in the $\gamma = 0$ plane) at which the angle $\beta = \alpha$ and covers the downstream part of the hemisphere between a plane inclined to the $\bar{r}$-axis at an angle α and the forward base of the cylinder. Calculations indicate that /524 for a cylinder with a hemispherical nose

$$c_{Rp} = \cos^4\frac{\alpha}{2}; \qquad \text{(XII-6-18)}$$

$$c_{xp} = \sin\alpha\cos^2\frac{\alpha}{2} + \frac{8}{3\pi}(2\lambda_b - 1)\sin^2\alpha; \qquad \text{(XII-6-19)}$$

$$m_{zp} = \frac{1}{2\lambda_b}\left[\sin\alpha\cos^2\frac{\alpha}{2} + \frac{4}{3\pi}(4\lambda_b^2 - 1)\sin^2\alpha\right], \qquad \text{(XII-6-20)}$$

where $\lambda_b = \ell_b/(2r_{mid})$ is the slenderness ratio of the body.

Application of improved Newton formula. The results given above were found on the basis of the ordinary Newton formula, according to which the excess pressure on a surface element that forms an angle α with the normal to the vector $\bar{V}_\infty$ is $p - p_\infty = \rho_\infty V_\infty^2\cos^2\alpha$, and the pressure coefficient $\bar{p} = 2\cos^2\alpha$. In flow around a cone or any other body with a spherical nose at a small angle of attack, the total-stagnation point lies on the sphere, and the improved Newton formula (X-3-1) can be used to calculate the flow around the blunted body. The corresponding expressions for the aerodynamic coefficients can be obtained from (XII-6-7), (XII-6-13), and (XII-6-16) by introducing the coefficient $\bar{p}_0$ and assuming small α:

$$c_{Rp} = \bar{p}_0\left[\sin^2\beta_c + \frac{\alpha^2}{2}(1 - 3\sin^2\beta_c) + \bar{R}_b^2\frac{\cos^4\beta_c}{4}(2 - 3\alpha^2)\right]; \qquad \text{(XII-6-21)}$$

$$c_{xp} = \bar{p}_0\alpha\cos^2\beta_c\left(1 - \frac{\bar{R}_b^2}{2}\cos^2\beta_c\right); \qquad \text{(XII-6-22)}$$

$$m_{zp} = \frac{\bar{p}_0}{\bar{l}}\alpha\cos^2\beta_c\left[\frac{2}{3\cos^2\beta_c} - (1 - \bar{l}) + \bar{R}_b^3\frac{\cos^3\beta_c}{6}(2 - 3\sin\beta_c)\right]. \qquad \text{(XII-6-23)}$$

On transition to a sharp cone, it is necessary to set $\bar{R}_b = 0$ in these formulas and substitute $\tilde{p}(k)$ for $\bar{p}_0$ in accordance with (X-3-3).

For a cylinder with a hemispherical nose, use of the improved Newtonian theory leads not to Formulas (XII-6-18)-(XII-6-20), but to the expressions

$$c_{Rp}=\frac{\bar{p}_0}{2}; \qquad \text{(XII-6-24)}$$

$$c_{Np}=\frac{\bar{p}_0}{2}\left[1+\frac{8}{3\pi}(2\lambda_b-1)\alpha\right]\alpha; \qquad \text{(XII-6-25)}$$

$$m_{zp}=\frac{\bar{p}_0}{2}\left[1+\frac{4}{3\pi}(4\lambda_b^2-1)\alpha\right]\frac{\alpha}{2\lambda_b}. \qquad \text{(XII-6-26)}$$

§XII-7. FLOW AROUND BLUNT BODIES OF CURVILINEAR SHAPE

The general solution. The problem of flow around blunt bodies with curvilinear generatrices can be solved on the basis of the law of plane sections, a manifestation of which is the analogy with nonsteady motion of a gas driven by a cylindrical piston.

As we know, this one-dimensional motion is described in general form by the system of equations (XII-3-2') and (XII-3-3'). Following G.G. Chernyy [38], we find the solution of the equations by expanding the unknown function in power series in $\delta = (k - 1)/(k + 1)$. For the gas variables behind the shock wave, these relationships, and Formula (III-4-12) for the pressure in particular, are expressed in terms of the density ratio ρ_∞/ρ_2. /525
With increasing velocity, this quantity becomes smaller, reaching $\rho_\infty/\rho_2 = \delta$ in the limiting case with $M_\infty \to \infty$ and $k = \text{const}$.

If we consider physicochemical transformations behind the shock, then ρ_∞/ρ_2 will be smaller. Thus, a layer of compressed gas in which the disturbed variables are of the same order of magnitude as directly behind the wave, i.e., they also have as a determining parameter the ratio of densities in the oncoming flow and in the undisturbed layer, forms near the shock-wave surface. The higher the velocity, the more intense the wave and the thinner the layer in which compression takes place.

This disturbed region of the gas behind the wave can be regarded as a kind of boundary layer of the wave, one in which most of the change in gas pressure occurs. In the limiting case in which the compression in this layer is infinite, i.e., $\rho_\infty/\rho_2 = 0$, the excess gas pressure behind the wave is $p_2 - p_\infty = \rho_\infty V_\infty^2 \sin^2 \beta$ and agrees with the value obtained from the Newtonian theory. The layer thickness becomes infinitesimal.

In real cases of flow, the pressure differs from the limiting value, and the parameter ρ_∞/ρ_2 is the criterion of this difference. The above implies that the possibility of finding the solution to the problem of gas flow in a thin layer near the wave

in the form of power series in the parameter $\delta = \rho_\infty/\rho_2$. It can be seen from the formulas given in §III-4 that the gas variables behind the shock wave are determined by precisely this small parameter.

Taking the system of equations (XII-3-2'), (XII-3-3'), and (XII-3-4), we present its solution in the form of the series

$$r = r_0 + \delta r_1 + \ldots; \quad p = p_0 + \delta p_1 + \ldots; \quad \rho = \frac{\rho_0}{\delta} + \rho_1 + \ldots. \qquad \text{(XII-7-1)}$$

Introducing the series into these equations and denoting $\partial r_0/\partial t = \dot{r}_0$; $\partial^2 r_0/\partial t^2 = \ddot{r}_0$, we obtain the equation system

$$\frac{\partial r_0}{\partial m} = 0; \quad \ddot{r}_0 = -r_0 \frac{\partial p_0}{\partial m}; \quad \frac{\partial}{\partial t}\left(\frac{p_0}{\rho_0^k}\right) = 0, \qquad \text{(XII-7-2)}$$

which serves for determination of the form of the functions r_0, p_0, and ρ_0. Integrating the equations, we find

$$r_0 = r_0(t); \quad p_0 = P(t) - \frac{\ddot{r}_0}{r_0} m; \quad p_0^{1/k} = \vartheta_0(m)\,\rho_0, \qquad \text{(XII-7-3)}$$

where $r_0(t)$, $P(t)$, $\vartheta(m)$ are arbitrary functions.

The same substitution gives the equation system

$$\left.\begin{aligned} &\frac{\partial r_1}{\partial m} = \frac{1}{\rho_0 r_0}; \quad r_0 \frac{\partial p_1}{\partial m} = \frac{\ddot{r}_0}{r_0} r_1 - \frac{\partial^2 r_1}{\partial t^2}; \\ &\frac{\partial}{\partial t}\left(\frac{p_1}{p_0} - k\frac{\rho_1}{\rho_0}\right) = 0, \end{aligned}\right\} \qquad \text{(XII-7-4)}$$

which the functions r_1, p_1, and ρ_1 satisfy. Integration of the equations gives expressions for these functions:

$$\left.\begin{aligned} &r_1 = \frac{1}{r_0}\int_{m^*}^{m} p_0^{1/k}\vartheta(m)\,dm + r_1^*(t); \quad \rho_1 = \frac{\rho_0}{k}\left[\frac{p_1}{p_0} - \vartheta_1(m)\right]; \\ &p_1 = \frac{\ddot{r}_0}{r^2}\int_{m^*}^{m} r_1\,dm - \frac{1}{r_0}\int_{m^*}^{m}\frac{\partial^2 r_1}{\partial t^2}\,dm + p_1^*(t), \end{aligned}\right\} \qquad \text{(XII-7-5)}$$

where $r_1^*(t)$, $p_1^*(t)$ and $\vartheta_1(m)$ are arbitrary functions and m^* is the lower limit of the integrals, which is also chosen arbitrarily.

The conditions on the shock wave and on the piston surface should be used to determine the arbitrary functions. The conditions on the shock wave moving at velocity D relative to the undisturbed flow take the form /526

$$\left.\begin{aligned} m &= 0{,}5\rho_\infty r_s^2; \quad p_s = (1-\delta)\rho_\infty D^2 - \delta p_\infty; \\ \rho_s &= \rho_\infty\left[\delta + (1-\delta)\frac{a_\infty^2}{D^2}\right]^{-1}. \end{aligned}\right\} \qquad \text{(XII-7-6)}$$

Exercising our freedom of choice of the arbitrary function $r_0(t)$, we take one that corresponds to the law of propagation of the shock wave, i.e., we set it equal to $r_0 = r_s(t)$. Then this propagation velocity will be $D = \partial r_s/\partial t = \dot{r}_s$. This selection obviously makes the function $r_1 = 0$ on the shock wave. The conditions that the other terms in the expansions must satisfy on the shock wave will be obtained if Expressions (XII-7-6) for p_s and ρ_s are set equal to their respective values presented in the form of the series (XII-7-1). We find as a result

$$\left.\begin{aligned} p_0 &= \rho_\infty \dot{r}_s^2; \quad p_1 = -p_\infty - \rho_\infty \dot{r}_s^2; \\ \rho_0 &= \delta\rho_\infty\left[\delta + (1-\delta)\frac{a_\infty^2}{\dot{r}_s^2}\right]^{-1}; \quad \rho_1 = 0. \end{aligned}\right\} \qquad \text{(XII-7-7)}$$

With Conditions (XII-7-6) and (XII-7-7) on the shock wave, we can determine the arbitrary functions in (XII-7-3) and (XII-7-5). In particular, introducing $p_0 = \rho_\infty \dot{r}_s^2$ and $m = 0.5\rho_\infty r_s^2$ into the second expression of (XII-7-3),

$$P(t) = \rho_\infty \dot{r}_s^2 + 0{,}5\rho_\infty \ddot{r}_s r_s.$$

The other functions can be found similarly, and p_0 and ρ_0 found after substitution of these functions into (XII-7-3) and simple rearrangement:

$$\left.\begin{aligned} p_0 &= \rho_\infty \dot{r}_s^2 + \frac{1}{2}\rho_\infty \ddot{r}_s r_s - \frac{\ddot{r}_s}{r_s} m; \\ \rho_0 &= \rho_\infty\left(1 + \frac{2}{k-1}\frac{a_\infty^2}{\dot{r}^2}\right)^{-1}\left(\frac{p_0}{\rho_\infty \dot{r}^2}\right)^{1/k}, \end{aligned}\right\} \qquad \text{(XII-7-8)}$$

where $\dot{r} = \partial r/\partial\tau$ is the derivative of the variable r, which defines the Lagrangian coordinate m. Here, if t is the time

corresponding to the coordinate $m^*(r_s)$, then a certain time τ defines the arbitrary Lagrangian coordinate m(r) of the shock wave.

Formulas for r_1, p_1 and ρ_1 are obtained in the same way:

$$\left.\begin{aligned} r_1 &= \frac{1}{r_s}\int_{m^*}^{m} \frac{\left(1+\frac{2}{k-1}\frac{a_\infty^2}{\dot r^2}\right)^{k/2} dm}{\rho_\infty\left(\dot r_s^2 + 0.5\ddot r_s r_s - \frac{\ddot r_s}{r_s}\frac{m}{\rho_\infty}\right)^{1/k}}; \\ p_1 &= \frac{\ddot r_s}{r_s^2}\int_{m^*}^{m} r_1\,dm - \frac{1}{r_s}\int_{m^*}^{m}\frac{\partial^2 r_1}{\partial t^2}\,dm - p_\infty - \rho_\infty \dot r_s^2; \\ \rho_1 &= \frac{\rho_0}{k}\left(\frac{p_1}{p_0}+1+\frac{a_\infty^2}{k\dot r^2}\right). \end{aligned}\right\} \qquad \text{(XII-7-9)}$$

Since the shape of the solid of revolution is usually assigned, and this corresponds to assigning the law of piston motion $r_b(t)$, it is necessary to link the function r_s to this law with an additional condition. The condition with which the terms of second and higher order of smallness can be dropped has the form /527

$$r = r_s + \delta r_1 = r_b.$$

We find from it that

$$r_s = r_b - \delta |r_1|_{m^*}^{0}, \qquad \text{(XII-7-10)}$$

where the function $|r_1|_{m^*}^{0}$ is determined by the first expression in (XII-7-9) with the upper limit of the integral m = 0 (condition on the piston). We note that in this expression, the quantity r_s in the right-hand member can be replaced by r_b. This follows from the fact that after substituting $r_s = r_b - \delta r_1$ for r_s, a third term of the order of δ^2 appears in it and can be disregarded.

Flow around solid of revolution with power-law generatrix. Let us consider application of the above method to calculation of flow around a solid of revolution with a power-law shape [38].

At very high flow velocities, when $a_\infty/D \ll 1$, the pressure in front of the shock wave can be disregarded. Its velocity will

then be determined by

$$\frac{\partial r_s}{\partial t} = f(t, \rho_\infty),$$

where $f(t,\rho_\infty)$ is a certain function of t and ρ_∞.

Since these two quantities have independent dimensions,

$$\frac{\partial r_s}{\partial t} = Bt^n \rho_\infty^m,$$

where B is a constant. Denoting $B\rho_\infty^m = C_1$, we write for the wave propagation velocity

$$\frac{\partial r_s}{\partial t} = C_1 t^n$$

and determine the law of its motion

$$r_s = \frac{C_1}{n+1} t^{n+1}. \qquad \text{(XII-7-11)}$$

The constant C_1 that appears here has the kinematic dimensions $LT^{-(n+1)}$.

By analogy with the expression for r_s, we can write a relation for the expansion law of the piston:

$$r_b = \frac{C}{n+1} t^{n+1}. \qquad \text{(XII-7-12)}$$

Substituting $t = x/V_\infty$ for t in this last expression, we obtain the equation of the body's generatrix:

$$r_b = \frac{C}{n+1} (xV_\infty^{-1})^{n+1}, \qquad \text{(XII-7-12')}$$

which has the form of a power monomial. In the particular case of n = 0, we arrive at the cone equation.

Having (XII-7-11) for r_s and the corresponding relation

$$r = \frac{C_1}{n+1}\tau^{n+1}, \qquad \text{(XII-7-11')}$$

we can determine the arbitrary functions that are represented in general form by (XII-7-8) and (XII-7-9). After substitution and the appropriate transformations, and remembering that a_∞/D is considered negligibly small, we obtain

$$\left.\begin{aligned} p_0 &= \rho_\infty D\left[1 + \frac{n}{2(n-1)}(1-\bar{m})\right]; \\ \rho_0 &= \rho_\infty^{\frac{k-1}{k}}\left(\frac{p_0}{C_1^2\tau^{2n}}\right)^{1/k}. \end{aligned}\right\} \qquad \text{(XII-7-13)}$$

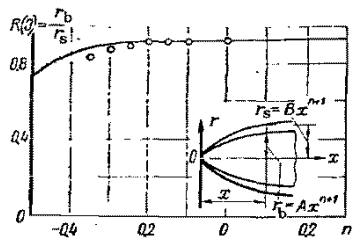

Figure XII-7-1. r_b/r_s for a Body of Power-Law Shape. ooo) exact solution; ———) solution according to (XII-7-22).

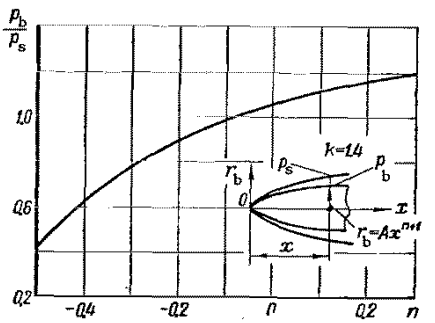

Figure XII-7-2. Ratio of Pressure on Surface of Solid of Revolution with Power-Law Generatrix to Pressure Behind Shock Wave.

/528

Similarly, we obtain relationships for the functions (XII-7-9):

$$\left.\begin{aligned} r_1 &= -\frac{r_s}{2}J(\bar{m}); \\ p_1 &= \rho_\infty D^2\left\{\bar{m}^2 J'(\bar{m}) - \frac{1}{2}\left(\frac{n}{n+1}+\frac{3}{2}\right)\bar{m}J(\bar{m}) - \right. \\ &\quad \left. - \left[\frac{n}{2(n+1)}+\frac{3}{2}\right]\int_{\bar{m}}^{1} J(\bar{m})\,d\bar{m}\right\}; \\ \rho_1 &= \frac{\rho_0}{k}\left(\frac{p_1}{p_0}+1\right), \end{aligned}\right\} \qquad \text{(XII-7-14)}$$

where

$$J(\bar{m}) = \int_{\bar{m}}^{1} \bar{m}^{\frac{n}{k(n+1)}} \left[1 + \frac{n}{2(n+1)}(1-\bar{m})\right]^{1/k} d\bar{m}, \qquad \text{(XII-7-15)}$$

and $J'(\bar{m}) = dJ(\bar{m})/d\bar{m}$.

We see from (XII-7-9) and (XII-7-14) that this motion is self-similar, since all dimensionless parameters are determined by the single dimensionless quantity $\bar{m} = m/m^*$.

The relation between the laws of piston and shock-wave motion, which is determined by the relationships between the coefficients C and C_1, is obtained from Formulas (XII-7-11) and (XII-7-12) by using (XII-7-14) for r_1:

$$\frac{r_b}{r_s} = \frac{C}{C_1} = 1 - \frac{\delta}{2} J(0), \qquad \text{(XII-7-16)}$$

where J(0) is the value of the function $J(\bar{m})$ at $\bar{m} = 0$.

In the problem of flow around the body, Relation (XII-7-16) gives the ratio of the coordinates of points on the body and shock-wave surfaces, respectively. This relation is presented graphically in Fig. XII-7-1.

Using (XII-7-13) and (XII-7-14), as well as Eqs. (XII-7-1), we can find relationships that determine the variables of the gas in the disturbed layer between the shock wave and the body. In particular, the pressure on the surface of the body ($\bar{m} = 0$) is

$$p_b = \rho_\infty D^2 \left[1 + \frac{n}{2(n+1)} - \delta\left(\frac{n}{n+1} + 3\right) \int_0^1 J(\bar{m})\, d\bar{m}\right] = p_s P(0), \qquad \text{(XII-7-17)}$$

and the pressure directly behind the shock is

/529

$$p_s = \frac{2}{k+1} \rho_\infty D^2,$$

while the function $P(0) = p_b/p_s$ [P(0) is determined from (XII-7-17)]. The drag of the power-law body can be calculated from this function, which is presented graphically in Fig. XII-7-2. Here we shall proceed from the formula

$$X = 2\pi \int_0^{r_b} p_b r_b\, dr_b$$

and the pressure expression

$$p_b = p_s P(0) = \frac{2}{k+1}\rho_\infty D^2 P(0) = \frac{2}{k+1}\rho_\infty C_1^2 t^{2n} P(0).$$

We express the product $C_1^2 t^{2n}$ that appears above in terms of r_s and r_b with consideration of (XII-7-11) and (XII-7-12). We then introduce the expression obtained for $\bar{p}$ into the integrand and evaluate it to obtain

$$X = \frac{4\pi}{k+1}\rho_\infty C^2 \frac{P(0)}{R^2(0)}\left(\frac{n+1}{C}\right)^{\frac{2n}{n+1}} \frac{n+1}{2(2n+1)} r_b^{2\left(\frac{n}{n+1}+1\right)}\Big|_0^{r_b}, \qquad \text{(XII-7-18)}$$

where $R(0) = r_b/r_s$ is calculated by Formula (XII-7-16).

To calculate the drag, it is necessary to know the equation of the body's generatrix in addition to the parameters of the oncoming flow. The radius of the largest cross section, $r_b = r_{mid}$, the exponent n, and the constant C appear in Formula (XII-7-18) as parameters characterizing the shape of the body.

In practical cases, we can assign n, r_{mid}, and the slenderness ratio $\lambda = x_{mid}/(2r_{mid})$ and construct the generatrix in accordance with the equation

$$r_b = Ax^{n+1} = \frac{1}{2}\lambda^{-(n+1)}(2r_{mid})^{-n} X^{n+1}.$$

Having determined the coefficient A with this equation, we can calculate the coefficient C, which, according to (XII-7-12') is $A(n+1)V_\infty^{n+1}$.

It follows from (XII-7-18) that a solution does not exist for all values of the exponent n in the piston-expansion law (XII-7-12), i.e., for all power-law shapes. For example, it is evident that the value of the integral

$$r_b^{2\left(\frac{n}{n+1}+1\right)}\Big|_0^{r_b}$$

diverges for $[n/(n+1)] < -1$. At n corresponding to this inequality, drag becomes infinite, and this cannot be.

The drag calculated by (XII-7-18) will be finite for bodies whose generatrix equations are characterized by an exponent $n > -1/2$. But if $n < -1/2$, then no self-similar solution exists. This means that the distribution of parameters in transverse planes between the body and the shock wave does not have the similarity property and, consequently, the pressure, density, and velocity cannot be expressed in the form

$$\frac{P(r)}{P(r_s)} = f\left(\frac{r}{r_s}\right).$$

In this case, the flow in a given cross section must depend on its prior history, which is determined by the geometric peculiarities of the body. It follows from analysis of the generatrix equation (XII-7-12) that with $n > -1/2$ this equation represents, in addition to sharp bodies ($n \geq 0$), also blunted shapes ($-1/2 < n < 0$).

The approximate nature of (XII-7-18), which is due to presentation of the solutions in series form (XII-7-1) with consideration of terms of the order $\delta = (k-1)/(k+1)$ restricts the application of this formula to values of n slightly larger than $-1/2$. This is seen in Fig. XII-7-3, which shows a curve of the drag coefficient corresponding to the formula /530

$$c_x = \frac{2X}{\rho_\infty V_\infty^2 \pi r_b^2} = \frac{2}{k+1}\frac{(n+1)^3}{2(2n+1)}\frac{P(0)}{R^2(0)}\frac{1}{\lambda_{mid}^2}, \qquad \text{(XII-7-19)}$$

in which the body's slenderness $\lambda_{mid} = x/(2r_b) = 1/\tau$. We note that Formula (XII-7-19) is obtained from (XII-7-18) if the value of the integral is zero at the lower limit and the constant

$$C = (n+1) r_b t^{-(n+1)} = (n+1) r_b \left(\frac{V_\infty}{x}\right)^{n+1}.$$

A comparison with the results of the exact solution (Fig. XII-7-3) indicates that the exactness of (XII-7-19) decreases around $n = -1/2$. The same can also be said as regards shock-wave shape. The corresponding working relationship (XII-7-16) gives less satisfactory results than the exact theory around the same value $n = -1/2$ (see Fig. XII-7-1).

Analysis of the results given in Fig. III-7-3 permits the conclusion that there exists a power-law solid of revolution that has the smallest drag of all such bodies with the same slenderness ratio. It follows from these results that the minimum of the function $c_x\lambda_{mid}^2$ is reached at approximately $n = -0.29$ and is equal

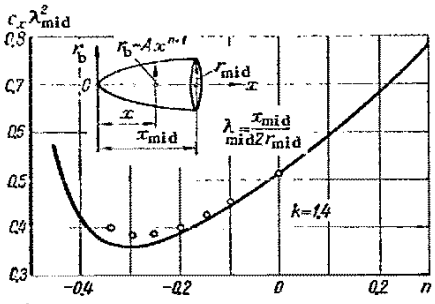

Figure XII-7-3. Drag Coefficient of Solids of Revolution with Power-Law Generatrices. ooo) exact solution; ———) solution according to (XII-7-25).

to 0.38, while $c_x\lambda^2_{mid} = 0.52$ for a cone, which is about 37% larger. For very high velocities, therefore, the blunt solid of revolution with a curvilinear generatrix, which has an advantage over the sharp cone in its superior conditions for dissipation of heat, may also compare favorably with the cone in that its drag is smaller.

The relationships derived above pertained to the case in which terms of the order of $\delta = (k - 1)/(k + 1)$ were considered in the expansions of (XII-7-1). Naturally, these relationships simplify if only the principal terms are considered. For example, Formulas (XII-7-16) and (XII-7-17) become

$$R(0)=\frac{r_b}{r_s}=\frac{C}{C_1}=1; \qquad \text{(XII-7-16')}$$

$$p_b=\rho_\infty D^2\left[1+\frac{n}{2(n+1)}\right]=p_s P(0), \qquad \text{(XII-7-17')}$$

and Formula (XII-7-19) for the drag coefficient

$$c_x=\frac{(n+1)^2}{4(2n+1)}\frac{3n+2}{\lambda^2_{mid}}. \qquad \text{(XII-7-19')}$$

Having determined the minimum of c_x for a fixed slenderness ratio λ_{mid}, we find that this minimum is reached at $n = -1/3$. The minimum

$$c_x=\frac{1}{3\lambda^2_{mid}}, \qquad \text{(XII-7-20)}$$

which is smaller than for a cone in this approximation, for which the Newtonian theory gives $c_x = 1/(2\lambda^2_{mid})$, corresponds to this value. /531

Application of the Newton formula. Pressure can be calculated by (XII-7-17) for points on the surface of a power-law solid of revolution at a certain distance from the blunt nose.

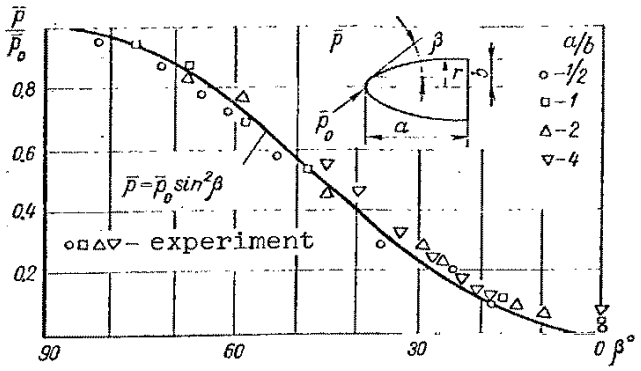

Figure XII-7-4. Comparison of Theoretical and Experimental Pressure Distributions Around an Ellipsoid in Symmetrical Flow.

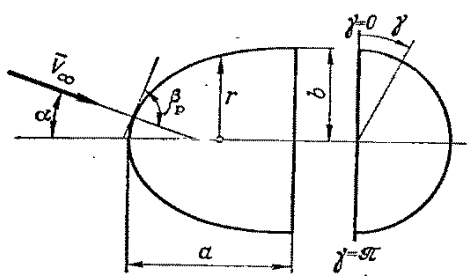

Figure XII-7-5. Diagram for Calculation of Flow Around Ellipsoid.

As concerns the nose surface, the improved Newton theory gives satisfactory results here in pressure-distribution calculations for spherical bodies. Studies have shown that the same results are obtained for bodies with other curvilinear shapes.

This is seen, for example, in Fig. XII-7-4, which presents, together with the results of a calculation by the formula $\bar{p} = \bar{p}_0 \sin^2 \beta$, experimental data on the pressure distribution around ellipsoids in symmetrical flow. Satisfactory results are also obtained from the improved Newton formula ([66], 1964, No. 4) for calculation of flow around an ellipsoid at an angle of attack (Fig. XII-7-5):

$$\bar{p} = \frac{\bar{p}_0}{\sin^2 \beta_p} \frac{(\cos\alpha \sqrt{1-\bar{r}^2} - \bar{r}\,\bar{t} \sin\alpha \cos\gamma)^2}{1+\bar{r}^2(\bar{t}^2-1)}, \qquad \text{(XII-7-21)}$$

where β_p is the angle between the tangent to the body's contour at its forward point and the direction of the vector $\bar{V}_\infty$; $\bar{r} = r/b$; $\bar{t} = a/b$ (b and a are the semiaxes of the ellipse, Fig. XII-7-5); $\bar{p}_0$ is the pressure coefficient at the critical point of the ellipsoid. The calculations can be simplified by using, instead of (XII-7-21), the empirical relation

$$\bar{p}(\bar{r}, \gamma) = \bar{p}_1(\bar{r}) + \bar{p}_2(\bar{r})\cos\gamma, \qquad \text{(XII-7-22)}$$

where

$$\bar{p}_1(\bar{r}) = \frac{1}{2}[\bar{p}(\bar{r}, \gamma = 0) + \bar{p}(\bar{r}, \gamma = \pi)]; \quad \bar{p}_2(\bar{r}) = \frac{1}{2}[\bar{p}(\bar{r}, \gamma = 0) - \bar{p}(\bar{r}, \gamma = \pi)]. \qquad \text{(XII-7-23)}$$

According to Formula (XII-7-22), the pressure is determined at any point on the surface by its value at points on the ellipsoid generatrices corresponding to the angles $\gamma = 0$ and π. /532

The axial-force coefficient can be determined by integrating pressure over the surface. Calculations and a comparison with experiment indicate that this coefficient varies insignificantly over a rather broad range of attack angles: $-15° \leq \alpha \leq 15°$. The comparison shows that better agreement between the experimental and theoretical results is observed at high supersonic speeds. However, the Newton theory gives an approximation that is quite satisfactory for practical purposes even at comparatively low speeds when the pressure is determined near the critical point. With increasing distance from the nose, the pressure found theoretically becomes smaller than the experimentally measured pressure.

The calculated results can be improved to some extent by "gluing" the pressure distribution found on the forward end by the Newton formula to the pressure distribution found on the downstream segment from the theory of Prandtl-Meyer expansion flow. In turn, the Prandtl-Meyer solution is "glued" to the solution found by Formula (XII-7-17).

§XII-8. INFLUENCE OF NONEQUILIBRIUM ON PARAMETERS OF INVISCID FLOW AROUND BLUNT BODIES

Nonequilibrium Flow in Regions with Strong Overexpansion and Small Pressure Gradients

Regions of gas flow around a blunt body. If we examine the nature of the flow around a blunt body, we can establish three regions of the gas flow (Fig. XII-8-1). The first lies directly over the blunt nose between the flow axis and the "sonic" line. It is characterized by an almost constant pressure close to the total-stagnation value. Moving along a streamline in this region of almost constant and very high pressure, the gas, which has entered a state of nonequilibrium dissociation after passage through the shock wave, will be able to recover quickly to the equilibrium state. Here the equilibrium corresponds to a certain average pressure and enthalpy in this region.

The second region of the flow begins at the "sonic" line and is characterized on a certain distance by a sharp pressure

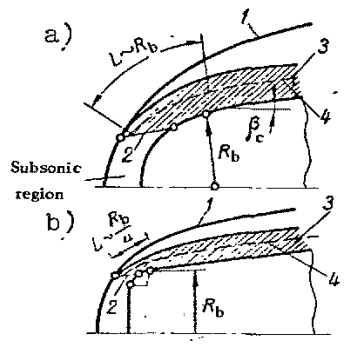

Figure XII-8-1. Diagram of Gas Flow Around Blunt Bodies. a) spherical bluntness; b) flat bluntness with circular bevel; 1) shock wave; 2) "sonic" line; 3) low-velocity shock layer; 4) streamline.

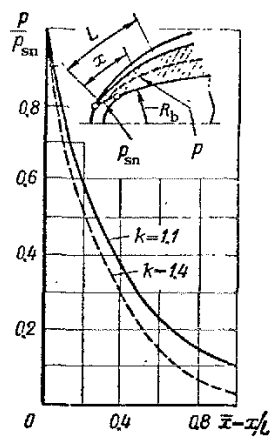

Figure XII-8-2. Pressure Drop Along Streamline During Expansion of Gas According to Prandtl-Meyer Law.

decrease. The region may terminate (depending on the shape of the body behind the nose) in a flow with positive, zero, or negative pressure gradients. In this zone of strong overexpansion, the state of the dissociating gas will lag behind equilibrium, so that thermodynamic nonequilibrium is an essential property of the moving gas. /533

In the third flow region, which is situated on the peripheral part of the body and is characterized by a small change in pressure, the gas will tend to its equilibrium state.

Thus, it becomes necessary to take departure from equilibrium into account in calculating inviscid flow. Here, research indicates that in practice, the pressure changes only slightly on passage from the nonequilibrium to the equilibrium state. On this basis, it has become possible to evaluate the influence of nonequilibrium molecular dissociation on such inviscid-flow variables as the degree of dissociation, density, and temperature for a given realistic pressure distribution. It is assumed here that the pressure distribution is subject to the same law irrespective of the conditions of the body's motion.

Calculation of nonequilibrium flow. This calculation requires integration of equation system (III-4-47) with certain assigned constants and boundary conditions. The results given here were obtained using $C = 6 \cdot 10^{14}$ cm^3/g·s and ρ_d = = 125 g/cm^3. The boundary conditions used in integrating the equations were the conditions on the "sonic" line, with the corresponding parameters on this line determined for a given flight speed V_∞ and a given altitude H as parameters of equilibrium flow in the total-stagnation region.

The streamline along which the nonequilibrium flow variables were calculated was downstream of the "sonic" region. It was assumed that the pressure established on this streamline is the same as in expansion of a one-dimensional flow in accordance with the Prandtl-Meyer law. It was also assumed that with this pressure distribution, the length of the selected streamline would be of the order of the radius of a spherical nose or one-quarter of the radius of a flat face (or a flat face with a small circular bevel). The length assumed for the initial supersonic expansion determines the characteristic linear dimension L.

Figure XII-8-2 shows the pressure distribution calculated on the basis of Prandtl-Meyer theory for a streamline crossing an expansion fan beginning at the "sonic" point ([72], 1960, No. 11). For a streamline with a constant radius of curvature r, the expansion angle was assumed to be $\nu = \bar{x} = x/r$. Figures XII-8-3 through XII-8-7 show certain results of numerical integration of System (III-4-47) for various altitudes and speeds. The calculations were also made in each case for several characteristic lengths L (or, which is the same thing, for several values of the parameter $\bar{\phi}$).

An inference as to the nature of the change in nonequilibrium dissociation can be drawn from Fig. XII-8-3. For comparison, this figure shows curves of the degree of equilibrium dissociation as obtained for real air (B) and a diatomic-gas model (A). We note that at speeds $V_\infty > 5$ km/s, the difference between the degrees of equilibrium dissociation is small in the last two cases. Analysis of these results shows that the change in the degree of dissociation α along the streamline is very small by comparison with the initial equilibrium value α_{0e} even at a considerable distance. Here the gas is close to the "frozen" state, in which no reactions take place in it and, consequently, its chemical composition does not change. /534

As a convention, we can consider the flow "frozen" in practical cases when the composition of the gas differs by about 5% from the original composition. Then if α_1 is the degree of nonequilibrium dissociation at the end of the expansion segment under consideration, the "frozen" state requires satisfaction of a condition according to which the nonequilibrium dissociation parameter

$$\tilde{\alpha}_1 = \frac{\alpha_1 - \alpha_{1e}}{\alpha_{0e} - \alpha_{1e}} \geqslant 0.95,$$

this parameter including α_{1e}, which is the degree of equilibrium dissociation at the end of the same segment. If the parameter $\tilde{\alpha}_1$ is zero, the transition to equilibrium is complete. In practice, it can be assumed that this state has intervened if $\tilde{\alpha}_1 \leq$

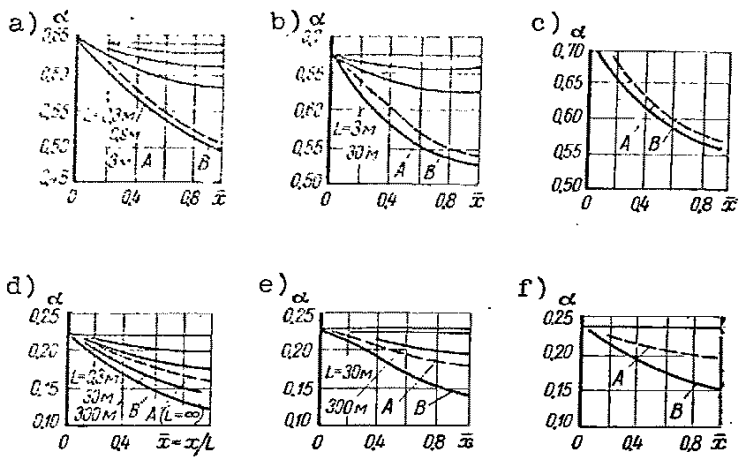

Figure XII-8-3. Influence of Nonequilibrium on the Degree of Dissociation along Streamline. A) diatomic gas; B) real air; a) H = 47 km, V_∞ = 7.6 km/s; b) H = 61 km, V_∞ = 7.6 km/s; c) H_∞ = 75 km, V_∞ = 7.6 km/s; d) H = 47km, V_∞ = 4.6 km/s; e) H_∞ = 61 km; V_∞ = 4.6 km/s; f) H = 75 km, V_∞ = 4.6 km/s.

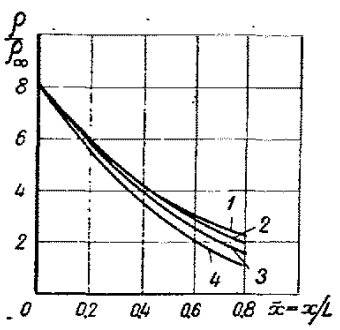

Figure XII-8-4. Variation of Density in Nonequilibrium Flow of Diatomic Gas Model. H = 47 km, V_∞ = 4.6 km/s; 1) L = 0.3 m; 2) L = = 6 m; 3) L = 30 m; 4) L = ∞ (equilibrium flow).

< 0.05. Returning to the diagrams of Fig. XII-8-3, we note that the flow in the region of supersonic expansion around blunt bodies will be practically "frozen" at altitudes above 47 km at speeds of 5-8 km/s.

For any given speed and length L, the flow will be found more nearly "frozen" with increasing altitude. With decreasing speed, other conditions the same, the parameter $\tilde{\alpha}_1$ increases owing to the decrease in local density. Increased "freezing" is observed at a decrease in the characteristic length L, which results in a shorter stay time of the gas particles at a particular point, during which only a few atoms manage to recombine. /535

It follows from the results presented in Figs. XII-8-4 and XII-8-5 that the deviation from equilibrium causes a decrease in density and a rise in temperature. In turn, this results in a

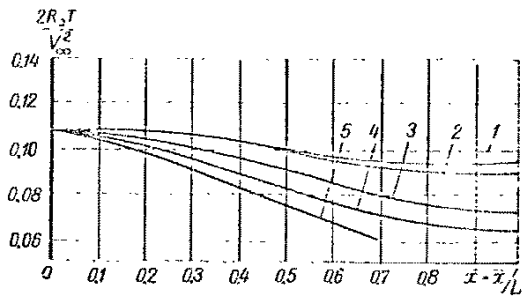

Figure XII-8-5. Temperature Distribution in Nonequilibrium Flow of Diatomic Gas Model. H = 47 km, V_∞ = 4.6 km/s. 1) L = ∞ (equilibrium flow); 2) L = 300 m; 3) L = 30 m; 4) L = 3 m; 5) L = 0.3 m.

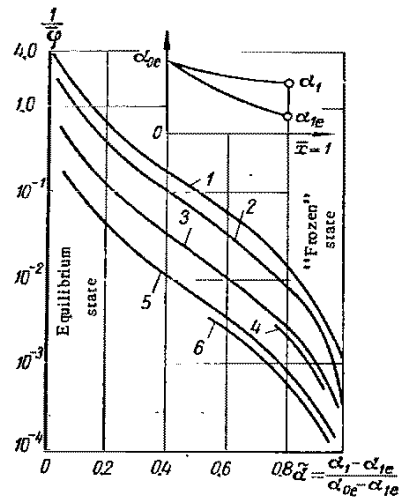

Figure XII-8-6. Variation of Nonequilibrium Dissociation Parameter under Various Conditions. 1) H = 47 km, V_∞ = 4.6 km/s; 2) H = 61 km, V_∞ = 4.6 km/s; 3) H = 47 km, V_∞ = 6.1 km/s; 4) H = 61 km, V_∞ = 6.1 km/s; 5) H = 47 km, V_∞ = 7.6 km/s; 6) H = 61 km, V_∞ = 7.6 km/s.

substantial change in the local Re. Here, calculations indicate that the deviation from equilibrium flow influences the pressure distribution weakly.

Curves that can be used to estimate the nonequilibrium dissociation parameter $\tilde{\alpha}_1$ for a known $\bar{\phi}$ have been plotted in Fig. XII-8-6 from the results of numerical integration of (III-4-47).

Behind the region of supersonic expansion, the flow enters a zone of weakly varying pressure that may be regarded in practice as a constant-pressure region, thus simplifying the analysis. This case is a close approximation of reality if the blunted nose is followed by a conical segment.

As they move in the constant-pressure zone, the gas particles are able to return to equilibrium, which corresponds to constant enthalpy and pressure. During this transition, the nonequilibrium parameters are determined by integrating only the last equation of System (III-4-47). The initial conditions are determined by the "frozen" parameters at the end of the supersonic-expansion segment considered above (the length $\bar{x}$ is measured from this cone). The results indicate that at speeds of 4.6-7.6 km/s, the flow on the segment next to the nose remains practically "frozen" at a distance of no less than 6-9 m, with this distance, which corresponds to an altitude of the order of 45-47 km, increasing with H. For example, at H = 61 km, the length L has increased to

30 m. Certain calculated results for H = 40 km are shown in Fig. XII-8-7. The deviation from the "frozen" state and the approach to equilibrium conditions take place most rapidly at high velocities.

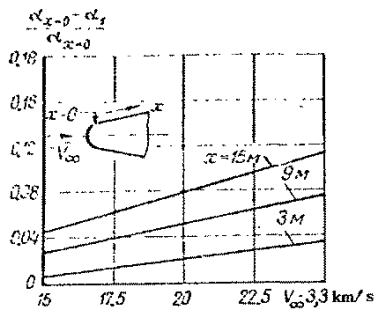

Figure XII-8-7. Variation of Degree of Dissociation along a Conical Surface under Constant-Pressure Conditions (H = 47 km).

The "freezing" phenomenon is inherent not only to the region with zero pressure gradient, but also, and to an even greater degree, to flow with negative pressure gradients, which arise, for example, in flow around a cylinder. This enhanced susceptibility to "freezing" is explained by the fact that a decrease in pressure causes a decrease in density. In the last equation of System (III-4-47), the recombination term in the right member depends essentially on density, varying approximately in proportion to its square. /536

The following practical conclusion can be drawn from the above analysis of nonequilibrium flow around a blunt body. Since the entire flow zone associated with the region of the strong shock wave remains "frozen" over almost the entire length of the blunt body, the inviscid-flow variables along a streamline in this shock layer can be calculated from the condition of isentropic flow with $k_2 = 1.1\text{-}1.2$ (the exact value of k_2 is calculated for total-stagnation conditions). Accordingly, the temperature and density at a given point are found from the expressions

$$\frac{T}{T_0'} = \left(\frac{p}{p_0'}\right)^{\frac{k_2-1}{k_2}}, \quad \frac{\rho}{\rho_0'} = \left(\frac{p}{p_0'}\right)^{1/k_2}. \qquad \text{(XII-8-1)}$$

Effect of Nonequilibrium on Position and Shape of Shock Wave

Let us consider the following two extreme cases, which characterize this effect qualitatively. The first is governed by completely "frozen" flow behind the shock, when the gas behaves as a medium with constant heat capacities that can be determined if it is assumed that the vibrational degrees of freedom are established instantaneously behind the shock. However, the maximum effect can be ascertained on the premise that equilibrium is not established for these degrees.

In our second limiting case, the gas in the compressed layer is under equilibrium-dissociation conditions.

We set forth above a method for calculating the relative detachment distance of the shock wave in both of the limiting flow cases. According to the calculated results, the wave is farthest from the critical point in the first case, while in the second it makes its closest approach to this point.

Real nonequilibrium flows, which are characterized by intermediate shock-wave positions, fall between these extreme cases. To characterize such flows, it is helpful to introduce a nonequilibrium parameter defined as follows. The last equation of System (III-4-47) implies that for flows behind a normal compression shock, $(C\rho_\infty)^{-1}$ can be regarded as the time scale of dissociation, and the parameter $V_\infty(C\rho_\infty)^{-1}$ as the linear scale of the flow. /537 Then we can take the ratio of some linear dimension of the body to the linear flow scale as a dimensionless parameter of nonequilibrium flow.

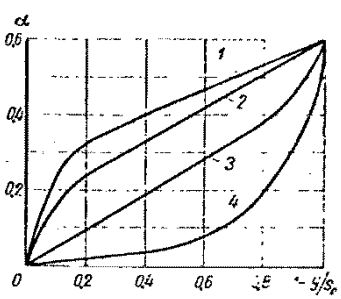

Figure XII-8-8. Variation of Degree of Dissociation along Zero Streamline (from shock wave to critical point of body). $(m_A V_\infty^2)/D = 1$; $\rho_\infty/\rho_d = 10^{-6}$; 1) $\Lambda = 100$; 2) $\Lambda = 50$; 3) $\Lambda = 10$; 4) $\Lambda = 1$.

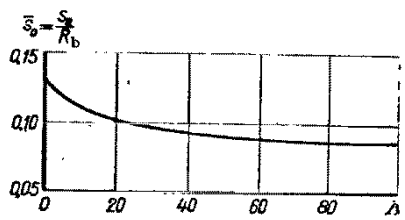

Figure XII-8-9. Relative Detachment Distance of a Shock Wave in Front of a Sphere as a Function of Nonequilibrium Parameter: $(m_A V_\infty^2)/D = 1$; $\rho_\infty/\rho_d = 10^{-6}$.

The linear dimension for a sphere may be its diameter D_b. Consequently, the nonequilibrium parameter in this case is

$$\Lambda = D_b C \rho_\infty V_\infty^{-1}. \qquad \text{(XII-8-2)}$$

If this parameter Λ is zero, we have undissociated ("frozen") flow owing to the infinitesimal rate of chemical reaction.

Large Λ correspond to rapid reactions and, consequently, dissociation begins near the wave and covers almost the entire region between the wave and the body's surface. As $\Lambda \to \infty$, equilibrium is reached immediately behind the wave.

The local value of the parameter $\Lambda = \lambda$, calculated from the local velocity V on the zero streamline, i.e.,

$$\lambda = D_b C \rho_\infty V^{-1} \qquad \text{(XII-8-2')}$$

can be used to analyze the flow between the wave and the body.

At the critical point, where $V = 0$, this parameter $\lambda = \infty$ and, consequently, equilibrium dissociation is reached near it. Physically, this effect is explained by the extremely slow flow in the neighborhood of the stagnation point, which aids in the establishment of thermodynamic equilibrium.

If we start with equilibrium flow on the surface of the body, the concentration distribution of the atomic component along the normal to the wall will be characterized qualitatively by a gradual concentration decrease toward the shock wave, where the degree of dissociation vanishes. The concentration profile can be calculated theoretically by solving the equation system for flow in the region of the critical point simultaneously with the last equation of the nonequilibrium-flow system (III-4-47). Figure XII-8-8 shows the concentration profile calculated in this manner for one of the particular cases.

Another result of solution is the possibility of calculating the distance from the shock wave to the body. Figure XII-8-9 is a graph of the relative detachment distance as a function of the nonequilibrium parameter Λ. Comparing the results, we see that the separations may differ by a factor of two in the two extreme cases, i.e., in "frozen" and equilibrium flows. The variation of the axial radius of curvature of the wave is similar.

Case of nonequilibrium at the surface. The ratio of the characteristic times $\bar{t}_D = t_D/t_{s_0}$ (t_{s_0} is the stay time of the particles in the nonequilibrium-reaction zone) can be used for approximate evaluation of the conditions under which nonequilibrium chemical reaction occurs at the wall. Clearly, this reaction occurs if $\bar{t}_D \geq 1$, i.e., when the atoms reach the surface of the body before reacting. /538

To estimate the length L of the surface segment with chemical reaction, it is necessary to compare the characteristic time of the reaction with the characteristic stay time of the particles in the nonequilibrium zone on the segment under consideration.

Here the stay time is calculated from $d\alpha/dt$, which determines the rate of the change in degree of dissociation due to the disappearance of atoms by recombination. This evanescence time, which is obviously equal to the characteristic stay time in the reaction zone, is determined from the equation

$$\frac{dt}{d\alpha} = \frac{dx}{d\alpha}\frac{1}{V}.$$

For approximate evaluation, we can set $dx/d\alpha \sim L/\alpha_0$, where α_0 is the degree of equilibrium dissociation at the stagnation point. The stay time can therefore be presented in the form $L/(\alpha_0 V)$, where V is the particle velocity along the surface near the stagnation point. Let us assume that this velocity is of the same order as the average velocity between the shock and the body, or $0.5V_0$. Thus, the characteristic-times ratio can be written

$$\bar{t}_L = \frac{t_D V \alpha_0}{L} = \frac{t_D V_0 \alpha_0}{2L}. \qquad \text{(XII-8-3)}$$

From this expression, we easily pass to

$$\bar{L}\bar{t}_L = \bar{t}_D \alpha_0 \bar{s}_0, \qquad \text{(XII-8-3')}$$

where $\bar{L} = L/R_b$.

Since we are concerned with the reaction zone, the condition $\bar{t}_L \geq 1$ must obviously be satisfied in it. The length of this zone from the stagnation point will therefore be

$$\bar{L} = \bar{t}_D \alpha_0 \bar{s}_0. \qquad \text{(XII-8-4)}$$

Atoms that have not reacted chemically enter the boundary layer on a surface segment of this length.

The recombination process culminates in the boundary layer and has some influence on friction and heat transfer. It should be stressed here that the pressure distribution is practically independent of the nonequilibrium effects.

Improvement of the flow regime in the stagnation zone (at the critical point and for a certain distance downstream) enables us to evaluate the change in density and temperature if this

regime is nonequilibrium. Increased temperature and decreased density at the outer layer boundary result in a change in the heat flow on this surface segment from the flow of the equilibrium state. It can be assumed that, despite the temperature increase, the heat flow diminishes to some degree owing to the decrease in density.

Up to this point, all calculations have been based on the assumption that the recombination-rate parameter k_R is independent of temperature. Actually, however, temperature has substantial influence on this parameter. For example, according to certain experimental data for oxygen

$$k_R = 8.4 \cdot 10^{14} \left(\frac{3500}{T}\right)^2 \text{ cm}^6/\text{mole}^2 \cdot \text{s} \qquad \text{(XII-8-5)}$$

According to this formula, the relaxation time calculated above can be improved by introducing a correction factor $(T/3500)^2$. The refined relaxation time will therefore be

$$\bar{t}' = \bar{t}\left(\frac{T}{3500}\right)^2. \qquad \text{(XII-8-6)}$$

Chapter XIII /539

NONSTATIONARY AERODYNAMICS OF BODIES

§XIII-1. LINEARIZED FLOW AROUND SOLIDS OF REVOLUTION

Basic Relationships

General definitions. Let us consider the problem of linearized nonsteady flow around a body. As in the case of steady flow, we shall use the method of sources for its solution, with the difference that the washed body is replaced by a system of nonsteady sources (sinks) and dipoles ([72], 1951, No. 8).

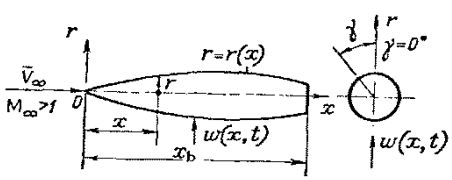

Figure XIII-1-1. Diagram of Nonsteady Flow Around Solid of Revolution in Transverse Direction.

Let us assume that in a linearized supersonic flow at a certain M_∞ there is a secondary transverse onflow at a velocity W(x,t) that depends on time t and the coordinate x of a given cross section of the solid of revolution (Fig. XIII-1-1). Thus, this additional flow is nonsteady. Following the method of sources, we can regard the velocity potential of this flow as the potential of nonsteady sources and dipoles whose strength and moment, respectively, vary in time.

Here the velocity potential from nonsteady sources and dipoles on the axis of a slender body is determined from the linearized equation (III-2-31). The integral ϕ' of this equation is sought as the sum of two potentials: ϕ_1', the axisymmetric-flow potential, which does not produce disturbances that lead to the appearance of a normal force, and ϕ_2', the potential from disturbance of symmetry, which does produce a normal force. As in the case of steady flow, the solution for the added potential ϕ_2' can be solved in the form (XI-1-14). As regards the solution for ϕ_1', it is the integral of the linearized nonsteady-flow equation

$$(\alpha')^2\varphi'_{xx}-\varphi'_{rr}-\frac{1}{r}\varphi'_r+\frac{2M_\infty}{a_\infty}\varphi'_{xt}+\frac{\varphi'_{tt}}{a_\infty^2}=0. \qquad \text{(XIII-1-1)}$$

where the subscripts x and r signify the corresponding partial derivatives.

Potential of nonsteady source (sinks). Let us write the solution of (XIII-1-1) in the form

$$\varphi_1' = \eta(x, r)\exp\left[i\omega\left(t - \frac{M_\infty x}{a_\infty (\alpha')^2}\right)\right], \qquad \text{(XIII-1-2)}$$

where ω is the angular frequency of the body's vibrations in the uninverted motion and $\eta(x,r)$ is a function of the variables x and r. Here, $\eta(0,r) = \eta_x(0,r) = 0$, which corresponds physically to the absence of disturbances on the $x = 0$ line.

After substituting (XIII-1-2) for ϕ_1' into (XIII-1-1), it becomes /540

$$\eta_{rr} + \frac{1}{r}\eta_r - (\alpha')^2\eta_{xx} - \frac{\omega}{a_\infty^2 (\alpha')^4}\eta = 0, \qquad \text{(XIII-1-3)}$$

Differential equation (XIII-1-3) can be solved by an operator method based on the Laplace integral transformation. Applied to the present case, this method consists in studying not the function $\eta(x,r)$ itself, which is known as the original, but instead its so-called transform. This transformation of the function $\eta(x,r)$ with respect to the variable x is accomplished as follows. The function $\eta(x,r)$ is multiplied by the exponential function $\exp(-sx)$, and then integration is carried out in the range from 0 to ∞. We obtain as a result

$$\bar{\eta}(s, r) = \int_0^\infty \exp(-sx)\,\eta(x, r)\,dx, \qquad \text{(XIII-1-4)}$$

where $\bar{\eta}(s,r)$ is a function known as the (Laplace) transform of the function $\eta(x,r)$ and s is a certain complex quantity, the transformation operator.

As a result of the Laplace transformation (XIII-1-4), we obtain an ordinary differential equation for the transform:

$$\frac{d^2\bar{\eta}}{dr^2} + \frac{1}{r}\frac{d\bar{\eta}}{dr} - (\alpha')^2\left[s^2 + \frac{\omega^2}{a_\infty^2 (\alpha')^4}\right]\bar{\eta} = 0. \qquad \text{(XIII-1-5)}$$

The sense of the transfromation becomes evident from the form of (XIII-1-5): it has reduced the number of variables by one and thereby enabled us to pass from a partial differential equation (XIII-1-3) to the ordinary differential equation (XIII-1-5). The equation obtained is one of the modifications

of the Bessel equation whose solution has a limit at infinity:

$$\overline{\eta} = K_0\left\{\alpha' r\left[s^2 + \frac{\omega^2}{a_\infty^2 (\alpha')^4}\right]^{1/2}\right\}, \qquad \text{(XIII-1-6)}$$

where K_0 is a Macdonald function.

Having found the transform $\overline{\eta}$, we must find the original η. The inverse Laplace transformation must be used for this purpose. The final expression for the unknown function takes the form

$$\eta(x, r) = [x^2 - (\alpha' r)^2]^{-1/2} \cos\left\{\frac{\omega}{a_\infty (\alpha')^2}[x^2 - (\alpha' r)^2]^{1/2}\right\}, \qquad \text{(XIII-1-7)}$$

which is valid for the condition $(x - \alpha' r) > 0$.

We obtain a relation for the potential of a nonsteady point source on the basis of (XIII-1-2) and (XIII-1-7). If sources of variable intensity $f(\varepsilon)$ are distributed continuously along the $\underline{x}$-axis, the potential function is

$$\varphi_1' = \exp(i\omega t) \times \int_0^{x-\alpha' r} \frac{f(\varepsilon) \exp\left[-\frac{i\omega M_\infty}{a_\infty (\alpha')^2}(x-\varepsilon)\right] \cos\left\{\frac{\omega}{a_\infty (\alpha')^2}[(x-\varepsilon)^2 - (\alpha' r)^2]^{1/2}\right\} d\varepsilon}{[(x-\varepsilon)^2 - (\alpha' r)^2]^{1/2}}. \qquad \text{(XIII-1-8)}$$

Potential of a nonsteady dipole. Differentiating the potential function ϕ_1' with respect to $\underline{r}$, we find the added potential ϕ_2' of a nonsteady dipole in accordance with (XI-1-14). Before differentiating, we transform Expression (XIII-1-8) to the variable $z = \text{arc cosh}\,[(x - \varepsilon)/(\alpha' r)]$. Then, differentiating with respect to $\underline{r}$ and transforming back to the variable $\varepsilon = x - \alpha' r \cosh z$, we find an expression for the nonsteady-dipole potential: /541

$$\varphi_2' = \exp(i\omega t)\cos\psi \left\{\frac{\omega}{r a_\infty (\alpha')^2}\int_0^{x-\alpha' r} f(\varepsilon) \exp\left[-\frac{i\omega M_\infty}{a_\infty (\alpha')^2}(x-\varepsilon)\right] \times \right.$$
$$\left. \times \sin\left\{\frac{\omega}{a_\infty (\alpha')^2}[(x-\varepsilon)^2 - (\alpha' r)^2]^{1/2}\right\} d\varepsilon + \right. \qquad \text{(XIII-1-9)}$$
$$\left. + \int_0^{x-\alpha' r} \frac{f(\varepsilon)(x-\varepsilon) \exp\left[-\frac{i\omega M_\infty}{a_\infty (\alpha')^2}(x-\varepsilon)\right] \cos\left\{\frac{\omega}{a_\infty (\alpha')^2}[(x-\varepsilon)^2 - (\alpha' r)^2]^{1/2}\right\} d\varepsilon}{r[(x-\varepsilon)^2 - (\alpha' r)^2]^{1/2}}\right.$$

$$+\frac{i\omega M_\infty}{a_\infty(\alpha')^2 r}\times$$

$$\times\int_0^{x-\alpha' r}\frac{f(\varepsilon)(x-\varepsilon)\exp\left[-\frac{i\omega M_\infty}{a_\infty(\alpha')^2}(x-\varepsilon)\right]\cos\left\{\frac{\omega}{a_\infty(\alpha')^2}[(x-\varepsilon)^2-(\alpha' r)^2]^{1/2}\right\}d\varepsilon}{[(x-\varepsilon)^2-(\alpha' r)^2]^{1/2}}\Bigg\}. \quad \text{(XIII-1-9)}$$

(Cont'd.)

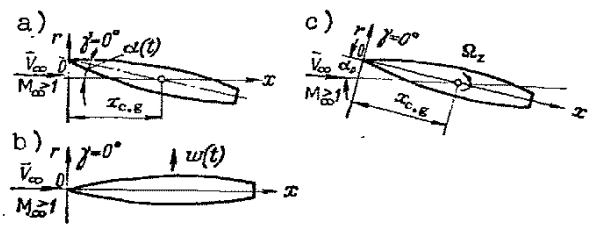

Figure XIII-1-2. Cases of Motion of Solid of Revolution. a) harmonic oscillatory motion about the body's center of gravity; b) harmonic oscillation of the body normal to its longitudinal axis; c) steady rotation of the body about a transverse axis passing through its center of gravity.

Boundary condition. The boundary condition for determination of the function f(ε) in (XIII-1-9) is obtained from the nonseparating-flow condition. This means that the disturbed-motion potential from the nonsteady dipole must be such that the normal velocity component vanishes on the surface of the body or, considering its small thickness, on the x-axis, i.e., such that a condition analogous to (XI-1-11') is satisfied:

$$\left(\frac{\partial\varphi_2}{\partial r}\right)_{r\to 0}=-W(x,t)\cos\gamma. \quad \text{(XIII-1-10)}$$

This condition assumes various forms depending on the specific case of flow accompanying the particular form of motion of the body.

Let us consider possible cases of motion that are of practical interest in connection with investigation of oscillatory stability.

Harmonic oscillatory motion of the body about a transverse axis passing through its center of gravity (Fig. XIII-1-2a). In this case, the motion is determined by the equation

$$\alpha=\alpha_0\exp(i\omega t), \quad \text{(XIII-1-11)}$$

where α_0 is the initial amplitude, which is equal to the attack angle at t = 0.

In the inverted motion, oscillations of the body give rise /542 to a nonsteady disturbed flow whose transverse velocity component

is

$$W(x, t) = V_\infty \alpha_0 \exp(i\omega t) + \frac{d\alpha}{dt}(x - x_{c.g}). \qquad \text{(XIII-1-12)}$$

Since

$$\frac{d\alpha}{dt} = \alpha_0 i\omega \exp(i\omega t), \qquad \text{(XIII-1-13)}$$

the boundary condition becomes

$$\frac{\partial \varphi_2'}{\partial r} = -\alpha_0 \exp(i\omega t)\cos\gamma\,[(V_\infty + i\omega(x - x_{c.g})]. \qquad \text{(XIII-1-14)}$$

Harmonic oscillation normal to the body's longitudinal axis (Fig. XIII-1-2b). In this case, the motion is characterized by a transverse velocity component

$$W(t) = W_0 \exp(i\omega t), \qquad \text{(XIII-1-15)}$$

where W_0 is the normal velocity of the oscillatory motion at time $t = 0$.

Consequently, Condition (XIII-1-10) is written

$$\frac{\partial \varphi_2'}{\partial r} = -W_0 \exp(i\omega t)\cos\gamma. \qquad \text{(XIII-1-16)}$$

Steady rotation of the body about its center of gravity (Fig. XIII-1-2c). The velocity component at a certain point on the surface of the body, which has a constant attack angle α_0 in this case, is determined by the expression

$$W(x) = \alpha_0 V_\infty + \Omega_z (x - x_{c.g}), \qquad \text{(XIII-1-17)}$$

where Ω_z is the angular velocity of rotation. The boundary condition will be

$$\frac{\partial \varphi_2'}{\partial r} = -[\alpha_0 V_\infty + \Omega_z (x - x_{c.g})]\cos\gamma. \qquad \text{(XIII-1-18)}$$

The boundary conditions serve for determination of the source-distribution law, i.e., the form of $f(\varepsilon)$. In the case of a very

slender body, the form of this function can be found as follows. First, Expression (XIII-1-9) is transformed to the variable z = = arc cosh [(x - ε)/α'r)] and the partial derivative ϕ'_{2r} is calculated. Then the expression obtained for this derivative is converted back to the variable ε = x - α'r cosh z, and the limit transition with r → 0 is made. The above boundary conditions are attached to the resulting limit relationship. Then the limiting value of the partial derivative ϕ'_{2r}, which is studied in slender-body theory for the case of nonsteady flow, will be

$$\frac{\partial \varphi'_2}{\partial r} = -\frac{\pi f(x)}{S(x)} \exp(i\omega t) \cos\gamma, \qquad \text{(XIII-1-19)}$$

where S(x) = πr^2 is the cross-sectional area at a distance x from the tip of the body.

Determination of the aerodynamic coefficients. The expression for the potential function and the boundary condition must be supplemented with relationships that determine the aerodynamic coefficients in general form. One of these relationships is Formula (XI-1-21) for the added pressure coefficient that appears as a result of nonsteady transverse flow. Substituting the expression for this coefficient according to (XI-1-21) for $\bar{p}_2$ into the integrand in (XI-3-1), we obtain for the normal-force coefficient /543

$$c_{Np} = -\frac{\pi}{S_{\text{mid}}} \int_0^{x_b} \frac{\bar{p}'_2}{\cos\gamma} r\, dx, \qquad \text{(XIII-1-20)}$$

where

$$\bar{p}'_2 = -2(q'_{2x} + q'_{2t}). \qquad \text{(XIII-1-21)}$$

Let us now examine the relationship that defines the moment coefficient about an axis passing through the center of gravity. To do so, we shall use Formula (I-5-8), which we transform to

$$m_{zp} = c_{Np} \frac{x_{c.g}}{x_b} + \frac{\pi}{S_{\text{mid}}\, x_b} \int_0^{x_b} \frac{\bar{p}'_2}{\cos\gamma} r x\, dx. \qquad \text{(XIII-1-22)}$$

As follows from (I-3-14) and (XI-1-21), the expression for the axial-force coefficient is the same as for the case of steady flow.

Aerodynamic Coefficients under the Conditions of Low-Frequency Oscillations

General expression for the potential function. Solution of the problem of determining aerodynamic characteristics for nonsteady supersonic flow around a solid of revolution is simplified if low-frequency oscillations correspond to this flow in the uninverted motion. If (XIII-1-9) is presented as a series in powers of the parameter $k = M_\infty \omega r/(\alpha' V_\infty)$, which is known as the reduced harmonic frequency, we can satisfy ourselves that for frequencies of the order of $a_\infty \alpha'/x_b$, the nonsteady-flow potential can be represented with sufficient accuracy in the form of a linear function of the parameter k. Transforming to the variable $z = \operatorname{arc\,cosh}[(x - \bar{e})/(\alpha' r)]$, in this relationship, we find in first approximation

$$\varphi_2' = \cos\gamma \exp(i\omega t)\left[\alpha' \int_0^{\operatorname{arch} u} \dot{f}(x - \alpha' r \operatorname{ch} z) \operatorname{ch} z\, dz - \right.$$
$$\left. - iM_\infty \alpha' k \int_0^{\operatorname{arch} u} \dot{f}(x - \alpha' r \operatorname{ch} z)\, dz\right]. \qquad \text{(XIII-1-23)}$$

We now calculate the derivatives of φ_2' with respect to x and t, which are needed for determination of the pressure coefficient. Setting $\dot{f} = m$, we obtain

$$\varphi_{2x}' = \alpha' \cos\gamma \exp(i\omega t)\left[\int_0^{\operatorname{arch} u} \dot{m}(x - \alpha' r \operatorname{ch} z) \operatorname{ch} z\, dz - \right.$$
$$\left. - iM_\infty k \int_0^{\operatorname{arch} u} \dot{m}(x - \alpha' r \operatorname{ch} z)\, dz\right]; \qquad \text{(XIII-1-24)}$$

$$\varphi_{2t}' = \alpha' i\omega \cos\gamma \exp(i\omega t)\left[\int_0^{\operatorname{arch} u} m(x - \alpha' r \operatorname{ch} z) \operatorname{ch} z\, dz - \right.$$
$$\left. - iM_\infty k \int_0^{\operatorname{arch} u} m(x - \alpha' r \operatorname{ch} z)\, dz\right]. \qquad \text{(XIII-1-25)}$$

The form of the functions $\dot{m}$ and m is determined from Condition (XIII-1-19) and the boundary conditions for each specific case of motion of the body. /544

Harmonic oscillatory motion of the body about its center of gravity. In this case, the form of the functions m and $\dot{m}$ can be determined as follows. First we find the function

$$f(\varepsilon) = \frac{S(\varepsilon)}{\pi} \alpha_0 [V_\infty + i\omega(\varepsilon - x_{c.g})] \qquad \text{(XIII-1-26)}$$

from Expressions (XIII-1-14) and (XIII-1-19).

Then, calculating the first and second derivatives,

$$m(\varepsilon) = \frac{S'(\varepsilon)}{\pi} \alpha_0 [V_\infty + i\omega(\varepsilon - x_{c.g})] + \frac{S(\varepsilon)}{\pi} i\omega\alpha_0; \qquad \text{(XIII-1-27)}$$

$$\dot{m}(\varepsilon) = \frac{S''(\varepsilon)}{\pi} \alpha_0 [V_\infty + i\omega(\varepsilon - x_{c.g})] + \frac{2S'(\varepsilon)}{\pi} i\omega\alpha_0. \qquad \text{(XIII-1-28)}$$

We introduce these expressions into (XIII-1-24) and (XIII-1-25) after first transforming to the variable z = arc cosh [(x - ε)/ /(α'r)]. Then, calculating the integrals and applying (XI-1-21), we obtain

$$\bar{p}_2' = \frac{2\alpha' \cos\gamma}{\pi} \left[\left(\alpha - \frac{\dot{\alpha} x_{c.g}}{V_\infty} \right) \frac{\partial Q_1}{\partial x} + \frac{\dot{\alpha}}{V_\infty} \left(\frac{\partial Q_2}{\partial x} + 2Q_1 \right) - \frac{\dot{\alpha} M_\infty^2 r}{V_\infty \alpha'} \frac{\partial Q_3}{\partial x} \right], \qquad \text{(XIII-1-29)}$$

where

$$Q_1 = \int_{\operatorname{arch} u}^{0} S'(x - \alpha' r \operatorname{ch} z) \operatorname{ch} z \, dz; \qquad \text{(XIII-1-30)}$$

$$Q_2 = \int_{\operatorname{arch} u}^{0} S'(x - \alpha' r \operatorname{ch} z)(x - \alpha' r \operatorname{ch} z) \operatorname{ch} z \, dz; \qquad \text{(XIII-1-31)}$$

$$Q_3 = \int_{\operatorname{arch} u}^{0} S'(x - \alpha' r \operatorname{ch} z) \, dz. \qquad \text{(XIII-1-32)}$$

Introducing $\bar{p}_2'$ from (XIII-1-29) into (XIII-1-19) and (XIII-1-22) and then calculating the derivatives

$$c_{Np}^{\dot{\alpha}} = \frac{V_\infty}{x_b} \frac{\partial c_{Np}}{\partial \dot{\alpha}}; \quad m_{zp}^{\dot{\alpha}} = \frac{V_\infty}{x_b} \frac{\partial m_{zp}}{\partial \dot{\alpha}}, \qquad \text{(XIII-1-33)}$$

we obtain

$$c_{Np}^{\dot{\alpha}} = -\frac{2\alpha'}{S_{\text{mid}} x_b} \int_0^{x_b} \left[2 \left(Q_1 + \frac{1}{2} \frac{\partial Q_2}{\partial x} \right) - \frac{M_\infty r}{\alpha'} \frac{\partial Q_3}{\partial x} - x_{c.g} \frac{\partial Q_1}{\partial x} \right] r \, dx; \qquad \text{(XIII-1-34)}$$

$$m_{zp}^{\dot{\alpha}} = \frac{x_{c.g}}{x_b} c_{Np}^{\dot{\alpha}} + \frac{2\alpha'}{S_{mid}\, x_b^2} \int_0^{x_b} \left[2\left(Q_1 + \frac{1}{2}\frac{\partial Q_2}{\partial x}\right) - \frac{M_\infty^2 r}{\alpha'}\frac{\partial Q_3}{\partial x} - x_{c.g}\frac{\partial Q_1}{\partial x} \right] rx\, dx. \quad \text{(XIII-1-35)}$$

The stability derivatives of very slender bodies can be obtained from the above expressions if the appropriate values from slender-body aerodynamics are substituted for the functions Q_n. To find these values, it is necessary to convert to the variable $\varepsilon = x - \alpha' r \cosh z$ in Expressions (XIII-1-30)-(XIII-1-32) and then make the limit transition with $r \to 0$. On substituting the values thus found for the function Q_n into (XIII-1-34) and (XIII-1-35), we obtain

/545

$$c_{Np}^{\dot{\alpha}} = 2\bar{S}_{bse}\left(1 - \frac{x_{c.g}}{x_b} + \frac{W_b}{x_b \bar{S}_{bse}}\right); \quad \text{(XIII-1-36)}$$

$$m_{zp}^{\dot{\alpha}} = -2\bar{S}_{bse}\left(1 - \frac{x_{c.g}}{x_b}\right)^2. \quad \text{(XIII-1-37)}$$

Harmonic oscillations in the direction normal to the body's longitudinal axis. For this type of motion, the function $f(\varepsilon)$ is defined as follows in accordance with (XIII-1-16) and (XIII-1-19):

$$f(\varepsilon) = \frac{S(\varepsilon)}{\pi} W_0, \quad \text{(XIII-1-38)}$$

and the function $\underline{m}$ and its derivative $\dot{m}$ take the form

$$m = \frac{S'(\varepsilon)}{\pi} W_0; \quad \dot{m} = \frac{S''(\varepsilon)}{\pi} W_0. \quad \text{(XIII-1-39)}$$

Converting to the variable $\underline{z}$ and substituting the functions $\underline{m}$ and $\dot{m}$ found from (XIII-1-39) into Formulas (XIII-1-24) and (XIII-1-25), we obtain the corresponding values of ϕ'_{2x} and ϕ'_{2t} and then, using (XIII-1-21), the pressure coefficient. Introducing the values of this coefficient into (XIII-1-20) and (XIII-1-22) and differentiating, we obtain the stability derivatives

$$c_{Np}^{\dot{w}} = -\frac{2\alpha'}{S_{mid}\, x_b} \int_0^{x_b} \left(Q_1 - \frac{M_\infty^2 r}{\alpha'}\frac{\partial Q_3}{\partial x}\right) r\, dx; \quad \text{(XIII-1-40)}$$

$$\dot{m}^{w}_{zp} = \frac{x_{c.g}}{x_b}\dot{c}^{w}_{Np} + \frac{2\alpha'}{S_{mid}\,x_b^2}\int_0^{x_b}\left(Q_1 - \frac{M_\infty^2 r}{\alpha'}\frac{\partial Q_3}{\partial x}\right) r x\,dx, \qquad \text{(XIII-1-41)}$$

where

$$\left.\begin{aligned} \dot{c}^{w}_{Np} &= \frac{V_\infty^2}{x_b}\frac{\partial c_{Np}}{\partial \dot{W}}; \quad \dot{m}^{w}_{zp} = \frac{V_\infty^2}{x_b}\frac{\partial m_{zp}}{\partial \dot{W}}; \\ \dot{W} &= \frac{\partial W}{\partial t}. \end{aligned}\right\} \qquad \text{(XIII-1-42)}$$

The relationships for the stability derivatives derived from the aerodynamic theory of the slender body take the form

$$\dot{c}^{w}_{Np} = \frac{2W_b}{S_{mid}\,x_b}; \qquad \text{(XIII-1-43)}$$

$$\dot{m}^{w}_{zp} = 2\bar{S}_{bse}\left[\frac{x_{c.g}W_b}{x_b S_{bse}\,x_b} - (x_b^2 S_{bse})^{-1}\int_0^{x_b} S(x)\,x\,dx\right]. \qquad \text{(XIII-1-44)}$$

Steady rotation about center of gravity. In this case, the function f(ε) is given by the equation

$$f(\varepsilon) = \frac{S(\varepsilon)}{\pi}[\alpha_0 V_\infty + \Omega_z(\varepsilon - x_{c.g})]. \qquad \text{(XIII-1-45)}$$

Differentiating this expression twice with respect to ε, we find

$$\ddot{f}(\varepsilon) = \dot{m} = \frac{S''(\varepsilon)}{\pi}[\alpha_0 V_\infty + \Omega_z(\varepsilon - x_{c.g})] + \frac{2S'(\varepsilon)}{\pi}\Omega_z. \qquad \text{XXIII-1-46)}$$

Converting in this formula to the variable $\underline{z}$ and substituting the expression found for $\dot{m}$ into (XI-3-2), we find ϕ'_{2x} and then the pressure coefficient

$$\bar{p}'_2 = -2\varphi'_{2x}/V_\infty.$$

With $\bar{p}'_2$, we can calculate the coefficients of normal force and moment due to the rotation and then their derivatives /546

$$c_{Np}^{\Omega_z} = -\frac{2\alpha'}{S_{\text{mid}}\, x_b}\int_0^{x_b}\left(Q_1 + \frac{\partial Q_2}{\partial x} - x_{c.g}\,\frac{\partial Q_1}{\partial x}\right) r\,dx; \qquad \text{(XIII-1-47)}$$

$$m_{zp}^{\Omega_z} = \frac{x_{c.g}}{x_b}\, c_{Np}^{\Omega_z} + \frac{2\alpha'}{S_{\text{mid}}\, x_b^2}\int_0^{x_b}\left(Q_1 + \frac{\partial Q_2}{\partial x} - x_{c.g}\,\frac{\partial Q_1}{\partial x}\right) rx\,dx, \qquad \text{(XIII-1-48)}$$

where

$$c_{Np}^{\Omega_z} = \frac{V_\infty}{x_b}\,\frac{\partial c_{Np}}{\partial \Omega_z}; \quad m_{zp}^{\Omega_z} = \frac{V_\infty}{x_b}\,\frac{\partial m_{zp}}{\partial \Omega_z}. \qquad \text{(XIII-1-49)}$$

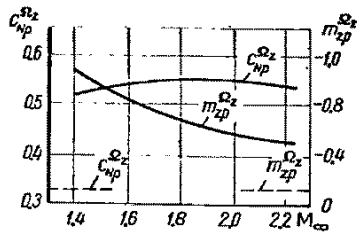

Figure XIII-1-3. Variation of Stability Derivatives of Solid of Revolution with M_∞ in Rotation at Constant Angular Velocity.

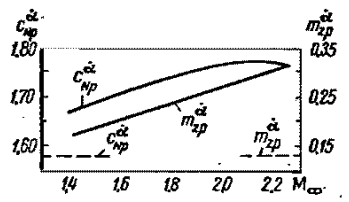

Figure XIII-1-4. Variation of Stability Derivatives of Solid of Revolution with M_∞ in Harmonic Oscillations About the Center of Gravity.

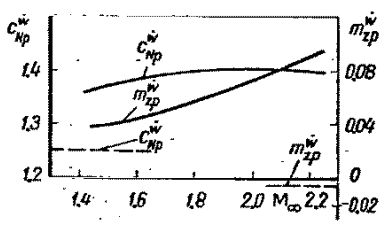

Figure XIII-1-5. Variation of Stability Derivatives of Solid of Revolution with M_∞ in Harmonic Oscillations Normal to the Longitudinal Axis.

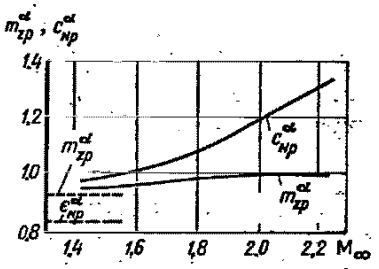

Figure XIII-1-6. Variation of Stability Derivatives of Solid of Revolution with M_∞ in Motion at Constant Angle of Attack.

The stability derivatives corresponding to slender-body aerodynamic theory take the form

$$c_{Np}^{\Omega_z} = 2\bar{S}_{\text{bse}}\left(1 - \frac{x_{\text{c.g}}}{x_{\text{b}}}\right); \qquad \text{(XIII-1-50)}$$

$$m_{zp}^{\Omega_z} = -2\bar{S}_{\text{bse}}\left[\left(1 - \frac{x_{\text{c.g}}}{x_{\text{b}}}\right)^2 + \frac{x_{\text{c.g}} W_{\text{b}}}{S_{\text{bse}} x_{\text{b}}^2} - (x_{\text{b}}^2 S_{\text{bse}})^{-1} \int_0^{x_{\text{b}}} S(x)\, x\, dx\right]. \qquad \text{(XIII-1-51)}$$

Results of calculation of the stability derivatives by these formulas for a parabolic solid of revolution are presented in Figs. XIII-1-3 through XIII-1-5. The generatrix of this solid has the form $r = 0.02(10x - x^2)$, while the coordinate of the center of gravity reckoned from the coordinate origin $x_{c.g} = 5$. The dashed lines on these figures indicate results obtained from slender-body theory. For comparison, Fig. XIII-1-6 shows static stability derivatives calculated for the same body by the formulas of linearized theory /547

$$c_{Np}^{\alpha} = \frac{\partial c_{Np}}{\partial \alpha} = -\frac{2\alpha'}{S_{\text{mid}}} \int_0^{x_{\text{b}}} \frac{\partial Q_1}{\partial x}\, r\, dx; \qquad \text{(XIII-1-52)}$$

$$m_{zp}^{\alpha} = \frac{\partial m_{zp}}{\partial \alpha} = \frac{x_{\text{c.g}}}{x_{\text{b}}} c_{Np}^{\alpha} + \frac{2\alpha'}{x_{\text{b}} S_{\text{mid}}} \int_0^{x_{\text{b}}} \frac{\partial Q_1}{\partial x}\, rx\, dx, \qquad \text{(XIII-1-53)}$$

and by the formulas of slender-body aerodynamic theory (dashed lines):

$$c_{Np}^{\alpha} = 2\frac{S_{\text{bse}}}{S_{\text{mid}}}; \qquad \text{(XIII-1-54)}$$

$$m_{zp}^{\alpha} = 2\frac{S_{\text{bse}}}{S_{\text{mid}}}\left(\frac{x_{\text{c.g}}}{x_{\text{b}}} + \frac{W_{\text{b}}}{x_{\text{b}} S_{\text{bse}}} - 1\right). \qquad \text{(XIII-1-55)}$$

§XIII-2. APPLICATION OF THE NEWTON METHOD

Tapered Solid of Revolution

Let us consider the aerodynamic characteristics of a body in hypersonic translational motion when it also rotates at a certain angular velocity Ω_z about its center of gravity.

The pressure coefficient is determined by the general formula (IV-7-7) as the sum of two components, one of which is governed by the translational motion and the other by the damping that arises as a result of the rotation.

The first component $\bar{p}_V$ is given by Formula (X-3-1), and the second is, according to (IV-7-9), equal to

$$\bar{p}_\Omega = -\frac{4\Omega_z}{V_\infty}(r\,\mathrm{tg}\,\beta + x - x_{c.g})(\cos\alpha\sin\beta - \\ -\sin\alpha\cos\beta\cos\gamma)\cos\beta\cos\gamma + \frac{2\Omega_z^2}{V_\infty^2}\cos^2\gamma\cos^2\beta(r\,\mathrm{tg}\,\beta + x - x_{c.g})^2. \quad \text{(XIII-2-1)}$$

According to (I-3-14), the axial-force coefficient of a body in rotation about its center of gravity is

$$c_{Rp} = \frac{4\lambda_{mid}}{\pi}\int_0^{\bar{x}_b'}\bar{r}\,\mathrm{tg}\,\beta\,d\bar{x}\int_{\gamma_b}^{\pi}(\bar{p}_V + \bar{p}_\Omega)\,d\gamma, \quad \text{(XIII-2-2)}$$

where $\bar{x} = x/x_{mid}$.

This formula can be written

$$c_{Rp} = (c_{Rp})_{\Omega=0} + \int_0^{\bar{x}_b'}(c_{Rp})_\Omega'\,d\bar{x}, \quad \text{(XIII-2-3)}$$

where

$$(c_{Rp})_\Omega' = \frac{dc_{Rp}}{d\bar{x}} = \frac{4}{\pi}\lambda_{mid}\bar{r}\,\mathrm{tg}\,\beta\int_{\gamma_b}^{\pi}\bar{p}_\Omega\,d\gamma. \quad \text{(XIII-2-4)}$$

The axial-force coefficient $(c_{Rp})_{\Omega=0}$ in the absence of rotation is determined by (X-3-5). The second term in (XIII-2-3) depends on the angular velocity Ω_z and is, as we see, expressed as the integral of the local axial-force coefficient c_{Rp}'. If we are concerned with the case of low angular velocities, which is usually encountered in practice, the second term in (XIII-2-1) can be dropped; then

/548

$$(c_{Rp})_\Omega' = \frac{4\Omega_z\bar{r}\lambda_{mid}}{\pi V_\infty}\sin 2\beta\sin\alpha(r\,\mathrm{tg}\,\beta + x - x_{c.g})\times \\ \times[(\pi - \gamma_b) - \sin\gamma_b(\cos\gamma_b - 2\,\mathrm{tg}\,\beta\,\mathrm{ctg}\,\alpha)]. \quad \text{(XIII-2-4')}$$

Evaluation of the limits $\bar{x}_b'$ and λ_b, which are determined by the length and shape of the "shaded" zone, is set forth in §X-3.

The rotary derivative

$$\frac{\partial c_{Rp}}{\partial \Omega_z} = \frac{\partial (c_{Rp})'_{\Omega}}{\partial \Omega_z} = \int_0^{\bar{x}'_b} \frac{(c_{Rp})'_{\Omega}}{\Omega_z} d\bar{x}. \qquad \text{(XIII-2-5)}$$

In analogy with (XIII-2-3), we can write for the normal-force coefficient

$$c_{Np} = (c_{Np})_{\Omega=0} + \int_0^{\bar{x}'_b} (c_{Np})'_{\Omega} d\bar{x}, \qquad \text{(XIII-2-6)}$$

where $\bar{x} = x/x_{mid}$.

In this formula, $(c_{Np})_{\Omega=0}$ is determined from (X-3-36), keeping the minus sign, and

$$(c_{Np})'_{\Omega} = \frac{\partial c_{Np}}{\partial \bar{x}} = -\frac{4\lambda_{mid}}{\pi} \bar{r} \int_{\gamma_b}^{\pi} \bar{p}_{\Omega} \cos\gamma \, d\gamma. \qquad \text{(XIII-2-7)}$$

With the first term in Ω_z/V_∞ retained, Expression (XIII-2-1) for $\bar{p}_{\Omega}$ is substituted into the integrand to obtain

$$(c_{Np})'_{\Omega} = -\frac{4\Omega_z \bar{r} \lambda_{mid}}{\pi V_\infty} \sin 2\beta \cos\alpha (r \operatorname{tg}\beta + x - x_{c.g}) \times$$
$$\times \left\{ (\gamma_b - \pi) - \sin\gamma_b \left[\cos\gamma_b - \operatorname{tg}\alpha \operatorname{ctg}\beta \left(1 - \frac{1}{3}\sin^2\gamma\right)\right]\right\}. \qquad \text{(XIII-2-8)}$$

The rotational derivative

$$\frac{\partial c_{Np}}{\partial \Omega_z} = \frac{\partial (c_{Np})'_{\Omega}}{\partial \Omega_z} = \int_0^{\bar{x}'_b} \frac{(c_{Np})'_{\Omega}}{\Omega_z} d\bar{x}. \qquad \text{(XIII-2-9)}$$

Let us examine expressions for the total longitudinal moment coefficient of the body about its center of gravity and the corresponding rotary derivative. The moment coefficient

$$m_{zp} = \frac{M_z}{qS_{mid}\, x_b} = \frac{2\lambda_{mid}}{\pi \lambda_b} \int_0^{\bar{x}'_b} \int_{\gamma_b}^{\pi} \bar{p}\bar{r} (\bar{r} \operatorname{tg}\beta + 2\bar{x}\lambda_{mid} - 2\bar{x}_{c.g}\lambda_{mid}) \cos\gamma \, d\bar{x}\, d\gamma, \qquad \text{(XIII-2-10)}$$

where

$$\bar{x} = \frac{x}{x_{mid}}; \quad \bar{r} = \frac{r}{r_{mid}}; \quad \bar{x}_{c.g} = \frac{x_{c.g}}{x_{mid}}.$$

Or, applying (XIII-2-7), /549

$$m_{zp} = \frac{1}{2\lambda_b} \int_0^{\bar{x}'_b} (\bar{r} \operatorname{tg} \beta + 2\bar{x}\lambda_{mid} - 2\bar{x}_{c.g}\lambda_{mid}) [(c_{Np})_{\Omega=0} + (c'_{Np})_\Omega] d\bar{x}, \quad \text{(XIII-2-11)}$$

where, according to (X-3-36),

$$(c_{Np})_{\Omega=0} = \frac{dc_{Np}}{d\bar{x}} = -\frac{4\lambda_{mid}}{\pi} B(\gamma_b)\bar{r}, \quad \text{(XIII-2-12)}$$

and the derivative $(c_{Np})'_\Omega$ is given by (XIII-2-7).

The rotary derivative

$$\frac{\partial m_{zp}}{\partial \Omega_z} = \frac{1}{2\lambda_b} \int_0^{\bar{x}'_b} (\bar{r} \operatorname{tg} \beta + 2\bar{x}\lambda_{mid} - 2\bar{x}_{c.g}\lambda_{mid}) \frac{(c_{Np})'_\Omega}{\Omega_z} d\bar{x}. \quad \text{(XIII-2-13)}$$

For the cylindrical section of the body, we must set $\beta = 0$ and $\gamma_b = \pi/2$ in the above formulas. Accordingly, $(c_{Rp})'_\Omega = (c_{Np})'_\Omega = 0$.

At certain angles of attack smaller than the β_0 at the point, the "shaded" zone on a curvilinear nose section may be short, so that we can set $\bar{x}'_b = 1$ and $\gamma_c = 0$. Then

$$\frac{\partial c_{Rp}}{\partial \Omega_z} = \frac{2x_{mid}}{V_\infty} \sin\alpha \int_0^1 \sin 2\beta (\bar{r} \operatorname{tg} \beta + 2\bar{x}\lambda_{mid} - 2\bar{x}_{c.g}\lambda_{mid}) \bar{r}\, d\bar{x}; \quad \text{(XIII-2-14)}$$

$$\frac{\partial c_{Np}}{\partial \Omega_z} = \frac{2x_{mid}}{V_\infty} \cos\alpha \int_0^1 \sin 2\beta (\bar{r} \operatorname{tg} \beta + 2\bar{x}\lambda_{mid} - 2\bar{x}_{c.g}\lambda_{mid}) \bar{r}\, d\bar{x}; \quad \text{(XIII-2-15)}$$

$$\frac{\partial m_{zp}}{\partial \Omega_z} = \frac{2x_{mid}}{V_\infty} \cos\alpha \int_0^1 \sin 2\beta (\bar{r} \operatorname{tg} \beta + 2\bar{x}\lambda_{mid} - 2\bar{x}_{c.g}\lambda_{mid})^2 \bar{r}\, d\bar{x}. \quad \text{(XIII-2-16)}$$

If the angles $\alpha \geq \beta_0$, the influence of the "shaded" zone will be significant and it is necessary to use the more general relationships, in which the angle $\gamma_c = \arccos(\tan\beta/\tan\alpha)$. In the "shaded" zone, we can set the pressure coefficient $\bar{p}_e = 0$.

The formulas to be used in calculating the total aerodynamic coefficients are

$$c_{Rp} = (c_{Rp})_{\Omega=0} + \frac{\partial c_{Rp}}{\partial \Omega_z}\Omega_z;\ c_{Np} = (c_{Np})_{\Omega=0} + \frac{\partial c_{Np}}{\partial \Omega_z}\Omega_z;\ m_{zp} = (m_{zp})_{\Omega=0} + \frac{\partial m_{zp}}{\partial \Omega_z}\Omega_z. \quad \text{(XIII-2-17)}$$

In the last formula

$$(m_{zp})_{\Omega=0} = \frac{2}{\pi}\int_0^{\bar{x}_b'} (\bar{r}\,\mathrm{tg}\,\beta + 2\bar{x}\lambda_{mid} - 2\bar{x}_{c.g}\lambda_{mid})\,B(\gamma_b)\,\bar{r}\,d\bar{x}. \quad \text{(XIII-2-18)}$$

The center of pressure coefficient $c_{c.p} = m_{zp}/c_{Np}$ is determined from the values found for m_{zp} and c_{Np}.

Blunted Cone

The aerodynamic coefficients of a spherically blunted cone in rotation at angular velocity Ω_z should be calculated by Formulas (XIII-2-3, (XIII-2-6) and (XIII-2-11), in which the integrals are represented as sums of three integrals, each of which corresponds to one of the flow regions established in §XII-6. With consideration of the lengths of the flow regions, the first integral is evaluated in the range from 0 to x_a, the second from x_a to x_b, and the third from x_b to ℓ_b (see Fig. XII-6-1). /550

According (XIII-2-3), the total axial force coefficient

$$c_{Rp} = (c_{Rp})_{\Omega=0} + \Delta(c_{Rp})_{\Omega}, \quad \text{(XIII-2-19)}$$

where $(c_{Rp})_{\Omega=1}$ is calculated by (XII-6-4) and the additional coefficient $\Delta(c_{Rp})_{\Omega}$ due to the rotation by

$$\Delta(c_{Rp})_{\Omega} = B_1 - \bar{x}_{c.g}B_2, \quad \text{(XIII-2-20)}$$

where $\bar{x}_{c.g} = x_{c.g}/\ell_b$ is the relative coordinate of the center of gravity.

The coefficients

$$\left.\begin{aligned} B_1 &= -\frac{2\omega_z}{\bar{l}}\left(1-\frac{\gamma_b}{\pi}\right)b_1\sin\alpha+\frac{\omega_z}{\bar{l}}\frac{\operatorname{tg}\beta_c}{2}\bar{R}_b b_2\sin 2\alpha+\\ &+\frac{2\omega_z}{\bar{l}}\frac{\sin\gamma_b}{\pi}\cos\alpha\operatorname{tg}\beta_c(b_1+\bar{R}_b^3\cos\beta_c\sin^3\beta_c);\\ B_2 &= 2\omega_z\left(1-\frac{\gamma_b}{\pi}\right)b_3\sin\alpha\cos^2\beta_c+\frac{\omega_z}{2}b_2\sin 2\alpha+\\ &+\omega_z\frac{\sin\gamma_b}{\pi}\cos\alpha\sin 2\beta_c(b_3+\bar{R}_b^2\sin^2\beta_c). \end{aligned}\right\} \qquad \text{(XIII-2-21)}$$

Here $\omega_x = \Omega_z \ell_b/V_\infty$; $\bar{R}_b = R_b/r_{mid}$; $\bar{\ell} = \ell_b/\ell_b'$ (ℓ_b' is the length of the unblunted cone and R_b is the radius of the spherical nose);

$$\left.\begin{aligned} b_1 &= \frac{2}{3}-\bar{R}_b\cos\beta_c(1-\sin\beta_c)+\frac{1}{6}\bar{R}_b^3\cos^3\beta_c(2-3\sin\beta_c);\\ b_2 &= \frac{1}{2}\bar{R}_b^2\left[1-\frac{2}{\pi}\operatorname{arctg}\left(\frac{\operatorname{ctg}\gamma_b}{\cos\alpha}\right)\right];\\ b_3 &= 1-\frac{1}{2}\bar{R}_b^2\cos^2\beta_c. \end{aligned}\right\} \qquad \text{(XIII-2-22)}$$

The normal-force coefficient

$$c_{Np} = (c_{Np})_{\Omega=0} + \Delta(c_{Np})_\Omega, \qquad \text{(XIII-2-23)}$$

where $(c_{Np})_{\Omega=0}$ is found from (XII-6-9) in the absence of rotation.

The added component due to an angular velocity is

$$\Delta(c_{Np})_\Omega = A_1 - \bar{x}_{c.g}A_2, \qquad \text{(XIII-2-24)}$$

where

$$\left.\begin{aligned} A_1 &= \frac{2\omega_z}{\bar{l}}\left(1-\frac{\gamma_b}{\pi}\right)b_1\cos\alpha+\frac{\omega_z}{\bar{l}}\bar{R}_b b_2\operatorname{tg}\beta_c(1+\sin^2\alpha)+\\ &+\frac{2}{3}\frac{\omega_z}{\bar{l}}\frac{\sin\gamma_b}{\pi}\cos\alpha(4\operatorname{tg}\alpha\operatorname{ctg}\beta_c-\operatorname{ctg}\alpha\operatorname{tg}\beta_c)\times\\ &\times(b_1-b_4\bar{R}_b\sin\beta_c\cos\beta_c);\\ A_2 &= 2\omega_z\left(1-\frac{\gamma_B}{\pi}\right)b_3\cos\alpha\cos^2\beta_c+\omega_z b_2(1+\sin^2\alpha)+\\ &+\frac{2}{3}\omega_z\cos^2\beta_c\frac{\sin\gamma_c}{\pi}\cos\alpha(4\operatorname{tg}\alpha\operatorname{ctg}\beta_c-\operatorname{ctg}\alpha\operatorname{tg}\beta_c)(b_3-b_4); \end{aligned}\right\} \qquad \text{(XIII-2-25)}$$

$$b_4 = \frac{\bar{R}_b^2}{2}\frac{\sin^2\alpha(4+3\sin^2\beta_c)-\sin^2\beta_c}{\sin^2\alpha(4-3\sin^2\beta_c)-\sin^2\beta_c}. \qquad \text{(XIII-2-26)}$$

The total longitudinal moment coefficient about a center of gravity at coordinate $x_{c.g}$ is determined from the expression /551

$$m_{zp} = (m_{zp})_{\Omega=0} + \Delta(m_{zp})_{\Omega}, \qquad \text{(XIII-2-27)}$$

where $(m_{zp})_{\Omega=0}$ is calculated without consideration of damping by Formula (XII-6-14). It must be remembered in the calculation that the moment is being determined with respect to the point $x_{c.g}$. Accordingly, $(m_{zp})_{\Omega=0} = m_{zp} - c_{Np}\bar{x}_{c.g}$, where m_{zp} is found from (XII-6-16) and c_{Np} from (X-3-36). The damping component

$$\Delta(m_{zp})_{\Omega} = F - 2A_1\bar{x}_{c.g} + A_2\bar{x}^2_{c.g}, \qquad \text{(XIII-2-28)}$$

where A_1 and A_2 are given by Expressions (XIII-2-25). The parameter

$$F = \frac{\omega_z}{\bar{l}^2 b_3 \cos^2\beta_c}\left[2\cos\alpha\left(1 - \frac{\gamma_b}{\pi}\right)(b_1^2 + b_5) + b_2 b_3 \bar{R}_b^2 \sin^2\beta_c (1 + \sin^2\alpha) + \right.$$
$$\left. + \frac{2}{3}\frac{\sin\gamma_b}{\pi}(4\operatorname{tg}\alpha\operatorname{ctg}\beta_c - \operatorname{ctg}\alpha\operatorname{tg}\beta_c)(b_1^2 + b_5 - b_3 b_4 \bar{R}_b^2 \sin^2\beta_c \cos^2\beta_c)\right], \qquad \text{(XIII-2-29)}$$

where

$$b_5 = \frac{1}{18} - \frac{\bar{R}_b^2\cos^2\beta_c}{4} + \frac{2}{9}\bar{R}_b^3\cos^3\beta_c - \frac{1}{36}\bar{R}_b^6\cos^6\beta_c. \qquad \text{(XIII-2-30)}$$

In the absence of a "shaded" zone, when $\alpha \leq \beta_c$ the angle $\gamma_b = 0$ and, consequently, the parameters determining damping will be simpler:

$$B_1 = \frac{2\omega_z b_1}{\bar{l}}\sin\alpha; \quad B_2 = 2\omega_z b_3 \sin\alpha\cos^2\beta_c; \qquad \text{(XIII-2-31)}$$

$$A_1 = \frac{2\omega_z b_1}{\bar{l}}\cos\alpha; \quad A_2 = 2\omega_z b_3 \cos\alpha\cos^2\beta_c; \qquad \text{(XIII-2-32)}$$

$$F = \frac{2\omega_z}{\bar{l}^2}\frac{\cos\alpha}{\cos^2\beta_c}\frac{b_1^2 + b_5}{b_3}. \qquad \text{(XIII-2-33)}$$

For a sharp cone, the damping characteristics can be obtained for $\bar{R}_b = 0$, $\bar{l} = 1$:

$$\left.\begin{aligned} B_1 &= \frac{4\omega_z\sin\alpha}{3}\left[\left(1 - \frac{\gamma_b}{\pi}\right) + \frac{\sin\gamma_b}{\pi}\operatorname{tg}\beta_c\operatorname{ctg}\alpha\right]; \\ B_2 &= 2\omega_z\sin\alpha\cos^2\beta_c\left[\left(1 - \frac{\gamma_b}{\pi}\right) + \frac{\sin\gamma_b}{\pi}\operatorname{tg}\beta_c\operatorname{ctg}\alpha\right]; \end{aligned}\right\} \qquad \text{(XIII-2-34)}$$

$$A_1 = \frac{4\omega_z \cos\alpha}{3}\left[\left(1-\frac{\gamma_b}{\pi}\right)+\frac{\sin\gamma_b}{3\pi}(4\operatorname{tg}\alpha\operatorname{ctg}\beta_c-\operatorname{tg}\beta_c\operatorname{ctg}\alpha)\right];$$
$$A_2 = 2\omega_z\cos\alpha\cos^2\beta_c\left[\left(1-\frac{\gamma_b}{\pi}\right)+\frac{\sin\gamma_b}{\pi}(4\operatorname{tg}\alpha\operatorname{ctg}\beta_c-\operatorname{tg}\beta_c\operatorname{ctg}\alpha)\right]; \quad \text{(XIII-2-35)}$$

$$F = \frac{\omega_z\cos\alpha}{\cos^2\beta_c}\left[\left(1-\frac{\gamma_b}{\pi}\right)+\frac{\sin\gamma_b}{3\pi}(4\operatorname{tg}\alpha\operatorname{ctg}\beta_c-\operatorname{tg}\beta_c\operatorname{ctg}\alpha)\right]. \quad \text{(XIII-2-36)}$$

If $\alpha \leq \beta_c$, there is no "shaded" zone, the angle $\gamma_b = 0$ and, consequently,

$$B_1 = \frac{4}{3}\omega_z\sin\alpha; \quad B_2 = 2\omega_z\sin\alpha\cos^2\beta_c; \quad \text{(XIII-2-37)}$$

$$A_1 = \frac{4}{3}\omega_z\cos\alpha; \quad A_2 = 2\omega_z\cos\alpha\cos\beta_c; \quad \text{(XIII-2-38)}$$

$$F = \frac{\cos\alpha}{\cos^2\beta_c}\omega_z. \quad \text{(XIII-2-39)}$$

/552

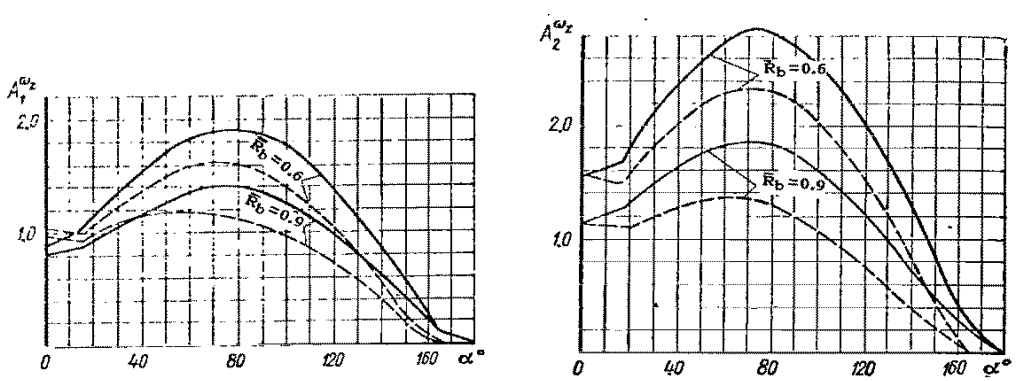

Figure XIII-2-1. Damping Parameters $\partial A_1/\partial\omega_z$ and $\partial A_2/\partial\omega_z$, Calculated by Newtonian Theory for a Spherically Blunted Nose ($\beta_c = 15°$). ———) cone with cylindrical tail section of length $0.334d_{mid}$; -----) without cylindrical section.

For a cylinder with a spherical nose, the coefficients $B_{1,2}$ and $A_{1,2}$ assume the form

$$B_1 = \frac{\omega_z}{4\lambda_b}\sin\alpha(1+\cos\alpha); \quad B_2 = \frac{1}{2}\omega_z\sin\alpha(1+\cos\alpha); \quad \text{(XIII-2-40)}$$

$$A_1 = \omega_z\left[\frac{1}{4\lambda_b}(1+\cos\alpha+\sin^2\alpha)+\frac{16}{3\pi}\lambda_b\sin\alpha\left(1-\frac{1}{4\lambda_b^2}\right)\right]; \quad \text{(XIII-2-41)}$$

$$A_2 = \omega_z\left[\frac{1}{2}(1+\cos\alpha+\sin^2\alpha)+\frac{16}{3\pi}\lambda_b\sin\alpha\left(1-\frac{1}{2\lambda_b}\right)\right]. \quad \text{(XIII-2-42)}$$

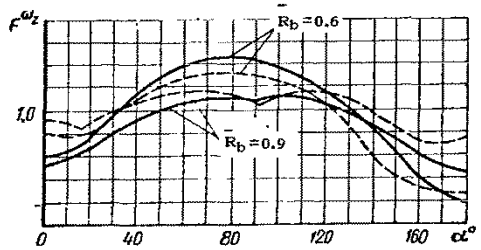

Figure XIII-2-2. Damping Parameter $\partial F/\partial\omega_z$, Calculated by Newtonian Theory for a Spherically Blunted Cone ($\beta_c = 16°$). ———) cone with cylindrical tail section of length $0.334d_{mid}$; -----) without cylindrical section.

Using these coefficients, we can determine the damping components by Formulas (XIII-2-20) and (XIII-2-24) for the axial- and normal-force coefficients. The damping-moment coefficient

$$\Delta(m_{zp})_\Omega = \omega_z\left\{\frac{1}{2}(1+\cos\alpha+\sin^2\alpha)\left(\frac{1}{2\lambda_b}-\bar{x}_{c.g}\right)^2+\right.$$
$$\left.+\frac{64}{3\pi}\lambda_b^2\sin\alpha\left[(1-\bar{x}_{c.g})^3-\left(\frac{1}{2\lambda_b}-\bar{x}_{c.g}\right)\right]\right\}. \qquad \text{(XIII-2-43)}$$

For circular onflow, when the attack angles reach $\alpha > 90°$, the influence of the base plane on damping must be taken into account by applying to $\Delta(m_{zp})_\Omega$ a correction

$$\Delta F = \omega_z\frac{\operatorname{tg}\beta_c}{\bar{l}}\cos\alpha. \qquad \text{(XIII-2-44)}$$

Results of calculations by these formulas are presented in Figs. XIII-2-1 and XIII-2-2. Figure XIII-2-1 shows values of the derivatives $\partial A_1/\partial\omega_z = A_1^{\omega_z}$; $\partial A_2/\partial\omega_z = A_2^{\omega_z}$ as functions of α, found for circular onflow onto a blunted cone with $\beta_c = 15°$ and $\bar{R}_b = 0.6$ and 0.9. In one of these cases, the cone has a cylindrical tail section of length $x_c = 0.334d_{mid}$. Figure XIII-2-2 presents calculated values of the derivative $dF/\partial\omega_z = F^{\omega_z}$ for the same conditions.

§XIII-3. ACTION OF ADDITIONAL FORCES DUE TO ROTATION OF BODY ABOUT LONGITUDINAL AXIS

/553

An additional lateral force ΔZ (the so-called Magnus force) appears when a body rotates about its longitudinal axis of symmetry; it can be calculated by the formula

$$\Delta Z = c_{\Delta z}qS_{mid}\omega_x, \qquad \text{(XIII-3-1)}$$

where

$$q = 0.5\rho_\infty V_\infty^2;\ \omega_x = \Omega_x d_{mid}/2V_\infty;\ c_{\Delta z} = (\partial c_{\Delta z}/\partial\alpha)\alpha;$$
$$\frac{\partial c_{\Delta z}}{\partial\alpha} = \frac{8\lambda^2}{\mathrm{Re}_l^{1/2}}(7.834-16.53\omega_x^2\lambda^2); \qquad \text{(XIII-3-2)}$$

$$\lambda = l/d_{mid},\ l = x_c + 0.5x_n,\ Re_l = V_\infty l/\nu_\infty. \qquad \text{(XIII-3-2)}$$
(Cont'd.)

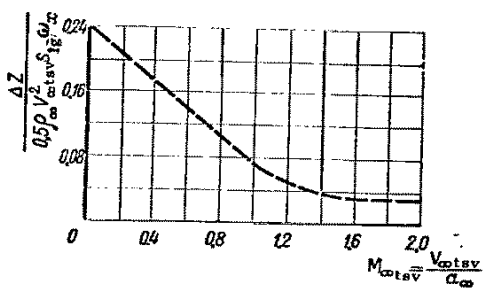

Figure XIII-3-1. Magnus Force at Large Body Attack Angles.

Formula (XIII-3-1) is derived for a cylindrical body with a flat base and is applicable for small attack angles $\alpha <$ 5-7° and flow conditions under which the boundary layer remains laminar.

The coordinate $(x_{c.p})_{\Delta z}$ of the point of application of the Magnus force, reckoned from the nose of the body, is calculated by the formula

$$\left(\frac{x_{c.p}}{l}\right)_{\Delta z} = \frac{x_b}{l} - 0.4 + 0.375\omega_x^2\lambda^2. \qquad \text{(XIII-3-3)}$$

The moment of this force with respect to the nose is $\Delta M = \Delta Z(x_{c.p})_{\Delta z}$. For a turbulent boundary layer, the Magnus effect increases by about 30-40%. This effect depends weakly on the shape of the nose, its degree of bluntness, and the presence of various annular projections or grooves on the body. At the same time, the tail section shape of the vehicle has substantial influence on ΔZ. For example, rounding the trailing edges at the base may change the Magnus force sharply and cause ΔZ to vary nonlinearly with attack angle α even at small values of this angle.

This nonlinearity becomes stronger with increasing attack angle. To take the effect into account, we can use the diagram in Fig. XIII-3-1, which gives experimental values of

$$\Delta Z/(0.5\rho_\infty V_{\infty\,tsv}^2 S_{lg}\omega_x)$$

as a function of

$$M_{\infty\,tsv} = V_{\infty\,tsv}/a_\infty = V_\infty \sin\alpha/a_\infty,$$

obtained for bodies with fineness ratios from 3 to 9. S_{lg} is the area of the body's longitudinal section. The data of Fig.

XIII-3-1 can be used to determine the Magnus force accurate to 10-20%.

Example. Determine the Magnus force and the moment of this force for an unfinned body in rotation about its longitudinal axis at an angular velocity Ω_x = 600 rad/s and in flight at an altitude of 5 km, M_∞ = 2, and at an angle of attack α = 5°. The geometrical dimensions of the body are as follows: x_c = 970 mm; /554
x_n = 560 mm; d_{mid} = 250 mm. The distance from the nose to the center of mass $x_{c.g}$ = 830 mm.

In accordance with these dimensions, the reference length $l = x_c + 0.5x_n = 970 + 0.5 \cdot 560 = 1250$ mm; the slenderness ratio $\lambda = l/d_{mid} = 1250/250 = 5$.

We find for an altitude of 5 km from the standard-atmosphere tables: $\rho_\infty = 0.07506$ kg·s^2/m^4; $\nu_\infty = 22.09 \cdot 10^{-6}$ m^2/s^2; $a_\infty = 320.4$ m/s.

The flight speed at this altitude is

$$V_\infty = M_\infty a_\infty = 2 \cdot 320.4 = 640.8 \text{ m/s},$$

and the Reynolds number

$$\mathrm{Re}_l = \frac{V_\infty l}{\nu_\infty} = \frac{640.8 \cdot 1.25}{22.09 \cdot 10^{-6}} = 0.36 \cdot 10^8.$$

According to (XIII-3-2)

$$\frac{\partial c_{\Delta z}}{\partial \alpha} = \frac{8 \cdot 5^2}{(0.36 \cdot 10^8)^{1/2}} \left[7.834 - 16.53 \left(\frac{600 \cdot 0.25}{2 \cdot 640.8}\right)^2 5^2\right] = 0.0721.$$

Since the velocity head

$$q = \rho_\infty V_\infty^2/2 = 0.07506 \cdot 640.8^2/2 = 1.54 \cdot 10^4 \text{ kg/m}^2,$$

and the midships-section area $S_{mid} = \pi d_{mid}^2/4 = \pi \cdot 0.25^2/4 = 0.0491$ m^2, then according to (XIII-3-1), the Magnus force is

$$\Delta Z = 0.0721 \left(\frac{5}{57.3}\right) 1.54 \cdot 10^4 \cdot 0.0491 \frac{600 \cdot 0.25}{2 \cdot 640.8} = 0.477 \text{ kg}.$$

We find from Formula (XIII-3-3)

$$\left(\frac{x_{c.p}}{l}\right)_{\Delta z}=\frac{1530}{1250}-0.4+0.375\left(\frac{600\cdot0.25}{2\cdot640.8}\right)^2 5^2=0.695.$$

The distance between the point of application of the Magnus force and the vehicle's center of mass is

$$\Delta x=\left(\frac{x_{c.p}}{l}\right)_{\Delta z} l-x_{c.g}=0.695\cdot1250-830=870-830=40\text{ mm}.$$

The moment of the Magnus force

$$\Delta M=\Delta Z\cdot\Delta x=0.477\cdot0.04=1.9\cdot10^{-2}\text{ kg-m}.$$

Let us assume that the attack angle is increased by 10° and that it is necessary to take the nonlinear effect into account. We find from Fig. XIII-3-1 for $M_{\infty tsv} = M_\infty \sin\alpha = 2\cdot\sin 10 = 0.347$

$$\Delta Z\Big/\left(\frac{1}{2}\rho_\infty V^2_{\infty tsv} S_{lg}\omega_x\right)=0.18.$$

For a vehicle with a conical nose section, the longitudinal-section area is

$$S_{lg}=\left(\frac{1}{2}x_n+x_C\right)d_{mid}=\left(\frac{1}{2}0.56+0.97\right)0.25=0.312\text{ m}^2.$$

From this longitudinal section and the transverse flow velocity $V_{\infty tsv} = M_{\infty tsv} a_\infty = 0.347\cdot320.4 = 111$ m/s, we calculate the Magnus force

$$\Delta Z=0.18\left[\frac{1}{2}0.07506\cdot111^2\cdot0.312\left(\frac{600\cdot0.25}{2\cdot111}\right)\right]=17.5\text{ kg}.$$

Chapter XIV

FRICTION AND HEAT TRANSFER AT HIGH VELOCITIES

§XIV-1. FRICTION AND HEAT TRANSFER ON THE BODY

Boundary layer around a solid of revolution. The equations for the boundary layer around a solid of revolution can be transformed to equations for the boundary layer of a plane two-dimensional gas flow [57]. The equations of motion and continuity for an axisymmetric laminar boundary layer (Fig. XIV-1-1) will be examined in the respective forms (III-2-12) and (III-2-21) for $\varepsilon = 1$ and the radius r set equal to its value r_0 for the body. Setting $\varepsilon = 1$ and $r = r_0$, we obtain the energy equation for an ideal gas with constant heat capacities from (III-2-45) in the form

$$c_p\left(V_x\frac{\partial T}{\partial x}+V_y\frac{\partial T}{\partial y}\right)=V_x\frac{\partial p}{\partial x}+\frac{\partial}{\partial y}\left(\lambda\frac{\partial T}{\partial y}\right)+\mu\left(\frac{\partial V_x}{\partial y}\right)^2. \qquad \text{(XIV-1-1)}$$

We shall use the transformation formulas proposed by Mangler [57]:

$$\bar{x}=\frac{c^2}{d^2}\int_0^x r_0^2\,dx;\quad \bar{y}=\frac{c}{d}r_0 y; \qquad \text{(XIV-1-2)}$$

$$\left.\begin{gathered}\bar{\psi}(\bar{x},\ \bar{y})=\frac{c}{d}\psi(x,\ y);\\ \bar{p}(\bar{x})=p(x);\ \bar{T}(\bar{x},\ \bar{y})=T(x,\ y);\ \bar{\rho}(\bar{x},\ \bar{y})=\rho(x,\ y);\\ \bar{\mu}(\bar{x},\ \bar{y})=\mu(x,\ y),\end{gathered}\right\} \qquad \text{(XIV-1-3)}$$

where d is a certain characteristic length and c is an arbitrary scale factor.

The velocity components are related to the stream function by

$$\rho r_0 V_x=\frac{\partial\psi}{\partial y};\ \rho r_0 V_y=-\frac{\partial\psi}{\partial x};\ \bar{\rho}\bar{V}_x=\frac{\partial\bar{\psi}}{\partial\bar{y}};\ \bar{\rho}\bar{V}_y=-\frac{\partial\bar{\psi}}{\partial\bar{x}}.$$

With the above transformation formulas, the equations of motion (III-2-12), continuity (III-2-21), and energy XIV-1-1) are transformed to the corresponding equations for a plane two-dimensional boundary layer along which the pressure distribution is

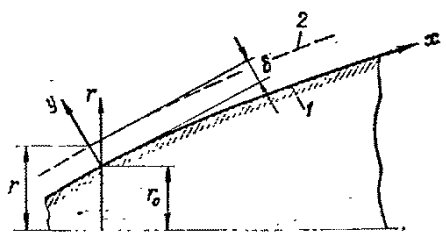

Figure XIV-1-1. Coordinate System for Mangler Transformation. 1) generatrix of body; 2) boundary of boundary layer.

subject to the condition $\bar{p}(\bar{x}) = p(x)$. The parameter $\bar{x}$ is related by Formula (XIV-1-2) to the arc length x of the solid-of-revolution generatrix. Obviously, the parameters of the gas on the outer boundaries of the boundary layer will have the same values at corresponding points of plane-parallel and axisymmetric flows.

Let us consider the relation between the frictional stresses. For plane-parallel flow, $\tau_{w1} = \mu_{w1}(\partial V_x/\partial y)_{w1}$, while for axisymmetric flow $\bar{\tau}_{w1} = \mu_{w1}\cdot(\partial V_x/\partial y)_{w1}$. Applying (XIV-1-2) for $\bar{y}$, we find the ratio $\tau_{w1}/\bar{\tau}_{w1} = (c/d)r_0$, in which c/d is determined from the first expression of (XIV-1-2). We obtain by substitution /556

$$\frac{\tau_{w1}}{\bar{\tau}_{w1}} = \left(\frac{\bar{x}r_0^2}{\int_0^{\bar{x}} r_0^2\,dx}\right)^{1/2}.$$

The $\bar{x}$-coordinate can be taken equal to the generatrix arc length x. If we convert to the axial coordinate x and write the generatrix equation in the form $r_0 = f(x)$, the arc length will be $\int_0^x \sqrt{1+(dr/dx)^2}\,dx$.

Consequently,

$$\frac{\tau_{w1}}{\bar{\tau}_{w1}} = \left[r_0^2\int_0^x \sqrt{1+\left(\frac{dr_0}{dx}\right)^2}\,dx\right]^{1/2}\left[\int_0^x r_0^2\sqrt{1+\left(\frac{dr_0}{dx}\right)^2}\,dx\right]^{-1/2}. \quad \text{(XIV-1-4)}$$

From the second relationship of (XIV-1-2), we obtain the relation between the boundary-layer thicknesses:

$$\frac{\delta}{\bar{\delta}} = \frac{\bar{\tau}_{w1}}{\tau_{w1}}. \quad \text{(XIV-1-4')}$$

To use these relationships, it is necessary to know the generatrix equation of the solid of revolution. If this equation is given in the form $r = ax^m$, the ratio $\tau_{wl}/\bar{\tau}_{wl}$ will be a function of the exponent m. On segments of the curvilinear surface far from the nose, where the pressure variation along the generatrix is negilgible, the flow in the boundary layer on a solid of revolution can be determined approximately from the flow in the boundary layer on a flat plate in uniform flow at zero angle of attack and the same gas-variable values as in inviscid flow around the body and at the same wall temperature.

For a fully turbulent boundary layer, the calculation can be made by the formulas

$$\frac{\tau_{wl}}{\bar{\tau}_{wl}} = (1+2m)^{1/5}; \quad \frac{\delta}{\bar{\delta}} = (1+2m)^{-1/5}. \qquad \text{(XIV-1-4")}$$

A relationship can be obtained [41] on the basis of (XIV-1-4) for the friction drag of a solid of revolution of arbitrary shape:

$$\frac{X_f}{(X_f)_{pl}} = \left(\int_0^{x_b} \frac{r_0}{x_b}\,dx\right)^{-1} \left(\int_0^{x_b} \frac{r_0^2}{x_b}\,dx\right)^{1/2}. \qquad \text{(XIV-1-5)}$$

where x is the arc length measured along the meridional contour and x_b is the length of the solid of revolution.

The friction drag is

$$(X_f)_{pl} = c_{xf} q S_{sde},$$

where c_{xf} is the average value of the coefficient of friction for a flat plate of length x_b and S_{sde} is the side (wetted) area of the body.

For turbulent flow, the Mangler transformation gives an expression for the frictional drag [41]: /557

$$\frac{X_f}{(X_f)_{pl}} = \left(\int_0^{x_b} \frac{r_0}{x_b}\,dx\right)^{-1} \left[\int_0^{x_b} (r_0^{5/4}/x_b)\,dx\right]^{4/5}. \qquad \text{(XIV-1-5')}$$

Cone. For a cone, the exponent m = 1; $dr_0/dx = \tan \beta_c$; $r_0 = x \tan \beta_c$, and, consequently, in the case of a laminar boundary layer

$$\tau_{wl}^{c} = \sqrt{3}\tau_{wl}^{pl}; \qquad \text{(XIV-1-6)}$$

$$\delta^{c} = \frac{\delta^{pl}}{\sqrt{3}}. \qquad \text{(XIV-1-6')}$$

Thus, the surface friction at corresponding points on the cone is larger by a factor $\sqrt{3}$ and the boundary-layer thickness smaller by a factor $\sqrt{3}$ than on the flat plate.

A formula analogous to (XIV-1-6) is used to determine the local c_{fx}^{c} and average c_{xf}^{c} values of the friction coefficients

$$c_{fx}^{c} = \sqrt{3}c_{fx}^{pl}; \quad c_{xf}^{c} = \sqrt{3}c_{xf}^{pl}, \qquad \text{(XIV-1-7)}$$

which pertain to the velocity head of the disturbed stream $q_b = \rho_b V_b^2/2$. If we convert to the free-flow velocity head $q_\infty = \rho_\infty V_\infty^2/2$, then a multiplier $\rho_b V_b^2/\rho_\infty V_\infty^2$ appears in Formulas (XIV-1-7).

In the case of a completely turbulent boundary layer on the cone

$$\left.\begin{aligned} \tau_{wl}^{c} &= \sqrt[5]{3}\tau_{wl}^{pl}; \\ c_{fx}^{c} &= \sqrt[5]{3}c_{fx}^{pl}; \end{aligned}\right\} \qquad \text{(XIV-1-8)}$$

$$\delta^{c} = \frac{\delta^{pl}}{\sqrt[5]{3}}. \qquad \text{(XIV-1-9)}$$

The formula for determination of the average friction-drag coefficient, which is calculated for the midships-section area of the cone, is

$$c_{xf}^{c} = \frac{X_f}{qS_{mid}} = \frac{2\tan\beta_c}{r_{mid}^2}\int_0^{x_c} c_{fx}^{c} x\,dx = \frac{2}{\tan\beta_c}\int_0^1 c_{fx}^{c}\bar{x}\,d\bar{x}, \qquad \text{(XIV-1-10)}$$

where $\bar{x} = x/x_c$ and the x-coordinate is reckoned along an axis that coincides with the axis of the cone. The coefficient c_{fx}^{c} depends on Reynolds number, which is determined for a length reckoned along the generatrix. Substituting the value of c_{fx}^{c} into the integrand, we obtain

$$c_{xf}^{c} = \frac{2}{\operatorname{tg}\beta_c}\frac{q_c}{q} C\,\mathrm{Re}^{n}\frac{A}{n+2}, \qquad \text{(XIV-1-11)}$$

where ℓ is the length of the cone generatrix and the values of C and n are determined from Table VI-1-1. The coefficient A is $\sqrt{3}$ for a laminar boundary layer and A = $\sqrt[5]{3}$ for a turbulent boundary layer.

Cylinder. For a cylindrical body, m = 0, so that

$$\tau_{w1}^{c} = \tau_{w1}^{pl}; \quad \delta^{c} = \delta^{w1}.$$

Thus, if we assume that the "inviscid" parameters remain constant on a cylinder, the frictional stress and boundary-layer thicknesses will be the same as on a flat plate with the same wall temperature and "inviscid" parameters as on the cylinder. The result obtained applies to both laminar and turbulent boundary layers. /558

Heat transfer. Heat transfer on a cone is calculated by Formula (IV-8-41'), in which the coefficient of friction is replaced by its values for a cone. The local and average Stanton numbers will be determined by the respective relationships

$$St_x = \frac{A}{2} c_{fx}^{pl} (Pr)^{-2/3}; \quad St = \frac{A}{2} c_{xf}^{pl} (Pr)^{-2/3}. \qquad (XIV-1-12)$$

The heat-transfer coefficients α_x and α are calculated on the basis of Formulas (IV-8-40').

Method of determining enthalpy. To take account of the influence of high temperatures, it is necessary to convert the above formulas to determining parameters.

The local coefficient of laminar friction calculated from these parameters for the cone is

$$c_{fx} = 1.15 \sqrt{\frac{c}{Re_x}}, \qquad (XIV-1-13)$$

where $c = \rho^* \mu^* / \rho_c \mu_c$, $Re_x = V_c \rho_c x / \mu_c$ are calculated from the free-stream parameters on a cone (the subscript c corresponds to the subscript δ).

The Stanton number

$$St_x^* = \frac{q_{w1}}{\rho_c V_c (i_r - i_{w1})} = d \sqrt{\frac{c}{Re_x}}, \qquad (XIV-1-14)$$

where d can be calculated by one of the formulas

$$d = 0.575\,(\mathrm{Pr}^*)^{-2/3} \text{ or } d = 0.251\,(1.3 + \mathrm{Pr}^*)/\mathrm{Pr}^*.$$

The Nusselt number, which can be calculated from the determining parameters, is

$$\frac{\mathrm{Nu}_x^*}{\sqrt{\mathrm{Re}_x}} = \frac{q_{w1} c_{pc} x}{\lambda_c (i_r - i_{w1})} = d\sqrt{c}\,\mathrm{Pr}^*. \qquad \text{(XIV-1-15)}$$

Turbulent friction and heat transfer can be calculated similarly. The "seventh-root law" is used here.

Studies have shown (V.M. Iyevlev) that satisfactory results for the local coefficient of friction and the specific heat flow are obtained from Formulas (VI-1-37) and (VI-2-8), respectively, in which the parameter

$$z = 0.54\,\mathrm{Re}_x. \qquad \text{(XIV-1-16)}$$

When the equilibrium radiation temperature is established preferentially, friction and heat transfer on a cone are calculated by successive approximations. In illustrating the procedure, we bear in mind that the gas is dissociated in the boundary layer. This calculation begins with determination of the parameters of ideal flow around a cone, i.e., the pressure p_c, density ρ_c, enthalpy i_c, and velocity V_c. Then approximate values are assigned to the Prandtl number, $\mathrm{Pr}^* = 0.71$, and to the enthalpy of a heat-insulated wall, $i_{w1} = i_c + 0.5\sqrt{\mathrm{Pr}^*}V_c^2$ and Formula (IV-8-7) is used to calculate the determining enthalpy i^*. The determining temperature T^* is found from tables or diagrams of the thermodynamic functions for this enthalpy and the pressure p_c. Then the equation of state is used to find the density $\rho^* = p_c \mu_{av}^*/(R_0 T^*)$, with the average molecular weight μ_{av}^* calculated from the values of T^* and p_c.

The viscosity is calculated to supplement these parameters, and then the Stanton number is calculated in first approximation from (XIV-1-12) and used to find the specific heat flow

$$q_{w1} = \mathrm{St}_x^* \rho_c V_c (i_r - i_{w1}),$$

where

/559

$$i_{w1} = f(T_{w1}, p); \quad q_{w1} = \varepsilon\sigma T_{w1}^4.$$

Then the equilibrium radiation temperature $T_{w1} = T_e$ is determined in second approximation by solving the equation $q_{w1} = \varepsilon\sigma T_{w1}^4$. The temperature found can be used to continue the calculations and improve Pr*, St*, and $T_{w1} = T_e$. The calculations are similar for a turbulent boundary layer.

When there is no dissociation, the equilibrium radiation temperature can be determined by solving the equation

$$St_x^* \rho_c V_c (c_p)_{w1} (T_r - T_{w1}) = \varepsilon\sigma T_{w1}^4.$$

In performing the calculations, it is necessary to evaluate the length of the laminar boundary layer by determining the critical Reynolds number. Research has shown (for particulars, see §XIV-3) that the critical Reynolds number is determined, apart from the local $M_\delta = M_c$, also by the relative wall temperature T_{w1}/T_r (Fig.XIV-3-4) and that there is approximate proportionality between Re_{cr} and T_{w1}/T_r (See Fig. XIV-3-4). Cooling of the wall increases the length of the boundary layer. The critical Reynolds number for the case of equilibrium radiation temperature is calculated by successive approximations. Analysis indicates that the equilibrium radiation temperature depends on the flow regime in the boundary layer and the coordinate of the point on the washed surface, increasing with the approach to the tip.

Transition to a turbulent boundary layer also tends to increase wall temperature, which may be so high that the skin material is damaged. The emissivity of the surface can be increased to cool the wall. However, it is not possible to provide emissivities greater than 0.8 in practice. It is therefore necessary to cool the inner surface of the wall or to protect the skin with insulation. If necessary, both measures are taken.

Let us assume that with internal cooling of a wall at $T_{w1} = T_e = 1500°K$, the heat flow taken off is $q_{cs} = 30$ kcal/m^2·s, the heat-transfer coefficient at the particular point on the surface $\alpha_{cs} = 2.56 \cdot 10^{-2}$ kcal/m^2·s·deg, and that the recovery temperature at that point is $T_r = 4400°K$. We find from these data $q_{cs}^*/(\alpha_{cs} T_r) = 0.27$ and a reduced temperature $T_r' = 3200°K$. According to

(VI-4-2), the equilibrium wall temperature $T_{w1} = T_e = 1380°K$, i.e., cooling has lowered the temperature by 120°.

From the value found for T_{w1}, we determine the outer and inner skin temperatures with Formula (VI-4-4).

§XIV-2. INFLUENCE OF VISCOSITY ON DRAG. WAKE DRAG

Influence of Viscous Interaction on Flow Variables

To calculate "inviscid" parameters with consideration of the boundary layer, it is necessary to find the law of variation of displacement thickness over the length of the body and introduce a correction into the generatrix equation. For this purpose, we can use the results from supersonic boundary-layer theory for a flat plate and a cone, which is based on use of the determining parameters. /560

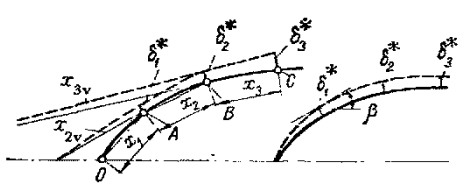

Figure XIV-2-1. Diagram Illustrating Calculation of Conventional Displacement Thickness.

Setting $\rho = \rho_\delta$ in (III-2-43) and substituting for V_x/V_δ in accordance with Eqs. (VI-1-1), we obtain the expression $\delta^*_{is.l} = 3\delta/8$ for the displacement thickness of a laminar layer and $\delta_{ic.t} = \delta/8$ for a turbulent layer. Introducing the appropriate formulas for the thicknesses into these expressions, we obtain

$$\delta^*_{ic} = B\left(\frac{\mu_\delta}{V_\delta \rho_\delta}\right)^n x^m, \qquad \text{(XIV-2-1)}$$

where B = 1.74, n = m = 1/2 for a laminar layer and B = 0.046; n = 1/5; m = 4/5 for a turbulent layer. Converting to the determining parameters, we find

$$\delta^*_{pl} = \delta^*_{ic}\left(\frac{\mu^*}{\mu_\delta}\right)^n \left(\frac{\rho_\delta}{\rho^*}\right)^n. \qquad \text{(XIV-2-2)}$$

If we are concerned with a cone in supersonic viscous flow, the displacement thicknesses can be calculated by the formula

$$\delta^*_c = A^{-1}\delta^*_{pl}, \qquad \text{(XIV-2-3)}$$

in which A = $\sqrt{3}$ for a laminar boundary layer and A = $\sqrt[5]{3}$ for a turbulent one.

Accordingly, the current radial coordinate of the generatrix of the virtual body $r^V = r + \delta_c^* \cos \beta_c$. The conventional thickness that appears here is

$$\delta_c^* = \bar{A} P^n x^m, \qquad \text{(XIV-2-4)}$$

where

$$P = \frac{\mu^*}{\mu_\delta} \frac{\rho_\delta}{\rho^*} \frac{\mu_\delta}{\rho_\delta V_\delta}. \qquad \text{(XIV-2-5)}$$

For a laminar layer, $\bar{A}$ = 1.02, for a turbulent layer $\bar{A}$ = = 0.037. In this formula, the x-coordinate is distance from the tip along the generatrix of the cone to an arbitrary cross section of the boundary layer and is equal to x = r/sin β_c. The virtual body differs from the cone and has a curvilinear generatrix. To simplify the calculation, however, we can keep the surface conical. Here we proceed from a certain average increment $\Delta\beta$ of the virtual-cone angle, calculated by the formula $\Delta\beta = \delta_b^*/L$. In this formula, the conventional thickness δ_b^* is determined from Expression (XIV-2-4) for x_b = L, i.e., for the base section of the boundary layer. Thus, the angle of the virtual cone is β_c^V = = $\beta_c + \Delta\beta$. It is for this angle that all calculations are made to determine the inviscid parameters on the cone.

Let us now consider a solid of revolution of arbitrary shape. Assuming that the nose of the body is a short conical element (Fig. XIV-2-1), we find the displacement thickness at the end of it:

$$\delta_1^* = \bar{A} P_1^n x_1^m, \qquad \text{(XIV-2-4')}$$

where P_1 is calculated from Expression (XIV-2-5) for the parameters on the conical nose.

We substitute a truncated cone with generatrix length x_2 for the next short segment of the curvilinear surface and assume that it is an extension of the virtual conical body with generatrix length x_{2V}. At the end of this virtual cone, the conventional thickness is δ_1^* and is calculated by (XIV-2-4'). Thus we have for the virtual cone the expression $\delta_1^* = \bar{A} P_2^n x_{2V}^m$, from which we find the length x_{2V} of its generatrix. Here the function P_2 is calculated for the parameters on the second section. Now that we

/561

know the generatrix length $x_{2_v} + x_2$ of the virtual cone with consideration of the second-section length, we can make an approximate calculation of the displacement thickness at point B on the surface of the body (Fig. XIV-2-1):

$$\delta_2^* = \bar{A}P_2^n (x_{2v} + x_2)^m.$$

The displacement thickness at point C can be calculated similarly:

$$\delta_3^* = \bar{A}P_3^n (x_{3v} + x_3)^m,$$

where the function P_3 is found for the parameters on the third segment and the length x_{3_v} of the virtual cone is calculated with the expression

$$\delta_2^* = \bar{A}P_2^n (x_{2v} + x_2)^m = \bar{A}P_3^n x_{3v}^m.$$

Generalizing the above relationships, we can write a relation for the conventional thickness on an arbitrary ith segment:

$$\delta_i^* = \bar{A}P_i^n (x_{iv} + x_i)^m, \qquad \text{(XIV-2-6)}$$

where the length x_{i_v} of the virtual-cone generatrix is found from the condition

$$\delta_{i-1}^* = \bar{A}P_{i-1}^n (x_{i-1v} + x_{i-1})^m = \bar{A}P_i^n x_{iv}^m. \qquad \text{(XIV-2-7)}$$

The same expression must be used to obtain the generatrix-point coordinate of the virtual body.

In the case of a heat-insulated surface, the above method presupposes simultaneous solution of two problems. The first involves determination of the inviscid parameters and the second calculation of the friction and heat-transfer variables.

To simplify the calculations, we may disregard the influence of heat transfer and high temperature on the thermodynamic characteristics and kinetic coefficients of the gas. Then the high-velocity effect will reduce to the influence of compressibility (M_∞) on the thickness of the boundary layer and, consequently, on the inviscid parameters. The inviscid parameters on

a curvilinear surface can be approximated by using the relationships for the conventional thickness of an incompressible boundary layer. In the case of strongly cooled flows (for example, in wind tunnels), the data agree well with experimental results even when the calculation is made by the formulas for a flat plate.

Viscous interaction on a slender cone at hypersonic flow velocity. The "inviscid" parameters on a slender cone at hypersonic velocities can be determined by the method of "local cones" and Formula (VIII-1-27), in which $K_1 = M_\infty \beta_c$ is replaced by $K^* = K_1 + M_\infty(d\delta^*/dx) = M_\infty(\beta_c + d\delta^*/dx)$. For a laminar boundary layer, the derivative $d\delta^*/dx$ is calculated from the expression [59]

$$\frac{d\delta^*}{dx} = \frac{d_1}{\sqrt{3}} \sqrt{c_1} \frac{M_1^2}{\sqrt{Re_{x\,1}}} = \frac{d_1}{\sqrt{3}} \frac{\bar{\chi}}{M_1}, \qquad \text{(XIV-2-8)}$$

where d_1, c_1, and $Re_{x\,1}$ are given by (V-6-9) and $\bar{\chi}$ by Formula (V-6-6). M_1 is found from the theory of flow around a slender cone without considering viscous interaction. The relation given for $d\delta^*/dx$ pertains to an arbitrary wall temperature T_{w1}. For the particular cases of heat-insulated and cold walls, the values of d_1 are determined from Formulas (V-6-10) and (V-6-11), respectively.

For weak interaction, when the induced pressure differs little from its initial value, $d\delta^*/dx < \beta_c$ (the values of $K_1 = M_\infty \beta_c$ are arbitrary). In this case, the hypersonic-interaction parameter $\bar{\chi}$ varies up to about 3-3.5. Values of $\bar{\chi}_1 > 3$-3.5 correspond to the strong interaction, for which $K^* \gg 1$ and $d\delta^*/dx > \beta_c$. /562

Friction

The friction-drag coefficient for a body can be approximated by the formulas

$$c_{xf\,1} = c'_{xf\,1} \frac{S_{sde}}{S_{mid}}; \quad c_{xf\,t} = c'_{xf\,t} \frac{S_{sde}}{S_{mid}}, \qquad \text{(XIV-2-9)}$$

the first of which is used in the case of a fully laminar boundary layer, and the second for full turbulence. The quantities $c'_{xf\,1}$ and $c'_{xf\,t}$ are the coefficients of friction drag of a flat plate for laminar and turbulent boundary layers, respectively.

The corresponding working formula for the friction-drag coefficient of a mixed boundary layer has the form of (VII-1-1). If the coefficients of turbulent and laminar friction in (VII-1-1) are defined respectively by (VI-1-8) and (VI-1-10) and compressibility is taken into account with (VI-1-18) and (VI-1-19), we obtain on setting the critical Reynolds number equal to $6.5 \cdot 10^6$

$$c_{xf} = \left[\frac{4.96 \cdot 10^{-4}}{\sqrt[3]{1 + 0.03M_\infty^2}} \frac{S_1}{S_{sde}} + \frac{0.0396}{\sqrt{1 + 0.12M_\infty^2}} \left(\frac{1}{Re^{0.145}} - \frac{0.1S_1}{S_{sde}} \right) \right] \frac{S_{sde}}{S_{mid}} . \quad \text{(XIV-2-10)}$$

Wind-tunnel experiments at moderate supersonic speeds ($M_\infty \simeq$ $\simeq$ 1.5-2) have shown that formulas derived for a flat plate on the assumption of an incompressible boundary layer can be used to calculate friction drag.

Improving the results of the friction-drag calculation requires taking account of the surface shape of the solid of revolution. Here a simplified method of calculating friction for a long slender body is to replace the nose section by an equivalent cone and the remainder by a cylinder. As on the equivalent cone, the variables of the gas can be considered constant on the cylinder. The values taken are usually those of the free stream.

The equivalent-cone angle can be determined by the formula $\beta_{c.e} = \int_0^1 \beta d\bar{x}$. In the particular case of a parabolic nose section $\beta_{c.e} = 0.5\beta_0$.

The total friction drag coefficient of the composite body (equivalent cone + cylinder) is

$$c_{xf} = Ac_{f\,c}^{pl} \frac{\rho_c V_c^2}{\rho_\infty V_\infty^2} \frac{S_{sde}^n}{S_{mid}} + c_{f\,C}^{pl} \frac{S_{sde}^C}{S_{mid}} , \quad \text{(XIV-2-11)}$$

where A is a constant for laminar and turbulent boundary layers and equal to $\sqrt{3}$ and $\sqrt[5]{3}$, respectively; S_{sde}^n is the side area of the real nose section; S_{sde}^C is the area of the rest of the body (the cylinder).

The coefficient $c_{f\,c}^{pl}$ in this formula is calculated from the flat-plate expressions, but for the parameters on the equivalent cone. The coefficient $c_{f\,C}^{pl}$ must be calculated as follows. The first step is determination of the virtual cylinder length x_v, on which a boundary layer of the same thickness as at the end of the cone would form with the parameters assigned on the cylinder. /563

Equating the corresponding expressions for the thicknesses, we find

$$x_v = x_{c.e}\left(\frac{V_\infty}{V_e}\frac{\rho_\infty}{\rho_e}\frac{\mu_e}{\mu_\infty}\right)^n, \qquad \text{(XIV-2-12)}$$

where $x_{c.e}$ is the generatrix length of the equivalent cone; n = 1 and 1/4, respectively, for laminar and turbulent layers.

We can now determine the coefficient of friction:

$$c_{fc}^{pl} = c_{f\,v+c}\frac{x_v + x_c}{x_c} - c_f\frac{x_v}{x_c}. \qquad \text{(XIV-2-13)}$$

Here the coefficient $c_{f,v+C}$ is calculated from the length $x_v + x_C$ and c_f from the virtual length x_v.

The significance of this formula is to define the friction drag of the cylindrical section as the difference between the drags of the cylinder with the virtual segment and of the virtual segment.

Instead of calculating by the equivalent-cone method, we might use the "local-cone" method and the notion of virtual cone length. Here the length of the virtual cone is determined from Formula (XIV-2-7). The distribution found for the local tangential stresses can be used to calculate the total frictional force and then the heat-flow distribution and total heat transfer.

Relationships that account for compressibility (and contain M_∞ directly) or, for very high velocities, relationships with determining parameters, can be used as a basis for calculation of friction coefficients.

In calculating heat-transfer parameters, it is necessary to convert to local coefficients of friction. The expressions for these coefficients on the equivalent cone and on the cylinder will be, respectively,

$$c_{fx} = Ac_{fc}^{pl};\quad c_{fx} = A'c_{fc}^{pl}. \qquad \text{(XIV-2-14)}$$

Here the coefficient $c_{f\,C}^{pl}$ is calculated for the length $x_v + x$, where $\underline{x}$ is the distance from the beginning of the cylindrical part.

In the first formula of (XIV-2-14), the value of the coefficient A is chosen as for an ordinary cone, in accordance with

whether the boundary layer is laminar or turbulent. In the second expression of (XIV-2-14), A' can be set equal to unity if the boundary-layer thickness is a small fraction of the cylinder radius. With this condition, the friction and heat transfer can be calculated by the thin-plate formulas for a turbulent boundary layer on the cylinder.

Wake Drag

Supersonic speeds. One of the components of total drag is the wake drag that results from the underpressure behind the blunt base of a body. This underpressure results from interaction between the boundary layer separating from the body at its base, the external flow, and the gas in the wake space (stagnation zone)(Fig. XIV-2-2). The external flow acts as an ejecting medium and the boundary layer as a kind of barrier to ejection; the gas in the stagnation zone again behaves as an ejecting medium. The ejecting effect and, consequently, the wake pressure p_{wke} depend on the kind of boundary layer in the region between the separation point A and the sticking point B, which is situated on the axis: fully laminar, mixed, or fully turbulent. The wake pressure also depends on a number of other factors, such as attack angle, the shape of the body as a whole and its base configuration in particular, Mach and Reynolds numbers, and wall temperature. /564

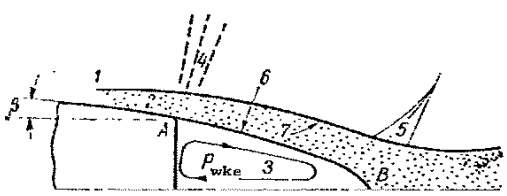

Figure XIV-2-2. Diagram of Gas Flow Behind Base of Solid of Revolution. 1) region of external flow; 2) boundary layer; 3) stagnation zone; 4) expansion region; 5) compression region; 6) lower edge of boundary layer; 7) upper edge of boundary layer.

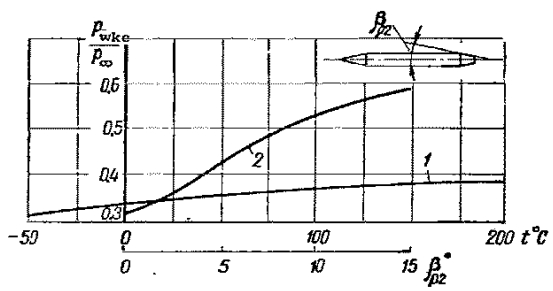

Figure XIV-2-3. Wake Pressure as a Function of Wall Temperature (1) and Half-Angle β_{p_2} of Stern (2) (Turbulent Boundary Layer).

As we know, the nature of the flow in the boundary layer determines the thickness of the layer, which will be smaller for laminar than for turbulent flows. The ejection effect is of the opposite nature: with a laminar layer, this effect is stronger than with a turbulent one. The wake pressure is therefore smaller in the former case and larger in the latter.

The case of mixed flow, which is characterized by location of the transition point between the separation and sticking points, is most complex for analysis. It can be assumed that the influence of such a mixed boundary layer on the wake pressure will be intermediate between the effects of purely laminar and purely turbulent boundary layers.

As a function of body shape, wake pressure is governed by the influence of surface configuration on the thickness of the boundary layer at the separation point and on the average pressure (denoted by p') and M' of the external inviscid flow in the neighborhood of the base. Figure XIV-2-3, whose data are experimental, indicates that an increase in the stern taper angle results in an increase in wake pressure and, consequently, a decrease in the wake-drag coefficient.

A change in Mach number is reflected in a change in the average pressure and velocity profile in the boundary layer at the separation point and, consequently, in an ejecting effect. The wake pressure always drops with increasing Mach number.

As we have noted, the wake effect depends on the form of the boundary layer in the neighborhood of the tail section. Wake pressure depends weakly on Reynolds number for a given boundary-layer form. This is evident, for example, from Fig. XIV-2-4, /565
which presents wake pressures measured in a case of turbulent flow. We observe only a minor, theoretically predictable increase in wake pressure with decreasing Reynolds number.

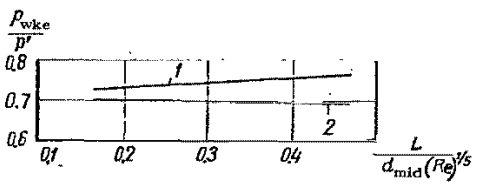

Figure XIV-2-4. Influence of Reynolds Number on Wake Pressure (Experiment). 1) M' = = 1.5; 2) M' = 2.

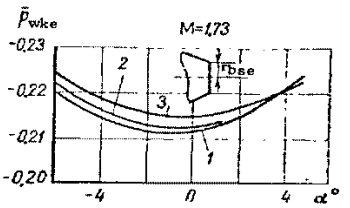

Figure XIV-2-5. Influence of Attack Angle on $\bar{p}_{wke}$. 1,2,3) for r/r_{bse} ratios of 0.876, 0.756, and 0.992, respectively.

The influence of small attack angles on wake pressure is slight. We see from the experimental data in Fig. XIV-2-5 that the wake pressure gradually decreases with increasing attack angle in turbulent flow. With rising flow velocities, wake pressure will also decrease, since it approaches its zero limiting value.

Wake pressure depends on the position of the tail-fin trailing edges. When the edges of rectangular tailplanes are situated at the base, the wake drag rises over that of the isolated body. Shifting the fins forward by approximately one chord makes the wake drag equal to that of the isolated body. In addition to changes in position, this drag is also influenced by the profile thickness and planform of the fins.

When the boundary layer is heated, its thickness increases, and there is a consequent increase in wake drag (see Fig. XIV-2-3). When the boundary layer is cooled by withdrawing heat through the surface, we observe the opposite effect: the layer thickness decreases and wake pressure drops. This effect is noted in flight at high supersonic speeds when forced cooling is applied to the wall and the boundary-layer temperature drops below the level established for an adiabatic wall.

Figure XIV-2-6 shows experimental results from a study of wake pressure for a series of solids of revolution with various shapes and turbulent layers on their surfaces. The shape differences involved different configurations of the tail sections. The curve of Fig. XIV-2-6 is universal by virtue of the introduction of parameters such as the average external-flow pressure p' and M', which is the average Mach number of the external flow along the mixing length and corresponds to the pressure p'. M' can be regarded as a similarity parameter: irrespective of the tail-section configuration, the ratio p_{wke}/p' remains constant for a given M'.

To use the curve in Fig. XIV-2-6 to determine wake pressure for a given solid-of-revolution shape, it is first necessary to find the average pressure p' over the length of the stagnation zone that corresponds to this shape. Here we can use the hypothesis that p' is equal to the pressure at the end of a conventional cylindrical extension of the body beyond the base section whose diameter and length are equal to the base-section diameter. The value of p' can be found either theoretically (for example, by the method of characteristics) or experimentally. Figure XIV-2-7 shows calculated results for the pressure p' as obtained by the method of characteristics for a cylindrical body with a nose cone. /566

For cylindrical bodies with a cylinder length three or four times d_{mid}, we can set $p' \simeq p_\infty$.

The wake pressure can be found from the formula

$$\frac{p_{wke}}{p_\infty} = \frac{p'}{p_\infty}\frac{p_{wke}}{p'}, \qquad \text{(XIV-2-15)}$$

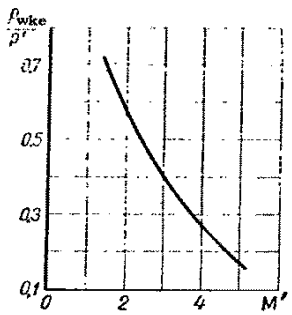

Figure XIV-2-6. Variation of p_{wke} as a Function of M' (Turbulent Boundary Layer).

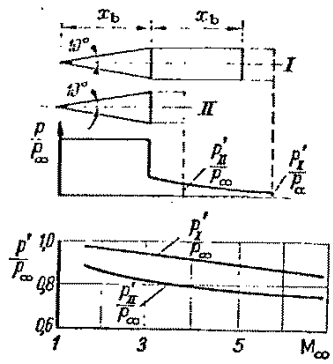

Figure XIV-2-7. Average Pressure in Stagnation Region.

where the ratio p_{wke}/p' is determined from Fig. XIV-2-6 for M'. The relation between p' and M' is also stated by

$$p' = p'_0 \left(1 + \frac{k-1}{2} M'^2\right)^{-\frac{k}{k-1}}, \qquad \text{(XIV-2-16)}$$

where p'_0 is the stagnation pressure corresponding to the part of the shock at the point of the nose section. The data of Fig. XIV-2-6 can be presented in the form of the dependence of wake pressure on a certain function $f_1(M')$:

$$\frac{p_{wke}}{p_\infty} = \frac{p'}{p_\infty} f_1(M'), \qquad \text{(XIV-2-17)}$$

which corresponds to negligible boundary-layer thickness. In a more general case, thickness influences wake pressure, and this can be taken into account by introducing a function $f(M', \delta_b/d_{mid})$:

$$\frac{p_{wke}}{p_\infty} = \frac{p'}{p_\infty} f\left(M', \frac{\delta_b}{d_{mid}}\right), \qquad \text{(XIV-2-18)}$$

where δ_b is the thickness of the boundary layer at the base. The thickness ratio of a turbulent layer of length ℓ is of the order of $\delta_b/\ell \sim Re^{-1/5}$, and that of a laminar layer $\delta_b/\ell \sim Re^{-1/2}$. For a turbulent layer, therefore,

$$\frac{p_{wke}}{p_\infty} = \frac{p'}{p_\infty} f_1\left(M', \frac{l}{d_{mid}\,Re^{1/5}}\right), \qquad \text{(XIV-2-19)}$$

and for a laminar layer /567

$$\frac{p_{wke}}{p_\infty} = \frac{p'}{p_\infty} f_2\left(M', \frac{l}{d_{mid}\,Re^{1/2}}\right), \qquad \text{(XIV-2-20)}$$

where f_1 and f_2 are certain functions of the parameters in the parentheses.

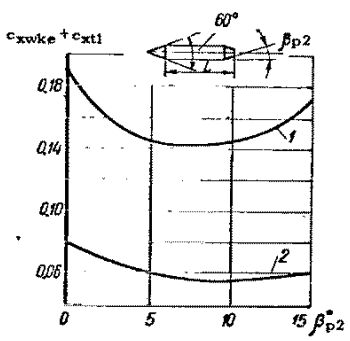

Figure XIV-2-8. Influence of Stern Taper on Stern Drag: Laminar (1) and Turbulent (2) Boundary Layers.

Wake pressure can be determined with a certain approximation without consideration of Reynolds number. The wake-pressure coefficient for turbulent flow is

$$\bar{p}_{wke} = -K_2 (0.29 + 0.13 \sin^{2/3} \beta_{p2})^{K_3}, \qquad \text{(XIV-2-21)}$$

where

$$K_2 = \left(4 - \frac{1.65k}{M_\infty^3}\right)(kM_\infty^2)^{-1}; \quad K_3 = 0.3\,(2 + M_\infty^{-1/2}). \qquad \text{(XIV-2-22)}$$

Formula (XIV-2-21) is valid for the range $1 < M_\infty < 5$ and for comparatively short bodies. According to (XIV-2-21), the wake-drag coefficient is

$$c_{x\,wke} = K_2 (0.22 + 0.13 \sin^{2/3} \beta_{p2})^{K_3} \bar{S}_{bse}. \qquad \text{(XIV-2-23)}$$

For a given stern-section length, an increase in the angle β_{p2} results in a smaller $\bar{S}_{bse}$ and, consequently, a lower $c_{x\,wke}$. But the drag component $c_{x\,tl}$ will then increase owing to the drop in pressure on the side of the stern. It is possible to find a taper angle β_{p2} that will produce minimum total drag $c_{x\,wke} + c_{x\,tl}$. The experimental curves in Fig. XIV-2-8 indicate that the drag minimum will occur at about $\beta_{p2} = 7°$.

If the body has a large slenderness ratio x_b/d_{mid}, it is advisable to take the effect of this slenderness on wake pressure into consideration. In deriving an empirical formula, we can start from the fact that the $Re^{1/5}$ that appears in the general

formula (XIV-2-19) has insignificant influence on wake pressure in a comparatively broad range of Re. Experimental studies then indicate that the coefficient

$$\bar{p}_{wke} = -1.144\,K_1(2-K_1)\,M_\infty^{-2}. \qquad \text{(XIV-2-24)}$$

Here $K_1 = M_\infty/\lambda_{ef}$, where the effective fineness ratio is

$$\lambda_{ef} = \frac{\lambda_b}{\bar{S}_{bse}} \qquad \text{(XIV-2-25)}$$

In accordance with the expression for $\bar{p}_{wke}$, the wake-drag coefficient

$$c_{x\,wke} = 1.144\,K_1(2-K_1)\,M_\infty^{-2}\bar{S}_{bse}. \qquad \text{(XIV-2-26)}$$

These formulas, which consider the effect of stern taper, give satisfactory results for $\bar{S}_{bse} \geq 0.4$-0.5 and comparatively small average generatrix inclination angles of the tail section (8-10°).

The parameter K_1 is a similarity parameter. At a given value of this parameter, $\bar{p}_{wke}M_\infty^2$ and $c_{x\,wke}M_\infty^2/\bar{S}_{bse}$ remain the same for various body shapes and M_∞. In using Formulas (XIV-2-24) and (XIV-2-26), it must be remembered that they are applicable for $K_1 \leq 1$. But if $K_1 > 1$, the calculation must be made by the formulas /568

$$\bar{p}_{wke} = -1.43\,M_\infty^{-2};\quad c_{x\,wke} = 1.43\,M_\infty^{-2}\bar{S}_{bse}, \qquad \text{(XIV-2-27)}$$

which correspond to the formation of an absolute vacuum behind the base.

Wake pressure with mixed boundary layer behind separation point. Mixed flow may appear behind the separation point when, for example, as a result of cooling of the wall below the equilibrium temperature a laminar boundary layer becomes longer and may extend beyond the separation point.

Wind-tunnel experiments indicate that the position of the transition point and, consequently, the wake pressure depend on the same variables M' and δ_b/d_{mid}. In evaluating wake pressure

for a mixed boundary layer, it must be remembered that it varies between limits corresponding to purely laminar and purely turbulent flow. For purely laminar flow, the transition occurs near the sticking point, and for a purely turbulent boundary layer it approaches the separation point.

Subsonic velocities. Measurements indicate that, as at supersonic velocities, the wake expansion and, consequently, the wake drag at $M_\infty < 1$ depend on the surface condition of the body, its length, and its base taper, i.e., on the same factors that determine the properties of the boundary layer. Consequently, there must be a relation between wake pressure, wake drag, and friction.

As a parameter characterizing wake pressure, we might introduce the coefficient $c_{xf\ wke} = \bar{c}_{fx}(S_{sde}/S_{bse})$, where $c_{xf\ wke}$ is the coefficient of friction referred to the base-section area and $\bar{c}_{xf}$ is the same coefficient calculated for the lateral area of the body.

Experimental data have made it possible to establish the following relation between the coefficient $c_{xf\ wke}$ and the wake-pressure coefficient:

$$\bar{p}_{wke} = -\frac{0.029}{\sqrt{c_{xf\ wke}}}. \qquad \text{(XIV-2-28)}$$

Introducing the coefficient of friction $c_{xf} = \bar{c}_{xf}(S_{sde}/S_{mid})$, which is referred to the midships section, we can find an expression for the wake-drag coefficient calculated for the area S_{mid}:

$$c_{x\,wke} = \frac{0.029}{\sqrt{c_{xf}}}\left(\frac{d_{bse}}{d_{mid}}\right)^2 \qquad \text{(XIV-2-29)}$$

Available experimental data indicate the possibility of using (XIV-2-28) and (XIV-2-29) for approximate calculations of wake pressure and drag even in the transonic-flow region, i.e., for M_∞ of the order of unity.

Wake pressure in the presence of a gas jet. Experimental studies of the wake pressure of solids of revolution with a working nozzle, i.e., under conditions corresponding to a running reaction engine, have shown that at a given M_∞ the pressure on the base ring of the body depends essentially on the pressure at the nozzle exit section. Here, the higher the pressure at this section, the higher will be the pressure on the ring.

Wake pressure also depends on the oncoming-flow parameters: velocity and static pressure. The following characteristic effects were observed during an investigation of this relationship: /569
1) at a nozzle-section pressure of 1 kg/cm^2 ($9.807 \cdot 10^4$ N/m^2), a static tunnel flow pressure of 0.4 kg/cm^2 ($3.921 \cdot 10^4$ N/m^2), and $M_\infty = 1.87$, an underpressure appeared on the ring; 2) with the nozzle-section pressure held at 1 kg/cm^2 and the static pressure in the tunnel lowered to 0.16 kg/cm^2 (the M_∞ of the flow then increased to 2.5), there was zero excess pressure on the ring; 3) when the tunnel static pressure was lowered even further to 0.1 kg/cm^2 (flow in tunnel accelerated to $M_\infty = 3$), the ring showed an overpressure instead of an underpressure. At this point, the flow velocity in the tunnel was equal to or greater than the velocity in the jet of gases issuing from the nozzle. The resulting difference between the static pressure at the nozzle section and in the tunnel results in vigorous mixing of the gas behind the base and filling of the vacuum. A propulsive force may arise as a result.

The first of the phenomena described arises when the nozzle is working at close to design conditions (pressure on section approximately equal to flow static pressure). If the static pressure on the nozzle section is much lower than the pressure in the flow, the resulting vacuum may be even greater than that which appears with the engine shut down. For near-design operation of the nozzle, the wake-drag coefficient can be evaluated approximately with Formula (XIV-2-26) by substituting $\bar{S}_r = S_r/S_{mid}$ for the taper $\bar{S}_{bse}$; here, S_r is the area of the base-section ring or, in the general case, of that part of the base not occupied by the nozzle systems.

The drop in wake pressure observed on deflection of the body is insignificant for small attack angles and has little influence on wake drag.

§XIV-3. DETERMINATION OF DEGREE OF BLUNTNESS FOR MAXIMUM REDUCTION OF HEAT FLOWS

Thickness of "inviscid" low-velocity layer. The method used to calculate the thickness of the "inviscid" low-velocity layer for a blunt cone is in principle the same as for a blunt wedge (see §VI-5).

Assuming that we can take as the upper boundary of the high-entropy "inviscid" layer the streamline passing through the "sonic" point at coordinate r_s on the detached shock wave in front of a blunted cone (Fig. IV-10-1), the gas flowrate across a cross section of area πr^2_s will be $\rho_\infty V_\infty \pi r^2_s$.

The same quantity crosses a so-called "low-Re" layer of a certain thickness Δ that corresponds to an arbitrary cross section of the body with radius r, and, consequently,

$$\rho_\infty V_\infty r_s^2 = 2\rho V r \Delta, \qquad \text{(XIV-3-1)}$$

hence the thickness of the "inviscid" layer

$$\Delta = \frac{1}{2}\frac{\rho_\infty}{\rho}\frac{r_s^2}{r}\frac{V_\infty}{V}, \qquad \text{(XIV-3-2)}$$

where ρ, and V are the density and velocity, respectively, in this section as calculated for inviscid flow on the surface with consideration of the bluntness effect.

/570

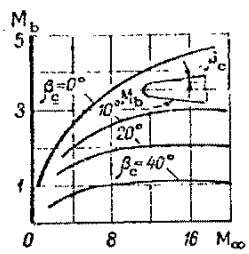

Figure XIV-3-1. M on Surface of Blunt Cone in Inviscid Flow.

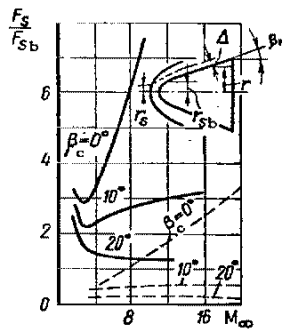

Figure XIV-3-2. Ratio of Cross-Sectional Area $F = 2\pi r\Delta$ of Low-Velocity Layer on Cone to Area $F_{sb} = \pi r_{sb}^2$; Solid Curves Represent Exact Calculations by (XIV-3-3) and Dashed Curves Approximate Values for the Ratio $r_s^2/r_{sb}^2 = 0.25$.

The determination of these parameters can be simplified in practical cases by assuming with some approximation that the pressure established at a certain distance from the bluntness is the same as that on the unblunted body. For example, this was evident in the example of flow past a blunted cone.

Calculation of the density ρ and velocity V for this condition, with dissociation taken into account on a blunt surface, was set forth in §VI-5. Formulas (VI-5-2) and (VI-5-4) are used to determine these parameters for K = const. The local Mach numbers M_b, calculated by Formula (VI-5-4) for a blunt cone and the condition that the pressure on it is the same as on a sharp

conical surface, are presented in Fig. XIV-3-1.

Introducing the values of the velocity and density into (XIV-3-2), we can determine the thickness of the "low-Re" layer and its cross-sectional area $2\pi r\Delta = F_s$ from the known "sonic"-point coordinate on the shock wave.

The diagram of Fig. XIV-3-2 shows curves for the area ratio

$$\frac{F_s}{F_{sb}} = \frac{2\pi r\Delta}{\pi r_{sb}^2} = \frac{1}{2}\frac{r_s^2}{r_{sb}^2}\frac{\rho_\infty}{\rho}\frac{V_\infty}{V}. \qquad \text{(XIV-3-3)}$$

Here r_{sb} is the coordinate of the "sonic" point on the spherical nose.

F_s/F_{sb} can be calculated approximately with the condition that the coordinate of point r_{sb} is twice the coordinate of the "sonic" point on the shock wave, i.e., the ratio $r_s^2/r_{sb}^2 = 0.25$.

We see from Fig. XIV-3-2 that with the above assumptions, the area ratio F_s/F_{sb} is of the order of unity for spherically blunted cones with small β_c angles. For flat-blunted cones, the low-velocity layer will be somewhat thicker. If we assume that the coordinates of the "sonic" points on the flat face and the shock wave are about the same, i.e., $r_s = r_{sb} = R_b$, then according to Formula (XIV-3-3), the area ratio F_s/F_{sb} will be four times that for the cone with the sphere. We can use Formula (XIV-3-2) to calculate the thickness of the low-velocity layer if the relation for the area ratio F_s/F_{sb} is given by the expression

$$\Delta = \frac{F_s}{F_{sb}}\frac{r_{s\tau}^2}{2r}. \qquad \text{(XIV-3-4)}$$

The thickness of the low-velocity layer can be calculated approximately for a spherical-nosed cone for the condition $F_s/F_{sb} = 0.25$, and with $F_s/F_{sb} = 1$ for a flat face. The corresponding working relationships take the form

$$\Delta = \frac{1}{8}\frac{r_{sb}^2}{r}; \quad \Delta = \frac{1}{2}\frac{r_{sb}^2}{r}. \qquad \text{(XIV-3-5)}$$

Calculation of required bluntness. In determining the required bluntness (r_{sb}), we can take as a condition that the

laminar-layer thickness δ_1 be equal to the thickness of the low- /571
velocity layer. Consequently, the conditions from which r_{sb} can be determined will be

$$\delta_1 = \frac{1}{2}\frac{\rho_\infty}{\rho}\frac{r_s^2}{r_t}\frac{V_\infty}{V} \quad \text{or} \quad \delta_1 = \frac{F_s}{F_{sb}}\frac{r_{sb}^2}{2r_t}, \qquad \text{(XIV-3-6)}$$

where r_t is the cross-section radius of the blunt cone at the expected transition point.

For example, it follows from the second formula of (XIV-3-6) that if $F_s/F_{sb} \simeq 1$, the coordinate r_{sb} must be of the order of $\sqrt{2r_t\delta_1}$ which is, as we see, equal to the geometric mean between the diameter of the body and the boundary-layer thickness at the transition point.

To determine the thickness of the laminar layer at the transition point on the surface of a blunt cone, we can use (XIV-1-6) with δ_1^{pl} calculated for the critical value Re^*_{cr} by the thin-plate formula

$$\frac{\delta_1^{pl}}{x_t} = 5.8\,(Re^*_{cr})^{-1/2},$$

in which x_t is the distance to the transition point.

The critical Reynolds number $Re^*_{cr} = V_\delta x_t \rho^*/\mu^*$ can be calculated in a general case from the determining parameters for a blunt cone.

To simplify the calculations, we can use the parameters of inviscid flow around a blunt cone, as obtained without consideration of determining temperature, instead of the determining parameters μ^* and ρ^*.

Since the critical Reynolds number is usually considered to be known, we can determine the laminar-segment length $x_t = \mu^* Re^*_{cr}/(V_\delta \rho^*)$, and then the boundary-layer thickness at the transition point:

$$\delta_1 = \frac{\delta_1^{pl}}{\sqrt{3}} = \frac{x_t}{\sqrt{3}}\left(\frac{\delta_1^{pl}}{x_t}\right) \qquad \text{(XIV-3-7)}$$

If we are concerned with the case of constant heat capacities, the formula for the required bluntness becomes

$$\Pi = \frac{r_{sb}^2}{x_t r_t} = 6.68\,(\mathrm{Re}_{cr}^*)^{-1/2}\,\frac{p_0'}{p_0}\left(\frac{1+\frac{k-1}{2}M_\infty^2}{1+\frac{k-1}{2}M^2}\right)^{\frac{k+1}{2(k-1)}}\frac{M}{M_\infty}\,\frac{r_{sb}^2}{r_s^2}. \qquad \text{(XIV-3-8)}$$

In this formula, as we have noted, Re_{cr}^* is usually assigned; the ratios p_0'/p_0 and r_{sb}^2/r_s^2 and M are determined on the blunt cone from the known M_∞. In rough calculations, the values of r_{sb}/r_s for a spherical nose and a flat face can be set equal to 2 and 1, respectively.

We can find the function Π by the necessary calculations in the right member of (XIV-3-8). Knowing the radius

$$r_t = R_b + x_t\beta_c$$

and the coordinate x_t, we can use the formula

$$r_{sb}^2 = \Pi x_t^2\beta_c + \Pi x_t R_b \qquad \text{(XIV-3-9)}$$

to compute the required blunting r_{sb} or, more precisely, the coordinate of the "sonic" point on the nose. For flat blunting, this coordinate will give the face radius, since $R_b = r_{sb}$, and for a spherical nose its radius will be found by the formula $R_b = r_{sb}/\sin\eta$, with the angle η at which the "sonic" point is located on the sphere found from Fig. XII-2-6.

Certain data on the critical Reynolds number. Determination of the critical Reynolds number requires investigation of boundary-layer stability. It has been established that with cooling of the wall, the stability of a laminar boundary layer increases. Physically, this is explained by the fact that with diminishing gas temperature near the surface, density rises, and hence so does the kinetic energy of the gas in a given volume. Understandably, particles with high energies are less subject to the influence of disturbing pulsations. It is noted here that at very high velocities, the Reynolds number, regarded as a stability criterion, is less important than such parameters as the wall-temperature ratio T_{wl}/T_δ (T_{wl}/T_∞ or T_{wl}/T_r) and the Mach

/572

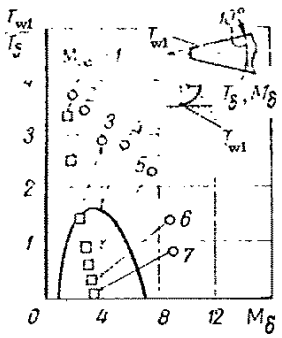

Figure XIV-3-3. Region of Stable Laminar Boundary Layer on Blunt Cone (Region Interior to Solid Curve). o) sharp cone; □) blunt cone.

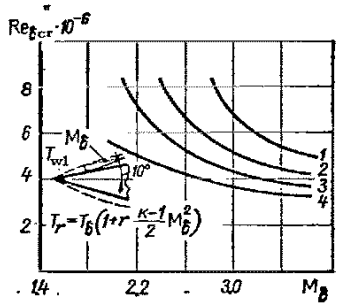

Figure XIV-3-4. Variation of Critical Reynolds Number on Cone. Values of T_{w1}/T_r: 1) 0.7; 2) 0.8; 3) 0.9; 4) 1.0.

number M_δ on the outer boundary of the boundary layer (or M_∞ for given flow conditions).

Theoretical studies have established the wall-temperature ratio required for complete stabilization of a laminar boundary layer as a function of the local M_δ (Fig. XIV-3-3). We see from this figure that with $M_\delta > 8$, the boundary layer cannot be stable regardless of intensity of cooling. It can also be noted that the stability boundaries broaden with diminishing ratio T_{w1}/T_δ. It follows from this that stagnation of the external flow, which is accompanied by a decrease in M_δ and a rise in the temperature T_δ, will have a stabilizing effect (if a constant wall temperature is maintained by appropriate cooling).

We noted above that such stagnation can be brought about by using a blunt rather than a sharp body. Thus, blunting is an important means of stabilizing a laminar boundary layer. In fact, the temperature at the outer boundary of the layer is higher on a blunt body than on a sharp one and, consequently, if constant wall temperature is maintained, the ratio T_{w1}/T_δ will be smaller. The local M_δ also decrease. This explains why bluntness shifts the conditions at the outer edge of the boundary layer from the instability region into the stable zone, as we see from Fig. XIV-3-3.

The instability region outside the curve in Fig. XIV-3-3 is necessarily a zone of full turbulization. In this region, the layer is characterized by turbulent inclusions whose appearance

is related to the point at which the laminar flow becomes turbulent. This transition culminates at the critical Reynolds number.

Figure XIV-3-4 shows wind-tunnel results obtained for this number by van Dreest. An experimental model of a shock cone was internally cooled, so that the ratio T_{w1}/T_δ could be varied. /573
The tests were run at various M_∞.

Analysis of the curves indicates that the critical Reynolds numbers increase with decreasing wall temperature and that the manner in which these numbers vary depends to a major degree also on M_δ. For $M_\delta > (3.8\text{-}4)$, the critical Reynolds numbers remain practically constant.

If the surface is cooled ($T_{w1}/T_r < 1$), the Re_{cr} increase, and in estimating the change in Re_{cr} we can proceed on the basis that its value is approximately inversely proportional to the wall temperature ratio T_{w1}/T_r defined by the expression

$$\frac{T_{w1}}{T_r} = \frac{T_{w1}}{T_\delta}\left(1 + r\frac{k-1}{2}M_\delta^2\right)^{-1} \qquad \text{(XIV-3-10)}$$

The pressure gradient at the wall exerts some influence on Re_{cr}. Here a negative gradient favors increased stability and, consequently, an increase in the critical Reynolds number. On the other hand, when the pressure increases downstream, i.e., the gradient is positive, conditions are set up for premature turbulization and Re_{cr} decreases.

If we consider flow around a blunted body, e.g., a cone, we find regions on its surface with various types of pressure variation. Immediately behind the total-stagnation point, the pressure decreases over a certain length of the body, setting up a negative static-pressure gradient that favors stabilization of the laminar boundary layer. Farther downstream, stagnation begins at a certain distance from the nose, with the result that a positive gradient appears. This lowers stability. However, this unfavorable effect of the positive gradient is not significant for practice. Nevertheless, it is advisable to take the negative gradient into account in final specification of the blunting dimension by increasing it slightly over the calculated value.

By way of example, let us calculate the transition-point shift for $M_\infty = 10$ on the smooth surface of a blunt cone with an angle $\beta_c = 10°$. We shall consider a spherical nose and first calculate the coordinate of the "sonic" point r_s. From the wave-generatrix equation $x = ar^2 = r^2/(2R_{s0})$ we find the ratio

$$\frac{r_s}{R_b}=\frac{R_{s0}}{R_b}\left(\frac{dr}{dx}\right)_s^{-1},$$

where the dimensionless wave radius of curvature R_{s0}/R_b is determined as a function of the density ratio ρ_s/ρ_∞ behind and in front of the normal part of the wave.

Taking dissociation into account for flight conditions near the ground at $M_\infty = 10$, we calculate the ratio $\rho_s/\rho_\infty = 7.4$, and then refer to the diagram of Fig. XII-2-12 to find $R_{s0}/R_b = 1.2$. Using the other diagram in Fig. XII-2-6, we determine the angular coordinate of the "sonic" point on the wave at $\omega = 22°30'$, and then find the shock inclination angle $\theta_{ss} = 67°30'$ and $\tan\theta_{ss} = (dr/dx)_s = 2.41$. Consequently, $r_s/R_b = 1.2/2.41 \simeq 0.5$. Also from Fig. XII-2-6, we find the angular coordinate of the "sonic" point on the sphere, $\eta_{sb} = 24°30'$ which determines the relative linear coordinate $r_{sb}/R_b = 0.676$. Thus, the ratio of the "sonic"-point coordinates $r_{sb}/r_s = 0.676/0.5 = 1.35$.

We then find the ratio of stagnation pressures p_0'/p_0 as the mean between their values at the apex and the "sonic" point of the shock wave. Applying (III-4-33), we calculate the ratio of the stagnation pressures after and before the shock for the values $M_\infty = 10$ and $M_\infty \sin\theta_{ss} = 10 \sin 67°30' = 9.24$, and then determine the mean pressure ratio /574

$$\frac{p_0'}{p_0}=\frac{3.14+4.52}{2}\cdot 10^{-3}=3.83\cdot 10^{-3}.$$

We then refer to Fig. XIV-3-1 to determine the Mach number M on the blunt cone ($M_b = 2.8$) and Fig. XIV-3-4 for the critical Reynolds number $Re_{cr} = 8.7\cdot 10^6$; in determining the latter, we assign the relative wall temperature $T_{w1}/T_r = 0.7$, which corresponds to the ratio

$$\frac{T_{w1}}{T_\delta}=0{,}7\left(1+r\frac{k-1}{2}M_\infty^2\right)=0.7\,(1+0.169\cdot 2.8^2)=1.58.$$

After substituting all of the values that we have found into (XIV-3-8), we obtain the function

$$\Pi = \frac{r_{sb}^2}{x_t r_t} = 2.47 \cdot 10^{-3}.$$

The transition-point coordinate on a sharp cone is

$$x_t = \mathrm{Re}_{cr} \left(\frac{1 + \frac{k-1}{2} M_c^2}{1 + \frac{k-1}{2} M_\infty^2} \right)^{\frac{k+1}{2(k-1)} - n} \frac{M_\infty}{M_c} \frac{\nu_\infty}{V_\infty}. \qquad \text{(XIV-3-11)}$$

For the cone selected, the local $M_c = 7.6$. Assuming further that the flight altitude is about 22 km, so that the kinematic viscosity coefficient $\nu_{\infty H} = 20\nu_{\infty 0}$, we obtain the value $x_t = 0.438$ m from Formula (XIV-3-11).

To determine the corresponding coordinate for the blunt cone, we refer to Fig. IV-10-2 to evaluate the Reynolds number for this cone, i.e., we find the ratio $\mathrm{Re}_b/\mathrm{Re}_c = 0.071$. Accordingly, the transition-point coordinate with the bluntness taken into account will be

$$x_t = \frac{0.438}{0.071} = 6.2 \text{ m}.$$

From this, we can calculate the coordinate of the "sonic" point on the sphere:

$$r_{sb} = 0.5\Pi x_t \cos\beta_c \sin^{-1}\eta_{sb} \mp [0.25(\Pi x_t \cos\beta_c \sin^{-1}\eta_{sb})^2 + \Pi x_t^2 \sin\beta_c]^{-1/2},$$

and then the spherical-blunting radius $R_b = r_{sb}/\sin\eta_{sb}$ and the ratio $\bar{s}_{sp}$ of the blunted-nose area to the cross-sectional area of the cone at the transition point. If this point is on the base section, the entire surface of the cone is covered by a laminar boundary layer.

The solution can be simplified by presenting the segment of the shock-wave generatrix as an arc of a circle of radius R_{s0}. In this case,

$$r_s = R_{s0}\cos\theta_{s\,s};\ r_{sb} = R_b \sin\eta_{sb}.$$

Consequently,

$$\frac{r_{s\,b}}{r_s} = \frac{R_b}{R_{s0}} \frac{\sin \eta_{s\,b}}{\cos \theta_{s\,s}} = 1.47.$$

The bluntness parameters are calculated from these data.

Effect of boundary layer. The required bluntness calculated in this way can be improved by considering the influence of the conditional boundary-layer displacement thickness. In fact, it follows from physical considerations that the effect of viscosity on the flow can indeed be taken into account if we consider inviscid flow around a conventional body whose transverse dimensions have been increased by the displacement thickness δ^*_1. Consequently, we find that the low-velocity layer has been shifted by δ^*_1. It is clear from this that in calculating the required bluntness, we must start with the equality $\Delta = \delta_1 - \delta^*_1$. The cone formula can be used to determine δ^*_1: /575

$$\delta_1^{*c} = \delta_1^{*pl}/\sqrt{3}.$$

The conventional thickness δ_1^{*pl} calculated from the determining parameters can, in turn, be found from the formula for an incompressible medium:

$$\delta_1^{*pl} = (3/8)\,\delta_1^{pl}.$$

Thus, for a blunt cone with the displacement thickness taken into account

$$\Delta = \delta_1 - \delta_1^* = 0.36 x_t \left(\frac{\delta_1^{pl}}{x_t}\right). \qquad \text{(XIV-3-12)}$$

Comparing this formula with (XIV-3-7), we may conclude that the required blunting is smaller in our case.

The method set forth above for calculating the required degree of bluntness is based on the assumption that the shape of the low-M layer profile does not change. However, deformation of this profile does occur downstream owing to dissipation of the "inviscid" low-velocity layer as it takes in increasing quantities of low-entropy air. This breakdown of the high-entropy flow is equivalent to a smaller bluntness.

Certain studies have shown that in flight at moderate altitude, dissipation of the low-velocity layer profile can be disregarded on a laminar-boundary-layer length of up to $x \simeq 1000\Delta$.

If the washed surface is longer, it is advisable to allow for the dissipation effect; this can be done by a slight increase in the originally calculated blunting.

§XIV-4. HEAT TRANSFER ON THE BODY

Curvilinear Surface

Relationships (IV-8-47) and (IV-8-48) should be used to calculate the specific heat flow from a laminar boundary layer to a strongly cooled curved wall in the case of equilibrium gas dissociation and $\rho\mu$ = const across the layer. Assuming $\varepsilon = 1$, we obtain

$$q = 0.5\ \mathrm{Pr}^{-2/3} \sqrt{V_\infty \rho_0' \mu_0'}\ i_r F, \qquad \text{(XIV-4-1)}$$

where the function

$$F = \frac{\sqrt{2}\ (p/p_0')\ (V_\delta/V_\infty)\ r}{2\left[\int_0^x (p/p_0')\ (V_\delta/V_\infty)\ r^2\, dx\right]^{1/2}}. \qquad \text{(XIV-4-2)}$$

In (XIV-4-1), the enthalpy i_r includes the acceleration of gravity $g = 9.81$ m/s^2, so that the dimensions of i_r will be kcal·m/kg·s^2.

Sharp Body

/576

Cone. For a conical curface, we must set $p = p_0'$, $V_\delta = V_c$, $\rho_0'\mu_0' = \rho_c\mu_c$ in (XIV-4-1) and (XIV-4-2). Consequently,

$$q_c = 0.508\ \mathrm{Pr}^{-2/3} i_r \sqrt{\frac{\rho_c \mu_c V_c}{x}}, \qquad \text{(XIV-4-3)}$$

where the subscript c signifies parameters on the cone; the x-coordinate is measured from the nose along the surface generatrix.

The total heat flow on the cone

$$Q_c = 2\pi \int_0^{x_c} q_c r\, dx. \qquad \text{(XIV-4-4)}$$

On substituting q_c from (XIV-4-3), we obtain

$$Q_c = 0.812\,\mathrm{Pr}^{-2/3}\,\mathrm{tg}\,\beta_c S_c i_r \sqrt{\rho_c \mu_c V_c x_c^{1/2}}, \qquad \text{(XIV-4-5)}$$

where $S_c = \pi x_c^2 \sin \beta_c$ is the lateral area of a cone with a generatrix length x_c and a semiapex angle β_c.

Sharp nose section of arbitrary shape. In calculating heat flows by Formula (XIV-4-1), we can set $p = \bar{p}^* \sin^2 \beta / \sin^2 \beta_0$ for high velocities; here $\bar{p}^*$ is the pressure coefficient on a tapered conical nose. Consequently,

$$\frac{p}{p^*} = \frac{1}{\sin^2 \beta_p}\left[\sin^2 \beta + \frac{p_\infty}{p^*}(\cos^2 \beta - \cos^2 \beta_p)\right]. \qquad \text{(XIV-4-6)}$$

Using the relation between pressure and velocity for isentropic flow, we can find the velocity V_δ on the surface of the layer. Introducing p and V_δ into (XIV-4-2), we can calculate the function F and then the specific heat flow from (XIV-4-1).

In approximate calculations for large M_∞, the local velocity on the nose section can be determined by the Newton formula $V_\delta = V_\infty \cos \beta_c$, so that a simpler relation can be obtained for F and hence for q.

At the same time, the "local-cone" method and (XIV-4-3) can be used to approximate the local-flow distribution. The specific heat flow at point A (Fig. IV-7-3) given by this formula corresponds to a local conical surface with a semiapex angle β and a distance $O'A = x_c$ along its generatrix. If the origin of the coordinate system taken is placed at the nose and the longitudinal axis is directed along the body's axis, the radial coordinate of point A at which the specific heat flow is determined is $r = x_c \sin \beta$. Accordingly, the specific heat flow at A is

$$q = 0.608\,\mathrm{Pr}^{-2/3} i_r \sqrt{\frac{\rho_\delta \mu_\delta V_\delta \sin \beta}{r}}, \qquad \text{(XIV-4-7)}$$

where ρ_δ, μ_δ, and V_δ are the inviscid-flow parameters on the local

If the specific heat flow on the local conical surface is calculated from the Stanton number $\underline{St_x^*} = \sqrt{3}\,St_{p1}^*$ found from the determining parameters $[q = St_x^* \rho_\delta V_\delta (i_r - i_{w1})]$, then /577

$$Q = 2\pi \int_0^x St_x^* \rho_c V_\delta (i_r - i_{w1}) r \cos^{-1}\beta \, dx, \qquad \text{(XIV-4-9)}$$

where $\underline{x}$ is the axial length of the body.

§XIV-5. TOTAL STAGNATION POINT ON BLUNT NOSE

Equilibrium dissociation. Setting $\varepsilon = 1$ in (IV-8-49), we obtain for the heat flow at the critical point on a blunted solid of revolution

$$q_0 = 0.664\, Pr^{-2/3} (\tilde{\lambda}\rho_0'\mu_0')^{1/2} i_r. \qquad \text{(XIV-5-1)}$$

This expression has been derived for an overcooled surface on which the temperature T_{w1} and therefore the enthalpy i_{w1} are negligibly small by comparison with the corresponding T_r and i_r. When cooling does not produce a low enough wall temperature, e.g., when heat is dissipated only by radiation and a comparatively high equilibrium radiation temperature is established, it is necessary to take i_{w1} into consideration.

Experimental studies have shown that for an overheated wall, the formula for q_0 retains the same basic form as (XIV-5-1). The difference is that instead of i_r, the new formula contains $i_r - i_{w1}$ and an additional factor to take account of the change in the product $\rho\mu$ across the boundary layer in the neighborhood of the critical point. The working relationship is

$$q_0 = 0.763\, Pr^{-0.6} (\tilde{\lambda}\rho_0'\mu_0')^{1/2} (i_r - i_{w1}) (\overline{\rho_{w1}\mu_{w1}})^{1/10}, \qquad \text{(XIV-5-2)}$$

where

$$\overline{\rho_{w1}\mu_{w1}} = \rho_{w1}\mu_{w1}/\rho_0'\mu_0'.$$

In accordance with (XIV-5-2) and the expressions

$$Nu = \frac{q_0 c_{p.w1} x}{\lambda_{w1}(i_r - i_{w1})}, \quad Re = \frac{\rho_{w1}}{\mu_{w1}} \tilde{\lambda} x^2 \qquad \text{(XIV-5-3)}$$

the dimensionless heat-transfer number is

$$\frac{\mathrm{Nu}}{\sqrt{\mathrm{Re}}} = 0.763\,\mathrm{Pr}^{0.4}\,(\overline{\rho_{w1}\mu_{w1}})^{-0.4}. \qquad \text{(XIV-5-2')}$$

Studies have shown that $\rho_{w1}\mu_{w1}/\rho_0'\mu_0' > 1$, so that the heat flow increases over its value for a strongly cooled surface. Formula (XIV-5-2) is valid for surface temperatures not in excess of the stagnation point. It implies that at high speeds, when dissociation becomes substantial, heat transfer is determined by the enthalpy gradient rather than the temperature gradient. At these velocities, the recovery enthalpy i_r can be calculated as the stagnation enthalpy by the formula $i_r = 0.5V_\infty^2$.

In the absence of dissociation, we can convert in (XIV-5-2) from the enthalpy difference to the temperature difference by using the substitution

$$i_r - i_{w1} = \bar{c}_{p,w1}\,(T_r - T_{w1}),$$

where the specific heat $c_{p.w1}$ is calculated as the mean between the values on cooled and insulated walls with the respective temperatures T_{w1} and T_r. It follows from these formulas that the heat brought to the wall depends on the parameters at the outer edge of the boundary layer. These parameters are in turn determined from the conditions of flow around the blunt nose at the total-stagnation point. /578

Reduction of calculated numerical results for very high supersonic velocities has made it possible to obtain an approximate formula for the specific heat flow at the total-stagnation point:

$$q_0 = \frac{31500}{\sqrt{R_b}}\sqrt{\frac{\rho_{\infty H}}{\rho_{\infty g}}}\left(\frac{V_\infty}{V_s}\right)^{3.25}\left(1 - \frac{i_{w1}}{i_r}\right)\frac{\mathrm{kcal}}{\mathrm{m^2\,s}}, \qquad \text{(XIV-5-4)}$$

where V_s is the earth-orbital velocity of 7.93 km/s; $\rho_{\infty\,H}$ and $\rho_{\infty g}$ are the densities of the atmosphere at a certain altitude H and at the ground, respectively; R_b is the radius of the sphere in meters.

The recovery enthalpy can be set equal to the stagnation enthalpy.

Formula (XIV-5-4) gives the heat flow determined not only by heat conduction, but also by diffusive heat transfer through recombination of atoms at a catalytic wall. If, on the other hand, the surface of the sphere is not catalytic (for example, the surface of a nonmetallic skin), Formula (XIV-5-4) will give a low value for the heat flow. The error of the formula will increase with altitude, as the state of the gas deviates farther from equilibrium. From the practical standpoint, use of a noncatalytic surface may be helpful, since the low recombination rates change insignificantly on a noncatalytic surface, heat is therefore absorbed by dissociation, and, as a consequence, the heat flow to the wall is lowered. In these calculations, the wall enthalpy can be assigned on the basis of the maximum permissible skin temperature.

The heat flows can also be calculated from their equality to the radiant heat flows. Under flight conditions, this equality can be guaranteed by appropriate adjustment of speed and altitude (air density). The surface emissivity ε and its temperature, which will be the equilibrium temperature in this case, are assigned for this purpose.

Having found the radiative heat flow $\sigma\varepsilon T_{w1}^4$ and introduced it into (XIV-5-4), we determine the required relation between velocity and air density and, consequently, between velocity and altitude. Under these flight conditions, cooling is by radiation from the heated surface.

At moderate supersonic speeds, the specific heat flow at the total stagnation point on the nose can be calculated by the formula

$$q_0 = 0.763\,\mathrm{Pr}_2^{-0.6}\sqrt{\rho_2\mu_2\tilde{\lambda}}\,c_p(T_r - T_{w1}), \qquad \text{(XIV-5-2")}$$

where $\lambda = (\partial V_\delta/\partial x)_{x=0}$ can be set equal to $(3/2)V_\infty/R_b$ (as for an incompressible fluid) or calculated by (VI-3-16).

According to experimental data, the specific heat flow at the stagnation point on a flat face is

$$q_{0s} = (0.55 \pm 0.05)\,q_{0sp}. \qquad \text{(XIV-5-5)}$$

Influence of vorticity in the external flow. The above heat-flow relationships were obtained for uniform flow in the "inviscid" layer next to the wall and, consequently, zero vorticity-controlled velocity gradients across the layer. Actually, however, the velocity is not constant, but increases from the value at the wall, /579

which corresponds to the stagnation parameters behind a normal shock, to a certain value on the conventional layer boundary, so that vorticity appears in the flow.

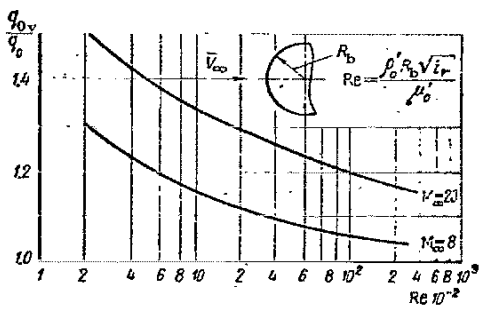

Figure XIV-5-1. Influence of Vorticity on Heat Transfer at the Critical Point. $i_r = V_\infty^2/2$; T_r = 2000°K.

Vorticity has its effects at every point on the surface, including the total-stagnation point; the ratio of the heat flow q_{0V} calculated with consideration of this effect to the q_0 found when vorticity is disregarded depends on a number of factors, including M_∞ and altitude.

Calculations have shown, for example, that at M_∞ = 20, this ratio q_{0V}/q_0 has the respective values 1.3 and 1.04 at the critical point on a hemisphere at altitudes of 90 and 60 km. The vorticity effect can therefore be disregarded for all practical purposes in the dense atmosphere, but in the thin layers it is advisable to correct the calculated heat transfer, increasing it slightly.

The most important parameter determining the influence of vorticity on heat transfer is the Reynolds number, calculated from the sphere radius and the gasdynamic characteristics at the critical point:

$$\mathrm{Re} = \frac{R_b \rho_0' \sqrt{i_r}}{\mu_0'}.$$

It must be remembered in determining this number that we can set $i_r = 0.5V_\infty^2$ for high velocities. Figure XIV-5-1 shows an experimental plot of the ratio q_{0V}/q_0 as a function of Re for two values of M_∞ = 8 and 20; this diagram can be used in refining the heat-flow value. We see that the vorticity effect is considerably smaller for M_∞ = 8 than for M_∞ = 20. The data of Fig. XIV-5-1 were obtained for a temperature T_0' = 2000°K at the critical point. The influence of vorticity increases with temperature. However, this increase is slight even for a substantial temperature rise. For example, when the temperature increases by 1000°K, heat transfer from the vorticity effect increases by only 3-4%.

Radiant flux from an overheated shock layer. The radiant heat flux in the neighborhood of the critical point can be calculated by the formula $q_{rad} = f(\varepsilon s_0)\sigma(T_0')^4$ if the wave detachment

distance s_0 is determined with consideration of the shape of the nose in three dimensions. At the same time, an experimental relationship can be used for the specific heat flow due to radiation of the gas in the neighborhood of the critical point of a sphere:

$$q_{rad} = 2.12 \cdot 10^7 R_b \left(\frac{V_\infty}{10^4}\right)^{8.5} \left(\frac{\rho_\infty H}{\rho_{\infty g}}\right)^{1.6} \frac{\text{kcal}}{\text{m}^2\text{s}}, \qquad \text{(XIV-5-6)}$$

or

$$q_{rad} = 89 \cdot 10^9 R_b \left(\frac{V_\infty}{10^4}\right)^{8.5} \left(\frac{\rho_\infty H}{\rho_{\infty g}}\right)^{1.6} \text{W/m}^2,$$

where R_b is in meters and V_∞ in m/s.

By determining the equivalent radius, we can calculate the radiant flux at the critical point of a nonspherical nose section, e.g., for a flat face.

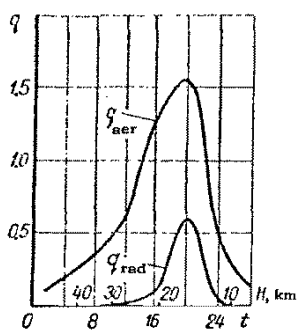

Figure XIV-5-2. Comparison of Aerodynamic and Radiant Heat Fluxes at Critical Point of Sphere. t is flight time in seconds and q is the heat flow (kcal/s·cm^2).

Figure XIV-5-2 shows a typical distribution of the radiant q_{rad} and aerodynamic q_{aer} heat fluxes on the trajectory for certain flight conditions. It can be noted that the radiant flux is greater at low altitudes. Its maximum corresponds to the maximum of the aerodynamic heat flow and represents about one-third of this maximum value. /580

Influence of diffusion. The influence of diffusion on heat transfer was examined in §IV-8. The variation of specific heat flow in the presence of diffusion is given by (IV-8-57), in which the catalytic coefficient ϕ takes account of the finite recombination rate. The largest amount of additional heat liberated by diffusion corresponds to infinite recombination rate, at which the coefficient $\phi = 1$ and, consequently,

$$q_{max} = q_c \left[1 + (\text{Le}^{2/3} - 1)\frac{i_D}{i_r}\right]. \qquad \text{(XIV-5-7)}$$

By way of example, let us estimate the maximum heat flow for infinitely fast catalysis and $M_\infty = 15$, $p_\infty = 0.1$ kg/cm^2 ($0.981 \cdot 10^4$ N/m^2) (an altitude $H \simeq 16$ km in the atmosphere corresponds to

this pressure). From the initial data, we calculate the pressure at the critical point: $p_0' = \overline{p}_0 k M_\infty^2 p_\infty/2$ = 30 kg/cm^2 ($29.4 \cdot 10^4$ N/m^2). The enthalpy at this point is

$$i_r = \frac{AV_\infty^2}{2g} = \frac{a_\infty^2 M_\infty^2 A}{2g} = 2430 \text{ kcal/kg} \quad (1018 \cdot 10^4 \text{ J/kg}).$$

We find the temperature T_r = 5500°K from Fig. III-1-3 for this value of i_r and the pressure p_0'. The corresponding enthalpy of the undissociated gas is

$$i_{\alpha=0} = c_{p\infty}\left(\frac{T_r}{T_\infty}\right)^{\varphi} T_r = 1780 \text{ kcal/kg} \quad (7460 \cdot 10^3 \text{ J/kg}).$$

Consequently, the dissociation enthalpy

$$i_D = i_r - i_{\alpha=0} = 2430 - 1780 = 650 \text{ kcal/kg} \quad (2720 \cdot 10^3 \text{ J/kg})$$

and the ratio i_D/i_r = 0.267. If we take Le = 1.45, the diffusion effect is determined according to (XIV-5-7) as q_{max}/q_c = 1.075.

At very high velocities, the ratio i_D/i_r closely approaches unity. If we set i_D/i_r = 1, then for ϕ = 1 the ratio q_{max}/q_c = = $Le^{2/3}$. For Le = 1.45, we have q_{max}/q_c = 1.28, i.e., the largest increase in heat flow is 28%. According to experimental data, the heat-transfer parameter, which takes diffusion into account, is.

$$\frac{Nu}{\sqrt{Re}} = 0.763 \, Pr^{0.4} (\overline{\rho_{w1}\mu_{w1}})^{-0.4} \left[1 + (Le^{0.52} - 1)\frac{i_D}{i_r}\right]. \qquad \text{(XIV-5-8)}$$

Formulas (XIV-5-3) must be used to calculate the specific heat flow from this parameter.

§XIV-6. CURVILINEAR BLUNTED SURFACE

/581

Laminar Heat Transfer

The case of thermodynamic equilibrium. Let us examine certain relationships that enable us to calculate the heat flow at an arbitrary point on a given curvilinear surface for thermodynamic equilibrium conditions. For this purpose, we shall use a formula that determines the ratio of the heat flow q at an

arbitrary point to its value q_0 at the total-stagnation point [50]:

$$\frac{q}{q_0}=\frac{F}{F_0}=\frac{1}{2}\frac{(p/p_0')\,V_\delta r}{\left[\int_0^x (p/p_0')\,V_\delta r^2\,dx\right]^{1/2}}\sqrt{\frac{1}{\tilde{\lambda}}}. \qquad \text{(XIV-6-1)}$$

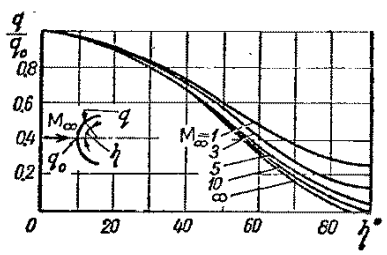

Figure XIV-6-1. Distribution of Heat Flow over Surface of Sphere (Laminar Boundary Layer). T_{w1} = const, $T_{w1}/T_\delta \ll 1$.

Hemisphere. Studies indicate that the heat-flow distribution over a spherical surface, calculated on the basis of (XIV-6-1) and the Newtonian pressure law $p = p_0 \cos^2 \eta$, agrees satisfactorily with experimental data for M_∞ of the order of two and larger. To calculate the heat flow, we shall bear in mind that the law of velocity variation with central angle on this surface is very close to linear up to $\eta = 75\text{-}80°$. We shall therefore assume henceforth that the velocity on the outer edge of the boundary layer $V_\delta = \tilde{\lambda} R_b \eta$. Remembering that

$$dx = R_b\,d\eta;\quad r = R_b \sin\eta,$$

and that according to the Newton formula, the pressure ratio at high velocities is

$$\frac{p}{p_0'}=\cos^2\eta+\frac{p_\infty}{p_0'}\sin^2\eta=\cos^2\eta+\frac{1}{kM_\infty^2}\sin^2\eta,$$

we write (XIV-6-1) in a more concrete form:

$$\frac{q}{q_0}=2\eta\sin\eta\left[\left(1-\frac{1}{k_\infty M_\infty^2}\right)\cos^2\eta+\frac{1}{k_\infty M_\infty^2}\right]D^{-1/2}, \qquad \text{(XIV-6-2)}$$

where the function

$$D=\left(1-\frac{1}{kM_\infty^2}\right)\left(\eta^2-\frac{\eta\sin 4\eta}{2}+\frac{1-\cos 4\eta}{8}\right)+ \\ +\frac{4}{k_\infty M_\infty^2}\left(\eta^2-\eta\sin 2\eta+\frac{1-\cos 2\eta}{2}\right). \qquad \text{(XIV-6-3)}$$

When $(k_\infty M_\infty^2)^{-1} \ll 1$, the following simpler expression can be used to evaluate the heat-flow distribution:

$$\frac{q}{q_0} = 2\eta \sin\eta \cos^2\eta \left(\eta^2 - \frac{\eta \sin 4\eta}{2} + \frac{1-\cos 4\eta}{8}\right)^{-1/2}. \qquad \text{(XIV-6-4)}$$

It is readily seen that this expression defines the heat flow exactly in the extreme case of $M_\infty = \infty$. In real cases, (XIV-6-4) can be used for $M_\infty > 10$; this is confirmed by Fig. XIV-6-1, which shows a family of curves plotted according to (XIV-6-2) and (XIV-6-4) on the assumption that the wall temperature is constant and quite low ($T_{w1}/T_\delta \ll 1$) at all points on the surface. These curves show that heat transfer reaches a maximum at the critical point and decreases on more remote zones of the hemisphere as a result of the lower densities. /582

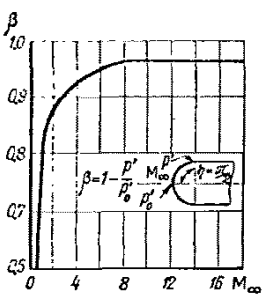

Figure XIV-6-2. Pressure Parameter β as a Function of M_∞.

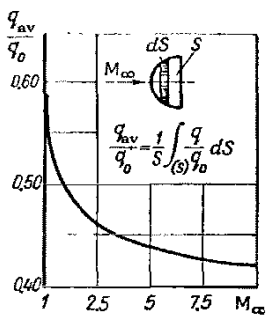

Figure XIV-6-3. Average Heat Flow to Hemispherical Surface (Laminar Boundary Layer).

Improvement based on experimental data [16]. Formula (XIV-6-2) reflects the real distribution of heat flows quite satisfactorily for the large M_∞ at which the relation $p_\infty/p_0' = (k_\infty M_\infty^2)^{-1}$ applies. However, the formula is not accurate enough for moderate velocities, especially for the segment of the surface near the point with coordinate $\phi = 90°$, where the effective heat-flow values are larger than those determined theoretically by (XIV-6-2). This is because the static pressure here is somewhat higher than atmospheric, which is obtained from the approximate Newtonian formula.

To improve (XIV-6-2), let us take the pressure distribution

$$\frac{p}{p_0'} = 1 - \left(1 - \frac{p'}{p_0'}\right)\sin^2\eta \qquad \text{(XIV-6-5)}$$

for the sphere, with p' representing the pressure at the $\eta = 90°$ point.

With this expression, Formula (XIV-6-4) becomes

$$\frac{q}{q_0} = \frac{(1-\beta\sin^2\eta)\,\eta\sin\eta}{[F_1(\eta)+\beta F_2(\eta)]^{1/2}}. \qquad \text{(XIV-6-6)}$$

In this formula, we have introduced the nomenclature

$$\left.\begin{aligned} \beta = 1-\frac{p'}{p_0'};\ F_1(\eta) = \eta^2 - \eta\sin 2\eta + \sin^2\eta; \\ F_2(\eta) = -\frac{1}{2}\left[\frac{3}{2}\eta^2 - \eta\sin 2\eta\left(\frac{3}{2}+\sin^2\eta\right)+\frac{3}{2}\sin^2\eta+\frac{1}{2}\sin^4\eta\right]. \end{aligned}\right\} \qquad \text{(XIV-6-7)}$$

The experimental dependence of the function β on M_∞ (Fig. XIV-6-2) indicates that β is practically constant for $M > 6$. The sharpest variation of β is observed at $M_\infty < 3$. At the corresponding velocities, therefore, the ratio of heat flows q/q_0 also varies considerably with pressure. Heat-flow studies made for $M_\infty > 10$, $i_{w1} < i_0$ and equilibrium-dissociation conditions ([66], 1966, No. 2) have shown that the distribution of q/q_0 can be approximated by the formula /583

$$\frac{q}{q_0} = 0.55 + 0.45\cos\eta. \qquad \text{(XIV-6-8)}$$

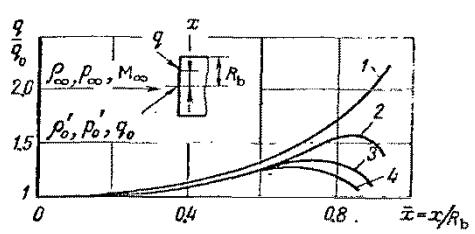

Figure XIV-6-4. Distribution of Heat Flow on Flat Face (Laminar Boundary Layer): Values of ρ_∞/ρ_0': 1) 0.05; 2) 0.15; 3) 0.25; 4) 0.35.

This formula is universal and also applies for low velocities and arbitrary i_{w1} if these values correspond to a strongly cooled wall.

The average value q_{av}/q_0 for the bluntness can be calculated from the pressure distribution around a sphere. Figure XIV-6-3 shows the variation of this quantity as a function of M_∞.

Flat face. Calculations indicate that the heat flows to a flat surface are considerably smaller than those to a spherical surface. This is explained not only by the smaller area of the flat face, but also by more intensive deceleration of the flow on it, one consequence of which

is a substantial decrease in velocity and the longitudinal gradient $\tilde{\lambda}$ at the outer edge of the boundary layer.

If the distribution pattern of the flow parameters is known, an approximate notion of the variation of q/q_0 can be obtained with Formula (XIV-6-1), in which we must set $r = x$. Figure XIV-6-4 shows the results of a calculation of this change for several values of ρ_∞/ρ_0' with different corresponding free-stream velocities. At very high M_∞ (curve 1, density ratio for total-stagnation point $\rho_\infty/\rho_0' = 0.05$), the specific heat flows increase with the approach to the sharp edge of the face. This is explained by the dominating influence of the pressure (density) rise in increasing the heat flows, which are to some extent diminished by the increase in velocity near the sharp edge.

As the flow velocity is lowered, the nature of the specific-heat-flow distribution changes (curves 2, 3, and 4, which correspond to density ratios $\rho_\infty/\rho_0' = 0.15$, 0.25, 0.35).

Up to a certain value of $\bar{x} = x/R_b < 1$, the ratio q/q_0 increases; it reaches a maximum at a certain $\bar{x}$, which depends on M_∞, and then decreases.

The decrease in specific heat flow is explained by the fact that the pressure decrease near the sharp edge may be a decisive factor at comparatively modest flow velocities and, despite the velocity increase, the heat flow begins to drop off after reaching a certain maximum.

Formula (XIV-6-1) can be used for approximate evaluation of the heat-flow distributions around arbitrary blunted surfaces with a given generatrix shape $r = f(x)$.

For this purpose, it is first necessary to calculate the distributions of the pressure p and the V_δ of inviscid flow over the blunt surface for given flight conditions (M, altitude H), remembering that the stagnation pressure p_0' is found for the conditions behind the "normal" part of the shock wave. The velocity and pressure distributions thus found are used to calculate the integral $\int_0^x \frac{p}{p_0'} V_\delta r^2 dx$. Then, having determined the velocity gradient $\tilde{\lambda}$ at /584

the total-stagnation point from the velocity distribution, we find the ratio of specific heat flows q/q_0 at the particular point on the surface of the blunt nose at the total-stagnation point. Figure XIV-6-5 shows the results of such a calculation for a flat face with a circular bevel of radius $r = 0.25R_b$. It also shows experimental data indicating that the rounding has some effect on the heat-flow distribution as compared with the flat face, but that the trend to increasing heat transfer with the approach to

the edge that is characteristic for a flat face in flow at very high M_∞ is nevertheless preserved.

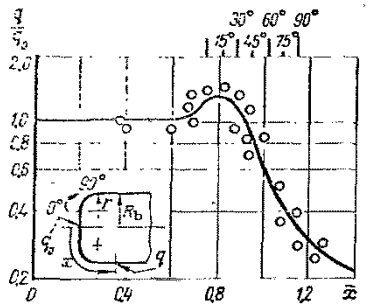

Figure XIV-6-5. Distribution of Heat Flow on Flat Face with Rounded Edges (Laminar Boundary Layer). o) experiment; ———) according to (XIV-6-1).

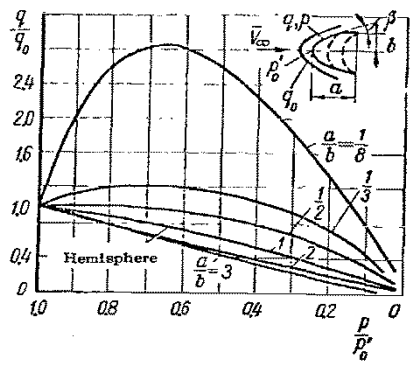

Figure XIV-6-6. Heat Transfer on Ellipsoid of Revolution.

$$p/p_0' - 1 = \frac{p_0' - p_\infty}{p_0'} \sin^2\beta$$

A significant decrease in the gas density where the blunted nose meets the cylindrical surface ($\bar{x} = x/R_b > 1$) causes a sharp decrease in the heat flows. The specific flow on the cylindrical surface is less than 10% of the value at the total-stagnation point, and can be calculated with some approximation for the conditions of flow around a flat plate.

Ellipsoid of revolution. Formula (XIV-6-1) can be used to calculate laminar heat transfer in flow around variously shaped solids of revolution. The results of this calculation, which show the variation of q/q_0 as a function of the dimensionless pressure on ellipsoids with various semiaxis ratios a/b, are shown in Fig. XIV-6-6. Small a/b ratios correspond to blunt noses with higher drag, while large a/b represent bodies with lower drag.

The heat flow at the critical point of an ellipsoid can be calculated, for example, by (XIV-5-4), in which $\sqrt{R_b}$ must be replaced by $\sqrt{b^2/a}$. Then the heat transfer can be found at any point on the surface from the diagram of Fig. XIV-6-6. The dimensionless pressure at this point is determined from the Newtonian theory or from experimental data.

Conical surface. Let us consider the calculation of heat flow on the surface of a truncated cone with a spherical nose. We shall assume that the "inviscid" gas parameters are constant /585

on the conical surface and equal to their corresponding values at the end of the sphere. For example, the velocity

$$V_\delta = \bar{\lambda} R_b \eta_c = \bar{\lambda} R_b \left(\frac{\pi}{2} - \beta_c\right),$$

and the pressure ratio

$$\frac{p}{p_0'} = \cos^2 \eta_c + \frac{1}{k_\infty M_\infty^2} \sin^2 \eta_c .$$

The radial coordinate of an arbitrary point on the surface of the cone $r = x_c \sin \eta_c$, where x_c is the distance along the surface measured from the imaginary apex of the sharp cone and defined by the relation

$$\frac{x_c}{R_b} = \operatorname{ctg} \beta_c + \frac{x}{R_b} - \left(\frac{\pi}{2} - \beta_c\right).$$

We can now substitute the above relationships for V_δ, p/p_0', and $\underline{r}$ into Formula (XIV-4-2). The integral in the denominator, which is definite in the range from 0 to x_c, is evaluated as the sum of two integrals: one with limits 0 and $x = R_b \eta_c$ (or for angles from 0 to η_c) and the other with the limits R_b cot β_c and x_c. The first integral corresponds to the heat flow at the end of the spherical segment (or, which is the same thing, at the beginning of the conical surface). Clearly, the heat-flow distribution on the forward curvilinear surface is the same as that obtained earlier for a sphere. The second integral

$$\int_{R_c \operatorname{tg} \eta_c}^{x_c} G x_c^2 \, dx_c = \frac{G}{3} (x_c^3 - R_b^3 \operatorname{tg}^3 \eta_c),$$

where the function

$$G = \bar{\lambda} R_b \eta_c \sin^2 \eta_c \left(\cos^2 \eta_c + \frac{1}{k_\infty M_\infty^2} \sin^2 \eta_c\right),$$

and the angle $\eta_c = \pi/2 - \beta_c$. After simple manipulation, we obtain for the heat flows

$$\frac{q}{q_0} = \frac{A \bar{x}_c}{\sqrt{B + \bar{x}_c^3}}, \qquad \text{(XIV-6-9)}$$

where

$$A(\beta_c)=\frac{\sqrt{3}}{2}\left\{\left[\left(1-\frac{1}{k_\infty M_\infty^2}\right)\sin^2\beta_c+\frac{1}{k_\infty M_\infty^2}\right]\left(\frac{\pi}{2}-\beta_c\right)\right\}^{1/2}; \quad \text{(XIV-6-10)}$$

$$B(\beta_c)=\frac{3}{16}\left[\frac{D(\eta)}{\eta}\right]_{\eta_c}\left[\left(1-\frac{1}{k_\infty M_\infty^2}\right)\sin^4\beta_c+\frac{\sin^2\beta_c}{k_\infty M_\infty^2}\right]^{-1}-\operatorname{ctg}\beta_c. \quad \text{(XIV-6-11)}$$

The function D that appears in the last expression is determined from (XIV-6-3) for $\eta = \eta_c$. The dimensionless quantity $\bar{x}_c$ in (XIV-6-9) is equal to x_c/R_b. It must be remembered that the relation is valid only on the cone, i.e., for $\bar{x}_c \geq \cot \beta_c$.

On the basis of the above formulas, we can calculate the heat-flow distribution in the extreme case with $M_\infty \to \infty$. The corresponding relationships for the functions $A(\beta_c)$ and $B(\beta_c)$ become

$$A(\beta_c)=\frac{\sqrt{3}}{2}\sin\beta_c\left(\frac{\pi}{2}-\beta_c\right)^{1/2}; \quad \text{(XIV-6-10')}$$

$$B(\beta_c)=\frac{3}{16\sin^4\beta_c}\left[\frac{D}{\eta}\right]_{\eta_c}-\operatorname{ctg}^2\beta_c. \quad \text{(XIV-6-11')}$$

These formulas can be used in practical cases if $M_\infty \sin \beta_c >> 1$. Figure XIV-6-7 shows curves plotted by the formulas (XIV-6-9)-(XIV-6-11) for a strongly cooled surface ($T_{w1} << T_\delta$). It also shows results calculated by (XIV-4-3) for the surface of the equivalent sharp cone, on which the velocity is computed by the expression $V_c = \tilde{\lambda} R_b \eta_c$. /586

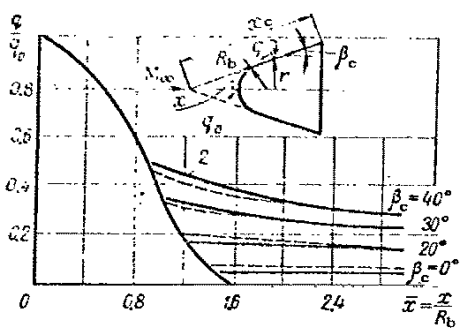

Figure XIV-6-7. Distribution of Heat Flow Along Surface of Blunted Cone (Laminar Boundary Layer). $T_{w1}/T_\delta < 1$; T_{w1} = const; $M_\infty \sin \beta_c >> 1$; 1) according to (XIV-4-3); 2) according to (XIV-6-9).

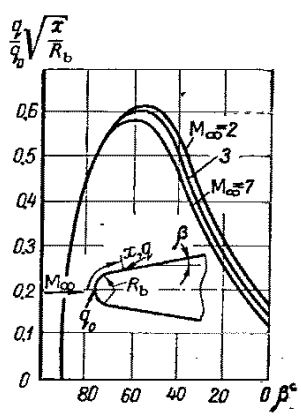

Figure XIV-6-8. Laminar Heat Transfer Parameter.

We see from Fig. XIV-6-7 that for angles β_c = 30 and 40°, the heat-flow distributions on the blunt and equivalent sharp cones are practically the same, while those on the surfaces of slender blunt bodies are smaller than on the surfaces of the corresponding equivalent cones.

Analysis of (XIV-6-9) indicates that the heat flow on surface areas downstream of the critical point is approximately proportional to $\bar{x}^{-1/2}$. It has therefore become possible to introduce as a heat-transfer parameter the quantity $(q/q_0)\sqrt{x/R_b}$, which depends on the local surface inclination angle β and M_∞. Using the corresponding calculated curve in Fig. XIV-6-8, we can quite easily determine the heat flow both on the surface of the blunt nose and on the peripheral zones. The results obtained from Fig. XIV-6-8 are better for surface regions near the nose.

Influence of dissipation of low-velocity profile. The relationships given above and the conclusions drawn pertain to the case in which dissipation of the low-velocity profile is not taken into account. The presence of dissociation reduces the effect bluntness, and this is manifested in increased heat flows. However, this effect is important for distant areas of the surface on which the heat flow increases to the value corresponding to the sharp cone. The heat flow near the nose will be close to the result of calculation.

The dissipation effect can be estimated by plotting the heat flows calculated for the blunt body near its nose and for the sharp body far from the nose and then drawing an interpolation curve over a certain assigned length. This length must be taken longer for the lower atmosphere than for rarefied layers.

Heat flows on cylindrical surface. When a spherical nose terminates in a cylindrical section, the heat-flow distribution can be calculated by Formulas (XIV-4-1) and (XIV-4-2) if on this section $p/p_0' = (k_\infty M_\infty^2)^{-1}$, $V_\delta = 0.5\lambda R_b \pi$, i.e., when the parameters /587 are taken the same as at the end of the sphere, where $\eta = \pi/2$. Since $r = R_b$ = const on the cylinder, Expression (XIV-4-1) for the heat flows becomes

$$\frac{q}{q_0} = \frac{\pi}{k_\infty M_\infty^2}\left(D_{\eta=\frac{\pi}{2}} + \frac{4\pi}{k_\infty M_\infty^2}\bar{x}_c'\right)^{-1/2}, \qquad \text{(XIV-6-12)}$$

where $\bar{x}_c' = x_c'/R_b$, and x_c' is measured from the beginning of the cylindrical segment. The function $D_{\eta=\pi/2}$ is determined by Formula (XIV-6-3), in which the angle η is set equal to $\pi/2$:

$$D_{\eta=\frac{\pi}{2}}=\frac{\pi^2}{4}+\frac{1}{k_\infty M_\infty^2}\left(\frac{3\pi^2}{4}+4\right). \qquad \text{(XIV-6-13)}$$

If we substitute $p/p_0' = \rho_\delta\mu_\delta/(\rho_0'\mu_0')$ in Formula (XIV-4-2), determine the heat flow q_0 at the critical point from Expression (XIV-5-1), and examine remote enough points on the cylinder, for which $\bar{x}_C >> 1$, we arrive at the relation

$$q=0.27\,\mathrm{Pr}^{-2/3}i_r\sqrt{\frac{\rho_\delta\mu_\delta u_\delta}{x_C'}}, \qquad \text{(XIV-6-14)}$$

which, for the equivalent velocity $u_\delta = 0.5\tilde{\lambda}R_b\pi$, is the same as the formula for the heat flow on a flat plate. At small M_∞, the velocity u_δ makes a close approach to V_δ, and in this case Formula (XIV-6-14) agrees exactly with the formula for the plate.

Experimental studies indicate that heat flows near the plate values are reached on the cylinder even somewhat earlier than would be indicated by the theory, practically at the seam. If we assume Pr = 0.71, the heat-transfer parameter according to Formula (XIV-6-14) in the present case with $u_\delta \approx V_\delta$ is

$$\mathrm{St}\sqrt{\mathrm{Re}}=0.34, \qquad \text{(XIV-6-15)}$$

which agrees with the value for an incompressible medium.

Calculation of heat flow to wall with arbitrary temperature. As we have noted, Relation (XIV-4-1) was derived for constancy of the product $\rho\mu$ across the boundary layer and does not take account of a pressure gradient. This assumption is correct if the wall is strongly cooled. Otherwise, it is necessary to reckon with a variable parameter $\rho\mu$, and the heat transfer will also depend on the parameter β, which is determined by the pressure gradient:

$$\beta=-2\frac{i_{0\delta}}{i_\delta}\frac{1}{\rho_\delta}\left(\int_0^x p_\delta V_\delta r^2\,dx\right)\frac{dp_\delta}{dx}\left(p_\delta V_\delta^2 r^2\right)^{-1}. \qquad \text{(XIV-6-16)}$$

Research has shown that the ratio of the specific heat flow at an arbitrary surface point to its value at the total-stagnation point is determined in this case by the expression

$$\frac{q}{q_0}=\frac{\rho_\delta\mu_\delta V_\delta r}{2\sqrt{\tilde{x}\rho_0'\mu_0'\tilde{\lambda}}}\frac{\varepsilon_{w1}'}{\varepsilon_{w1\,0}'} \qquad \text{(XIV-6-17)}$$

where

$$\tilde{x} = \int_0^x \rho_\delta \mu_\delta V_\delta r^2 \, dx.$$

The ratio

$$\frac{g'_{w1}}{g'_{w1\,0}} = \frac{0.937\,(1-g_{w1})}{1-g_{w1\,0}}\,(1+0.096\sqrt{\beta}). \qquad \text{(XIV-6-18)}$$

The specific heat flow q_0 at the total stagnation point is determined from Formula (XIV-5-2). /588

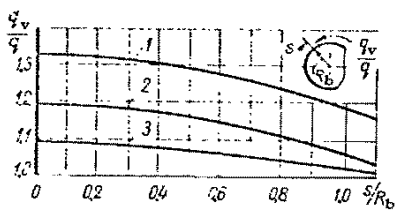

Figure XIV-6-9. Influence of Flow Vorticity on Heat Transfer at Arbitrary Point of Spherical Surface: 1) H = 60 km; M_∞ = = 20; Re = $\rho'_0 R_b \sqrt{i_r}/\mu'_0$ = =1470; k = 1.4; R_b = 0.6 m; 2) T'_0 = 2900°K; Re = = 1000, M_∞ = 8; 3) T'_0 = = 2000°K; Re = 3570; M_∞ = 8.

Influence of vorticity. In our discussion of heat transfer at the critical point, we noted that the influence of vorticity is manifested in increased heat transfer. The same phenomenon is also observed at any other point on the surface.

Figure XIV-6-9 shows results of a study of the vorticity effect under various conditions. With these curves and values of the heat transfer at the critical point, we can construct a tentative curve for given specific conditions and estimate the heat flow q_v with consideration of the vorticity effect at an arbitrary surface point.

Influence of diffusion. Relationships similar to those used in analysis of critical-point heat flows can be used to improve the calculations with consideration of the diffusion effect. Research has shown that one of these relationships might be the expression

$$q = q_c\left[1 + (\mathrm{Le}^{\bar{\beta}} - 1)\frac{i_D}{i_r}\right], \qquad \text{(XIV-6-19)}$$

where q_c, the heat flow without consideration of diffusion at an arbitrary surface point, is calculated in the general case by Formula (XIV-6-17). The exponent $\bar{\beta}$ depends on flow conditions in the boundary layer.

It was shown earlier that this exponent $\bar{\beta}$ = 2/3 at the critical point for "frozen" dissociation, while $\bar{\beta}$ = 0.52 for the

equilibrium process. No exact data on $\bar{\beta}$ are available for peripheral regions of the surface. Approximate calculations indicate that we can set $\bar{\beta} = 2/3$ in the case of "frozen" flow for a strongly cooled flat plate. Comparing the data for the critical point and the plate, we can try the value $\bar{\beta} = 2/3$ for evaluation of the diffusion effect on heat transfer to remote surface areas of a solid of revolution. Here the expression in brackets in (XIV-6-19) can be interpreted as a correction for diffusion applied to the coefficient of friction. Therefore,

$$c_f = c_{f0}\left[1 + (\mathrm{Le}^{\bar{\beta}} - 1)\frac{i_D}{i_r}\right], \qquad \text{(XIV-6-20)}$$

where c_{f0} is the coefficient of friction without allowance for diffusion.

Heat Transfer Across Turbulent Boundary Layer

Method of calculation. In practice, a certain part of the peripheral surface of a blunt body is washed by a turbulent boundary layer. On this part, therefore, heat transfer from the gas to the body increases significantly. By way of illustration, Fig. XIV-6-10 shows experimental results obtained on a cylinder with a spherical nose ([72], 1958, No. 12). We see that in the Re range from $4 \cdot 10^5$ to $6 \cdot 10^5$, the laminar flow (region I) changes to turbulent (region II), and that heat transfer increases by almost five times in this process.

The measurements showed that Formula (IV-8-38) can be used /589
to calculate turbulent heat transfer with the Prandtl number of the laminar boundary layer, although this number will be different in a turbulent flow. The surface-friction coefficient needed for calculations by Formula (IV-8-38) is assumed to be the same as for an incompressible fluid in the case of a strongly cooled surface, and is found for the parameters on the outer edge of the layer on the assumption that the sectionwise velocity distribution in the boundary layer is subject to the seventh-root law.

If the wall is cooled weakly, it is better to use the determining parameters in calculating heat transfer and, consequently, friction. Here the external form of the relationships used remains the same as for the incompressible medium.

On a curvilinear surface with a turbulent boundary layer, the following formula can be used to calculate the heat transfer at moderate supersonic speeds in the neighborhood of the sphere critical point, where the velocity distribution is subject to the law $V_\delta = \lambda x$:

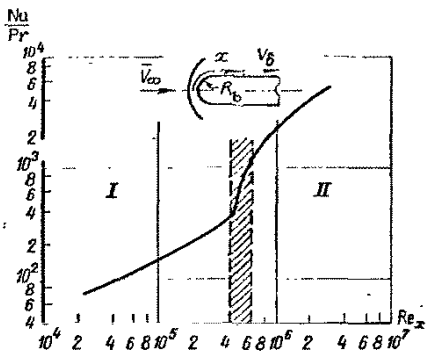

Figure XIV-6-10. Heat Transfer on Cylinder with Spherical Nose Section as a Function of Reynolds Number.

$$Re_x = \frac{\rho_\delta V_\delta x}{\mu_\delta};\quad \frac{Nu}{Pr} = \frac{qx}{\mu_\delta (i_r - i_{w1})};\quad Pr = 0.72$$

$$q = 0.042\,Pr^{-2/3}\,\bar{\lambda}^{4/5}\rho_\delta^{4/5}\mu_\delta^{1/5}x^{3/5}c_p(T_r - T_{w1}). \qquad \text{(XIV-6-21)}$$

At comparatively low Reynolds numbers, the boundary layer is fully laminar and the distribution of specific heat transfer is characterized by a maximum of q at the stagnation point. At high Reynolds numbers, when the boundary layer is turbulized at a certain distance from the stagnation point, we observe a second peak of the heat-transfer rate near the point of passage through the speed of sound. Research has shown [78] that for a relatively cold hemispherical nose section in hypersonic flow with Pr = Le = 1, the ratio of the maximum specific heat transfer $q_{max\ t}$ at the sonic transition point for the turbulent boundary layer to the maximum specific heat flow $q_{max\ l}$ at the stagnation point is

$$\frac{q_{max\ t}}{q_{max\ l}} = 21.1\,(R_b\rho_\infty)^{3/10}, \qquad \text{(XIV-6-22)}$$

where R_b is in meters and the density has the dimensions $kg \cdot s^2/m^4$ and is taken for the appropriate height in the atmosphere. The value of $q_{max\ l} = q_0$ is calculated by (XIV-5-4).

Influence of diffusion. We may expect the heat-transfer mechanism governed by diffusion to be similar to that observed in a fully laminar boundary layer. On this basis, we can use (XIV-6-19), which proceeds from laminar heat transfer theory. According to experimental data, $Le^{\bar{\beta}} - 1$ is put at about 0.4 in this relationship. Accordingly, the relation for calculation of heat transfer on the blunted surface takes the form /590

$$q = q_c\left(1 + 0.4\frac{i_D}{i_r}\right). \qquad \text{(XIV-6-23)}$$

The theory of flow around a flat plate yields useful information on heat transfer at a blunt surface with a small longitudinal pressure gradient. One of the relationships for the

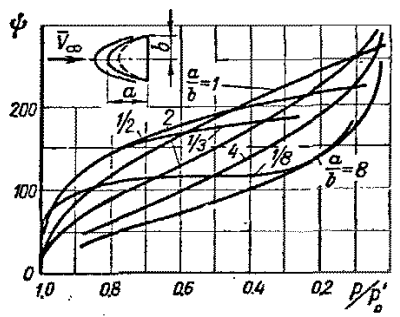

Figure XIV-6-11. Parameter Allowing for Influence of Local Pressure Gradient and Body Geometry on Critical Reynolds Number.

plate, extended to a surface of revolution, takes the form

$$q = A\rho_\delta V_\delta \mathrm{Pr}^{-2/3} \frac{c_{f0}}{2}\left[2\left(\frac{1+\alpha_{w1}}{1+\alpha_\delta}\right)^{1/7} - 1\right]\left[1+(\mathrm{Le}^{\bar{\beta}}-1)\frac{i_D}{i_r}\right](i_r - i_{w1}), \qquad \text{(XIV-6-24)}$$

(for a cone A = $\sqrt[5]{3}$; for a cylinder A ≈ 1).

If we proceed from Formula (XIV-6-19), we must set $\mathrm{Le}^{\bar{\beta}} - 1$ equal to 0.4 and calculate q_t from the expression

$$q_t = A\rho_\delta V_\delta \mathrm{Pr}^{-2/3} \frac{c_{f0}}{2}\left[2\left(\frac{1+\alpha_{w1}}{1+\alpha_\delta}\right)^{1/7} - 1\right](i_r - i_{w1}). \qquad \text{(XIV-6-25)}$$

The dissociation enthalpy, which appears in (XIV-6-24), is calculated for an atomic-molecular mixture of nitrogen and oxygen for degrees of dissociation $\alpha_{w1} \neq 0$ at the wall by the formula

$$i_D = (\alpha_\delta - \alpha_{w1})\frac{\sum\limits_{k=0,N}(c_{c\delta} - c_{c\,w1})\,i_{R\,c}}{\sum\limits_{k=0,N}(c_{c\delta} - c_{c\,w1})}. \qquad \text{(XIV-6-26)}$$

The calculations are simpler for a strongly cooled surface, since $\alpha_{w1} = c_{c\,w1} = 0$. Moreover, $i_{w1} \ll i_r$, so that the influence of the enthalpy of the gas at the wall can be disregarded.

Heat transfer on a blunted nose section. Under certain conditions, a turbulent boundary layer forms on the surface of a blunt nose. The point of transition from laminar to turbulent flow can be determined if we know the critical Reynolds number. Under these conditions, it is preferable to calculate this number for the momentum thickness δ^{**}, i.e., to assume that

$$\mathrm{Re}_{cr} = \frac{V_\delta \rho_\delta \delta^{**}}{\mu_\delta}.$$

Experimental studies made on a series of blunt surfaces in the form of ellipsoids of revolution (including a hemisphere)

gave the critical Reynolds number as

$$\mathrm{Re}_{cr} = 11.2\sqrt{b}\left(\frac{\beta_{\infty H}}{\beta_{\infty v}}\right)^{0.51}\left(\frac{V_\infty}{10}\right)^{0.48}\psi, \qquad \text{(XIV-6-27)}$$

where the dimensions of b, the length of the ellipse semiaxis, are in meters, and velocity is in m/s. The parameter ψ depends on the position of the point being considered on the surface of the body and on the shape of this surface. For example, ψ can be determined from Fig. XIV-6-11 for an ellipsoid.

The momentum thickness for which the critical Reynolds number is determined is calculated by the formula /591

$$\delta^{**} = \frac{\sqrt{2\varepsilon}}{\rho_\delta V_\delta r}\left[0.491\,(1-0.09\beta^{0.4})\left(\frac{\rho_\delta V_\delta}{\rho_{w1}\mu_{w1}}\right)^{0.39}\right], \qquad \text{(XIV-6-28)}$$

where the function ε is given by the formula $\varepsilon = \int_0^x \rho_\delta V_\delta \mu_\delta r^2\,dx$, and the coefficient β is determined from the expression

$$\beta = 2\frac{d\ln V_\delta}{d\ln \varepsilon}.$$

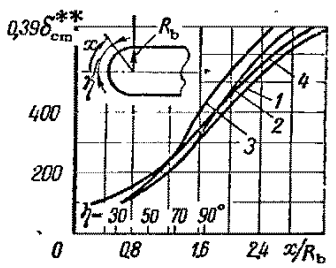

Figure XIV-6-12. Momentum Thickness on Blunt Surfaces with Various Degrees of Cooling. 1) i_0/i_{w1} = = 29.5, M_∞ = 2.5; 2) i_0/i_{w1} = 17.5, M_∞ = = 2.2; 3) i_0/i_{w1} = = 9.5, M_∞ = 1.8; 4) ellipsoid of revolution: i_0/i_{w1} = 17.5, M_∞ = 2.2.

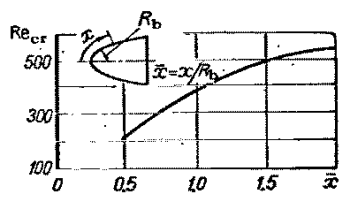

Figure XIV-6-13. Variation of Critical Reynolds Number Along Surface of Cone (the Characteristic Length is the Momentum Thickness).

We see from (XIV-6-28) that the momentum thickness depends on the amount of wall cooling. This is confirmed by experimental results obtained on a cylindrical body with a hemispherical nose (Fig. XIV-6-12).

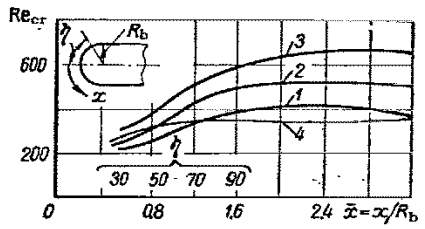

Figure XIV-6-14. Critical Reynolds Number on Cooled Surface. 1) i_0/i_{w1} = 9.5; M_∞ = 1.8; 2) i_0/i_{w1} = = 17.5; M_∞ = 2.2; 3) i_0/i_{w1} = 29.5; M_∞ = 2.5; 4) ellipsoid of revolution: i_0/i_{w1} = 17.5; M_∞ = = 2.2; $Re_{cr} = \rho_\delta V_\delta \delta^{**}/\mu_\delta$.

Having determined Re_{cr} and δ^{**}, we can find the coordinate of the transition point, behind which the heat-transfer processes will be determined by the turbulent flow region in the boundary layer. Here the critical Reynolds number can be found with the experimental curve in Fig. XIV-6-13, which was obtained for a spherical nose with an attached 30-degree cone. The data of this curve correspond to a very strongly cooled wall. The critical Reynolds number depends strongly on the degree to which wall temperature is reduced. The influence of degree of cooling on Re_{cr} can be evaluated from Fig. XIV-6-14, which shows experimental data for a cylinder with a hemispherical nose. The curves in this figure can be used not only for the curvilinear surface of the nose, but also for its periphery. The corresponding relationship between Re_{cr} and the cooling parameter i_0/i_{w1} is presented more palpably in graphical form in Fig. XIV-6-15.

The turbulent heat transfer that occurs behind the transitional zone must be calculated with consideration of the prior history of the boundary layer, i.e., with consideration of the processes that take place upstream in the layer. The corresponding working relationship is similar to the formula for laminar heat transfer and takes the form /592

$$\frac{\tilde{N}u}{\tilde{R}e^{4/5}} = \frac{0.029\,Pr^{1/3}(\bar{\rho}_\delta\bar{\mu}_\delta)^{5/4}\bar{V}_\delta\bar{r}^{1/4}}{\left[\int_0^{\bar{x}}\bar{\rho}\bar{V}_\delta(\bar{r}\bar{\mu}_\delta)^{5/4}\,d\bar{x}\right]^{1/5}}\,\bar{h}_r^{-2/5}, \qquad \text{(XIV-6-29)}$$

where the Nusselt number

$$\tilde{N}u = \frac{qc_{pr}R_b}{\lambda_r(i_r - i_{w1})}. \qquad \text{(XIV-6-30)}$$

$\tilde{R}e$ is given by the formula

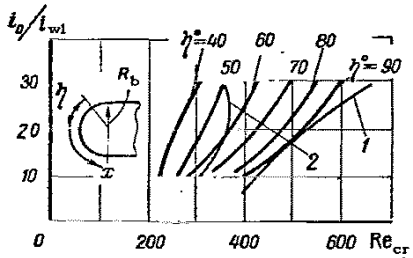

Figure XIV-6-15. Variation of Critical Reynolds Number as a Function of Degree of Cooling. 1) cylinder with sphere, x/R_b = 2.4-3.2; 2) cylinder with ellipsoid, x/R_b = 2.0-3.0.

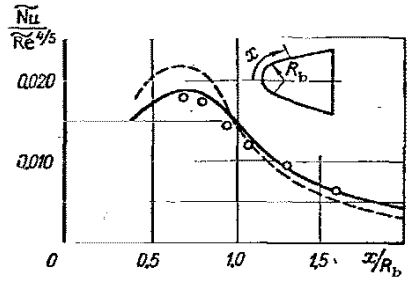

Figure XIV-6-16. Distribution of Turbulent Heat Transfer Parameter. o) experiment.

$$\overline{\mathrm{Re}} = \mathrm{Re}\, h_r^{1/2}; \quad \mathrm{Re} = \frac{\rho_r R_b \sqrt{i_r}}{\mu_r}. \qquad \text{(XIV-6-31)}$$

The density, dynamic-viscosity-coefficient, and velocity ratios are defined thus:

$$\bar{\rho} = \frac{\rho_\delta}{\rho_r}; \quad \bar{\mu}_\delta = \frac{\mu_\delta}{\mu_r}; \quad \bar{V}_\delta = \frac{V_\delta}{\sqrt{i_r}}. \qquad \text{(XIV-6-32)}$$

The parameter that appears in (XIV-6-29) is

$$h_r = \frac{p_\delta'}{\rho_r i_r}. \qquad \text{(XIV-6-33)}$$

All quantities with the subscript r correspond to the recovery enthalpy (temperature) and can be calculated with a certain approximation for stagnation conditions. The linear dimensionless parameters in this formula are referred to the sphere of radius R_b.

As we see from (XIV-6-29), integration begins with the conditions at the critical point, where $\bar{x} = 0$. Here the value sought for the heat-transfer parameter will correspond to the surface zones (or $\bar{x}$-values), that lie behind the point of transition from laminar to turbulent flow. Figure XIV-6-16 presents experimental data and (dashed curve) the results of calculation of the turbulent heat transfer parameter by (XIV-6-29). With the exception of the transitional region, the theoretical results agree satisfactorily with experiment. /593

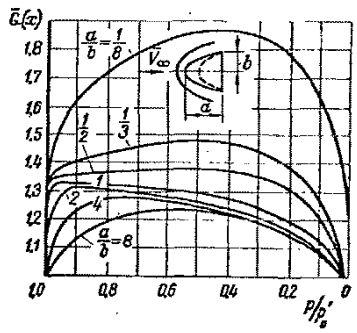

Figure XIV-6-17. Parameter Accounting for Influence of Pressure Gradient and Body Shape on Heat Transfer.

Having computed the heat flow, we can determine the local coefficient of turbulent friction by using the equation that expresses the Reynolds analogy:

$$q = \mathrm{Pr}^{-2/3}\rho_\delta V_\delta (i_r - i_{w1})\frac{c_{f_x}}{2}. \quad \text{(XIV-6-34)}$$

Studies indicate that heat transfer can be calculated on the basis of relationships derived for a thin plate, which, as we know, do not consider the longitudinal pressure gradient. If, moreover, the effect of diffusion in the boundary layer is disregarded, the formulas for the heat-exchange parameter can be used in the form

$$\frac{\bar{\mathrm{Nu}}}{\bar{\mathrm{Re}}^{4/5}} = \frac{0.029\,\mathrm{Pr}^{1/3}}{h_r^{2/5}}\left(\frac{\bar{\rho}_\delta \bar{V}_\delta \bar{x}}{\bar{\mu}_\delta}\right)^{4/5}\frac{\bar{\mu}_\delta}{\bar{x}}, \quad \text{(XIV-6-35)}$$

or

$$\mathrm{Nu}^0 \equiv \mathrm{Nu}_{\mathrm{Le}=1,\,G=1} = 0.029\,\mathrm{Re}_x^{4/5}\mathrm{Pr}^{1/3}. \quad \text{(XIV-6-36)}$$

The results of calculation by (XIV-6-35) are represented by the solid line in Fig. XIV-6-16. Somewhat higher accuracy is obtained if the calculation is made for the determining enthalpy. The latter can be improved by using, instead of (IV-8-7), the expression

$$i^* = 0{,}5i_{w1} + 0.22\,\mathrm{Pr}^{1/3} i_r + i_\delta (0.5 - 0.22\,\mathrm{Pr}^{1/3}), \quad \text{(XIV-6-37)}$$

in which the Prandtl number appears in explicit form. The determining parameters corresponding to this enthalpy are part, for example, of the Reynolds and Nusselt numbers:

$$\mathrm{Re}_x = \frac{\rho^* V_\delta x}{\mu^*};$$

$$\mathrm{Nu} = \frac{q c_p^* x}{\lambda^* (i_r - i_{w1})}. \quad \text{(XIV-6-38)}$$

Further refinement of the above formulas involves consideration of the longitudinal pressure gradient and diffusion. This should be done with the semiempirical relation

$$\frac{\mathrm{Nu}_{\mathrm{Le}\neq 1;\, G\neq 1}}{\mathrm{Nu}^0} = \frac{q_{\mathrm{Le}\neq 1,\, G\neq 1}}{q^0} = 1.037\bar{G}(x)\left[1 + (\mathrm{Le}^{\bar{\beta}} - 1)\frac{i_D}{i_r - i_{w1}}\right]. \quad \text{(XIV-6-39)}$$

The coefficient $\bar{G}(x)$ takes account of the local pressure gradient. As we see from the diagram in Fig. XIV-6-17, $\bar{G}(x)$ depends on the pressure ratio at the particular point of the surface and on the shape of this surface. The expression in brackets is the correction for diffusion. Experimental data indicate that $\mathrm{Le}^{\bar{\beta}} - 1$ can be set equal to 0.58 in this expression.

§XIV-7. COMPARISON OF FRICTION AND HEAT FLOWS ON SHARP AND BLUNT CONES /594

Cone and spherical nose. By way of evaluating the effect of bluntness on total heat flow, it is interesting to determine first the difference between the heat flows on a blunt cone and the corresponding spherical nose (Fig. XIV-7-1). Let us consider laminar heat transfer [50].

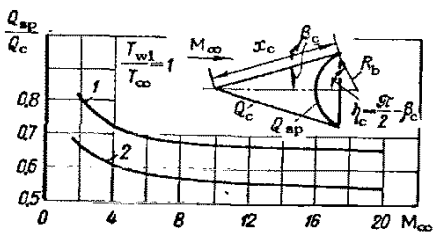

Figure XIV-7-1. Comparison of Heat Flows for Spherical and Conical Noses (Laminar Boundary Layer). 1) $\beta_c = 20°$; 2) $\beta_c = 10°$.

The total of this heat transfer on a sharp cone is determined by Formula (XIV-4-5). The heat flow on the surface of the corresponding inscribed spherical segment can be calculated by the formula

$$Q_{sp} = 0.5 S_{sp} q_0 \int_0^{\eta_c} \left(\frac{q}{q_0}\right) \sin\eta \, d\eta,$$

where the ratio q/q_0 is taken from Formulas (XIV-6-1) or (XIV-6-6) and the area of the spherical segment is

$$S_{sp} = 4\pi R_b^2 = 4\pi x_c^2 \operatorname{tg}^2 \beta_c.$$

The integral upper limit $\eta_c = \pi/2 - \beta_c$. Assigning various flow conditions or, which is the same thing, the system of parameters M_∞, T_{w1}/T_δ, β_c, and x_b, we can determine the ratio of the heat flows on the sphere and the cone, i.e., Q_{sp}/Q_c. Figure

XIV-7-1 presents some of the results of these calculations, which were made for cones with semiapex angles β_c = 10 and 20° for a surface cooled to the free-stream temperature. It follows from these results that the heat flows are smaller for a spherical nose than for a cone.

Conical body with sharp and blunt noses. If the boundary layers on the blunted and sharp conical surfaces are of the same type, the friction and heat-transfer values on the two surfaces will not differ substantially. For example, calculations indicate that the decrease in heat transfer on a blunt cone is no more than 5%.

A substantial advantage of the blunt surface makes its appearance when most of it is covered with a laminar layer, in contrast to the sharpened body, on which the boundary layer is turbulent.

To satisfy ourselves of the above, let us examine the relationships between the coefficients of friction and heat transfer for sharp and blunt cones. According to the formulas for the local coefficients of friction, their ratio is

$$\frac{c_{fb}}{c_{fc}} = \frac{A_b}{A_c} \frac{c_{fb}^{pl}}{c_{fc}^{pl}}, \qquad \text{(XIV-7-1)}$$

where $A_b = \sqrt{3}$, $A_c = \sqrt[5]{3}$.

Then

$$\frac{c_{fb}}{c_{fc}} = 16 \left(\frac{Re_c}{Re_b}\right)^{1/2} Re_c^{-3/10}. \qquad \text{(XIV-7-2)}$$

To evaluate the effect of bluntness on the average coefficient of friction, it is necessary to substitute 25.6 for the coefficient 16 in (XIV-7-2). As we see, we must first find the Reynolds numbers for given points on the blunted and sharp conical surfaces in order to use this formula. /595

To gain an idea of the order of magnitude of the decrease in friction, we can assign certain expected values to these numbers. If, for example, we assume that $Re_c = 10^{10}$ on a sharp cone and $Re_b = Re_c/25$ on a blunt cone, the laminar local and average friction coefficients on the blunt surface will decrease from their values for the turbulent boundary layer by factors of 12 and 7.5, respectively.

Formula (XIV-7-2) can also be used to evaluate the decrease in heat transfer to the blunt surface if we attach to it a relation reflecting the Reynolds analogy. To simplify, we may assume here with some approximation that the Prandtl numbers of the two bodies are the same. Then if $i_{w1} \ll i_r$, the heat-flow ratio is

$$\frac{q_b}{q_c} = 16 \left(\frac{\mathrm{Re}_b}{\mathrm{Re}_c}\right)^{1/2} \mathrm{Re}^{-3/10} \frac{\mu_b}{\mu_c} \frac{c_{p\,b}}{c_{p\,c}} \frac{T_{r\,b}}{T_{r\,c}}. \qquad \text{(XIV-7-3)}$$

Assuming that the last two ratios in the right member vary little, we can calculate the dynamic viscosity coefficient by (III-1-3) and $\mathrm{Re}_b/\mathrm{Re}_c$ by (IV-10-2), and set $n = 3/4$ to obtain a simpler relation for the ratio of local heat flows on the blunt and sharp cones:

$$\frac{q_b}{q_c} = 16 \left(\frac{M_b}{M_c}\right)^{4/5} \mathrm{Re}_b^{-3/10}. \qquad \text{(XIV-7-3')}$$

The coefficient 16 must be replaced by 25.6 in evaluating the ratio of average heat flows. In accordance with (XIV-7-3'), the heat flows may decrease substantially on the blunt body. For example, on a 10-degree cone with $M_\infty = 20$, $M_b = 3$ and $\mathrm{Re}_b = 10^6$, the local heat flow decreases by a factor of 17, and the average flow by a factor of 11. Experimental investigations indicate that the decrease is actually not as great. This is explained basically by the fact that turbulization intervenes before the calculated critical Reynolds number is reached, and the turbulent boundary layer covers a substantial part of the surface, on which the heat flow remains practically the same as on the sharp cone.

Experimental studies indicate that the coefficient of turbulent heat transfer at low flow velocities around a cone [46] is

$$\alpha = \frac{q_{w1}}{T_r - T_{w1}} = 0.022 \frac{\lambda_\infty}{x} \mathrm{Re}_x^{0.8} \beta_c^{0.33}, \qquad \text{(XIV-7-4)}$$

where β_c is the cone angle in radians and x is the distance from the nose along the generatrix to the point at which the heat transfer is determined; $\mathrm{Re}_x = V_\infty x/\nu_\infty$.

Applying (XIV-7-4), we can use (VI-4-6) to determine the temperature of a thin skin at a given time in flight.

§XIV-8. VISCOSITY EFFECT ON EXTERNAL FLOW AROUND A BLUNT BODY

Evaluation of viscous-interaction effect. In studying the influence of viscosity on the parameters of the external (inviscid) flow, and on the static pressure distribution in particular, it is necessary to consider the role of bluntness in shaping the boundary layer. It has been established that if the Reynolds number calculated from the nose diameter D_b by the formula $Re_{D_b} = V_\infty \rho_\infty D_b / \mu_\infty$ is large enough, the effect of pressure in the inviscid flow at a blunt nose becomes dominant, and it is its magnitude and distribution that determine the development of the boundary layer. /596

The back effect of the boundary layer on the external flow is minor. However, this influence becomes stronger with increasing distance from the nose as a result of the increase in boundary-layer thickness. For example, the increase in layer thickness may increase pressure substantially, and this, in turn, influences the boundary-layer variables. Studies have shown that for solids of revolution, the distance L from the blunt nose at which the additional drag due to the pressure increase in viscous interaction becomes commensurate with the bluntness drag is determined by the formula

$$\frac{L}{D_b} = b \frac{Re_{D_b}}{M_\infty^2}, \qquad \text{(XIV-8-1)}$$

where b is a certain coefficient that depends on flow conditions.

As a result of experimental wind-tunnel studies on a heat-insulated cylindrical surface ($T_{w1} = T_r$) at $M_\infty = 15$ it has been found that b is approximately two.

Viscosity has considerably weaker influence under free-stream conditions, at which the temperature is substantially lower than the recovery temperature; as a result, the boundary layer is thinner than on a heat-insulated wall. For example, $b \simeq 20$ at $T_{w1} = 5T_\infty$ and $M_\infty = 15$.

Thus, the effect of the viscous interaction depends on the thermal regime of the wall and on M_∞ and Re_{D_b}. By way of example, let us evaluate this interaction on the surface of a sphere with $D_b = 1$ m for flight at an altitude of the order of 82-83 km at a velocity $M_\infty = 15$. Calculations with these data give $Re_{D_b} = 2640$. For a heat-insulated wall (b = 2), therefore, Formula (XIV-8-1)

gives $L/D_b = 23$, while in the free stream (b = 20) at a wall temperature $T_{w1} = 5T_\infty$, this figure will be ten times larger, i.e., $L/D_b = 230$.

As we see, the viscosity effect can be disregarded at the selected Re_{D_b} for shorter real bodies, i.e., with length ratios L/D_b smaller than those found in the example. With decreasing Re_{D_b} or increasing M_∞, however, the calculated L/D_b may be smaller than the length ratio of the real body, and the viscous interaction will have substantial influence. For example, with $Re_{D_b} = 225$, $M_\infty = 15$ and $T_r = T_{w1}$, the value of $L/D_b = 2$. In this case, the additional nose drag due to the pressure increase associated with increasing boundary layer thickness becomes commensurate with the drag of the nose near the bluntness at a length $L = 2D_b$. These recommendations for calculation of the viscous interaction apply only for large Re_{D_b} and become doubtful for small values of this number. At the present time, it is difficult to state the exact limit of applicability of the theory of this interaction in terms of a certain limiting Re_{D_b}. Isolated data indicate that $Re_{D_b} \simeq 10^2$ might be used as a tentative lower limit.

"Effective" shape of body. Allowing for the effect of viscous interaction on the external-flow parameters consists in calculating the inviscid flow about a body with an "effective" shape obtained by shifting the contour of the given body by an amount equal to the boundary-layer displacement thickness. If we consider distant zones of the body, where the longitudinal pressure gradient is small, the displacement thickness can be calculated with a certain approximation on the basis of the theory of boundary layer near a plate, by use of the Mangler transformation. /597

The generalized formula for the displacement thickness of a laminar boundary layer takes the form

$$\delta^* = \frac{A}{N_1 N_2} x \, \mathrm{Re}_x^n. \qquad \text{(XIV-8-2)}$$

A and n are given in Table VI-1-1. The coefficient $N_1 = 8/3$ for a laminary boundary layer and $N_1 = 8$ for a turbulent one. The coefficient $N_2 = 1$ for a cylinder in flow with either a laminar or a turbulent boundary layer. For a conical surface, it takes various values: in the case of a laminar boundary layer $N_2 = \sqrt{3}$, while for a turbulent one $N_2 = \sqrt[5]{3}$. In Formula (XIV-8-2), Re_x should be calculated for the equivalent velocity computed with

the bluntness taken into account. For spherically blunted body, this velocity is equal to the velocity at the end of the nose, $V_\delta = \lambda R_b \eta_c$, where $\eta_c = \pi 2 - \beta_c$ for a cone and $\eta_c = \pi/2$ for a cylinder. The viscosity and density for which Re_x is calculated are found for a hot, e.g., heat-insulated, wall from the determining temperature, and for a strongly cooled surface ($T_{w1} << T_r$), they are assumed the same as at the outer edge of the boundary layer, i.e., are calculated as inviscid-flow parameters with the bluntness taken into account. The length $\underline{x}$ can be reckoned along the curvilinear generatrix of the nose from the stagnation point.

In practical calculations, Re_x can be calculated by (IV-10-2) or found from the curves in Fig. IV-10-2.

To illustrate application of (XIV-8-2), let us consider calculation of the displacement thickness for a spherically (R_b = = 0.25 m) blunted cone with the angle $\beta_c = 10°$ and a cylinder 10 m long with a strongly cooled wall. We shall take the same flight conditions as in the example given above (M_∞ = 15, H = = 30 m). For a sharp cone 10 m long, $Re = 9 \cdot 10^7$, and the corresponding Reynolds number calculated for the cylinder from the undisturbed parameters is $Re = 5.28 \cdot 10^7$. This cylinder can be regarded as a sharp cone with zero generatrix inclination angle.

The Reynolds numbers obtained are above critical, so that the boundary layer will be turbulent on the sharp surfaces. Since bluntness lowers the Reynolds number on the cone by a factor of 30 and on a cylinder by a factor of 48, the boundary layer is laminarized over practically the entire length and, consequently, (XIV-8-2) can be used. Substituting the smaller Reynolds number into it, we obtain $\delta^* = 7.2$ mm at the end of the cone and $\delta^* = 20.7$ mm at the end of the cylinder. The influence of viscosity will be stronger for turbulent flow. Calculations give $\delta^* = 18.7$ mm for the cone and $\delta^* = 29.3$ mm for the cylinder.

The change in δ^* for a heat-insulated wall is larger than for a cooled wall. Calculations indicate that the determining temperature will be approximately 10 times smaller than at the outer boundary. Considering the variation of ρ and μ with temperature, therefore, the Reynolds number found for the determining parameters is 50 times smaller. Accordingly, the displacement thickness is increased by a factor of about 7 for a laminar boundary layer and by a factor of 2.2 for a turbulent one. A substantial increase in displacement thickness is associated with a decrease in the local Reynolds numbers. Thus, blunting of the body, increase in flight altitude, and an increase in the average boundary-layer temperature are all factors contributing to change in the "effective" shape. /598

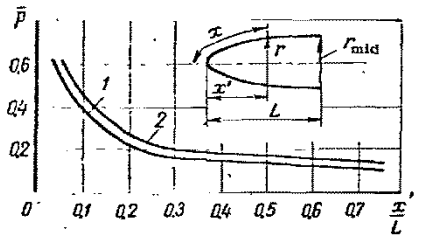

Figure XIV-8-1. Influence of Boundary Layer on Pressure Distribution. 1) inviscid flow; 2) with consideration of boundary-layer effect; $M_\infty = 18.4$; $Re = V_\infty L/\nu_\infty = 3.3 \cdot 10^5$.

After the "effective" shape of the body has been determined by shifting the contour by δ^* in the direction of the normal, the pressure distribution and other "inviscid" parameters are calculated for this new shape. One of the characteristics of the new shape, e.g., for a cone, is its "effective" angle, which can be found approximately by the formula $\beta_c^e = \beta_c + \delta^*/L$, where δ^* is the conventional thickness at the given generatrix length L. If, on the other hand, a cylinder is given, a cone whose angle is δ^*/L can be regarded as its "effective" shape.

Definition of the "effective" shape of a cone or cylinder as a modified surface of revolution with a curvilinear generatrix is more accurate. The "effective" curvilinear contour is also preserved when the body in the flow has a given curvilinear contour.

Pressure can be calculated for the "effective" curvilinear surfaces thus obtained by use of the Newton formula $\bar{p} = \bar{p}_0 \sin^2 \beta^e$, in which the angle $\beta^e = \beta_c + \text{arc tan}\,(d\delta^*/dx)$ for a cone is determined by the inclination of the "effective" generatrix to the free-stream velocity vector.

TABLE XIV-8-1. DRAG OF BLUNT CONE

Drag coefficient and its components	Absolute value	Percent	Drag coefficient and its components	Absolute value	Percent
c_x	0.1300	100	Δc_{xpp}	0.0069	5.3
c_{xp}	0.0427	32.9	Δc_{xfp}	0.0037	2.8
c_{xf}	0.0643	49.5	Δc_{xfc}	0.0063	4.8
c_{xwke}	0.0061	4.7			

For zones of the body far enough from the blunting, Formula (XIV-8-2) can be used to calculate the increment $\Delta\beta = \text{arc tan}\,(d\delta^*/dx)$ in the inclination angle of the contour that results from the displacement-thickness effect. Differentiating with respect to x,

$$\frac{d\delta^*}{dx} = \frac{A(n+1)}{N_1 N_2} \mathrm{Re}_x^n. \qquad \text{(XIV-8-3)}$$

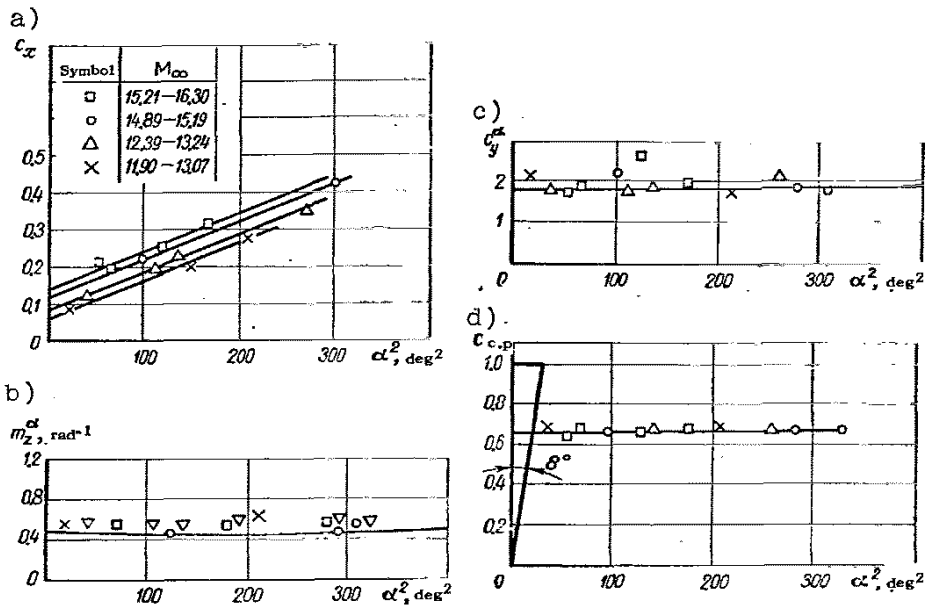

Figure XIV-8-2. Aerodynamic Characteristics of a Cone with Small Spherical Bluntness ($\beta_c = 8°$, $R_b/r_{bse} = 0.035$).

For a slender body, the "effective" contour inclination angle $\beta^e = \beta_c + d\delta^*/dx$. Figure XIV-8-1 shows the influence of the boundary layer on pressure distribution in the example of a helium flow over the surface of a power-law solid of revolution. The substantial increase in pressure due to the viscous interaction is explained by the very large M_∞, the comparatively small Re, and the presence of a heat-insulated surface.

Drag is increased not only by an increase in free-stream pressure, but also by an increase in the friction governed by the influence of induced pressure on the boundary layer. As a result, the over-all drag coefficient will be determined by the relation

$$c_x = c_{xp} + c_{xf} + c_{x\,wke} + \Delta c_{xpp} + \Delta c_{xfp} + \Delta c_{xfc},$$

where c_{xp}, c_{xf} and $c_{x\ wke}$ are the coefficients of pressure drag, friction drag, and the drag in question, respectively, calculated without consideration of viscous interaction and Δc_{spp} and Δc_{xfp} are the coefficients of the additional drags caused by the changes

in pressure and friction, respectively, as a result of the viscous interaction.

The coefficient Δc_{xfc} characterizes the change in friction drag due to the transverse curvature of the body. Table XIV-8-1 lists calculated results for the components of the drag coefficient of a spherically blunted cone with the angle $\beta_c = 8°$ and the degree of blunting $R_b/r_{wke} = 0.035$ for the conditions $M_\infty = 15.3$ and $Re = V_\infty R_b/\nu_\infty = 8.4 \cdot 10^4$ ([70], 1964, No. 11). /599

The over-all c_x given in Table XIV-8-1 agrees well with the experimental value $c_x = 0.1290$. Analysis of the total-drag components indicate that the drags $c_{xp} + c_{xf} + c_{x\ wke}$, calculated without consideration of the viscous interaction, make up most of it (87.1%). The additional drag components due to the viscous interaction and the transverse curvature of the surface can be estimated in practical cases on the basis of the data in Table XIV-8-1.

Figure XIV-8-2 presents experimental data on the aerodynamic coefficients for a cone with a slight spherical bluntness ($\beta_c = 8°$, $R_b/r_{wke} = 0.035$) for various hypersonic M_∞. These data were obtained with consideration of viscous interaction. The frontal-drag coefficient varies as a square-law function of attack angle and increases with M_∞. The static derivatives c_y^α, m_z^α and the center of pressure coefficient $c_{c.p} = x_{c.p}/x_b$ can be regarded as independent of attack angle and Mach number. /600

Part Four /601

AERODYNAMIC CHARACTERISTICS OF THE FLIGHT VEHICLE /602

Chapter XV /603

STEADY-STATE FLOW

§XV-1. CALCULATION OF AERODYNAMIC COEFFICIENTS WITH CONSIDERATION OF INTERFERENCE FOR A SLENDER BODY-WING COMBINATION

General Definitions

A solid of revolution or a body with some other geometrical shape used as a design element of a vehicle may be fitted with wings, tail, and control elements.

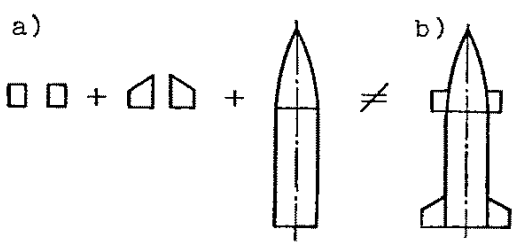

Figure XV-1-1. Scheme of Interference Between Body and Wing and Tailplanes Mounted on it. a) isolated elements; b) elements combined into one configuration.

The complex and still inadequately developed problem of allowing for the interference between the various elements of the vehicle arises in study of the aerodynamics of bodies in combination with lifting, stabilizing, and control surfaces.

As a result of interference, the sum of the aerodynamic forces and moments taken separately for the (isolated) wing and body, tail and body, body, wing and tail, etc., is not equal to the complete force or moment of the combination consisting of the corresponding elements and forming a single whole (Fig. XV-1-1). Thus, when the individual elements - body, wings, tail, control surfaces - are combined into a single vehicle design, they lose, so to speak, their individual aerodynamic characteristics and acquire new ones as a result of interference.

The over-all aerodynamic characteristics of a vehicle can be defined as the sum of these characteristics for the isolated component elements plus added amounts known as interference corrections. In the particular case examined below, the corrections arise from interference between a body and a wing. Accordingly, the normal force of the body-wing combination (Fig. XV-1-2) is presented in slender-body aerodynamic theory [51] in the form

$$N_{b.wg} = N_b + N_{wg} + \Delta N_b + \Delta N_{wg},$$

where the first two terms represent the normal forces for the isolated body and wing, respectively, ΔN_b is the additional normal force of the body that is governed by the wing, and ΔN_{wg} is the additional wing normal force due to interference with the body. /604
Let us introduce the nomenclature $\Delta N_b = N_{b(wg)}$ and $N_{wg} + \Delta N_{wg} = N_{wg(b)}$ (normal force of wing in presence of body). Then

$$N_{b.wg} = N_b + N_{b(wg)} + N_{wg(b)}. \qquad \text{(XV-1-1)}$$

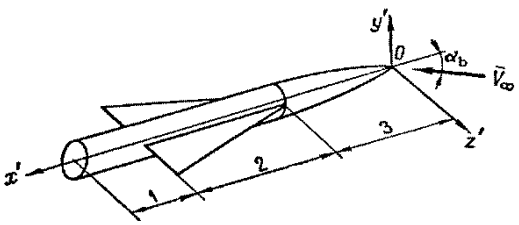

Figure XV-1-2. Principal Parts of Wing-Body Combination ($\phi = 0$, $\alpha_b \neq 0$); 1) tail section; 2) wing section; 3) nose section.

For convenience in the calculations, the last two terms in (XV-1-1) can be written

$$N_{wg(b)} = K_{wg} N_{wg}; \qquad \text{(XV-1-2)}$$

$$N_{b(wg)} = K_b N_{wg}, \qquad \text{(XV-1-3)}$$

where N_{wg} is the normal force of the isolated wing and K_b and K_{wg} are interference coefficients. An isolated wing is a wing consisting of the two cantilevers joined together.

According to Formulas (XV-1-2) and (XV-1-3), the normal force of the body-wing combination is

$$N_{b.wg} = N_b + (K_b + K_{wg}) N_{wg}. \qquad \text{(XV-1-4)}$$

In the presence of roll, an additional interference effect arises and changes the wing normal force. The normal-force increment is

$$\Delta N_{wg} = \overline{K}_\varphi N_{wg}, \qquad \text{(XV-1-5)}$$

where $\overline{K}_\phi$ is the interference coefficient governed by the roll.

The total normal force with roll is

$$N_{b.wg} = N_b + (K_b + K_{wg} + \overline{K}_\varphi) N_{wg}. \qquad \text{(XV-1-6)}$$

The expression for the moment can be presented similarly. Thus, calculation of the reciprocal effect between the body and the wing involves determination of interference coefficients. The body normal force is

$$N_b = K_{b.i} N_{wg}, \qquad \text{(XV-1-7)}$$

where $K_{b.i}$ is a certain coefficient linking the normal forces of the isolated body and wing. Thus,

$$N_{b.wg} = (K_{b.i} + K_b + K_{wg} + \bar{K}_\varphi) N_{wg}. \qquad \text{(XV-1-8)}$$

Converting to the aerodynamic coefficients, we obtain

$$(c_N)_{b.wg} = (K_{b.i} + K_b + K_{wg} + \bar{K}_\varphi) c_{N\,wg}. \qquad \text{(XV-1-8')}$$

If we take a linear relation for normal force as a function of attack angle, then $c_N = c_N^\alpha \alpha$ and, consequently, /605

$$(c_N^\alpha)_{b.wg} = (K_{b.i} + K_b + K_{wg} + \bar{K}_\varphi) c_{N\,wg}^\alpha, \qquad \text{(XV-1-9)}$$

where the coefficients K should be regarded as ratios of the angle derivatives of the corresponding normal-force coefficients to the derivative $c_{N\ wg}^\alpha$.

Relationships for Aerodynamic Calculation with Consideration of Interference

Slender-body aerodynamic theory yields relationships for the aerodynamic characteristics of wing-body combinations with consideration of interference. The combination may be not only monoplane, consisting of a body with a pair of lifting cantilevers, but also cruciform, with two pairs. In defining the forces and moments, we shall use an x', y', z'-coordinate system (Fig. XV-1-2) whose axes coincide with the symmetry axes of the body at $\phi = 0$ and $\alpha_b \neq 0$, along with an x_1, y_1, z_1-system whose axes are bound to the body at all values of α_b and ϕ. Here the forces acting on the cantilevers in a roll ($\phi \neq 0$) are more conveniently defined in the x_1, y_1, z_1-system (Fig. XV-1-3).

The cantilever hinge moment M_h is calculated about an axis directed normal to the body's longitudinal axis, as the product

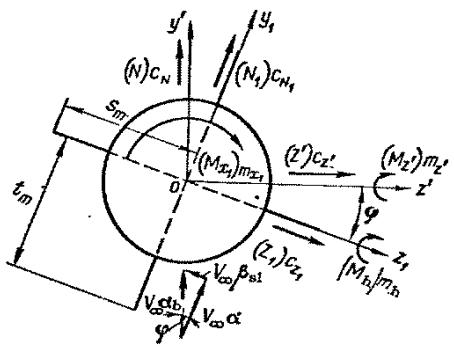

Figure XV-1-3. Coefficients of Forces and Moments Acting on Wing Halves and on Entire Wing-Body Combination.

of the normal forces and the center of pressure coordinate reckoned from the nose of the cantilever's root section. The moment can be converted to any other point by the usual methods.

Interference of cruciform wing with body. Let us consider the most general case, in which a combination consisting of a cruciform wing and a body is in flow at an angle of attack α_b and banked at an angle ϕ (Fig. XV-1-3). Investigation of the aerodynamic characteristics of such a combination and determination of the interference interaction between the wings and the body are based on presentation of the disturbed-flow potential function in the form of the sum $\phi = \phi_{\alpha=0} + \phi_\alpha + \phi_\beta$. The values of ϕ_α and ϕ_β represent the disturbance potentials for independent flows with velocities $V_\infty\alpha$ and $V_\infty\beta_{sl}$, i.e., in the directions of the respective normals to the plane of the horizontal cantilevers with their half-span s(x) and the plane of the vertical cantilevers with half-span t(s).

The potentials ϕ_α and ϕ_β are determined from the complex potentials W_α and W_β, which, in turn, are found by conformal mapping of a circle on the $\sigma = \xi + i\eta$ plane into a circle with a pair of plane cantilevers on the $\zeta = z_1 + iy_1$ plane. This mapping is accomplished by the formula given in Table IV-4-1. The potential W_α is obtained from (IV-4-33) for $\phi = 0$ by substituting $\sigma - r_0^2/\sigma$ according to the indicated formula from Table IV-4-1) and the substitution $V_0 = V_\infty\alpha = V_\infty\alpha_b\cos\phi$. To find the full potential W_α, it is necessary to incorporate into it /606
the potential function of the flow parallel to the y_1-axis, which is $iV_\infty\alpha\zeta$. Having performed these operations, we find

$$W_\alpha = -iV_\infty\alpha\left\{\left[\left(\zeta-\frac{r^2}{\zeta}\right)^2-\left(s+\frac{r^2}{s}\right)^2\right]^{1/2}-\zeta\right\}. \qquad \text{(XV-1-10)}$$

The transverse-flow velocity components are computed by the formula $w_\alpha - iv_\alpha = dW_\alpha/d\zeta$.

The complex potential W_β for transverse flow in the direction β_{sl} at velocity $V_\infty\beta_{sl} = V_\infty\alpha_b \sin\phi$ is obtained by substituting β_{sl} for α and $\underline{t}$ for $\underline{s}$ in (XV-1-10). As for the velocity components, they are calculated by the formula $w_\beta = iv_\beta = dW_\beta/d\zeta$. Separating the real parts from the complex quantities W_α and W_β, we find the potentials ϕ_α and ϕ_β. Adding the potential $\phi_{\alpha=0}$ (IV-4-8) to the sum of these functions, we determine the total potential function $\phi = \phi_{\alpha=0} + \phi_\alpha + \phi_\beta$.

The full velocity components are found by adding the three terms:

$$\left.\begin{aligned} u &= \varphi_x = u_{\alpha=0} + u_\alpha + u_\beta; \\ v &= \varphi_y = v_{\alpha=0} + v_\alpha + v_\beta; \\ w &= \varphi_z = w_{\alpha=0} + w_\alpha + w_\beta. \end{aligned}\right\} \qquad \text{(XV-1-11)}$$

Introducing $\underline{u}$, $\underline{v}$, and $\underline{w}$ into (III-3-12'), we find the pressure coefficients in the disturbed flow around the body-wing combination being considered. In the general case, the pressure coefficient is

$$\bar{p} = f(\alpha_b, \varphi, s, t, r, x_1, y_1, z_1), \qquad \text{(XV-1-12)}$$

where x_1 is reckoned from the beginning of the cantilever root chord. Referring the expression for $\bar{p}$ to conditions on the body ($y_1^2 = r^2 - z_1^2$), we find the pressure coefficient $\bar{p}_{b(wg)}$ on the body in the presence of the wing. Denoting the pressure coefficient at the bottom of the body by the subscript $\underline{l}$ and the value of this coefficient at the symmetrical point on the top of the body by the subscript $\underline{u}$, we find the excess pressure coefficient $\Delta\bar{p}_{b(wg)} = \bar{p}^l_{b(wg)} + \bar{p}^u_{b(wg)}$:

$$\Delta\bar{p}_{b(wg)} = \frac{4\alpha_b \cos\varphi\,[(1-r_s^4)\,s' + 2r_s\,(1+r_s^2-2z_r^2)\,r']}{[(1+r_s^2)^2-4z_s^2]^{1/2}} + \\ + \frac{64 z_s z_t\,(1-z_r^2)\,\alpha_b^2 \cos\varphi \sin\varphi}{[(1+r_s^2)^2-4z_s^2]^{1/2}\,[(1-r_t^2)^2+4y_t^2]^{1/2}}, \qquad \text{(XV-1-13)}$$

where $r_s = r/s$; $r_t = r/t$, $z_r = z_1/r$, $y_t = y_1/t$;

$$z_s = z_1/s;\ z_t = z_1/t;\ r' = dr/dx_1;\ s' = ds/dx_1.$$

To determine the pressure coefficient $\bar{p}_{wg(b)}$ on the cantilever in the presence of the body, we must set $z_1 = 0$ (for the vertical cantilevers) and $y_1 = 0$ (for the horizontal cantilevers) in the general expression (XV-1-12). For the vertical cantilevers, y_1 varies from $\pm r$ to $\pm t$. The z_1-coordinate for the horizontal cantilevers varies from $\pm r$ to $\pm s$. Calculations indicate that the excess pressure coefficient for the starboard cantilever in the presence of the body is

$$\Delta\bar{p}_{wg(b)} = \frac{4\alpha_b \cos\varphi \{(1-r_s^4)\, s' + r_s r' [2(r_s^2-1)+(1-r_z^2)^2]\}}{[(1+r_s^4)-y_s^2(1+r_z^4)]^{1/2}} + \\ + \frac{4 z_s z_t (1-r_z^4)^2 \alpha_b^2 \sin\varphi\cos\varphi}{[(1+r_s^4)-z_s^2(1+r_z^2)]^{1/2}[(1+r_t^4)+z_t^2(1+r_z^2)]^{1/2}}, \qquad \text{(XV-1-14)}$$

where we have introduced the new variables $r_z = r/z_1$ and $y_s = y_1/s$.

For the port cantilever, the angle ϕ used in the above expression should be increased by π. The expression for the excess pressure coefficient on the vertical cantilevers will be similar to (XV-1-14), except that y_1 must be substituted for z_1. The angle ϕ is replaced for the lower cantilever by $\phi + \pi/2$, and for the upper cantilever by $-\phi + 3\pi/2$. This definition of the angles ϕ should also be applied to (XV-1-13) when it is used to calculate pressure at the points of attachment to the cantilevers. /607

Analyzing Expressions (XV-1-13) and (XV-1-14), we can conclude that the first terms on the right (we shall denote them by $\Delta\bar{p}^0_{b(wg)}$ and $\Delta\bar{p}^0_{wg(t)}$, respectively) determine a load distributed symmetrically over the right and left cantilevers and dependent on the parameters of only the horizontal cantilevers. For a fixed angle $\alpha = \alpha_b \cos\phi$, the values of $\Delta\bar{p}^0_{b(wg)}$ and $\Delta\bar{p}^0_{wg(b)}$ will be the same for any ϕ, even in the absence of roll, when $\phi = 0$ and, consequently, $\alpha = \alpha_b$.

The second terms in Formulas (XV-1-13) and (XV-1-14) ($\Delta\bar{p}^{\varphi}_{b(wg)}$ and $\Delta\bar{p}^{\varphi}_{wg(b)}$, respectively) give equal but opposite loads on the right and left cantilevers. These loads, which are asymmetrical in nature, depend on roll angle and the shape of the vertical cantilevers. Thus, the pressure coefficients can be regarded as sums of two quantities:

$$\Delta\bar{p}_{b(wg)} = \Delta\bar{p}^0_{b(wg)} + \Delta\bar{p}^{\varphi}_{b(wg)}; \qquad \text{(XV-1-13')}$$

$$\Delta\bar{p}_{wg(b)} = \Delta\bar{p}^0_{wg(b)} + \Delta\bar{p}^{\varphi}_{wg(b)}. \qquad \text{(XV-1-14')}$$

The derivative $r' = dr/dx_1$, which characterizes the influence of variable radius at the junction with the wing, appears in (XV-1-13) and (XV-1-14). Studies have shown that its influence is insignificant. We shall therefore assume $r' = 0$.

Aerodynamic forces. By integrating the pressure over the body and wing surfaces, we can find the normal force N_1 in the plane of the attack angle $\alpha = \alpha_b \cos \phi$ and the lateral force Z_1 normal to this plane:

$$N_1 = 2\pi\alpha s_m^2 (1 - r_s^2 + r_s^4) q_\infty; \qquad \text{(XV-1-15)}$$

$$Z_1 = -2\pi\beta_{s1} t_m^2 (1 - r_t^2 + r_t^4) q_\infty; \qquad \text{(XV-1-16)}$$

where $r_s = r/s_m$; $r_t = r/t_m$; s_m and t_m are the respective spans of the horizontal and vertical cantilevers.

The normal force N, which lies in the plane of the attack angle α_b, is

$$N = N_1 \cos\varphi - Z_1 \sin\varphi. \qquad \text{(XV-1-17)}$$

The lateral force, which coincides with the direction of the z'-axis, is

$$Z_1' = N_1 \sin\varphi + Z_1 \cos\varphi. \qquad \text{(XV-1-18)}$$

For a symmetrical cruciform combination, $t_m = s_m$, so that

$$N = 2\pi\alpha_b s_m^2 (1 - r_s^2 + r_s^4) q_\infty. \qquad \text{(XV-1-19)}$$

It follows from (XV-1-18) that the lateral force is zero. Thus, the normal force in the plane of the attack angle α_b remains constant regardless of roll angle.

Interference coefficients. As we noted above, we may assume that the derivative $r' = 0$. This means that we shall be examining the case in which the body is a circular cylinder at the point of attachment of the wing. The normal force of the part of the body in front of the wing is equal, as we see from (XV-1-19), to $N_b = 2\pi\alpha_b r^2 q_\infty$ and is developed by the nose section on the length in front of the joint with the cylinder, which does not lift.

Since $N_{wg} = \alpha_b (c_N^{\alpha})_{wg} S_{wg} q_\infty$ for the wing, the coefficient $K_{b.i}$ in (XV-1-7) will be /608

$$K_{b.i} = \frac{2\pi r^2}{S_{wg}(c_N^{\alpha})_{wg}}. \qquad \text{(XV-1-20)}$$

TABLE XV-1-1. INTERFERENCE COEFFICIENTS AND CENTER OF PRESSURE COORDINATES IN THE PRESENCE OF AN ANGLE OF ATTACK

$\frac{r}{s_m}$	K_{wg}	K_b	$\left(\frac{x_{c.p\alpha}}{b_{rt}}\right)_{wg(b)}$	$\left(\frac{x_{c.p\alpha}}{b_{rt}}\right)_{b(wg)}$	$\frac{z_{c.p\alpha}-r}{s_m-r}$
0	1.000	0	0.667	0.500	0.424
0.1	1.077	0.133	0.657	0.521	0.421
0.2	1.162	0.278	0.650	0.542	0.419
0.3	1.253	0.437	0.647	0.563	0.418
0.4	1.349	0.611	0.646	0.581	0.417
0.5	1.450	0.800	0.647	0.598	0.417
0.6	1.555	1.005	0.650	0.613	0.416
0.7	1.663	1.227	0.654	0.628	0.418
0.8	1.774	1.467	0.658	0.641	0.420
0.9	1.887	1.725	0.662	0.654	0.422
1.0	2.000	2.000	0.667	0.667	0.424

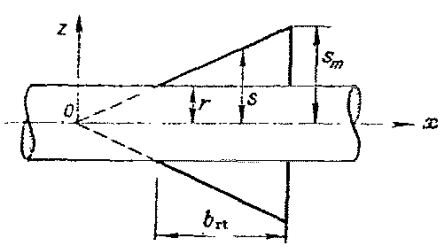

Figure XV-1-4. Combination of Delta Wing and Body.

If the cylindrical section of the body between the wing and the nose section is long, a component generated by this segment and governed by flow separation must be taken into account in determining the normal force.

According to (XV-1-2), the interference coefficient for the wing $K_{wg} = N_{wg(t)}/N_{wg}$. The wing normal force $N_{wg(t)}$ with consideration of the body effect can be calculated by integrating the pressure over the wing surface and setting the derivative $r' = 0$ in (XV-1-14). Table XV-1-1 presents results of an interference calculation for a body/delta wing combination (Fig. XV-1-4) with consideration of the fact that for the isolated wing $N_{wg} = 2\pi\alpha_b \cos\phi(s_m - r)^2$.

The interference coefficient is a function of the ratio $r_s = r/s_m$. The body radius may vary chordwise along a wing or tail. In this case, the calculations are simplified by taking the average value of the radius on the length of the chord. In the

extreme case, when r = 0, the combination becomes a wing and K_{wl} = = 0. As r/s_m approaches unity, the wing cantilevers become very small, and it follows from the formula

$$\alpha_z = \alpha_b \left(1 + \frac{r^2}{z^2}\right), \qquad \text{(XV-1-21)}$$

where α_b is the body angle of attack and z is the distance from the body axis to the cantilever section under consideration, that the local angle of attack of this very small cantilever will be $2\alpha_b$. The interference coefficient K_{wg} = 2, so that the effectiveness of the cantilever has doubled. Values of K_{wg} obtained for the delta wing may be used in practice for all slender combinations irrespective of span.

The interference coefficient for the body is determined from (XV-1-3) in the form of the ratio $K_b = N_{b(wg)}/N_{wg}$, in which /609

$$N_{b(wg)} = N_{b.wg} - N_{wg(b)} = N_b. \qquad \text{(XV-1-22)}$$

TABLE XV-1-2. INTERFERENCE COEFFICIENTS AND CENTER OF PRESSURE COORDINATES IN THE PRESENCE OF ROLL (BODY AND DELTA WING)*

	Plane combinations			Cruciform combinations		
$\frac{r}{s_m}$	K_φ	$\left(\frac{x_{c.p\varphi}}{b_{rt}}\right)_{wg(b)}$	$\frac{z_{c.p\varphi} - r}{s_m - r}$	K_φ	$\left(\frac{x_{c.p\varphi}}{b_{rt}}\right)_{wg(b)}$	$\frac{z_{c.p\varphi} - r}{s_m - r}$
0	0.637	0.667	0.524	0.352	0.667	0.556
0.1	0.687	0.667	0.518	0.447	0.654	0.552
0.2	0.681	0.677	0.531	0.490	0.660	0.550
0.3	0.649	0.688	0.546	0.508	0.673	0.540
0.4	0.597	0.699	0.560	0.502	0.687	0.554
0.5	0.529	0.709	0.575	0.471	0.700	0.569
0.6	0.447	0.719	0.588	0.417	0.714	0.585
0.7	0.382	0.729	0.601	0.342	0.725	0.598
0.8	0.246	0.736	0.614	0.244	0.734	0.612
0.9	0.128	0.744	0.616	0.127	0.743	0.625
1.0	0	0.750	0.647	0	0.750	0.637

The over-all normal force $N_{b.wg}$ is calculated by Formula (XV-1-15) for the attack angle α. If we remember that $N_{wg(b)} = N_{wg}K_{wg}$, and $N_b = 2\pi\alpha r^2 q_\infty$, we obtain for the interference coefficient

$$K_b = (1 + r_s)^2 - K_{wg}. \qquad \text{(XV-1-23)}$$

Values of K_b calculated by Formula (XV-1-23) appear in Table XV-1-1. These values do not depend on the planform of the wing, but are determined only by the parameter $r_s = r/s_m$.

Let us consider how the wing interference coefficient governed by roll is calculated. It is determined from (XV-1-5) in the form $\bar{K}_\phi = \Delta N_{wg}/N_{wg}$. The additional wing normal force ΔN_{wg} in roll is found by integrating the pressure coefficient $\Delta\bar{p}^{\phi}_{wg(b)}$ which is equal to the second term in (XV-1-14), over the surface. Since the resultant force ΔN_{wg} for the two halves is zero, one cantilever, e.g., the starboard one, for which $N_{wg} = \pi\alpha(s_m - r)^2 q_\infty$, must be examined to determine $\bar{K}_\phi$. Integrating over the surface of the cantilever, we find that $\bar{K}_\phi$ is proportional to the ratio $\beta_{s1}/\tan\varepsilon$ ($\tan\varepsilon = ds/dx_1 = \text{const}$) and to a certain function K_ϕ, which depends on the parameter $r_s = r/s_m$. This function, which is also used as an interference coefficient, is

$$K_\varphi = \frac{\Delta N_{wg}}{N_{wg}} \frac{\operatorname{tg}\varepsilon}{\beta_{s1}} = \bar{K}_\varphi \frac{\operatorname{tg}\varepsilon}{\beta_{s1}}. \qquad \text{(XV-1-24)}$$

Values of the coefficient K_ϕ are listed in Table XV-1-2 as functions of the ratio $r_s = r/s_m$. They were calculated for a body-delta-wing combination and will change on passage to another wing form. In this case, the data of Table XV-1-2 can be used for orientation.

The coefficient K_ϕ, which determines the unbalanced load, is needed for calculation of the rolling moment from the forces acting on the wings. Calculation of an analogous interference coefficient for the body would be pointless, since the unbalanced load has practically no influence on the forces and moment acting on the body. /610

Center of pressure. Let us calculate the center of pressure coordinates for the right horizontal cantilever $(z_{c.p\alpha})_{wg(b)}$, $(x_{c.p\alpha})_{wg(b)}$ considering the case in which roll angle has no influence. The coordinate

$$(z_{c.p\alpha})_{wg(b)} = \int_{(S)} \Delta\bar{p}^{0}_{wg(b)} z_1 ds \left[\int_{(S)} \Delta\bar{p}^{0}_{wg(b)} dS\right]^{-1}, \qquad \text{(XV-1-25)}$$

where $dS = dx_1 dz_1$, and the excess pressure coefficient $\Delta\bar{p}^0_{wg(b)}$ on the cantilever is equal to the first term in (XV-1-14).

The coordinate

$$(x_{c.p\,\alpha})_{wg(b)} = \int_{(S)} \Delta\bar{p}^0_{wg(b)} x_1 dS \Big[\int_{(S)} \Delta\bar{p}^0_{wg(b)}\, dS\Big]^{-1}. \qquad \text{(XV-1-26)}$$

Here x_1 and, consequently, the coordinate $(x_{c.p\alpha})_{wg(b)}$ is reckoned from the front of the cantilever. The dimensionless values of $(x_{c.p\alpha}/b_{rt})_{wg(b)}$ and $(z_{c.p\alpha} - r)_{wg(b)}/(s_m - r)$, calculated with Formulas (XV-1-26) and (XV-1-25), are given in Table XV-1-1. The values of $(x_{c.p\alpha}/b_{rt})_{wg(b)}$ differ little from 2/3 for the isolated wing composed of the cantilevers, indicating that the influence of interference is weak.

A similar calculation yields the coordinates $(z_{c.p\phi})_{wg(b)}$ and $(x_{c.p\phi})_{wg(b)}$ of the center of pressure, which is the point of application of the additional lifting force caused by rotation through the roll angle. The working formulas will be the same except that instead of $\Delta\bar{p}^0_{wg(b)}$ it is necessary to take $\Delta\bar{p}^{\phi}_{wg(b)}$, which is equal to the second term in (XV-1-14). Instead of the dimensional coordinates, it is preferable to use the dimensionless parameters $(z_{c.p\phi} - r)_{wg(b)}/(s_m - r)$; $(x_{c.p\phi})_{wg(b)}/b_{rt}$. Values of these parameters calculated by the above method appear in Table XV-1-2. The body center of pressure $(x_{c.p\alpha})_{b(wg)}$ with consideration of the wing influence can be determined for $\phi = 0$, since the wing has insignificant influence. The working formula is

$$(x_{c.p\,\alpha})_{b(wg)} = \int_{(S)} \Delta\bar{p}^0_{b(wg)} x \sin\Theta\, dS \Big[\int_{(S)} \Delta\bar{p}^0_{b(wg)} \sin\Theta\, dS\Big]^{-1}, \qquad \text{(XV-1-27)}$$

where $dS = r\,d\Theta\,dx_1$, and the angle Θ is reckoned along the oz_1 axis. Values of $(x_{c.p\alpha}/b_{rt})_{b(wg)}$ calculated by (XV-1-27) and referred to the cantilever root chord b_{rt} are given in Table XV-1-1. The distance from the nose to the center of pressure

$$(x_{c.p\,\alpha})_{b(wg)} = x_n + \left(\frac{x_{c.p\,\alpha}}{b_{rt}}\right)_{b(wg)} b_{rt}, \qquad \text{(XV-1-28)}$$

where x_n is the distance from the nose of the body to the beginning of the cantilever root chord.

The values of $(z_{c.p\alpha} - r)/(S_m - r)$ given in Table XV-1-1 approach $4/3\pi$, which applies for elliptical distribution of the load, and do not depend on wing planform. This result indicates that interference of the wing with the body has no substantial effect on the spanwise position of the wing center of pressure.

The longitudinal position of the wing center of pressure depends on planform, and the values of $(x_{c.p\alpha}/b_{rt})_{wg(b)}$ in Table XV-1-1 were calculated by Formula (XV-1-26) for a delta wing.

The result of applying slender-body theory to rectangular wings is that the center of pressure is on the leading edge, and this is physically impossible. To determine the real center of pressure coordinate, we can assume, as for the delta wing, that interference has little effect on it and, consequently, that this coordinate can be assumed equal to its value for the isolated wing. If we use the linearized theory, /611

$$\left(\frac{x_{c.p\alpha}}{b_{rt}}\right)_{wg(b)} = \frac{3\alpha'\lambda_{wg} - 2}{6\alpha'\lambda_{wg} - 3}, \qquad \text{(XV-1-29)}$$

where

$$\alpha'\lambda_{wg} > 1. \qquad \text{(XV-1-30)}$$

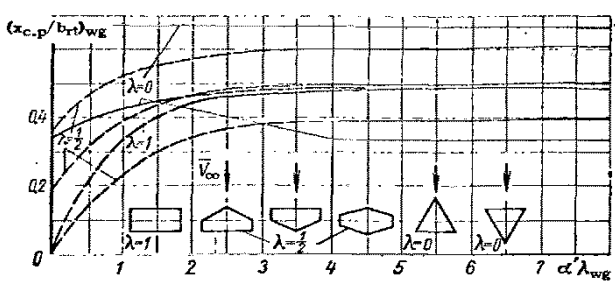

Figure XV-1-5. Coordinates of Center of Pressure for Isolated Wings as Calculated from the Linearized Theory for Supersonic Speeds ($\alpha' > 1$).

Research has shown that the center of pressure coordinate of a trapezoidal wing in the presence of a body can be assumed with good approximation to be equal to that of the isolated wing. Figure XV-1-5 shows values of $(x_{c.p}/b_{rt})_{wg}$ for isolated delta ($\lambda = b_{tp}/b_{rt} = 0$), trapezoidal ($\lambda = 1/2$) and rectangular ($\lambda = 1$)

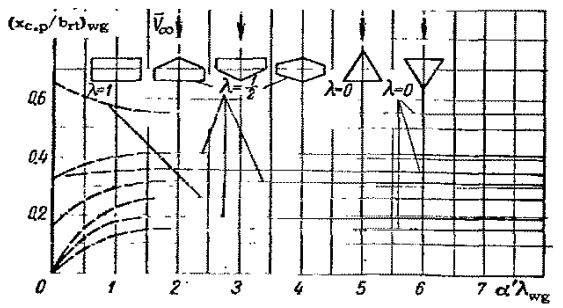

Figure XV-1-6. Center of Pressure Coefficients for Isolated Wings as Calculated by Linearized Theory for Subsonic Speeds ($\alpha' < 1$).

wings. The curves calculated from supersonic linearized theory are extrapolated to the limits obtained from slender-body theory for $\alpha'\lambda_{wg} = 0$. Figure XV-1-6 gives values of $(x_{c.p}/b)_{wg}$ for subsonic speeds.

According to the curves, $(x_{c.p\alpha}/b_{rt} = (x_{c.p\alpha}/b_{rt})_{wg(b)}$, and the distance from the nose of the body to the center of pressure is

$$x_{c.p\,\alpha} = x_n + (x_{c.p\,\alpha}/b_{rt})_{wg(b)}\, b_{rt}. \qquad \text{(XV-1-31)}$$

Plane body-wing combination. To obtain the corresponding expressions for the aerodynamic parameters of a plane body-wing combination, we must set t = r. In particular, Formulas (XV-1-13) and (XV-1-14) for the excess pressure coefficient assume the following form (provided that, in addition to t = r, the derivative $r' = dr/dx_1 = 0$): /612

$$\Delta\bar{p}_{b(wg)} \quad \frac{4\alpha_b \cos\varphi\,(1-r_s^2)\,s'}{[(1-r_s^2)^2-4z_s^2]^{1/2}} + \frac{32 z_s z_r\,(1-z_r^2)^{1/2}\,\alpha_b^2 \cos\varphi \sin\varphi}{[(1+r_s^2)^2-4z_s^2]^{1/2}}; \qquad \text{(XV-1-32)}$$

$$\Delta\bar{p}_{wg(b)} \quad \frac{4\alpha_b \cos\varphi\,(1-r_s^2)\,s'}{[(1+r_s^2)^2-z_s^2\,(1+r_s^2)]^{1/2}} + \frac{4z_s\,(z_r^2-1)\,(z_r^2-1)\,\alpha_b^2 \sin\varphi\cos\varphi}{(z_r^2+1)\,z_r^2\,[(1+r_s^2)^2-z_s^2\,(1+r_s^2)]^{1/2}}. \qquad \text{(XV-1-33)}$$

These pressure values for the plane combination were used to calculate the interference coefficients K_ϕ and the centers of pressure $(x_{c.p\phi})_{wg(b)}$ and $(z_{c.p\phi})_{wg(b)}$, which are listed in Table XV-1-2.

For the case of no roll ($\phi = 0$), the formulas for the pressure coefficients become even simpler:

$$\Delta\bar{p}_{b(wg)} = \frac{4\alpha_b\,(1-r_s^2)\,s'}{[(1+r_s^2)^2-4z_s^2]^{1/2}}; \qquad \text{(XV-1-34)}$$

$$\Delta\bar{p}_{wg(b)} = \frac{4\alpha_b (1-r_s^4)\, s'}{[(1+r_s^4) - z_s^2 (1+r_2^4)]^{1/2}}. \qquad \text{(XV-1-35)}$$

These relationships can also be applied to a cruciform combination in motion without roll. The corresponding aerodynamic characteristics, calculated by (XV-1-34) and (XV-1-35), are given in Table XV-1-1.

Formulas for calculating the aerodynamic coefficient. Knowledge of the interference coefficients, center of pressure coordinates, and the aerodynamic characteristics of the isolated wing and body enables us to calculate the aerodynamic characteristics of the individual elements of the vehicle and of the combination as a whole with consideration of the interference effects.

Table XV-1-3 gives all formulas needed for such calculation of the aerodynamic coefficients of slender plane cruciform combinations. These formulas were derived for wings of zero thickness, which do not disturb longitudinal flow at zero angle of attack.

TABLE XV-1-3. FORMULAS FOR AERODYNAMIC CALCULATION OF SLENDER PLANE AND CRUCIFORM COMBINATIONS WITH CONSIDERATION OF INTERFERENCE

Coefficient	Working Formula
Body-Wing (Plane combination)	
I. Forces and moments acting on right cantilever	
Force coefficient (Fig. XV-1-3)	$(c_{N1})_c = K_{wg}\left(\frac{1}{2}c_N^{\alpha}\right)_{wg}\alpha_b\cos\varphi + \frac{K_\varphi}{\operatorname{tg}\varepsilon}\left(\frac{1}{2}c_N^{\alpha}\right)_{wg}\alpha_b^2\sin\varphi\cos\varphi$
Cantilever hinge moment coefficient	$m_h = -K_{wg}\left(\frac{1}{2}c_N^{\alpha}\right)_{wg}\frac{(x_{c.p.\,\alpha})_{wg(b)}}{x_b}\alpha_b\cos\varphi - \frac{K_\varphi}{\operatorname{tg}\varepsilon}\left(\frac{1}{2}c_N^{\alpha}\right)_{wg}\times \frac{(x_{c.p.\,\varphi})_{wg(b)}}{x_b}\alpha_b^2\sin\varphi\cos\varphi$; x_b is the body length
Rolling moment coefficient	$(m_{x1})_b = -K_{wg}\left(\frac{1}{2}c_N^{\alpha}\right)\frac{(z_{c.p.\,\alpha})_{wg(b)}}{x_b}\alpha_b\cos\varphi - \frac{K_\varphi}{\operatorname{tg}\varepsilon}\left(\frac{1}{2}c_N^{\alpha}\right)_{wg}\times \frac{(z_{c.p.\,\varphi})_{wg(b)}}{x_b}\alpha_b^2\sin\varphi\cos\varphi$
II. Forces and moments induced on body by wing	/613
Normal force coefficient (Fig. XV-1-3)	$(c_N)_{b(wg)} = K_b\,(c_N^{\alpha})_{wg}\,\alpha_b\cos^2\varphi$

TABLE XV-1-3 (Cont'd.)

Coefficient	Working Formula
Lateral force coefficient	$(c_{z'})_{b(wg)} = K_b (c_N^\alpha)_{wg} \alpha_b \sin\varphi \cos\varphi$
Pitching moment coefficient	$(m_{z'})_{b(wg)} = -K_b (c_N^\alpha)_{wg} \frac{(x_{c.p.\,\alpha})_{b.wg}}{x_c} \alpha_b \cos^2\varphi$
Rolling moment coefficient	$m_{x'} = 0$

III. Total forces and moments of plane combination

Normal force coefficient	$c_N = c_{N\,b} + (c_N)_{b(wg)} + K_{wg} (c_N^\alpha)_{wg} \alpha_b \cos^2\varphi$
Lateral force coefficient	$c_{z'} = c_{z'\,b} + (c_{z'})_{b(wg)} + K_{wg} (c_N^\alpha)_{wg} \alpha_b \sin\varphi \cos\varphi$
Pitching moment coefficient	$m_{z'} = m_{z'\,b} + (m_{z'})_{b(wg)} - K_{wg} (c_N^\alpha)_{wg} \frac{(x_{c.p\ \ \alpha})_{wg(b)}}{x_b} \alpha_b \cos^2\varphi$
Rolling moment coefficient	$m_{x'} = -K_{wg} (c_N^\alpha)_{wg} \frac{(x_{c.p.\,\alpha})_{wg(b)}}{x_b} \alpha_b \cos\varphi$

Body and Cruciform Wing (Cruciform Combination)

I. Forces and moments acting on right cantilever

Normal force coefficient	$(c_{N^1})_c$	Formulas same as for plane combination. In these formulas, K_ϕ and $(x_{c.p\phi})_{wg(b)}$ must be determined from Table XV-1-2 for the cruciform combination.
Cantilever hinge moment coefficient	m_h	
Rolling moment coefficient	$(m_z)_c$	

II. Forces and moments induced on body by wing

Normal force coefficient	$(c_N)_{b(wg)} = K_b (c_N^\alpha)_{wg} \alpha_b$
Lateral force coefficient	$(c_{z'})_{b(wg)} = 0$
Pitching moment coefficient	$(m_{z'})_{b(wg)} = -K_b (c_N^\alpha)_{wg} \frac{(x_{c.p.\,\alpha})_{b(wg)}}{x_b} \alpha_b$

TABLE XV-1-3 (Cont'd.)

Rolling moment coefficient	$(m_{x'})_{b(wg)}=0$

III. Total forces and moments of cruciform combination /614

Normal force coefficient	$c_N=c_{N\,b}+(K_b+K_{wg})(c_N^{\alpha})_{wg}\alpha_b$
Lateral force coefficient	$c_{z'}=0$
Pitching moment coefficient	$m_{z'}=(m_{z'})_b-\frac{1}{x_b}[K_b(x_{c.p}\ \alpha)_{b(wg)}+K_{wg}(x_{c.p}\ \alpha)_{wg(b)}](c_N^{\alpha})_{wg}\alpha_b$
Rolling moment coefficient	$m_{x'}=0$
Normal force	$N_1=2\pi\alpha s_m^2(1-r_s^2+r_s^4)q_\infty$
Lateral force	$Z_1=-2\pi\beta_{s1}t_m^2(1-r_t^2+r_t^4)q_\infty$
Normal force into x-axis direction	$N=N_1\cos\varphi-Z_1\sin\varphi$ $N=2\pi\alpha_b s_m^2(1-r_s^2+r_s^4)q_\infty$

Calculation of Interference for "Nonslender" Combinations

Interference coefficients. The results of interference-coefficient calculations for slender combinations can be used as a basis for determining the lift of "nonslender" configurations. In this method, the aerodynamic coefficient of the configuration is calculated from the interference coefficient found from slender-body theory and the isolated-wing aerodynamic coefficient taken from linearized theory or from experiment. For example, the coefficient $(c_N)_{wg(b)} = K_{wg}(c_N)_{wg}$, where K_{wg} is found from Table XV-1-1 and $(c_N)_{wg}$ is determined with consideration of the influence of M_∞ as established in linearized theory. The other interference characteristics are also written similarly.

It is therefore assumed that the interference coefficients do not change at transition to nonslender combinations. Studies have shown that this hypothesis is fully justified for the coefficient K_{wg}. As for K_b, the values corresponding to slender-body theory apply for the condition

$$\alpha'\lambda_{wg}\left(1+\frac{b_{tp}}{b_{rt}}\right)\left(\frac{1}{\alpha'\operatorname{tg}\varepsilon}+1\right)\leqslant 4. \qquad \text{(XV-1-36)}$$

If the condition

$$\alpha'\lambda_{wg}\left(1+\frac{b_{tp}}{b_{rt}}\right)\left(\frac{1}{\alpha' \operatorname{tg}\varepsilon}+1\right)>4, \qquad \text{(XV-1-37)}$$

is satisfied, the results from slender-body aerodynamic theory are not as good as in the previous case.

More satisfactory interference data can be obtained by calculating the actual normal force that arises in the presence of the wing for the cross-hatched area of the body (Fig. XV-1-7). In this scheme, the body is assumed to be plane and set at zero attack angle.

For a wing with a supersonic leading edge, this normal force developed on a body with a tail section (Fig. XV-1-7b) is /615

$$N_{b(wg)}=\frac{8q_\infty\alpha \operatorname{tg}\varepsilon}{\pi\sqrt{(\alpha' \operatorname{tg}\varepsilon)^2-1}}\int_0^{2r}d\eta\int_{\alpha'\eta}^{b_{rt}+\alpha'\eta}\arccos\frac{\xi/\alpha'+\alpha'\eta \operatorname{tg}\varepsilon}{\eta+\xi \operatorname{tg}\varepsilon}d\xi, \qquad \text{(XV-1-38)}$$

where α' tan $\varepsilon > 1$.

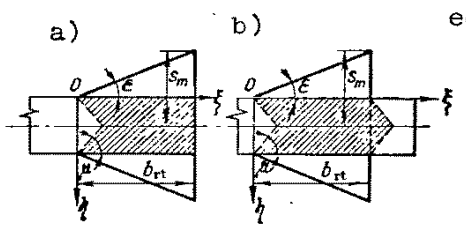

Figure XV-1-7. Diagram of Lift Calculation with Consideration of Interference Between Wing and Body. a) plane model for calculating the effect of wing on body without tail section; b) plane model for calculating the effect of wing on body with tail section.

Similarly, for subsonic leading edges

$$N_{b(wg)}=\frac{16q_\infty\alpha(\alpha' \operatorname{tg}\varepsilon)^{3/2}}{\pi\alpha'(\alpha' \operatorname{tg}\varepsilon+1)}\int_0^{2r}d\eta\int_{\alpha'\eta}^{b_{rt}+\alpha'\eta}\sqrt{\frac{\xi/\alpha'-\eta}{\xi \operatorname{tg}\varepsilon+\eta}}d\xi, \qquad \text{(XV-1-39)}$$

where α' tan $\varepsilon < 1$.

The integrals of (XV-1-38) and (XV-1-39) are expressed in elementary functions. Dividing each of the values found by the normal force of an isolated wing $q_\infty S_{wg}(c_N)_{wg} = q_\infty S_{wg}(c_N^\alpha)_{wg}\alpha$ with the aspect ratio

$$\lambda_{wg}=\frac{4(s_m-r)}{b_{rt}(1+\lambda)}\left(\lambda=\frac{b_{tp}}{b_{rt}}\right), \qquad \text{(XV-1-40)}$$

we obtain the corresponding relationships for the interference coefficients K_b. Analysis of these

relationships indicates that $\overline{K}_b = K_b(1 + \lambda)(s_m/r - 1)\alpha'(c_N^{\alpha})_{wg}$ is a function of only α' tan ε and $2\alpha' r/b_{rt}$. Values of K_b are given in Fig. XV-1-8b. The data in this figure correspond to the case in which the tip effect has no influence on the part of the body cross-hatched in Fig. XV-1-7. With this condition, the Mach wave AB originating at the leading edge of the wing root chord passes behind point C on the root-chord trailing edge. The diagram in Fig. XV-1-8b is used if the distance from the wing trailing edge to the base section satisfies the inequality

$$x_{wg} \geqslant 2r\sqrt{M_\infty^2 - 1}. \qquad \text{(XV-1-41)}$$

If this inequality is not satisfied, the interference coefficients and the center of pressure relative coordinate can be found by linear interpolation between the values determined from the diagram of Fig. XV-1-8b.

If the body has no tail section behind the wing, the interference coefficient is again to be calculated with Formulas (XV-1-38) and (XV-1-39), in which b_{rt} is substituted for the upper limit $b_{rt} + \alpha'\eta$ of the integral. The corresponding values of $\overline{K}_b$ are given in Fig. XV-1-8a. Comparison with Fig. XV-1-8b shows that for large $2\alpha' r/b_{rt}$, the tail section of the body behind the wing has a substantial influence on the normal force governed by interference with the wing.

At subsonic speeds, the effect of the tail section is about the same, since downstream zones of the body produce much less lift than at supersonic speeds. /616

Influence of wing on position of body center of pressure. The center of pressure coordinate of the body may be sensitive to change in M_∞ even if the body-wing combination is slender. It is determined by different methods for supersonic and subsonic speeds.

Supersonic speeds. The plane body model used to determine the normal force on the body in the presence of a wing can be used for supersonic velocities. The normal-force moment of a body-and-tail governed by a wing with a supersonic leading edge is

$$M_{b(wg)} = \frac{4q_\infty \alpha \operatorname{tg}\varepsilon}{\pi\sqrt{(\alpha' \operatorname{tg}\varepsilon)^2 - 1}} \int_0^{2r} d\eta \times \int_{\alpha'\eta}^{b_{rt}+\alpha'\eta} \xi \arccos \frac{\xi/\alpha' + \alpha'\eta \operatorname{tg}\varepsilon}{\eta + \xi\alpha'} d\xi. \qquad \text{(XV-1-42)}$$

a)

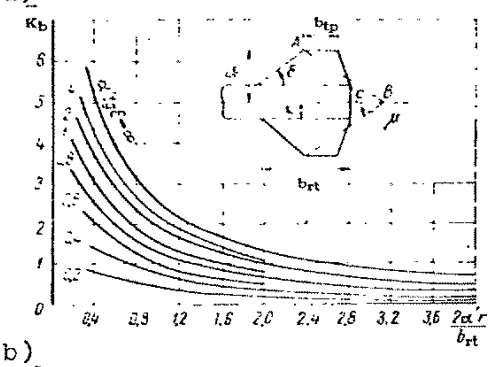

b)

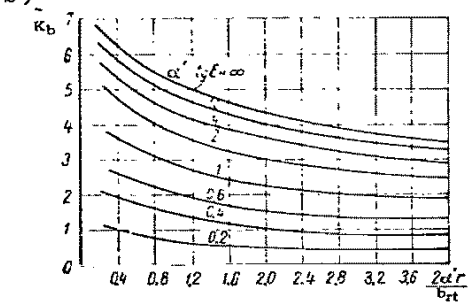

Figure XV-1-8. Diagrams for Calculating the Effect of Wing on Body Normal Force. a) without tail section; b) with tail section;

$$K = K_b(\alpha' dc_N/d\alpha)_{wg}\left(1 - \frac{b_{tp}}{b_{rt}}\right)\left(\frac{sm}{r} - 1\right);$$

$$\lambda = \frac{b_{tp}}{b_{rt}};\ \alpha' = \sqrt{|M_\infty^2 - 1|};\ \lambda_{wg} = \lambda_{rt}\frac{4(sm - r)}{(1 - b_{tp}/b_{rt})};$$

$$\alpha'\lambda_{wg}(1 + b_{tp}/b_{rt})(1/\alpha' \operatorname{tg}\varepsilon + 1) \geqslant 4$$

This result must be doubled to obtain the body moment that results from both halves of the wing. Similarly, for a wing with a subsonic leading edge,

$$M_{b(wg)} = -\frac{8q_\infty\alpha(\alpha' \operatorname{tg}\varepsilon)^{3/2}}{\pi\alpha'(\alpha' \operatorname{tg}\varepsilon + 1)}\int_0^{2r} d\eta \int_{\alpha'\eta}^{b_{rt}+\alpha'\eta} \frac{\xi\sqrt{\xi/\alpha' - \eta}}{\sqrt{\xi \operatorname{tg}\varepsilon + \eta}}\, d\xi. \qquad \text{(XV-1-43)}$$

The center of pressure coefficient is obtained by dividing the $M_{b(wg)}$ determined from (XV-1-42) and (XV-1-43) by the $N_{b(wg)}$ determined by Formulas (XV-1-38) and (XV-1-39), respectively:

$$\left(\frac{x_{c.p\alpha}}{b_{rt}}\right)_{b(wg)} = \frac{M_{b(wg)}}{N_{b(wg)}b_{rt}} = \frac{M_{b(wg)}}{K_b N_{wg} b_{rt}}. \qquad \text{(XV-1-44)}$$

The results of calculation of $(x_{c.p\alpha}/b_{rt})_{b(wg)}$ for the combination of a body with wings having supersonic and subsonic leading edges appear in Fig. XV-1-9b. We note that the parameter α' tan ε has little influence on the center of pressure coordinate. /617

In the absence of a body tail section behind the wing, Formulas (XV-1-42) and (XV-1-43) are integrated with b_{rt} as the upper limit. Figure XV-1-9a shows calculated results for the relative center of pressure coordinate. The curves in Fig. XV-1-9 apply for $\alpha'\lambda_{wg}(1 + \lambda)|1 + (\alpha' \operatorname{tg}\varepsilon)^{-1}| > 4$. The diagrams in Fig. XV-1-10 correspond to the range of small aspect ratios, for which $\alpha'\lambda_{wg}(1 + \lambda)|1 + (\alpha' \operatorname{tg}\varepsilon)^{-1}| < 4$; they were constructed on the assumption that part of the body projects behind the wing and the effective aspect ratio $\alpha'\lambda_{wg}$ and the reciprocal taper $\lambda = b_{tp}/b_{rt}$ are independent variables; the ratio of the radius to the half-span $r_s = r/s_m$ was taken as the

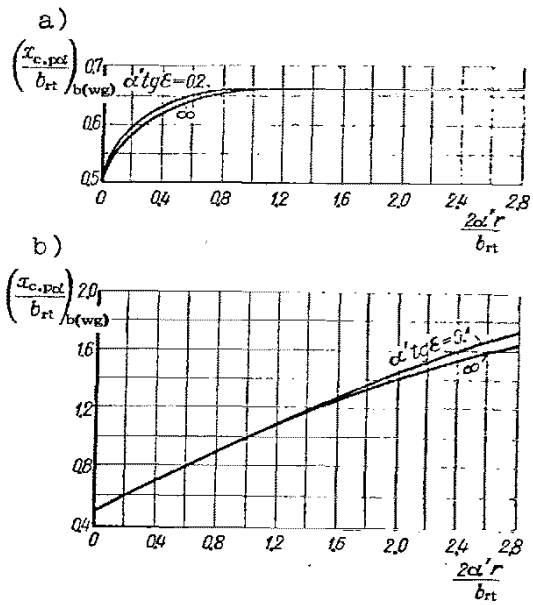

Figure XV-1-9. Curves for Calculating the Wing Effect on Body Center of Pressure Position. a) without tail section; b) with tail section.

parameter. The values of $(x_{c.p\alpha}/b_{rt})_{b(wg)}$ for $\alpha'\lambda_{wg} = 0$ were obtained from slender-body theory, and those for $r_s = r/s_m = 0$ from linearized theory for the isolated wing; the dashed curves were constructed by extrapolation to $(x_{c.p\alpha}/b_{rt})_{b(wg)}$ for $\alpha'\lambda_{wg} = 0$. Comparison shows that the values of $(x_{c.p\alpha}/b_{rt})_{b(wg)}$ calculated by the linearized theory in the presence of a body tail section for $\alpha'\lambda_{wg} > 0$ differ sharply from the values found from slender-body theory. When there is no tail section, the difference becomes much smaller, as we noted in particular for wings with subsonic leading edges. In this case, we can apply slender-body aerodynamic theory in practice to evaluate the effect of interference on the body center of pressure coordinate.

Subsonic speeds. In the presence of a wing, the body center of pressure is determined by use of a horseshoe-vortex model the top of which runs along the quarter-chord line of the wing (attached vortex), while the two lateral vortex lines follow the stream (free vortices) and one of them may lie inside the body tail section (see Fig. XV-2-7). Let us consider a quarter-chord line with an elliptical distribution of circulation:

$$\Gamma = \Gamma_0 \sqrt{1 - \left(\frac{z-r}{s_m - r}\right)^2}. \qquad \text{(XV-1-45)}$$

We shall assume that z_1 is the coordinate of the free vortex inside the body. As a result, the lift of an elementary lifting-line segment due to the attached vortex is /618

$$dY_{b(wg)} = \Gamma dz_1 = \Gamma d\left(\frac{r^2}{z}\right) = -\Gamma r^2 \frac{dz}{z^2}.$$

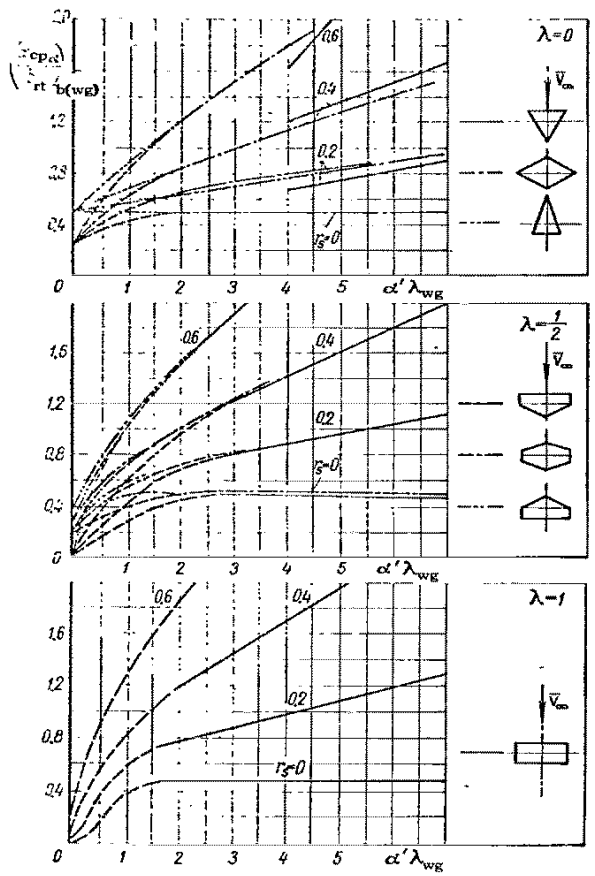

Figure XV-1-10. Diagrams for Determination of Relative Center of Pressure Coordinate of Body with Tail Section Behind Wing at Supersonic Speed (Dashed Lines Obtained by Extrapolation). Condition of use:

$$\alpha'\lambda_{wg}(1+\lambda)(1+1/\alpha'\operatorname{tg}\varepsilon)<4$$

The moment element about a z-axis passing through the apex of the quarter-chord line is

$$dM_{b(wg)} = -\frac{\Gamma r^2 x\,dz}{z^2}.$$

Consequently, the distance to the center of pressure from the beginning of the lifting line

$$\left(\frac{M}{N}\right)_{b(wg)} = (x_{c.p\ \alpha})_{b(wg)} - \frac{b_{rt}}{4} = \int_r^{s_m} \frac{\Gamma x\,dz}{z^2}\left(\int_r^{s_m}\Gamma\frac{dz}{z^2}\right)^{-1}, \qquad \text{(XV-1-46)}$$

where $(x_{c.p\alpha})_{b(wg)}$ is measured from the leading edge of the root (inboard) chord.

Introducing Γ from (XV-1-45), substituting x in accordance with the expression $x = (\tan\varepsilon)_{1/4}(z-r)$ and integrating, we obtain the distance to the center of pressure and the relative quantity $(x_{c.p\alpha}/b_{rt})_{b(wg)}$. The calculated results appear in Fig. XV-1-11, and correspond to the condition $\alpha'\lambda_{wg} = 0$ for the slender body. As we see, these results depend on the shape of the leading edge and the ratio r/s_m and are independent of M_∞. /619

More exact analyses based on the linearized theory indicate that the center of pressure coefficient depends on the parameters $\alpha'\lambda_{wg}$ and r/s_m and on the form of the wing. This is evident from

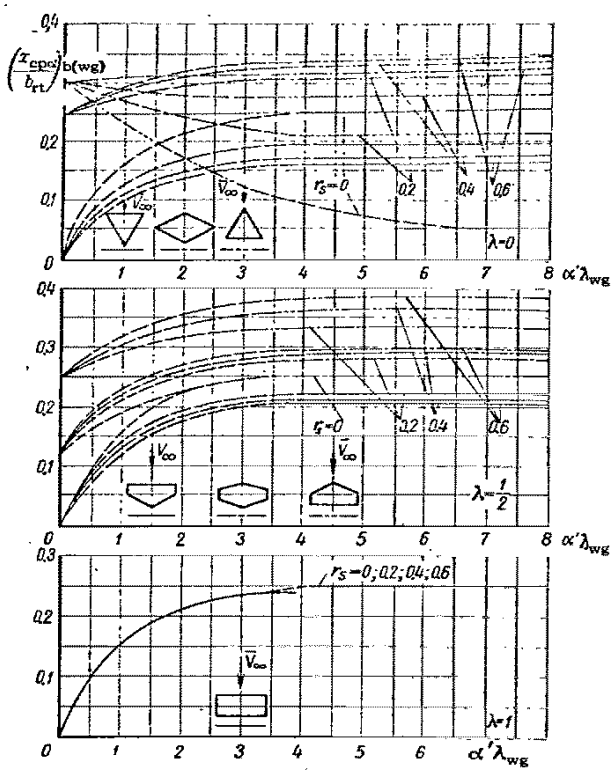

Figure XV-1-11. Diagrams for determination of body relative center of pressure coefficient with consideration of wing effect at subsonic speed (dashed lines obtained by extrapolation).

Fig. XV-1-1, which shows calculated results for three wing forms: delta, trapezoidal (λ = 1/2), and rectangular. The curves for $\alpha'\lambda_{wg} < 4$ are extrapolated to the value $(x_{c.p\alpha}/b_{rt})_{n(wg)}$, which corresponds to slender-body theory.

Example. Taking interference into account, calculate the forces and moments acting on a starboard cantilever in the form of a delta wing on a body, and on the entire cruciform body-wing combination (the dimensions are indicated in Fig. XV-1-12). We take angles $\alpha_b = 0.3$ (17.2°) and $\phi = 22.5°$ and $M_\infty = 2$ and use the formulas, tables, and diagrams given above. We enter all results in Table XV-1-4, from which the sequence of the computational work is obvious. /620

It is assumed in the calculation that the pitching-moment axis passes through the point on the leading edge at which the wing meets the body. The root chord b_{rt} is taken as the characteristic length ℓ, and the area of the isolated wing as the characteristic area.

In this example, the calculations take into consideration the fact that the derivative $(c_N^\alpha)_{wg}$ was determined not from slender-body aerodynamic theory, but from linearized theory. Linearized theory was also used in improving $(x_{c.p\alpha}/b_{rt})_{b(wg)}$ with consideration of the tail-section effect (see Fig. XV-1-9). This quantity was found to be 0.85, i.e., substantially larger than the value of 0.556 obtained in slender-body theory.

TABLE XV-1-4. EXAMPLE OF CALCULATION OF FORCES AND MOMENTS FOR CRUCIFORM BODY-WING COMBINATION WITH CONSIDERATION OF INTERFERENCE

/621

1	2	3	4	5	6	7	8	9	10	11	12	13	14
$\frac{r}{s_m}$	K_{wg}	K_b	$\left(\frac{x_{c.p}\,\alpha}{b_{rt}}\right)_{wg(b)}$	$\left(\frac{x_{c.p}\,\alpha}{b_{rt}}\right)_{b(wg)}$	$\frac{z_{c.p}\,\alpha - r}{s_m - r}$	$\bar{z}_{c.p}\,\alpha$	K_φ	$\frac{z_{c.p}\,\varphi - r}{s_m - r}$	$z_{c.p}\,\varphi$	$\left(\frac{x_{c.p}\varphi}{b_{rt}}\right)_{wg(b)}$	α'	$\frac{2\alpha' r}{b_{rt}}$	tg ε
0,75/2.75	From Tbl. XV-1-1 for (1)	From Tbl. XV-1-1 for (1)	From Tbl. XV-1-1 for (1)	From Tbl. XV-1-1 for (1)	From Tbl. XV-1-1 for (1)	From 6	From Tbl. XV-1-2 for (1)	From Tbl. XV-1-2 for (1)	From 9	From Tbl. XV-1-2 for (1)	$\sqrt{M_\infty^2 - 1}$	from Fig. XV-1-12 and (12)	From Fig. XV-1-15
0.27	1.23	0.39	0.648	0.556	0.418	1.586	0.500	0.537	1.91	0.669	1.730	0.650	0.500

15	16	17	18	19	20	21	22	23	24	25	26	27	28	29
$\alpha' \operatorname{tg}\varepsilon$	$\left(\frac{x_{c.p}\,\alpha}{b_{rt}}\right)_{b(wg)}$	k	$E(k)$	$(c_N^\alpha)_{wg}$	$(c_{N_1})_c$	m_b	$(m_{x_1})_c$	$(c_N)_{b(wg)}$	$(c_{z'})_{b(wg)}$	$(m_{z'})_{b(wg)}$	$(c_N)_{wg.b}$	$(c_{z'})_{wg.b}$	$(m_{z'})_{wg.b}$	$(m_{x'})_{wg.b}$
From (12) and (14)	From Fig. XV-1-9, b for (13) and (15)	$\sqrt{1-(\alpha' \operatorname{tg}\varepsilon)^2}$	From Formula (V-3-18')	From (V-10-51) ($\gamma_1 = \varepsilon$), (14) и (18)	Table XV-1-3 for (19), (14), (2), (8)	Table XV-1-3 for (14), (19) (2), (8), (4), (11)	Table XV-1-3 for 10), (7), (2) (8), (4), (19)	Table XV-1-3 for (3), (19)	Table XV-1-3 for (3)	Table XV-1-3 for (3), (16), (19)	Table XV-1-3 for (2), (3), (19)	Table XV-1-3	Table XV-1-3 for (2), (3), (16) (4), (19)	Table XV-1-3
0.866	0.850	0.500	1.47	2.14	0.399	—0.526	—0.160	0.25	0	—0.242	$(c_N)_b$ + 1.04	0	$(m_{z'})_b$ — —0.725	0

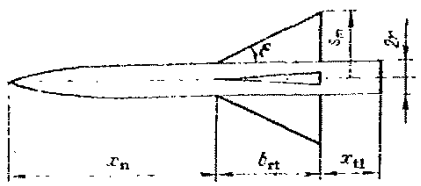

Figure XV-1-12. Model Form and Dimensions Used in Examples of Interference Calculation for Cruciform Combination:

x_n	b_{rt}	x_{tl}	r	s_m
4.50	4.00	2.67	0.75	2.75

The coordinates of the wing and body centers of pressure can be found from Table XV-1-1 with consideration of interference. The distance from the nose to the point of application of the normal force $N_{wg(b)}$ is

$$(x_{c.p\ \alpha})_{wg(b)} = x_n + \left(\frac{x_{c.p\ \alpha}}{b_{rt}}\right)_{wg(b)} b_{rt}. \quad \text{(XV-1-47)}$$

On substituting the data, we find

$$(x_{c.p\ \alpha})_{wg(b)} = 4.5 + 0.648 \cdot 4 = 7.09.$$

The point of application of the body normal force $N_{b(wg)}$ due to the influence of the wing on the body is determined by the coordinate

$$(x_{c.p\ \alpha})_{b(wg)} = x_n + \left(\frac{x_{c.p\ \alpha}}{b_{rt}}\right)_{b(wg)} b_{rt}, \quad \text{(XV-1-48)}$$

which in our example is equal to

$$(x_{c.p\ \alpha})_{b(wg)} = 4.5 + 0.85 \cdot 4 = 7.9.$$

The distance to the body center of pressure is determined in slender-body theory by the formula

$$(x_{c.p})_b = x_{mid}\left(1 - \frac{W_n}{\pi r_{mid}^2 x_{mid}}\right), \quad \text{(XV-1-49)}$$

which is derived on the assumption that the only lifting part of the body is a curvilinear nose section of length x_{mid}. In (XV-1-49), W_n is the volume of this nose section. With consideration of the $(x_{c.p})_b$ for an isolated body that creates a normal force N_b, the center of pressure coordinate of the body-wing combination is

$$x_{c.p} = \frac{(x_{c.p.\alpha})_{wg(b)} N_{wg(b)} + (x_{c.p.\alpha})_{b(wg)} N_{b(wg)} + (x_{c.p})_b N_b}{N_{wg(b)} + N_{b(wg)} + N_b}. \quad \text{(XV-1-50)}$$

In using this formula, we can take account of the generation of a certain part of the lift by the cylindrical section aft of the curvilinear nose at high Mach numbers for long bodies, so that $x_{c.p}$ will be larger than indicated by (XV-1-49). To obtain more accurate data, therefore, it is preferable to use the results of linear theory or experimental data. When the wings create the largest part of the total lift and the contribution of the body is small, the linear theory and Formula (XV-1-49) can be applied.

§XV-2. CHANGE IN TAIL AERODYNAMIC PROPERTIES UNDER THE INFLUENCE OF THE WING /622

General Expression for Normal Force

If there are no other lifting or control surfaces forward of a tailplane attached to a body, the interference calculation for the tail and body is made in exactly the same way as for a wing and body. But if there is a wing on the body forward of the tail, the additional effect of the wing must be taken into account in determining the aerodynamic characteristics of the tail.

Let us consider the case in which the vehicle's wing and tail are mounted rigidly on the body and have zero setting angles relative to the vehicle's longitudinal axis. We shall assume that there is no slip and that the normal force is a linear function of attack angle. Then the normal-force coefficient with consideration of interference will be

$$c_N = (c_N^\alpha)_{wg}\alpha (K_{wg} + K_b)_{wg}\frac{S_{wg}}{S} + (K_{wg} + K_b)_{h.t} \times \\ \times (c_N^\alpha)_{h.t}(\alpha - \varepsilon)\frac{S_{h.t}}{S} + (c_N^\alpha)_b \alpha \frac{S_{mid}}{S}. \qquad \text{(XV-2-1)}$$

Here $(c_N^\alpha)_{h.t} = (\partial c_N/\partial\alpha)_{h.t}$ is the derivative of the normal-force coefficient c_N of the isolated horizontal tailplane with respect to the attack angle α; $(K_{wg} + K_b)_{wg}$ is the total interference coefficient for the body-wing combination; $(K_b + K_{wg})_{h.t}$ is the same coefficient for the body-tail combination; S_{wg} and $S_{h.t}$ are the areas of the isolated wing and horizontal tail without consideration of the parts occupied by the body; S is the wing plan area counting the part occupied by the body; ε is the downwash angle behind the wing at the angle of attack α; $\alpha - \varepsilon = \alpha_{e.h.t}$ is the effective attack angle of the tailplane as a result of the downwash behind the wing.

Formula (XV-2-1) can also be used to determine normal force when there is a slip (or roll) angle. For this purpose, it is necessary to add a coefficient $\overline{K}_\phi$ to the sum of the coefficients $K_{wg} + K_b$ to take account of interference on the appearance of the roll angle ϕ and to substitute $\alpha = \alpha_b \cos \phi$ for the angle α. The force calculated with (XV-2-1) will be equal in absolute magnitude to the length of a vector in the plane of the attack angle α.

In the range in which c_N varies linearly with attack angle,

$$c_N = c_N^\alpha \alpha. \qquad \text{(XV-2-2)}$$

The c_N^α in (XV-2-2) is determined by differentiating (XV-2-1) with respect to α: /623

$$c_N^\alpha = (c_N^\alpha)_{wg}\left[(K_{wg} + K_b)_{wg}\frac{S_{wg}}{S} + \right.$$
$$\left. + (K_{wg} + K_b)_{h.t}\frac{S_{h.t}}{S}\frac{(c_N^\alpha)_{h.t}}{(c_N^\alpha)_{wg}}\left(1 - \frac{d\varepsilon}{d\alpha}\right)\right] + (c_N^\alpha)_b\frac{S_{mid.}}{S}. \qquad \text{(XV-2-3)}$$

In many current vehicle configurations, $S_{h.t} \ll S$ and $S_{h.t}/S \ll 1$. Moreover, $1 - d\varepsilon/d\alpha$ is often much smaller than unity. Formula (XV-2-3) can therefore be replaced by the approximate expression

$$c_N^\alpha = (c_N^\alpha)_{wg}(K_{wg} + K_b)_{wg}\frac{S_{wg}}{S} + (c_N^\alpha)_b\frac{S_{mid}}{S}. \qquad \text{(XV-2-4)}$$

The above relationships are not applicable for large disturbances, when the aerodynamic force does not vary linearly and it is necessary to consider nonlinear effects. This makes the problem considerably more complex. In many cases that are of practical interest, the influence of large attack angles can be determined only by experiment. As a rule, the "limiting" attack angle at which the linear relationships still apply is also determined experimentally. Study has shown that the "limiting" attack angle becomes smaller with increasing M_∞.

Downwash Angle Behind Wing

Subsonic flow. The downwash angle at a point behind the wing at a distance of $L_{h.t}$ from the center of pressure (aerodynamic center) can be determined by the formula [6]:

$$\varepsilon = \frac{c_N}{2\pi\lambda_{wg}} k \left[1 + \sqrt{1 + \frac{1}{k^2}\left(\frac{y_t}{2L_{r.0}}\right)^2}\right] \text{rad}, \qquad \text{(XV-2-5)}$$

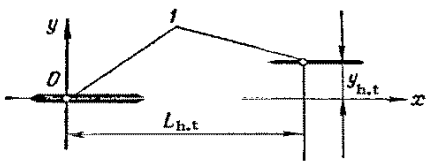

Figure XV-2-1. Vertical Shift of Tail from Wing Plane. 1) Aerodynamic center.

where ℓ is the span and $\lambda_{wg} = \ell/b_{mn}$ is the wing aspect ratio.

The parameter

$$k = \frac{c_{N0} b_{rt}}{c_N b_{mn}}, \qquad \text{(XV-2-6)}$$

where c_{N0} is the root-section normal-force coefficient.

The downwash angle can be assumed constant over the span of the tail and equal to its value at a point that coincides with the center of pressure (aerodynamic center) of the tail, the distance to which is $L_{h.t}$. Formula (XV-2-5) can be used with a certain approximation for wings and tails of any planform if they lie in the same plane.

If the wing and tail lie in different horizontal planes and the distance between them is $y_{h.t}$ (Fig. XV-2-1), the calculation will be more complex. An approximate relationship that is also suitable for such cases can be indicated:

$$\varepsilon = 46.2 \frac{c_N}{\lambda_{wg}} k_1 k_2 k_3 \text{ deg}. \qquad \text{(XV-2-7)}$$

The coefficients k_p that appear in this formula correct the downwash angle for the influence of the distance $L_{h.t}(k_1)$, the vertical position of the tail with respect to the wing chord plane (k_2), and wing taper (k_3). Values of these coefficients are given in Figs. XV-2-2-XV-2-4. /624

Supersonic flow. The characteristics of a tailplane positioned behind a wing can be determined approximately from the flow downwash angle behind the isolated wing. In this case, therefore, the effect of interference between the wing and body on downwash angle is not taken into account.

Figure XV-2-5 [6] presents values of the downwash angles behind isolated rectangular-planform wings with two different aspect ratios as a function of the distance L from the leading edge referred to the chord b. The curves shown in Fig. XV-2-6 enable us to determine the downwash angle at any point behind

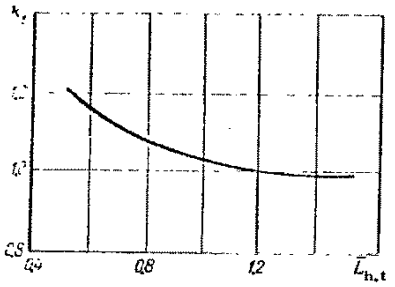

Figure XV-2-2. Curve for Calculation of Coefficient k_1 in (XV-2-7).

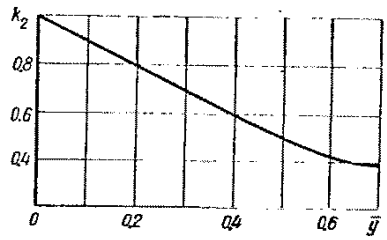

Figure XV-2-3. Curve for Calculation of Coefficient k_2 in (XV-2-7).

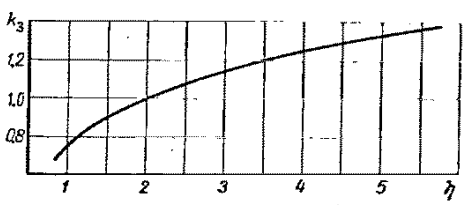

Figure XV-2-4. Curve for Calculation of Coefficient k_3 in (XV-2-7).

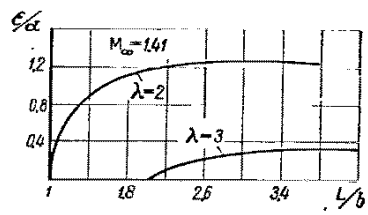

Figure XV-2-5. Downwash behind Rectangular Wing.

delta wings as a function of the relative longitudinal coordinate of the point $\bar{L} = L/b_{rt}$ and its dimensionless distance from the plane $\bar{y} = y_{h.t}/b_{rt}$, as well as the parameter $\theta_0 = (\operatorname{tg}\chi_1)^{-1}\sqrt{M_\infty^2 - 1}$.

The calculation for the tail must be made for the effective attack angle with consideration of tail-body interference. In rough evaluations of tail aerodynamic characteristics, we can limit ourselves to the influence of the effective attack angle only.

Lifting Capacity of Vehicle with Fixed Wings and Tail at Supersonic Speeds

Coefficients of interference of tail with wing. The real characteristics of the tail can be considered to depend on the angle $\alpha_{e.h.t}$ only in rough approximation. They can be improved by assuming that the average downwash angle and, consequently, also $\alpha_{e.h.t}$ will also be determined by the interference between the wing and the body. /625

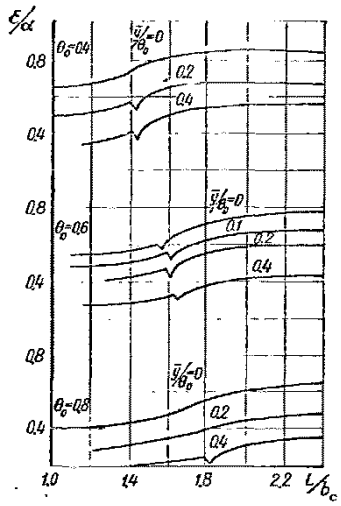

Figure XV-2-6. Downwash Behind Delta Wing.

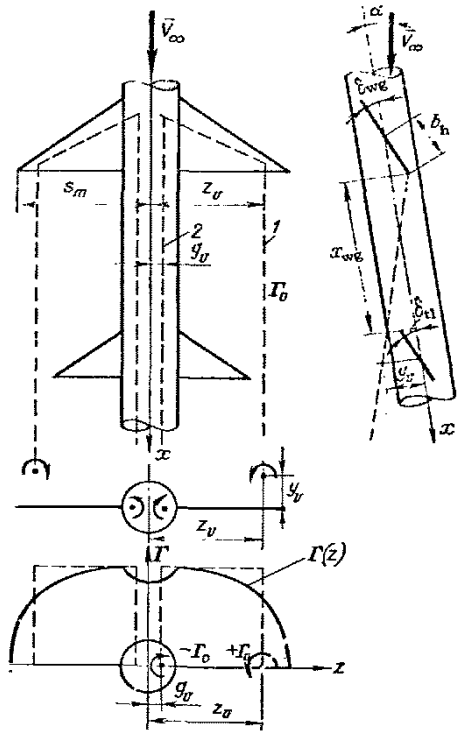

Figure XV-2-7. Vortex Scheme Used in Calculating Interference of Wing and Tail. 1) outboard vortex; 2) inboard vortex.

The conclusions of vortex theory from slender-body aerodynamics, which enable us to calculate directly that part of the aerodynamic coefficient that is created by the tail under the influence of interference with the wing, can also be used. In this theory, which is equally applicable for subsonic and supersonic speeds, a vortex diagram such as that shown in Fig. XV-2-7 is used for a wing joined to a body. At positive attack angles, the vortices lie above the plane of the tail, and their direction coincides with the oncoming-flow velocity.

Thus, the problem of interference of the tail with the wing is reduced to one of interference of the tail with a vortex. The effect of the interference is determined by the intensity and position of the outboard vortex relative to the tail. As one of the characteristics of tail interference that depend not on intensity, but only on the position of the vortex, we introduce the dimensionless parameter i_{t1}, which is determined from the expression [51]:

$$N_{(b.tl)v} = i_{tl} \frac{\Gamma_0}{2\pi V_\infty (s_m - r)_{tl}} \frac{N_{tl}}{\alpha}. \qquad \text{(XV-2-8)}$$

Like K_{wg}, the parameter i_{tl} is known as an interference coefficient. Unlike K_{wg}, however, the coefficient i_{tl} takes account /626 of the change in the lift of the tail-body combination under the influence of the wing (vortex).

In (XV-2-8), $N_{(b.tl)v}$ is the normal force of the tailplane that is governed by the wing (vortex) in the presence of the body; Γ_0 is the vorticity; N_{tl}/α is the normal force of the isolated tailplane per degree of attack angle; $(s_m - r)_{tl}$ is the difference between the span of the tail and the radius of the body at the point at which it meets the trailing edge of the tail.

$N_{(b.tl)v}$ must be added to the value determined with (XV-2-1) if the calculation is being made not for the effective attack angle but for the body attack angle (α). Usually, $N_{(b.tl)v}$ is negative, since the normal force is lowered by the presence of vortices trailing off the wing.

If interference of the wing with the tail does not lower the lift of the tail, then $N_{(b.tl)v} = 0$ and $i_{tl} = 0$. We can take the other extreme case in which, as a result of interference with the wing, the tailplane lift vanishes altogether. In this case, $i_{tl} < 0$ and takes the smallest of all of its possible values.

Calculation of tailplane normal force due to interference with the wing ($N_{(b.tl)v}$). This calculation can be made by Formula (XV-2-8), which applies for a plane body-wing-tail combination (or for a cruciform combination at zero angle of roll). The vorticity Γ_0 in this formula can be determined as follows. Let Γ be the vorticity behind the half-wing (see Fig. XV-2-7) on segment $(s_m - r)_{wg}$, i.e., between the outboard edge of the wing and the body. Then the wing normal force $N_{wg(b)} = 2\rho_\infty V_\infty \int_{r_{wg}}^{(s_m)_{wg}} \Gamma dz$. If we assume that the vortex sheet is replaced by a vortex of intensity Γ_0 equal to the circulation in the wing-half root section, then $\int_{r_{wg}}^{(s_m)_{wg}} \Gamma dz = \Gamma_0 (z_v - r)_{wg}$, where z_v is the lateral coordinate of the vortex. Remembering that the additional normal force of the fixed wing ($\delta_{wg} = 0$) is

$$N_{wg(b)} = q_\infty S_{wg} K_{wg} \alpha \left(\frac{\partial c_N}{\partial \alpha}\right)_{wg}, \qquad \text{(XV-2-9)}$$

we can find the circulation Γ_0. Introducing it into (XV-2-8), we obtain

$$N_{(b,tl)v} = i_{tl} \frac{K_{wg}\alpha \left(\frac{\partial c_N}{\partial \alpha}\right)_{wg} \left(\frac{\partial c_N}{\partial \alpha}\right)_{tl} S_{wg} S_{tl} q_\infty}{8\pi (s_m - r)_{tl} (z_v - r)_{wg}}, \qquad \text{(XV-2-8')}$$

where $\left(\frac{\partial c_N}{\partial \alpha}\right)_{tl}$, $\left(\frac{\partial c_N}{\partial \alpha}\right)_{tl}$ are the derivatives for the isolated wing and tail, respectively; S_{wg} and S_{tl} are the areas of the two cantilevers of the isolated wing and tail; $(s_m)_{tl}$ is the span of the tail, including the body; r_{wg} and r_{tl} are the respective radii of the body at the positions of the wing and tail.

Taking a certain figure S as the characteristic area, we obtain the normal-force coefficient

$$(c_N)_{(b,tl)v} = \frac{N_{(b,tl)v}}{q_\infty S} = i_{tl} \frac{K_{wg}\alpha \left(\frac{\partial c_N}{\partial \alpha}\right)_{wg} \left(\frac{\partial c_N}{\partial \alpha}\right)_{tl} (s_m - r)_{tl} \frac{S_{wg}}{S}}{2\pi \lambda_{tl} (z_v - r)_{wg}}, \qquad \text{(XV-2-10)}$$

where the aspect ratio of the isolated tail is /627

$$\lambda_{tl} = \frac{4 (s_m - r)^2_{tl}}{S_{tl}}. \qquad \text{(XV-2-11)}$$

TABLE XV-2-1. HORIZONTAL COORDINATE OF TRAILING VORTEX (TRANSVERSE POSITION OF VORTEX-SHEET CENTER OF GRAVITY)

$\bar{r}_s = \frac{r}{s_m}$	0	0.1	0.2	0.3	0.4	0.5	0.6	0.7	0.8	0.9	1.0
$\left(\frac{z_v - r}{s_m - r}\right)_{wg}$	0.785	0.769	0.760	0.757	0.757	0.759	0.763	0.768	0.774	0.780	0.786

To use (XV-2-10), it is necessary to know the vortex coordinates x_v and y_v in the tail section of the vehicle. It may be assumed to simplify the calculations that the vortices trailing off the wing trailing edge coincide with the flow direction and do not shift transversely. If we also assume that the coordinate lies over the center of gravity of the tail area including that

part of the area which is occupied by the body, then the coordinate

$$y_v = x'_{wg}\alpha - b_h \delta_{wg}, \qquad \text{(XV-2-12)}$$

where x'_{wg} is the distance from the wing trailing edge to the center of gravity of this area and b_h is the distance from the trailing edge to the hinge line of the wing (Fig. XV-2-7). The values of the coordinate z_v, which can be determined from Table XV-2-1, do not depend on the planform of the wing or the shape of the body forward of the maximum-wingspan line, since potential and, consequently, circulation are determined in slender-body theory only by the transverse flow in the plane under consideration.

The maximum deviation between the values of the ratio $\left(\frac{z_v - r}{s_m - r}\right)_{wg}$ from Table XV-2-1 and the corresponding values for the isolated wing ($\pi/4 = 0.786$) is about 3%. This small difference permits determination of the z_v of the body-wing combination from the data for the isolated wing, even in analysis of nonslender combinations.

For the isolated wing, the linearized theory gives

$$z_v = \frac{(c_N)_{wg} S_{wg}}{2 (c_N)_{mn} b_{mn}}, \qquad \text{(XV-2-13)}$$

where $(c_N)_{mn} b_{mn}$ is the product of the profile normal force coefficient in the mean section by the mean chord.

Formula (XV-2-13) was derived on the assumption that maximum circulation corresponds to the mean-section position. The results of calculation of the ratio $(z_v - r)/(s_m - r)$ with (XV-2-13) are given in Fig. XV-2-8 for rectangular ($\lambda = b_{tp}/b_{rt} = 1$), trapezoidal ($\lambda = 1/2$), and delta ($\lambda = 0$) wings. The dashed curves were found by extrapolating data from the linearized theory to the value $\pi/4$ obtained from slender-body theory for zero aspect ratio.

The expressions found for z_v determine the lateral position of the vortex on the wing. Research has shown that this value of z_v differs from the lateral coordinate of the tail vortex. In the absence of more accurate data, the z_v for the tail was /628

assumed to be the same as on the wing.

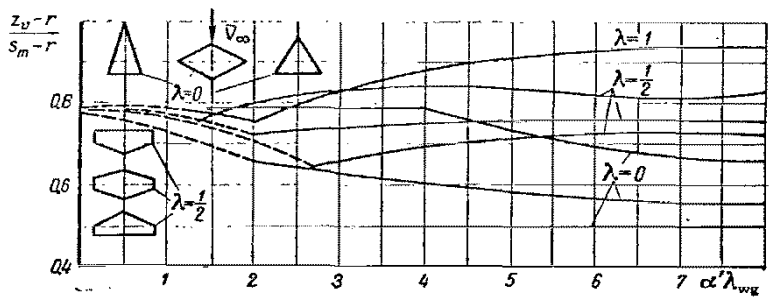

Figure XV-2-8. Relative Coordinate Determining Transverse Position of Vortex Filament.

According to (XV-2-8), the interference coefficient can be regarded as the ratio of two dimensionless quantities: the normal force and the dimensionless vorticity. If the normal forces are calculated by the linearized theory rather than by slender body theory, the interference coefficient remains practically constant. Thus, having calculated the coefficient i_{tl} by slender-body theory, we can use that value to calculate the interference for nonslender configurations that fit into the framework of linearized theory. This is the point of introducing the tail interference coefficient. In the general case, it depends on the parameters $\lambda = (b_{tp}/b_{rt})_{tl}$; $(r/s_m)_{tl}$; $(b_{rt}/\alpha' s_m)_{tl}$; $(z_v/s_m)_{tl}$ and $(y_v/s_m)_{tl}$. The method of strips is effective for calculation of i_{tl} provided that a plane model is considered. Calculations by this method indicate that i_{tl} is practically independent of the ratio $(b_{rt}/\alpha' s_m)_{tl}$. The results of these calculations are shown in Figs. XV-2-9, XV-2-10, and XV-2-11 for combinations of a body with delta ($\lambda = 0$), trapezoidal ($\lambda = 1/2$), and rectangular ($\lambda = 1$) tails. Curves of $i_{tl} = \text{const}$ plotted for the parameters λ and $(r/s_m)_{tl}$ as functions of $(z_v/s_m)_{tl}$ and $(y_v/s_m)_{tl}$ appear in these figures. For the delta wing, the maximum value corresponds to a vortex in the plane of the tail near the inboard end. For the other wings, an infinite maximum appears when the vortex is located at the end. Thus, with the exception of delta wings with supersonic leading edges, strip theory is unsuitable for vortex positions near the end.

The strip method gives more satisfactory data when the vortex lies outside the tail and less accurate results for inboard positions. Figure XV-2-12 shows $[(i_{tl.l} - i_{tl}/i_{tl.l}]$ 100% calculated

from the value of $i_{tl.l}$ found from linearized theory with $(r/s_m)_{tl} = 0.2$, $(b_{rt}/\alpha' s_m)_{tl} = 0.5$ for a combination with a rectangular tail ($\lambda = 1$), as functions of the ratio $(z_v/s_m)_{tl}$. The curves in this figure can be used to improve the values of i_{tl} determined by the strip method using the diagrams in Figs. XV-2-9, XV-2-10 and XV-2-11. This refinement is advisable when the interference coefficient is determined for an inboard vortex position.

As we see from Figs. XV-2-9, XV-2-10, and XV-2-11, the interference coefficient is for fixed values of λ, $(r/s_m)_{tl}$ a function of only the vortex dimensionless coordinates $(z_v/s_m)_{tl}$, $(y_v/s_m)_{tl}$ and does not depend on vorticity. Practical interest attaches to an interference parameter that depends on vorticity. One such parameter, which characterizes degree of interference, is the tail effectiveness coefficient /632

$$\eta_{tl} = \frac{N_{b.wg.tl} - N_{b.wg}}{N_{b.tl} - N_b}, \qquad \text{(XV-2-14)}$$

which is equal to the ratio of the normal-force increment when mounting the empennage on the body-wing combination to the normal-force increment when it is mounted on the isolated body. The tail effectiveness indicates the factor by which the bearing capacity of the tail is lowered as a result of interference with the wings. Another expression for η_{tl} is

$$\eta_{tl} = 1 - \frac{N_{(b.tl)v}}{N_{b.tl} - N_b}. \qquad \text{(XV-2-15)}$$

The force difference $\Delta N = N_{b.tl} - N_b$ can be presented in the form $\Delta N = \alpha i$, where the coefficient i is determined from a relationship that takes account of interference between the body and tail. By analogy with the relation for ΔN, we can write a relation $N_{(b.tl)v} = -\varepsilon i$, which takes account of the change in tail normal force as a result of downwash at an angle ε due to interference from the wing. We can thus establish a relation between the effectiveness coefficient and the wing downwash angle:

$$\eta_{tl} = 1 - \frac{\varepsilon}{\alpha}. \qquad \text{(XV-2-16)}$$

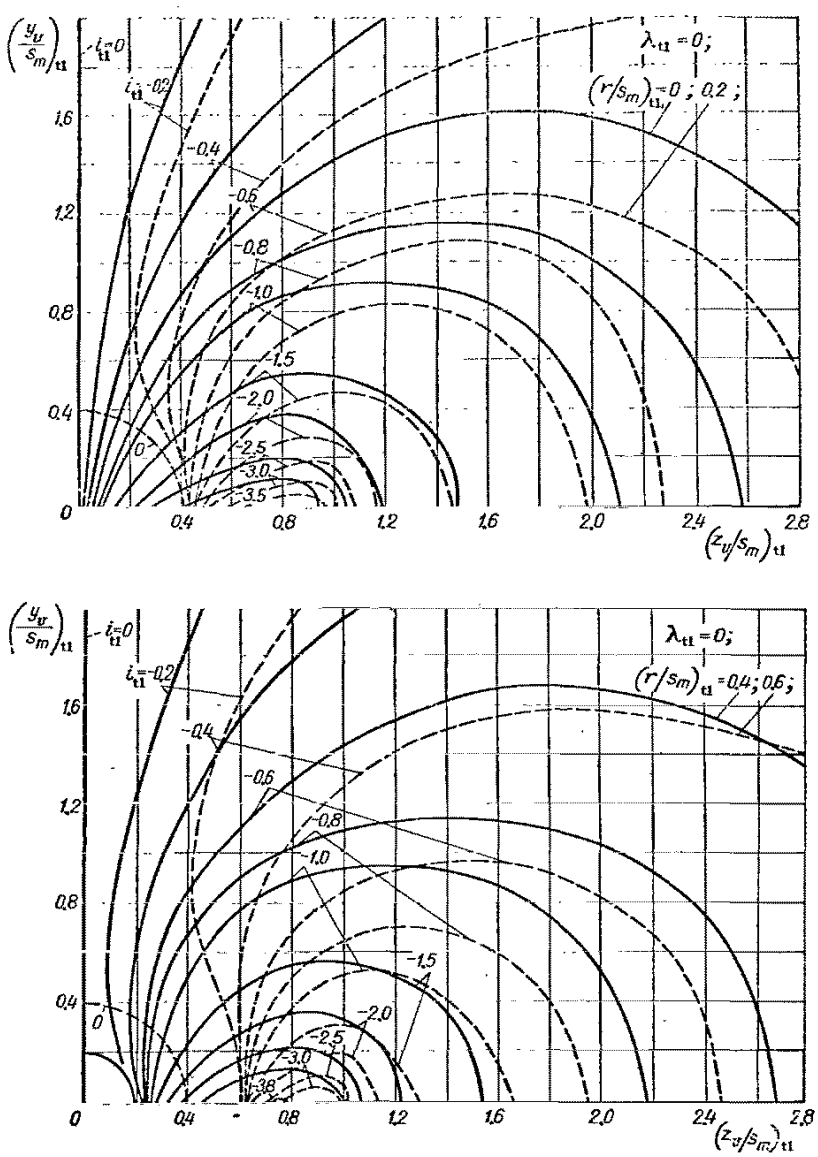

Figure XV-2-9. Variation of Interference Coefficient for Body-Delta-Tail Combination.

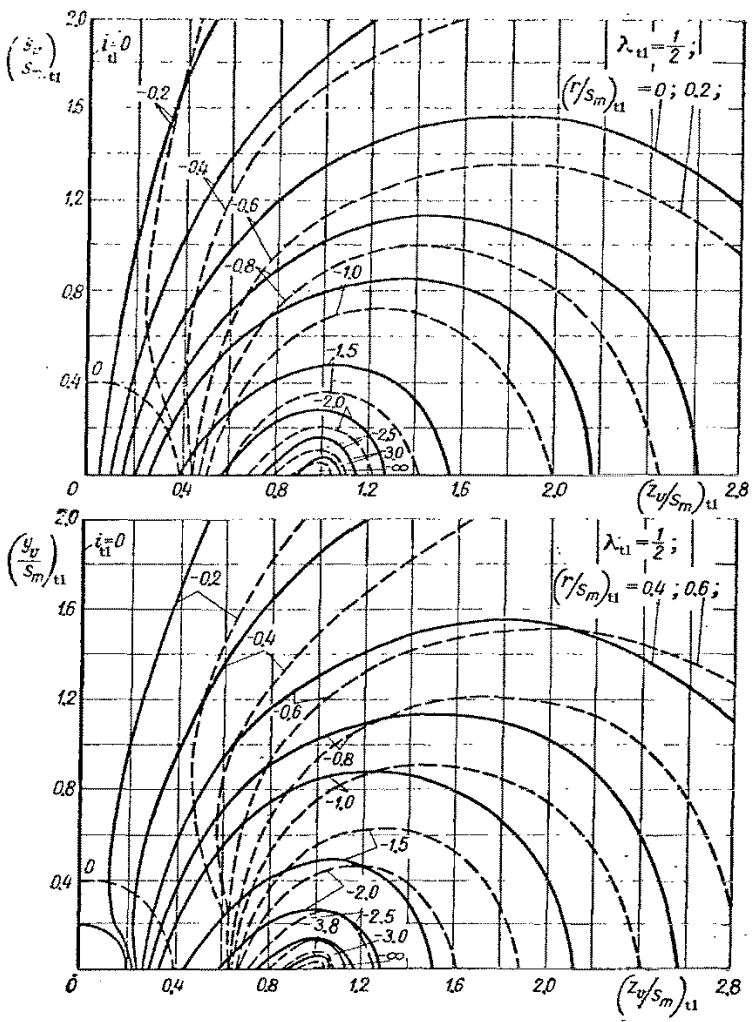

Figure XV-2-10. Variation of Interference Coefficient for Body-Trapezoidal-Wing Combination.

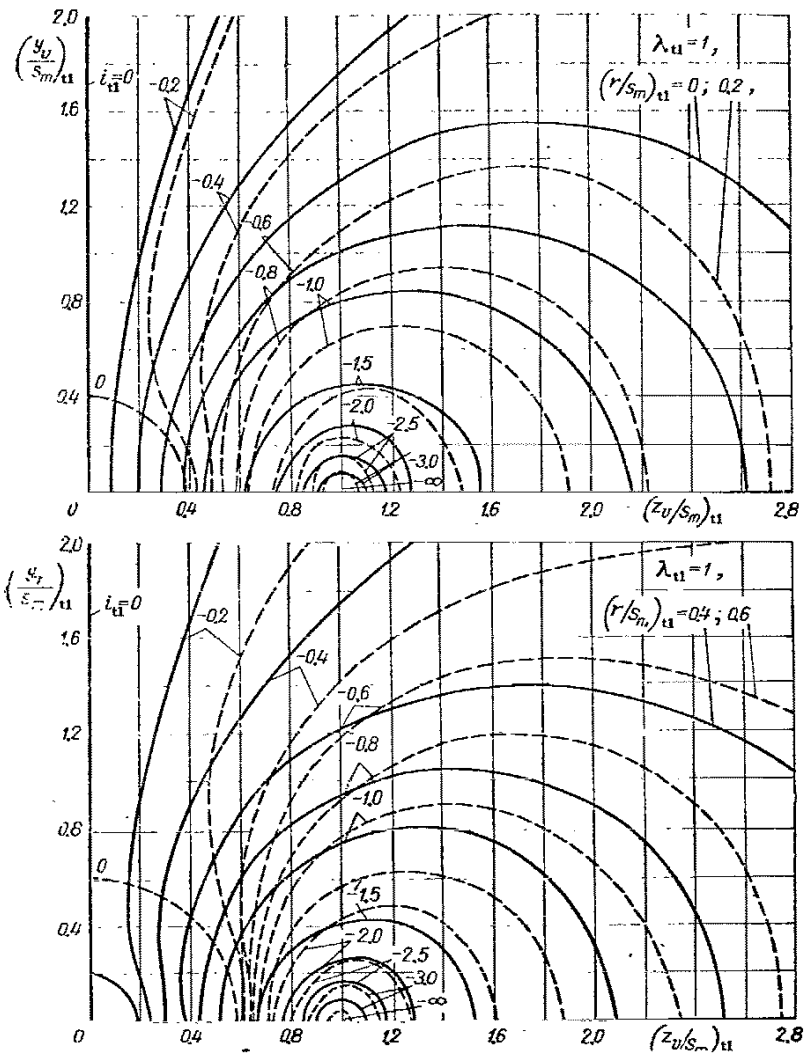

Figure XV-2-11. Variation of Interference Coefficient for Body-Rectangular-Wing Combination.

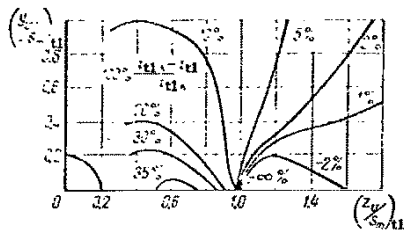

Figure XV-2-12. Error in Calculation of Interference Coefficient by Method of Strips for Body-Rectangular-Wing Combination [$r/s_m = 0.2$; $(b_{rt}/\alpha' s_m)_{tl} = 0.5$, $\lambda_{tl} = 1$].

Remembering that ε and α are small, we can replace ε/α by the derivative $(d\varepsilon/d\alpha)_{\alpha=0}$.

Expression (XV-2-16) is used for approximate evaluation of the sidewash angle σ in the presence of slip. In this case, the effectiveness should be referred to the vertical tail and the ratio ε/α replaced by $\sigma/\beta_{sl} \approx d\sigma/d\beta_{sl}$.

Tail center of pressure. Like the normal force, the center of pressure coordinate of the tail varies under the influence of wing vortices. It can be assumed with sufficient approximation that the point of application of the normal force due to the wing vortices coincides with the tail center of pressure for a body-tail combination, i.e.,

$$(x_{c.p}\ \alpha)_{tl(v)} = (x_{c.p}\ \alpha)_{tl(b)}. \qquad \text{(XV-2-17)}$$

Approximate evaluation of tail interference. Let us consider two methods of estimating the interference. One is based on a simplified model of the flow in which a plane vortex sheet forms behind the wing in the plane of the tail. It is assumed that the tail is in the plane of the wing. Thus, those areas of the tail that are "coated" by the vortex sheet will not produce a normal force. If the tail span $(s_m)_{tl}$ is smaller than or equal to the wing span $(s_m)_{wg}$, the tail effectiveness is zero. This follows directly from (XV-2-14), in which we must set $N_{b.wg.tl} = N_{b.wg}$.

When $(s_m)_{tl} > (s_m)_{wg}$, the total normal force $N_{b.wg.tl}$ of the body-wing-tail combination (including the nose section) is calculated by Formula (XV-1-15), in which $(s_m)_{wg}$ must be replaced by $(s_m)_{tl}$ and the body radius r assumed constant behind the wing. Obviously, this value of $N_{b.wg.tl}$ will be exactly equal to the normal force $N_{b.tl}$ of the body-tail combination in the absence of the wing. Introducing the expressions for $N_{b.wg.tl}$ and $N_{b.tl}$ into (XV-2-14) and applying (XV-1-15) for $N_{b.wg}$ and the relation $N_b = 2\pi r^2 q_\infty \alpha$, we find the empennage effectiveness: /633

$$\eta_{tl} = 1 - \frac{(1-r_{wg}^2)^2}{(1-r_{tl}^2)^2}\frac{r_{tl}^2}{r_{wg}^2}, \qquad \text{(XV-2-18)}$$

where $r_{wg} = r(s_m)_{wg}$, $r_{tl} = r(s_m)_{tl}$.

Formula (XV-2-18) can be used for $(s_m)_{tl} \geq (s_m)_{wg}$.

Let us pass to the second method of evaluating the interference. Unlike the first, it is based on a flow scheme in which the vortex sheet is replaced by two horseshoe vortices in the plane of the tail wing. In fact, the direction of the vortices is nearer to that of the free-flow than to that of the tailplane cantilevers. For this model, the tail effectiveness can be calculated by (XV-2-18) or from the expression

$$\eta_{tl} = 1 - \frac{16}{\pi^2}\frac{(1-r_v)^2}{(1-r_{tl})^2}\frac{r_{tl}^2}{r_v^2}, \qquad \text{(XV-2-19)}$$

where $r_v = r/z_v$ and z_v is the transverse coordinate of the trailing vortex.

Formulas (XV-2-18) and (XV-2-19) are used for cases in which $z_v \leq (s_m)_{tl}$. In calculating r_{tl}, the body radius may be assumed equal to r_{tl}, which differs from the r_{wg} at the wing.

Cruciform combination. The methods set forth above for calculation of interference for a plane body-wing-tail combination can be applied to calculation of interference for a cruciform combination at any angle of roll and for arbitrary spans of the vertical and horizontal tailplanes.

The method is based on the assumption that the cruciform combination is presented as an additive combination of two plane combinations, one of which is formed by the body and the horizontal wing and tail cantilevers, while the other is formed by the body and the vertical cantilevers. It is assumed that the horizontal cantilevers are washed by the transverse velocity component $\alpha V_\infty = V_\infty \alpha_b \cos\phi$, and the vertical cantilevers by the component $\beta_{sl} V_\infty = V_\infty \alpha_b \sin\varphi$.

Interference is calculated independently for the horizontal and vertical tails in y_1 and z_1 body axes. Then the aerodynamic characteristics of the combination are converted to the y' and z' body axes. For a plane combination with roll, the vertical-tail span must be set equal to the body radius in the resulting expressions.

TABLE XV-2-2. EXAMPLE OF CALCULATION

1	2	3	4	5	6
$\left(\frac{r}{s_m}\right)_{wg}$	$\left(\frac{z_v - r}{s_m - r}\right)_{wg}$	$(z_v)_{wg}$	$\frac{(z_n)_{wg}}{(s_m)_{tl}}$	x_{wg}	$(y_v)_{wg}$
From Fig. XV-2-13	From Table XV-2-1 according to (1)	From Fig. XV-2-13 according to (2)	From Fig. XV-2-7 and according to (3)	From Fig. XV-2-13	From Eq. (XV-2-12) and according to (5)
0.2	0.760	2.27	1.25	3.99	0.348

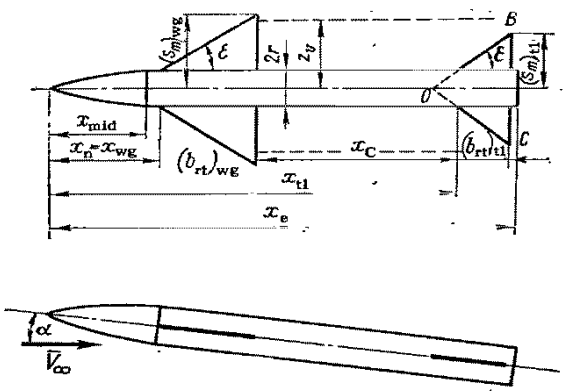

Figure XV-2-13. Illustrating Example Calculation of Tail-Wing Interference:

x_n	$(b_{rt})_{wg}$	x_C	$(b_{rt})_{tl}$	x_e	$(sm)_{wg}$	$(sm)_{tl}$	2r	α°	ε°
3.75	2.25	3.16	1.25	10.5	2.81	1.81	1.125	5	45

As an example, let us calculate the normal-force coefficient due to the vortices formed behind the wing (Fig. XV-2-13), for a tail-body configuration on the assumption that $M_\infty = 2$, $\alpha = 5°$, $\beta_{sl} = 0$ (there is no slip). The results and procedure of the calculation are presented in Table XV-2-2.

To determine the coordinate y_v, we first find the coordinate of the tail center of gravity (triangle OBC in Fig. XV-2-13) and then the distance $x_{wg} = 3.99$. /634 Formula (XV-2-12) is used to calculate y_v.

The derivatives $(\partial c_N/\partial\alpha)_{wg}$ and $(\partial c_N/\partial\alpha)_{tl}$ are determined by Formula (V-10-51) of the linearized theory. Here it is remembered that the leading edges of the wing and tail cantilevers are supersonic for $M = 2$. In calculating $(c_N)_{(b.tl)v}$ by (XV-2-20), the area S_{wg} of the isolated wing (the pair of cantilevers) is taken as the characteristic area. The tail effectiveness coefficient can be calculated from the data of Table XV-2-2. For this purpose, we use (XV-2-15), which can be presented with the normal-force coefficients in the form

OF TAIL-WITH-BODY INTERFERENCE

7	8	9	10	11	12
$\frac{(y_n)_{wg}}{(s_m)_{tl}}$	i_{tl}	K_{wg}	$\left(\frac{\partial c_N}{\partial \alpha}\right)_{wg}$	$\left(\frac{\partial c_N}{\partial \alpha}\right)_{tl}$	$(c_N)_{(b.tl)v}$
From Fig. XV-2-13 and according to (6)	From Fig. XV-2-9 according to (1), (4), (7)	From Table XV-1-1 according to (1)	From Eq. (V-10-51) and $M_\infty = 2$	From Eq. (V-10-51) and $M_\infty = 2$	From Eq. (XV-2-10) at $S = S_{cr}$
0.19	—1.80	1.16	2.31	2.31	—0.029

$$\eta_{tl} = 1 + \frac{(c_N)_{(b.tl)v}}{(c_N)_{b.tl} - (c_N)_b}.$$

Any area S, such as the wing area $S = S_{wg}$, can be taken as characteristic in this formula. Then the normal-force coefficient of the wing-body combination, calculated with consideration of interference, is $(c_N)_{b.tl} = (K_{wg} + K_b)(c_N)_{wg} = 1.62\alpha$, and the normal-force coefficient of the isolated body is $(c_N)_b = 2\alpha S_{mid}/S_{wg} = 0.396\alpha$. According to the data obtained, the tail effectiveness is /635

$$\eta_{tl} = 1 + \frac{-0.029}{(1.62 - 0.396)(5/57.3)} = 1 - 0.27 = 0.73.$$

Thus, the tail effectiveness has been lowered to 73%. This decrease in tail bearing capacity does not cause any substantial decrease in the total lift of the combination, since the wing area is substantially larger than that of the tail. However, the influence of interference on the moment characteristics and, consequently, on static stability may prove to be more substantial owing to the long arm of the tail. In the example considered here, the static stability margin decreases by approximately 3% as $\alpha \to 0$.

The adverse effect of interference diminishes with increasing attack angle. This is because the vortex continues to move in the direction of the flow, and the tail drops down with increasing α, with the result that the coordinates z_v and y_v increase and hence $|i_{tl}|$ decreases. If the position of the vortex with respect to the tail did not change, the unfavorable effect of interference would be linear, since vorticity is proportional to attack angle. It follows from this that in reality, the moment

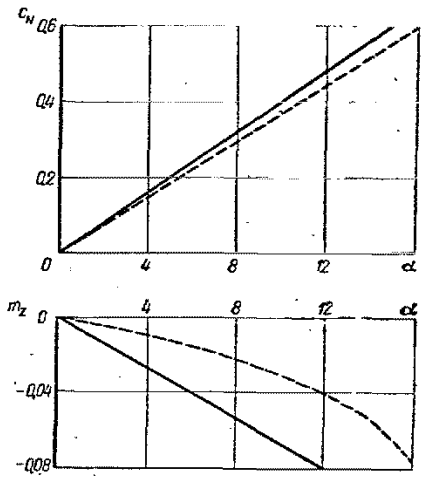

Figure XV-2-14. Coefficients of Moment and Normal Force for Body-Wing-Tail Combination. ———) without interference; -----) with consideration of interference.

characteristic will be nonlinear (Fig. XV-2-14), and that static stability will increase with increasing attack angle.

The unfavorable influence of interference on stability can be reduced by placing the tail higher than the wing (Fig. XV-2-15). Then the characteristics of the tail, which will be cruciform, improve at small attack angles, when the vortices are quite far from it. With increasing attack angle, the upper cantilevers of the tail come steadily closer to the vortices, and the detrimental effect of interference becomes stronger. After the tail has passed through the vortex and moved away from it again, the unfavorable effect diminishes. /636

Tail-wing interference due to presence of compression shocks. In addition to the interference related to vortex formation, there is another interference interaction that arises at high supersonic speeds. At these speeds, compression shocks form on the wing (Fig. XV-2-16) and interact with the tail to change its characteristics further. We see from Fig. XV-2-16 that at a small attack angle ($\alpha = 5°$), the horizontal tail lies in a zone between a tail shock and an expansion fan. As a result, it is at zero angle of attack for the flow passing through the expansion fan and will not create lift. For practical purposes, the tail effectiveness is near zero ($\eta_{tl} = 0$). With increasing attack angle (by way of example, Fig. XV-2-16 shows $\alpha = 20°$), the shock angle to the plane of the wing increases and its plane may pass forward of the tail. Since the streamline behind the shock nearly coincides with the direction of the oncoming flow, the tail recovers much of its effectiveness. Some decrease in lift results from the lower M and velocity head behind the shock. A curve indicating the manner in which the tail moment changes as a result of compression and expansion shocks appears in Fig. XV-2-16. It passes between the lines corresponding on the one hand to total loss of effectiveness ($\eta_{tl} = 0$) and, on the other, to full recovery ($\eta_{tl} = 1$).

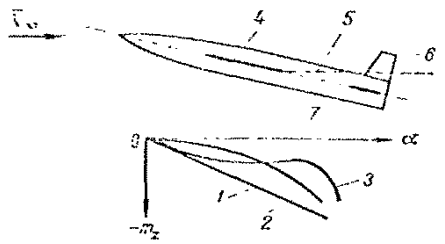

Figure XV-2-15. Effect of Horizontal Tail on Moment Characteristics of Body-Wing-Tail Combination. 1) without interference; 2) with interference considered for conventional tail; 3) with interference considered for nontandem cruciform tail; 4) wing; 5) vortex; 6) vertical tailplane; 7) horizontal tailplane.

§XV-3. EFFECT OF INTERFERENCE ON AERODYNAMIC CHARACTERISTICS OF CONTROLS

All-Moving Plane Controls

Deflection angles. Let these angles for the horizontal cantilevers be δ_1 for the port and δ_2 for the starboard cantilever. We shall assume that the angle will be positive if the wing is deflected downward (Fig. XV-3-1). The longitudinal δ_e and lateral δ_a deflection angles can be calculated from δ_1 and δ_2

$$\delta_e = \frac{\delta_1 + \delta_2}{2}; \quad \delta_a = \frac{\delta_1 - \delta_2}{2}. \qquad \text{(XV-3-1)}$$

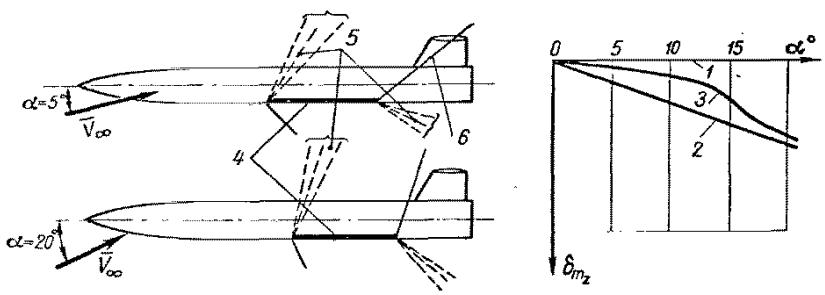

Figure XV-2-16. Effect of Wing-Tail Interference at Appearance of Compression Shocks. 1) effectiveness coefficient $\eta_{tl} = 0$; 2) $\eta_{tl} = 1$; 3) real curve; 4) wing; 5) expansion fan; 6) tail compression shock.

If δ_1 and δ_2 are equal and of the same sign, i.e., $\delta_1 = \delta_2$, then $\delta_e = \delta_1 = \delta_2$. This value of the deflection angle δ_e corresponds to longitudinal [pitch] control. If, on the other hand, the deflection angles are equal but opposite, $\delta_a = \delta_1 = -\delta_2$. The angle δ_a will correspond to transverse control with the aid of horizontal wings.

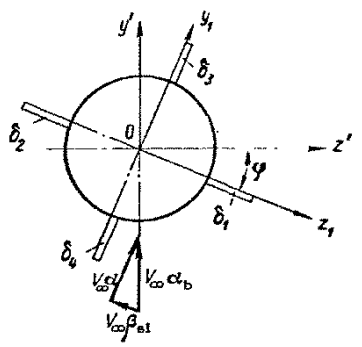

Figure XV-3-1. Cruciform Configuration of All-Moving Controls.

Let the angles δ_3 and δ_4 characterize the deflections of the upper and lower cantilevers, respectively, and let the deflection angle to the right be positive (Fig. XV-3-1). The directional δ_r and transverse δ_a, deflection angles can be determined from these angles:

$$\delta_r = \frac{\delta_3 + \delta_4}{2}; \quad \delta_{a'} = \frac{\delta_3 - \delta_4}{2}. \qquad \text{(XV-3-2)}$$

If $\delta_3 = \delta_4$ (angles δ_3 and δ_4 equal and of the same sign), then the angle δ_r, which is equal $\delta_3 = \delta_4$, characterizes directional control; in this case, when $\delta_3 = -\delta_4$ (angles δ_3 and δ_4 equal and opposite), the angle $\delta_{a'} = \delta_3 = -\delta_4$ and defines the deflection set up for transverse control.

Change in normal force. Let us consider how the normal force is determined for all-moving controls located on the body in a plane configuration. When the deflection angle δ_e of the horizontal cantilevers is not zero and the body is inclined at a certain angle of attack α, the normal force of the wing-body combination can be represented as the sum

$$N_{b.wg} = N_{(b.wg)\alpha} + N_{(b.wg)\delta_e}, \qquad \text{(XV-3-3)}$$

where $N_{(b.wg)\alpha}$ is the normal force at zero control deflection at a certain angle of attack ($\delta_e = 0$, $\alpha \neq 0$); $N_{(b.wg)\delta_e}$ is the normal force of the combination with the controls deflected at zero body angle of attack ($\delta_e' \neq 0$, $\alpha = 0$).

Figure XV-3-2 presents a diagram of the action of the forces. /638 $N_{(b.wg)\alpha}$ has already been determined. To determine the second component $N_{(b.wg)\delta_e}$, we can use results from slender-body aerodynamic theory, extending them with the aid of linearized solutions to nonslender bodies and thus finding the dependence of lift on M_∞. According to slender-body theory, $N_{(b.wg)\delta_e}$ can be presented as the sum

$$N_{(b.wg)\delta_e} = N_{wg(b)\delta_e} + N_{b(wg)\delta_e}, \qquad \text{(XV-3-4)}$$

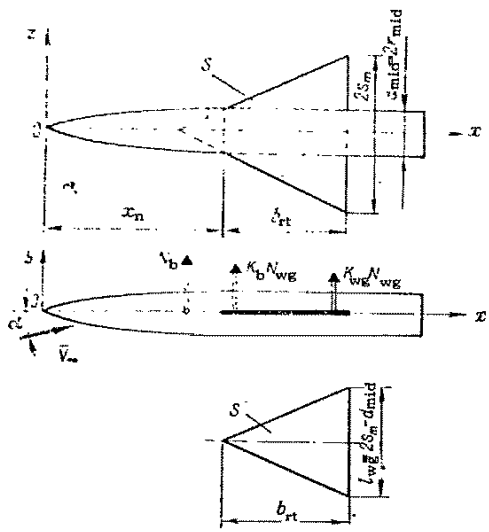

Figure XV-3-2. Diagram of Action of Normal Forces for Moving Control.

where the first term is the normal force of the wing deflected through angle δ_e in the presence of the body effect and the second is the body normal force due to its interference with the wing. Each of these components can be expressed in the form

$$N_{wg(b)\delta_e} = k_{wg} N_{wg},$$
$$N_{b(wg)\delta_e} = k_b N_{wg}, \qquad \text{(XV-3-5)}$$

where k_{wg} and k_b are the interference coefficients due to deflection of the controls through angle δ_e at $\alpha = 0$; N_{wg} is the normal force of the isolated wing. Thus,

$$N_{(b.wg)\delta_e} = (k_{wg} + k_b) N_{wg}. \qquad \text{(XV-3-6)}$$

We can also write

$$N_{(b.wg)\delta_e} = q_\infty S_{wg} \left(\frac{\partial c_N}{\partial \alpha}\right)_{wg} (k_{wg} + k_b)\, \delta_e, \qquad \text{(XV-3-7)}$$

from which the normal force coefficient of the combination, referred to a certain arbitrary area S, is

$$(c_N)_{(b.wg)\,\delta_e} = \left(\frac{\partial c_N}{\partial \alpha}\right)_{wg} (k_{wg} + k_b)\, \delta_e \frac{S_{wg}}{S}. \qquad \text{(XV-3-8)}$$

In the presence of a body attack angle and simultaneous deflection of the wings and tail through the respective angles $(\delta_e)_{wg}$ and $(\delta_e)_{tl}$, the components of the coefficient of the normal force acting on the body-wing-tail combination will be as follows:

1. Normal force coefficient of body nose section

$$(c_N)_b = K_{b.1}\, (c_N^\alpha)_{wg} \alpha. \qquad \text{(XV-3-9)}$$

2. Normal force coefficient of wing in the presence of body

$$(c_N)_{wg(b)} = [K_{wg}\alpha + k_{wg}(\delta_e)_{wg}](c_N^\alpha)_{wg}. \qquad \text{(XV-3-10)}$$

3. Normal force coefficient of body in the presence of wing

$$(c_N)_{b(wg)} = [K_b\alpha + k_b(\delta_e)_{wg}](c_N^\alpha)_{wg}. \qquad \text{(XV-3-11)}$$

4. Normal force coefficient of tail in the presence of body (without consideration of wing-vortex effect) /639

$$(c_N)_{tl(b)} = [K_{tl}\alpha + k_{tl}(\delta_e)_{tl}](c_N^\alpha)_{tl}\frac{S_{tl}}{S_{wg}}, \qquad \text{(XV-3-12)}$$

where K_{tl} and k_{tl} are determined for the tail in the same way as for the wing.

5. Normal force coefficient of body in the presence of body [sic] (without consideration of wing-vortex effect)

$$(c_N)_{b(tl)} = [(K_b)_{tl}\alpha + (k_b)_{tl}(\delta_e)_{tl}](c_N^\alpha)_{tl}\frac{S_{tl}}{S_{wg}}, \qquad \text{(XV-3-13)}$$

where $(K_b)_{tl}$ and $(k_b)_{tl}$ are found from the parameters for the tail in the same way as the coefficients K_b and k_b are found from the wing parameters.

6. Normal force coefficient for tail section due to wing vortices

$$(c_N)_{(b,tl)v} = i_{tl}\frac{(c_N^\alpha)_{wg}(c_N^\alpha)_{tl}[K_{wg}\alpha + k_{wg}(\delta_e)_{wg}](s_m - r)_{tl}}{2\pi\lambda_{tl}(z_v - r)_{wg}}. \qquad \text{(XV-3-14)}$$

This formula was derived from (XV-2-10), in which $K_{wg}\alpha + k_{wg}(\delta_e)_{wg}$ was substituted for $K_{wg}\alpha$, and S_{wg} was taken as the characteristic area.

Together with this component, a force due to the influence of wing vortices on the part of the body between the tail and the wing also makes its appearance. This force is

$$N_{b(v)} = -2\rho_\infty V_\infty \Gamma_0 \times [(z_v - g_v)_{wg} - (z_v - g_v)_{tl}] \qquad \text{(XV-3-15)}$$

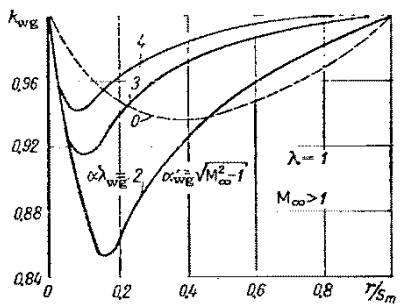

Figure XV-3-3. Values of k_{wg} for Body-Rectangular-Wing Combination.

and depends on the positions of line vortices of vorticity Γ_0 on the wing and tail. Since this position is assumed to be the same on the wing as on the tail, $N_{b(v)} \simeq 0$.

In slender-body aerodynamic theory, the coefficient k_{wg} is determined as a function of the parameter $r_s = r/s_m$. The corresponding values of this coefficient are listed in Table XV-3-1. We see from the tabulated data, which apply for slender body-wing combinations, that the coefficient k_{wg} differs insignificantly from one. This means that the bearing capacity of all-moving thin wings or tails in the presence of a body undergoes practically no change by comparison with the isolated wings.

In application to nonslender combinations, the values of k_{wg} differ under certain conditions from the linearized-theory data, as follows from Fig. XV-3-3, where these data are shown for a body-rectangular-wing combination. If $\alpha'\lambda_w < 2$, we can use the values of k_{wg} from slender-body theory for rectangular wings in combination with a body. When the effective aspect ratio $\alpha'\lambda_{wg} > 2$ and $M_\infty > 1$, then the results obtained are better if the data available from the linearized theory for k_{wg} are used.

The method of calculation of k_{wg} from slender-body theory can also be applied at subsonic speeds; to some extent, this is explained by the independence of the interference coefficient of M_∞.

To determine the coefficient k_b, we have only the data of slender-body theory, which indicate that

$$k_b = K_{wg} - k_{wg}. \qquad \text{(XV-3-16)}$$

Table XV-3-1 gives values of k_b as functions of the ratio r/s_m. /640

The coefficient k_b can differ sharply from unity, indicating substantial influence of the wing on the lifting properties of the

TABLE XV-3-1. INTERFERENCE COEFFICIENTS AND CENTER OF PRESSURE COORDINATE FOR ALL-MOVING CANTILEVER AT $\delta_e \neq 0$ and $\alpha = 0$

$\frac{r}{s_m}$	K_{wg}	k_{wg}	k_b	$\frac{k_b}{k_{wg}}$	$\frac{K_b}{K_{wg}}$	$\left(\frac{x_{c.p}\,\delta}{b_{rt}}\right)^*_{wg(b)}$
0	1.000	1.000	0	0	0	0.667
0.1	1.077	0.963	0.114	0.118	0.123	0.669
0.2	1.162	0.944	0.218	0.231	0.239	0.668
0.3	1.253	0.936	0.317	0.338	0.349	0.666
0.4	1.349	0.935	0.414	0.442	0.454	0.665
0.5	1.450	0.940	0.510	0.542	0.551	0.664
0.6	1.555	0.948	0.607	0.641	0.646	0.663
0.7	1.663	0.958	0.705	0.736	0.737	0.664
0.8	1.774	0.971	0.803	0.827	0.827	0.666
0.9	1.887	0.985	0.902	0.916	0.915	0.667
1.0	2.000	1.000	1.000	1.000	1.000	0.667

*Delta wing.

body. An approximate relation for the interference coefficient follows from Table XV-3-1:

$$k_b = r_a = \frac{r}{s_m}. \qquad \text{(XV-3-17)}$$

If we assume that the wing "transmits" part of its lift to the body irrespective of whether this force is created under the influence of an attack angle α or a setting angle δ_e, we can write the equality $k_b/k_{wg} = K_b/K_{wg}$, from which another approximate relation follows:

$$k_b = k_{wg}\frac{K_b}{K_{wg}}. \qquad \text{(XV-3-18)}$$

Like the coefficients k_{wg}, the values of k_b are applicable for slender configurations. However, they are also used for nonslender configurations in approximate calculations. The values of k_b can be improved by applying Formula (XV-3-18) and available data for k_{wg} and K_b from linearized theory.

The calculation method presented above is applicable when there are no lifting surfaces forward of the control. Otherwise it is necessary to take account of a decrease in lift due to the influence of the wing by applying the interference-calculating methods set forth above.

Center of pressure. The center of pressure position will change as a result of pivoting of the controls. The center of pressure coordinate for $\alpha = 0$ and $\delta_e \neq 0$ can be determined from the expression

$$(x_{c.p\,\delta})_{wg} = x_{wg} + \left(\frac{x_{c.p\,\delta}}{b_{rt}}\right)_{wg(b)} b_{rt}. \qquad \text{(XV-3-19)}$$

This coordinate is measured from the nose of the body. The quantity x_{wg} is the distance from the nose to the forward end of the root chord, and the second term in (XV-3-19) determines the relative distance from this point to the center of pressure of the control when its rotation angle $\delta_e \neq 0$. The values of $(x_{c.p\delta}/b_{rt})_{wg(b)}$ for a delta wing are given in Table XV-3-1. The /641 effect of interference on the center of pressure coordinate is small for delta cantilevers. This gives reason to assume that the center of pressure for a wing of any planform may with good approximation be assumed the same as for the isolated wing, i.e., $(x_{c.p\delta})_{wg(b)} = (x_{c.p\delta})_{wg}$.

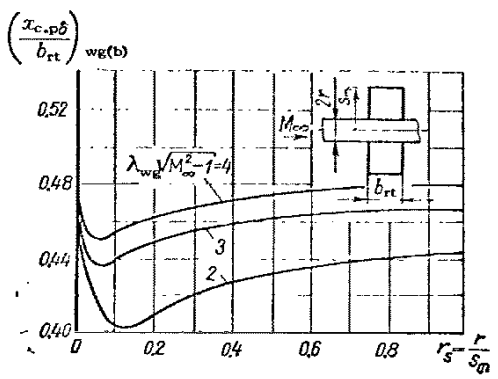

Figure XV-3-4. Curves for Calculation of Shift of Wing Center of Pressure under the Influence of the Body for $\alpha = 0$ and $\delta_e \neq 0$.

The isolated-wing $(x_{c.p\delta})_{wg}$ can be calculated by linearized theory instead of slender-body theory. For comparatively simple combinations of a body and a rectangular-planform pivoting wing, this theory also permits more accurate calculation of the center of pressure shift due to the body for $\alpha = 0$ and $\delta_e \neq 0$ (Fig. XV-3-4).

If the body is deflected to an attack angle α and the wing is also deflected through an angle δ_e with respect to the body axis, the wing center of pressure

$$(x_{c.p})_{wg(b)} = x_{wg} + \left(\frac{x_{c.p}}{b_{rt}}\right)_{wg(b)} b_{rt}, \qquad \text{(XV-3-20)}$$

where

$$\left(\frac{x_{c.p}}{b_{rt}}\right)_{wg(b)} = \frac{K_{wg}\alpha\left(\frac{x_{c.p}\ \alpha}{b_{rt}}\right)_{wg(b)} + k_{wg}\delta_e\left(\frac{x_{c.p}\ \delta}{b_{rt}}\right)_{wg(b)}}{K_{wg}\alpha + k_{wg}\delta_e}. \qquad \text{(XV-3-21)}$$

A similar expression will also apply for a body-tail combination.

When rotation of the control is accompanied by a change in the wing center of pressure position because of interference with the body, the coordinate of the point of application of the additional body normal force due to the wing effect also changes. It can be assumed in approximation that the change will be the same as in the case of formation of the normal force under the influence of a body attack angle, i.e.,

$$(x_{c.p\ \alpha})_{b(wg)} = x_{wg} + \left(\frac{x_{c.p\ \alpha}}{b_{rt}}\right)_{b(wg)} b_{rt}. \qquad \text{(XV-3-22)}$$

The center of pressure coordinate can also be reckoned from the center of gravity. If the distance to it from the forward point of the root chord is $(x_{c.g})_{wg}$, the center of pressure coordinate is

$$(x_{c.p\ \alpha})_{b(wg)} = (x_{c.g})_{wg} + \left(\frac{x_{c.p.\alpha}}{b_{rt}}\right)_{b(wg)} b_{rt}. \qquad \text{(XV-3-23)}$$

In calculating the center of pressure position on the body with consideration of the wing effect, it is assumed that the center of pressure is insensitive to whether the lift is developed from an attack angle or from a wing (tail)rotation angle. Accordingly, $(x_{c.p\alpha})_{b(wg)} = (x_{c.p\delta})_{b(wg)}$.

For the complete body-wing-tail combination, the center of pressure is determined by the formula

$$x_{c.p} = \frac{(x_{c.p})_b (c_N)_b + (x_{c.p})_{wg(b)} (c_N)_{wg(b)} + (x_{c.p})_{b(wg)} (c_N)_{b(wg)} + (x_{c.p})_{tl(b)} (c_N)_{tl(b)} + \\ + (x_{c.p})_{b(tl)} (c_N)_{b(tl)} + (x_{c.p})_{tl(v)} (c_N)_{tl(v)}}{(c_N)_b + (c_N)_{wg(b)} + (c_N)_{b(wg)} + (c_N)_{b(tl)} + (c_N)_{tl(b)} + (c_N)_{tl(v)}}, \qquad \text{(XV-3-24)}$$

where $(c_N)_{tl(v)}$ and $(x_{c.p})_{tl(v)}$ are the normal-force coefficient and center of pressure governed by wing vortices. /642

The quantity $(x_{c.p})_{tl(v)}$ is assumed equal to $(x_{c.p})_{tl(b)}$. The values of $x_{c.p}$ and c_N, which appear in (XV-3-24), are determined in the general case with consideration of the attack angle

and the wing and tail rotation angles. In particular, $(x_{c.p})_{wg(b)}$ is found from Formula (XV-3-20) in which $(x_{c.p}/b_{rt})_{wg(b)}$ is determined from (XV-3-21). The corresponding coordinate for a body in the wing is

$$(x_{c.p})_{b(wg)} = x_{wg} + \left(\frac{x_{c.p}}{b_{rt}}\right)_{b(wg)} b_{rt}, \qquad \text{(XV-3-25)}$$

where

$$\left(\frac{x_{c.p}}{b_{rt}}\right)_{b(wg)} = \frac{K_b\alpha\left(\frac{x_{c.p.\alpha}}{b_{rt}}\right)_{b(wg)} + k_b\delta_e\left(\frac{x_{c.p.\delta}}{b_{rt}}\right)_{b(wg)}}{K_b\alpha + k_b\delta_e}. \qquad \text{(XV-3-26)}$$

A quantity that defines the normal-force coefficient of the body in accordance with the formula

$$(c_N)_{b(wg)} = (K_b\alpha + k_b\delta_e)(c_N^\alpha)_{wg} \qquad \text{(XV-3-27)}$$

appears in the denominator of this expression. The relationships for the tail section can be written similarly.

Longitudinal effectiveness. The longitudinal effectiveness of the controls is determined by the change in the pitching-moment coefficient m_z as a function of a change in the angle δ_e on a symmetrical deflection of the horizontal cantilevers, and is equal to the derivative $\partial m_z/\partial\delta_e$. This derivative is usually negative for tailplanes and positive for controls of the "canard" configuration. If the longitudinal moment is determined with respect to the center of gravity, the longitudinal effectiveness is

$$\frac{\partial m_z}{\partial\delta_e} = \frac{b_{rt}}{l}\left\{k_{wg}\left[\left(\frac{x_{c.p.\delta}}{b_{rt}}\right)_{wg} + \left(\frac{x_{c.g}}{b_{rt}}\right)_{wg}\right] + k_b\left[\left(\frac{x_{c.p.\alpha}}{b_{rt}}\right)_{b(wg)} + \left(\frac{x_{c.g}}{b_{rt}}\right)_{wg}\right]\right\}(c_N^\alpha)_{wg}, \qquad \text{(XV-3-28)}$$

where l is a characteristic length.

If some lifting element is located forward of the control, it is necessary to take account of the effect of interference with this element on pitching moment.

Lateral effectiveness. Lateral effectiveness is determined by the derivative of the rolling moment m_x with respect to the angle δ_a on a differential deflection of the horizontal controls. The derivative $\partial m_x/\partial\delta_a$, which is usually negative, is equal to

$$\frac{\partial m_x}{\partial \delta_a} = -\lambda_{wg} f\left(\frac{r}{s_m}\right). \qquad \text{(XV-3-29)}$$

Here $\lambda_{wg} = 4(s_m - r)^2/S_{wg}$ is the wing aspect ratio; f is a certain function of the ratio $r_s = r/s_m$, and for a linear relationship is defined by the equality

$$f = 0.167(1 + 3.71 r_s). \qquad \text{(XV-3-30)}$$

The values of the function f correspond to a very slender body. By applying the theory of linearized flow, we can improve these values for a real slender body and thereby take account of M_∞:

$$f = f_{s.b} \frac{(c_N^\alpha)_{wg.ln}}{(c_N^\alpha)_{wg.sb}}, \qquad \text{(XV-3-31)}$$

where f_{sb} is calculated by Formula (XV-3-30), which is derived from slender-body theory.

The fraction in Formula (XV-3-31) is the ratio of the slopes of the $c_N(\alpha)$ curves for the isolated wing, as calculated by the linearized and slender-body theories. For delta wings, this ratio takes the form /643

$$\frac{(c_N^\alpha)_{wg.ln}}{(c_N^\alpha)_{wg.sb}} = \begin{cases} \dfrac{1}{E(k)} & \text{for } \alpha'\lambda_{wg} < 4, \\ \dfrac{8}{\pi\alpha'\lambda_{wg}} & \text{for } \alpha'\lambda_{wg} > 4, \end{cases} \qquad \text{(XV-3-32)}$$

where E(k) is a complete elliptic integral of the second kind with modulus $k = [1 - (0.25\alpha'\lambda_{wg})^2]^{1/2}$; λ_{wg} is the wing aspect ratio.

The following ciruumstance must be kept in mind in locating controls that are to set up a lateral moment. If there are any lifting surfaces aft of the controls, those surfaces will set up a rolling moment opposed to the moment from the controls when the latter are given a differential deflection, as a result of interference between them. For this reason, controls positioned forward of the lifting surfaces, such as "canard"-type controls, are not effective enough for lateral control.

Example. Determine the longitudinal and lateral effectiveness of all-moving tail cantilevers at $M_\infty = 2$ for the body-wing-tail combination whose dimensions and shape are indicated in Fig. XV-2-13. Let the center of gravity of the combination be situated at a distance $(x_{c.g})_{tl} = 3.95$ from the forward end of the tail root chord (we substitute the subscript tl for wg).

We use Formula (XV-3-28) to calculate $\partial m_z/\partial \delta_e$. The coefficients k_{tl} and k_b that appear in it are found from Table XV-3-1 for the value $(r/s_m)_{tl} = 0.562/1.81 = 0.310$; $k_{tl} = 0.936$, $k_b = 0.327$.

The relative center of pressure coordinate $(x_{c.p\delta}/b_{tl})_{tl(b)}$ is assumed equal to $(x_{c.p\alpha}/b_{tl})_{tl(b)}$ and is determined from Table XV-1-1. For a delta cantilever we find $(x_{c.p\delta}/b_{tl})_{tl(b)} = 2/3$. We determine the center of pressure on the body in accordance with Formula (XV-3-25) with the aid of Table XV-1-1, bearing in mind that there is no tail section aft of the empennage. The relative center of pressure coordinate is $(x_{c.p\delta}/b_{tl})_{b(tl)} = 0.556$.

Taking the wing mean aerodynamic chord $b_{MAC} = 1.5$ passing through the cantilever's center of gravity as the characteristic length ℓ and remembering that $(c_N^\alpha)_{tl} = 2.31$ for the isolated tail, we obtain after substituting all quantities into Formula (XV-3-28)

$$\frac{\partial m_z}{\partial \delta_e} = -\frac{1.25}{1.5}\left[0.936\left(0.667+\frac{3.95}{1.25}\right)+0.327\left(0.556+\frac{3.95}{1.25}\right)\right]2.31 = -9.24.$$

We then calculate the lateral effectiveness. From Formula (XV-3-30) and $r_s = r/s_m = 0.310$ we find $f_{sb} = 0.359$.

Since the aspect ratio of the isolated tail is

$$\lambda_{tl} = \frac{4(s_m - r)^2}{S_{tl}} = \frac{4(1.812-0.562)^2}{1.25^2} = 4.00,$$

and $\alpha' = \sqrt{M_\infty^2 - 1} = 1.73$, we have $\alpha'\lambda_{tl} = 6.92$. In accordance with the second formula of (XV-3-32), therefore,

$$\frac{(c_N^\alpha)_{tl.in}}{(c_N^\alpha)_{tl.sb}} = 0.368.$$

According to (XV-3-29),

$$\frac{\partial m_x}{\partial \delta_a} = -0.359 \cdot 0.368 \cdot 4 = -0.53.$$

Applying (XV-3-8) and taking $S = S_{tl}$ as the characteristic area, we determine the slope of the $c_N(\delta_e)$ curve for the tail:

$$\left(\frac{\partial c_N}{\partial \delta_e}\right)_{(b.tl)\,\delta} = 2.31\,(0.936 + 0.327) = 2.9.$$

All-Moving Cruciform Controls /644

Longitudinal effectiveness. For a cruciform configuration of all-moving control surfaces, the longitudinal effectiveness in the plane of the angle $\alpha = \alpha_b \cos \phi$ can be found in the presence of roll from Formula (XV-3-28), leaving out of account the effect of slip rate, i.e., assuming that there is no interaction between the cantilevers. It follows from (XV-1-17) that longitudinal effectiveness increases in the presence of a roll angle. While the normal force N of the entire combination is created at $\phi = 0$ only by the horizontal cantilevers, which are deflected through an angle δ, all four cantilevers participate in generation of normal force when the system is rotated through a certain angle ϕ. The total normal force in the vertical plane will be $N(\cos \phi + \sin \phi)$, which, for example at $\phi = 45°$, gives $N\sqrt{2}$.

Directional effectiveness. This characteristic, which is determined by the derivative $\partial m_y/\partial \delta_r$, depends on the change in directional moment at a symmetrical deflection of the vertical control surfaces. Formula (XV-3-28) can be used to calculate $\partial m_z/\partial \delta_r$ in the plane of the angle $\beta_{sl} = \alpha_b \sin \phi$ without considering the influence of the angle α.

Lateral effectiveness. Longitudinal and directional effectiveness is analyzed for cruciform surfaces in the same way as for plane controls, and without considering interference between the cantilevers. However, these methods do not give satisfactory results for lateral effectiveness, since pressure is redistributed on the vertical cantilevers under the influence of the horizontal controls when they are given a differential deflection, with a positive pressure set up on one of the halves and a negative pressure on the other. The result is a reverse lateral moment that opposes the moment from the control deflection. As a result, the resultant lateral moment and the corresponding lateral effectiveness will be smaller. The change in lateral effectiveness can be calculated from the approximate relationship

$$\frac{1}{\lambda_{wg}}\Delta\left(\frac{\partial m_x}{\partial \delta_a}\right)=0.16\cos\left(\frac{\pi}{2}r_s\right)-0.12r_s(1-r_s). \qquad \text{(XV-3-33)}$$

Despite the lower lateral effectiveness of the horizontal controls, the resultant lateral effectiveness of the cruciform combination will nevertheless be greater than that of the plane configuration owing to the influence of the vertical surfaces.

In calculations for nonslender bodies, the values obtained from slender-body theory must be improved with the aid of (XV-3-31).

Interaction Between Controls

To obtain a complete picture of the aerodynamic properties of a vehicle, it is necessary to know, in addition to the characteristics related to the direct influence of attack, slip, and control-deflection angles, the effects that appear as a result of interaction between controls. One of these effects is a lateral moment from the vertical wings that appears on a differential deflection of the horizontal control surfaces. Let us examine the qualitative aspects of the possible forms of interaction between controls.

Interaction not related to deflection of controls. Let us assume that a body-wing combination is in flight at a certain angle of attack with simultaneous roll, and analyze the effects of interaction for the case in which the wings, which act as controls, are not deflected. /645

1. Owing to the interaction of the pressure fields from the finite-thickness body and wings in the presence of attack and slip (roll) angles, additional lifting forces arise from the horizontal and vertical cantilevers. In the presence of only the attack angle, the interaction governed by body thickness can be defined by convention as an interaction of the "attack angle-vs. -thickness" type that results in the creation of a unidirectional lifting force on the horizontal cantilevers. On the appearance of a slip angle, an additional interaction of the "slip angle-vs.-thickness" type appears and produces lift, again unidirectional, on the vertical cantilevers. The forces that arise as a result of the two interaction types act in the planes of the angles α and β_{sl}, respectively.

2. A second type of interaction is governed by the reciprocal effects between the pressure fields from the body and wings in the presence of attack and slip angles ("attack angle-vs.-slip angle" type of interaction). For a plane combination, this results in the appearance of additional lifting forces of opposite directions on the starboard and port cantilevers and, as a consequence, the formation of a lateral moment that tends to reduce the roll.

In the case of a cruciform combination, the "attack angle-vs.-slip angle" interaction also results in the formation on the vertical cantilevers of a moment equal in magnitude but opposite in sign to the moment on the horizontal cantilevers. The resultant rolling moment is therefore zero.

Interaction governed by deflection of horizontal controls. An interaction of this type arises on deflection of the horizontal control surfaces to set up a pitching moment or produce a certain desired lateral moment. The most general case of the interaction is characterized by the presence of attack and slip angles.

1. Let us consider the interaction effects when the controls are deflected symmetrically through an angle δ_e to support longitudinal control.

a. Let us assume for the time being that there is no slip ($\beta_{sl} = 0$). In the case of a plane combination, symmetrical deflection of the cantilevers through angle δ_e results in the appearance of an additional lift of the same magnitude and sign on the starboard and port cantilevers. This is also observed in the case of the cruciform configuration, since there is no interaction with the vertical cantilevers.

This interaction is of the "angle δ_e-vs.-thickness" type and is qualitatively the same as the "attack angle vs.-thickness" interaction.

b. If deflection of the controls through angle δ_e is accompanied by slip, an interaction of the "angle δ_e-vs.-angle β_{sl}" type appears. For a plane combination, it is qualitatively the same as interaction of the "angle β_{sl}-vs.-attack angle" type, which results in a lateral moment that tends to reduce roll angle. For a cruciform combination, the interaction effect is similar: additional lifting forces appear on the vertical cantilevers and set up a lateral moment of the same sign as that on the horizontal cantilevers.

2. Let us consider the interaction effects that appear when the horizontal controls are used to create lateral moments, i.e., when they act as ailerons.

a. Assume that there are no slip or attack angles. Secondary lateral moments appear as a result of interaction of the body with the horizontal controls when they are given a differential deflection through angle δ_a (interaction of the "angle δ_a-vs.-thickness" type). A lateral moment that reduces the roll angle /646

then appears on the horizontal and vertical cantilevers.

If the attack angle is not zero, an interaction of the "angle α -vs.-angle δ_a" type appears in the case of a cruciform combination and creates a lateral force of one sign (negative) on the vertical cantilevers. No additional forces arise on the horizontal cantilevers. Thus, this interaction does not occur for the plane combination. The phenomenon is similar to the "angle β_{sl}-vs.-thickness" interaction discussed above and, as we see, leads to the formation of a directional moment for a cruciform combination.

b. In the presence of slip, differential deflection of the horizontal cantilevers through angle δ_a results in the appearance of an additional positive lift for a plane combination. In the case of a cruciform configuration, no interaction appears on the vertical cantilevers. Thus, when the horizontal cantilevers are used as ailerons, a pitching moment is created for either a plane or a cruciform configuration.

3. Finally, we might examine the interaction due to use of the horizontal controls for longitudinal and lateral control simultaneously. The deflection of the controls, which is characterized by the angles δ_e and δ_a, sets up an additional lifting force on the vertical cantilevers, but no additional force arises on the horizontal controls. The general conclusion drawn from analysis of the interaction in these cases is that the lateral effectiveness changes and a pitching moment appears for a plane configuration when the lateral controls are deflected. A directional moment also appears in the case of a cruciform configuration.

These interaction effects are governed by deflection of the horizontal cantilevers. New interference effects appear when the vertical controls are deflected. They can be analyzed in the same way as in the case of the horizontal cantilevers. It must also be borne in mind that these conclusions pertain to slender bodies and small-aspect-ratio wings.

Controls Along Trailing Edges of Lifting Surfaces

Controls located along the trailing edges of lifting surfaces may occupy all or part of the cantilever trailing edge. If they occupy the entire trailing edge, they may be regarded as all-moving controls and the aerodynamic calculation methods set forth above can be applied to them. Cases in which the controls occupy part of the edge, and then not a very large part, are frequently encountered. If the interference of the body with the lifting surface has insignificant influence on the aerodynamic characteristics of the control, such as, for example, its center of pressure coordinate, these characteristics can be calculated by

applying the results of regular supersonic theory as they apply to the isolated surfaces.

Aerodynamic analysis of the controls becomes more complicated when interference between the body and wing exerts substantial influence on the control surfaces. If a trailing-edge control has a large aspect ratio, its aerodynamics can be investigated by elementary swept-wing theory.

Application of ordinary supersonic theory. Attention must be drawn to the following factors when this theory is applied: /647

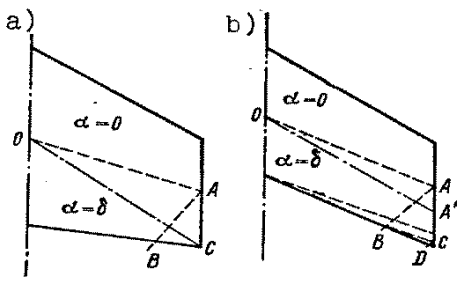

Figure XV-3-5. Reflection Diagram for Controls with Subsonic Leading Edge. a) trailing edge supersonic; b) trailing edge subsonic; -----) Mach line; -•-•-) rotation axis of control surface.

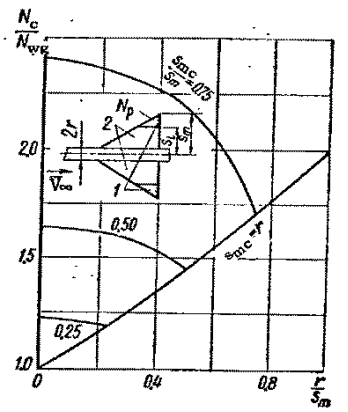

Figure XV-3-6. Effectiveness of Controls. 1) outboard controls; 2) inboard controls; 3) $s_i = s_{m\,c}$; $s_m = s_{m\,wg}$.

1) whether the leading and trailing edges of the controls are supersonic or subsonic;

2) whether the tip chords of the control coincide with the stream direction;

3) how the control is located: does it extend to the tip chord of the wing or is it at a certain distance from this chord; in the latter case, it is important to know whether the outboard Mach cone of the control intersects the wing tip chord;

4) finally, whether the inboard Mach cone of the control crosses the wing root chord.

A certain amount of difficulty is encountered in investigation of controls with subsonic leading and trailing edges owing to multiple reflection of disturbance waves on the control surface (Fig. XV-3-5).

Consideration of interference between wing and body. Such consideration is necessary when the controls are mounted on short wings. In combination with slender-body theory, the reversibility principle can be used to calculate the effectiveness of wingtip controls with respect to lift.

Let us consider a body-wing-control combination (Fig. XV-3-6) with a fixed wing and a moving wingtip control whose transverse dimension is defined by $s_{m\ wg} - s_{m\ c}$. Let us find the effectiveness of the controls for zero angles of attack of the body and hence of the wing ($\alpha_b = \alpha_{wg} = 0$) and a control-surface deflection angle $\delta(\alpha_c = \delta)$.

To find the normal force N_c of the combination that results from control deflection, we shall examine the reversed motion and assume that in this motion (see Fig. IV-5-2), the combination is set at a common angle of attack $\alpha_2 = \delta$. Then we find from (IV-5-2)

$$\iint\limits_{(s_c+s_{wg}+s_b)} \Delta\bar{p}_1\, dS = \iint\limits_{(s_c)} \Delta\bar{p}_2\, dS. \qquad \text{(XV-3-34)}$$

Here the left member defines the unknown normal force N_c of one cantilever referred to the velocity head q_∞. To calculate the right member, we introduce into the integrand the quantity $\Delta\bar{p}_2 = \Delta\bar{p}_{wg(b)}$, expressed by Formula (XV-1-14), in which we take $\phi = 0$, $\alpha_b = \delta$, $r' = 0$, $s = x \tan \varepsilon$, $s' = \tan \varepsilon = \text{const}$. Assuming that $dS = dxdz$ and integrating over x with $z/\tan \varepsilon$ and $s_m/\tan \varepsilon$ as limits and over y from s_i to s_m (Fig. XV-3-6), we obtain an expression for N_c. Referring it to the force $N_{wg} = 2q_\infty \delta \pi [(s^2_{m\ wg} - s^2_{m\ c})]$ of the isolated wing formed by combining the two wingtip controls, we obtain the ratio

/648

$$\frac{N_c}{N_{wg}} = 2(1-\bar{s}_c^2)^{-1}\left[\frac{\pi}{4}(1-r_s^2)^2 - (\bar{s}_c^2 - r_s^2)^{1/2}(1-\bar{s}_c^2)^{1/2} + \right.$$
$$\left. + \frac{1}{2}(1-r_s^4)\arcsin\frac{1-2\bar{s}_c^2+r_s^4}{1-r_s^4} + r_s^2 \arcsin\frac{(1+r_s^2)\bar{s}_c^2 - 2r_s^4}{(1-r_s^4)\bar{s}_c^2}\right], \qquad \text{(XV-3-35)}$$

where $r_s = r/s_m$, $\bar{s}_c = s_{m\ c}/(s_m)_{wg}$.

Although this ratio was obtained with Formula (XV-1-14), which refers to conditions on a delta wing, research has nevertheless shown that it can be used for wings of arbitrary form.

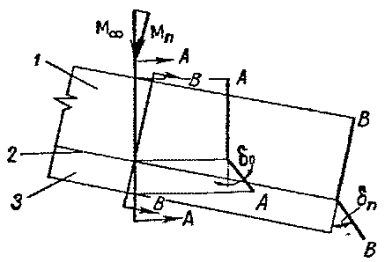

Figure XV-3.7. Swept Large-Aspect-Ratio Control. 1) wing; 2) axis of rotation; 3) control surface.

The quantity N_c/N_{wg} depends only on the geometry at the trailing edge. Figure XV-3-6 shows a curve characterizing the variation of N_c/N_{wg}.

Having calculated N_{wg} for the isolated wing with consideration of its shape and taking the ratio N_c/N_{wg} as in slender-body theory, we can take account of the influence of M_∞ on the effectiveness of wingtip controls. For example, an isolated wing (control surface) may be triangular with root chords going with the stream as shown in Fig. XV-3-6. The data of Fig. XV-3-6 can also be used to calculate the effectiveness of inboard controls. The figure is used to find the effectiveness $(N_c/N_{wg})_r$ of controls that extend from the body to the wingtip ($s_{m\,c} = r$); then the value of $(N_c/N_{wg})_{ob}$ is determined for the outboard control ($s_{m\,c} > r$). The forces $(N_c)_r$ and $(N_c)_{ob}$ are found from these values. Now, regarding the inboard control surface as the difference of two outboard controls extending to the wingtip, $N_c = (N_c)_r - (N_c)_{ob}$ is found for the inboard control. If the normal force for the joined inboard control surfaces is N_{wg}, the effectiveness will be N_c/N_{wg}.

Elementary theory of sweep. If a trailing-edge control surface has a large enough aspect ratio, its effectiveness can be calculated by elementary sweep theory. Let us assume that the axis of rotation of the control surface (Fig. XV-3-7), which coincides with its swept leading edge, is supersonic. Then the normal force developed by the control on deflection through an angle δ_n measured in the direction of the normal to the rotation axis will be determined in accordance with the two-dimensional sweep theory by the expression

$$N_n = N_0 \sqrt{\frac{M_\infty^2 - 1}{M_\infty^2 - \cos^{-2}\chi}} = N_0 \sqrt{\frac{\cos^2\chi\,(M_\infty^2 - 1)}{M_\infty^2 \cos^2\chi - 1}}. \qquad \text{(XV-3-36)}$$

Here N_0 is the normal force at zero sweep, calculated from the control-surface area S_c by the expression

$$N_0 = q_\infty \delta_0 (c_N^\alpha)_0 S_c, \qquad \text{(XV-3-37)}$$

where q_∞ is the velocity head calculated from M_∞; δ_0 is the control deflection angle in the direction of the oncoming flow ($\delta_0 = \delta_n \cos\chi$); $(c_N^\alpha)_0$ is the derivative of the normal-force coefficient with respect to attack angle and is equal to $(c_N^\alpha)_0 = 4(M_\infty^2 - 1)^{-1/2}$. /649

As we see from Formula (XV-3-36), which is applicable for $M_\infty \cos\chi > 1$, sweep results in an increase in normal-force effectiveness of the control. As $M_\infty \cos\chi \to 1$, the formula becomes invalid. The shock separates from the controls; this can be avoided by making certain that the pivot-axis position is supersonic.

Nonlinear Effects

Influence of slots. One factor disturbing linearity of control aerodynamic characteristics as functions of deflection angle is formation of slots between the controls and the body or around the pivot axis. These slots tend to reduce the pressure drop at the root chord (Fig. XV-3-8) and, consequently, normal force. Under real viscous-flow conditions, the boundary layer may be thought of as covering small slots, so that their detrimental effects are not manifested in practice and linearity is not disturbed.

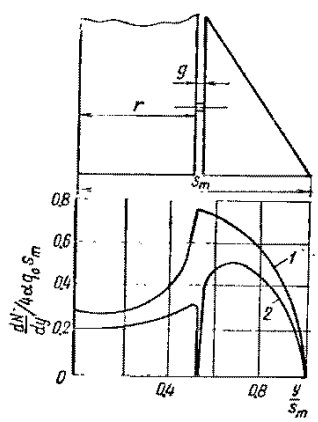

Figure XV-3-8. Influence of Slots on Distribution of Normal Force (Without Consideration of Viscosity). 1) no slots ($g/s_m = 0$); 2) slot dimension $g/s_m = 0.0025$.

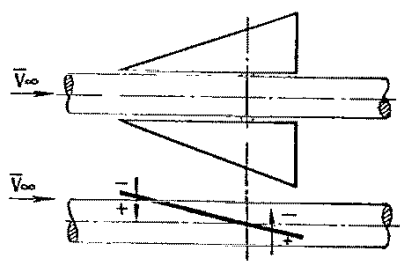

Figure XV-3-9. Influence of Slots at Large Control Deflection.

Effectiveness drops off and nonlinearity appears when the slots are longer and their shape changes when the moving controls are given large deflections (Fig. XV-3-9). In this case, the

change in aerodynamic characteristics and departure from linearity are explained by redistribution of pressure on the body owing to the influence of the wing. Compression of the flow on the lower surface of the cantilever increases the pressure on the body and, as a result, gives rise to a force couple.

Influence of large control-surface deflection angles and profile thickness. These factors may change aerodynamic characteristics from those of the linear theory. Unfortunately, no nonlinear theory has been developed for wings of small and medium aspect ratio.

If the controls have large enough aspect ratios, shock-and-expansion-flow theory can be used to evaluate the higher-order effects of attack angle on aerodynamic characteristics. The nonlinear effect can also be taken into account comparatively simply /650
with the Busemann second-order-approximation theory, which is useful, for example, in evaluating the influence of the thickness of wing-trailing-edge control surfaces (Fig. XV-3-10). In this theory, the pressure coefficients on the profile surface are expressed by Formulas (V-2-16) and (V-2-17). The normal-force coefficient of the control can be calculated by integration with these formulas. For a symmetrical control-surface profile form, the normal-force coefficient referred to the chord is

$$c_N = \frac{1}{b - x_{ro}} \int_a^b (\bar{p}_1 - \bar{p}_{ro})\, dx = 2c_1\delta - \frac{2c_2\delta^2 (s_{max} - s_{bse})}{b - x_{ro}}, \qquad \text{(XV-3-38)}$$

where x_{ro} is the distance from the forward end of the root chord to the axis of rotation of the control.

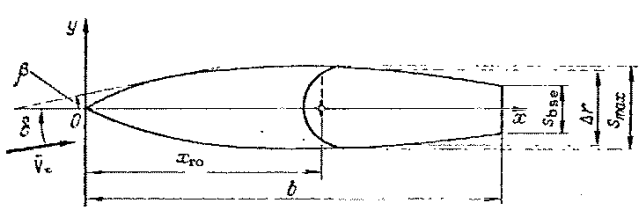

Figure XV-3-10. Control with Symmetrical Profile (x_{ro} is the distance to the axis of rotation; s_{max} and Δr are the maximum thicknesses of the wing and control, respectively).

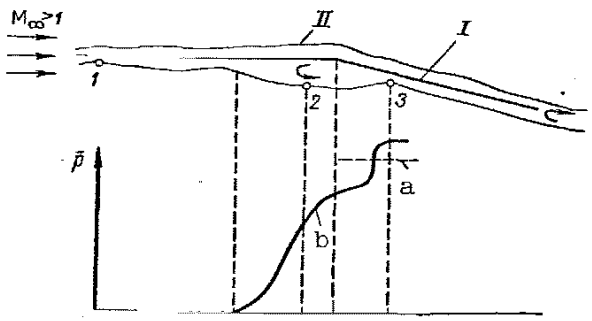

Figure XV-3-11. Boundary-Layer Separation on Trailing-Edge Control. I) control; II) boundary layer; 1) transition point; 2) separation point; 3) sticking point; a) pressure without consideration of viscosity; b) pressure with consideration of separation.

The nomenclature of the other geometrical parameters is given in Fig. XV-3-10. The coefficients c_1 and c_2 are found from Formula (V-2-7). The first term in (XV-3-38) defines the normal force $(c_N)_{s=0}$ of a zero-thickness lifting surface, while the second gives the correction for the thickness effect. Thus, although the linear effect is preserved with respect to control rotation angle, there is still a deviation from linear theory owing to the influence of thickness. The decrease in control normal force is determined by the expression

$$\frac{c_N}{(c_N)_{s=0}} = 1 - \frac{c_2}{c_1}\frac{s_{max} - s_{bse}}{b - x_{r\cdot}}. \qquad \text{(XV-3-39)}$$

If the trailing edge is not blunted, $s_{bse} = 0$ in this formula. /651

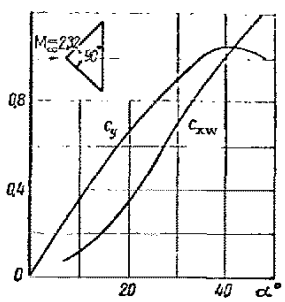

Figure XV-3-12. Lift and Drag of Delta Wing.

Effect of flow separation. Boundary-layer separation, which usually begins near the rotation axis of the control surface, results in redistribution of pressure (Fig. XV-3-11) and, as a consequence, a certain change in the aerodynamic characteristics.

Maximum lift. Around the attack angle at which $c_{y\ max}$ is reached, lift shows a substantial deviation from linearity as a function of attack angle. In most practical cases, the nonlinear relation for lift is obtained experimentally. Figure XV-3-12 shows typical curves of the aerodynamic coefficients for an isolated delta wing at large angles of attack, including a lift-coefficient curve.

If such a wing were mounted on a body as an all-moving control, its maximum lift would be determined by the sum of the control deflection angle and the body attack angle, which would be smaller than the critical attack angle in Fig. XV-3-12. This is explained by the secondary influence of the body on the wing. Slots could also influence the critical attack angle. Studies made for isolated wings in the M_∞ range from 1.6 to 2.3 resulted in the observation that for wings with aspect ratios greater than 1.4 and various planforms - delta, rectangular, swept, trapezoidal - the maximum values of the lift coefficient are approximately the same at 1.05 ± 0.05. Here the critical attack angles were near 40° in all cases. This result may prove useful in study of the large-attack-angle aerodynamic characteristics on various combinations that include lifting elements of the shape indicated above.

Hinge Moment of All-Moving Wings

The hinge moment of a control with respect to its rotation axis is calculated by the following procedure.

1. The control's normal-force coefficients $(c_N)_\alpha$ (for attack angle) and $(c_N)_\delta$ (for deflection angle) are determined with consideration of interference with the body.

2. The wing center of pressure coordinate $x_{c.p\alpha}$ is found for $\alpha \neq 0$ and zero control deflection. To do so, the center of pressure coordinate of the isolated wing is determined first and then corrected for interference and thickness effects. Interference has little influence on center of pressure position. Calculations indicate that for delta wings, the maximum center of pressure shift is 2% of root chord. The change in the center of pressure coordinate due to the thickness effect is also small and can be taken into account with Busemann's second-approximation theory. For a profile that is symmetrical about the vertical axis, the center of pressure shift is determined from the formula

$$\Delta\bar{x}_{c.p} = \frac{m_z}{c_N}, \qquad \text{(XV-3-40)}$$

where $\Delta\bar{x}_{c.p} = \Delta x_{c.p}/b_{MAC}$.

The coefficients m_z and c_N for the profile are determined by the formulas /652

$$m_z = \frac{2}{3} c_1 (\bar{s}_1 - \bar{s}_0) + \frac{4}{3} c_2 \alpha (\bar{s}_1 + \bar{s}_0); \qquad \text{(XV-3-41)}$$

$$c_{N_\alpha} = 2c_1\alpha + \frac{16}{3}c_2(\bar{s}_l^2 - \bar{s}_u^2), \qquad \text{(XV-3-42)}$$

where $\bar{s}_l$ and $\bar{s}_u$ are the maximum thicknesses of the bottom and top of the profile, respectively, referred to the chord b_{MAC}.

The distance to the center of pressure from the forward point of the root chord, calculated with consideration of thickness and referred to b_{rt}, will be

$$\frac{x_{c.p}}{b_{rt}} = \left(\frac{x_{c.p}}{b_{rt}}\right)_{wg} - \Delta\bar{x}_{c.p}\frac{b_{MAC}}{b_{rt}}, \qquad \text{(XV-3-43)}$$

where $(x_{c.p}/b_{rt})_{wg}$ is the relative center of pressure coordinate of the isolated thin wing.

For a delta wing, this quantity may be assumed equal to 2/3. Research indicates that the thickness correction is no more than 3-4% of root chord.

3. The correction to the center of pressure coordinate of the isolated thin wing to allow for the thickness of the control and interference when it is deflected is calculated, and the distance to the center of pressure, $x_{c.p\delta}$, is found for $\alpha = 0$. The interference coefficient is small; for example, it is no more than 1% of root chord for triangular control surfaces.

4. The hinge moment is found as the sum of the moments produced by the attack and control-deflection angles:

$$m_h = \frac{b_{rt}}{b_{MAC}}\left\{(c_N)_\alpha\left[\frac{x_{ro}}{b_{rt}} - \left(\frac{x_{c.p}}{b_{rt}}\right)_\alpha\right] + (c_N)_\delta\left[\frac{x_{ro}}{b_{rt}} - \left(\frac{x_{c.p}}{b_{rt}}\right)_\delta\right]\right\}, \qquad \text{(XV-3-44)}$$

where x_{ro} is the distance from the forward point of the root chord to the control-surface axle. The hinge moment coefficient in Formula (XV-3-44) is referred to mean aerodynamic chord.

The method set forth above is applicable for controls of any planform, but the interference data used in it, which are taken from slender-body aerodynamic theory, give more satisfactory results for the delta form and are less accurate for rectangular wings. In determining the reciprocal influence of a body and a deflected rectangular control on lift and center of pressure position, it is better to use data from the linearized theory, according to which the correction for the center of pressure shift, at the deflection of the control, is approximately twice that

according to slender-body theory.

Example. Calculate the hinge-moment coefficient for $M_\infty = 2$, $\alpha = 0.1$, $\delta = 0.2$ for a fully deflected triangular control surface with the dimensions indicated in Fig. XV-3-13. The control profile is symmetrical and biconvex with the thickness ratio $\bar{s}_{max} = s_{max}/b_{rt} = 0.05$.

First we find the normal-force coefficients for the values of the angles α and δ:

$$(c_N)_\alpha = K_{wg}\alpha\,(c_N^\alpha)_{wg};\quad (c_N)_\delta = k_{wg}\delta\,(c_N^\alpha)_{wg}.$$

Since the wing has a supersonic leading edge,

$$(c_N^\alpha)_{wg} = (c_N^\delta)_{wg} = 4\,(M_\infty^2 - 1)^{-1/2} = 2.31.$$

For the value $r_s = r/s_m = 0.25$, we find the interference coefficients $K_{wg} = 1.21$ and $k_{wg} = 0.94$ in Table XV-3-1. Now we use Formula (XV-3-43) to determine the center of pressure coordinate with consideration of thickness, remembering that in this formula

$$\Delta\bar{x}_{c.p} = \frac{2c_2}{3c_1}\frac{s_{max}}{b_{MAC}} = \frac{2}{3}\frac{1.47}{1.16}0.05 = 0.042.$$

Assuming that $b_{MAC}/b_{rt} = 2/3$ and setting $x_{c.p}/b_{rt} = 2/3$, we find after substitution into (XV-3-43) /653

$$\frac{x_{c.p}}{b_{rt}} = \frac{2}{3} - 0.042\frac{2}{3} = 0.667 - 0.028 = 0.639.$$

This figure must be improved with a view to the influence of attack angle, using the formula

$$\Delta\bar{x}_{c.p\ \alpha} = \left(\frac{x_{c.p}\ \alpha}{b_{rt}}\right)_{wg} - \left(\frac{x_{c.p}\ \alpha}{b_{rt}}\right)_{wg(b)}, \qquad \text{(XV-3-45)}$$

in which the first term defines the center of pressure coordinate of the isolated wing and the second represents the combination with the body.

From Table XV-1-1, we find for $r_s = 0$ and $r_s = 0.25$ the

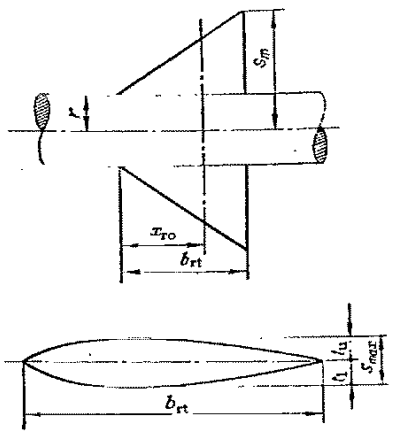

Figure XV-3-13. Moving Control in Calculation Example.

r	s_m	x_{ro}	b_{rt}	s_{max}	$t_u = t_l$
1	4	2	3	0.05	0.025

respective values $(x_{c.p\alpha}/b_{rt})_{wg}$ = = 0.667 and $(x_{c.p\alpha}/b_{rt})_{wg(b)}$ = = 0.648. Consequently, $\Delta x_{c.p\alpha}$ = = 0.019 and the relative center of pressure coordinate with consideration of thickness is $(x_{c.p\alpha}/b_{rt})_{wg}$ = = 0.639 - 0.019 = 0.620. The center of pressure shift on deflection of the control is

$$\Delta\bar{x}_{c.p.\delta} = \left(\frac{x_{c.p.\delta}}{b_{rt}}\right)_{wg} - \left(\frac{x_{c.p\ \delta}}{b_{rt}}\right)_{wg(b)}, \quad \text{(XV-3-46)}$$

where the first term defines the center of pressure coordinate of the isolated wing and the second that of the wing in combination with the body.

From Table XV-3-1, we find $(x_{c.p\delta}/b_{rt})_{wg}$ = 0.667 and $(x_{c.p\delta}/b_{rt})_{wg(b)}$ = 0.667 for r_s = 0 and r_s = 0.25, respectively. Consequently, $\Delta\bar{x}_{c.p\delta}$ = 0 and according to our data the relative control-deflected center of pressure coordinate is $(x_{c.p}/b_{rt})_{\delta}$ = 0.639 - 0 = 0.639. After substitution into (XV-3-44), we find the hinge-moment coefficient

$$m_h = \frac{b_{rt}}{(2/3)\,b_{rt}} 2.31\left[1.21\cdot 0.1\left(\frac{2}{3}-0.620\right)+0.94\cdot 0.2\left(\frac{2}{3}-0.639\right)\right]=0.038.$$

Example of aerodynamic-characteristic calculation for a body-wing-tail combination. Experimental data.

By way of example, Table XV-3-2 shows the results of a calculation of the over-all M_∞ = 2 aerodynamic characteristics of the plane body-wing-tail combination diagrammed in Fig. XV-2-13. The characteristic geometrical dimensions used were the length x_b of the combination and the area of the two wing cantilevers not counting the area occupied by the body. All linear geometrical parameters are dimensionless and are referred to the radius of the body cylindrical section, which is taken as the unit (r = = r_{mid} = 1). The distance from the nose to the center of rotation is, according to Fig. XV-2-13, x_{ro} = 9.35.

TABLE XV-3-2. EXAMPLE OF CALCULATION OF AERODYNAMIC CHAR- /654

Body-

1	2	3	4	5	6	7	8	9	10	11	12	13
M_∞	α'	r	s_m	$b_{e.C}$	b_{rt}	$\operatorname{tg}\varepsilon$	x_{wg}	λ	r_s	$\alpha'\operatorname{tg}\varepsilon$	S_{wg}	λ_{is}
By hypothesis	M_∞^2-1	By hypothesis						$\frac{(5)}{(6)}$	$\frac{(3)}{(4)}$	(2)(3)	$[(4)-(3)]\cdot(6)$	$\frac{[(4)-(3)]^3}{(12)}\cdot 4$
2	1.73	1	5	0	1	1	6.66	0	0.2	1.73	16	4

Body-

24	25	26	27	28	29	30	31
λ	r_s	$\alpha'\operatorname{tg}\varepsilon$	S_{tl}	λ_{is}	$\alpha'\lambda_{is}$	$\frac{2\alpha' r}{b_{rt}}$	$\alpha'\lambda_{is}\left(1+\frac{1}{\alpha'\operatorname{tg}\varepsilon}\right)(1+\lambda)$
$\frac{(20)}{(21)}$	$\frac{(18)}{(19)}$	(2)(22)	$[(19)-(18)]\times(21)$	$\frac{[(19)-(18)]^2}{(27)}\cdot 4$	(2)(28)	$\frac{2(2)(18)}{(21)}$	$(29)\left[1+\frac{1}{(26)}\right][1+(24)]$
0	0.31	1.73	4.94	4	6.92	1.56	10.9

Interference of body-

42	43	44	45	46	47
$\left(\frac{x_{c.p}\,\delta}{b_{rt}}\right)_{wg(b)}$	$(x_{c.p}\,\alpha)_{wg}$	$(x_{c.p}\,\delta)_{wg}$	$x_{ro}-(x_{c.p}\,\alpha)_{wg}$	$x_{ro}-(x_{c.p}\,\delta)_{wg}$	$\left(\frac{x_{c.p}\,\alpha}{b_{rt}}\right)_{b(wg)}$
Table XV-3-1 from (10)	(8)+(41)(6)	(8)+(42)·(6)	(17)−(43)	(17)−(44)	Fig. XV-1-9b from (15)
0.67	9.26	9.34	0.09	0.01	0.94

Interference of body-

56	57	58	59	60
$\left(\frac{x_{c.p}\,\alpha}{b_{rt}}\right)_{tl(b)}$	$\left(\frac{x_{c.p}\,\delta}{b_{rt}}\right)_{tl(b)}$	$(x_{c.p}\,\alpha)_{tl}$	$(x_{c.p}\,\delta)_{tl}$	$x_{ro}-(x_{c.p}\,\alpha)_{tl}$
Table XV-1-1 from (25)	Table XV-3-1 from (25)	(23)+(56)(21)	(23)+(57)(21)	(17)−(58)
0.647	0.666	17.7	17.8	−8.40

ACTERISTICS FOR BODY-WING-TAIL COMBINATION (Fig. XV-2-13). /655

wing						Body-tail					
14	15	16	17	17′	18	19	20	21	22	23
$\alpha'\lambda_{is}$	$\frac{2\alpha' r}{b_{rt}}$	$\alpha'\lambda_{is}\left(1+\frac{1}{\alpha' \operatorname{tg}\varepsilon}\right)(1+\lambda)$	x_{ro}	x_b	r	s_m	b_{tp}	b_{rt}	$\operatorname{tg}\varepsilon$	x_{tl}
(2) (13)	$2\frac{(2)(3)}{(6)}$	(14) $\left[1+\frac{1}{(11)}\right]$ [1 + (9)]	By hypothesis		By hypothesis					By hypothesis
6.92	0.86	10.9	9.35	16.7	1	3.22	0	2.22	1	16.3

tail	Body				Interference of body-wing combination					
32	33	34	35	36	37	38	38′	39	40	41
$\frac{S_{tl}}{S_{wg}}$	r_{mid}	x_{mid}	S_{mid}	W_b	K_{wg}	K_b	K_b	k_{wg}	k_b	$\left(\frac{x_{c.p}\,\alpha}{b_{rt}}\right)_{wg(b)}$
$\frac{(27)}{(12)}$	By hypothesis				Table XV-3-1 from (10)	Table XV-1-1 from (10)	Fig. XV-1-8b from 15),(11) and $\alpha' c_N^{\alpha}=4$	Table XV-3-1 from(10)	Table XV-3-1 from(10)	Table XV-1-1 from(10)
0.308	1	5.67	3.14	6.82	1.16	0.28	0.23	0.94	0.22	0.65

wing combination				Interference of body-tail combination			
48	49	50	51	52	53	54	55
$(x_{c.p}\,\alpha)_b$	$x_{ro}-(x_{c.p}\,\alpha)_b$	$\left(\frac{z_p-r}{s_m-r}\right)_{wg}$	$(c_N^{\alpha})_{wg}$	K_{tl}	K_b	k_{tl}	k_b
(8) + (47) (6)	(17) − (48)	Fig. XV-2-8 from (14) and $\lambda=0$	Chap. II (theory) (4/57.3)(2)	Table XV-3-1 from(25)	Fig. XV-1-8, a from (30), (26) and $\alpha' c_N^{\alpha}=4$	Table XV-3-1 from(25)	Table XV-3-1 from(25)
10.4	−1.05	0.678	0.0404	1.26	0.130	0.940	0.330

tail combination				
61	62	63	64	65
$x_{ro}-(x_{c.p}\,\delta)_{tl}$	$\left(\frac{x_{c.p}\,\alpha}{b_{rt}}\right)_{b(tl)}$	$(x_{c.p}\,\alpha)_b$	$x_{ro}-(x_{c.p}\,\alpha)_b$	$\frac{S_{tl}}{S_{wg}}(c_N^{\alpha})_{tl}$
(17) − (59)	Fig. XV-1-9a from (30)′	(23) + (62) (21)	(17) − (63)	(32) $\frac{4}{57.3\,(2)}$
−8.40	0.670	17.8	−8.40	0.0124

Aerodynamic characteristics of isolated body (curvilinear

66	67	68	69
$\frac{S_{mid}}{S_{wg}}$	$(c_N^{\alpha})_b$	$K_{sb} = \frac{(c_N^{\alpha})_{b}}{(c_N^{\alpha})_{wg}} \frac{S_{mid}}{S_{wg}}$	$\frac{W_b}{x_{mid} S_{mid}}$
$\frac{(35)}{(12)}$	$\frac{2}{57.3}$	$\frac{(67)}{(51)}(66)$	$\frac{(36)}{(34)(35)}$
0.196	0.035	0.171	0.495

Complete combination (body-wing-tail) without consideration of

74	75
$(c_N^{\delta})_{tl.b}$	$(m_z^{\alpha})_{b.wg.tl}$
[(54) + (55)] (65)	{[(37) (45) + (38') (49) + (68) (71)] (51) + + [(52) (60) + (53) (64)] (65)} $\frac{1}{(17)'}$
0.0158	−0.00573

Normal force of complete combination without consideration of wing vortices

79	80	81	82	83	84	85
			$(c_N^{\alpha})_{b.wg.tl}$ α	$(c_N^{\delta})_{wg.b}$ $(\delta_e)_{wg}$	$(c_N^{\delta})_{tl.b}$ $(\delta_e)_{tl}$	c_N
α°	$(\delta_e)^\circ_{wg}$	$(\delta_e)^\circ_{tl}$	(72) (79)	(73) (80)	(74) (81)	(82) + (83) + (84)
0	4.9	0	0	0.229	0	0.229
5	4.9	0	0.402	0.229	0	0.631
10	4.9	0	0.804	0.229	0	1.03
15	4.9	0	1.20	0.229	0	1.43

Normal force of complete combination with wings

91	92	93	94	95	96
b_h	x'_{wg}	$(v_b/v_m)_{tl}$	i_{tl}	$K_{mn}\alpha$	k_{av} $(\delta_e)_{wg}$

Table XV-3-2 (Cont'd.)

nose section)		Aerodynamic characteristics	
70	71	72	73
$(x_{c.p})_b$	$x_{ro} - (x_{c.p})_b$	$(c_N^{\alpha})_{b.wg.tl}$	$(c_N^{\delta})_{wg.b}$
from (69) and (34)	(17) — (70)	[(37) + (38') + (68)] (51) + [(52) + (53)] (65)	[(39) + (40)] (51)
2.87	6.48	0.0804	0.0468

wing vortices	Distance of wing vortex from tail	
76	77	78
$(m_z^{\delta})_{wg.b}$	$(m_z^{\delta})_{tl.b}$	$\left(\frac{z_v}{s_m}\right)_{tl}$
$[(39)(46) + (40)(49)]\frac{(5)}{(17')}$	$[(54)(61) + (55)(64)]\frac{(65)}{(17')}$	$\{(50)[1 - (10)] + (10)\}\frac{(4)}{(19)}$
—0.00048	—0.0071	1.152

Moment and C.P of complete combination without consideration of wing vortices

86	87	88	89	90
$(m_z^{\alpha})_{b.wg.tl}$ α	$(m_z^{\delta})_{wg.b}$ $(\delta_e)_{wg}$	$(m_z^{\delta})_{tl.b}$ $(\delta_e)_{tl}$	m_z	$(x_{ro} - x_{c.p})/x_b$
(75) (79)	(76) (80)	(77) (81)	(86) + (87) + (88)	(89)/(85)
0	0.00235	0	—0.00235	—0.0105
—0.0287	—0.00235	0	—0.0310	—0.0492
—0.0573	—0.00235	0	—0.0596	—0.0577
—0.0862	—0.00235	0	—0.0886	—0.0621

vortex effect			Moment and C.P of complete combination with consideration of wing vortices		
97	98	99	100	101	102
$k_{wg}\alpha + k_{wg}(\delta_e)_{wg}$	Formula (XV-3-14) $(c_N)_{(b.tl)v}$	c_N	$(m_z)_{(b.tl)v}$	m_z	$(x_{ro} - x_{c.p})/x_b$

Normal force of complete combination with consideration of					
91	92	93	94	95	96
1.560	7.12	$\frac{[(92)(79)-(91)(80)]}{57.3\,(19)}$	Fig. XV-2-9 from (93), (78) and (25)	(37) (79)	(39) (80)
$\alpha = 0°$	$\delta = 4.9°$	−0.0413	−2.16	0	4.60
$\alpha = 5°$	$\delta = 4.9°$	0.151	−2.02	5.80	4.60
$\alpha = 10°$	$\delta = 4.9°$	0.344	−1.71	11.6	4.60
$\alpha = 15°$	$\delta = 4.9°$	0.536	−1.44	17.4	4.60

Resultant values of static stability	
	103
	$(c_N^\alpha)_\alpha = (\delta_e)_{wg} = 0$
body	(68) (51) = 0.0069
body-wing	[(37) + (38') + (68)] (51) = 0.0631
body-tail without body nose	[(52) + (53)] (65) = 0.0172
body-wing-tail	$(72) + \frac{(98)}{(97)}(37)\frac{i_{tl} = -2.20}{(94)} = 0.0726$
remark	from Fig. XV-2-9 for $y_0 = 0, z_0/s_m = 1.152$ and $r_s = 0.31$ we find $i_{tl} = -2.2$.

Note. The column numbers from which the working data are taken

Wherever possible, experimental data or the results of supersonic linearized theory given in Chapters II and III were used in determining the coefficients $(c_N^\alpha)_{wg}$, $(c_N^\alpha)_{tl}$ and $(c_N^\alpha)_b$, so that the calculations were more accurate than in the case of slender-body theory.

In Table XV-3-2, columns 1-36 contain the initial geometry of the combination and the auxiliary parameters calculated with consideration of the given M_∞. Columns 37-51 and 52-65 present

wing vortices.			Moment and C.P of complete combination with consideration of wing vortices		
97	98	99	100	101	102
(95) + (96)	$\frac{(94)\,(97)\,(51)\,(65)\,[(19)-(18)]\,57,3}{2\pi\,(28)\,(50)\,[(4)-(3)](32)}$	(85) ÷ (96)	$\frac{(98)\,(51)}{(17')}$	(89) + (100)	$\frac{(101)}{(99)}$
4.60	−0.0303	0.1987	0.0136	+0.0112	0.6565
10.4	−0.0636	0.5674	0.0286	−0.0024	−0.0842
16.2	−0.0840	0.9460	0.0378	−0.0218	−0.0230
22.0	−0.0965	1.3340	0.0434	−0.0452	−0.0338

derivatives and their components		
104	105	106
$(m_z^{\alpha})_{\alpha} = (\delta_e)_{wg} = 0$	$(c_N^{\delta})_{\alpha} = (\delta_e)_{wg} = 0$	$(m_z^{\delta})_{\alpha} = (\delta_e)_{wg} = 0$
$\frac{(103)\,(71)}{(17')} = 0.0024$		
$[(37)\,(45) + (38')\,(49) + + (68)\,(71)]\,\frac{(51)}{(17')} = 0.0021$	(73) = 0.0464	(76) = − 0.00048
[(52)+(53)] (65)=0.0172	$[(52)\,(61) + (53)\,(64)]\,\frac{(65)}{(17')} = = -0.00775$	
$(75) + [(103) - (72)]\,\frac{(60)}{(17')} = -0.00228$	$(73) + [(103) - (72)]\,\frac{(39)}{(37)} = = 0.0405$	$(76) + [(104) - (75)]\,\frac{(39)}{(37)} = = 0.00236$

are indicated in the parentheses.

the results of calculation of the interference characteristics for the body-wing and body-tail combinations, respectively. Here, columns 38 and 38' give the coefficients k_b as calculated by slender-body aerodynamic theory and the linearized theory, respectively. The subsequent calculations use the k_b = 0.23 obtained from linearized theory.

Columns 66-71 present data on the flow around the isolated curvilinear nose section, while columns 72-102 contain the over-

TABLE XV-3-3. THEORETICAL AND EXPERIMENTAL VALUES OF AERODYNAMIC CHARACTERISTICS FOR PLANE WING-BODY COMBINATIONS. GEOMETRICAL PARAMETERS OF COMBINATION; VALUES OF M_∞, $Re = V_\infty (b_{MAC})_{wg}/\nu_\infty$*

No.	Diagram of combination	M_∞	Re·10⁻⁶	$\frac{x_e}{r_{mid}}$	$\frac{x_{ro}}{x_e}$	$\frac{x_{wg}}{x_e}$	$a'\lambda_{ls,wg}$	$\varkappa_1^\circ$	$\lambda = \frac{b_{tp}}{b_{rt}}$	$\frac{r}{r_{mid}}$	$\frac{r}{e_m}$
				1—a							
1a	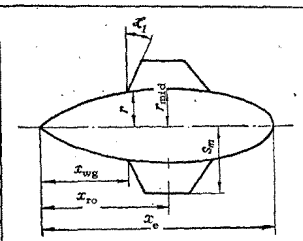	0.20	1.86	22.5	0.483	0.440	3.43	9.45	0.546	0.992	0.179
b		0.70	1.86	22.5	0.483	0.440	2.49	9.45	0.546	0.992	0.179
c		0.90	1.86	22.5	0.483	0.440	1.52	9.45	0.546	0.992	0.179
2a	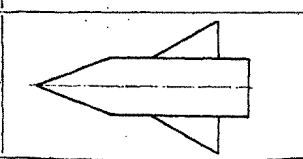	1.50	1.0	14.7	—	0.450	4.47	45.0	0.000	1.000	0.201
b		2.00	1.0	14.7	—	0.450	6.93	45.0	0.000	1.000	0.201
3a	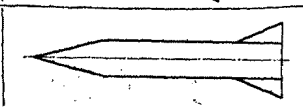	1.20	0.59	31.8	—	0.912	2.66	45.0	0.000	1.000	0.254
b		1.70	0.59	31.8	—	0.912	5.50	45.0	0.000	1.000	0.254

Table XV-3-3 (Cont'd.) /661

No.	Diagram of combination	M_∞	$Re \cdot 10^{-6}$	$\frac{x_e}{r_{mid}}$	$\frac{x_{ro}}{x_e}$	$\frac{x_{wg}}{x_e}$	$\alpha'\lambda_{ls.wg}$	$\varkappa_1^\circ$	$\lambda = \frac{b_{tp}}{b_{rt}}$	$\frac{r}{r_{mid}}$	$\frac{r}{r_m}$
4a	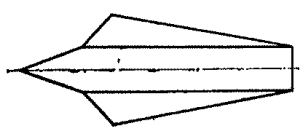	0.50	4.25	19.6	1.000	0.380	1.73	26.5	0.000	1.000	0.243
b		0.90	6.58	19.6	1.000	0.380	0.87	26.5	0.000	1.000	0.243
c		1.45	2.76	19.6	1.000	0.380	2.10	26.5	0.000	1.000	0.243
d		1.99	2.34	19.6	1.000	0.380	3.45	26.5	0.000	1.000	0.243
5	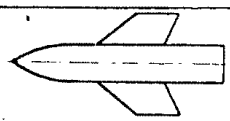	0.60	3.67	16.7	0.521	0.386	2.19	35.0	0.352	1.000	0.160
6	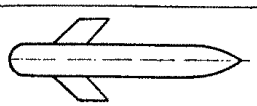	0.10	0.57	11.7	0.322	0.260	5.62	0.0	0.88	1.000	0.115
7	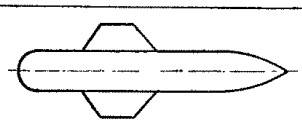	0.10	0.62	11.7	0.322	0.185	5.52	18.3	0.38	1.000	0.115
8a	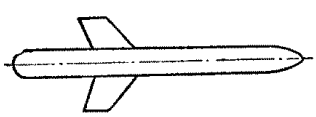	0.10	0.62	11.7	0.322	0.223	5.52	9.3	0.38	1.000	0.115
b		0.10	0.62	11.7	0.322	0.261	5.52	0.0	0.38	1.000	0.115

Table XV-3-3 (Cont'd.) /662

No.	Diagram of combination	M_∞	Re·10⁻⁶	$\frac{x_e}{r_{mid}}$	$\frac{x_{ro}}{x_e}$	$\frac{x_{wg}}{x_e}$	$\alpha'\lambda_{1s.wg}$	$\varkappa_1^\circ$	λ $\frac{b_{tp}}{b_{rt}}$	$\frac{r}{r_{mid}}$	$\frac{r}{s_{r/s}}$
9a	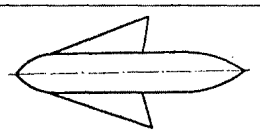	0.75	1.27	24.0	0.606	0.388	1.49	60.0	0.0	0.981	0.158
b		1.07	1.25	24.0	0.606	0.388	0.83	60.0	0.0	0.981	0.158
10a	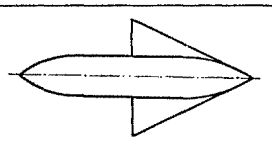	0.75	1.31	24.0	0.637	0.499	1.60	0.0	0.0	0.861	0.139
b		1.07	1.29	24.0	0.637	0.499	0.90	0.0	0.0	0.861	0.139
				2—a							
11a	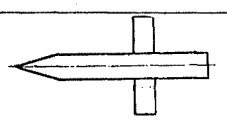	1.62	0.40	19.5	—	0.501	1.66	0.0	1.000	1.000	0.350
b		1.93	0.40	19.5	—	0.501	2.14	0.0	1.000	1.000	0.350
c		2.40	0.40	19.5	—	0.501	2.84	0.0	1.000	1.000	0.350
12	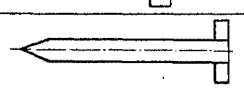	2.00	—	27.9	—	0.860	1.73	0.0	1.000	1.000	0.333
13	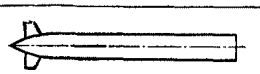	1.50	0.26	22.9	—	0.148	2.98	26.6	0.500	0.986	0.486

Table XV-3-3 (Cont'd.) /663

No.	Diagram of combination	M_∞	$Re \cdot 10^{-6}$	$\frac{x_e}{r_{mid}}$	$\frac{x_{ro}}{x_e}$	$\frac{x_{wg}}{x_e}$	$\alpha'\lambda_{is.wg}$	$\varkappa_1^\circ$	$\lambda=\frac{b_{tp}}{b_{rt}}$	$\frac{r}{r_{mid}}$	$\frac{r}{e_m}$
14a	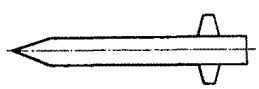	1.50	0.70	22.9	—	0.632	3.30	14.0	0.461	1.000	0.250
b		2.00	0.70	22.9	—	0.632	5.11	14.0	0.461	1.000	0,250
15a	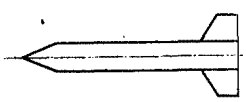	1.62	0.31	21.8	—	0.870	1.57	60.0	0.305	1.000	0.465
b		1.93	0.28	21.8	—	0.870	2.03	60.0	0.305	1.000	0,465
16a	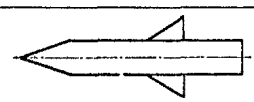	1.50	1.00	14.7	—	0.450	0.75	80.4	0.000	1.000	0.600
b		2.00	1.00	14.7	—	0.450	1.16	80.4	0.000	1.000	0.600
					3—a						
17	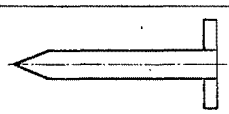	1.92	0.20	25.0	—	0.920	5.13	0.0	1.0	1.0	0.228
18	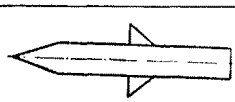	1.40	1.25	31.8	—	0.412	2.27	0.0	0.0	1.0	0.216

Table XV-3-3 (Cont'd.) /664

No.	Diagram of combination	M_{cr}	Re·10⁻⁶	$\frac{x_e}{r_{mid}}$	$\frac{x_{ro}}{x_e}$	$\frac{x_{wg}}{x_e}$	$\alpha'\lambda_{1s.wg}$	$\varkappa_1^e$	$\lambda = \frac{b_{tp}}{b_{rt}}$	$\frac{r}{r_{mid}}$	$\frac{r}{s_{ns}}$
19a	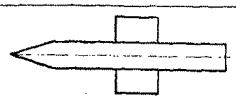	1.40	1.51	31.8	—	0.389	1.13	0.0	1.0	1.0	0.216
b		1.90	1.51	31.8	—	0.389	1.87	0.0	1.0	1.0	0.216

Aerodynamic characteristics

1 — b ($\alpha \neq 0$, $\delta = 0$)

No.	$K_{b.i}$	K_b	K_{wg}	Theory: normal force			Theory: center of pressure				Experiment: normal force		Experiment: center of pressure
				$(\alpha' c_N^\alpha)_{wg}$	$(\alpha' c_N^\alpha)_b$	$(\alpha' c_N^\alpha)_{b.wg}$	$\left(\frac{x_{c.p}}{x_e}\right)_b$	$\left(\frac{x_{c.p}\,\alpha}{x_e}\right)_{b(wg)}$	$\left(\frac{x_{c.p}\,\alpha}{x_e}\right)_{wg(b)}$	$\left(\frac{x_{c.p}}{x_e}\right)_{b.wg}$	$(\alpha' c_N^\alpha)_b$	$(\alpha' c_N^\alpha)_{b.wg}$	$\left(\frac{x_{c.p}}{x_e}\right)_{b.wg}$
1a	0.08	0.24	1.14	3.47	0.27	5.05	0.229	0.480	0.485	0.47	—	4.70	0.47
b	0.07	0.24	1.14	2.83	0.19	4.10	0.229	0.478	0.485	0.47	—	3.94	0.47
c	0.06	0.24	1.14	2.02	0.12	2.90	0.229	0.474	0.485	0.47	—	3.08	0.47
2a	0.11	0.23	1.16	4.00	0.44	6.01	0.190	0.675	0.636	0.60	0.43	5.69	0.60
b	0.17	0.23	1.16	4.00	0.68	6.24	0.190	0.710	0.636	0.59	0.90	7.09	0.60
3a	0.15	0.20	1.21	3.10	0.48	4.86	0.207	0.966	0.969	0.89	—	4.91	0.90
b	0.25	0.14	1.21	4.00	1.00	6.40	0.207	0.969	0.969	0.84	—	7.26	0.85
4a	0.14	0.35	1.20	1.97	0.28	3.34	0.102	0.452	(0.428)	0.40	—	3.36	0.40
b	0.12	0.35	1.20	1.13	0.16	1.89	0.102	0.441	(0.428)	0.40	—	2.18	0.40
c	0.13	0.35	1.20	2.69	0.34	4.50	0.102	0.606	(0.477)	0.47	—	4.40	0.43
d	0.15	0.35	1.20	3.71	0.55	6.31	0.102	0.632	(0.477)	0.47	—	5.95	0.43
5	0.05	0.22	1.13	2.51	0.13	3.51	—	0.505	0.541	—	—	3.64	0.52

Table XV-3-3 (Cont'd.) /665

No.	$K_{b.1}$	K_b	K_{wg}	Theory							Experiment		
				normal force			center of pressure				normal force		center of pressure
				$(\alpha' c_N^{\alpha})_{wg}$	$(\alpha' c_N^{\alpha})_b$	$(\alpha' c_N^{\alpha})_{b,wg}$	$\left(\frac{x_{c.p}}{x_e}\right)_b$	$\left(\frac{x_{c.p(\alpha)}}{x_e}\right)_{b,wg}$	$\left(\frac{x_{c.p\,\alpha}}{x_e}\right)_{wg(b)}$	$\left(\frac{x_{c.p}}{x_e}\right)_{b,wg}$	$(\alpha' c_N^{\alpha})_b$	$(\alpha' c_N^{\alpha})_{b,wg}$	$\left(\frac{x_{c.p}}{x_e}\right)_{b,wg}$
6	0.14	0.15	1.09	4.13	0.60	5.30	0.100	0.322	0.319	0.31	—	5.81	0.32
7	0.14	0.15	1.09	4.12	0.58	5.27	0.100	0.290	0.338	0.33	—	4.83	0.32
8a	0.14	0.15	1.09	4.12	0.58	5.27	0.100	0.316	0.334	0.33	—	4.83	0.32
b	0.14	0.15	1.09	4.12	0.58	5.27	0.100	0.341	0.325	0.32	—	4.83	0.32
9a	0.05	0.23	1.13	1.76	0.09	2.48	0.217	0.548	0.592	0.57	—	2.40	0.56
b	0.04	0.21	1.13	1.22	0.05	1.68	0.217	0.584	0.631	0.60	—	1.53	0.59
10a	0.05	0.19	1.11	1.84	0.09	2.48	0.217	0.566	0.558	0.54	—	2.38	0.50
b	0.04	0.19	1.11	1.31	0.05	1.74	0.217	0.578	0.539	0.52	—	1.76	0.53
							2—b						
11a	0.27	0.52	1.30	2.79	0.76	5.84	0.207	0.646	0.568	0.51	0.80	4.71	0.49
b	0.32	0.44	1.30	3.07	0.98	6.32	0.207	0.657	0.566	0.50	1.05	5.66	0.50
c	0.39	0.38	1.30	3.30	1.29	6.84	0.207	0.679	0.568	0.49	1.34	6.72	0.51
12	0.24	0.25	1.28	2.84	0.68	5.02	0.083	0.992	0.920	0.78	0.68	5.48	0.80
13	1.38	0.56	1.44	3.49	4.83	11.81	0.090	0.213	0.175	0.13	4.98	11.05	0.13
14a	0.16	0.29	1.21	3.56	0.57	5.91	0.090	0.742	0.688	0.62	0.59	6.10	0.62
b	0.24	0.27	1.21	3.78	0.89	6.48	0.090	0.766	0.691	0.60	1.09	7.15	0.61
15a	0.71	0.31	1.41	2.62	1.87	6.38	0.165	0.956	0.949	0.69	2.15	6.12	0.68
b	0.78	0.16	1.41	3.12	2.42	7.32	0.165	0.960	0.949	0.67	2.91	7.78	0.64
16a	2.33	0.97	1.56	1.13	2.63	5.48	0.190	0.675	0.636	0.42	2.56	6.35	0.44
b	2.44	0.94	1.56	1.67	4.08	8.25	0.190	0.710	0.636	0.42	5.38	10.02	0.41

Note. Values of $\alpha' c_N^{\alpha}$ are given in radians. ( ) Experimental values used in theoretical calculations.

TABLE XV-3-3 (Cont'd.) /666

3—b ($\alpha \neq 0$, $\delta = 0$)

No.	$K_{b,l}$	K_b	K_{wg}	Theory							Experiment	
				normal force			center of pressure				normal force	center of pressure
				$(\alpha' c_N^{\alpha})_{wg}$	$(\alpha' c_N^{\alpha})_b$	$(\alpha' c_N^{\alpha})_{b,wg}$	$\left(\frac{x_{c.p.}}{x_e}\right)_b$	$\left(\frac{x_{c.p}\,\alpha}{x_e}\right)_{b(wg)}$	$\left(\frac{x_{c.p}\,\alpha}{x_e}\right)_{jwg(b)}$	$\left(\frac{x_{c.p.}}{x_e}\right)_{b,wg}$	$(\alpha' c_N^{\alpha})_{wg(b)}$	$\left(\frac{x_{c.p}}{x_e}\right)_{wg(b)}$
17	0.29	0.07	1.19	3.61	1.06	5.61	0.19	0.954	0.954	0.78	5.61	0.75
18	0.10	0.31	1.18	2.83	0.27	4.48	0.21	0.548	0.457	0.45	4.60	0.45
19a	0.06	0.31	1.18	2.23	0.13	3.48	0.21	0.525	0.460	0.43	3.59	0.45
b	0.08	0.31	1.18	2.93	0.22	4.58	0.21	0.545	0.475	0.45	4.54	0.47

3—c ($\alpha = 0$, $\delta \neq 0$)

No.	k_b	k_{wg}	Theory					Experiment			
			normal force		center of pressure			normal force		center of pressure	
			$(\alpha' c_N^{\delta})_{wg(b)}$	$(\alpha' c_N^{\delta})_{lwg,b}$	$\left(\frac{x_{c.p}\,\delta}{x_e}\right)_{b(wg)}$	$\left(\frac{x_{c.p}\,\delta}{x_e}\right)_{wg(b)}$	$\left(\frac{x_{c.p}\,\delta}{x_e}\right)_{lwg,b}$	$(\alpha' c_N^{\delta})_{wg(b)}$	$(\alpha' c_N^{\delta})_{lwg,b}$	$\left(\frac{x_{c.p}\,\delta}{x_e}\right)_{wg(b)}$	$\left(\frac{x_{c.p}}{x_e}\right)_{wg,b}$
17	0.25	0.98	3.53	4.43	0.954	0.953	0.96	—	3.03	—	0.98
18	0.24	0.94	2.67	3.34	0.548	0.467	0.47	2.58	3.26	0.450	0.48
19a	0.24	0.94	2.10	2.63	0.525	0.457	0.44	2.25	2.75	0.458	0.46
b	0.24	0.94	2.76	3.46	0.545	0.475	0.46	2.96	3.52	0.467	0.48

TABLE XV-3-4. THEORETICAL AND EXPERIMENTAL VALUES OF AERODYNAMIC CHARACTERISTICS /667
FOR PLANE BODY-WING-TAIL COMBINATIONS. 1-a. GEOMETRICAL PARAMETERS OF COMBINATION; VALUES OF M_∞ AND Re*

No.	Diagram of combination	M_∞	Re·10⁻⁶	$\frac{x_e}{r_{mid}}$	$\frac{x_{ro}}{x_e}$	$\frac{S_{tl}}{S_{wg}}$	Surface	$\frac{x_{wg}/x_e}{x_{tl}/x_e}$ or	$\frac{s_{max}}{b}$	$\alpha'\lambda_{1z}$	$\varkappa_1^\circ$	$\lambda=\frac{b_{tp}}{b_{rt}}$	$\frac{r}{r_{mid}}$	$\frac{r}{s_m}$
1	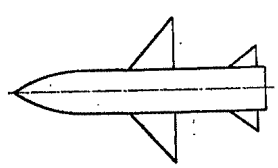	1.99	0.81	18.6	0.500	0.309	wing	0.357	0.08	6.88	45.00	0.000	1.000	0.200
							tail	0.872	0.08	6.88	45.00	0.000	1.000	0.340
2a	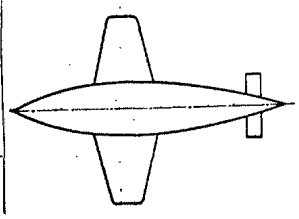	0.20	1.86	22.5	0.483	0.252	wing	0.440	0.042	3.43	9.45	0.546	0.992	0.179
							tail	0.895	0.042	3.43	9.45	0.548	0.488	0.176
2b		0.70	1.86	22.5	0.483	0.252	wing	0.440	0.042	2.49	9.45	0.546	0.992	0.179
							tail	0.895	0.042	2.50	9.45	0.548	0.488	0.176
2c		0.90	1.86	22.5	0.483	0.252	wing	0.440	0.042	1.52	9.45	0.546	0.992	0.179
							tail	0.895	0.042	1.53	9.45	0.548	0.488	0.176

Table XV-3-4 (Cont'd.) /668

No.	Diagram of combination	M_∞	$Re \cdot 10^{-6}$	$\frac{x_e}{r_{mid}}$	$\frac{x_{ro}}{x_e}$	$\frac{S_{tl}}{S_{wg}}$	Surface	$\frac{x_{wg}/x_e}{x_{tl}/x_e}$ or	$\frac{s_{max}}{b}$	$\alpha'\lambda_{ls}$	$\varkappa_1^\circ$	$\lambda=\frac{b_{tp}}{b_{rt}}$	$\frac{r}{r_{mid}}$	$\frac{t}{s_m}$
3a	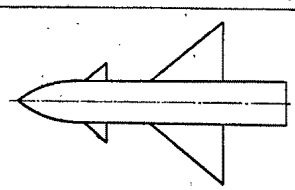	0.89	6.0	32.6	0.525	9.00	wing	0.226	—	1.05	60.00	0.000	1.000	0.467
							tail	0.597	—	1.05	60.00	0.000	1.000	0.226
b		1.25	9.2	32.6	0.525	9.00	wing	0.226	—	1.73	60.00	0.000	1.000	0.467
							tail	0.597	—	1.73	60.00	0.000	1.000	0.226
4	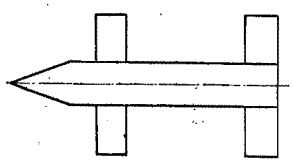	1.90	1.51	31.8	0.508	0.392	wing	0.389	0.03	1.87	0.00	1.000	1.000	0.216
							tail	0.809	0.02	0.78	0.00	1.000	1.000	0.405
5	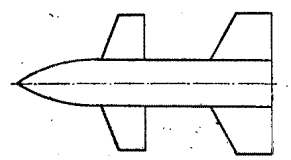	1.93	0.33	21.9	0.522	0.839	wing	0.486	—	1.69	60.00	0.323	1.000	0.465
							tail	0.869	0.049	2.03	60.00	0.305	1.000	0.465

Table XV-3-4 (Cont'd.) /669

No.	Diagram of combination	M_{co}	$Re \cdot 10^{-6}$	$\frac{x_e}{r_{mid}}$	$\frac{x_{ro}}{x_e}$	$\frac{S_{tl}}{S_{wg}}$	Surface	$\frac{x_{wg}/x_e}{x_{tl}/x_e}$ or	$\frac{s_{max}}{b}$	$\alpha'\lambda_{is}$	$\varkappa_1^\circ$	$\lambda=\frac{b_{tp_i}}{b_{rt_i}}$	$\frac{r}{r_{mid}}$	$\frac{r}{s_m}$
6	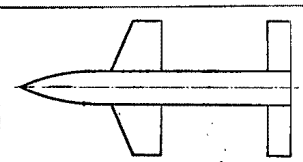	1.93	0.33	22.8	0.541	0.931	wing tail	0.507 0.947	— 0.064	1.69 5.51	60.00 0.00	0.323 1.000	1.000 1.000	0.465 0.333
7	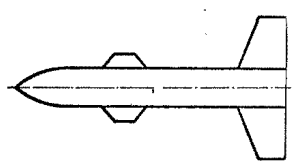	1.93	0.33	22.8	0.541	1.01	wing tail	0.507 0.893	— —	1.69 3.16	60.00 45.00	0.323 0.352	1.000 1.000	0.465 0.388
8	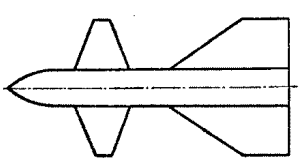	1.93	0.83	22.8	0.541	5.74	wing tail	0.290 0.636	— —	1.69 1.03	60.00 70.00	0.323 0.400	1.000 1.000	0.508 0.356

Table XV-3-4 (Cont'd.) /670

No.	Diagram of combination	M_{∞}	Re·10⁻⁶	$\frac{x_e}{r_{mid}}$	$\frac{x_{ro}}{x_e}$	$\frac{S_{tl}}{S_{wg}}$	Surface	$\frac{x_{wg}/x_e}{x_{tl}/x_e}$ or	$\frac{s_{max}}{b}$	$c'\lambda_{ls}$	$\varkappa_1^o$	λ	$\frac{b_{tp}}{b_{rt}}$	$\frac{r}{r_{mid}}$	$\frac{r}{s_m}$
9		1.93	0.83	22.8	0.541	23.10	wing	0.404	—	3.81	60.00	0.000	1.000	1.000	0.579
							tail	0.636	—	1.03	70.00	0.400	1.000	1.000	0.356
10		1.93	0.83	22.8	0.541	10.30	wing	0.376	—	3.81	60.00	0.000	1.000	1.000	0.479
							tail	0.636	—	1.03	70.00	0.400	1.000	1.000	0.356
11		1.93	0.83	22.8	0.541	5.79	wing	0.349	—	3.81	60.00	0.000	1.000	1.000	0.408
							tail	0.636	—	1.03	70.00	0.400	1.000	1.000	0.356
12		1.62	0.23	25.7	0.486	1.000	wing	0.355	—	3.31	0.00	0.000	1.000	1.000	0.350
							tail	0.880	—	3.31	0.00	0.000	1.000	1.000	0.350

1-b. Aerodynamic Characteristics

No.	$K_{b,1}$	K_b	K_{wg}	$K_{b(t)}$	$K_{t(b)}$	Theory: normal force $(\alpha' c_N^{\alpha})_{wg}$	$(\alpha' c_N^{\alpha})_{t}$	$(\alpha' c_N^{\alpha})_b$	$(\alpha' c_N^{\alpha})^*_{cm}$	$(\alpha' c_N^{\alpha})_{cm}$	Theory: center of pressure $\left(\frac{x_{c.p}}{x_b}\right)_b$	$\left(\frac{x_{c.p}\,\alpha}{x_b}\right)_{wg(b)}$	$\left(\frac{x_{c.p}\,\alpha}{x_b}\right)_{b(wg)}$	$\left(\frac{x_{c.p}\,\alpha}{x_b}\right)_{b(t)}$	$\left(\frac{x_{c.p}\,\alpha}{x_b}\right)_{t(b)}$	$\left(\frac{x_{c.p}}{x_b}\right)^*_{cm}$	$\left(\frac{x_{c.p}}{x_b}\right)_{cm}$	Experiment: normal force $(\alpha' c_N^{\alpha})_b$	$(\alpha' c_N^{\alpha})_{cm}$	Experiment: center of pressure $\left(\frac{x_{c.p}}{x_b}\right)_{cm}$
1	0.17	0.23	1.16	0.12	1.27	4.00	4.00	0.68	7.99	7.20	0.154	0.558	0.500	0.951	0.951	0.575	0.535	—	7.74	0.550
2a	0.08	0.24	1.14	0.24	1.14	3.47	3.48	0.27	6.45	5.56	0.229	0.480	0.485	0.915	0.918	0.557	0.521	—	5.20	0.505
b	0.07	0.24	1.14	0.24	1.14	2.83	2.83	0.19	4.70	4.21	0.229	0.478	0.485	0.915	0.918	0.565	0.525	—	4.25	0.493
c	0.06	0.24	1.14	0.24	1.14	2.02	2.02	0.12	3.60	3.17	0.229	0.474	0.485	0.912	0.918	0.559	0.510	—	3.11	0.483
3a	0.96	0.74	1.42	0.32	1.19	1.32	1.32	0.14	2.51	2.06	0.104	0.257	0.261	0.683	0.701	0.602	0.581	—	1.97	0.583
b	0.89	0.62	1.42	0.27	1.19	2.34	2.34	0.23	4.17	3.40	0.104	0.281	0.267	0.714	0.719	0.627	0.607	—	3.38	0.603
4	0.08	0.31	1.18	0.62	1.36	2.93	1.50	0.22	5.74	5.19	0.182	0.547	0.475	0.931	0.864	0.559	0.508	—	5.00	0.485
5	(0.82)	0.63	1.41	0.26	1.41	2.94	3.12	2.01	12.77	8.70	(0.165)	0.640	0.574	0.956	0.948	0.635	0.488	2.41	8.39	—
6	(0.82)	0.63	1.41	0.06	1.29	2.94	3.64	2.01	12.87	11.73	(0.118)	0.655	0.591	0.982	0.973	0.647	0.616	2.41	11.15	0.599
7	(0.82)	0.63	1.41	0.14	1.34	2.94	3.67	1.99	13.81	10.31	(0.118)	0.655	0.591	0.964	0.959	0.662	0.561	2.39	10.72	0.555
8	(1.15)	0.69	1.46	0.54	1.31	2.94	1.94	0.49	4.98	4.26	(0.118)	0.431	0.364	0.868	0.830	0.666	0.625	0.59	[3.90]	[0.593]
9	(3.48)	0.70	1.54	0.54	1.31	3.91	1.94	0.49	4.54	4.16	(0.118)	0.505	0.440	0.868	0.830	0.718	0.705	0.59	3.77	0.683
10	(1.55)	0.54	1.43	0.54	1.31	3.91	1.94	0.49	4.92	4.16	(0.118)	0.492	0.432	0.868	0.830	0.698	0.675	0.59	3.82	0.668
11	(0.87)	0.44	1.36	0.54	1.31	3.91	1.94	0.49	5.39	4.26	(0.118)	0.482	0.431	0.868	0.830	0.672	0.629	0.59	4.00	[0.604]
12	(0.48)	0.53	1.30	0.53	1.30	3.62	3.62	1.51	14.97	9.78	(0.162)	0.450	0.390	0.953	0.914	0.609	0.446	1.72	9.09	[0.486]

*Values without consideration of wing vortices.
( ) Experimental values used in calculation.
[ ] Experimental values nonlinear around $\alpha = 0$.
The subscript cm pertains to the combination as a whole.
The coordinate $(x_{c.p}/x_b)_{cm}$ is measured from the nose of the body.

all aerodynamic characteristics of the body-wing-tail combination. Some of these characteristics are given without consideration of wing vortices, but the final results (columns 78-102) incorporate the interference correction governed by wing-tail interaction. Lastly, the over-all values of the static derivatives $(c_N^{\alpha})_{\alpha=(\delta_e)_{wg}=0}$, $(m_z^{\alpha})_{\alpha=(\delta_e)_{wg}=0}$, $(c_N^{\delta})_{\alpha=(\delta_e)_{wg}=0}$ and $(m_z^{\delta})_{\alpha=(\delta_e)_{wg}=0}$ and their components for the isolated body (curvilinear nose section) and the body-wing and body-tail combinations (without the body nose section) are calculated. We see from the results that the wing section is the dominant factor in generating normal force for the combination, while the tail section dominates in the generation of moment.

Calculations similar to those in Table XV-3-2 were carried out for other combinations. Table XV-3-3 presents the results of these calculations for body-wing combinations and Table XV-3-4 for body-wing-tail combinations. For comparison, these tables /659
indicate the experimental characteristics obtained for various M_{∞} and $Re = V_{\infty}b_{MAC}/\nu$ (b_{MAC} is the mean aerodynamic chord of the isolated wing) ([75], 1307). For some combinations, the body radius was variable at the wing or tail attachment. In these tables, s_{max}/b is the maximum profile thickness referred to the chord.

The theoretical and experimental figures are compared for the α-derivatives of the normal-force coefficients (at $\alpha = 0$) and for the center of pressure coefficients $(x_{c.p}/x_b)_{b.wg}$ of the combinations, since comparisons for the individual components of the combinations were impossible owing to the shortage of appropriate experimental data. The satisfactory agreement of the over-all theoretical and experimental results confirms indirectly /672
that the distribution of the interference components of normal force between the body and the wing has been calculated correctly. However, this problem requires further investigation.

Some difficulty was encountered in determining the slopes of the moment curves during reduction of the experimental data ([75], 1307), since a nonlinearity, although a small one, was observed around $\alpha = 0$. It was assumed that linearity exists for $\alpha = \pm 2°$ and the average slope on this segment was taken.

The moment characteristics were found to be so nonlinear for certain wing-body-tail combinations that it was impossible to determine the center of pressure position accurately at $\alpha = 0$; the corresponding center of pressure coordinates are not shown in Tables XV-3-3 and XV-3-4 for these cases.

It was also difficult to determine the inclination angles of the normal-force curves for the isolated bodies in some cases

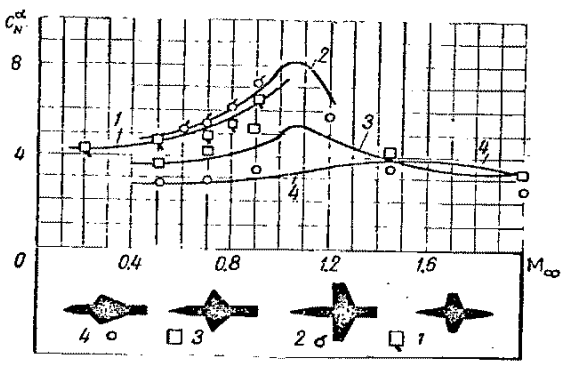

Figure XV-3-14. Variation of Derivative c_N^α ($\alpha = 0$) of Body-Wing Combination as a Function of M_∞: ——— : calculated; □(1); ◇(2); □(3); ○(4) – experimental data.

owing to the very small sizes of these angles and the unreliability of available experimental data. The error in determination of the inclinations does not exceed 10%.

Body-wing combination. Comparison with the experimental data indicates that the calculated slopes of the normal-force curves for the body-wing combinations differed from the experimental values ([75], 1307) by as much as 10%, and that they averaged larger than the experimental slopes for the combination with the part of the body behind the wing.

The most reliable data are those calculated for the normal forces of bodies with delta wings. Figure XV-3-14 indicates the accuracy of the method of determining the slopes of the body-wing normal-force curves as functions of M_∞. Although the trend of variation of the calculated parameters was predicted correctly, there are differences in magnitude; for example, the calculated values are smaller than the experimental ones in the transonic range.

The inclinations of the normal-force curves for isolated wings were calculated by the linear theory, which, for example, for rectangular wings, gives better agreement with experiment in the neighborhood of $M_\infty = 1$ if a certain conventional parameter $\lambda_{wg}(s_{max}/b)^{1/3} < 1$. However, the theoretical and experimental slopes /673
of the normal-force curves do not agree well for all four combination forms represented in Fig. XV-3-14. Analysis of the data in this figure indicates that the behavior of the normal-force curve with M_∞ in the neighborhood of $M_\infty = 1$ is qualitatively the same for the combination as a whole as for an isolated small-aspect-ratio wing.

Study of the effect of wing setting angle on normal force indicates that the theoretical and experimental $\alpha' c_N^\delta$ values of the body-wing combination agree well when the c_N^α are determined experimentally for the isolated wings.

For comparison, Table XV-3-2 presents experimental data on the centers of pressure, whose dimensionless coordinates are

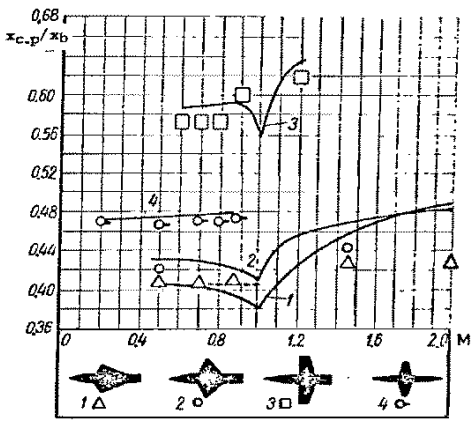

Figure XV-3-15. Change in Center of Pressure Coordinate of Body-Wing Combination as a Function of M_∞ for $\alpha \to 0$. ———) calculated; △(1); ○(2); □(3); ○—(4) experimental data.

determined by the formula

$$\left(\frac{\Delta x_{c.p}}{x_b}\right)_\alpha = \frac{x_{ro} - \frac{m_z^\alpha}{c_N^\alpha} x_b}{x_b}, \qquad \text{(XV-3-47)}$$

where m_z^α and c_N^α are the experimental moment and normal-force coefficients; x_{ro} is the distance from the nose to the center of rotation; and x_b is the length of the combination.

The comparison shows that when a theory that does not consider the effect of the body behind the wing is used, the theoretical and experimental data show better agreement. As in the case of lift, the influence of the part of the body behind the wing on the center of pressure coordinate may be strong.

Analysis of the pressure centers indicates that their calculated coordinates, reckoned from the nose, will be larger than the experimental coordinates. Here the center of pressure lies closer to the stern for rectangular wings than for delta wings. For the trapezoidal wing form, the error of calculation of the center of pressure coordinate will be of intermediate magnitude. According to experimental data ([75], 1307), the error in determination of the center of pressure coordinate is $0.026x_b$ in the presence of a rectangular wing, $0.009x_b$ in the presence of a delta wing, and $0.017x_b$ for a trapezoidal wing. A comparison of the theoretical and experimental centers of pressure for subsonic and supersonic velocities is made in Fig. XV-3-15, which presents data for four body-wing combinations. Our attention is drawn to the small change in the center of pressure coordinate with M_∞ until transonic speeds are reached. The experimental and theoretical values found for $(\Delta x_{c.p}/x_b)_\delta$ with $\delta_e \neq 0$, $\alpha = 0$ appear in Table XV-3-2.

Body-wing-tail combination. It has been established that the interaction between the tail and the wing may affect the overall aerodynamic characteristics by roughly 30-40%. Correction for /674

the type of interference by the method set forth above yields the over-all characteristics accurate to within ±10%.

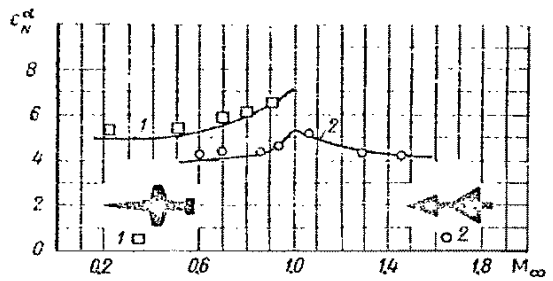

Figure XV-3-16. Variation of Derivative c_N^α as $\alpha \to 0$ as a Function of M_∞ for Body-Wing-Tail Combination. ———) calculation; □(1); ○(2) experiment.

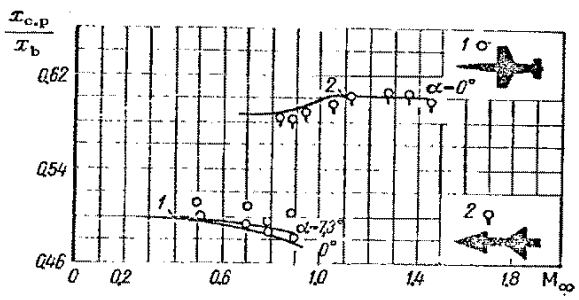

Figure XV-3-17. Variation of Center of Pressure Position as Function of M_∞ as $\alpha \to 0$ for Body-Tail Combination. ———) theory; ○(1); ○(2) experiment.

Figure XV-3-16 shows the variation of the derivative c_N^α as $\alpha \to 0$ for two body-wing-tail combinations as a function of M_∞. We see that a theory that takes account of interference between the tail and the wing agrees with experiment for practically the entire range of M_∞ from subsonic to supersonic, including the transonic region.

According to theory and experiment ([75], 1307), the influence of interference between the tail and wing on the combination's center of pressure position is usually stronger at supersonic than at subsonic speeds. The errors in the theoretical calculations amount to about $0.02x_b$.

The influence of Mach number and attack angle on the relative center of pressure coordinate as $\alpha \to 0$ is shown in Fig. XV-3-17 for two body-wing-tail combinations at sub- and supersonic speeds. For the combination with the trapezoidal wing, the theoretical data do not agree as well with experimental results as they do for a combination with a delta wing. This indicates that nonlinear effects are substantial for the trapezoidal combination. /675

When the wing is rotated through a positive angle δ_e, an additional upward normal force is created, but the resultant wing vortices give rise to an opposed tail normal force. The result is a substantial pitching moment that tends to shift the center of pressure forward. This is confirmed by theoretical and experimental data ([75], 1307) in Table XV-3-2. Figure XV-3-18 presents similar data for two combinations with different wing forms.

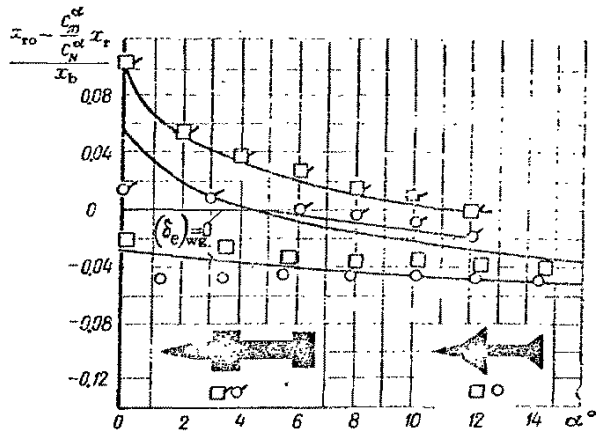

Figure XV-3-18. Influence of Wing Rotation Angle of Body-Wing-Tail Combination on Center of Pressure Position. ———) calculation; experiment:

$M_\infty=1.9$; C $-(\delta_e)_{wg}=0°$; □ $-(\delta_e)_{wg}=4°$; $M_\infty=2.0$; ○ $-(\delta_e)_{wg}=0°$; ◌ $-(\delta_e)_{wg}=4.9°$

In the attack-angle range studied, we observe good agreement between theory and experiment for the rectangular-wing combination and less satisfactory agreement for the model with the delta wing; this is explained by the inadequacy of the single-wing-vortex scheme adopted for this model.

§XV-4. DAMPING MOMENT OF VEHICLE DUE TO MOTION OF FUEL AND COMBUSTION PRODUCTS

As a result of rotation of the vehicle about its center of mass, the moving fuel (or fuel-combustion products) create centrifugal and Coriolis forces, and this gives rise to a damping moment. Research has shown that centrifugal forces are negligibly small by comparison with the Coriolis forces. For the vehicle whose scheme is shown in Fig. XV-4-1, the lateral force R_z and the damping moment $M_{y\,d}$ produced by rotation about the center of mass (oy-axis) can be determined by the respective formulas

/676

$$R_z = 2\Omega_y \dot{m}\left[x_a - \frac{1}{2}(x_1 + x_0)\right]; \qquad \text{(XV-4-1)}$$

$$M_{y\,d} = \Omega_y \dot{m}\left\{\left[x_a^2 - \frac{1}{3}(x_1^2 + x_1 x_0 + x_0^2)\right] + \left[z_a^2 - \frac{1}{3}(z_1^2 + z_1 z_0 + z_0^2)\right]\right\}, \qquad \text{(XV-4-2)}$$

where $\dot{m}$ is the mass of fuel consumed by the powerplant per second; x_a, x_1, x_0, z_a, z_1, z_0 are the coordinates identified in Fig. XV-4-1.

Formulas (XV-4-1) and (XV-4-2) should be applied for uniform rotation (Ω_y = const). These formulas were derived on the assumption that rotation of the vehicle about the ox- and oz-axes has no effect on the damping moment $M_{y\,d}$ and that the fuel or fuel-combustion products move in the direction of the powerplant thrust

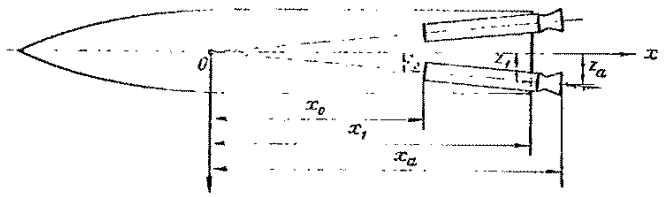

Figure XV-4-1. Diagram Illustrating Calculation of Damping Moment Due to Motion of Fuel or Combustion Products Relative to Vehicle.

vector. The combustion process for which the calculation is made corresponds to that of solid-fuel grains having central channels and burning from both ends.

§XV-5. DESIGN OF ROLLERONS

The design of rollerons (Fig. II-3-4') consists in determining the control-surface geometry, disk dimensions and its angular velocity that will ensure the required longitudinal angular velocity of the vehicle, Ω_{x1}, at an acceptable rolleron deflection angle δ_r, which must be less than critical. The calculation may involve solution of the inverse problem, i.e., calculation of δ_r and Ω_{x1} for specified rolleron parameters and vehicle aerodynamic characteristics. These calculations can be accomplished by solving the following equation system, which describes the disturbed rolling motion of a vehicle fitted with rollerons:

$$J_{x1}\ddot{\gamma} = M_{x1} + M_{x1d} + M_d; \qquad \text{(XV-5-1)}$$

$$J_{rz1}\ddot{\delta}_r = M_g + M_h, \qquad \text{(XV-5-2)}$$

where J_{x1} and J_{rz1} are the respective moments of inertia of the vehicle about the x_1-axis and the rolleron about the z_1-axis; γ and δ_r are the roll and rolleron-rotation angles, respectively; M_{x1} is the rolling moment created by the rollerons; $M_{x\,d}$ is the roll damping moment; M_d is the disturbing rolling moment; M_g is the gyroscopic moment; M_h is the rolleron hinge moment. /677

Equation (XV-5-1) describes the rotary motion of the vehicle about the x_1-axis, and (XV-5-2) the rotation of the rolleron about its axis without consideration of its weight and bearing friction. In these equations, the moments are replaced by the

expressions

$$M_{x1} = nq_\infty S_r r_r c_y^\delta \delta_r; \qquad \text{(XV-5-3)}$$

$$M_{x1d} = q_\infty S_{wg} \frac{l^2}{2V_\infty} m_x^{\omega_x} \Omega_{x1}; \qquad \text{(XV-5-4)}$$

$$M_g = \Omega_{y1} \Omega_{x1} J_{r\,y1}; \qquad \text{(XV-5-5)}$$

$$M_h = q_r S_r b_{MAC\,r} m_h^\delta \delta_r, \qquad \text{(XV-5-6)}$$

where $\underline{n}$ is the number of rollerons; S_r is the plan area of a rolleron; r_r is the distance from the x_1-axis to the rolleron center of pressure; c_y^δ is the static derivative of the rolleron lift coefficient with respect to its rotation angle; $m_x^{\omega_x}$ is the rotational derivative of the roll damping moment coefficient with respect to the dimensionless roll angular velocity

$$\omega_x = \frac{\Omega_{x1} l}{2V_\infty}; \quad (\Omega_{x1} = \dot{\gamma});$$

$J_{r\,y1}$ is the moment of inertia of the rolleron disk, in rotation at angular velocity Ω_{y1}, with respect to the y_1-axis (Fig. II-3-4'); $b_{MAC\ r}$ is the mean aerodynamic chord of the rolleron; m_h^δ is the static derivative of the rolleron hinge moment coefficient with respect to its turn angle.

The velocity heads $\underline{q}$ and q_∞ are calculated for the disturbed flow in front of the rollerons and for the free stream, respectively. The disturbing moment M_d is assigned as a time function $M_d(t)$.

After this substitution, our equation system becomes

$$\ddot{\gamma} + A\dot{\gamma} + B\delta_r = \frac{1}{J_{x1}} M_d(t); \qquad \text{(XV-5-7)}$$

$$\ddot{\delta}_r + D\delta_r + E\dot{\gamma} = 0, \qquad \text{(XV-5-8)}$$

where

$$\left.\begin{aligned} A &= -\frac{q_\infty S_{wg} l^2 m_x^{\omega_x}}{2V_\infty J_{x1}}; \quad & B &= -\frac{nq_\infty S_r r_r c_y^\delta}{J_{x1}}; \\ E &= -\frac{J_{r\,y1}}{J_{r\,x1}} \Omega_{y1}; \quad & D &= -\frac{q_\infty S_r b_{MAC\,r} m_h^\delta}{J_{r\,x1}}. \end{aligned}\right\} \qquad \text{(XV-5-9)}$$

In first approximation, the values of A, B, E, and D can be found from calculated data on the translational trajectory of the vehicle center of mass without considering roll. Solution of Eqs. (XV-5-7) and (XV-5-8) is simplified substantially if we assume $\ddot{\gamma} = 0$, which is possible for many vehicle classes. For this case,

$$\ddot{\delta}_r + \left(D - \frac{E}{A}B\right)\delta_r = -\frac{1}{J_{x1}}M_d(t); \qquad \text{(XV-5-10)}$$

$$\dot{\gamma} = \Omega_{x1} = \frac{1}{A}\left[\int\frac{1}{J_{x1}}M_d(t) - B\delta_r\right]. \qquad \text{(XV-5-11)}$$

We assume the parameters A, B, E, and D to be independent of time and equal to their average values on a certain length of the trajectory, and that the moment M_d = const. In this case, we obtain the solution of (XV-5-10) in the following form /678

$$\delta_r = C\sin(kt + \varphi) + F\frac{1}{k^2}(1 - \cos kt), \qquad \text{(XV-5-12)}$$

where

$$k^2 = D - \frac{E}{A}B; \quad F = -E(J_{x1}AM_d)^{-1} = \text{const}.$$

The constants of integration C and ϕ are determined from the initial data for δ_r and $\dot{\delta}_r$.

For steady rotation of the rolleron ($\ddot{\delta}_r = 0$)

$$\delta_r = -\frac{EM_d}{J_{x1}A}\left(D - \frac{E}{A}B\right)^{-1}. \qquad \text{(XV-5-13)}$$

The roll angular velocity $\dot{\gamma} = \Omega_{x1}$ is calculated directly from (XV-5-11).

Example. Calculate δ_r and $\dot{\gamma} = \Omega_{x1}$ from the following data: $M_\infty = 1.8 (V_\infty = 540$ m/s); $q_\infty = 1.3 \cdot 10^4$ kg/m^2;

$$S_{wg} = 0.187 \text{ m}^2; \; l = 0.48 \text{ m}; \; \Omega_{y1} = 2090 \text{ s}^{-1}; \; m_x^{\omega_x} = -0.19;$$
$$J_{r\,y1} = 0.2 \cdot 10^{-3} \text{ kgf-s}^2\text{-m}; \quad J_{x1} = 0.025 \text{ kgf-s}^2\text{-m};$$
$$J_r = 0.18 \cdot 10^{-3} \text{ kgf-s}^2\text{-m}; \quad M_d = 10 \text{ kgf-m}.$$

Four rectangular rollerons (n = 4) are placed on the trailing edges of a cruciform tail behind a wing, and have the dimensions

$$b_r = 0.068 \text{ m};\quad l_r = 0.064 \text{ m};\quad r_r = 0.15 \text{ m};\quad S_r = b_r l_r = 4.35 \cdot 10^{-3} \text{ m}^2.$$

Let us assume that the velocity head forward of the rolleron $q = 0.85 q_\infty$ and, consequently, $M^2 \approx 0.85\, M_\infty^2$. Without consideration of the rolleron tip effect, the derivative

$$c_y^\delta = \frac{4}{\sqrt{M^2-1}} = \frac{4}{\sqrt{1.8^2 \cdot 0.85 - 1}} = 3.02.$$

From the formula

$$m_h^{\delta_r} = -c_y^\delta \frac{h}{b_r},$$

where h is the distance from the rolleron center of pressure to the axis of rotation and is equal to $b_r/2$, we determine

$$m_h^\delta = -\frac{1}{2} c_y^\delta = -1.51.$$

We then calculate

$$A = \frac{1.3 \cdot 10^4 \cdot 0.187 \cdot 0.48^2 \cdot 0.19}{2 \cdot 540 \cdot 0.025} = 3.93;$$

$$B = -\frac{4.13 \cdot 10^4 \cdot 0.85 \cdot 4.35 \cdot 10^{-3} \cdot 0.15 \cdot 3.02}{0.025} = -3480;$$

$$E = \frac{0.2 \cdot 10^{-3}}{0.18 \cdot 10^{-3}} 2090 = -2320;$$

$$D = \frac{1.3 \cdot 10^4 \cdot 0.85 \cdot 4.35 \cdot 10^{-3} \cdot 0.068 \cdot 1.51}{0.18 \cdot 10^{-3}} = 27\,400.$$

From Formula (XV-5-13), we determine

$$\delta_r = \frac{2320 \cdot 10}{0.025 \cdot 3.93} \left(27400 - \frac{2320 \cdot 3480}{3.93}\right)^{-1} = -0.116 \text{ rad } (-6.66^\circ),$$

and find from (XV-5-11)

$$\dot{\gamma} = \omega_{x1} = \left(\frac{10}{0.025} + 3480 \cdot 0.116\right) / 3.93 = 204 \text{ s}^{-1}.$$

§XV-6. FRONTAL DRAG

Drag at Zero Lift

The total drag of a vehicle is determined by the sum of the drags of its individual elements, calculated with consideration of interference. At subsonic and moderate supersonic speeds ($M_\infty < 5$), the total drag can be resolved into a drag that does not depend on lift and is equal to the drag of the vehicle at $c_y = 0$ and an induced drag that does depend on lift. The drag at $c_y = 0$ can be written

$$X_0 = X_b + X_{wg} + X_{tl} + \Delta X_{b(wg)} + \Delta X_{b(tl)} + \Delta X_{wg(b)} + \Delta X_{tl(b)} + \Delta X_{tl(wg)}, \quad \text{(XV-6-1)}$$

where the first three terms represent the drags of the isolated body, wings, and tail, while the sum of the remaining terms yields a correction for interference. In each term, the subscript in parentheses indicates the design element as a result of interference with which the additional body, wing, or tail drag appears. For example, $\Delta X_{b(wg)}$ represents the additional body drag due to interference with the wing, $\Delta X_{b(tl)}$ the body drag due to interference with the tail, and so forth.

Drag can be determined in the first approximation without considerating interference, as the sum of the drags of the body, wing, and tail in isolation:

$$X_0 = X_b + X_{wg} + X_{tl}. \quad \text{(XV-6-2)}$$

Isolating from each component the drag due to vacuum in the wake of the body, we write

$$X_0 = X'_b + X'_{wg} + X'_{tl} + X_{b.wke} + X_{wg.wke} + X_{tl.wke}, \quad \text{(XV-6-3)}$$

where the first three quantities represent the drags due to pressure and friction for the body, wing, and tail, and the second three the corresponding wake-drag components.

Body. The total drag of the body is determined with consideration of its shape, which may differ in the general case from that of a solid of revolution. If this difference is small, the body is regarded as a solid of revolution whose radius is distributed along the longitudinal x-axis in accordance with the law

$$r(x) = \sqrt{\frac{1}{\pi} S(x)}, \qquad \text{(XV-6-4)}$$

where S(x) is the cross-sectional area of the assigned body shape.

Study shows that the lift and moment characteristics of such a solid of revolution remain the same as for the assigned body shape. The drag difference is found to be more substantial and must be taken into account. The shape of the body may deviate from the solid of revolution owing to various types of "superstructures", e.g., fairings, antenna installations, etc.

The aerodynamic drag of the body depends on the positions of superstructures. Research has shown that drag is lowest when the superstructures are centered on the body. If they are shifted forward, drag rises owing to the increased pressure on the nose section, and when they are shifted aft it increases because of flow detachment and increased vacuum behind the base.

Wings and tail. To calculate the drag of the isolated wings and tail, they can be regarded in their simplest form as the combined cantilevers. The corresponding wing (tail) has the same area but a shorter span. At the same time, the isolated wing can be formed from cantilevers that project outside the body and fictitious sections inside the body. The span of this wing remains the same, but its area is increased. The value of X_{wg} (or X_{tl}) taken into account by Formula (XV-6-2) is equal to the wing (tail) drag less the drag on the fictitious central part of the area occupied by the body. In either case, determination of the drag is approximate. It must be improved experimentally or by a more rigorous theoretical calculation. Remembering that the vertical and horizontal cantilevers of the tail need not be the same, it is advisable to make separate drag calculations, determining the components $X_{v.t}$ and $X_{h.t}$. Accordingly, (XV-6-2) can be written

/680

$$X_0 = X_b + X_{wg} + X_{v.t} + X_{h.t}. \qquad \text{(XV-6-5)}$$

Denoting the characteristic area of the entire vehicle by S, we obtain an expression for the over-all frontal-drag coefficient:

$$c_{x0} = c_{xb}\frac{S_{mid}}{S} + c_{xwg}\frac{S_{wg}}{S} + c_{xv.t}\frac{S_{v.t}}{S} + c_{xh.t}\frac{S_{h.t}}{S}, \qquad \text{(XV-6-6)}$$

where S_{mid}, S_{wg}, $S_{v.t}$, and $S_{h.t}$ are the respective areas of the body midships section, the wing plan area, and the areas of the vertical and horizontal tail cantilevers.

The values of S_{wg}, $S_{v.t}$, and $S_{h.t}$ are found without consideration of the in-body areas of the wing and tail, and $c_{x\ b}$, $c_{x\ wg}$, $c_{x\ v.t}$, and $c_{x\ h.t}$ are the drag coefficients of the body, wing, and vertical and horizontal tail cantilevers, calculated from the respective characteristic parameters S_{mid}, S_{wg}, $S_{v.t}$, and $S_{h.t}$.

Without consideration of interference with the body, the wing drag coefficient is

$$c_{x\,wg} = (c_{x\,wg})_{is}\left(1 - \frac{\Delta S}{S'_{wg}}\right), \qquad \text{(XV-6-7)}$$

where S'_{wg} is the wing area counting the part inside the body; ΔS is the wing area inside the body; $(c_{x\ wg})_{is}$ is the drag coefficient of the isolated wing with consideration of the area inside the body.

The effect of interference on drag can be taken into account by introducing a correction into (XV-6-7) in the form

$$c_{x\,wg} = (c_{x\,wg})_{is}\left(1 - k_{int}\frac{\Delta S}{S'_{wg}}\right), \qquad \text{(XV-6-8)}$$

where k_{int} is an interference coefficient that varies over a broad range depending on the position of the wing on the body and the way in which they are joined, as well as on wing shape and aspect ratio. When wings with small sweep and aspect ratio ($\lambda_{wg} > 2$) are properly attached to the body, k_{int} differs little from one. In the presence of positive interference, which reduces drag, $k_{int} > 1$.

The drags of the horizontal and vertical tails at $c_y = 0$ are calculated in the same way as wing drag.

Total drag. Experimental studies indicate that the effect of interference on total vehicle drag is usually small and can be taken into account by applying a resultant correcting interference coefficient k_r to the drag X_0. Accordingly, the total drag /681

$$X_t = X_0 k_r. \qquad \text{(XV-6-9)}$$

Depending on conditions (flight speed, vehicle design, etc.), the coefficient k_r may be larger or smaller than unity; in most of the cases that are of practical interest, it differs little from one.

Approximate calculation of total drag at $c_y = 0$. In practical cases, it may be assumed for calculation of total drag that friction drag is independent of interference. Then it is necessary to consider only the change in pressure drag that results from reciprocal effects between the wings and body. This change is negligibly small if the wings are mounted on a cylindrical body surface.

When the wings are on a tapering or expanding section of the body, it is advisable to take interference drag into account. $X_{wg(b)}$ can be found in approximation by assuming that the cantilevers are situated in the pressure field of the isolated body, and $X_{b(wg)}$ can be determined on the assumption that the body is in the pressure field of the isolated wing, which is calculated by supersonic wing theory.

Practical interest also attaches to calculation of drag with consideration of interference by the equivalent-body method [51]. This method is based on the following rule: the drag of a body-wing combination is equal to the drag of an isolated body with the same cross-sectional-area distribution as the body-wing combination. This isolated body is known as the equivalent body. The above rule is known in aerodynamics as the rule of areas.

Construction of the equivalent body is the crucial point in this method. For this purpose, the body-wing combination is cut by transverse planes perpendicular to the longitudinal axis and the area is measured in a chosen section through the combination. This area is regarded as that of the equivalent body, whose external form differs from that of the original body in that, it becomes convex beginning at the section passing through the wing leading edges. If the wing trailing edges lie forward of the body's base section, the equivalent body will be the same as the original on the stern section behind the wings.

If the equivalent body is known, the drag of the body-wing combination can be determined by two methods. First, we can use Formula (IV-4-30). The expressions for the second derivatives $S''(x)$ and $S''(\varepsilon)$ in the integrands of these formulas are determined for the equivalent body. Secondly, if the experimentally determined drag of the equivalent body is known, it can be used to determine the drag of the given body-wing combination. In this case, it is necessary to proceed as follows. A curve of $\Delta c_x^e = f(M_\infty)$, where $\Delta c_x^e = c_x^e - c_{x0}^e$ is equal to the difference

between the drag c_x^e at a given M_∞ and the constant drag c_{x0}^e at subsonic speed, is constructed from the experimental data. Assuming further that the drag c_{x0}^c is known for the given body-wing combination, we can calculate its total drag with consideration of interference: $c_x^c = c_{x0}^c = \Delta c_x^e$.

The above method is applicable in the supersonic speed range only for very slender configurations that lie near the axis of the Mach cone and, consequently, have swept small-aspect-ratio wings. The method can also be used for unswept wings if $M_\infty \leq 1$. /682

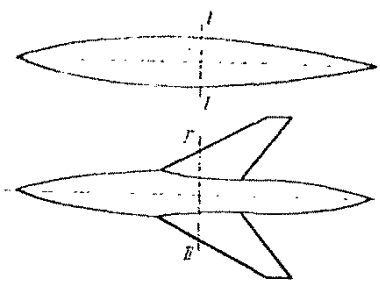

Figure XV-6-1. Construction of Optimum Shape of Body-Wing Combination. Top: solid of revolution with minimum drag; bottom: corresponding optimum shape of body-wing combination. The areas of sections I-I and II-II are equal.

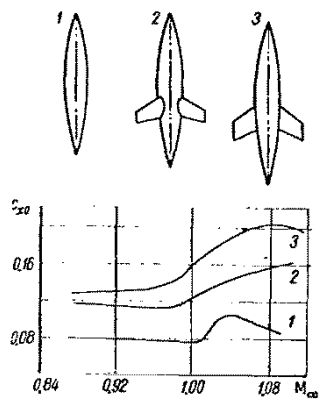

Figure XV-6-2. Drag of Vehicle Constructed by "Area Rule": 1) minimum-drag body; 2) body-wing combination designed by "area rule"; 3) same combination with "area rule" not observed.

Experimental studies have shown that the area rule can be used to obtain a vehicle layout that will deliver minimum drag in the transonic speed range. In accordance with this rule, the vehicle should be designed in such a way that the areas of its cross sections perpendicular to the flow will vary along the vehicle's axis in the same way as for the minimum-drag solid of revolution (Fig. XV-6-1).

Figure XV-6-2 shows an experimental curve of the drag coefficient as a function of M_∞ at $c_y = 0$; it shows that the body-wing combination designed by the area rule has lower drag than the combination constructed without consideration of this rule.

The equivalent-body method can produce satisfactory results for the transonic M_∞ range and, consequently, is limited for a given combination to a certain maximum $M_\infty > 1$.

Supersonic area rule [51]. If M_∞ exceeds the limiting M_∞ and the equivalent-body method cannot be used, the supersonic area rule can be applied for the drag calculation. When this rule is used, we determine the areas of cross sections cut through the given combination by planes that are not perpendicular to the longitudinal axis (as in the equivalent-body method), but are inclined and tangent to the Mach cone (Fig. XV-6-3) with the equation

$$x + \alpha' (z \sin \gamma + y \cos \gamma) = x_0. \qquad \text{(XV-6-10)}$$

The area $S(x_0, \gamma)$ that this plane cuts off the body-wing combination is a function of the meridional angle γ and the coordinate x_0 of the origin of the Mach cone (Fig. XV-6-3). The projection of this area onto the plane normal to the x-axis can be calculated from $S(x_0, \gamma)$:

$$S_n (x_0, \gamma) = \sin \mu S (x_0, \gamma), \qquad \text{(XV-6-11)}$$

where $\sin \mu = 1/M_\infty$.

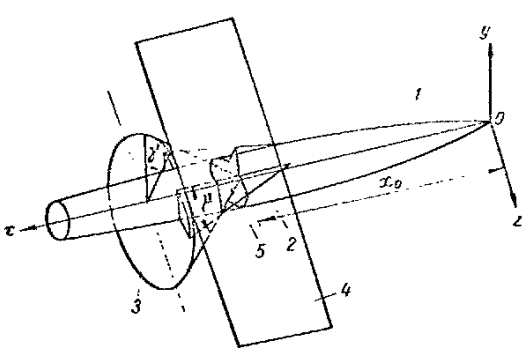

Figure XV-6-3. Supersonic "Area Rule": 1) body; 2) wings; 3) Mach cone with angle μ = arc sin $(1/M_\infty)$; 4) secant plane inclined at angle γ ; 5) sectional area determined by supersonic "area rule."

Formula (IV-4-30) can be used to calculate drag after substituting $S''(x,\gamma)$. For a fixed angle γ, these formulas will yield $c_x^e = dc_x/d\gamma$ for the given combination, which is equal to the equivalent-body drag coefficient. To obtain the drag coefficient c_x of the entire combination, the drags of the equivalent bodies are averaged over the angle γ: /683

$$c_x = \frac{2}{\pi} \int_0^{\pi} c_x^e d\gamma. \qquad \text{(XV-6-12)}$$

Drag at $c_y \neq 0$

The total drag X of the vehicle for $c_y \neq 0$ can be represented as the sum of the drag X_0 at zero lift, the induced drag X_i of the wings and tail, and the drag ΔX_α, which includes certain unaccounted drags (increase in drag due to pressure on the body at $\alpha \neq 0$, drag increase due to flow separation on the wing, tail, and body, etc.). Thus,

$$X = X_0 + X_i + \Delta X_\alpha. \tag{XV-6-13}$$

According to this formula, the expression for the total drag coefficient will be written

$$c_x = c_{x0} + c_{xi} + \Delta c_{x\alpha}, \tag{XV-6-13'}$$

where the induced drag coefficient c_{xi} can be regarded as the sum of the induced drags of the wing $(c_{xi})_{wg}$ and tail $(c_{xi})_{h.t}$, which are respectively equal to

$$(c_{xi})_{wg} = (\bar{c}_{xi})_{wg} \frac{S_{wg}}{S_{mid}}; \quad (c_{xi})_{h.t} = (\bar{c}_{xi})_{h.t} \frac{S_{h.t}}{S_{mid}}. \tag{XV-6-14}$$

Here, S_{wg} and $S_{h.t}$ are the areas of the isolated wing and tail, including the areas occupied by the body. The coefficient $\Delta c_{x\alpha}$ in (XV-6-13') is calculated by the formula $\Delta c_{x\alpha} = \Delta X_\alpha / q_\infty S_{mid}$, and the force ΔX_α can be regarded as the sum of three terms. The first is the added body drag at the appearance of an angle of attack, and the second and third terms are respectively equal to the unaccounted wing or tail drag. Thus, the over-all drag coefficient is

$$c_x = c_{x0} + (c_{xi})_{wg} \frac{S_{wg}}{S_{mid}} + (\bar{c}_{xi})_{h.t} \frac{S_{h.t}}{S_{mid}} + \Delta c_{x\alpha}. \tag{XV-6-15}$$

At subsonic speeds, the induced drag coefficients of the wing and tail can be calculated by the respective formulas

$$(\bar{c}_{xi})_{wg} = \frac{(c_y^a)_{wg}}{\pi (\lambda_{ef})_{wg}}; \quad (\bar{c}_{xi})_{h.t} = \frac{(c_y^a)_{h.t}}{\pi (\lambda_{ef})_{h.t}}, \tag{XV-6-16}$$

where the lift coefficients are found for the isolated wings and tail from the actual spans of the cantilevers. Interference has been taken into account by introducing the empirical coefficients $(\lambda_{ef})_{wg}$ and $(\lambda_{ef})_{h.t}$, which are effective aspect ratios calculated by the formulas /684

$$(\lambda_{ef})_{wg} = \lambda_{wg}\left(1 + \frac{S_i}{S}\right)_{wg}^{-1}; \quad (\lambda_{ef})_{h.t} = \lambda_{h.t}\left(1 + \frac{S_i}{S}\right)_{h.t}^{-1}, \qquad \text{(XV-6-17)}$$

where λ_{wg} and $\lambda_{h.t}$ are the aspect ratios of the isolated wings and tail and $(S_i)_{wg}$ and $(S_i)_{h.t}$ are the wing and tail areas inside the body.

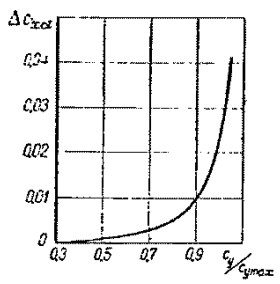

Figure XV-6-4. Drag Correction for Large Angles of Attack.

Tail induced drag is not calculated in practice, and its value for the entire vehicle is set equal to $c_{xi} = (c_{xi})_{wg}$. The lift coefficient from which c_{xi} is calculated may be that of the vehicle as a whole, i.e., it may be assumed that $(c_y)_{wg} = c_y$. Then the overall drag coefficient will be

$$c_x = c_{x0} + \frac{c_y^2}{\pi\lambda_{ef}} + \Delta c_{x\alpha}, \qquad \text{(XV-6-18)}$$

where $\lambda_{ef} = (\lambda_{ef})_{wg}$.

The correction $\Delta c_{x\alpha}$ can be determined experimentally. Figure XV-6-4 shows experimental data [23] for $\Delta c_{x\alpha}$ as a function of the ratio $c_y/c_{y\ max}$. It may be assumed in using the diagram that $c_y/c_{y\ max}$ is practically the same for the vehicle as for the wing.

Formula (XV-6-18) gives the frontal drag coefficient as a function of lift coefficient. In graphical form, this dependence is a polar of the vehicle; a family of these curves can be constructed by assigning various M_∞.

In those cases of supersonic speed in which there are no suction forces, the coefficients of the wing and tail drags that depend on lift will be

$$(c_{xi})_{wg} = (c_y)_{wg}\alpha_{wg}; \quad (c_{xi})_{h.t} = (c_y)_{h.t}\alpha_{h.t} \qquad \text{(XV-6-19)}$$

or

$$(c_{xi})_{wg} = \frac{(c_y^2)_{wg}}{(c_y^\alpha)_{wg}}; \quad (c_{xi})_{h.t} = \frac{(c_y^2)_{h.t}}{(c_y^\alpha)_{h.t}}. \qquad \text{(XV-6-19')}$$

Suction forces that appear on subsonic leading edges lower induced drag. In practice, however, it is not possible to produce suction forces on thin wings. Accordingly, Formulas (XV-6-19) can also be used for subsonic leading edges on swept wings.

The attack angles α_{wg} and $\alpha_{h.t}$ include the body attack angle α and the wing and tail setting angles δ_{wg} and $\delta_{h.t}$. The values of $(c_y)_{wg}$ and $(c_y)_{h.t}$ are determined with consideration of interference with the body; in addition, the coefficient $(c_y)_{h.t}$ must be calculated with consideration of the wing effect.

The quantity $\Delta c_{x\alpha}$ can be assumed equal to the added body drag on the appearance of an attack angle. At small angles of attack, it is calculated by the formula

$$\Delta c_{x\alpha} = \alpha c_{y\,h} \qquad \text{(XV-6-20)}$$

in which the lift (or normal-force) coefficient can be calculated considering the interference with the wing and tail. The following method of calculating total drag can be used as an alternative. The attack-angle component of the drag coefficient for the entire vehicle is assumed equal to /685

$$c_{xi} \quad c_y(\alpha \quad \alpha_0) \text{ or } c_{xi} \quad \frac{c_y^2}{c_y^\alpha}. \qquad \text{(XV-6-21)}$$

The subject here is an unsymmetrical vehicle layout in which lift is zero at a certain body angle of attack $\alpha = \alpha_0$. For small α, the lift coefficient c_y can be assumed equal to its value for the wing with a certain approximation. To improve the accuracy of the calculations, it is advisable to calculate the coefficient c_y with consideration of the body and tail effects. Applying (XV-6-21), we can write the equation for the polar curve in the form

$$c_x = c_x^0 + \frac{c_y^2}{c_y^\alpha}, \qquad \text{(XV-6-22)}$$

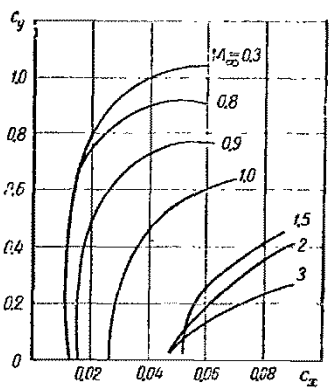

Figure XV-6-5. Polars of Vehicle.

where c_x^0 corresponds to zero lift.

A family of polar curves is shown in Fig. XV-6-5 by way of illustration. Use of small-aspect-ratio swept wings makes it possible to lower c_x^0 in the range of M_∞ = 1-3. However, this is detrimental to the lifting properties of the vehicle, i.e., c_y^α becomes smaller and the total drag of the vehicle increases as a result. For large c_y, the c_{xi} of a vehicle with small-aspect-ratio swept wings increases to such a degree that their advantage — the smaller c_x^0 — is lost, since total drag increases.

This recommendation for calculation of polar curves for the vehicle applies when the total drag can be resolved into c_x^0 and the lift-dependent drag. Such resolution is impossible for large M_∞ > > 5, and it is necessary to find the drag coefficient separately for each attack angle, using the recommendations given above for wings and bodies.

Lift/Drag Ratio

The lift/drag ratio is

$$K = \frac{c_y}{c_x}.$$

Substituting Expression (XV-6-13') for c_x in this formula and disregarding $\Delta c_{x\alpha}$, we obtain

$$K = \frac{c_y}{c_x^0 + Ac_y^2}, \qquad \text{(XV-6-23)}$$

where $A = 1/(\pi\lambda_{ef})$ for subsonic and $A = 1/c_y^\alpha$ for supersonic speeds.

An important characteristic of a vehicle is its maximum lift/drag ratio. At subsonic speeds, it is

$$K_{max} = \frac{1}{2}\sqrt{\frac{\pi\lambda_{ef}}{c_x^0}}. \qquad \text{(XV-6-24)}$$

The optimum lift coefficient, which corresponds to this value, is /686

$$c_{y\ optm} = \sqrt{\pi \lambda_{ef} c_x^0}. \qquad \text{(XV-6-25)}$$

At supersonic speeds,

$$K_{max} = \frac{1}{2}\sqrt{\frac{c_y^\alpha}{c_x^0}}, \qquad \text{(XV-6-26)}$$

$$c_{y\ optm} = \sqrt{c_y^\alpha c_x^0}. \qquad \text{(XV-6-27)}$$

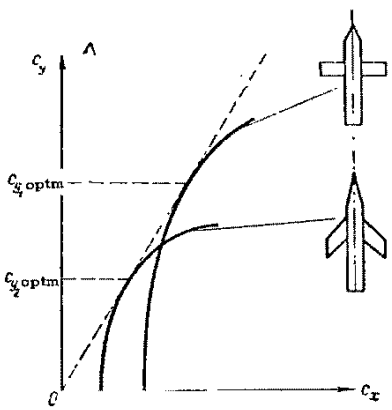

Figure XV-6-6. Polar Curves of Vehicles.

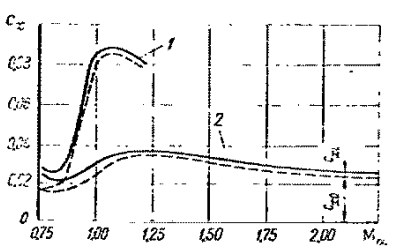

Figure XV-6-7. Variation of Drag for Two Aircraft Types. 1) subsonic airplane; 2) supersonic airplane.

Use of swept wings and wings of small aspect ratio lowers $c_{y\ optm}$ since c_x^0 and c_y^α diminish with diminishing aspect ratio and increasing sweep angle. Figure XV-6-6 shows the manner in which $c_{y\ otpm}$ varies with wing sweep.

The aerodynamic layout of a vehicle must provide for increased lift/drag ratios. The first step toward this objective is to choose thin enough profiles with small curvatures, so that drag will be low. As regards planform, the delta wing is optimal from the standpoint of increasing lift/drag ratio. Secondly, we can vary the sweep angle and aspect ratio of the wing. A lower c_x^0 can be obtained by increasing the angle χ in the M_∞ range corresponding to a subsonic leading edge and by reducing the aspect ratio. The χ of modern aircraft range up to 70° [23], and their aspect ratios λ_{wg} range downward from 2. It must be remembered, however, that increasing sweep and reducing aspect ratio are detrimental to the lifting properties of the wing, i.e., they lower c_y^α. In aerodynamic design

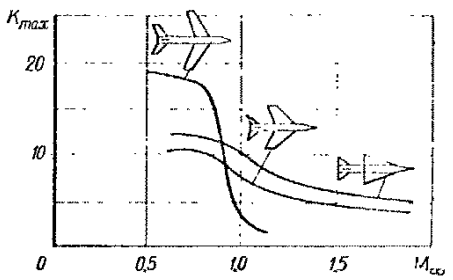

Figure XV-6-8. Maximum Vehicle Lift/Drag Ratios.

work, it is necessary to determine the optimum aspect ratio and sweep at which the largest lift/drag ratio will be obtained. This conclusion pertains basically to transonic M_∞. For larger $M_\infty > 3$ the wing planform has practically no influence on lift/drag ratio, and profile thickness is the deciding factor.

Thirdly and lastly, the shape of the body must be chosen properly and matched to the wing and tail in order to obtain maximum lift/drag ratio. The body shape chosen is that of the isolated body with minimum drag at the given M_∞ or, at least, one that approaches this optimum.

In laying out all elements of the vehicle, and the wing and body in particular, an effort must be made to obtain positive interference, which lowers drag. Figure XV-6-7 shows that the /687
aerodynamic layout of the modern supersonic airplane (quite thin swept wing of small aspect ratio) can lower drag substantially, especially under the conditions of transonic flights, and this also raises the lift/drag ratio. Irrespective of layout, however, the maximum lift/drag ratio K_{max} is always considerably smaller at supersonic speeds than in the subsonic range (Fig. XV-6-8).

Vehicles whose wings have small sweep angles and large aspect ratios have the largest lift/drag ratios at subsonic speeds. As flight speed approaches that of sound, their lift/drag ratios drop off sharply. Those of vehicles with trapezoidal and delta wings vary much less as functions of M_∞. Here the delta wing with small thickness ratio on a "tailless" vehicle offers a certain increase in lift/drag ratio owing to its strong sweep and small aspect ratio.

Chapter XVI /688

AERODYNAMICS OF CONTROLS

§XVI-1. FORCES CREATED BY AERODYNAMIC CONTROLS

Spoilers

Let us examine certain results of wind-tunnel tests on spoilers mounted on the end of a flat plate ([76], 1962, Nos. 4-5).

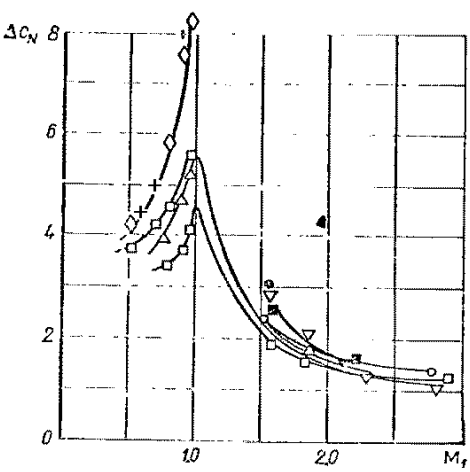

Figure XVI-1-1. Coefficient ΔC_N of Normal Force Created by Terminal Spoiler as a Function of M_1 and Spoiler Dimensions:

Symbol	h, mm	l_s, mm
○ □ △ ◇	2 3 4 6 8	100
● ▼ ■	2 6 8	50

◇ + with side plates

Figure XVI-1-1 presents data for the dimensionless coefficient Δc_N, which is equal to the ratio of the normal force ΔN created by the spoiler to qh (q is the velocity head and h is the height of the spoiler). Figure XVI-1-2 gives experimental data for $\Delta c_N/\Delta c_R$, where $\Delta c_R = \Delta R/qh$ (ΔR is the axial force created by the spoiler). The coefficients Δc_N and Δc_R were calculated for a spoiler 1 cm wide and therefore having an area equal to h.

These data indicate that the force exerted by a spoiler depends on its length l_s and height h and the M_1 forward of the spoiler.

Experiments have shown ([76], 1962, No. 4-5) that Δc_N and Δc_R increase with increasing positive attack angles and, conversely, that Δc_N decreases to some degree with increasing negative attack angles. High-speed motion pictures made during these experiments as the spoiler was deployed at a speed of 7 mm in $5 \cdot 10^{-3}$ s at

M_1 = 2.21 made it possible to establish that the flow pattern around the spoiler corresponds to the flow pattern in steady flow at any point in time. The compression shocks vanished in $2 \cdot 10^{-4}$ s after the spoiler was retracted into the plate. This provides a basis for use of the steady-state hypothesis in calculations for vibrating spoilers. For such spoilers, normal force is determined by the formula /689

$$\Delta N = \Delta c_N q h l_s k, \qquad \text{(XVI-1-1)}$$

where $k = (t_1 - t_2)/(t_1 + t_2)$ is the so-called coefficient of command; t_1 is the time for which the spoiler is in the up position; t_2 is the time for which the spoiler is in the down position.

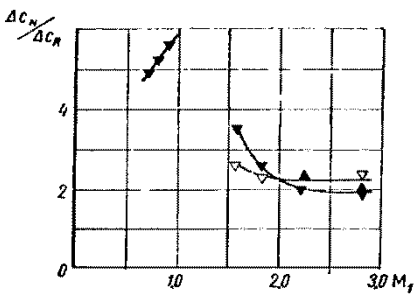

Figure XVI-1-2. Ratio of Coefficients of Normal and Longitudinal Forces Created by Terminal Spoiler as a Function of M_1 and Spoiler Dimensions:

Symbol	h, mm	Remarks
▲	4	with side plates
▽	6	without side plates
▼	6	with side plates

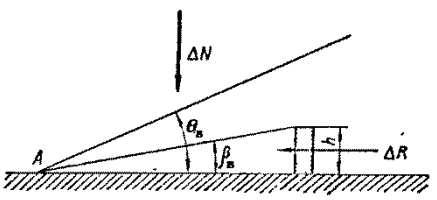

Figure XVI-1-3. Diagram for Spoiler Calculation.

Data from the experiments indicate that the presence of plates set parallel to the flow and preventing flow of air across the lateral edges of the spoiler increases Δc_N ([76], 1962, No. 4-5).

At supersonic velocities of the flow past the spoiler, spoiler height should be set equal to $h > 5\delta$, where δ is the thickness of the boundary layer ahead of the spoiler (Fig. XVI-1-3). The following procedure can be recommended for calculation of spoiler effectiveness.

1. The pressure coefficient in the separation zone behind the compression shock and ahead of the spoiler is calculated from the M_1 of the flow in front of the spoiler and the Re determined for the distance from the wing leading edge to the spoiler. For a laminar boundary layer,

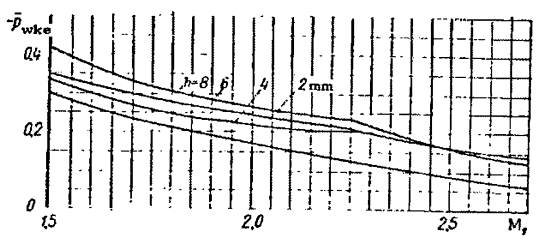

Figure XVI-1-4. Diagram of Wake-Pressure Coefficient Behind a Plate as a Function of M_1 of the Flow Past a Spoiler and the Spoiler Deployment Height h in mm.

$$\bar{p}_2 = \frac{1.69}{Re^{1/4}(M_1^2-1)^{1/4}}, \quad \text{(XVI-1-2)}$$

and for a turbulent layer /690

$$\bar{p}_2 = \frac{2.04}{Re^{0.1}(M_1^2-1)^{1/4}}. \quad \text{(XVI-1-3)}$$

2. Assuming that the boundary of the stagnation zone is straight and passes through the apex of the spoiler, we determine

$$\Delta c_N = \bar{p}_2 / \operatorname{tg}\beta_s. \quad \text{(XVI-1-4)}$$

To calculate the axial force set up by the spoiler, we can refer to the diagram in Fig. XVI-1-4, which presents the results of an experimental study of the wake-pressure coefficients $\bar{p}_{wke}$ behind a spoiler as a function of M_1 and spoiler height h for a case in which there were no lateral plates. Knowing the pressure coefficient behind the spoiler, we can calculate the coefficient of the longitudinal force that it creates:

$$\Delta c_R = \frac{p_2 - p_{wke}}{q} \quad \text{or} \quad \Delta c_R = \bar{p}_2 - \bar{p}_{wke}.$$

Example. Determine the normal and axial forces crated by a terminal spoiler situated at a distance x = 0.140 m from the wing leading edge and in a stream of air moving at M_1 = 1.83. The spoiler height h = 8 mm and its length ℓ_s = 100 mm. The flight is being made at sea level (trajectory altitude H ≈ 0).

The data are used to find the flight speed $V_1 = M_1 a$ = 1.83 × × 340 = 622 m/s and $Re = V_1 x/\nu = 622 \cdot 0.140/1.46 \cdot 10^{-5} = 6 \cdot 10^6$. Assuming the flow conditions in the boundary layer ahead of the spoiler to be turbulent, we find the pressure coefficient in the stagnation zone:

$$\bar{p}_2 = \frac{2.04}{Re^{0.1}(M_1^2-1)^{1/4}} = \frac{2.04}{(6\cdot 10^6)^{0.1}(1.83^2-1)^{1/4}} = 0.346.$$

The pressure ratio

$$p_2/p_1 = 1 + kM_1^2\bar{p}_2/2 = 1 + 1.40 \cdot 1.83^2 \cdot 0.346/2 = 1.81.$$

The shock inclination angle

$$\theta_s = \arcsin \sqrt{(p_2/p_1 + \delta)/[(1 + \delta) M_1^2]} =$$

$$= \arcsin \sqrt{(1.81 + 0.167)/[(1 + 0.167) 1.83^2]} = 45.5°,$$

where $\delta = \frac{k-1}{k+1} = \frac{1.4-1}{1.4+1} = 0.167.$

We then calculate the rotation angle of the flow behind the compression shock:

$$\operatorname{tg}(\theta_s - \beta_s) = (\delta p_2/p_1 + 1)(\delta + p_2/p_1)^{-1} \operatorname{tg}\theta_s =$$

$$= (0.167 \cdot 1.81 + 1)(0.167 + 1.81)^{-1} \operatorname{tg} 45.5° = 0.669;$$

$$\operatorname{tg}\beta_s = 0.2065.$$

The normal-force coefficient

$$\Delta c_N = \bar{p}_2/\operatorname{tg}\beta_s = 0.346/0.2065 = 1.67.$$

Consequently, the normal force

$$\Delta N = \Delta c_N \frac{\rho_1 V_1^2}{2} h l_s = 1.67 \frac{0.125 \cdot 622^2}{2} 8 \cdot 10^{-3} \cdot 0.1 = 32.4 \text{ kgf (318 N)}.$$

From the diagram in Fig. XVI-1-4, we find $\bar{p}_{wke} = -0.3$ for $M_1 = 1.83$ and $h = 8$ mm. Remembering that $p_2 = 0.346$, we determine the coefficient $\Delta c_R = 0.346 + 0.3 = 0.646$ and the force $\Delta R = \Delta c_R q l_s h = 12.5$ kg (123 N).

Increasing Lift of Aerodynamic Controls by Blowing Gas into Boundary Layer /691

By blowing a certain amount of gas into the boundary layer, we can shift the separation point toward the trailing edge of the control and thereby increase the controlling force ([70], 1965, No. 5).

Determination of the required amount of injection gas involves calculation of the gas jet momentum coefficient, which is calculated from the expression

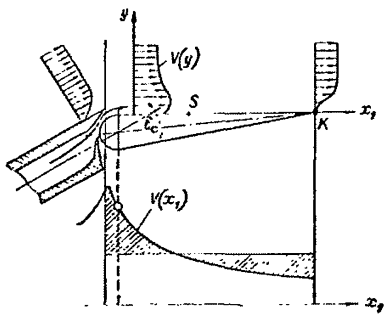

Figure XVI-1-5. Diagram of Velocity Distribution at Surface of Aerodynamic Control when Gas is Injected into Boundary Layer. V(y) is the flow-velocity diagram in a section perpendicular to the control surface and $V(x_1)$ is the velocity variation over the length of the control.

$$c = \frac{2,35\Delta\delta^{**}}{b(1-\bar{V}_\infty/V_j)^2} = \frac{\rho_j V_j^2}{q_\infty}\frac{\Delta}{b}, \qquad \text{(XVI-1-5)}$$

where ρ_j and V_j are the mass density and average velocity of the gas in the jet respectively; Δ is the width of the slot; b is the chord of the control surface.

The parameter $\Delta\delta^{**}$ is the increment of boundary-layer momentum thickness in the absence of injection on the segment from the separation point S to point K on the control's trailing edge (Fig. XVI-1-5). This parameter is calculated by the formula

$$\frac{\Delta\delta^{**}}{b} = \frac{0.037}{\mathrm{Re}^{0.2}}\left(\frac{V_{\delta K}}{V_\infty}\right)^{-3}\times$$

$$\times\left[\int_{\bar{x}_S}^{\bar{x}_K}\left(\frac{V_\delta}{V_\infty}\right)^{3.5} d\left(\frac{x}{b}\right)\right]^{0.8}, \qquad \text{(XVI-1-6)}$$

where $\bar{x}_S = x_S/b$; $\bar{x}_K = x_K/b$; $\mathrm{Re} = V_\infty b/\nu_\infty$; V_δ is the velocity of inviscid nonseparating flow; $V_{\delta K}$ is the velocity at point K.

If an aerodynamic control is placed along a wing trailing edge, the average velocity on the control should be taken in the formulas instead of V_∞. By way of example, let us determine the coefficient of momentum of the gas jet for a case in which the flow velocity along an aileron varies linearly from a certain value $V_{\delta S}$ to $V_{\delta K} = V_{\delta S}/2$, so that the average velocity is

$$V_{av} = (V_{\delta S} + V_{\delta K})/2 = (3/2)V_{\delta K}.$$

The average velocity in the jet is $V_j = 2V_{av} = 3V_{\delta K}$, and $\mathrm{Re} = 10^5$. For these data, (XVI-1-6) gives

$$\frac{\Delta\delta^{**}}{b} = \frac{0.00967}{\mathrm{Re}^{0.2}}\frac{\left[\left(\frac{V_{\delta S}}{V_{\delta K}}\right)^{1.5}-1\right]^{0.8}}{\left(1-\frac{V_{\delta S}}{V_{\delta K}}\right)^{0.8}\left(\frac{V_{\delta S}}{V_{\delta K}}-1\right)^{0.8}} = \frac{(2^{1.5}-1)^{0.8}}{(1.5)^{0.2}(1.2)^{0.6}(2-1)^{0.8}}\,0.00583.$$

The corresponding value of the momentum coefficient is

$$c = 2.35\frac{\Delta\delta^{**}}{b}\left(1-\frac{V_{ev}}{V_j}\right)^{-2} = 2.35\cdot 0.00583\left(1-\frac{1}{2}\right)^{-2} = 0.0548.$$

§XVI-2. CALCULATION OF FORCES DEVELOPED BY GASDYNAMIC CONTROLS /692

Calculation of Thrust of Gasdynamic Controls with Consideration of Losses in Air Intakes

The thrust developed when air is taken from the atmosphere and fuel-combustion products are expelled through a nozzle can be calculated by the formula

$$P = \frac{G_f}{g}w_a + \frac{G_a}{g}(w_a - V_\infty) + (p_a - p_\infty)S_a - \frac{dQ}{dt}, \qquad \text{(XVI-2-1)}$$

where P is the thrust; G_f is the per-second flow rate, by weight, of fuel combustion products; G_a is the per-second flow rate, by weight, of the air taken from the atmosphere; V_∞ is the velocity of the vehicle's center of mass; w_a is the velocity of outflow of fuel-combustion products through the nozzle; p_a is the pressure in the jet at the nozzle exit section; S_a is the exit-section area of the nozzle; Q is the momentum of the air and fuel-combustion products with respect to the vehicle.

The derivative dQ/dt is known as the variational force.

For rocket engines, which do not use atmospheric air, Formula (XVI-2-1) becomes simpler:

$$P = \frac{G_f}{g}w_a + (p_a - p_\infty)S_a - \frac{dQ}{dt} \qquad \text{(XVI-2-2)}$$

When air is taken in, frontal drag is increased by the added air-intake drag ΔX_{ai}, which results from the fact that the pressure p_1 and air velocity w_1 in the entry section of the air intake differ from the corresponding values in the undisturbed free stream, p_∞ and $w_\infty = V_\infty$. This additional drag is

$$\Delta X_{ai} = S_1(p_1 - p_\infty) - \frac{G_a}{g}(V_\infty - w_1). \qquad \text{(XVI-2-3)}$$

Relation (XVI-2-1) defines thrust as it is affected by a stationary atmosphere. However, the presence of air intakes, nozzle assemblies, and the jets of fuel-combustion products issuing from them changes the pattern of air flow around the vehicle. In determining the aerodynamic coefficients, therefore, it is necessary to consider the influence of a compression shock in front of the air intake, forces on the exposed surfaces of the air intakes and nozzles, interference between the air intakes and the wing or body of the vehicle, and, finally, the influence of the jets on the flow of air at the surface of the vehicle.

The frontal drag coefficient of the body nose section of a vehicle or engine pods housing air intakes is determined by the relation

$$c_{x\,\mathrm{nos}} = (c_{x\,\mathrm{nos}})_{\varphi=1} + (\Delta c_{x\,\mathrm{ai}} - c_{s,\mathrm{ai}})\frac{S_1}{S_{\mathrm{mid}}}, \qquad \text{(XVI-2-4)}$$

where $\varphi = G_{\mathrm{a}}/(\rho_\infty g V_\infty S_1)$ is the air flowrate coefficient, which is equal to the ratio of the actual per-second air flow to the maximum possible flow [21]; $(c_{x\,\mathrm{nos}})_{\phi=1}$ is the frontal drag coefficient of the nose section at $\phi = 1$; $\Delta c_{x\,\mathrm{ai}}$ is the coefficient of the air-intake drag increment; $c_{s.\mathrm{ai}}$ is the coefficient of the air-intake suction force; S_1 is the entry-section area of the air intake. /693

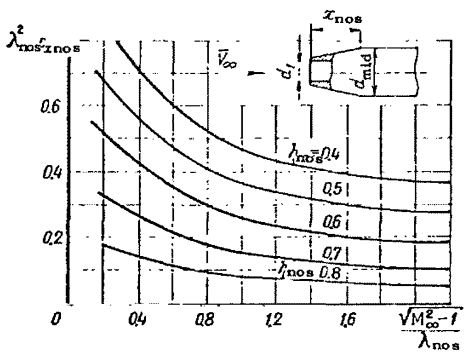

Figure XVI-2-1. Diagram for Determination of Frontal Drag Coefficient of Parabolic Vehicle Nose Section with Throat at $\phi = 1$ ($\lambda_{\mathrm{nos}} = x_{\mathrm{nos}}/d_{\mathrm{mid}}$; $\eta_{\mathrm{nos}} = d_1/d_{\mathrm{mid}}$).

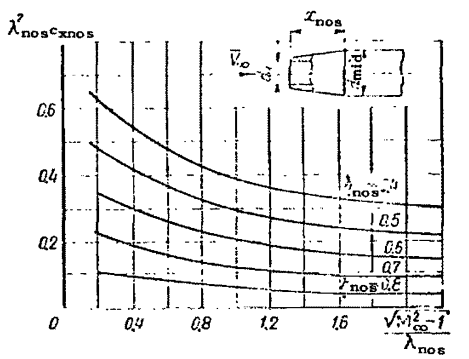

Figure XVI-2-2. Diagram for Determination of Frontal Drag Coefficient of Conical Vehicle Nose Section with Throat at $\phi = 1$.

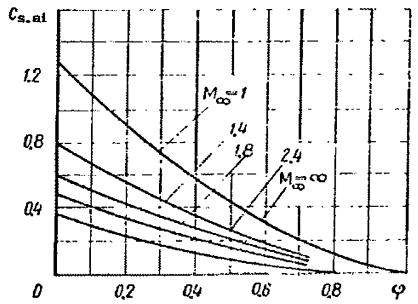

Figure XVI-2-3. Diagram for Determination of Suction-Force Coefficient of Air Intake.

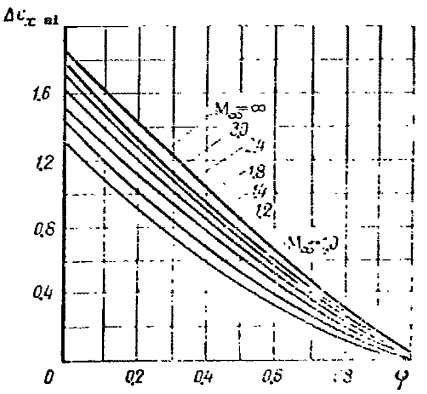

Figure XVI-2-4. Diagram for Determination of Coefficient of Added Air-Intake Drag.

Air intakes without central body. With $\phi = 1$ and supersonic velocities, the coefficient $c_{x\,nos} = (c_{x\,nos})_{\phi=1}$ and can be determined from the curves presented in Figs. XVI-2-1 and XVI-2-2.

For $\phi < 1$ and subsonic speeds, we may assume $c_{x\,nos} \approx (c_{x\,nos})_{\phi=1}$ provided that the outer surface is well enough rounded at the air-intake entry section. This is because the suction force is quite large and equal to the added drag force of the air intake. With $\phi < 1$ and supersonic speeds, calculation of the nose-section drag becomes more complicated, since a detached compression shock forms ahead of the nose. However, $(c_{x\,nos})_{\phi=1}$ can be found approximately from the same Figs. XVI-2-1 and XVI-2-2, and $c_{s.ai}$ can be determined from the diagram shown in Fig. XVI-2-3 [21], which is valid for air intakes that have rounded leading edges when the rim of the nose section is curvilinear. Otherwise, $c_{s.ai}$ will be much smaller than would follow from the diagram. The value of the coefficient Δc_{xai} is determined from the diagram of Fig. XVI-2-4.

/694

Example. Find the frontal drag coefficient of a parabolic vehicle nose section whose air intake has no central body, using the following data:

$$M_\infty = 2;\ a_\infty = 340\ \text{m/s};\quad \rho_\infty = 0.125\ \text{kg-s/m}^4;$$
$$G_a = 141\ \text{kg/s};\quad d_a = 0.56\ \text{m};\ d_{mid} = 0.80\ \text{m};\ \lambda_{nos} = 3.$$

We determine

$$\eta_{nos} = d_a/d_{mid} = 0.56/0.80 = 0.70;\ S_{mid} = \pi d_{mid}^2/4 = \pi \cdot 0.8^2/4 = 0.503\ m^2;\ S_1 = \pi d_a^2/4 = \pi \cdot 0.56^2/4 = 0.246\ m^2;$$
$$\sqrt{M_\infty^2 - 1}/\lambda_{nos} = \sqrt{2^2 - 1}/3 = 0.577;\ V_\infty = M_\infty a_\infty = 2 \cdot 340 = 680\ m/s.$$

We find from the diagram of Fig. XVI-2-1

$$\lambda_{nos}^2 (c_{x\,nos})_{\varphi=1} = 0.22,$$

from which

$$(c_{x\,nos})_{\varphi=1} = 0.22/3^2 = 0.024.$$

The coefficient

$$\varphi = G_a/(\rho_\infty g V_\infty S_1) = 1.44/(0.125 \cdot 9.81 \cdot 680 \cdot 0.246) = 0.70.$$

From the diagram of Fig. XVI-2-3, we find $c_{s.ai} = 0.06$, while Fig. XVI-2-4 gives $\Delta c_{xai} = 0.38$.

According to these data,

$$c_{x\,nos} = (c_{x\,nos})_{\varphi=1} + (\Delta c_{x.\,ai} - c_{s.ai}) \frac{S_1}{S_{mid}} = 0.024 + (0.38 - 0.06) \frac{0.246}{0.503} = 0.18.$$

Air intakes with central body. Use of such air intakes is advantageous at speeds corresponding to $M_\infty > (1.8\text{-}2.0)$. Below we present data for double-shock air intakes. The air flow through such an intake can be calculated from the relationships for conical flows. The results of such calculations are given in Fig. XVI-2-5 in the form of curves of the maximum flowrate coefficient Φ as a function of M, the central-body cone angle β_c, and the projection angle β_{prj} of the body with respect to the air-intake leading edge (Fig. XVI-2-6). The coefficient

$$\Phi = \frac{G_{a\,max}}{\rho_\infty g V_\infty S_1}, \qquad \text{(XVI-2-5)}$$

where $G_{a\,max}$ is the maximum possible per-second flowrate with consideration of deflection of air filaments by the shock system in front of the air intake and $S_1 = \pi d_1^2/4$.

Various positions of the compression shocks are possible, as indicated in Fig. XVI-2-6, depending on ϕ and Φ. It must be remembered here that air intakes are designed for a definite $M_\infty = M_{design}$ (case a in Fig. XVI-2-6).

As M_∞ varies in flight, it is necessary to adjust the air-intake parameters, since otherwise ϕ will be smaller than 1 and an additional drag Δc_{xai} will appear (cases c and d) or high total-pressure losses will be incurred behind the shock system (case b). In case d, which occurs with small "throat" areas (sectional areas at the narrowest point of the intake-air passage), operation of the intake may become unstable owing to periodic displacements of compression shocks along its central body. This phenomenon, which is known as surging, results from separation of the flow from the central body behind the compression shock and from flow pulsation, and causes vibration of the engine, flameout, or perhaps even engine damage. Unstable engine operation may occur in the case $M_\infty > M_{dsgn}$ (case b) or when the throat area is too large. If the air-intake passage expands too abruptly, flow separates from the walls, vortices form, and the flow pulsates. Since these pulsations are at higher frequency than in the case of surging, they produce a "tickling" sensation. This operating condition is also unacceptable.

/695

/696

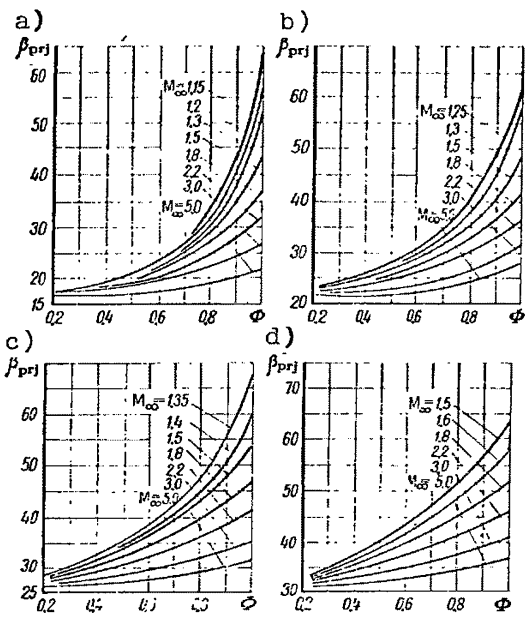

Figure XVI-2-5. Diagram for Determination of Ideal Air Flowrate Coefficient for the Following Central Body Cone Angles: a) $\beta_c = 15°$; b) $\beta_c = 20°$; c) $\beta_c = 25°$; d) $\beta_c = 30°$.

If the air intake is in an air flow at a substantial angle of attack α (or at large angle of slip β_{sl}), a complex flow pattern that is difficult to calculate forms at its entry (Fig. XVI-2-7). In this case, engine performance deteriorates and Δc_{xai} rises sharply. This imposes limits on the angles α and β_{sl}, complicates the control system, and increases its weight.

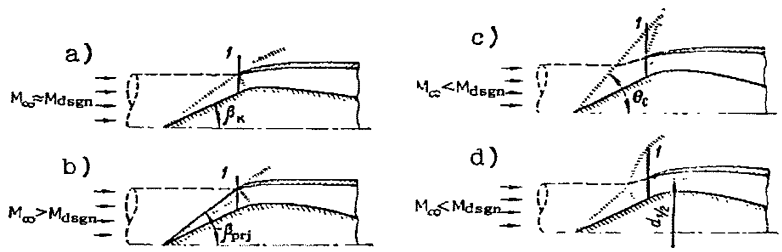

Figure XVI-2-6. Various Types of Compression Shocks in Front of Air Intake with Conical Central Body. a) design condition $\Phi = \phi = 1$; nondesign conditions: b) $\Phi = \phi = 1$; c) $\phi = \Phi > 1$; d) $\phi < \Phi \leq 1$.

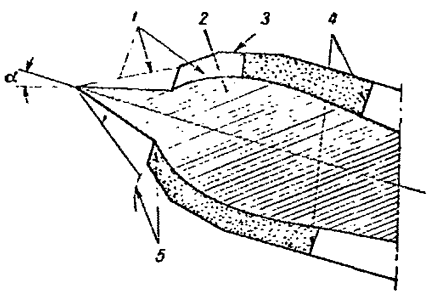

Figure XVI-2-7. Diagram of Flow Around Air Intake at Large Angle of Attack. 1) oblique compression shocks; 2) central body; 3) casing; 4) closed shocks in throat; 5) curvilinear compression shocks.

Knowing the parameters β_c, β_{prj} and M_∞, and having determined Φ from Fig. XVI-2-5, we can use the data of Fig. XVI-2-8 [21] to find Δc_{xai}. The dashed lines in this figure indicate the minimum possible Δc_{xai} when $\phi = \Phi$. The coefficient $(c_{xnos})_{\phi=0}$ in Formula (XVI-2-4) is determined, as in the preceding case, from the curves of Figs. XVI-2-1 and XVI-2-2, and the coefficient $c_{s.ai}$ can be disregarded in first approximation, since the air-intake leading edges for $M_\infty > 1.8$-2.0 are sharp and their rims are, as a rule, rectilinear.

Side air intakes with conical central bodies, e.g., semicircular types, are synthesized in much the same way. For side air intakes with the same initial data as circular ones, the values of the coefficient ϕ and the pressure recovery factor are found to be 3-6% smaller, but on the other hand lateral air intakes do not increase the vehicle's frontal-drag coefficient as much as do circular intakes.

Calculations for multiple-shock, annular, and other air-intake types are given in the specialized literature.

Example. For the data of the preceding example, find the frontal-drag coefficient of a parabolic vehicle nose section

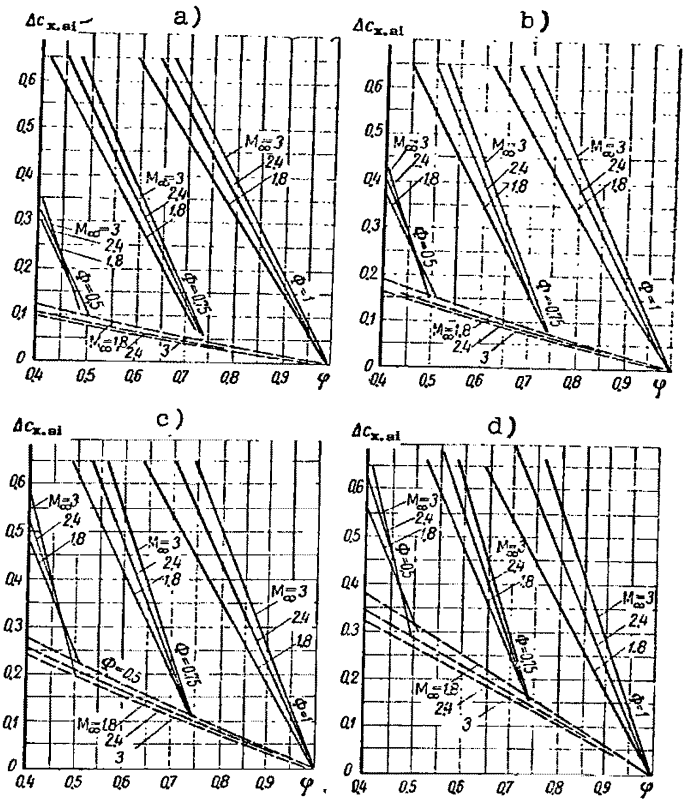

Figure XVI-2-8. Diagrams for Determining Coefficient of Added Drag of Air Intake with Conical Central Bodies with the Following Angles: a) $\beta_c = 15°$; b) $\beta_c = 20°$; c) $\beta_c = 25°$; d) $\beta_c = 30°$.

having an air intake with a central body (double-shock diffuser) with the parameters $\beta_{prj} = 32°, \beta_c = 20°$.

From the diagram (Fig. XVI-2-5b), we find $\Phi = 0.75$; then according to Formula (XVI-2-5), $G_{a\ max} = 0.75 \cdot 0.125 \cdot 9.81 \cdot 680 \cdot 0.246 = 154$ kg/s. From the diagram (Fig. XVI-2-8b), we find $\Delta c_{xai} = 0.175$. Then we refer to the diagram (Fig. XVI-2-1) to determine $(c_{x\ nos})_{\phi=0} = 0.024$ as in the previous example. We set $c_{xai} = 0$ and thus find from Formula (XVI-2-4)

$$c_{x\ nos} = 0.024 + (0.175 - 0)\frac{0.246}{0.503} = 0.11.$$

Influence of air intake on vehicle lift. This effect is felt owing to the change in the direction of the air stream at the entry into the air-intake passage at angles of attack $\alpha \neq 0$. The lift coefficient will be changed by an amount

$$\Delta c_{y\ al} = 0.035\varphi\alpha, \qquad \text{(XVI-2-6)}$$

where α is the attack angle in degrees; ϕ is the flowrate coefficient of the air passing through the intake.

In the process of vehicle design, the presence of air intakes calls for close coordination of the aerodynamic research with powerplant design in view of the reciprocal effects.

Fixed and Movable Control Engines /698

When fixed multiple-start control engines (usually rocket engines) are used for flight control, calculation of the forces that they develop reduces to determination of the thrust forces from Relation (XVI-2-1). If the engine burn time is short, the variational component of thrust will be substantial during pressure buildup and decay and it will not be possible to disregard it.

If the sustainer or special pivoting vernier engines are deflected to control flight, the controlling forces that they set up are calculated by determining the projections of the thrust onto the direction of interest. For example, rotation of a sustainer engine with thrust P through an angle δ_p creates a controlling force

$$P_{y1} = P \sin \delta_p, \qquad \text{(XVI-2-7)}$$

directed along the normal to the original position of the engine longitudinal axis and acting in the plane of the turn angle.

The loss of thrust from rotation of the sustainer engine is small, since the projection of the thrust onto the original direction of the engine's longitudinal axis (this direction usually coincides with the vehicle longitudinal axis) will be

$$P_{x1} = P \cos \delta_p. \qquad \text{(XVI-2-8)}$$

In first approximation for small turn angles, therefore, it is assumed that the thrust does not change ($P_{x1} \approx P$), and that the controlling force varies linearly as a function of turn angle, i.e., $P_{y1} \approx P\delta_P$.

The line of action of the controlling force P_{y1} passes through the engine pivot axis, and this makes it easy to find its point of application and calculate the moment about the vehicle's center of mass.

Pivoting Nozzles

When the entire nozzle is pivoted, including the part upstream of the critical cross section (Fig. XVI-2-9), no difficulty is encountered in calculating the controlling forces, since it can be assumed with sufficient accuracy that the entire thrust force vector rotates. Hence Relationships (XVI-2-7) and (XVI-2-8) also remain valid for this case. /699 The application point of the controlling force can also be found by assuming that its line of action passes across the nozzle pivot axis. The thrust loss that results from rotation of the nozzle may be larger than in the case of engine pivoting, since there are no gap losses in the latter case.

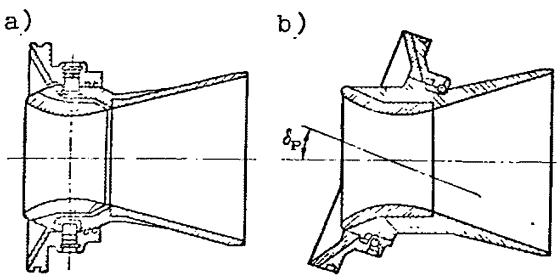

Figure XVI-2-9. Diagrams of Pivoting Nozzles. a) pivot axis in plane perpendicular to vehicle axis; b) pivot axis in plane perpendicular to line forming an angle δ_P with the vehicle axis.

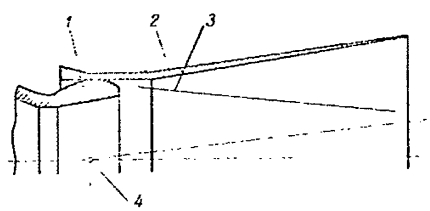

Figure XVI-2-10. Diagram of Flow in Supersonic Nozzle with Pivoted Section.

Calculation of the controlling forces becomes much more complicated if only a certain section of the supersonic part of the nozzle is pivoted (sectional nozzle, Fig. XVI-2-10). This is because it is necessary to provide certain clearances between the rotating 2 and fixed 1 parts of the nozzle for rotation about axis 4. This results in local flow separation from the nozzle walls and in the formation of a compression shock at the beginning of the movable part of the nozzle

even in the absence of a turn angle ($\delta_P = 0$). The flow pattern changes when part of the nozzle is rotated: the intensity of compression shock 3 increases in front of the pivoting section that has moved down onto the flow, and decreases at the diametrally opposite position, so that a spatial expansion wave may appear at that point at certain pivot angles.

The controlling forces developed by a sectional nozzle can be calculated in approximation on the basis of certain experimental data. The controlling force

$$Y_P = K_e c_{yP}^{\delta} q_P S_P \delta_P, \qquad \text{(XVI-2-9)}$$

where c_{yP}^{δ} is the derivative of the controlling force with respect to nozzle pivot angle; q_P is the velocity head of the fuel-combustion products at the center of the pivoting nozzle section; $S_P = D_{cr}\ell_P$ is the longitudinal-section area of the sectional nozzle; D_{cr} is the inside diameter at the center of the rotating section; ℓ_P is the length of the pivoting nozzle section; δ_P is the turn angle of the nozzle in radians; K_e is a coefficient of agreement with experiment.

If M is determined in the center section of the pivoting part of the nozzle and c_{yP}^{δ} is expressed by

$$c_{yP}^{\delta} = \frac{4}{\sqrt{M^2-1}}\left(1 - \frac{1}{2\lambda\sqrt{M^2-1}}\right), \qquad \text{(XVI-2-10)}$$

where $\lambda = D_{cr}/\ell_P$, then $K_e \approx 1.24$. The application point of force Y_P is assumed to be at the center of the pivoting nozzle section. In first approximation, the force Y_P can be assumed to be directed normal to the axis of symmetry of the rotating nozzle section drawn in the plane of rotation.

The thrust loss in control by rotating the supersonic nozzle section is composed of the losses at $\delta_P = 0$ and the losses caused by turning the nozzle section through an angle $\delta_P \neq 0$. As a rule, experimentation produces reliable data on these losses.

Relationships (XVI-2-9) and (XVI-2-10) enable us to specify the length necessary for the supersonic part of the nozzle in order to set up the desired maximum force Y_P. For this purpose,

experimental data are used as a basis for choosing the maximum rotation angle $\delta_{P\ max}$ that ensures an approximately linear $Y_P(\delta_P)$ relationship for $0 \leq \delta_P \leq \delta_{P\ max}$, $\delta_{P\ max} \approx 15°$. Then, by assigning a series of values to ℓ_P, the center of the rotating section /700 is determined for the complete selected nozzle and all parameters are found for it (D_{cr}, q_P, M, λ, S_P). This enables us to find the corresponding values of Y_P/δ_P from Formulas (XVI-2-9) and (XVI-2-10). Plotting a diagram of Y_P/δ_P against ℓ_P, we find the required ℓ_P from the ratio $Y_{P\ max}/\delta_{P\ max}$.

Example. Determine the controlling force set up by rotating the supersonic section of a nozzle through an angle $\delta_P = 5°$. The gas variables are as follows in the center section of the pivoting part of the nozzle: M = 2.43; ρ = 0.0822 kg·s^2/m^4; V = 1637 m/s. The dimensions of the pivoting nozzle section: ℓ_P = 0.0331 m; D_{cr} = 0.057 m. From these data we find

$$\lambda = \frac{D_{cr}}{l_P} = \frac{0.057}{0.0331} = 1.722;$$

$$c_{yP}^{\delta} = \frac{4}{\sqrt{M^2-1}}\left(1 - \frac{1}{2\lambda\sqrt{M^2-1}}\right) = \frac{4}{\sqrt{2.43^2-1}}\left(1 - \frac{1}{2\cdot 1.722\sqrt{2.43^2-1}}\right) = 1.57;$$

$$q_P = \frac{\rho V^2}{2} = \frac{0.0822\cdot 1637^2}{2} = 1.1\cdot 10^5,\ \text{kg/m}^2;$$

$$S_P = D_{cr} l_P = 0.0331\cdot 0.057 = 0.001887\ \text{m}^2.$$

Setting the coefficient K_e = 1.24, we calculate the controlling force:

$$Y_P = K_e c_{yP}^{\delta} q_P S_P \delta_P = 1.24\cdot 1.57\cdot 1.1\cdot 10^5\cdot 0.001887 \times \frac{5}{57.3} = 35.2\ \text{kg}.$$

Rotary Mouthpieces

If a mouthpiece is to develop its controlling force at the smallest possible deflection angles δ_P (to prevent the formation of "dead" zones), its internal surface must be profiled to conform to the shape of the jet issuing from the nozzle. However, the need to rotate the nozzle requires that a certain space be left open between the nozzle exit section and the mouthpiece, and this will change the shape of the jet and exert a certain influence on flow through the nouthpiece. On emerging from the nozzle, the flow expands and is accelerated, and then, striking the surface of the mouthpiece, it is decelerated. This produces a curvilinear detached compression shock. Then the flow expands

in the mouthpiece behind this shock. The flow pattern inside a rotary mouthpiece is highly similar to that inside a nozzle with a pivoting supersonic section.

A number of assumptions can be adopted to simplify determination of the controlling force developed by the mouthpiece. Chief among these is solution of the corresponding plane problem (in the plane of the mouthpiece rotation angle) instead of the spatial problem of gas flow in the mouthpiece. Straight oblique shock waves are substituted for the curvilinear compression shocks. The positions of possible points of separation of the flow from the nozzle walls can be determined from the relationships of separating-flow theory. This method will be outlined below as it is applied to calculate forces set up by a deflector. The applicability of this method in the synthesis of rotary mouthpieces or pivoting supersonic nozzle sections requires experimental confirmation.

One important point must be borne in mind in making calculations by this approximate method. For the supersonic part of the mouthpiece, the pressure on its walls will be variable over its length even if the compression shock is straight. This is because the flow expands. It would therefore be more correct to consider the pressure on the mouthpiece wall in an arbitrary cross section equal to the pressure behind the compression shock at the corresponding point of this section.

/701

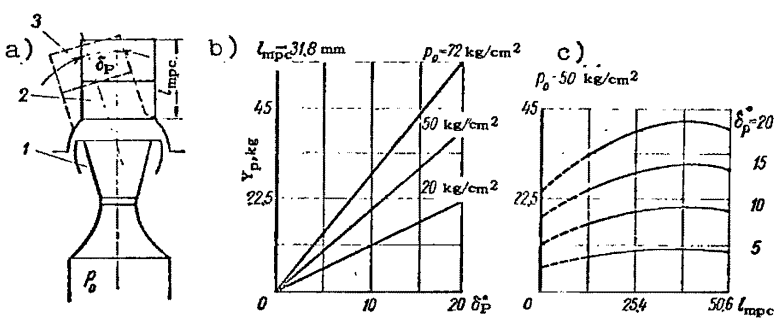

Figure XVI-2-11. Controlling Force Y_p of Rotary Cylindrical Mouthpiece (a) as Function of Rotation Angle δ_p (b) and Mouthpiece Length l_{mpc} (c). 1) nozzle; 2) mouthpiece; 3) position of mouthpiece after rotation through angle δ_p.

Interest attaches to experimental data for cylindrical mouthpieces ([74], 1958, No. 565). The shape of the mouthpiece and the curves of controlling force as a function of rotation angle,

mouthpiece length, and engine-chamber pressure are given in Fig. XVI-2-11. For the rotary-mouthpiece design studied, the hinge moment reached 1.54 kg·cm per 1 kg (1.54 N·cm per 1 N) of lateral controlling force, while it is 0.92 kg·cm/kg for a central gas vane. The thrust losses are insignificant and depend little on the design of the mouthpiece entry section. It may be expected that the erosion stability of the mouthpiece will depend strongly on design shape.

The experiments indicate that the optimum length of a cylindrical mouthpiece is about 1.5 times its diameter.

Deflectors

Two cases are possible in controlling-force calculations.

If the deflector rotation angle δ_p is small, so that its surface forms an angle $\beta_d = \delta_p + \beta_{nz}$ smaller than the critical angle (β_{nz} is the nozzle angle, Fig. XVI-2-12a) with the direction of the gas flow out of the nozzle, then a nearly straight compression shock will form in front of the deflector. Knowing the flow parameters in the nozzle in front of the deflection in its plane of symmetry passing through the nozzle axis perpendicular to the deflector rotation axis (M_1, p_1, k_1), we can find the shock angle θ_s for any δ_p (provided that δ_d is smaller than critical) from the relationships for the oblique compression shock. Assuming further that the pressure is distributed over the surface in the same way as behind a oblique compression shock AA' (for example, the pressure in the cross section passing through point K is equal to the pressure p_2 behind the shock at point N of the same cross section), we determine the controlling force:

$$Y_p = \iint_{(S)} (p_2 - p_\infty)\, dS, \qquad \text{(XVI-2-11)}$$

where S is the area of the projection of the deflector surface washed by the flow from the nozzle onto the plane passing through the nozzle axis and the deflector pivot axis.

If the angle β_d exceeds a certain critical size, the boundary layer separates at the point of its interaction with the compression shock. The pressure rise at the separation point is transmitted upstream along the subsonic part of the boundary layer. This shifts the separation point into the interior of the nozzle. /702
The flow pattern will be the same as in Fig. XVI-2-12a. The flow separates from point A on the inner surface of the nozzle and, passing across the compression shock AA', is rotated through an angle β_{s1}. This flow then attaches to the deflector surface at

point B, at which the second compression shock BB' is formed. A stagnant zone ("fluid wedge") lies below line AB. Pressure p_3 will act on the deflector surface behind the attached compression shock with angle θ_{s2} at point B.

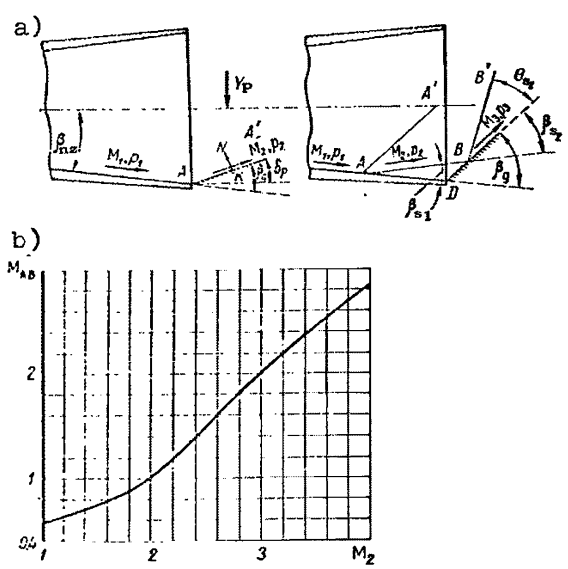

Figure XVI-2-12. Diagram of Flow at Small and Large Deflector Rotation Angles (a); M_{AB} on Line AB as a Function of M_2(b).

Assuming shocks AA' and BB' and line AB to be straight, assuming further that the stagnation pressure p_0 on line AB is equal to the pressure p_3 behind shock BB', and applying (XVI-1-2) or (XVI-2-3) for separating flows and the relationships of compression-shock theory, we can find the positions of point A and B and calculate the pressures p_2 and p_3.

The procedure of the calculation is as follows. We assign a position to point A. For M_1 and Re_1, we find the pressure coefficient p_2 behind the shock from Formula (XVI-1-2) if the boundary layer is laminar or from (XVI-1-3) if it is turbulent, and then use the formula $p_2 = p_1(1 + k_1 M_1^2 p_2/2)$ to find the absolute pressure p_2. Using the relationships of compression-shock theory, we find β_{s1}, M_2, and θ_{s1} from M_1 and p_2. Then line AB is drawn at an angle β_{s1} to the nozzle generatrix and the position of point B on the deflector surface and the flow rotation β_{s2} behind this point are determined. Using the same relationships for the compression shocks, we find θ_{s2} and p_3 from the known M_2 and β_{s2} and calculate the stagnation pressure on line AB:

$$p_0 = p_2\left(1 + \frac{k_1 - 1}{2} M_{AB}^2\right)^{k_1/(k_1-1)},$$

which is compared with p_3. In this formula, M_{AB} is the Mach number on line AB, which is found from M_2 with the aid of a diagram /703

(Fig. XVI-2-12b) constructed from the data of ([79], 1957, No. 5). The positions of points A and B and the pressure values p_2 and p_3 will be assumed correct if it is found that $p_0 = p_3$.

All calculations are to be made in the deflector symmetry plane passing perpendicular to its pivot axis. Assuming that the pressure is the same on the surfaces of the nozzle and deflector in the cross sections (perpendicular to the nozzle axis) and equals the pressure behind compression shock AA' (or BB') in the same sections, we can determine the controlling force and thrust loss:

$$\left.\begin{aligned} Y_P &= \iint_{(S_1)} (p_2 - p_{2,\,cp})\, dS_1 + \iint_{(S_2)} (p_2 - p_\infty)\, dS_2 + \iint_{(S_3)} (p_3 - p_\infty)\, dS_3, \\ \Delta P &= \iint_{(S_{1x})} (p_2 - p_{2,\,cp})\, dS_{1x} + \iint_{(S_{2x})} (p_2 - p_\infty)\, dS_{2x} + \iint_{(S_{3x})} (p_3 - p_\infty)\, dS_{3x}, \end{aligned}\right\} \quad \text{(XVI-2-12)}$$

where S_1 and S_2 are the projections of the nozzle and deflector surfaces, on which the variable pressure p_2 acts; S_3 is the projection of the deflector surface with the variable pressure p_3 (projection onto the plane passing through the nozzle axis and the deflector rotation axis); S_{1X}, S_{2X}, and S_{3X} are the projections of the above surfaces onto the plane perpendicular to the nozzle axis; $p_{2,av}$ is the average pressure on nozzle section AD provided that flow does not separate.

It is assumed in determining S_1, S_2, and S_3, as well as S_{1X}, S_{2X}, and S_{3X}, that they are limited by conical compression shocks with rectilinear generatrices AA' and BB' and with axes of symmetry on the nozzle and deflector walls, respectively.

Line AB may not strike the deflector wall at certain deflector rotation angles. Then the position of the flow separation point must be determined for a line AB passing across the edge of the deflector. By assigning a series of separation points and determining the direction of the AB lines, we can find the deflector rotation angle corresponding to each separation point.

The methods described above do not take account of a certain decrease in controlling force and increase in thrust loss that are associated with the presence between the nozzle and the deflector of the clearances necessary for reliable operation.

Gas Vanes

To simplify the calculations to be set forth below, let us adopt the following assumptions.

1. The flow of fuel combustion products in the powerplant is assumed uniform at the exit from the nozzle.

2. The influence of the slot between the control surface and the nozzle walls, the boundary layer at the nozzle walls, and the profile and planform of the vane on vane lift is taken into account indirectly through an empirical coefficient K_v.

3. The vane leading edges are supersonic.

The lift and drag of the vanes are determined by the formulas

$$Y_v = q_v S_v c_{y\,v}^{\delta} \delta_v, \qquad \text{(XVI-2-13)}$$

$$X_v = q_v S_v c_{x\,v}, \qquad \text{(XVI-2-14)}$$

where $q_v = 0.5\rho_a w_a^2$ is the velocity head in the nozzle exit section; S_v is the vane area; δ_v is the vane rotation angle; $c_{y\,v}^{\delta}$ is the static derivative of vane lift coefficient with respect to vane rotation angle; $c_{x\,v}$ is the frontal drag coefficient of the vanes. /704

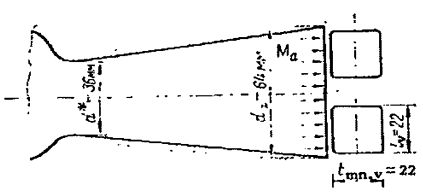

Figure XVI-2-13. Diagram of Nozzle with Gas Vanes.

The derivative

$$c_{y\,v}^{\delta} = \frac{4}{\sqrt{M_a^2 - 1}} K_v, \qquad \text{(XVI-2-15)}$$

where M_a is the Mach number in the nozzle exit section.

In first approximation for $M_a \geq 2.5$, we can assume that $K_v \approx 0.7$. The following semiempirical relationship, which is applicable for wings of small aspect ratio with nearly rectangular planform, is recommended for determination of $c_{x\,v}$:

$$c_{xv} = \underbrace{\left(1 - \frac{0.3}{\lambda_e + 0.3}\right) \frac{B\bar{c}^2}{\sqrt{M_a^2 - 1}} + c_{xf\,v}}_{c_{x\,v0}} + \underbrace{\frac{4\delta_v^2}{\sqrt{M_a^2 - 1}} \left(1 - \frac{1}{2\lambda_e}\right)}_{c_{x\,v\delta}}, \qquad \text{(XVI-2-16)}$$

where $\lambda_e = \lambda_v \sqrt{M_a^2 - 1}$; $\lambda_v = \ell_v / b_{mn.v}$ is the vane aspect ratio; ℓ_v is the span of a vane; $b_{mn.v}$ is the mean chord of a vane; $B = 2K_1$

is a coefficient taking profile shape into account (see Table V-2-2); $\bar{c}$ is the relative thickness of a vane; $c_{xf\ v}$ is the friction drag coefficient of the vanes (see §VI-1).

Formulas (XVI-2-15) and (XVI-2-16) are valid for nonseparating flow around the vanes ($\delta_v > \delta_{v.cr}$), which is the case for $\delta_v < 15°$.

The values of the coefficient K_v and those of $c_{x\ v0}$ and $c_{x\ v\delta}$ in (XVI-2-16) must be improved experimentally for specific vane and nozzle designs. In addition, the vanes may suffer burn damage owing to the high temperature of the flow around their surfaces. This may result in a substantial change in Y_v and X_v during operation of the gas vanes.

The frontal drag of the vanes is taken into account by a reduction in the actual thrust. The calculations work with an effective thrust

$$P_e = P - X_v. \qquad \text{(XVI-2-17)}$$

It may be assumed in first approximation that Y_v and X_v are applied at the center of gravity of the vane surface.

Example. Determine X_v and Y_v for the control surfaces whose dimensions are indicated in Fig. XVI-2-13. The variables of the gas in the powerplant combustion chamber are as follows: $p_0 = 40$ kg/cm^2 (392 N/cm^2), $T_0 = 2500°$K, $k = 1.33$, $R = 30.0$ kg·m/kg·deg (30 Nm/N·deg).

In accordance with the drawing of the nozzle, we find:

$$S_a = \frac{\pi d_a^2}{4} = \frac{\pi (6.4 \cdot 10^{-2})^2}{4} = 3.22 \cdot 10^{-3}\ м^2$$

for the nozzle exit section area and

$$S^* = \frac{\pi d^{*2}}{4} = \frac{\pi (3.6 \cdot 10^{-2})^2}{4} = 1.02 \cdot 10^{-3}\ м^2$$

for the nozzle critical section area.

We determine the relative flowrate

$$q = \frac{S^*}{S_a} = \frac{1.02 \cdot 10^{-3}}{3.22 \cdot 10^{-3}} = 0.316.$$

Referring to the gasdynamic-function tables for k = 1.33 [8] /705
or to the corresponding formulas for one-dimensional steady-state isentropic flow of an ideal compressible fluid (III-3-4), we find

$$M_a = 2.60;\ \lambda_a = 1.93;\ \frac{T_a}{T_0} = 0.472;\ \frac{p_a}{p_0} = 0.103;$$

$$\frac{\rho_a}{\rho_0} = 0.0487;\ f_a = 0.487.$$

We determine the density of the gas in the combustion chamber from the equation of state:

$$\rho_0 = \frac{p_0}{gRT_0} = \frac{40 \cdot 10^4}{9.81 \cdot 30 \cdot 2500} = 0.544 \text{ kg-s}^2/\text{m}^4 \quad (5.33 \text{ kg/m}^3).$$

We calculate the temperature, pressure, and density in the nozzle exit section:

$$T_a = T_0\left(\frac{T_a}{T_0}\right) = 2500 \cdot 0.472 = 1181^\circ \text{ K};$$

$$p_a = p_0\left(\frac{p_a}{p_0}\right) = 40 \cdot 10^4 \cdot 0.0487 = 1.948 \cdot 10^4 \text{ kg/m}^2 \ (19.1 \cdot 10^4 \text{ N/m}^2);$$

$$\rho_a = \rho_0\left(\frac{\rho_a}{\rho_0}\right) = 0.544 \cdot 0.103 = 0.0560 \text{ kg-s}^2/\text{m}^4 \quad (0.549 \text{ kg/m}^3).$$

We calculate the thrust developed by the powerplant in a vacuum:

$$P_{max} = S_a p_0 f_a = 3.22 \cdot 10^{-3} \cdot 40 \cdot 10^4 \cdot 0.487 = 627 \text{ kg} \ (6150 \text{ N}).$$

The thrust at sea level (for the standard atmosphere) is

$$P = P_{max} - p_\infty S_a = 627 - 1.033 \cdot 10^4 \cdot 3.22 \cdot 10^{-3} = 594 \text{ kg} \ (5830 \text{ N}).$$

The critical speed of sound

$$a^* = a_0\sqrt{\frac{2}{k+1}} = \sqrt{kgRT_0\frac{2}{k+1}} = \sqrt{1.33 \cdot 9.81 \cdot 30 \cdot 2500\frac{2}{1.33+1}} = 916 \text{ m/s}.$$

The velocity of the gases in the nozzle exit section

$$w_a = \lambda_a a^* = 1.93 \cdot 916 = 1768 \text{ m/s}.$$

The velocity head in the nozzle exit section

$$q_a = \frac{\rho_a w_a^2}{2} = \frac{0.056 \cdot 1768^2}{2} = 8.76 \cdot 10^4 \text{ kg/m}^2 \ (86.0 \cdot 10^4 \text{ N/m}^2).$$

The aspect ratio of the vane (see drawing of vane) is

$$\lambda_v = \frac{l_v}{b_{mn.v}} = \frac{22}{22} = 1.0.$$

We calculate λ_e:

$$\lambda_e = \lambda_v \sqrt{M_a^2 - 1} = 1 \sqrt{2.60^2 - 1} = 2.40.$$

Setting the Re on the surface of the vane equal to 10^7 and assuming that the flow is turbulent, we find that at $\delta_v = 10°$ (0.174 rad), $\bar{c} = 0.12$, and B = 5.33, (XVI-2-16) gives

$$c_{xv} = \left(1 - \frac{0.3}{2.40 + 0.3}\right) \frac{5.33 \cdot 0.12}{\sqrt{2.60^2 - 1}} + \frac{2 \cdot 0.074}{\sqrt{1 + 0.12 \cdot 2.60^2}\,(10^7)^{0.2}} +$$
$$+ \frac{4\,(0.174)^2}{\sqrt{2.60^2 - 1}} \left(1 - \frac{1}{2\sqrt{2.60^2 - 1}}\right) = 2.83 \cdot 10^{-2} + 0.44 \cdot 10^{-2} + 4.01 \cdot 10^{-2} = 7.28 \cdot 10^{-2}$$

According to (XVI-2-15),

$$c_{y\,v}^{\delta} = \frac{4 \cdot 0.7}{\sqrt{2.60^2 - 1}} = 1.16.$$

The plan area of two vane cantilevers is

$$S_v = 2 b_{mn.v} l_v = 2 \cdot 2.2 \cdot 10^{-2} \cdot 2.2 \cdot 10^{-2} = 9.68 \cdot 10^{-4} \text{ m}^2.$$

The values of X_v and Y_v at $\delta_v = 10°$ will be /706

$$X_v = q_a S_v c_{x\,v} = 8.76 \cdot 10^4 \cdot 9.68 \cdot 10^{-4} \cdot 7.28 \cdot 10^{-2} = 6.2 \text{ kg } (60.8 \text{ N}).$$
$$Y_v = q_a S_v c_y^{\delta} \delta_v = 8.76 \cdot 10^4 \cdot 9.68 \cdot 10^{-4} \cdot 1.16 \cdot 0.174 = 17.2 \text{ kg } (169 \text{ N}).$$

The effective thrust (counting only one pair of vanes) is

$$P_e = P - X_v = 594 - 6 = 588 \text{ kg } (5760 \text{ N}).$$

Control by Gas Injection into Supersonic Section of Nozzle

Gases and liquids are usually injected into the supersonic section of a nozzle through round holes placed around the perimeter of a certain nozzle section. Injection is against the flow, at about a 30° angle to the normal to the nozzle inner wall. The interaction of the injected stream with the expanding axisymmetric flow produces a highly complex flow pattern inside the nozzle ([70], 1965, No. 1).

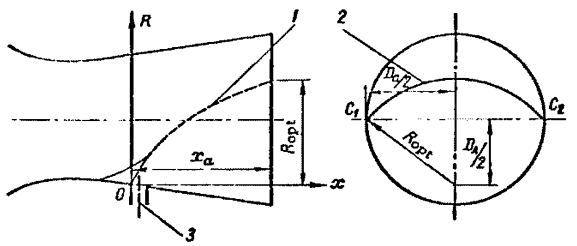

Figure XVI-2-14. Diagram Showing Position of Compression-Shock Front.

The nucleus of the injected gas, which expands relatively weakly downstream, is found directly downstream of the injection orifice. Outside the nucleus, immediately after emerging from the injection orifice, the jet experiences considerable expansion and is acted upon by the main flow to form a rotational flow that deflects toward the nozzle walls; the pressure reaches its largest values at these points on the wall. The flow of injected gas is also displaced in the vortical zone. At the boundary between the vortical zone and the injection-gas nucleus on the wall of the nozzle, the pressure drops off sharply and boundary-layer separation results.

The injected-gas nucleus and the vortical zone are surrounded by the flow passing through the λ-shaped compression shock that forms in front of the injected stream. In Fig. XVI-2-14, we see the front 1 of this shock in the meridional plane passing through the injection orifice 3. The shock front is crossed at nearly circular lines 2 by planes perpendicular to the nozzle axis.

In investigation of the magnitude, direction, and point of application of the controlling force that results from injection of gas into the supersonic section of a nozzle, one of the basic problems is to determine the configuration of the compression shock that forms in front of the injected-gas nucleus. This can be done in first approximation with the formula

$$R \quad R_c\left(\frac{4k}{\pi J}\right)^{1/4}\left[1+\lambda\left(\frac{\pi J}{4k}\right)^{1/2}\frac{1}{M_A^2}\frac{x}{R_c}\right]^{1/2}\left(\frac{x}{R_c}\right)^{1/2}, \qquad \text{(XVI-2-18)}$$

where R is the front radius of the λ-shaped compression shock /707

(not counting the front branch), measured from the x-axis (the x-axis runs parallel to the nozzle axis in the meridional plane passed through the center of the injection orifice); here the origin of the x-axis is placed directly in front of this orifice (Fig. XVI-2-14); k is the ratio of heat capacities for the gas flowing through the nozzle; J and λ are constants that depend on k (for k = 1.4, J = 0.88, λ = -1.989); M_a is the Mach number of the gas flow in the nozzle immediately ahead of the orifice in the absence of injection and corresponds to the velocity w_a at this point;

$$R_c = \left(\eta_1\eta_2 S_A \frac{m_i w_a}{m_n w_A}\right)^{1/2}$$

is the characteristic radius; $\eta_1 = 1 \pm (w_i \cos \beta_i)/w_a$ is a correction factor that takes account of the deflection angle β_n of the injection-port axis from the normal to the nozzle axis (the "+" is taken when the gas is injected against the nozzle flow); w_i is the velocity of the injected gas in the injection-orifice exit section; w_a is the gas velocity in the nozzle exit section without consideration of injection; S_A and w_A are the cross-sectional area of the nozzle and the gas velocity directly ahead of the injection orifice (without considering injection); m_n and m_i are the per-second mass flowrates of gas through the nozzle and the injection orifice; $\eta_2 = 1 \pm \Delta h/(w_A w_a)$ is a coefficient that takes account of the influence of vaporization and chemical reaction of the injected fluid on the position of the compression shock; $\pm\Delta h$ is the energy liberated (+) or absorbed (-) by a unit mass of the injected fluid during its vaporization or chemical reaction. Studies have shown ([70], 1965, No. 2), that Formula (XVI-2-18) gives satisfactory agreement with experiment for injection of either gas or liquid into the supersonic part of the nozzle.

Since the pressure increases behind the shock, we can assume that the lateral force arising from the pressure redistribution over the inner nozzle wall on gas injection reaches its maximum value when the compression-shock front in the nozzle exit section falls at a point of intersection of the nozzle inner surface and the meridional plane perpendicular to the plane passing through the nozzle axis and the injection orifice (points C_1 and C_2 in Fig. XVI-2-14). The corresponding optimum compression-shock radius in the nozzle exit section is

$$R_{opt} = \left[\left(\frac{D_a}{2}\right)^2 + \left(\frac{D_A}{2}\right)^2\right]^{1/2}, \qquad \text{(XVI-2-19)}$$

where D_A is the cross-sectional diameter of the nozzle immediately in front of the injection orifice.

By using (XVI-2-18) and (XVI-2-19), we can either find the injection rate that guarantees maximum lateral force for a given position of the injection orifice or find the injection-orifice position for a given flowrate that produces the same force.

The lateral controlling force forms as a result of the pressure rise on the surface of the nozzle in the zone of flow separation between the legs of the λ-shaped shock (and behind the compression shock) and as a result of the pressure drop behind the injection orifice. However, (XVI-2-18) does not consider the influence of the high-pressure zone between the legs of the λ-shaped shock (this zone increases the resultant force) and the zone of reduced pressure behind the injection orifice (this zone lowers the resultant force), but this is to some extent justified by the offsetting directions of these factors.

To construct the separation zone and determine the influence of pressure $p_{2,\lambda}$ behind the front leg of the λ-shaped shock, we can use Formula (XVI-1-2) or (XVI-1-3) for separating flows and the formulas for the equivalent-barrier height $\underline{h}$ and the length ℓ of the separation zone in the nozzle meridional plane passing through the center of the injection orifice (Fig. XVI-2-15). /708

The equivalent-barrier height is

$$h = \left[\frac{2S_A}{\pi}\right]^{1/2} \left\{ \frac{2k_n M_i \left(1 + \frac{k_n - 1}{2} M_i^2\right)}{\left(\frac{S_A}{S_i}\right)^2 \left(\frac{p_A}{p_i}\right)^2 \left(\frac{p_{2,mn}}{p_A} - 1\right)\left[(k_n + 1) - (k_n - 1)\frac{p_{2,mn}}{p_A}\right]} \right\}^{1/4}, \quad \text{(XVI-2-20)}$$

where M_i and p_i are the Mach number and pressure in the injected jet at the exit section of the injection orifice; k_n is the heat-capacity ratio of the injected gas; S_i is the exit-section area of the injection orifice; $p_{2,av} = \frac{1}{3}(p_i + 2p_{2,\lambda})$.

If an incompressible fluid is injected, Formula (XVI-2-20) should be replaced by

$$h = \frac{0.3 m_n w_a}{d_i (p_{2,\lambda} - p_i)}, \quad \text{(XVI-2-21)}$$

where d_i is the exit-section diameter of the injection orifice ([69], 1966, No. 1).

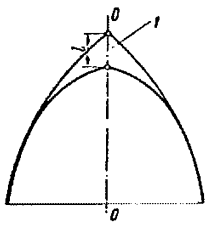

Figure XVI-2-15. Diagram Illustrating Determination of Pressure and Dimensions of Separation Zone in Front of Injection Orifice in Nozzle.

The length of the separation zone, i.e., the distance along the nozzle wall from the separation point to the edge of the injection orifice, is

$$l = h\,[\operatorname{ctg}\beta_s + \operatorname{tg}(\beta_{nz} \div \beta_i)], \qquad \text{(XVI-2-22)}$$

where β_s is the flow deflection angle behind the forward leg of the λ-shaped shock; β_{nz} is the inclination angle of the nozzle wall to its axis.

The problem is solved by trial and error. Assigning a position to the separation point (and, consequently, a length l), we find the pressure $p_{2,\lambda}$ from (XVI-1-2) or (XVI-1-3) and use the formulas of compression-shock theory to find the angle β_s. Then we determine the height h by Formula (XVI-2-20). This enables us to find the length l of the separation zone by Formula (XVI-2-22) and compare it with that originally assigned. An effort should be made to have these figures agree.

The lateral boundaries of the separation zones are the lines of intersection of the nozzle inner surface with the conical surface generated by the straight line of the forward leg of the λ-shaped shock, and its axis of symmetry is the tangent to the nozzle surface at the separation point.

The lateral force behind the compression shock can be found by assuming that the pressure on the nozzle wall in any cross section will be the same as that behind the compression shock:

$$Y_v = 0.95\left[(p_{2,\lambda} - p_{2\min})\,S_1 + \iint\limits_{(S_2)} (p_2 - p)\,dS_2\right] + [m_i w_i + (p_i - p_{2,\lambda})\,S_i], \qquad \text{(XVI-2-23)}$$

where the factor 0.95 takes account of the decrease in Y_p due to the zone of underpressure behind the injection orifice; $p_{2,av}$ is the average separation-zone pressure for nonseparating flow; S_1 and S_2 are the projections of the separation-zone area and the surface area of the nozzle behind the compression shock onto a plane parallel to the nozzle axis and perpendicular to the meridional section passing through the injection-orifice axis; p_2 and p are the pressures behind the shock and in front of the shock in the nozzle cross section under consideration; the second term /709

is the thrust developed by the injected-gas jet.

Throttling Individual Nozzles

Multiple-nozzle systems can be used to create controlling forces by throttling individual nozzles (by closing off the critical cross sections partly or even completely). For this purpose, a central body ("slug") is mounted in the critical cross section of the nozzle and displaced along the nozzle axis to regulate its critical-section area and, consequently, the thrust produced by this nozzle. By throttling one or more of a group of nozzles positioned unsymmetrically around the longitudinal axis of a vehicle, we can produce a moment about this axis that tends to turn the vehicle in the corresponding direction.

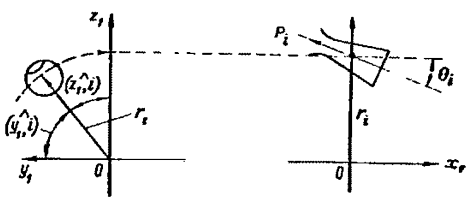

Figure XVI-2 16. Nomenclature of Parameters of ith Nozzle in a Nozzle Cluster.

Let a nozzle cluster consist of n nozzles, each of which creates a thrust P_i and is located on a circle of radius r_i at an angle θ_i to the vehicle longitudinal axis. Then on D_i-percent throttling of each ith nozzle, we obtain the following moments about the y_1 and z_1-axes:

$$\Delta M_{y_1} = 10^{-2} \sum_{i=1}^{n} D_i P_i r_i \cos\theta_i \sin(\widehat{y_1, r_i}); \qquad \text{(XVI-2-24)}$$

$$\Delta M_{z_1} = 10^{-2} \sum_{i=1}^{n} D_i P_i r_i \cos\theta_i \sin(\widehat{z_1, r_i}), \qquad \text{(XVI-2-25)}$$

where $(\widehat{y_1, r_i})$ and $(\widehat{z_1, r_i})$ are the angles between the corresponding axes y_1 and z_1 and the radius r_i (Fig. XVI-2-16).

Relationships (XVI-2-24) and (XVI-2-25) assume that when all nozzles are fully opened $\Delta M_{y1} = \Delta M_{z1} = 0$, and that the axis of any ith nozzle lies in a plane passing through the vehicle longitudinal axis x_1.

If all nozzles have equal $P_i = P$, $r_i = r$, $\theta_i = \theta$, we can write instead of (XVI-2-24) and (XVI-2-25)

$$\Delta M_{y_1} = 10^{-2} Pr \cos 0 \sum_{i=1}^{n} D_i \sin(\widehat{y_1, r_i}); \qquad \text{(XVI-2-26)}$$

$$\Delta M_{z_1} = 10^{-2} Pr \cos 0 \sum_{i=1}^{n} D_i \sin(\widehat{z_1, r_i}). \qquad \text{(XVI-2-27)}$$

Nozzles positioned in this way can be used to control a vehicle in pitch and yaw. For roll control, it is necessary to place some of the nozzles with their axes forming a certain angle with the vehicle meridional plane or to provide special controls.

Determination of Controlling Efforts Created by Gasdynamic Controls in Nozzle Assemblies with a Central Body /710

A nozzle with a central body performs well in a broad range of atmospheric pressures. If we consider the ratio of the mea-

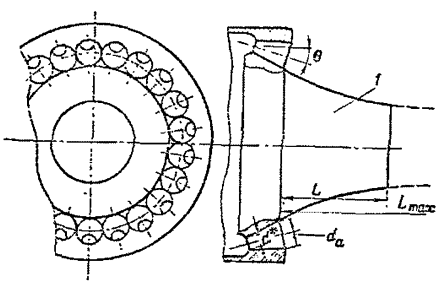

Figure XVI-2-17. Clustered Nozzle Assembly. L_{max} is the maximum length of the central body.

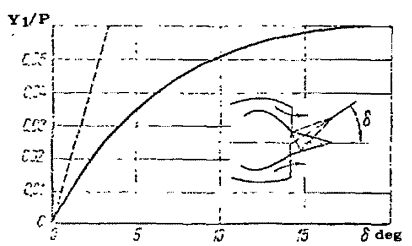

Figure XVI-2-18. Ratio of Lateral Thrust Component Y_1 to Axial Force P as a Function of Central-Body Rotation Angle. -----) theory; ———) experiment.

sured thrust to the thrust obtained by calculation for isentropic expansion to atmospheric pressure, we find, for example, for a powerplant-chamber pressure of 35 kg/cm^2 (343 N/cm^2), and $S_a/S^* = 16$, that this ratio will vary from 0.95 at sea level to 0.98 at H = 20 km for a nozzle with a central body, and from 0.80 to 0.98 under the same conditions for an ordinary nozzle.

The central-body nozzle has an unquestionable advantage in its smaller base area S_{bse}, which, other conditions the same, lowers the frontal drag coefficient of the vehicle. The central-body nozzle arrangement may be either annular or multiple (Fig. XVI-2-17). Here the central body can be made very short without

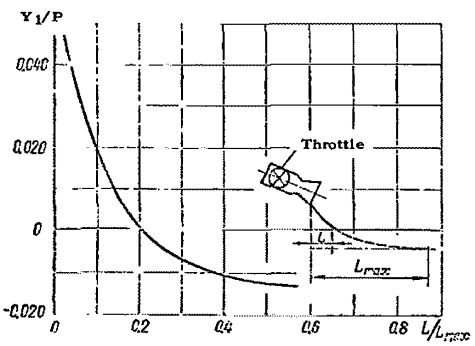

Figure XVI-2-19. Ratio of Lateral Thrust Component Y_1 to Axial Force P as a Function of Length of Stubby Central Body at 12.5% Throttling of One of the Nozzles.

any substantial loss of thrust. Experiments have shown that reducing its length by 75% has practically no effect on thrust, while the thrust loss amounts to about 3% when the central body is absent altogether. Note should be taken of a substantial thrust decrease that occurs when the distance between the exit sections of the nozzles in the clustered variant is increased. An effort should therefore be made to keep this distance as near zero as possible or to give the central body a special profile. Attempts to create controlling forces by rotating the central body, throttling individual nozzles (or rotating them), and injecting gas through orifices in the lateral surface of the central body have been reported.

Experiments have shown that it is necessary to turn the central body through large angles δ in order to create large enough controlling forces Y_1 (Fig. XVI-2-18), and that when individual nozzles are throttled, it is necessary to reckon with the influence of central-body length (Fig. XVI-2-19). An elongated central body retunes asymmetrical flows behind the nozzles to nearly perfect uniformity. This is why the controlling force changes direction when long central bodies are used. /711

The data in Figs. XVI-2-18 and XVI-2-19 were obtained from an experiment with a multinozzle installation having the following characteristics:

$$\theta = 23^\circ; \quad n = 24; \quad \varepsilon_n = \frac{D_n^2}{nd^{*2}} = 16; \quad \varepsilon_n = \frac{d_n^2}{d^{*2}};$$
$$S^* = 3.72 \text{ cm}^2.$$

A literature report states that control by injection of gas from the lateral surface of the central body is just as effective as in ordinary expanding nozzles ([70], 1964, No. 7).

It may prove helpful in calculations to use the following relation between the characteristics of the multinozzle version, which has been obtained on the assumption that the nozzle exit sections are in contact:

$$\frac{\varepsilon_n}{\varepsilon_n} = \frac{1}{n}\left(\frac{n}{\pi} + \cos\theta\right)^2. \qquad \text{(XVI-2-28)}$$

§XVI-3. CALCULATION OF FORCES SET UP BY COMBINED CONTROLS

Controls with Fixed Slot Nozzle on Trailing Edge of Plate

Let us examine experimental data ([76], 1962, No. 4-5) that can be used to calculate forces for interaction of a jet issuing from a slot nozzle on the trailing edge of a plate perpendicular to its surface and the undisturbed air stream washing this plate. The outflow velocity of the jet was sonic in the experiments; the Re calculated from the distance from the leading edge of the plate to the slot varied from $1.4 \cdot 10^6$ to $1.2 \cdot 10^7$ and had no marked influence on the results; the slot length ℓ_s = 48 mm. The gas jet was air at standard temperature.

Figures XVI-3-1 and XVI-3-2 show values of the gain K_a as a function of the free-airstream M and the ratio of the jet stagnation pressure p_{0i} to the static pressure p_∞ in the oncoming flow and as a function of slot width ℓ_s and the presence of lateral plates that prevent spillage of the airflow across the lateral edges of the jet [sic].

The gain K_a is the ratio of the total force acting in the direction of the normal to the plate to the thrust P_{max} that could be obtained using a gas flow in a Laval nozzle operating under design conditions, i.e.,

$$K_a = \frac{\Delta N + P}{P_{max}},$$

where ΔN is the change in the force normal to the plate in front of the slot nozzle; P is the thrust developed by the gas flow in the slot nozzle.

Having determined K_a and knowing the parameters of the slot nozzle and k, p_{0i}, and p_∞, we can calculate the force set up by the control device under consideration: /712

$$Y_{\text{ср}} = K_a P_{max}, \qquad \text{(XVI-3-1)}$$

where

$$P_{max} = k\mu S_s p_{0i} \sqrt{\frac{2}{k-1}\left(\frac{2}{k+1}\right)^{\frac{k+1}{k-1}}\left[\left(1 - \frac{p_\infty}{p_{0i}}\right)^{\frac{k-1}{k}}\right]}, \qquad \text{(XVI-3-2)}$$

μ = 0.90-0.99 is the flowrate coefficient; S_s is the critical sectional area of the slot.

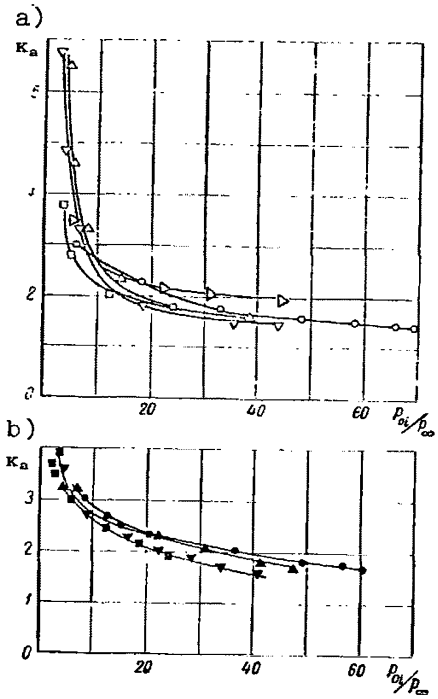

Figure XVI-3-1. Curves of Gain K_a as a Function of Pressure Ratio p_{0i}/p_∞ and M_1. a) without side plates; b) with side plates at slot nozzle. Slot nozzle width 1 mm, length 48 mm.

Side plates: no	Side plates: yes	M_1
○	●	2.80
△	▲	2.21
▽	▼	1.83
□	■	1.57
▷	–	1.83*

*Slot nozzle width 0.33 mm.

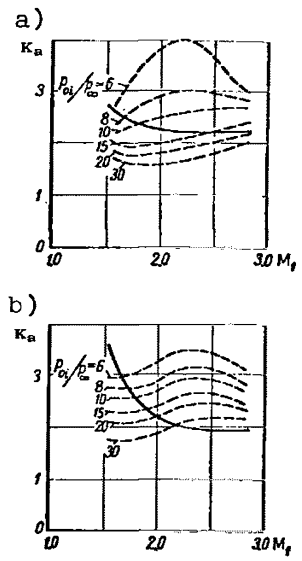

Figure XVI-3-2. Curves of Gain K_a as Function of M_1 and Pressure Ratio p_{0i}/p_∞. a) without side plates; b) with side plates at slot nozzle. Nozzle dimensions: width 1 mm, length 48 mm. The solid lines are curves of the ratio of the normal-force coefficient to the axial force created by a spoiler (see Fig. XVI-1-2).

Analysis of the diagrams in Figs. XVI-3-1 and XVI-3-2 indicates that it is necessary to reduce the stagnation pressure p_{0i} in the jet and the slot width b_s and to place the plates along the sides of the slot parallel to the air flow in order to increase the gain at a given M and air-stream pressure p_∞. Here the smaller p_{0i} and b_s lower P_{max} and make it difficult

to obtain the desired Y_p. In fact, it is evident from (XVI-3-1) and (XVI-3-2) that Y_p can be increased only through S_s, by using a long slot. However, it may be found that the surface of the vehicle will not accomodate a long slot anywhere. /713

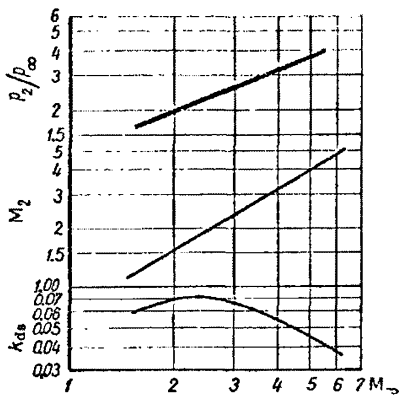

Figure XVI-3-3. Variation of Air Parameters in Stagnation Zone and Coefficient of Displacement Velocity as Function of M_∞ for a Turbulent Boundary Layer.

The response speed of this type of control is evaluated from experimental data. For the specific case of a gas line 3 m long, experimental studies indicated that the time from the admission of the gas to the appearance of Y_p was of the order of 0.01 s.

The force ΔN can be calculated approximately with the aid of the following relationships ([69], 1966, No. 1):

$$\Delta N = (p_2 - p_\infty)\Delta x, \qquad \text{(XVI-3-3)}$$

$$\frac{\Delta x}{d_n} = \frac{p_{0i}M_a\left(1+\frac{k_c-1}{2}M_a^2\right)e^{\frac{1+k_c}{2(1-k_c)}}k_c}{kp_2M_2^2\sqrt{(k_c-1)/2}\,k_{ds}}, \qquad \text{(XVI-3-4)}$$

$$\frac{p_2}{p_1} = 1 + 1.27M_\infty^{3/2}\mathrm{Re}_L^{1/4}\left(\frac{L}{L-\Delta x}\right)^{1/4}, \qquad \text{(XVI-3-5)}$$

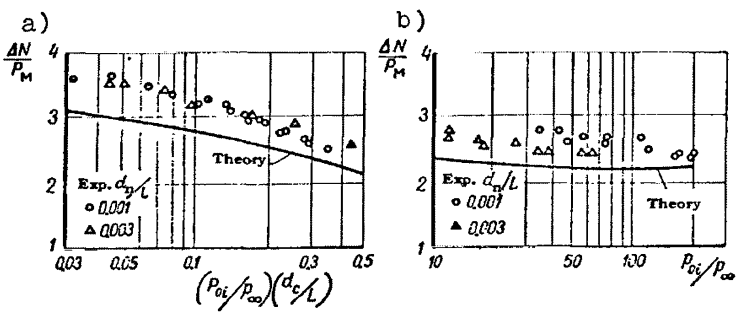

Figure XVI-3-4. Comparison of Experimental and Calculated Data for Laminar (a) and Turbulent (b) Boundary Layers. P_M is the maximum thrust for outflow from the slot into a vacuum.

where $Re = V_2(L - \Delta x)/\nu$, $Re_L = V_\infty L/\nu$; $k_{ds} = 8.37/Re^{0.5}$ is the coefficient of displacement velocity at the boundary of the stagnation zone; Δx is the length of the stagnation zone from the point of flow separation to the beginning of the jet; L is the distance from the orifice leading edge to the beginning of the jet; p_2, V_2, and M_2 are the pressure, velocity, and Mach number in the stagnation zone, and can be determined from the conditions of isentropic compression of the air.

Formula (XVI-3-5) is empirical and was obtained for $M_\infty = 4$ for the case of a laminar boundary layer. If the boundary layer is turbulent, we can use the diagrams in Fig. XVI-3-3 instead of Formula (XVI-3-5) to determine k_{ds}, M_2, and p_2/p_∞. The results of comparison of the calculated and experimental data for $M_\infty = 4$ appear in Fig. XVI-3-4 ([69], 1966, No. 1). Certain Supplementary data indicate that the proposed relationships should not be used when $M_\infty \geq 5$ and $p_{0i} \leq 30$ simultaneously. /714

Example. Determine the lateral controlling force for outflow of gas through a slot in a plate for the following data:

$$M_\infty = 1.83;\ V_\infty = 622\ \text{m/s};\quad p_\infty = 1\ \text{kg/cm}^2;$$
$$\nu_\infty = 1.45 \cdot 10^{-5}\ \text{m}^2/\text{s};\quad p_{0i} = 31.2\ \text{kg/cm}^2;\quad k = 1.4;\quad k_n = 1.4;$$
$$M_a = 1;\quad L = 0.17\ \text{m}.$$

The width of the slot $d_n = 10^{-3}$ m, and its length is 10 mm. The Reynolds number corresponding to these data is

$$Re_L = V_\infty L/\nu_\infty = 622 \cdot 0.17/1.45 \cdot 10^{-5} = 7.29 \cdot 10^6.$$

Let us consider the case in which a laminar boundary layer is formed on the plate. Assigning $\Delta x = 0.149$ m, we find

$$\frac{p_2}{p_\infty} = 1 + 1.27 M_\infty^{3/2} Re_L^{-1/4} \left(\frac{L}{L - \Delta x}\right)^{1/4} =$$
$$= 1 + 1.27 \cdot 1.83^{3/2} (7.29 \cdot 10^6)^{-1/4} \left(\frac{0.17}{0.17 - 0.149}\right)^{1/4} = 1.1.$$

Consequently,

$$p_2 = 1.1 p_\infty = 1.1\ \text{kg/cm}^2.$$

From compression-shock theory, knowing $M_\infty = 1.83$ and the pressure behind the shock $p_2 = 1.1$ kg/cm^2, we find

$$M_2 = 1.77 \text{ and } V_2 = 601 \text{ m/s}.$$

The Reynolds number

$$\mathrm{Re} = \frac{V_2 (L - \Delta x)}{\nu_\infty} = \frac{601\,(0.17 - 0.149)}{1.45 \cdot 10^{-5}} = 8.7 \cdot 10^5.$$

We then determine

$$k_{ds} = 8.37/\mathrm{Re}^{0.5} = 8.37/(8.7 \cdot 10^5)^{0.5} = 8.97 \cdot 10^{-3}$$

and find

$$\frac{\Delta x}{d_n} = \frac{1.4 \cdot 1\left(1 + \frac{1.4-1}{2} 1^2\right) e^{\frac{1+1.4}{2(1-1.4)}} \cdot 34.2}{1.4 \cdot 1.1 \cdot 1.77^2 \sqrt{(1.4-1)/2 \cdot 8.97 \cdot 10^{-3}}} = 0.148 \cdot 10^3.$$

From this

$$\Delta x = 0.148 \cdot 10^3 \cdot d_n = 0.148 \cdot 10^3 \cdot 10^{-3} = 0.148 \text{ м}.$$

This value differs little from the assigned $\Delta x = 0.149$ m, so that no further approximations are necessary. From the resulting data, we determine the unknown lateral force

$$\Delta N = (p_2 - p_\infty)\, \Delta x 10^2 = (1.1 - 1)\, 0.148 \cdot 10^2 = 1.48 \text{ kg}.$$

We now consider the case of a fully turbulent boundary layer. From the diagram of Fig. XVI-3-3, we find for $M_\infty = 1.83$

$$k_{ds} = 0.067; \quad M_2 = 1.5; \quad p_2/p_\infty = 1.75.$$

We then calculate $\Delta x/d_n = 17.3$ and find:

$$\Delta x = (\Delta x/d_n)\, d_n = 17.3 \cdot 10^{-3} = 1.73 \cdot 10^{-2} \text{ m}.$$

The lateral force corresponding to these data is

$$\Delta N = (p_2 - p_\infty)\, \Delta x 10^2 = (1.75 - 1.0)\, 1.73 \cdot 10^{-2} \cdot 10^2 = 1.3 \text{ kg}.$$

Controls with Rotating Slot Nozzle on Wing Trailing Edge at Subsonic Speeds /715

When a vehicle leaves a stationary launcher, it is moving at low speed, and this means that the controlling forces developed by aerodynamic controls are also small. Combined controls with a slotted nozzle on the wing trailing edge — a simple jet flap (Fig. XVI3-5a) — are used to increase the control forces. Some versions may use plain flaps with gas blown either over the upper surface (Fig. XVI-3-5b) or simultaneously over the upper and lower surfaces (Fig. XVI-3-5c).

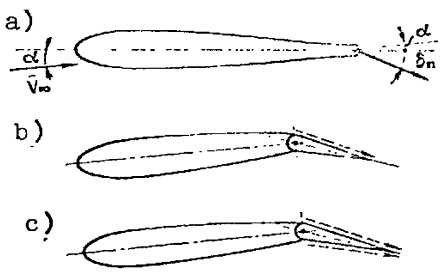

Figure XVI-3-5. Types of Combined Controls. a) simple jet flap; b) flap with gas blown over its upper surface; c) flap with gas blown over both surfaces.

Let us examine experimental data that can be used to calculate the above varieties of the combined control for wings with aspect ratios $\lambda_{wg} > 10$.

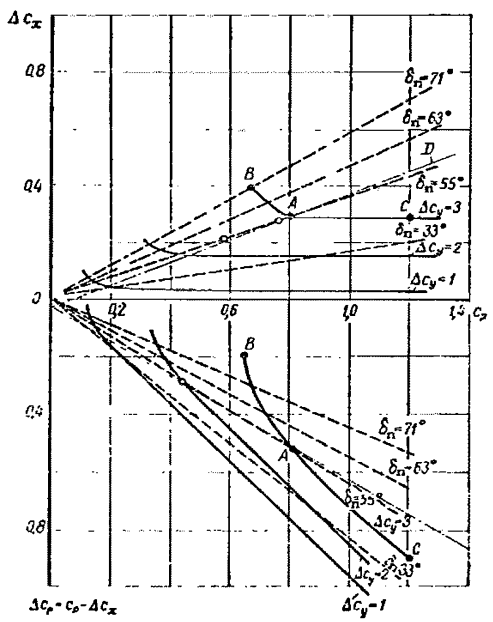

Figure XVI-3-6. Curves of Coefficients of Frontal Drag (Δc_x), Thrust (Δc_P) and Lift (Δc_y) of Wing for Various Values of the Jet Momentum Coefficient c_P and Jet Rotation Angle δ_n.

1. Wing attack angle $\alpha = 0$. The diagram of Fig. XVI-3-6 presents curves of the coefficients of frontal drag Δc_x and thrust $\Delta c_P = c_P - \Delta c_x$ of the wing and the increment in the wing lift coefficient Δc_y owing to action of the gas jet on the air stream. These characteristics are given as functions of the jet momentum coefficient $c_P = mw_a/q_\infty S_{wg}$, where

$\dot{m}$ is the mass flow rate of gas through the nozzle, w_a is the velocity at the exit from the nozzle, q_∞ is the velocity head of the oncoming undisturbed flow, and s_{wg} is the area of the wing in plan, and as functions of jet rotation angle δ_n ([70], 1964, No. 1).

This diagram enables us, for example, to establish that the desired increase in wing lift coefficient can be obtained at the minimum values of Δc_x and c_P. /716

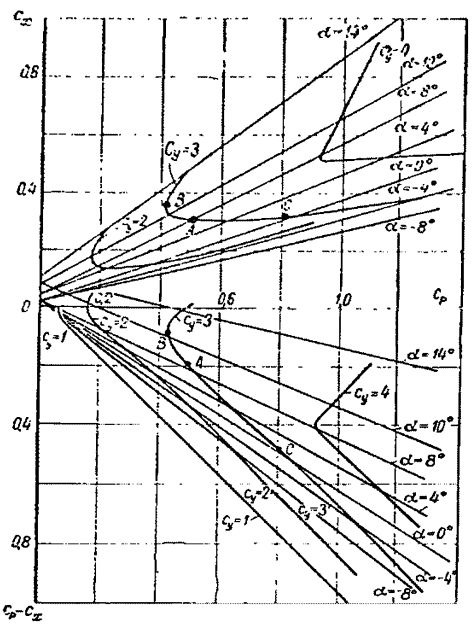

Figure XVI-3-7. Curves of c_x, c_y, and $(c_P - c_x)$ as Functions of c_P and Wing Attack Angle α at $\delta_n = 55°$.

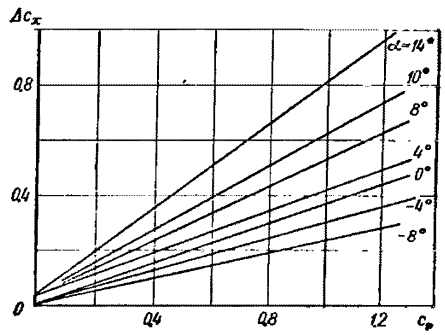

Figure XVI-3-8. Curves of Wing Frontal Drag Coefficient (Δc_x) as Function of c_P and α for $\delta_n = 55°$.

The shape of the Δc_y = = const lines indicates that this requirement can be met by selecting the necessary points where the Δc_y = const lines begin to turn up. The geometrical locus of these points forms line D of operating modes. Below these lines, thrust is fully recovered and the entire reaction force created by outflow of gas through the nozzle is converted into wing thrust regardless of the angle δ_n, while Δc_x remains constant. Outside of this zone, Δc_x increases, since the profile drag of the wing begins to increase.

2. Wing attack angle $\alpha \neq 0$. The cuaracteristics of combined controls can be improved by varying the wing attack angle α.

With increasing α, the c_y and c_x of an ordinary wing increase, although the increase in c_x is comparatively small at small α. For wings with slotted nozzle, an increase in α with δ_n = const further increases c_y, since the vertical component of reaction force increases. Here Δc_x remains unchanged over a broad range of α. It is evident from this that to obtain the desired Δc_y for $\alpha \neq 0$, we can reduce c_P, which ultimately results in a Δc_x smaller than in the case of $\alpha = 0$.

At large attack angles, however, we observe a sharp increase in $c_x(\alpha)$ and flow detachment occurs. All this results in a substantial increase in Δc_x and loss of effectiveness of the combined control device.

Figure XVI-3-7 shows curves of c_x, c_y and $c_P - c_x$ as functions of c_P and α for $\delta_n = 55°$.

In this case, the line of operating modes will be the geometric locus of all points on the c_y = const lines at which the tangents to these lines are parallel to the line of total thrust recovery.

Figure XVI-3-8 shows the variation of wing frontal drag coefficient as a result of mounting a control at various angles of attack and coefficient c_P for $\delta_n = 55°$. /717

The following relationships apply in the range of total thrust recovery:

$$\Delta c_x \quad c_P (C_1 \sin^2 \delta_n + C_2 \sin^2 \alpha); \qquad \text{(XVI-3-6)}$$

$$\Delta c_x \quad \frac{C_1}{K^2} \Delta c_y^2, \qquad \text{(XVI-3-7)}$$

where C_1, C_2 and K are experimentally obtained coefficients.

For a simple jet flap, we may set $C_1 = 0.55$, $C_2 = 7.7$, $K = 3.65 + 0.35 c_P$ (or, approximately, $K = 4$).

For gas-washed flaps, $K = 5.3$ at $\alpha = 0$, and the C_1/K ratios are 0.0270 (flow over the top only) and 0.0225 (flow over both sides).

Example. Determine the parameters of a simple jet flap that provides a wing lift coefficient $\Delta c_y = 3.0$.

TABLE XVI-3-1. CALCULATION OF JET-FLAP PARAMETERS FOR $\alpha = 0$

Point	Δc_y	c_P	Δc_x	Δc_P	δ_n	$\Delta c_y/\Delta c_x$	$\Delta c_y/(c_P \sin \delta_n)$	α
A	3.0	0.80	0.29	0.51	55°	10.3	4.58	0
B	3.0	0.67	0.38	0.29	71°	7.9	4.74	0
C	3.0	1.20	0.29	0.91	44°	10.3	3.64	0

TABLE XVI-3-2. CALCULATION OF JET-FLAP PARAMETERS FOR $\alpha \neq 0$ and $\delta_n = 55°$

Point	c_y	c_P	c_x	Δc_P	n	c_y/c_x	$c_y/(c_P \sin \delta_n)$	α	Δc_x
A	3.0	0.50	0.296	0.204	55°	10.1	6.73	8	0.28
B	3.0	0.42	0.350	0.07	55°	8.57	7.88	10	0.29
C	3.0	0.80	0.312	0.488	55°	9.61	4.58	0	0.29

In the $\alpha = 0$ case, we take a point A at the intersection of the operating-mode line in Fig. XVI-3-6 with the $\Delta c_y = 3$ line and determine from its coordinates $\Delta c_x = 0.29$, $\Delta c_P = 0.51$, $c_P = 0.8$, $\delta_n = 55°$. For comparison, we find the analogous parameters for points B and C, which also endow the wing with $\Delta c_y = 3$. The corresponding data are given in Table XVI-3-1.

We see from Table XVI-3-1 that the operating mode corresponding to point A will be most economical, since Δc_x rises sharply and the wing thrust Δc_P drops under the conditions corresponding to point B; the third point C corresponds, firstly, to a high gas flowrate ($c_P = 1.2$ as against $c_P = 0.8$ at point A), and hence a heavier control, and, secondly, to smaller values of the gain $\Delta c_y/(c_P \sin \delta_n)$.

For $\alpha \neq 0$ and an assigned angle $\delta_n = 55°$, we determine the parameters at points A, B, and C from the diagram of Fig. XVI-3-7 for $\Delta c_y = 3$, and use Fig. XVI-3-8 to find Δc_x. All of the resulting data are listed in Table XVI-3-2.

We see from Table XVI-3-2 that the operating mode corresponding to A, which lies on the line of operating modes, will be most economical.

Comparison of the data of Tables XVI-3-1 and XVI-3-2 indicates that if we set the wing at an angle of attack $\alpha = 8°$, we can obtain the same lift $c_y = 3$ with a substantially lower gas flow ($c_p = 0.5$ as compared to $c_p = 0.8$ for $\alpha = 0$), and, consequently, with a lighter control device. The increase in the frontal drag coefficient Δc_x due to mounting the control on the wing at $\alpha = 8°$ is found to be smaller than for $\alpha = 0$ ($\Delta c_x = 0.28$ and $\Delta c_x = 0.29$, respectively). Note should also be taken of the larger gains for $\alpha \neq 0$. /718

Controls in the Form of a Fixed Slot Nozzle on a Cylindrical Body Surface at Supersonic Speeds

Only empirical relationships that do not take account of Reynolds number for the air stream interacting with the jets issuing from orifices or slots on the body stern section are available for design of controls of this type. Figure XVI-3-9 shows the influence of Re on gain for various ratios of jet stagnation pressure to free-air-stream pressure, p_{0i}/p_1. These data were obtained from wind-tunnel tests in which cold air was blown through a slit 0.38 mm wide perpendicular to the surface. The slot was at a distance of 6.35 mm from the base and ran parallel to the base section between two stabilizers of an "X" configuration. The stabilizers prevented spreading of the flow interacting with the jet and increased controlling force. The velocity of outflow from the slot was sonic. Figure XVI-3-9 indicates a substantial influence of Re on gain at $M_\infty = 6$ ([70], 1965, No.3). /719

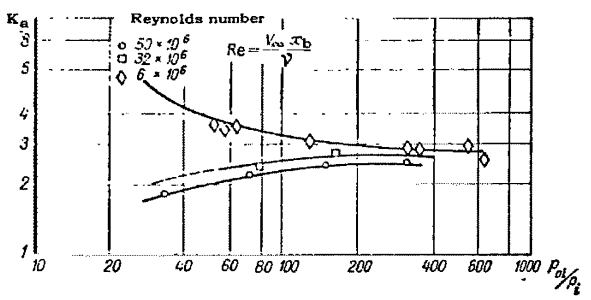

Figure XVI-3-9. Gain as a Function of Ratio of Stagnation Pressure in Jet to Static Pressure in Airstream for Various Re and $M_1 = 6$. ----) extrapolation.

Figure XVI-3-10 shows values of the gain for $Re = 6 \cdot 10^6$ and various attack angles and, consequently, various M_1 of the air flow in front of the slot. These data were obtained for various values of p_{0i}/p_1 for the conditions indicated above. The high

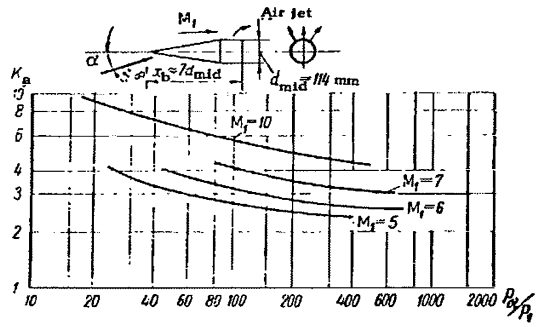

Figure XVI-3-10. Influence of Attack Angle on Gain (Re = $= V_\infty x_b/\nu_\infty = 6 \cdot 10^6$; Boundary Layer Turbulent).

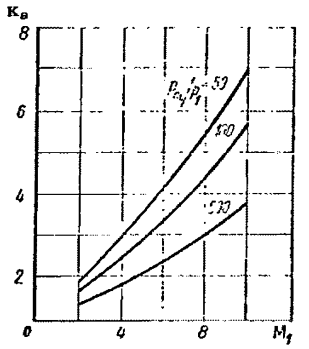

Figure XVI-3-11. Gain as a Function of M_1 and p_{0i}/p_1.

values of K_a for small p_{0i}/p_i and large M_1 confirm that combined controls can be just as effective as aerodynamic controls.

Tentative determinations of gain can be made by referring to Fig. XVI-3-11, which presents experimental data from a number of published papers.

Knowing K_a, we can find the thrust developed by a slot nozzle for a given controlling force and calculate the necessary parameters (slot dimensions, gas flowrate, etc.)

According to experimental data ([76], 1962, No. 4-5), the shape and dimensions of the slot have no substantial influence on K_a, although a trend to increasing K_a is noted as slot width is reduced.

§XVI-4. DETERMINATION OF HINGE MOMENTS OF GASDYNAMIC AND COMBINED CONTROLS

In the general case, the hinge moment M_h can be expressed as follows:

$$M_h = M_{h(\omega=0)} + M_h^d,$$

where $M_{h(\omega=0)}$ is the hinge moment when the control is stationary; M_h^d is the hinge moment due to damping.

In turn,

$$M_{h\,(\omega=0)} = M_{h.i} + M_{h.e} + M_{h.in},$$

where $M_{h.i}$ is the hinge moment determined for the conditions of gas flow through the nozzle in the absence of misalignment and manufacturing errors and with an ideally formed entry into the nozzle; $M_{h.e}$ is the hinge moment that arises from the geometri and gasdynamic eccentricity of the thrust; $M_{h.in}$ is the hinge moment caused by asymmetry of the nozzle entry.

The damping hinge moment appears when the control is rotated at an angular velocity ω. The principal component of the moment is caused by Coriolis forces. M_h^d should be calculated by Formula (XV-4-2), with the appropriate values of the coordinates for the gas inlet and outlet of the rotating part of the control. /720

Certain factors must be borne in mind in determining M_h for the various controls. Firstly, $M_h = 0$ for all controls that have no rotating parts, e.g., for fixed control engines, controls with gas or liquid injection into the supersonic part of a nozzle, and all combination-type controls (except for those shown in Fig. XVI-3-5, b and c). Secondly, it has been found that as a rule, $M_{h.i} = 0$ for rotary engines and nozzles. The only exceptions are nonaxisymmetric nozzle designs, such as those having oblique exit sections.

Theoretical determination of the parameters of certain controls involves calculation of spatial gas flows inside the nozzle when they sweep control elements. Since this is a highly complex calculation, a number of simplifications are adopted. As in calculation of the controlling forces, two-dimensional flows in the plane of rotation of the control are often examined.

When the supersonic section of a nozzle rotates, $M_{h.i} = Y_p \ell_{c.p}$, where $\ell_{c.p}$ is the distance from the rotation axis to the application point of the lateral controlling force Y_p. It can be assumed in first approximation that the force Y_p is applied at the center of the rotating nozzle section.

$M_{h.i}$ is calculated similarly for a deflector, but in this case it is necessary to determine $\ell_{c.p}$ by direct determination of the point of application of Y_p from known values and application points of its components.

For rotary mouthpieces,

$$M_{h.l} = Y_p x_{c.g} - \Delta X y_{c.g},$$

where Y_p is the lateral controlling force, ΔX is the change in the axial thrust component due to the rotary mouthpiece; $x_{c.g}$ and $y_{c.g}$ are the center-of-gravity coordinates of the projections of the surface the pressure on which produces the lateral controlling force onto planes passing through the nozzle axis and perpendicular to this axis, respectively.

Chapter XVII /721

NONSTATIONARY CHARACTERISTICS OF THE VEHICLE

§XVII-1. DETERMINATION OF STABILITY DERIVATIVES FROM SLENDER-BODY AERODYNAMIC THEORY

Working formulas [5]. The stability derivatives of vehicles formed by combining very slender bodies and small-aspect-ratio tail fins can be calculated for moderate supersonic speeds by Formulas (IV-6-11)-(IV-6-45). The coefficients $\bar{A}_{ik}$ and E_{ik} that appear in these formulas depend on the cross-sectional shape of the vehicle and on the manner in which this cross section varies lengthwise.

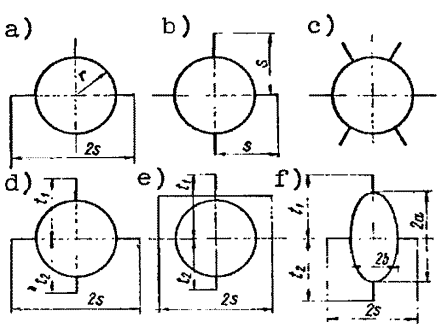

Figure XVII-1-1. Combination of Body with Wings. a) Body and plane wing; b) body and cruciform wing; c) body and six fins; d) body and symmetrical horizontal and unsymmetrical vertical tails; e) body and symmetrical tangent horizontal and unsymmetrical vertical tails; f) elliptical body with symmetrical horizontal and unsymmetrical vertical tails.

A definite attached-mass coefficient λ_{ik} corresponds to each cross-sectional shape. Analyzing the stability-derivative expressions (IV-6-11)-(IV-6-45) we note that only the stability derivative $m_x^{\omega_x}$ (roll damping coefficient) depends on λ_{33}, and that all other derivatives are independent of it.

Let us examine the most commonly encountered cross-sectional shape, that of a combination of a slender solid of revolution of radius $\underline{r}$ with a cruciform wing that has cantilevers of equal size S in the vertical and horizontal planes (Fig. XVII-1-1b). The attached-mass coefficients are

$$\lambda_{11} = \lambda_{22} = \pi\rho_\infty s^2 (1 - r_s^2 + r_s^4);$$
$$\lambda_{12} = \lambda_{13} = \lambda_{23} = 0, \qquad \text{(XVII-1-1)}$$

where $r_s = r/s$.

For the simpler combination of a body and a plane horizontal wing (Fig. XVII-1-1a), the corresponding coefficients can be obtained from (XVII-1-1) in the form

$$\lambda_{11}=\pi\rho_\infty r^2;\ \lambda_{22}=\pi\rho_\infty s^2(1-r_s^2+r_s^4);\ \lambda_{12}=\lambda_{13}=\lambda_{23}=0. \qquad \text{(XVII-1-2)}$$

We present the attached-mass coefficients for certain other cross-sectional shapes. For a circular-section body with three or more fins (in Fig. XVII-1-1c the number of fins n = 6) of the same span s, /722

$$\left.\begin{aligned}\lambda_{11}=\lambda_{22}=2\pi\rho_\infty s^2\left[\left(\frac{1+r_s^n}{2}\right)^{4/n}-\frac{r_s^2}{2}\right];\\ \lambda_{12}=\lambda_{13}=\lambda_{23}=0,\end{aligned}\right\} \qquad \text{(XVII-1-3)}$$

where n is the number of fins.

If a circular-cross-section body is fitted with fins in the midwing configuration and the fin in the upper half-plane has a span t_1 and that in the lower half-plane has a span t_2 (Fig. XVII-1-1d), then

$$\lambda_{11}=\frac{\pi\rho_\infty s^2}{4}\left\{\bar{t}_1^2(1+r_1^4)+\bar{t}_2^2(1+r_2^4)-2(1+r_s^2)^2+\right.$$
$$\left.+2[(1+r_s^2r_1^2)(1+\bar{t}_1^2)(1+r_s^2r_2^2)(1+\bar{t}_2^2)]^{1/2}\right\}; \qquad \text{(XVII-1-4)}$$

$$\lambda_{22}=\pi\rho_\infty s^2(1-r_s^2+r_s^4);\ \lambda_{12}=\lambda_{23}=0, \qquad \text{(XVII-1-5)}$$

where $r_1=r/t_1;\ r_2=r/t_2;\ r_s=r/s;\ \bar{t}_1=t_1/s;\ \bar{t}_2=t_2/s.$

The coefficient λ_{13} is determined from [51]. For a circular-section body with tangential horizontal fins and vertical fins with span t_1 in the upper half-plane and t_2 in the lower (Fig. XVII-1-1e), the attached-mass coefficients are written

$$\lambda_{11}=2\pi\rho_\infty\left\{c^2-\frac{r^2}{2}+\frac{4c^2\sin\lambda\cos^2\frac{\lambda}{2}}{3(\lambda+\sin\lambda)}\left[\sin^2\frac{\lambda}{2}-\frac{3\lambda\cos^2\frac{\lambda}{2}}{\lambda+\sin\lambda}\right]+2(r^2-c^2)\right\}; \qquad \text{(XVII-1-6)}$$

$$\lambda_{22}=2\pi\rho_\infty\left\{c^2-\frac{r^2}{2}-\frac{4c^2\sin\lambda\cos^2\frac{\lambda}{2}}{3(\lambda+\sin\lambda)}\left[\sin^2\frac{\lambda}{2}-\frac{3\lambda\cos^2\frac{\lambda}{2}}{\lambda+\sin\lambda}\right]\right\}; \qquad \text{(XVII-1-7)}$$

$$\lambda_{12}=\lambda_{23}=0. \qquad \text{(XVII-1-8)}$$

The following auxiliary relationships should be used in applying the formulas for λ_{11} and λ_{22}:

$$\left.\begin{aligned} r_s &= \frac{1}{\pi}\left\{\operatorname{arcsh}\left(\frac{\lambda}{2}\operatorname{tg}\frac{\lambda}{2}\right)^{1/2}+\left[\frac{\lambda}{2}\operatorname{tg}\frac{\lambda}{2}+\left(\frac{\lambda}{2}\right)^2\operatorname{tg}^2\frac{\lambda}{2}\right]^{1/2}\right.; \\ \frac{c}{r} &= \frac{\pi}{\lambda+\sin\lambda}; \quad 2+\frac{t_1}{r}=\pi\left(\frac{\lambda}{h/c-1}+\operatorname{arctg}\frac{\sin\lambda}{h/c-\cos\lambda}\right)^{-1}; \\ \frac{t_2}{r} &= \pi\left(\frac{\lambda}{f/c-1}+\operatorname{arctg}\frac{\sin\lambda}{f/c+\cos\lambda}\right)^{-1}; \\ r &= \frac{1}{4}\left(h+\frac{c^2}{h}+f+\frac{c^2}{f}\right). \end{aligned}\right\} \qquad \text{(XVII-1-9)}$$

The attached-mass coefficients for a combination consisting of an elliptical-section body and tail fins (Fig. XVII-1-1f) have the form

$$\lambda_{11} = \pi\rho_\infty(4c^2-k^2-2ab-b^2); \qquad \text{(XVII-1-10)}$$

$$\lambda_{22} = \frac{\pi\rho_\infty}{(a-b)^2}[s^2(a^2+b^2)+2ab^2(a-b)-2abs(s^2-a^2+b^2)^{1/2}]; \qquad \text{(XVII-1-11)}$$

$$\lambda_{12} = \lambda_{13} = 0. \qquad \text{(XVII-1-12)}$$

In these formulas, we have used the nomenclature /723

$$\left.\begin{aligned} k &= \frac{as-b(s^2+a^2-b^2)^{1/2}}{r-b}; \quad c = \frac{f_1+f_2}{4}; \\ f_{1,2}^2 &= k^2+\left[\tau_{1,2}+\frac{(a+b)^2}{4\tau_{1,2}}\right]^2; \quad \tau_{1,2} = \frac{1}{2}[t_{1,2}+(t_{1,2}^2-a^2+b^2)^{1/2}]. \end{aligned}\right\} \qquad \text{(XVII-1-13)}$$

Formula (IV-6-47) is used to determine the values of A_{ik}, including $\overline{A}_{ik}$, from the known attached-mass coefficients for the given combination sectional shape. Then the coefficients B_{ik}, C_{ik} and D_{ik} are calculated by Formula (IV-6-46). In this formula, the lower limit of the integral is equal to the distance from the combination center of gravity to the trailing edge of the tail, and the upper limit is the distance to the cross section of the body at the cantilever leading edges.

To obtain the over-all stability derivative, it is necessary to add to the derivative calculated by the above method for the body-tail combination the derivative for the remaining forward part of the body.

§XVII-2. DAMPING COEFFICIENTS

Roll damping coefficient. In the most general case of motion at angles of attack, the roll-damping coefficient of a given combination is calculated by (IV-6-27) for $m_x^{\omega_x}$. The quantity $\bar{A}_{33}$, which depends on the attached-mass coefficient λ_{33} determined from the base-section parameters, appears in this formula. For one of the most common body-cruciform-tail combinations, the coefficient λ_{33} can be found with the diagram in Fig. XVII-2-1, where we have a curve of the ratio $\bar{A}_{33}/(\bar{A}_{33})_{r=0} = \lambda_{33}/(\lambda_{33})_{r=0}$, in whose denominator the quantity $(\bar{A}_{33})_{r=0} = (\lambda_{33})_{r=0} = 2\rho_\infty s^4/\pi$ for the pure cruciform tail appears. The same Fig. XVII-2-1 shows the curve for a body-and-plane-tail combination, which corresponds to the formula

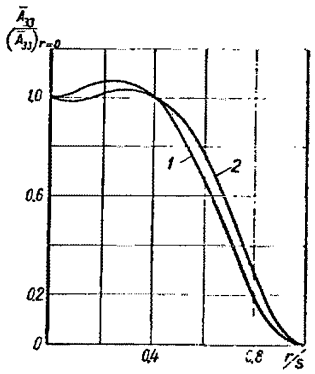

Figure XVII-2-1. Coefficient Used to Calculate Stability Derivatives with Consideration of Interference. 1) Body and plane wing; 2) body and cruciform wing.

$$\lambda_{33} = \frac{\pi\rho_\infty s^4}{8}\left\{\left[(1+r_s^2)^2 \operatorname{arctg}\frac{1}{r_s}\right]^2 + 2r_s(1-r_s^2)(r_s^4-6r_s^2+1)\operatorname{arctg}\frac{1}{r_s} - \pi^2 r_s^4 + r_s^2(1-r_s^2)^2\right\}. \quad \text{(XVII-2-1)}$$

We note that the coefficients λ_{33} are quite close together for the two combinations. Consequently, Formula (XVII-2-1) can also be used with a certain approximation for a combination of the body with a cruciform tail.

The damping coefficient can also be calculated by a simplified method based on the assumption that there are no forms of motion other than the roll, i.e., $\alpha = \beta_{sl} = 0$. In this case, therefore, $\omega_z = \omega_y = 0$ and

/724

$$m_x^{\omega_x} = -4\bar{A}_{33}. \quad \text{(XVII-2-2)}$$

For cruciform and plane combinations, $\bar{A}_{33}$ can be found with the diagram of Fig. XVII-2-1. Here it is more convenient to go from Formula (XVII-2-2) to the expression

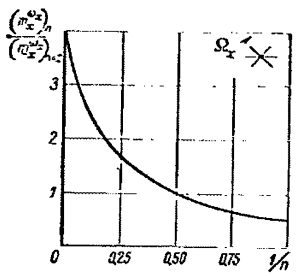

Figure XVII-2-2. Damping Parameter in Roll as a Function of Number of Cantilevers n.

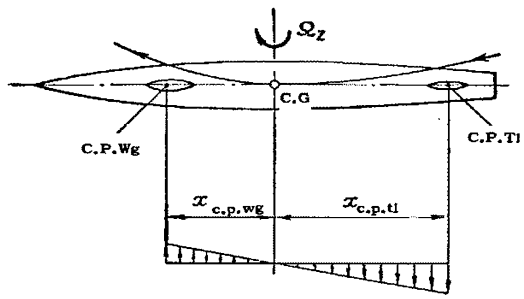

Figure XVII-2-3. Motion of Body-Wing-Tail Combination Along Circular Trajectory (Ω_z is the Angular Velocity).

$$\frac{m_x^{\omega_x}}{(m_x^{\omega_x})_{r=0}} = \frac{\bar{A}_{33}}{(\bar{A}_{33})_{r=0}}, \qquad \text{(XVII-2-3)}$$

where $(m_x^{\omega_x})_{r=0}$ is the damping coefficient of the "pure" tail, i.e., when the body radius r = 0.

The damping coefficient can be found with (XVII-2-3) and Fig. XVII-2-1 as a function of body radius for cases in which the number of cantilevers n = 2 and 4. Cases in which the number of cantilevers is arbitrary may also be of practical interest.

Analysis of the stability derivatives as functions of the number of cantilevers becomes simpler in the extreme case in which the radius $r \to 0$. Studies have shown that this dependence can be represented graphically in the form of a curve (Fig. XVII-2-2) reflecting the variation of the quantity

$$\frac{(m_x^{\omega_x})_n}{(m_x^{\omega_x})_{n=2}} = \frac{(\bar{A}_{33})_n}{(\bar{A}_{33})_{n=2}}. \qquad \text{(XVII-2-4)}$$

The denominator in this expression represents the parameters for a two-cantilever tail (n = 2), while the numerator gives the corresponding parameters for the multicantilever tail. The curve in Fig. XVII-2-2 can also be used for approximate evaluation of the influence of the number of cantilevers on the damping coefficient when the body radius is nonzero but sufficiently small.

Longitudinal damping. Let us consider methods of calculating the longitudinal-damping coefficients on the assumption that the vehicle is moving in the longitudinal plane without slip or

roll. The particular longitudinal-damping characteristics obtained by this calculation are helpful in evaluating vehicle dynamic properties.

Damping governed by angular velocity Ω_z. Let us assume that the vehicle is moving along a circular trajectory (Fig. XVII-2-3). For investigation of longitudinal damping, this motion can be replaced by rotation of the vehicle about its center of gravity at a certain angular velocity Ω_z, which we shall henceforth assume constant. As a result of the rotation, the tail will acquire an additional attack angle of $\Delta\alpha = \Omega_z x_{c.p.tl}/V_\infty$, where $x_{c.p.tl}$ is the distance from the combination center of gravity to the tail center of pressure. A change in attack angle will produce an increment of tail normal force /725

$$\Delta c_{N\,tl} = \left(\frac{\partial c_N}{\partial \alpha}\right)_{tl} \frac{q}{q_\infty} \frac{\Omega_z x_{c.p.tl}}{V_\infty}; \qquad \text{(XVII-2-5)}$$

where the derivative $(\partial c_N/\partial\alpha)_{tl}$ is found from the local M in front of the tail ($q = 0.5kM^2p$ is the velocity head calculated for this M).

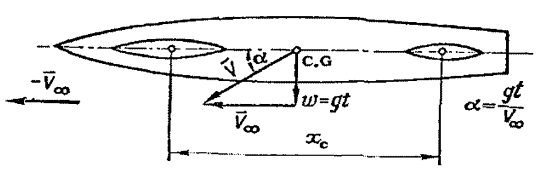

Figure XVII-2-4. Motion of Body-Wing-Tail Combination with Constant $\dot{\alpha} = g/V_\infty$.

The normal-force increment enables us to calculate the rotary derivatives for the normal-force coefficients and the tail damping moment:

$$(c_N^{\omega_z})_{tl} = 2\left(\frac{\partial c_N}{\partial \alpha}\right)_{tl} \frac{q}{q_\infty} \frac{x_{c.p.tl}}{l}; \qquad \text{(XVII-2-6)}$$

$$(m_z^{\omega_z})_{tl} = -2\left(\frac{\partial c_N}{\partial \alpha}\right)_{tl} \frac{q}{q_\infty} \left(\frac{x_{c.p.tl}}{l}\right)^2; \quad \omega_z = \frac{\Omega_z l}{2V_\infty}. \qquad \text{(XVII-2-7)}$$

We find the wing derivatives in the same way:

$$(c_N^{\omega_z})_{wg} = 2\left(\frac{\partial c_N}{\partial \alpha}\right)_{wg} \frac{x_{c.p.wg}}{l}; \qquad \text{(XVII-2-8)}$$

$$(m_z^{\omega_z})_{wg} = -2\left(\frac{\partial c_N}{\partial \alpha}\right)_{wg} \left(\frac{x_{c.p.wg}}{l}\right)^2. \qquad \text{(XVII-2-9)}$$

It is assumed in these formulas that the velocity head in front of the wing is equal to the free-stream velocity head. The over-all effect of the wing and tail on longitudinal damping can be expressed as the sum of the corresponding derivatives.

By analyzing the components of the over-all derivative, we can evaluate the parts played by the wing and tail in damping. The total damping characteristic for body-wing-tail combinations can be obtained with consideration of the isolated-body derivative.

Damping governed by derivative $\dot{\alpha}$. To investigate the damping governed by time variation of the attack angle, we shall use the diagram in Fig. XVII-2-4. The motion under study is characterized by the values $\Omega_z = 0$ and $\dot{\alpha} \neq 0 = \text{const}$ in the absence of rotation but in the presence of displacement (free fall) in the direction of the normal to the trajectory with constant acceleration.

Damping arises as a result of the added moments that appear as a result of time variation of the tail and wing attack angles. Let $\Delta\alpha_{wg}$ be the change in wing attack angle. Then the change in the attack angle of the horizontal tail due to wing downwash is /726

$$\Delta\alpha_{tl} \quad \left(\frac{d\varepsilon}{d\alpha}\right)_n \Delta\alpha_{wg}. \qquad \text{(XVII-2-10)}$$

To find $\Delta\alpha_{wg}$ for a given $\dot{\alpha}$, we can use the principle of downwash lag, according to which the downwash angle at the tail lags behind the wing attack angle by the amount of time taken by the wake in covering the distance from the wing to the tail, which is equal to $t = x_c/V_\infty$. Substituting this time into the expression $\Delta\alpha_{wg} = -\dot{\alpha}t$, we obtain the change in wing attack angle $\Delta\alpha_{wg} = -\dot{\alpha}x_c/V_\infty$. Thus, the attack-angle change for the horizontal tail is $\Delta\alpha_{tl} = (\dot{\alpha}x_c/V_\infty)(d\varepsilon/d\alpha)_{tl}$, where x_c is the distance from the wing center of area to the tail center of area.

A change in tail attack angle by $\Delta\alpha_{tl}$ results in the appearance of an added normal force

$$(\Delta c_N)_{tl} = \left(\frac{\partial c_N}{\partial \alpha}\right)_{tl} \frac{q}{q_\infty} \frac{\dot{\alpha} r_c}{V_\infty} \left(\frac{d\varepsilon}{d\alpha}\right)_{tl}, \qquad \text{(XVII-2-11)}$$

which, if known, can be used to find the stability derivatives:

$$(c_N^{\dot{\bar{\alpha}}})_{tl} = 2\left(\frac{\partial c_N}{\partial \alpha}\right)_{tl}\frac{q}{q_\infty}\left(\frac{d\varepsilon}{d\alpha}\right)_{tl}\frac{x_c}{l}; \qquad \text{(XVII-2-12)}$$

$$(m_z^{\dot{\bar{\alpha}}})_{tl} = -2\left(\frac{\partial c_N}{\partial \alpha}\right)_{tl}\frac{q}{q_\infty}\left(\frac{d\varepsilon}{d\alpha}\right)_{tl}\left(\frac{x_c}{l}\right)^2; \qquad \text{(XVII-2-13)}$$

$$\dot{\bar{\alpha}} = \frac{\dot{\alpha} l}{2V_\infty}.$$

Yaw damping. The technique of calculating longitudinal damping can be used to calculate the stability derivatives of the tail in yawing motion provided that all other forms of motion are absent. Using this method, we can obtain the following values for the stability derivatives:

$$(c_z^{\omega_y})_{tl} = -2\left(\frac{\partial c_z}{\partial \beta_{sl}}\right)_{tl}\frac{q}{q_\infty}\frac{x_{c.p.tl}}{l}; \qquad \text{(XVII-2-14)}$$

$$(m_y^{\omega_y})_{tl} = 2\left(\frac{\partial c_z}{\partial \beta_{sl}}\right)_{tl}\frac{q}{q_\infty}\left(\frac{x_{c.p.tl}}{l}\right)^2; \qquad \text{(XVII-2-15)}$$

$$(c_z^{\dot{\beta}})_{tl} = 2\left(\frac{\partial c_z}{\partial \beta_{sl}}\right)_{tl}\frac{q}{q_\infty}\frac{d\sigma}{d\beta_{sl}}\frac{x_c}{l}; \qquad \text{(XVII-2-16)}$$

$$(m_y^{\dot{\beta}})_{tl} = -2\left(\frac{\partial c_z}{\partial \beta_{sl}}\right)_{tl}\frac{q}{q_\infty}\frac{d\sigma}{d\beta_{sl}}\frac{x_c}{l}\frac{x_{c.p.tl}}{l}, \qquad \text{(XVII-2-17)}$$

where x_c is the distance between the wing and tail centers of area; $d\sigma/d\beta_{sl}$ is the change in the sidewash angle corresponding to a change in slip angle and is calculated in much the same way as the change in downwash angle with attack angle.

§XVII-3. ANALYSIS OF STABILITY DERIVATIVES FOR FINNED BODY

Resolution of given combination into individual elements [51]. The method of calculation set forth above, which is based on use of the attached-mass coefficients, enables us to calculate the over-all values of the stability derivatives. At the same time, practical interest attaches to estimating the contribution of one or another tail element to the total stability-derivative value as a result of interference with the body and mutual interference. In particular, it is important to establish how the body stability derivative changes when vertical and horizontal cantilevers are attached to it. /727

Nor does this method enable us to take account of interference between the tail and wing as it affects the stability derivatives. Finally, it is not possible in calculating the over-all characteristics to establish the dependence of these derivatives on M_∞. The method set forth below for stability-derivative analysis eliminates these shortcomings. Its prime advantage is that it enables us to analyze the individual components of which

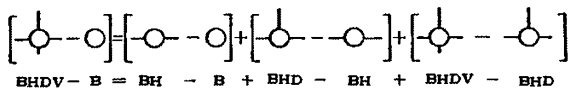

Figure XVII-3-1. Diagram Showing Breakdown of Body-Tail Combination into Elements.

the over-all stability derivative is made up.

For convenience in the interference analysis, it is helpful to break the tail up into individual elements with a view to the known aerodynamic characteristics of each such element. In other words, the tail is conventionally represented as the sum of its individual elements, while the over-all aerodynamic characteristics are presented as sums of the corresponding element aerodynamic characteristics corrected for interference. We shall use the following nomenclature: B for the isolated body; H for the isolated horizontal tail; D for an isolated dorsal tail; V for an isolated ventral tail; TL for the tail.

With these designations, a body-tail combination will be denoted by BHDV, the tail by BHDV-B, and so forth. By way of illustration, Fig. XVII-3-1 shows the dismemberment of a body-tail combination with unlike dorsal and ventral cantilevers. The first term on the right indicates the effect of adding a horizontal tail on the force or moment, and the second and third terms indicate that of the dorsal and ventral cantilevers, respectively. We note that the combination can be broken up in ways other than that indicated in Fig. XVII-3-1.

Static stability derivatives. By way of illustrating the method set forth here, let us examine the determination of the stability derivative of the tail lateral force coefficient with respect to slip angle, considering only interference between the body and the tail. According to Fig. XVII-3-1, the tail lateral force is

$$Z_{TL} = Z_{BHDV} - Z_B + (Z_{BH} - Z_B) + (Z_{BHD} - Z_{BH}) + (Z_{BHDV} - Z_{BHD}) =$$
$$= \frac{Z_{BH} - Z_B}{Z_B} Z_B + \frac{Z_{BHD} - Z_{BH}}{Z_D} Z_D + \frac{Z_{BHDV} - Z_{BHD}}{Z_V} Z_V. \qquad \text{(XVII-3-1)}$$

The interference forces are referred to the forces for the isolated elements, with the isolated body regarded as a sharp solid of revolution with a base cross sectional area equal to the body area at the tail. The lateral force of the isolated dorsal or ventral cantilever is assumed equal to half the lateral force of a tail composed of a pair of identical cantilevers. /728

The differences between the forces in the right member of (XVII-3-1), which are referred to the forces for the isolated elements, represent the interference coefficients

$$\left.\begin{aligned} K_{1B} &= \frac{Z_{BH}-Z_B}{Z_B} = \frac{(\lambda_{11})_{BH}-(\lambda_{11})_B}{(\lambda_{11})_B}; \\ K_{1D} &= \frac{Z_{BHD}-Z_{BH}}{Z_D} = \frac{(\lambda_{11})_{BHD}-(\lambda_{11})_{BH}}{(\lambda_{11})_D}; \\ K_{1V} &= \frac{Z_{BHDV}-Z_{BHD}}{Z_V} = \frac{(\lambda_{11})_{BHDV}-(\lambda_{11})_{BHD}}{(\lambda_{11})_V}. \end{aligned}\right\} \qquad \text{(XVII-3-2)}$$

The values of the attached-mass coefficients λ_{11} were given earlier for a variety of configurations. Converting in (XVII-3-1) from forces to coefficients and calculating the derivative with respect to β_{sl}, we find a formula for the static derivative of lateral force with respect to slip angle :

$$(c_z^\beta)_{TL} = K_{1B}(c_z^\beta)_B + K_{1D}(c_z^\beta)_D + K_{1V}(c_z^\beta)_V. \qquad \text{(XVII-3-3)}$$

The static derivative of the yawing moment for the tail is

$$(m_y^\beta)_{tl} = -\frac{x_{c.m}}{l}(c_z^\beta)_{TL}, \qquad \text{(XVII-3-4)}$$

where $x_{c.m}$ is the distance between the center of moments and the point of application of the tail lateral force.

A peculiarity of Formulas (XVII-3-3) and (XVII-3-4) is that they can also be used for not particularly slender combinations. In this case, the derivatives c_z^β for the isolated elements are calculated by linearized theory, i.e., with consideration of M_∞, and the interference coefficients K_1, which do not depend on M_∞, are found from slender-body theory.

The calculation given above corresponds to the condition $\alpha = 0$. If the attack angle is nonzero, terms proportional to α and reflecting the interaction between the attack and slip angles appear in the expressions for c_z^β and m_y^β for the general case.

The relationships given for c_z^β and m_y^β do not consider the effect of interference of the tail with a wing. In the presence of a wing, this effect can be taken into account by the methods set forth earlier.

Roll damping. According to Fig. XVII-3-1, the roll stability derivative for a finned body is

$$(m_x^{\omega_x})_{TL} = (m_x^{\omega_x})_{BHDV} - (m_x^{\omega_x})_B = [(m_x^{\omega_x})_{BH} - (m_x^{\omega_x})_B] + \\ + [(m_x^{\omega_x})_{BHD} - (m_x^{\omega_x})_{BH}] + [(m_x^{\omega_x})_{BHDV} - (m_x^{\omega_x})_{BHD}]. \qquad \text{(XVII-3-5)}$$

This expression can also be written

$$(m_x^{\omega_x})_{TL} = K_{3H}(m_x^{\omega_x})_H + K_{3D}(m_x^{\omega_x})_D + K_{3V}(m_x^{\omega_x})_V, \qquad \text{(XVII-3-6)}$$

where the K_3 are interference coefficients as follows:

$$\left.\begin{aligned} K_{3H} &= \frac{(\lambda_{33})_{BH} - (\lambda_{33})_B}{(\lambda_{33})_H}; \\ K_{3D} &= \frac{(\lambda_{33})_{BHD} - (\lambda_{33})_{BH}}{(\lambda_{33})_D}; \\ K_{3V} &= \frac{(\lambda_{33})_{BHDV} - (\lambda_{33})_{BHD}}{(\lambda_{33})_V}. \end{aligned}\right\} \qquad \text{(XVII-3-7)}$$

/729

The values of the attached-mass coefficients λ_{33}, on which the K_3 depend, are listed in Fig. XVII-2-1.

The results obtained for $m_X^{\omega_X}$ pertain to the $\alpha = 0$ case. For $\alpha \neq 0$, they can be improved by considering wing and body vortices. Here the vortex system is replaced by a single vortex trailing from the wing and having coordinates determined by the method set forth above. Although the vortex has a tendency to rotate as a result of banking the wing, we can disregard this rotation and consider the displacement of only the tail relative to the vortex. Thus, the influence of the vortex will be examined on the assumption that this effect is determined at any point in time by the position of the tail with respect to the vortex. The results of the calculation can be improved by considering a certain average vortex position. The vortex formed by the body keeps a fixed position that depends only on attack angle. To simplify the calculations, it can be assumed that the vortices from the body and wing do not interact.

Example of stability-derivative calculation. Let us calculate the stability derivatives for the cruciform tail of the vehicle diagrammed in Fig. XV-2-13 for $M_\infty = 2$.

The derivatives $(c_z^\beta)_{TL}$, $(m_y^\beta)_{TL}$. In calculating the derivatives, we shall proceed from Formulas (XVII-3-3) and (XVII-3-4) and determine the interference coefficients from Expressions (XVII-3-2), using the data of Table XV-1-1. The values of the attached-mass coefficients are as follows:

$$(\lambda_{11})_B = (\lambda_{11})_{BH} = \pi\rho_\infty r^2;$$

$$(\lambda_{11})_{BHD} = \frac{\pi\rho_\infty s^2}{4}\left(1+\frac{r^2}{s^2}\right)\left[-\left(1+\frac{r^2}{s^2}\right)+2\sqrt{2}\left(1+\frac{r^4}{s^4}\right)^{1/2}\right];$$

$$(\lambda_{11})_{BHDV} = \pi\rho_\infty s^2\left(1-\frac{r^2}{s^2}+\frac{r^4}{s^4}\right);$$

$$(\lambda_{11})_D = (\lambda_{11})_V = \frac{1}{2}\pi\rho_\infty (s-r)^2.$$

After substituting the r and s values given in Fig. XV-2-13, we obtain

$$(\lambda_{11})_B = (\lambda_{11})_{BH} = 0.316\pi\rho_\infty;\ (\lambda_{11})_{BHD} = 1.56\pi\rho_\infty;$$
$$(\lambda_{11})_{BHDV} = 3\pi\rho_\infty;\quad (\lambda_{11})_D = (\lambda_{11})_V = 0.782\pi\rho_\infty.$$

Introducing these values into (XVII-3-2), we find

$$K_{1B} = 0;\quad K_{1D} = 1.602;\quad K_{1V} = 1.832.$$

To use Formula (XVII-3-3), it is necessary to know the values of $(c_z^\beta)_D$ and $(c_z^\beta)_V$, which can be determined by assuming that they are equal to $-0.5(c_N^\alpha)_H$ (it will be recalled that the dorsal and ventral cantilevers of the tail are identical). Referring the coefficients to the wing plan area S_{wg}, we find

$$(c_z^\beta)_D = (c_z^\beta)_V = -\frac{1}{2}\frac{4}{(M_\infty^2-1)^{1/2}}\frac{S_V}{S_{wg}} = -0.356.$$

After the appropriate substitutions into Eq. (XVII-3-3), we obtain /730

$$(c_z^\beta)_{TL} = 1.602(-0.356)+1.832(-0.356) = -0.571-0.652 = -1.223.$$

We may conclude from these figures that addition of the ventral cantilever to the other three increases the tail lateral force by about 14%.

We determine the static derivative $(m_y^\beta)_{TL}$ from Formula (XVII-3-4), in which we assume $x_{c.m}$ to be equal to the distance between the centers of area of the wing and tail cantilevers. According to Fig. XV-2-13, $x_{c.m} = 4.74$. The characteristic dimension ℓ is equal to the wing mean aerodynamic chord $\ell = (2/3)b_{rt} = 1.50$. After substitution of the numerical values for $(c_z^\beta)_{TL}$, $x_{c.m}$ and ℓ into (XVII-3-4), we obtain

$$(m_y^\beta)_{TL} = \frac{4.74}{1.50} 1.223 = 3.87.$$

The values of $(c_z^\beta)_{TL}$ and $(m_y^\beta)_{TL}$ are found without consideration of wing and body interference, i.e., without consideration of the vortices formed by a slipping body and wing.

The derivative $m_x^{\omega_x}$. It is convenient to use Figs. XVII-2-1 and XVII-2-2 to calculate this derivative. The diagram in Fig. XVII-2-2 enables us to evaluate tail effectiveness in the absence of the body when the number of cantilevers differs from two. It follows from the resulting data that the rolling moment increases by a factor of 1.625 for the case under consideration (n = 4).

The diagram in Fig. XVII-2-1 establishes the influence of the body on the same moment as a function of the parameter r/s. In our example, r/s = 0.31, so that the diagram indicates a 2% rolling-moment increase on addition of the body to the pair of horizontal cantilevers. Accordingly, we have for a four-cantilever tail

$$(m_x^{\omega_x})_{TL} = 1.625 \cdot 1.02 (m_x^{\omega_x})_H,$$

where $(m_x^{\omega_x})_H$ is the rolling moment of the isolated horizontal tail with the span including part of the body.

Linearized theory can be used to determine $m_x^{\omega_x}$ for an isolated horizontal tail composed of a pair of cantilevers:

$$(m_x^{\omega_x})_H = -\frac{11}{3\alpha'} = -\frac{1}{3}\frac{1}{\sqrt{M_\infty^2 - 1}} = -0.192.$$

Counting the area inside the body and the new wingspan, we find

$$(m_x^{\omega_x})_H = -0.192\frac{1.812}{2.812}\left(\frac{1.812}{2.250}\right)^2 = -0.080.$$

Thus, the wing moment due to the tail is

$$(m_x^{\omega_x})_{TL} = 1.625 \cdot 1.02\,(-0.080) = -0.133.$$

The derivatives $(c_N^{\omega_z})_{TL}$, $(m_z^{\omega_z})_{TL}$, $(c_N^{\dot{\alpha}})_{TL}$, $(m_z^{\dot{\alpha}})_{TL}$. We shall calculate $(c_N^{\omega_z})_{TL}$ by Formula (XVII-2-6), in which we set $q = q_\infty$. Using the values found for $(c_N^{\alpha})_{TL} = -(c_Z^{\beta})_{TL} = -1.223$ and $x_{c.p.tl} = 4.74$, we obtain

$$(c_N^{\omega_z})_{TL} = 2 \cdot 1.223 \cdot 1 \cdot \frac{4.74}{1.50} = 7.75.$$

Assuming that the center of moment coincides with the center of gravity, we find from (XVII-2-7): /731

$$(m_z^{\omega_z})_{TL} = -2 \cdot 1.223\left(\frac{4.74}{1.50}\right)^2 = -24.5.$$

The derivatives thus found are referred to $\Omega_z b_{MAC}/2V_\infty$. To calculate the other two derivatives $(c_N^{\dot{\alpha}})_{TL}$ and $(m_Z^{\dot{\alpha}})_{TL}$, we shall use Formulas (XVII-2-12) and (XVII-2-13), in which the derivative $d\varepsilon/d\alpha$, determined from the condition:

$$\eta_H = 1 - \left(\frac{d\varepsilon}{d\alpha}\right)_H,$$

appears.

We found earlier that the effectiveness coefficient $\eta_H = 0.73$, so that $(d\varepsilon/d\alpha)_H = 0.27$. Remembering that the distance between the area centers and the tail $x_c = 4.74$ and assuming that M is the same in front of the tail as in the free stream, we find after substituting these values into (XVII-2-12)

$$(c_N^{\dot{\alpha}})_{TL} = 2 \cdot 1.223 \cdot 0.27\,\frac{4.74}{1.50} = 2.08.$$

Applying (XVII-2-13), we get

$$(m_z^{\dot{\alpha}})_{TL} = -2 \cdot 2.08 \frac{4.74}{1.50} = -6.59.$$

§XVII-4. THE MAGNUS EFFECT

Pitched tail fins. A finned body can be made to rotate about its longitudinal axis of symmetry by mounting the tailplanes at a

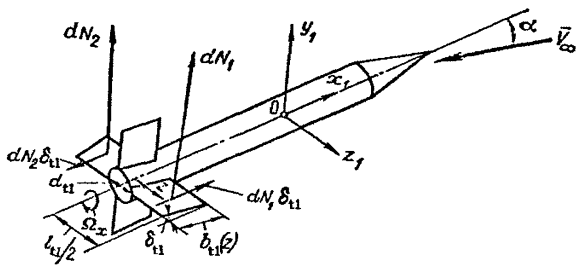

Figure XVII-4-1. Diagram of Flow Around Body with Pitched Tail Fins.

certain angle δ_{TL} to this axis (Fig. XVII-4-1). The rotation produces an additional yawing moment ΔM_y owing to the action of Magnus forces on the pitched tail. For a body with a cruciform tail in the absence of slip, this moment is

$$\Delta M_y = 2q_\infty \delta_{TL} \alpha \int_{d_{TL}/2}^{l_{TL}/2} c_\Lambda^\alpha b_{TL}(z) z\, dz, \qquad \text{(XVII-4-1)}$$

where $b_{TL}(z)$ is the tail chord at a distance z from the body axis; /732
d_{TL} is the diameter of the body at the point of tail attachment;
ℓ_{TL} is the tail span.

The relation between the angle δ_{TL} and the vehicle's angular velocity Ω_x is determined from the expression

$$\delta_{TL} \int_{d_{TL}/2}^{l_{TL}/2} b_{TL}(z) z\, dz = \int_{d_{TL}/2}^{l_{TL}/2} \frac{\Omega_x z}{V_\infty} b_{TL}(z) z\, dz. \qquad \text{(XVII-4-2)}$$

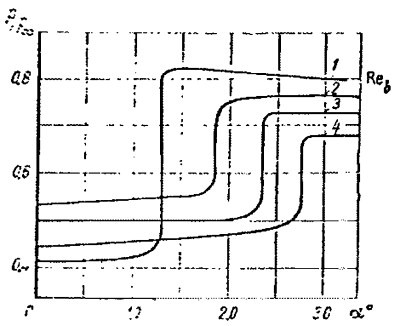

Figure XVII-4-2. Influence of Flow Detachment on Pressure in Flow Around a Flat Plate. 1) $Re_b = 0.5 \cdot 10^6$; 2) $Re_b = 0.7 \cdot 10^6$; 3) $Re_b = 0.9 \cdot 10^6$; 4) $Re_b = 1.3 \cdot 10^6$.

For example, for a rectangular tail

$$\delta_{TL} = \frac{\Omega_x d_{TL}}{3V_\infty}\left(\frac{\lambda_{TL}^2}{\lambda_{TL}+1}+1\right), \quad \text{(XVII-4-3)}$$

where $\lambda_{TL} = \ell_{TL}/d_{TL}$ is the tail aspect ratio.

During rotation of a four-bladed tail with a 90° angle between the blades, the Magnus-force yawing moment will vary as a function of the turn angle γ_1 measured from the horizontal plane in accordance with the expression

$$\Delta M_y = \Delta(M_y)_{\gamma_1=0}(\sin\gamma_1 + \cos\gamma_1), \quad \text{(XVII-4-4)}$$

where $\Delta(M_y)_{\gamma_1=0}$ is the yawing moment corresponding to $\gamma_1 = 0$.

In motion with slip ($\beta_{sl} \neq 0$) at zero angle of attack, a secondary pitching moment appears owing to rotation about the longitudinal axis; it can be calculated by a formula analogous to (XVII-4-1).

Influence of flow separation. The boundary layer may separate from a thin tail ($\bar{s} < 0.05$) in flow at small Mach and Reynolds numbers. The critical attack angle, at which separation occurs, depends on $Re = V_\infty b_{rt}/\nu$ and can be determined from Fig. XVII-4-2 for a thin plate with a laminar boundary layer. Boundary-layer detachment causes a pressure increase and the appearance of an additional moment.

The pressures p_{lft} and p_{rght} on the left and right cantilevers can be determined from Fig. XVII-4-2 when their attack angles are

$$\alpha_{lft} = \alpha + \delta_{TL} - \frac{\Omega_x z}{V_\infty}; \quad \text{(XVII-4-5)}$$

$$\alpha_{rght} = \alpha - \delta_{TL} + \frac{\Omega_x z}{V_\infty}, \quad \text{(XVII-4-6)}$$

where z is the distance from the axis to the cantilever center of gravity.

The pitching moment that results from the difference between the pressures on the left and right cantilevers is /733

$$\Delta M_z = \left(\frac{p_{\text{right}}}{p_\infty} - \frac{p_{\text{left}}}{p_\infty}\right) S_{\text{TL}} p_\infty x_{1\text{TL}}, \qquad \text{(XVII-4-7)}$$

where x_{1TL} is the distance from the vehicle center of gravity to the center of gravity of the tail area.

The vehicle's moment characteristics depend on the interference of the tail with the body. However, studies have shown that the moment from the interference is small and that in approximate calculations, the total Magnus-force moment can be determined from the value for the isolated pitched tail.

Example. Determine the tail setting angle δ_{tl} necessary to impart an angular velocity of $\Omega_x = 5\ s^{-1}$ to a finned body and the Magnus-force yawing moment ΔM_y at $\alpha = 5°$.

The vehicle flies at a speed $V_\infty = 640.8$ m/s ($M_\infty = 2$) at an altitude H = 5 km. The diameter of the body at the tail attachment is $d_{tl} = 0.25$ m, the aspect ratio of the rectangular tail is $\lambda_{tl} = 3$, and its chord $b_{tl} = d_{tl}$. We find from (XVII-4-3)

$$\delta_{tl} = \frac{5 \cdot 0.25}{3 \cdot 640.8}\left(\frac{3^2}{3+1} + 1\right) = 0.00211\ (0°7'16'').$$

According to (XVII-4-1), the moment

$$\Delta M_y = \frac{1}{4} q_\infty \delta_{tl} d_{tl}^3 c_N^\alpha \alpha (\lambda_{tl}^2 - 1).$$

Since

$$c_N^\alpha = 4(M_\infty^2 - 1)^{-1/2};\ q_\infty = 1.54 \cdot 10^4\ \text{kg/cm}^2,$$

we have

$$\Delta M_y = 1.54 \cdot 10^4 \cdot 0{,}00211 \cdot 0.25^3 \frac{5}{57.3} \frac{3^2 - 1}{\sqrt{4-1}} = 0.204\ \text{kg-m}.$$

We calculate the pitching moment due to boundary-layer separation from the stabilizer cantilevers for the conditions

$$\Omega_x = 5\ s^{-1};\quad \alpha = 2.5°;\quad \delta_{tl} = 1°;\quad z = 0.25\ \text{m},\quad V_\infty = 200\ \text{m/s};$$

$$Re_b = 1.3 \cdot 10^6 \ (b = b_{min} = 0.25 \text{ m};\ H \approx 10.7 \text{ km});$$

tail area $S_{tl} = 0.0625$ m^2; distance between centers of gravity of vehicle and tail $x_{1tl} = 0.35$ m; atmospheric pressure $p_\infty = 0.56$ kg/cm^2.

We find from Formulas (XVII-4-5) and (XVII-4-6)

$$\alpha_{lft} = 2.5 + 1 - \frac{5 \cdot 0.25}{200} 57.3 = 3.14°;$$

$$\alpha_{rght} = 2.5 - 1 + \frac{5 \cdot 0.25}{200} 57.3 = 1.86°.$$

We determine $p_{rght}/p_\infty = 0.47$, $p_{lft}/p_\infty = 0.68$ from Fig. XVII-4-2 and calculate the moment from (XVII-4-7):

$$\Delta M_z = (0.47 - 0.68)\ 0.0625 \cdot 0.56 \cdot 10^4 \cdot 0.35 = -25.7 \text{ kg-m}.$$

TABLE VIII-1-1. GASDYNAMIC FUNCTIONS OF AIR IN AXISYMMETRIC FLOW AROUND CONE (k = 1.4).*

$M_\infty = 2$

ξ		$\beta_c°$ 10	15	20	30	ξ		$\beta_c°$ 10	15	20	30
0	V_x	1.5299	1.4356	1.3213	1.0374	0.6	V_x	1.5754	1.5024	1.4057	1.1528
	V_r	0.2697	0.3847	0.4809	0.5989		V_r	0.1029	0.2034	0.3016	0.4577
	p	0.6157	0.7460	0.9103	1.3364		p	0.5691	0.6860	0.8413	1.2765
	ρ	1.2014	1.3773	1.5841	2.0491		ρ	1.1358	1.2973	1.4973	1.9542
0.1	V_x	1.5398	1.4491	1.3379	1.0602	0.8	V_x	1.5885	1.5229	1.4317	1.1859
	V_r	0.2182	0.3376	0.4379	0.5611		V_r	0.0754	0.1661	0.2617	0.4030
	p	0.6121	0.7425	0.9069	1.3323		p	0.5486	0.6651	0.8235	1.2941
	ρ	1.1965	1.3727	1.5798	2.0446		ρ	1.1064	1.2553	1.4490	1.9021
0.2	V_x	1.5483	1.4611	1.3529	1.0810	1.0	V_x	1.6083	1.5495	1.4620	1.2198
	V_r	0.1829	0.3010	0.4026	0.5294		V_r	0.0406	0.1252	0.2294	0.3710
	p	0.6050	0.7316	0.8984	1.3221		p	0.5165	0.6126	0.7554	1.1509
	ρ	1.1864	1.3623	1.5692	2.0335		ρ	1.0598	1.1966	1.3864	1.8417
0.4	V_x	1.5626	1.4825	1.3801	1.1186						
	V_r	0.1356	0.2458	0.3465	0.4784						
	p	0.5877	0.7125	0.8732	1.2906		W_x	0.6077	0.6724	0.7756	1.1137
	ρ	1.1621	1.3329	1.5377	1.9988						

$M_\infty = 3$

ξ		$\beta_c°$ 10	20	30	40	ξ		$\beta_c°$ 10	20	30	40
0	V_x	1.8607	1.6468	1.3439	0.9696	0.2	V_x	1.8734	1.6674	1.3723	1.0062
	V_r	0.3281	0.5994	0.7759	0.8436		V_r	0.2635	0.5459	0.7289	0.7698
	p	0.4749	0.8544	1.4151	2.1170		p	0.4685	0.8475	1.4067	2.1053
	ρ	1.3678	2.0422	2.7580	3.3696		ρ	1.3548	2.0304	2.7462	3.3563
0.1	V_x	1.8673	1.6574	1.3584	0.9895	0.4	V_x	1.8845	1.6865	1.3987	1.0429
	V_r	0.2924	0.5713	0.7514	0.7905		V_r	0.2177	0.5009	0.6885	0.7340
	p	0.4730	0.8525	1.4129	2.1138		p	0.4554	0.8303	1.3850	2.0766
	ρ	1.3640	2.0389	2.7549	3.3660		ρ	1.3275	2.0009	2.7159	3.3235

TABLE VIII-1-1 (Cont'd)

$M_\infty = 3$

ξ		β_c° 10	20	30	40	ξ		β_c° 10	20	30	40
0.6	V_x	1.8951	1.7052	1.4241	1.0750	1.0	V_x	1.9217	1.7461	1.4757	1.1354
	V_r	0.1807	0.4607	0.6525	0.7035		V_r	0.1060	0.3832	0.5864	0.6523
	p	0.4388	0.8057	1.3536	2.0367		p	0.3891	0.7339	1.2651	1.9333
	ρ	1.2927	1.9584	2.6717	3.2777		ρ	1.1863	1.8321	2.5458	3.1580
0.8	V_x	1.9064	1.7246	1.4494	1.1056						
	V_r	0.1466	0.4226	0.6189	0.6766		W_x	0.3983	0.5684	0.8327	1.2702
	p	0.4186	0.7742	1.3136	1.0884						
	ρ	1.2499	1.9033	2.6151	3.2221						

$M_\infty = 5$

ξ		β_c° 10	20	30	40	ξ		β_c° 10	20	30	40
0	V_x	2.1394	1.9189	1.5892	1.1813	0.6	V_x	2.1600	1.9545	1.6433	1.2586
	V_r	0.3772	0.6984	0.9175	0.9913		V_r	0.2764	0.6079	0.8299	0.9462
	p	0.3298	0.7940	1.4990	2.3737		p	0.3095	0.7646	1.4561	2.3123
	ρ	1.8023	3.0370	3.9858	4.5878		ρ	1.7225	2.9562	3.9040	4.5027
0.1	V_x	2.1430	1.9250	1.5986	1.1952	0.8	V_x	2.1672	1.9665	1.6609	1.2825
	V_r	0.3570	0.6818	0.9014	0.9751		V_r	0.2476	0.5803	0.8038	0.8825
	p	0.3290	0.7931	1.4976	2.3716		p	0.2961	0.7437	1.4260	2.2711
	ρ	1.7993	3.0344	3.9831	4.5850		ρ	1.6685	2.8985	3.8160	4.4454
0.2	V_x	2.1465	1.9310	1.6078	1.2085	1.0	V_x	2.1757	1.9792	1.6790	1.3064
	V_r	0.3387	0.6659	0.8861	0.9598		V_r	0.2160	0.5523	0.7779	0.8599
	p	0.3269	0.7903	1.4937	2.3657		p	0.2779	0.7172	1.3881	2.2218
	ρ	1.7911	3.0268	3.9756	4.5768		ρ	1.5946	2.8240	3.7734	4.3761
0.4	V_x	2.1533	1.9428	1.6257	1.2341						
	V_r	0.3060	0.6361	0.8571	0.9318						
	p	0.3198	0.7862	1.4789	2.3443		W_x	0.2796	0.4651	0.7160	1.0811
	ρ	1.7632	2.9991	3.9475	4.5472						

TABLE VIII-1-1 (Cont'd.)

/736

$M_\infty = 7$

ξ		β_c° 10	20	30	40	ξ		β_c° 10	20	30	40
0	V_x	2.2120	2.0177	1.6765	1.2542	0.6	V_x	2.2561	2.0446	1.7216	1.3224
	V_r	0.3953	0.7344	0.9680	1.0524		V_r	0.3231	0.6646	0.8940	0.9763
	p	0.2695	0.7683	1.5316	2.4774		p	0.2566	0.7463	1.4955	2.4221
	ρ	2.3092	3.8706	4.7600	5.2245		ρ	2.2294	3.7911	4.6796	5.1411
0.1	V_x	2.2445	2.0223	1.6843	1.2663	0.8	V_x	2.2610	2.0536	1.7364	1.3440
	V_r	0.3818	0.7219	0.9546	1.0383		V_r	0.3011	0.6427	0.8713	0.9544
	p	0.2691	0.7676	1.5304	2.4754		p	0.2475	0.7303	1.4695	2.3842
	ρ	2.3065	3.8682	4.7576	5.2218		ρ	2.1725	3.7328	4.6214	5.0834
0.2	V_x	2.2468	2.0268	1.6919	1.2780	1.0	V_x	2.2664	2.0631	1.7515	1.3653
	V_r	0.3691	0.7099	0.9418	1.0268		V_r	0.2778	0.6206	0.8489	0.9333
	p	0.2679	0.7656	1.5271	2.4703		p	0.2355	0.7099	1.4370	2.3381
	ρ	2.2990	3.8610	4.7503	5.2139		ρ	2.0968	3.6580	4.5480	5.0130
0.4	V_x	2.2514	2.0357	1.7068	1.3006						
	V_r	0.3454	0.6868	0.9173	0.9996						
	p	0.2634	0.7581	1.5149	2.4512		W_x	0.2408	0.4354	0.6854	1.0372
	ρ	2.2715	3.8339	4.7228	5.1852						

TABLE VIII-2-1. GASDYNAMIC FUNCTIONS OF AIR IN FLOW AROUND CONE AT ATTACK ANGLE (k = 1.4)

$M_\infty = 2$ $\beta_c = 15°$ $\alpha = 5°$

ξ		φ° 0	45	90	135	180	ξ		φ° 0	45	90	135	180
0	V_x	1.3786	1.3927	1.4270	1.4649	1.4825	0.1	V_x	1.3950	1.4084	1.4419	1.4765	1.4908
	V_r	0.3694	0.3732	0.3826	0.3925	0.3972		V_r	0.3120	0.3188	0.3369	0.3586	0.3689
	V_ϕ	0.0000	0.1352	0.2029	0.1513	0.0000		V_ϕ	0.0000	0.1220	0.1808	0.1328	0.0000
	p	0.8674	0.8223	0.7309	0.6675	0.6504		p	0.8627	0.8207	0.7337	0.6687	0.6486
	ρ	1.5322	1.4749	1.3558	1.2707	1.2494		ρ	1.5262	1.4732	1.3606	1.2741	1.2469

TABLE VIII-2-1 (Cont'd.)

$M_\infty = 2$, $\beta_c = 15°$, $\alpha = 5°$

ξ		$\vartheta°$ 0	45	90	135	180	ξ		$\vartheta°$ 0	45	90	135	180
0.2	V_x	1.4093	1.4221	1.4537	1.4857	1.4989	0.8	V_x	1.4800	1.4897	1.5136	1.5377	1.5481
	V_r	0.2670	0.2763	0.3014	0.3312	0.3452		V_r	0.1017	0.1211	0.1706	0.2246	0.2477
	V_ϕ	0.0000	0.1126	0.1654	0.1205	0.0000		V_ϕ	0.0000	0.0900	0.1303	0.0942	0.0000
	p	0.8520	0.8127	0.7299	0.6654	0.6441		p	0.7485	0.7214	0.6611	0.6087	0.5868
	ρ	1.5126	1.4629	1.3558	1.2697	1.2407		ρ	1.3790	1.3437	1.2634	1.1915	1.1636
0.4	V_x	1.4344	1.4460	1.4744	1.5029	1.5147	1.0	V_x	1.5067	1.5159	1.5388	1.5629	1.5746
	V_r	0.1988	0.2123	0.2478	0.2885	0.3071		V_r	0.0551	0.0768	0.1308	0.1880	0.2108
	V_ϕ	0.0000	0.1005	0.1464	0.1059	0.0000		V_ϕ	0.0000	0.0885	0.1279	0.0927	0.0000
	p	0.8223	0.7877	0.7130	0.6517	0.6301		p	0.6996	0.6757	0.6214	0.5722	0.5513
	ρ	1.4749	1.4307	1.3334	1.2510	1.2214		ρ	1.3140	1.2823	1.2087	1.1400	1.1103
0.6	V_x	1.4572	1.4678	1.4937	1.5196	1.5305							
	V_r	0.1467	0.1634	0.2067	0.2551	0.2763							
	V_ϕ	0.0000	0.0938	0.1360	0.0982	0.0000		W_x	0.6081	0.6251	0.6725	0.7315	0.7625
	p	0.7876	0.7569	0.6897	0.6327	0.6119							
	ρ	1.4301	1.3906	1.3022	1.2249	1.1960							

$M_\infty = 2$, $\beta_c = 15°$, $\alpha = 10°$

ξ		$\vartheta°$ 0	45	90	135	180	ξ		$\vartheta°$ 0	45	90	135	180
0	V_x	1.3113	1.3370	1.4041	1.4791	1.5180	0.2	V_x	1.3444	1.3682	1.4292	1.4934	1.5185
	V_r	0.3514	0.3583	0.3762	0.3963	0.4067		V_r	0.2391	0.2553	0.3022	0.3671	0.4067
	V_ϕ	0.0000	0.2503	0.4025	0.3218	0.0000		V_ϕ	0.0000	0.2123	0.3279	0.2483	0.0000
	p	1.0153	0.9039	0.6914	0.5852	0.5821		p	0.9968	0.9034	0.7203	0.6066	0.5813
	ρ	1.7097	1.5735	1.2993	1.1534	1.1542		ρ	1.6874	1.5668	1.3204	1.1678	1.1531
0.1	V_x	1.3289	1.3537	1.4185	1.4887	1.5164	0.4	V_x	1.3717	1.3933	1.4478	1.5041	1.5265
	V_r	0.2890	0.3006	0.3342	0.3814	0.4124		V_r	0.1624	0.1867	0.2547	0.3417	0.3889
	V_ϕ	0.0000	0.2285	0.3594	0.2775	0.0000		V_ϕ	0.0000	0.1915	0.2893	0.2161	0.0000
	p	1.0097	0.9082	0.7120	0.6003	0.5822		p	0.9608	0.8806	0.7191	0.6068	0.5753
	ρ	1.7029	1.5708	1.3026	1.1440	1.1544		ρ	1.6436	1.5423	1.3304	1.1814	1.1446

TABLE VIII-2-1 (Cont'd.)

$M_{\infty} = 2$, $\beta_c = 15°$, $\alpha = 10°$

ξ		φ° 0	45	90	135	180	ξ		φ° 0	45	90	135	180
0.6	V_x	1.3963	1.4157	1.4648	1.5161	1.5374	1.0	V_x	1.4472	1.4634	1.5058	1.5558	1.5758
	V_r	0.1031	0.1344	0.2185	0.3192	0.3700		V_r	0.0021	0.0445	0.1516	0.2657	0.3204
	V_ϕ	0.0000	0.1799	0.2683	0.1994	0.0000		V_ϕ	0.0000	0.1712	0.2516	0.1873	0.0000
	p	0.9185	0.8491	0.7058	0.5983	0.5646		p	0.8161	0.7641	0.6500	0.5500	0.5178
	ρ	1.5916	1.5051	1.3189	1.1744	1.1293		ρ	1.4627	1.3975	1.2478	1.1083	1.0617
0.8	V_x	1.4204	1.4378	1.4822	1.5302	1.5512							
	V_r	0.0522	0.0896	0.1868	0.2972	0.3501							
	V_ϕ	0.0000	0.1737	0.2566	0.1902	0.0000		W_x	0.5636	0.5909	0.6755	0.8037	0.8795
	p	0.8715	0.8118	0.6849	0.5832	0.5487							
	ρ	1.5330	1.4587	1.2940	1.1552	1.1065							

$M_{\infty} = 2$, $\beta_c = 20°$, $\alpha = 5°$

ξ		φ° 0	45	90	135	180	ξ		φ° 0	45	90	135	180
0	V_x	1.2541	1.2703	1.3108	1.3535	1.3787	0.6	V_x	1.3487	1.3626	1.3970	1.4323	1.4471
	V_r	0.4565	0.4623	0.4771	0.4926	0.5018		V_r	0.2498	0.2650	0.3033	0.3452	0.3622
	V_ϕ	0.0000	0.1217	0.1820	0.1360	0.0000		V_ϕ	0.0000	0.0928	0.1346	0.0976	0.0000
	p	1.0615	1.0087	0.8972	0.8112	0.7839		p	0.9759	0.9353	0.8442	0.7634	0.7331
	ρ	1.7613	1.6982	1.5620	1.4534	1.4262		ρ	1.6586	1.6108	1.5065	1.3988	1.3596
0.1	V_x	1.2729	1.2894	1.3304	1.3732	1.3912	0.8	V_x	1.3766	1.3896	1.4221	1.4560	1.4704
	V_r	0.4072	0.4152	0.4359	0.4589	0.4694		V_r	0.2045	0.2219	0.2648	0.3097	0.3290
	V_ϕ	0.0000	0.1138	0.1688	0.1250	0.0000		V_ϕ	0.0000	0.0893	0.1287	0.0930	0.0000
	p	1.0572	1.0066	0.8982	0.8110	0.7815		p	0.9307	0.8936	0.8093	0.7325	0.7030
	ρ	1.7561	1.6970	1.5674	1.4600	1.4231		ρ	1.6033	1.5593	1.4569	1.3581	1.3195
0.2	V_x	1.2899	1.3058	1.3454	1.3864	1.4030	1.0	V_x	1.4073	1.4197	1.4511	1.4851	1.5002
	V_r	0.3665	0.3763	0.4014	0.4295	0.4423		V_r	0.1600	0.1792	0.2256	0.2724	0.2919
	V_ϕ	0.0000	0.1075	0.1584	0.1165	0.0000		V_ϕ	0.0000	0.0872	0.1253	0.0902	0.0000
	p	1.0466	0.9981	0.8931	0.8061	0.7756		p	0.8763	0.8426	0.7645	0.6904	0.6609
	ρ	1.7436	1.6870	1.5615	1.4540	1.4155		ρ	1.5358	1.4952	1.3980	1.3019	1.2625
0.4	V_x	1.3205	1.3354	1.3721	1.4097	1.4253							
	V_r	0.3016	0.3143	0.3468	0.3824	0.3983							
	V_ϕ	0.0000	0.0985	0.1438	0.1048	0.0000		W_x	0.7260	0.7402	0.7788	0.8248	0.8466
	p	1.0152	0.9709	0.8727	0.7882	0.7573							
	ρ	1.7060	1.6540	1.5363	1.4310	1.3915							

TABLE VIII-2-1 (Cont'd.)

$M_{co} = 2$ $\beta_c = 20°$ $\alpha = 10°$

ξ		ϑ° 0	45	90	135	180	ξ		ϑ° 0	45	90	135	180
0	V_x	1.1765	1.2069	1.2857	1.3734	1.4264	0.6	V_x	1.2780	1.3041	1.3765	1.4414	1.4709
	V_r	0.4282	0.4383	0.4680	0.4999	0.5192		V_r	0.2025	0.2322	0.3086	0.3956	0.4353
	V_ϕ	0.0000	0.2293	0.3626	0.2865	0.0000		V_ϕ	0.0000	0.1795	0.2666	0.1985	0.0000
	p	1.2348	1.1084	0.8594	0.7085	0.6828		p	1.1340	1.0443	0.8537	0.7016	0.6516
	ρ	1.9501	1.8053	1.5053	1.3114	1.2931		ρ	1.8350	1.7350	1.5107	1.3177	1.2507
0.1	V_x	1.1968	1.2275	1.3073	1.3952	1.4323	0.8	V_x	1.3073	1.3314	1.3932	1.4611	1.4904
	V_r	0.3750	0.3900	0.4301	0.4791	0.5041		V_r	0.1531	0.1877	0.2743	0.3676	0.4104
	V_ϕ	0.0000	0.2153	0.3349	0.2599	0.0000		V_ϕ	0.0000	0.1737	0.2549	0.1884	0.0000
	p	1.2297	1.1109	0.8735	0.7178	0.6818		p	1.0814	1.0014	0.8272	0.6804	0.6291
	ρ	1.9443	1.8110	1.5311	1.3371	1.2918		ρ	1.7738	1.6812	1.4777	1.2892	1.2198
0.2	V_x	1.2150	1.2451	1.3222	1.4051	1.4391	1.0	V_x	1.3384	1.3604	1.4183	1.4865	1.5189
	V_r	0.3307	0.3491	0.3982	0.4582	0.4890		V_r	0.1059	0.1451	0.2506	0.3373	0.3781
	V_ϕ	0.0000	0.2043	0.3139	0.2403	0.0000		V_ϕ	0.0000	0.1706	0.2477	0.1821	0.0000
	p	1.2172	1.1052	0.8783	0.7208	0.6788		p	1.0205	0.9499	0.7917	0.6482	0.5930
	ρ	1.9302	1.8052	1.5391	1.3424	1.2878		ρ	1.7018	1.6222	1.4323	1.2553	1.1693
0.4	V_x	1.2479	1.2761	1.3476	1.4232	1.4542							
	V_r	0.2595	0.2839	0.3480	0.4236	0.4609							
	V_ϕ	0.0000	0.1890	0.2848	0.2143	0.0000		W_x	0.6927	0.7170	0.7890	0.8894	0.9417
	p	1.1891	1.0800	0.8720	0.7157	0.6680							
	ρ	1.8880	1.7766	1.5330	1.3363	1.2731							

$M_{co} = 2$ $\beta_c = 30°$ $\alpha = 5°$

ξ		ϑ° 0	45	90	135	180	ξ		ϑ° 0	45	90	135	180
0	V_x	0.9499	0.9689	1.0160	1.0652	1.1130	0.1	V_x	0.9752	0.9969	1.0511	1.1082	1.1328
	V_r	0.5484	0.5591	0.5866	0.6150	0.6426		V_r	0.5034	0.5206	0.5661	0.5867	0.6100
	V_ϕ	0.0000	0.1664	0.1567	0.1153	0.0000		V_ϕ	0.0000	0.1046	0.1538	0.1131	0.0000
	p	1.5390	1.4672	1.3229	1.2012	1.1580		p	1.5282	1.4650	1.3220	1.1994	1.1547
	ρ	2.2371	2.1680	2.0135	1.8794	1.8652		ρ	2.2321	2.1693	2.0284	1.9053	1.8605

TABLE VIII-2-1 (Cont'd.)

$M_\infty = 2$						$\beta_c = 30°$						$\alpha = 5°$	
ξ		$\vartheta°$					ξ		$\vartheta°$				
		0	45	90	135	180			0	45	90	135	180
0.2	V_x	0.9983	1.0196	1.0725	1.1275	1.1509	0.8	V_x	1.1126	1.1307	1.1760	1.2238	1.2444
	V_r	0.4711	0.4866	0.5252	0.5655	0.5828		V_r	0.3313	0.3521	0.4023	0.4524	0.4731
	V_ϑ	0.0000	0.1021	0.1498	0.1102	0.0000		V_ϑ	0.0000	0.0927	0.1334	0.0962	0.0000
	p	1.5159	1.4536	1.3145	1.1920	1.1466		p	1.3773	1.3265	1.2077	1.0945	1.0494
	ρ	2.2193	2.1590	2.0216	1.8978	1.8511		ρ	2.0723	2.0235	1.9051	1.7865	1.7376
0.4	V_x	1.0397	1.0600	1.1100	1.1618	1.1837	1.0	V_x	1.1482	1.1653	1.2087	1.2558	1.2766
	V_r	0.4143	0.4319	0.4753	0.5200	0.5390		V_r	0.2971	0.3191	0.3717	0.4231	0.4449
	V_ϑ	0.0000	0.0979	0.1427	0.1043	0.0000		V_ϑ	0.0000	0.0912	0.1305	0.0935	0.0000
	p	1.4783	1.4200	1.2874	1.1672	1.1212		p	1.3178	1.2702	1.1579	1.0479	1.0030
	ρ	2.1798	2.1238	1.9931	1.8700	1.8218		ρ	2.0075	1.9618	1.8490	1.7320	1.6823
0.6	V_x	1.0772	1.0963	1.1438	1.1933	1.2143							
	V_r	0.3693	0.3886	0.4358	0.4836	0.5037							
	V_ϑ	0.0000	0.0949	0.1374	0.0997	0.0000							
	p	1.4310	1.3765	1.2508	1.1339	1.0883		W_x	1.0803	1.0995	1.1248	1.1504	1.1609
	ρ	2.1297	2.0774	1.9530	1.8321	1.7834							

$M_\infty = 3$						$\beta_c = 15°$						$\alpha = 5°$	
ξ		$\vartheta°$					ξ		$\vartheta°$				
		0	45	90	135	180			0	45	90	135	180
0	V_x	1.7049	1.7182	1.7522	1.7891	1.8145	0.2	V_x	1.7238	1.7379	1.7734	1.8108	1.8266
	V_r	0.4568	0.4604	0.4695	0.4794	0.4862		V_r	0.3904	0.3970	0.4142	0.4347	0.4448
	V_ϑ	0.0000	0.1295	0.1902	0.1540	0.0000		V_ϑ	0.0000	0.1207	0.1822	0.1379	0.0000
	p	0.8213	0.7577	0.6263	0.5301	0.5024		p	0.8129	0.7533	0.6277	0.5300	0.4985
	ρ	1.9920	1.8815	1.6422	1.4578	1.4232		ρ	1.9783	1.8781	1.6578	1.4761	1.4152
0.1	V_x	1.7146	1.7289	1.7651	1.8040	1.8206	0.4	V_x	1.7410	1.7545	1.7884	1.8237	1.8384
	V_r	0.4216	0.4268	0.4404	0.4565	0.4643		V_r	0.3363	0.3456	0.3695	0.3971	0.4105
	V_ϑ	0.0000	0.1250	0.1903	0.1456	0.0000		V_ϑ	0.0000	0.1138	0.1692	0.1260	0.0000
	p	0.8190	0.7574	0.6288	0.5314	0.5014		p	0.7929	0.7372	0.6181	0.5216	0.4887
	ρ	1.9889	1.8847	1.6583	1.4781	1.4210		ρ	1.9434	1.8502	1.6411	1.4599	1.3952

TABLE VIII-2-1 (Cont'd.)

$M_\infty = 3$ $\beta_c = 15°$ $\alpha = 5°$

ξ		$\vartheta°$ 0	45	90	135	180	ξ		$\vartheta°$ 0	45	90	135	180
0.6	V_x	1.7576	1.7704	1.8027	1.8364	1.8507	1.0	V_x	1.7933	1.8049	1.8347	1.8682	1.8835
	V_r	0.2893	0.3012	0.3311	0.3641	0.3795		V_r	0.2010	0.2177	0.2571	0.2953	0.3106
	V_ϕ	0.0000	0.1089	0.1599	0.1177	0.0000		V_ϕ	0.0000	0.1036	0.1490	0.1081	0.0000
	p	0.7654	0.7138	0.6016	0.5076	0.4744		p	0.6891	0.6459	0.5481	0.4594	0.4251
	ρ	1.8951	1.8085	0.6103	1.4321	1.3659		ρ	1.7581	1.6842	1.5074	1.3337	1.2631
0.8	V_x	1.7745	1.7867	1.8175	1.8503	1.8644							
	V_r	0.2456	0.2600	0.2952	0.3322	0.3487							
	V_ϕ	0.0000	0.1056	0.1533	0.1119	0.0000		W_x	0.4384	0.4476	0.4735	0.5067	0.5237
	p	0.7315	0.6840	0.5790	0.4882	0.4550							
	ρ	1.8347	1.7545	1.5674	1.3928	1.3259							

$M_\infty = 3$ $\beta_c = 15°$ $\alpha = 10°$

ξ		$\vartheta°$ 0	45	90	135	180	ξ		$\vartheta°$ 0	45	90	135	180
0	V_x	1.6315	1.6558	1.7205	1.7970	1.8522	0.6	V_x	1.6870	1.7105	1.7710	1.8390	1.8672
	V_r	0.4371	0.4437	0.4610	0.4815	0.4963		V_r	0.2576	0.2821	0.3453	0.4179	0.4575
	V_ϕ	0.0000	0.2368	0.3919	0.3338	0.0000		V_ϕ	0.0000	0.2077	0.3139	0.2427	0.0000
	p	1.0437	0.8882	0.5900	0.4206	0.4059		p	0.9763	0.8574	0.6178	0.4432	0.3946
	ρ	2.3214	2.0687	1.5445	1.2128	1.2230		ρ	2.2132	2.0337	1.6345	1.3008	1.1988
0.1	V_x	1.6416	1.6676	1.7363	1.8174	1.8530	0.8	V_x	1.7046	1.7265	1.7830	1.8485	1.8771
	V_r	0.4001	0.4098	0.4365	0.4716	0.4937		V_r	0.2102	0.2407	0.3168	0.3974	0.4376
	V_ϕ	0.0000	0.2297	0.3724	0.3103	0.0000		V_ϕ	0.0000	0.2039	0.3012	0.2286	0.0000
	p	1.0410	0.8919	0.6043	0.4315	0.4057		p	0.9352	0.8281	0.6075	0.4359	0.3830
	ρ	2.3171	2.0831	1.5931	1.2681	1.2228		ρ	2.1463	1.9835	1.6170	1.2857	1.1735
0.2	V_x	1.6513	1.6772	1.7450	1.8226	1.8546	1.0	V_x	1.7236	1.7435	1.7960	1.8615	1.8950
	V_r	0.3669	0.3796	0.4142	0.4596	0.4886		V_r	0.1631	0.1999	0.2885	0.3726	0.4063
	V_ϕ	0.0000	0.2235	0.3565	0.2914	0.0000		V_ϕ	0.0000	0.2022	0.2926	0.2185	0.0000
	p	1.0337	0.8910	0.6134	0.4386	0.4051		p	0.8852	0.7907	0.5898	0.4204	0.3595
	ρ	2.3055	2.0844	1.6165	1.2875	1.2214		ρ	2.0638	1.9221	1.5846	1.2531	1.1215
0.4	V_x	1.6695	1.6945	1.7588	1.8307	1.8598							
	V_r	0.3087	0.3272	0.3767	0.4379	0.4744							
	V_ϕ	0.0000	0.2140	0.3317	0.2626	0.0000		W_x	0.4176	0.4323	0.4789	0.5526	0.5994
	p	1.0096	0.8789	0.6206	0.4446	0.4016							
	ρ	2.2670	2.0678	1.6367	1.3028	1.2139							

TABLE VIII-2-1 (Cont'd.)

$M_\infty = 3$, $\beta_c = 20°$, $\alpha = 5°$

ξ		ϕ = 0°	45	90	135	180
0	V_x	1.5736	1.5885	1.6263	1.6669	1.7076
	V_r	0.5727	0.5782	0.5919	0.6067	0.6215
	V_ϕ	0.0000	0.1132	0.1716	0.1309	0.0000
	ρ	1.0808	1.0044	0.8417	0.7117	0.6686
	ρ	2.3673	2.2466	1.9801	1.7565	1.7347
0.1	V_x	1.5850	1.6027	1.6476	1.6956	1.7164
	V_r	0.5422	0.5496	0.5683	0.5887	0.5978
	V_ϕ	0.0000	0.1137	0.1712	0.1300	0.0000
	p	1.0785	1.0036	0.8427	0.7118	0.6672
	ρ	2.3637	2.2544	2.0111	1.8041	1.7321
0.2	V_x	1.5959	1.6137	1.6581	1.7049	1.7249
	V_r	0.5143	0.5227	0.5438	0.5665	0.5767
	V_ϕ	0.0000	0.1120	0.1688	0.1272	0.0000
	p	1.0723	0.9989	0.8404	0.7092	0.6635
	ρ	2.3540	2.2484	2.0101	1.8040	1.7252
0.4	V_x	1.6168	1.6341	1.6772	1.7222	1.7413
	V_r	0.4644	0.4748	0.5004	0.5272	0.5391
	V_ϕ	0.0000	0.1106	0.1633	0.1213	0.0000
	p	1.0510	0.9811	0.8280	0.6977	0.6508
	ρ	2.3206	2.2211	1.9918	1.7815	1.7016
0.6	V_x	1.6370	1.6537	1.6953	1.7390	1.7577
	V_r	0.4198	0.4321	0.4620	0.4923	0.5052
	V_ϕ	0.0000	0.1086	0.1585	0.1162	0.0000
	p	1.0206	0.9545	0.8078	0.6796	0.6322
	ρ	2.2724	2.1787	1.9585	1.7490	1.6668
0.8	V_x	1.6576	1.6736	1.7136	1.7566	1.7753
	V_r	0.3779	0.3922	0.4264	0.4589	0.4721
	V_ϕ	0.0000	0.1071	0.1545	0.1120	0.0000
	p	0.9821	0.9201	0.7807	0.6553	0.6077
	ρ	2.2108	2.1230	1.9122	1.7045	1.6202
1.0	V_x	1.6797	1.6949	1.7337	1.7769	1.7965
	V_r	0.3360	0.3522	0.3897	0.4234	0.4356
	V_ϕ	0.0000	0.1061	0.1515	0.1086	0.0000
	p	0.9344	0.8770	0.7453	0.6225	0.5738
	ρ	2.1336	2.0518	1.8505	1.6432	1.5553
W_x		0.5457	0.5527	0.5716	0.5941	0.6048

$M_\infty = 3$, $\beta_c = 20°$, $\alpha = 10°$

ξ		ϕ = 0°	45	90	135	180
0	V_x	1.4872	1.5155	1.5893	1.6748	1.7566
	V_r	0.5413	0.5516	0.5785	0.6096	0.6394
	V_ϕ	0.0000	0.2128	0.3428	0.2842	0.0000
	p	1.3423	1.1617	0.8069	0.5745	0.5255
	ρ	2.6884	2.4247	1.8690	1.4662	1.4683
0.1	V_x	1.4993	1.5322	1.6176	1.7167	1.7622
	V_r	0.5088	0.5230	0.5605	0.6026	0.6246
	V_ϕ	0.0000	0.2130	0.3371	0.2762	0.0000
	p	1.3396	1.1640	0.8163	0.5807	0.5248
	ρ	2.6843	2.4449	1.9329	1.5537	1.4663

TABLE VIII-2-1 (Cont'd.)

$M_\infty = 3$		$\beta_c = 20°$						$\alpha = 10°$					
ξ		$\Phi°$					ξ		$\Phi°$				
		0	45	90	135	180			0	45	90	135	180
0.2	V_x	1.5111	1.5442	1.6295	1.7250	1.7677	0.8	V_x	1.5763	1.6055	1.6804	1.7667	1.8064
	V_r	0.4791	0.4957	0.5380	0.5862	0.6111		V_r	0.3326	0.3637	0.4375	0.5068	0.5357
	V_Φ	0.0000	0.2121	0.3316	0.2683	0.0000		V_Φ	0.0000	0.2081	0.3040	0.2275	0.0000
	p	1.3322	1.1618	0.8218	0.5842	0.5228		p	1.2242	1.0887	0.8021	0.5663	0.4859
	ρ	2.6742	2.4467	1.9534	1.5682	1.4628		ρ	2.5170	2.3173	1.9410	1.5424	1.3884
0.4	V_x	1.5333	1.5656	1.6484	1.7400	1.7792	1.0	V_x	1.5992	1.6262	1.6965	1.7826	1.8270
	V_r	0.4256	0.4470	0.5000	0.5571	0.5858		V_r	0.2883	0.3245	0.4087	0.4806	0.5032
	V_Φ	0.0000	0.2102	0.3298	0.2523	0.0000		V_Φ	0.0000	0.2083	0.2984	0.2182	0.0000
	p	1.3067	1.1474	0.8238	0.5847	0.5153		p	1.1685	1.0461	0.7802	0.5470	0.4580
	ρ	2.6376	2.4305	1.9682	1.5746	1.4478		ρ	2.4348	2.2834	1.9058	1.5053	1.3310
0.6	V_x	1.5546	1.5856	1.6647	1.7531	1.7917							
	V_r	0.3776	0.4037	0.4673	0.5314	0.5614							
	V_Φ	0.0000	0.2088	0.3115	0.2387	0.0000							
	p	1.2700	1.1225	0.8166	0.5784	0.5033		W_x	0.5322	0.5444	0.5813	0.6328	0.6608
	ρ	2.5837	2.3962	1.9621	1.5647	1.4237							

$M_\infty = 3$		$\beta_c = 30°$						$\alpha = 5°$					
ξ		$\Phi°$					ξ		$\Phi°$				
		0	45	90	135	180			0	45	90	135	180
0	V_x	1.2480	1.2647	1.3064	1.3502	1.4272	0.2	V_x	1.2786	1.3027	1.3627	1.4258	1.4529
	V_r	0.7206	0.7302	0.7543	0.7795	0.8240		V_r	0.6897	0.6854	0.7239	0.7640	0.7810
	V_Φ	0.0000	0.0950	0.1398	0.1028	0.0000		V_Φ	0.0000	0.1053	0.1549	0.1147	0.0000
	p	1.7089	1.6121	1.3986	1.2148	1.1479		p	1.6989	1.6045	1.3940	1.2095	1.1408
	ρ	3.0491	2.9248	2.6424	2.3895	2.4447		ρ	3.0364	2.9386	2.7143	2.5119	2.4353
0.1	V_x	1.2636	1.2876	1.3475	1.4121	1.4402	0.4	V_x	1.3073	1.3310	1.3898	1.4506	1.4765
	V_r	0.6942	0.7088	0.7454	0.7844	0.8014		V_r	0.6256	0.6428	0.6847	0.7272	0.7450
	V_Φ	0.0000	0.1020	0.1501	0.1112	0.0000		V_Φ	0.0000	0.1091	0.1594	0.1172	0.0000
	p	1.7063	1.6106	1.3983	1.2138	1.1462		p	1.6730	1.5819	1.3764	1.1928	1.1234
	ρ	3.0458	2.9462	2.7142	2.5151	2.4434		ρ	3.0032	2.9114	2.6955	2.4900	2.4080

TABLE VIII-2-1 (Cont'd.)

$M_\infty = 3$ $\theta_c = 30°$ $\alpha = 5°$

ξ		φ° 0	45	90	135	180	ξ		φ° 0	45	90	135	180
0.6	V_x	1.3351	1.3580	1.4149	1.4741	1.4995	1.0	V_x	1.3908	1.4118	1.4651	1.5213	1.5467
	V_r	0.5860	0.6048	0.6497	0.6945	0.7129		V_r	0.5141	0.5358	0.5863	0.6344	0.6534
	V_Φ	0.0000	0.1112	0.1613	0.1176	0.0000		V_Φ	0.0000	0.1138	0.1625	0.1164	0.0000
	p	1.6352	1.5479	1.3490	1.1677	1.0977		p	1.5302	1.4521	1.2689	1.0950	1.0254
	ρ	2.9547	2.8683	2.6600	2.4539	2.3691		ρ	2.8478	2.7423	2.5501	2.3454	2.2566
0.8	V_x	1.3626	1.3846	1.4397	1.4975	1.5224							
	V_r	0.5494	0.5696	0.6175	0.6641	0.6831							
	V_Φ	0.0000	0.1127	0.1621	0.1172	0.0000		W_x	0.8254	0.8293	0.8380	0.8467	0.8498
	p	1.5876	1.5047	1.3132	1.1352	1.0656							
	ρ	2.8929	2.8119	2.6118	2.4060	2.3196							

$M_\infty = 3$ $\beta_c = 30°$ $\alpha = 10°$

ξ		φ° 0	45	90	135	180	ξ		φ° 0	45	90	135	180
0	V_x	1.1392	1.1724	1.2580	1.3535	1.4973	0.6	V_x	1.2333	1.2766	1.3865	1.5069	1.5597
	V_r	0.6577	0.6769	0.7263	0.7814	0.8644		V_r	0.5125	0.5308	0.6425	0.7323	0.7700
	V_Φ	0.0000	0.1872	0.2882	0.2221	0.0000		V_Φ	0.0000	0.2149	0.3175	0.2400	0.0000
	p	2.0196	1.8014	1.3517	1.0156	0.9154		p	1.9330	1.7457	1.3388	0.9906	0.8772
	ρ	3.3111	3.0515	2.4856	2.0264	2.1282		ρ	3.2091	3.0393	2.6297	2.2247	2.0644
0.1	V_x	1.1560	1.2003	1.3152	1.4469	1.5090	0.8	V_x	1.2630	1.3041	1.4092	1.5270	1.5890
	V_r	0.6294	0.6569	0.7276	0.8075	0.8446		V_r	0.4729	0.5150	0.6140	0.7071	0.7443
	V_Φ	0.0000	0.1965	0.2989	0.2329	0.0000		V_Φ	0.0000	0.2193	0.3194	0.2370	0.0000
	p	2.0165	1.8023	1.3573	1.0181	0.9139		p	1.8771	1.7027	1.3158	0.9761	0.8519
	ρ	3.3075	3.0858	2.6022	2.2259	2.1257		ρ	3.1425	2.9901	2.6055	2.1953	2.0216
0.2	V_x	1.1721	1.2175	1.3334	1.4622	1.5198	1.0	V_x	1.2933	1.3317	1.4315	1.5476	1.6024
	V_r	0.6030	0.6332	0.7091	0.7909	0.8273		V_r	0.4350	0.4809	0.5872	0.6828	0.7179
	V_Φ	0.0000	0.2021	0.3063	0.2389	0.0000		V_Φ	0.0000	0.2230	0.3203	0.2334	0.0000
	p	2.0078	1.7983	1.3592	1.0180	0.9100		p	1.8102	1.6498	1.2853	0.9492	0.8191
	ρ	3.2974	3.0887	2.6247	2.2405	2.1191		ρ	3.0621	2.9269	2.5682	2.1541	1.9658
0.4	V_x	1.2032	1.2482	1.3621	1.4860	1.5400							
	V_r	0.5553	0.5898	0.6739	0.7598	0.7971							
	V_Φ	0.0000	0.2096	0.3139	0.2416	0.0000		W_x	0.8257	0.8343	0.8559	0.8753	0.8802
	p	1.9774	1.7783	1.3539	1.0109	0.8966							
	ρ	3.2616	3.0736	2.6385	2.2416	2.0969							

TABLE VIII-2-1 (Cont'd.)

$M_\infty = 5$ $\beta_c = 15°$ $\alpha = 5°$

ξ		$\vartheta°$ 0	45	90	135	180	ξ		$\vartheta°$ 0	45	90	135	180
0	V_x	1.9796	1.9905	2.0186	2.0501	2.0929	0.6	V_x	2.0104	2.0247	2.0607	2.0993	2.1161
	V_r	0.5304	0.5333	0.5409	0.5493	0.5608		V_r	0.4252	0.4346	0.4564	0.4762	0.4843
	V_Φ	0.0000	0.1070	0.1663	0.1316	0.0000		V_Φ	0.0000	0.1202	0.1763	0.1316	0.0000
	p	0.7716	0.6884	0.5168	0.3873	0.3476		p	0.7389	0.6649	0.5069	0.3768	0.3316
	ρ	3.0009	2.7663	2.2538	1.8342	1.8645		ρ	2.9095	2.7426	2.3431	1.9551	1.8026
0.1	V_x	1.9849	1.9995	2.0369	2.0783	2.0969	0.8	V_x	2.0208	2.0346	2.0693	2.1074	2.1245
	V_r	0.5111	0.5157	0.5273	0.5401	0.5461		V_r	0.3933	0.4049	0.4311	0.4529	0.4605
	V_Φ	0.0000	0.1123	0.1722	0.1355	0.0000		V_Φ	0.0000	0.1217	0.1757	0.1285	0.0000
	p	0.7705	0.6885	0.5182	0.3880	0.3471		p	0.7159	0.6463	0.4951	0.3684	0.3199
	ρ	2.9979	2.7967	2.3505	1.9810	1.8623		ρ	2.8447	2.6901	2.3085	1.9179	1.7569
0.2	V_x	1.9900	2.0049	2.0425	2.0831	2.1008	1.0	V_x	2.0320	2.0450	2.0785	2.1166	2.1347
	V_r	0.4927	0.4982	0.5117	0.5260	0.5326		V_r	0.3607	0.3748	0.4056	0.4282	0.4335
	V_Φ	0.0000	0.1150	0.1748	0.1363	0.0000		V_Φ	0.0000	0.1231	0.1749	0.1255	0.0000
	p	0.7674	0.6867	0.5183	0.3876	0.3456		p	0.6868	0.6221	0.4769	0.3518	0.3033
	ρ	2.9894	2.7967	2.3621	1.9864	1.8565		ρ	2.7616	2.6199	2.2575	1.8640	1.6913
0.4	V_x	2.0002	2.0150	2.0520	2.0914	2.1083							
	V_r	0.4580	0.4653	0.4828	0.5001	0.5078							
	V_Φ	0.0000	0.1181	0.1764	0.1345	0.0000		W_x	0.3520	0.3561	0.3676	0.3821	0.3893
	p	0.7561	0.6785	0.5147	0.3839	0.3401							
	ρ	2.9579	2.7787	2.3622	1.9786	1.8353							

$M_\infty = 5$ $\beta_c = 15°$ $\alpha = 10°$

ξ		$\vartheta°$ 0	45	90	135	180	ξ		$\vartheta°$ 0	45	90	135	180
0	V_x	1.8091	1.9197	1.9751	2.0439	2.1279	0.1	V_x	1.9048	1.9312	2.0004	2.0853	2.1297
	V_r	0.5089	0.5144	0.5292	0.5477	0.5702		V_r	0.4882	0.4970	0.5203	0.5477	0.5639
	V_Φ	0.0000	0.2011	0.3346	0.3070	0.0000		V_Φ	0.0000	0.2083	0.3356	0.2977	0.0000
	p	1.0700	0.8668	0.4897	0.2623	0.2296		p	1.0687	0.8694	0.4976	0.2682	0.2297
	ρ	3.5095	3.0193	2.0079	1.2855	1.4016		ρ	3.5063	3.0757	2.1582	1.4800	1.4008

TABLE VIII-2-1 (Cont'd.)

$M_{\infty} = 5$ $\beta_c = 15°$ $\alpha = 10°$

ξ		$\Phi°$ 0	45	90	135	180	ξ		$\Phi°$ 0	45	90	135	180
	V_x	1.9104	1.9377	2.0082	2.0919	2.1312		V_x	1.9439	1.9689	2.0318	2.1070	2.1450
	V_r	0.4682	0.4794	0.5084	0.5398	0.5587		V_r	0.3587	0.3865	0.4527	0.5047	0.5291
0.2	V_Φ	0.0000	0.2135	0.3382	0.2948	0.0000	0.8	V_Φ	0.0000	0.2352	0.3469	0.2666	0.0000
	p	1.0648	0.8700	0.5044	0.2732	0.2290		p	0.9984	0.8392	0.5241	0.2893	0.2172
	ρ	3.4973	3.0931	2.2454	1.5308	1.3988		ρ	3.3401	3.0618	2.3661	1.6354	1.3469
	V_x	1.9214	1.9488	2.0184	2.0987	2.1347		V_x	1.9561	1.9790	2.0374	2.1106	2.1546
	V_r	0.4303	0.4464	0.4871	0.5259	0.5478		V_r	0.3228	0.3574	0.4378	0.4956	0.4972
0.4	V_Φ	0.0000	0.2218	0.3405	0.2843	0.0000	1.0	V_Φ	0.0000	0.2413	0.3407	0.2493	0.0000
	p	1.0505	0.8659	0.5146	0.2811	0.2270		p	0.9008	0.8168	0.5241	0.2906	0.2052
	ρ	3.4636	3.1037	2.2903	1.5866	1.3903		ρ	3.2496	3.0130	2.3801	1.6437	1.2934
	V_x	1.9325	1.9590	2.0257	2.1032	2.1391							
	V_r	0.3941	0.4158	0.4688	0.5145	0.5353							
0.6	V_Φ	0.0000	0.2288	0.3411	0.2724	0.0000							
	p	1.0282	0.8554	0.5210	0.2863	0.2234		W_x	0.3460	0.3530	0.3763	0.4140	0.4363
	ρ	3.4109	3.0920	2.3374	1.6177	1.3743							

$M_{\infty} = 5$ $\beta_c = 20°$ $\alpha = 5°$

ξ		$\Phi°$ 0	45	90	135	180	ξ		$\Phi°$ 0	45	90	135	180
	V_x	1.8389	1.8510	1.8819	1.9158	1.9330		V_x	1.8522	1.8714	1.9198	1.9714	1.9938
	V_r	0.6663	0.6737	0.6850	0.6973	0.7247		V_r	0.6338	0.6421	0.6625	0.6837	0.6928
0	V_Φ	0.0000	0.0935	0.1414	0.1073	0.0000	0.2	V_Φ	0.0000	0.1090	0.1624	0.1233	0.0000
	p	1.0968	0.9955	0.7800	0.6060	0.5469		p	1.0920	0.9928	0.7798	0.6049	0.5442
	ρ	3.5371	3.3006	2.7729	2.3155	2.4749		ρ	3.5262	3.3516	2.9523	2.5956	2.4659
	V_x	1.8456	1.8645	1.9125	1.9650	1.9885		V_x	1.8652	1.8845	1.9323	1.9825	2.0040
	V_r	0.6512	0.6587	0.6775	0.6977	0.7067		V_r	0.6004	0.6104	0.6341	0.6574	0.6671
0.1	V_Φ	0.0000	0.1034	0.1548	0.1178	0.0000	0.4	V_Φ	0.0000	0.1163	0.1714	0.1283	0.0000
	p	1.0955	0.9951	0.7807	0.6061	0.5462		p	1.0789	0.9825	0.7738	0.5989	0.5369
	ρ	3.5343	3.3508	2.9393	2.5898	2.4725		ρ	3.4959	3.3346	2.9523	2.5862	2.4422

TABLE VIII-2-1 (Cont'd.)

$M_\infty = 5$ $\beta_c = 20°$ $\alpha = 5°$

ξ		φ° 0	45	90	135	180
0.6	V_x	1.8783	1.8971	1.9438	1.9930	2.0142
	V_r	0.5686	0.5803	0.6076	0.6329	0.6430
	V_φ	0.0000	0.1214	0.1768	0.1304	0.0000
	p	1.0584	0.9657	0.7627	0.5888	0.5257
	ρ	3.4483	3.2986	2.9317	2.5595	2.4058
0.8	V_x	1.8917	1.9099	1.9552	2.0036	2.0248
	V_r	0.5375	0.5511	0.5820	0.6092	0.6192
	V_φ	0.0000	0.1254	0.1804	0.1311	0.0000
	p	1.0302	0.9427	0.7408	0.5747	0.5106
	ρ	3.3841	3.2458	2.8947	2.5185	2.3563

ξ		φ° 0	45	90	135	180
1.0	V_x	1.9058	1.9232	1.9669	2.0148	2.0364
	V_r	0.5061	0.5217	0.5565	0.5851	0.5943
	V_φ	0.0000	0.1286	0.1830	0.1310	0.0000
	p	0.9961	0.9131	0.7258	0.5560	0.4998
	ρ	3.3020	3.1755	2.8413	2.4619	2.2906
	W_x	0.4590	0.4616	0.4684	0.4756	0.4786

$M_\infty = 5$ $\beta_c = 20°$ $\alpha = 10°$

ξ		φ° 0	45	90	135	180
0	V_x	1.7432	1.7672	1.8310	1.9079	2.0317
	V_r	0.6345	0.6432	0.6664	0.6944	0.7395
	V_φ	0.0000	0.1831	0.2945	0.2479	0.0000
	p	1.4452	1.2064	0.7439	0.4356	0.3621
	ρ	3.9538	3.4754	2.4604	1.6789	1.9125
0.1	V_x	1.7505	1.7850	1.8748	1.9817	2.0362
	V_r	0.6148	0.6289	0.6650	0.7066	0.7274
	V_φ	0.0000	0.1969	0.3066	0.2536	0.0000
	p	1.4437	1.2081	0.7494	0.4389	5.3616
	ρ	3.9509	3.5559	2.6932	2.0308	1.9107
0.2	V_x	1.7577	1.7936	1.8855	1.9909	2.0402
	V_r	0.5957	0.6120	0.6531	0.6965	0.7169
	V_φ	0.0000	0.2065	0.3181	0.2617	0.0000
	p	1.4393	1.2077	0.7540	0.4415	0.3604
	ρ	3.9424	3.5748	2.7536	2.0808	1.9059
0.4	V_x	1.7721	1.8084	1.8999	2.0021	2.0479
	V_r	0.5590	0.5797	0.6298	0.6771	0.6980
	V_φ	0.0000	0.2213	0.3337	0.2673	0.0000
	p	1.4228	1.2005	0.7600	0.4446	0.3559
	ρ	3.9101	3.5801	2.8268	2.1273	1.8802

ξ		φ° 0	45	90	135	180
0.6	V_x	1.7866	1.8220	1.9109	2.0105	2.0558
	V_r	0.5236	0.5490	0.6087	0.6601	0.6798
	V_φ	0.0000	0.2330	0.3442	0.2671	0.0000
	p	1.3968	1.1868	0.7623	0.4451	0.3490
	ρ	3.8589	3.5741	2.8697	2.1464	1.8629
0.8	V_x	1.8016	1.8352	1.9202	2.0178	2.0645
	V_r	0.4888	0.5193	0.5895	0.6548	0.6611
	V_φ	0.0000	0.2431	0.3518	0.2644	0.0000
	p	1.3617	1.1656	0.7611	0.4434	0.3392
	ρ	3.7894	3.5429	2.8933	2.1507	1.8253
1.0	V_x	1.8173	1.8487	1.9288	2.0248	2.0751
	V_r	0.4537	0.4898	0.5714	0.6305	0.6394
	V_φ	0.0000	0.2520	0.3577	0.2603	0.0000
	p	1.3172	1.1372	0.7565	0.4396	0.3249
	ρ	3.7005	3.4929	2.9014	2.1441	1.7700
	W_x	0.4571	0.4624	0.4782	0.4983	0.5055

TABLE VIII-2-1 (Cont'd.)

$M_{\infty} = 5$ $\beta_c = 30°$ $\alpha = 5°$

ξ		φ° 0	45	90	135	180	ξ		φ° 0	45	90	135	180
0	V_x	1.4831	1.4968	1.5315	1.5680	1.6806	0.6	V_x	1.5436	1.5606	1.6339	1.7063	1.7284
	V_r	0.8563	0.8642	0.8842	0.9053	0.9703		V_r	0.7584	0.7784	0.8260	0.8732	0.8928
	V_ϕ	0.0000	0.0805	0.1172	0.0844	0.0000		V_ϕ	0.0000	0.1249	0.1809	0.1319	0.0000
	p	1.8898	1.7612	1.4770	1.2326	1.1429		p	1.8360	1.7160	1.4453	1.2020	1.1098
	ρ	4.3129	4.1011	3.6177	3.1783	3.5809		ρ	4.2248	4.1212	3.8684	3.6127	3.5065
0.1	V_x	1.4934	1.5196	1.5860	1.6577	1.6892	0.8	V_x	1.5637	1.5889	1.6513	1.7161	1.7437
	V_r	0.8387	0.8545	0.8943	0.9369	0.9555		V_r	0.7287	0.7501	0.8008	0.8501	0.8702
	V_ϕ	0.0000	0.0959	0.1397	0.1025	0.0000		V_ϕ	0.0000	0.1315	0.1892	0.1369	0.0000
	p	1.8882	1.7602	1.4774	1.2320	1.1418		p	1.7976	1.6825	1.4198	1.1794	1.0869
	ρ	4.3101	4.1751	3.8802	3.6478	3.5783		ρ	4.1615	4.0678	3.8283	3.5685	3.4548
0.2	V_x	1.5035	1.5303	1.5969	1.6672	1.6975	1.0	V_x	1.5844	1.6086	1.6688	1.7321	1.7594
	V_r	0.8217	0.8385	0.8800	0.9233	0.9418		V_r	0.6993	0.7223	0.7762	0.8274	0.8478
	V_ϕ	0.0000	0.1046	0.1527	0.1126	0.0000		V_ϕ	0.0000	0.1368	0.1956	0.1504	0.0000
	p	1.8833	1.7564	1.4750	1.2294	1.1386		p	1.7497	1.6404	1.3875	1.1510	1.0584
	ρ	4.3021	4.1759	3.8932	3.6534	3.5713		ρ	4.0820	3.9980	3.7725	3.5102	3.3898
0.4	V_x	1.5236	1.5503	1.6161	1.6843	1.7132							
	V_r	0.7892	0.8076	0.8523	0.8974	0.9164							
	V_ϕ	0.0000	0.1165	0.1696	0.1246	0.0000							
	p	1.8648	1.7409	1.4638	1.2188	1.1271		W_x	0.7192	0.7197	0.7200	0.7184	0.7170
	ρ	4.2720	4.1581	3.8917	3.6422	3.5456							

$M_{\infty} = 5$ $\beta_c = 30°$ $\alpha = 10°$

ξ		φ° 0	45	90	135	180	ξ		φ° 0	45	90	135	180
0	V_x	1.3628	1.3916	1.4670	1.5523	1.7569	0.1	V_x	1.3741	1.4224	1.5476	1.6939	1.7648
	V_r	0.7868	0.8034	0.8470	0.8962	1.0143		V_r	0.7675	0.7969	0.8726	0.9584	1.0008
	V_ϕ	0.0000	0.1648	0.2508	0.1858	0.0000		V_ϕ	0.0000	0.1870	0.2789	0.2127	0.0000
	p	2.3023	2.0125	1.4173	0.9701	0.8333		p	2.3003	2.0132	1.4208	0.9715	0.8324
	ρ	4.5738	4.1546	3.2342	2.4670	3.0955		ρ	4.5709	4.2627	3.5965	3.1384	3.0931

TABLE VIII-2-1 (Cont'd.)

$M_\infty = 5$, $\beta_c = 30°$, $\alpha = 10°$

ξ		φ° 0	45	90	135	180	ξ		φ° 0	45	90	135	180
0.2	V_x	1.3853	1.4355	1.5635	1.7068	1.7720	0.8	V_x	1.4528	1.5006	1.6212	1.7532	1.8111
	V_r	0.7487	0.7810	0.8619	0.9494	0.9888		V_r	0.6450	0.6895	0.7934	0.8897	0.9286
	V_ϕ	0.0000	0.2019	0.3012	0.2328	0.0000		V_ϕ	0.0000	0.2554	0.3714	0.2768	0.0000
	p	2.2944	2.0110	1.4230	0.9717	0.8300		p	2.1890	1.9428	1.4059	0.9514	0.7926
	ρ	4.5625	4.2813	3.6600	3.1900	3.0867		ρ	4.4118	4.2399	3.7787	3.2354	2.9867
0.4	V_x	1.4077	1.4585	1.5864	1.7250	1.7854	1.0	V_x	1.4763	1.5213	1.6365	1.7659	1.8245
	V_r	0.7127	0.7493	0.8383	0.9283	0.9672		V_r	0.6120	0.6606	0.7724	0.8720	0.9096
	V_ϕ	0.0000	0.2241	0.3323	0.2557	0.0000		V_ϕ	0.0000	0.2675	0.3849	0.2819	0.0000
	p	2.2719	1.9983	1.4228	0.9689	0.8216		p	2.1296	1.9006	1.3897	0.9373	0.7719
	ρ	4.5304	4.2000	3.7302	3.2328	3.0043		ρ	4.3259	4.1870	3.7747	3.2136	2.9306
0.6	V_x	1.4301	1.4798	1.6048	1.7398	1.7983							
	V_r	0.6783	0.7180	0.8153	0.9083	0.9474							
	V_ϕ	0.0000	0.2412	0.3544	0.2687	0.0000		W_x	0.7256	0.7280	0.7323	0.7391	0.7242
	p	2.2364	1.9754	1.4170	0.9620	0.8090							
	ρ	4.4799	4.2746	3.7654	3.2433	3.0308							

$M_\infty = 7$, $\beta_c = 15°$, $\alpha = 5°$

ξ		φ° 0	45	90	135	180	ξ		φ° 0	45	90	135	180
0	V_x	2.0796	2.0889	2.1131	2.1406	2.1953	0.2	V_x	2.0871	2.1023	2.1408	2.1826	2.2011
	V_r	0.5572	0.5597	0.5662	0.5736	0.5882		V_r	0.5296	0.5350	0.5482	0.5615	0.5674
	V_ϕ	0.0000	0.0925	0.1430	0.1118	0.0000		V_ϕ	0.0000	0.1092	0.1645	0.1280	0.0000
	p	0.7536	0.6586	0.4695	0.3267	0.2823		p	0.7478	0.6576	0.4708	0.3270	0.2810
	ρ	3.8496	3.5063	2.7533	2.4252	2.3685		ρ	3.8391	3.5913	3.0250	2.5205	2.3603
0.1	V_x	2.0833	2.0982	2.1361	2.1787	2.1983	0.4	V_x	2.0947	2.1100	2.1482	2.1888	2.2065
	V_r	0.5433	0.5478	0.5593	0.5717	0.5774		V_r	0.5032	0.5103	0.5271	0.5425	0.5488
	V_ϕ	0.0000	0.1029	0.1560	0.1220	0.0000		V_ϕ	0.0000	0.1180	0.1751	0.1338	0.0000
	p	0.7499	0.6537	0.4705	0.3272	0.2820		p	0.7396	0.6522	0.4691	0.3250	0.2774
	ρ	3.8469	3.5835	2.9049	2.5107	2.3663		ρ	3.8091	3.5846	3.0495	2.5364	2.3386

TABLE VIII-2-1 (Cont'd.)

$M_{\infty} = 7$ $\beta_c = 15°$ $\alpha = 5°$

ξ		θ° 0	45	90	135	180	ξ		θ° 0	45	90	135	180
0.6	V_x	2.1023	2.1173	2.1546	2.1945	2.2149	1.0	V_x	2.1185	2.1322	2.1670	2.2058	2.2240
	V_r	0.4775	0.4866	0.5073	0.5248	0.5312		V_r	0.4261	0.4399	0.4697	0.4904	0.4945
	V_ϕ	0.0000	0.1245	0.1820	0.1364	0.0000		V_ϕ	0.0000	0.1341	0.1905	0.1368	0.0000
	p	0.7266	0.6927	0.4648	0.3209	0.2717		p	0.6860	0.6115	0.4481	0.3063	0.2536
	ρ	3.7610	3.5570	3.0489	2.5228	2.3047		ρ	3.6100	3.4461	2.9946	2.4499	2.1939
0.8	V_x	2.1102	2.1246	2.1608	2.2000	2.2176							
	V_r	0.4520	0.4634	0.4884	0.5077	0.5135							
	V_ϕ	0.0000	0.1297	0.1868	0.1369	0.0000		W_x	0.3272	0.3293	0.3353	0.3422	0.3450
	p	0.7088	0.6292	0.4578	0.3147	0.2640							
	ρ	3.6952	3.5110	3.0302	2.4940	2.2578							

$M_{\infty} = 7$ $\beta_c = 15°$ $\alpha = 10°$

ξ		θ° 0	45	90	135	180	ξ		θ° 0	45	90	135	180
0	V_x	1.9958	2.0142	2.0644	2.1285	2.2283	0.6	V_x	2.0216	2.0396	2.1191	2.1986	2.2376
	V_r	0.5348	0.5397	0.5532	0.5703	0.5971		V_r	0.4440	0.4651	0.5162	0.5556	0.5662
	V_ϕ	0.0000	0.1810	0.3008	0.2808	0.0000		V_ϕ	0.0000	0.2370	0.3489	0.2770	0.0000
	p	1.0798	0.8544	0.4426	0.1974	0.1560		p	1.0471	0.8494	0.4728	0.2184	0.1518
	ρ	4.3666	3.6941	2.3094	1.2971	1.6110		ρ	4.2717	3.8957	2.9513	1.9568	1.5801
0.1	V_x	2.0000	2.0267	2.0959	2.1809	2.2302	0.8	V_x	2.0308	2.0573	2.1233	2.2003	2.2415
	V_r	0.5191	0.5278	0.5504	0.5763	0.5903		V_r	0.4145	0.4416	0.5059	0.5517	0.5549
	V_ϕ	0.0000	0.1917	0.3081	0.2709	0.0000		V_ϕ	0.0000	0.2500	0.3594	0.2734	0.0000
	p	1.0788	0.8564	0.4482	0.2010	0.1538		p	1.0225	0.2388	0.4810	0.2251	0.1480
	ρ	4.3638	3.8072	2.5978	1.6692	1.6102		ρ	4.1999	3.8892	3.0424	2.0290	1.5520
0.2	V_x	2.0043	2.0322	2.1038	2.1886	2.2317	1.0	V_x	2.0404	2.0650	2.1264	2.2009	2.2473
	V_r	0.5037	0.5147	0.5427	0.5712	0.5852		V_r	0.3843	0.4182	0.4971	0.5501	0.5391
	V_ϕ	0.0000	0.2052	0.3189	0.2760	0.0000		V_ϕ	0.0000	0.2620	0.3682	0.2675	0.0000
	p	1.0760	0.8573	0.4536	0.2047	0.1554		p	0.9908	0.8234	0.4883	0.2321	0.1413
	ρ	4.3550	3.8424	2.6978	1.7656	1.6074		ρ	4.1065	3.8626	3.1200	2.0783	1.5016
0.4	V_x	2.0129	2.0414	2.1131	2.1954	2.2345							
	V_r	0.4736	0.4893	0.5284	0.5621	0.5759							
	V_ϕ	0.0000	0.2224	0.3358	0.2797	0.0000		W_x	0.3261	0.3305	0.3449	0.3679	0.3776
	p	1.0649	0.8556	0.4637	0.2117	0.1541							
	ρ	4.3236	3.8818	2.8413	1.8796	1.5973							

TABLE VIII-2-1 (Cont'd.)

$M_\infty = 7$ $\beta_c = 20°$ $\alpha = 5°$

ξ		$\phi°$ 0	45	90	135	180	ξ		$\phi°$ 0	45	90	135	180
0	V_x	1.9345	1.9451	1.9722	2.0020	2.0838	0.6	V_x	1.9656	1.9852	2.0339	2.0849	2.1067
	V_r	0.7041	0.7080	0.7178	0.7287	0.7585		V_r	0.6235	0.6354	0.6631	0.6889	0.6992
	V_ϕ	0.0000	0.0826	0.1235	0.0913	0.0000		V_ϕ	0.0000	0.1263	0.1836	0.1355	0.0000
	p	1.1020	0.9901	0.7524	0.5608	0.4956		p	1.0717	0.9677	0.7411	0.5493	0.4806
	ρ	4.3785	4.0561	3.3339	2.7026	3.2050		ρ	4.2920	4.1324	3.7328	3.3137	3.1355
0.1	V_x	1.9397	1.9592	2.0087	2.0633	2.0879	0.8	V_x	1.9763	1.9953	2.0425	2.0925	2.1142
	V_r	0.6901	0.6978	0.7171	0.7380	0.7473		V_r	0.5976	0.6114	0.6429	0.6708	0.6813
	V_ϕ	0.0000	0.0969	0.1434	0.1078	0.0000		V_ϕ	0.0000	0.1334	0.1921	0.1399	0.0000
	p	1.1011	0.9899	0.7529	0.5609	0.4951		p	1.0491	0.9496	0.7300	0.5397	0.4700
	ρ	4.3759	4.1612	3.6848	3.3074	3.2027		ρ	4.2272	4.0851	3.7095	3.2803	3.0856
0.2	V_x	1.9448	1.9648	2.0148	2.0684	2.0918	1.0	V_x	1.9875	2.0057	2.0513	2.1004	2.1221
	V_r	0.6764	0.6849	0.7059	0.7276	0.7369		V_r	0.5714	0.5872	0.6228	0.6527	0.6629
	V_ϕ	0.0000	0.1055	0.1558	0.1175	0.0000		V_ϕ	0.0000	0.1394	0.1988	0.1429	0.0000
	p	1.0985	0.9882	0.7525	0.5601	0.4937		p	1.0202	0.9261	0.7152	0.5271	0.4563
	ρ	4.3683	4.1688	3.7148	3.3258	3.1962		ρ	4.1437	4.0191	3.6685	3.2343	3.0210
0.4	V_x	1.9551	1.9752	2.0249	2.0770	2.0992							
	V_r	0.6496	0.6598	0.6840	0.7077	0.7176							
	V_ϕ	0.0000	0.1175	0.1723	0.1288	0.0000		W_x	0.4349	0.4361	0.4386	0.4403	0.4403
	p	1.0882	0.9806	0.7486	0.5562	0.4886							
	ρ	4.3391	4.1612	3.7370	3.3307	3.1724							

$M_\infty = 7$ $\beta_c = 20°$ $\alpha = 10°$

ξ		$\phi°$ 0	45	90	135	180	ξ		$\phi°$ 0	45	90	135	180
0	V_x	1.8348	1.8566	1.9154	1.9877	2.1327	0.1	V_x	1.8406	1.8760	1.9676	2.0774	2.1363
	V_r	0.6678	0.6758	0.6972	0.7235	0.7763		V_r	0.6521	0.6663	0.7029	0.7452	0.7666
	V_ϕ	0.0000	0.1676	0.2684	0.2223	0.0000		V_ϕ	0.0000	0.1873	0.2866	0.2308	0.0000
	p	1.4853	1.2211	0.7121	0.3750	0.2027		p	1.4842	1.2225	0.7163	0.3771	0.2023
	ρ	4.7533	4.1325	2.8414	1.7783	2.4138		ρ	4.7506	4.2780	3.2315	2.4458	2.4117

TABLE VIII-2-1 (Cont'd.)

$M_\infty = 7$ $\beta_c = 20°$ $\alpha = 10°$

ξ		φ° 0	45	90	135	180	ξ		φ° 0	45	90	135	180
0.2	V_x	1.8465	1.8835	1.9780	2.0868	2.1394	0.8	V_x	1.8828	1.9185	2.0079	2.1089	2.1565
	V_r	0.6365	0.6531	0.6946	0.7383	0.7584		V_r	0.5456	0.5763	0.6467	0.7099	0.7165
	V_ϕ	0.0000	0.2016	0.3053	0.2469	0.0000		V_ϕ	0.0000	0.2589	0.3726	0.2810	0.0000
	p	1.4807	1.2225	0.7202	0.3791	0.2915		p	1.4148	1.1921	0.7363	0.3873	0.2775
	ρ	4.7427	4.3128	3.3360	2.5473	2.4065		ρ	4.5911	4.3453	3.6522	2.7583	2.3237
0.4	V_x	1.8583	1.8961	1.9913	2.0971	2.1451	1.0	V_x	1.8960	1.9224	2.0141	2.1130	2.1631
	V_r	0.6058	0.6269	0.6774	0.7241	0.7438		V_r	0.5150	0.5543	0.6332	0.6919	0.7018
	V_ϕ	0.0000	0.2240	0.3336	0.2657	0.0000		V_ϕ	0.0000	0.2720	0.3872	0.2835	0.0000
	p	1.4672	1.2181	0.7270	0.3826	0.2884		p	1.3757	1.1702	0.7388	0.3889	0.2689
	ρ	4.7117	4.3485	3.4750	2.6544	2.3885		ρ	4.5001	4.3128	3.7138	2.7892	2.2721
0.6	V_x	1.8704	1.9076	2.0005	2.1038	2.1507							
	V_r	0.5757	0.6014	0.6644	0.7116	0.7302							
	V_ϕ	0.0000	0.2422	0.3552	0.2757	0.0000							
	p	1.4452	1.2080	0.7323	0.3852	0.2838		W_x	0.4368	0.4398	0.4482	0.4561	0.4545
	ρ	4.6612	4.3575	3.5746	2.7165	2.3613							

$M_\infty = 7$ $\beta_c = 30°$ $\alpha = 5°$

ξ		φ° 0	45	90	135	180	ξ		φ° 0	45	90	135	180
0	V_x	1.5662	1.5787	1.6102	1.6434	1.7716	0.2	V_x	1.5836	1.6113	1.6806	1.7537	1.7851
	V_r	0.9043	0.9115	0.9296	0.9488	1.0228		V_r	0.8748	0.8922	0.9354	0.9804	0.9997
	V_ϕ	0.0000	0.0741	0.1068	0.0757	0.0000		V_ϕ	0.0000	0.1047	0.1506	0.1106	0.0000
	p	1.9609	1.8194	1.5075	1.2384	1.1399		p	1.9553	1.8154	1.5055	1.2359	1.1365
	ρ	5.0293	4.7673	4.1681	3.6220	4.3957		ρ	5.0191	4.8938	4.6262	4.4336	4.3863
0.1	V_x	1.5749	1.6021	1.6710	1.7456	1.7785	0.4	V_x	1.6008	1.6286	1.6971	1.7679	1.7978
	V_r	0.8894	0.9058	0.9470	0.9914	1.0109		V_r	0.8466	0.8657	0.9121	0.9591	0.9789
	V_ϕ	0.0000	0.0928	0.1342	0.0977	0.0000		V_ϕ	0.0000	0.1188	0.1726	0.1266	0.0000
	p	1.9585	1.8186	1.5074	1.2380	1.1390		p	1.9394	1.8023	1.4966	1.2275	1.1274
	ρ	5.0267	4.8887	4.6023	4.4201	4.3932		ρ	4.9898	4.8821	4.6389	4.4319	4.3610

TABLE VIII-2-1 (Cont'd.)

$M_\infty = 7$ $\beta_c = 30°$ $\alpha = 5°$

ξ		$\vartheta°$ 0	45	90	135	180	ξ		$\vartheta°$ 0	45	90	135	180
0.6	V_x	1.6180	1.6452	1.7122	1.7811	1.8101	1.0	V_x	1.6535	1.6788	1.7416	1.8070	1.8349
	V_r	0.8194	0.8401	0.8895	0.9388	0.9593		V_r	0.7665	0.7902	0.8462	0.9001	0.9219
	V_ϑ	0.0000	0.1299	0.1880	0.1371	0.0000		V_ϑ	0.0000	0.1461	0.2092	0.1504	0.0000
	p	1.9140	1.7809	1.4814	1.2140	1.1132		p	1.8362	1.7142	1.4331	1.1725	1.0713
	ρ	4.9430	4.8496	4.6260	4.4088	4.3219		ρ	4.7988	4.7318	4.5451	4.3151	4.2050
0.8	V_x	1.6355	1.6619	1.7269	1.7940	1.8224							
	V_r	0.7929	0.8150	0.8677	0.9193	0.9405							
	V_ϑ	0.0000	0.1387	0.1998	0.1447	0.0000		IV_x	0.6919	0.6913	0.6888	0.6842	0.6814
	p	1.8796	1.7515	1.4602	1.1956	1.0946							
	ρ	4.8794	4.7994	4.5941	4.3695	4.2700							

$M_\infty = 7$ $\beta_c = 30°$ $\alpha = 10°$

ξ		$\vartheta°$ 0	45	90	135	180	ξ		$\vartheta°$ 0	45	90	135	180
0	V_x	1.4413	1.4682	1.5391	1.6198	1.8508	0.6	V_x	1.5003	1.5524	1.6830	1.8232	1.8830
	V_r	0.8321	0.8477	0.8886	0.9352	1.0686		V_r	0.7361	0.7778	0.8772	0.9739	1.0153
	V_ϑ	0.0000	0.1550	0.2337	0.1668	0.0000		V_ϑ	0.0000	0.2508	0.3675	0.2787	0.0000
	p	2.4136	2.0943	1.4397	0.9491	0.7990		p	2.3546	2.0636	1.4436	0.9418	0.7804
	ρ	5.2304	4.7263	3.6163	2.6853	3.9035		ρ	5.1388	4.9437	4.4657	4.0074	3.8382
0.1	V_x	1.4510	1.5009	1.6303	1.7825	1.8570	0.8	V_x	1.5205	1.5708	1.6972	1.8340	1.8928
	V_r	0.8155	0.8458	0.9238	1.0142	1.0579		V_r	0.7056	0.7513	0.8583	0.9585	1.0003
	V_ϑ	0.0000	0.1823	0.2681	0.2006	0.0000		V_ϑ	0.0000	0.2693	0.3917	0.2927	0.0000
	p	2.4118	2.0950	1.4427	0.9501	0.7983		p	2.3108	2.0354	1.4373	0.9382	0.7678
	ρ	5.2277	4.8917	4.1788	3.7890	3.9012		ρ	5.0704	4.9204	4.5131	4.0240	3.7940
0.2	V_x	1.4608	1.5128	1.6455	1.7946	1.8627	1.0	V_x	1.5414	1.5891	1.7102	1.8440	1.9028
	V_r	0.7991	0.8324	0.9159	1.0069	1.0483		V_r	0.6751	0.7249	0.8400	0.9411	0.9855
	V_ϑ	0.0000	0.2008	0.2963	0.2265	0.0000		V_ϑ	0.0000	0.2854	0.4118	0.3028	0.0000
	p	2.4067	2.0934	1.4448	0.9504	0.7964		p	2.2553	1.9982	1.4272	0.9293	0.7522
	ρ	5.2197	4.9211	4.2755	3.8786	3.8946		ρ	4.9831	4.8774	4.5406	4.0236	3.7386
0.4	V_x	1.4804	1.5334	1.6666	1.8107	1.8731							
	V_r	0.7671	0.8049	0.8967	0.9902	1.0311							
	V_ϑ	0.0000	0.2288	0.3371	0.2585	0.0000		IV_x	0.7002	0.7008	0.6997	0.6903	0.6849
	p	2.3867	2.0830	1.4462	0.9490	0.7900							
	ρ	5.1888	4.9459	4.3926	3.9664	3.8719							

TABLE VIII-2-2. AERODYNAMIC COEFFICIENTS OF CONE IN BODY COORDINATE SYSTEM ($k = 1.4$)

/754

	β_c	α	M_∞ 2	3	5	7		β_c	α	M_∞ 2	3	5	7
c_{Rp}	10°	0°	0.1046	0.0875	0.0748	0.0698	m_{zp}	20°	10°	0.1919	0.1954	0.1990	0.2009
		2°30′	0.1040	0.0876	0.0757	0.0710			15°	—	0.2916	0.2923	0.2930
		5°	—	0.0881	0.0785	0.0746							
		7°30′	—	—	0.0831	0.0805	c_{Rp}	30°	0°	0.6452	0.5750	0.5425	0.5335
									2°30′	0.6448	—	—	—
c_{Np}		0°	0	0	0	0			5°	0.6435	0.5742	0.5416	0.5325
		2°30′	0.0802	0.0801	0.0814	0.0827			10°	—	0.5719	0.5391	0.5301
		5°	—	0.1625	0.1645	0.1658			15°	—	0.5689	0.5381	0.5281
		7°30′	—	—	0.2508	0.2506			20°	—	—	0.5398	0.5304
$-m_{zp}$		0°	0	0	0	0	c_{Np}		0°	0	0	0	0
		2°30′	0.0535	0.0534	0.0543	0.0551			2°30′	0.0611	—	—	—
		5°	—	0.1083	0.1097	0.1106			5°	0.1220	0.1261	0.1294	0.1306
		7°30′	—	—	0.1672	0.1670			10°	—	0.2487	0.2549	0.2572
c_{Rp}	15°	0°	0.2024	0.1732	0.1542	0.1478			15°	—	0.3648	0.3723	0.3756
		5°	0.2015	0.1752	0.1581	0.1519			20°	—	—	0.4773	0.4803
		10°	0.2015	0.1814	0.1698	0.1648	$-m_{zp}$		0°	0	0	0	0
c_{Np}		0°	0	0	0	0			2°30′	0.0508	—	—	—
		5°	0.1525	0.1550	0.1586	0.1607			5°	0.0813	0.0840	0.0863	0.0871
		10°	0.3003	0.3142	0.3163	0.3175			10°	—	0.1658	0.1699	0.1715
$-m_{zp}$		0°	0	0	0	0			15°	—	0.2432	0.2482	0.2504
		5°	0.1017	0.1033	0.1057	0.1071			20°	—	—	0.3182	0.3202
		10°	0.2002	0.2095	0.2108	0.2117	c_{Rp}	40°	0°	—	0.9390	0.8923	0.8809
c_{Rp}	20°	0°	0.3256	0.2843	0.2605	0.2532			2°30′	—	0.9378	—	—
		5°	0.3253	0.2862	0.2632	0.2557			5°	—	—	0.8871	0.8755
		10°	0.3244	0.2919	0.2718	0.2645			10°	—	—	0.8718	0.8599
		15°	—	0.3015	0.2875	0.2816	c_{Np}		0°	0	0	0	0
c_{Np}		0°	0	0	0	0			2°30′	—	0.0499	—	—
		5°	0.1435	0.1471	0.1512	0.1531			5°	—	—	0.1014	0.1021
		10°	0.2878	0.2931	0.2985	0.3014			10°	—	—	0.1997	0.2011
		15°	—	0.4374	0.4385	0.4396	$-m_{zp}$		0°	0	0	0	0
									5°	—	—	0.0676	0.0681
$-m_{zp}$		0°	0	0	0	0			10°	—	—	0.1332	0.1341
		5°	0.0956	0.0981	0.1008	0.1021							

TABLE IX-2-1. GASDYNAMIC FUNCTIONS IN AXISYMMETRIC FLOW OF CHEMICALLY REACTIVE AIR AROUND SOLID OF REVOLUTION BUILT UP FROM CONICAL ELEMENTS

/755

Semiapex angles: nose cone $\beta_c = 40°$, main cone $\beta_c = 10°$, $M_\infty = 20$.

ξ		x = 1.0	1.24	1.88	5.8	28.52	ξ		x = 1.0	1.24	1.88	5.8	28.52
0	V_x	1.377	1.748	2.031	2.028	2.053	0.8	V_x	1.418	1.493	1.869	2.323	2.376
	V_r	1.156	0.830	0.355	0.354	0.358		V_r	1.109	1.053	0.680	0.349	0.343
	p	2.524	0.745	0.160	0.163	0.193		p	2.483	2.020	0.657	0.154	0.164
	ρ	10.757	4.001	1.075	1.090	1.305		ρ	10.612	8.987	3.812	2.436	4.935
0.2	V_x	1.388	1.636	2.033	2.035	2.263	1.0	V_x	1.428	1.511	2.003	2.337	2.377
	V_r	1.143	0.946	0.330	0.352	0.378		V_r	1.098	1.087	0.857	0.426	0.322
	p	2.521	1.159	0.167	0.164	0.192		p	2.460	2.258	1.060	0.248	0.150
	ρ	10.747	5.729	1.123	1.105	2.228		ρ	10.584	10.551	8.150	5.113	4.373
0.4	V_x	1.398	1.570	1.978	2.100	2.362							
	V_r	1.131	1.002	0.435	0.359	0.377	W		0.917	1.132	1.540	2.769	6.712
	p	2.513	1.487	0.260	0.164	0.188							
	ρ	10.719	7.013	1.634	1.208	4.975							
0.6	V_x	1.408	1.524	1.904	2.262	2.372	W_x		0.917	0.849	0.503	0.229	0.177
	V_r	1.120	1.035	0.566	0.350	0.361							
	p	2.500	1.765	0.437	0.151	0.178							
	ρ	10.674	8.053	2.566	1.626	5.212	B		—	1.007	1.143	1.827	5.792

Semiapex angles: nose cone $\beta_c = 40°$, main cone $\beta_c = 20°$, $M_\infty = 20$

ξ		x = 1.0	1.12	1.88	5.0	29.8	ξ		x = 1.0	1.12	1.88	5.0	29.8
0	V_x	1.377	1.540	1.875	1.844	1.854	0.4	V_x	1.398	1.449	1.896	2.019	2.158
	V_r	1.156	1.037	0.655	0.644	0.647		V_r	1.131	1.097	0.574	0.650	0.725
	p	2.524	1.565	0.420	0.648	0.680		p	2.513	2.167	0.438	0.626	0.675
	ρ	10.757	7.308	2.467	3.589	3.376		ρ	10.719	9.505	2.531	4.406	6.835
0.2	V_x	1.388	1.483	1.892	1.837	2.154	0.6	V_x	1.408	1.429	1.867	2.171	2.162
	V_r	1.143	1.077	0.604	0.607	0.738		V_r	1.120	1.106	0.597	0.658	0.763
	p	2.521	1.912	0.424	0.646	0.679		p	2.500	2.352	0.513	0.590	0.669
	ρ	10.747	8.590	2.498	3.482	6.888		ρ	10.674	10.154	2.868	5.771	6.771

TABLE IX-2-1 (Cont'd.)

Semiapex angles: nose cone $\beta_c = 40°$, main cone $\beta_c = 20°$, $M_\infty = 20$

ξ		x					ξ		x				
		1.0	1.12	1.88	5.0	29.8			1.0	1.12	1.88	5.0	29.8
0.8	V_x	1.418	1.421	1.918	2.230	2.466		W	0.917	—	1.529	2.624	11.949
	V_r	1.109	1.107	0.708	0.645	0.701							
	p	2.482	2.459	0.695	0.549	0.661		W_x	0.917	—	0.492	0.337	0.382
	ρ	10.612	10.529	4.366	7.042	6.700							
1.0	V_x	1.428	1.428	2.020	2.227	2.171		B	—	—	1.222	2.311	1.097
	V_r	1.098	1.098	0.843	0.617	0.689							
	p	2.460	2.460	1.020	0.516	0.651							
	ρ	10.534	10.534	8.002	6.190	6.617							

Semiapex angles: nose cone $\beta_c = 40°$, main cone $\beta_c = 20°$, $M_\infty = 15$

ξ		x					ξ		x				
		1.0	1.12	1.88	5.0	29.8			1.0	1.12	1.88	5.0	29.8
0	V_x	1.363	1.526	1.874	1.860	1.824	0.8	V_x	1.410	1.409	1.863	2.217	2.156
	V_r	1.144	1.028	0.654	0.649	0.637		V_r	1.090	1.091	0.747	0.627	0.688
	p	2.519	1.641	0.496	0.594	0.687		p	2.471	2.469	0.866	0.533	0.665
	ρ	9.480	6.544	2.310	2.736	2.164		ρ	9.324	9.318	4.082	5.728	5.775
0.2	V_x	1.375	1.466	1.886	1.857	2.140	1.0	V_x	1.421	1.422	1.937	2.212	2.161
	V_r	1.129	1.068	0.613	0.610	0.731		V_r	1.077	1.077	0.875	0.605	0.674
	p	2.515	1.983	0.508	0.593	0.685		p	2.445	2.444	1.194	0.529	0.652
	ρ	9.469	7.711	2.367	2.695	5.918		ρ	9.240	9.240	6.710	5.389	5.680
0.4	V_x	1.387	1.432	1.890	2.005	2.146							
	V_r	1.116	1.086	0.582	0.620	0.716		W	0.930	1.039	1.532	2.734	12.197
	p	2.506	2.227	0.523	0.584	0.681							
	ρ	9.439	8.525	2.414	3.104	5.908		W_x	0.930	0.929	0.555	0.346	0.388
0.6	V_x	1.398	1.413	1.841	2.143	2.151							
	V_r	1.103	1.094	0.634	0.634	0.702		B	—	—	1.194	2.311	10.967
	p	2.491	2.394	0.652	0.558	0.674							
	ρ	9.390	9.073	2.913	4.429	5.849							

TABLE IX-2-2. COMPARISON OF GASDYNAMIC FUNCTIONS CALCULATED WITH AND WITHOUT CONSIDERATION OF CHEMICAL REACTIONS

/757

Semiapex angles: nose cone $\beta_c = 40°$, main cone $\beta_c = 0°$ (cylinder); $M_\infty = 20$

ξ		x: with consideration of chemical reactions				ξ		x: with consideration of chemical reactions			
		1.0	1.160	2.040	10.60			1.0	1.160	2.040	10.60
0	V_x	1.377	1.516	2.132	2.133	0.8	V_x	1.418	1.431	1.893	2.371
	V_r	1.156	1.056	0	0		V_r	1.109	1.100	0.617	0.194
	p	2.524	—	0.057	0.056		p	2.482	2.389	0.541	0.061
	ρ	10.757	7.752	0.443	0.433		ρ	10.612	10.281	3.172	1.314
0.2	V_x	1.388	1.478	2.119	2.138	1.0	V_x	1.428	1.433	2.040	2.383
	V_r	1.143	1.080	0.040	0.072		V_r	1.098	1.097	0.826	0.304
	p	2.521	1.940	0.069	0.054		p	2.460	2.448	0.971	0.135
	ρ	10.747	8.691	0.519	0.430		ρ	10.534	10.433	7.820	4.225
0.4	V_x	1.398	1.454	2.043	2.159						
	V_r	1.131	1.093	0.287	0.113						
	p	2.513	2.135	0.160	0.052		W	0.917	1.062	1.632	3.730
	ρ	10.719	9.392	1.083	0.417						
0.6	V_x	1.408	1.439	1.952	2.317						
	V_r	1.120	1.099	0.470	0.132						
	p	2.500	2.294	0.319	0.043		W_x	0.917	0.913	0.478	0.168
	ρ	10.674	9.919	1.951	0.532						

ξ		x: without consideration of chemical reactions (k = 1.4)				ξ		x: without consideration of chemical reactions (k = 1.4)			
		1.0	1.16	2.040	10.60			1.0	1.16	2.040	10.60
0	V_x	1.329	1.486	2.207	2.239	0.2	V_x	1.349	1.446	2.180	2.236
	V_r	1.115	1.035	0	0		V_r	1.091	1.043	0.090	0.068
	p	2.591	1.865	0.091	0.056		p	2.585	2.111	0.125	0.056
	ρ	6.065	4.796	0.660	0.399		ρ	6.055	5.240	0.705	0.399

TABLE IX-2-2 (Cont'd.)

/758

Semiapex angles: nose cone $\beta_c = 40°$, main cone $\beta_c = 0°$ (cylinder); $M_\infty = 20$

ξ		x				ξ		x			
		without consideration of chemical reactions ($k = 1.4$)						without consideration of chemical reactions ($k = 1.4$)			
		1.0	1.16	2.040	10.60			1.0	1.16	2.040	10.60
0.4	V_x	1.369	1.426	2.053	2.242	1.0	V_x	1.426	1.426	1.967	2.372
	V_r	1.069	1.041	0.390	0.111		V_r	1.009	1.009	0.848	0.335
	p	2.568	2.280	0.310	0.057		p	2.465	2.465	1.148	0.161
	ρ	6.027	5.536	1.316	0.408		ρ	5.854	5.854	5.694	4.353
0.6	V_x	1.388	1.416	1.940	2.309						
	V_r	1.048	1.034	0.571	0.137						
	p	2.542	2.395	0.533	0.055		W	0.999	1.157	1.801	4.159
	ρ	5.983	5.733	1.956	0.577						
0.8	V_x	1.407	1.416	1.905	2.357						
	V_r	1.028	1.024	0.706	0.212		W_x	0.999	0.999	0.551	0.185
	p	2.508	2.460	0.775	0.072						
	ρ	5.925	5.845	2.888	1.233						

TABLE IX-2-3. GASDYNAMIC FUNCTIONS OF AIR IN AXISYMMETRIC FLOW AROUND SOLID OF REVOLUTION ($M_\infty = 20$, $\alpha = 5°$)

ξ		$x = 1.3$					ξ		$x = 1.4$				
		$\Phi°$							$\Phi°$				
		0	45	90	135	180			0	45	90	135	180
0	V_x	1.047	1.077	1.156	1.247	1.290	0	V_x	1.309	1.342	1.430	1.531	1.576
	V_r	0.984	1.012	1.086	1.172	1.212		V_r	0.840	0.862	0.918	0.983	1.012
	V_Φ	0.000	0.039	0.054	0.038	0.000		V_Φ	0.000	0.041	0.057	0.039	0.000
	p	3.095	2.937	2.575	2.237	2.101		p	1.705	1.578	1.291	1.018	0.907
	ρ	9.990	9.681	9.061	8.688	8.676		ρ	5.951	5.652	5.018	4.535	4.393

TABLE IX-2-3 (Cont'd.)

		$x = 1.2$						$x = 1.4$				
		$\vartheta°$						$\vartheta°$				
ξ		0	45	90	135	180	ξ	0	45	90	135	180
0.1	V_x	1.044	1.076	1.156	1.242	1.280	0.1	1.270	1.302	1.384	1.472	1.510
	V_r	0.981	1.012	1.091	1.177	1.214		0.861	0.888	0.957	1.031	1.064
	V_ϑ	0.000	0.068	0.099	0.073	0.000		0.000	0.069	0.101	0.074	0.000
	p	3.155	3.001	2.648	2.318	2.186		1.913	1.790	1.512	1.246	1.140
	ρ	10.159	9.889	9.347	9.004	8.964		6.575	6.321	5.787	5.385	5.278
0.2	V_x	1.042	1.074	1.153	1.236	1.272	0.2	1.242	1.273	1.350	1.432	1.468
	V_r	0.977	1.010	1.092	1.179	1.216		0.872	0.903	0.979	1.058	1.093
	V_ϑ	0.000	0.084	0.123	0.091	0.000		0.000	0.085	0.124	0.092	0.000
	p	3.210	3.059	2.714	2.390	2.261		2.085	1.966	1.692	1.428	1.321
	ρ	10.313	10.066	9.574	9.257	9.217		7.086	6.861	6.389	6.035	5.947
0.5	V_x	1.040	1.070	1.146	1.224	1.257	0.5	1.192	1.219	1.288	1.362	1.394
	V_r	0.966	1.002	1.090	1.179	1.217		0.883	0.919	1.006	1.094	1.131
	V_ϑ	0.000	0.117	0.170	0.124	0.000		0.000	0.117	0.170	0.124	0.000
	p	3.345	3.203	2.876	2.565	2.440		2.486	2.374	2.109	1.846	1.737
	ρ	10.687	10.494	10.114	9.858	9.817		8.256	8.096	7.750	7.487	7.421
0.8	V_x	1.042	1.071	1.144	1.219	1.250	0.8	1.202	1.221	1.274	1.336	1.364
	V_r	0.951	0.989	1.082	1.175	1.214		0.910	0.944	1.028	1.115	1.152
	V_ϑ	0.000	0.141	0.202	0.146	0.000		0.000	0.139	0.200	0.145	0.000
	p	3.459	3.322	3.000	2.689	2.563		2.789	2.682	2.423	2.159	2.047
	ρ	10.996	10.840	10.519	10.281	10.228		9.347	9.210	8.915	8.678	8.618
1.0	V_x	1.079	1.102	1.163	1.230	1.259	1.0	1.297	1.309	1.345	1.393	1.416
	V_r	0.969	1.003	1.089	1.178	1.216		0.989	1.020	1.097	1.179	1.214
	V_ϑ	0.000	0.153	0.220	0.158	0.000		0.000	0.149	0.215	0.156	0.000
	p	3.526	3.392	3.070	2.754	2.625		3.001	2.893	2.629	2.359	2.244
	ρ	11.410	11.249	10.904	10.633	10.564		10.835	10.733	10.569	10.541	10.547
W		1.437	1.435	1.430	1.421	1.415	W	1.645	1.646	1.645	1.638	1.633
W_x		1.140	1.147	1.159	1.163	1.161	W_x	0.939	0.954	0.984	1.003	1.006

TABLE IX-2-3 (Cont'd.)

$x = 1.6$							$x = 1.8$						
ξ		$\Phi°$					ξ		$\Phi°$				
		0	45	90	135	180			0	45	90	135	180
0	V_x	1.643	1.679	1.775	1.878	1.923	0	V_x	1.844	1.881	1.971	2.065	2.108
	V_r	0.499	0.510	0.539	0.570	0.584		V_r	0.099	0.101	0.106	0.111	0.113
	V_Φ	0.000	0.044	0.062	0.043	0.000		V_Φ	0.000	0.049	0.069	0.048	0.000
	p	0.637	0.761	0.304	0.256	0.212		p	0.234	0.194	0.117	0.067	0.052
	ρ	2.553	2.342	1.881	1.480	1.324		ρ	1.111	0.984	0.705	0.465	0.391
0.1	V_x	1.545	1.578	1.661	1.746	1.779	0.1	V_x	1.751	1.784	1.864	1.944	1.980
	V_r	0.612	0.635	0.694	0.761	0.792		V_r	0.305	0.324	0.378	0.438	0.462
	V_Φ	0.000	0.070	0.100	0.072	0.000		V_Φ	0.000	0.069	0.098	0.068	0.000
	p	0.914	0.834	0.652	0.489	0.435		p	0.414	0.366	0.261	0.180	0.153
	ρ	3.474	3.282	2.858	2.527	2.415		ρ	1.773	1.643	1.368	1.099	0.999
0.2	V_x	1.472	1.502	1.577	1.655	1.685	0.2	V_x	1.667	1.697	1.772	1.845	1.878
	V_r	0.679	0.708	0.782	0.859	0.895		V_r	0.438	0.465	0.533	0.612	0.643
	V_Φ	0.000	0.085	0.123	0.089	0.000		V_Φ	0.000	0.083	0.118	0.084	0.000
	p	1.168	1.087	0.856	0.714	0.652		p	0.610	0.556	0.429	0.323	0.285
	ρ	4.291	4.118	3.733	3.439	3.364		ρ	2.457	2.326	2.041	1.802	1.696
0.5	V_x	1.346	1.372	1.437	1.507	1.537	0.5	V_x	1.492	1.516	1.579	1.646	1.674
	V_r	0.765	0.801	0.892	0.982	1.019		V_r	0.632	0.669	0.760	0.852	0.890
	V_Φ	0.000	0.116	0.168	0.122	0.000		V_Φ	0.000	0.112	0.161	0.117	0.000
	p	1.740	1.660	1.466	1.261	1.178		p	1.148	1.091	0.948	0.799	0.740
	ρ	6.043	5.934	5.684	5.479	5.432		ρ	4.213	4.124	3.929	3.780	3.738
0.8	V_x	1.390	1.401	1.435	1.482	1.507	0.8	V_x	1.527	1.533	1.557	1.596	1.617
	V_r	0.863	0.896	0.977	1.060	1.094		V_r	0.788	0.822	0.904	0.987	1.019
	V_Φ	0.000	0.135	0.195	0.142	0.000		V_Φ	0.000	0.130	0.188	0.137	0.000
	p	2.154	2.072	1.869	1.657	1.568		p	1.627	1.566	1.412	1.254	1.184
	ρ	7.866	7.761	7.535	7.404	7.381		ρ	6.386	6.307	6.166	6.113	6.051
1.0	V_x	1.511	1.515	1.531	1.560	1.578	1.0	V_x	1.676	1.673	1.673	1.686	1.699
	V_r	0.970	1.002	1.079	1.156	1.187		V_r	0.929	0.962	1.040	1.117	1.148
	V_Φ	0.000	0.145	0.210	0.153	0.000		V_Φ	0.000	0.140	0.205	0.150	0.000
	p	2.478	2.391	2.179	1.956	1.859		p	2.069	2.002	1.836	1.658	1.574
	ρ	10.534	10.537	10.542	10.411	10.287		ρ	10.504	10.455	10.252	9.923	9.737
W		1.816	1.820	1.826	1.824	1.820	W		1.958	1.966	1.981	1.986	1.984
W_x		0.773	0.790	0.829	0.860	0.869	W_x		0.657	0.676	0.723	0.764	0.777

TABLE IX-2-3 (Cont'd.)

$x = 2.0$							$x = 4.008$						
		$\theta°$							$\theta°$				
ξ		0	45	90	135	180	ξ		0	45	90	135	180
0	V_x	1.871	1.907	1.995	2.089	2.131	0	V_x	1.878	1.904	1.978	2.071	2.117
	V_r	0.000	0.000	0.000	0.000	0.000		V_r	0.000	0.000	0.000	0.000	0.000
	V_θ	0.000	0.055	0.077	0.053	0.000		V_θ	0.000	0.108	0.153	0.114	0.000
	p	0.187	0.153	0.089	0.049	0.037		p	0.174	0.150	0.099	0.058	0.045
	ρ	0.928	0.810	0.561	0.356	0.289		ρ	0.875	0.799	0.609	0.408	0.338
0.1	V_x	1.855	1.889	1.969	2.052	2.090	0.1	V_x	1.879	1.906	1.980	2.072	2.118
	V_r	0.047	0.060	0.103	0.146	0.161		V_r	0.011	0.013	0.012	0.003	0.006
	V_θ	0.000	0.070	0.098	0.067	0.000		V_θ	0.000	0.122	0.177	0.128	0.000
	p	0.217	0.185	0.121	0.077	0.062		p	0.174	0.150	0.099	0.059	0.045
	ρ	1.049	0.948	0.731	0.527	0.453		ρ	0.870	0.801	0.616	0.407	0.332
0.2	V_x	1.793	1.824	1.899	1.976	2.011	0.2	V_x	1.882	1.908	1.982	2.076	2.120
	V_r	0.201	0.225	0.294	0.363	0.387		V_r	0.019	0.021	0.018	0.003	0.017
	V_θ	0.000	0.081	0.114	0.079	0.000		V_θ	0.000	0.123	0.176	0.124	0.000
	p	0.332	0.294	0.215	0.152	0.128		p	0.172	0.149	0.098	0.057	0.044
	ρ	1.476	1.377	1.172	0.952	0.855		ρ	0.867	0.800	0.612	0.401	0.329
0.5	V_x	1.618	1.643	1.709	1.772	1.801	0.5	V_x	1.898	1.909	1.944	2.005	2.038
	V_r	0.488	0.524	0.613	0.708	0.742		V_r	0.046	0.077	0.167	0.251	0.280
	V_θ	0.000	0.106	0.153	0.110	0.000		V_θ	0.000	0.116	0.165	0.117	0.000
	p	0.746	0.701	0.588	0.484	0.441		p	0.173	0.163	0.144	0.121	0.110
	ρ	2.903	2.829	2.654	2.526	2.442		ρ	0.903	0.873	0.840	0.770	0.735
0.8	V_x	1.622	1.626	1.646	1.680	1.698	0.8	V_x	2.068	2.060	2.048	2.046	2.054
	V_r	0.691	0.726	0.811	0.896	0.927		V_r	0.300	0.342	0.445	0.550	0.589
	V_θ	0.000	0.124	0.180	0.131	0.000		V_θ	0.000	0.116	0.167	0.120	0.000
	p	1.201	1.156	1.042	0.927	0.874		p	0.331	0.319	0.292	0.267	0.252
	ρ	4.952	4.890	4.798	4.744	4.665		ρ	2.250	2.181	2.038	1.908	1.845
1.0	V_x	1.803	1.796	1.784	1.787	1.796	1.0	V_x	2.220	2.208	2.182	2.159	2.151
	V_r	0.874	0.900	0.993	1.073	1.103		V_r	0.501	0.551	0.667	0.779	0.821
	V_θ	0.000	0.137	0.199	0.146	0.000		V_θ	0.000	0.118	0.173	0.127	0.000
	p	1.748	1.698	1.567	1.421	1.347		p	0.659	0.646	0.608	0.564	0.539
	ρ	10.105	10.006	9.719	9.334	9.118		ρ	6.646	6.605	6.485	6.331	6.252
W		2.081	2.093	2.117	2.131	2.133	W		2.861	2.918	3.052	3.177	3.218
W_x		0.572	0.594	0.645	0.692	0.706	W_x		0.287	0.309	0.364	0.423	0.446

TABLE IX-2-4. FUNCTION (x, ϑ) FOR DETERMINATION OF COORDINATE ξ BY FORMULA (IX-2-1) /762

x	$\vartheta°$				
	0	45	90	135	180
1.4	0.849	0.842	0.826	0.811	0.800
1.6	0.874	0.872	0.864	0.856	0.839
1.8	0.809	0.806	0.799	0.790	0.776
2.0	0.930	0.929	0.927	0.924	0.917
2.4	0.859	0.856	0.850	0.843	0.837

APPENDIX No. 2

PARAMETERS OF AIR AT VARIOUS ALTITUDES (STANDARD ATMOSPHERE)

Altitude H, km	Temperature T_H, K	$\frac{p_H}{p_g}$	$\frac{\rho_H}{\rho_g}$	Speed of sound a_H, m/s	Kinematic viscosity ν_H, m^2/s	Acceleration of free fall g_H, m/s^2	Av. molecular weight, $\mu_{av\,H}$
0	288.15	1.0000	1.0000	340.28	$1.4607 \cdot 10^{-5}$	9.80665	28.966
0.5	284.90	$9.4205 \cdot 10^{-1}$	$9.5282 \cdot 10^{-1}$	338.36	1.5196	9.80511	28.966
1	281.65	8.8701	9.0751	336.43	1.5812	9.80357	28.966
1.5	278.40	8.3460	8.6384	334.48	1.6461	9.80203	28.966
2	275.14	7.8458	8.2171	332.52	1.7146	9.80049	28.966
2.5	271.89	7.3716	7.8127	330.55	1.7866	9.79896	28.966
3	268.64	6.9208	7.4237	328.56	1.8624	9.79742	28.966
4	262.13	6.0850	6.6891	324.56	2.0271	9.79435	28.966
5	255.63	5.3338	6.0125	320.51	2.2103	9.79128	28.966
6	249.13	4.6595	5.3895	316.41	2.4153	9.78820	28.966
7	242.63	4.0560	4.8171	312.25	2.6452	9.78514	28.966
8	236.14	3.5182	4.2931	308.05	2.9030	9.78207	28.966
9	229.64	3.0388	3.8132	303.78	3.1942	9.77900	28.966
10	223.15	2.6144	3.3761	299.45	3.5232	9.77594	28.966
11	216.66	2.2393	2.9784	295.07	3.8966	9.77287	28.966
12	216.66	1.9137	2.5453	295.07	4.5595	9.76981	28.966
14	216.66	1.3979	1.8593	295.07	6.2420	9.76369	28.966
16	216.66	1.0213	1.3584	295.07	8.5437	9.75758	28.966
18	216.66	$7.4630 \cdot 10^{-2}$	$9.9257 \cdot 10^{-2}$	295.07	$1.1694 \cdot 10^{-4}$	9.75146	28.966
20	216.66	5.4546	7.2547	295.07	1.5997	9.74537	28.966
22	216.66	3.9875	5.3033	295.07	2.1883	9.73927	28.966
24	216.66	2.9155	3.8776	295.07	2.9929	9.73318	28.966
25	219.40	2.1341	2.8030	296.93	4.1842	9.72710	28.966
28	221.87	1.5736	2.0164	300.61	5.9370	9.72102	28.966
30	230.35	1.1681	1.4613	304.25	8.3565	9.71494	28.966
32	235.82	$8.7337 \cdot 10^{-3}$	1.0676	307.84	$1.1661 \cdot 10^{-3}$	9.70888	28.966
34	241.28	6.5820	$7.8608 \cdot 10^{-3}$	311.38	1.6135	9.70282	28.966
36	246.74	4.9900	5.8276	314.89	2.2165	9.69676	28.966
38	252.20	3.8042	4.3465	318.36	3.0248	9.69071	28.966
40	257.66	2.9199	3.2656	321.78	4.0956	9.68466	28.966
45	271.28	1.5436	1.6397	330.17	8.4977	9.66957	28.966
50	274.00	$8.3475 \cdot 10^{-4}$	$8.7788 \cdot 10^{-4}$	331.82	$1.5997 \cdot 10^{-2}$	9.65452	28.966
55	270.56	4.5166	4.8105	329.74	2.8903	9.63950	28.966
60	253.40	2.3896	2.7071	319.11	4.8749	9.62452	28.966
65	236.26	1.2006	1.4642	308.13	8.5151	9.60957	28.966
70	219.15	$5.7580 \cdot 10^{-5}$	$7.5712 \cdot 10^{-5}$	296.76	$1.5475 \cdot 10^{-1}$	9.59466	28.966
80	185.00	1.0995	1.7126	272.66	5.9202	9.56494	28.966
90	185.00	$1.8203 \cdot 10^{-6}$	$2.8354 \cdot 10^{-6}$	272.60	$3.5759 \cdot 10^{0}$	9.53536	28.966
100	209.22	$3.1987 \cdot 10^{-7}$	$4.4075 \cdot 10^{-7}$			9.50591	28.962

(Cont'd.)

Altitude H, km	Temperature T_H° K	$\frac{p_H}{p_g}$	$\frac{\rho_H}{\rho_g}$	Speed of sound a_H, m/s	Kinematic viscosity ν_H, m^2/s	Acceleration of free fall g_H, m/s^2	Av. molecular weight, $\mu_{av\ H}$
120	332.24	$2.5217 \cdot 10^{-8}$	$1.0633 \cdot 10^{-8}$			9.43288	28.624
140	768.00	$7.2887 \cdot 10^{-9}$	$2.6748 \cdot 10^{-9}$			9.38948	28.314
160	1155.3	3.7628	$9.0457 \cdot 10^{-10}$			9.33205	27.950
180	1193	2.2199	5.0883			9.27400	27.476
200	1226.8	1.3455	2.9477			9.21750	27.000
225	1269.9	$7.4584 \cdot 10^{-10}$	1.5404			9.14762	26.348
250	1302.8	4.2900	$8.3835 \cdot 10^{-11}$			9.07850	25.577
275	1334.6	2.5554	4.7024			9.01021	24.672
300	1358.0	1.5731	2.7364			8.94270	23.731
400	1480	$5588 \cdot 10^{-14}$	0.7342			8.680	19.56
500	1576	1566	0.1806			8.428	18.28
600	1691	$5240 \cdot 10^{-15}$	$0.5402 \cdot 10^{-12}$			8.187	17.52
700	1812	2011	$0.1879 \cdot 10^{-12}$			7.957	17.03

Notes:
1. The data in Appendix No. 2 up to the altitude H = 200 km are taken from GOST 4401-64.
2. The data in the altitude range from 225 to 300 km correspond to recommendations cited in GOST 4401-64.
3. The remaining data (up to H = 700 km) are taken from [17].

At H = 0, $p_H = p_g = 25\ N/m^2 = 760$ mmHg = 10,332.3 kg/m^2; $\rho_H = \rho_g = 1.225\ kg/m^3 = 0.12492 \frac{kg/s^2}{m^4}$.

APPENDIX No. 3

TABLE FOR CONVERSION OF UNITS USED IN AERODYNAMICS TO MEASURE VARIOUS QUANTITIES FROM MKGFS SYSTEM TO INTERNATIONAL SYSTEM (SI), GOST 9867-61

Designation	Old Unit (MKGFS System)	New Unit (SI)
Fundamental Units		
Length	1 m	1 m
Mass	1 kg	1 kg
Time	1 s	1 s
Thermodynamic Temperature	1°K	1°K
Derived Units		
Velocity	1 m/s	1 m/s
Acceleration	1 m/s^2	1 m/s^2
Acceleration of gravity	9.8 m/s^2	9.8 m/s^2
Force	1 kgf	9.807 N

Designation	Old Unit (MKGFS System)	New Unit (SI)
Pressure	1 kg/cm^2	$9.807 \cdot 10^4$ N/m^2
Dynamic viscosity	1 kg/s^2	9.807 $N \cdot s/m^2$
Kinematic viscosity	1 m^2/s	1 m^2/s
Work, energy	1 kgf-m	9.807 J
Amount of heat	1 kcal	$4.187 \cdot 10^3$ J
Thermal equivalent of work	1/427 kcal/kgf-m	1 J/N-m
Mechanical equivalent of heat	427 kgf-m/kcal	1 N-m/J
Specific heat	1 kcal/kgf·deg	$4.187 \cdot 10^3$ J/kg·deg
Entropy	1 kcal/kgf·deg	$4.187 \cdot 10^3$ J/kg·deg
Enthalpy	1 kcal/kgf	$4.187 \cdot 10^3$ J/kg
Specific heat flux	1 $kcal/m^2 \cdot h$	1.163 W/m^2
Heat transfer coefficient	1 $kcal/m^2 \cdot h \cdot deg$	1.163 $W/m^2 \cdot deg$
Coefficient of thermal conductivity	1 kcal/m·h·deg	1.163 W/m·deg
Emissive power of absolutely black body	4.88 $kcal/m^2 \cdot h \cdot deg^4$	5.68 $J/m^2 \cdot deg^4$
Gas constant	1 kgf-m/kgf·deg	9.807 J/kg·deg
Coefficient of thermal diffusivity	1 m^2/h	$2.778 \cdot 10^{-4}$ m^2/s

REFERENCES

/764

1. Arzhanikov, N.S. and Mal'tsev, V.N. Aerodinamika (Aerodynamics), Oborongiz, 1956.

2. Arzhanikov, N.S. and Sadekova, G.S. Aerodinamika bol'shikh skorostey (High-Speed Aerodynamics), "Vysshaya Shkola" Press, 1965.

3. Aerodinamika razrezhennykh gazov (Aerodynamics of Rarefied Gases), Collected papers edited by S.V. Vallander. Leningrad University Press, 1963.

4. Babenko, K.I., Voskresenskiy, G.P., Lyubimov, A.N., and Rusanov, V.V. Prostranstvennoye obtekaniye gladkikh tel ideal'nym gazom (Spatial Flow of an Ideal Gas Around Smooth Bodies), "Nauka" Press, 1964.

5. Belotserkovskiy, S.M. Tonkaya nesushchaya poverkhnost' v dozvukovom potoke gaza (Thin Lifting Surface in a Subsonic Gas Flow), "Nauka" Press, 1965.

6. Burago, G.F. and Votyakov, V.D. Aerodinamika (Aerodynamics), Part II. VVIA im. N.Ye. Zhukovskiy Press, 1961.

7. Vukalovich, M.P., Kirillin, V.A., Remizov, S.A., Siletskiy, V.S. and Timofeyev, V.N. Termodinamicheskiye svoystva gazov (Thermodynamic Properties of Gases), Gostekhizdat, 1953.

8. Davidson, V.Ye. Osnovy gazovoy dinamiki v zadachakh (Fundamentals of Gas Dynamics in Problems), "Vysshaya Shkola" Press, 1965.

9. Ginzburg, I.P. Aerogazodinamika (Aerogasdynamics), "Vysshaya Shkola" Press, 1966.

10. Dorodnitsyn, A.A. Metod integral'nykh sootnosheniy dlya chislennogo resheniya differentsial'nykh uravneniy v chastnykh proizvodnykh (A Method of Integral Relationships for Numerical Solution of Partial Differential Equations), Trudy in-ta tochnoy mekhaniki i vychislitel'noy tekhniki AN SSSR (Transactions of the Institute of Precision Mechanics and Computer Engineering of the USSR Academy of Sciences), 1958.

11. Drakin, I.I. Aerodinamicheskiy i luchistyy nagrev v polete (Aerodynamic and Radiant Heating in Flight), Oborongiz, 1961.

12. Kalikhman, L.Ye. Turbulentnyy pogranichnyy sloy na krivolineynoy poverkhnosti, obtekayemoy gazom (Turbulent Boundary Layer on Curvilinear Surface in Gas Flow), Oborongiz, 1956.

13. Kibardin, Yu.A., Kuznetsov, S.I., Lyubimov, L.N., and Shumyatskiy, B.Ya. Atlas gazodinamicheskikh funktsiy pri bol'shikh skorostyakh i vysokikh temperaturakh vozdushnogo potoka (Atlas of the Gasdynamic Functions for High Velocities and High Airstream Temperatures), Gosenergoizdat, 1961.

14. Kochin, N.Ye., Kibel', I.A., and Roze, N.V. Teoreticheskaya gidromekhanika (Theoretical Hydromechanics), Parts I-II. Fizmatgiz, Moscow, 1963.

15. Krasil'shchikova, Ye.A. Krylo konechnogo razmakha v szhimayemom potoke (Finite-Span Wing in Compressible Flow), Gostekhizdat, 1962.

16. Krasnov, N.F. Aerodinamika tel vrashcheniya (Aerodynamics of Solids of Revolution), Oborongiz, 1958.

17. Krasnov, N.F. Aerodinamika tel vrashcheniya (Aerodynamics of Solids of Revolution), "Mashinostroyeniye" Press, 1964.

18. Kuznetsov, S.I. Diagrammy i tablitsy techeniya dissotsiiruyushchego vozdukha okolo klina, konusa i vypukloy poverkhnosti (Diagrams and Tables of Flow of Dissociating Air Around the Wedge, Cone, and Convex Surface), Oborongiz, 1962.

19. Landau, L.D. and Lifshits, Ye.M. Mekhanika sploshnykh sred (Fluid Mechanics), Gostekhizdat, 1954.

20. Landau, L.D. and Lifshits, Ye.M. Statisticheskaya fizika (Statistical Physics), Moscow, GITTL, 1951.

21. Lebedev, A.A. and Chernobrovkin, L.S. Dinamika poleta (Dynamics of Flight), Oborongiz, 1962. /765

22. Loytsyanskiy, L.G. Mekhanika zhidkosti i gaza (Fluid and Gas Mechanics), Gostekhizdat, 1950.

23. Mel'nikov, A.P. Aerodinamika bol'shikh skorostey (Aerodynamics of High Velocities), Voyenizdat, Ministry of Defense USSR, 1961.

24. Orlov, B.V. and Mazing, G.Yu. Gasodinamicheskiye i ballisticheskiye osnovy proyektirovaniya raketnykh dvigateley na tverdom toplive (Gasdynamic and Ballistic Fundamentals of Solid Rocket Engine Design), Mashinostroyeniye, 1964.

25. Osnovy teploperedachi v aviatsionnoy i raketnoy tekhnike (Fundamentals of Heat Transfer in Aviation and Rocket Engineering), Edited by Prof. V.K. Koshkin, Oborongiz, 1960.

26. Ostoslavskiy, I.V. Aerodinamika samoleta (Aerodynamics of the Airplane), Oborongiz, 1957.

27. Panichkin, I.A. and Lyakhov, A.V. Osnovy gazovoy dinamiki i ikh prilozheniye k raschetu sverkhzvukovykh aerodinamicheskikh trub (Fundamentals of Gasdynamics and Their Application in the Design of Supersonic Wind Tunnels), Kiev University Press, 1965.

28. Predvoditelev, A.S., Stupochenko, Ye.V., Ionov, V.P., Pleshanov, A.S., Rozhdestvenskiy, I.B., and Samuylov, Ye.V. Termodinamicheskiye funktsii vozdukha dlya temperatur ot 1000 do 12000°K i davleniy ot 0.001 do 1000 at (grafiki funktsiy) (Thermodynamic Functions of Air for Temperatures from 1000 to 12,000°K and Pressures from 0.001 to 1000 atm (Curves of the Functions)), USSR Academy of Sciences Press, 1960.

29. Predvoditelev, A.S., Stupochenko, Ye.V., Samuylov, Ye.V., Stakhanov, I.P., Pleshanov, A.S., and Rozhdestvenskiy, I.B. Tablitsy termodinamicheskikh funktsiy vozdukha (dlya temperatur ot 6000 do 12000°K i davleniy ot 0.0001 do 1000 at) (Tables of Thermodynamic Functions of Air (For Temperatures from 6000 to 12,000°K and Pressures from 0.0001 to 1000 atm)), USSR Academy of Sciences Press, 1957.

30. Martynov, A.K. Eksperimental'naya aerodinamika (Experimental Aerodynamics), Oborongiz, 1951.

31. Sedov, L.I. Metody podobiya i razmernosti v mekhanike (Methods of Similarity and Dimensional Analysis in Mechanics), "Nauka" Press, 1965.

32. Fabrikant, I.Ya. Aerodinamika (Aerodynamics), "Nauka" Press, 1964.

33. Fedorov, V.I. Konstruktsiya reaktivnykh dvigateley (Design of Reaction Engines), Voyenizdat, 1960.

34. Feodos'yev, V.I. and Sinyarev, G.B. Vvedeniye v raketnuyu tekhniku (Introduction to Rocket Engineering), Oborongiz, 1960.

35. Fizicheskaya gazodinamika (Physical Gasdynamics), Collected Papers. USSR Academy of Sciences Press, 1959.

36. Frankl', F.I. and Karpovich, Ye.A. Gazodinamika tonkikh tel (Gasdynamics of Slender Bodies), Gostekhizdat, 1948.

37. Khristianovich, S.A. Obtekaniye tel gazom pri bol'shikh skorostyakh (High-Velocity Gas Flows Around Bodies), Trudy TsAGI

(Transactions of the Central Aerohydrodynamics Institute), No. 481, 1940.

38. Chernyy, G.G. Techeniya gaza s bol'shoy sverkhzvukovoy skorost'yu (Gas Flows at High Supersonic Velocity), Fizmatgiz, 1959.

39. Chislennyye metody v gazovoy dinamike (Numerical Methods in Gasdynamics), Collection of papers edited by G.S. Roslyakov and L.A. Chudov. Moscow University Press, 1963.

40. Shirokov, M.F. Fizicheskiye osnovy gazodinamiki (Physical Foundations of Gasdynamics), Fizmatgiz, 1958.

41. Aerodinamika chastey samoleta pri bol'shikh skorostyakh (Aerodynamics of Aircraft Components at High Speeds), IL*, 1959.

42. Bers**, L. Matematicheskiye voprosy dozvukovoy i okolozvukovoy gazovoy dinamiki (Mathematical Problems of Subsonic and Transonic Gasdynamics), IL, 1961.

43. Gazovaya dinamika (Gasdynamics), Collection of articles. IL, 1950.

44. Gazodinamika razrezhennykh gazoy (Gasdynamics of Rarefied Gases), Collection of articles. IL, 1963.

45. Guderley, K.G. Teoriya okolozvukovykh techniy (Theory of Transonic Flows), IL, 1960.

46. Dou, R.B. Osnovy teorii sovremennykh snaryadov (Fundamentals of Modern Missile Theory), "Nauka" Press, 1964.

47. Issledovaniye giperzvukovykh techeniy (Analysis of Hypersonic Flows), "Mir" Press, 1964.

48. Kurant, R. and Fridrikhs, K. Sverkhzvukovoye techeniye i udarnyye volny (Supersonic Flow and Shock Waves), IL, 1950. /766

49. Lippman, G.V. and Roshko, A. Elementy gazovoy dinamiki (Elements of Gasdynamics), IL, 1960.

50. Nauchnyye problemy iskusstvennykh sputnikov Zemli (Scientific Problems of Artificial Earth Satellites), IL, 1959.

51. Nil'sen, D. Aerodinamika upravlyaemykh snaryadov (Aerodynamics of Guided Missiles), Oborongiz, 1962.

*Translator's Note: "IL" refers to the Foreign Literature Press, Moscow.

**Translator's Note: Non-Russian authors, here and below, are transliterated from the Russian text.

52. Obshchaya teoriya aerodinamiki bol'shikh skorostey (General Theory of High-Speed Aerodynamics), Edited by Prof. I.A. Panichkin. Voyenizdat Min. oborony SSSR, 1962.

53. Patterson, G.N. Molekulyarnoye techeniye gazov (Molecular Flow of Gases), Fizmatgiz, 1960.

54. Problemy vysokikh temperatur v aviatsionnykh konstruktsiyakh (Problems of High Temperatures in Aircraft Design), IL, 1961.

55. Problemy dvizheniya golovnoy chasti raket dal'nego deystviya (Problems of Nose-Cone Motion for Long-Range Missiles), IL, 1959.

56. Problemy poleta s bol'shimi skorostyami (Problems of Flight at High Velocities), IL, 1960.

57. Sovremennoye sostoyaniye aerodinamiki bol'shikh skorostey (Contemporary State of High-Speed Aerodynamics), IL, Vols. 1-2, 1955-1956.

58. Ferri, A. Aerodinamika sverkhzvukovykh techeniy (Aerodynamics of Supersonic Flows), Gostekhizdat, 1953.

59. Kheyz, U.D. and Probstin, R.F. Teoriya giperzvukovykh techeniy (Theory of Hypersonic Flows), IL, 1962.

60. Khilton, U.F. Aerodinamika bol'shikh skorostey (Aerodynamics of High Speeds), IL, 1955.

61. Etkin, B. Dinamika poleta (Flight Dynamics), "Mashinostroyeniye" Press, 1964.

62. Kopal, Z. Tables of Supersonic Flow Around Cones of Large Yaw, Technical Report No. 5, MIT, 1949.

63. Kopal, Z. Tables of Supersonic Flow Around Yawing Cones, Technical Report No. 3, MIT, 1947.

64. Kopal, Z. Tables of Supersonic Flow Around Cones, Technical Report No. 1, MIT, 1947.

65. Sigard, F., and Hoerner. Aerodynamic Drag, Ohio, USA, 1951.

66. Izvestiya AN SSSR, Mekhanika i mashinostroyeniye. Izvestiya AN SSSR, Mekhanika zhidkosti i gaza.

67. Inzhenernyy zhurnal.

68. Prikladnaya matematika i mekhanika. AN SSSR.

69. Voprosy raketnoy tekhniki (Problems of Rocket Engineering) "Mir" Press.

70. Raketnaya tekhnika i kosmonavtika (AIAA Journal).

71. Jet Propulsion (ARS Journal).

72. Journal of the Aeronautical Sciences.

73. Journal of the Fluid Mechanics.

74. Journal of the Royal Aeronautical Society.

75. National Advisory Committee for Aeronautics (NACA).

76. Zeitschrift für Flugwissenschaften.

77. Zhurnal vychislitel'noy matematiki i matematicheskoy fiziki.

78. Miyele, A. Mekhanika poleta (Mechanics of Flight), "Nauka" Press, 1965.

79. Mekhanika. Sbornik sokrashchennykh perevodov i referatov inostrannoy periodicheskoy literatury (Mechanics. Collection of condensed translations and abstracts from the foreign periodical literature), IL.

80. Dmitriyevskiy, A.A. and Koshevoy, V.N. Osnovy teorii poleta raket (Fundamentals of Rocket Flight Theory), Military Press, Ministry of Defense USSR, 1964.

81. Lebedev, A.A. and Karabanov, V.A. Dinamika sistem upravleniya bespilotnymi letatel'nymi apparatami (Guidance-System Dynamics for Pilotless Aircraft), "Mashinostroyeniye" Press, 1965.

NASA-Langley, 1971 – 01
ComL, Phila., Penn.

TIONAL AERONAUTICS AND SPACE ADMINISTRATION
WASHINGTON, D. C. 20546
OFFICIAL BUSINESS
PENALTY FOR PRIVATE USE $300

FIRST CLASS MAIL

POSTAGE AND FEES PAID
NATIONAL AERONAUTICS AND
SPACE ADMINISTRATION

National Aeronautics and Space Administration
WASHINGTON, D. C. 20546
OFFICIAL BUSINESS
Penalty For Private Use, $300.00

POSTAGE AND FEES PAID
NATIONAL AERONAUTICS AND
SPACE ADMINISTRATION

032 001 C1 U 01 710730 S00903DS
DEPT OF THE AIR FORCE
WEAPONS LABORATORY /WLOL/
ATTN: E LOU BOWMAN, CHIEF TECH LIBRARY
KIRTLAND AFB NM 87117

If Undeliverable (Section 158
Postal Manual) Do Not Return

conducted so as ...
edge of phenomena in the atmos...
shall provide for the widest practicable and appro...
of information concerning its activities and the results thereof.

—NATIONAL AERONAUTICS AND SPACE ACT OF 1958

NASA SCIENTIFIC AND TECHNICAL PUBLICATIONS

TECHNICAL REPORTS: Scientific and technical information considered important, complete, and a lasting contribution to existing knowledge.

TECHNICAL NOTES: Information less broad in scope but nevertheless of importance as a contribution to existing knowledge.

TECHNICAL MEMORANDUMS: Information receiving limited distribution because of preliminary data, security classification, or other reasons.

CONTRACTOR REPORTS: Scientific and technical information generated under a NASA contract or grant and considered an important contribution to existing knowledge.

TECHNICAL TRANSLATIONS: Information published in a foreign language considered to merit NASA distribution in English.

SPECIAL PUBLICATIONS: Information derived from or of value to NASA activities. Publications include conference proceedings, monographs, data compilations, handbooks, sourcebooks, and special bibliographies.

TECHNOLOGY UTILIZATION PUBLICATIONS: Information on technology used by NASA that may be of particular interest in commercial and other non-aerospace applications. Publications include Tech Briefs, Technology Utilization Reports and Technology Surveys.

Details on the availability of these publications may be obtained from:

SCIENTIFIC AND TECHNICAL INFORMATION OFFICE

NATIONAL AERONAUTICS AND SPACE ADMINISTRATION

Washington, D.C. 20546

"The aeronautical and space activities of the United States shall be conducted so as to contribute . . . to the expansion of human knowledge of phenomena in the atmosphere and space. The Administration shall provide for the widest practicable and appropriate dissemination of information concerning its activities and the results thereof."

—NATIONAL AERONAUTICS AND SPACE ACT OF 1958

NASA SCIENTIFIC AND TECHNICAL PUBLICATIONS

TECHNICAL REPORTS: Scientific and technical information considered important, complete, and a lasting contribution to existing knowledge.

TECHNICAL NOTES: Information less broad in scope but nevertheless of importance as a contribution to existing knowledge.

TECHNICAL MEMORANDUMS: Information receiving limited distribution because of preliminary data, security classification, or other reasons.

CONTRACTOR REPORTS: Scientific and technical information generated under a NASA contract or grant and considered an important contribution to existing knowledge.

TECHNICAL TRANSLATIONS: Information published in a foreign language considered to merit NASA distribution in English.

SPECIAL PUBLICATIONS: Information derived from or of value to NASA activities. Publications include conference proceedings, monographs, data compilations, handbooks, sourcebooks, and special bibliographies.

TECHNOLOGY UTILIZATION PUBLICATIONS: Information on technology used by NASA that may be of particular interest in commercial and other non-aerospace applications. Publications include Tech Briefs, Technology Utilization Reports and Notes, and Technology Surveys.

Details on the availability of these publications may be obtained from:

SCIENTIFIC AND TECHNICAL INFORMATION DIVISION

NATIONAL AERONAUTICS AND SPACE ADMINISTRATION

Washington, D.C. 20546